SIMULATING THE MEDIUM TEMPERATURE CHALCOPYRITE OXIDATION SYSTEM IN BATCH AND CONTINUOUS AUTOCLAVES

by

Johann du Toit Steyl

Dissertation presented for the Degree

of

DOCTOR OF PHILOSOPHY
(Extractive Metallurgical Engineering)

in the Faculty of Engineering
at Stellenbosch University

Supervisor
Prof. S. Bradshaw

Co-Supervisor
Prof. G. Akdogan

December 2012

Stellenbosch University http://scholar.sun.ac.za

Declaration

By submitting this dissertation electronically, I declare that the entirety of the work contained therein is my own, original work, that I am the sole author thereof (save to the extent explicitly otherwise stated), that reproduction and publication thereof by Stellenbosch University will not infringe any third party rights after a three year period of receiving the degree has passed as requested by Anglo American and that I have not previously in its entirety or in part submitted it for obtaining any qualification.

JOHANN DU TOIT STEYL

……
Signature

23 NOVEMBER 2012

……
Date

Copyright © 2012 Stellenbosch University
All rights reserved

Stellenbosch University http://scholar.sun.ac.za

ABSTRACT

A detailed mathematical description of the pressure oxidation of chalcopyrite concentrates in acidic sulfate solutions is presented in this dissertation, including descriptions of the most important accompanying reactions under typical medium operating temperatures (140-155ºC) in batch and steady-state continuous stirred tank reactors. The mathematical framework consists of various modules, each addressing particular thermodynamic and kinetic aspects of the primary processes occurring in a pressure oxidation reactor. Comprehensive literature investigations are presented which constituted the departure point of this study, supplemented by phenomenological data obtained from controlled batch and continuous experimentation.

The different modules are each covered in a chapter of this dissertation, and include the following: i) the solution thermodynamic framework, ii) the interfacial oxygen mass transfer rate, iii) the iron(II) oxidation rate, iv) the iron(III) precipitation rate, (v) the intrinsic oxidation kinetics of the sulfide minerals, and vi) the particulate batch and continuous reactor frameworks. These modules are imbedded within a continuous mass and energy balance platform of a primary leaching – solvent extraction circuit, while the batch reactor analogy describes the conservation of mass, and its movement between phases, in a stand-alone configuration.

Literature information proved particularly important in deriving the generic functional forms of the most important reaction rate expressions, while the phenomenological expressions were refined, and the associated constants obtained, from low pulp density batch experimentation. Higher pulp density batch reactor and continuous (pilot plant) data were then used to confirm the successful integration of these expressions in the overall simulation.

This is the first truly comprehensive study of chalcopyrite concentrate pressure oxidation, the kinetics of the accompanying reactions and each of the underlying thermodynamic aspects. Consistent theoretical arguments and insights are presented, while conceptual proposals are tabled in cases where the fundamental information is lacking. This dissertation presents an internally consistent simulation, with each of the modules contributing to an overall mathematical description of the pressure oxidation of chalcopyrite concentrates. It provides a powerful research and process engineering tool, and may be used to simulate the performance of a primary leaching circuit on a full-scale plant. As an example, the simulation was used to study the impact of selected intrinsic properties and control parameters on the autoclave and primary leach circuit performance. Various recommendations on improving the simulation are highlighted, as well as the aspects to explore in follow-up studies.

Stellenbosch University http://scholar.sun.ac.za

OPSOMMING

Hiedie verhandeling stel 'n gedetailleerde wiskundige beskrywing van die drukoksidasie van chalkopiriet-konsentrate in suuragtige sulfaatoplossings bekend, sowel as die evaluering van die belangrikste meegaande reaksies by tipiese gemiddelde bedryftemperature (140-155ºC) in enkellading en gestagdigde-vloei mengvatreaktore. Die wiskundige raamwerk bestaan uit verskeie modules, wat elk beide die termodinamiese- en kinetiese-aspekte aanspreek van die primêre prosesse wat binne in 'n drukoksidasie reaktor plaasvind. Gedetailleerde literatuurondersoeke word aangebied wat the vertrekpunt van hierdie studie gevorm het, aangevul deur fenomenologiese data wat uit gekontroleerde enkellading en gestagdigde-vloei eksperimentering verkry is.

Die verskillende modules, wat elk 'n hoofstuk van hierdie verhandeling beslaan, sluit die volgende in i) die oplossings termodinamika raamwerk, ii) gas/vloeistof massaoordrag van suurstof, iii) die kinetika van yster(II) oksidasie, iv) die kinetika van yster(III) presipitasie, v) die intrinsieke oksidasiekinetika van die sulfiedminerale, en vi) die partikelraamwerke van die enkellading en gestadigde-vloei reaktore. Hierdie modules is ingebed in 'n gestadigde massa- en energiebalans-platform van 'n primêre loog – oplosmiddel ekstraksievloeidiagram, terwyl die enkellading reaktor-analogie beskryf word deur die behoud van massa, en die beweging daarvan tussen fases, in 'n losstaande konfigurasie.

Literatuur inligting was veral belangrik in die afleiding van die generiese funksionele vorme van die belangrikste reaksietempovergelykings, terwyl die fenomenologiese uitdrukkings verfyn, en die gepaardgaande konstantes, uit lae pulpdigtheid enkellading eksperimentering verkry is. Hoër pulpdigtheid enkellading reaktor en gestadigde-vloei (loods aanleg) data is toe gebruik om die suksesvolle integrasie van hierdie vergelykings in die algehele simulasie te bevestig.

Hierdie is die eerste volledige studie van die drukoksidasie van chalkopiriet-konsentrate, die kinetika van elk van die gepaardgaande reaksies en die onderliggende termodinamiese aspekte. Konsekwente teoretiese argumente en insigte word aangebied, terwyl konseptuele voorstelle ter tafel gelê word in gevalle waar die fundamentele inligting ontbreek. Hierdie verhandeling bied 'n interne konsekwente simulasie aan, met elk van die modules wat bydra tot 'n algehele wiskundige beskrywing van die drukoksidasie van chalkopiriet-konsentrate. Dit bied 'n kragtige navorsings en proses-ingenieurswese instrument aan, wat gebruik kan word om die gedrag van 'n primêre loogvloeidiagram op 'n volskaalse aanleg te simuleer. As 'n voorbeeld, is die simulasie gebruik om die impak van geselekteerde intrinsieke eienskappe en beheerparameters op die gedrag van die autoklaaf en primêre loogvloeidiagram te bestudeer.Verskeie aanbevelings oor die verbetering van die simulasie word uitgelig, asook die aspekte om in opvolgstudies te verken.

Stellenbosch University http://scholar.sun.ac.za

ACKNOWLEDGEMENTS

I would like to thank the following people and organizations:

Anglo American Technical Solutions (Research) for the logistical and financial assistance. Paul Dempsey (Group Head of Metallurgy, AA plc) is sincerely thanked for his support and allowing me to finish this project, despite significant research and role shifts during the course of this study.

The help of the staff of the Technology Department is gratefully acknowledged, in particular the autoclave operator, Mr. Sibusiso Mdlalose, for doing most of the administrative work and also for his dedicated help in recording quality experimental data.

Dr. Kathy Sole for her encouragement and for reviewing the thesis on relatively short notice, despite a busy schedule.

Dr. Maggie Burger of the Technology Department, for assisting with some of the computational chemistry calculations.

Dr. Frank Crundwell, on whose knowledge and experience of particulate leaching processes I drew.

Dr. Alison Lewis, at the University of Cape Town, for reviewing the iron(III) precipitation chapter and giving helpful feedback.

Prof. Steven Bradshaw, my supervisor during the final year of registration, for his assistance and encouragement.

Last, but not least, I would like to thank my wife, Alexandra, son, Jack, and daughter, Zara, for their support and love, which made this work possible.

Stellenbosch University http://scholar.sun.ac.za

CONTENTS

Stellenbosch University http://scholar.sun.ac.za

VOLUME I: SOLUTION CHEMISTRY, MASS TRANSFER & REACTIONS

Stellenbosch University http://scholar.sun.ac.za

Stellenbosch University http://scholar.sun.ac.za

Stellenbosch University http://scholar.sun.ac.za

Stellenbosch University http://scholar.sun.ac.za

Stellenbosch University http://scholar.sun.ac.za

Stellenbosch University http://scholar.sun.ac.za

Stellenbosch University http://scholar.sun.ac.za

VOLUME II: MINERAL OXIDATION REACTIONS, REACTORS & SYSTEMS

Stellenbosch University http://scholar.sun.ac.za

Stellenbosch University http://scholar.sun.ac.za

Stellenbosch University http://scholar.sun.ac.za

Stellenbosch University http://scholar.sun.ac.za

Stellenbosch University http://scholar.sun.ac.za

Stellenbosch University http://scholar.sun.ac.za

Stellenbosch University http://scholar.sun.ac.za

Stellenbosch University http://scholar.sun.ac.za

Stellenbosch University http://scholar.sun.ac.za

Stellenbosch University http://scholar.sun.ac.za

Stellenbosch University http://scholar.sun.ac.za

NOTATION A

Symbol	Standard Unit (Unless specified differently in text)	Description
a	m^2/kg	Total interfacial area between a solid or gas & aqueous liquid per unit mass water.

The symbol a_{Fe} represents the total iron(III) precipitate surface area.

a	m^2	Surface area (general).

The symbols $\mathbf{a}_A$ & $\mathbf{a}_C$ refer to the anodic & cathodic (*ref.* electrochem. reactions) surface areas, respectively. The symbol a_p refers to an outer particle surface area, while a_s refers to the unreacted sulfide mineral particle or particle core area.

a	–	Activity of a solution species (molality scale).

The symbol a_w refers to the activity of water as solvent. The symbol a^* refers to the activity at thermodynamic equilibrium, whereas a^*_L refers to the equilibrium with a solid particle of finite size (L).

A_T	J/mol.K	Primary parameter of the Correspondence Principle.
A_γ	$(kg/mol)^{1/2}$	DH parameter of the activity coefficient (infinite dilution).

The symbol A_ϕ refers to the DH (Debye-Hückel) parameter of the osmotic coefficient (at infinite dilution).

Â	1/min	Pre-exponential factor.

B	kg/mol	Binary virial coefficient of the activity coefficient of a pure electrolyte (Pitzer ion-interaction theory).

B' refers to its ionic strength derivative. The symbol B^ϕ refers the binary virial coefficient of the osmotic coefficient.

B	1/kg.m.min	Birth rate of new particles.

The symbol B_L refers the formation rate of new hematite particles of characteristic size, L_{Hem}.

B_T	–	B-parameter (Correspondence Principle).

C	$(kg/mol)^2$	Ternary virial coefficient of the activity coefficient of a pure electrolyte (Pitzer ion-interaction theory).

The symbol C^ϕ refers the ternary virial coefficient of the osmotic coefficient (solvent).

C_p	J/mol.K	Heat capacity at constant pressure.

C_p° refers to the value at the standard state of infinite dilution.

d_x	m	Particle diameter below, which a specified volume percentage (d_x percentile) of material lies.
d[3,2]	m	Equivalent surface area mean diameter.

Also known as the surface area moment mean diameter or Sauter mean (Rawle, 1995).

d[4,3]	m	Equivalent volume mean diameter.

Also known as the volume moment mean diameter or De Broucker mean (Rawle, 1995).

D	m^2/min	Free (effective) diffusion coefficient (diffusivity) in sln.

The symbol D_e refers to the effective diffusivity in a product layer, surrounding an unreacted sulfide mineral core.

D	1/min	Death rate of particles.

Stellenbosch University http://scholar.sun.ac.za

e_c	J/mol.K^2	Constant in Lewis linearization of the Criss-Cobble Correspondence Principle.
E	V	Electromotive force (EMF) of a cell.

All the cell potentials are expressed as reduction reactions, unless indicated otherwise. E° refers to the standard state value, *i.e.*, the ideal solution at an imaginary state of unit activity of the contributing redox species. The symbol E_{red} refers to the general reduction reaction. The symbol E_h refers to potential measured against the standard hydrogen electrode (SHE). The symbol E_{Ag} refers to the Ag|AgCl reference system.

E_a	J/mol	Activation energy.

The subscript hom refers to homogeneous nucleation, while *Hem* refers to specifically the apparent activation energy of secondary hematite nucleation. The subscripts *Jar* & *Jar*/*Hem* refer to the apparent activation energies of continuous hydronium jarosite growth & shrinkage (due to its conversion to hematite), respectively.

E_c	eV	Lowest molecular orbital of the conduction band.
E_{corr}	V	Open circuit (corrosion) potential of a mineral.
E_g	eV	Band gap energy of a semiconductor.
E_k	J/mol	Kinetic energy.
E_L	−	Enhancement factor.

The factor by which a chem. reaction increases the rate of gas absorption (interfacial gas/liquid mass transfer).

E_m	V	Mixed potential.

The default scale refers to the standard hydrogen electrode (SHE).

E_p	J/mol	Potential energy.

The symbol E_{coh} refers to the cohesive energy of a solid material, E_{metal} refers to the energy of an atom in a metal structure, while E_{atom} refers to the calculated energy of an atom on its own.

E_{pp}	V	Passivation potential of a mineral.
E_{rest}	V	Rest potential of a mineral.

This is the potential that a mineral assimilates when brought in contact with an electrolyte solution, *i.e.*, before anodic or cathodic current flows. The default scale refers to the standard hydrogen electrode (SHE).

E_{tpp}	V	Transpassive potential of a mineral.
E_v	eV	Uppermost molecular orbital of the valence band.
E	−	Absolute relative error.

Eq. 2.72.

E_F	−	Error function (*ref.* minimising an objective function).
f	atm	Fugacity of a species in the gas phase.
f°	mol/kg	Standard state fugacity of a species in solution.

Standard state in an ideal solution, where f° = m° = 1 mol/kg. The standard state of the solvent is its pure form fugacity at the solution temperature & corresponding pressure of the pure solvent.

f	−	Denotes a mathematical function.

Stellenbosch University http://scholar.sun.ac.za

F	mol/min	Molar flowrate.

The symbol F_g refers to the molar flowrate of the gas phase.

F_H	–	Acidity factor.

Empirical parameter, describing the change in the sulfur yield on a mineral surface as a function of the hydrated proton & dissolved oxygen concentrations (Eq. 8.3).

F	–	Function value.
F	–	Residual function value.

The bold symbol ***F*** refers to a vector of residual function values.

F	C/mol	Faraday constant (Table A.1).

---

g_c	1/K	Constant in Lewis linearization of the Criss-Cobble Correspondence Principle.
g	m/s^2	Gravitational acceleration (Table A.1).
G	J/mol	Gibbs free energy.

G° refers to the value at the standard state of infinite dilution. $^{\ddagger}G$ refers to the Gibbs energy of activation. The symbols G_a & G_c refer to the free energy of the anodic & cathodic directions of an electrochemical half-cell reaction, respectively. The symbol ΔG_V refers to the free energy change due to bulk volume creation.

ΔG_{hom}	J/kg	Total Gibbs free energy change per unit mass water due to homogeneous nucleation.

ΔG_A represents the free energy change due to surface creation.

ΔG_{het}	J/kg	Total Gibbs free energy change per unit mass water due to heterogeneous nucleation.
G	m/min	Linear growth rate (refers to precipitation).

The subscript *Jar* refers to the hydronium jarosite phase. The superscripts + & – refer to the positive (growth) & negative (shrinkage or conversion) rates, respectively.

h	–	Step-size value (numerical routine).

The bold symbol **h** refers to a vector of step-size values.

---

h	J.s	Planck's constant (Table A.1).
H	J/mol	Enthalpy.

H° refers to the value at the standard state of infinite dilution. $^{\ddagger}H$ refers to the enthalpy of activation. The symbol H_{at} refers to the enthalpy of atomisation, H_{ion} to the enthalpy of ionisation, H_{hyd} to the enthalpy of hydration, H_{red} to the enthalpy of reduction, & H_{dil} to the enthalpy of dilution.

Ha	–	Hatta number.

Eq. 3.8.

I	mol/kg	Ionic strength of an electrolyte solution.

---

j	A/m^2	Current density.

The symbols j_a & j_c refer to the anodic & cathodic directions of an electrochemical half-cell reaction, respectively. The symbols j_A & j_C refer to the anodic & cathodic directions of the net processes, respectively.

Stellenbosch University http://scholar.sun.ac.za

j_{cc}	A/m^2	Critical current density (corresponding to the passivation potential of a mineral).
j_o	A/m^2	Exchange current density (corresponding to the equilibrium potential of an electrochemical reaction).
j_{ps}	A/m^2	Passive current density of a mineral.
J	1/kg.min	Nucleation rate.

Number of particles formed in 1 kg water per unit time. The subscripts hom, prim & sec refer to the homogeneous, primary & secondary nucleation rates, respectively. The symbol J_{Hem} refers to the total nucleation rate of new hematite particles of characteristic size L_{Hem}, *via* a nucleation – rapid growth mechanism. Surface nucleation, J_{surf}, refers to the nucleation rate per unit area precipitate surface ($1/m^2$.min).

J	–	Jacobian matrix.

---

k	$(mol/kg)^{(1-n)}.min^{-1}$	Intrinsic reaction rate constant per unit mass water.

The superscript n refers to the total reaction order.

k	$kg^n.mol^{(1-n)}/m^2.min^1$	Intrinsic reaction rate constant per unit surface area.

Unit area refers to the surface per unit mass water & n refers to the total reaction order. The symbols k_a & k_c refer to the anodic & cathodic directions of an electrochemical half-cell reaction, respectively. The symbol k_C refers to the rate constant of pyrite-catalysed iron(II) oxidation in solution.

k_G	m/min	Linear growth rate constant (refers to precipitation).

The symbol k^-_G refers to the linear conversion rate constant of hydronium jarosite to hematite.

k_{hom}	1/kg.min	Homogeneous nucl. rate constant per unit mass water.
k_l	$(mol/m^3)^{(1-n)}/min$	Intrinsic reaction rate constant per unit volume solution.

where n is to the total reaction order.

k_ℓ	m/min	One-dimensional (linear) rate constant (rate of particle shrinkage) under intrinsic reaction control.

Relevant to the unreacted shrinking particle (or particle core) model, under surface reaction control (Eq. 6.156 & F.28).

k_L	m/min	Liquid-side mass transfer coefficient.
k_{prim}	1/kg.min	Primary nucleation rate constant per unit mass water.
k_s	1/min	Overall (observed) intrinsic leaching rate constant of a sulfide mineral.
k_{surf}	$1/m^2.min$	Surface nucleation rate constant per unit surface area.

Unit area refers to iron(III) precipitate surface per unit mass water.

k_υ	(varies)	Refers to the intrinsic constant in linear particle shrinkage rate expressions (also see k_ℓ).
$k^{\sim}$	(varies)	Proportionality constant.

The subscripts *Hem* & *Jar* refer to the hematite & hydronium jarosite phases, respectively (units of mol Fe/μm^3).

k_b	J/K	Boltzmann constant (Table A.1).

Stellenbosch University http://scholar.sun.ac.za

K	$(mol/kg)^n$	Equilibrium constant (*ref.* stepwise reaction).

All equilibria, except for the solubility product of a solid phase, K_{sp}, are expressed as association reactions in this study. The symbol K' refers to the dissociation reaction, *p*K refers to the *-log* K value & K° refers to the value at the standard state of infinite dilution.

K_H	mol/kg.atm	Henry's law constant for diatomic oxygen in equilibrium with an electrolyte mixture.

The symbol $K_{H,w}$ refers to Henry's law constant for diatomic oxygen in equilibrium with pure water.

$\mathbf{K}_{Hem}$	–	Dimensionless temperature-dependent constant used to describe the primary nucleation rate of hematite.

It originates from the fundamental homogeneous nucleation rate expression (Eq. 5.35). The symbol K_{Hem} refers to the same constant, but without the temperature & interfacial energy terms (units of m^6K^3/J^3; Eq. 5.43).

$\mathbf{K}_{Jar}$	–	Dimensionless hydronium jarosite growth rate constant.

ℓ	m	One-dimensional size of an unreacted sulfide mineral or other solid phase in a particle or particle core.

The symbol ℓ_{max} refers to the largest unreacted size of a particle or particle core in a PSD
When the subscript (ℓ) is used with a chemical species, it refers to the liquid phase.

L	m	Total (one-dimensional) size of a particle.

The symbol L_o refers to the initial size of a sulfide mineral particle. The symbol $L_{o,n}$ refers to the average initial particle size in size-class *n*. The symbol L_{crit} is the critical size of a nucleus, above which its existence becomes stable. The symbol L_c is used as a general description of a characteristic particle size, while L_{Hem} refers to the characteristic hematite particle size, following nucleation & rapid growth. The symbol L_{max} refers to the maximum particle size in a distribution, while L_∞ denotes some particle size larger than this maximum. The symbol L_{OD} refers to the Ostwald diameter (Eq. 5.28), while L_{Fe} represents the iron(III) precipitate particle size.

---

m	mol/kg	Molality of a species in solution.

Unit mass refers to pure water. The symbol m^* refers to the molality at thermodynamic equilibrium, while m^{st} refers to the stoiciometric (formal) molality value. The bold symbol, **m**, refers to a vector of species molalities. The symbols m_{ox} & m_{red} refer to the molalities of an oxidised & reduced species, respectively.

M	mol/L	Molarity of a species in solution.

Unit volume refers to solids- & bubble-free solution. M^* refers to the molarity at thermodynamic equilibrium.

M	kg/min	Mass flowrate of a species.

Sign convention: positive flow out & negative flow into a reactor. M_s refers to the mass flowrate of a sulfide mineral, while M_w refers to the mass flowrate of water. M_{cl} denotes the total cooling liquid flow to a multi-compartment autoclave.

Mw	g/mol	Molecular weight of a species.

The symbol Mw_s refers to the molecular weight of a sulfide mineral or another solid phase.

---

n	mol/kg	Total moles per unit mass water.
n_s	mol	Total moles of a sulfide mineral or other solid phase in a particle or particle core.
n	mol	Total moles of a species.

n_s refers to the total moles of a sulfide mineral or other solid phase in a particle or particle core

n(*p*)	$1/m^4$	Particle number density distribution of any property, *p*.

Referring to the number continuity equation of the PB in particle phase space (App. H.1).

Stellenbosch University http://scholar.sun.ac.za

N	1/kg	Particle number or particle number distribution per unit mass water.

The symbol $N_{Fe,L}$ represents the total number of iron(III) precipitate particles in size class L_{Fe}.

N_{Fe}	–	Mole ratio of iron dissolved in sphalerite.

The ratio refers to mol Fe/mol Zn in the mineral lattice.

$N_{FeIII,m}$	–	Moles Fe(III) reduced on a mineral surface.

Refers to mol Fe(III) reduced per mol mineral (*m*) oxidised, where *m* could refer to *Cpy* (chalcopyrite), *Sph* (sphalerite), *Chc* (chalcocite), *Cov* (covellite), *Bor* (bornite), *Py* (pyrite) or *Ph* (pyrrhotite) mineral.

N	–	Number of data evaluation points.
N_a	1/mol	Avogadro's constant (Table A.1).

---

p	atm	Partial pressure of a species in the gas phase.

The symbol p_w refers to the vapour pressure of water over an electrolyte solution. The symbol $p_w°$ refers to the vapour pressure of pure water, while $p_{O2}°$ is the equivalent oxygen partial pressure over pure water at the relevant temperature.

$p_{1,2,3,...}$	(varies)	General notation used for a parameter.
P	atm	Total pressure of the gas phase.

The symbol P_g refers to gauge pressure, P_a refers to absolute pressure, while P_{atm} refers to atmospheric pressure.

P	(varies)	General notation used for an interaction parameter.

Q	m^3/min	Volumetric flowrate of a substance to & from a reactor.

Sign convention: positive for flow out & negative for flow into a reactor. The symbol Q_{sl} refers to the total (gas-free) flowrate of slurry 'at temperature', while Q_l refers to the total (solids- & gas-free) flowrate of solution 'at temperature'.

Q	J/min	Rate of energy (heat) flow.

Sign convention: positive for energy flow out & negative for energy flow into a reactor. The symbols Q_{in} & Q_{out} refer to the total energy flow in & out of a unit operation, respectively, while Q_{loss} signifies the net heat loss to the surroundings. The symbol Q_{mech} denotes the energy introduced to a reactor by mechanical action. The symbol Q_{ext} denotes the amount of energy that has to be removed externally in order to achieve isothermal operation.

---

r	mol/m^2.min	Intrinsic reaction rate per unit interfacial area.

The symbols r_a & r_c refer to the anodic & cathodic directions of an electrochemical half-cell reaction, respectively. The symbols r_A & r_C refer to the anodic & cathodic directions of the net processes, respectively. The symbols r^+ & r^- indicate the rate of movement of the cation & anion, respectively. The symbol r_s refers to the intrinsic dissolution rate of an unreacted sulfide mineral particle or particle core. The intrinsic oxidation rate of a homogeneous solution species can also be expressed per unit interfacial area between the oxidant (gas) & unit mass water.

R	mol/kg.min	Reaction rate per unit mass water.

The symbols R_J & R_G refer to the overall nucleation & growth rate of solid particles during precipitation from solution, respectively. The symbol R_{FeII} denotes the overall rate of iron(II) oxidation. $R_{FeII,SI}$ & $R_{FeII,SD}$ refers to the sulfate-independent & sulfate-dependent pathways, while $R_{FeII,C}$ refers to the catalysed iron(II) oxidation rate. $R_{FeII,hom}$ & $R_{FeII,het}$ refers to the overall homogeneous & heterogeneous reaction rates. The symbol R^F_{FeII} refers to the formal production rate of iron(II) (without any oxidation in solution or on mineral surfaces), while $R_{FeII,net}$ refers to the net oxidation rate. R_{FeIII} refers to the overall rate of iron(III) precipitation & subscripts *Hem* & *Jar* identify the phases, while hom, prim & surf refer to homogeneous, primary & surface nucleation mechanisms, respectively.

R_l	mol/m^3.min	Intrinsic reaction rate per unit volume solution.
R_g	J/mol.K	Gas constant (Table A.1).

Stellenbosch University http://scholar.sun.ac.za

R_{O2}	g/kg	Oxygen demand of a sulfide concentrate.

S	J/mol.K	Entropy.

S° refers to the value at the standard state of infinite dilution. $^{\ddagger}S$ refers to the entropy of activation. The symbol S_{red} refers to the entropy of reduction & $S^{\circ(abs)}$ is the absolute partial molal entropy.

S_a	–	Thermodynamic supersaturation (activity) ratio.

See Eq. 5.15. The subscript crit refers to the critical supersaturation ratio. The subscripts surf, het & hom refer to surface, heterogeneous & homogeneous nucleation mechanisms, respectively. S_{Hem} & S_{Jar} refer to the simplified supersaturation ratios (*ref.* unity species activity coefficients) of the hematite & hydronium jarosite phases, respectively. The symbol S_L refers to the supersaturation ratio with respect to a particle of size L.

Sc	–	Schmidt number

Eq. 4.23.

S_e	m^2	Sum of all moving surfaces in a reactor due to changes in the void fraction of solids in the reactor.

Refers to the derivation of the macroscopic PB (App. H.1).

S_k	m^2	Sum of all moving surfaces in a reactor due to the in- & outflow of streams.

Refers to the derivation of the macroscopic PB (App. H.1).

S_l	m^2	Sum of all moving surfaces in a reactor due to the changes in the solids- & gas-free liquid volume.

Refers to the derivation of the macroscopic PB (App. H.1).

S_m	m^2	Sum of all moving surfaces in a reactor.

Refers to the derivation of the macroscopic PB (App. H.1).

---

t	min	Time.

The symbol t_p refers to an oxygen electrode response time, *i.e.*, to record 63% of a step change.

T	K	Temperature.

The symbol T_c refers to the Celsius scale, T_d refers to the temperature difference between T & the reference temperature, T_r. The symbol T_o refers to unit temperature, *i.e.*, 1 K or 1°C.

---

v	m^3	Volume.

The symbol v_s refers to the volume of an unreacted sulfide mineral particle or particle core.

V	m^3	Reactor volume.

The symbol V_{sl} refers to the volume of (gas-free) slurry, while V_l denotes the volume of (solids- & gas-free) solution.

---

w	kg	Mass.

The symbol w_s refers to the mass of an unreacted sulfide mineral particle or core, while $w_{s,o}$ refers to the initial mass.

$w_s(\ell)$	$m^{-1}.kg^{-1}$	Mass density distribution of sulfide mineral particles *ref.* around unreacted core size ℓ per unit mass water.

The symbol $w_{s,o}(L_o)$ refers to the analogous mass distribution of sulfide particles in the feed to the reactor.

w(L)	m^{-1}	Mass density distribution of particles *ref.* size L.

The symbol $w_o(L_o)$ refers to the mass density distribution of the feed material.

Stellenbosch University http://scholar.sun.ac.za

W	kg	Total mass in a reactor.

This symbol W_i refers to batch test mass balancing, *i.e.*, total mass of element *i* in a solid or solution phase (Ch. 6). The symbol W_{H2O} denotes the total mass of water & W_o the original solids mass in a batch reactor.

W_f	–	Fractional mass.

The symbol $W_{f,}(L_{o,n})$ refers to the fractional mass of mineral feed material in size-class *n*, with average size $L_{o,n}$ (also denoted by $W_{f,,n}$). This distribution is directly obtained from the particle size analyser (histogram). The symbol $W_{f,t}$ refers to the mass fraction of residue material (*cf.* the original sample) after reaction time t ($W_{f,tot}$ may also be used). The symbol $W_{f,Hem}$ refers to the fractional hematite content in the solid phase, *i.e.*, normalised to the total hematite plus hydronium jarosite mass.

W_s	g/kg	Total mass or mass distribution of sulfide mineral particles per unit mass water.

$W_{s,o}$ refers to the initial mass of sulfide mineral or the mass in the feed to a reactor. The symbol $W_s(\ell)$ refers to the cumulative mass distribution of sulfide particles in an unreacted particle core of size, ℓ, per unit mass water in the outflow. It could also refer to specific sulfide minerals, *e.g.*, *Cpy* (chalcopyrite), *Sph* (sphalerite), *Chc* (chalcocite), *Cov* (covellite), *Bor* (bornite), *Py* (pyrite) or *Ph* (pyrrhotite).

---

x_i	–	Mass fraction of species, *i*, in the solid phase.
x_{O2}	–	Mole fraction of oxygen in the gas phase.
x	–	Denotes a variable in a mathematical function.
$X_{p,Fe}$	–	Fractional amount of total iron precipitated from solution.

The symbol $X_{p,FeIII}$ refers to the fractional amount of iron(III) precipitated from solution.

$X_{FeII,ox}$	–	Fractional amount of total iron(II) oxidised.
X_s	–	Fractional amount of sulfide mineral leached.

The symbol X_i refers to the fractional amount of element *i* leached from solids material (based on solids analyses; see Eq. 6.159). The symbol $X_{s,j}$ refers to the fractional amount of sulfide leached in reactor *j*, while $X_{s,n}$ refers to the fractional amount of sulfide leached from original particles in size-class *n*. X_{Hem} & X_{Jar} refer to the redissolution of hematite & hydronium jarosite after slurry discharge from the continuous or batch autoclaves.

---

y_F	–	Error function coefficient (weighed).

Eq. 2.72.

---

z	–	Charge of an ion or the number of elementary charges taking part in a charge transfer process.

Negative sign for the transfer of a negative charge. The symbol z_{rx} refers to the stoichiometric number of charges taking part in a charge transfer reaction.

Z	–	Total ionic charge of an electrolyte solution.

Stellenbosch University http://scholar.sun.ac.za

NOTATION B

Symbol	Standard Unit (Unless specified differently in text)	Description
α_1, α_2	$(kg/mol)^{1/2}$	Electrolyte parameters (Pitzer ion-interaction theory). These numeric subscripts refer to different parameters of the same electrolyte.
α_i	–	Mole fraction of a species, *i*. Molality of a species divided by the formal molality of its reference ion. The symbol α'_i refers to the degree of dissociation of the same species, *i.e.*, 1-α_i for the binary case.
α	1/K	Coefficient of thermal expansion.
β	$(mol/kg)^n$	Equilibrium constant of a cumulative reaction. All equilibria, except for the solubility of a solid phase, are expressed as association reactions in this study. The symbol $\beta°$ refers to the thermodynamic equilibrium constant at infinite dilution.
$\beta^{(0)}$, $\beta^{(1)}$, $\beta^{(2)}$	kg/mol	Ion-specific binary interaction parameters of a pure electrolyte (Pitzer ion-interaction theory). These symbols refer to different parameters of the same binary interaction.
β	–	Charge transfer coefficient *ref.* Butler-Volmer equation. β_A & β_C refer to the transfer coefficient of the net anodic & cathodic processes, respectively (App. F.2).
γ	–	Activity coefficient of a species in solution. $\gamma_\pm$ refers to the mean activity coefficient of a salt, while $\gamma^*_\pm$ is the relative value in a mixture *ref.* the binary system (Eq. 2.77). The symbol γ^{st} refers to the stoiciometric (formal) value (the superscript is omitted in general use).
γ	J/m^2	Average interfacial energy at a solid surface.
δ	m	Thickness of a film layer around a particle or gas bubble.
ε	$C^2/J.m$	Permittivity of a medium. The symbol ε_w refers to the relative permittivity (dielectric constant) of water, while ε_ℓ refers to the relative permittivity of a pure liquid, *e.g.*, 100% sulfuric acid solution. The symbol ε_o refers to the vacuum permittivity (Table A.1).
ξ	–	Correction factor for heterogeneous nucleation on a substrate surface.
η	kg/m.s	Dynamic viscosity. cP = 1×10^{-3} kg/(m.s). The symbols η_c & η_w refer to the continuous (liquid) phase & water viscosity, respectively.
η	V	Overpotential. Difference between the applied & equilibrium potential.

Stellenbosch University http://scholar.sun.ac.za

θ	–	Fractional coverage of particle surface area.

The symbol θ_{Cov} refers to the fractional coverage of sulfide particles by a covellite phase. The symbol θ_{Pyc} refers to the catalytic fraction pyrite surface area that produces reactive oxidant (radical) species.

θ_{ij}	kg/mol	Short-range binary interaction parameter for mixing like-charged ions, *i* & *j* (Pitzer ion-interaction theory).

The symbol θ^{ϕ} refers the binary virial coefficient of the osmotic coefficient (solvent).

${}^{E}\theta_{ij}$	kg/mol	Long-range (electrostatic) binary interaction parameter for unsymmetrical mixing of like-charged ions, *i* & *j*. (Pitzer ion-interaction theory).

The symbol ${}^{E}\theta'$ refers to its ionic strength derivative.

θ	–	Temperature correction factor (mass transfer coefficient).

κ	–	Catalytic enhancement factor.

Refers to the catalytic effect of iron(III) precipitate surface area on the rate of surface nucleation.

λ	kg/mol	Binary virial coefficient of a mixed system that involves neutral species (Pitzer ion-interaction theory).

μ	$(kg/mol)^2$	Ternary virial coefficient of a mixed system that involves neutral species (Pitzer ion-interaction theory).
μ	J/mol	Chemical potential.

ν	–	Stoichiometric coefficient.

ρ	kg/m^3	Density.

The symbols ρ_c & ρ_s refer to the density of the continuous & solid (or sulfide mineral) phase, respectively. The symbol ρ_w refers to the density of water.

ρ_{Fe}	kg/kg	Pulp density (fraction or %) of an iron(III) precipitate.

Mass solids per unit mass water.

$\rho_{s/w}$	kg/kg	Pulp density (fraction or %) of solids in a slurry.

Mass solids per unit mass water.

ρ_{sl}	kg/m^3	Pulp density of solids material per unit volume slurry.

Mass solids per unit volume (bubble-free) slurry. $\rho_{sl,o}$ refers the original pulp density in a batch or semi-batch reactor.

σ	–	Relative supersaturation.

Refers to the supersaturation ratio S_a, *i.e.*, $\sigma = S_a - 1$. The subscripts *Hem* & *Jar* refer to the hematite & hydronium jarosite phases, respectively. The symbol σ_{Fe} refers to the relative iron(III) saturation ratio of the hematite & hydronium jarosite phases, based on the bulk solution properties.

Stellenbosch University http://scholar.sun.ac.za

τ	min	Average (mean) residence time in a continuous reactor.
τ_s	min	Time constant of a sulfide mineral or other solid material (time required for complete oxidation in a batch reactor).

Refers to the shrinking particle (or particle core) model, under surface reaction control (App. F.4). The symbols τ_{Hem} & τ_{Jar} refer to the time constants of hematite & hydronium jarosite redissolution, respectively.

υ	m/min	General symbol used to describe the velocity vector of the particle phase space (*ref.* PB model).

See derivation of the macroscopic PB (App. H.1). The subscripts i & e refer to the internal & external terms of this property. The symbol υ_ℓ refers to the rate of change of the particle core size, while $\upsilon_{\ell,n}$ refers to the corresponding rate of change of the core size in original particle size-class *n*. The symbol υ_L refers to the growth rate of hydronium jarosite on an iron(III) precipitate particle of size, L_{Fe}. The superscript Py_c refers to the accelerated velocity term of mineral oxidation due to the catalytic effect of pyrite surface.

ϕ	–	Molal osmotic coefficient of an electrolyte solution.

The symbol ϕ^{st} refers to the stoiciometric (formal) value.

ϕ	V	Electric potential.

ϕ° refers to the standard state value at infinite dilution, *i.e.*, the ideal solution at an imaginary state of unit activity of the contributing redox species. The symbol ϕ^e refers to the electric potential of an electrochemical reaction at equilibrium.

ϕ_c	–	Thermodynamic driving force of crystallisation.
ø	–	Fugacity coefficient.
Φ	kg/mol	Binary virial coefficient of the activity coefficient when mixing ions of same charge (Pitzer ion-interaction theory).

The symbol Φ' refers to its ionic strength derivative, while the symbol Φ^ϕ refers to the binary virial coefficient of the osmotic coefficient (solvent).

Φ_a	–	Area shape factor of a particle.
Φ_v	–	Volume shape factor of a particle.

$\psi(\ell)$	1/kg.m	Particle size number density distribution.

This distribution is defined per unit mass water in the reactor outflow. The symbol ψ' represents the normalised (fractional) density distribution (units of 1/m), while ψ_o refers to the density distribution flowing into the first reactor. The symbol ψ_l refers to distribution, per unit volume solution in the reactor outflow (units of $1/m^4$).

ψ	$(kg/mol)^2$	Ternary interaction virial coefficient for mixing three different ions (Pitzer ion-interaction theory).

Stellenbosch University http://scholar.sun.ac.za

NOTATION C

Symbol	Standard Unit (Unless specified differently in text)	Description
AARD Eq. 2.73.	%	Absolute average relative deviation.
AC Eq. 6.158.	%	Accountability.
CV App. D (table footnotes).	%	Coefficient of variance.
R^2	–	Coefficient of determination.
RSS	–	Residual sum of squares.
[ ]	mol/kg or mol/L	Molality or molarity of a species in solution.
The symbol [ ]* refers to the molality or molarity at thermodynamic equilibrium.		
{ }	–	Refers to a metastable phase.

LIST OF ABBREVIATIONS

AA-UBC	Anglo American – University of British Columbia
AATSR	Anglo American Technical Solutions Research
AC	Autoclave
AR	Analytical-grade (chemicals)
BE	Binding energy
BFS	Basic ferric sulfate
BH	Born-Haber
BLCM	Balanced Like Charge Method
BMS	Base metal sulfide
BSE	Backscattered electron (images)
BSSE	Basis set superposition errors
BSTR	Batch stirred-tank reactor

Stellenbosch University http://scholar.sun.ac.za

BZS	Basic zinc sulfate
CASTEP	Cambridge Serial Total Energy Package
CCRMP	Canadian Certified Reference Materials Project
CIP	Contact ion pair
COSMO	Conductor-Like Screening Model
CSTR	Continuous stirred-tank reactor
DFT	Density function theory
DH	Debye-Hückel
DNP	Double numerical atomic basis sets incl. polarisation functions
DO	Dissolved oxygen
DOS	Density of states
DRS	Dielectric spectroscopy
EC	Electrochemical-chemical (mechanism)
EDX	Energy dispersive X-ray
EMF	Electromotive force
EW	Electrowinning
FEG	Field emission gun
FEL	Fluctuating energy-level (model)
GGA	Gradient-generalised approximation
GT	Gibbs-Thompson
HBMS	Hudson Bay Mining & Smelting Co. Ltd.
HOMO	Highest molecular orbital
HP	High pressure
HPLC	High performance liquid chromatography
HR	High resolution
HT	High temperature (>180ºC)
HX	Heat exchanger
ICP-OES	Inductively coupled plasma – optical emission spectroscopy

Stellenbosch University http://scholar.sun.ac.za

IHP	Inner Helmholtz plane
IR	Infra red
LALLS	Low angle laser light scattering
LAXS	Large angle X-ray scattering
LDA	Local density approximation
LDOS	Local density of states
LL	Lewis linearization
LLD	Lower limits of determination
LS	Lignosulfonate
LSD	Local spin density
LT	Low temperature (<115ºC)
LUMO	Lowest unoccupied molecular orbitals
MD	Molecular dynamics
MES	Mössbauer-effect spectroscopy
MLA	Mineral liberation analyser
MP	Mixed potential (theory)
MSE	Mixed solvent electrolyte
MT	Medium temperature (115-160ºC)
NBS	National Bureau of Standards
NLSD	Non-local spin density
OHP	Outer Helmholtz plane
PB	Population balance
PDOS	Partial density of states
PGE	Platinum group element
PHT	Potassium hydrogen phthalate
PID	Proportional-integral-differential (controller)
PLC	Programmable logic controller

Stellenbosch University http://scholar.sun.ac.za

PLS	Pregnant leach solution
PPD	Particle penetration depth
PSD	Particle size distribution
PZC	Point of zero charge
QB	Quebracho
QM	Quantum mechanical
QMCF	Quantum mechanical charge field
RS	Raman spectroscopy
RTD	Residence time distribution
SC	Semiconductor
SCADA	Supervisory control & data acquisition
SCF	Self-consistent field
SD	Sulfate-dependent (reaction pathway)
SEI	Secondary electron images
SEM	Scanning electron microscope
SHE	Standard hydrogen electrode
SI	Sulfate-independent (reaction pathway)
SMD	Stirred-media detritor
SSA	Specific surface area
SSIP	Solvent-separated ion pair
SX	Solvent extraction
TEM	Transmission electron microscopy
TIP	Triple ion pair
TMS	Trace mineral search
TPOX	Total pressure oxidation
TPSA	Total particle surface area
USC	Unreacted shrinking core (model)
USP	Unreacted shrinking particle (model)

Stellenbosch University http://scholar.sun.ac.za

XAES	X-ray Auger electron spectroscopy
XPS	X-ray photoelectron spectroscopy
XRD	X-ray diffraction
XRF	X-ray fluorescence
XRFS	X-ray fluorescence spectrometer

MINERAL ABBREVIATIONS

Bor	Bornite
Cov	Covellite
Cpy	Chalcopyrite
Chc	Chalcocite
G	Gangue
Hem	Hematite
Jar	Hydronium jarosite
Ph	Pyrrhotite
Py_c	Pyrite catalysed
Py	Pyrite
Sph	Sphalerite

Stellenbosch University http://scholar.sun.ac.za

CHAPTER 1. INTRODUCTION

1.1 Background

Numerous processes have been proposed to commercially treat chalcopyrite ores and concentrates, the most abundant copper-containing mineral. The vast majority of these processes have, thus far, failed to reach commercial maturity due to economic, high process risk and environmental factors. Technologically proven processes, such as smelting, are falling out of favour due to the high cost of electricity, sulfur dioxide emissions (unless a market for concentrated acid or a local oxide ore can be used to 'sink' sulfur economically), deleterious impurities and its scale sensitivity (*e.g.*, Berezowsky & Trytten, 2002; Dreisinger, 2006).

1.1.1 High temperature (HT) processing

With regards to new technology risks, the best alternative to smelting would be a high temperature (HT; >180ºC), total pressure oxidation (TPOX) process, which is ideally suited to copper-gold concentrates. This is because all sulfides are oxidised to sulfate and no cyanide-consuming sulfur reports to the residue, which would allow easy and economic recovery of the precious metals. Furthermore, iron is rejected as a stable hematite phase, which is the preferred hydrometallurgical process residue. However, if no relatively cheap oxide ore or other neutralising source is available, the cost associated with sulfate removal may become prohibitive, unless the copper and/or gold grade is high enough to warrant such neutralisation expense. Another drawback of the TPOX process is that the autoclave heat balance requires the reactor to run moderately diluted, *i.e.*, at relatively low pulp densities. The Platsol process (Dreisinger 2003), although not yet commercialised, is a variation of the TPOX process and could allow *in situ* platinum group element (PGE) extraction due to the presence of ~6 g/L chloride.

1.1.2 Medium temperature (MT) operation in context of LT and HT processing options

A host of non-commercial (some demonstration plant) low temperature (LT; <115ºC) processes have been proposed in sulfate medium (*e.g.*, the Sherrit Gordon (Vizsolyi *et al.*, 1967), Activox (Corrans & Angove, 1993), MIM Albion (Hourn *et al.*, 1999), BioCOP (Dew & Batty, 2003) and Galvanox (Dixon & Tshilombo, 2005; Dixon, 2007; Dixon *et al.*, 2008) processes), in chloride medium (*e.g.*, the Cymet (McNamara *et al.*, 1978), Clear (Schweitzer & Livingstone, 1982), Cuprex (Dalton, 1991), Intec (Moyes *et al.*, 2002), and HydroCopper (Hyvärinen & Hämäläinen, 2005) processes), in ammonia medium (*e.g.*, the Anaconda Arbiter (Kuhn *et al.*, 1975) and Escondida (BHP) processes), and in nitric acid medium (*e.g.*, the NSC (Anderson 1999) process). It is beyond the scope of this study to attempt to rate these processes in terms of their economical viabilities, which may favour whole-ore heap leaching options because of the concentrator

Stellenbosch University http://scholar.sun.ac.za

redundancy and lower capital investment. Besides the controllability issues associated with heaps, most LT processes do not deal well with deleterious elements, are complex and are prone to produce environmentally unstable residues. In terms of both economic and new technology risk factors, the TPOX processes, combined with oxide co-treatment, *e.g.*, as was applied at Freeport McMoRan's Bagdad Operation (Arizona), may be the more viable option for higher grade ore bodies. However, if the oxide source is limited and spare capacity exists in a downstream refinery circuit, *i.e.*, in the solvent extraction (SX) and electrowinning (EW) unit operations, a medium temperature (MT; 115-160ºC) autoclave process may become an attractive alternative.

The different operating regimes are schematically illustrated in Figure 1.1. The LT processing options generally fall in a temperature region below the melting point of sulfur, whereas the HT processing options drive all sulfide sulfur to the sulfate form, *i.e.*, to S(VI). Most of the difficulties associated with MT operation are associated with liquid sulfur, as elaborated upon in later chapters. Surfactants or fine coal are used in MT processes to overcome the stifling effects of liquid sulfur, while ultra-fine milling and high oxygen overpressures are applied to reduce the average autoclave residence time. However, it would also be economically beneficial to operate the primary leaching – SX circuit close to acid neutral, *i.e.*, to prevent excessive acid neutralisation or addition. This aspect depends heavily on the mineralogy of a specific concentrate, the temperature, the oxygen overpressure and the effectiveness of the surfactant(s). The upper temperature boundary is limited by the sulfur transition region (Figure 1.1), which is associated with a rapid increase in the viscosity of liquid sulfur, followed by a rapid decrease in the overall elemental sulfur yield. If the economics of the MT process demand operation close to this transition point due to the slow chalcopyrite leaching rate, which is also related to the total available surface area, *i.e.*, the cost of milling, the elemental sulfur yield would be lower and more variable.

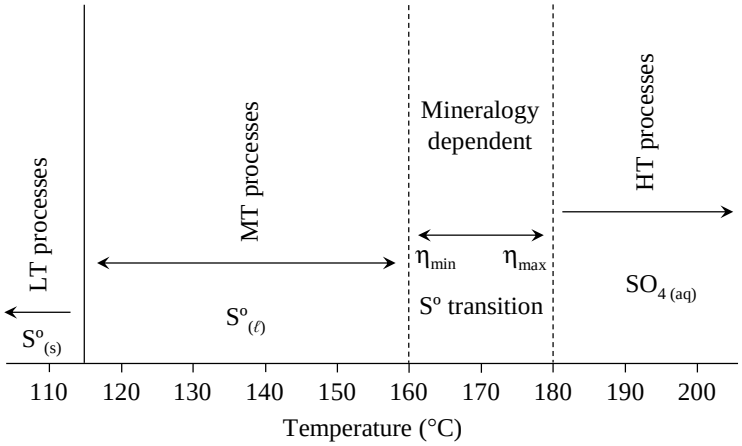

Figure 1.1
Schematic diagram showing different temperature regimes for chalcopyrite concentrate oxidation.

Stellenbosch University http://scholar.sun.ac.za

Since the exact transition temperature depends on specific impurity levels and viscous liquid sulfur is difficult to disperse, only MT operation below ~160ºC would generally be considered. MT processes that, at the present time, have come closest to commercial success are the Anglo American (AA) and University of British Columbia (UBC), *i.e.*, the AA-UBC process (Dempsey & Dreisinger, 2003) (extensively piloted at Anglo American's Technical Solution's (ATS) Research department), a similar process applied by Freeport McMoRan Copper & Gold Inc. to their Morenci operation (now converted to TPOX) and Tech Cominco's CESL process (10 000 tpy Cu plant demonstrated at Vale's Sossego site). These processes are similar, except for the lower surfactant (<3 g/L) and ~12 g/L chloride additions in the case of the CESL process (McDonald & Muir, 2007). The major difference is that the presence of chloride ion, an effective electron-transfer agent (see pioneering work of Taube & co-workers, *e.g.*, Taube, 1952; Nobel lecture, 1983), relaxes the tight particle size requirement of the AA-UBC process ($d_{90} \approx 10$ µm) to a d_{90} of about 20 to 40 µm. The presence of chlorides also results in a higher sulfide to sulfur conversion (>80%, McDonald & Muir, 2007) compared to the AA-UBC process (50-70%, Dreisinger *et al.*, 2002; Steyl, 2004; McDonald & Muir, 2007). These and other MT processes (*e.g.*, the Dynatec process; Berezowsky & Trytten, 2002) could be very competitive, as they produce a more concentrated pregnant leach solution (PLS) as compared to both TPOX and LT processes (Berezowsky & Trytten, 2002) and pose low environmental risk (Jansen & Taylor, 2000). MT operating conditions, on average, produce one third of the acid compared to TPOX and consume about half the oxygen, despite needing about on third more reaction time (~90 min). An important observation from these MT processes is that different surfactants and additives (*e.g.*, chlorides or coal) may result in significant changes in the sulfide oxidation rate, elemental sulfur yield and post-leach cyanide consumption (Berezowsky & Trytten, 2002; McDonald & Muir, 2007). For example, the Dynatec process uses fine coal as a surfactant, which not only better withstands degradation, but also renders elemental sulfur at a slightly lower (~5%) yield and consumes ~50% less cyanide as compared to the AA-UBC process (Berezowsky & Trytten, 2002).

1.2 Overall research objective

Numerous studies of the oxidation of sulfide minerals and, in particular, chalcopyrite concentrates can be found in the open literature. Most electrochemical studies focused on developing a better fundamental understanding of chalcopyrite oxidation, while others were more geared towards engineering and commercial objectives. Although such studies have contributed tremendously to our knowledge of chalcopyrite oxidation over the past few decades, no attempts have been made to generalise and capture this knowledge in an internally consistent mathematical framework. There is a therefore need to develop a deeper understanding of the process fundamentals of MT chalcopyrite oxidation in acidic sulfate solutions. Although this quest is process-(engineering) orientated, it

Stellenbosch University http://scholar.sun.ac.za

demands a better fundamental understanding of each of the chemical steps in the autoclave, as well as the integration of the continuous reactor into the primary leach – SX circuit.

The objective of this study is to develop such a fundamental mathematical framework and, in so doing, to quantify the effects of the key control parameters on the important AA-UBC process targets, both in technical and economical terms. The comparative behaviour of the batch autoclave reactor is also important to understand and mathematically describe because such equipment is typically used to generate the reaction rate constants required to design the commercial (continuous) autoclave.

1.3 Thesis structure, specific objectives and research methodologies

The thesis structure and specific objectives are summarised below, with reference to each chapter.

1.3.1 Chapter 2: Solution chemistry

The first step is to establish a solution chemistry framework, *i.e.*, to calculate the speciation, the solubilities of the iron(III) precipitates and the vapour pressure, which, in turn, forms the departure point when describing the reaction kinetics. Due to the complicated electrolyte system (consisting of numerous solute species) and to prevent over-parameterisation of the model, a simplified methodology is required. Furthermore, since this study is primarily concerned with reaction kinetics, only thermodynamic data from the open literature are available to constrain the phenomenological model. Since no quantitative speciation behaviour at high temperatures is currently available for the mixed electrolyte systems encountered in this study, such behaviour needs to be inferred by the model. A qualitative interpretation of the quantum-level chemistry needs to be developed as a complementary tool to add more confidence to the ambiguous nature of the published thermodynamic data and to better understand the various simplifying assumptions.

1.3.2 Chapter 3: Interfacial oxygen mass transfer

Oxygen gas/liquid mass transfer rate expressions are required in order to allow the oxidative processes in both the batch and continuous reactors to be described in terms of the (actual) dissolved oxygen concentration, *i.e.*, the primary oxidation agent. Such expressions are not only required for all the reactors used in this study, but they also need to be described in terms of the most important system variables. For the sake of quality control, the overall rate constants also need to be verified by a completely different measurement method. Most importantly, it is necessary to quantitatively establish the importance of specific internal reactor configurations, in particular, the slurry level in relation to the position of the impeller(s).

Stellenbosch University http://scholar.sun.ac.za

1.3.3 Chapter 4: Iron(II) oxidation

The overall reactor simulation requires a quantitative description of the iron(II) oxidation rate because it not only affects the solution speciation, but also the oxidation potential of the solution, as well as the acid balance in the reactor. Furthermore, it affects the supersaturation of iron(III), and, hence, the rate of iron(III) precipitation and the type of precipitates formed (Ch. 5). Although iron(II) oxidation kinetics have been studied extensively over the past century, adequate consideration of the interfacial oxygen mass transfer limitations has been lacking, while the resulting rate expressions have either totally neglected the different iron(II) sulfate species reactivities towards oxidation or are inconsistent with chemical reaction theory. Therefore, an iron(II) oxidation module needs to be developed using sound experimental procedures, it needs to be internally consistent with the solution chemistry description (Ch. 2) and current mechanistic understanding, and it also needs to quantitatively account for the interfacial mass transfer limitations of the batch and continuous pilot autoclave test reactors (Ch. 3).

1.3.4 Chapter 5: Iron(III) precipitation

Accounting for the rate of iron(III) precipitation is important in terms of the overall simulation because it affects the acid, sulfur and iron balances in the autoclave. Although particular aspects of iron(III) precipitation have been extensively studied, the complexities associated with aqueous iron(III) speciation and hydrolysis, the complicated nucleation and growth mechanisms in sparingly soluble solution environments at high temperatures, as well as the formation of metastable iron phases make this an unattractive research field in the context of hydrometallurgical processing. Very few studies deal with the kinetics of iron precipitation, while no publications are known of that address the relative precipitation rates of hematite and hydronium jarosite under typical autoclave conditions, not to mention the practical quantification of such processes in a sulfide mineral oxidation reactor. A brief but sufficiently detailed journey into reactive crystallisation (precipitation) theory is therefore warranted, with the aim of gaining the necessary insights in order to derive a kinetic model of iron(III) precipitation. Controlled (low pulp density) batch experimentation and scanning electron microscope (SEM) imaging are then embarked upon in order to derive sufficiently simple rate expressions, *i.e.*, to prevent over-parameterisation of the phenomenological model. Again, thermodynamics form the departure point when deriving these rate expressions, emphasising the importance of the solution chemistry platform (Ch. 2). Finally, the performance of the low pulp density simulation needs to be verified under high pulp density conditions, *i.e.*, to quantify the relative abundance of hematite, the preferred product, relative to hydronium jarosite in practical leaching systems. However, this verification is conducted retrospectively because the oxidation rates of the iron-bearing sulfide minerals in the batch and continuous autoclaves (Ch. 6, 7 & 8) also need to be considered in such a regression exercise.

Stellenbosch University http://scholar.sun.ac.za

1.3.5 Chapter 6: Sulfide mineral oxidation

In order to develop intrinsic mineral leaching rate expressions, some mechanistic level of understanding is required for each charge-transfer step during the sulfide mineral oxidation sequence. The objective of this chapter is to establish the initial mechanistic concepts, with particular reference to the MT oxidation of the sulfide minerals in the Hudson Bay Mining and Smelting Co. Ltd. (HBMS) copper (777) concentrate, *i.e.*, the reference material used in most of the batch and continuous leaching testwork. Mechanistic knowledge of sulfide mineral oxidation is so widely scattered (over several disciplines) in the current literature, that the rate-limiting steps required to formulate the leaching process are severely obscured. Semiconductor theory, surface phenomena and the nature of the various oxidants are considered when formulating the theoretical bases of these dissolution rate expressions. Again, various simplifications are required to prevent over-parameterisation of the model. Preliminary (qualitative) quantum-level modelling of the interaction of the most important oxidants with the different mineral surfaces is conducted in order to guide this process, *i.e.*, to reveal the dominant oxidation mechanisms on each mineral. Finally, the intrinsic oxidation rates of these minerals are measured under well-controlled conditions, *e.g.*, at low pulp densities in a batch autoclave, in order to refine these expressions on a phenomenological level and to obtain the overall intrinsic rate constants.

1.3.6 Chapter 7: Batch and continuous reactor simulation

The batch and continuous reactor models, as well as the architecture of the integrated mass and energy balance model of the primary circuit (autoclave leaching, thickening-filtration & SX-EW) are established first. The rates of all the reactions involving particulates (Ch. 5 & 6) are incorporated into these batch and continuous mass balance frameworks *via* the population balance approach, *i.e.*, to account for changes in the particle number and surface area over the reaction time. Since the interfacial oxygen mass transfer rate is quantified for each reactor (Ch. 3) and the solution thermodynamic model (Ch. 2) relates the formal and actual species concentrations, the phenomenological iron(II) oxidation (Ch. 4), iron(III) precipitation (Ch. 5) and mineral oxidation (Ch. 6) rate expressions can be solved sequentially (in the case of the batch reactor) or iteratively (in the case of a continuous reactor compartment). Although the generic mass, energy and population balance equations are well-established and have been applied to hydrometallurgical leaching or precipitation reactors in the open literature, it is the first attempt to also incorporate such elaborate mineral oxidation and iron(III) precipitation reaction kinetics, all imbedded within the solution thermodynamic, particle population, mass and energy balance frameworks. The intrinsic rate constants and activation energies of the primary sulfide minerals are derived from batch experimentation. This low pulp density leach approach is unique because it prevents iron(III) precipitation, and, hence, allows detailed bulk modal analysis of the residues, which, in turn, reveals the comparative oxidation behaviour of the different sulfide minerals in different

Stellenbosch University http://scholar.sun.ac.za

concentrates. In order to verify the accuracy of the simulation under MT autoclave conditions, the continuous model calculations are compared to integrated pilot plant results during selected operating periods, focusing on the performance of the iron(III) precipitation module (Ch. 5) and more specifically, the impact of the existing surface area on the iron(III) precipitation rate.

1.3.7 Chapter 8: Model application

This chapter focuses on the performance of the overall autoclave reactor simulation. Due to the high costs associated with conducting pilot plant investigations, laboratory-scale batch experimentation at high pulp densities is used to verify the model, in particular with regard to the sulfide mineral oxidation and iron(III) precipitation kinetics. In addition, possible changes in the intrinsic mineral oxidation rates under these high pulp density conditions need to be determined, using two of the chalcopyrite concentrates studied in Chapter 7. Since the degrees of freedom of the observed system are reduced to only a selected few unknown reaction stoichiometries, the simulation can be used to infer more detail around the primary oxidation reactions, specifically the intrinsic elemental sulfur yields and the interactions of the major sulfide minerals with aqueous iron(III). Armed with this addition information, the continuous simulation (Ch. 7) is expanded to also include energy optimisation around the autoclave, *i.e.*, to maintain isothermal operation in each autoclave compartment. In order to illustrate the power of the overall simulation as a process design tool, a number of operating and intrinsic parameters are systematically varied, while recording the autoclave and circuit responses.

1.3.8 Chapter 9: Study overview and key outcomes

This chapter presents a summary of the key outcomes and recommendations of this study, which tie in with the above objectives.

1.3.9 Dissertation roadmap

Due to large volume of work, the numerous citations and frequent cross-referencing to other chapters, the dissertation is subdivided into three volumes. As a quick guide, these chapters are grouped as follows in each of the volumes:

VOL I:	SOLUTION CHEMISTRY, MASS TRANSFER & REACTIONS:	CH. 2 - 5
VOL II:	MINERAL OXIDATION REACTIONS, REACTORS & SYSTEMS:	CH. 6 - 8
VOL III:	**STUDY OVERVIEW & KEY OUTCOMES**:	CH. 9
	REFERENCES	
	APPENDICES	

Stellenbosch University http://scholar.sun.ac.za

CHAPTER 2. SOLUTION CHEMISTRY

2.1 Introduction

The effort expended to describe the chemistry of sulfuric acid – divalent metal, M(II), sulfate aqueous mixtures does not reflect its industrial importance. This is especially prevalent at higher temperatures, *e.g.*, under oxidative pressure leaching conditions. The application of solution thermodynamic theory to hydrometallurgical processes is usually directed towards calculating specific equilibria, *e.g.*, to simulate salt solubility (Liu & Papangelakis, 2005a, 2005b). In selected cases, it is more explicitly directed to the understanding of the process kinetics, *e.g.*, by deriving the actual solution acidity from potentiometric or conductivity measurements (Baghalha & Papangelakis, 2000; Seneviratne *et al.*, 2003). The objective of this chapter is to develop a solution chemistry platform to interpret iron(II) and sulfide mineral oxidation, and iron(III) precipitation kinetics, *i.e.*, to calculate the speciation of the important contact ion pairs (CIPs), in addition to obtaining selected thermodynamic properties, *e.g.*, the solubility and solution vapour pressure.

The development roadmap of this phenomenological model is as follows:

- Developing the methodology and mathematical framework to describe the relevant thermodynamic properties of the electrolyte system (Sect. 2.2)
- Selecting and explicitly recognising the most important (minimum number) CIPs that may impact on the above-mentioned kinetic processes (Sect. 2.3)
- Selecting the thermodynamic properties of the known CIPs from the literature and using this to build a thermodynamic basis from first principles (Sect. 2.3.2)
- Using this fundamental basis to estimate the thermodynamic properties of the lesser-known CIPs (Sect. 2.3.2 & 2.3.3)
- Adopting and testing the surrogate salt approach, *i.e.*, to overcome the complexities of the mixed H_2SO_4-$CuSO_4$-$ZnSO_4$-$FeSO_4$-$MgSO_4$-H_2O electrolyte system (Sect. 2.4)
- Using the available thermodynamic and speciation data from the literature to regress the most important (minimum number) interaction parameters and their temperature dependencies, up to 200°C and up to 1 mol/kg total sulfate concentration (Sect. 2.4.2)
- Testing the consistency of the overall chemistry model and generating indicative trends for the mixed salt system at varying temperatures (Sect. 2.4.3)
- Developing a simplified strategy for dealing with the oxidised iron(III) metal sulfate species within the above modelling framework (Sect. 2.4.3), and
- Comparing the calculated vapour pressure of the mixed electrolyte system to other data sources (Sect. 2.4.3).

Stellenbosch University http://scholar.sun.ac.za

2.2 Theoretical framework

2.2.1 Outlining the general thermodynamic basis

By definition (Smith & Van Ness, 1987), the activity (*a*) of a dissolved species is related to its molality in the following manner:

$$a = \gamma m/f^{o} = \gamma m \qquad 2.1$$

The final term on the right incorporates an imaginary standard state, which is conveniently chosen at unit molality, so that f° = m° = 1 (Stokes, 1991). This asymmetrical reference state is so chosen that as the molality approaches zero, the activity coefficient (γ) tends to unity. The reference state of the solvent is therefore its pure liquid form and is considered suitable for this low to medium ionic strength application. For the same reason, the proton is modelled as an unhydrated species. The molality scale is the preferred scale in solution thermodynamics, because it has the advantage that it is independent of temperature and pressure. However, the concentration scale has more practical significance and it is often necessary to convert between the scales. The following relation is easily derived, where M refers to concentration in the molarity scale, ρ is the solution density (g/L) and Mw_i is the molecular weight of species *i*:

$$m_i = \frac{10^3 \cdot M_i}{\rho - \sum_i M_i Mw_i} \qquad 2.2$$

In order to calculate the activity coefficient of a species in a non-ideal solution, an interaction-type framework needs to be selected from the following commonly used models (references indicate recent examples): the Bromley-Zemaitis (Liu & Papangelakis, 2005a), Mixed Solvent Electrolyte (MSE) (Liu & Papangelakis, 2005b), Pitzer (Casas *et al.*, 2005b) and Electrolyte NRTL (Haghtalab *et al.*, 2004) models. Despite the fact that these models have been successfully applied to simulate chemical systems, each having their own subtleties, the relatively low salt concentrations (< 1 mol/kg H_2SO_4 and $M(II)SO_4$) covered in this study make the choice somewhat ambiguous. Although the ion-interaction model of Pitzer is more complicated, it has been widely applied to thermodynamic studies over the past 35 years and its theoretical framework is also adopted in this study, albeit phenomenologically (Sect. 2.4).

2.2.2 Pitzer ion-interaction model

The standard Pitzer ion-interaction model, which is based on statistical mechanics, has been widely applied. It expresses the excess Gibbs energy of the solution and consists of an extended Debye-Hückel (DH) term and virial expansion terms. A relatively dilute electrolyte concentration makes the ionic strength dependencies of the third virial coefficients (Clegg *et al.*, 1994) redundant; these generalised equations can be found in numerous publications (*e.g.*, Pitzer, 1991). The activity

Stellenbosch University http://scholar.sun.ac.za

coefficient of a cation (M), anion (X) and neutral ion (N) may respectively be represented as follows ('c' is the general notation for a cation, 'a' for an anion and 'n' for a neutral ion):

$$\gamma_M = z_M^2 F + \sum_a m_a (2B_{Ma} + ZC_{Ma}) + z_M \sum_c \sum_a m_c m_a C_{ca} + \sum_c m_c (2\Phi_{Mc} + \sum_a m_a \psi_{Mca}) + \sum_a \sum_{a'} m_a m_{a'} \psi_{Maa'} + 2\sum_n m_n \lambda_{Mn} + 3\sum_n m_n^2 \mu_{Mnn} + \ldots \quad 2.3$$

$$\gamma_X = z_X^2 F + \sum_c m_c (2B_{cX} + ZC_{cX}) + |z_X| \sum_c \sum_a m_c m_a C_{ca} + \sum_a m_a (2\Phi_{Xa} + \sum_c m_c \psi_{cXa}) + \sum_c \sum_{c'} m_c m_{c'} \psi_{cc'X} + 2\sum_n m_n \lambda_{Xn} + 3\sum_n m_n^2 \mu_{Xnn} + \ldots \quad 2.4$$

$$\gamma_N = 2\sum_c m_c \lambda_{Nc} + 2\sum_a m_a \lambda_{Na} + 6\sum_n \sum_c m_n m_c \mu_{Nnc} + 6\sum_n \sum_a m_n m_a \mu_{Nna} + \ldots \quad 2.5$$

The primed indices refer to summation over all distinguishable pairs, z_i is the charge of ion, *i*, and:

$$F = f^{\gamma} + \sum_c \sum_a m_c m_a B'_{ca} + \sum_c \sum_{c'} m_c m_{c'} \Phi'_{cc'} + \sum_a \sum_{a'} m_a m_{a'} \Phi'_{aa'} \quad 2.6$$

The water activity (a_w), more appropriately expressed as the osmotic coefficient (ϕ), may then be written as (Clegg & Whitfield, 1991):

$$\phi - 1 = -[1 - (55.509/\sum_k m_k) \cdot ln\, a_w] = (2/\sum_k m_k) \cdot [f^{\phi} I + \sum_c \sum_a m_c m_a (B^{\phi}_{ca} + ZC_{ca}) + \sum_c \sum_{c'} m_c m_{c'} (\Phi^{\phi}_{cc'} + \sum_a m_a \psi_{cc'a}) + \sum_a \sum_{a'} m_a m_{a'} (\Phi^{\phi}_{aa'} + \sum_c m_c \psi_{aa'c}) + \sum_n \sum_c m_n m_c \lambda_{nc} + \sum_n \sum_a m_n m_a \lambda_{na} + 3\sum_n \sum_c m_n^2 m_c \mu_{nnc} + 3\sum_n \sum_a m_n^2 m_a \mu_{nna} + \ldots] \quad 2.7$$

The total absolute ionic change, Z, and ionic strength, I, of the electrolyte solution are defined in terms of *k* ionic charges, z_k as follows, respectively:

$$Z = \sum_k m_k |z_k| \quad 2.8$$

$$I = \tfrac{1}{2} \sum_k m_k z_k^2 \quad 2.9$$

The ionic strength dependence of the DH terms may be represented as follows (Pitzer, 1991):

$$f^{\phi} = -A_{\phi} I^{\frac{1}{2}} / (1 + bI^{\frac{1}{2}}) \quad 2.10$$

$$f^{\gamma} = f^{\phi} - A_{\phi} (2/b)\, ln(1 + bI^{\frac{1}{2}}) \quad 2.11$$

The universal parameter b has a value of 1.2 $(kg/mol)^{1/2}$ (Pitzer, 1991). The DH parameter of the osmotic coefficient at infinite dilution, A_{ϕ}, follows from the DH derivation (*e.g.*, Atkins, 1986):

Stellenbosch University http://scholar.sun.ac.za

$$A_\phi = \frac{1}{3}\cdot A_\gamma = \frac{1}{3}\cdot\frac{(2\rho_w)^{\frac{1}{2}}F^3}{8\pi N_a[(\varepsilon_w\varepsilon_o)(R_g T)]^{\frac{3}{2}}} \qquad 2.12$$

This equation, by definition, refers to the natural logarithm scale. The relative permittivity of water (ε_w), reported by Bradley and Pitzer (1979), its density (ρ_w), reported by Cooper and Le Fevre (1982), and the fundamental constants (Table A.1) yield a value of 0.3914 $(kg/mol)^{1/2}$ at 25ºC; this is in excellent agreement with the value of 0.3915±0.001 $(kg/mol)^{1/2}$, suggested by Pitzer (1991). The binary (B_{ca}, B'_{ca}, B^ϕ_{ca}) and ternary (C_{ca}) virial coefficients may be expressed in terms of their interaction parameters, β_{ca} and C^ϕ_{ca}, respectively (Pitzer, 1991):

$$B_{ca} = \beta^{(0)}_{ca} + \beta^{(1)}_{ca}\cdot f(\alpha_1 I^{\frac{1}{2}}) + \beta^{(2)}_{ca}\cdot f(\alpha_2 I^{\frac{1}{2}}) \qquad 2.13$$

$$B'_{ca} = [\beta^{(1)}_{ca}\cdot f'(\alpha_1 I^{\frac{1}{2}}) + \beta^{(2)}_{ca}\cdot f'(\alpha_2 I^{\frac{1}{2}})]/I \qquad 2.14$$

$$B^\phi_{ca} = \beta^{(0)}_{ca} + \beta^{(1)}_{ca}\cdot exp(-\alpha_1 I^{\frac{1}{2}}) + \beta^{(2)}_{ca}\cdot exp(-\alpha_2 I^{\frac{1}{2}}) \qquad 2.15$$

$$C_{ca} = C^\phi_{ca}/2|z_c z_a|^{\frac{1}{2}} \qquad 2.16$$

The values of parameters α_1 and α_2 are usually set to 1.4 and 12 $(kg/mol)^{1/2}$, respectively, for 2-2 electrolytes but 2 and 0 $(kg/mol)^{1/2}$, respectively, for other types of interactions (Pitzer, 1991). The ionic strength functionalities for calculating the binary virial coefficient and its derivative are represented by the following two equations, respectively (Pitzer, 1991):

$$f(x) = 2[1-(1+x)exp(-x)]/x^2 \qquad 2.17$$

$$f'(x) = -2[1-(1+x+x^2/2)exp(-x)]/x^2 \qquad 2.18$$

In mixed electrolyte systems, binary interaction between ions of like charge (Φ) and various ternary interactions (ψ) may have to be accounted for. In addition to the binary short-range (θ) forces, long-range electrostatic forces ($^E\theta$), *i.e.*, for unsymmetrical mixing, may have to be included. The binary mixing term, its derivative and the corresponding mixing term for the osmotic coefficient are then expressed by Equations 2.19, 2.20 and 2.21, respectively.

$$\Phi_{ij} = \theta_{ij} + {}^E\theta_{ij}(I) \qquad 2.19$$

$$\Phi'_{ij} = {}^E\theta'_{ij}(I) \qquad 2.20$$

$$\Phi^\phi_{ij} = \Phi_{ij} + I\Phi'_{ij} \qquad 2.21$$

The values of the electrostatic terms may be calculated using Chebyshev approximations (see Pitzer, 1991). Although the above thermodynamic framework is capable of simulating complicated

Stellenbosch University http://scholar.sun.ac.za

electrolyte mixtures in an internally consistent manner, the way it is applied in this study is phenomenological in nature due to the surrogate salt approach that is followed (see later).

2.2.3 General modelling methodology

The methodology of modelling thermodynamic properties has traditionally followed an ion-interaction-only approach, *i.e.*, it is based on complete electrolyte dissociation. However, certain electrolyte mixtures, such as the H_2SO_4-H_2O system, require the explicit recognition of the strong covalent complexes (the bisulfate inner-sphere complex, HSO_4^-, in this case) in order to accurately describe their thermodynamic properties (Pitzer *et al.*, 1977). Although such 'modifications' introduce more interaction parameters, this is compatible with the full dissociation framework. At the other extreme, many researchers studying hydrometallurgical systems frequently opt for a speciation-only type approach, *e.g.*, to predict solubility (*e.g.*, Papangelakis *et al.*, 1994) or to support a specific reaction mechanism (*e.g.*, Crundwell, 1987). In cases where such speciation models also confirm independent measurements, *e.g.*, spectroscopic or pH data, they become an attractive alternative to the interaction-type approach (*e.g.*, Casas *et al.*, 2005a). Casas *et al.* (2005b) compared the performance of three different chemical models, *i.e.*, the DH B-dot, Pitzer and Bromley-Zemaitis models at high temperatures (>200ºC). Although the three models differ in complexity and recognised species (equilibria), they demonstrated almost the same ability to fit the solubility of magnesium and aluminium in ternary systems. This illustrates that interaction parameters can make up for differences in the number of explicitly recognised species and *vice versa*. The choice of an interaction compared to a speciation approach should be guided by the minimum parameter space required to adequately describe the experimental data and the ultimate objective of the model.

Measured species abundance data are severely restricted in the open literature, especially at higher temperatures. It is therefore natural to limit the model to explicitly contain only the CIPs that are most likely to impact on the kinetic processes, *i.e.*, the driving force behind this study. A combined interaction-speciation framework is therefore selected for this study, which is in line with modern chemical modelling methodology (see Liu & Papangelakis, 2005a). Published experimental information at room temperature is then used to infer the speciation behaviour at higher temperatures, where only limited solubility, mean activity and osmotic coefficient data are currently available. This is important because the formation of these CIPs is entropy driven (Sect. 2.3.2) and would be expected to impact on the reaction kinetics at high temperatures.

Data regression

Since colligative properties, *e.g.*, vapour pressure lowering and boiling point elevation, are difficult to measure accurately (Rard & Platfort, 1991), it is most appropriate to use water activity data

Stellenbosch University http://scholar.sun.ac.za

(expressed as the stoichiometric osmotic coefficient, ϕ^{st}) from isopiestic measurements (see Rard & Platfort, 1991), albeit referring mostly to lower solution temperatures (<100ºC). Similarly, reported speciation data, utilising a range of different measurement techniques, are mostly limited to lower temperatures. Activity coefficient data from electromotive force (EMF; see Butler & Roy, 1991) and isopiestic measurements proved most useful to this study (Sect. 2.4.2). Since individual ions cannot be isolated, only the mean activity coefficient, $\gamma_{\pm}$, of a salt is obtained from experimentation. For a salt, $M_{\nu 1}X_{\nu 2}$, the mean activity coefficient is defined as follows (Robinson & Stokes, 1959):

$$\gamma_{\pm} = (\gamma_M^{\nu 1}\,\gamma_X^{\nu 2})^{\frac{1}{\nu}} \qquad 2.22$$

The ion number, ν, of the salt is equal to the sum of its individual stoichiometric coefficients, *i.e.*, $\nu_1+\nu_2$. In order to maintain internal consistency, all calculations should be based on the calculated species properties. However, the experimental data regression requires their stoichiometric (also called formal or observed) values. The following two equations convert the calculated activity and osmotic coefficients to their stoichiometric values, respectively:

$$\gamma^{st} = \frac{m}{m^{st}}\gamma \qquad 2.23$$

$$\phi^{st} = \frac{\sum_k m_k}{\sum_k m_k^{st}}\phi \qquad 2.24$$

Solute mean activity coefficients inferred from salt solubility measurements (*e.g.*, Linke & Seidell, 1958, 1965) provide valuable information at higher temperatures for both pure and mixed electrolyte systems. The generalised solubilisation reaction for the hydrated salt may be written as follows (Pabalan & Pitzer, 1991):

$$M_{\nu 1}X_{\nu 2}\cdot nH_2O_{(s)} \Leftrightarrow \nu_1 M_{(aq)}^{y+} + \nu_2 X_{(aq)}^{z-} + nH_2O_{(aq)} \qquad 2.25$$

The thermodynamic solubility product, $K°_{sp}$, is derived by taking the activity of the solid phase as unity (pure substance):

$$K_{sp}^{o} = exp\frac{-\Delta G_{rx}^{o}}{R_g T} = a_M^{\nu 1}\,a_X^{\nu 2}\,a_w^{n} = (m_M\gamma_M)^{\nu 1}\,(m_X\gamma_X)^{\nu 2}\,a_w^{n} = m_M^{\nu 1}m_X^{\nu 2}\,\gamma_{\pm}^{\nu}\,a_w^{n} \qquad 2.26$$

The last two terms follow from the substitution of Equations 2.1 and 2.22, respectively.

Complexation

As mentioned above, the Pitzer ion-interaction framework becomes more complicated when strong interactions are explicitly treated as separate species and should therefore be limited to a minimum. Thermodynamically, a complex species is considered to be a new entity in solution when the

Stellenbosch University http://scholar.sun.ac.za

mutual electronic attraction of the individual ions is considerably greater than their thermal energy (Robinson & Stokes, 1959). In aqueous solution, water molecules are chemically bonded to the ion and this forms the inner coordination sphere. An inner-sphere complex, *i.e.*, a CIP, is formed when water molecules are replaced from the inner coordination sphere of the metal ion by a ligand (such as the sulfate ion), forming a direct chemical bond. When ligand ions do not replace any water molecules from the inner sphere, and are attached to the positive ions only by virtue of electrostatic considerations, they form an outer-sphere complex (Hancock, 1976). Activity coefficients of outer-sphere complexes are strikingly similar up to high concentrations, and this is reflected in very similar values of their association constants.

Inner-sphere complexes on the other hand, always show large differences in stability (Prue, 1966). Inner- and outer-sphere complexes represent two extremes and although most ion complexes would show predominance of one type, both are likely to be present. The ionic strength (Eq. 2.9) defines the net charge in the electrolyte solution and would obviously be affected by the number of explicitly recognised complex species, while the condition of electrical neutrality always needs to be fulfilled:

$$\sum_k \mathrm{m}_k \mathrm{z}_k = 0 \qquad 2.27$$

This study approaches all complexation reactions from an association perspective. Either a step-wise or cumulative description may be used, represented by the following two equations, respectively:

$$\mathrm{MX}_{n-1} + \mathrm{X} \Leftrightarrow \mathrm{MX}_n \qquad 2.28$$

$$\mathrm{M} + n\mathrm{X} \Leftrightarrow \mathrm{MX}_n \qquad 2.29$$

The thermodynamic association constants (at infinite dilution) for the step-wise (K°) and cumulative (β°) reactions are then represented as follows, respectively:

$$\mathrm{K}_n^{\mathrm{o}} = exp\frac{-\Delta \mathrm{G}_{\mathrm{rx}}^{\mathrm{o}}}{R_g \mathrm{T}} = \frac{a_{\mathrm{MX}_n}}{a_{\mathrm{MX}_{n-1}} a_{\mathrm{X}}} = \frac{\mathrm{m}_{\mathrm{MX}_n}}{\mathrm{m}_{\mathrm{MX}_{n-1}} \mathrm{m}_{\mathrm{X}}} \cdot \frac{\gamma_{\mathrm{MX}_n}}{\gamma_{\mathrm{MX}_{n-1}} \gamma_{\mathrm{X}}} = \mathrm{K}_n \cdot \frac{\gamma_{\mathrm{MX}_n}}{\gamma_{\mathrm{MX}_{n-1}} \gamma_{\mathrm{X}}} \qquad 2.30$$

$$\beta_n^{\mathrm{o}} = exp\frac{-\Delta \mathrm{G}_{\mathrm{rx}}^{\mathrm{o}}}{R_g \mathrm{T}} = \frac{a_{\mathrm{MX}_n}}{a_{\mathrm{M}} a_{\mathrm{X}}^n} = \frac{\mathrm{m}_{\mathrm{MX}_n}}{\mathrm{m}_{\mathrm{M}} \mathrm{m}_{\mathrm{X}}^n} \cdot \frac{\gamma_{\mathrm{MX}_n}}{\gamma_{\mathrm{M}} \gamma_{\mathrm{X}}^n} = \beta_n \cdot \frac{\gamma_{\mathrm{MX}_n}}{\gamma_{\mathrm{M}} \gamma_{\mathrm{X}}^n} \qquad 2.31$$

Choosing appropriate thermodynamic properties for these association reactions is an important aspect of the overall solution chemistry model. The next section is therefore devoted to establishing a sound thermodynamic platform, *i.e.*, at the transcendent condition of infinite dilution.

Stellenbosch University http://scholar.sun.ac.za

2.3 Thermodynamics at infinite dilution

2.3.1 Temperature extrapolation

This section summarises the various thermodynamic relationships utilised in this study to extrapolate over temperature. No partial molal volume terms are included in these equations, since temperatures are limited to 200ºC and below, and hence to relatively insignificant pressure effects.

Background

A standard thermodynamic property (generic symbol, X) of an equilibrium reaction is constituted from the sum of the primary components (partial molal properties) taking part in the reaction:

$$\Delta X = \sum_{prod} \nu_p X_p - \sum_{react} \nu_r X_r \qquad 2.32$$

The equilibrium constant can be calculated if the partial molal enthalpy (H^o) of the constituent species or the standard molal enthalpy of the reaction (ΔH^o) are known. The following equation (also known as the Van't Hoff isochore) is derived from the Gibbs-Helmholtz relationship (Atkins & De Paula, 2006) and requires knowledge of the temperature dependency of the reaction enthalpy.

$$R_g \frac{d(ln\, K^o)}{dT} = \frac{\Delta H^o}{T^2} \qquad 2.33$$

The temperature dependency of the heat capacity cannot be predicted and mathematical correlation is used to represent the experimental data. The partial molal heat capacity of a species ($C_p°$) is often reported by the following mathematical expression, also known as the Maier-Kelley equation (see original reference in Horvath, 1985):

$$C_p^o = a + b \cdot 10^{-3} \cdot T + c \cdot 10^5 \cdot T^{-2} + d \cdot 10^{-6} \cdot T^2 \qquad 2.34$$

The coefficients a, b, c, and d are temperature independent. If such coefficients are available for the constituent species taking part in a reaction (follows from Eq. 2.32), Kirchhoff's Law (Atkins & De Paula, 2006) may be used to calculate the reaction enthalpy at temperature, T, if it is known at some reference temperature, T_r:

$$\Delta H_T^o - \Delta H_{T_r}^o = \int_{T_r}^{T} \Delta C_p^o \, dT \qquad 2.35$$

The equilibrium constant is directly related to the Gibbs free energy of the reaction:

$$ln\, K^o = \frac{-\Delta G^o}{R_g T} \qquad 2.36$$

where the definition of the standard Gibbs free energy stipulates that (Atkins & De Paula, 2006):

Stellenbosch University http://scholar.sun.ac.za

$$\Delta G^{o} = \Delta G^{o}_{T_r} + (\Delta H^{o} - \Delta H^{o}_{T_r}) - (T\Delta S^{o} - T_r \Delta S^{o}_{T_r}) \qquad 2.37$$

The standard entropy of a reaction is related to the standard heat capacity as follows (Atkins & De Paula, 2006):

$$\Delta S^{o} - \Delta S^{o}_{T_r} = \int_{T_r}^{T} \frac{\Delta C^{o}_{p}}{T} dT \qquad 2.38$$

Substitution of Equations 2.35, 2.37 and 2.38 into Equation 2.36, and rearranging, yields the following general equation, *i.e.*, for the case where the temperature dependence of the reaction heat capacity is known:

$$ln\,K^{o} = \frac{1}{R_g}\left(\Delta S^{o}_{T_r} + \int_{T_r}^{T} \frac{\Delta C^{o}_{p}}{T} dT\right) - \frac{1}{R_g T}\left(\Delta H^{o}_{T_r} + \int_{T_r}^{T} \Delta C^{o}_{p} dT\right) \qquad 2.39$$

Constant heat capacity

When no functional expression for the heat capacity is available, it is often assumed to be constant, *i.e.*, the enthalpy of reaction varies linearly with temperature (after integrating Eq. 2.35):

$$\Delta H^{o}_{T} - \Delta H^{o}_{T_r} = \Delta C^{o}_{p,T_r}(T - T_r) \qquad 2.40$$

and the entropy value may be estimated after integration of Equation 2.38:

$$\Delta S^{o}_{T} - \Delta S^{o}_{T_r} = \Delta C^{o}_{p,T_r} \cdot ln\frac{T}{T_r} \qquad 2.41$$

Balanced Like Charge Method (BLCM)

The assumption of constant heat capacity has found particular application in the Balanced Like Charge Method (BLCM). This method utilises equilibrium reactions with balanced like charges to extrapolate over temperature (see, *e.g.*, Oscarson *et al.*, 1988; Papangelakis, 2004). Lindsay (1980), referring to these reactions as isocoulombic equilibria, found that their heat capacity is usually relatively constant with temperature. Substitution of Equations 2.40 and 2.41 into Equation 2.37 and simplifying, yields the following relationship, which is used to test the validity of the BLCM:

$$\Delta G^{o}_{T} = \Delta G^{o}_{T_r} - \Delta S^{o}_{T_r}(T - T_r) + \Delta C^{o}_{p}\left(T - T_r - T \cdot ln\frac{T}{T_r}\right) \qquad 2.42$$

If the BLCM is found to be valid, Equation 2.36 may be used to calculate the equilibrium constant.

Zero heat capacity

When no heat capacity data are available, it is often assumed to be zero, *i.e.*, the enthalpy of the reaction is assumed to be constant, and integration of Equation 2.33 then yields

Stellenbosch University http://scholar.sun.ac.za

$$ln\,K^{o} = ln\,K^{o}_{T_r} - \frac{\Delta H^{o}_{T_r}}{R_g}\left(\frac{1}{T} - \frac{1}{T_r}\right) \qquad 2.43$$

This approximation is usually only valid over a very short temperature range.

Other extrapolation techniques

Instead of using Equation 2.43, a more accurate approach may be to consider predictive models to estimate the average heat capacity between T and T_r, such as the method of Criss and Cobble (see Zemaitis *et al.*, 1986). This method is, however, questionable when applied the non-simple cations (like metal sulfate ions) and metal-oxy-anions (like the bisulfate ion) (Blakey & Papangelakis, 1996). Alternatively, a close approximation of the value of K^{o} may be obtained using Helgeson extrapolation (see original references in Liu & Papangelakis, 2005a). However, this method may give an over-estimation at higher temperatures (>100ºC) (Papangelakis, 2004).

Density function

The Density function (Anderson *et al.*, 1991) is remarkably accurate in estimating equilibrium constants of reactions at higher temperatures when the molal heat capacity value is known at the reference temperature. The model is based on the observation of almost linear behaviour of $ln\,K°$ with $ln\,\rho$ and adopts the form as presented in Equation 2.44:

$$ln\,K^{o} = ln\,K^{o}_{T_r} - \frac{\Delta H^{o}_{T_r}}{R_g}\left(\frac{1}{T} - \frac{1}{T_r}\right) + \frac{\Delta C^{o}_{p,T_r}}{R_g T_r (\partial\alpha/\partial T)_{P_r}} \cdot \left(\frac{1}{T} ln\frac{\rho_{T_r}}{\rho} - \frac{\alpha_{T_r}}{T}(T - T_r)\right) + \frac{\Delta a}{R_g}\left(ln\frac{T}{T_r} + \frac{T_r}{T} - 1\right) + \frac{\Delta b}{2R_g}\left(T + \frac{T_r^2}{T} - 2T_r\right) + \frac{\Delta c}{R_g}\left(\frac{-T^2 - T_r^2 + 2TT_r}{2T^2T_r^2}\right) \qquad 2.44$$

The density (ρ) and coefficient of thermal expansion (α) of water are well documented, *e.g.*, the study of Anderson *et al.* (1991). The two terms on the first line refer to the solute species, whereas the three terms on the second line encapsulate the influence of solid phases.

2.3.2 Thermodynamic framework based on quantum-level calculations

The above relationships illustrate the importance of realistic partial molal properties at the reference temperature (25ºC). As mentioned before, only the CIPs that are most likely to impact on the kinetic processes are explicitly recognised in this study. The results of quantum chemistry calculations under the transcendent condition of infinite dilution are now used to gain some insight into these CIP formation reactions, albeit semi-quantitatively, and attempt to add more confidence to the ambiguous nature of the published thermodynamic data. A basic understanding of ion solvation is an essential part of this analysis. An ion in water may be considered to be surrounded by concentric shells of water molecules, where the successive shells become more weakly bound to

Stellenbosch University http://scholar.sun.ac.za

the preceding shells until a bulk water structure is reached (Pye & Rudolph, 1998). The concept of the hydration shell has been verified for cations and anions by spectroscopic measurement and is also supported by quantum-level calculations (*e.g.*, Pye & Rudolph, 2001).

Calculation methodology

Density function theory (DFT)

All quantum-level calculations are carried out using the DMol^3 (Delley, 1990) density function theory (DFT) code imbedded in the *Materials Studio* (*MS*, Release 4.2) quantum chemistry package from Accelrys Software Inc (2008), *i.e.*, the calculations are conducted within the Kohn-Sham formulism (Kohn & Sham, 1965). In order to increase the accuracy when optimising the transition metal complexes, an all-electron scalar relativistic basis set is employed. The gradient correction method (gradient-generalised approximation, GGA) is employed throughout, utilising two DFT Hamiltonians, *i.e.*, the local spin density (LSD) method, utilising the Vosko *et al.* (1980) (VWN) parameterisation of the Ceperley-Alder Monte Carlo result for a homogeneous gas, and the non-local spin density (NLSD) method, utilising a combination of the Becke (B) gradient-corrected exchange energy (Becke, 1988) and the Perdew (P) gradient-corrected correlation energy (Perdew & Wang, 1992). Fully self-consistent field (SCF) calculations are conducted using the VWN-BP functional throughout. High quality double numerical atomic basis sets including polarisation functions (DNP) are used throughout, *i.e.*, to yield best accuracy, especially since hydrogen bonding is an important aspect of this study. Because these functions are treated numerically (rather than analytically) in DMol^3, basis set superposition errors (BSSE) are minimised (Delley, 1990; *MS*, 2008, help file). The aim of this chemical modelling exercise is more qualitative in nature and no additional effort is therefore expended to quantify the effect of BSSE errors or to test alternative basis sets or exchange-correlation functionals.

Conductor-Like Screening Model (COSMO)

The Conductor-Like Screening Model (COSMO) (Klamt & Schüürman, 1993) is used to account for long-range electrostatic solvent effects, using the dielectric constant of pure water. COSMO is an example of a continuum solvent model where the solvent molecules are not treated explicitly but are expressed as a homogeneous medium characterised by a bulk dielectric constant. The effect of the solvent may be modelled by imposing charges on the continuum surface, which leads to a polarisation of the wave function within the solute cavity (Ziegler & Autschbach, 2005). Whereas the electronic structure and geometry of the solute are treated on a quantum-level (DFT), the electrostatic impact of the bulk solvent is treated classically. The solute is placed inside a cavity which is determined by the solvent-accessible surface area of the solute. Outside of the cavity, the solvent is represented by a homogeneous dielectric medium (Andzelm *et al.*, 1995). The approach followed in this study is based on the default DMol^3-COSMO recommendations imbedded within

Stellenbosch University http://scholar.sun.ac.za

the software. The DMol^3-COSMO model can predict solvation energies for neutral solutes with accuracy better than 10 J/mol (Andzelm *et al.*, 1995) and has been tested extensively (Andzelm *et al.*, 1995; Klamt & Schüürman, 1993).

Explicit recognition of the first hydration shell

Although continuum models are effective when the impact of the solvent is predominantly electrostatic in nature, the lack of an explicit solvent treatment is an oversimplification and neglects specific information on intermolecular interactions, such as hydrogen bonding in the first hydration shell. In this study, the total coordination of a solute is restricted by explicitly using water as a coordination filling species in its first hydration shell, while treating the effect of the solvent beyond this level *via* the COSMO methodology. The most energetically stable structures are confirmed to be minima *via* analytic second-derivative calculation.

Basis of comparison with the literature

Since the entropy of the solvated species cannot be obtained using the above methodology, as well as the difficulties associated with obtaining the vibrational energy, the enthalpy rather than the total free energy forms the basis of comparison with the reported literature values. This approach is based on the assumption that the enthalpy can be represented by the potential energy (E_p), *i.e.*, it assumes that the kinetic energy (translational, rotational, *etc.*) cancels approximately between the solvated reactant and product species at constant temperature. All calculations are conducted from a static viewpoint, which is sufficient for the purpose of this study, *i.e.*, this first principles (*ab initio*) approach is meant to be semi-quantitative in nature, but of sufficient quality to guide the selection of the important equilibria and their thermodynamic properties.

Ab initio calculation results and the resulting thermodynamic framework

The objective of the following discussion is to create an internally consistent thermodynamic framework for the key solute species, while maintaining consistency with the reported standard state properties at infinite dilution in water, *e.g.*, the National Bureau of Standards (NBS) tables (Wagman *et al.*, 1982).

Hydrated proton

Within the context of the conventionally defined zero Gibbs energy of formation of the hydrated proton, the hydrogen electrode is the appropriate starting point. The absolute electrode potential in electrochemistry is the difference in electronic energy between the Fermi-level energy of a metal electrode and a universal reference system *in vacuo* (Trasatti, 1986). The standard hydrogen electrode (SHE) is a redox half cell and forms the basis of the thermodynamic scale of oxidation-reduction potentials:

Stellenbosch University http://scholar.sun.ac.za

$$H^{+}_{(aq)} + e^{-} \Leftrightarrow \tfrac{1}{2}H_{2(g)} \qquad 2.45$$

This reaction can be achieved at a practical level with the use of a platinum electrode, because it possesses the ability to catalyse the reduction of the proton to form hydrogen gas at a high exchange current density, and *vice versa*. The recommended value of the absolute electrode potential of this cell in water, often referred to as the vacuum-scale potential, is 4.44±0.02 V at 25ºC (Trasatti, 1986). This number is the required link between the electrochemical potential scale and the physical energy scale. Reported literature values vary considerably for such an important quantity, with an average around 4.6 V (see Bockris & Khan, 1993). Furthermore, the exact nature of the hydrated proton is clouded by the fact that the proton is geometrically very small and forms fluctuating bonds in the highly structured, hydrogen-bonded network of water (Marx *et al.*, 1999). Although both the $H_5O_2^+$ and $H_9O_4^+$ species might exist in a dilute chemical environment, these authors emphasised that such a description is only important in the sense of ideal structures. Numerous unclassifiable situations exist in between so that an unambiguous distinction between these species cannot be achieved. Senanayake and Muir (1988) used EMF measurement (with some 'extra'-thermodynamic assumptions) in chloride media to estimate ionic activities and hydration numbers. The hydration number of seven, obtained for the proton in dilute solution, indicated further hydration beyond the first hydration shell. Based upon the acidity function and other physical evidence (Bell, 1959; Bockris & Reddy, 1977), the existence of well-defined species only predominates in strongly acidic solutions.

In view of these complexities, a thermodynamic basis for the hydrated proton may be defined by comparing the calculated enthalpy of hydration with reported literature values. The thermochemical Born-Haber (BH) cycle (Atkins & De Paula, 2006) consists of atomising the gas ($\Delta H°_{at}$), ionising the gas ($\Delta H°_{ion}$), followed by solvation in water medium ($\Delta H°_{hyd}$), and finally, reduction on a platinum electrode ($\Delta H°_{red}$), to again form hydrogen gas:

$$\begin{array}{ccc} H_{(g)} & \xrightarrow{\Delta H^{o}_{ion}} & H^{+}_{(g)}\ (+e^{-}) \\ \uparrow \Delta H^{o}_{at} & & \downarrow \Delta H^{o}_{hyd} \\ \tfrac{1}{2}H_{2(g)} & \xleftarrow{\Delta H^{o}_{red}} & H^{+}_{(aq)}\ (+e^{-}) \end{array} \qquad 2.46$$

The hydrated isomer structures are arranged in order of increasing degree of hydration in Figure 2.1, while Table 2.1 compares the calculated and literature values of the total ionisation enthalpy of the gas molecule, $H_{2(g)}$, the free enthalpy of hydration of the gas ion, $H^{+}_{(g)}$, and the reduction enthalpy of the hydrated proton, $H^{+}(H_2O)_n$, with all values normalised to 1 mol hydrogen atom.

Stellenbosch University http://scholar.sun.ac.za

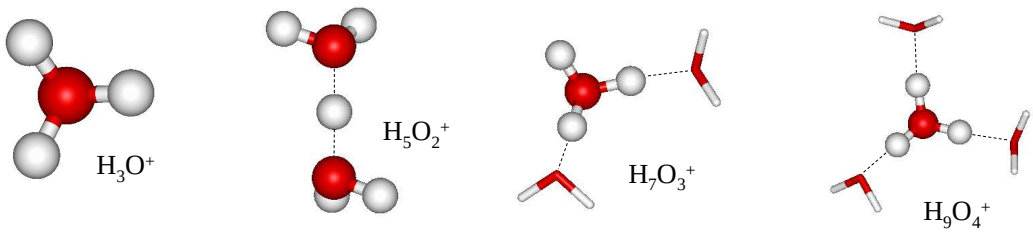

Figure 2.1
Geometrically optimised isomer structures of $H^+(H_2O)_n$ (n = 1 to 4) in H_2O at 25°C (ε_w = 78.38).

Table 2.1
Calculated & literature values of the various energy contributions (kJ/mol H) to the BH cycle for the SHE in H_2O at 25°C (ε_w = 78.38).

BH cycle	$\Delta E_{p,rx\ (calc.)}$	$(H_2O)_1$	$(H_2O)_2$	$(H_2O)_3$	$(H_2O)_4$	Reference
$\Delta H°_{at} + \Delta H°_{ion}$	1543					[a] 1536
$\Delta H°_{hyd}$	-524	**-1081**	**-1147**	-1185	-1216	[b] -1103
$\Delta H°_{red}$	-1019	**-462**	**-396**	-358	-327	[c] -424

All calculations based on a single optimised E_p value (-76.6240464 hartrees) for a H_2O molecule in the dielectric continuum. [a] Wagman *et al.* (1982); [b] Marcus (1987); [c] Corresponds to $E°_{red\ (avg)}$ = 4.6 V from Bockris & Khan (1993), using Eq. 2.48 & $\Delta S°_{red}$ = 131 J/mol.K $H_{2\ (g)}$[(a)].

Comparison between the calculated and literature values (of $\Delta H°_{hyd}$) points to either the H_3O^+ or the $H_5O_2^+$ species (highlighted in bold), prompting the following thermodynamic basis:

$$H_3O^+_{(aq)} + H_5O^+_{7(aq)} + 2e^- \Leftrightarrow H_{2(g)} + 3H_2O_{(aq)} \qquad 2.47$$

This approach yields a $\Delta H°_{hyd}$ value of -1114 kJ/mol $H^+_{(aq)}$ and a $\Delta H°_{red}$ value of -859 kJ/mol $H_{2(g)}$. The standard EMF of a redox reaction (E°) is directly related to its enthalpy and entropy values *via* the standard Gibbs free energy (Atkins & De Paula, 2006):

$$\Delta G^o = -|z|FE^o = \Delta H^o - T \cdot \Delta S^o \qquad 2.48$$

An entropy value of 131 J/mol.K (Wagman *et al.*, 1982), for the reaction $2H^+_{(aq)} + 2e^- \rightarrow H_{2(g)}$, yields an $E°_{red}$ value of 4.6(5) V (*ref.* an electron at rest *in vacuo*), which is in excellent agreement with the average value reported by Bockris and Khan (1993) of 4.6 V.

Sulfur reference

A thermodynamic basis is also required for all aqueous sulfur species. The difficulty in modelling a unit cell of rhombic sulfur (the reference in Wagman *et al.*, 1982) prompted a more direct approach, *i.e.*, the enthalpy of dilution of concentrated sulfuric acid, according to the following description, where the ions refer to the formal species in excess water:

$$H_2SO_{4(\ell)} \Rightarrow 2H^+_{(aq)} + SO^{2-}_{4\,(aq)} \qquad 2.49$$

Stellenbosch University http://scholar.sun.ac.za

The structure of a H_2SO_4 molecule in concentrated sulfuric acid solution consists of extensive hydrogen bond networks. This is evident from its exceptionally high dielectric constant (ε_ℓ) of 110 (Lide, 1991). Kazansky and Solkan (2003) used *ab initio* quantum chemical calculations, whilst Walrafen *et al.* (2000) used experimental methods to show that these hydrogen bonds form ionic clusters. These localised structures may be cationic, anionic or neutral in nature, *e.g.*, in the case of the dimer, $(H_3SO_4\ H_2SO_4)^+$, $(HSO_4\ H_2SO_4)^-$ or $(2{\cdot}H_2SO_4)°$, respectively. The modelling of periodic structures, using a number of interacting molecules (*e.g.*, Arrouvel *et al.*, 2005), would obviously yield the best results. In the context of this study, only the most stable electro-neutral complexes, similar to the structures reported by Kazansky and Solkan (2003), are considered. These optimised symmetrical monomeric, dimeric and trimeric complexes are illustrated in Figure 2.2, while their corresponding molecular energies are represented in Table 2.2.

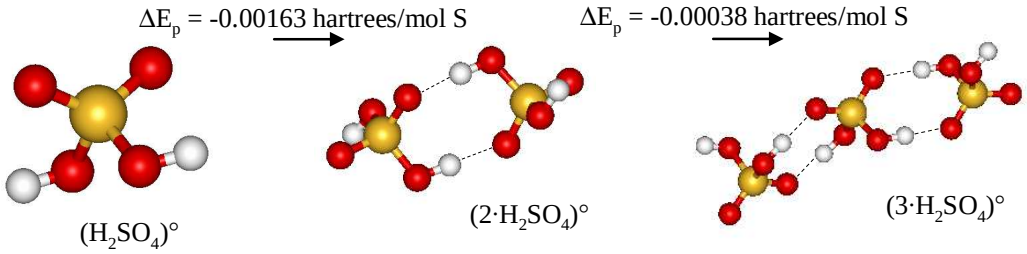

Figure 2.2
Geometrically optimised structures of $(n{\cdot}H_2SO_4)°$ (n = 1 to 3) in 100% $H_2SO_{4\,(\ell)}$ at 25°C (ε_ℓ = 110).

Table 2.2
Geometrically optimised molecular energies & hydrogen bond lengths of $(n{\cdot}H_2SO_4)°$ (n = 1 to 3) in 100% $H_2SO_{4\,(\ell)}$ at 25°C (ε_ℓ = 110).

Molecule	$E_{p\,(calc.)}$ (hartrees)	$\Delta E_{p\,(calc.)}$ (hartrees/mol S)	H-bond O–O length (Å)	H-bond O–H length (Å)
$(H_2SO_4)°$	-702.0775021	–	–	–
$(2{\cdot}H_2SO_4)°$	-1404.1582559	-0.0016259	2.74 (avg.)	1.72(min), 1.74(max)
$(3{\cdot}H_2SO_4)°$	-2106.2385225	-0.0003795	2.74 (avg.)	1.70 (min), 1.78(max)

The average calculated O−O bond length of 2.74Å is comparable to the experimentally observed average distance of around 2.9Å (Walrafen *et al.*, 2000), while the average O−H bond length of 1.74Å is close to the average calculated value of Kazansky and Solkan (2003) of 1.8Å. The trimer is assumed to be sufficiently stable (ΔE_p) to justify its use as a first-estimate thermodynamic basis for the sulfur-containing solutes in water.

Hydrated sulfate ion

Pye and Rudolph (2001) proposed that water coordinates with the sulfate ion in a bidentate fashion to form two hydrogen bonds per pair of sulfate oxygen atoms. However, comparison between

Stellenbosch University http://scholar.sun.ac.za

calculated and experimental S–O bond lengths suggested that more than six waters should be present in the primary hydration shell. Cannon *et al.* (1994) used *ab initio* calculations to show that, unlike most anions, the tetrahedral sulfate dianion can be considered to be a structure-making ion with respect to the solvent around it, with roughly three water molecules coordinated with each of the sulfate oxygen atoms. Water in the primary hydration shell is orientated with one hydrogen pointing towards the sulfate oxygen and the other hydrogen pointing towards the neighbouring water oxygen. Based on diffraction data, the number of waters in the first hydration shell of the sulfate ion varied between approximately six and fourteen. A more recent study by Vchirawongkwin *et al.* (2007) characterised the hydrated sulfate ion using *ab initio* quantum mechanical (QM) charge field (CF) – molecular dynamics (MD) simulation and large angle X-ray scattering (LAXS) methods. The LAXS data revealed an average coordination number of up to twelve, while the QMCF-MD simulation displayed a range between eight and fourteen. Experimental investigations in several sulfate solutions (in Vchirawongkwin *et al.*, 2007) reported coordination numbers between six and eight. The study of Wang *et al.* (2000) indicated that an isolated sulfate ion is unstable in the gas phase due to the strong Coulomb repulsion between the two excess electrons, and a minimum of three water molecules is necessary to stabilise the dianion. In solution, around twelve water molecules were claimed to be present in the first hydration shell, with four water molecules each forming two direct hydrogen bonds with the sulfate oxygen atoms.

As pointed out by Cannon *et al.* (1994), the above wide range of values for the hydration number in the primary hydration shell exemplifies the difficulties involved in building solvation models for polyatomic ions. The more accurate approach would have been to use a QM-MD formulation, *e.g.*, as suggested by Sterzel and Autschbach (2006) and recently illustrated by Balasubramanian *et al.* (2011). Due to the qualitative nature of the calculations in this study and in order to maintain internal consistency, the (above) static methodology for the hydrated proton is also expanded to the hydrated sulfate ion (& its CIPs; see later).

The sulfate ion is a polyatomic group with the double charge evenly distributed over the four oxygen atoms in tetrahedral symmetry. The hydrogen bond network in this first shell must therefore adopt the geometry imposed by this sulfate group (Gao & Liu, 2004). All the above references suggested at least six waters in the first hydration sphere. Therefore, the initial optimisations of this study utilised the T_d structure of Pye and Rudolph (2001), *i.e.*, the starting structure consisted of six water molecules, each acting as a bidentate hydrogen bond donor to two sulfate oxygen atoms. Various preliminary optimisations were conducted, each time modifying the starting structure slightly. On each occasion the structure relaxed to form only one direct hydrogen bond (per water molecule) with sulfate oxygen, while the other hydrogen orientated itself towards the dielectric continuum. However, at least one and often two water molecules donated their ‘free’

Stellenbosch University http://scholar.sun.ac.za

hydrogen to other water oxygen atoms (in close proximity). The water molecules would therefore be expected to form clusters in the primary hydration sphere. In fact, as illustrated by Gao and Liu (2004), the geometrical coincidence of the sulfate group, with its tetrahedron structure, forms cyclic rings (up to three water molecules) to accommodate more water in the primary hydration shell. They considered up to twelve water molecules in the primary hydration shell at 100 K, using MD simulations. However, when the induced conditions approached 200 K, a 'crowding-out' of the first hydration shell was observed, with four molecules moving to the second shell and eight remaining in the primary hydration shell.

With this in mind, the water molecules are arranged in two- or three-water clusters. For example, with six molecules in the primary hydration shell, either two clusters of three water molecules or three clusters of two water molecules could be considered. As would be expected, the highest combination of three-water clusters always resulted in the lower overall energy for the total structure. In most cases, one of the water molecules in these clusters orientated itself towards the dielectric continuum during further geometric optimisation, which is in line with the observations of Gao and Liu (2004). The following reaction represents the dilution of concentrated sulfuric acid in a large excess of water:

$$H_2SO_{4(\ell)} + (3+n)H_2O_{(aq)} \Rightarrow H_3O^+_{(aq)} + H_5O^+_{7(aq)} + SO_4^{2-}(H_2O)_{n(aq)} \qquad 2.50$$

The unsymmetrical nature of the less hydrated complexes, *e.g.* six or seven waters in the primary hydration shell, makes them unlikely candidates at infinite dilution. Figure 2.3 presents the optimised structures with eight water molecules in the primary hydration shell. The geometrically optimised energies ($6 \leq n \leq 9$) are listed in Table 2.3. The best agreement with literature (highlighted in bold) corresponds to the second isomer in Figure 2.3. Although these optimised energies do not necessarily represent absolute global minima, further 'modification' resulted in only a marginal improvement of ΔE_p (*ref.* Rx. 2.50).

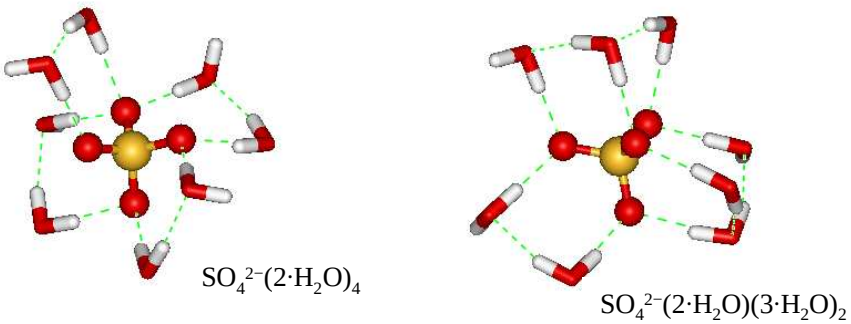

Figure 2.3
Geometrically optimised structures of $SO_4^{2-}(H_2O)_8$ isomers in H_2O at 25°C (ε_w = 78.38).

Stellenbosch University http://scholar.sun.ac.za

Table 2.3
Geometrically optimised energies of $SO_4^{2-}(H_2O)_n$ (n = 6 to 9) in H_2O at 25°C (ε_w = 78.38), & comparing the corresponding reaction values with the dilution enthalpy (ΔH^o_{dil}) of $H_2SO_{4\,(\ell)}$.

n	$E_{p\,(calc.)}$ (hartrees)	[a] $\Delta E_{p,rx\,(calc.)}$ (kJ/mol)	[b] $\Delta H°_{dil\,(litr.)}$ (kJ/mol)
$SO_4^{2-}(2{\cdot}H_2O)_3$	-1160.989182	-38.8 (n = 6)	-95.3
$SO_4^{2-}(3{\cdot}H_2O)_2$	-1160.993309	-49.6 (n = 6)	-95.3
$SO_4^{2-}(2{\cdot}H_2O)_2(3{\cdot}H_2O)$	-1237.624055	-67.2 (n = 7)	-95.3
$SO_4^{2-}(2{\cdot}H_2O)_4$	-1314.254551	-84.1 (n = 8)	-95.3
$SO_4^{2-}(2{\cdot}H_2O)(3{\cdot}H_2O)_2$	-1314.260114	**-98.7** (n = 8)	**-95.3**
$SO_4^{2-}(2{\cdot}H_2O)_3(3{\cdot}H_2O)$	-1390.889044	-111.6 (n = 9)	-95.3
$SO_4^{2-}(3{\cdot}H2O)_3$	-1390.894635	-126.2 (n = 9)	-95.3

All calculations based on a single optimised E_p value (-76.6240464 hartrees) for a H_2O molecule in the dielectric continuum. [a] Rx. 2.50; [b] Wagman *et al.* (1982).

If more than eight water molecules occupy the primary hydration sphere, bonding is likely to be less structured than depicted by the static snapshots in Figure 2.3. This could be the reason for the more negative (calculated) $\Delta H°_{hyd}$ value of the sulfate ion ($SO_4^{2-}{}_{(g)} + 8H_2O_{(aq)} \rightarrow SO_4^{2-}(H_2O)_{8(aq)}$) of -1213 kJ/mol (*ref.* $\Delta H°_{hyd}$ = -1114 kJ/mol H^+; Rx. 2.47) as compared to the average reported value of -1026 kJ/mol (Marcus, 1987; *ref.* $\Delta H°_{hyd}$ = -1103 kJ/mol H^+).

Hydrated bisulfate and neutral acid species

The nature of the hydrated bisulfate (HSO_4^-) and neutral acid ($H_2SO_4°$) species is discussed next. In view of the strong interaction between the hydrated proton and sulfate oxygen, the net reduction in the total anionic charge, as well as the asymmetrical geometries of these species, fever water molecules would be expected in their primary hydration shells (*cf.* the sulfate dianion). The association of the hydrated sulfate and bisulfate ions with the hydrated proton, *i.e.*, the protonation reactions, are represented by the following two reactions, respectively:

$$H_3O^+_{(aq)} + H_5O^+_{7(aq)} + 2SO_4^{2-}(H_2O)_{8(aq)} \Leftrightarrow 2HSO_4^-(H_2O)_{n(aq)} + (19-2n)H_2O_{(aq)} \qquad 2.51$$

$$H_3O^+_{(aq)} + H_5O^+_{7(aq)} + 2HSO_4^-(H_2O)_{n(aq)} \Leftrightarrow 2H_2SO_4^o(H_2O)_{2(aq)} + (2n-1)H_2O_{(aq)} \qquad 2.52$$

Walrafen *et al.* (2000) suggested three or four water molecules in association with the bisulfate species in more dilute acid environment. In order to find the optimum hydration structure for the bisulfate species, water molecules (not associated with the proton) are arranged in either two- or three-water clusters, similar to the approach followed for the sulfate dianion. The dilution enthalpy may therefore be compared to energy released by the following general reaction:

$$2H_2SO_{4(\ell)} + (3+n)H_2O_{(aq)} \Rightarrow H_3O^+_{(aq)} + H_5O^+_{7(aq)} + 2HSO_4^-(H_2O)_{n(aq)} \qquad 2.53$$

Stellenbosch University http://scholar.sun.ac.za

With reference to the neutral acid molecule, the measured Raman frequencies of Walrafen *et al.* (2000) point to strong hydrogen bonding resulting from direct H_3O^+-HSO_4^- ion pair interaction. In order to be consistent with the way in which the hydration of the proton is dealt with, a single water molecule is bound to both O–H pairings (of the optimised $H_2SO_4°$ structure), *i.e.*, to form two –O–$H_3O^{(+)}$ groups, and then optimised further. The calculated reaction energies and equilibrium constants are compared to the corresponding literature values in Table 2.4, while the optimised bisulfate and neutral species structures are represented in Figure 2.4.

Table 2.4
Geometrically optimised energies of $HSO_4^-(H_2O)_n$ (n = 3 to 5) & $H_2SO_4°(H_2O)_2$ in H_2O at 25°C (ε_w = 78.38), the corresponding reaction values & equilibrium constants, & comparison with the corresponding literature protonation constants & dilution enthalpy ($\Delta H°_{dil}$) of $H_2SO_{4\,(\ell)}$.

Species	$E_{p\,(calc.)}$ (hartrees)	[a] $½\Delta E_{p,rx\,(calc.)}$ (kJ/mol)	[c] $\Delta H°_{dil\,(litr.)}$ (kJ/mol)	$log(K°)_{(calc.)}$	$log(K°)_{(litr.)}$
$(H_2O)HSO_4^-(2{\cdot}H_2O)$ (a)	-931.546511	-51.3 (n = 3)	-73.35	–	
$(H_2O)HSO_4^-(2{\cdot}H_2O)$ (b)	-931.547928	-55.1 (n = 3)	-73.35	–	
$(H_2O)HSO_4^-(3{\cdot}H_2O)$	-1008.180816	**-78.3** (n = 4)	**-73.35**	[d] 2.2	[c] 1.99; [f] 1.96
$(H_2O)HSO_4^-(2{\cdot}H_2O)_2$ (a)	-1084.809288	-89.9 (n = 5)	-73.35		
$(H_2O)HSO_4^-(2{\cdot}H_2O)_2$ (b)	-1084.811148	-94.8 (n = 5)	-73.35		
$(H_2O)_2H_2SO_4°$	-855.3544882	[b] **7.7** (n = 4)	–	[e] -1.3	[g] -4.7 to -2.0

[a] Rx. 2.53; [b] Rx. 2.52; [c] Wagman *et al.* (1982); [d] $½\Delta E_p$ (Rx. 2.51) & $\Delta S°_{rx}$ = 111.7 J/mol.K [(c)]; [e] $½\Delta E_p$ (Rx 2.52) & $\Delta S°_{rx}$ = 0 J/mol.K (assumed); [f] Dickson *et al.* (1990); [g] Perrin (1982).

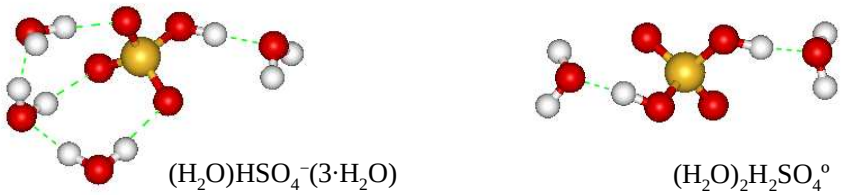

$(H_2O)HSO_4^-(3{\cdot}H_2O)$ $(H_2O)_2H_2SO_4°$

Figure 2.4
Geometrically optimised structures of $HSO_4^-(H_2O)_4$ & $H_2SO_4°(H_2O)_2$ in H_2O at 25°C (ε_w = 78.38).

Taking into consideration the assumptions made thus far, the calculated pK'_2 of 2.2 is in good agreement with the values listed in the literature (~2). This calculation includes a reaction entropy ($\Delta S°_{rx}$) value of 111.7 J/mol.K (Wagman *et al.*, 1982). The calculated pK'_1 of -1.3 (assuming $\Delta S°_{rx}$ = 0 J/mol.K) is higher than most values listed in the literature, but may be considered acceptable in view of the wide spread of the reported values (see Figure 2.11 *b*). In conclusion, the above results suggest that the hydrated sulfate ion, $SO_4^{2-}(H_2O)_8$, sheds half its water upon protonation to form the $HSO_4^-(H_2O)_4$ species, and then another half upon further protonation to form the neutral $H_2SO_4°(H_2O)_2$ species.

Stellenbosch University http://scholar.sun.ac.za

Hydrated divalent metal cation

Magnesium fulfilled the role of surrogate metal for all the other divalent metal ions in solution in this study (see later). The thermodynamic basis for this ion is its pure metal crystal phase. This alkaline earth element has a hexagonal crystal structure at 25°C and the unit cell (q = 2) is modelled using space group P63/mmc and experimental cell dimensions (a = 3.2088Å; c = 5.2099Å) from the *Inorganic Crystal Structure Database* (*ICSD*, 2008). The optimised potential energy (-400.837182 hartrees) and cell dimensions (a = 3.1811Å; c = 5.1493Å) are obtained using periodic DFT calculation, while keeping the number of k points within reasonable limits. The cohesive energy (E_{coh}) is obtained after calculating the optimised energy of the magnesium atom *in vacuo* (-200.360445 hartrees):

$$E_{coh} = \frac{E_{metal}}{q} - E_{atom} \qquad 2.54$$

The calculated value of -1.58 eV compares well with the literature value of -1.51 eV (Kittel, 1996). The energy required to decompose the metal into a single atom (atomisation) is thus 153 kJ/mol and this is in close agreement with literature (Table 2.5). The complete thermochemical BH cycle for the divalent metal cation (M) may be represented as follows:

$$\begin{array}{ccc} M_{(g)} & \xrightarrow{\Delta H^{o}_{ion}} & M^{2+}_{(g)}\ (+2e^{-}) \\ \uparrow \Delta H^{o}_{at} & & \downarrow \Delta H^{o}_{hyd} \\ M_{(s)} & \xleftarrow{\Delta H^{o}_{red}} & M^{2+}_{(aq)}\ (+2e^{-}) \end{array} \qquad 2.55$$

A comparison between the calculated gas-phase energies of the magnesium ion (-199.533566 hartrees) and the atom (above) yields an ionisation energy of 2171 kJ/mol, which also compares well with the literature (Table 2.5).

Table 2.5
Calculated energy contributions (kJ/mol) to the BH cycle for divalent Mg & Fe (per mol metal) in H_2O at 25°C (ε_w = 78.38), & comparison to the corresponding literature values.

BH cycle	**Mg** $\Delta E_{p,rx\ (calc.)}$	Literature (kJ/mol)	**Fe** $\Delta E_{p,rx\ (calc.)}$	Literature (kJ/mol)
$\Delta H°_{at}$	153	[e] 148	687	[e] 416
$\Delta H°_{ion}$	2171	[e] 2201	2199	[e] 2334
$\Delta H°_{hyd}$	[a] -1961	[f] -1949	[a] -2107	[f] -1972; [i] -2177
$\Delta H°_{red}$	[b] -362; [c,d] -2.51V	[g] -2.36V	[b] -779; [h,d] -0.36V	[g] -0.44V

[a] Rx. 2.56; [b] Rx. 2.57 (*ref.* electrons at rest *in vacuo*); [c] $E°_h$; $\Delta S°_{red}$ = 171 J/mol.K Mg [(e)]; [d] *Ref.* Eq. 2.48, $\Delta H°_{red}$ = -859 kJ/mol $H_{2\ (g)}$, $\Delta S°_{red}$ = 131 J/mol.K $H_{2\ (g)}$ [(e)]; [e] Wagman *et al.* (1982); [f] Marcus (1987; $\Delta H°_{hyd}$ = -1103 kJ/mol H^+); [g] Atkins & De Paula (2006); [h] $E°_h$; $\Delta S°_{red}$ = 165 J/mol.K Fe [(d)]; [i] Remsungnen & Rode (2004; calc.).

Stellenbosch University http://scholar.sun.ac.za

The ferrous cation, Fe^{2+}, is an important solute species in this study and in order to test the validity of the (magnesium) surrogate salt approach (see later), it is treated in analogous fashion to the magnesium cation. Although the optimised cell dimensions (a = 2.4739Å; c = 3.9084Å; potential energy = -2541.965845 hartrees) compare well with the experimental cell dimensions (a = 2.473Å; c = 3.962Å) (*ICSD*, 2008), some discrepancy with the literature (Table 2.5) appears to be associated with the calculated energy of the iron atom *in vacuo* (-1270.721106 hartrees), yielding an atomisation energy of 687 kJ/mol (Eq. 2.54). However, its context within this study it did not warrant further optimisation, especially since the calculated Fe–O distance of 2.11Å of the octahedral solute species (Figure 2.5) is in close agreement with the experimental value of 2.12Å (Remsungnen & Rode, 2004). In addition, the calculated energy of the ferrous ion *in vacuo* (-1269.883622 hartrees) yields an ionisation energy of 2199 kJ/mol, which lies within experimental error (10%) of the literature value.

Divalent transition metal cations are strongly hydrated at room temperature in a dilute aqueous environment and hydration arrangements consist of six waters in an octahedral arrangement in the primary hydration shell (Horvath, 1985; Pye & Rudolph, 1998; Remsungnen & Rode, 2004; Rudolph *et al.*, 2003). The geometrically optimised structures of aqueous magnesium (-660.024857 hartrees) and iron(II) (-1730.430504 hartrees) are illustrated in Figure 2.5, corresponding to the following general hydration and reduction reactions, respectively:

$$M^{2+}_{(g)} + 6H_2O_{(aq)} \Leftrightarrow M^{2+}(H_2O)_{6(aq)} \qquad 2.56$$

$$M^{2+}(H_2O)_{6(aq)} + 2e^- \Leftrightarrow M_{(s)} + 6H_2O_{(aq)} \qquad 2.57$$

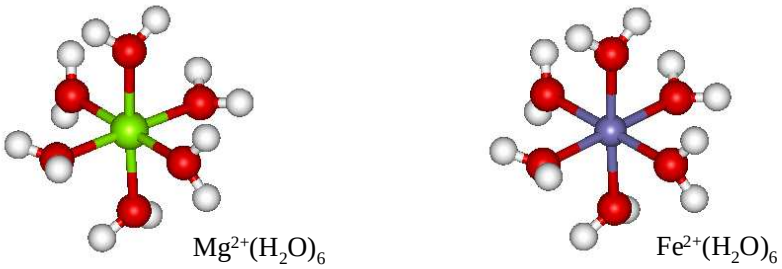

Figure 2.5
Geometrically optimised structures of $Mg^{2+}(H_2O)_6$ & $Fe^{2+}(H_2O)_6$ in H_2O at 25°C (ε_w = 78.38).

The free enthalpy of hydration of both the metal gas ions is seen to be in excellent agreement with the corresponding literature values (Table 2.5). The standard EMF of the cell with reference to the SHE ($E°_h$) is readily obtained from Equation 2.48. For example, in the case of the reduction of the aqueous Mg^{2+} ion, the enthalpy change is approximated by the calculated ΔE_p values, *i.e.*, -362-(-859) = 497 kJ/mol. The entropy change for the reduction reaction is based on the reported literature

Stellenbosch University http://scholar.sun.ac.za

values (Wagman *et al.*, 1982), *i.e.*, 171-131 = 40 J/mol.K, yielding an $E°_h$ value of -2.51 V. This is reasonably close to the literature value of -2.36 V (Atkins & De Paula, 2006). Similarly, the $E°_h$ value of the aqueous Fe^{2+} ion is calculated as -0.36 V, which is in good agreement with the literature value of -0.44 V, considering that no ΔE_k term has been included in these calculations.

First magnesium sulfate CIP

Internally consistent thermodynamic references have been established for the hydrated magnesium cation and the hydrated sulfate anion. The reaction between these solvated ions to form the first metal sulfate CIP, $MgSO_4°$, may therefore be evaluated, *i.e.*, for the general case:

$$M^{2+}(H_2O)_6 + SO_4^{2-}(H_2O)_8 \Leftrightarrow MSO_4^o(H_2O)_n + (14-n)H_2O \qquad 2.58$$

Considering the number of possible permutations of water molecules in the primary hydration shell of the CIP, a simplification is required. Since the primary hydration shell around the cation is comparatively stronger and more structured compared to the sulfate dianion, monodentate and bidentate bonding are assumed to release one and two water molecules around the cation, respectively. Therefore, in the case of monodentate CIP, the molecule may be represented as $(H_2O)_5MgSO_4°(H_2O)_{n-5}$. Three geometrically optimised structures (n = 8, 9 & 10, respectively) are illustrated in Figure 2.6, while their corresponding reaction energies are summarised in Table 2.6. As would be expected, the most stable structures are obtained with the sulfate tilted sideways and its oxygen atoms forming hydrogen bonds with two adjacent magnesium waters.

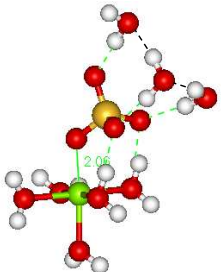

$(H_2O)_5MgSO_4°(3{\cdot}H_2O)$

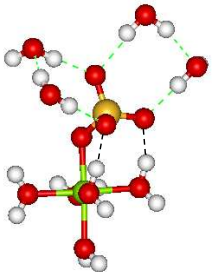

$(H_2O)_5MgSO_4°(2{\cdot}H_2O)_2$

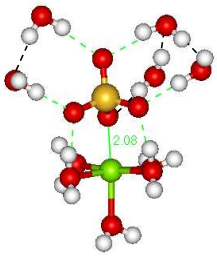

$(H_2O)_5MgSO_4°(2{\cdot}H_2O)(3{\cdot}H_2O)$

Figure 2.6
Geometrically optimised structures of monodentate $(H_2O)_5MgSO_4°(H_2O)_{n-5}$ (n = 8 to 10) in H_2O at 25°C (ε_w = 78.38).

Comparison with the reaction enthalpy of Akilan *et al.* (2006a) points to the second optimised structure in Figure 2.6, *i.e.*, n = 9. Dielectric spectroscopy (DRS) (Akilan *et al.*, 2006a) and ultrasonic relaxation values (Atkinson & Petrucci, 1966) have proven the existence of a stepwise mechanism, commonly referred to as the Eigen mechanism. The enthalpy and entropy terms in Table 2.6 for the overall reaction (Rx. 2.58) represent the sum of the thermodynamic contributions of each of these mechanistic steps which, in context of this study, are represented as follows:

Stellenbosch University http://scholar.sun.ac.za

$$\Delta G^{o}_{CIP} = \Delta G^{o}_{2SSIP} + \Delta G^{o}_{2SSIP/SSIP} + \Delta G^{o}_{SSIP/CIP} \quad 2.59$$

$$\Delta G^{o}_{2SSIP}: \quad M^{2+}(H_2O)_6 + SO_4^{2-}(H_2O)_{14} \Leftrightarrow M^{2+}(H_2O)_6(H_2O)_8SO_4^{2-} \quad 2.60$$

$$\Delta G^{o}_{2SSIP/SSIP}: \quad M^{2+}(H_2O)_6(H_2O)_8SO_4^{2-} \Leftrightarrow M^{2+}(H_2O)_mSO_4^{2-} + (14-m)H_2O \quad 2.61$$

$$\Delta G^{o}_{SSIP/CIP}: \quad M^{2+}(H_2O)_mSO_4^{2-} \Leftrightarrow MSO_4^{o}(H_2O)_n + (m-n)H_2O \quad 2.62$$

where 2SSIP refers to the double solvent-separated ion pair, $M^{2+}(OH_2)_6(OH_2)_8SO_4^{2-}$, and SSIP to the single solvent-separated ion pair, $M^{2+}(OH_2)_mSO_4^{2-}$. This mechanism presents a general description of the association of free hydrated ions to first form the 2SSIPs, then the SSIPs, and ultimately, the CIPs.

Table 2.6
Geometrically optimised energies of monodentate $(H_2O)_5MgSO_4{}^o(H_2O)_{n\text{-}5}$ (n = 8 to 10) in H_2O at 25°C (ε_w = 78.38), & comparing the corresponding equilibrium reaction values with the literature.

Species	$E_{p\ (calc.)}$ (hartrees)	[a] $\Delta E_{p,rx\ (calc.)}$ (kJ/mol)	[b] $\Delta H°_{rx\ (litr.)}$ (kJ/mol)	[a] *log* $K°_{(calc.)}$	*log* $K°_{(litr.)}$
$(H_2O)_5MgSO_4°(3{\cdot}H_2O)$	-1514.523722	44.6 (n = 8)	32	–	–
$(H_2O)_5MgSO_4°(2{\cdot}H_2O)_2$	-1591.154526	**26.7** (n = 9)	**32**	[c] 1.1 ([d] 2.2)	[e] 1.2
$(H_2O)_5MgSO_4°(2{\cdot}H_2O)(3{\cdot}H_2O)$	-1667.787060	-10.1 (n = 10)	32	–	–

[a] Rx. 2.58; [b] Akilan *et al.* (2006a); [c] $\Delta S°_{rx}$ = 110 J/mol.K [(b)]; [d] $\Delta S°_{rx}$ = 131 J/mol.K [(e)]; [e] Atkinson & Petrucci (1966).

The alternative value of $\Delta S°_{rx}$ = 131 J/mol.K refers to the ultrasonic relaxation data of Atkinson and Perucci (1966): the enthalpies for each of the Eigen reaction steps are fixed at the values reported by Akilan *et al.* (2006a), while the entropy is calculated (Eq. 2.36 & 2.48) to reflect the average equilibrium constant of Atkinson and Perucci (1966). This doubles the value of *log* K°, which illustrates the sensitivity of the equilibrium constant to the entropy change, a thermodynamic property that is not readily obtained from the DMol^3-COSMO methodology.

Second magnesium sulfate CIP

Various studies (*e.g.*, Rudolph *et al.*, 2003; Zhang *et al.*, 2002) have speculated on the possibility of bidentate CIP formation in the aqueous magnesium sulfate system. Two optimised structures are illustrated in Figure 2.7, while the corresponding energies are presented in Table 2.7. Although the reported thermodynamic values of the stepwise equilibria (Rx. 2.60, 2.61 & 2.62) are qualitative in nature (Akilan *et al.*, 2006a), comparison of the calculated energies with the overall reaction (Rx. 2.58) enthalpy suggests that the second magnesium sulfate CIP could be this bidentate species, rather than the triple ion pair (TIP), $Mg_2SO_4^{2+}$. On the other hand, the formation of this TIP is also supported by the Raman spectroscopy (RS) study of Rudolph *et al.* (2003).

Stellenbosch University http://scholar.sun.ac.za

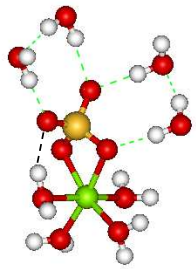

$(H_2O)_4MgSO_4°(2{\cdot}H_2O)_2$

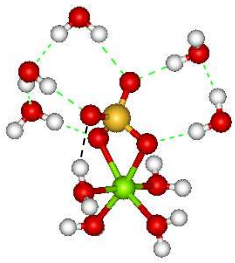

$(H_2O)_4MgSO_4°(2{\cdot}H_2O)\ (3{\cdot}H_2O)$

Figure 2.7
Geometrically optimised structures of bidentate $(H_2O)_4MgSO_4°(H_2O)_{n-4}$ (n = 8 to 9) in H_2O at 25°C (ε_w = 78.38).

However, the formation of the corresponding anion, $Mg(SO_4)_2^{2-}$, cannot be ruled out. This is because the geometry of this TIP is close to linear (Figure 2.8) and therefore has a zero dipole moment, *i.e.*, it cannot be detected by DRS (Akilan *et al.*, 2006a; Buchner *et al.*, 2004). The study of Zhang *et al.* (2002) has considered even longer and more complex magnesium sulfate clusters in concentrated solution. The above calculations suggest that the hydrated sulfate ion loses about half its waters from the primary hydration shell when forming the monodentate or bidentate CIP, and, hence, no such waters are likely to be associated with sulfate in the $M_2SO_4^{2+}$ structure, yielding the following general reactions for the monodentate and bidentate TIPs, respectively:

$$M^{2+}(H_2O)_6 + (H_2O)_5MSO_4^o(2\cdot H_2O)_2 \Leftrightarrow [(H_2O)_5M]_2SO_4^{2+} + 5H_2O \qquad 2.63$$

$$M^{2+}(H_2O)_6 + (H_2O)_4MSO_4^o(2\cdot H_2O)(3\cdot H_2O) \Leftrightarrow [(H_2O)_4M]_2SO_4^{2+} + 7H_2O \qquad 2.64$$

Various structures were considered for these monodentate and bidentate TIPs, but the energy differences between the structures had a relatively insignificant effect on the calculated equilibrium constants. The *log* K° values reported in Table 2.7 suggest that the $Mg_2SO_4^{2+}$ species is an unlikely candidate for the second CIP, even when using a relatively large reaction entropy change of 100 J/mol.K. The formation reactions for the anionic $M(SO_4)_2^{2-}$ species follow directly from adding another partially hydrated sulfate ion to the corresponding first CIPs in symmetrical fashion, *i.e.*, for the monodentate and bidentate anionic TIPs, respectively:

$$SO_4^{2-}(H_2O)_8 + (H_2O)_5MSO_4^o(2\cdot H_2O)_2 \Leftrightarrow (H_2O)_4M[(SO_4)(2\cdot H_2O)_2]_2^{2-} + 5H_2O \qquad 2.65$$

$$SO_4^{2-}(H_2O)_8 + (H_2O)_4MSO_4^o(2\cdot H_2O)(3\cdot H_2O) \Leftrightarrow (H_2O)_2M[(SO_4)(2\cdot H_2O)(3\cdot H_2O)]_2^{2-} + 5H_2O \qquad 2.66$$

The more likely TIP is the monodentate anionic $Mg(SO_4)_2^{2-}$ species, as can be seen from the calculated *log* K° value reported in Table 2.7. The geometrically optimised structure of this species is illustrated in Figure 2.8. The presence of anionic metal sulfate species is in line with the potentiometric study of Fedorov *et al.* (1973), who considered the formation of a series of anionic

Stellenbosch University http://scholar.sun.ac.za

sulfate complexes of zinc and cadmium, *i.e.*, $M(SO_4)_n^{(2-2n)}$, up to n = 5, at high ionic strengths. However, it should be emphasised that this claim of a high degree of anionic pairing has been questioned on the basis of anion-exchange data (Rudolph, 1998). On the other hand, the iron(III) CIPs, $Fe(SO_4)_n^{(3-2n)}$, are known to form (Magini, 1979) and although this can be partially explained by virtue of the high positive charge of the ferric (Fe^{3+}) ion, it does suggest that this kind of anionic pairing may also be present in the divalent case, albeit to a lesser extent.

Table 2.7
Geometrically optimised energies of the second Mg sulfate CIPs in H_2O at 25°C (ε_w = 78.38), & comparing the calculated equilibrium reaction values with the corresponding literature values.

Species	$E_{p\ (calc.)}$ (hartrees)	$\Delta E_{p,rx\ (calc.)}$ (kJ/mol)	[f] $\Delta H°_{rx\ (litr.)}$ (kJ/mol)	*log* $K°_{(calc.)}$	[f] *log* $K°_{(litr.)}$
$(H_2O)_4MgSO_4°(2{\cdot}H_2O)_{2\ (bident.)}$	-1514.511298	[a] 77.2 (*n*=8)	43	–	–
$(H_2O)_4MgSO_4°(2{\cdot}H_2O)(3{\cdot}H_2O)_{(bident.)}$	-1591.146776	[a] **47.1** (*n*=9)	**43**	[g] -0.9	-0.2
$[(H_2O)_5Mg]_2SO_4^{2+}{}_{(monodent.)}$	-1868.033131	[b] 68.3	–	[h] -6.9	-0.4
$[(H_2O)_4Mg]_2SO_4^{2+}{}_{(bident.)}$	-1714.746198	[c] 149.9	–	[h] -21	-0.4
$(H_2O)_4Mg[SO_4(2{\cdot}H_2O)_2]_2^{2-}{}_{(monodent.)}$	-2522.275826	[d] 48.8	–	[h] **-3.5**	-0.4
$(H_2O)_2Mg[SO_4(2{\cdot}H_2O)(3{\cdot}H_2O)]_2^{2-}{}_{(bident.)}$	-2522.259313	[e] 71.8	–	[h] -7.5	-0.4

[a] Rx. 2.58; [b] Rx. 2.63; [c] Rx. 2.64; [d] Rx. 2.65; [e] Rx. 2.66; [f] Akilan *et al.* (2006a); [g] $\Delta S°_{rx}$ = 140 J/mol.K [(f)]; [h] $\Delta S°_{rx}$ = 97 J/mol.K (see discussion below).

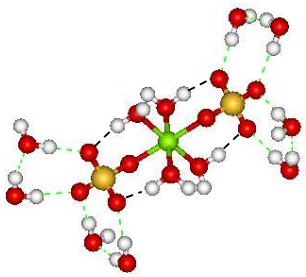

$(H_2O)_4Mg[SO_4(2{\cdot}H_2O)_2]_2^{2-}$

Figure 2.8
Geometrically optimised structure of monodentate $Mg(SO_4)_2^{2-}(H_2O)_{12}$ in H_2O at 25°C (ε_w = 78.38).

The presence of this anionic triple ion may become more predominant at higher temperatures, especially if the reaction (Rx. 2.65) entropy is higher than the estimated value of 30 J/mol.K (Akilan *et al.*, 2006a). That the entropy may be closer to 100 J/mol.K stems from a comparison between the solvent cavity volume changes of the various reactions, as computed within the continuum solvent methodology. The calculated volume increase for the formation of the first CIP (Rx. 2.58, n = 9) is approximately 20Å^3, and the entropy change for this reaction is 110 J/mol.K (Table 2.6). The calculated volume change for the formation of the anionic monodentate TIP (Rx. 2.65) is very similar, *i.e.*, around 23Å^3. Since the negative charge of this species would cause some structuring effect in the secondary solvation shell and beyond, the (convenient) entropy change of

Stellenbosch University http://scholar.sun.ac.za

97 J/mol.K assumes that this effect only partially compensates for the disruption caused by accommodating such large molecules in the surrounding solvent, yielding a rounded *log* K° value of -3.5. Although this constant is significantly smaller than the corresponding value of Akilan *et al.* (-0.4), there is no conceivable way of accommodating more water molecules in the primary hydration shell of the symmetrical TIP structure (Figure 2.8) without significantly overestimating the *log* K° value of first CIP (Table 2.6). Clearly, more experimental data are required, while the above static QM framework ideally needs to be expanded to a QM-MD simulation methodology.

Iron(II) sulfate CIPs

The RS study of Rudolph *et al.* (1997) confirmed the presence of CIPs in the iron(II) sulfate system. No quantitative results were obtained due to the rapid oxidation of iron(II) and the low solubility of the salt, especially at elevated temperatures. Three structures (analogous to the magnesium system) are considered as possibilities in this study, *i.e.*, the $(H_2O)_5FeSO_4°(H_2O)_4$ monodentate, $(H_2O)_4FeSO_4°(H_2O)_4$ bidentate and $(H_2O)_4FeSO_4°(H_2O)_5$ bidentate complexes. The optimised results are presented in Table 2.8, while the corresponding structures of the two bidentate complexes are illustrated in Figure 2.9.

Table 2.8
Geometrically optimised energies of the first & second Fe(II) CIPs in H_2O at 25°C (ε_w = 78.38), & comparing the calculated equilibrium reaction values with the corresponding literature values.

Species	$E_{p\ (calc.)}$ (hartrees)	[a] $\Delta E_{p,rx\ (calc.)}$ (kJ/mol)	[c] $\Delta H°_{rx\ (Mg)}$ (kJ/mol)	*log*(K°) $_{(calc.)}$
$(H_2O)_5FeSO_4°(2{\cdot}H_2O)_{2\ (monodent.)}$	-2661.599500	-76.5 (*n* = 9)	26.7	–
$(H_2O)_4FeO_4°(2{\cdot}H_2O)_{2\ (bident.)}$	-2584.925802	53.9 (*n* = 8)	26.7	–
$(H_2O)_4FeSO_4°(2{\cdot}H_2O)(3{\cdot}H_2O)_{(bident.)}$	-2661.560160	**26.9** (*n* = 9)	26.7; [d] (15)	[e] 1.0
$(H_2O)_2Fe[SO_4(2{\cdot}H_2O)(3{\cdot}H_2O)]_2^{2-}{}_{(bident.)}$	-3592.677911	[b] 58.1	48.8	[f] -5.1

[a] Rx. 2.58; [b] Rx. 2.66; [c] Calc. *ref.* Mg (Table 2.6 & Table 2.7); [d] Rudolph *et al.* (1997) (RS in 1.95 mol/kg $FeSO_4$, incl. SSIPs); [e] $\Delta S°_{rx}$ = 110 J/mol.K (*ref.* Mg; Table 2.6); [f] $\Delta S°_{rx}$ = 97 J/mol.K (*ref.* Mg TIP, Table 2.6; see below).

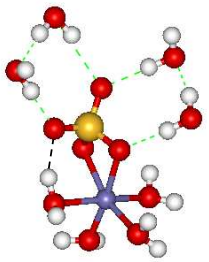

$(H_2O)_4FeSO_4°(2{\cdot}H_2O)_2$

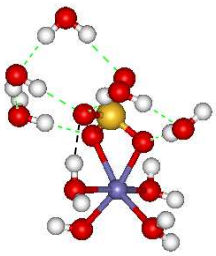

$(H_2O)_4FeSO_4°(2{\cdot}H_2O)\ (3{\cdot}H_2O)$

Figure 2.9
Geometrically optimised structures of bidentate $(H_2O)_4FeSO_4°(H_2O)_{n-4}$ (*n* = 8 to 9) in H_2O at 25°C (ε_w = 78.38).

Stellenbosch University http://scholar.sun.ac.za

The calculated values (Table 2.8) suggest that significantly fewer than nine waters of hydration are required in order to yield a realistic ferrous sulfate monodentate analogy to the magnesium system. Therefore, assuming similar degrees of hydration between the two systems, the hydrated ferrous and sulfate ions are expected to bond in a bidentate rather than in a monodentate fashion. This assumption is supported by the symmetry offered by the *d*-orbital of iron (a transition metal), lending itself more to bidentate bonding. Major uncertainty around the entropy change of the reaction does not warrant a more in-depth evaluation of other possibilities. The bidentate $(H_2O)_4FeSO_4°(2{\cdot}H_2O)(3{\cdot}H_2O)$ species is clearly the most consistent with the magnesium system. The calculated volume change of this reaction is approximately 19Å^3, which is conveniently close to the 20Å^3 calculated for the first magnesium sulfate CIP reaction (2.58, n = 9) in order to justify a similar reaction enthalpy, *i.e.*, 110 J/mol.K, and yielding a similar log K^o value of around 1.The geometrically optimised structure for the bidentate TIP is illustrated in Figure 2.10, while the corresponding energy is listed in Table 2.8. The total calculated volume change of this reaction is close to 18Å^3 and the reaction entropy of 97 J/mol.K, assumed for the magnesium TIP (Table 2.6), is also adopted for this species, yielding a relatively small *log* K^o value of -5.1.

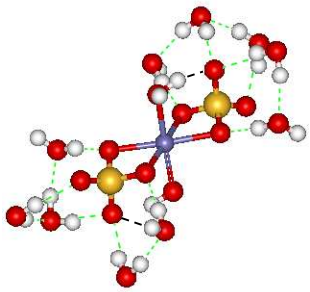

$(H_2O)_2Fe[SO_4(2{\cdot}H_2O)\ (3{\cdot}H_2O)]_2^{2-}$

Figure 2.10
Geometrically optimised structure of bidentate $Fe(SO_4)_2^{2-}(H_2O)_{12}$ in H_2O at 25°C (ε_w = 78.38).

The above results should be viewed as semi-quantitative due to the static QM approach that is followed. Nevertheless, these calculations reveal unique insights into the solution chemistry of typical sulfide mineral leach solutions. Bonding between the magnesium and iron(II) sulfate CIPs is shown to be different, while the TIPs are most likely anionic species. The equilibrium constants of these TIPs are significantly smaller than the corresponding first CIPs (*log* K^o ≈ 1), and, therefore, more uncertain. Not only are the CIP formation extents driven by positive entropy changes, and, hence, would increase with temperature, but cognisance has to be taken of the higher complexation tendencies of the softer transition metals, *e.g.*, copper(II) (*cf.* the harder alkali-earth element, magnesium; Pitzer, 1972). These aspects are expanded upon in Section 2.4, particularly in context of the proposed magnesium surrogate salt approach.

Stellenbosch University http://scholar.sun.ac.za

2.3.3 Quantification of the thermodynamic equilibrium constants in sulfate medium

The following discussion is devoted to the quantification of the equilibrium constants involving sulfate ions, either by adopting correlations from the literature or using the thermodynamic relationships of Section 2.3.1 to best represent the published data.

Hydrogen and sulfate ion association

The first association of the hydrogen ion (second protonation of the sulfuric acid) is as follows:

$$K_B^o: \quad H^+ + SO_4^{2-} \Leftrightarrow HSO_4^- \qquad 2.67$$

This study utilises the published correlation of Dickson *et al.* (1990) for the thermodynamic association constant, K^o_B (details in Appendix A.2.1). This correlation is also consistent with the most important results from the literature between 1952 and 1990. One of the most important studies during that period was the work of Pitzer *et al.* (1977), but their equations are only valid up to 55°C. Figure 2.11 *a* illustrates the good comparison between this empirical correlation (Eq. A.1) and the thermodynamic data (symbols) obtained from a detailed scan of the open literature (Table A.3), utilising over fifteen databases. The broken line represents the calculated equilibrium constant after integration of the enthalpy and entropy terms (Eq. 2.39). The Kelley heat capacity coefficients (Eq. 2.34), based on Helgeson extrapolation (Shock & Helgeson, 1988), as well as the thermodynamic data at the reference temperature (25ºC), are obtained from the *HSC* (2006) database. The dotted line illustrates how well the Density function (Eq. 2.44) performs, utilising only the $\Delta H°$ and $\Delta C_p°$ values of the association reaction (no solid phase) at the reference temperature.

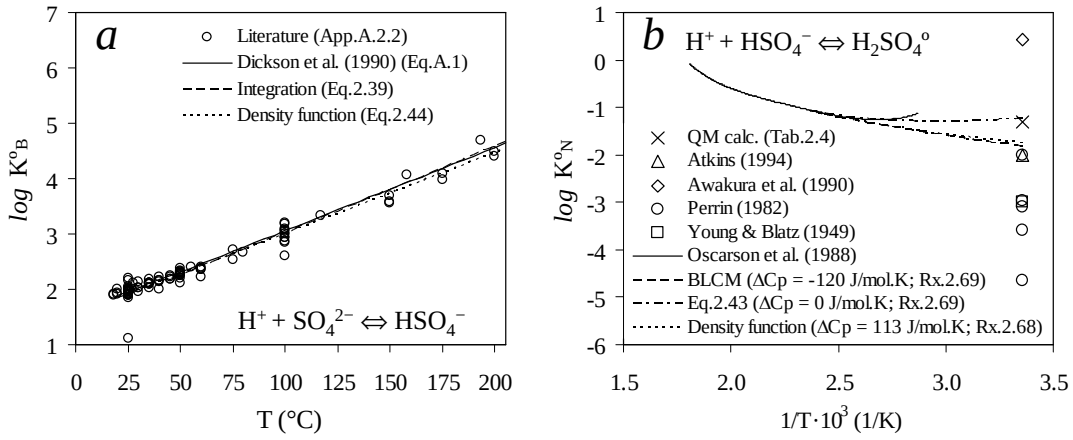

Figure 2.11
Temperature extrapolation of the thermodynamic association constants of hydrogen & sulfate ions: *a*) K^o_B (T_r = 25ºC); *b*) K^o_N (T_r = 150ºC).

The second association of the proton (first protonation of the sulfuric acid) is as follows:

Stellenbosch University http://scholar.sun.ac.za

$$K^{o}_{N}: \quad H^{+} + HSO^{-}_{4} \Leftrightarrow H_{2}SO^{o}_{4} \qquad 2.68$$

Reported thermodynamic values of this association constant, K^{o}_{N} are rare because the concentration of the neutral species, $H_2SO_4^o$, can only be accurately determined at high temperatures and concentrations. In most studies of the dilute sulfuric acid system, even at high temperatures (*e.g.*, Dickson *et al.*, 1990; Marshall & Jones, 1966; Rudolph, 1996), the formation of the neutral species was ignored. Some of the older RS studies (*e.g.*, Young & Blatz, 1949; Young *et al.*, 1959) and the Nuclear Magnetic Resonance (NMR) study of Hood and Reilly (1957) quantitatively took the existence of the neutral ion pair into account, even at low temperatures (<50ºC), albeit at high acid concentrations. The RS study of Rao (1940) suggested (qualitatively) around 95% dissociation of the neutral species in 1 mol/litre acid. More recent work includes the RS investigation of Walrafen *et al.* (2002), the spectroscopic measurements of Xiang *et al.* (1996) and the flow calorimetric work of Oscarson *et al.* (1988), all conducted at high temperatures (>150ºC). Agreement between the studies of Xiang *et al.* and Oscarson *et al.* is good, and the latter is used in this study as the primary source of data for K^{o}_{N} at the reference temperature (150ºC). An isocoulombic reaction is obtained by also considering the water dissociation reaction, *i.e.*:

$$HSO^{-}_{4} + H_{2}O \Leftrightarrow H_{2}SO^{o}_{4} + OH^{-} \qquad 2.69$$

Both the BLCM model (Eq. 2.42) and the assumption of zero reaction heat capacity (Eq. 2.43) for this reaction fit their respective linearity assumptions well over the 150-200ºC range (Figure 2.12 *a* & *b*, respectively). The thermodynamic data of Sweeton *et al.* (1974) are used to represent the water dissociation reaction.

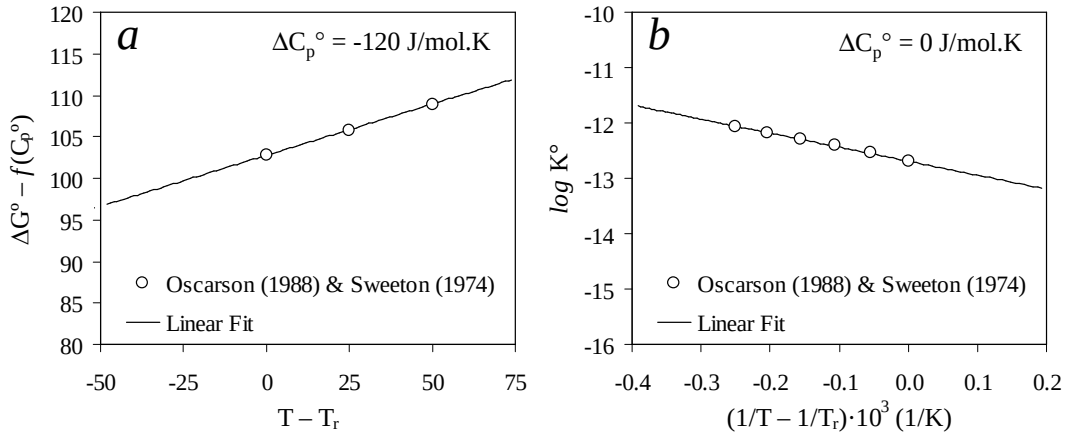

Figure 2.12
Linear relationships for the isocoulombic reaction (Rx. 2.69) (*ref.* the data of Oscarson *et al.*, 1988 & Sweeton *et al.*, 1974, at T_r = 150 ºC): *a*) BLCM function, where $f(C_p^o) = \Delta C_p^o[T - T_r - T \cdot ln(T/T_r)]$, *vs.* $T - T_r$ (Eq. 2.42); *b*) *log* K° *vs.* 1/T (Eq. 2.43).

Stellenbosch University http://scholar.sun.ac.za

Figure 2.11 *b* illustrates that the Density function and BLCM yield similar values of *log* K^{o}_{N} at 25ºC, *i.e.*, -1.7 and -1.8, respectively. The considerable spread in reported values exemplifies the difficulties in measuring this equilibrium constant in dilute sulfuric acid solutions, especially since the neutral molecule is typically not present in measurable quantities at room temperature.

In conclusion, the above results justify the use of the Dickson *et al*. (1990) correlation for the first hydrogen ion association (with sulfate ion), while the Density function and thermodynamic values of Oscarson *et al*. (1988) (T_r = 150ºC) are adequate in describing the second hydrogen ion association (with bisulfate ion) in the phenomenological model (Table 2.10).

Divalent metal and sulfate ion association

Earlier discussions have highlighted the lack of information on the structure and thermodynamic properties of CIP formation between the divalent metal ion and sulfate dianion. Spectroscopic studies of magnesium sulfate solutions (Akilan *et al.*, 2006a; Buchner *et al.*, 2004; Rudolph *et al.*, 2003), copper sulfate solutions (Akilan *et al.*, 2006b), zinc sulfate solutions (Rudolph *et al.*, 1999a, 1999b), cadmium sulfate solutions (Rudolph, 1998), iron(II) sulfate solutions (Rudolph *et al.*, 1997) and, nickel and cobalt sulfate solutions (Chen *et al.*, 2005) have contributed to the understanding of species complexation in the metal sulfate self-medium, despite various uncertainties (see Akilan *et al.*, 2006a). For example, the RS study of Rull *et al.* (1994) has even gone as far as dismissing the presence of CIPs altogether in magnesium sulfate solutions, at least up to 2.9 mol/kg $MgSO_4$ and 80ºC. Figure A.1 in Appendix A.2.3 exemplifies the disagreement in the literature, especially when extrapolating to higher temperatures. From a modelling perspective, Casas *et al.* (2005b) illustrated that the explicit recognition of species is not actually required. As mentioned before, various studies (*e.g.*, Holmes & Mesmer, 1983; Phutela & Pitzer, 1986; Reardon & Beckie, 1987) used an ion-interaction approach without any explicit species recognition to describe the thermodynamics of metal sulfate systems up to high temperatures. However, as pointed out by Akilan *et al.* (2006b), models that take no note of the actual species present "cannot be much more than exercises in numerology, with little physical significance". Since this study is concerned with building a framework to assist with the interpretation of kinetic processes, it is important to recognise the existence of the CIPs, despite the various complexities and general lack of thermodynamic data (Sect. 2.3.2).

Although the speciation reactions have been simulated (semi-quantitatively) in Section 2.3.2, these reactions need to be consistent with the rationale of the ion-interaction framework. In particular, the equilibrium constant of the CIP formation reaction needs to be described in terms of the apparent unassociated moles of ions (y), *i.e.*, the sum of the actual free hydrated ions (z) and all the SSIPs:

Stellenbosch University http://scholar.sun.ac.za

$$K_C^o: \quad (\tfrac{z}{y})\{M^{2+} + SO_4^{2-}\} + (1-\tfrac{z}{y})M(OH_2)_n SO_4^o \Leftrightarrow MSO_4^o + n(1-\tfrac{z}{y})H_2O \qquad 2.70$$

Although this constant should be expressed as β^o (Eq. 2.31), the step-wise notation is retained here in order to be consistent with the ion-interaction framework. However, as highlighted by Rudolph *et al.* (1999a), these thermodynamic constants cannot be obtained by extrapolating the experimental values to infinite dilution because of the stepwise Eigen mechanism (Rx. 2.60 to 2.62). With γ_C representing the activity coefficient of the CIP, M(II)SO_4^o, the following relationship is obtained (see derivation in Appendix A.2.4):

$$K_C^o = \frac{\gamma_C}{(\gamma_\pm^{st})^2} \cdot \frac{\alpha_C}{m^{st}} \qquad 2.71$$

Published spectroscopic information of the mole fraction CIPs, α_C, is then used, in conjunction with Equation 2.71 and the stoichiometric mean activity coefficient of the salt, $\gamma_\pm^{st}$, to estimate the thermodynamic constant, K^o_C, *i.e.*, the equilibrium between the apparent free ions $(1 - \alpha_C)$ and the CIPs. Table 2.9 summarises the results of the salts systems relevant to this study, assuming $\gamma_C = 1$.

Table 2.9
Average calculated thermodynamic association constants from RS & DRS (literature) data.

System	Method	[a] *log* $K°_C$	Reference
$MgSO_4$-H_2O	RS	1.5	Rudolph *et al.* (2003)
	DRS	1.6	Akilan *et al.* (2006a)
$FeSO_4$-H_2O	RS	[b] 1.5	Rudolph *et al.* (1997)
$CuSO_4$-H_2O	RS	[c] (1.0)	Akilan *et al.* (2006b)
$ZnSO_4$-H_2O	RS	1.5	Rudolph *et al.* (1999a)

[a] Using Eq. 2.71, exp. data between 0.1 & 1 mol/kg M(II)SO_4, smoothed $\gamma_\pm^{st}$ data (*ref.* Figure 2.13) & $\gamma_C = 1$; [b] Single data point at 1.95 mol/kg $FeSO_4$, using $\gamma_\pm^{st}$ from Reardon & Beckie (1987); [c] Value taken directly from the reference.

These calculated values should be considered as relatively crude due to experimental error, as well as the (likely) dipole moment of the neutral molecule (see, *e.g.*, Figure 2.6), *i.e.*, γ_C might deviate notably from one at these experimental concentrations. Although an offset in *log* K^o_C would propagate into a species abundance error (phenomenological model calculations; Sect. 2.4), it would ultimately be absorbed in the rate constants of the simulated kinetic processes (later chapters), provided that these calculations are conducted in an internally consistent manner.

2.4 Phenomenological model

As mentioned before, the phenomenological model consists of a combined ion-interaction-speciation framework, using multi-variable regression to align the model with the experimental observations. The following section presents a summary of the selected equilibrium constants.

Stellenbosch University http://scholar.sun.ac.za

2.4.1 Final selection of the thermodynamic values for the CIP formation reactions

Table 2.10 summarises the thermodynamic values of all the CIP associations (discussed above) in the H_2SO_4-M(II)SO_4-H_2O system, as adopted by the phenomenological model (Sect. 2.4). For the sake of internal consistency and due to the complexities of simulating the mixed H_2SO_4-$CuSO_4$-$ZnSO_4$-$FeSO_4$-$MgSO_4$-H_2O electrolyte system, the primary assumption of the phenomenological model is the use of magnesium as a surrogate metal to represent all the metal(II) sulfate salts. The *log* $K°_C$ value of 1.5 (Table 2.9) is therefore retained for the surrogate CIP, *i.e.*, $MgSO_4°$.

Table 2.10
Thermodynamic values of the CIP formation reactions used by phenomenological model.

Reaction		T_r (°C)	*log* K°	$\Delta H°_{rx}$ (kJ/mol)	$\Delta S°_{rx}$ (J/mol.K)	$\Delta C_p°_{rx}$	Reference
$H^+ + SO_4^{2-} \Leftrightarrow HSO_4^-$	$K°_B$	25	[a] 1.964	(22.8)	(114)	–	Dickson *et al.* (1990)
$H^+ + HSO_4^- \Leftrightarrow H_2SO_4°$	$K°_N$	150	[b] -1.05	19.62	(26)	113	Oscarson *et al.* (1988)
$Mg^{2+} + SO_4^{2-} \Leftrightarrow MgSO_4°$	$K°_C$	25	[c] 1.5	[e] 10	[g] 62	[h] *330*	Collated (this study)
$MgSO_4° + SO_4^{2-} \Leftrightarrow Mg(SO_4)_2^{2-}$	$K°_T$	25	[d] -3.5	[f] 49	(97)	[h] *0*	Calculated (this study)

Temperature extrapolation using: [a] Eq. A.1 (Dickson correlation); [b] Eq. 2.44 (Density function); [c] Eq. 2.75; [d] Eq. 2.43 [(h)]; [e] Avg. of various M(II) sulfate salts from RS (Rudolph, 1998; Rudolph *et al.*, 1997, 1999a, 1999b); [f] Estimated using QM calcs. (Sect. 2.3.2); [g] Based on $\Delta G°_{rx}$ & $\Delta H°_{rx}$ (*ref.* Eq. 2.48); [h] Regressed phenomenologically (Sect. 2.4.2).

The smaller reaction enthalpy value (10 kJ/mol) of the first CIP as compared to the *ab initio* value (~27 kJ/mol) in Table 2.6 stems from the fact that the apparent free ion concentrations ($1 - \alpha_C$) obtained by RS actually include various SSIPs (see previous section). It is therefore paramount to the internal consistency of the phenomenological model to use this reaction enthalpy value. The positive enthalpy values in Table 2.10 may be ascribed to the energy required to break the coordination water molecules of the reacting species, while the positive entropy values are related to a decrease in structure around the ion pairs due to the release of water molecules. The increase in reaction entropy compensates for the positive reaction enthalpy, especially at higher temperatures (*ref.* Eq. 2.48), *i.e.*, these reactions may be viewed as being entropy driven.

The inclusion of the relatively large *log* $K°_T$ (*ab initio*) estimate of the surrogate $Mg(SO_4)_2^{2-}$ species (-3.5; Table 2.7), as opposed to the smaller value of the $Fe(SO_4)_2^{2-}$ species (-5.1; Table 2.8), is justified considering that this TIP formation reaction is also likely to involve SSIPs. No explicit interaction between the bisulfate anion and the divalent metal cation is considered because the bisulfate ion has a noble gas electronic structure, similar to the perchlorate (ClO_4^-) ion, and is therefore not expected to form CIPs (Rudolph *et al.*, 1997; Tremaine *et al.*, 2004).

Stellenbosch University http://scholar.sun.ac.za

2.4.2 Model regression

This section focuses on the model regression, first for the binary H_2SO_4-H_2O and M(II)SO_4-H_2O systems, and then for the ternary H_2SO_4-M(II)SO_4-H_2O system, up to 200ºC. A Newton-Raphson numerical routine, similar to the one proposed by I and Nancollas (1972), is adopted in order to solve the system of mass balance equations within the ion-interaction (Pitzer) framework, while the computation has to fulfil the condition of electrical neutrality (Eq. 2.27). This method is summarised in Appendix A.3, allowing fast convergence of the species molalities. Due to a lack of speciation data at high temperatures, the model relies on the following regression methodology:

- Careful selection of thermodynamic reference data and extrapolation strategies (Sect.2.4.1)
- Selecting a minimum number of adjustable interaction parameters
- Constraining the system to the thermodynamic data at non-zero ionic strength, and
- Accounting for the observed speciation trends, albeit available at lower temperatures only.

Available experimental data are incorporated into the regression analysis by minimising the objective function $F(E_F)^2$ at each temperature *j*:

$$E_{F,j} = \sum_k y_{F,k} \sum_i E_{i,k} = \sum_k y_{F,k} \sum_i \left| k_i^{calc} / k_i^{exp} - 1 \right| \qquad 2.72$$

where E represents the absolute relative error at datapoint *i* and y_F is the weighed error function coefficient of each thermodynamic property *k*, so that $\sum y_{F,k} = 1$. A statistical evaluation is used to determine how well the model represents the average experimental trend. This study uses the absolute average relative deviation (*AARD*) (Jones *et al.*, 2008), defined as a percentage (N, represents the total number of data evaluation points):

$$AARD_{j,k}\ (\%) = \frac{100}{N_j} \cdot \sum_i E_{i,j} \qquad 2.73$$

H_2SO_4-H_2O system

Although the thermodynamic properties of this system have been studied extensively, uncertainty still exists with regard to the actual species concentrations. The MSE model of Liu and Papangelakis (2005b) suggested almost 40% $H_2SO_4^o$ species in a 0.5 mol/kg H_2SO_4 solution at 200ºC. Wang *et al.* (2006) adjusted this model by explicitly treating the hydrogen ion as the hydrated species, H_3O^+, and adjusting the interaction parameters to reflect the experimental observations (*e.g.*, Hood & Reilly, 1957; Walrafen *et al.*, 2000; Young *et al.*, 1959). Due to the relatively dilute range of this study, it is not deemed necessary to follow the hydrated cation approach of Wang *et al.* (2006). The problem is that quantitative information concerning the neutral $H_2SO_4^o$ species abundance is only available at relatively high acid concentrations and temperatures. However, as indicated above, the speciation trends at high temperatures would

Stellenbosch University http://scholar.sun.ac.za

become more accurate by incorporating the experimentally observed distribution of the primary species, HSO_4^- and SO_4^{2-}, in the regression analysis, albeit available at room temperature only. The studies of Clegg *et al.* (1994), Clegg and Brimblecombe (1995) and Pitzer *et al.* (1977) include reviews of the most important thermodynamic studies of the H_2SO_4-H_2O system from the 20th century, all of which were limited to temperatures below 60ºC. Only one high temperature study, based on own experimental measurement and where a description of the self-medium was attempted, is known to the author, *i.e.*, the isopiestic study of Holmes and Mesmer (1992).

Available experimental literature data, including the recommended (calculated) values of Holmes and Mesmer, are incorporated into the regression analysis, using the phenomenological framework presented earlier and minimising the weighed objective function (Eq. 2.72). The relevant regression results are presented in Table 2.11. Depending on the available data at each temperature, up to three thermodynamic properties are considered simultaneously, *i.e.*, ϕ, $\gamma_{\pm}$ and α_B'. The symbol α_B' refers to the extent (mole fraction) of bisulfate dissociation, *i.e.*, $1 - \alpha_B$. The activity coefficient of the neutral complex is assumed to be unity, *i.e.*, no interaction parameters involve the neutral acid molecule. Various combinations and the relative importance of the interaction parameters ($\beta^{(0)}_{HB}$, $\beta^{(1)}_{HB}$, C^{ϕ}_{HB}, $\beta^{(0)}_{HS}$, $\beta^{(1)}_{HS}$, C^{ϕ}_{HS}, θ_{BS}, ψ_{HBS}) are evaluated, both with and without the inclusion of the long-range electrostatic parameters ($^{E}\theta_{BS}$, $^{E}\theta'_{BS}$). In accordance with previous notation, the subscripts H, B and S refer to the hydrogen, bisulfate and sulfate ions, respectively, while the (above) thermodynamic properties are the stoichiometric values (for the sake of simplicity, the superscript 'st' is omitted in the rest of this study). A power series is used to describe the temperature dependence of an interaction parameter, *P* (Holmes & Mesmer, 1992):

$$P(T) = \sum_j p_j \cdot \left(\frac{T_d}{T_o} \right)^{j-1} \qquad 2.74$$

where $T_d = T - T_r$ (298.15 K) and $T_o = 1$ K. The lower concentration end is limited to 0.1 mol/kg H_2SO_4 since isopiestic measurements are generally regarded to be inaccurate below this concentration (Rard & Platford, 1991). Excellent results are obtained by considering only three interaction parameters, *i.e.*, $\beta^{(0)}_{HB}$, $\beta^{(1)}_{HB}$ and θ_{BS}, with inclusion of the long-range electrostatic terms. Due to the lack of thermodynamic data and species abundance information at the higher temperatures, these three interaction parameters are only allowed to vary linearly, *i.e.*, $j \leq 2$. These optimised parameters are presented in Table 2.12, yielding *AARD* values of less than 1% for ϕ and $\gamma_{\pm}$ between 25 and 200ºC, and less than 3% in the case of α_B', albeit referring to 25ºC only.

Stellenbosch University http://scholar.sun.ac.za

Table 2.11
Objective functions & their relative *AARD* values for the binary H_2SO_4-H_2O system.

Temp. (°C)	[a] Obj. func. coeff. $y_F(\phi, \gamma_\pm, {}^c\alpha_B')$	[b] *AARD* (%) $\phi, \gamma_\pm, {}^c\alpha_B'$	Temp. (°C)	[a] Obj. func. coeff. y_F ($\phi, \gamma_\pm, {}^c\alpha_B'$)	[b] *AARD* (%) $\phi, \gamma_\pm, {}^c\alpha_B'$
25	⅓, ⅓, ⅓	0.24, 0.14, 2.47	125	½, ½, 0	0.13, 0.42, –
50	½, ½, 0	0.47, 0.36, –	150	½, ½, 0	0.12, 0.19, –
75	½, ½, 0	0.09, 0.23, –	175	½, ½, 0	0.13, 0.08, –
100	½, ½, 0	0.07, 0.30, –	200	½, ½, 0	0.64, 0.76, –

[a] Eq. 2.72; [b] Eq. 2.73; [c] Refers to the degree of dissociation of HSO_4^-, *i.e.*, $1 - \alpha_B$.

Table 2.12
Optimised interaction parameters for the binary H_2SO_4-H_2O system (including ${}^E\theta_{BS}$ & ${}^E\theta'_{BS}$).

	[a] p_1 (kg/mol)	[a] $p_2 \cdot 10^3$ (kg/mol)
$\beta^{(0)}_{HB}$	0.2214	-0.4412
$\beta^{(1)}_{HB}$	0.4025	-0.0541
θ_{BS}	0.1271	-0.1381

[a] Eq. 2.74.

Comparisons between the experimental (literature) and calculated (this study) coefficients are presented in Figure 2.13, which emphasises the consistent performance of the simulation over the relatively wide temperature range of 25 to 200ºC, utilising only six regression parameters.

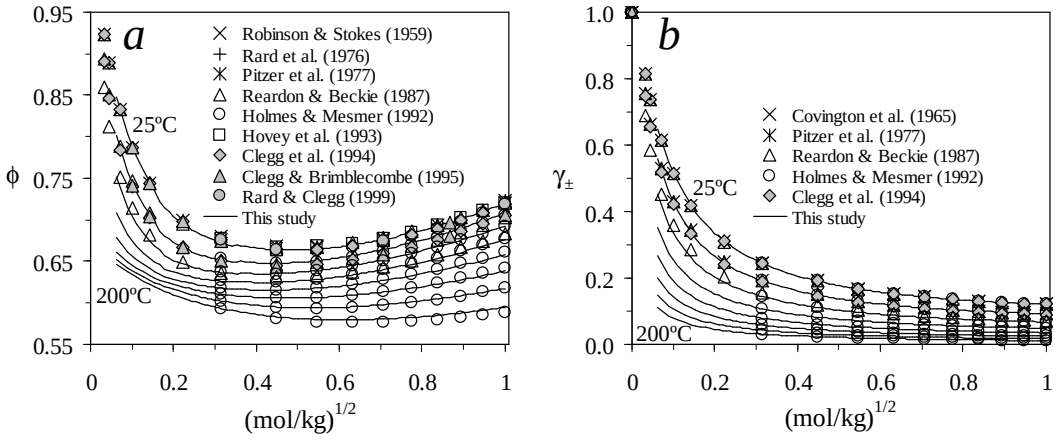

Figure 2.13
Comparison between the experimental & calculated stoichiometric coefficients for the binary H_2SO_4-H_2O system at 25ºC intervals: *a*) ϕ *vs.* $[H_2SO_4]^{1/2}$; *b*) $\gamma_\pm$ *vs.* $[H_2SO_4]^{1/2}$.

With the regression constraints discussed above, the model is used to infer the speciation behaviour at higher temperatures, where no actual speciation data are available. Figure 2.14 *a* compares the simulated bisulfate dissociation extents with the reported values (25 & 50ºC), while Figure 2.14*b*

Stellenbosch University http://scholar.sun.ac.za

presents the (calculated) speciation at 1 mol/kg H_2SO_4. Clearly, the neutral $H_2SO_4^o$ species plays a relatively minor role (< 5%), even at 200ºC. This is in line with Wang *et al.* (2006).

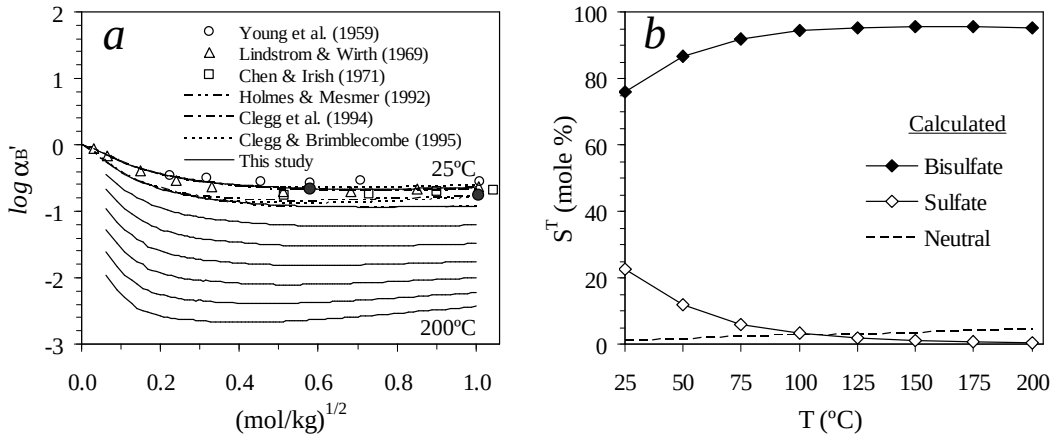

Figure 2.14
Comparison between experimental & calculated speciation for the binary H_2SO_4-H_2O system at 25ºC intervals: *a*) *log* α_B' *vs.* $[H_2SO_4]^{1/2}$ (closed symbols refer to 50ºC); *b*) S^T distribution at 1 mol/kg H_2SO_4.

M(II)SO_4-H_2O system

Thermodynamic data for the individual binary M(II)SO_4-H_2O systems are scattered throughout the literature. Sources of osmotic and mean activity coefficient data can be found in Guendouzi *et al.* (2003), Majima *et al.* (1988), Pitzer (1972) and Robinson and Stokes (1959). Additional data for the $CuSO_4$-H_2O system have been reported by Downes and Pitzer (1976), Harned and Owen (1958) and Majima and Awakura (1988). The more recent measurements of Albright *et al.* (2000) and Miladinovic *et al.* (2002) provide useful information about the $ZnSO_4$-H_2O system. However, only the study of Oykova and Balarew (1974) reveals information about the $FeSO_4$-H_2O system, which exemplifies the difficulties in obtaining accurate experimental data for this system. Additional information about the $MgSO_4$-H_2O system has been reported by Archer and Rard (1998), Archer and Wood (1985), Phutela and Pitzer (1986) and Snipes *et al.* (1975) for the osmotic coefficient, and Holmes and Mesmer (1983), Pitzer and Mayorga (1974) and Rard and Miller (1981) for the mean activity coefficient. Agreement between the above studies is reasonable, except for the measurements of Majima *et al.* (1988), whose data are omitted for the zinc and magnesium sulfate systems. Figure 2.15 *a* and *b* present the average of these reported stoichiometric osmotic and mean activity coefficients (at 25ºC), respectively.

The exact degree of CIP formation would be expected to vary significantly between the softer transition metal ions, such as copper(II), and the harder magnesium ions (Sect. 2.3.2; also see below). The relative insensitivity of the average measured coefficients in Figure 2.15 suggests that

Stellenbosch University http://scholar.sun.ac.za

CIP formation is not significant at 25ºC, which has been confirmed by the RS measurements of Rudolph *et al.* (2003) (~10% in 1 mol/kg $MgSO_4$), Rudolph *et al.* (1999a) (8% in 1.1 mol/kg $ZnSO_4$) and Rudolph *et al.* (1997) (13% in 1.95 mol/kg $FeSO_4$). Therefore, the major excess free energy contributions stem from electrostatic forces, which are less sensitive to the metal ion type. This is also evident from the similar values of the total thermodynamic equilibrium constants of these salts at 25ºC (Helgeson, 1967; Högfeldt, 1982; Izatt *et al.*, 1969; Nair & Nancollas, 1958, 1959; Pitzer, 1972).

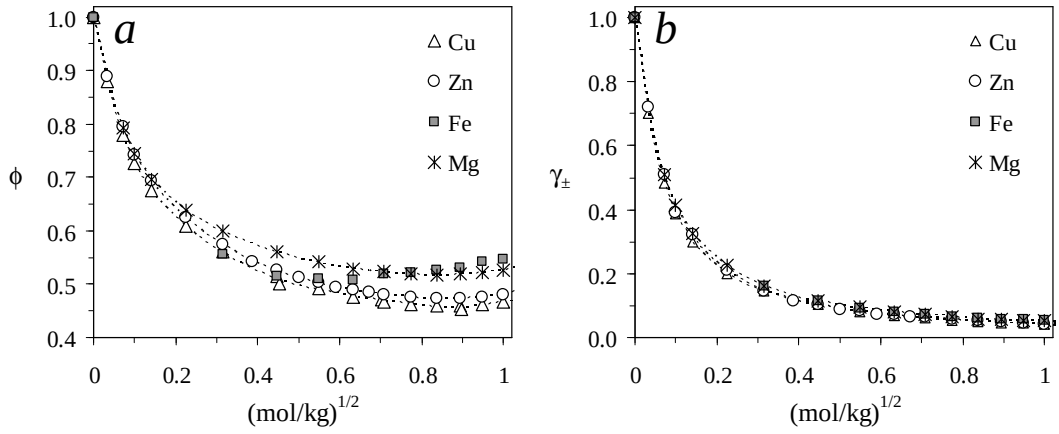

Figure 2.15
Average stoichiometric coefficients of metal(II) sulfates in water at 25ºC (the datapoints represent the average literature values; see text above): *a*) ϕ *vs.* $[MSO_4]^{1/2}$; *b*) $\gamma_{\pm}$ *vs.* $[MSO_4]^{1/2}$.

Despite these similarities, the discussions of Section 2.3.2 and Figure 2.15 *a* suggest that some degree of oversimplification is introduced by using magnesium sulfate to represent the total metal(II) sulfate concentration. In an attempt to gauge if an increase in temperature would result in significantly different behaviour between these salts, their reported thermodynamic values may be compared. For example, the EMF study of Nair and Nancollas (1959), conducted up to 45ºC, yielded very similar overall reaction enthalpies, *i.e.*, 16.8 and 20.3 kJ/mol, and entropies, *i.e.*, 102 and 110 J/mol.K, for zinc and magnesium sulfate, respectively. Helgeson extrapolation (Helgeson, 1967) also yielded similar overall equilibrium constant values up to high temperatures, *e.g.*, *log* Kº = 4.6 and 4.8 at 200ºC for zinc and magnesium sulfate, respectively (Högfeldt, 1982). However, various studies (*e.g.*, Izatt *et al.*, 1969; Powell, 1973) suggested higher reaction enthalpies for copper and cadmium sulfate (compared to the other metal(II) sulfates), which may be ascribed to preferential CIP formation (Sect. 2.3.2) and which is in line with the experimental findings of Larson (1970) and Mironov *et al.* (1970). Larson (1970) rated the tendency to form sulfate CIPs as follows: Cd > Cu > Zn. In contrast, the studies of Rudolph (1998) and Rudolph *et al.* (1999a) reported similar degrees of CIP formation for zinc and cadmium, *i.e.*, 25% in 2.33 mol/kg $ZnSO_4$ (115°C) and 22% in 2.86 mol/kg $CdSO_4$ (109°C), respectively. Despite these uncertainties, CIP

Stellenbosch University http://scholar.sun.ac.za

formation appears to be favoured in the case of copper (Méndez De Leo *et al.*, 2005) as compared to the other metal(II) sulfates (Zn, Fe & Mg). Since no quantitative information is available in the self-medium under autoclave temperatures, it is assumed that these salts behave similarly up to 200ºC. The premise of this assumption is that any offset in the actual CIP formation extent between these metal sulfates can be accommodated in the rate constants of the kinetic processes that make use of this phenomenological chemistry framework. The regression is therefore only constrained using the experimental data of the surrogate salt, magnesium sulfate.

Various combinations, from a minimum of three to a maximum of six parameters, involving the main interactions between the explicit ions, *i.e.*, $\beta^{(0)}_{MS}$, $\beta^{(1)}_{MS}$, $\beta^{(2)}_{MS}$, C^{ϕ}_{MS}, $\beta^{(0)}_{MT}$, $\beta^{(1)}_{MT}$, C^{ϕ}_{MT}, θ_{ST}, ψ_{MST}, are evaluated. Again, to be consistent with the notation used to describe the equilibrium constants, the subscripts M, C and T refer to the aqueous metal ion, Mg^{2+}, the neutral CIP, $MgSO_4^o$, and the TIP, $Mg(SO_4)_2^{2-}$, respectively. The regression may also be expanded to include the binary interactions involving the neutral CIPs (λ_{MC}, λ_{SC}, λ_{CC}, λ_{CT}) and the ternary interactions (μ_{MCC}, μ_{SCC}, μ_{CCC}, μ_{MSC}). The best regression at 25ºC, with a minimum number of four parameters, is obtained with the parameters $\beta^{(0)}_{MS}$, $\beta^{(1)}_{MS}$, $\beta^{(2)}_{MS}$, in addition to one of the following: C^{ϕ}_{MS}, λ_{MC} or λ_{SC}. Although previous studies of magnesium sulfate at high temperatures (Holmes & Mesmer, 1983; Phutela & Pitzer, 1986) only utilised the parameters, $\beta^{(0)}_{MS}$, $\beta^{(1)}_{MS}$, $\beta^{(2)}_{MS}$, and C^{ϕ}_{MS}, the explicit inclusion of the two metal sulfate CIPs demands a modified approach. Excellent results at high temperatures are obtained with the inclusion of one of the neutral CIP interaction parameters, λ_{MC} or λ_{SC}. These parameters may be perceived to capture the electrostatic interactions between the dipole of the first CIP and the charged metal cation or sulfate dianion, respectively. The inclusion of the $\beta^{(2)}_{MS}$ term in the conventional treatment of 2-2 electrolytes (Pitzer & Mayorga, 1974) is related to the rapid decrease in the ion activity coefficient in the dilute range (~0.03 to 0.1 mol/kg), which, in turn, is related to a maximum degree of association found for typical 2-2 electrolytes in this dilute range. With optimised $\beta^{(2)}_{MS}$ values for magnesium sulfate in the range -37.23 (Pitzer & Mayorga, 1974) to -32.7 kg/mol (Rard & Miller, 1981), its value needs to be adjusted because of the explicit recognition of the CIPs. Figure 2.16 *a* illustrates the results of this optimisation, which yields a value close to -31 kg/mol, while maintaining the conventional 2-2 electrolyte parameter values of 1.4 and 12 $(kg/mol)^{1/2}$ for α_1 and α_2, respectively, *i.e.*, the explicit recognition of the CIPs lowers the absolute value of the second virial coefficient. The optimised interaction parameters at 25ºC are presented in the first column of Table 2.14. In order to determine the temperature dependence of the various interaction parameters, Equation 2.74 is again utilised. However, as highlighted in Table 2.10, no heat capacity information is available for the formation of the neutral CIP and the TIP, and hence, no accurate description of their enthalpy and entropy changes with temperature can be made. The heat capacities of these two reactions may therefore be viewed as

Stellenbosch University http://scholar.sun.ac.za

adjustable, and incorporated into the regression analysis *via* integration of the entropy and enthalpy contributions (Eq. 2.39). In order to prevent over-parameterisation, these heat capacities are assumed to remain constant over temperature, *i.e.*:

$$ln\,K^{o} = \frac{1}{R_g}\left(\Delta S^{o}_{T_r} + \Delta C^{o}_{p,T_r} \cdot ln\frac{T}{T_r}\right) - \frac{1}{R_g}\left(\frac{\Delta H^{o}_{T_r}}{T} + \Delta C^{o}_{p,T_r}\left(1 - \frac{T_r}{T}\right)\right) \qquad 2.75$$

At least for the isocoulombic TIP formation reaction (Table 2.10), a constant heat capacity should be a reasonable assumption (Lindsay, 1980). In fact, the best results are obtained by setting the heat capacity equal to zero for this reaction (Eq. 2.43). The regression then simplifies to finding the heat capacity value of the first CIP formation reaction (Eq. 2.75), in addition to finding the temperature dependencies of the interaction parameters (Eq. 2.74). The optimised value of 330 J/mol.K is illustrated in Figure 2.16 *b*, based on the regression methodology and data below.

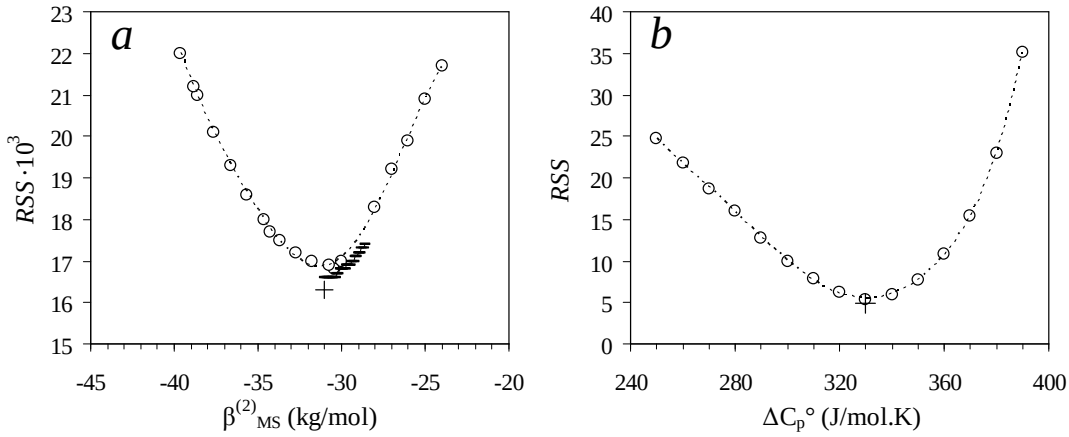

Figure 2.16
Residual sum of squares (*RSS*) (○ represents the initial optimisation, while − & + represent progressively lower tolerance levels): *a*) Second virial coefficient (at 25°C); *b*) ΔC_p^o of the first CIP formation reaction, K^o_C (assuming ΔC_p^o = 0 J/mol.K for the TIP formation reaction, K^o_T).

Experimental data at higher temperatures for the $MgSO_4$-H_2O system are limited to the heats of dilution measurements of Snipes *et al.* (1975) (up to 80ºC), the isopiestic vapour pressure measurements of Holmes and Mesmer (1983) (at 110ºC) and the heat capacity measurements of Phutela and Pitzer (1986) (up to 150ºC). The studies of Archer and Rard (1998) and Archer and Wood (1985) also considered other data sources and their model outputs provide good generalisations of the available data up to 150ºC. Although the study of Phutela and Pitzer (1986) considered temperatures up to 200ºC, information is limited to low molalities (~0.1 mol/kg) and shows discrepancies with the model of Archer and Wood (1985) above 140ºC. Therefore, this study requires additional information at higher temperatures (>150ºC) and the incorporation of kieserite ($MgSO_4 \cdot H_2O$) solubility data is ideally suited for that purpose:

Stellenbosch University http://scholar.sun.ac.za

$$MgSO_4 \cdot H_2O_{(s)} \Leftrightarrow Mg^{2+}_{(aq)} + SO^{2-}_{4(aq)} + H_2O \qquad 2.76$$

The temperature dependence of the thermodynamic solubility product, K^o_{sp}, is unknown. However, based on the partial molal heat capacity of the crystal phase and the aqueous species at the reference temperature, $C_p{}^o_{25^oC}$, this equilibrium constant may be extrapolated to higher temperatures using the Density function (Eq. 2.44). Appendix A.2.5 compares *log* K^o_{sp} using this function and reference values from the *HSC* (2006) database, with *log* K^o_{sp} values reported in other studies (based on Helgeson extrapolation and alternative reference values). Archer and Rard (1998) and Pabalan and Pitzer (1987) proposed values of 126 J/mol.K and 134 J/mol.K, respectively, for the partial molal heat capacity of kieserite, while this study uses the value of 145 J/mol.K (*HSC*, 2006), yielding *log* K^o_{sp} = 0.0662, $\Delta C_p{}^o$ = -355.92 J/mol.K and ΔH^o = -52.43 kJ/mol at 25ºC. The regression makes use of Equation 2.26 and the experimental solubility values of Linke and Seidell (1965) and Marshall and Slusher (1965) (170 to 200 ºC). The objective functions and regression results are summarised in Table 2.13, while the optimised parameters are listed in Table 2.14.

Table 2.13
Objective functions & their relative *AARD* values for the binary $MgSO_4$-H_2O system.

Temp. (°C)	[a] Obj. func. coeff. $y_F(\phi, \gamma_\pm,$ [c] $\alpha_C)$	[b] *AARD* (%) $\phi, \gamma_\pm,$ [c] α_C	Temp. (°C)	[a] Obj. func. coeff. $y_F(\phi, \gamma_\pm,$ [d] *log* $K°_{sp}{}^{100})$	[b] *AARD* (%) $\phi, \gamma_\pm,$ [d] *log* $K°_{sp}$
25	⅓, ⅓, ⅓	0.86, 1.41, 1.11	130	½, ½, 0	1.11, 0.58, –
45	½, ½, 0	1.41, 1.67, –	140	½, ½, 0	0.92, 0.90, –
65	½, ½, 0	2.44, 1.39, –	150	½, ½, 0	1.49, 0.90, –
80	½, ½, 0	2.42, 1.42, –	170	0, 0, 1	– , – , 0.10
100	½, ½, 0	1.56, 1.37, –	180	0, 0, 1	– , – , 0.58
110	½, ½, 0	1.05, 1.57, –	190	0, 0, 1	– , – , 0.75
120	½, ½, 0	1.36, 0.68, –	200	0, 0, 1	– , – , 0.12

[a] Eq. 2.72; [b] Eq. 2.73; [c] Refers to the degree of $MgSO_4°$ association; [d] Refers to kieserite solubility (Rx. 2.76).

Table 2.14
Optimised interaction parameters for the binary $MgSO_4$-H_2O system.

	[a] p_1 (kg/mol)	[a] $p_2 \cdot 10^2$ (kg/mol)	$\Delta C_p°_{rx}$ (J/mol.K)
$\beta^{(0)}_{MS}$	0.2658	0.2809	–
$\beta^{(1)}_{MS}$	3.1502	0.3196	–
$\beta^{(2)}_{MS}$	-31	–	–
λ_{SC}	-0.1236	-0.4801	–
K^o_C	–	–	[b] 330
K^o_T	–	–	[c] (0)

[a] Eq. 2.74; [b] Eq. 2.75; [c] Eq. 2.43.

Stellenbosch University http://scholar.sun.ac.za

Figure 2.17 and Figure 2.18 illustrate the generally good agreement between the experimental data and the simulation, using only the adjustable parameters λ_{SC}, $\beta^{(0)}_{MS}$, $\beta^{(1)}_{MS}$, $\beta^{(2)}_{MS}$ and ΔC_p^o (*ref.* K^o_C), and linear temperature dependencies for the first three parameters ($j \leq 2$; Eq. 2.74). *AARD* values better than 3% are obtained at 150ºC and below for both the stoichiometric osmotic (Figure 2.17 *a*) and mean activity (Figure 2.17 *b*) coefficients. Figure 2.18 *a* illustrates the reasonably good kieserite solubility simulation between 170 and 200ºC, while Figure 2.18 *b* compares the calculated fraction CIPs with the available experimental data at 25ºC. The predictions at higher temperatures are also illustrated, suggesting preferential ion association at low molalities (discussed previously), while the formation of the TIP only becomes notable at higher salt concentrations and temperatures (>150ºC).

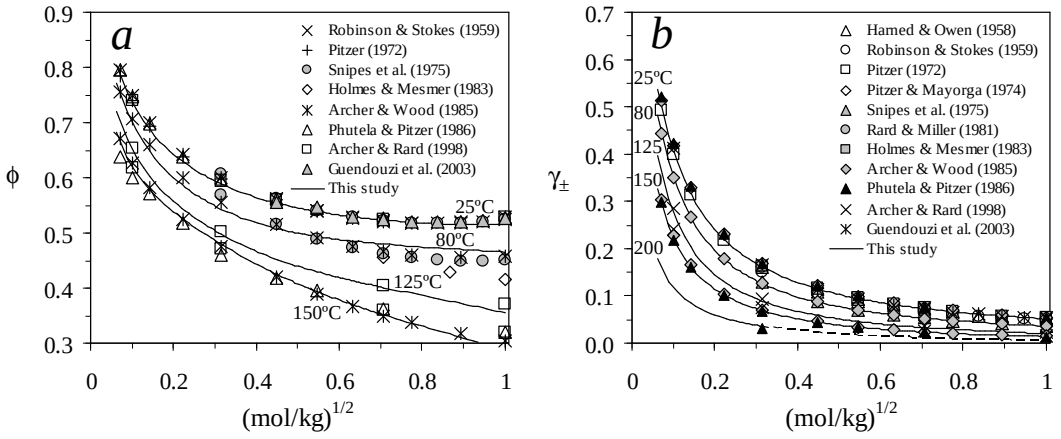

Figure 2.17
Comparison between the experimental & calculated stoiciometric coefficients for the binary $MgSO_4$-H_2O system at selected temperatures: *a*) ϕ *vs.* $[MgSO_4]^{1/2}$; *b*) $\gamma_{\pm}$ *vs.* $[MgSO_4]^{1/2}$ (the broken line artificially exceeds the solubility limit).

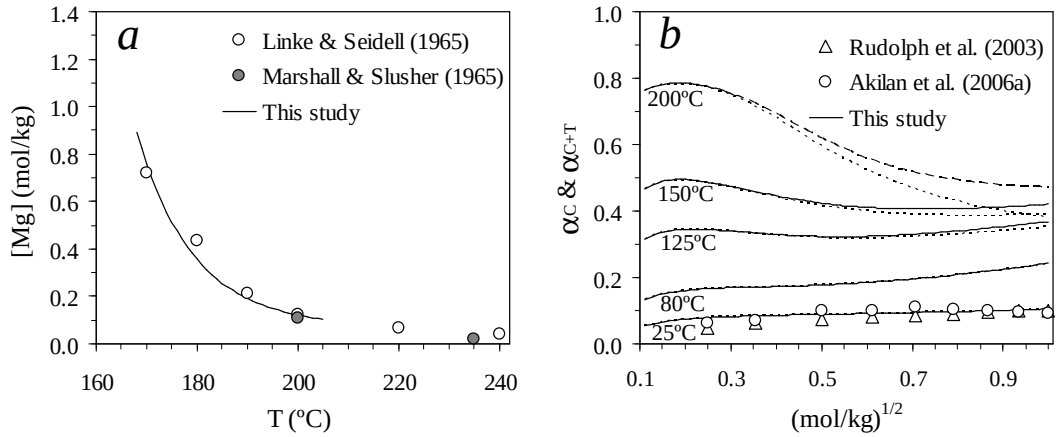

Figure 2.18
Experimental *vs.* calculated properties for the binary $MgSO_4$-H_2O system at different temperatures: *a*) Kieserite solubility; *b*) First (α_C; dotted lines) & total (α_{C+T}; solid lines) CIP fractions *vs.* $[MgSO_4]^{1/2}$. The broken line (200ºC) is an artificial region above the kieserite solubility.

Stellenbosch University http://scholar.sun.ac.za

H_2SO_4-M(II)SO_4-H_2O system

Reliable experimental information for these ternary systems is rare, which is surprising in view of their industrial importance. The most comprehensive set of isopiestic data for various salt mixtures was generated by Majima *et al.* (1988) at 25ºC. Valuable information at 25ºC, including reference to other data sources, is also obtained from the isopiestic measurements of Rard and Clegg (1999) for the H_2SO_4-$MgSO_4$-H_2O system, and the vapour pressure and EMF measurements of Tartar and Ness (1941) for the H_2SO_4-$ZnSO_4$-H_2O system. Unfortunately, the study of Jaskula and Hotloś (1992) for the H_2SO_4-$CuSO_4$-H_2O system at 60ºC is of little use to this study because no comparative values were reported for the same system at 25ºC. Various researchers have applied the Pitzer ion-interaction model to these types of ternary systems, *e.g.*, Guerra and Bestetti (2006) (H_2SO_4-$ZnSO_4$-H_2O system; ≤ 45ºC), Rard and Clegg (1999) (H_2SO_4-$MgSO_4$-H_2O system; 25ºC) and Reardon and Beckie (1987) (H_2SO_4-$FeSO_4$-H_2O system; ≤ 90ºC). Due to the explicit recognition of the selected CIPs, this study has to derive its own unique mixing parameters. However, poor agreement between the experimental data of Majima *et al.* (1988) and the other studies, even for the same salt system, complicates this exercise. A relative mean activity coefficient, $\gamma^*_{\pm}$, is therefore defined:

$$\gamma^*_{\pm,m} = \frac{\gamma^{ternary}_{\pm,m}}{\gamma^{binary}_{\pm,m}} \qquad 2.77$$

This relationship normalises the mean activity coefficient in the ternary system to its value in the binary system at the same molality (m), and thus provides a more suitable basis for comparison.

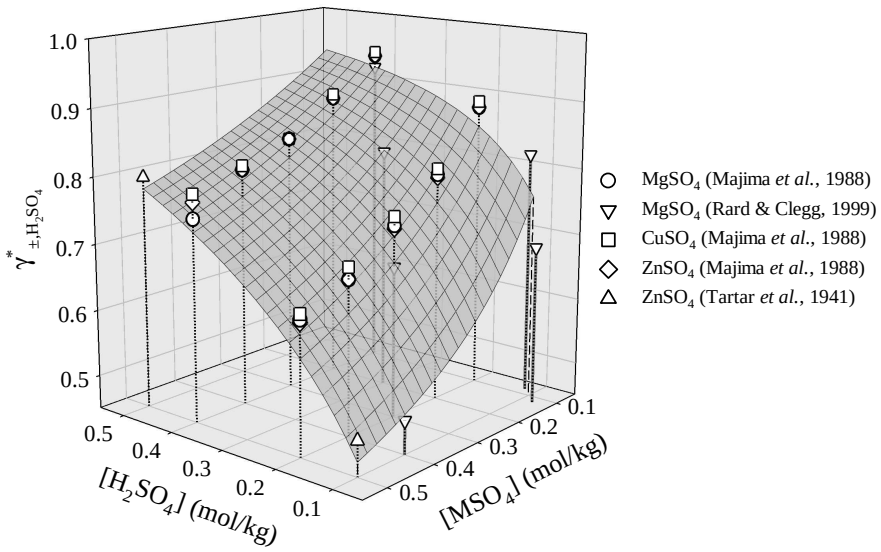

Figure 2.19
Summary of $\gamma^*_{\pm,H2SO4}$ values in ternary mixtures with M(II)SO_4 & H_2O from different studies at 25ºC. The mesh surface represents the calculated results (this study) from 0.1 to 0.5 mol/kg H_2SO_4 & $MgSO_4$ (regression discussed below).

Stellenbosch University http://scholar.sun.ac.za

Figure 2.19 compares this relative stoichiometric mean activity coefficient of sulfuric acid in various ternary mixtures, confirming a relatively close agreement between the different salt systems. On the other hand, there is a notable disagreement between the different relative mean activity coefficients of the metal sulfate salts in ternary mixtures with sulfuric acid and water, in particular between the measured data of Rard and Clegg (1999) and Majima *et al.* (1988). Since the stoichiometric mean activity and osmotic coefficient data of Rard and Clegg (1999) are most consistent with each other, they form the basis of the regression analysis for the ternary system at 25ºC. Due to the general lack of accurate experimental data, only three mixing parameters are selected. Furthermore, due to the relative obscurity of the metal(II) sulfate CIPs in acidic media (Rudolph *et al*., 1997), their mixing parameters are not considered. Only combinations of the following mixing parameters are therefore considered, $\beta^{(0)}_{MB}$, $\beta^{(1)}_{MB}$, C^{ϕ}_{MB}, θ_{HM}, ψ_{HMB}, ψ_{HMS} and ψ_{MBS}, with at least two of the binary interaction terms $\beta^{(0)}_{MB}$, $\beta^{(1)}_{MB}$ or θ_{HM} required. Since the mixing of metal and bisulfate ions does not form CIPs (Rudolph *et al.*, 1997), the inclusion of the first two terms is most consistent with the ion-interaction approach. The limited experimental data available for the mixed ternary system make the choice of the ternary interaction term somewhat arbitrary. The same ternary interaction term is therefore used as in the work of Reardon and Beckie (1987), *i.e.*, ψ_{HMB}, but with the inclusion of the long-range electrostatic terms, ${}^{E}\theta_{HM}$ and ${}^{E}\theta'_{HM}$. The objective functions and their relative deviations are summarised in Table 2.15. The optimised parameters (at 25ºC) are summarised in Table 2.16, corresponding to a Pitzer α_1-value of 2 $(kg/mol)^{1/2}$. Therefore the calculated surfaces in Figure 2.19 (mean activity coefficient) and Figure 2.20 (osmotic coefficient) involve only three adjustable parameters, *i.e.*, $\beta^{(0)}_{MB}$, $\beta^{(1)}_{MB}$ and ψ_{HMB}.

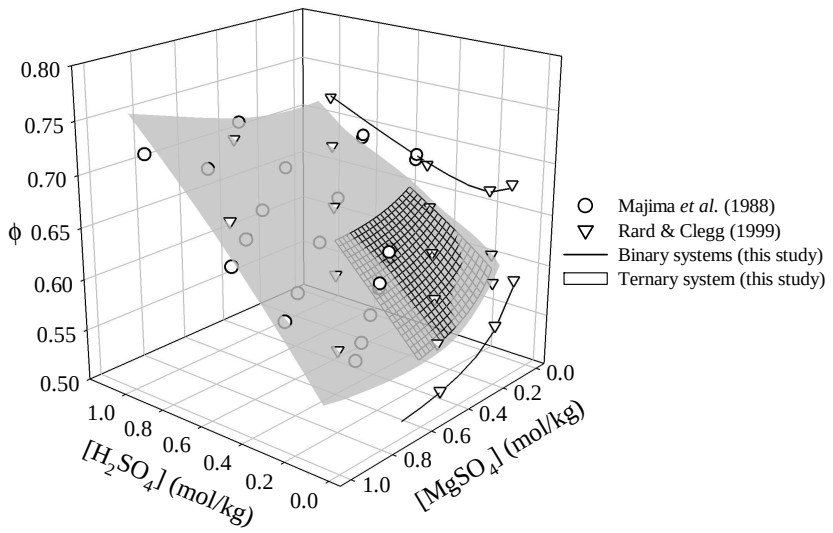

Figure 2.20
Osmotic coefficients for the H_2SO_4-$MgSO_4$-H_2O system at 25ºC. The smooth surface represents the data of Rard & Clegg, while the solid lines & mesh surface represent the calculated results (this study) for the binary & ternary systems, respectively, from 0.1 to 0.5 mol/kg H_2SO_4 & $MgSO_4$.

Stellenbosch University http://scholar.sun.ac.za

Table 2.15
Objective functions & their relative *AARD* values for the ternary H_2SO_4-$MgSO_4$-H_2O system.

Temp.	[a] Obj. func. coeff.	[b] *AARD* (%)
(°C)	$y_F(\phi, \gamma_{\pm, MgSO4}$, [c] *log* $K°_{sp})$	$\phi, \gamma_{\pm, MgSO4}$, [c] *log* $K°_{sp}$
25	½, ½, 0	2.37, 7.91, –
200	0, 0, 1	– , – , 0.11

[a] Eq. 2.72; [b] Eq. 2.73; [c] Refers to kieserite solubility (Rx. 2.76).

Table 2.16
Optimised interaction parameters for the ternary H_2SO_4-$MgSO_4$-H_2O system (with inclusion of the long-range electrostatic terms, ${}^{E}\theta_{HM}$ & ${}^{E}\theta'_{HM}$).

	[a] p_1 (kg/mol)	[a] $p_2 \cdot 10^2$ (kg/mol)
$\beta^{(0)}_{MB}$	0.2757	-0.0580
$\beta^{(1)}_{MB}$	2.0833	1.3418
ψ_{HMB}	[b] 0.2324	[b] -0.1500

[a] Eq. 2.74; [b] Units of $(kg/mol)^2$.

The only thermodynamic data known to the author for the ternary system at higher temperatures are the solubility data of kieserite at 200ºC from Marshall and Slusher (1965). This lack of data, once again, only justifies a linear dependency of the three adjustable mixing parameters on temperature (j = 2; Eq. 2.74). Figure 2.21 illustrates the good agreement between the measured solubility data in the ternary system and the calculated output, even though some concentration regions (dotted lines) fall outside the regression range.

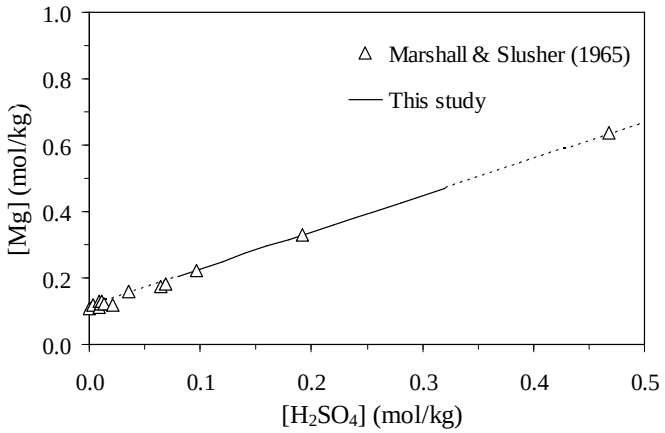

Figure 2.21
Comparison between the experimental & calculated (this study) values of kieserite solubility in the ternary H_2SO_4-$MgSO_4$-H_2O system at 200ºC (the dotted lines represent the simulated results outside the regression range).

Stellenbosch University http://scholar.sun.ac.za

2.4.3 Application of the phenomenological solution chemistry model

The methodology of explicitly recognising the strongest CIPs, within a solution thermodynamic framework, allows the direct use of the species molalities to interpret the reaction kinetics. This approach is considered simpler as compared to the alternative, *i.e.*, recognising only formal species within a solution thermodynamic framework, which requires the complex task of splitting mean activity coefficients into single ion activity coefficients in order to interpret the reaction kinetics.

Typical speciation trends

Figure 2.22 and Figure 2.23 present examples of typical trends resulting from this simulation.

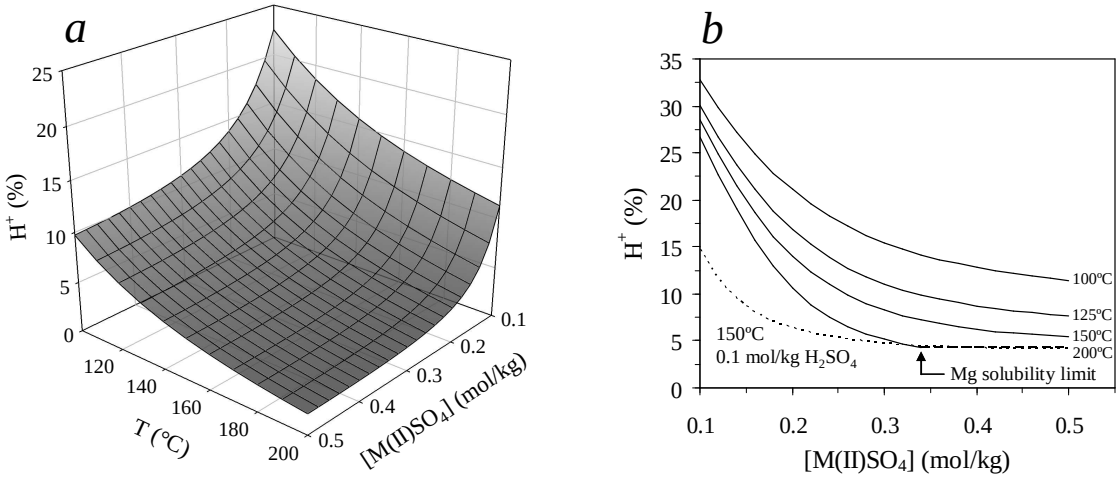

Figure 2.22
Indicative (calculated) trends of the unassociated % H^+ with varying metal sulfate concentration & temperature at 0.2 mol/kg H_2SO_4 in the ternary H_2SO_4-M(II)SO_4-H_2O system: *a*) Surface plot; *b*) Contour plots (the dotted line represents the 150ºC contour at 0.1 mol/kg H_2SO_4).

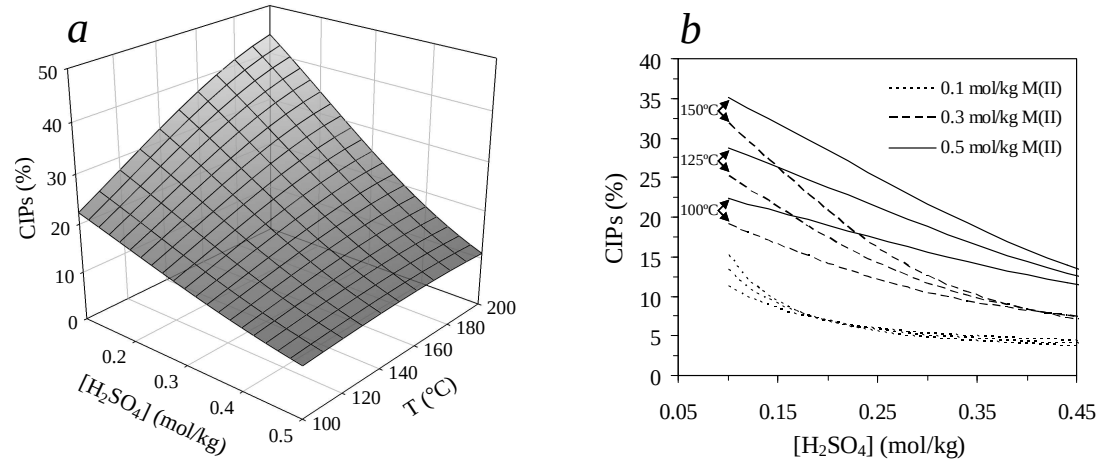

Figure 2.23
Indicative (calculated) trends of the % metal(II) sulfate CIPs with varying acid concentration & temperature in the ternary H_2SO_4-M(II)SO_4-H_2O system: *a*) Surface plot at 0.5 mol/kg M(II)SO_4; *b*) Contour plots at selected metal(II) sulfate concentrations.

Stellenbosch University http://scholar.sun.ac.za

Figure 2.22 illustrates that the unassociated H^+ concentration (as a percentage of the total hydrogen ion concentration) is more sensitive to varying metal(II) concentration at higher H_2SO_4:M(II)SO_4 ratios. Figure 2.23 *a* illustrates that the metal(II) sulfate CIPs (as a percentage of the total metal(II) concentration) are favoured at higher temperatures and lower acid concentrations. At higher metal(II) tenors, the abundance of these CIPs is more sensitive to the temperature and acid concentration (Figure 2.23 *b*).

Model application to redox solutions

Leach solutions also contain redox species, with the iron(II)/iron(III) couple being the most dominant in acidic sulfate solutions emanating from oxidative autoclave leaching: $E°_h$ ($Cu^{2+}|Cu^+$) of 0.16 V *vs.* $E°_h$ ($Fe^{3+}|Fe^{2+}$) of 0.77 V (Atkins & De Paula, 2006). Despite the buffering action of the temperature-driven precipitation reactions (Ch. 6), the mere presence of iron(III) species in the mixed electrolyte system would impact on the equilibrium constants. Various investigations have opted to use speciation calculations to estimate the relative abundance of the iron(III) sulfate (& other) species (*e.g.*, Casas *et al.*, 2005a; Crundwell, 1987; Filippou *et al.*, 1995; Hirato *et al.*, 1987; Lee & Tavlarides, 1985; Liddel & Bautista, 1981; Liu & Papangelakis, 2005a; Senanayake & Muir, 1988), albeit backed by insufficient experimental verification. By virtue of the highest K^o values, the $FeSO_4^+$, $Fe(SO_4)_2^{2-}$ and $FeHSO_4^{2+}$ species usually predominate in acidic sulfate solutions (see, *e.g.*, Stipp, 1990), with the latter species unlikely to be a CIP (Tremaine *et al.*, 2004). Crundwell (1987) modelled the kinetics of sphalerite oxidation by considering both free ferric ion and $FeHSO_4^{2+}$ as electro-active species, but not the CIP, $FeSO_4^+$. Another species of importance, albeit somewhat controversial, was originally proposed by Lister and Rivington (1955). Their calorimetric study (25°C) demanded the inclusion of an additional species at higher acidities (0.2 mol/L H^+), which was postulated as the $Fe(SO_4)(HSO_4)°$ species. Filippou *et al.* (1995) discarded this postulation, based on the study of Magini (1979), who found no spectroscopic evidence of such species. Instead, Magini used spectroscopic evidence to propose the polysulfate complexes $Fe(SO_4)_n^{(3-2n)}$, with $n > 2$. More recent studies have again brought the predominance of the neutral iron(III) complexes to the fore, even at room temperature, *e.g.*, Ciavatta *et al.* (2002) (potentiometric study) proposed that the neutral $Fe(OH)SO_4°$ species dominates in a dilute acid environment (~0.001 to 0.01 mol/kg H^+), whilst Casas *et al.* (2005a) suggested the presence of the neutral $FeH(SO_4)_2°$ species in acidic solutions. This latter species was required in order to regress their speciation model to the solubility data of iron(III) sulfate in equilibrium with rhomboclase, $FeH(SO_4)_2°_{(s)}$, *vs.* pH at 25 and 50°C. The free acidity decreases with an increased iron(III) concentration, confirming a strong association between the hydrogen ion and iron(III) sulfate species. They also conducted RS in acidic iron(III) sulfate solutions and attributed the bands at high iron(III) concentration (> 0.64 mol/kg) in the 242 to 282 cm^{-1} range to vibrations of Fe–OH–S,

Stellenbosch University http://scholar.sun.ac.za

which was seen as evidence of the neutral $FeH(SO_4)_2^\circ$ species. The model was further validated by comparing calculated solution conductivities with the experimental values. This chemical model was later extended to higher temperatures (70°C) in order simulate the precipitation of sodium jarosite (Casas *et al.*, 2007). Once again, the solubility of rhomboclase was used to derive the thermodynamic equilibrium constant for the $FeH(SO_4)_2^\circ$ formation reaction. Speciation calculations conducted using this model (Cifuentes *et al.*, 2006) confirmed that iron(III) is highly associated in sulfate solutions at 70°C, forming predominantly $FeH(SO_4)_2^\circ$ at higher acid concentrations. Elgersma *et al.* (1993) and McAndrew *et al.* (1975) also assumed that this species predominates at higher temperatures. Papangelakis *et al.* (1994) simulated the solubility of hematite at high temperatures (170 to 200°C) and acidity (30 to 100 g/L H_2SO_4), which required recognition of the $FeH(SO_4)_2^\circ$ species in order to describe its inverse solubility behaviour with temperature. Rubisov and Papangelakis (2000) found the best representation of metal solubilities for laterite autoclave solution conditions (230 to 270°C, & terminal acidities of 10 to 75 g/L H_2SO_4) by assuming the neutral species, $Fe_2(SO_4)_3^\circ$, rather than $FeH(SO_4)_2^\circ$. In another study of hematite solubility at 230 to 270°C (Liu *et al.*, 2003), a new species, $Fe(OH)_2(SO_4)^-$, was introduced in order to obtain good agreement with experimental measurement.

The above discussion suggests that iron(III) forms predominantly neutral or negatively charged polyatomic complexes at higher temperatures and in excess sulfate solution. This is to be expected due to the low dielectric constant of water at higher temperatures, which would make the solvation of the small and highly charged ferric cation unfavourable (Papangelakis *et al.*, 1994). Even in the case of the anionic species, the net charge would be delocalised and hence would be expected to yield relatively stable complexes. Existing Pitzer models of the H_2SO_4-$Fe_2(SO_4)_3$-H_2O system (*e.g.*, Christomir, 2004; Kobylin *et al.*, 2007) are untested at higher temperatures, besides the fact that the interaction parameters would be inconsistent with the model developed in this study. Furthermore, thermodynamic data of the ternary H_2SO_4-$Fe_2(SO_4)_3$-H_2O system are limited to low temperatures (Casas *et al.*, 2005a, 2007; Majima *et al.*, 1988; Rumyantsev *et al.*, 2004; Velázquez-Rivera *et al.*, 2007), while high temperature solubility data (Liu *et al.*, 2003; Papangelakis *et al.*, 1994; Umetsu *et al.* 1977) are clouded by the formation of metastable phases (Ch. 6). Therefore, the low overall charge of the iron(III) complex species, the lack of thermodynamic and spectroscopic information at higher temperatures, especially in mixtures with metal(II) sulfate salts, as well as its relatively low concentration under typical autoclave leaching conditions, justify a number of simplifications. In its simplest form, the phenomenological model artificially deals with the mixed system by reducing the (free) acidity according to the following stoichiometric reaction:

$$Fe_2(SO_4)_3 + H_2SO_4 \Rightarrow 2FeH(SO_4)_2^\circ \qquad 2.78$$

Stellenbosch University http://scholar.sun.ac.za

Calculating the solution vapour pressure

The vapour pressure of the solution is an important thermodynamic property due to the fact that most of this study is concerned with elevated temperatures. The activity of the solvent is thermodynamically related to its relative fugacity as follows (Robinson & Stokes, 1959):

$$a_w = \frac{f_w}{f_w^o} = \frac{p_w}{p_w^o} \qquad 2.79$$

The symbol $p_w°$ refers to the vapour pressure of pure water at the same temperature as the solution. The second equality term arises from the fact that the vapour pressure of the solution and pure water are of similar magnitude, so that the gas phase correction factor is practically the same for both (see Robinson & Stokes, 1959). The activity of water is directly obtained from the chemistry model (Eq. 2.7). Figure 2.24 compares the calculated vapour pressure ratio as a function of the temperature and sulfuric acid concentration in ternary mixtures with 0.5 mol/kg $M(II)SO_4$.

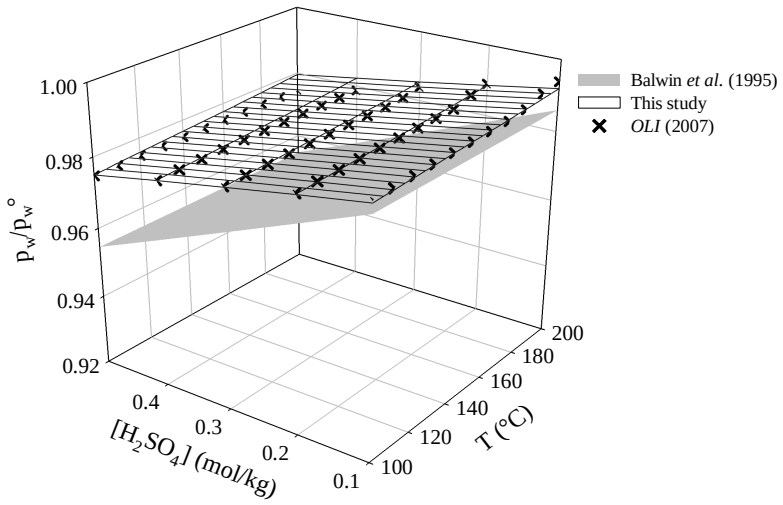

Figure 2.24
The vapour pressure ratio, $p_w/p_w°$, of the H_2SO_4-$M(II)SO_4$-H_2O system as a function of temperature & sulfuric acid concentration at 0.5 mol/kg M(II). The grey surface represents the correlation of Baldwin *et al.* (1995) at 0.25 mol/kg Zn & 0.25 mol/kg Fe^T, while the grid surface represents the simulation from this study. The datapoints represent the *OLI* software (2007; public databank) output values at 0.5 mol/kg Mg, based on the MSE model.

Unfortunately, the public databank of the commercial *OLI* software package (2007, based on the MSE model; Sect. 2.2.1) is not sufficiently populated (with regressed parameters) in order to deal with the quaternary system and the accuracy of the empirical correlation of Baldwin *et al.* (1995) cannot be verified. However, the fact that this correlation significantly underestimates (> 2%) the vapour pressure (*ref.* the *OLI* simulation) for the binary H_2SO_4-H_2O system, casts doubt on its accuracy. Since there is reasonable agreement (< 0.2% deviation) between this study and the *OLI* simulation for the binary and ternary mixtures (even at 0.5 mol/kg H_2SO_4 & $MgSO_4$ at 150ºC), the

Stellenbosch University http://scholar.sun.ac.za

above thermodynamic framework is assumed adequate. However, since the effect of the iron(III) species is not incorporated into the above framework *via* ion-interaction parameters, a modified approach is required. These predominantly neutral complexes would be hydrated, albeit less so than the free ferric ion. The simplest approach is to assume that the average interaction of these highly associated iron(III) complexes with water is similar to the reduced, but less associated, metal(II) species. Figure 2.25 evaluates this assumption by comparing published isopiestic data with the simulation for the ternary H_2SO_4-$Fe_2(SO_4)_3$-H_2O system.

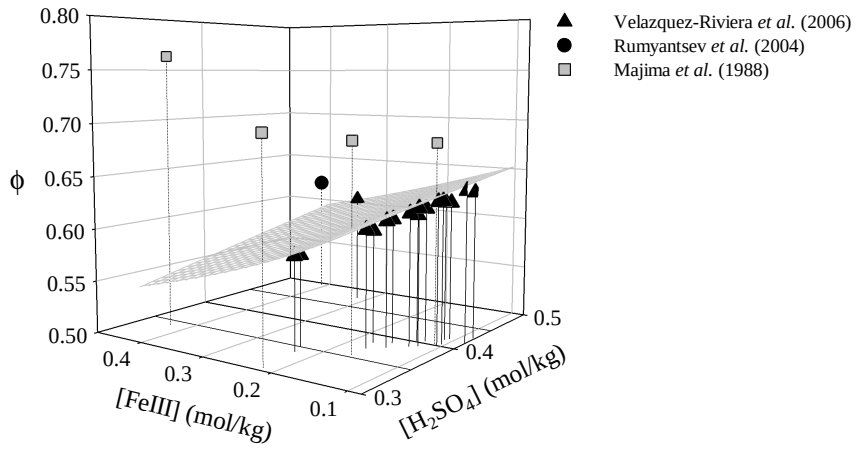

Figure 2.25
Osmotic coefficient of the ternary H_2SO_4-$Fe_2(SO_4)_3$-H_2O system at 25°C. The surface represents the simulated output from this study, assuming that the $FeH(SO_4)_2^o$ species exerts the same effect on the water activity as the equivalent concentration metal(II) sulfate salts.

The relatively small discrepancies with the data of Rumyantsev *et al.* (2004) and Velázquez-Rivera *et al.* (2007) again highlight the poor agreement with the data of Majima *et al.* (1988) (also see Sect. 2.4.2). The error introduced by not differentiating between the metal(II) and metal(III) sulfates, *i.e.*, after adjusting the acid concentration according to Reaction 2.78, is therefore significantly less than the experimental error, at least for the ternary H_2SO_4-$Fe_2(SO_4)_3$-H_2O system.

To summarise, the above approach does not capture the impact of the iron(III) species on the activity coefficients of the other solutes, other than by lowering the (free) solution acidity. Without more experimental (including speciation) data, at least for the ternary H_2SO_4-$Fe_2(SO_4)_3$-H_2O system at typical autoclave temperatures, a dedicated ion-interaction treatment of the iron(III) sulfate salt is considered superfluous, especially at relatively low iron(III) concentrations (due to precipitation) in high metal(II) sulfate backgrounds. The above assumption that the $FeH(SO_4)_2^o$ species lowers the water activity in a similar (stoichiometric) fashion to a metal(II) sulfate salt is therefore only used to estimate the solution vapour pressure in ternary mixtures, but is otherwise omitted in order to maintain the internal consistency of the thermodynamic model.

Stellenbosch University http://scholar.sun.ac.za

2.5 Overview and recommendations

2.5.1 General

The theoretical framework provided by the Pitzer ion-interaction approach is used to simulate the ternary H_2SO_4-M(II)SO_4-H_2O system, using magnesium sulfate as a surrogate salt to represent the other metal(II) sulfate salts, making this model phenomenological in nature. Since this model aims at developing a platform to interpret hydrometallurgical process kinetics, the most important contact ion pairs (CIPs) are explicitly recognised. Thermodynamic data at finite ionic strength are then used to constrain the phenomenological model, thereby inferring the speciation behaviour at autoclave temperatures, where limited experimental information is currently available. Iron(III) is also dealt with phenomenologically, not only due to the lack of thermodynamic data at high temperatures, but also because of its relatively low solubility and unresolved speciation behaviour at typical autoclave temperatures. Special effort is made to ensure that the thermodynamic data of the various CIP formation reactions are consistent with the rationale of the ion-interaction framework.

2.5.2 Thermodynamics at infinite dilution

Due to the relatively dilute nature of the electrolyte modelled in this study, all thermodynamic expressions refer back to the transcendent position of infinite dilution.

Quantum-level calculations (at 25ºC)

All calculations are conducted from a static viewpoint, which is sufficient for the purpose of this study, *i.e.*, this first-principles approach is meant to be semi-quantitative in nature, but of sufficient quality to guide the selection of the important CIPs. It is used as a complementary tool to add more confidence to the ambiguous nature of the thermodynamic data published in the literature and to better understand the simplifying assumptions.

Calculation methodology

Molecular geometries are optimised using a density function theory ($DMol^3$) – Conductor-Like Screening Model (COSMO) theoretical framework. The total coordination of the solute species is restricted by explicitly using water as a coordination filling species in the first hydration shell, while treating the effect of the solvent beyond this level *via* the COSMO methodology. Since the entropy of the solvated species cannot be obtained using the above methodology, as well as the difficulties associated with obtaining the vibrational energy, the enthalpy rather than the total free energy forms the basis of comparison with the reported literature values. This approach is based on the assumption that the enthalpy can be represented by the potential energy (E_p), *i.e.*, it assumes

Stellenbosch University http://scholar.sun.ac.za

that the kinetic energy (translational, rotational, *etc.*) cancels approximately between the solvated reactant and product species at a constant temperature.

Thermodynamically most favourable CIPs

Besides the bisulfate, HSO_4^-, species, the neutral (first metal sulfate) CIP, $M(II)SO_4^o$, is recognised in the open literature as potentially important when simulating reaction kinetics. The above calculation methodology is used to identify other species that need to be explicitly included in the overall model, *i.e.*, the CIPs that fall in a thermodynamically favourable regime, albeit less so than the above-mentioned two species. Based on an average proton hydration of between H_3O^+ and $H_5O_2^+$, a structured and static approach to the solvation of sulfate suggests that the dianion contains eight water molecules in the primary hydration shell. It is estimated to lose half its water molecules when reacting with the proton to form the bisulfate ion. Based on this framework, the neutral acid molecule, $H_2SO_4^o$, consists of two water molecules in its primary shell, yielding *log* K° of -1.3 (assuming zero entropy change for the bisulfate protonation reaction).

The first CIP of magnesium sulfate, $MgSO_4°$, is likely a monodentate complex, but the presence of a 'second' CIP can be explained by the $MgSO_4°$ bidentate complex. The formation of a triple ion pair (TIP), $Mg_2SO_4^{2+}$, as reported in the literature, is not supported by these calculations. Instead, its anionic analogue, $Mg(SO_4)_2^{2-}$, seems more plausible (*log* K^o of -3.5, based on an estimated reaction entropy of about 100 J/mol.K). The iron(II) sulfate CIPs are shown to bond in a bidentate rather than monodentate fashion, despite yielding similar equilibrium constant values. It is recommended to explore a quantum mechanical (QM) – molecular dynamics (MD) (QM-MD) calculation methodology in future modelling exercises, due to the difficulties involved in building static QM solvation models for polyatomic ions. Nevertheless, these calculations reveal unique insights into the solution chemistry of typical sulfide mineral leach solutions. Cognisance is taken of the different complexation tendencies of the different metal(II) cations with the sulfate dianion.

Temperature extrapolation

The equation of Dickson *et al.* (1990) gives a good description of the bisulfate formation constant (derived from experimentation) up to high temperatures, and is also adopted in this study. The Density function (Eq. 2.44) and thermodynamic values of Oscarson *et al.* (1988) (T_r = 150ºC) are used to calculate the neutral acid formation constant, yielding *log* K° of -1.7, which compares reasonably well with the above quantum-level calculations.

Despite exhibiting different bonding mechanisms, a typical *log* K° value of 1.5 (at 25 ºC) is obtained for the first CIP of different metal(II) sulfate salts, based on spectroscopic data (reported in the literature) and assuming unity activity coefficient of this neutral species. Since no heat

Stellenbosch University http://scholar.sun.ac.za

capacity data are available for the CIP formation reactions, it is considered a variable in the regression analysis (below). An average reaction enthalpy of 10 kJ/mol is adopted from the literature for the first CIP, while an estimated value of 49 kJ/mol for the formation of the TIP is obtained from the (above) quantum calculations. These positive reaction enthalpy values are ascribed to the energy required to break the coordination water molecules of the reacting species, but are compensated for by positive reaction entropy values, especially at higher temperatures, *i.e.*, these reactions may be viewed as being entropy driven.

2.5.3 Phenomenological model

The explicit recognition of the four CIPs, *i.e.*, HSO_4^- (B) $H_2SO_4^o$ (N), $M(II)SO_4^o$ (C) and $M(II)(SO_4)_2^{2-}$ (T), requires an iterative approach around the ion-interaction framework. Due to a lack of experimental data at high temperatures, only selected interaction parameters are allowed to vary with temperature, and only in a linear manner, *i.e.*, to prevent over-parameterisation of the model. The final regression of the binary H_2SO_4-H_2O system only makes use of the interaction parameters $\beta^{(0)}_{HB}$, $\beta^{(1)}_{HB}$ and θ_{BS}. The neutral acid species, $H_2SO_4^o$, is shown to play an insignificant role, even at 1 mol/kg H_2SO_4 and 200ºC, which is in line with recent reports in the literature.

Although the binary $MgSO_4$-H_2O system represents an oversimplification of the complexities introduced by a mixed system of various metal(II) sulfates, their activity coefficient and equilibrium constant values exhibit enough similarities to justify the surrogate approach. These similarities pay testimony to the fact that these salts consist predominantly of outer-sphere complexes at room temperature, *i.e.*, they are dominated by electrostatic forces. The interaction parameters may be regarded as capturing the electrostatically induced effects, including the formation of outer-sphere complexes, while the explicit inclusion of equilibrium constants recognises the important covalent interactions. The formation of the first CIP, $MgSO_4^o$, becomes more important at higher temperatures, based on a regressed (& constant) reaction heat capacity of 330 J/mol.K, while the TIP, $Mg(SO_4)_2^{2-}$, only becomes apparent above 150ºC, based on an optimal zero reaction heat capacity. The disadvantage of the magnesium surrogate approach is that the extent of CIP formation may be underestimated in the case of the softer transition metal cations, *e.g.*, copper(II). Since this study is concerned with trends rather than exact values, these discrepancies may be absorbed in the rate constants of the simulated reactions that make use of this thermodynamic framework. This simplification is justified by the fact that the thermodynamic data, especially in mixtures with sulfuric acid, are mostly limited to the magnesium case.

To summarise, the binary $MgSO_4$-H_2O system is adequately described by the interaction parameters $\beta^{(0)}_{MS}$, $\beta^{(1)}_{MS}$, $\beta^{(2)}_{MS}$ and λ_{SC}, while the lack of reliable experimental data for the ternary H_2SO_4-$MgSO_4$-H_2O system demands only the mixing parameters $\beta^{(0)}_{MB}$, $\beta^{(1)}_{MB}$ and ψ_{HMB}. The

Stellenbosch University http://scholar.sun.ac.za

solubility of kieserite ($MgSO_4 \cdot H_2O$) is particularly valuable in deriving the (linear) temperature dependencies of these parameters, resulting in consistent simulation trends, even beyond the ranges used in the regression. The abundance of the total metal(II) sulfate CIPs is favoured at higher temperatures and lower acid concentrations. At higher metal(II) tenors, the abundance of these CIPs is more sensitive to the temperature and acid concentration.

Due to the lack of experimental speciation data, the impact of iron(III) under oxidative autoclave conditions is treated phenomenologically by reducing the (free) acidity to form the neutral $FeH(SO_4)_2^\circ$ species. Although the existence of this species has yet to be proven convincingly, it is conveniently assigned a unity activity coefficient, *i.e.*, the interaction of this neutral inner-sphere complex with the surrounding solution is assumed weak at higher temperatures. Without more experimental (including speciation) data, at least for the ternary H_2SO_4-$Fe_2(SO_4)_3$-H_2O system at typical autoclave temperatures, a dedicated ion-interaction treatment of the iron(III) sulfate salt is considered superfluous, especially at relatively low iron(III) concentrations (due to precipitation) in high metal(II) sulfate backgrounds. It is therefore recommended to generate more thermodynamic and speciation data for these mixed electrolyte systems, especially at higher temperatures.

2.5.4 Achieving the overall modelling objective

An internally consistent model of the solution thermodynamics and equilibrium species concentrations has been developed, which may be used as a departure point from which to mathematically describe the kinetics of various reactions in the complicated H_2SO_4-$CuSO_4$-$FeSO_4$-$Fe_2(SO_4)_3$-$ZnSO_4$-$MgSO_4$-H_2O system, up to 200ºC. The effect of iron(III) on the electrolyte system is dealt with *via* the stoichiometric lowering of the (free) solution acidity, 'H_2SO_4'. The overall thermodynamic description is then treated in an internally consistent manner by adopting magnesium sulfate as a surrogate salt, reducing the above complicated mixture to the ternary 'H_2SO_4'-'$MgSO_4$'-H_2O system and explicitly recognising the most important CIPs that may impact on the kinetic processes. Speciation predictions at higher temperatures are made possible by careful selection of the thermodynamic reference data and extrapolation strategies, by selecting a minimum number of adjustable interaction parameters, and by constraining the system to the available thermodynamic data as well as the experimentally observed (lower temperature) species distributions. It also allows the calculation of the solution vapour pressure and selected salt solubilities. All these thermodynamic properties are required in order to simulate the important reactions in the chalcopyrite oxidation autoclave.

Stellenbosch University http://scholar.sun.ac.za

CHAPTER 3. INTERFACIAL OXYGEN MASS TRANSFER

3.1 Introduction

An accurate mathematical description of the interfacial mass transfer rate of the primary oxidant, the diatomic oxygen (O_2) molecule, from the gas to the liquid phase is required for all the reactors utilised in this study. This allows the intrinsic rate of all oxidation reactions to be quantified in terms of the dissolved oxygen concentration at any point in time.

The most important aspects covered in this chapter are:

- Based on the information available in the open literature, the reaction regimes required to obtain the mass transfer coefficients and the most important system properties that need to be accounted for in the final rate expressions, are identified (Sect. 3.2)
- Confidence in the experimental equipment and procedures, *i.e.*, in order to correctly interpret and maintain the interfacial mass transfer of oxygen, is established (Sect. 3.4 & 3.5), and
- The interfacial mass transfer characteristics of each reactor as a function of the most important operating parameters are quantified (Sect. 3.5).

3.2 Review and theory

The rate of physical absorption of a soluble gas has been experimentally found to be represented by the following equation (Danckwerts, 1970):

$$\frac{d[O_2]}{dt} = k_L a\left([O_2]^* - [O_2]\right) \qquad 3.1$$

The overall mass transfer coefficient, k_La (1/min), is the primary parameter dealt with in this chapter. Equation 3.1 follows directly from the film model (Danckwerts, 1970) and pictures a stagnant film of thickness δ at the surface of the liquid adjacent to the gas phase. While the rest of the liquid is kept uniform in composition by agitation, the oxygen concentration in the film falls from the saturation or equilibrium concentration, $[O_2]^*$, at the solution interface between the gas and the liquid, to its bulk solution value, $[O_2]$. There is no convection in the stagnant film and the dissolved gas crosses it by molecular diffusion alone. The driving force for the interfacial mass transfer of oxygen from the gas to the liquid phase is the difference in its chemical potential between the two phases (Filippou *et al.*, 2000). Equation 3.1 neglects the gas-side resistance of the two-film theory because it has been experimentally proven to be of minor importance for the O_2-H_2O system (see references in Filippou *et al.*, 2000). The symbol, a, represents the total interfacial area (per unit mass water) between the gas and liquid phase. The film model expresses the liquid-side mass transfer coefficient, k_L, simply as:

Stellenbosch University http://scholar.sun.ac.za

$$k_L = \frac{D}{\delta} \qquad 3.2$$

where D is the effective diffusivity of the dissolved gas in the stagnant film layer. Danckwerts (1970) pointed out that this film model is simple but not very realistic. Nevertheless, it incorporates an essential feature of the real system, namely, that the gas must dissolve and diffuse into the liquid before it can be transported by convection. Danckwerts further pointed out that predictions based on this model are usually remarkably similar to those based on more sophisticated models, such as still-surface and surface-renewal models, and indeed sometimes identical.

The k_La is strongly influenced by factors such as the agitation speed (power input), agitator type (*e.g.*, radial impellers are more efficient in dispersing gas), agitator position, reactor (& baffle) design and liquid-phase properties (ionic strength, density, surface tension, viscosity, the presence of solid particles, *etc.*). Filippou *et al.* (2000), Linek *et al.* (1987) and Van't Riet (1979) have presented good overviews of these and other aspects. Although some of these aspects have been captured in mathematical correlations, quantitative account of their effects still remains specific to the system investigated. This study therefore requires its own experimental verification.

3.2.1 Direct measurement

The k_La-value may be directly obtained by physical absorption measurements. However, due to the small autoclaves used in this study, pressure-change measurements (Filippou *et al.*, 2000) are inaccurate. Mass-flow measurements were also found to be inaccurate due to the suboptimal design of the pilot autoclave and polarographic oxygen electrodes had to be used. Although simple in concept, the interpretation is complicated because an instantaneous concentration value cannot be obtained by commercially available electrodes due to the following reasons (Linek *et al.*, 1987):

- Oxygen has to diffuse through the electrode membrane, which results in a response lag
- Gas bubbles are likely to be in regular contact with the membrane, causing a chaotic response and an average signal that may be higher or lower than the actual liquid-phase concentration, and
- Electrodes are unsuitable for determining the k_La-value at elevated temperatures.

On the other hand, Van't Riet (1979) pointed out that if the electrode response time (t_p) to record 63% of a step change, conforms to the inequality presented in Equation 3.3, the measurement error will be less than 6%:

$$t_p < \frac{1}{k_L a} \qquad 3.3$$

This study only utilised direct oxygen absorption (electrode) measurement as a confirmatory tool because it was mainly concerned with kinetic processes at autoclave temperatures and pressures.

Stellenbosch University http://scholar.sun.ac.za

3.2.2 Indirect measurement

The primary measurement method used in this study was indirect, *i.e.*, mass transfer accompanied by a chemical reaction, which consumes the dissolved gas on the solution side of the diffusion film. This method of measuring the k_La-value is also preferred due to its experimental simplicity. A drawback of this method is that the physical properties of the liquid phase cannot be varied to a great extent because high concentrations of a reducing species, *e.g.*, sulfite ion (SO_3^{2-}), are required in solution. The conditions under which the treatment of simultaneous mass transfer and chemical reaction is allowed are complicated (see Danckwerts, 1970). The enhancement factor is the factor by which the rate of gas absorption is increased due to the chemical reaction in the film layer. If the rate of absorption is to be used to calculate the k_La-value, an error would be introduced due to this enhancement of the physical transfer of oxygen by the chemical reaction. This scenario is especially prevalent when the chemical reaction rate is high compared to the k_La-value. For example, Phillips and Johnson (1959) identified operating conditions where increased agitation did not result in an increase in the mass transfer rate, indicating that the system was not under film diffusion control. In order to measure the true k_La-value, the conditions should be controlled so that no appreciable amount of the dissolved gas reacts in the film, but at the same time, the reaction should be fast enough to ensure that the gas levels in the bulk solution are reduced to zero. Under these conditions, only the saturation concentration needs to be known:

$$\frac{d[O_2]}{dt} = k_L a[O_2]^* \qquad 3.4$$

Implicit in this equation is the assumption that the thickness of the reaction zone is small, compared to the thickness of the liquid film. As illustrated by Danckwerts (1970), the conditions where no chemical reaction occurs in the film layer can be restrictive when the k_L-value is low.

Sodium sulfite solution is commonly used to determine the mass transfer characteristics in gas/liquid contactors:

$$SO_3^{2-} + \tfrac{1}{2}O_2 \Rightarrow SO_4^{2-} \qquad 3.5$$

The use of this oxidation reaction to measure the overall k_La-value is often applied without considering the restrictions involved. Danckwerts (1970) illustrated that for negligible reaction to occur in the film, *i.e.*, with no enhancement of the physical absorption process and with the bulk oxygen concentration approximately zero, the following condition (expressed per unit interfacial area) must be satisfied:

$$\frac{D_{O_2}}{k_L} \nu R_1([O_2]^*, [Red]) << k_L[O_2]^* \qquad 3.6$$

Stellenbosch University http://scholar.sun.ac.za

where R_1 is the intrinsic reaction rate per unit volume solution at the interface, [Red] is the reduced species concentration and ν is the stoichiometric coefficient. Equation 3.6 is readily manipulated to yield the following condition where no reaction occurs in the film layer (Danckwerts, 1970):

$$\frac{D_{O_2} \nu k_l [O_2]^{*(n_1-1)} [Red]^{n_2}}{k_L^2} << 1 \qquad 3.7$$

where n_1 and n_2 are the reaction orders and k_l is the intrinsic reaction rate constant (per unit volume solution at the interface). A more general description of the dimensionless left-hand side of this equation, referred to as the Hatta (Ha) number, is as follows:

$$Ha = \left(\frac{2}{n_1 + 1} \frac{D_{O_2} \nu k_1 [O_2]^{*(n_1-1)} [Red]^{n_2}}{k_L^2} \right)^{\frac{1}{2}} \qquad 3.8$$

The system is under interfacial mass transfer control only if the experimental conditions are such that $0.02 < Ha < 0.3$ (Sharma & Danckwerts, 1970). Equation 3.4 may then be used to quantify the k_La-value, but obviously only if the bulk oxygen concentration is approximately zero. The intrinsic oxidation rate of the reduced species, *e.g.*, sulfite or iron(II), is normally slow, but is catalysed by small amounts of metallic cations, such as cobalt(II) or copper(II). However, the reaction kinetics are complex and vary considerably with the type of catalyst and other solution properties, *e.g.*, the reduced species concentration, pH, and solution ionic strength (Linek & Vacek, 1981). Therefore, if the pH drops, *e.g.*, due to chemical equilibria shifts, to levels where the above condition is no longer valid (pH < 7.5; Linek & Vacek, 1981), the k_La-value may be underestimated.

Under conditions where a pseudo steady-state bulk oxygen concentration is maintained and the reaction kinetics fall in the slow regime, oxygen mass conservation requires that:

$$R([O_2],[Red]) = k_L a ([O_2]^* - [O_2]) \qquad 3.9$$

If R represents the intrinsic rate (per unit mass water), Equation 3.9 may be expressed as follows:

$$\frac{[O_2]}{[O_2]^*} = \frac{k_L a}{k_L a + \nu k [O_2]^{n_1} [Red]^{n_2}} \qquad 3.10$$

Most studies have found either a first- or second-order dependency of oxidation rate on the oxygen concentration in heterogeneous gas absorbers where a metal catalyst was used (see tables in Linek & Vacek, 1981). Under conditions where oxygen is absorbed in the presence of 1×10^{-5} to 2×10^{-5} mol/L Co(II) catalyst and 1.2 to 1.3 mol/L sulfite, the reaction has mostly been found to be zero-order in sulfite concentration (Danckwerts, 1970; Linek & Vacek, 1981). However, there is some critical value below which absorption would be dependent on the sulfite concentration: in terms of

Stellenbosch University http://scholar.sun.ac.za

determining an accurate k_La-value, this should be avoided. This critical concentration is generally in the region of 0.3 to 0.5 mol/L sulfite (Linek & Vacek, 1981). However, as pointed out by Linek and Vacek (1981), the higher the value of k_1 relative to k_L, the higher the critical sulfite concentration becomes, *i.e.*, the local sulfite concentration is more likely to drop near the interface. Various soluble impurities, *e.g.*, species introduced by a particular sulfite source or additives, may also influence the value of k_1. Therefore, the critical reaction regimes and sulfite concentrations should always be verified experimentally for each particular reactor system.

There are also other experimental methods that could be utilised to identify the correct mass transfer test regime. For example, Linek and Vacek (1981) presented typical oxygen absorption rate profiles over changing catalyst concentrations, while keeping the remaining operating conditions unchanged. A distinct region was identified where the oxygen absorption rate was independent of the catalyst loading. This is the region where the chemical enhancement of the physical oxygen absorption process would be minimal and the bulk oxygen concentration would be approximately zero, justifying the use of Equation 3.4.

3.2.3 Effect of solution composition on the k_La-value

The addition of ions to water is known to reduce the average bubble size, and hence to increase the gas/liquid interfacial area, compared to that of pure water, *i.e.*, electrolytes act as coalescence-inhibiting media. This effect is further enhanced by the tendency of the gas holdup to increase when the bubbles are smaller (Van't Riet, 1979). However, the value of k_L is also reduced due to changes in the hydrodynamics (smaller bubbles have lower k_L values; Van't Riet, 1979) and also due to a decrease in the oxygen diffusivity (Filippou *et al.*, 2000). The net effect of ions can therefore be to increase or decrease the k_La-value. There is a limiting concentration, above which the k_La is no longer concentration dependent. The limiting concentrations of 2-1 salts have generally been found to be modest, *e.g.*, about 0.1 mol/L for K_2SO_4 and Na_2SO_4 (Linek *et al.*, 1987), but are even lower for 2-2 salts (Zuidervaart *et al.*, 2000).

Surfactants can also increase the gas/liquid interfacial area by reducing the gas/liquid interfacial tension, in addition to hindering bubble coalescence. Similar to ions, surfactants will not only reduce the value of k_L by impeding diffusion, but also by reducing turbulence on a microscopic scale in the interfacial region (Filippou *et al.*, 2000). Once again, the net effect can be an increase or decrease in the overall k_La-value. Reference to various studies that investigated the effect of surfactants on the oxygen mass transfer rate can be found in Hwang and Stenstrom (1979). Surfactants were generally found to reduce the oxygen mass transfer rate, although in some instances showed no significant effect. On the other hand, a selected few cases indicated a dramatic increase in the mass transfer rate (also see Filippou *et al.*, 2000). No information is currently

Stellenbosch University http://scholar.sun.ac.za

available regarding the surfactants used in this study, *i.e.*, lignosulfonate (LS) and Quebracho (QB): their effects therefore needed to be quantified experimentally.

3.2.4 Effect of solids particles on the k_La-value

Gas/liquid mass transfer in slurry reactors is usually treated in a similar fashion to systems that contain no solids, *i.e.*, the solid-liquid phase can be treated as a pseudo-liquid phase (Sánchez *et al.*, 2005). The k_La-value is usually found to decrease with increasing solids concentration (Filippou *et al.*, 2000), although this is an oversimplification, since it also depends on the particle-specific characteristics, such as surface properties, density, size and shape (Filippou *et al.*, 2000; Hallet *et al.*, 1981, Kawase *et al.*, 1997; Sánchez *et al.*, 2005), and liquid properties (Kawase *et al.*, 1997).

Smaller particle sizes have sometimes been found to decrease the k_La-value more than larger particles, but to have the opposite effect in other cases (Filippou *et al.*, 2000). The review of Mills *et al.* (1987) pointed out that the presence of solids may affect the k_L by modifying interfacial turbulence or by creating a diffusion blocking effect. The effect of solids' loading on the k_La-value also depends on whether the liquid phase is a Newtonian fluid (the viscosity is independent of the fluid shear rate) or non-Newtonian fluid (the viscosity decreases with increasing shear rate). A decrease in the interfacial area due to increased viscosity and coalescence rates at increasing solids' loading appears to have a more significant effect in Newtonian liquids (Kawase *et al.*, 1997). However, Oguz *et al.* (1987) observed a decrease in the k_La-value of non-Newtonian aqueous suspensions of hydrophilic hematite (Fe_2O_3) and sea sand particles, amongst others, which was also (partly) attributed to a lowering of the interfacial area by enhanced bubble coalescence.

Contrary to the above trends, Zuidervaart (2000) found slurries of pyrite mineral particles to increase the k_La-value with increased solids' loading. However, it was concluded that the dissolution of oxidised metal sulfate surface layers accounted for at least 60% of this phenomenon, probably due to an increase in the ionic strength (see Sect. 3.2.3). Derksen *et al.* (2000) also observed an increase in the k_La-value in pyrite slurries using oxygen electrode measurements, whereas silica was found to impair oxygen mass transfer. However, these measurements were conducted in gas-water-solid mixtures, which would be expected to behave differently to coalescence-inhibiting gas-electrolyte-solid mixtures.

In conclusion, most researchers have found both hydrophobic sulfides and hydrophilic oxides to decrease the k_La-value (see references in Filippou *et al.*, 2000). However, the above discussion highlights the contradictory observations by different studies, which may be related to the large effect that electrolyte solutions have on gas dispersion and coalescence, as well as the varying characteristics of solid particles and their dissimilar behaviour in three-phase suspensions.

Stellenbosch University http://scholar.sun.ac.za

Although some of these effects may also be related to a gas hold-up reduction in the presence of solids particles (Filippou *et al.*, 2000; Nicolella *et al.*, 1998), the gas hold-up in agitated dispersions would be small compared to airlift- or flotation-type reactors. This highlights the need to experimentally verify the effect of solid particles on the k_La-value in the three-phase systems encountered in this study.

3.2.5 Effect of temperature on the k_La-value

Caution should be exerted when sulfite is used to measure the k_La-value, since the temperature at the interface may be raised significantly above the bulk temperature due to the rapid exothermic chemical reaction (Danckwerts, 1970; Linek & Vacek, 1981). The temperature of the bulk solution should also be controlled as far as possible, to ensure that the saturation concentration of oxygen is maintained over the course of the experiment. In order to prevent a significant change in the temperature at the interface, the chemical reaction should be slowed down, but not excessively (Sect. 3.2.2). According to Aebi (1974), the k_La increases with temperature by about 2%/°C. The following empirical equation is often used to correlate this temperature effect:

$$k_L a\,(T) = k_L a_{(T_r)}\,\theta^{T-T_r} \qquad 3.11$$

The generally accepted value of the temperature correction factor θ is 1.024 (Stenstrom & Gilbert, 1981), but values as low as 1.01 and as high as 1.09 have been reported (Hwang & Stenstrom, 1979). It should be realised that temperature affects various physical properties of the system and Equation 3.11 attempts to lump all of these together. An increase in temperature will increase the diffusivity of oxygen, and hence the value of k_L (Filippou *et al.*, 2000). However, higher temperature may decrease the interfacial surface area as the bubbles tend to coalesce more due to changes in the physical properties of the solution. The overall effect on the k_La-value depends therefore on the properties of a specific chemical system and should be checked experimentally. It is, however, generally accepted that the k_La-value increases with temperature and that it follows an Arrhenius relationship (see, *e.g.*, Atkins & De Paula, 2006), with measured activation energies between 18 and 33 kJ/mol (Filippou *et al.*, 2000). This range falls comfortably within the more extreme correction factor range stated above.

3.2.6 Effect of pressure on the k_La-value

Yoshida and Arakawa (1968) reported a decrease in the k_La-value with increasing pressure, while Shin *et al.* (1995) observed the opposite effect. Filippou *et al.* (2000) cited two cases from the literature that reported the k_La-value to be independent of the total pressure over a wide range. This insensitivity is explained by the fact that the physical properties of a solution are relatively unaffected by the total pressure.

Stellenbosch University http://scholar.sun.ac.za

The oxygen absorption rate of sulfite solutions should be proportional to the oxygen partial pressure, as long as the mass transfer rate is not enhanced by the chemical reaction and the bulk concentration of oxygen is negligible (Phillips & Johnson, 1959). According to the film model, the absorption rate should be identical for air and pure oxygen, at the same oxygen partial pressure. However, when the oxygen absorption process is measured using dilute gases, *e.g.*, air, care should be taken to ensure that the degree of oxygen depletion remains low. This is because the dilution of oxygen in an air bubble, due to its reaction with sulfite, would result in a partial pressure change. According to Linek *et al.* (1987), the error in the measured k_La-value would be less than 10%, provided that the relative decrease in concentration of oxygen in the gas phase is below 25%. In the case of pure oxygen, bubble shrinkage may influence the k_La-value in reactors with high gas hold-up characteristics. The effect of the oxygen partial pressure on its saturation (thermodynamic equilibrium) concentration is discussed next.

Oxygen solubility

Knowledge of the oxygen solubility in an electrolyte solution is important because it is the starting point of the mass transfer process across the liquid boundary layer (Eq. 3.1). The gas phase adjacent to the interfacial area is assumed to be saturated with liquid vapour and at the same temperature as the bulk solution. The solubility of oxygen in solution is related to its partial pressure by the following thermodynamic relationship (Clegg & Whitfield, 1991):

$$K^{o} = \frac{a}{f} = \frac{\gamma m}{\phi p} \qquad 3.12$$

where K° is the equilibrium constant. The pressures in mineral processing autoclaves are usually low enough to assume that the fugacity coefficient, ø, is close to unity. Since diatomic oxygen is a non-polar gas, it exhibits a very low solubility in water. Hence, the activity coefficient, γ, is also close to unity. Under conditions where $\gamma / \phi \approx 1$, oxygen would exhibit Henry-type behaviour and $K° = K_H$ (Henry's law constant). The study of Tromans (1998a) has shown that this simplification holds to within 1%, at least up to 20 atm oxygen partial pressure at the temperatures encountered in this study (< 200°C). The empirical equation of Tromans (1998a) was therefore adopted in this study to obtain the K_H values (App. A.4). Although various other empirical equations exist in the literature (see Filippou *et al.*, 2000), none of these were found to yield significantly different answers from the equation of Tromans under the conditions encountered in this study.

Increased salt concentration decreases the gas solubility due to the 'salting-out' effect of aqueous ions (Weisenberger & Schumpe, 1996). Most correlations in the literature are based on the well-known Sechenov-type relationship (see Filippou *et al.*, 2000). Although earlier correlations (Danckwerts, 1970) are limited to single-salt solutions, Schumpe *et al.* (1982) presented equations

Stellenbosch University http://scholar.sun.ac.za

that are applicable to mixed electrolyte systems. Since these equations rely solely on the temperature variation of the solubility in pure water, Weisenberger and Schumpe (1996) included gas-specific constants to enable linear extrapolation to higher temperatures. Unfortunately, these published parameters have only been tested up to 90°C, and it is uncertain at what temperature the assumed linear dependency would collapse. The use of these equations for weak electrolyte solutions has also been questioned (Narita *et al.*, 1983). The approach of Narita *et al.* (1983), *i.e.*, to use the actual species concentrations, overcomes these limitations. However, the accuracy of their Van't Hoff-type solubility dependency (see Sect. 2.3.1) is, by their own admission, questionable above 100°C. The correlation of Tromans (1998b) is most useful to this study, because it can handle multiple salt systems up to (at least) 200°C. Their approach is different in that only a fraction of the total water in an electrolyte solution is available to interact with the oxygen molecule. This conceptual basis led to the following expression for Henry's law constant (mol/kg.atm) of diatomic oxygen in equilibrium with an electrolyte mixture:

$$K_H = K_{H,w} \cdot \left(\frac{1}{1+\kappa_1 m_1^{\,y_1}} \right)^{\eta_1} \left\{ \prod_{i=2}^{j} \left(\frac{1}{1+\kappa_i m_i^{\,y_i}} \right)^{\eta_i} \right\}^{q} \qquad 3.13$$

where $K_{H,w}$ refers to the Henry's law constant of diatomic oxygen in equilibrium with pure water (App. A.4, Eq. A.17). The coefficient κ and exponents y and η are solute-specific empirical parameters (Table A.6), while an average value for parameter q of 0.8 was found, following the regression of 21 solutes (Tromans, 1998b). Since no parameters were listed for iron(II) sulfate, the value of zinc sulfate is adopted for that purpose in this study, which is substantiated by the fact that the Schumpe-model parameters (Weisenberger & Schumpe, 1996) for Fe(II) (0.1523) and Zn(II) (0.1537) are almost identical. Similarly, for sodium sulfite the parameter values of sodium sulfate are adopted, despite the fact that this type of simplification has been criticised before (Hermann *et al.*, 1993). The error due to this assumption is thought to be less than 2% (Filippou *et al.*, 2000) and is, again, justified by similar Schumpe-model parameters for SO_3^{2-} (0.1270) and SO_4^{2-} (0.1117) (Weisenberger & Schumpe, 1996).

3.3 Reaction vessels used in this study

A detailed description of the internals of the reactors is required since all of the oxidation reactions demand proper mixing, while the mathematical model requires a quantitative knowledge of the oxygen mass transfer rates. The testwork in this study was conducted in either a 2-litre (nominal size; Model 4522) (Figure 3.1) or 1-gallon (3.75 L nominal size; Model 4551) autoclave from Parr Instrument Company. The tops of these autoclaves could be easily removed and all the internal parts cleaned of adhering solid material. All wetted parts were manufactured from titanium (Grade 2). Both these autoclaves were operated at around two-thirds of their maximum work volume, *i.e.*,

Stellenbosch University http://scholar.sun.ac.za

around 1 to 1.2 L in the case of the small autoclave (1.5 L maximum work volume) and 2 L in the case of the 1-gallon autoclave (3 L maximum work volume). These work volumes resulted in a solution height-to-vessel inside diameter ratio of around 1.2 to 1.5 in the case of the 2-litre autoclave, whereas this ratio was closer to 0.7 in the case of the 1-gallon autoclave.

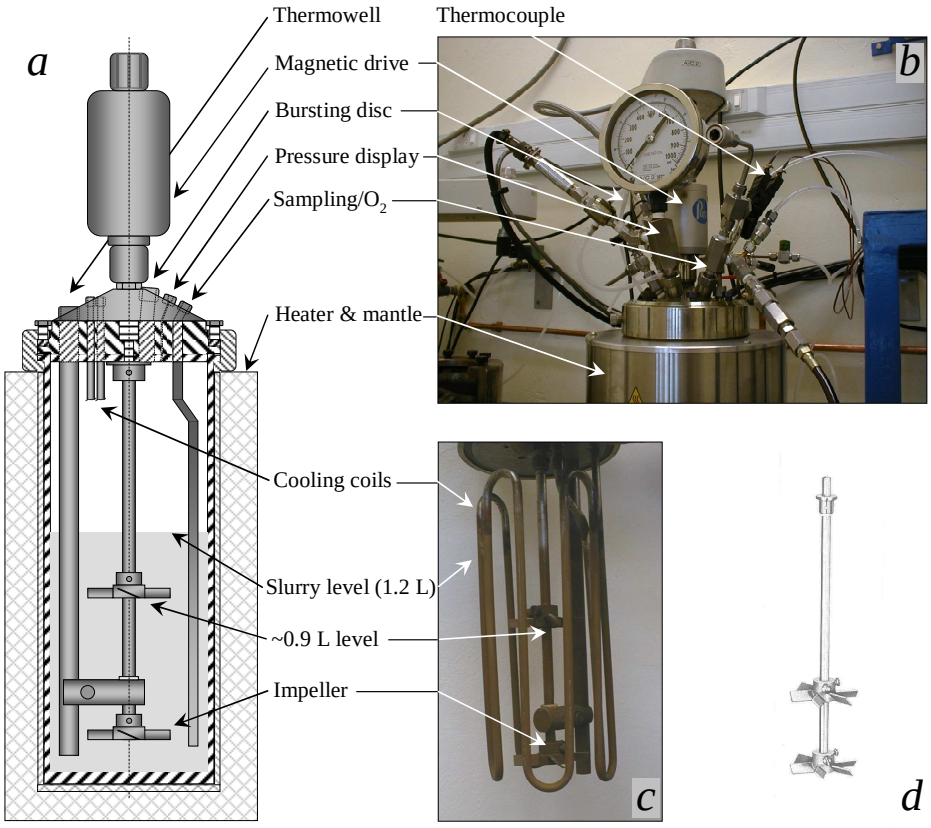

Figure 3.1
Parr batch autoclave: *a*) Schematic diagram of the 2-litre autoclave; *b*) Photo of the 2-litre autoclave; *c*) Photo of the 2-litre autoclave internals; *d*) Diagram of the 1-gallon autoclave impeller.

Despite being fitted with variable speed drives, the 2-litre autoclave was usually operated at 1000 rev/min and the 1-gallon autoclave at 500 rev/min to prevent splashing. The actual agitation speeds were regularly checked using a hand-held optical tachometer. Agitation was provided by down-thrusting turbine impellers. The 2-litre autoclave was fitted with a dual four-blade impeller system, while the 1-gallon autoclave was fitted with a dual six-blade impeller system (Figure 3.1). The top impeller in the 2-litre autoclave was fixed (for the purpose of this study) at the position illustrated in Figure 3.1; starting with 1.2 L solution or slurry, a limited number of samples could be withdrawn without significantly affecting the rate of oxygen mass transfer. In the case of the 1-gallon autoclave, the diameter was large enough to ensure that various small samples could be withdrawn from an initial 2 L volume, without significantly affecting the mass transfer rate.

Stellenbosch University http://scholar.sun.ac.za

Baffling was provided by the internal thermowells, support brackets and dip tubes. Both reactors were also fitted with serpentine cooling coils, which further improved turbulence and allowed rapid cooling after completion of a test. A built-in proportional-integral-differential (PID) controller acted on the signal from the thermocouple (type J), which was inserted in the thermowell (oil-filled). Ceramic heating mantles provided heat to the reactor; the heat-up time of the 1-gallon reactor was, however, significantly longer than that of the 2-litre autoclave. The reactor pressure was set by the pressure regulator on the feed cylinder. Each autoclave pressure gauge and transducer was calibrated with a certificate of approval. This allowed accurate steam pressure readings (using pure water) to be obtained as a function of temperature for each autoclave. These readings were, in turn, used to determine the accuracy of the thermocouples and temperature controllers, *i.e.*, by comparing the measured pressures to standard steam table values (Cooper & Le Fevre, 1982). Gas was vented through a needle release valve on each vessel head. Safety rupture discs were permanently in place for protection. Samples were taken through the dip tube, needle valve and cooling bomb system (Sect. 4.3.1). Due to the fast heat-up and cool-down times, small sample requirement and ease of operation, the bulk of the experimental testwork in this study was conducted in the smaller 2-litre autoclave. The 1-gallon autoclave was only used to generate characteristic information on the variation of the k_La-value with temperature and solids' loading.

A limited number of confirmatory iron(II) oxidation tests (Sect. 4.4.1) were conducted in the atmospheric reactor vessel (Figure 3.2), which also demanded knowledge of its mixing and oxygen mass transfer characteristics. The experimental setup consisted mainly of a glass vessel (~7.4 L total volume) with polypropylene lid, overhead motor and impeller, reflux condenser, mass-flow controller (gas), Pt100 sensor and oil bath with heating circulator and control (Julabo F12-SL HighTech Series). The bath was filled with Thermal H (Julabu) fluid which was continuously circulated through the reactor jacket. The temperature in the reactor vessel was controlled to within 1°C by the oil bath heating circulator, using feedback from the external Pt100 sensor in the glass reactor. The glass reactor was also insulated from the surroundings by an insulation jacket (see Figure 3.2). The over-sized reflux condenser consisted of an external cooling jacket and an internal cooling coil. Chilled water (~5°C) (Julabo F12-ED bath & refrigeration circulator) was continuously circulated through the condenser to reduce water loss to the environment. The impeller was also fitted with a liquid (water) seal to reduce water loss. The variable overhead drive was set at the required speed using an optical hand-held tachometer. The agitator system consisted of a shaft, down-pumping pitched-blade impeller (with fluoropolymer coating) and a polypropylene gas inductor. Anti-swirl polypropylene baffles were fitted at 90° intervals around the circumference, which increased turbulence, and hence improved the gas/liquid mass transfer rate. The working volume and design of this reactor were specifically aimed at providing excellent gas/liquid mass transfer. The inductor continuously re-entrained gas from the atmosphere above the

Stellenbosch University http://scholar.sun.ac.za

liquor surface, *i.e.*, from the point where the gas was introduced into the reactor. Samples were taken with a syringe through the feed port (Figure 3.2).

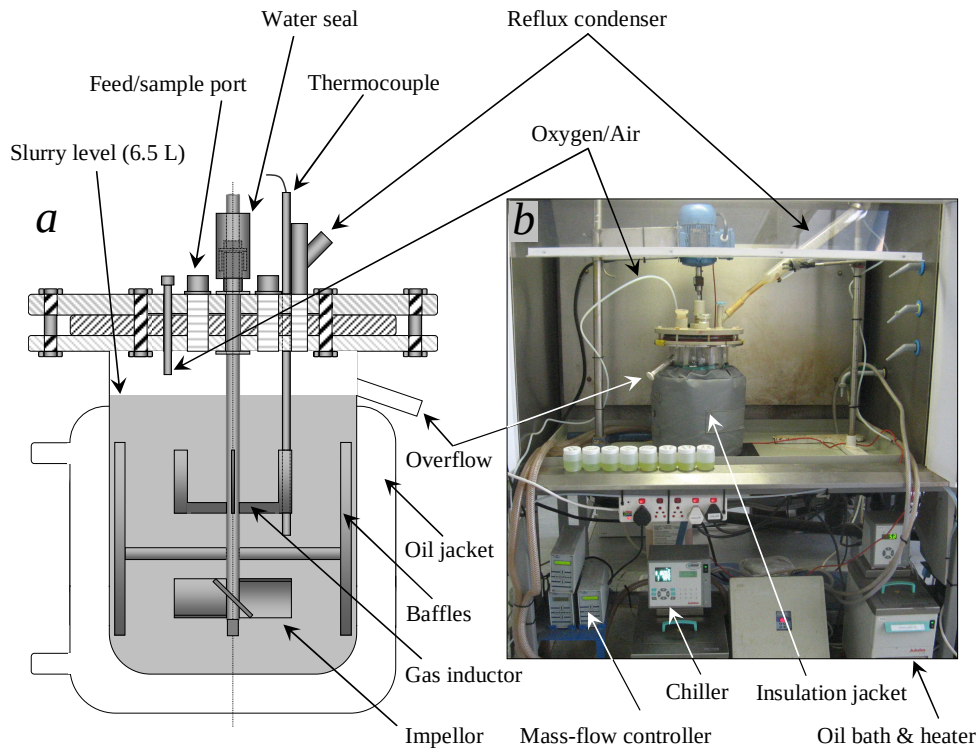

Figure 3.2
Batch atmospheric reactor: *a*) Schematic diagram of the 7-litre glass reactor; *b*) Photo of reactor with jacket & peripheral equipment.

The only other reactor used in this study was a six-compartment horizontal pilot autoclave (Ch. 7). This vessel is schematically illustrated in Figure 3.3. The complete autoclave body and internals were manufactured from Grade 2 titanium. The detailed operating procedure is presented in Section 7.3.1. The slurry was continuously fed to the first (dual) compartment and then cascaded down to last compartment, before overflowing into the autoclave letdown system. Small differences in weir heights (see Figure 3.3) ensured one-way flow through the autoclave, but this resulted in a gradual reduction in the compartment work volume along the autoclave. Each compartment was equipped with a Lightnin A315 (axial flow) impeller for mixing, solids suspension and gas dispersion, whilst a flat-blade top impeller created high bubble surface area, *i.e.*, surface entrainment *via* the formation of a vortex. As illustrated in Figure 3.3, the autoclave consisted of three sections, each containing two compartments. Each inter-sectional compartment was divided by means of an overflow weir plate, whilst an upcomer assembly separated each of the sections. This arrangement of alternating overflows and upcomers prevented short-circuiting of material.

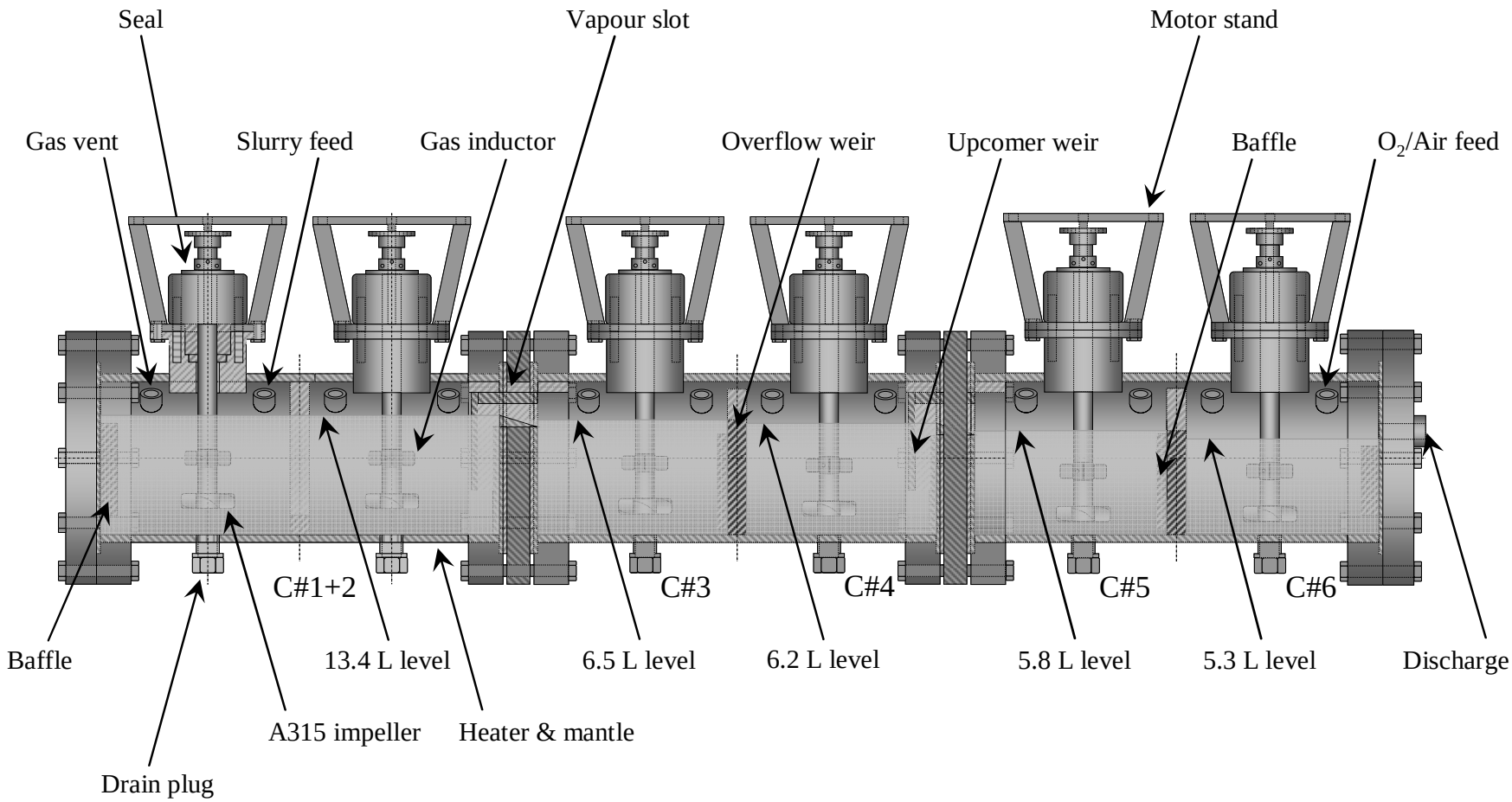

Figure 3.3
Six-compartment horizontal pilot autoclave

Stellenbosch University http://scholar.sun.ac.za

Each compartment was also fitted with baffles to enhance turbulence. Oxygen gas was originally sparged *via* a dip tube, but persistent blockage problems necessitated a modified approach, *i.e.*, introducing the gas above the slurry level and relying on the agitation system to create bubbles (*via* surface entrainment) and maintain gas hold-up. The oxygen flowed counter-currently to the slurry at a set rate, utilising a mass-flow meter and controller. The pressure inside the autoclave was controlled by a needle valve on the vent system.

The autoclave was also equipped with a series of safeguards, *i.e.*, an emergency vent valve, a pressure release valve and a bursting disc. The temperature in each compartment was individually controlled using the feedback signal from a Pt100 sensor inside each oil-filled thermowell. Heating was provided by a ceramic heating mantle around each compartment, while each section was also covered with an isolation jacket in order to reduce heat losses to the environment. Each impeller shaft was sealed using a water-cooled mechanical seal arrangement. The agitation speed in each compartment was maintained at 1000 rev/min during the initial campaign, but this was later increased to 1200 rev/min, except in the final compartment. The measured volumes, reflected in Figure 3.3, refer to the static system with all the internals in place. Table 3.1 summarises these and other measured compartment volumes at the different agitation speeds.

Table 3.1
Measured solution volume of each compartment of the horizontal pilot autoclave.

Agitation speed (rev/min)	C#1+2 (L)	[a] C#1+2 (L)	C#3 (L)	C#4 (L)	[a] C#3+4 (L)	C#5 (L)	[b] C#6 (L)	Total (L)
Static	13.39	(15.69)	6.47	6.25	(15.65)	5.77	5.28	37.16
1000	11.71	(13.61)	5.68	5.43	(13.69)	5.07	4.64	32.53
1200	11.51	(13.31)	5.52	5.37	(13.36)	4.97	4.55	31.92

[a] Represents the total volume up to the vapour slot; [b] Compartment six was always maintained at 1000 rev/min.

Despite a gradual decrease in the compartmental volumes, the distance between the normal overflow level and the top impeller was kept approximately constant by lowering each of the corresponding impeller shafts down the autoclave (see Figure 3.3). Table 3.1 also lists the volumes (in brackets) of the first two autoclave sections (C#1+2 & C#3+4), up to the vapour slot level. These values represent the volumes when the corresponding upcomer arrangements blocked (see Sect. 7.3.1 & 7.4.1). Finally, the agitation speed in the last compartment was always controlled at 1000 rev/min, in order to allow consistent overflow into the autoclave discharge system.

3.4 Experimental

This section describes the procedures and results of the gas/liquid mass transfer testwork conducted in each of the reaction vessels described above.

Stellenbosch University http://scholar.sun.ac.za

3.4.1 Equipment and procedures

Indirect (chemical) method

Mass transfer testwork in the two batch autoclaves and the atmospheric glass reactor was conducted using the indirect (chemical) method, without the need to modify the vessels or to operate them differently. However, the continuous autoclave had to be dismantled and each section operated individually in order to prevent hazardous (possible titanium fire) conditions, to prevent contamination of a test compartment with solution from an upstream compartment, and to correctly simulate the different operating volumes (Table 3.1). This experimental setup is illustrated in Figure 3.4. The perspex endplate was used to simulate the volume in each compartment during both normal and high overflow (upcomer blockage) conditions.

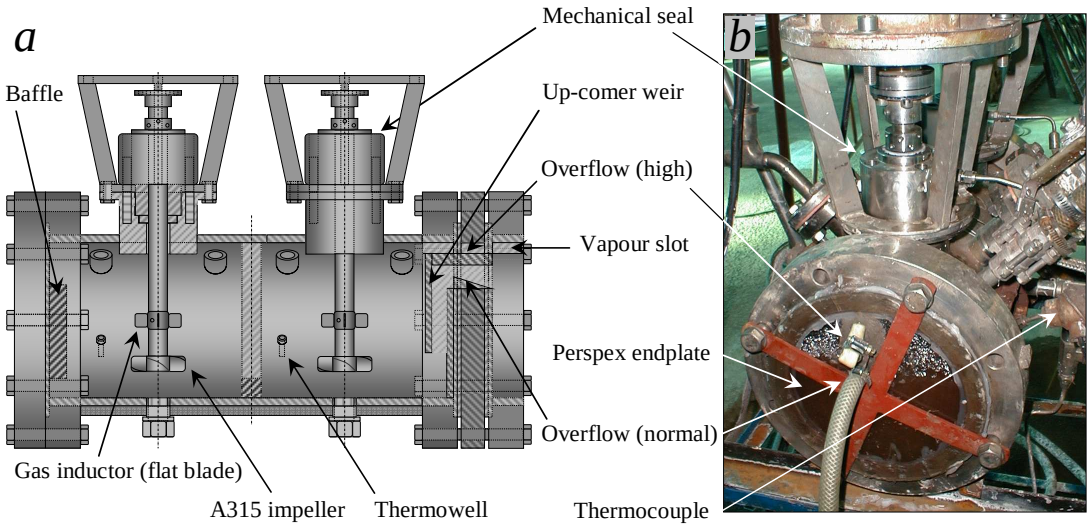

Figure 3.4
Experimental setup used to indirectly measure the O_2 mass transfer rate in a horizontal autoclave compartment: *a*) Schematic diagram of an autoclave section; *b*) Photo of the experimental setup.

The experimental procedure was virtually the same for all the reactors and is summarised in Appendix C.1.1. This method is based on an iodometric back-titration procedure (App. B.2.3) to determine the oxidation rate of a sodium sulfite solution (Rx. 3.5), which, in turn, yields the interfacial mass transfer rate of the reactor.

Direct (oxygen electrode) method

Direct electrode measurement of the oxygen absorption rate was only used as a confirmatory tool in this study. Since the 2-litre autoclave was most frequently utilised in this study, it was important to experimentally verify the results obtained by the indirect method. The experimental setup is illustrated in Figure 3.5 and Figure 3.6, consisting of electrodes of known response times and a data acquisition unit to log the increase in dissolved oxygen (DO) concentration in electrolyte solutions over time. The detailed experimental procedures are summarised in Appendix C.1.2. During the

Stellenbosch University http://scholar.sun.ac.za

initial testwork programme, it was found that entrained gas bubbles remained in the down-flow pipe, resulting in unstable and inconsistent electrode signals. The quality of the data improved after a pneumatic vibration unit was mounted on the electrodes (Figure 3.6), which continuously dispersed the small bubbles from the membrane surface.

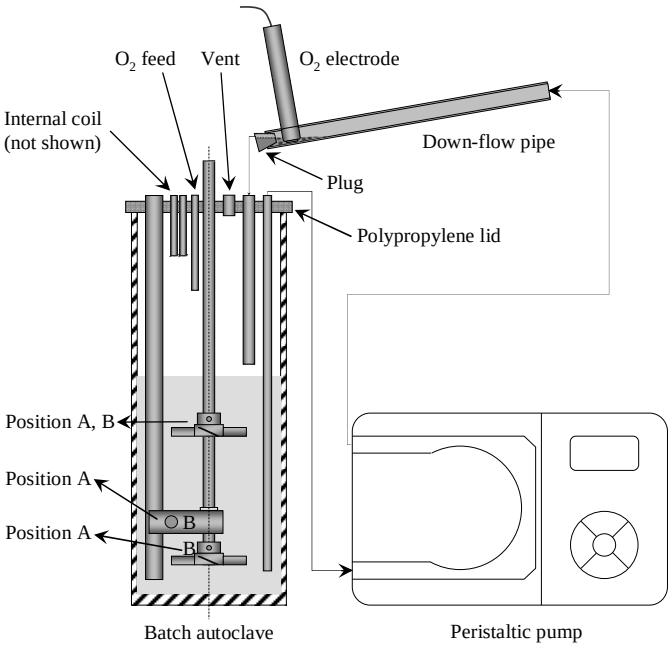

Figure 3.5
Schematic diagram of the experimental setup used to directly measure the O_2 mass transfer rate in the 2-litre batch autoclave.

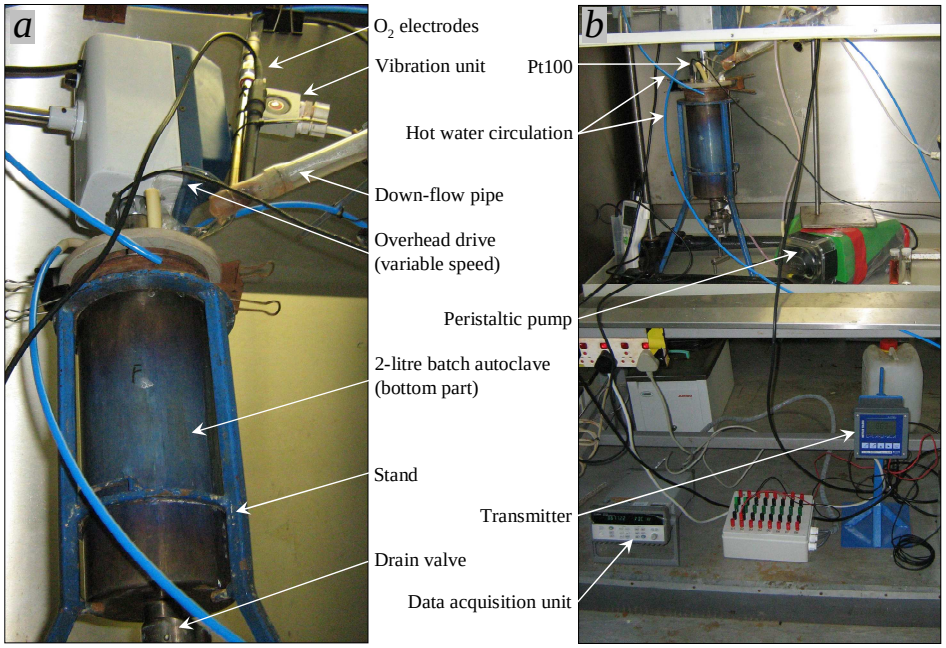

Figure 3.6
Direct measurement of the O_2 mass transfer rate in the 2-litre batch autoclave: *a*) Photo of the vessel attachments; *b*) Photo of the peripheral equipment.

Stellenbosch University http://scholar.sun.ac.za

3.4.2 Data interpretation

Indirect (chemical) method

A steady-state flow-through approach (see Linek *et al.*, 1990) was not deemed suitable, due to the relatively small sizes of the vessels used in this study and the requirement to also evaluate k_La-values at high temperatures, *i.e.*, at positive pressures. If the test conditions are such that no oxygen reacts with sulfite ion in the film layer around the gas bubbles, and, at the same time, the bulk oxygen concentration levels are close to zero (Sect. 3.2), Equation 3.4 may be integrated to yield the following relationship:

$$\Delta[O_2]_{absorbed} = k_L a [O_2]^* \cdot \Delta t \qquad 3.14$$

The thiosulfate titrant values (iodometric back-titration; App. B.2.3) were used to calculate the sulfite ion concentration in the reactor, which, in turn, revealed the amount of oxygen absorbed at each data point. Equation 3.14 was then utilised to obtain the value, $k_La\ [O_2]^*$, *i.e.*, from the straight-line region (slope) of the plot. The oxygen solubility was also calculated at each data point (App. A.4), knowing the absolute pressure and the solution vapour pressure (App. A.5). The average solubility over the straight-line region was then used to obtain the k_La-value, which is assumed to correspond to the average temperature over the same region. The detailed experimental and calculated data are presented in Appendices C.2 to C.10, including the straight-line plots for each test.

Direct (oxygen electrode) method

As mentioned above, the DO levels were automatically logged at 0.1 sec intervals until the reading had stabilised at the thermodynamic equilibrium value, $[O_2]^*$. Equation 3.1 is directly applicable in this case and may be represented in the following discrete differential form:

$$\frac{\Delta[\overline{O}_2]}{\Delta t} = k_L a (1 - [\overline{O}_2]) \qquad 3.15$$

where the over-bar refers to the normalised oxygen concentration:

$$[\overline{O}_2] = \frac{[O_2]}{[O_2]^*} \qquad 3.16$$

The recorded experimental data were manipulated into the normalised form (Eq. 3.16) and then regressed to fit Equation 3.15 by searching for the optimum k_La-value. This procedure was executed numerically in *Matlab* (2011) by minimising the objective function $F(E_F)^2$ over all the relevant data points *i*, with the error function defined as follows:

$$E_F = \sum_i \left| ([\overline{O}_2]_i^{calc} / [\overline{O}_2]_i^{exp}) - 1 \right| \qquad 3.17$$

Stellenbosch University http://scholar.sun.ac.za

The detailed results and statistical information (*AARD*; Eq. 2.73) are presented in Appendices C.11 to C12 (due to the large number of recorded data points, the raw-data presentations are limited to 5 sec intervals). The electrode readings often behaved erratically around the saturation point, $[O_2]^*$, and the experimental equilibrium values could only be obtained after extended reaction times.

3.5 Results and discussion

3.5.1 The effect of different operating conditions on the k_La-value in the 1-gallon autoclave

The 1-gallon autoclave (AC), with its favourable operating height-to-diameter ratio, was used to quantify the variation of the k_La-value with changes in the operating environment (the detailed results can be found in App. C.2, C.3 & C.4). This ratio (~0.7), as well as the larger work volume (~2 L), allowed the top impeller to remain covered, *i.e.*, sample-taking (max. 10 samples of 40 mL each, incl. 'dead' samples) has a negligible effect on the mass transfer characteristics in this vessel.

Identifying the physical absorption regime (indirect method)

The temperature range was limited to 100°C in these tests, which allowed fast sample-taking, without a significant degree of flashing. Nevertheless, these temperatures required the indirect sulfite oxidation method to be used, which, in turn, demanded identification of the correct mass transfer regime (Chaudhari *et al.*, 1987; Danckwerts, 1970; Levenspiel & Godfrey, 1974; Linek & Vacek, 1981). Hence, the cobalt(II) catalyst concentration (Sect. 3.2.2) and oxygen partial pressure were varied in the first series of tests, while keeping the other conditions as constant as possible. These results are summarised in Table 3.2 and are illustrated in Figure 3.7.

Table 3.2
Sulfite oxidation tests in the 1-gallon AC at different O_2 partial pressures & Co(II) concentrations.

Test no.	Feed gas	P_g	[Co]	[b] Temp.	Slope	[b] $[O_2]^*$	k_La
–	(% O_2)	(kPa)	(mg/L)	(°C)	(mg/kg.min)	(mg/kg)	(1/min)
MTA1	100	100	0.1	80.6	277.7	15.4	**18.1**
MTA2	100	100	5.0	82.0	351.0	15.0	**23.3**
MTA3	[a] 21	250	0.1	80.4	60.9	6.7	**9.0**
MTA4	[a] 21	250	5.0	80.6	60.1	6.7	**8.9**
MTA5	100	50	5.0	80.2	103.5	9.9	**10.5**
MTA6	100	75	5.0	81.0	179.3	12.5	**14.3**

2250 g initial sln. mass & 500 rev/min agitation speed used in all these tests; [a] 21 vol.% O_2 (rounded) used for air; [b] Avg.

The k_La-values in Table 3.2 suggest that the absorption rates at the higher oxygen partial pressures are enhanced by the sulfite oxidation reaction. On the other hand, the tests conducted at the lower oxygen partial pressures (< 10 mg/kg O_2 solubility) yield similar k_La-values, irrespective of the initial catalyst concentration.

Stellenbosch University http://scholar.sun.ac.za

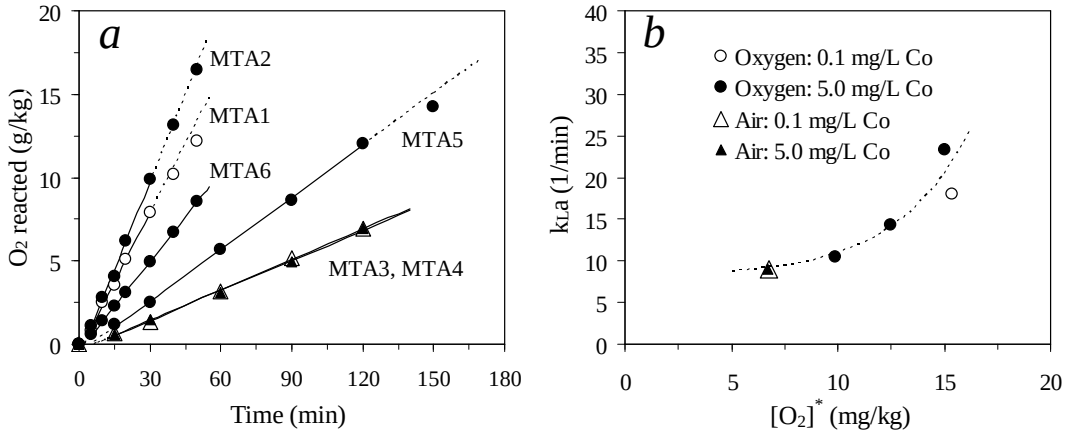

Figure 3.7
Sulfite oxidation tests in the 1-gallon AC at different O_2 partial pressures & Co(II) concentrations: *a*) O_2 absorption curves; *b*) k_La (~80°C) *vs.* $[O_2]^*$ (avg.).

It should be emphasised that some cobalt would be expected to hydrolyse and precipitate over time. The initial pH of these sodium sulfite solutions was around 9.8 and dropped only by about half a pH unit over the course of an experiment. Ji and King (2004) found an average drop of 6 to 2 mg/L Co(II) at temperatures below 50°C, whilst oxidising 0.5 mol/kg Na_2SO_3 in about 3 min. Therefore, the catalyst concentration effects are likely overemphasised in Figure 3.7, suggesting that the oxygen partial pressure is the more important controlling parameter. Although an artificial lowering of the starting pH may reduce the cobalt precipitation rate, this option was not considered in this study due to the strong reduction in the intrinsic reaction rate with pH (Sect. 3.2). Such a scenario could result in comparable values of the two denominator terms in Equation 3.10, *i.e.*

$$\frac{[O_2]}{[O_2]^*} << 1 \qquad 3.18$$

which would result in underestimated k_La-values. It would, however, been practically challenging to control the pH in this small autoclave vessel under pressure. The above results suggest that an air overpressure of 250 kPa results in a relatively insignificant enhancement of the physical absorption rate. It is also assumed that the gas hold-up in these stirred vessels is low as compared to the oxygen absorption rate and that the vapour-phase vent rate is fast enough to assume that the oxygen partial pressure in each bubble is maintained at the bulk gas-phase value.

Quantifying the effect of temperature on the k_La-value

The relatively low air overpressure of 250 kPa was also used to study the effect of temperature on the k_La-value over a relatively narrow range of 40 to 100°C. These results are presented in Table 3.3 and are illustrated in Figure 3.8.

Stellenbosch University http://scholar.sun.ac.za

Table 3.3
Sulfite oxidation tests in the 1-gallon AC at different temperatures, using air (P_g = 250 kPa).

Test no.	[a] Temp.	Sln. mass (start)	Slope	[a, b] $[O_2]^*$	k_La
–	(°C)	(g)	(mg/kg.min)	(mg/kg)	(1/min)
MTB1	40.0	2300	42.5	10.0	**4.3**
MTB2	60.0	2280	54.2	8.0	**6.7**
MTA3	80.4	2252	60.9	6.7	**9.0**
MTA4	80.6	2250	60.1	6.7	**8.9**
MTB3	100.0	2220	87.7	5.5	**16.0**

500 rev/min agitation speed & 0.1 mg/L Co(II) added initially; [a] Avg.; [b] 21 vol.% O_2 (rounded) used for air.

The solution volume 'at temperature' was kept constant by varying the initial solution mass in the autoclave. Although an Arrhenius-type relationship would suffice, a superior result is obtained by Equation 3.11, using the 40°C test (MTB1) as the point of reference (Figure 3.8 *b*). The best regression is obtained with a correction factor of 1.021, while the Arrhenius plot corresponds to an activation energy of 20.0 kJ/mol. These values compare well with the literature (Sect. 3.2.5) and suggest that minimal chemical enhancement of the oxygen absorption rate was prevalent under these conditions. The value of $\theta = 1.021$ is therefore adopted in the rest of this study.

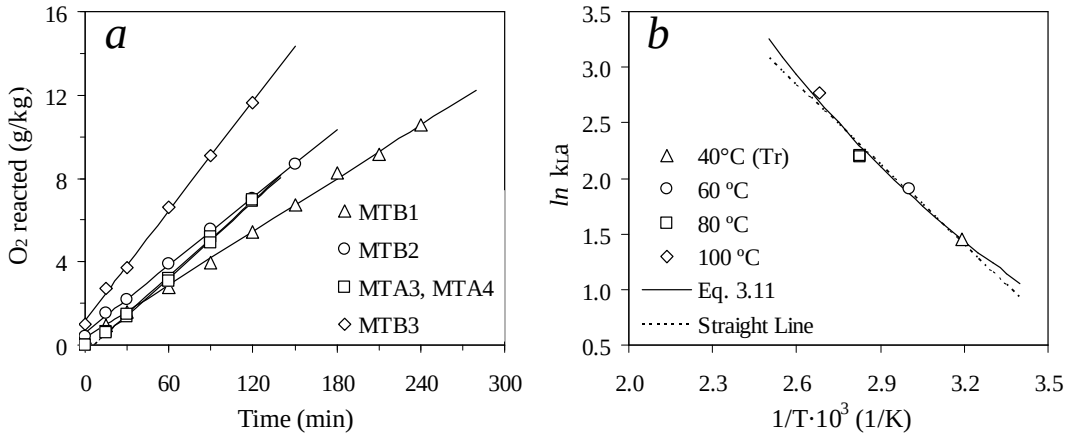

Figure 3.8
Sulfite oxidation tests in the 1-gallon AC at different temperatures, using air (P_g = 250 kPa): *a*) O_2 absorption curves; *b*) *ln* k_La *vs.* 1/T (Arrhenius coordinates).

The effect of increasing sulfide concentrate pulp density on the k_La-value

The next series of tests aimed at quantifying the effect of fine hydrophobic sulfide mineral particles on the k_La-value. Section 3.2.4 has highlighted the disagreement that exists in the open literature with regard to the effect of sulfide particles, especially under conditions of low bubble coalescence. The concentrate contained 34% total sulfide and consisted predominantly of the mineral sphalerite (54% Zn, 7% Fe), with minor amounts of pyrite and pyrrhotite (3% Fe) and trace amount of

Stellenbosch University http://scholar.sun.ac.za

chalcopyrite (1% Cu). The particle size distribution (PSD) is as follows: d_{10} = 15 µm, d_{50} = 36 µm and d_{90} = 92 µm. The initial solution mass was adjusted to give a constant slurry volume 'at temperature'. These results are summarised in Table 3.4 and are illustrated in Figure 3.9.

Table 3.4
Sulfite oxidation tests (1-gallon AC) at various sulfide pulp densities, $\rho_{s/w}$, using air (P_g = 250 kPa).

Test no.	$\rho_{s/w}$	Sln. mass (start)	Slope	[a, b] $[O_2]^*$	[c] k_La (80°C)
–	% (kg/kg H_2O)	(g)	(mg/kg.min)	(mg/kg)	(1/min)
MTA3	0.0	2252	60.9	6.7	**9.0**
MTA4	0.0	2250	60.1	6.7	**8.8**
MTC1	2.9	2250	64.2	6.8	**9.5**
MTC2	8.7	2240	59.3	6.8	**8.8**
MTC3	17.7	2215	56.0	6.8	**8.3**

500 rev/min agitation speed & 0.1 mg/L Co(II) added; [a] Avg.; [b] 21 vol.% O_2 (rounded) used for air; [c] Calc. (Eq. 3.11).

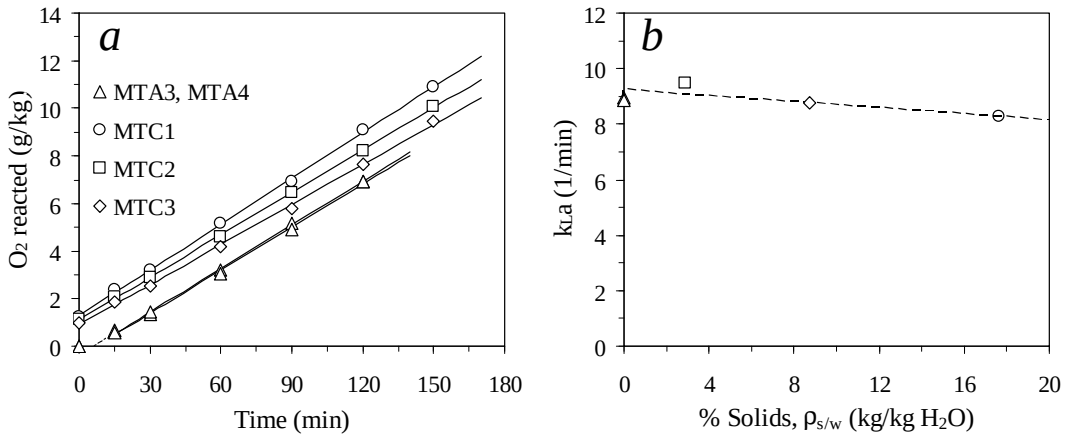

Figure 3.9
Sulfite oxidation tests in the 1-gallon AC at different sulfide mineral pulp densities, using air (P_g = 250 kPa): *a*) O_2 absorption curves; *b*) k_La (80°C) *vs.* $\rho_{s/w}$ (%).

Although these tests were conducted under similar conditions, their temperatures are corrected (Eq. 3.11) to a common reference temperature of 80°C. Although the apparent increase in the k_La-value at 2.9% solids (Figure 3.9 *b*) could be related to the dissolution of copper(II) from the oxidised mineral surface, the chalcopyrite content (1% Cu) and copper hydroxide solubility product ($K°_{sp}$ = 4.8×10^{-20} for $Cu(OH)_2$ *cf.* 1.3×10^{-15} for $Co(OH)_2$; Söhnel & Garside, 1992) are both very low. Chemical enhancement of the oxygen absorption process by dissolving copper(II) ions is therefore less likely here (*cf.* Sect. 3.5.5) and this apparent anomaly may be due to experimental error, rather than any physical effect. It is therefore concluded that the presence of sulfide mineral particles decreases the k_La-value only slightly in typical electrolyte solutions (low bubble coalescence tendency *cf.* pure water) and at pulp densities less than 20 wt% solids.

Stellenbosch University http://scholar.sun.ac.za

3.5.2 The kLa-value of the 2-litre autoclave at different temperatures, oxygen partial pressures, cobalt catalyst concentrations and initial reactor volumes

The more versatile 2-litre autoclave could be heated or cooled at significantly faster rates (*cf.* the 1-gallon autoclave) and was therefore used in most of the testwork conducted in this study. However, its comparatively smaller volume, combined with excessive sample-taking, may result in undesirable variations of its oxygen mass transfer characteristics. It was also necessary to check whether the temperature correlation (Eq. 3.11) is valid up to MT autoclave conditions. These results are summarised in Table 3.5 (the detailed results can be found in App. C.5 & C.6).

Table 3.5
Sulfite oxidation tests in the 2-litre AC at different temperatures, O_2 partial pressures, Co(II) concentrations & initial reactor volumes.

Test no.	Temp.	[a] Gas feed	P_g	[b] Sln. mass	[b] [Co]	Slope	$[O_2]^*$	k_La
–	(°C)	(% O_2)	(kPa)	(g)	(mg/L)	(mg/kg.min)	(mg/kg)	(1/min)
MTD1	100	100	100	1300	0.1	88.2	9.3	**9.5**
MTD2	150	21	550	1301	5.0	158.1	4.7	**33.7**
MTD3	150	21	500	1300	1.0	89.5	3.4	**26.5**
MTD4	150	10	500	950	0.1	23.2	1.6	**14.5**
MTE1	80	21	300	1300	1.0	64.9	7.6	**8.6**
MTE2	100	21	350	1300	1.0	83.8	7.4	**11.3**
MTE3	120	21	350	1300	0.1	84.8	5.6	**15.2**

1000 rev/min agitation speed, using impeller config. A (Fig. 3.1 & 3.5); [a] Vol% O_2 (21% in air); [b] Starting sln.

The first interesting comparison is made in Figure 3.10, *i.e.*, between the tests conducted at 150°C, using different initial solution volumes. Test MTD3 commenced at about 1250 mL initial solution volume, with both impellers being submerged over the course of the experiment, while Test MTD4 (~900 mL initially) commenced with the solution level at the top impeller (Figure 3.1). The sample volumes in these two tests were deliberately increased to about 50 mL/sample to accentuate the effect of sampling on the oxygen absorption rates. Besides the different oxygen absorption rates due to the different operating partial pressures (21% *vs.* 10% O_2), the lower initial rate in the case of Test MTD3 and the upward curvature at the end of Test MTD4 are clear indications that the distance between the liquid surface and the closest working impeller affects the oxygen absorption rate. This is confirmed by an almost 50% reduction in the k_La-value when only the bottom impeller is active, *i.e.*, about 15 1/min for Test MTD4 (only the bottom impeller active) *vs.* about 27 1/min in the case of Test MTD3 (both impellers active). This dependency of the mass transfer rate on the liquid level is exploited later in the chapter, in order to quantify the effect of hematite and chalcopyrite particles on the k_La-value *via* direct oxygen electrode measurements in the lower mass transfer rate regime (Sect. 3.5.6).

Stellenbosch University http://scholar.sun.ac.za

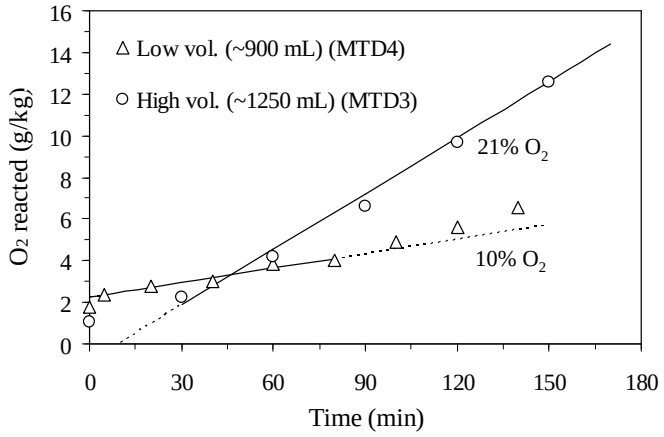

Figure 3.10
O_2 absorption curves at different initial solution volumes in the 2-litre AC at 150°C (P_g = 500 kPa).

Since the 2-litre and 1-gallon autoclave internals and operating conditions were similar, despite utilising different impellers and agitation speeds, these absorption rates would not be expected to be enhanced by the sulfite oxidation reaction. Variations in the oxygen partial pressure may be used to check this assumption, utilising Equation 3.11 as the comparison basis (Figure 3.11). Once again, differences in the initial cobalt catalyst concentration are likely of less importance here because of its low solubility in basic sulfite solutions (see Sect. 3.5.1), especially at these higher temperatures.

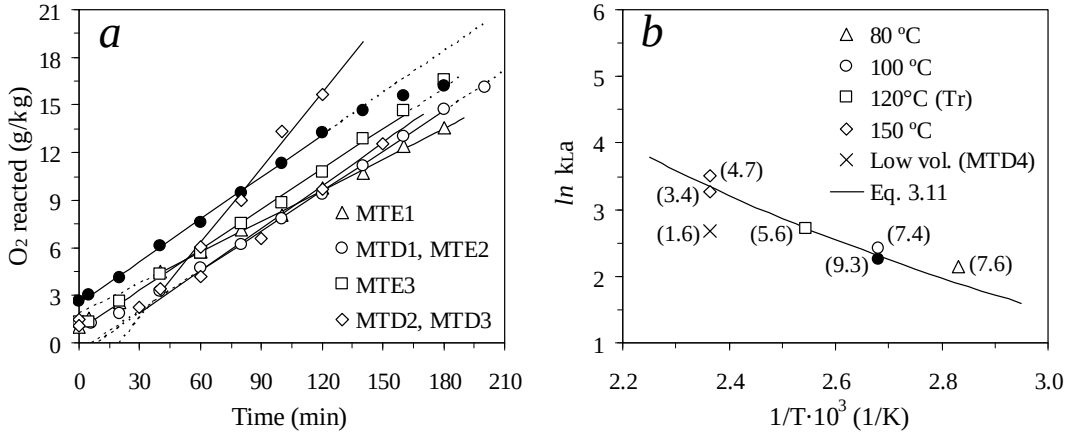

Figure 3.11
Sulfite oxidation tests in the 2-litre AC at different temperatures & O_2 partial pressures: *a*) O_2 absorption curves; *b*) *ln* k_La *vs.* 1/T (Arrhenius coordinates). The bracketed values refer to $[O_2]^*$ (mg/kg) & the closed symbol refers to 100% O_2.

Figure 3.11 *b* illustrates that the temperature correlation (Eq. 3.11, for $\theta = 1.021$) is maintained up to 150°C, with the reference temperature best represented by Test MTE3, *i.e.*, at 120°C. Whilst the small difference between the two k_La-values at 100°C may be due to experimental error, the

Stellenbosch University http://scholar.sun.ac.za

comparatively larger variation at 150°C suggests some chemical enhancement effect. This may also be true for the 80°C point, which deviates slightly from Equation 3.11.

3.5.3 Comparison between the absorption regimes in the 1-gallon and 2-litre autoclaves

Assuming that the intrinsic reaction rate is first-order with respect to the dissolved oxygen concentration and zero-order with respect to the sulfite concentration (Sect.3.2.2), the following restriction appears to hold for the 1-gallon reactor, which follows directly from Equation 3.7:

$$D_{O_2} \nu k_1 << k_L^2 \qquad 3.19$$

However, this condition appears to be more marginal in the case of the 2-litre autoclave. This is supported by the comparative k_La-values of these reactors, based on their respective reference values (Tests MTB1 & MTE3) and using Equation 3.11 to extrapolate to a common temperature. The k_La-value (at 25°C) of the 2-litre autoclave (2.1 1/min) is about one-third lower than the corresponding value of the 1-gallon autoclave (3.1 1/min). Follow-up tests were therefore conducted in the 2-litre autoclave, utilising direct oxygen electrode measurements (Sect. 3.5.6).

3.5.4 The k_La-value in the continuous pilot autoclave at different operating conditions

Table 3.6 summarises the results obtained in selected compartments of the continuous pilot autoclave (see Figure 3.3; the detailed results can be found in App. C.7). Similar to the 2-litre autoclave, the k_La-value is sensitive to the liquid level above the top impeller. A reduction in the k_La-value is observed at the high (H), as compared to the normal (N), overflow levels (Table 3.6).

Table 3.6
Sulfite oxidation tests in the continuous pilot autoclave at different conditions & compartments.

Test no.	[a] AC comp.	Speed	[b] Sln.	[c] Temp.	P_g	Slope	[c] $[O_2]^*$	k_La	[d] k_La (25°C)
–	–	(rev/min)	(g)	(°C)	(kPa)	(mg/kg.min)	(mg/kg)	(1/min)	(1/min)
MTF1	C #1 (N)	1000	6500	82.3	500	116.2	11.9	9.8	**3.0**
MTF2	C #1+2 (N)	1000	13000	80.2	100	27.6	3.1	8.9	**2.8**
MTF3	C #1+2 (H)	1200	14000	155.8	650	31.5	5.5	5.7	**0.4**
MTF4	C #4 (N)	1200	5500	152.8	650	351.3	6.5	53.9	**3.8**
MTF5	C #4 (H)	1200	7500	81.0	100	5.9	3.1	1.9	**0.6**

Air (21 vol% O_2) & 1 mg/L Co(II); [a] At norm.(N) & high (H) overflow levels; [b] Starting sln.; [c] Avg.; [d] Calc. (Eq. 3.11).

Under normal operating conditions and 1000 rev/min, the calculated (using Eq. 3.11) k_La-value at 25°C in the combined first two compartments (2.8 1/min) compares well with the 1-gallon batch autoclave (3.1 1/min). Therefore, under these conditions, the chemical enhancement of the physical absorption process is minimal. However, this is not necessarily true at a lower k_La-value (Sect. 3.6), *e.g.*, due to a high overflow level (Sect. 7.3.1). Also, differences between the single and double compartment k_La-values (3.0 & 2.8 1/min, respectively) appear less than the experimental error.

Stellenbosch University http://scholar.sun.ac.za

3.5.5 The effect of different operating conditions on the k_La-value in the 7-litre glass reactor

The 7-litre glass reactor (Figure 3.2) was used to conduct confirmatory iron(II) oxidation testwork under atmospheric pressure conditions (Ch. 4, Sect. 4.3.1). This vessel was designed to give excellent gas/liquid mass transfer rates and to reduce the effect of sample-taking, hence, the relatively large working volume. Table 3.7 summarises the results of all these tests, using the indirect method (the detailed results can be found in App. C.8, C.9 & C.10). The last column presents the calculated (Eq. 3.11) k_La-values at 80°C, which are used as the basis of comparison.

Table 3.7
Sulfite oxidation tests in the 7-litre glass atm. reaction vessel at different operating conditions.

Test no.	Variable	[d] Temp.	[e] Sln. mass	Slope	[d] $[O_2]^*$	k_La	[f] k_La (80°C)
–	–	(°C)	(g)	(mg/kg.min)	(mg/kg)	(1/min)	(1/min)
MTG1	[a] 6.15 L	45.0	6800	25.9	2.3	11.2	**23.2**
MTG2	[a] 6.65 L	52.8	7358	28.3	2.0	14.0	**24.6**
MTG3	[a] 7.15 L	49.6	7925	29.0	2.1	13.6	**25.5**
MTG4	[b] 21% O_2	80.4	7100	25.0	1.0	26.2	**26.0**
MTG5	[b] 21% O_2	79.7	7100	28.1	1.0	28.5	**28.7**
MTG6	[b] 100% O_2	83.3	7100	198.9	3.8	51.9	**48.5**
MTG7	[c] 20% O_2	82.9	7100	19.2	0.8	24.3	**22.9**
MTG8	[c] 10% O_2	80.4	7100	13.0	0.5	28.6	**28.4**
MTG9	[c] 21% O_2	77.9	7100	30.4	1.1	28.4	**29.7**
MTG10	[c, g] 0.35 g/L LS, QB	79.6	7100	29.1	1.0	29.4	**29.7**
MTG11	[c, g] 0.50 g/L LS, QB	79.8	7100	24.5	1.0	25.0	**25.1**
MTG12	[a] 3.5% Cpy	80.5	7050	41.6	0.9	44.0	**43.6**
MTG13	[a] 7.0% Cpy	80.5	7000	40.4	0.9	42.6	**42.2**
MTG14	[a] 15% Cpy	80.7	6850	36.9	0.9	39.3	**38.8**
MTG15	[a] 7% Cpy, [g] 0.5 g/L LS, QB	80.0	7000	39.8	1.0	40.0	**40.0**

Gas flowrate ~10 L/min (excess O_2), 1000 rev/min, ~6.5 L, air (21 vol% O_2), unless indicated otherwise; [Co(II)]: [a] 0 mg/L; [b] 0.0001 mg/L; [c] 0.001 mg/L; [d] Avg.; [e] Starting sln.; [f] Calc. (Eq. 3.11); [g] Norlig A, Orfom 2 (no pre-drying).

Identifying the absorption regime at different volumes, O_2 pressures and Co(II) concentrations

The solution starting volumes, oxygen partial pressures and cobalt catalyst concentrations were varied in the first nine tests, all of which are presented in Figure 3.12. The first three tests (open symbols) illustrate that the impact of relatively large sample volumes on the k_La-value is comparable to or, more likely, less than the experimental error (~10%) in the 7-litre reactor.

Figure 3.12 *b* also illustrates the chemical enhancement of the absorption rate when using pure oxygen (Test MTG6), whereas no conclusive evidence exists regarding the role of the oxidation reaction in the other tests. The average k_La-value is significantly higher in the 7-litre reactor (~8.3

Stellenbosch University http://scholar.sun.ac.za

1/min at 25°C) compared to the 1-gallon autoclave (3.1 1/min). Since the bubbles appeared very small, this high k_La-value is probably the result of the extensive bubble surface area created by the inductor (Figure 3.2) shear forces. On the other hand, the smaller bubbles are also associated with smaller k_L-values (Sect. 3.2.3). Therefore, the fact that the three lower temperature tests (~50C°; MTG1, MTG2 & MTG3) exhibit lower than average k_La-values and no cobalt(II) catalyst was added in those tests, suggests that the restrictive condition (Eq. 3.19) may be violated at higher temperatures, especially in the presence of cobalt(II). This is consistent with the well-known notion that the activation energy of a chemical reaction is higher than that of a physical diffusion process.

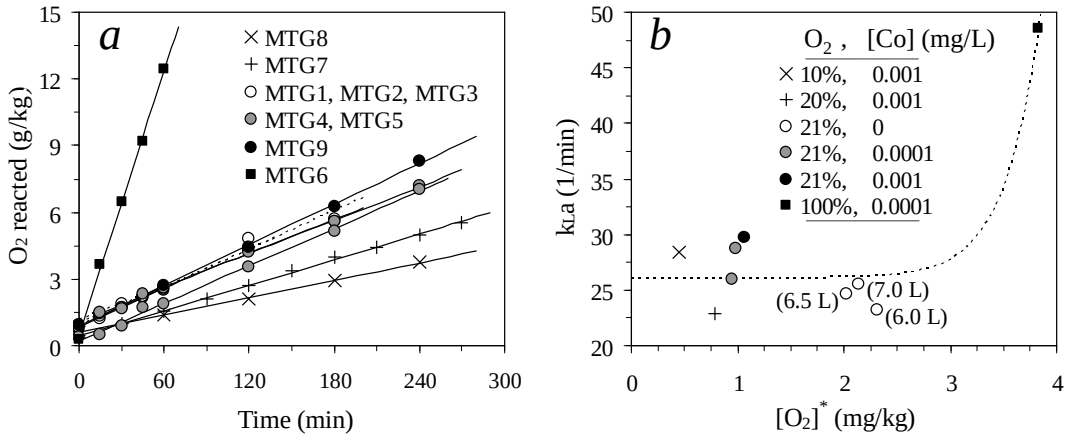

Figure 3.12
Sulfite oxidation tests in the 7-litre reactor at different initial reactor volumes, O_2 partial pressures & Co(II) concentrations: *a*) O_2 absorption curves; *b*) k_La (80°C) *vs.* $[O_2]^*$ (avg.). The bracketed values are the avg. (rounded) static solution volumes 'at temperature'.

The effect of sulfur-dispersing surfactants and sulfide concentrate pulp density on the k_La-value

Sulfur-dispersing surfactants are used during MT autoclave oxidation to prevent the occlusion of the unleached sulfide mineral particles by liquid sulfur (Sect. 6.3.3). However, Section 3.2.3 has highlighted the possibility of strong interference in the mass transfer process by such surface-active agents. Tests MTG10 and MTG11 (Table 3.7) investigated the effects of the surfactants, LS (Norlig A) and QB (Orfom grade 2 Tannin) (Sect. 6.3.3), on the k_La-value: the results are illustrated in Figure 3.13.

These surfactants clearly retard the k_La-value, which agrees with most observations from the literature (Sect. 3.2.3). It is also clear that these surfactants degrade over time, with the higher concentration taking longer to degrade due to a slower oxygen mass transfer rate. The ultimate k_La-value, after long reaction times (> t), would therefore not be affected by these surfactants, because the degradation products seemingly have no influence on the physical absorption process.

Stellenbosch University http://scholar.sun.ac.za

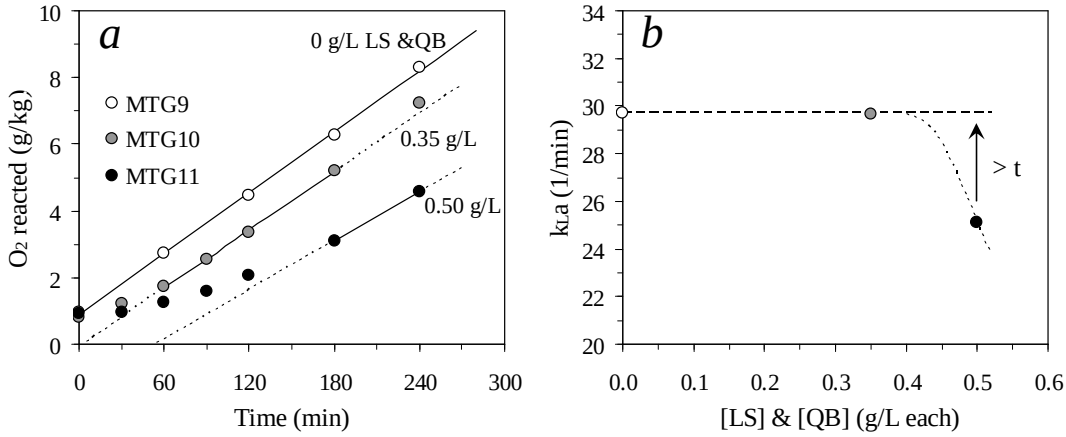

Figure 3.13
Sulfite oxidation tests in the 7-litre glass reactor at different surfactant concentrations, using air: *a*) O_2 absorption curves; *b*) k_La (80°C) *vs.* initial surfactants (LS & QB) concentrations (g/L each).

The final four tests (Table 3.7) investigated the effect of fine chalcopyrite mineral particles on the mass transfer rate, and also the effect of the above-mentioned surfactants in the presence of these mineral particles. The mineral composition and PSD of this concentrate are similar to the feed material used in the continuous pilot autoclave campaigns (Sect. 7.3.3 & 7.4.1). It consists predominantly of chalcopyrite (~69%), with some pyrite (~10%) and sphalerite (~8%), and minor amounts of pyrrhotite (~1%). The balance constitutes gangue minerals. The PSD is as follows: d_{10} = 1.7 µm, d_{50} = 3.6 µm and d_{90} = 10 µm. The initial test solution mass was adjusted to give constant slurry volume 'at temperature'. These results are illustrated in Figure 3.14.

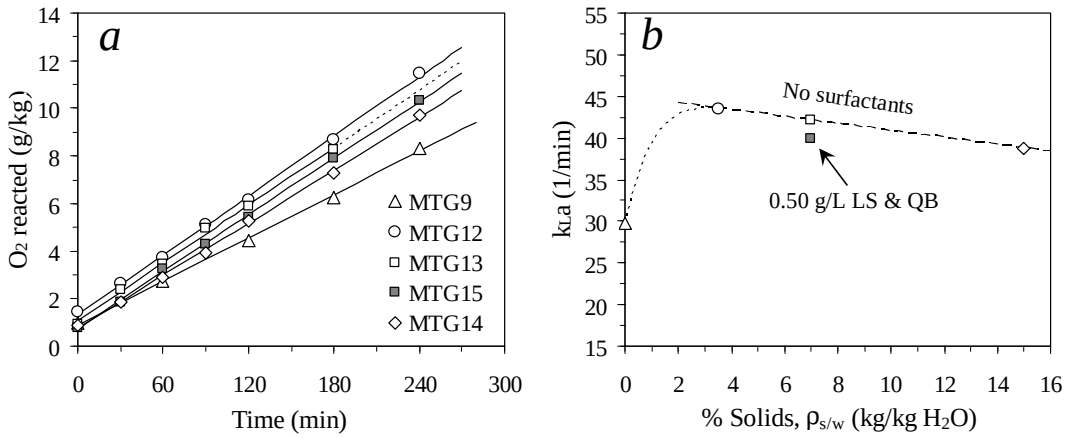

Figure 3.14
Sulfite oxidation tests in the 7-litre glass reactor at increasing chalcopyrite mineral pulp densities, using air: *a*) O_2 absorption curves; *b*) k_La (80°C) *vs.* $\rho_{s/w}$ (%).

No cobalt catalyst was initially added in any of these test solutions. The reason for the relative k_La-value increase in the presence of the chalcopyrite mineral particles may be related to the dissolution

Stellenbosch University http://scholar.sun.ac.za

of copper(II) from the mineral surface. However, prior to conducting these mass transfer tests, the concentrate was washed with dilute (~1%) sulfuric acid in order to remove any oxide layers. Nevertheless, the oxidation or reduction of the minerals and the consequent release of copper(II) ions may have accelerated the sulfite oxidation reaction to such an extent, that Equation 3.19 is no longer valid. It can be assumed that this enhancement effect is similar in all the tests where chalcopyrite concentrate was added initially due to the low solubility product of $Cu(OH)_2$ (Sect. 3.5.1), thereby accounting for the gradual decrease in the k_La-value with increasing pulp density, similar to the observed trend when adding progressively more sphalerite concentrate (Figure 3.9). An important observation from Figure 3.14 *b* is that relatively high surfactant concentrations (0.5 g/L LS & QB) have an insignificant effect on the oxygen absorption rate at 7 wt% solids. The oxygen also absorbs almost linearly (*cf.* Figure 3.13 *b*) over the course of the experiment, suggesting that the surfactant concentrations in the bulk solution are low. Since these surfactants are always associated with sulfide slurries in this study, there is no need to quantify their effects on the k_La-value in the leaching reactors, especially not at typical sulfide oxidation pulp densities (~7 wt% solids).

3.5.6 The effect of different operating conditions on the k_La-value in the 2-litre autoclave, incl. chalcopyrite and hematite pulp density, based on direct oxygen electrode measurements

The indirect method (above results) has yielded interesting and insightful information on the rate of gas/liquid mass transfer in the different reactors. However, the influence of solid particles on the k_La-value needed to be quantified, while the absolute k_La-value in the 2-litre autoclave required clarity (see Sect. 3.5.3), utilising the direct oxygen electrode measurement method. In particular, the k_La-value required confirmation at different impeller configurations, *i.e.*, using operating modes A and B (Figure 3.5). The results of the two test programmes are summarised in Table 3.8 (detailed results can be found in App. C.11 & C.12, respectively). The simulated oxygen concentration, normalised to the saturation concentration, *i.e.*, $[O_2]/O_2]^*$, generally agrees well with the measured data (see Sect. 3.4.2). Figure 3.15 and Figure 3.16 present some of the most important results, including the responses of the two electrodes, *i.e.*, the InLab 605 and InPro 6800 probes (see App. C.1.2 & C.11). The electrode response times (t_p) are short enough so that all these tests conform to Equation 3.3, with Test OPA4 showing the closest margin, *i.e.*, t_p (~16 sec) < $1/k_La$ (~24 sec).

The first important observation is the lower than expected k_La-values for impeller configuration A, *i.e.*, 1.3 to 1.4 1/min at 25°C (Tests OPA1 & OPD1, using Eq. 3.11 to extrapolate to room temperature), as compared to the corresponding value of 2.1 1/min obtained by the indirect method (Sect. 3.5.3). This represents a discrepancy of about 33% between the indirect and direct measurement methods, and is most likely due to the chemical enhancement of the k_La-value. Alternative explanations may be increased oxygen solubility and/or non-coalescent behaviour in

Stellenbosch University http://scholar.sun.ac.za

sulfite (*cf.* sulfate) solutions. On the other hand, the exact influence of the gas bubbles on the oxygen electrode readings is unknown. Although various precautions were taken to obtain reliable readings (App. C.1.2 & C.12), some interference did occur. This is illustrated in Figure 3.17, which presents the results of the three lowest quality tests. Therefore, the two measurements techniques are assumed to yield two extreme estimates of the actual k_La-value.

Table 3.8
Direct oxygen electrode measurement in the 2-litre autoclave at different atm. operating conditions.

Test	$[SO_3^{2-}]$	[b] Imp. conf. & spd.	$[SO_4]$	$\rho_{s/w}$	[d] Temp.	*AARD*	k_La	[e] k_La (40°C)
–	(*ref.* $[O_2]^*$)	(rev/min)	(mol/kg)	% (kg/kg H_2O)	(°C)	(%)	(1/min)	(1/min)
OPA1	0	Double (A), 1000	0.50	0	22.0	2.67	1.33	**1.93**
OPA2	0	Double (A), 1000	0.25	0	39.2	3.65	1.74	**1.77**
OPA3	0	Double (A), 1000	[c] 1.30	0	42.9	3.00	2.05	**1.93**
OPA4	0	Double (A), 1100	0.50	0	42.0	2.10	2.53	**2.42**
OPB1	0.5 × stoic.	Double (B), 1000	0.50	0	44.0	5.12	1.24	**1.14**
OPB2	1.5 × stoic.	Double (B), 850	0.50	0	51.0	4.75	0.67	**0.53**
OPC1	1.1 × stoic.	Single (B), 1000	0.50	0	46.7	3.80	0.41	**0.36**
OPC2	1.5 × stoic.	Single (B), 1000	0.50	1.0 (Cpy)	40.5	2.07	0.36	**0.36**
OPC3	0.5 × stoic.	Single (B), 1000	0.50	7.5 (Cpy)	43.3	0.88	0.37	**0.34**
OPC4	1.5 × stoic.	Single (B), 1000	0.50	7.5 (Hem)	42.8	1.47	0.35	**0.33**
OPD1	1.1 × stoic.	Double (A), 1000	0.50	0	41.8	0.21	1.88	**1.81**
[a] OPD2	1.5 × stoic.	Single (A), 1000	0.50	0	43.7	0.31	0.46	**0.43**
[a] OPD3	1.5 × stoic.	Single (A), 1000	0.50	15.0 (Hem)	41.2	0.69	0.40	**0.39**
[a] OPD4	1.1 × stoic.	Single (A), 1000	0.50	7.5 (Cpy)	39.0	3.77	0.39	**0.40**

1.2 L (static) starting sln., using $MgSO_4$ background salt, unless indicated otherwise; [a] 0.9 L starting sln.; [b] Figure 3.5; [c] Na_2SO_4 background salt; [d] Avg. values; [e] Calc. (Eq. 3.11).

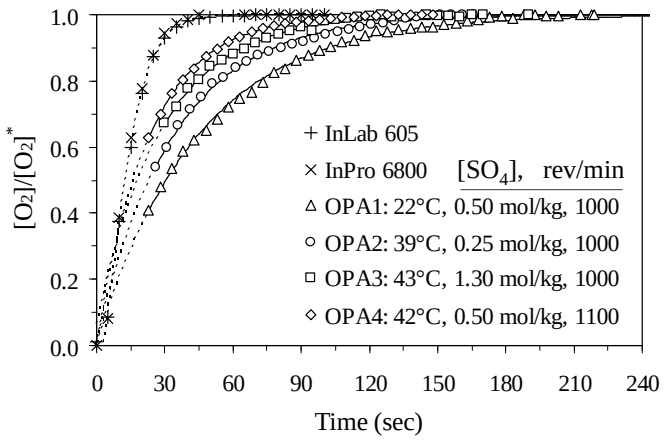

Figure 3.15
Direct O_2 electrode measurements (incl. probe responses) in the 2-litre autoclave, using impeller config. A (double) at 1.2 L (static) volume. The lines represent the (optimised) simulated values.

Stellenbosch University http://scholar.sun.ac.za

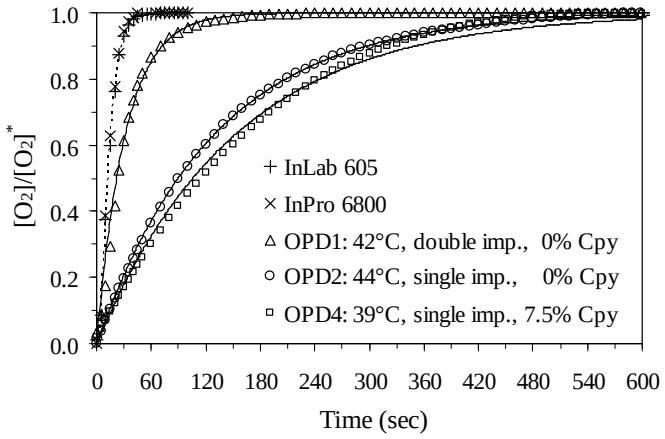

Figure 3.16
Direct O_2 electrode measurements (incl. probe responses) in the 2-litre autoclave, using impeller configuration A (double: 1.2 L or single: 0.9 L) at 1000 rev/min & 0.5 mol/kg SO_4. The lines represent the (optimised) simulation values.

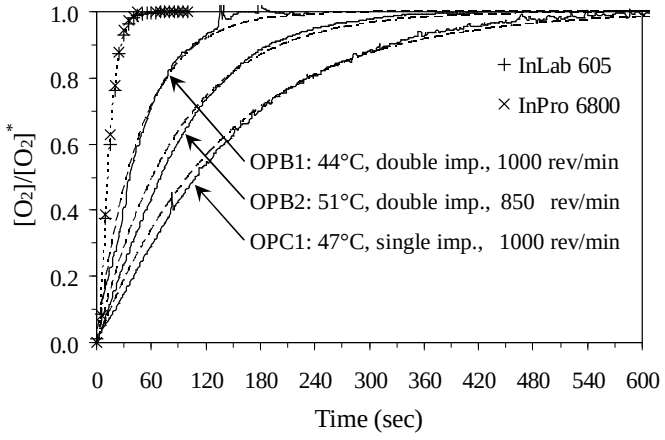

Figure 3.17
Direct O_2 electrode measurement (incl. probe responses) in the 2-litre autoclave, using impeller configuration B at 1.2 L (static) volume & 0.5 mol/kg SO_4. The solid & broken lines represent the measured data & (optimised) simulation values, respectively.

General observations regarding the effect of selected operating parameters on the k_La-value

Agreement between Test OPA1 (without sulfite) and OPD1 (with sulfite) confirms insignificant (< 7%) interference by the initial small amount of sulfite salt added to remove all the dissolved oxygen. Most of this sulfite is oxidised before commencing with the data recording (App. C.1.2).

The minimum k_La-value for impeller configuration B is 0.8 1/min (at 25°C) at normal operating conditions (Test OPB1), but this value falls to around 0.4 1/min (~50% decrease) at 850 rev/min (Test OPB2) and to 0.3 1/min with only a single bottom impeller at 1000 rev/min (Test OPC1). The

Stellenbosch University http://scholar.sun.ac.za

k_La-values (~1.9 1/min, at 40°C) obtained in the 0.5 mol/kg $MgSO_4$ (Test OPA1) and 1.3 mol/kg Na_2SO_4 (Test OPA3) background solutions are only marginally higher than the corresponding value in the 0.25 mol/kg $MgSO_4$ solution (~1.8 1/min; Test OPA2). Since these tests were conducted at different temperatures, this insensitivity validates the correlation adopted before (Eq. 3.11, $\theta = 1.021$). It also suggests that these electrolyte solutions are above their limiting concentrations and of similar non-coalescent character (Sect. 3.2.3). The higher agitation speed of 1100 rev/min (Test OPA4) increases the k_La-value by about 25% (*cf.* 1000 rev/min).

The second test series (OPC & OPD) focussed on the effect of hydrophobic chalcopyrite (Cpy) and hydrophilic hematite (Hem) particles on the k_La-value (Table 3.8). The chalcopyrite concentrate is identical to the pilot plant feed sample (d_{90} = 10 µm) described earlier (Sect. 3.5.5), while the hematite sample (97% pure) was obtained from a chemical supplier. These tests all utilised a pneumatic vibrator to dislodge gas bubbles from the electrode membrane surface, an initial small amount of sulfite to prevent premature oxygen dissolution, and a single impeller system in order to operate in a lower mass transfer rate regime, *i.e.*, to completely rule out any electrode response time issues. The final column in Table 3.8 suggests that the impact of both these types of solids is relatively small, similar to the results obtained by the indirect method. No increase in the k_La-value at low pulp densities (Figure 3.14 *b* & Figure 3.9 *b*) is prevalent, confirming that this anomalous behaviour is specific to the indirect method.

Another interesting observation is the almost 75% drop in the k_La-value between the double (Test OPD1) and single (Test OPD2) impeller systems for configuration A, which is similar to the 70% drop observed for impeller configuration B (Tests OPB1 & OPC1), but different from the 50% drop measured by the indirect method (Sect. 3.5.2). Once again, this suggests that the sulfite oxidation reaction may artificially enhance the k_La-value, especially in a regime where the liquid-side mass transfer coefficient, k_L, is low.

3.6 Overview and summary of k_La-values

3.6.1 General

A general framework is presented in order to understand and mathematically describe the interfacial oxygen mass transfer rate between the gas and bulk solution phases. The experimental programme, supported by literature information, quantifies the effects of the most important system variables on the k_La-values of the stirred tank reactors used in this study. Although the impact of the operating environment on the absorption process in the interfacial layer is complicated, it is treated phenomenologically in this study *via* empirical correlations, with special consideration of the equipment, procedures and testing regimes when quantifying the k_La-values.

Stellenbosch University http://scholar.sun.ac.za

3.6.2 Experimental objectives and methodology

In order to obtain quality data, two different methods of determining the k_La-value are applied, *i.e.*, the indirect (chemical, *i.e.*, sulfite oxidation) and direct (oxygen electrode) methods, each with their own limitations. Since the mixing environment depends on the reaction vessel, the internal configuration of each reactor is described in detail, as applied in other parts of this study. Although the oxygen solubility 'at temperature and pressure' (thermodynamic property) impacts greatly on the overall gas absorption rate, it does not have to be incorporated into the solution chemistry model (Ch. 2). Instead, it is treated empirically *via* correlations from the literature, valid over the full operating range of this study. Also, because of the non-polar character (low solubility) of the oxygen molecule (O_2) and the relatively low overpressures used in this study (< 2000 kPa), both the liquid and vapour phases are assumed to exhibit ideal behaviour. According to the film model, the absorption rate should be identical for air and pure oxygen at the same oxygen partial pressure.

Although selected system parameters, *e.g.*, temperature, have been correlated in the literature, quantitative account of their effects may still be specific to the system investigated. Also, besides the temperature and oxygen concentration, other system properties may impact greatly on the k_La-value, *e.g.*, the solution solute concentration, the presence of surfactants, hydrophobic sulfide and hydrophilic oxide particles. This highlights the need to experimentally verify these parameters on the k_La-value in the three-phase systems encountered in this study.

Direct oxygen electrode measurements are only used as a confirmatory tool in this study, because it is mainly concerned with kinetic processes at autoclave temperatures and pressures. The indirect method requires that the conditions be controlled so that no appreciable amount of the dissolved oxygen reacts in the film, but at the same time, the sulfite oxidation reaction should be fast enough to ensure that the gas levels in the bulk solution are reduced to zero. These conditions can be very restrictive when the k_L-value is low in comparison to the oxidation reaction rate, *e.g.*, at high dissolved oxygen, cobalt(II) or copper(II) catalyst concentrations.

The following sections summarise the most important outcomes of the experimental programme, including best estimates of the k_La-value ranges in each reactor used in this study.

3.6.3 1-gallon autoclave

The 1-gallon autoclave, with its larger operating volume, is relatively insensitive to sample-taking, provided the top impeller remains covered with liquid. Due to its low solubility in the alkaline solution environments, the effect of varying cobalt(II) catalyst concentration on the absorption rate is less important than the oxygen partial pressure. Tests conducted at different oxygen partial pressures indicate that the absorption rates at high pressures are enhanced by the sulfite oxidation

Stellenbosch University http://scholar.sun.ac.za

reaction. Solubility levels of less than about 10 mg/kg O_2, *e.g.*, by using air, yield accurate k_La-values, assuming that the oxygen partial pressure in each bubble is maintained at the bulk gas-phase value.

These optimised test conditions are also used to determine the effect of temperature over the 40 to 100°C range. A correction factor, θ (Eq. 3.11), of 1.021 gives the best representation of the experimental data, which corresponds to an activation energy (Arrhenius plot) of 20 kJ/mol. This is a typical value for a diffusion process, validating the insignificant chemical enhancement of the physical absorption process. Under these conditions, hydrophobic sphalerite particles decrease the k_La-value only slightly in typical electrolyte solutions (low bubble coalescence tendency *cf.* pure water) and at pulp densities less than 20 wt% solids.

3.6.4 Continuous pilot autoclave

Similar to the other reactors used in this study, the interfacial gas/liquid mass transfer in the continuous pilot autoclave also relies on surface entrainment *via* a high-shear top impeller. However, due to upcomer blockages (Ch. 7, Sect. 7.3.1), an increase the distance between this impeller and the slurry level significantly reduces the k_La-value. Considering the possibility of chemical enhancement in this low absorption regime, a mere 20% increase in the overflow level (height) is estimated to reduce the k_La-value by as much as 85 to 95% (Table 3.9). However, under normal operating conditions, the k_La-value in any one compartment is comparable to the values measured in the 1-gallon batch autoclave (above) and the chemical enhancement of the physical absorption process is minimal. Also, differences between the single and double compartment k_La-values appear less than the experimental error.

3.6.5 7-litre glass reactor

The 7-litre atmospheric glass reactor, equipped with a high-shear gas inductor, is ideal for studying the effects of solid particles and the sulfur-dispersing surfactants, lignosulfonate (LS) and Quebracho (QB) (*ref.* sulfide mineral leaching; Ch. 6, Sect. 6.3.3), on the k_La-value. This is because of the negligible impact of typical sample volumes on the k_La-value in this reactor. The k_La-value is significantly (~2.5 times) higher compared to the corresponding value in the 1-gallon autoclave, primarily due to the high bubble surface area created by the inductor. However, since smaller bubbles are also associated with smaller k_L-values, some enhancement of the physical absorption rate may occur. Nevertheless, the tests conducted with dilute oxygen gas yield relatively consistent absorption rates, with minimal chemical enhancement.

This operating regime also reveals that the surfactants retard the k_La-value, which agrees with most observations in the literature. However, this retardation effect dissipates over time. Importantly,

Stellenbosch University http://scholar.sun.ac.za

these results provide unequivocal proof that the LS and QB are degraded by dissolved oxygen and that the degradation products seemingly have no influence on the physical absorption process. Furthermore, insignificant retardation of the initial oxygen absorption rate occurs in the presence of sulfide mineral particles. Since these surfactants are always associated with sulfide slurries in this study, there is no need to quantify their effects on the k_La-value in the leaching reactors, especially not at typical sulfide oxidation pulp densities (~7 wt% solids).

With regard to the effect of chalcopyrite particles on the k_La-value, the results are somewhat clouded by the apparent catalytic effect of dissolving copper(II) ions on the rate of oxidation reaction, resulting in some chemical enhancement of the oxygen absorption rate. Notwithstanding, a gradual decrease in the k_La-value with increasing sulfide pulp density is observed, similar to the (sphalerite concentrate) trend in the 1-gallon reactor (see above).

3.6.6 2-litre autoclave

The more versatile 2-litre autoclave is used in most of the testwork conducted in this study and a description of its mass transfer characteristics is important. Volume changes due to sample-taking are important, since the k_La-value decreases by almost 50% when the liquor level drops below the top impeller, *i.e.*, the distance between the slurry surface and the closest working impeller greatly affects the overall oxygen absorption rate. The k_La-value of the 2-litre autoclave (2.1 1/min at 25°C) is about one-third lower than the corresponding value of the 1-gallon autoclave (3.1 1/min). Therefore, the conditions under which the physical absorption of oxygen is chemically enhanced by the sulfite oxidation reaction are more favourable in the case of the 2-litre autoclave, especially when only the bottom impeller is operational. These differences between these two autoclaves are partly due to a significantly more favourable solution height-to-diameter ratio in the case of the 1-gallon autoclave, while they were also equipped with different impeller types and arrangements. Notwithstanding, tests conducted at high temperatures in the 2-litre autoclave indicate that the general temperature correlation ($\theta = 1.021$, Eq. 3.11) is maintained up to at least 150°C.

Due to the relatively low k_La-value in the 2-litre autoclave, direct oxygen electrode measurements are ideally suited to check the above results, obtained using the indirect method, *i.e.*, the electrode response times are short enough (*cf.* the k_La-value) to allow a direct interpretation of the oxygen absorption rate. Firstly, the general temperature correlation, as quantified by the indirect method (above), also holds in sulfite-free sulfate solutions, *i.e.*, the typical electrolyte solutions in a MT autoclave are above their limiting concentrations and of similar non-coalescent character. However, the absolute k_La-values are about 33% lower than the corresponding values obtained by the indirect method. This is most likely due to the chemical enhancement of the k_La-value. On the other hand,

Stellenbosch University http://scholar.sun.ac.za

the exact influence of the gas bubbles on the oxygen electrode readings is unknown. Therefore, the two measurements techniques are assumed to yield two extreme estimates of the actual k_La-value. Direct electrode measurements suggest a 70 to 75% reduction in the k_La-value between the double and single impeller systems, which is higher than the 50% reduction measured by the indirect method. Once again, this suggests that the sulfite oxidation reaction may artificially enhance the k_La-value, especially in a regime where the liquid-side mass transfer coefficient, k_L, is low.

3.6.7 Generalising the effect of the pulp density on the k_La-value

A small decrease in the k_La-value with increasing pulp density for both sulfide (sphalerite & chalcopyrite) and oxide (hematite) particles is obtained, irrespective of whether the direct or indirect measurements methods are used. However, this excludes the apparent increase in k_La-values (*cf.* pure liquid) when using the indirect method in sulfide slurries, especially for chalcopyrite concentrate, which is probably related to the catalytic enhancement of oxygen absorption rate by dissolving copper(II) ions.

Figure 3.18 summarises the results from the different reactors and temperatures. Except for the fact that both the hydrophobic sulfides and hydrophilic hematite particles result in a decrease in the k_La-value, no general trend is obvious from these data. The average value (-0.9) of the slope, $\Delta k_La/\Delta\rho_{s/w}$, is, for the purpose of this study, rounded to -1 and assumed to be constant up to 20 wt% solids, irrespective of the type or size of the particles. As mentioned above, a correlation to describe the retardation of the k_La-value by surfactants is not required because these substances adsorb readily on sulfide particles, without significantly affecting the gas/liquid interfacial mass transfer rate. However, this simplification may not necessarily hold under low pulp density conditions.

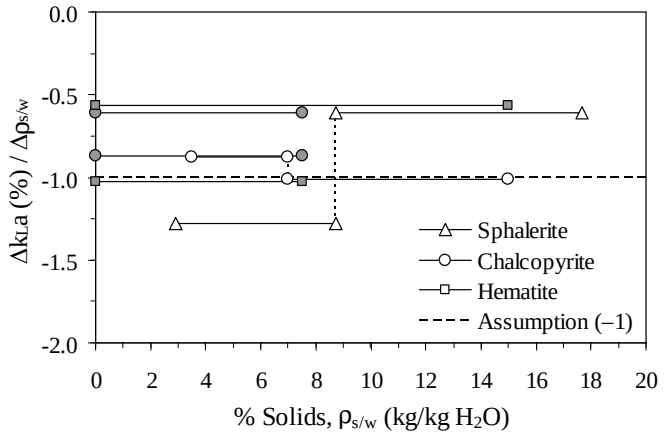

Figure 3.18
The relative effect of different types of solids particles on the reduction of the k_La-value, using both the indirect (open symbols) & direct (closed symbols) measurement methods.

Stellenbosch University http://scholar.sun.ac.za

3.6.8 Summary of k_La-values

Table 3.9 summarises the k_La-values of the reactors used in this study. Since the electrolyte concentrations in this study typically are over their limiting values (> 0.1 mol/kg), no correlation is required to account for solution coalescence changes.

Table 3.9
Summary of k_La-values, incl. the relative effects of the different impeller configurations & speeds.

Reactor	Volume	[a] Config.	Agitation speed	k_La (25°C)	[b] Change
–	(L)	–	(rev/min)	(1/min)	(%)
2-litre batch autoclave	0.95 – 1.25	Mode A	1000	**1.7 ± [c] 25%**	–
	0.95 – 1.25	Mode A	1100	–	+25
	0.95 – 1.25	Mode B	1000	–	-40
	0.95 – 1.25	Mode B	850	–	-50
	< 0.9	Mode A, B	1000	–	-75
7-litre glass reactor	6.0 – 7.0	–	1000	**8.3 ± [d] 15%**	–
[e] Continuous pilot autoclave	Normal	Single/double	1000	**2.9 ± [f] 10%**	–
	Normal	Single/double	1200	–	+25
	High	Single/double	1200	–	-85± [g] 10

[a] Figure 3.5; [b] % Var. (*ref*. std. value); [c] Var. between indirect & direct methods; [d] Exp. error; [e] Var. between individual & single or double compartment modes less than exp. error; [f] Uncertainty (est.); [g] Possible chemical enhancement & uncertainty due to different impeller heights in each compartment (Figure 3.3).

Stellenbosch University http://scholar.sun.ac.za

CHAPTER 4. IRON(II) OXIDATION

4.1 Introduction

This chapter focuses on the rate of iron(II) oxidation by dissolved diatomic oxygen (O_2) in acidic base metal sulfate solutions, both without and in the presence of aqueous copper(II). The iron(II) oxidation rate affects the dissolved oxygen and iron(III) concentrations under typical medium temperature (MT) autoclave conditions (130-155ºC), which in turn influence the oxidation rates of the sulfide minerals (Ch. 6). Furthermore, the iron(II) oxidation rate affects the supersaturation level of iron(III), which not only determines its precipitation rate but also the relative abundance of metastable phases, *e.g.*, hydronium jarosite (Ch. 5). Although the final rate expressions are phenomenological in nature, the adopted functionalities aim to reflect the (currently) perceived oxidation mechanisms. All the rate expressions are therefore quantified in terms of the actual dissolved species concentrations, accounting for the interfacial (gas/liquid) oxygen mass transfer rate (Ch. 3) and the formation of inner-sphere complexes, *i.e.*, the contact ions pairs (CIPs) (Ch. 2).

The development roadmap of the iron(II) oxidation rate model is as follows:

- Review of the literature to identify the most important factors that may impact on the iron(II) oxidation rate in sulfide mineral oxidation systems and to expand current mechanistic understanding of the oxidation reaction in acidic sulfate solutions (Sect. 4.2)
- Establishing confidence in the experimental procedures and identifying the relevant reaction regimes for interpreting the intrinsic iron(II) oxidation rate (Sect. 4.3 & 4.4.1)
- Developing phenomenological expressions to describe the oxidation rate as a function of the actual species concentrations in acidic low and high sulfate solutions, with and without dissolved copper, as well as validating the final rate expression (Sect. 4.4.2-4.4.6), and
- Simplifying, quantifying (regressing) and verifying the phenomenological model in order to simulate the iron(II) oxidation rate in sulfide mineral oxidation reactors (Sect. 4.4.7).

4.2 Review and theory

Iron(II) oxidation is widely covered in the open literature, spanning several disciplines. This review is limited to the typical conditions expected in MT sulfide mineral oxidation systems, excluding a vast number of publications covering lower temperatures and less acidic aqueous systems, *e.g.*, in waste water treatment. Various older references, from the late 19th to the early 20th century, can be found in the open literature (*e.g.*, Mellor, 1935). The stoichiometry of the overall reaction is as follows (Lowson, 1982):

$$Fe(II) + \tfrac{1}{4}O_2 + H^+ \Rightarrow Fe(III) + \tfrac{1}{2}H_2O \qquad 4.1$$

Stellenbosch University http://scholar.sun.ac.za

Various studies have reported the effects of the solution composition, *e.g.*, hydrogen ion (H^+) and sulfate concentration, catalysts, *e.g.* copper(II), and the temperature on the iron(II) oxidation rate. Table 4.1 summarises some of these reported rate expressions, reaction orders and activation energies, specifically where oxygen was used in acidic sulfate solutions.

Table 4.1
Fe(II) oxidation rate expressions in acidic sulfate solutions.

Rate law	E_a (kJ/mol)	[a] Other effects	Ref.
[b] $k[Fe\ II]^2\,[O_2]$, $k \propto [H^+]^{-0.23}$	74 (25-40ºC)	$[Cu\ II]^y$ (2.5·k), I	1
$k[Fe\ II]^2\,p_{O2}$	74 (40-80ºC)	$[H_2SO_4]^{-x}{}_{\leq 60\ g/L}$	[c] 2
$k_1[Fe\ II]p_{O2} + k_2[Fe\ II]^2\,p_{O2}$ $k_3[Fe\ II][Cu\ II]_{\sim 30ºC}$	56 $_{k1}$, 68 $_{k2}$ (140-180ºC)	$k_2 > k_1$ (<T & <SO_4) pH^x, [d] $[Fe\ III]^0$	3
$k[Fe\ II]^2\,p_{O2}$	62 (130-165ºC)	–	4
$k[Fe\ II]^2\,[Cu\ II]^{0.5}\,p_{O2}$, $k \propto [H_2SO_4]^{-0.3}$	69 (100-130ºC)	–	5
$k[Fe\ II]^2\,p_{O2}$	56 (100-150ºC)	–	[c] 6
$k[Fe\ II]^2\,[H^+]^{-0.35}\,[O_2]$	94 (20-50ºC)	–	7
$k[Fe\ II]^{1.84}\,[H^+]^{-0.25}\,[O_2]$, $k \propto [Cu\ II]^{0.28}$	74 (20-80ºC)	[d] $[SO_4]^0$	8
[e] $k[Fe\ II]^2\,[O_2]$, $\propto [Fe\ II]_{<3\text{-}8\ g/L}$	57 (40-135ºC)	$[H_2SO_4]^{-x}$; $[Cu\ II]^y$	9
[f] $k_1[Fe\ II]^2\,p_{O2} + k_2[SO_4][Fe\ II]^2\,p_{O2}$	52 $_{k1}$, 94 $_{k2}$ (70-90ºC)	$[H^+]^{-x}{}_{f(SO4)}$, $[Fe\ III]^{-z}$	10, 11
[e] $k_3[Fe\ III]^{-1} + k_4[H^+][SO_4][Fe\ III]^{-1}$ k_3, $k_4 \propto [Fe\ II]p_{O2}\,[Cu\ II]_{<\sim 3\ g/L}$	26 $_{k3}$; 134 $_{k4}$ (70-90ºC)	–	11
$k[Fe\ II]^{1.84}\,[H^+]^{-0.36}\,[O_2]$	69 (25-85ºC)	–	12
$(k_1[Fe\ II]^2 + k_2[Fe\ II][FeSO_4^o] + k_3[FeSO_4^o]^2)$ $\times (1+5[Cu\ II]^{0.5})\,p_{O2}$	80 (120-155ºC)	–	13
$k[Fe\ II]^2\,p_{O2}$	[g] 51 (50-200ºC)	$[H^+]^{-x}$	14
[h] $k_1[Fe\ II]^2\,[O_2]/(1 + k_2[Fe\ II])$	34 (60-130ºC)	–	15
$k[Fe\ II]^2\,[H^+]^{-0.25}\,[O_2]$ $\times (1+5.75[Cu\ II]\,\{[Fe\ II]/[Fe^T]\}^{0.5})$	[i] 80 (60-80ºC)	[j] a_{Py}	16

[a] Not quantified in rate expressions (x, y, z > 0); [b] Perchloric acid sln.; [c] In Lowson (1982); [d] No effect at constant pH; [e] Cu(II) present; [f] Perchloric acid/sulfate sln. & no Cu(II); [g] Mass transfer limitations; [h] High acid (> 100 g/L H_2SO_4) & Fe(II) (> 50 g/L) at ~constant pH; [i] Adopted from Dreisinger & Peters (1989); [j] Pyrite surface area. **References**: [1] George (1954); [2] Belopol'skii & Urusov (1948); [3] Huffman & Davidson (1956); [4] Cornelius & Woodcock (1958); [5] McKay & Halpern (1958); [6] Hotta & Suzuki (1963); [7] Keenen (1969); [8] Mathews & Robins (1972); [9] Chmielewski & Charewicz (1984); [10] Iwai *et al.* (1982); [11] Awakura *et al.* (1986); [12] Verbaan & Crundwell (1986); [13] Dreisinger & Peters (1989); [14] Vračar & Cerović (1997); [15] Rönnholm *et al.* (1999); [16] Littlejohn & Dixon (2008).

4.2.1 Mechanistic considerations in copper-free solutions

The general consensus is that the uncatalysed reaction follows a termolecular path, with second-order (bimolecular) and first-order (unimolecular) dependencies on iron(II) and dissolved oxygen concentrations, respectively. Most studies observed retarded kinetics at increased acid concentration, while some found the effect to become saturated above a threshold limit, *e.g.*, 0.1

Stellenbosch University http://scholar.sun.ac.za

mol/L H_2SO_4 at 30°C (Lamb & Elder, 1931), 0.6 mol/L H_2SO_4 at 40 to 80°C (Belopol'skii & Urusov, 1948) and 1 mol/L H_2SO_4 at 70 to 90°C (Awakura *et al.*, 1986). Various researchers, *e.g.*, Awakura *et al.* (1986), Dreisinger and Peters (1989) and Huffman and Davidson (1956), have proposed that the iron(II)-sulfate CIPs oxidise faster than the unassociated ferrous ion (Fe^{2+}); this explains the beneficial effect of adding 'inert' sulfate salts (see Ch. 2) on the overall oxidation rate.

It is unclear what (direct) role hydrogen ion plays in the oxidation mechanism of the sulfate-independent (SI) reaction pathway. George (1954) found the rate constant to increase only slightly with decreasing acid concentration in a perchlorate medium at lower temperatures (25-40°C) (see Table 4.1). He proposed that the ionisation of a water molecule in the ferrous ion (Fe^{2+}) solvation shell accompanies the simultaneous transfer of two electrons to the oxygen molecule, which explains the relative insensitivity of the overall oxidation rate on hydrogen ion concentration:

$$Fe^{2+} + O_{2(aq)} \Leftrightarrow FeO_2^{2+} \qquad 4.2$$

$$FeO_2^{2+} + Fe(H_2O)^{2+} \Rightarrow FeO_2H^{2+} + HOFe^{2+} \qquad 4.3$$

This proposal utilises the energy released when forming the $HOFe^{2+}$ species ($\Delta H°_{rx} \approx$ -5 kJ/mol) to drive the formation of the other ferric ion species (FeO_2H^{2+}; $\Delta H°_{rx} \approx$ 7.5 kJ/mol), by resorting to the transfer of two oxidation equivalents at the same time, one inter-molecularly and the other intra-molecularly (George, 1954). The existence of these complexes was established experimentally and might involve the formation of an intermediate Fe^{2+}-O_2 species, which would be more thermodynamically viable than the initial electron transfer reaction to form the FeO_2^{2+} species.

Assuming the reduction of diatomic oxygen proceeds *via* a series of one-electron transfer steps (energetically more favourable), special conditions have to prevail in order to prevent the resulting radical species from driving the reverse reactions at appreciable rates (analogous to the discussions around mineral oxidation in Ch. 6, Sect. 6.3.2 & 6.5). The above proposal of George (1954) captures some aspects of such a mechanism, while Astanina and Rudenko (1971) presented a multistep mechanism involving the diatomic oxygen molecule linked to two ferrous ions *via* the solvation shell water molecules. When broken down into individual steps, it resembles the Weiss mechanism (Weiss, 1935), involving perhydroxyl ($HO_2\cdot$) radical species:

$$Fe^{2+} + O_{2(aq)} + H^+ \Leftrightarrow Fe^{3+} + HO_2\cdot \qquad \text{(or)}$$

$$Fe^{2+}(H_2O)_n + O_{2(aq)} \Leftrightarrow Fe(OH)^{2+}(H_2O)_{n-1} + HO_2\cdot \qquad 4.4$$

followed by:

$$Fe^{2+} + HO_2\cdot + H^+ \Rightarrow Fe^{3+} + H_2O_2 \qquad \text{(or)}$$

Stellenbosch University http://scholar.sun.ac.za

$$Fe^{2+}(H_2O)_n + HO_2\cdot \Rightarrow Fe(OH)^{2+}(H_2O)_{n-1} + H_2O_2 \qquad 4.5$$

For the purpose of this study, it is assumed that the oxidation of iron(II) by the peroxide intermediate species (H_2O_2), *i.e.*, if it survives disproportionation at high temperatures, proceeds *via* a mechanism analogous to diatomic oxygen, but at a faster (non-limiting) rate *via* the hydroxyl radical (OH·):

$$Fe^{2+} + H_2O_2 + H^+ \Leftrightarrow Fe^{3+} + OH\cdot + H_2O \qquad 4.6$$

$$Fe^{2+} + OH\cdot + H^+ \Rightarrow Fe^{3+} + H_2O \qquad 4.7$$

Besides the thermodynamic justification for assuming faster oxidation by the peroxide molecule, compared to the diatomic oxygen molecule (see Sect. 4.2.2), Pham and Waite (2008) proposed a three-order magnitude difference between these two reaction rate constants (~0.1 L/mol.sec for Rx. 4.4 *cf.* 620 L/mol.sec for Rx. 4.6, both at pH 6), albeit referring to the analogous deprotonated reactions in neutral water systems. Notwithstanding, over 90% of the iron(II) species was estimated by these authors to be unassociated ferrous ion and the rate constants should therefore show a similar comparative difference at lower pH values. The above reaction sequences capture the reaction stoichiometry, as portrayed by Reaction 4.1, but reveal little about the actual mechanism. The formation of binuclear complexes of iron was proposed in various earlier publications (*e.g.*, Huffman & Davidson, 1956; Weiss, 1935, 1953). One such scheme (out of many possibilities) is represented in Figure 4.1.

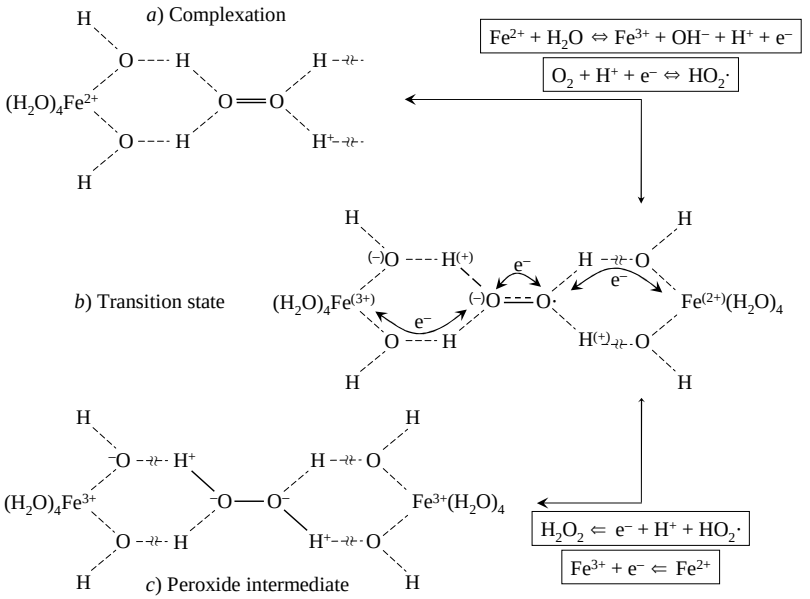

Figure 4.1
Simplified mechanistic proposal of uncatalysed Fe^{2+} oxidation by O_2: *a*) Complexation of aqueous Fe^{2+} & O_2; *b*) Oxidation of Fe^{2+}, simultaneous reduction of O_2 to form the $HO_2\cdot$ intermediate & oxidation of nearby solvated Fe^{2+} species; *c*) H_2O_2 intermediate, after consuming another H^+.

Stellenbosch University http://scholar.sun.ac.za

Unlike the oxidation of sulfide mineral surfaces, where electrons may also be transferred *via* the conduction band (Figure 6.66), the reaction pathway would depend heavily on electron wave function overlap between the reacting species. This would allow the diatomic oxygen molecule to accept two electrons *via* intra-molecular transfer. The crossing of the energy barrier at the transition state may thus be viewed as being driven by the approach of a second iron(II) species (Figure 4.1 *b*), hence the bimolecular dependence of the observed reaction rate on the iron(II) concentration, as noted in nearly all studies listed in Table 4.1. Hydrogen ion is an intrinsic part of this mechanism but should not be limiting at low acidities because ferric ion (Fe^{3+}) would release the equivalent amount of hydrogen ion during its hydrolysis (Rx. 4.4). This provides an explanation of why the oxidation rate is often found to be zero-order in hydrogen ion concentration, despite being a reagent (Rx. 4.1). An electrostatic argument may also (at least partially) explain why iron(II) typically oxidises orders of magnitude faster in neutral or basic solutions as compared to acidic solutions (see typical rate constants in Lowson, 1982).

4.2.2 General iron(II) rate expressions in copper-free solutions

The following discussions are based on the unfavourable thermodynamic driving force for the first reduction step of diatomic oxygen, compared to the peroxide molecule, *i.e.*, an E^o_h of -0.65 V for O_2 at pH 0 *cf.* 0 to -0.3 V for H_2O_2 at pH 7 (based on the $Fe^{3+}|Fe^{2+}$ couple *ref.* Lide (2004), ΔG^o of $O_{2\,(aq)}$ *ref.* Wagman *et al.* (1982), *p*K of $HO_2\cdot$, E^o_h of the $O_2|HO_2\cdot$ couple *ref.* Bielski *et al.* (1985), and E^o_h of the $H_2O_2|HO\cdot$ couple *ref.* Wardman (1989); see Table 6.1 & related discussions). This leads to the following expression for the oxidation rate, R (mol Fe(II)/kg.min), *via* the SI pathway:

$$R_{FeII,SI} = k_F[Fe^{2+}]^2[O_2] \qquad 4.8$$

The rate constant, k_F, is assumed to be insensitive to the hydrogen ion molality. However, over a relatively wide concentration span, the simulation may also have to consider the increased probability of the reverse reactions occurring, *e.g.*, using $k_F/[H^+]^n$ to account for ferric ion reduction by the perhydroxyl radical at higher acidities (*ref.* Figure 4.1).

The low sensitivity of the oxidation rate to the acid concentration in pure perchloric acid medium (George, 1954) suggests that the rate is to a large extent dominated by the 'reluctant' approach of two (unassociated) ferrous ions at lower temperatures. Such electrostatic considerations also seem to account for the relatively slow oxidation rate of iron(II) in perchlorate as compared to sulfate solutions ($1\text{-}2\times10^6$ & $3\text{-}4\times10^6$ mol/L.atm.sec, respectively, at 30ºC & ~1 mol/L H^+; Lowson, 1982). At higher oxidation temperatures, the abundance of the iron(II) sulfate CIPs becomes more variable, especially at lower acidities (Ch. 2, Sect. 2.4.3). The higher the temperature, the higher the threshold acid levels where the total fraction of CIPs becomes insensitive to the acid concentration. This may explain the apparent literature trend (Sect. 4.2.1) of increasing threshold

Stellenbosch University http://scholar.sun.ac.za

acid concentration with temperature. This study assumes that the approach of the initial Fe^{2+}-O_2 complex by an iron(II) sulfate CIP, *e.g.*, $FeSO_4^o$, (sulfate-dependent (SD) reaction pathway) is electrostatically more favourable compared to the unassociated ferrous ion (SI pathway), leading to faster overall oxidation rates. This is in line with the proposals of various authors, *e.g.*, Awakura *et al*. (1986), Dreisinger and Peters (1989) and Iwai *et al*. (1982).

Dreisinger and Peters (1989) applied a mutual activation energy (~80 kJ/mol) to the SI and SP pathways, while Iwai *et al.* (1982) found significantly higher activation energy for the SD pathway (~145 kJ/mol; re-analysed by Awakura *et al.* (1986), as ~94 kJ/mol in an insensitive H^+ regime) compared to the SI pathway (~52 kJ/mol). Both of these proposals contradict the fact that the SD pathway exhibits faster kinetics, *i.e.*, is characteristic of lower activation energy barriers at the transition state, hence it would be expected to exhibit a lower activation energy than the SI pathway. Assuming that the termolecular reaction order is also consistent with the SD pathways, the following rate expression is adopted in this study:

$$R_{FeII,SD} = (k_{CIP}[Fe_{CIP}]^2 + k_{CIP/F}[Fe_{CIP}][Fe^{2+}])[O_2] \qquad 4.9$$

This expression is in agreement with the notion that the oxidation rate appears largely unaffected by the hydrogen ion concentration in high sulfate solutions, other than by changing the relative abundance of the iron(II) sulfate CIPs (Fe_{CIP}). The dependence of the oxidation rate on the relative abundance of the CIPs is reflected by its insensitivity to the total ionic strength when using sodium perchlorate, while a rate increase is seen with the addition of sodium sulfate (see Awakura *et al.*, 1986). Magnesium sulfate forms the basis of the surrogate salt approach of the solution chemistry model, assuming that the speciation changes are relatively consistent between the different divalent metal sulfates (Ch. 2). However, Dreisinger and Peters (1989) reported differences in the oxidation rate in different sulfate backgrounds and it is therefore imperative to regress the final simulation to the most relevant salt system, *i.e.*, the sulfuric acid, zinc(II), copper(II) and iron(III) sulfate mixture, in this study.

Validating the general rate model, based on qualitative observations from the literature

The first interesting observation is that the studies of both Dreisinger and Peters (1989) and Iwai *et al*. (1982) started with 0.1 to 0.2 mol/L Fe(II), but showed different and variable acid dependencies. Iwai *et al.* (reaffirmed by Awakura *et al.*, 1986) found a variable acid threshold, depending on the total sulfate level at 90°C. Increased hydrogen ion and sulfate levels, *i.e.*, when increasing the total sulfuric acid concentration, exhibited slower oxidation kinetics (~$[H_2SO_4]^{-0.6}$), up to the threshold concentration level of 1 mol/L H_2SO_4. However, when sulfate and hydrogen ion concentrations were independently controlled, using perchloric acid and sodium sulfate salts, the oxidation rate was independent of hydrogen ion concentration in the 0.1 to 0.4 mol/L range at very low sulfate

Stellenbosch University http://scholar.sun.ac.za

levels (0.005 mol/L SO_4), but showed a decreased rate at higher total sulfate levels (> 0.2 mol/L SO_4). Dreisinger and Peters (1989) also reported a consistent decrease in the oxidation rate over the 0.2 to 1 mol/L H_2SO_4 range at 150°C and a constant high sulfate level (2.7 mol/L SO_4), while Lamb and Elder (1931) recorded insignificant rate enhancement at 30°C when adding 0.1 mol/L sulfate salts to a stock solution containing 0.15 mol/L Fe(II) and 0.5 mol/L H_2SO_4.

Although the background salt matrices and temperatures differed significantly between these studies, the trends are in qualitative agreement with the relative abundance of the metal(II)-sulfate CIPs, as a function of acid, sulfate and temperature (Sect. 2.4.3, *e.g.*, Figure 2.23). This is in agreement with earlier discussions (related to Figure 4.1) suggesting that the mechanism is largely unaffected by the hydrogen ion concentration in high sulfate solutions, *i.e.*, hydrogen ion is an unlikely participant in the rate-limiting step, but changes the relative abundance of iron(II)-sulfate CIPs and, hence, indirectly affects the overall observed oxidation rate.

Awakura *et al*. (1986) claimed an inversely proportional relationship of the oxidation rate with increasing iron(III) concentration and ascribed this to the large formation constants of the iron(III) sulfate complexes, which, in turn, reduce the relative abundance of the iron(II) sulfate CIPs over time. On the other hand, Dreisinger and Peters (1989) and Huffman and Davidson (1956) found no effect when adding small amounts (<0.05 mol/L) of iron(III) as a sulfate salt at relatively high temperatures (150 & 160°C, respectively). This is again in qualitative agreement with the phenomenological treatment of iron(III) sulfate complexation in this study (Sect. 2.4.3).

Huffman and Davidson (1956) proposed that the addition of complexation agents, including sulfate ion, accelerates the oxidation rate *via* transition-state stabilisation. This statement is in line with earlier mechanistic discussions (Figure 4.1) but differs fundamentally in that they assigned a bimolecular pathway, first-order in iron(II) concentration, to such a stabilisation route. This is also in contradiction with the uncatalysed oxidation rate expressions listed in Table 4.1; most of these results, and various other publications in the open literature, agree on a general second-order dependence on the iron(II) concentration.

Another exception is the first-order dependence on the iron(II) concentration observed by Chmielewski and Charewicz (1984) during pressure oxidation at 95°C and lower (< 3-8 g/L) iron(II) concentrations, while the oxidation rate exhibited the expected second-order dependence at higher iron(II) concentrations. Besides the possibility of a different oxidation mechanism in the presence of copper(II) (Sect. 4.2.3), it is important to note that their experimental conditions consisted of high initial iron(II) (0.55 mol/L) and acid (0.5 mol/L H_2SO_4) concentrations, which, in

Stellenbosch University http://scholar.sun.ac.za

turn, may have resulted in significant compositional changes over the course of the experiment. This would have resulted in significant speciation changes over time, which, in turn, may have been the reason for this apparent change in the 'reaction order'.

Three other studies, listed in Table 4.1, also used high initial iron(II) concentrations, *i.e.*, Belopol'skii and Urusov (1948), Rönnholm *et al.* (1999) and Vračar and Cerović (1997). The first two studies observed a second-order dependence on the iron(II) concentration over a wide concentration range, even when starting with 0.9 to 1.2 mol/L Fe(II), while the study of Rönnholm *et al.* (1999), relevant to even higher iron(II) (2 mol/L) and acid (1.2 mol/L H_2SO_4) concentrations, used a somewhat more complicated relationship (see Table 4.1). However, this rate expression reduced to the conventional second-order relationship when using the regressed rate constants at a lower concentration, *i.e.*, in the range claimed by Chmielewski and Charewicz (1984) to exhibit first-order kinetics (see above). The relatively low overall activation energy recorded by Rönnholm *et al.* (1999) (34 kJ/mol; see Table 4.1), casts some doubt on the results when conducted at such high initial iron(II) concentrations, despite claims by the authors that no oxygen mass transfer limitations existed. For example, the study of Vračar & Cerović (1997) found a comparatively higher intrinsic activation energy (51 kg/mol), despite experiencing significant oxygen mass transfer limitations. The effect of interfacial oxygen mass transfer limitations on the iron(II) oxidation rate is therefore an important factor, especially when the rate is catalysed by copper(II).

4.2.3 Mechanistic considerations in copper(II) sulfate solutions

Contrary to the similarities in the reported rate equations of the uncatalysed reaction pathway, a range of fundamentally different expressions have been published to account for the copper-catalysed reaction pathway (Table 4.1).

Reaction orders

George (1954) revealed a marginal acceleration of the oxidation rate at 35ºC in the perchlorate system, but no change in the reaction order with respect to the iron(II) concentration. Lamb and Elder (1931) witnessed a significant acceleration of the oxidation rate by copper(II) in the sulfate system at 30ºC, and, interestingly, also reported higher rates at increasing acid concentration. The only other report of similar behaviour is that of Awakura *et al.* (1986), who proposed a first-order dependence on the hydrogen ion concentration for the SD pathway at 70 to 90ºC and copper(II) sulfate concentrations below 0.05 mol/L. They proposed first-order relationships in iron(II) and copper(II) concentration for both the SI and SD pathways, while the rate was first-order in oxygen concentration. In fact, all the rate expressions listed in Table 4.1 for the copper-catalysed reaction show a first-order (or close to this) dependence on the oxygen concentration (or partial pressure).

Stellenbosch University http://scholar.sun.ac.za

Huffman and Davison (1956) proposed that the copper-catalysed reaction is independent of the oxygen concentration, while exhibiting first-order dependencies on the iron(II) and copper(II) concentrations at about 30ºC. Whether the interfacial mass transfer rate was sufficient in their reaction vessels, *i.e.*, rotating 15 mm Pyrex tubes, is questionable, which could explain this apparent first-order dependence of the rate on the iron(II) concentration. This is particularly pertinent to testwork conducted in copper(II) sulfate solutions, since the intrinsic oxidation rate is significantly higher than the uncatalysed route. Furthermore, independence of the reaction rate on the agitation speed may not necessarily constitute evidence that no mass transfer limitations exist, *e.g.*, in a region where the contribution of oxygen mass transfer by agitation is relatively small compared to its enhancement by the chemical reaction itself (Ch. 3).

It may also be tempting to draw parallels between the catalytic action of copper and the accelerating effect imposed by other ions. Although second-order dependencies on the iron(II) concentration have been claimed in the chloride system (*e.g.*, Colborn & Nicol, 1973; Lepin & Matseevskii, 1967; Yano *et al.*, 1974, *ref.* in Iwai *et al.*, 1979), other studies conducted at both high (~30, *e.g.*, Iwai *et al.*, 1979) and low HCl to Fe(II) molar ratios (~0.08, *e.g.*, Bouboukas *et al.*, 1987) suggest first-order relationships, with high (> 75 kJ/mol) activation energies. The recent oxygen isotope fractionation study of Oba and Poulson (2009) presents evidence of a significant change in the reaction mechanism with changing pH and this appears to be related to the oxygen reduction reaction. At higher pH (>3), the catalytic role of the iron(II) hydroxide species shifts the rate of iron(II) oxidation to a first-order dependence, *i.e.*, exhibiting analogous behaviour to the chloride system. This suggests that the iron(II) oxidation mechanism is intrinsically different in aqueous basic and chloride systems.

Besides the higher rate constant values in the presence of copper(II), the majority of studies in the sulfate system suggest that the uncatalysed reaction orders are retained, *i.e.*, second-order and first-order with respect to the iron(II) and oxygen concentrations, respectively (*e.g.*, Dreisinger & Peters, 1989; Littlejohn & Dixon, 2008; Mathews & Robins, 1972; McKay & Halpern, 1958).

Rate dependence on the copper(II) concentration

Various studies have revealed saturation effects at increasing copper(II) concentration, *e.g.*, Kobe and Dickey (1945) (~0.02 mol/L Cu at 100ºC & low ionic strength in sulfate medium), George (1954) (perchlorate medium at 35ºC), Awakura *et al.* (1986) (~0.05 mol/L Cu at 60ºC in low sulfate medium), while Littlejohn and Dixon (2008) noted reduced catalytic activity at higher solution redox potentials (at 80ºC). Higher sulfate and iron(II) concentrations appear to extend the catalytic efficiency of copper(II) to higher concentrations. For example, Chmielewski and Charewicz (1984) noticed a rate sensitivity, even as high as 1.4 mol/kg Cu at 95ºC in 0.5 mol/L

Stellenbosch University http://scholar.sun.ac.za

Fe(II) and high sulfate background. Dreisinger and Peters (1989) conducted testwork at 150ºC and in an even higher sulfate background environment, but starting with only 0.2 mol/L Fe(II); they observed a half-order dependence on the copper concentration up to 0.25 mol/L Cu. These apparent trends are assumed to be related to speciation changes in the electrolyte solution, which would be highly dependent on temperature, acid and total sulfate concentration (Sect. 2.4.3).

Simplified mechanism of copper-catalysed iron(II) oxidation

In view of the above discussions, a simplified mechanistic proposal is presented in Figure 4.2. This mechanism is similar to the uncatalysed reaction pathway, except that it assumes the preferential association of copper with the dissolved diatomic oxygen molecule to form an inner-sphere complex. This proposal is based on the instability of the unassociated cuprous ion (Cu^{+}) in the aqueous sulfate system, combined with its favourable electronic structure for a reaction with oxygen (Sect. 6.3.2). Although the electrocatalytic role of cuprous ion in the first reduction step of oxygen is thermodynamically marginal (~0 V at pH 0; Sect. 6.6.2), it is more favourable than the reduction reaction by the ferrous ion (-0.65 V at pH 0; Sect. 4.2.2). From a kinetic perspective, the reduction of oxygen by ferrous ion (~0.1 L/mol.sec at pH 6; Pham & Waite, 2008) is more than six orders of magnitude slower than the corresponding reaction with cuprous ion (4.6×10^{5} L/mol.sec at pH 2.1; Cabelli *et al.*, 2000, Table 6.2). It is therefore assumed that electron transfer between the diatomic oxygen and ferrous ion occurs more readily *via* the stabilised copper-oxygen inner-sphere complex, which supports a first-order dependency on the most reactive copper(II) sulfate species.

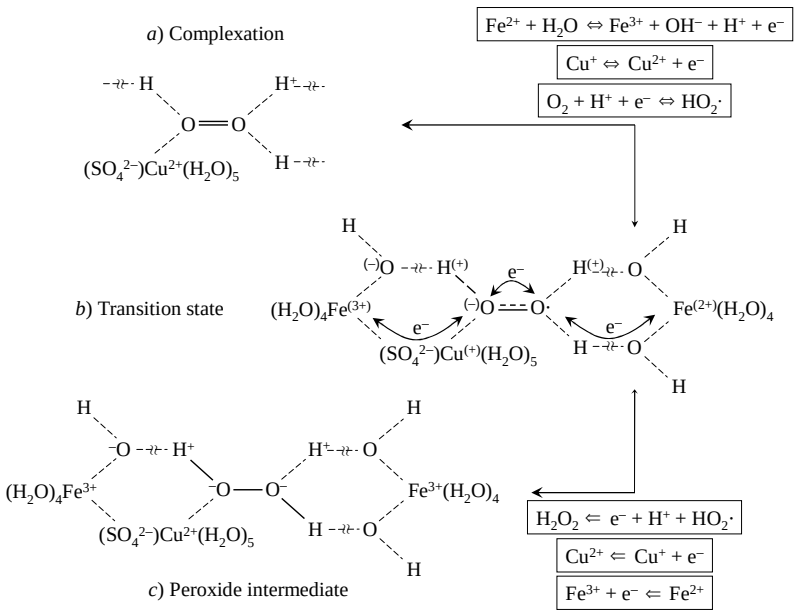

Figure 4.2
Simplified mechanistic proposal of copper-catalysed Fe^{2+} oxidation by O_2: *a*) Complexation of aqueous Cu(II) & O_2; *b*) Oxidation of Fe^{2+}, simultaneous reduction of O_2 to form the $HO_2\cdot$ intermediate *via* the Cu(II)|Cu(I) couple & oxidation of nearby solvated Fe^{2+} species; *c*) H_2O_2 intermediate, after consuming another H^{+}.

Stellenbosch University http://scholar.sun.ac.za

The reverse reaction, *i.e.*, between the perhydroxyl radical and the copper(II) species, is typically three orders of magnitude faster than the forward reaction (~1×10^8 L/mol.sec; Bielski *et al.*, 1985), which places heavy emphasis on the presence of two iron(II) species in the vicinity of the copper-oxygen inner-sphere complex. It is therefore not surprising that various studies have reported a second-order dependence on the iron(II) concentration in copper sulfate solutions (Table 4.1).

Electrostatic considerations should also come into play for the copper-catalysed oxidation reaction, again separating the overall reaction into distinct SI and SD pathways. This may be the reason that the catalytic effect of copper is significantly reduced in media with low complexation tendencies, *e.g.*, in perchlorate medium (George, 1954), while diminished catalytic activity is to be expected at lower iron(II) to iron(III) concentration ratios. This may explain the apparent decrease in the 'reaction order' and catalytic activity, as observed by Chmielewski and Charewicz (1984) and Littlejohn and Dixon (2008), respectively (see above).

4.2.4 Catalysed iron(II) oxidation rate expression in acidic copper-containing mineral slurries

The precipitation of iron(III) (Ch. 5) during the MT autoclave oxidation of sulfide mineral slurries introduces another level of complexity. This is because iron(III) hydrolysis products may also catalyse iron(II) oxidation (*e.g.*, El Azher *et al.*, 2008; Lowson, 1982). However, studies under acidic conditions (pH < 3) revealed that the adsorption of iron(II) onto hydrous iron(III) oxides is not favourable, and that the heterogeneous reduction of oxygen by such surfaces would not be likely to affect the oxidation rate (Oba & Poulson, 2009). On the other hand, Littlejohn and Dixon (2008) presented experimental evidence that pyrite mineral surfaces enhance the iron(II) oxidation rate initially (at lower redox potential), but refrained from giving a mechanistic explanation for this.

These observations are in line with the discussions of Chapter 6, which are used to derive a qualitative picture of the pyrite-catalysed (Py_c) mechanism. The reversible behaviour of the iron(III)|iron(II) couple on pyrite surfaces is discussed in Section 6.3.2. The electrocatalytic role of the non-bonding t_{2g} orbital of iron in the pyrite surface lattice and the enhanced electron-attracting capability of surface-coordinated diatomic oxygen is emphasised. At lower redox potentials, the catalytic reduction of oxygen and the subsequent oxidation of water may create a highly oxidised pyrite surface (Figure 6.16 & 6.17), but without significant electron exchange between the bonding orbitals in the pyrite surface lattice and these species. This represents a highly catalytic environment for aqueous iron(II) oxidation in close proximity to the pyrite surface, probably *via* a Grotthuss-type tunnelling mechanism (see Horne & Axelrod, 1964). However, as the solution potential increases, *i.e.*, with a build-up of iron(III) species in solution, pyrite bonding orbitals may be increasingly subjected to direct oxidation (Figure 6.10); alternatively, the surface concentration of oxidised species may reach a critical level, in combination with temperature, to allow internal

Stellenbosch University http://scholar.sun.ac.za

transfer of electrons *via* a conduction mechanism (Figure 6.11). This may signify the inflection point, as observed by Littlejohn and Dixon (2008), which represents a decrease in the surface concentration of oxidised species and holes, making the surface less catalytic towards iron(II) oxidation. These factors may therefore combine in a unique way to catalyse iron(II) oxidation to a greater or lesser degree, depending on the characteristics of the specific pyrite sample and the operating conditions.

In conclusion, the catalytic enhancement of the iron(II) oxidation reaction is deeply imbedded within the electronic structures at the transition states and more insight into the observed phenomena will only be gained by comprehensive molecular modelling and detailed experimentation, which was outside the scope of this study. Furthermore, different intrinsic reaction pathways, out of many possibilities, may become dominant in specific solution environments, creating apparent 'anomalies', not to mention the subtle effects induced by interfacial mass transfer limitations, especially in catalytic systems where the intrinsic oxidation rate is fast. It is therefore justified to base the catalysed iron(II) oxidation rate expression on the currently perceived mechanisms, as presented above. The most general description of the catalysed oxidation rate, $R_{FeII,C}$, is obtained by retaining the second-order and first-order dependencies on the iron(II) and dissolved oxygen concentrations, respectively, and by representing the catalytic effect of copper(II) as some function of its concentration, $f([Cu])$:

$$R_{FeII,C} = (k_{CIP}[Fe_{CIP}]^2 + k_{CIP/F}[Fe_{CIP}][Fe^{2+}] + k_F[Fe^{2+}]^2) \cdot f([Cu]) \cdot [O_2] + \theta_{Py_c} a_{Py} k_C [FeII][O_2]^n \quad 4.10$$

Again, the direct hydrogen ion dependence of the SI pathway is assumed to be weak (constant k_F; *ref.* Eq. 4.8) compared to the changing speciation trends at higher temperatures. The second term accounts for the catalytic pyrite surface (Py_c), which is represented as a fraction (θ) of the total available pyrite surface area at any point in time, a_{Py} (Sect. 6.3.4). This rate is also assumed to exhibit a first-order dependence on the total iron(II) concentration. Chapter 8 briefly discusses the importance of this term, *i.e.*, whether it is actually required to describe the iron(II) oxidation rate in high pulp density leaching systems under typical MT autoclave conditions.

Besides scrutinising the most important assumptions, the testwork programme aimed to simplify the above rate expressions as far as possible, *i.e.*, to prevent over-parameterisation of the phenomenological oxidation rate model. For example, it was unclear whether both the SI and SD pathways are required in order to describe the uncatalysed or catalysed reaction rates, and whether the total CIP (*e.g.*, $[FeSO_4^o] + [Fe(SO_4)_2^{2-}]$) or only the neutral species (*ref.* Ch. 2) gives the best description over relatively wide temperature and acidity ranges.

Stellenbosch University http://scholar.sun.ac.za

4.3 Experimental

Although the focus is on MT autoclave temperatures (130-155 ºC), the experimental programme covered a relatively wide temperature range (90-180ºC) in order to instil confidence in and generalise the phenomenological rate model.

4.3.1 Equipment

This part of the study utilised the 2-litre Parr autoclave (Figure 4.3 *a*), as well as the 7-litre glass reactor under atmospheric pressure conditions (these reactors, their internals, control and operating procedures are discussed in detail in Ch.3, Sect. 3.3). Similar to the mineral oxidation testwork (Ch. 6, Sect. 6.4), a high-pressure feed bomb was used to inject the reagents 'at temperature' (Figure 6.23). On the other hand, the relatively fast intrinsic kinetics of iron(II) oxidation demanded samples to be rapidly withdrawn from the vessel, using a sampling bomb (Figure 4.3 *b*).

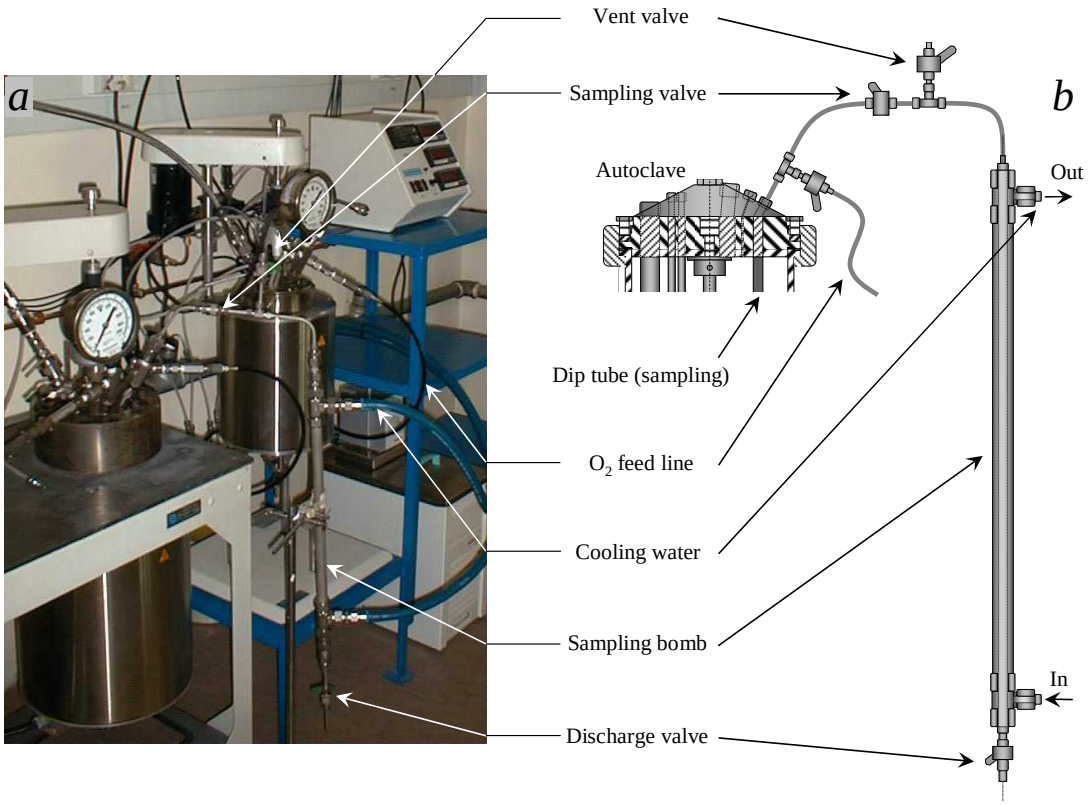

Figure 4.3
Iron(II) oxidation testwork apparatus: *a*) Photo of the 2-litre autoclave & peripheral equipment; *b*) Schematic diagram of the custom built sampling bomb.

4.3.2 Experimental procedure

The detailed experimental procedure is presented in Appendix D.1. The autoclave was charged with the required amount of water and background sulfate salts and then heated to the required operating temperature, with the impeller stirring slowly, and applying about 100 kPa oxygen

Stellenbosch University http://scholar.sun.ac.za

overpressure. Once the required operating temperature was reached, the overpressure was increased to the target gauge pressure, using pure oxygen. The impeller speed was then increased to the setpoint value of 1000 rev/min, while the vapour phase was slowly vented for a minute to remove inert gas from the head space. The feed bomb was then charged with the required amount of iron(II) sulfate solution and injected into the autoclave 'at temperature', *i.e.*, to initiate the oxidation reaction at 5 g/L Fe(II), corresponding to 1000 or 1200 g starting mass in the autoclave. The clock was started when the feed bomb discharge valve was opened. The reaction proceeded for a predetermined time and samples were removed at regular intervals *via* the sampling bomb.

A 'dead' volume of around 15 mL was taken first in order to prevent contamination of the actual sample by stagnant solution in the dip and connection tubes. Before discharging, the actual samples were rapidly cooled to below 90ºC by passing cooling water from a chiller unit through the sampling bomb jacket. Iron(II) oxidation ceased almost instantaneously (< 15 sec) after entering the sampling bomb. The above procedure was therefore initiated about 15 sec before the sample was due. The glass sample holder was immediately covered and placed in a waterbath, which was controlled at 20ºC. An accurate 10 mL volume was then pipetted into a volumetric flask and titrated against a standardised (0.05 or 0.1 N) potassium dichromate solution. For quality control, selected samples were also titrated potentiometrically.

4.3.3 Data interpretation

Small (25 mL) burettes were used when conducting colorimetric titrations (App. B.2.3), yielding accuracies as high as ±0.05 mL titrant, depending on the analyst and equipment used. In some cases, *e.g.*, when using the potentiometric method, titrant volumes were reported to the nearest 0.1 mL, which translates into accuracies of ±0.001 mol/kg Fe(II). Therefore, by focussing on the initial rate data, *i.e.*, down to 0.01 mol/kg Fe(II), the rate constant values obtained from the initial experimental programme (uncatalysed system) are generally accurate within ±10%. Only data points with variation coefficients (between the colorimetric & potentiometric data) of less than 15% were subjected to further interpretation. Due to the rapid oxidation in the copper system, only the smaller burettes (calibrated at 0.05 mL intervals) were utilised. These results are therefore assumed accurate within ±0.0005 mol/kg Fe(II), unless using the lower (0.05 N) dichromate concentration, which is adequate to distinguish between the real experimental trends. The error bars on each figure specify these (conservative) titration errors, which are assumed to also encapsulate the overall experimental error. Finally, the background acid and iron(III) concentrations are related stoichiometrically (Eq. 4.1), rather than relying on their measured values.

The advantage of working in a relatively low iron(II) concentration range (≤ 5 g/L Fe) is that less 'interference' is likely due to interfacial mass transfer limitations.

Stellenbosch University http://scholar.sun.ac.za

4.4 Results and discussion

The objective of this section is to derive a phenomenological description of the iron(II) oxidation rate, based on the general theoretical framework presented in Section 4.2 and the data from the experimental programme. Before deriving the oxidation rate constants, the experimental procedure and the intrinsic oxidation reaction regime require verification.

4.4.1 Validating the experimental procedure and the intrinsic oxidation reaction regime

Besides the meticulous execution of the experimental procedure, interference by 'external' factors has to be clarified as far as possible.

Copper impurity levels introduced by the other salts

Section 4.2.3 has highlighted the significant accelerating effect of copper(II) on the oxidation rate. Standard (1 mol/L) solutions of all the reagents were therefore prepared and analysed to determine their copper content. These results are summarised in Table 4.2 and clearly show low copper contamination levels when using analytical-grade (AR) grade chemicals. Iron(III) and zinc sulfate salts contained the highest copper(II) levels, yet resulted in less than 0.2 mg/L Cu under the highest salt concentration conditions. Soluble copper impurity in other salts is therefore assumed to have an insignificant influence on the observed rate constants.

Table 4.2
Copper impurity levels resulting from other salts used in this study.

Salt	[a] Cu impurity	Salt	[a] Cu impurity
–	(µg/L)	–	(µg/L)
H_2SO_4	< 2	$Fe_2(SO_4)_3$	700 (<150)
$ZnSO_4$	230 (<150)	$MgSO_4$	< 2
$FeSO_4$	300 (<50)	–	–

[a] Cu levels in 1 mol/L salt sln. (bracketed values are the highest Cu levels at the salt conc. ranges used in this study).

The effect of the interfacial oxygen mass transfer limitations

The first series of tests aimed to assess the roles of interfacial mass transfer rate limitations and the reaction product, iron(III), on the oxidation rate (the detailed test results can be found in App. D.2). The first four tests (FOA1-FOA4) were conducted at lower initial mass, *i.e.*, 1000 g starting solution, and at different oxygen partial pressures (p_{O2}°, *ref.* pure water), with and without adding copper to the solution. This lower initial solution mass was selected, knowing that sampling would reduce the oxygen mass transfer rate (Ch. 3), *i.e.*, the lower k_La-value is exploited in order to shed some light on the limiting role of the interfacial mass transfer rate. The liquid level dropped below the top impeller with the removal of about two samples (~30 mL/sample), and an (at least) 75% reduction in the k_La-value resulted (Table 3.9). Figure 4.4 summarises these results.

Stellenbosch University http://scholar.sun.ac.za

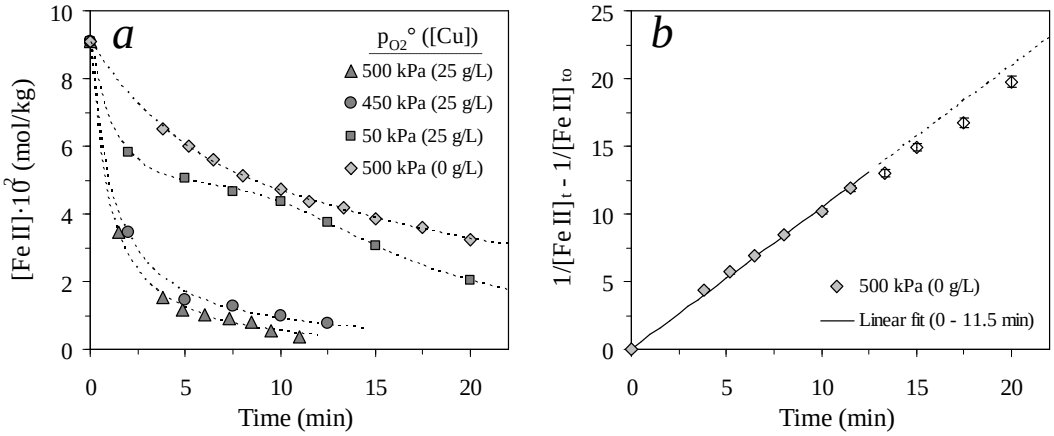

Figure 4.4
Effect of p_{O2}° at 150ºC & 25 g/L H_2SO_4, using a lower initial solution mass of 1000 g: *a*) [Fe(II)] *vs.* time; *b*) Second-order plot.

The agitation speed was maintained at 1000 rev/min, using impeller configuration A (Figure 3.5; no further reference is made to the mixing intensity in this chapter). The most prominent feature of these tests is the S-shape kinetics of the test conducted with 25 g/L Cu at 50 kPa p_{O2}° (Test FOA3), whereas the test conducted without any copper (Test FOA4) reacted in a predominantly second-order fashion (Figure 4.4 *b*). The two tests conducted with copper at the higher oxygen pressures (Tests FOA1 & FOA2) show no interfacial mass transfer effects because the iron(II) levels dropped rapidly (< 5 min) to very low levels. These results confirm that copper dramatically accelerates the overall oxidation rate, requiring the simultaneous consideration of the interfacial oxygen mass transfer rate. Most of the tests utilised a higher initial solution mass of 1200 g, *i.e.*, ensuring higher initial mass transfer rates by virtue of the dual mixing system (Figure 3.1).

Test repeatability and the impact of start-up effects

Linear regression of the first six data points of Test FOA4 (Figure 4.4 *b*) yields an overall rate constant of 1.05 ± 0.02 kg/mol.min. Despite the initial linearity, there is a deviation, albeit small, from second-order kinetics after about 12 min. Due to the lower density (without copper in solution), five to six samples would have caused the liquid level to drop below the top impeller. However, due to the rapidly decreasing oxygen consumption over time, this deviation is unlikely to be related to oxygen mass transfer limitations. Other possible experimental errors first need to be ruled out, before trying to explain this phenomenon.

All the tests were initiated by injecting iron(II) solution into the autoclave 'at temperature'. The experimental procedure (Sect. 4.3.1) aimed to minimise any start-up effects. Nevertheless, Figure 4.5 (Tests FOB1 & FOB2; App. D.2) illustrates the difference in the initial rates when pre-heating the solution, as compared to injecting cold solution.

Stellenbosch University http://scholar.sun.ac.za

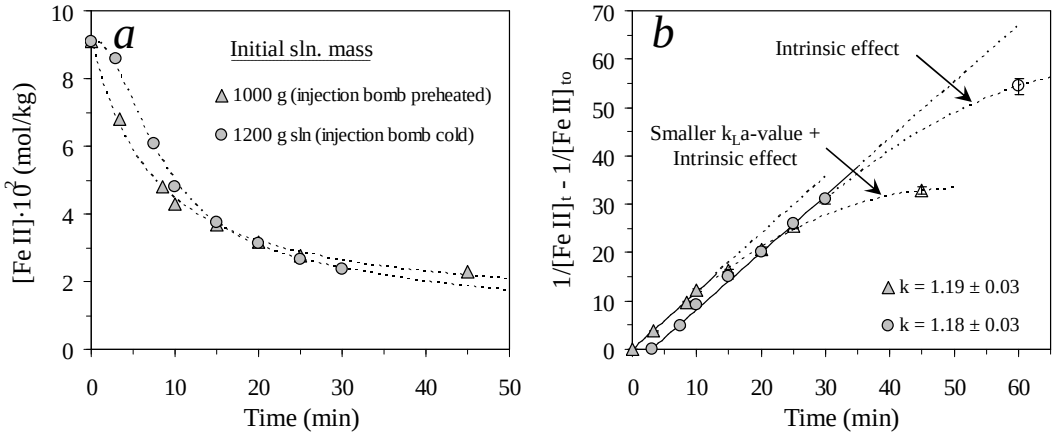

Figure 4.5
The effects of different start-up conditions at 150°C, 650 kPa p_{O2}°, 25 g/L H_2SO_4 & 0 g/L Cu: *a*) [Fe(II)] *vs.* time; b) Second-order plots (units of k, kg/mol.min).

Test FOB1 was conducted by injecting preheated (~130°C) iron(II) solution into the autoclave to yield 1000 g of 5 g/L Fe(II) solution 'at temperature'. Test FOB2, in turn, was initiated by injecting cold (room temperature) iron(II) solution into the hot autoclave to yield 1200 g solution. The initial temperature upset, albeit small, clearly impacted on the observed reaction rate (Figure 4.5 *a*). Nevertheless, these two tests yield almost identical rate constants if the initial 'time zero' datapoint is omitted from the regression analysis (Figure 4.5 *b*). Although the injection of hot solution may be preferred from an accuracy point of view, the preheating procedure was time consuming and difficult to regulate. More accurate rate constants are therefore obtained by omitting the 'time zero' samples from the regression analyses, *i.e.*, by using the subsequent (> 0 min) datapoint as the reference point to obtain the overall observed rate constant.

Again, initial second-order kinetics are prevalent but a downward deviation is observed as the solution level dropped below the top impeller. In the case of Test FOB2 (1200 g), the solution level was high enough to prevent major mass transfer limitations and consequently maintains linearity for a longer reaction time. The deviation at high reaction extents may be ascribed to an intrinsic effect, most probably due to an increase in ferrous ion to total iron(II) concentration ratio (Ch.2, Sect. 2.4.3), which, in turn, results in a slower apparent reaction rate (Sect. 4.2.2). Alternatively, the build-up of iron(III) species may alter the solution speciation by lowering the sulfate concentration and thereby decreasing the observed oxidation rate; this possibility is investigated in the next section. Less emphasis is therefore placed on the datapoints at high reaction extents, *e.g.*, below 0.02 mol/kg Fe(II), especially under lower background sulfate conditions.

The next two tests (FOC1 & FOC2; App. D.2) were conducted at 130°C and aimed to determine the repeatability of the experimental procedure. These results are illustrated in Figure 4.6.

Stellenbosch University http://scholar.sun.ac.za

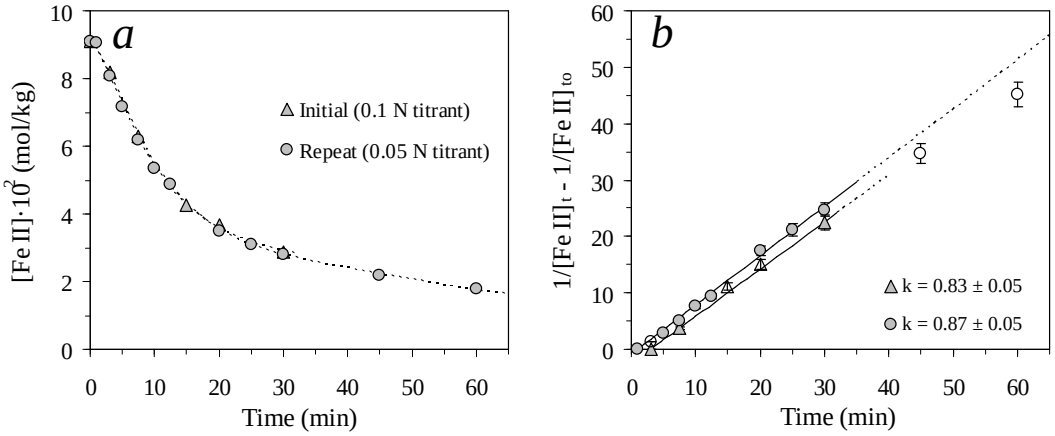

Figure 4.6
Repeatability testwork at 130°C, 1000 kPa p_{O2}°, 25 g/L H_2SO_4 & 0 g/L Cu: *a*) [Fe(II)] *vs.* time; *b*) Second-order plots (units of k, kg/mol.min; open symbols excl. from linear regression).

The coefficient of variance (*CV*) between these two datasets is, without exception, less than 10%. As illustrated in Figure 4.6 *b*, the different dichromate titrant stock solution concentrations yield results that are generally of the same order or smaller than the chemical analysis errors. Therefore, the repeatability of these tests was good and the rate constants of the repeat tests generally agree with the original set within the average range of the chemical analysis errors.

The effect of the reaction product species

Having verified the experimental repeatability, the effect of the reaction product, iron(III), is assessed. Test FOC3 (App. D.2) was conducted at a high oxygen partial pressure of 2000 kPa p_{O2}° and adding 10 g/L Fe(III) initially. It is compared to the baseline test (Test FOD2; App. D.3) in Figure 4.7, *i.e.*, without adding iron(III) sulfate salt initially, under otherwise similar conditions. The higher iron(III) concentration results in a marginal improvement of the initial oxidation rate, whilst the deviation from linearity at the higher reaction extents (Figure 4.7 *b*) appears similar to the baseline test. These deviations at high reaction extents are therefore not likely to be due to a build-up of iron(III) product species. Instead, they may be due to implicit changes in the prevalence of the iron(II) CIPs.

The increase in the initial oxidation rate, albeit inconclusively, may be due to the complexation of hydrogen ion, *e.g.*, as the $FeH(SO_4)_2$° species (Eq. 2.78). The relatively high iron(III) concentration of 10 g/L was chosen to allow substantial sulfate (~0.09 mol/kg, over-and-above sulfate from the iron(III) salt itself) to be locked up as this iron(III) sulfate species. Yet, the lowering of the hydrogen ion concentration appears to outweigh the sulfate complexation effect. The impact of the hydrogen ion concentration on the oxidation rate is explored in more detail in Section 4.4.2.

Stellenbosch University http://scholar.sun.ac.za

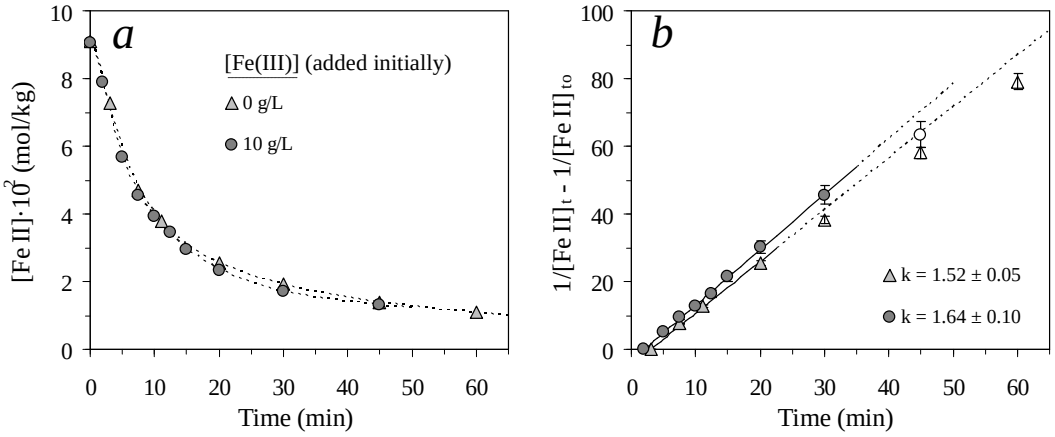

Figure 4.7
Effect of adding Fe(III) sulfate at 130°C, 2000 kPa p_{O2}°, 25 g/L H_2SO_4 & 0 g/L Cu: *a*) [Fe(II)] *vs.* time; *b*) Second-order plots (units of k, kg/mol.min).

4.4.2 Reaction orders in comparatively low sulfate solution environments (no copper)

This section presents the experimentally observed dependencies of the oxidation rate on the primary variables in the lower sulfate solution environment, *i.e.*, starting with the ternary H_2SO_4-$FeSO_4$-H_2O system. Results from Section 4.4.1 strongly support a second-order dependence on the iron(II) concentration, which is in line with most studies in the open literature (Table 4.1). In order to validate this, a range of integer orders were tested. The following expressions represent the overall *n*th-order reaction rate (at constant solution composition) and the integrated functionalities, f_n, corresponding to first-, second- and third-order kinetics, respectively:

$$R_{FeII} = k \cdot [Fe\,II]^n \qquad 4.11$$

$$f_{1st} = ln\frac{[Fe\,II]_{to}}{[Fe\,II]_t} = k_{1st} \cdot t \qquad 4.12$$

$$f_{2nd} = \frac{1}{[Fe\,II]_t} - \frac{1}{[Fe\,II]_{to}} = k_{2nd} \cdot t \qquad 4.13$$

$$f_{3d} = \frac{1}{[Fe\,II]_t^2} - \frac{1}{[Fe\,II]_{to}^2} = k_{3d} \cdot t \qquad 4.14$$

Figure 4.8 compares these different reaction order functionalities for Test FOC2 (App. D.2), confirming that the second-order dependence gives the best representation of the oxidation kinetics over a relatively wide iron(II) concentration range. It is also worth noticing that the datapoints surround the second-order regression line in a subtle S-shape fashion (Figure 4.8 *a*). Although this is a marginal trend, it emphasises the importance of evaluating the reaction rate constants in terms of the actual dissolved oxygen and other species concentrations over time.

Stellenbosch University http://scholar.sun.ac.za

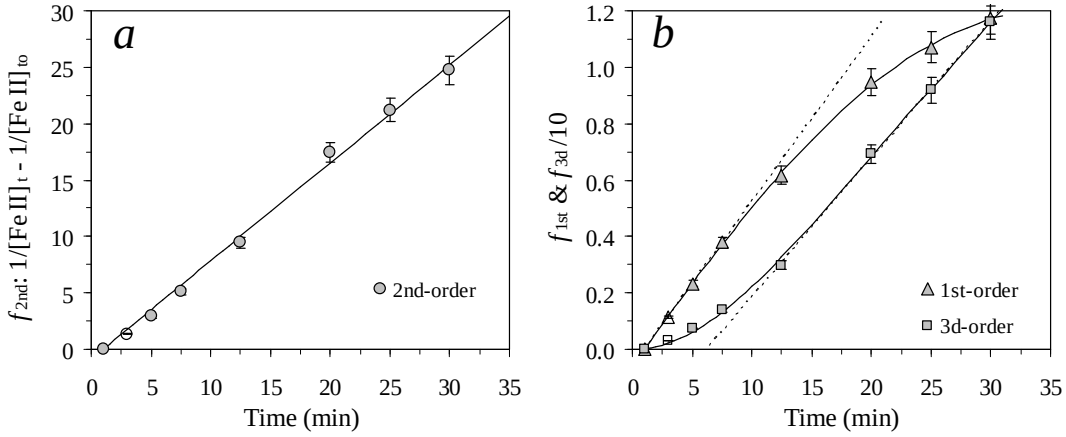

Figure 4.8
Validating the reaction order *ref.* [Fe(II)] at 130°C, 1000 kPa p_{O2}°, 25 g/L H_2SO_4 & 0 g/L Cu: *a*) Second-order plot; *b*) First- & third-order plots.

There is general agreement in the literature that the rate is first-order with respect to the oxygen concentration (Table 4.1). A series of tests was therefore conducted at 1500, 2000 and 2500 kPa p_{O2}° (Tests FOD1-FOD3) and compared to Test FOC2 (1000 kPa p_{O2}°) in Figure 4.9 (also see detailed comparisons in App. D.3.1). The dissolved oxygen concentration is assumed to be constant in this analysis, *i.e.*, at its initial saturated concentration, $[O_2]^*_{to}$. In view of the care that was taken to generate these experimental results, the regressed reaction order (robust line: R^2 = 0.94) of 0.9 is lower than expected. Nevertheless, it can be seen that the two rate constants at the lowest oxygen partial pressures deviate only marginally from the idealised first-order line, based on the 2000 kPa test (FOD2) as the point of reference. The assumption of a constant oxygen saturation concentration is scrutinised in more detail later in this chapter.

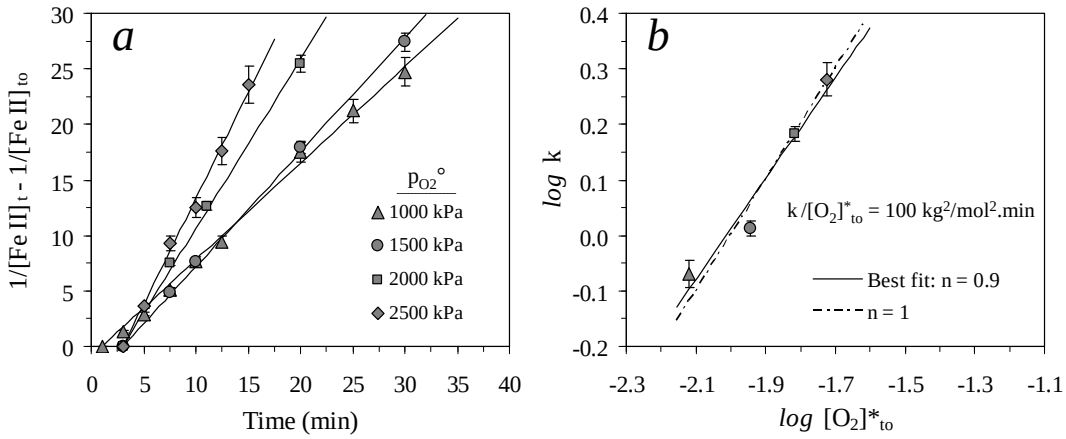

Figure 4.9
Effect of p_{O2}° on the oxidation rate at 130°C, 25 g/L H_2SO_4 & 0 g/L Cu: *a*) Second-order plots ; *b*) *log* k (kg/mol.min) *vs. log* $[O_2]^*_{to}$ (mol/kg).

Stellenbosch University http://scholar.sun.ac.za

Section 4.2 highlighted the various uncertainties with regard to the effect of changing hydrogen ion concentration on the rate of iron(II) oxidation. The next series of tests (FOE1-FOE3; App. D.2) was conducted at different initial acid concentrations, under otherwise similar starting conditions (5 g/L Fe(II), 130ºC & 2000 kPa p_{O2}º). These results, presented in Figure 4.10, including the baseline test at 25 g/L H_2SO_4 (Test FOD2), confirm that the oxidation rate increases when utilising lower initial acid concentrations, which is consistent with the literature (Table 4.1).

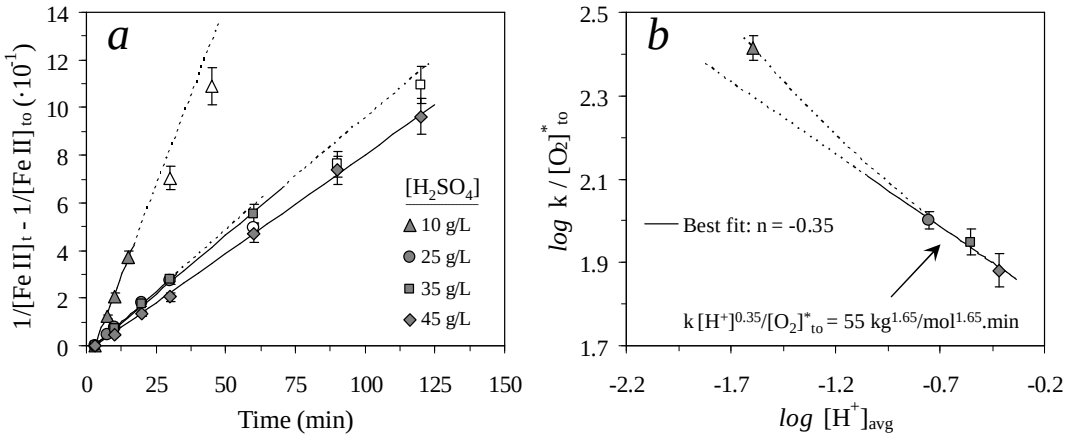

Figure 4.10
Effect of $[H_2SO_4]$ on the oxidation rate at 130°C, 2000 kPa p_{O2}° & 0 g/L Cu: *a*) Second-order plots; *b*) *log* $k/[O_2]^*_{to}$ ($kg^2/mol^2.min$) *vs. log* $[H^+]_{avg}$ (mol/kg).

An interesting observation is that the second-order dependence (linearity) extends to lower iron(II) concentrations in the case of the higher initial acid concentrations (Figure 4.10 *a*), suggesting that acid consumption is an important factor (Eq. 4.1). On the other hand, the initial oxidation rate decreases with increasing acid concentration, which supports the notion that this negative deviation is driven by solution speciation changes.

To determine the reaction order with regards to the acid concentration, the experimental rate constants are evaluated against the average unassociated hydrogen ion concentration for each regression period (Figure 4.10 *b*). All the species concentrations, including the hydrogen ion, are obtained *via* the solution chemistry model (Ch. 2), which also accounts for the complexation of iron(III), hydrogen and sulfate ions to form the $FeH(SO_4)_2^o$ species. Due to the consumption of acid by the oxidation reaction (Rx. 4.1) and the strong complexation tendency of iron(III) (Rx. 2.78), the hydrogen ion concentration effect cannot be accurately described by a fixed 'reaction order', especially under conditions of lower excess acid. Based on the initial oxidation rates of the three tests conducted at higher acidities (25, 35 & 45 g/L H_2SO_4; Figure 4.10), the reaction order of -0.35 (R^2 = 0.965) is in good agreement with the values obtained by Keenen (1969) and Verbaan and Crundwell (1986), albeit referring to temperatures below 100ºC (Table 4.1). This yields an intrinsic

Stellenbosch University http://scholar.sun.ac.za

rate constant of 55 $kg^{1.65}/mol^{1.65}$.min, as indicated in Figure 4.10 *b*. The only study found to have quantified this effect above 100ºC is that of McKay and Halpern (1958), claiming a reaction order of -0.3 with respect to the total acid (H_2SO_4) concentration: this varies slightly from the corresponding value of -0.435, obtained from the three tests at higher acidities (see App. D.3.1). The negative deviation from the second-order dependence on the iron(II) concentration, *i.e.*, the linearity in Figure 4.10 *a*, also noted by Verbaan and Crundwell (1986) and Chmielewski and Charewicz (1984), albeit in the presence of copper(II), is assumed to be compounded by an ever-increasing concentration of the iron(III) species. The $FeH(SO_4)_2^{o}$ species, if indeed the primary iron(III) sulfate CIP, removes two sulfate ions for every hydrogen ion, resulting in an increasing Fe^{2+} to Fe(II) concentration ratio (over time), especially in lower sulfate solution environments. The final simulation (Sect. 4.4.7) accounts for these effects at each time step, instead of relying on average solution tenors and an apparent fractional reaction order.

4.4.3 Reaction orders in comparatively high sulfate solution environments (no copper)

Tests FOF1 to FOF4 (App. D.3) were conducted at different oxygen partial pressures (1000, 1500, 2000 & 2500 kPa p_{O2}°, respectively), utilising zinc sulfate (25 g/L Zn) and constant (excess) acid levels (25 g/L H_2SO_4). These tests, also conducted at 130°C and without copper, are illustrated in Figure 4.11 (also see detailed comparisons in App. D.3.1).

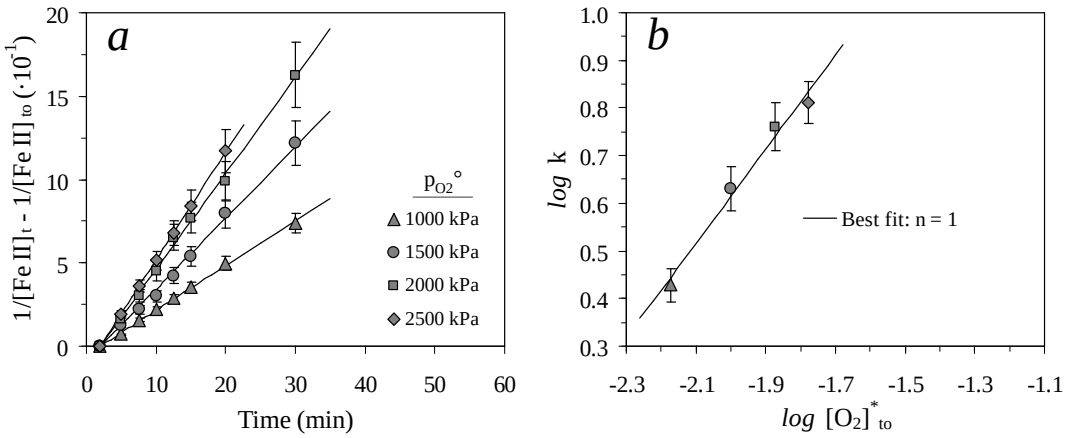

Figure 4.11
Effect of p_{O2}° on the oxidation rate at 130°C, 25 g/L H_2SO_4, 15 g/L Zn & 0 g/L Cu: *a*) Second-order plots; b) *log* k (kg/mol.min) *vs. log* $[O_2]^*_{to}$ (mol/kg).

The regressed (robust line; R^2 = 0.98) reaction order of about one (0.99) is rather fortuitous, considering the experimental uncertainty. Nevertheless, this confirms that the uncatalysed reaction pathway maintains its linear dependence on the dissolved oxygen concentration under comparatively high total sulfate concentration levels.

Stellenbosch University http://scholar.sun.ac.za

The next series of tests (FOG1-FOG3; App. D.3) investigated the effect of increasing zinc sulfate concentration, under otherwise similar starting conditions (130°C, 1000 kPa p_{O2}° & 25 g/L H_2SO_4). These tests are compared to the baseline series at 0 g/L Zn (Tests FOC1 & FOC2) and 15 g/L Zn (Test FOF1) in Figure 4.12, which illustrates the enhancement of the oxidation rate when adding an 'inert' metal(II) sulfate salt. Test FOG1 (25 g/L Zn) was conducted at the lower initial solution mass (1000 g), while Test FOG3 (35 g/L Zn) is a repeat, again validating the generally good experimental repeatability.

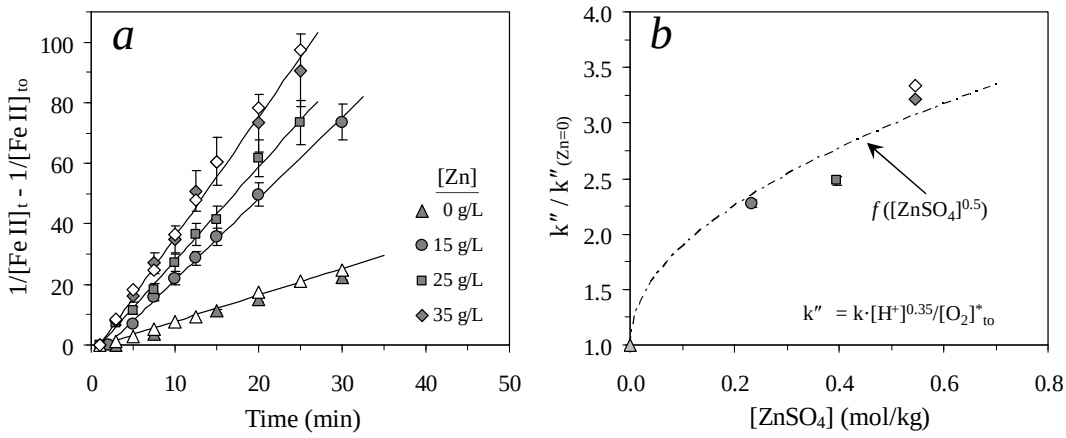

Figure 4.12
Effect of $[ZnSO_4]$ at 130°C, 1000 kPa p_{O2}°, 25 g/L H_2SO_4 & 0 g/L Cu: *a*) Second-order plots; *b*) $k''/k''_{(Zn=0)}$ *vs.* $[ZnSO_4]$. The open symbols denote the repeat tests, while a lower initial solution mass (1000 g) was utilised for the 25 g/L Zn test.

The comparative rate constant values (*cf.* the baseline value at 0 g/L Zn) are presented in Figure 4.12 *b*, after accounting for minor hydrogen ion and oxygen concentration differences. These results, again, reflect the increasing prevalence of the iron(II) sulfate CIPs (as compared to the unassociated ferrous ions) at higher total sulfate concentrations, which is consistent with the solution chemistry model (Sect. 2.4.3) and previous discussions (Sect. 4.2.2).

The lower apparent rate constant value of the 25 g/L Zn test, assuming a power function response to the zinc sulfate concentration (analogous to copper sulfate; see Figure 4.15 & App. D.3.1), may suggest that interfacial mass transfer limitations were prevalent at the lower initial solution mass (revisited in Sect. 4.4.7). Nevertheless, the intrinsic rate constant derived from this test (0.4 mol/kg $ZnSO_4$) is about 2.5 times the baseline value, which is roughly comparable to the 2.5-fold increase observed by Dreisinger and Peters (1989) when adding 0.3 mol/L $ZnSO_4$, albeit referring to higher temperature (150°C), initial baseline iron(II) (~11 g/L) and acid (~50 g/L H_2SO_4) concentrations.

Figure 4.12 *a* illustrates that the linear (second-order) relationship often extends to lower terminal iron(II) concentrations compared to the tests conducted without any zinc sulfate (Figure 4.7 *b* &

Stellenbosch University http://scholar.sun.ac.za

Figure 4.10 *a*). This, again, suggests that the deviation from a second-order dependence on the iron(II) concentration at higher reaction extents may be associated with speciation changes, *i.e.*, due to a drop in the relative prevalence of the iron(II) sulfate CIPs. These results also illustrate that it is imperative that the simulation 'dynamically' accounts for changes in the solution chemistry and interfacial oxygen mass transfer limitations, *i.e.*, at each time interval (Sect. 4.4.7).

4.4.4 Activation energy in comparatively low and high sulfate solution environments (no Cu)

Various tests were conducted at different temperatures in low (0 g/L Zn) and relatively higher (15 g/L Zn) sulfate concentrations to determine the overall activation energy of the uncatalysed reaction (see Figure 4.13 *a*). The first three tests (FOH1-FOH3; App. D.4) were conducted at 105°C, 150°C and 180°C, respectively, without any additional sulfate and at similar starting conditions (1000 kPa $p_{O2}°$, 25 g/L H_2SO_4). The baseline is represented by the two repeat tests at 130°C (Tests FOC1 & FOC2; App D.2). Comparative tests were also conducted in solutions containing 15 g/L Zn, *i.e.*, Test FOI1 (105°C, 1000 kPa $p_{O2}°$) and Test FOI2 (150°C, 650 kPa $p_{O2}°$) (App. D.4). The baseline (130°C, 1000 kPa $p_{O2}°$) is represented by Test FOF1 (App. D.3).

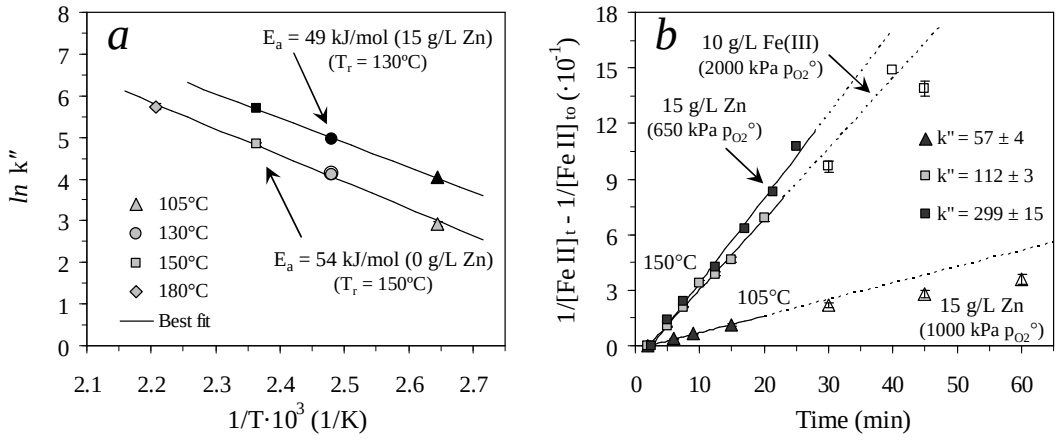

Figure 4.13
Effect of temperature at 1000 kPa $p_{O2}°$, 25 g/L H_2SO_4 & 0 g/L Cu, without Zn (grey symbols) & with 15 g/L Zn (650 kPa $p_{O2}°$ at 150ºC) (black symbols): *a*) k″ ($kg^{1.65}/mol^{1.65}$.min) in Arrhenius coordinates; *b*) Second-order plots, incl. the test at 10 g/L Fe(III) at 2000 kPa $p_{O2}°$.

The formal definition of a chemically activated reaction is adopted here (Atkins & De Paula, 2006), giving rise to the following well-known dependence of the intrinsic rate constant on the temperature (see App. F.3), *i.e.*, the Arrhenius relationship:

$$k'' = \frac{k[H^+]^{0.35}}{[O_2]^*_{t_o}} = \hat{A}k^{\sim} \cdot exp\frac{-E_a}{R_g T} \qquad 4.15$$

The pre-exponential factor, Â, represents the frequency (1/min) of successful reaction exchanges, with the proportionality constant, $k^{\sim}$, adopting the units of $(mol/kg)^{1.65}$. As indicated in Equation

Stellenbosch University http://scholar.sun.ac.za

4.15, the measured rate constants are consolidated over the varying experimental space, assuming a linear dependence on the initial dissolved oxygen concentration (*e.g.*, Figure 4.9 *b*) and adopting the $[H^+]^{-0.35}$ dependence from Figure 4.10 *b*. Figure 4.13 *a* represents the rate constants in Arrhenius coordinates, assuming that the temperature dependencies of both the pre-exponential factor and the activation energy, E_a, are small compared to the temperature term in the exponent, *i.e.*, yielding a straight line with slope E_a/R_g. The detailed oxidation rate comparisons are presented in Appendix D.4.1.

The calculated activation energies of 54 (R^2 = 0.995) and 49 (R^2 = 0.999) kJ/mol in the lower and higher sulfate environments, respectively, compare reasonably well with some of the reported activation energies (Table 4.1) for the uncatalysed reaction in the higher temperature regime (> 100ºC), *e.g.*, 56 kJ/mol (Hotta & Suzuki, 1963) and 51 kJ/mol (Vračar & Cerović, 1977). The activation energy decrease of about 5 kJ/mol with the addition of a relatively small amount of sulfate (15 g/L Zn equiv.) is consistent with the proposal that the iron(II) sulfate CIPs are more easily oxidised, *i.e.*, they are associated with lower activation energy barriers compared to the ferrous ions. This also suggests that each reaction pathway (Eq. 4.8 & 4.9) should be assigned its own unique activation energy, rather than using an overall activation energy approach.

Figure 4.13 *b* compares the second-order dependencies at 105ºC and 150ºC (Tests FOI1 & FOI2, respectively) under relatively high sulfate background concentration (15 g/L Zn), with the test conducted at 150°C and in the presence of 10 g/L Fe(III) only (Test FOJ1; App. D.4). An approximate two- to three-fold decrease in the intrinsic rate constant at 150°C (299±15 *vs.* 112±3 $kg^{1.65}/mol^{1.65}$.min) is observed between about 0.27 and 0.04 mol/kg average metal(II) sulfate background concentrations, which is consistent with the relative abundance of the metal(II) sulfate CIPs in Chapter 2 (Figure 2.23 *b*). Furthermore, the deviation from linearity is clearly less prevalent at the higher temperatures, even at relatively low free sulfate concentrations when the iron(III) concentration levels are high. This suggests that the oxidation pathways involving unassociated ferrous ions are strongly activated, which is in line with the above statements.

4.4.5 Reaction orders in the presence of copper

This section evaluates the reaction orders with respect to the iron(II) and oxygen concentrations in the presence of dissolved copper(II) sulfate. Tests FOK1 to FOK3 (App. D.5) evaluated different oxygen partial pressures at 130°C (500, 750 & 1000 kPa p_{O2}°, respectively) at the same initial acid (25 g/L H_2SO_4) and copper (15 g/L Cu) concentrations. Since these tests started at lower initial solution masses (950-1000 g), the initial rates were likely to be influenced by interfacial mass transfer limitations, especially when only the bottom impeller was functional (see Sect. 4.4.1, *ref.* Figure 4.4). As illustrated in Figure 4.14 *a*, the rate constants of these tests (open symbols) are

Stellenbosch University http://scholar.sun.ac.za

obtained from the latter part of the each relevant kinetic curve, *i.e.*, in a lower iron(II) concentration regime, thereby alleviating the influence of the oxygen mass transfer rate. However, as reflected by the error bars, the accuracy of these results is less certain (*cf.* the uncatalysed rate constants) due to the comparatively low residual iron(II) concentration levels. An additional two tests were conducted at 1000 and 2500 kPa $p_{O2}°$ (Tests FOL1 & FOL2, respectively; App. D.5), utilising the dual impeller system over the full reaction time, *i.e.*, by starting with the higher solution mass (1200 g). These results are represented by the closed symbols in Figure 4.14.

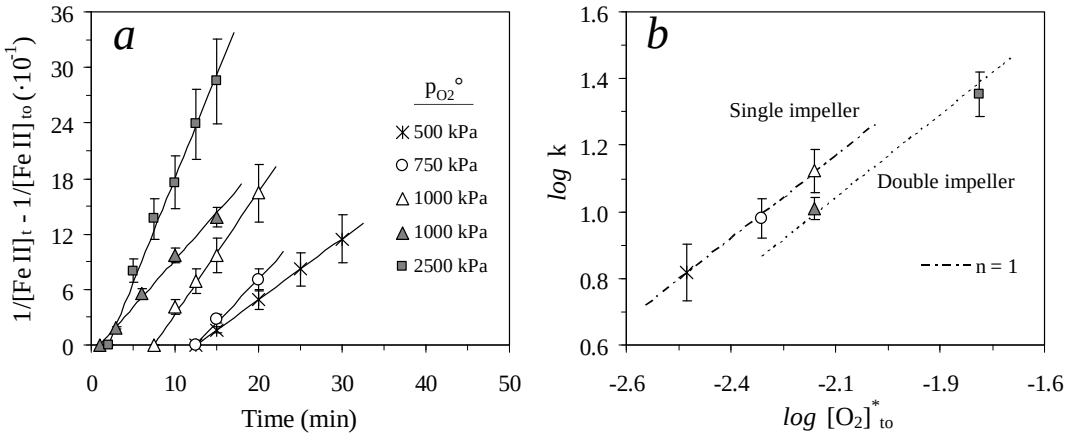

Figure 4.14
Effect of $p_{O2}°$ on the oxidation rate at 130°C, 25 g/L H_2SO_4 & 15 g/L Cu: *a*) Second-order plots; *b*) *log* k (mol/kg.min) *vs. log* $[O_2]^*_{to}$ (mol/kg). The open & closed symbols denote the 950-1000 & 1200 g initial solution masses, respectively.

Clearly, the second-order dependence on the iron(II) concentration (Figure 4.14 *a*) and first-order dependence on the oxygen concentration (Figure 4.14 *b*) are maintained down to very low iron(II) concentrations, supporting the proposed rate expression (Eq. 4.10) for the catalysed reaction pathway(s). Furthermore, a comparison of the average rate constants with their corresponding values in (15 g/L) zinc solution (Figure 4.14 *b vs.* Figure 4.11 *b*) reveals a four- to five-fold rate increase by copper (see the detailed comparisons in App. D.5.1 *vs.* D.3.1: 412±44 $kg^2/mol^2.min$ & 142±44 $kg^{1.65}/mol^{1.65}.min$ for k′ & k″, respectively, in 15 g/L Zn solution *cf.* the corresponding values of 1654±258 $kg^2/mol^2.min$ & 538±84 $kg^{1.65}/mol^{1.65}.min$ in 15 g/L Cu solution). This provides clear evidence that the role of copper is catalytic and not merely related to solution speciation changes, especially since copper(II) is a softer transition metal than zinc. In other words, copper sulfate substantially increases the oxidation rate, despite rendering less iron(II) sulfate CIPs compared to zinc sulfate (Sect. 2.3.2 & 2.4.2).

Figure 4.14 *b* also suggests that interfacial mass transfer limitations may initially be prevalent in the copper system, even with the dual impeller functional, *i.e.*, under at least two times higher mass transfer rates compared to the single bottom impeller (Sect. 3.6.6). Determining the rate constants

Stellenbosch University http://scholar.sun.ac.za

from the average second-order slopes presents therefore an oversimplification. The final regression of the phenomenological oxidation rate model (Sect. 4.4.7) simultaneously considers both the changing mass transfer rate and solution chemistry at each reaction time interval.

Since there is little agreement in the literature (Table 4.1) on the catalytic efficiency of copper at higher concentrations, the next two tests (FOM1 & FOM2; App. D.5) evaluated the effect of different initial copper tenors (25 & 35 g/L Cu, respectively), under otherwise similar starting conditions (130°C, 1000 kPa $p_{O2}°$ & 25 g/L H_2SO_4). These tests are compared to the baseline series at 0 g/L Cu (Tests FOC1 & FOC2) and 15 g/L Cu (Test FOL1, 1000 kPa $p_{O2}°$ & Test FOL2, 2500 kPa $p_{O2}°$) in Figure 4.15. These tests utilised the dual impeller (1200 g initial solution mass) and the rate constants are derived from the initial kinetics (Figure 4.15 *a*). However, this does not imply that interfacial mass transfer limitations were not prevalent in these tests (see later).

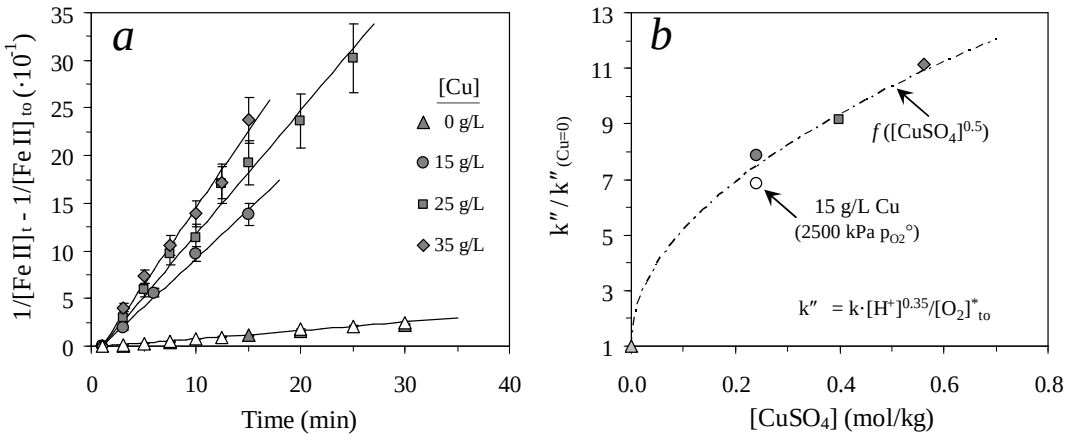

Figure 4.15
Effect of [$CuSO_4$] at 130°C, 1000 kPa $p_{O2}°$ & 25 g/L H_2SO_4: *a*) Second-order plots; *b*) $k''/k''_{(Cu=0)}$ *vs.* [$CuSO_4$]. The open symbols denote repeat tests. The regressed power function exponent is 0.48.

The regressed power function exponent of about 0.5 in Figure 4.15 *b* (0.48, R^2 = 0.92; see detailed calcs. in App. D.5.1) is in agreement with Dreisinger and Peters (1989). If it is assumed that the copper sulfate CIPs are more effective catalysts due to electrostatic and transition-state considerations (Sect. 4.2.3), the shape of Figure 4.15 *b* should roughly reflect the relative abundance of the copper(II) sulfate CIPs with increasing metal(II) concentration. The solution chemistry model (Sect. 2.4.3) suggests that this may be the case between 15 and 35 g/L M(II) in the 10 to 30 g/L H_2SO_4 range. The solution speciation model provides the mathematical methodology for simulating the apparent reduction in the catalytic efficiency of copper at increasing concentrations. This methodology is also consistent with the apparent inefficiency of copper(II) in (low complexation) perchlorate media (George, 1954), the observations of Littlejohn and Dixon

Stellenbosch University http://scholar.sun.ac.za

(2008) at high redox potentials, as well as the apparent second- to first-order change at high reaction extents, as observed by Chmielewski and Charewicz (1984) (Table 4.1).

Despite the notable experimental uncertainty, Figure 4.16 *a* (Tests FOL2 & FOM1) suggests that higher copper sulfate concentrations extend the second-order rate dependence to relatively lower terminal iron(II) concentrations. Figure 4.16 *b* (Tests FOG3 & FOM2) illustrates that the linear range in the copper sulfate system, despite its relatively higher complexation tendency, far exceeds the linear range in the zinc sulfate system (at same concentration), which supports the notion that the copper(II) sulfate CIPs are the most effective catalyst species of unassociated ferrous ion. In view of these insights, Equation 4.10 may be simplified as follows, to prevent over-parameterisation of the phenomenological rate model in homogeneous solutions:

$$R_{FeII,C} \approx k_{F/Cu}[Fe^{2+}]^2 \cdot f([Cu_{CIP}]) \cdot [O_2] \qquad 4.16$$

This assumption is scrutinised later (see regression analysis of the final rate model; Sect. 4.4.7).

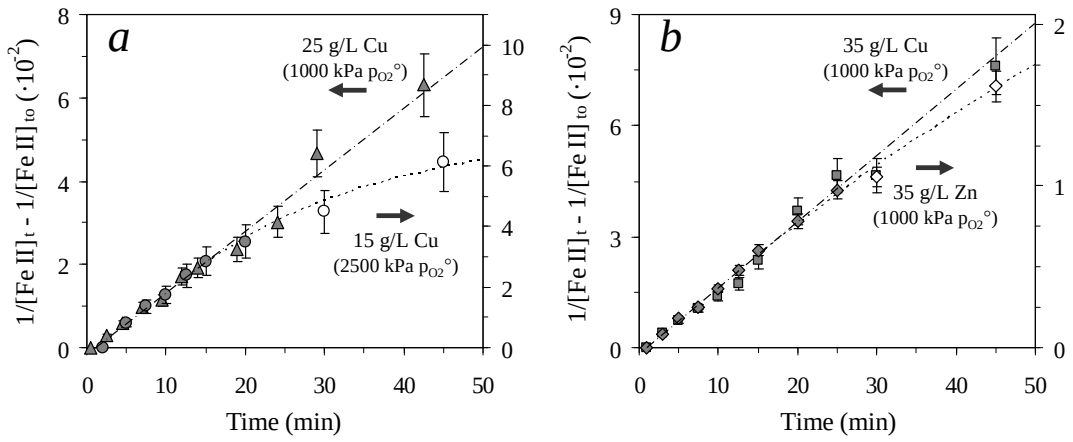

Figure 4.16
Effect of different background metal(II) sulfate salts on the second-order dependence of the rate on [Fe(II)] at 130°C & 25 g/L H_2SO_4: *a*) 25 g/L Cu *vs.* 15 g/L Cu; *b*) 35 g/L Cu *vs.* 35 g/L Zn.

4.4.6 Activation energies in the presence of copper

The final two tests in the 2-litre autoclave (Tests FON1 & FON2; App. D.5) investigated the effect of temperature (105°C & 150°C, respectively) on the oxidation rate in copper(II) sulfate solutions. In order to obtain more accurate measurements at 150°C, the copper concentration and oxygen partial pressure were lowered to 10 g/L Cu and 650 kPa p_{O2}°, respectively, while maintaining the initial acid concentration at 25 g/L H_2SO_4. The previous tests conducted at 15 g/L Cu (at 1000 & 2500 kPa p_{O2}°, *i.e.*, Tests FOL1 & FOL2, respectively) represent the datapoints at 130°C. The results of these tests are presented in Figure 4.17 *a*, while the activation energy regression is

Stellenbosch University http://scholar.sun.ac.za

illustrated in Figure 4.17 *b*, using the power function, $f([CuSO_4]^{0.5})$, to normalise the rate constants to the same copper molality of 0.24 mol/kg Cu (for illustrative purposes).

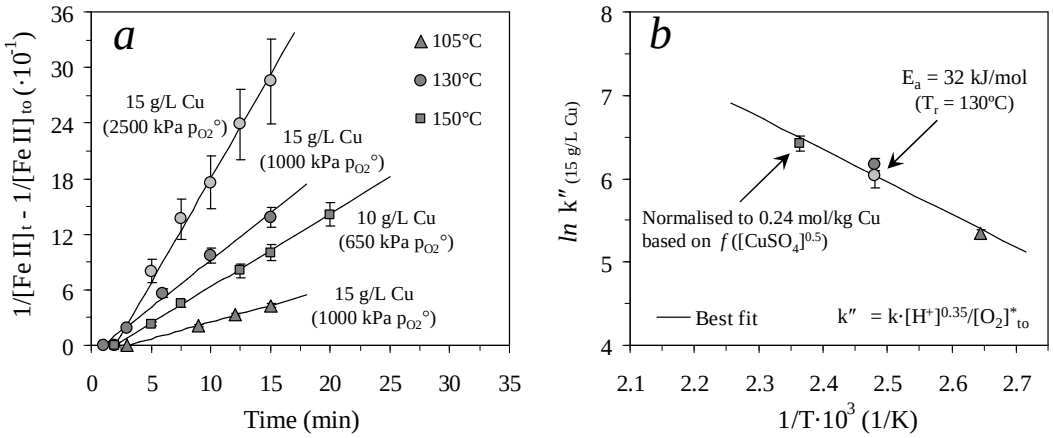

Figure 4.17
Effect of temperature at 25 g/L H_2SO_4 & 10-15 g/L Cu: *a*) Second-order plots; *b*) k″ ($kg^{1.65}/mol^{1.65}$.min) in Arrhenius coordinates (at 0.24 mol/kg Cu).

The relatively low value of 32 kJ/mol (R^2 = 0.96), compared to the copper-free sulfate system (Figure 4.13 *a*), is consistent with the catalysed reaction pathway. However, these activation energies are only indicative due to the interfacial oxygen mass transfer limitations and the changing solution speciation over time. These aspects are discussed in the regression analysis (Sect. 4.4.7).

4.4.7 Simulating the iron(II) oxidation rate

The above discussions of the higher apparent catalytic efficiency of copper in the low iron(II) concentration regime leads the following expression of the overall oxidation rate in homogeneous solutions, after combining Equations 4.9 and 4.16, and assuming a first-order relationship in the copper(II) sulfate CIP concentration (in line with the mechanistic proposal *ref.* Figure 4.2):

$$R_{FeII,\hom} = \frac{d[\mathrm{Fe\,II}]}{dt} = (k_{CIP}[Fe_{CIP}]^2 + k_{CIP/F}[Fe_{CIP}][Fe^{2+}] + k_{F/Cu}[Fe^{2+}]^2[Cu_{CIP}]) \cdot [O_2] \qquad 4.17$$

This equation neglects the other possible catalytic pathways between the copper(II) and iron(II) species, *e.g.*, $k_{CIP/Cu}[Fe_{CIP}]^2[Cu^{2+}]\cdot[O_2]$, which may be required when attempting to simulate a more complex electrolyte mixture or wider concentration ranges. Equation 4.17 is sufficient under typical MT autoclave conditions (see below) and prevents over-parameterisation of the overall model. Besides the three adjustable parameters, k_{CIP}, $k_{F/CIP}$ and $k_{F/Cu}$, only their respective activation energies, $E_{a,F/CIP}$, $E_{a,CIP}$, $E_{a,F/Cu}$, are required. This section concludes with a comparison between the simulation performance and other test results (not used in the regression) from the 2-litre autoclave, as well as from the 7-litre glass reactor at 90°C, *i.e.*, at atmospheric conditions and under high interfacial mass transfer rates.

Stellenbosch University http://scholar.sun.ac.za

Regression results and model verification

The regression analysis consists of minimising the objective function, $F(E_F)^2$, where the error function, E_F, is defined as the absolute error between the calculated and measured iron(II) concentrations for *k* tests, consisting of *i* datapoints, *i.e.*:

$$E_F = \sum_k \sum_i E_{i,k} = \sum_k \sum_i \left| [Fe\,II]_i^{calc} / [Fe\,II]_i^{exp} - 1 \right| \qquad 4.18$$

Only the tests that were conducted under well defined and higher mass transfer rates are included in the regression analysis, *i.e.*, when using the higher initial solution mass (1200 g), with both impellers submerged over the course of the test. Due to the experimental uncertainty, a minimum cut-off concentration of 0.01 mol/kg Fe(II) is used for all tests conducted without copper, while the improved experimental procedure (Sect.4.3.3) allowed this cut-off to be extended to 0.005 mol/kg Fe(II) in the presence of copper. The regression only considers the data obtained after the reactor temperature had stabilised, *i.e.*, at the first actual kinetic sample and not from the beginning of the test. The oxygen concentration at this initiation point, as well as at each time step, relies on the intrinsic iron(II) oxidation rate (Eq. 4.17) and the following oxygen mass balance expression:

$$\frac{d[O_2]}{dt} = k_L a([O_2]^* - [O_2]) - \nu_{O_2} \cdot \frac{d[Fe\,II]}{dt} \qquad 4.19$$

According to the stoichiometric reaction (Rx. 4.1), ν_{O2} is equal to ¼. All species molalities, including the oxygen solubility, are updated after each time step, utilising the solution chemistry model (Ch. 2) and the correlations of Tromans (1998a, b) (Sect. 3.2.6 & App. A.4), respectively.

Copper-free solutions

Fourteen tests were used to minimise the objective function of the uncatalysed reaction, while six tests were used to determine the corresponding activation energies. These optimised constants are summarised in Table 4.3, while the test conditions and absolute average relative deviation (*AARD*; Eq. 2.73) values of each test are summarised in Table 4.4 (the overall *AARD* value of these twenty tests is 4.3%). The majority of these tests were conducted at 130°C, making this the logical reference temperature choice, assuming Arrhenius-like behaviour:

$$k_T = k_{T_r} \cdot exp \frac{-E_a}{R_g} \left(\frac{1}{T} - \frac{1}{T_r} \right) \qquad 4.20$$

Different combinations of the iron(II) species, Fe^{2+}, $FeSO_4^o$ and $Fe(SO_4)_2^{2-}$, both with and without the explicit inclusion of a $[H^+]$ term (*e.g.*, $k_{CIP}/[H^+]$; Sect. 4.2) may be considered. The lowest overall *AARD* value (~6%) is obtained with Equation 4.17. The overall oxidation rate is therefore insensitive to the hydronium ion concentration, except for that accounted for by the solution chemistry model (Ch. 2). Replacing the total iron(II) sulfate CIP concentration with the first

Stellenbosch University http://scholar.sun.ac.za

bidentate ion pair concentration, [$FeSO_4^o$], causes some minor but inconclusive changes (less than experimental error) in the *AARD* values. This is thought to be due to the relatively low sulfate concentration used, *i.e.*, the bidentate triple anion concentration, [$Fe(SO_4)_2^{2-}$], is relatively low under these conditions (Sect. 2.4.2) and there is no reason to suspect that either of the two iron(II) sulfate CIPs is chemically more reactive than the other.

Table 4.3
Optimised intrinsic rate constants & activation energies for the uncatalysed oxidation reaction in acidic sulfate solutions.

Reaction pathway	T_r (°C)	k $(kg/mol)^2.min$	[a] *AARD* (%)	E_a (kJ/mol)	Range (°C)	[a] *AARD* (%)
k_{CIP}	130	4623	4	38.2	105 – 180	5
$k_{CIP/F}$		2144.5		60.5(4)		

[a] See Eq. 2.73: $AARD\,(\%) = \frac{100}{N_i} \cdot \sum_i E_i$

The lower activation energy of about 38 kJ/mol is associated with the interaction between two CIPs, while the higher activation energy of about 61 kJ/mol corresponds to the interaction between the CIPs and the unassociated ferrous ion. Again, these regression results are consistent with chemical reaction theory, which implies that the less favourable reaction pathway should exhibit comparatively higher activation energy.

Figure 4.18 *a* compares the simulation and test results at the higher (35 g/L Zn, 130ºC) and lower (15 g/L Zn, 150ºC) zinc sulfate concentrations (Tests FOG3 & FOI2, respectively). Figure 4.18 *b* compares the actual and corresponding saturation concentrations of oxygen, using Equation 3.11 (θ = 1.021, Sect. 3.5.2) to correlate the k_La-value (1.7 1/min; Table 3.9) with the test temperatures.

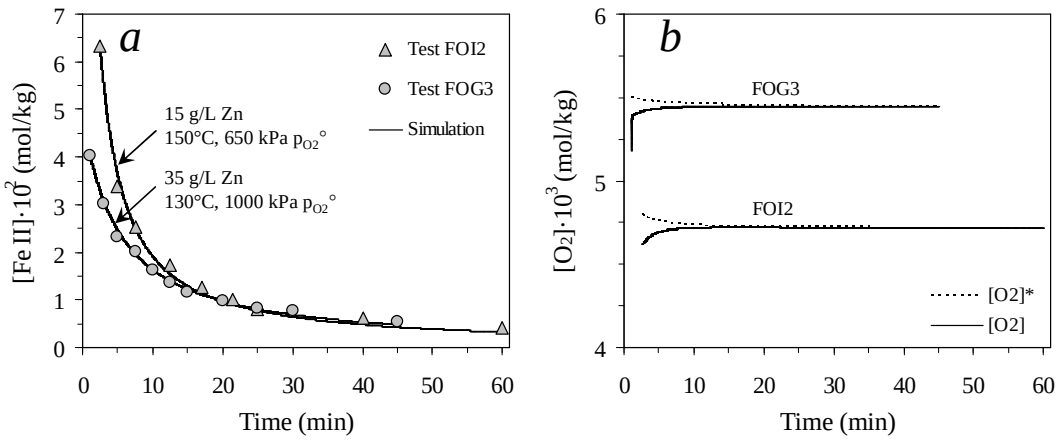

Figure 4.18
Measured *vs.* simulated [Fe(II)] & [O_2] for the Zn sulfate system, starting with 1200 g solution & 25 g/L H_2SO_4: *a*) [Fe(II)] *vs.* time; *b*) [O_2] & $[O_2]^*$ *vs.* time.

Stellenbosch University http://scholar.sun.ac.za

Despite the relatively fast intrinsic oxidation rates, differences between the actual and saturation oxygen concentrations are clearly small. This suggests that the interfacial oxygen mass transfer rate has an insignificant impact on the kinetics of the uncatalysed oxidation reaction in the 2-litre autoclave, provided both impellers are submerged (~1200 g sln. initially).

Table 4.4
Tests used to regress the intrinsic rate constants & activation energies of the uncatalysed reaction.

Test no.	Temp.	p_{O2}°	$[H_2SO_4]\cdot10^2$	$[Zn]\cdot10^2$	$[Fe(II)]\cdot10^2$	[a] *AARD*
–	(°C)	(kPa)	(mol/kg)	(mol/kg)	(mol/kg)	(%)
FOC1	130	1000	25.90	0	9.09	5.5 {99}
FOC2	130	1000	25.90	0	9.09	3.9 {>99}
FOD1	130	1500	25.90	0	9.09	6.2 {99}
FOD2	130	2000	25.90	0	9.09	0.7 {>99}
FOD3	130	2500	25.90	0	9.09	2.1 {>99)
FOE1	130	1500	10.24	0	8.99	6.5 {99}
FOE2	130	1500	36.40	0	9.13	5.3 {99}
FOE3	130	1500	46.94	0	9.16	4.8 {>99}
FOF1	130	1000	25.82	23.24	9.07	3.2 {97}
FOF2	130	1500	25.82	23.24	9.07	2.1 {97}
FOF3	130	2000	25.82	23.24	9.07	2.6 {98}
FOF4	130	2500	25.82	23.24	9.07	5.7 {98}
FOG2	130	1000	26.04	54.68	9.15	4.1 {95}
FOG3	130	1000	26.04	54.68	9.15	3.3 {94}
FOH1	105	1000	25.90	0	9.09	1.6(5) {>99}
FOI1	105	1000	25.82	23.24	9.07	6.9 {96}
FOB2	150	650	25.90	0	9.09	4.6 {99}
FOH2	150	1000	25.90	0	9.09	3.3 {99}
FOI2	150	650	25.82	23.24	9.07	8.3 {96}
FOH3	180	1000	25.90	0	9.09	4.9 {99}

All tests utilised 1200 g initial sln. mass; [a] *Ref.* [Fe(II)] & the {values} refer to % $[O_2]/[O_2]^*$ at the first kinetic datapoint.

Copper-containing solutions

Before evaluating the impact of the interfacial mass transfer rate on the catalysed reaction rate, the impact of the oxidation reaction itself on the oxygen absorption process needs to be assessed. The dimensionless Hatta (Ha) number (Eq. 3.8) is adopted for this purpose, *i.e.*, to determine whether the chemical reaction or the physical absorption process is controlling. Since the oxidation reaction is first-order in the dissolved oxygen concentration, the following expression is obtained:

Stellenbosch University http://scholar.sun.ac.za

$$Ha = \left(\frac{2}{n_1 + 1} \frac{D_{O_2} \nu k_1 [O_2]^{*(n_1-1)} [Red]^{n_2}}{k_L^2} \right)^{\frac{1}{2}} = \left(\frac{D_{O_2}}{k_L^2} \frac{\frac{1}{4} k [Fe\,II]^2}{[O_2]^*_{t_o}} \right)^{\frac{1}{2}} \quad 4.21$$

Calderbank and Moo-Young (1961) correlated the liquid-side mass transfer coefficient (k_L) for a liquid film in stirred vessels. Larger gas bubbles (> 2.5 mm), produced when pure liquids are aerated in stirred vessels, do not behave like rigid spheres and the following correlation is utilised:

$$k_L (Sc)^{\frac{1}{2}} = 0.42 \left(\frac{\Delta \rho \eta_c g}{\rho_c^2} \right)^{\frac{1}{3}} \quad 4.22$$

where Sc is the Schmidt number:

$$Sc = \left(\frac{\eta_c}{\rho_c D_{O_2}} \right)^{\frac{1}{3}} \quad 4.23$$

The terms η_c and ρ_c refer to the viscosity and density of the continuous phase, respectively, while $\Delta\rho$ (the density difference between the two phases) is assumed to be close to the liquid density since the oxygen bubbles are significantly less dense than the aqueous solution. Equation 4.22 then simplifies to:

$$k_L = 0.42\, D_{O_2}^{\frac{1}{2}} \cdot \left(\frac{g^2 \rho_c}{\eta_c} \right)^{\frac{1}{6}} \quad 4.24$$

Substitution of Equation 4.24 into Equation 4.21, and rearranging then results in the following estimate of the Hatta number:

$$Ha \approx \frac{(k')^{\frac{1}{2}}}{0.84} [Fe(II)] \cdot \left(\frac{\mu_w}{g^2 \rho_w} \right)^{\frac{1}{6}} \quad 4.25$$

where water viscosity and density are used as a first estimate and the average intrinsic rate constant $k' = k/[O_2]^*_{to}$ is obtained from the intrinsic kinetic regime at a low terminal iron(II) concentration.

The enhancement factor, E_L, is the ratio by which the oxidation reaction increases the rate of oxygen absorption, compared to absorption without any reaction (Danckwerts, 1970). This depends on the concentration profile in the diffusion layer. A limiting case may be derived to give a conservative estimate of the enhancement factor if the chemical reaction is first order in oxygen concentration and the bulk concentration is approximately zero (Danckwerts, 1970):

$$E_L = \frac{Ha}{tanh(Ha)} \quad 4.26$$

Stellenbosch University http://scholar.sun.ac.za

The tests most likely to have experienced chemical enhancement, *i.e.*, fastest intrinsic kinetics, are Tests FOA3 (150°C, 25 g/L Cu) and FOM2 (130°C, 35 g/L Cu). A summary of these calculations is presented in Table 4.5. These calculations reveal that Ha < 0.3, confirming that minimal iron(II) oxidation occurs in the interfacial layer (Beek & Mutzall, 1991). Since the enhancement factors are close to unity, Equation 4.19 may also be directly applied to obtain the dissolved oxygen concentration in the copper sulfate system.

Table 4.5
Enhancement factors at high intrinsic oxidation rates in the presence of copper(II).

Test no.	Temp.	[Cu]	k′	[a] [Fe(II)]·10^2	[b] μ_w	[b] ρ_w	[c] Ha	[d] E_L
–	(°C)	g/L	(kg/mol)^2/sec	(mol/kg)	(cP)	(kg/m^3)	–	–
FOA3	150	25	[e] 39.310	9.084	0.180	916.6	0.242	1.019
FOM2	130	35	41.373	9.113	0.211	934.6	0.255	1.022

[a] Initial [Fe(II)]; [b] Cooper & Le Fevre (1982); [c] Eq. 4.25; [d] Eq. 4.26; [e] *Ref*. Test FON2 (10 g/L Cu), using [Cu]$^{0.5}$ to scale.

All combinations involving the second-order interaction between two iron(II) (Fe^{2+}, $FeSO_4°$, $Fe(SO_4)_2^{2-}$) and a copper(II) species (Cu^{2+}, $CuSO_4°$, $Cu(SO_4)_2^{2-}$) were evaluated, both with and without [H^+]-terms (Sect. 4.2). Again, the best results are obtained using Equation 4.17, but the regression improves marginally when using the neutral copper(II) sulfate species concentration, [$CuSO_4^o$]. The optimal description of the iron(II) oxidation rate in homogeneous acidic copper sulfate solutions, with a minimum number of adjustable parameters, is therefore as follows:

$$R_{FeII,\text{hom}} = \frac{d[\text{Fe II}]}{dt} = (k_{CIP}[FeSO_4^o + Fe(SO_4)_2^{2-}]^2 + k_{CIP/F}[FeSO_4^o + Fe(SO_4)_2^{2-}][Fe^{2+}] + k_{F/Cu}[Fe^{2+}]^2[CuSO_4^o]) \cdot [O_2] \qquad 4.27$$

The oxidation rate at the lowest copper concentration (10 g/L Cu; Test FON2) reveals the rate constant at 150ºC, while the five remaining tests (FOL1-FOL2, FOM1-FOM2 & FON1) were used to determine the activation energy. The optimised values for the catalysed reaction are summarised in Table 4.6, while the test conditions and individual *AARD* values are summarised in Table 4.7.

Table 4.6
Optimised intrinsic rate constant & activation energy for the copper-catalysed oxidation reaction.

Reaction	T_r	k	[a] *AARD*	E_a	Range	[a] *AARD*
pathway	(°C)	(kg/mol)^3.min	(%)	(kJ/mol)	(°C)	(%)
$k_{F/Cu}$	150	54655	2	34	105 – 150	7

[a] Table 4.3 footnote.

The optimised activation energy value of 34 kJ/mol for the copper-catalysed reaction is again consistent with a more favourable pathway, compared to the apparent activation energy of 49 to 54 kJ/mol for the uncatalysed reaction (Figure 4.13 *a*).

Stellenbosch University http://scholar.sun.ac.za

Table 4.7
Tests used to regress the intrinsic rate constant & activation energy of the catalysed reaction.

[a] Test no.	Temp.	$p_{O2}°$	$[H_2SO_4]\cdot10^2$	$[Cu]\cdot10^2$	$[Fe(II)]\cdot10^2$	[a] *AARD*
–	(°C)	(kPa)	(mol/kg)	(mol/kg)	(mol/kg)	(%)
FON2	150	650	25.82	15.94	9.07	1.7 {96}
FOL1	130	1000	25.89	23.97	9.09	5.3 {95}
FOL2	130	2500	25.89	23.97	9.09	3.1 {99}
FOM1	130	1000	25.86	39.92	9.08	6.7 {94}
FOM2	130	1000	25.95	56.06	9.11	14.1 {90}
FON1	105	1000	25.89	23.97	9.09	10.4 {96}

All tests utilised 1200 g initial sln. mass; [a] *Ref.* [Fe(II)] & the {values} refer to % $[O_2]/[O_2]^*$ at the first kinetic datapoint.

Figure 4.19 *a* compares the calculated and measured iron(II) values at relatively low (10 g/L Cu; 150°C) and high (35 g/L Cu; 130°C) copper concentrations with the zinc sulfate system (Figure 4.18) under similar operating conditions, while Figure 4.19 *b* compares the actual oxygen concentration with the saturation concentration. Although the simulation gives a good representation of the experimental data, the slightly 'faster' simulation output at 35 g/L Cu suggests that interfacial mass transfer limitations may be more significant than depicted by Figure 4.19 *b*, *i.e.*, the k_La-value (at 25°C) may be lower than 1.7 1/min (previous section), and possibly as low as 0.75 1/min (Table 3.9). However, even when utilising this lower estimate, the simulation is only marginally improved (13.2% *AARD*, *ref.* Test FOM2), confirming that the oxygen mass transfer rate has an insignificant impact on the oxidation kinetics after the first five minutes at these low iron(II) tenors, provided both impellers are submerged.

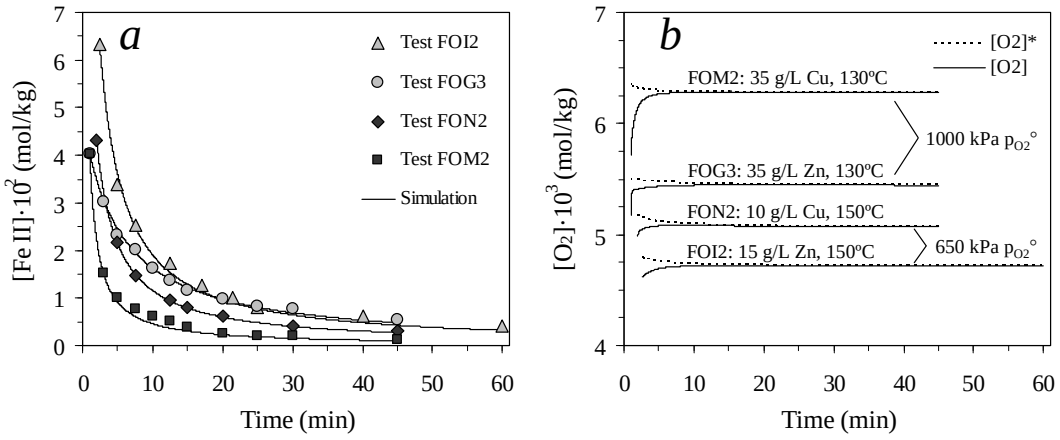

Figure 4.19
Measured *vs.* simulated [Fe(II)] & $[O_2]$ for the Zn & Cu sulfate systems, starting with 25 g/L H_2SO_4 & 1200 g solution: *a*) [Fe(II)] *vs.* time; *b*) $[O_2]$ & $[O_2]^*$ *vs.* time (k_La = 1.7 1/min).

Stellenbosch University http://scholar.sun.ac.za

Model verification using experimental data not included in the above regressions

The simulation performance was verified by eleven tests, conducted in the 2-litre autoclave and not utilised in the above regression, referring mostly to the tests that used a lower initial solution mass (≤ 1000 g). These results are summarised in Table 4.8.

Table 4.8
Summary of tests & conditions used to verify the phenomenological iron(II) oxidation rate model.

[a] Test no.	Temp.	p_{O2}°	$[H_2SO_4]\cdot10^2$	$[Metal]\cdot10^2$	$[Fe(II)]\cdot10^2$	[b] *AARD*
–	(°C)	(kPa)	(mol/kg)	(mol/kg)	(mol/kg)	(%)
FOA1	150	500	25.86	39.92 (Cu)	9.08	[c] 5.9, 7.3 (8.5)
FOA2	150	450	25.86	39.92 (Cu)	9.08	[c] 10.3, 8.7 (7.5)
FOA3	150	50	25.86	39.92 (Cu)	9.08	[c] 7.8, 3.5 (10)
FOA4	150	500	25.90	0 (Cu)	9.09	[c] 0.5, 0.9 (11.5)
FOB1	150	650	25.90	0 (Cu)	9.09	[c] 7.4, 7.1 (45)
[d] FOJ1	150	2000	25.79	18.12 (FeIII)	9.06	[e] 6.3, 6.0 (45)
[d] FOC3	130	2000	25.79	18.12 (FeIII)	9.06	[e] 5.3, 5.0 (45)
FOG1	130	1000	26.29	39.43 (Zn)	9.23	[c] 8.1, 6.6 (45)
FOK1	130	500	25.89	23.97 (Cu)	9.09	[c] 4.8, 3.2 (10)
[f] FOK2	130	750	25.89	23.97 (Cu)	9.09	[c] 6.2, 4.8 (12.5)
FOK3	130	1000	25.89	23.97 (Cu)	9.09	[c] 4.4, 4.9 (10)
[g] FOO1	90	16.1	24.20	40 (Cu), 1.6 (FeIII)	8.40	2.2 (180)
[g] FOO2	90	15.5	12.03	10 (Cu), 0.9 (FeIII)	9.06	3.2 (180)
[g] FOO3	90	15.8	12.50	10 (Cu), 30 (Mg)	10.0	11.2 (180)
[g] FOO4	90	15.8	12.29	10 (Cu), 30 (Zn), 0.4 (FeIII)	9.58	6.3 (180)
[g] FOO5	90	16.7	49.53	10 (Cu), 30 (Zn), 0.9 (FeIII)	9.06	12.8 (180)
[g] FOO6	90	16.4	49.59	10 (Cu), 0.8 (FeIII)	9.18	11.8 (180)

[a] 1000 g initial sln. mass (2-litre AC), unless indicated otherwise; [b] *Ref.* [Fe(II)] (eval. range (min) in brackets); [c] k_La of 0.425 & 0.25 1/min, respectively; [d] 1200 g initial sln. mass; [e] k_La of 1.7 & 0.75 1/min, respectively; [f] 950 g initial sln. mass; [g] 7-litre glass reactor (~7000 g initial sln. mass; App. D.6) under atm. pressure & k_La of 8.3 1/min (Tab.3.9).

Figure 4.20 compares the first four tests (FOA1-FOA4), conducted at different oxygen overpressures and k_La-values. The k_La-value of 0.425 1/min refers to the average mass transfer coefficient as the solution volume dropped below the top impeller, while the value of 0.25 1/min represents the estimated lower boundary for impeller configuration B (Ch. 3) and clearly yields a better result for Test FOA3. This suggests an even lower k_La-value for the single impeller than depicted in Table 3.9 and emphasises the importance of considering interfacial mass transfer limitations when copper(II) is present. Test FOA4, on the other hand, shows less sensitivity towards the oxygen mass transfer rate because no copper was present in the test solution.

Stellenbosch University http://scholar.sun.ac.za

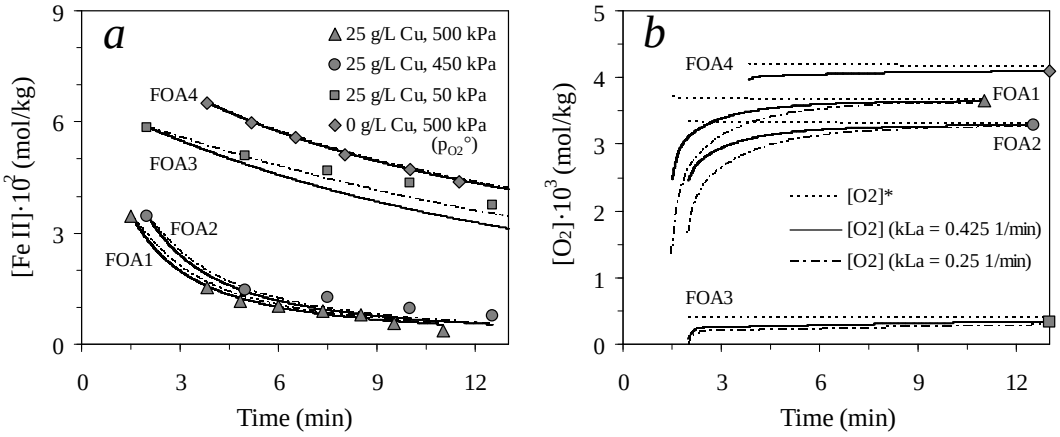

Figure 4.20
Measured *vs.* simulated [Fe(II)] & [O_2] at 150°C, starting with 25 g/L H_2SO_4 & 1000 g sln in the 2-litre AC: *a*) [Fe(II)] *vs.* time; *b*) [O_2] & [O_2]* *vs.* time. The lines represent the simulation results.

Tests FOK1 to FOK3, conducted at 130°C and various oxygen overpressures, also utilised lower initial solution volumes in the presence of copper (15 g/L Cu). These results are illustrated in Figure 4.21 and, once again, highlight the importance of the interfacial oxygen mass transfer rate during the initial oxidation period in the copper-catalysed system, especially with only the single (bottom) impeller functional. However, this figure suggests that the k_La-value of 0.425 1/min for the single impeller gives an accurate representation of the data. Therefore, no further analysis of the mass transfer rate is made in this regard and the k_La-values reported in Table 3.9 are assumed to be sufficiently accurate for the purpose of this study.

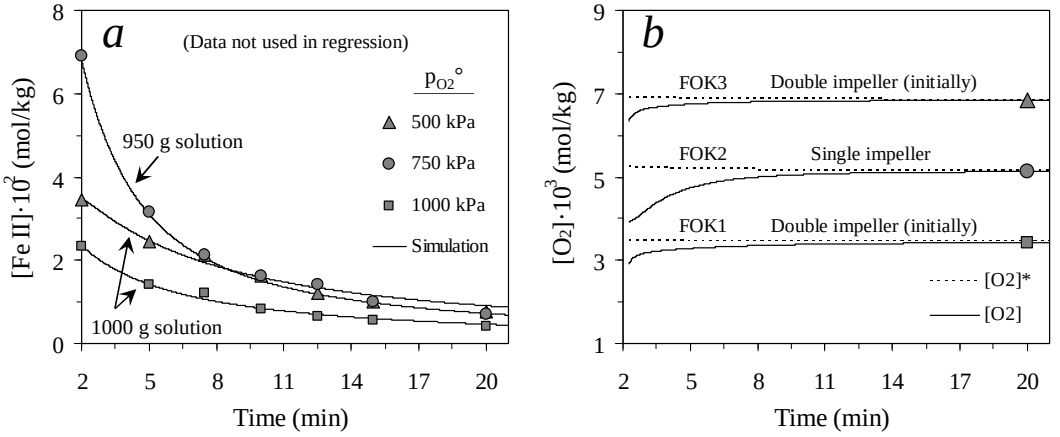

Figure 4.21
Measured *vs.* simulated [Fe(II)] & [O_2] at 130°C, starting with 25 g/L H_2SO_4, 15 g/L Cu & 950 to 1000 g sln. in the 2-litre AC: *a*) [Fe(II)] *vs.* time; *b*) [O_2] & [O_2]* *vs.* time (k_La = 0.425 1/min).

Figure 4.22 compares the simulation performance and experimental values at 130°C in the presence of sulfate salts, but without copper in solution, *i.e.*, for Test FOC3 (10 g/L Fe(III), 2000 kPa pO_2°,

Stellenbosch University http://scholar.sun.ac.za

1200 g initial solution) and Test FOG1 (25 g/L Zn, 1000 kPa p_{O2}° & 1000 g initial solution). The simulation performance is again acceptable and illustrates that the interfacial oxygen mass transfer rate in the 2-litre autoclave is unimportant in the case of the uncatalysed iron(II) oxidation reaction, provided the initial concentration is lower than about 5 g/L Fe(II).

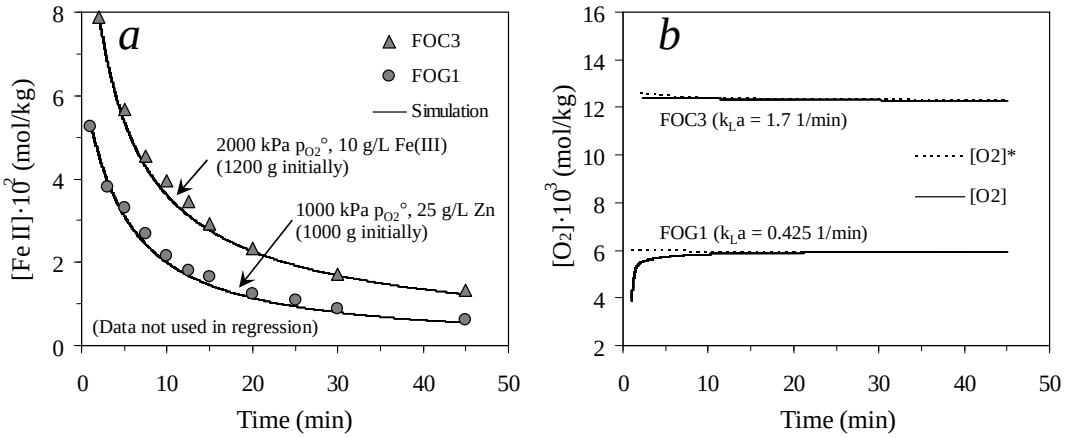

Figure 4.22
Measured *vs.* simulated [Fe(II)] & [O_2] at 130°C, starting with 25 g/L H_2SO_4 & Fe(III) or Zn sulfate in the 2-litre AC: *a*) [Fe(II)] *vs.* time ; *b*) [O_2] & $[O_2]^*$ *vs.* time.

Figure 4.23 evaluates the simulation performance at two significantly different temperatures, *i.e.*, at 105 (Tests FOI1 & FON1) and 150ºC (Tests FOB1 & FOJ1), and in different sulfate backgrounds. Since the iron(II) oxidation reaction is more activated than the interfacial diffusion of diatomic oxygen, insignificant mass transfer limitations are prevalent at 105ºC, even in the presence of copper (Figure 4.23 *a*).

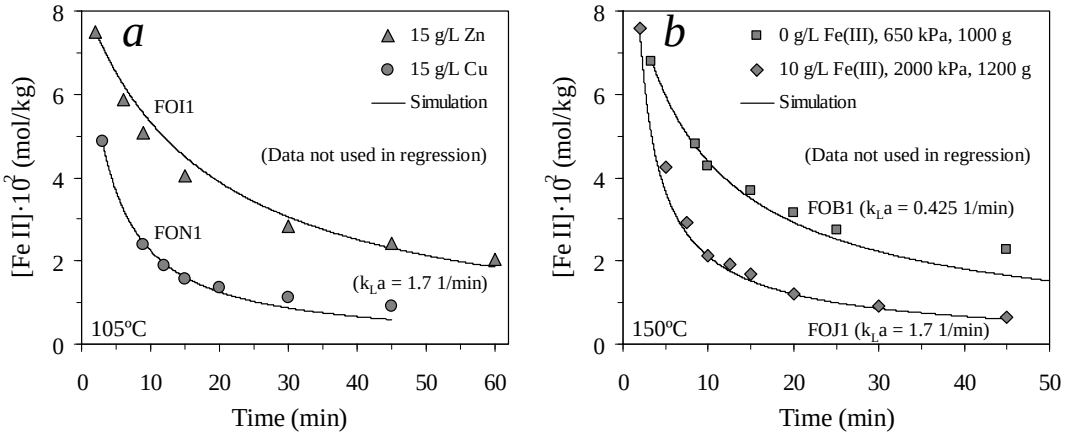

Figure 4.23
Measured *vs.* simulated [Fe(II)], starting with 25 g/L H_2SO_4 in the 2-litre AC: *a*) [Fe(II)] *vs.* time at 105°C, 1200 g sln. & 1000 kPa p_{O2}°; *b*) [Fe(II)] *vs.* time at 150°C, with & without Fe(III) (no Zn & Cu sulfate salts added).

Stellenbosch University http://scholar.sun.ac.za

Figure 4.22 *a* and Figure 4.23 *b* illustrate that the reduction of the free acid concentration (Rx. 2.78), as well as the associated changes in the CIPs, adequately account for the presence of iron(III) sulfate salt in the solution background. As illustrated above, the lower *AARD* values for Test FOB1 (Table 4.8) are related to the deviation from second-order kinetics at higher reaction extents.

As suggested by the above figures, an increase in the prevalence of the iron(II) sulfate CIPs at higher temperatures and background sulfate concentrations appears to extend the second-order kinetics to lower terminal iron(II) concentrations. Confirmatory tests (FOO1-FOO6) were therefore conducted in the 7-litre glass reactor at even lower temperatures (90°C, under atmospheric pressure conditions), characterised by a high interfacial mass transfer rate (Table 3.9) which remains relatively unaffected by sample removal (see experimental procedure in App. D.1). The detailed test results can be found in Appendix D.6. The test conditions (at the initiation point) are also summarised in Table 4.8. The phenomenological oxidation rate model is again evaluated from the first sample, *i.e.*, after 5 minutes. The second-order (linear) plots of the first two tests (FOO1 & FOO2) are illustrated in Figure 4.24. The most interesting aspect of these lower temperature tests is that the deviation from linearity occurs at significantly higher iron(II) concentrations as compared to the MT autoclave tests (see previous results).

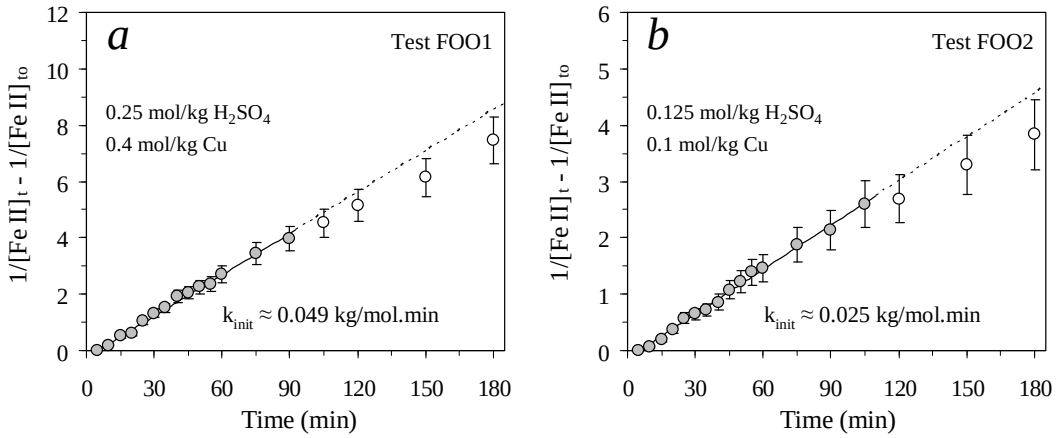

Figure 4.24
Second-order plots at 90°C in the 7-litre glass reactor, starting with 0.1 mol/kg Fe(II): *a*) 0.25 mol/kg H_2SO_4 & 0.4 mol/kg Cu; *b*) 0.125 mol/kg H_2SO_4 & 0.1 mol/kg Cu.

The following two tests (FOO3 & FOO4) were conducted at relatively low acid (0.125 mol/kg H_2SO_4) and copper (0.1 mol/kg Cu) concentrations, but in the presence of 0.3 mol/kg Mg and Zn, respectively. Contrary to autoclave results at higher temperatures, Figure 4.25 suggests that these sulfate background salts increase the deviation from second-order kinetics, especially magnesium sulfate (Figure 4.25 *a*). Furthermore, the initial rate is significantly (~40%) faster in the case of magnesium compared to the zinc sulfate background, while the final rate (> 60 min) is very similar

Stellenbosch University http://scholar.sun.ac.za

(~0.03 kg/mol.min). The latter observation supports the main assumption of the solution chemistry model (Ch. 2), *i.e.*, the surrogate metal(II) salt approach.

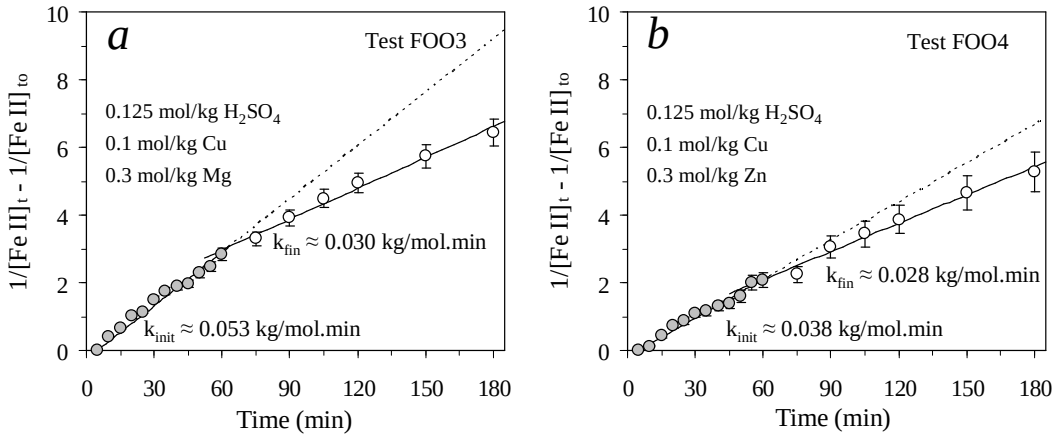

Figure 4.25
Second-order plots at 90°C in the 7-litre reactor, starting with 0.1 mol/kg Fe(II): *a*) 0.125 mol/kg H_2SO_4, 0.1 mol/kg Cu & 0.3 mol/kg Mg; *b*) 0.125 mol/kg H_2SO_4, 0.1 mol/kg Cu & 0.3 mol/kg Zn.

The final two tests (FOO5 & FOO6) were conducted at high acid (0.5 mol/kg H_2SO_4) and low copper (0.1 mol/kg Cu) concentrations, with and without 0.3 mol/kg Zn, respectively. The second-order plots, illustrated in Figure 4.26, are consistent with MT autoclave trends, *i.e.*, a higher sulfate background concentration results in less deviation from second-order kinetics. However, under these conditions (90°C, ~50 g/L H_2SO_4), the zinc sulfate causes a relatively small (< 20%) acceleration of the oxidation rate compared to the addition of 15 g/L Zn in the 2-litre autoclave at 105°C and 25 g/L H_2SO_4 (~270%; compare Tests FOH1 & FOI1; App. D.4).

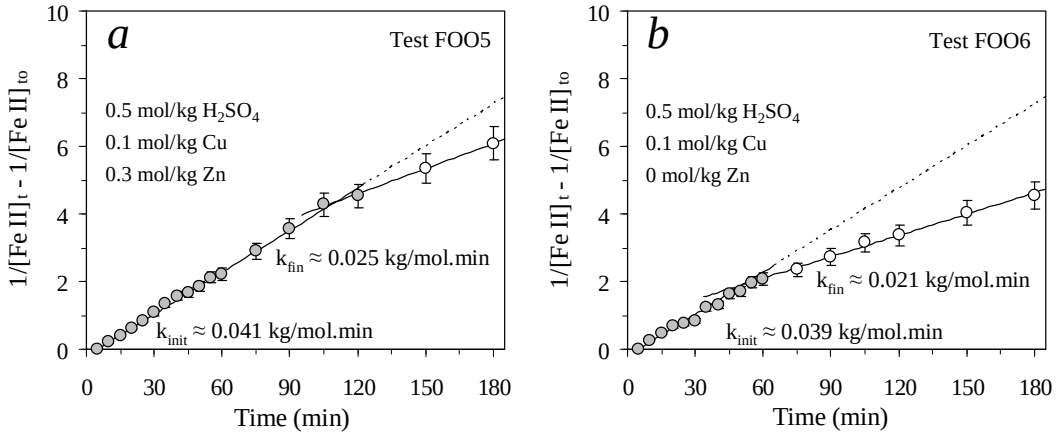

Figure 4.26
Second-order plots at 90°C in the 7-litre reactor, starting with 0.1 mol/kg Fe(II): *a*) 0.5 mol/kg H_2SO_4, 0.1 mol/kg Cu & 0.3 mol/kg Zn; *b*) 0.5 mol/kg H_2SO_4, 0.1 mol/kg Cu & 0 mol/kg Zn.

Stellenbosch University http://scholar.sun.ac.za

Nevertheless, the tests conducted at 105°C (see, *e.g.*, Figure 4.23 *a*) also exhibit significant deviation from second-order kinetics, albeit at higher conversion extents compared to the 90°C tests. Figure 4.27 *b* illustrates that the simulation is less accurate at 90°C, especially at the higher acid concentration of 0.5 mol/kg H_2SO_4 (Tests FOO5 & FOO6). The initial observed rates are significantly (up to 40%) higher than anticipated, especially in quaternary mixtures with magnesium sulfate, while the final observed rates (after ~25% oxidation extent) are reasonably well described by the simulation. The step-change adjustments are included in order to illustrate that the simulation gives an acceptable representation of the final rate, but not the initial rate.

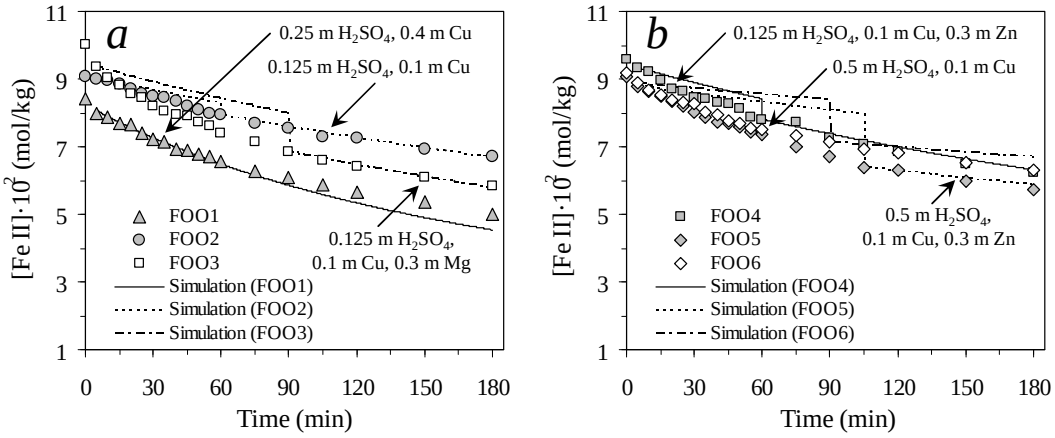

Figure 4.27
Measured *vs.* simulated [Fe(II)] at 90°C in the 7-litre reactor (k_La = 8.3 1/min): *a*) Tests FOO1, FOO2 & FOO3 (k_La = 8.3 1/min); *b*) Tests FOO4, FOO5 & FOO6. The step-change adjustments serve to illustrate that the simulation best represents the final oxidation rate and not the initial rate.

To summarise, as the temperature decreases, other effects, whether kinetic or speciation related, appear to come into play and the simulation becomes less accurate. It should, however, be noted that this model makes use of a limited number of adjustable parameters and it would be unrealistic to expect an accurate extrapolation outside the regressed parameter space, at least without a more elaborative description of the solution speciation.

Stellenbosch University http://scholar.sun.ac.za

4.5 Overview and recommendations

4.5.1 General

This chapter presents a phenomenological model of the rate of iron(II) oxidation under typical medium temperature (MT) autoclave leach conditions. In order to prevent over-parameterisation of the rate model, various assumptions are made, based on literature information and scrutinised using experimental observation. Regression analyses are then used to simplify and verify the rate model, while maintaining consistency with the main proposals of this study.

The experimental results confirm that the uncatalysed and copper-catalysed iron(II) oxidation reactions follow a termolecular pathway, with second- and first-order dependencies on the iron(II) and dissolved oxygen concentrations, respectively. It is also shown that the iron(II) sulfate contact ion pairs (CIPs) oxidise faster than the unassociated ferrous ion (Fe^{2+}). The negative impact of increasing hydrogen ion concentration on the oxidation rate is likely an artefact of the solution speciation changes. In fact, an accurate solution thermodynamic description, as well accounting for the interfacial oxygen mass transfer limitations, is shown to be paramount to the consistent behaviour of the oxidation rate model utilising a minimum number of adjustable parameters.

4.5.2 Uncatalysed iron(II) oxidation reaction

There is considerable evidence in the literature to suggest that the iron(II) sulfate CIPs oxidise faster than unassociated ferrous ion, which explains the beneficial effect of adding 'inert' sulfate salts (see Ch. 2) on the overall oxidation rate. A clear distinction is therefore made between the sulfate-independent (SI) and sulfate-dependent (SD) reaction pathways.

It is assumed that the oxidation of iron(II) by the peroxide (H_2O_2) intermediate, if it survives disproportionation at high temperatures, proceeds *via* a mechanism analogous to diatomic oxygen, but at a faster (non-limiting) rate. The oxidation rate expression is therefore based on the thermodynamically less favourable and kinetically slower first reduction step of diatomic oxygen by ferrous ion compared to the peroxide molecule. It is also assumed that this oxygen molecule can accept two electrons *via* intra-molecular transfer. The crossing of the energy barrier at the transition state may thus be viewed as being driven by the approach of a second iron(II) species, hence the second-order dependence of the observed reaction rate on the iron(II) concentration. An electrostatic argument may therefore (at least partially) explain why iron(II) typically oxidises orders of magnitude faster in neutral or basic solutions compared to acidic solutions. Clarity on these aspects, as well as the direct role of the hydrogen ion in the oxidation mechanism of the SI reaction pathway, may, however, only be obtained after comprehensive quantum mechanical (including molecular dynamic) simulations of the oxidation reaction. Nevertheless, the general

Stellenbosch University http://scholar.sun.ac.za

consensus is that an increase in the hydrogen ion concentration negatively affects the oxidation rate, and appears to be more prominent at higher temperatures and sulfate concentrations and less prominent at lower temperatures and in non-complexing media, *e.g.*, in perchlorate solutions.

From a phenomenological modelling perspective, it is assumed that the intrinsic oxidation mechanisms of both the SI and SD pathways are unaffected by the hydrogen ion concentration, *i.e.*, the hydrogen ion does not participate in the rate-limiting step and the overall observed oxidation rate is merely an artefact of the speciation changes that accompany the changing solution composition. This assumption is not only supported by the regression results (see below), but it is also consistent with various studies cited in the literature, suggesting that the higher the temperature, the higher the threshold acid levels at which the oxidation rate becomes insensitive to the acid concentration. Although the background salt matrix and temperature differed significantly between these studies, the trends are in qualitative agreement with the relative abundance of the metal(II)-sulfate CIPs as a function of acid, sulfate and temperature (Ch. 2, Sect. 2.4.3). In fact, many of the apparent reaction order 'anomalies' reported for the sulfate system can either be ascribed to such speciation changes or to interfacial mass transfer limitations, especially at high iron(II) concentrations. For example, high concentrations of the reaction 'product', iron(III), can be assumed to reduce the relative abundance of the iron(II) sulfate CIPs, due to the large formation constants of the iron(III) sulfate complexes. Again, only the most fundamental studies would reveal whether iron(III) directly partakes in the intrinsic oxidation mechanism, *e.g.*, by accelerating the reverse reaction at the transition state. The aim of the experimental programme (see below) is to scrutinise this assumption, amongst others, from a phenomenological modelling perspective.

4.5.3 Copper-catalysed iron(II) oxidation reaction

Although the rate expression for the copper-catalysed oxidation reaction differs widely in the open literature, most of the studies retain the second- and first-order dependencies on the iron(II) and dissolved oxygen concentration, respectively. Therefore, unlike the fundamentally different oxidation mechanisms in aqueous basic and chloride systems, the copper-catalysed reaction in the sulfate system may be treated analogously to the uncatalysed reaction. However, a number of studies fail to maintain consistency with the fundamentals of chemical reaction theory, which proposes that the copper-catalysed, as well as the SD, pathway should reflect a lower activation energy barrier compared to the SI pathway. Furthermore, due to the high oxidation rates in the presence of copper(II), the deviation from these reaction orders may also be related to interfacial oxygen mass transfer rate limitations, as elaborated upon in the literature review.

Findings from literature studies at lower temperatures suggest that the catalytic action of copper is more substantial in high sulfate environments compared to perchlorate solutions. It also appears

Stellenbosch University http://scholar.sun.ac.za

that higher sulfate and iron(II) concentrations extend the catalytic efficiency to higher copper(II) concentrations, which is again assumed to be related to solution speciation changes, which, in turn, are dependent on temperature, acid and total sulfate concentration. Electrostatic considerations therefore also come into play for the copper-catalysed reaction, again separating the overall reaction into distinct SI and SD pathways. The mechanistic proposal of this study envisages that electron transfer between the diatomic oxygen and iron(II) species occurs more readily *via* a copper-oxygen inner-sphere complex, with heavy emphasis being placed on the presence of two iron(II) species in the vicinity of this intermediate species. This proposal is consistent with the second-order rate dependence on the iron(II) concentration in copper sulfate solutions, as observed in various experimental studies, as well as a general first-order dependence on the most reactive copper(II) sulfate species (Figure 4.2).

4.5.4 Surface-catalysed iron(II) oxidation reaction

In this study, the catalytic role of solid surfaces on the iron(II) oxidation rate is particularly relevant to the chalcopyrite concentrate leaching system at high pulp densities in the batch and continuous autoclaves. The catalytic role of iron(III) precipitates is assumed to be insignificant due to the negligible adsorption of iron(II) onto hydrous iron(III) oxides in acidic solutions (pH < 3), according to the literature. In contrast, pyrite mineral surfaces are shown to enhance the oxidation rate of iron(II). This mechanism is related to the electrocatalytic role of the non-bonding t_{2g} orbital of iron in the pyrite surface lattice and the enhanced electron-attracting capability of surface-coordinated diatomic oxygen on pyrite. This may create highly oxidised surface species, which, under certain conditions and at specific crystal faces, may not necessarily result in electron exchange with the bonding orbitals of pyrite itself. Instead, this mechanism provides an oxygen reduction pathway that can oxidise other less noble minerals and solution species, *e.g.*, iron(II). The rate expressions derived for pyrite oxidation (Ch. 6, Sect. 6.3.2) lead to a qualitative expression of the currently perceived heterogeneous iron(II) oxidation mechanism, assuming that the heterogeneous reaction pathway is insensitive to the hydrogen ion concentration under typical MT autoclave acidities.

$$R_{FeII,\text{het}} = R_{FeII,\text{hom}} + \theta_{Py_c} a_{Py} k_C [\text{Fe II}][O_2]^n \qquad 4.28$$

where catalytic pyrite (Py_c) is represented as a fraction (θ) of the total available pyrite surface area (a_{Py}) at any point in time.

4.5.5 Model validation (experimental results)

Different intrinsic reaction pathways may become dominant in specific solution environments, creating apparent ‘anomalies’. Subtle effects are also imposed by the solution speciation changes and interfacial mass transfer limitations, especially in catalytic systems where the intrinsic

Stellenbosch University http://scholar.sun.ac.za

oxidation rate is fast. The experimental programme aimed to simplify and validate the phenomenological oxidation rate model, which is primarily based on the information and insights gained from the open literature.

The following summary highlights the most important outcomes of the experimental programme:

- Due to the various quality control measures, the residual iron(II) titration errors appear to encapsulate the overall experimental errors. This is especially true when omitting the 'time zero' samples from the regression analyses, *i.e.*, more accurate rate constants are obtained after the temperature has stabilised (> 0 min). Since none of the background salts introduced more than 0.2 mg/L Cu under the most extreme concentration ranges used, soluble copper impurity is assumed to have an insignificantly influence on the observed rate constants. The test repeatability is good and the rate constants of the repeat tests mostly agree with the original set within the average range of chemical analysis errors. Furthermore, since the initial iron(II) concentration is limited to 5 g/L Fe, less 'interference' is likely due to interfacial mass transfer limitations
- Before validating the general functional form of the oxidation rate expression, the limiting role of the interfacial oxygen mass transfer rate was assessed. Tests conducted under varying k_La-values (solution level *vs.* impeller positions) confirmed that copper significantly accelerates the overall oxidation rate, requiring the simultaneous consideration of the interfacial oxygen mass transfer rate. In contrast, the uncatalysed reaction is slow enough under typical MT autoclave conditions to allow direct interpretation of the observed oxidation rate. Under such conditions, the observed oxidation rate shows a first-order dependence on the dissolved oxygen concentration
- Despite overwhelming proof of a second-order rate dependency on the iron(II) concentration, 'reaction order' deviations are observed after an initial oxidation period. Although the second-order dependency is maintained to relatively higher reaction extents under high and constant interfacial mass transfer rates, the downward deviations are still prevalent. Due to the rapidly decreasing oxygen consumption rate accompanying the iron(II) concentration drop, this deviation is not related to oxygen mass transfer limitations. Instead, it may be ascribed to an intrinsic speciation phenomenon. The most obvious consideration is the build-up of iron(III) sulfate species as the oxidation reaction proceeds, resulting in the complexation of free sulfate. This may reduce the relative prevalence of the iron(II) sulfate CIPs and, subsequently, reduce the overall oxidation rate. On the other hand, the introduction of iron(III), as a sulfate salt, actually increases the rate slightly. This is likely due to a lowering of the free acidity levels *via* formation of the $FeH(SO_4)_2^\circ$ species (Sect. 2.4.3). Most importantly, insignificant changes in the second-order deviation are

Stellenbosch University http://scholar.sun.ac.za

observed with this additional iron(III) sulfate salt. These deviations are therefore not directly related to the build-up of iron(III), but are likely due to the implicit changes in the prevalence of the iron(II) sulfate CIPs. These insights emphasise the importance of evaluating the reaction rate constants in terms of the evolving electrolyte species and dissolved oxygen concentration over time. Notwithstanding, it is recommended that future studies also investigate the effects of adding iron(III) salt of a non-complexing anion, *e.g.*, as iron(III) perchlorate

- The oxidation rate increases when utilising lower initial acid concentrations, which is consistent with the literature. Reaction orders of -0.75 and -0.35 are observed with respect to the average total and unassociated hydrogen ion concentrations ('at temperature'), respectively, as obtained by the solution chemistry model (Ch. 2). These orders are in relatively close agreement with the findings of other researchers, some of whom also noted a deviation from second-order kinetics at higher oxidation reaction extents. Changes in the metal(II) sulfate CIP concentrations are most profound at relatively low acid concentrations (Figure 2.23), which is qualitatively in line with the experimental observations of this study, *i.e.*, that the highest deviations from second-order kinetics occur at the lowest acid concentrations and in a negative direction. This sensitivity of the oxidation rate to the speciation changes is compounded by an ever increasing concentration of the iron(III) species. The $FeH(SO_4)_2^\circ$ species, as the primary iron(III) sulfate CIP, removes two sulfate ions for every hydrogen ion, resulting in an increasing Fe^{2+} to Fe(II) concentration ratio (over time), especially in lower sulfate solution environments. The simulation accounts for these effects at each time step, instead of relying on average solution tenors and an apparent fractional reaction order
- The next series of tests focussed on obtaining the reaction orders at higher sulfate background conditions without any copper in solution. The uncatalysed reaction pathway maintains its linear dependence on the dissolved oxygen concentration under these comparatively high total sulfate concentration levels, while showing a substantial acceleration of the second-order oxidation rate. A 0.4 mol/kg $ZnSO_4$ background solution increases the rate constant more than 2.5-fold at 130°C, which is comparable to the reported literature values. These trends are consistent with the increasing prevalence of the iron(II) sulfate CIPs (compared to ferrous ions) at higher total sulfate concentrations. The second-order dependence also extends to lower terminal iron(II) concentrations compared to the tests conducted without any zinc sulfate, which supports the notion that these deviations are related to the above-mentioned speciation changes.
- The uncatalysed oxidation reaction exhibits Arrhenius-like behaviour over the 105 to 180°C range, yielding an overall observed activation energy of about 54 kJ/mol in lower

Stellenbosch University http://scholar.sun.ac.za

sulfate environment (no additional metal(II) sulfate salts added). This activation energy decreases by about 5 kJ/mol with the addition of a relatively small amount of sulfate (15 g/L Zn equiv.), which is consistent with the proposal that the iron(II) sulfate CIPs are more easily oxidised, *i.e.*, they are associated with lower activation energy barriers compared to the unassociated ferrous ions. This also suggests that the SI and SD reaction pathways should be assigned their own unique activation energies, rather than using an overall activation energy approach. Nevertheless, these apparent activation energies are close to the average of typical values reported in the literature (35-75 kJ/mol). A final observation is that the deviation from second-order kinetics appears more substantial at low temperature (105°C), even in the presence of 15 g/L Zn, compared to the kinetics at higher temperature (150°C) and low sulfate concentration. This suggests that the oxidation pathways involving unassociated ferrous ions are strongly activated, which is in line with the above discussions

- Tests conducted in the presence of 15 g/L Cu increased the oxidation rate four- to five-fold compared to a background sulfate solution consisting of 15 g/L Zn, even though the copper system renders less iron(II) sulfate CIPs by virtue of its comparatively stronger complexation tendency with sulfate ion (copper(II) is a softer transition metal than zinc; Sect. 2.3.2 & 2.4.2). This provides clear evidence that the role of copper is catalytic and not merely related to solution speciation changes, as is the case for the other metal(II) sulfate salts, *e.g.*, zinc sulfate. The relatively low apparent activation energy value of 32 kJ/mol, compared to the copper-free sulfate system (49-54 kJ/mol), is also consistent with a catalysed reaction pathway. However, special consideration needs to be given to the initial interfacial mass transfer limitations in the copper system: these restrictions become even more prevalent at higher iron(II) concentrations, especially when the solution level drops below the top impeller, *e.g.*, due to sampling (Ch. 3)
- Based on the rate constants obtained at different oxygen partial pressures and high reaction extents (no interfacial mass transfer limitations), a first-order dependence of the oxidation rate on the saturated oxygen concentration in the copper system is validated. The fundamental form of the uncatalysed oxidation rate expression is therefore maintained in the copper sulfate system, and
- The catalytic efficiency of copper decreases in half-'order' fashion, which is line with another relevant study in the literature. More importantly, this catalytic efficiency is mimicked, to some extent, by the relative abundance of the metal(II)-sulfate CIPs, *i.e.*, according to the solution chemistry model in the 10 to 30 g/L H_2SO_4 range (Sect. 2.4.3). This supports the proposal in Section 4.2.3 (Figure 4.2) that the copper(II) sulfate CIPs are effective in catalysing the oxidation of unassociated ferrous ions, as well as themselves

Stellenbosch University http://scholar.sun.ac.za

acting in first-order fashion. This approach is also consistent with the diminished copper activity in low complexation media, *e.g.*, in perchlorate solutions, and at atmospheric temperatures (literature), while explaining why the second-order dependence of the oxidation rate is maintained down to lower terminal iron(II) concentration levels in copper sulfate solutions compared to the equivalent zinc sulfate background. These insights provide the mathematical methodology to simulate the iron(II) oxidation rate in copper sulfate solutions, without changing the fundamental form of the rate expression (Eq. 4.29).

4.5.6 Model verification and quantification (regression analyses)

The importance of the oxygen mass transfer rate in the copper system is highlighted above, *i.e.*, to account for the interfacial mass transfer limitations during the regression. However, the impact of the oxidation reaction itself on the oxygen absorption process first needed to be assessed. The highest intrinsic reaction rates, based on the rate constants at low terminal iron(II) concentrations (no mass transfer limitations), reveal that the Hatta (Ha) number is less than 0.3, confirming that the oxidation reaction falls in the slow regime, *i.e.*, insignificant iron(II) oxidation occurs in the interfacial layer. This justifies the methodology of simultaneously considering the intrinsic oxidation and interfacial mass transfer rate expressions in a conventional manner.

The experimental results summarised in the previous section allow the general form of the rate expression to be greatly simplified, thereby preventing over-parameterisation of the model. Nevertheless, all possible permutations were evaluated, including an explicit hydrogen ion concentration term for each of the reaction pathways. Fourteen tests were used to minimise the objective function for the uncatalysed reaction pathway at 130°C, while six tests were used to determine the corresponding activation energies. Another six tests were used to determine the rate constant and activation energy of the copper-catalysed reaction pathway. The best regressions were obtained without any explicit hydrogen ion concentration terms. The overall oxidation rate is therefore insensitive to the hydronium ion concentration, other than as accounted for by the solution chemistry model (Ch. 2).

These regressions were repeated by replacing the total iron(II) sulfate CIP concentration with the first bidentate ion pair concentration, $[FeSO_4^o]$, which causes some minor but inconclusive changes (less than experimental error) in the *AARD* values. This is thought to be due the relatively low sulfate concentration used, *i.e.*, the bidentate triple anion concentration, $[Fe(SO_4)_2^{2-}]$, is relatively low under these conditions (Sect. 2.4.2) and there is no reason to suspect that either of the two iron(II) sulfate CIPs is chemically more reactive than the other. However, in terms of the copper-catalysed reaction pathway, marginally better results were obtained when only using the neutral copper(II) sulfate species concentration, $[CuSO_4^o]$, *i.e.*, in combination with a second-order

Stellenbosch University http://scholar.sun.ac.za

dependence on the ferrous ion concentration, [Fe^{2+}] (discussed above). The optimal oxidation rate expression in homogeneous acidic copper sulfate solutions, with the minimum number of adjustable parameters and on overall *AARD* value of about 6%, is as follows:

$$R_{FeII,\text{hom}} = \frac{d[\text{Fe II}]}{dt} = (k_{CIP}[FeSO_4^o + Fe(SO_4)_2^{2-}]^2 + k_{CIP/F}[FeSO_4^o + Fe(SO_4)_2^{2-}][Fe^{2+}] + k_{F/Cu}[Fe^{2+}]^2[CuSO_4^o]) \cdot [O_2] \quad 4.29$$

The final regression results (Table 4.3 & Table 4.6) are also consistent with chemical reaction theory, which implies that the less favourable reaction pathway should exhibit comparatively higher activation energy. The final regression analysis yielded optimised activation energies of 38, 61 and 34 kJ/mol for each of these three rate terms, respectively. This homogeneous rate equation also represents a first estimate of the bulk iron(II) oxidation rate in heterogeneous systems (Ch. 5, 7 & 8). If required, this equation could be expanded to include the enhancement effects of catalytic surfaces, *e.g.*, pyrite (Eq. 4.28). In this study, such an expansion was not justified due to the uncertainties associated with the pyrite oxidation mechanism (Ch. 7 & 8) and the increase in the number of adjustable parameters. It is therefore recommended that future studies also focus on the oxidation of iron(II) in heterogeneous systems, using relative pure pyrite concentrate samples.

Whereas the interfacial oxygen mass transfer rate has an insignificant impact on the kinetics of the uncatalysed oxidation reaction in the 2-litre autoclave, provided the initial iron(II) concentration is lower than about 5 g/L Fe(II), considerable mass transfer limitations are initially present in copper system, especially with only a single (bottom) impeller functional. With knowledge of the k_La-values under the different operating conditions, the above rate expression gives a reasonable representation of the experimental results not used in the regression. For example, the reduction in the free acid concentration (Rx. 2.78), as well as the associated changes in the metal(II) sulfate CIPs, adequately account for the presence of iron(III) sulfate salt in the solution background.

Since the activation energy of the iron(II) oxidation reaction is higher than the interfacial diffusion of diatomic oxygen, insignificant mass transfer limitations are prevalent at 105ºC, even in the presence of copper. However, deviations from the second-order rate dependence occur at higher iron(II) concentrations at these temperatures, compared to the MT autoclave conditions. Six confirmatory tests were therefore conducted at 90°C under atmospheric pressure in the 7-litre glass reactor, characterised by high and relatively constant (with sampling) interfacial mass transfer rate. The most striking aspect of these results is the substantial deviation in second-order kinetics at relatively low oxidation extents (~25%). The initial rate is significantly (~40%) faster in the case of magnesium compared to the zinc sulfate background, while the final rate (> 60 min) is very similar (~0.03 kg/mol.min). The latter observation is in line with the main assumption of the solution

Stellenbosch University http://scholar.sun.ac.za

chemistry model (Ch. 2), *i.e.*, the surrogate metal(II) salt approach. The model generally only represents the oxidation rate well after the initial period (~25% oxidation), suggesting that other effects, whether kinetic or speciation related, come into play at lower temperatures and the simulation becomes less accurate. This model makes use of a limited number of adjustable parameters and it would be unrealistic to expect an accurate extrapolation outside the regressed parameter space, at least without a more elaborative description of the solution speciation. It is therefore recommended that more data be generated in future work to improve the solution thermodynamic model (Ch. 2), especially in more complicated metal sulfate salt mixtures over a relatively wide acid concentration range.

4.5.7 Achieving the overall modelling objective

In conclusion, interesting insights are gained from this kinetic study, while various mechanistic proposals are tabled from a phenomenological reaction rate perspective. In context of simulating the overall copper sulfide mineral leaching system, the model developed in this chapter gives an acceptable estimate of the iron(II) oxidation rate under typical medium MT autoclave conditions.

It should however be realised that the iron(II) oxidation mechanism is deeply imbedded within the electronic structures at the reaction transition states and more insight into the observed phenomena will only be gained by comprehensive quantum-level modelling and detailed experimentation, which were outside the scope of this study.

Stellenbosch University http://scholar.sun.ac.za

CHAPTER 5. IRON(III) PRECIPITATION

5.1 Introduction

The objective of this chapter is to describe the rate of iron(III) precipitation and the relative amounts of hematite compared to hydronium jarosite precipitation during batch and continuous chalcopyrite oxidation under typical medium temperature (MT) autoclave conditions (130 to 155ºC). Published information has not yet revealed sufficient mechanistic insights about this sparingly soluble salt system under these conditions. The rate expressions in this chapter are based in part on current literature information, supplemented by qualitative experimental observation at low pulp density conditions, in particular the backscattered electron (BSE) images and particle size distributions (PSDs) of the precipitates. A summary of this work and insights from the literature are presented first, after which the behaviour of iron(III) in high pulp density leaching systems (Ch. 7 & 8) is used to derive a phenomenological expression of the effect of existing iron(III) precipitate surface area on the precipitation rate. The overall regression encapsulates all the experimental results, *i.e.*, those obtained in both batch and continuous autoclave configurations.

The development roadmap of this phenomenological model is as follows:

- Review of the literature to identify the most important factors that may impact on the rate of iron(III) precipitation, to derive the thermodynamic (supersaturation) framework and also to obtain the general functional forms of the precipitation rate expressions (Sect. 5.2)
- Experimentation at low pulp densities, complimented by BSE images, qualitative energy dispersive X-ray (EDX) spot analyses and PSDs, to reveal the most apparent precipitation mechanisms and validate the general modelling methodology (Sect. 5.3 & 5.4.1)
- Quantifying the thermodynamic description of iron(III) supersaturation with respect to the primary precipitates, *i.e.*, hematite and hydronium jarosite (Sect. 5.4.2)
- Deriving a phenomenological model of iron(III) precipitation to mathematically describe these mechanisms as a function of the bulk solution composition (Sect. 5.4.3), and
- Expanding, verifying and quantifying (regressing) the phenomenological model in order to simulate the iron(III) precipitation rate and the relative abundance of the primary phases at low and high pulp densities in batch and continuous reactor configurations (Sect. 5.4.4).

5.2 Review and theory

This section gives a detailed account of the background theory used to develop the phenomenological precipitation rate model, but not necessarily to address all the fundamental questions. The following subsections present the theoretical building blocks, as well as the various assumptions made to construct the phenomenological model.

Stellenbosch University http://scholar.sun.ac.za

5.2.1 Background (thermodynamics and kinetics)

The nature of iron(III) hydrolysis and precipitation is complex and still poorly understood. Firstly, like any crystallisation process, both thermodynamic and kinetic aspects are important, *i.e.*, the thermodynamics determine the solution speciation and saturation concentration, while the precipitation rate depends on the driving force, *e.g.*, supersaturation, surface type and area. The relative thermodynamic stabilities of hematite and other phases in the Fe(III)-S-O-metal(II) system at higher temperatures have been studied by various investigators (*e.g.*, Liu *et al*., 2003; McAndrew *et al*., 1975; Posnjak & Merwin, 1922; Reid & Papangelakis, 2006; Sasaki *et al*., 1993; Tozawa & Sasaki, 1986; Umetsu *et al*., 1977; Walter-Lévy & Quéméneur, 1964). Figure 5.1 illustrates that the two most important factors determining iron(III) precipitation are temperature and hydrogen ion concentration. One of the complexities associated with iron precipitation is its tendency to generate acid, *i.e.*, the hydrolysis process itself affects the intrinsic acidity of the particle environment. This is illustrated in the study of Vračar and Cerović (1997); oxidation of high iron(II) concentrations released substantial amounts of acid during hydrolysis, which, in turn, significantly raised the iron(III) equilibrium level. A lower degree of supersaturation slowed the iron(III) precipitation kinetics, while the solid-phase composition was greatly affected by the free acid and iron(III) sulfate concentrations.

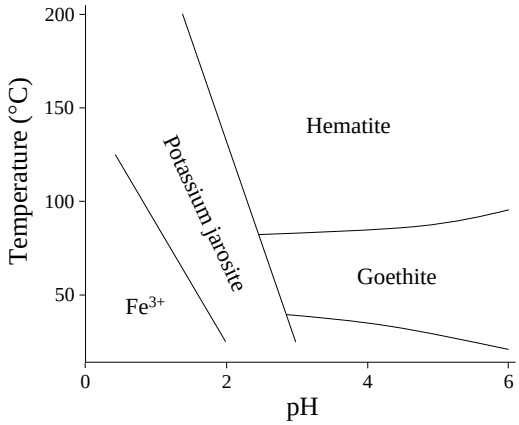

Figure 5.1
Schematic representation of the major stability areas in the Fe(III)-S-O system, starting with 0.5 mol/L $Fe_2(SO_4)_3$ solution between 20 & 200°C (after Babcan, 1971; adapted from Miller, 1986).

In general, higher temperatures favour phases with fewer waters of hydration, while increased saturation levels (at higher acidities) incorporate more sulfates into the crystal structure (see Figure 5.2). The most common iron phases encountered in pressure oxidation systems are goethite (FeO(OH)), hematite (Fe_2O_3), jarosites (general formula $XFe_3(SO_4)_2(OH)_6$, where X may be K^+, Na^+, NH_4^+, Ag^+, H_3O^+, *etc.*; see Dutrizac & Jambor, 2000), and basic ferric sulfate (BFS) ($Fe(OH)SO_4$). Various factors determine the precipitation rate and precipitate composition in hydrometallurgical processes (Cheng & Demopoulos, 1997; Dutrizac, 1980). From a

Stellenbosch University http://scholar.sun.ac.za

thermodynamic perspective, jarosites are more stable at lower pH, while goethite is favoured at higher pH and lower temperature (Figure 5.1). Higher temperature favours hematite formation, while BFS only forms under more severe acidity (< pH 0) and temperature (> 170ºC) conditions. Tozawa and Sasaki (1986) have shown that the addition of metal sulfates, *e.g.*, copper or zinc sulfate, may extend hematite stability to higher acid levels by reducing the free hydrogen ion concentration, *i.e.*, the solution thermodynamics underpin the stability of the precipitated phase. Hematite is the preferred phase, both from environmental (relatively inert towards weathering) and economical viewpoints, *e.g.*, low metal losses (Dutrizac & Jambor, 2000), faster liquid/solid separation (Lahtinen *et al.*, 2006), higher wash efficiencies, lower tailings neutralisation requirements and smaller residue storage ponds.

Metastability

Since only small amounts of potassium and sodium are usually present in copper sulfide concentrates, hematite formation would be expected to dominate under MT autoclave conditions. However, stability diagrams only refer to thermodynamic time frames and neglect the metastability of phases such as hydronium jarosite, $(H_3O)Fe_3(OH)_6(SO_4)_2$. High supersaturation is most likely to produce metastable phases (Cheng & Demopoulos, 1997), which would then convert to the thermodynamically preferred phase over time. However, in particular bulk solution environments at high acidity, hydroxy-sulfate salts may actually become thermodynamically stable. This is illustrated in Figure 5.2, based on the thermodynamic data of Posnjak and Merwin (1922) and assuming that their $3Fe_2O_3.4SO_3.9H_2O$ phase is the ideal hydronium jarosite end member. The transition between hematite and hydroxy-sulfate phases is clearly affected by temperature.

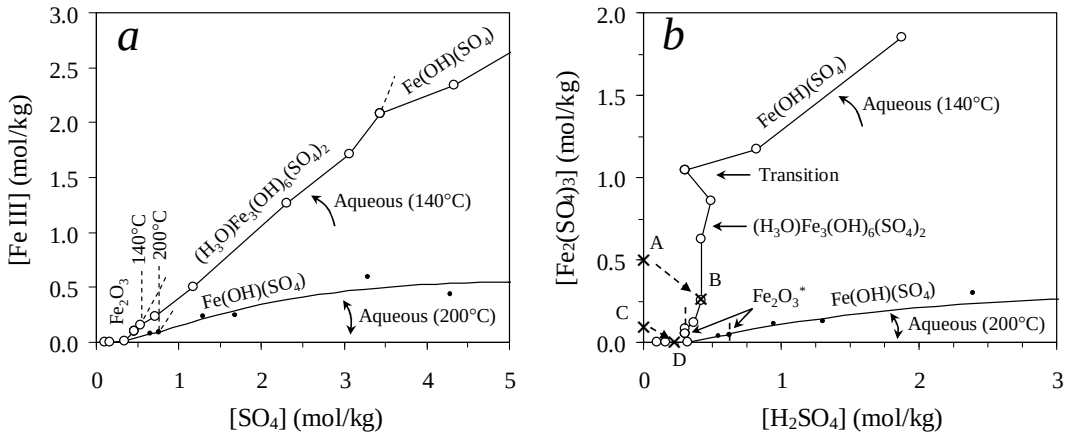

Figure 5.2
Isotherms at 140 & 200°C for the Fe(III)-S-O system from the data of Posnjak & Merwin (1922): *a*) Isotherms plotted over varying sulfate concentration; *b*) Isotherms plotted over varying acid concentration ($Fe_2O_3^*$ represents the transition from hematite to the hydroxy-sulfate phases).

Stellenbosch University http://scholar.sun.ac.za

Figure 5.2 *b* illustrates that, contrary to the hematite and BFS phases, the stability region of hydronium jarosite is not that well defined. An example of a system where hydronium jarosite may be the thermodynamically stable product is represented by line A-B, *i.e.*, 0.5 mol/kg $Fe_2(SO_4)_3$ injected into water at 140°C; around 0.25 mol/kg $Fe_2(SO_4)_3$ should precipitate, producing close to 0.4 mol/kg H_2SO_4. A more realistic example of the behaviour of iron in a leaching system, where rapid dissolution occurs, may be represented by line C-D, *i.e.*, injecting ~0.15 mol/kg Fe(III) into water; although hematite would be the thermodynamically stable product, the ultimate end-point (D) (after extended reaction time) may lie very close to the phase boundary, and significant metastable hydronium jarosite would be expected to form initially, with slow conversion to hematite. It may be expected that the further the ultimate end-point is positioned from the phase boundary, the faster the conversion of the metastable to the thermodynamically stable phase.

According to Figure 5.2 *b*, the transition point between hematite and stable hydronium jarosite lies around 0.3 mol/kg H_2SO_4 and 0.1 mol/kg Fe(III) at 140ºC, which is only marginally different from the conditions experienced in a typical MT autoclave (Ch. 7). The conversion of metastable hydronium jarosite to stable hematite would therefore be slow in a MT autoclave and the jarosite phase could, for all practical purposes, be considered stable (while in the autoclave). This is particularly relevant to MT chalcopyrite oxidation since this mineral typically requires acid concentrations higher than 0.15 to 0.2 mol/kg H_2SO_4 in order to oxidise at acceptable rates (Ch. 4), while the system is self-compensating in that more hydronium jarosite is produced at higher acidities (Ch. 7 & 8). In contrast, the corresponding solution composition at 200°C would heavily favour hematite formation. This highlights the drawback of operating under MT autoclave conditions.

5.2.2 Precipitation chemistry

Overall reaction stoichiometry

Besides the (undesirable) process factors associated with hydronium jarosite formation, mentioned above, there is the possibility of metal cation substitution, *e.g.*, copper and zinc losses due to their incorporation into the crystal structure (Dutrizac & Jambor, 2000). However, substitution of these metals is known to only occur in lead jarosite, with minor quantities in alkali jarosites (< 3% Cu and Zn). Cation substitution is therefore also assumed to play an insignificant role in the leaching system encountered in this study and hydronium jarosite, similar to hematite, is considered to be present as a pure phase. However, it should be noted that the existence of the hydronium species in jarosite is somewhat controversial, as it cannot be measured directly (see Dutrizac & Jambor, 2000). Stoffregen *et al.* (2000) highlighted that all jarosite minerals have a stoichiometric deficiency on the trivalent metal site and also non-stoichiometry on the monovalent ion site.

Stellenbosch University http://scholar.sun.ac.za

Majzlan *et al.* (2004) suggested that the hydronium jarosite phase may be represented by the following general formula: $(H_3O)_{1.00-x}Fe_{2.91}(SO_4)_2[(OH)_{5.73-x}(H_2O)_{2x}]$. They synthesised hydronium jarosite by the hydrothermal treatment of iron(III) sulfate solution and determined the value of x to be 0.09 from single-crystal X-ray powder diffraction (XRD) and other data. Notwithstanding, the exact structural formula of hydronium jarosite is of less importance to this study, as long as its thermodynamic properties are consistent with the selected end-member composition. For the sake of simplicity, the nominal compositions and corresponding published thermodynamic data of hematite, α-Fe_2O_3 (Liu *et al.*, 2003), and hydronium jarosite, $(H_3O)Fe_3(OH)_6(SO_4)_2$ (Majzlan *et al.*, 2004), are assumed. Iron(III) precipitation under typical MT autoclave conditions is therefore represented by the overall reaction stoichiometries of these two major phases:

$$Fe_2(SO_4)_{3(aq)} + 3H_2O_{(aq)} \Leftrightarrow Fe_2O_{3(s)} + 3H_2SO_{4(aq)} \qquad 5.1$$

$$3Fe_2(SO_4)_{3(aq)} + 14H_2O_{(aq)} \Leftrightarrow 2(H_3O)Fe_3(OH)_6(SO_4)_{2(s)} + 5H_2SO_{4(aq)} \qquad 5.2$$

The extents and relative rates of these two reactions are the most important aspects to be captured by the phenomenological model.

Iron(III) complexation

In general, precipitation reaction kinetics depend on various factors, which are difficult to capture in a simplistic mathematical description. In particular, the complicated (solution) reactions leading to nucleation demand a number of simplifications. Dutrizac (1980) discussed some aspects of the pathways that lead to iron(III) precipitation, *i.e.*, the hydrolysis reactions, followed by dimerisation and subsequent polymerisation of the iron hydroxyl (OH) groups and then the precipitation step. Dutrizac argued that it can be assumed that the compound precipitated by hydrolysis is closely related to the aqueous iron(III) complexes present in the bulk solution at that point in time.

Section 2.4.3 has highlighted the complexities and general lack of information regarding iron(III) complex formation in acidic sulfate solutions, especially at higher temperatures. Based on a limited number of investigations at higher temperatures, iron(III) appears to form predominantly neutral or negatively charged polyatomic complexes, with very low free ferric ion (Fe^{3+}) concentrations. This is because the formation of contact ion pairs (CIPs) would be most effective in reducing the free energy of the system, especially when the highly charged ferric ion is solvated in a medium of lower permittivity, *i.e.*, the hot supersaturated solution. The assumption is made (see Sect. 2.4.3) that the polyatomic neutral molecule, $FeH(SO_4)_2^\circ$, predominates under MT autoclave conditions in acidic and sulfate-excess solutions, which is in line with recent proposals from the literature (Casas *et al.*, 2005a). However, the presence of iron(III) hydroxide species, *e.g.*, $Fe(OH)^{2+}$, $Fe(OH)_2^+$, $Fe(OH)_3^\circ$ and $Fe_2(OH)_2^{4+}$ or hydroxy-sulfate species, *e.g.*, $Fe(OH)_2SO_4^-$, may become

Stellenbosch University http://scholar.sun.ac.za

progressively more important at higher temperatures and lower acid concentrations (Liu *et al.*, 2003; McAndrew *et al.*, 1975; Papangelakis *et al.*, 1994). The total contribution of these iron(III) hydroxide species would be small compared to the iron(III) sulfate species in acidic sulfate solutions: their relative abundance would therefore not be expected to impact strongly on the other rate processes, such as mineral oxidation. Their relative abundance is, however, important when attempting to describe the relative precipitation rates of hematite and hydronium jarosite (degrees of freedom of the system) and needs, therefore, to be considered in the phenomenological model.

The thermodynamic properties of some of these species have been regressed in order to correctly predict hematite solubility behaviour at high temperatures (*e.g.*, Liu *et al.*, 2003). In principle, any number of these species may be included in a process model, while selecting a reference species (usually the ferric ion; Papangelakis *et al.*, 1994; Papangelakis & Demopoulos, 1990) as the basis to represent the solubility behaviour of the precipitate. For the sake of simplicity, the two neutral complex species $Fe(OH)_3^\circ$ and $FeH(SO_4)_2^\circ$ are selected to act as surrogate species for the different iron(III) hydroxide and sulfate species, respectively.

Polymerisation reaction pathways

In order to develop a deeper understanding of iron(III) precipitation under MT autoclave conditions, the various reaction steps leading up to nucleation are briefly discussed. Assuming $FeH(SO_4)_2^\circ$ to be the major iron(III) species at these temperatures, the first hydrolysis step may be represented by the following reaction, driven by the strong electron affinity of the highly charged Fe^{3+} ion towards oxygen electrons in the hydration shell surrounding the complex:

$$FeH(SO_4)_2^o + H_2O \Leftrightarrow Fe(OH)^{2+} + 2H^+ + 2SO_4^{2-} \qquad 5.3$$

This reaction reflects the fact that the low molecular weight species tend to form first. Two of these monomeric species in close vicinity may then form dimerised polynuclear species, according to the following reaction (Cornell & Schwertmann, 2003):

$$2Fe(OH)^{2+} \Leftrightarrow Fe_2(OH)_2^{4+} \qquad 5.4$$

This dimer may then react with monomer or other dimeric species to form longer polymer structures. In general, the following reaction describes the elongation of the polymeric structure *via* hydroxyl cross-linking of iron atoms:

$$Fe_2(OH)_2^{4+} + nFe^{3+} + nH_2O \Leftrightarrow Fe_{(n+2)}(OH)_{(n+2)}^{(2n+4)+} + nH^+ \qquad 5.5$$

Although these reactions are presented as reversible, Cornell and Schwertmann (2003) indicated that acid dissociation of polymers may become progressively slower as they grow larger. Dutrizac (1980) suggested, citing references from the literature, that these polymers may include significant

Stellenbosch University http://scholar.sun.ac.za

amounts of anions. Sylva (1972) suggested that precipitation occurs most readily *via* lower molecular weight species and that polymerisation and precipitation may be competing processes. Matijevic *et al.* (1975) emphasised the role that complex iron(III) sulfate species, *e.g.*, $FeSO_4^+$, may play in promoting BFS formation, while suppressing the polymerisation process and the formation of oxides and oxyhydroxides. With regard to this study, Reaction 5.3 may be viewed as an equilibrium that involves the crossing of an energy barrier before the complexing sulfate species are shed from the inner sphere. At increasing acidity and sulfate concentration, the reverse reaction may predominate to such an extent that the formation of colloidal hydronium jarosite particles involves the cross-linking of the iron atoms *via* hydroxyl bridges with the $FeH(SO_4)_2^\circ$ species, *i.e.*, according to the following overall reaction stoichiometry:

$$2n\mathrm{Fe(OH)_3^o} \Leftrightarrow n\mathrm{Fe_2(OH)_6^o} \qquad 5.6$$

$$n\mathrm{FeH(SO_4)_2^o} + n\mathrm{Fe_2(OH)_6^o} + n\mathrm{H_2O} \Leftrightarrow n(\mathrm{H_3O})\mathrm{Fe_3(OH)_6(SO_4)_2} \qquad 5.7$$

These reactions do not capture the true structure of the hydronium jarosite precursor phase, which is currently unknown.

At higher temperatures (> 160°C), hydronium jarosite formation starts to diminish, broadening the hematite stability field (Figure 5.2). The driver behind hematite formation appears to be the replacement of hydroxyl bridges by oxygen bridges, *i.e.*, the so-called oxolation reactions (Dutrizac 1980; Sylva, 1972). This oxolation process may occur more readily at higher temperature, *i.e.*, the activation energy barrier may be readily overcome, even in the presence of a relatively high acid concentration. The presence of low molecular weight hydroxide species may be instrumental in providing a lower activation energy path (see Shang & Van Weert, 1993). Cornell and Schwertmann (2003) emphasised that the key factor which governs the formation of the oxide and its crystallinity is the rate at which these species, mainly monomers and dimers, are supplied to the crystal. The slower these species are supplied, the better ordered the resulting phase becomes, *e.g.*, ferrihydrite may be favoured when the rate of supply of growth units is relatively rapid, whereas crystalline goethite or hematite may result from slower supply rates. They also highlighted the directing factors to be acidity (pH), iron(III) concentration and temperature. Again, using the neutrally charged surrogate hydroxide species to represent a number of different reaction routes, the overall reaction stoichiometry of hematite formation may be represented as follows:

$$n\mathrm{Fe_2(OH)_6^o} \Leftrightarrow n\mathrm{Fe_2O_3} + (3n)\mathrm{H_2O} \qquad 5.8$$

Once again, this generalised reaction does not capture the true nature of the metastable precursor structure of hematite, which would only be revealed upon comprehensive experimental measurement and modelling.

Stellenbosch University http://scholar.sun.ac.za

The general statement can be made that hematite formation only predominates when strong enough covalency between the 3*d* orbitals of iron(III) and the 2*p* orbitals of oxygen exists in order to overcome the bonding energy between oxygen and the other atoms in the iron(III) inner sphere, *e.g.*, the hydrogen in a hydronium (H_3O^+) or -$H(SO_4)_2^{3+}$ moiety. Higher hydrogen ion concentrations therefore slow down the hematite precipitation route, relative to alternative pathways, *e.g.*, hydronium jarosite and BFS formation under MT and HT autoclave conditions, respectively. In this study, all solution-phase equilibria are assumed to be established at a rate faster than the hydrolysis and precipitation reactions.

5.2.3 The driving force of precipitation (bulk perspective)

The modelling of iron(III) precipitation is most appropriately described by crystallisation theory (*e.g.*, Cheng & Demopoulos, 1997; Demopoulos, 2009), although some researchers (*e.g.*, Baxter *et al.*, 2004; Crundwell & Bryson, 1992) opted, for obvious reasons, to exclusively use a thermodynamic equilibrium approach. The leach results in Appendix G reveal the preferential formation of a sulfate-containing iron(III) precipitate during the rapid oxidation of fine iron-containing mineral particles compared to the slower-leaching coarser fractions, even at relatively low acid concentrations. This suggests that the degree of supersaturation is an important factor that influences metastability and, hence, the precipitation rate. Oswald's rule of stages (Söhnel & Garside, 1992) also implies that the thermodynamically stable phase will be preceded by that of several metastable precursor phases.

Thermodynamic description

The relative rates of the following two reactions are most important in context of the overall model:

$$Fe_2O_{3(s)} + 3H_2O_{(aq)} \Leftarrow \{Fe_2O_3 \cdot 3H_2O\}_{(s)} \Rightarrow 2Fe(OH)^o_{3(aq)} \qquad 5.9$$

$$(H_3O)Fe_3(OH)_6(SO_4)_{2\,(s)} \Leftarrow \{(H_3O)Fe_3(OH)_6(SO_4)_2\}_{(s)} \Rightarrow FeH(SO_4)^o_{2(aq)} + 2Fe(OH)^o_{3(aq)} + H_2O_{(aq)} \qquad 5.10$$

where the two complex species, $Fe(OH)_3°$ and $FeH(SO_4)_2°$, act as surrogate species for the different iron(III) hydroxide and sulfate species, respectively. This is also in line with the above discussions that precipitation occurs most readily *via* lower molecular weight species. The $\{Fe_2O_3{\cdot}3H_2O\}$ and $\{(H_3O)Fe_3(OH)_6(SO_4)_2\}$ phases represent the metastable precursor hematite and hydronium jarosite phases, respectively. Since the free energies of formation of these phases are unknown, their solubility products (Ch. 2, Sect. 2.2.3) are estimated from their stable analogues, *i.e.*, assuming nominal hematite (*Hem*), α-Fe_2O_3 (Liu *et al.*, 2003), and hydronium jarosite (*Jar*) (Majzlan *et al.*, 2004) compositions, respectively:

Stellenbosch University http://scholar.sun.ac.za

$$K^{o}_{sp,Hem} = exp\frac{-(2\Delta G^{o}_{Fe(OH)^{o}_{3}} - \Delta G^{o}_{Hem} - 3\Delta G^{o}_{w})}{R_g T} = \frac{a^{2}_{Fe(OH)^{o}_{3}}}{a^{3}_{w}} \approx \frac{\{K^{o}_{sp,Hem}\}}{a^{3}_{w}} \quad 5.11$$

$$K^{o}_{sp,Jar} = exp\frac{-(\Delta G^{o}_{FeH(SO4)^{o}_{2}} + 2\Delta G^{o}_{Fe(OH)^{o}_{3}} + \Delta G^{o}_{w} - \Delta G^{o}_{Jar})}{R_g T} = a_{FeH(SO_4)^{o}_{2}} a^{2}_{Fe(OH)^{o}_{3}} a_{w} \quad 5.12$$

$$\approx \{K^{o}_{sp,Jar}\}$$

This simplified treatment therefore makes no distinction between the metastable and stable phase solubilities and implicitly assumes that the conversion of the metastable to the stable phase at some reaction front has an insignificant impact on the bulk precipitation driving force. This thermodynamic driving force of crystallisation (ϕ_c) is simply the chemical potential difference ($\Delta\mu$) of the reaction species, *i.e.*, between the supersaturated and equilibrium states (Söhnel & Garside, 1992). The following representation of the thermodynamic driving force follows directly from the basic definition of the chemical potential and substituting the thermodynamic solubility product:

$$\phi_c = \Delta\mu_i = R_g T \cdot ln\left(\frac{\prod_i a_i^{\nu_i}}{(\prod_i a_i^{\nu_i})^{*}}\right) = R_g T \cdot \nu\, ln\left(\frac{\prod_i a_i^{\nu_i}}{K^{o}_{sp}}\right)^{\frac{1}{\nu}} \quad 5.13$$

The asterisk indicates the activity at thermodynamic equilibrium and ν represents the overall stoichiometric coefficient of the reaction species:

$$\nu = \sum_i \nu_i \quad 5.14$$

The solubility product in Equation 5.13 originates from the unit activity of the solid phase (pure phase). The term in parentheses, also known as the thermodynamic supersaturation ratio, S_a, is an important parameter when describing precipitation kinetics (Söhnel & Garside, 1992):

$$S_a = \left(\frac{\prod_i a_i^{\nu_i}}{K^{o}_{sp}}\right)^{\frac{1}{\nu}} \quad 5.15$$

In this study, this parameter artificially caters for the nucleation and growth of both the initial amorphous phases and the stable phases forming during the later stages of a typical high pulp density leaching process. Furthermore, unity activity coefficients are conveniently assigned to the two iron(III) surrogate species, *i.e.*, the interactions of these neutral inner-sphere complexes with the surrounding solution are assumed weak at higher temperatures, so that the supersaturation ratios of the hematite and hydronium jarosite phases may be expressed as follows, respectively:

Stellenbosch University http://scholar.sun.ac.za

$$S_{Hem}^{2} = \frac{a_{Fe(OH)_3^o}^{2}}{\{K_{sp,Hem}^{o}\}} \approx \frac{1}{K_{sp,Hem}^{o}} \frac{m_{Fe(OH)_3^o}^{2}}{a_w^3} \qquad 5.16$$

$$S_{Jar}^{4} = \frac{a_{FeH(SO_4)_2^o} a_{Fe(OH)_3^o}^{2} a_w}{\{K_{sp,Jar}^{o}\}} \approx \frac{1}{K_{sp,Jar}^{o}} m_{FeH(SO_4)_2^o} m_{Fe(OH)_3^o}^{2} a_w \qquad 5.17$$

These supersaturation ratios are linked by the equilibrium reaction between the two iron(III) surrogate species and imbedded within the Pitzer ion-interaction framework of the background H_2SO_4-M(II)SO_4-H_2O electrolyte (Ch. 2):

$$Fe(OH)_3^o + 2H_2SO_4 \Leftrightarrow FeH(SO_4)_2^o + 3H_2O \qquad 5.18$$

This equilibrium is represented by the following constant, *i.e.*, at the thermodynamic transcendent condition of infinite dilution, again utilising the unit activity coefficient assumption for the two neutral species:

$$K_{FeIII}^{o} = \frac{a_{FeH(SO_4)_2^o} a_w^3}{a_{Fe(OH)_3^o} a_{H_2SO_4}^{2}} = \frac{m_{FeH(SO_4)_2^o}}{m_{Fe(OH)_3^o}} \frac{a_w^3}{a_{H_2SO_4}^{2}} \qquad 5.19$$

The activity of sulfuric acid is related to its mean molality ($m_{\pm}$) and activity coefficient ($\gamma_{\pm}$), as follows (Ch. 2, Sect. 2.2.3):

$$a_{H_2SO_4} = m_{\pm}^{\nu} \gamma_{\pm}^{\nu} = 4 m_{H_2SO_4}^{3} \gamma_{\pm}^{3} \qquad 5.20$$

The use of the formal acid molality in the second equality arises from expressing the stoichiometric mean activity coefficient in an internally consistent manner (Eq. 2.23).

The $Fe(OH)_3°$ species, in particular, assumes extremely low equilibrium molalities when based on published thermodynamic data (*e.g.*, Liu et al., 2003). Simple mass balancing is utilised to obtain the values of the two surrogate species as a function of the total iron(III) molality, *i.e.*, outside the iterative scheme described in Appendix A.3:

$$2 m_{Fe_2(SO_4)_3} = m_{FeH(SO4)_2^o} + m_{Fe(OH)_3^o} \qquad 5.21$$

Equation 5.19 is then utilised to close the degrees of freedom of the system, yielding the following expression to obtain the $Fe(OH)_3°$ species molality:

$$m_{Fe(OH)_3^o} = \frac{2 m_{Fe_2(SO_4)_3}}{1 + K_{FeIII}^{o} \frac{a_{H_2SO_4}^{2}}{a_w^3}} \qquad 5.22$$

Alternatively, the $FeH(SO_4)_2°$ species may be treated in analogous fashion to $Fe(OH)_3°$ (Eq. 5.22).

Stellenbosch University http://scholar.sun.ac.za

Formation of the bulk material

The above internally consistent thermodynamic framework may now be used to describe the free energy change as the solute moves between the liquid and solid states:

$$\Delta\vec{G}^{o}_{V} = R_g T \cdot \nu \, ln S_a \quad \text{or} \quad \Delta\overleftarrow{G}^{o}_{V} = -R_g T \cdot \nu \, ln S_a \qquad 5.23$$

The second term refers to the reverse reaction, *i.e.*, the thermodynamic driving force of precipitation from solution. The symbol ΔG°_{V} (Randolph & Larson, 1988) refers to the free energy change due to the homogeneous creation of a new solid phase, as a bulk substance, but neglects the creation of solids' surface area (discussed below).

5.2.4 The solid/solution interface

Surface structures are less stable than bulk structures and therefore require more energy to be created. This free energy contribution, ΔG°_{A}, is rooted in the physics of a solid surface and its surrounding solution (see Söhnel & Garside, 1992). The material-specific interfacial energy of the surface ($\gamma = \partial G^{\circ}_{A}/\partial a$; J/m^2) accounts for the work required to achieve the formation of unit surface area. This is a collective property, as it depends on crystal morphology, structure and, in particular, particle size. It is most reliable if derived from experimental measurements under well-controlled conditions, but no such values could be found for hematite or hydronium jarosite. However, hematite solubility is lower than jarosite solubility under typical autoclave conditions (Figure 5.29). Based on the generally inverse relationship between the interfacial energy and the logarithm of the solubility (Söhnel & Garside, 1992), a higher interfacial energy would therefore be expected for hematite than for hydronium jarosite. This is also reflected by the high apparent surface enthalpy of hematite in comparison to iron(III) hydroxide and oxyhydroxide surfaces (Diakonov *et al.*, 1994; Marchand & Rancourt, 2009; Navrotsky *et al.*, 2008). Before the important precipitation mechanisms can be explored, the basics of homogeneous precipitation need to be reviewed.

Homogeneous generation of solid surface

The condition for homogeneous nucleation may be represented as follows (expressed per unit mass water), using Equation 5.23 to replace ΔG°_{V} (Randolph & Larson, 1988):

$$\Delta G_{hom} = n\,\Delta\overleftarrow{G}^{o}_{V} + \Delta G^{o}_{A} = -(n R_g T) \cdot \nu \, ln S_a + a \cdot \gamma \qquad 5.24$$

where n and a refer to the total moles and interfacial area of nuclei per unit mass water, respectively. The volume and area free energy terms may also be expressed in terms of the size (L) and number (N) of nuclei (per unit mass water):

$$\frac{\Delta G_{hom}}{N} = \frac{-\Phi_v L^3 \rho_s}{Mw_s} R_g T \cdot \nu \, ln S_a + \Phi_a L^2 \cdot \gamma \qquad 5.25$$

Stellenbosch University http://scholar.sun.ac.za

Assuming that the volume and area shape factors (Φ_v & Φ_a) and solid-state density (ρ_s) are constant and that the system is supersaturated, *i.e.*, $S_a > 1$, Equation 5.25 reveals negative and positive values for the first and second terms, respectively. In order to achieve homogeneous nucleation, the supersaturation ratio needs to exceed unity by some degree, here referred to as the critical supersaturation ratio, $S_{a,crit}$. Nucleation only becomes possible above this critical point, *i.e.*, where the free energy is a maximum, or $\partial\Delta G_{hom}/\partial L = 0$, which then yields:

$$\nu ln S_a > \nu ln S_{a,crit} = \frac{2\Phi_a \gamma M w_s}{3\Phi_v \rho_s R_g T} \cdot \frac{1}{L_{crit}} \qquad 5.26$$

The critical nucleus size, L_{crit}, signifies the minimum size that a nucleus needs to attain in order to become a stable particle entity. This is illustrated in Figure 5.3, using assumed (for illustrative purposes) interfacial energy values of 0.1 and 0.5 J/m^2 for hydronium jarosite and hematite, respectively. It can be seen that a higher supersaturation ratio and a higher interfacial energy both produce smaller critical nuclei sizes in a region of spontaneous homogeneous nucleation.

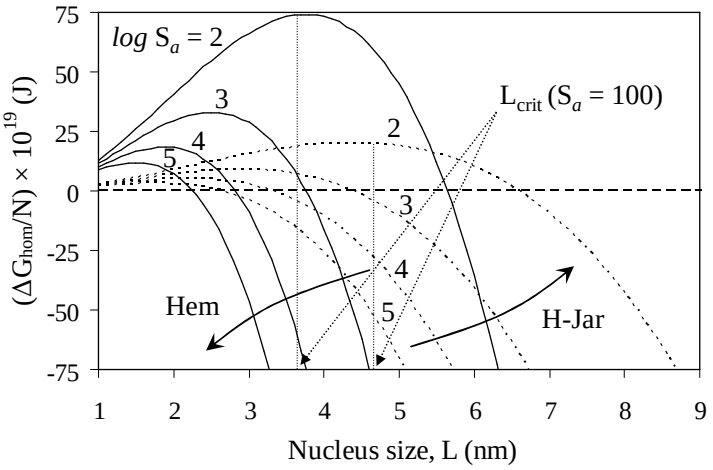

Figure 5.3
Indicative free energy changes accompanying homogeneous nucleation as a function of nuclei size at different supersaturation ratios (at 150°C), using Φ_v & Φ_a factors for a spherical particle, ρ_s = 2700 (Roberts *et al.*, 1990) & 5240 kg/m^3 (Lide, 2004), & γ = 0.5 & 0.1 J/m^2 for hematite (solid lines) & hydronium jarosite (broken lines), respectively.

Considering that hematite is significantly less soluble than hydronium jarosite under typical autoclave conditions (Figure 5.2), hematite precipitation would be expected to dominate in a region of spontaneous nucleation, especially at lower acid concentrations and higher temperatures. Demopoulos (2009) has, however, emphasised the need to treat equilibrium diagrams with caution because they neglect kinetics, besides the fact that many of them have been built on inaccurate experimental procedures. Particle size (discussed next) is particularly important in this regard.

Stellenbosch University http://scholar.sun.ac.za

Effect of particle size on the solubility

The effect of the size (L) on the solubility of a particle is described by the (Ostwald-modified) Gibbs-Thomson (GT) or Kelvin relationship (Söhnel & Garside, 1992):

$$a_L^* = a^* \cdot exp\left(\frac{L_{OD}}{L}\right) \qquad 5.27$$

where a^*_L and a^* refer to the activity of the solute in equilibrium with finite and infinite particle size, respectively. The Ostwald diameter, L_{OD}, is defined as follows:

$$L_{OD} = \frac{2\Phi_a}{3\Phi_v}\frac{\gamma M w_s}{\nu \rho_s R_g T} \qquad 5.28$$

Equation 5.27 may also be used to explain the so-called Ostwald ripening phenomenon (see David & Klein, 2001): at the end of a precipitation process, the solution should approach equilibrium with the bulk material particle size, *i.e.*, the smaller particles would become undersaturated:

$$\frac{a^*_{L<L_c}}{a^*_{L_c}} > 0 \qquad 5.29$$

In effect, the smaller particles would tend to redissolve and supersaturation would then lead to growth onto the larger particles, establishing equilibrium between the solution and the bulk particle mass of characteristic size L_c.

The application of the above equations is only justified for small particle sizes (< 1 µm), as illustrated by David and Klein (2001). For the sake of simplicity, the effect of particle size on the solubilities of the iron(III) precipitates is neglected in this study. However, the GT relationship is of qualitative use after recognising that the thermodynamic supersaturation, S_a, is equivalent to a/a^*:

$$\frac{S_L}{S} = exp\frac{-L_{OD}(\gamma)}{L} \qquad 5.30$$

The supersaturation experienced by a particle of size L, S_L, would therefore be lower than envisaged by the bulk thermodynamic formulations (Sect. 5.2.3). The higher the interfacial energy of the phase, the more rapidly particle growth would tend to dissipate, *i.e.*, as the supersaturation is consumed. The formation of a high number of small hematite particles would therefore be expected in a region of spontaneous nucleation. This is in line with Papangelakis *et al*. (1996), who observed the rapid formation of hematite particles during the acid pressure leaching of limonite ore, without additional growth.

In contrast to hematite, the lower comparative interfacial energies of hydronium jarosite and other metastable phases would tend to form larger surfaces. The already slow conversion (in

Stellenbosch University http://scholar.sun.ac.za

hydrometallurgical terms) of hydronium jarosite to hematite would therefore be decelerated further in the 0.15 to 0.30 mol/kg H_2SO_4 range (Sect. 5.2.1), which justifies the treatment of hydronium jarosite as a stable phase under typical MT autoclave leaching conditions. This assumption is also in agreement with Zerella *et al.* (1983), who found that higher temperatures (>150ºC) and/or significant neutralisation (< 10 g/L H_2SO_4 at 150ºC) are required in order to rapidly convert hydronium jarosite to hematite. These assumptions are experimentally verified later in this study.

5.2.5 Mechanistic considerations

The above discussions have been based on classical crystallisation theory, as precipitation is correctly defined as reactive crystallisation (Demopoulos, 2009). Since it is typically associated with high supersaturation ratios, a multitude of amorphous precursor phases of varying metastability and interlinked precipitation mechanisms may be important. An accurate description of the iron(III) precipitation rate in batch and continuous autoclaves is therefore a daunting task that stretches beyond the scope of this study. The following mechanistic considerations provide the theoretical backdrop required to interpret the experimental results, to justify the simplifying assumptions and to derive the phenomenological precipitation rate model.

The 'grey' area in the current understanding of surface nucleation

The critical supersaturation ratio varies between different nucleation mechanisms and is generally in the order $S_{a,crit,surf} < S_{a,crit,het} < S_{a,crit,hom}$, where the subscripts refer to surface (on same surface), heterogeneous (on foreign surface) and homogeneous (from solution) nucleation mechanisms, respectively (Cheng & Demopoulos, 1997). An increase in supersaturation leads to an increase in the number of nucleation events, whichever mechanism predominates at a specific point in time.

Surface nuclei are especially prevalent at higher supersaturation ratios, where high surface area is available, *e.g.*, in seeded batch and continuous operations, which can lead to polynuclear spike-like, skeletal or dendritic growth (see Mersmann *et al.*, 2001a). Different modes of growth can therefore be identified and the exact means by which particle growth occurs in sparingly soluble systems remains complicated. Furthermore, the previous section has emphasised the mechanistic shift at higher supersaturation ratios towards a regime where more homogeneous nucleation events and less growth (per particle) occur. The same trend is also applicable in the case of surface nucleation. This creates ambiguity between the formal nucleation and growth mechanisms, since surface integration events are not that easily differentiated from secondary nucleation events in the case of sparingly soluble systems. Figure 5.4 presents the full spectrum, emphasising the 'grey' area that becomes apparent at higher supersaturations (diffusion-controlled growth is neglected here, as it is unlikely to prevail in mineral oxidation-precipitation systems characterised by vigorous agitation).

Stellenbosch University http://scholar.sun.ac.za

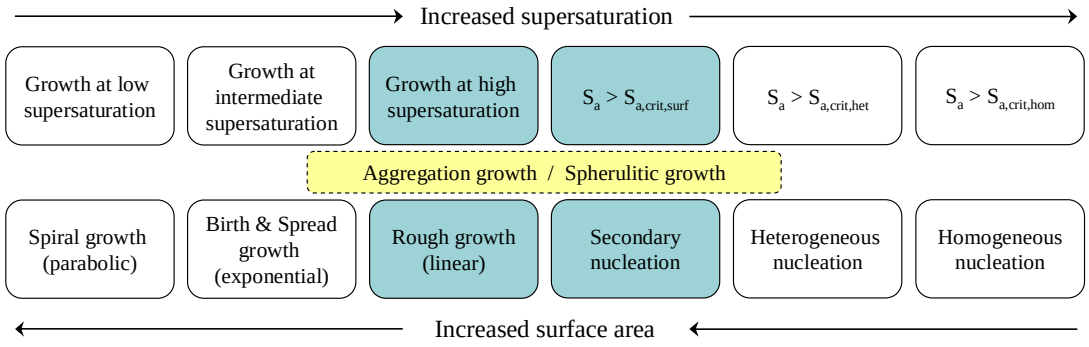

Figure 5.4
Schematic representation of the different precipitation regimes over the supersaturation spectrum (expanded *ref.* Lewis, 2011).

Mono-nuclear (layered) growth is observed at lower supersaturations and results in smooth surfaces (on a molecular level). The growth rate may be controlled by surface integration or nucleation, leading to a parabolic or exponential response to the supersaturation, respectively. Polynuclear (continuous) growth is characterised by rough surfaces and occurs where the rate-limiting step is the integration of a growth unit at the site of the lowest energy for its orientation (Randolph & Larson, 1988). Such a mechanism is commonly observed in industrial precipitation systems (Demopoulos, 2009) and, due to the higher supersaturation and random location of growth sites, the rate would typically be proportional to the supersaturation ratio (Randolph & Larson, 1988). This mode of growth falls in the 'grey' area, barely distinguishable from secondary nucleation on existing crystal surfaces (elaborated upon in Section 5.4.3).

With reference to the above 'grey' area (Figure 5.4), particle aggregation also involves some degree of growth. As pointed out by Demopoulos (2009), small particulates, most prevalent in uncontrolled batch precipitation systems, tend to promote compact aggregate formation. Surface nucleation and molecular growth ($> S_{a,crit,surf}$) is the mechanism by which these particulates are cemented together. On the other hand, Beck and Adreassen (2010) proposed an alternative mechanism to nano-aggregation during the spontaneous precipitation of calcite particles, as aggregation could not explain the differences in the observed subunit size of the spherulites. A spherulitic growth mechanism was proposed as the underlying enlargement mechanism of some polycrystalline particles. Sasaki *et al.* (1999) used such a mechanism to explain how a peanut-shaped hematite particle is formed.

Aggregation

In this study, "aggregate" means a particle comprising of fused particles. "Agglomerate" means a collection of more weakly bound particles or aggregates where the resulting external surface area is similar to the sum of the surface areas of the individual components. In general, aggregation is

Stellenbosch University http://scholar.sun.ac.za

promoted by small particles sizes, high particle concentrations and increased turbulence, while it diminishes above a certain critical size (~50 µm) (Mersmann, 2001; Mersmann & Braun, 2001). When particles collide and the attractive forces prevail long enough, crystalline bridges (due to growth) will form, and the particles will be cemented together. This is especially true at high supersaturations, while the disruptive forces, *e.g.*, the strong shear stresses from vigorous mixing, may result in agglomerate disintegration at lower supersaturations. This is in line with the observations of Shang and Van Weert (1993). They produced looser agglomerates in nitrate solutions at lower operating temperatures (140°C), but they became larger and more compact at higher temperatures (160 & 180°C). However, Mersmann (2001) indicated that the opposite may also occur, *e.g.*, at medium supersaturation, inter-particle cemented aggregates may remain intact under vigorous agitation, but at high supersaturation, nucleation and growth may reduce the supersaturation level so rapidly that only weakly bonded agglomerates are formed.

In this study, the complex task of accounting for these mechanisms is avoided by treating each crystallite as an individual particle, suspended in the slurry and in full contact with the surrounding solution. Although this is a major simplification, it is largely inconsequential since the precipitation rate does not have to be directly related to the observed (experimental) PSD in a phenomenological-type model. In any event, as shown later (Sect. 5.4.1), the surface morphology of most particles is so irregular that a realistic estimation of the particle surface area over varying surface and solution composition would have been difficult.

Literature examples of hematite precipitation

Various observations from the literature regarding hematite precipitation are summarised below. Although the test conditions and context of these studies were different, small hematite particles (<1 µm) were generally produced.

Papangelakis *et al*. (1996) used transmission electron microscopy (TEM) to study hematite particle morphology during acid pressure leaching of limonite ores (> 240ºC). They observed uniform, dense and almost spherical particles, with an average size of 0.1 to 0.25 µm. High temperature pressure leaching of laterite materials (270ºC) (Rubisov & Papangelakis, 1999) also produced nano-sized particles (~0.2 µm), the bulk of which agglomerated into larger units. Rubisov and Papangelakis found the shape of the hematite particles to change from thin flakes at lower acidity to progressively more spherical structures at higher acidity. The transition was shown to occur at the point of zero charge (PZC) of the hematite (~0.16 mol/L H^+, 'at temperature') and was ascribed to the preferential adsorption of specific ions on the surface. Above the PZC, hydroxyl complexes may preferentially adsorb onto a particular face, causing retarded growth and promoting platelet-type particle formation. At higher acidity, sulfate adsorption controls the shape (see next section).

Stellenbosch University http://scholar.sun.ac.za

The more recent study of Ruiz *et al.* (2007b) in the 180 to 220°C range revealed relatively narrow hematite PSDs. Particles produced at 200°C, in the presence of 10 g/L H_2SO_4, were significantly larger (d_{50} 31.4 µm) than particles produced at 1 g/L H_2SO_4 (d_{50} 2.5 µm). Ruiz *et al.* (2007b) attributed the smaller average size at the lower acid concentration to a higher supersaturation, while the rapid formation of these small particles may have inhibited aggregation growth (see previous section). Increased temperature produced lower sulfur contents and smaller particles, while increased acidity produced higher sulfur contents and larger particles. This is in agreement with earlier discussions, in that higher temperature would be expected to yield higher supersaturation (lower hematite solubility), and hence would favour the formation of a high number of small hematite particles over excessive growth. However, the higher sulfur content of the precipitate produced under higher acidity and its apparent impact on the overall particle size was not addressed in that study, which may have involved the formation of metastable hydronium jarosite (Sect. 5.4).

Dutrizac and Chen (2009) found hematite crystallinity to increase with increasing temperature in the 135 to 180°C range. The hematite particles produced in a mixed sulfate-chloride solution at 150°C typically consisted of ~10 µm 'cauliflower-like' agglomerates, with modest porosity. Interestingly, varying amounts of poorly crystalline goethite were also detected when a lower initial acid concentration (< 0.125 mol/kg H_2SO_4) was utilised, but this was suppressed at higher initial acid levels, yielding hematite of typically 60% Fe and 5 to 7% SO_4 (see next section). Since most of this testwork was conducted at ~0.3 mol/kg Cl for 5 hours, in the presence of various sulfate salts (~1.9 mol/kg SO_4^T), the stabilising role of chloride ion on goethite formation should not be underestimated. Importantly, the presence of goethite seed did not suppress sodium jarosite formation nor promote hematite or goethite precipitation. It is also worth noting that a test conducted in the presence of both 15 g/L reagent-grade hematite and 15 g/L sodium jarosite seed, yielded a similar precipitate composition to a test conducted using only 15 g/L jarosite seed. This suggests that jarosite growth dominated hematite growth under the conditions investigated.

The experimental procedure is also of critical importance. Dutrizac and Chen (2009), Riveros and Dutrizac (1997) and Shang and Van Weert (1993) added the reagents together (incl. seed material & acid) before heating the autoclave contents to temperature: this may have complicated their test results. On the other hand, Rubisov and Papangelakis (1999) initiated the leaching of iron from laterite ores by injecting the acid 'at temperature'. Ruiz *et al.* (2007b) heated iron(II) (& acid) solution to temperature before adding oxygen to the autoclave, which is considered an attractive experimental procedure and is also adopted in this study (Sect. 5.3).

Stellenbosch University http://scholar.sun.ac.za

Sulfate adsorption on hematite surfaces

Dutrizac and Chen (2009) suggested that 5 to 7% sulfate occurred as adsorbed species on individual hematite crystallites formed in a mixed sulfate-chloride solution at 150°C. They reached this conclusion as no discrete sulfate phases were detected using XRD analysis. However, since crystalline hydronium jarosite is often preceded by amorphous structures (Sect. 5.4), this sulfate content range is only considered indicative. A sudden increase in sulfate content (> 20% SO_4) below 135°C was, in fact, ascribed to hydronium jarosite formation. On the other hand, electron microscope (SEM) – Energy dispersive X-ray (EDX) analyses of polished cross-sections of these particles revealed uniform distribution of sulfur throughout, suggesting that the sulfate adsorbed on individual crystallites. They argued further that, since sulfate is unlikely to be incorporated in the crystal structure of hematite (based on the XRD diffractogram *d*-values), all sulfate present in the precipitate was associated with hematite as an adsorbed species. Therefore, some baseline sulfur content in hematite appears to stem from the surface adsorption of sulfate species.

The intimate association of sulfate with hematite has also been reported in other investigations (see Table 11.1 in Cornell & Schwertmann, 2003). Various studies have focussed on the bonding aspects of sulfate, suggesting that it is strongly chemisorbed onto the hematite surface (Sugimoto & Wang, 1998; Watanabe *et al.*, 1994), while others (Sugimoto *et al.*, 1998) utilised sulfate ion as an additive to control particle shape. The so-called "gel-sol method" was developed in order to produce hematite particles of uniform size. Chloride medium was utilised and, under the correct conditions, finely dispersed akaganeite (β-FeOOH) formed, after which hematite crystallised *via* a redissolution-crystallisation mechanism (Sugimoto *et al.*, 1998). While pure chloride led to pseudo-cubes, the presence of sulfate promoted ellipsoidal and peanut-shaped crystals, depending on the sulfate levels. Again, EDX and chemical analysis revealed that the sulfate ions were uniformly incorporated into the particles during their growth (Sugimoto & Wang, 1998). The peanut-shaped particles were found to be polycrystals composed of rod-like subcrystals and the uniform distribution of sulfate was consistent with the uniform distribution of these internal surfaces. Lu *et al.* (2006) managed to produce hollow polycrystalline hematite particles from solid spindle-type particles by exploiting the strong adsorption tendency of the sulfate ions. The particle interiors could be dissolved, while the exteriors were protected by the coordinated sulfate ions.

The adsorbed sulfate content of hematite particles is therefore dependent on the total internal surface area of each particulate, which may be variable (*e.g.*, Liu *et al.*, 2007; Sasaki *et al.*, 1999). The ranges suggested by Dutrizac and Chen (2009), Sugimoto and Wang (1998), Umetsu *et al.* (1977) and Zerella *et al.* (1983) average at 2% S^T, which is applied as a fixed constituent of the hematite phase produced in this study.

Stellenbosch University http://scholar.sun.ac.za

Hydronium jarosite growth and its reversible behaviour at lower acidities

Kandori *et al.* (2004) found relatively large cubic or hexagonal BFS particles to form preferentially during the early stages of precipitation after adding relatively high iron(III) concentrations to a mixed sulfate-chloride system at 100°C. This phase then transformed over time, probably *via* a redissolution-precipitation mechanism, to form irregular hydronium jarosite particles. It can be argued that these hydronium jarosite particles may also have been readily transformed to goethite, the thermodynamically preferred phase under their conditions, had the bulk acid concentration been lower. In fact, Kandori *et al.* cited other references from the literature where the addition of lower iron(III) concentrations favoured a single goethite phase, while higher relative iron(III) concentrations accelerated the condensation of hydrolysed iron(III) ions to first form amorphous precipitates which then transformed to hydronium jarosite.

The reversible role of hydronium jarosite has been illustrated in the study of Zerella *et al.* (1983). They confirmed that the conversion of hydronium jarosite (& other jarosites) to hematite can be achieved in a crystalliser, showing increased rate with an increase in temperature and decrease in acid concentration. They assumed that the mechanisms for nucleation, growth and conversion are the same when they occur simultaneously as when they occur individually. They developed a model, assuming that the formation of the initial surface area and subsequent growth was confined to hydronium jarosite, followed by its conversion to hematite at separate sites on the crystal surface. In a previous investigation, one of the authors determined that the conversion of jarosite followed classical shrinking core kinetics, without a change in particle size or shape (see Zerella *et al.*, 1983). The original jarosite particles did, however, become less dense due to the loss of sulfuric acid and water, and the overall conversion reaction may be represented as follows:

$$2(H_3O)Fe_3(OH)_6(SO_4)_{2(s)} \Rightarrow 3Fe_2O_{3(s)} + 4H_2SO_{4(aq)} + 5H_2O_{(aq)} \qquad 5.31$$

They used an intrinsic expression, with the rate proportional to the surface area, multiplied by an acid driving force, to describe this transformation process within a population balance (PB) framework (App. H). The acid driving force was taken as the difference between the equilibrium acid concentration at the hematite/jarosite phase boundary (from Posnjak & Merwin, 1922) and in the bulk solution. The driving force for hydronium jarosite growth was described in terms of the locus of the hydronium jarosite/solution boundary (again, using the data of Posnjak & Merwin, 1922). These terms were correlated empirically, assuming that the residual sulfate (~3% S^T) was present as unconverted hydronium jarosite. It is clear that hydronium jarosite could be considered stable over autoclave timeframes if retained in the mother liquor above threshold acidity levels.

Hydronium jarosite and the metastable precursor phases grow to larger sizes, compared to the thermodynamically stable phase due to their comparatively lower interfacial energies.

Stellenbosch University http://scholar.sun.ac.za

5.2.6 Rate expressions for primary hematite nucleation and hydronium jarosite growth

High supersaturation of hematite would be expected due to its low solubility (Sect. 5.4.2), especially during the initial stages of mineral oxidation, *i.e.*, when the acid consumption and iron dissolution rates are the highest (Ch. 6 to 8). Later on during the leaching process, the acid concentration typically increases again due to the advancing iron(III) precipitation reactions, as well as to the lower elemental sulfur yields of the slower oxidising refractory sulfide minerals, *e.g.*, pyrite and chalcopyrite (Ch. 6 to 8). The growth of hydronium jarosite would therefore be expected to be most dominant during these final stages in the autoclave reactor, and therefore demands a different approach to Zerella *et al.* (1983).

Primary hematite nucleation

Assuming that the overall precipitation mechanism in both batch and continuous autoclaves is primarily driven by nucleation, a large number of hematite particles of relatively small size (typically 0.1-10 µm, according to Söhnel & Garside, 1992) would be formed. In terms of batch operation, it is also assumed that the induction period, *i.e.*, the time required for the critical nucleus to form (David & Klein, 2001; Söhnel & Garside, 1992), is short enough to be neglected.

The activation energy, E_a (kJ/mol), of homogeneous nucleation is obtained after substituting the $\Delta G°_V$ free-energy term (Eq. 5.23) into Equation 5.25:

$$E_a = \frac{N_a \Delta G_{hom}}{N} = \frac{N_a \Phi_v L^3 \rho_{Hem}}{Mw_{Hem}} \cdot \tilde{G}^o_V + N_a \Phi_a L^2 \cdot \gamma_{Hem} \qquad 5.32$$

The following relationship is obtained after substituting L with an expression for L_{crit} (Eq. 5.26):

$$\frac{E_a}{R_g T} = \frac{4N_a}{27}\left(\frac{Mw_{Hem}}{\rho_{Hem}\Phi_v}\frac{1}{\nu \ln S_{Hem}}\right)^2\left(\frac{\gamma_{Hem}\Phi_a}{R_g T}\right)^3 \qquad 5.33$$

The exponent of this expression represents the classical probability of nuclei crossing the activation energy barrier from a supersaturated solution state during homogeneous nucleation (Mersmann *et al.*, 2001a; Söhnel & Garside, 1992). The well-known Arrhenius equation (App. F.3) is therefore utilised to obtain the homogeneous nucleation rate, J_{hom} (number/kg H_2O.min):

$$J_{hom} = \hat{A}k^{\sim} \cdot exp\frac{-E_a}{R_g T} = k_{hom} \cdot exp\frac{-\mathbf{K}_{Hem}}{(\nu \ln S_{Hem})^2} \qquad 5.34$$

where $\mathbf{K}_{Hem}$ represents a dimensionless temperature-dependent constant:

$$\mathbf{K}_{Hem} = \frac{4N_a}{27}\left(\frac{Mw_{Hem}}{\rho_{Hem}\Phi_v}\right)^2\left(\frac{\gamma_{Hem}\Phi_a}{R_g}\right)^3\frac{1}{T^3} \qquad 5.35$$

Stellenbosch University http://scholar.sun.ac.za

The proportionality constant, $k^{\sim}$, adopts the units of number/kg H_2O, while the pre-exponential factor, Â, gives the frequency (1/min) of successful energy-barrier crossings. Although the pre-exponential efficiency factor, $Âk^{\sim}$, also depends on the supersaturation ratio, interfacial energy and temperature, amongst other parameters (see Mersmann *et al.*, 2001a), their impact on the nucleation rate is confined to the above exponential term. Since the batch data, presented later in this chapter, do not differentiate between the elementary precipitation steps, the pre-exponential factor is treated as an adjustable constant, *i.e.*, $Âk^{\sim} = k_{hom}$ (1/kg.min). Pre-exponential values of the order of 10^{31} to 10^{36} 1/sec.m^3 have been reported for sparingly soluble salts, such as barium sulfate (Randolph & Larson, 1988), while Söhnel and Garside (1992) reported a wider range of 10^{25} to 10^{56} 1/sec.m^3 for slightly soluble salts.

Randolph and Larson (1988) pointed out that an equation of this form (Eq. 5.34) only predicts homogeneous nucleation at extremely high supersaturation ratios. Nevertheless, this equation gives a reasonable representation of the primary nucleation rate, J_{prim}, in some precipitation systems. Alternatively, an empirical power function may be used (Söhnel & Garside, 1992):

$$J_{prim} = k_{prim} S_{Hem}^{n} \qquad 5.36$$

where neither the rate constant, k_{prim} (1/kg.min), nor the power function order, n, have any physical meaning. As one would expect, high orders, in a wide range of six to twelve, have been found in practice (Demopoulos, 2009), while k_{prim} may have to be subjected to an Arrhenius relationship if such an equation is to be applied over a range of temperatures.

The phenomenological model (Sect. 5.4.3), comprising various non-linear functions, is more stable when based on Equation 5.34, rather than searching for a value of n (Eq. 5.36). However, as pointed out by David and Klein (2001), primary nucleation cannot be considered as being homogeneous because various foreign surfaces are always present in practice. The theory behind heterogeneous nucleation is complex and unpredictable (*e.g.*, Mersmann et al., 2001a). In essence, foreign surfaces act as a catalyst by decreasing the energy barrier of nucleation (Söhnel & Garside, 1992). The simplest treatment reduces the homogeneous activation energy barrier *via* a correction factor ξ, which is a function of the contact angle between the nuclei and the substrate at the solid/solution interface (David & Klein, 2001; Söhnel & Garside, 1992). The formation of primary hematite nuclei in the autoclave is therefore best represented by the following equation:

$$J_{prim} = k_{prim} \cdot exp \frac{-\xi \mathbf{K}_{Hem}}{(\nu \, ln S_{Hem})^2} \qquad 5.37$$

Stellenbosch University http://scholar.sun.ac.za

Hydronium jarosite growth

The above discussions have highlighted the fact that hydronium jarosite precipitation is kinetically favoured over hematite precipitation at higher acid concentrations. In this study, the acid concentration generally increases with reaction time in the batch and continuous autoclaves (see above). It is therefore reasonable to assume that hydronium jarosite nucleation occurs under conditions of higher acid concentration, and hence lower supersaturation, resulting in very limited primary nucleation in the bulk solution, *i.e.*, most nucleation would occur on existing precipitate surfaces and would most likely lead to a continuous growth mechanism.

The rate of hydronium jarosite precipitation would depend on the total surface area present in the reactor, as well as the average linear growth rate, G_{Jar} (µm/min), which depends on the supersaturation level. A general description of a surface integration mechanism is as follows:

$$G_{Jar} = k_G \cdot f(S_{Jar}) \cdot exp\frac{-K_{Jar}}{4 \ln S_{Jar}} \qquad 5.38$$

where k_G is the linear growth rate constant (µm/min) and the function $f(S_{Jar})$ can take one of several forms, depending on the mechanism (see, *e.g.*, Söhnel & Garside, 1992). One such mechanism, evaluated in Section 5.4.4, is the birth and spread (B+S) model (Mersmann *et al.*, 2001b), which is characterised by a non-linear response in the supersaturation ratio:

$$f(S_{Jar}) = \sigma_{Jar}^{\frac{2}{3}} \cdot (4 \ln S_{Jar})^{\frac{1}{6}} \qquad 5.39$$

where σ_{Jar} is the relative supersaturation of hydronium jarosite ($\sigma = S_a - 1$).

Incorporation of these highly non-linear types of equations into the phenomenological model becomes rather arbitrary because they to not cater for a range of different mechanisms at different supersaturation levels (Figure 5.4). The overall model ultimately also depends on the rate-limiting regime, *i.e.*, diffusion or surface integration, while particles of similar size may also exhibit a distribution of growth rates (see, *e.g.*, Mersmann *et al.*, 2001b). Therefore, the most appropriate generalised growth rate expression in a phenomenological-type model is the power function:

$$G_{Jar} = k_G (S_{Jar} - 1)^n = k_G \sigma_{Jar}^n \qquad 5.40$$

where the function order, n, is typically found to vary between one and two in practice (Demopoulos, 2009; Mersmann *et al.*, 2001b; Söhnel & Garside, 1992). Despite the general applicability of this equation, the lower order simplifies the regression of the overall phenomenological model. This rate expression and the alternative growth rate models are evaluated later in this chapter (Sect. 5.4.4), based on the experimental data presented below.

Stellenbosch University http://scholar.sun.ac.za

5.3 Experimental

The aim of the experimental programme was to derive adequate rate expressions, based on the above general theoretical framework, and obtain constants that are valid under typical MT autoclave operating conditions (130-155°C), assuming Arrhenius-like behaviour. Since supersaturation is difficult to control in a sparingly soluble system, the phenomenological model is also based on the BSE images and qualitative EDX spectroscopy results (App. B.3.4).

5.3.1 Equipment

The experimental programme utilised the 2-litre Parr autoclave, discussed in detail in Chapter 3 (Sect. 3.3). It also made use of a high-pressure (HP) feed pump to inject the reagents 'at temperature' (Ch. 7, Fig. 7.5). Since hydronium jarosite may redissolve or other phases precipitate during autoclave or sample cooling, the internal pressure of the autoclave was used to obtain representative samples *via* a pressure filter (0.4 µm polycarbonate membrane) (Figure 5.5).

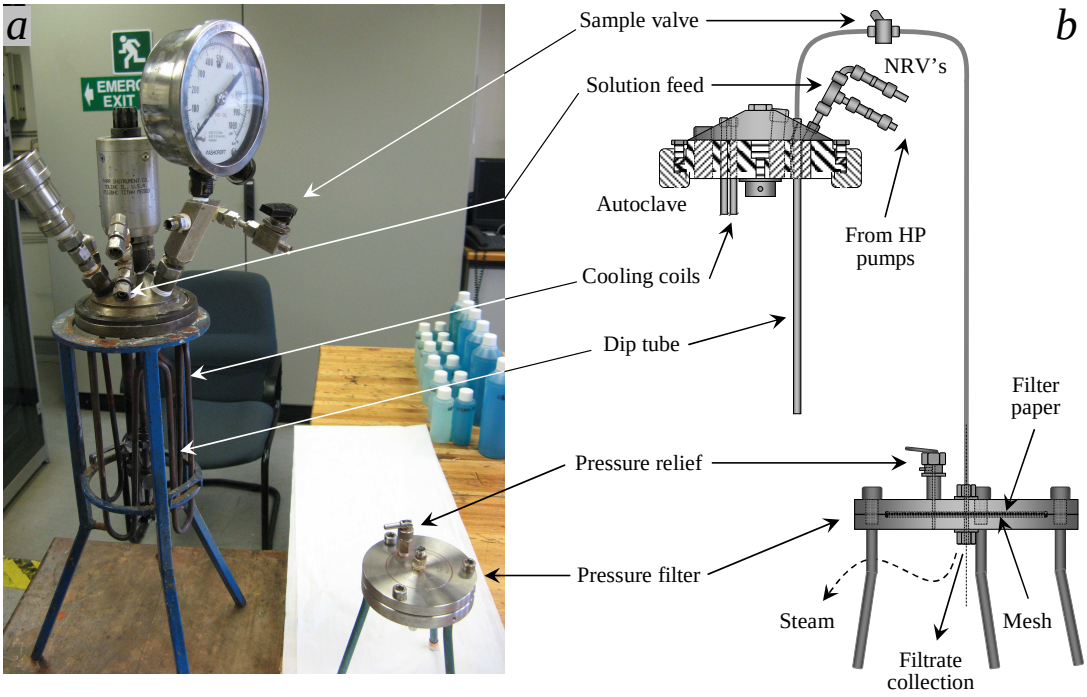

Figure 5.5
2-litre autoclave & high-pressure filter arrangement: *a*) Photo of the autoclave (lid & internals) & pressure filter; *b*) Schematic diagram of the pressure filter & its connection to the autoclave.

5.3.2 Experimental procedure

The detailed experimental procedure is presented in Appendix E.1. The autoclave was charged with the required amount of water and background salts, and then heated. The measuring tube of the HP feeding system (Fig. 7.5) was then charged with the required amount of dissolved iron(II) sulfate and pumped into the autoclave, to yield 1200 g solution. The overpressure was increased to the

Stellenbosch University http://scholar.sun.ac.za

setpoint gauge pressure using pure oxygen, while the agitation speed was increased to 1000 rev/min (impeller configuration A; see Ch. 3, Fig. 3.5), signifying the start of the kinetic test. Iron(III) precipitation was therefore driven by iron(II) oxidation, which has been quantified (Ch. 4), in addition to the rate of interfacial oxygen gas/liquid mass transfer (Ch. 3).

The filter cake (washed with propanol solution) was split into three parts: one part was dried in an oven at 40ºC and the total iron, copper (or zinc) and sulfur contents were determined. The second part was immediately subjected to PSD measurement, while the third part was used to produce the BSE images of the precipitates. EDX spectroscopy (App. B.3.4) was used to estimate the total sulfur to iron (S^T:Fe) mass ratio, *i.e.*, to qualitatively identify the dominant iron precipitate phases. Selected samples were also analysed by XRD (App. B.3.2) analysis to identify the major phases.

5.3.3 Data interpretation

A separate test was conducted for each kinetic data point in order to generate statistically superior results. This procedure also ensured that enough (solid) sample mass could be collected at each time interval, allowing various analyses to be conducted without creating artificially high supersaturation conditions in the autoclave. A total mass balance was used to determine the water loss (as steam) during pressure filtration, which, in turn, was used to back-calculate the aqueous species concentrations in the autoclave 'at temperature'. The reaction extents are determined from the solid phase sulfur and iron balances, as well as the overall iron balance (see below).

Sulfur balance

In order to determine the hydronium jarosite content, a constant average sulfur (S^T) value of 2% is assumed to be present as adsorbed sulfate on the hematite polycrystals (Sect. 5.2.5). It is further assumed that all the residual copper in the solid phase is present as antlerite, $Cu_3(SO_4)(OH)_4$. This is the only crystalline phase identified by XRD analysis in the copper sulfate system at low acidity (Figure 5.6). No such analogous zinc salts were detected in the zinc sulfate systems and, for the sake of simplicity, it is assumed that all residual zinc was present as basic zinc sulfate (BZS), $ZnSO_4.2Zn(OH)_2$. All sulfur, not present as these salts and adsorbed sulfate, is therefore assumed to be present as the ideal hydronium jarosite end member.

Iron balance

The solid phase iron balance then (iteratively) yields the idealised hematite content, while the extent of precipitation, $X_{p,Fe}$, is based on the residual amount of iron left in solution and the original amount of iron(II) at the start. These normalised fractions (weight %) of hematite ($W_{f,Hem}$) and hydronium jarosite phases ($1 - W_{f,Hem}$) are obtained after assuming that the other iron(III) precipitates, *e.g.*, goethite, constitute a minor portion of the total precipitated mass.

Stellenbosch University http://scholar.sun.ac.za

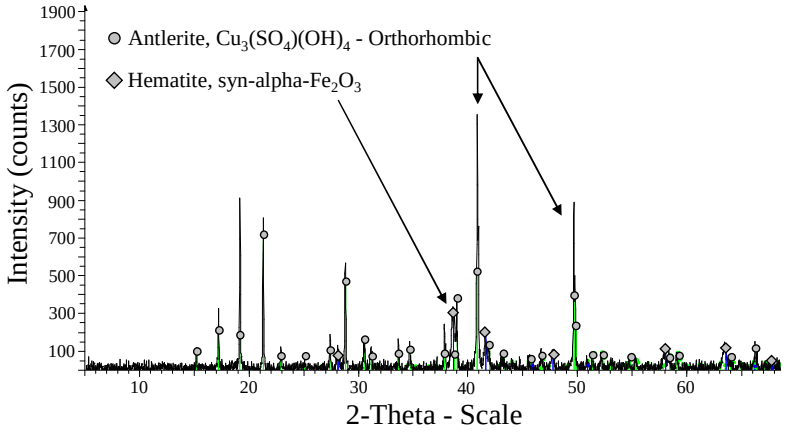

Figure 5.6
XRD pattern of the precipitate after 2.5 min at 155°C (1000 kPa $p_{O2}{}^{o}$), starting with 4 g/L H_2SO_4, 3 g/L Fe(II) & 15 g/L Cu (Test FPB11, App. E.3).

5.4 Results and discussion

Before any rate constants can be regressed, the phenomenological model of iron(III) precipitation (based on the general theoretical framework; Sect. 5.2) first needs to be validated using the batch experimental results at low pulp densities (< 1 wt% solids).

5.4.1 Measured reaction extents and qualitative BSE images obtained from low pulp density (< 1 wt% solids) batch precipitation testwork, and validating the overall modelling methodology

Table 5.1 presents a summary of the various tests and their respective aims. The experimental results are presented, based on the temperature, as well as the initial acid and iron(II) concentration regimes, *i.e.*, low (L), medium (M) and high (H) (see footnote). These subsections, and the corresponding appendixes (App. E), include various BSE images. The particle morphologies of the hematite and hydronium jarosite phases are quite distinct (see below), which lends qualitative support to the main assumptions of the phenomenological model.

Table 5.1
Experimental precipitation regimes & the primary aims of each test series.

[a] Regime (L, M, H)	[b] Salt	Test series	Aims (identify, qualify or quantify)
155ºC, L Acid, L Fe	Zn	FPA1–FPA3	Hem morph., charac. size, pptn. rate
155ºC, L-M Acid, L Fe	Zn, Cu	FPB1–FPB4	Hem morph., charac. size, pptn. rate
150ºC, M-H Acid, ~M Fe	Cu	FPC1–FPC6	Hem & H-Jar morph., size, pptn. rate, surf. interactions
150ºC, H Acid, H Fe	Cu	FPD1-FPD5	H-Jar morph., size, pptn. rate
140ºC, M-H Acid, M-H Fe	Cu	FPE1-FPE5	H-Jar & Hem morph., size, pptn. rate, surf. interactions
130ºC, L-M Acid, ~L Fe	Cu	FPF1-FPF3	H-Jar & Hem morph., size, pptn. rate, surf. interactions

[a] Acid regimes: L (< 5 g/L), M (5-15 g/L), H (> 15 g/L); Fe(II) regimes: L (< 5 g/L), M (5-7.5 g/L), H (> 7.5 g/L);
[b] Background sulfate salt (15 g/L Zn or Cu).

Stellenbosch University http://scholar.sun.ac.za

Hematite precipitation at 155°C and different oxygen partial pressures, in the low acid (< 5 g/L H_2SO_4) and low iron(II) (< 5 g/L Fe) concentration regimes, in zinc sulfate background

The first part of the experimental programme focussed on determining the typical hematite particle morphology and size. A low and narrow acid concentration window could be maintained by limiting the initial acid and iron(II) concentrations to less than 5 g/L. A temperature of 155°C in zinc sulfate (15 g/L Zn) background was utilised for this purpose. Table 5.2 presents the results of these tests, carried out at different oxygen partial pressures (p_{O2}° refers to pure water), within the typical ranges applied during MT mineral oxidation, in order to gain insight into the effect of supersaturation on the precipitation rate (detailed results & BSE images can be found in App. E.2).

Table 5.2
Results of the iron(III) precipitation tests at 155ºC & different oxygen partial pressures, starting with 3.5 g/L H_2SO_4, 3.5 g/L Fe(II) and 15 g/L Zn.

[a] Test	p_{O2}°	Time	$[H_2SO_4]$	[b] $[Fe^T]\cdot10^2$	[c] Zn	[c] Fe	[c] S^T	[d] S^T:Fe	$X_{p,Fe}$	$W_{f,Hem}$
–	(kPa)	(min)	(mol/kg)	(mol/kg)	(%)	(%)	(%)	(%)	(%)	(%)
FPA12	350	40	0.110	0.21 (24)	1.45	56.7	3.2	5.6 (4)	97	88
FPA22	700	15	0.105	0.49 (78)	0.76	56.0	2.3	4.1 (4)	93	94
FPA31	1000	5	0.090	1.07 (52)	1.15	53.3	2.7	5.1 (8)	84	90
FPA32	1000	15	0.095	0.31 (58)	1.09	53.6	3.1	5.8 (5)	95	86

[a] 0.05 g/L Arbo A02 (LS) & Orfom 2 (QB) added initially; [b] Bracketed values refer to Fe(II) left in sln. (wt. % of Fe^T); [c] Wt. % in residue; [d] S^T:Fe wt. ratio (avg. ratio from EDX spot analyses in brackets).

Clearly, the precipitation rate is fast and the hematite content high (> 85%) at these low acidity conditions. Since the iron(II) oxidation rate is also fast under these conditions (Ch. 4), high initial supersaturation ratios would have been prevalent, even at 350 kPa p_{O2}°, resulting in similar size particles (see images in App. E.2). Figure 5.7 *a* illustrates that most particles appear spheroidal, are roughly 0.5 to 1 µm in diameter and comprise smaller particulates. The image at a shorter residence time (Figure 5.7 *b*) confirms that these spheroidal particles were preceded by nano-aggregates of similar sized (0.1 to 0.2 µm), spindle-like particulates. Another interesting feature is the appearance of hollow particles (circled). This is in line with the observations of Lu *et al.* (2006), who claimed that the strong adsorption tendency of sulfate ions may protect particle exteriors, while the interiors could redissolve, yielding the apparent hollow particles upon aging. This suggests that the precursor phase at shorter reaction times may indeed have contained some waters of hydration, *e.g.*, $Fe_2O_3\cdot3H_2O$, which ties in with the thermodynamic assumptions of Section 5.2.3.

Small amounts (0.05 g/L) of the surfactants, lignosulfonate (LS) and Quebracho (QB) were added upfront to approximate the solution environment during leaching (Ch. 6). Although these surfactants degrade relatively rapidly in the presence of dissolved oxygen (Ch. 3 & 6), they would adsorb on oxide precipitates, especially at lower pH values (see Nanthakumar *et al.*, 2010). This

Stellenbosch University http://scholar.sun.ac.za

could affect the precipitation behaviour of iron(III), but such investigation was outside the scope of this study. On the other hand, the strong association of sulfate with hematite surfaces could prevent the adsorption of the negatively charged surface-active portion of these surfactants.

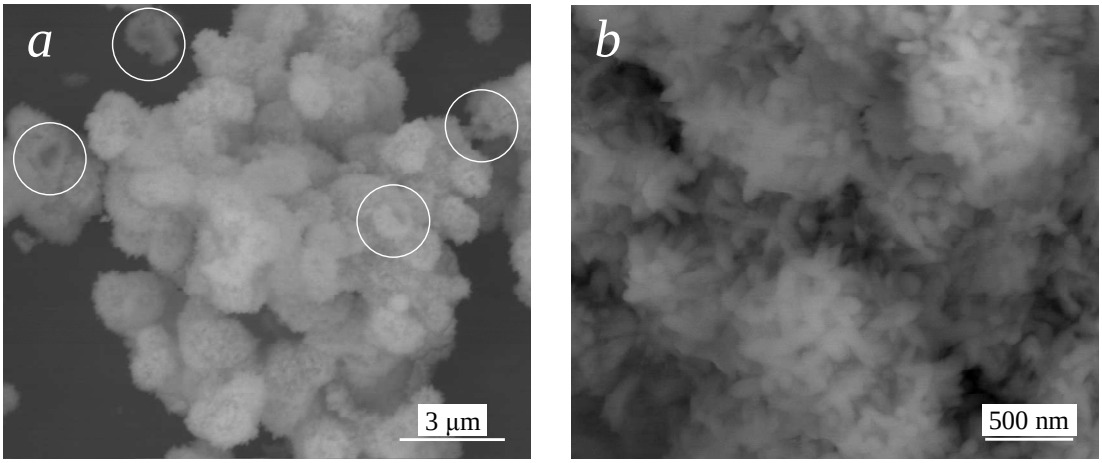

Figure 5.7
BSE images of residues produced at 155ºC (700 kPa $p_{O2}{}^{o}$) & 15 g/L Zn, starting with 3.5 g/L H_2SO_4 & 3.5 g/L Fe(II): *a*) After 15 min (FPA22); *b*) After 5 min (FPA21).

Table 5.2 confirms that the average sulfur-to-iron ratios obtained by the EDX spot analyses are comparable to the chemically analysed values, confirming the presence of about 4% S^T in the final residue. This yields a high proportion of hematite (> 85%), after subtracting the contributions of BZS and adsorbed sulfate (2% S^T). In addition to the characteristic deep red colour of these samples, XRD analyses (*e.g.*, Figure 5.6) confirm that hematite is the primary iron(III) precipitate at low acidities. Unfortunately, the presence of amorphous phases prevented the use of semi-quantitative XRD to support these calculated compositions, *i.e.*, based on the chemical analyses.

Hematite precipitation at 155 ºC (1000 kPa oxygen), in the low-medium acid (4-12 g/L H_2SO_4) and low iron(II) (< 5 g/L Fe) concentration regimes, in zinc and copper sulfate backgrounds

The next set of tests focussed on comparing the particle morphology and size and the rate of iron(III) precipitation at 155ºC and high oxygen partial pressure (1000 kPa $p_{O2}{}^{o}$) in the H_2SO_4-$ZnSO_4$ and H_2SO_4-$CuSO_4$ systems, starting with 4 to 12 g/L H_2SO_4 and a low initial iron(II) concentration regime (< 5 g/L Fe). Besides the speciation changes between these two chemical systems, the presence of copper in solution greatly enhances the oxidation rate of iron(II) (Ch. 4), which, in turn, would affect the level of iron(III) supersaturation. The detailed mass balances and BSE images can be found in Appendix E.3, while a summary is presented in Table 5.3.

The initial acid and iron(II) concentrations seem to be the dominant factor that determine the precipitation rate: this supports the use of supersaturation as the main parameter in the nucleation and growth rate expressions (Sect. 5.2.6).

Stellenbosch University http://scholar.sun.ac.za

Table 5.3
Results of the iron(III) precipitation tests at 155ºC (1000 kPa $p_{O2}{}^{o}$), starting with 4 to 12 g/L H_2SO_4, 2.5 to 4 g/L Fe(II) & 15 g/L Cu or Zn.

[a] Test –	Time (min)	[b] [A, Fe] (g/L)	$[H_2SO_4]$ (mol/kg)	[c] $[Fe^T]\cdot10^2$ (mol/kg)	[d] Cu or Zn (%)	[d] Fe (%)	[d] S^T (%)	[e] S^T:Fe (%)	$X_{p,Fe}$ (%)	$W_{f,Hem}$ (%)
FPB11	2.5	4, 3	0.069	2.46 (8.9)	1.44 (Cu)	52.9	3.4	6.4 (9)	59	84
FPB12	5	4, 3	0.080	1.76 (3.4)	0.78 (Cu)	55.7	2.5	4.6 (7)	70	92
FPB13	10	4, 3	0.091	1.13 (6.2)	0.74 (Cu)	54.3	2.9	5.3 (6)	81	88
FPB21	5	4, 4	0.1095	1.33 (46)	0.56 (Zn)	53.4	2.8	5.3 (5)	82	88
FPB22	10	4, 4	0.120	0.63 (38)	0.53 (Zn)	55.7	2.6	4.7 (5)	91	91
FPB23	15	4, 4	0.125	0.38 (39)	0.51 (Zn)	56.0	2.45	4.4 (4)	95	92.5
FPB31	2.5	12, 2.5	0.128	4.71 (9.3)	1.11 (Cu)	53.3	3.1	5.9 (8)	9	86
FPB32	5	12, 2.5	0.123	4.44 (5.2)	0.90 (Cu)	55.3	2.6	4.7 (8)	12.5	92
FPB33	10	12, 2.5	0.127	3.99 (4.3)	0.70 (Cu)	54.35	3.1	5.7 (10)	20	86
FPB42	10	7, 3.5	0.100	3.44 (9.3)	0.57 (Zn)	56.7	3.5	6.2 (5)	50	84
FPB43	15	7, 3.5	0.115	2.34 (8.1)	0.91 (Zn)	55.2	3.6	6.5 (5)	67	82.5

[a] 0.05 g/L Arbo A02 (LS) & Orfom 2 (QB) added initially; [b] Initial H_2SO_4 & Fe(II), respectively; [c] Bracketed values refer to Fe(II) left in sln. (wt. % of Fe^T); [d] Wt. % in residue; [e] S^T:Fe wt. ratio (avg. from EDX spot analyses in brackets).

Even in the presence of copper, the hematite precipitation rate is dominant (> 80%), confirming that the hematite phase is highly insoluble below about 15 g/L H_2SO_4. Furthermore, since the iron(II) oxidation reaction consumes acid (Ch. 4; Rx. 4.1), the initial iron(II) concentration also influences the nucleation rate in this low acidity range. Figure 5.8 compares the BSE images of Tests FPB11 and FPFE31 at high magnifications. Similarly to the tests conducted at different oxygen partial pressures (previous section), iron(II) oxidation rate differences at different solution compositions seem to be relatively unimportant at these high temperatures and low acidities, *i.e.*, these differences have an insignificant impact on the particulate size (Figure 5.7 *b* & Figure 5.8) and nucleation rate (Table 5.3), at least from a phenomenological modelling perspective. Even at slightly lower hematite content (Test PFB43), no appreciable hydronium jarosite growth appears to have occurred under these conditions (see App. E.3).

The differences in supersaturation ratios under these low acidity conditions are therefore relatively inconsequential with regard to the individual particulate sizes (0.1-0.2 µm), in particular compared to the sizes at higher acidities (next section). An average characteristic particulate size (L_{Hem}) of around 0.15 µm is therefore adopted in the phenomenological model, notwithstanding that these particulates are not spherical and transform into nano-aggregates and agglomerates of different overall sizes.

Stellenbosch University http://scholar.sun.ac.za

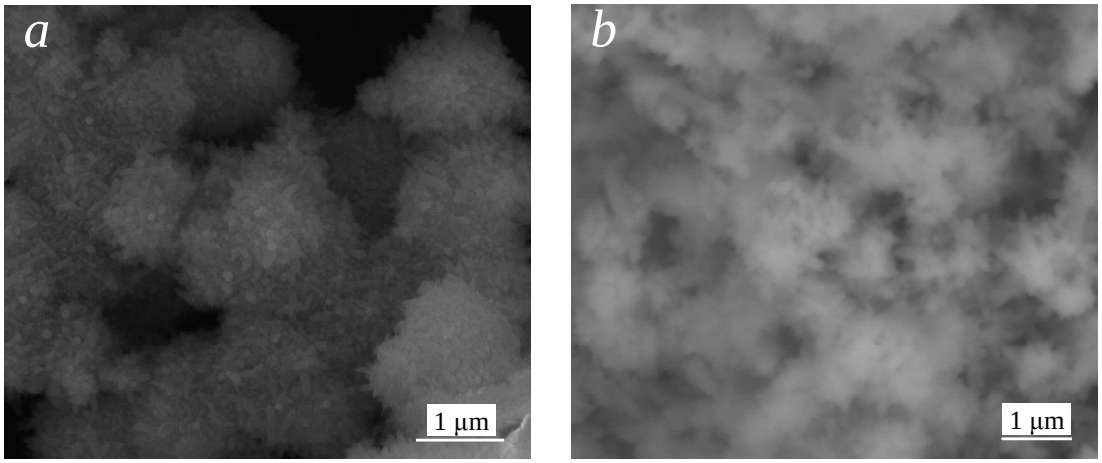

Figure 5.8
BSE images of residues produced at 155ºC (1000 kPa $p_{O2}{}^{o}$) & 15 g/L Cu in different acid concentration regimes: *a*) After 2.5 min, starting with 4 g/L H_2SO_4 & 3 g/L Fe(II) (FPB11); *b*) After 15 min, starting with 12 g/L H_2SO_4 & 2.5 g/L Fe(II) (FPB31).

Iron(III) precipitation at 150 ℃ (1000 kPa oxygen) in the medium-high acid (10-16 g/L H_2SO_4) and medium iron(II) (4-8.5 g/L) concentration regimes, in copper sulfate background

The tests targeted a slightly higher initial acidity range (10-16 g/L H_2SO_4) at the baseline temperature of 150ºC and medium iron(II) concentrations (4-8.5 g/L) in the H_2SO_4-$CuSO_4$ system. Besides the particle morphology and precipitation rate, these tests aimed to identify possible surface interactions between the different precipitates. The detailed mass balances and BSE images are presented in Appendix E.4, while a summary is presented in Table 5.4.

Table 5.4
Results of iron(III) precipitation tests at 150ºC (1000 kPa $p_{O2}{}^{o}$), starting with 10 to 16 g/L H_2SO_4, 4 to 8.5 g/L Fe(II) & 15 g/L Cu.

[a] Test	Time	[b] [A, Fe]	[H_2SO_4]	[c] [Fe^T]·10^2	[d] Cu	[d] Fe	[d] S^T	[e] S^T:Fe	$X_{p,Fe}$	$W_{f,Hem}$
–	(min)	(g/L)	(mol/kg)	(mol/kg)	(%)	(%)	(%)	(%)	(%)	(%)
FPC11	5	10, 8.5	0.090	10.62 (4.4)	0.42	43.6	7.7	17.7 (14)	33.5	41
FPC12	7.5	10, 8.5	0.1105	9.08 (3.7)	0.44	44.8	8.5	18.9 (21)	44	38
FPC21	15	12.5, 4	0.117	6.67 (2.8)	0.9	49.2	5.2	10.6 (11)	13	65
FPC22	20	12.5, 4	0.127	5.94 (2.7)	1.0	47.2	4.6	9.8 (13)	23	68
FPC32	10	13.5, 5.5	0.111	10.05 (2.8)	0.9	47.7	6.8	14.2 (17)	6	52
FPC42	10	14, 6	0.111	10.67 (2.7)	0.90	41.6	8.0	19.2 (19)	6	38
FPC43	15	14, 6	0.126	9.37 (2.0)	0.67	47.3	6.0	12.7 (12)	19	57
FPC52	10	15, 7.5	0.111	13.59 (2.2)	0.57	40.5	9.4	23.2 (21)	5	27.5
FPC53	15	15, 7.5	0.122	11.92 (1.2)	0.30	36.9	11.6	31.4 (35)	17	11
FPC62	15	16, 8.5	0.1475	11.82 (1.9)	0.57	40.9	9.7	23.7 (18)	28	26

[a] 0.05 g/L Arbo A02 (LS) & Orfom 2 (QB) added initially; [b] Initial H_2SO_4 & Fe(II), respectively; [c] Bracketed values refer to Fe(II) left in sln. (wt. % of Fe^T); [d] Wt. % in residue; [e] S^T:Fe wt. ratio (avg. from EDX spot analyses in brackets).

Stellenbosch University http://scholar.sun.ac.za

The first two tests (FPC11 & FPC12) conducted at relatively high iron(III) supersaturation, by starting with 8.5 g/L Fe(II) and relatively low acid (10 g/L H_2SO_4), yielded a significant amount of hydronium jarosite (~60%). Figure 5.9 presents the BSE images after 5 and 7.5 minutes, respectively. This jarosite phase appears rather amorphous at first (Figure 5.9 *a*), but becomes more crystalline over time (Figure 5.9 *b*). The comparatively bright (higher average atomic number) hematite centres are visible in the amorphous structures (small circles; Figure 5.9 *a*), suggesting that hematite can act as substrate surface for nucleation, followed by crystal growth.

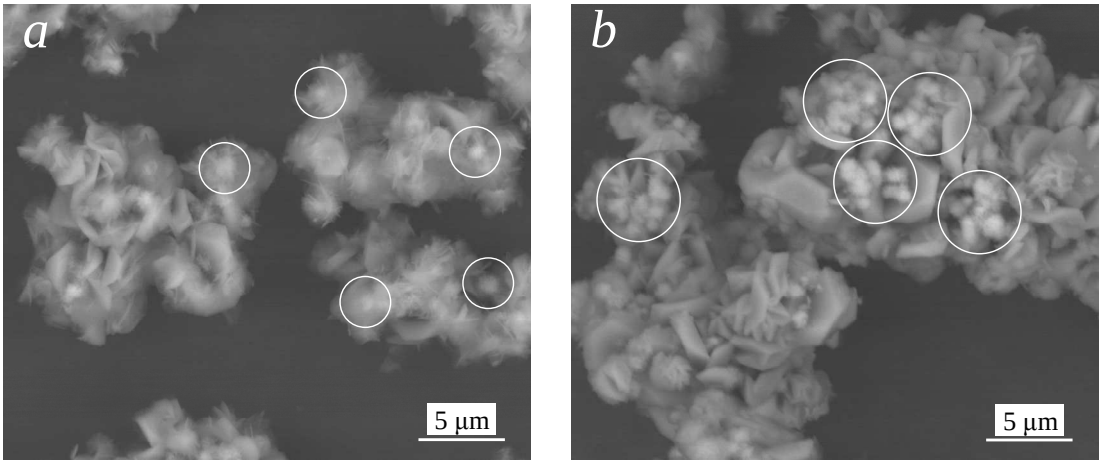

Figure 5.9
BSE images of residues produced at 150ºC (1000 kPa $p_{O2}{}^{o}$), 15 g/L Cu & relatively high iron(III) supersaturation, starting with 10 g/L H_2SO_4 & 8.5 g/L Fe(II): *a*) After 5 min (FPC11: 34% $X_{p,Fe}$, 41% $W_{f,Hem}$); *b*) After 7.5 min (FPC12: 44% $X_{p,Fe}$, 38% $W_{f,Hem}$).

On the other hand, some bright spheroidal hematite clusters are also visible on the crystalline hydronium jarosite outer surface after 7.5 minutes (large circles; Figure 5.9 *b*). Either the hematite and jarosite particles formed separately and then agglomerated, or secondary hematite nucleation could be catalysed by existing hydronium jarosite surfaces. If hematite surfaces could act as a substrate for jarosite nucleation, the reverse might also be true. Contact angle calculations (*e.g.*, Mersmann *et al.*, 2001a) might confirm this, but they are outside the scope of this study due to the unknown interfacial energies of the amorphous (& other) phases.

It is not unreasonable to expect that the interfacial energy of secondary hematite nucleation on hydronium jarosite surfaces is lower than the high interfacial energy between hematite and the solvent during primary nucleation (Sect. 5.2.6). It is assumed that the strong adsorption of sulfate ion on hematite is the driving force that makes these mechanisms possible.

Besides these surface nucleation mechanisms, the above images also suggest that significant particle aggregation occurred. Figure 5.10 presents the residue volume distributions, particle masses and numbers (N) of the above two tests.

Stellenbosch University http://scholar.sun.ac.za

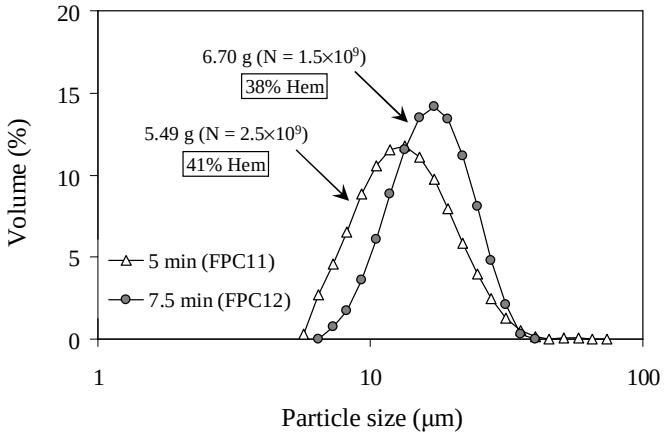

Figure 5.10
PSD, particle mass & number (in parentheses), per kg H_2O, at 150ºC (1000 kPa $p_{O2}{}^{o}$) & 15 g/L Cu after 5 & 7.5 min, starting with 10 g/L H_2SO_4 & 8.5 g/L Fe(II).

Clearly, the increase in residue mass (growth) is accompanied by a decrease in the number of particles, confirming that particle aggregation also occurred during the course of these batch experiments. The overall precipitation mechanism therefore consists of various interactions between the hematite and hydronium jarosite surfaces, highlighting the complexity of this system. More experimental evidence is required in this intermediate acid regime, as discussed below.

Figure 5.11 represents the BSE images of residues after 15 and 20 minutes at relatively lower supersaturation (*cf*. Series FPC1), starting with 12.5 g/L H_2SO_4 and 4 g/L Fe(II) (Series FPC2).

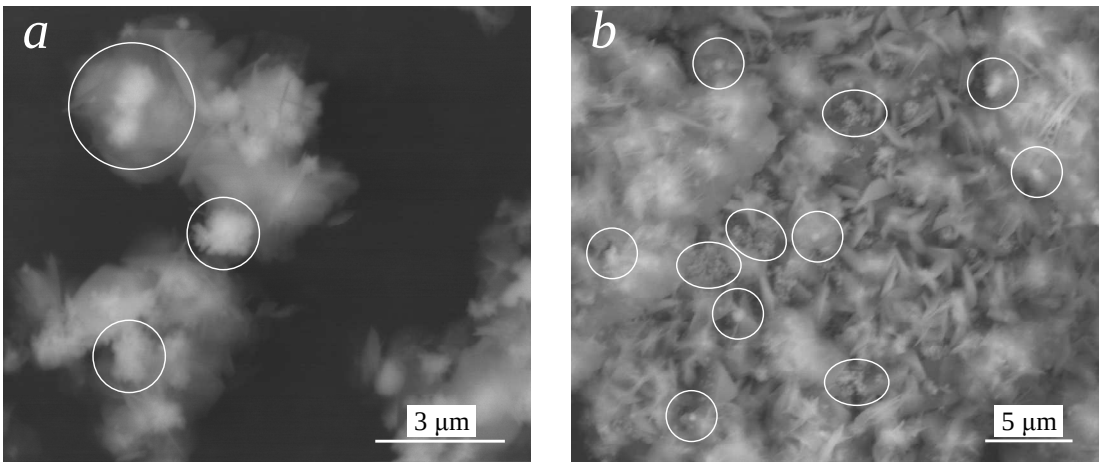

Figure 5.11
BSE images of residues produced at 150ºC (1000 kPa $p_{O2}{}^{o}$), 15 g/L Cu & relatively low iron(III) supersaturation, starting with 12.5 g/L H_2SO_4 & 4 g/L Fe(II): *a*) After 15 min (FPC21: 13% $X_{p,Fe}$, 65% $W_{f,Hem}$); *b*) After 20 min (FPC22: 23% $X_{p,Fe}$, 68% $W_{f,Hem}$).

This intermediate acid regime is more typical of the conditions experienced during the initial stage of precipitation in a batch leaching reactor. Again, the initial agglomerates consist of comparatively

Stellenbosch University http://scholar.sun.ac.za

bright hematite nano-aggregates, often surrounded by what appears to be precursor hydronium jarosite structures (large circle; Figure 5.11 *a*). This suggests that the initial drop in acidity due to iron(II) oxidation promotes hematite formation, which then acts as a substrate surface for the hydronium jarosite precursor phase. In other cases, hematite appears on the outer surfaces, either due to agglomeration, or as a result of a role reversal between the two phases, *i.e.*, hematite nucleation catalysed by other surfaces (smaller circles; Figure 5.11 *a*). With an increase in jarosite crystallinity over time, the initial agglomerates transform into more compact aggregate structures (Figure 5.11 *b*). This particular test is insightful in that the hematite content remains relatively constant over time (65 to 68%). Despite an increase in the acid concentration due to the advancing precipitation reactions, both jarosite growth and the continuous formation of dispersed hematite particulates are sustained. These comparatively bright hematite particulates are visible on the outer proximity of the amorphous structures (small circles; Figure 5.11 *b*), again suggesting that these surfaces could catalyse secondary hematite nucleation. The oval-shaped rings highlight what appear to be surface nuclei. Due to the integrated nature of these aggregates, EDX analysis could not be used to identify these phases. However, dispersed particulates of similar appearance, 'coating' larger hydronium jarosite crystal facets, are elaborated upon in the next section. These surfaces are low in sulfur and are therefore assumed to be the hematite precursor phase.

Series FPC3, FPC4, FPC5 and FPC6 systematically investigated the effects of pumping higher acid and iron(II) concentrations into the autoclave. All these residues comprised a significant amount of hydronium jarosite, which generally increased with increasing initial acid and iron(II) concentrations (Table 5.4). The BSE images of these residues (App. E.4) confirm the presence of amorphous structures surrounding small (comparatively bright) hematite aggregates of varying overall size. A particularly interesting transition appears to have occurred between Series FPC4 and FPC5. The former series contained initial concentrations of 14 g/L H_2SO_4 and 6 g/L Fe(II), while the latter series corresponds to 15 g/L H_2SO_4 and 7.5 g/L Fe(II). Although the overall precipitation extents are very similar, hematite formation dominated at longer reaction times in the case of Series FPC4 (57% $W_{f,Hem}$), while hydronium jarosite formation dominated in the case of Series FPC5 (11% $W_{f,Hem}$). These observations are in line with the BSE images presented in Figure 5.12 (Series FPC4) and Figure 5.13 (Series FPC5), respectively. Therefore, these initial test conditions of 14 to 15 g/L H_2SO_4 and 6 to 7.5 g/L Fe(II) represent a cusp, promoting either phase depending on the actual supersaturation ratios and the existing surface areas (see Figure 5.4). Hydronium jarosite particles, which are clearly the more stable phase at the higher acid and iron concentrations, not only increase in size but also become more crystalline over time (Figure 5.13 *b*). This is in line with the GT relationship (Eq. 5.30), suggesting that the large crystalline hydronium jarosite particles are often the more stable phase, compared to the nano-sized hematite particulates, despite the fact that the thermodynamics might suggest otherwise (Sect. 5.4.2).

Stellenbosch University http://scholar.sun.ac.za

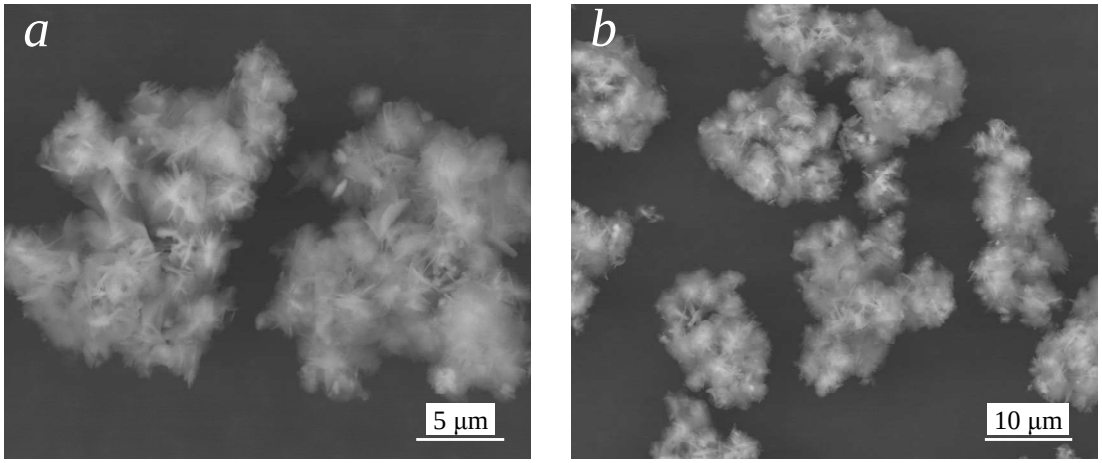

Figure 5.12
BSE images of residues produced at 150ºC (1000 kPa p_{O2}º) & 15 g/L Cu, starting with 14 g/L H_2SO_4 & 6 g/L Fe(II): *a*) After 10 min (FPC42: 6% $X_{p,Fe}$, 38% $W_{f,Hem}$); *b*) After 15 min (FPC43: 19% $X_{p,Fe}$, 57% $W_{f,Hem}$).

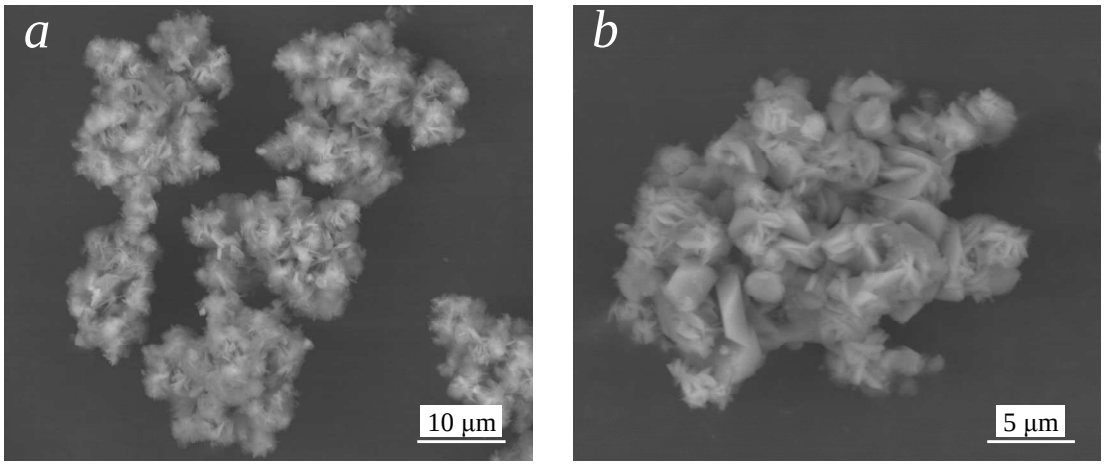

Figure 5.13
BSE images of residues produced at 150ºC (1000 kPa p_{O2}º) & 15 g/L Cu, starting with 15 g/L H_2SO_4 & 7.5 g/L Fe(II): *a*) After 10 min (FPC52: 5% $X_{p,Fe}$, 28% $W_{f,Hem}$); *b*) After 15 min (FPC53: 17% $X_{p,Fe}$, 11% $W_{f,Hem}$).

The PSD, particle mass and number of these residues are compared in Figure 5.14. Despite the increase in total precipitate mass and number of particles over time, the average particle size decreases with increasing hematite content in the case of Series FPC4, while the average particle size increases with increasing hydronium jarosite content in the case of Series FPC5.

Despite the clouded relationship between the overall precipitation rate and the observed PSDs due to aggregation, hematite growth is confined to forming nano-sized particulates of similar size (L_{Hem} ≈ 0.15 µm) over relatively wide acid and iron concentration regimes.

Stellenbosch University http://scholar.sun.ac.za

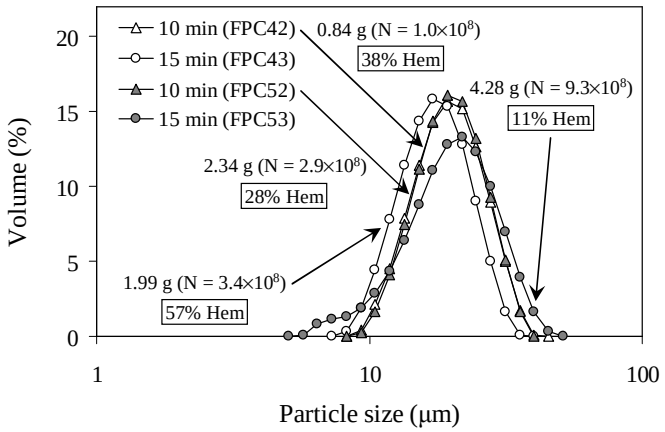

Figure 5.14
PSD, particle mass & number (in parentheses), per kg H_2O, at 150ºC (1000 kPa $p_{O2}{}^{o}$) & 15 g/L Cu after 10 & 15 min. Comparing the effects of starting with 14 g/L H_2SO_4 & 6 g/L Fe(II) (Series FPC4) *cf.* 15 g/L H_2SO_4 & 7.5 g/L Fe(II) (Series FPC5).

The above images provide qualitative, yet strong, support in favour of primary and secondary hematite nucleation, accompanied by rapid (but limited) growth. Hydronium jarosite precipitation, on the other hand, manifests *via* a continuous growth mechanism on existing surfaces, which is in line with the general rate expressions in Section 5.2.6 (investigated in more detail below).

Iron(III) precipitation at 150 ℃ (1000 kPa oxygen) in the high acid (> 15 g/L H_2SO_4) and high iron(II) (> 7.5 g/L Fe) concentration regimes, in copper sulfate background

These tests focussed on determining the particle morphology and size and the precipitation rate in the H_2SO_4-$CuSO_4$ system, at progressively higher initial acid (20 to 30 g/L) and iron(II) (9 to 15 g/L) concentrations, where hydronium jarosite growth is most prevalent. Table 5.5 presents a summary of these results (the detailed mass balances and BSE images can be found in App. E.5).

Figure 5.15 (*ref.* Series FPD1) illustrates the polycrystalline nature of the relatively large hydronium jarosite particles, which clearly increased in overall size over time. Since the increase in size is accompanied by a notable increase in precipitate mass, particle growth dominates in the case of hydronium jarosite precipitation (Figure 5.16). However, the number of particles decreased significantly over time, *i.e.*, the increase in the overall particle size can also be ascribed to agglomeration and aggregation (relatively loose agglomerate structures are clearly visible in Figure 5.15 *b*). Therefore, a direct relationship between the precipitation rate and the overall particle size is not readily obtained from the measured PSDs, as with hematite precipitation in the lower acid regimes. The reaction extents in Table 5.5 illustrate the sensitivity of the precipitation rate to varying acid concentration. This is also reflected by the solubility curves in Figure 5.2, highlighting the importance of the supersaturation term in the general jarosite growth rate expression (Eq. 5.40).

Stellenbosch University http://scholar.sun.ac.za

Table 5.5
Results of iron(III) precipitation tests at 150ºC (1000 kPa $p_{O2}{}^{o}$), starting with 20 to 30 g/L H_2SO_4, 9 to 15 g/L Fe(II) & 15 g/L Cu.

[a] Test	Time	[b] [A, Fe]	$[H_2SO_4]$	[c] $[Fe^T]\cdot10^2$	[d] Cu	[d] Fe	[d] S^T	[e] S^T:Fe	$X_{p,Fe}$	$W_{f,Hem}$
–	(min)	(g/L)	(mol/kg)	(mol/kg)	(%)	(%)	(%)	(%)	(%)	(%)
FPD11	10	20, 10	0.1215	18.71 (2.8)	0.14	35.6	11.2	31.5 (30)	2	11
FPD12	15	20, 10	0.143	18.59 (2.0)	0.15	36.3	11.8	32.5 (31)	4	9
FPD13	20	20, 10	0.138	17.76 (1.7)	0.15	35.9	11.9	33.1 (33)	10.5	8
FPD14	25	20, 10	0.165	17.77 (1.5)	0.24	35.5	12.3	34.6 (39)	12	6
FPD21	15	20, 9	0.143	15.57 (2.4)	0.18	37.2	10.5	28.2 (33)	8	17
FPD22	20	20, 9	0.153	15.56 (2.0)	0.27	37.4	10.9	29.1 (32)	8	15
FPD23	25	20, 9	0.1595	15.70 (1.9)	0.19	36.4	10.8	29.7 (31)	11	14
FPD24	30	20, 9	0.159	14.84 (1.3)	0.20	38.6	10.0	25.9 (28)	13	21
FPD31	10	25, 15	0.152	24.79 (3.1)	0.10	35.4	12.3	34.7 (36)	13	5
FPD32	20	25, 15	0.184	21.39 (2.0)	0.06	35.6	12.3	34.6 (36)	25	6
FPD33	30	25, 15	0.193	20.35 (1.4)	0.09	35.4	11.6	32.8 (31)	29	8.5
FPD41	30	25, 12	0.174	21.19 (1.2)	0.14	36.8	11.0	29.9 (31)	8	13.5
FPD42	45	25, 12	0.179	20.31 (1.0)	0.10	36.0	12.6	35.0 (35)	10	5
FPD43	60	25, 12	0.200	18.30 (0.9)	0.15	35.7	11.9	33.3 (32)	20	8
FPD51	45	30, 15	0.212	26.24 (0.9)	0.07	36.4	11.9	32.7 (32)	10	9
FPD52	60	30, 15	0.210	23.87 (0.8)	0.06	35.5	11.8	33.2 (36)	14	8

[a] 0.05 g/L Arbo A02 (LS) & Orfom 2 (QB) added initially; [b] Initial H_2SO_4 & Fe(II), respectively; [c] Bracketed values refer to Fe(II) left in sln. (wt. % of Fe^T); [d] Wt. % in residue; [e] S^T:Fe wt. ratio (avg. from EDX spot analyses in brackets).

Spherical nano-aggregates of another phase are also visible on selected hydronium jarosite particles, as illustrated in Figure 5.15 *a* (circled). This, again, suggests that the system is initially close to a cusp, which depends strongly on the prevailing acid concentration. In most cases in this high acid regime, this phase appears as dispersed particulates on the jarosite surfaces (see Figure 5.17 *a*). Qualitative EDX spot analysis (App. B.3.2) at the top position of Figure 5.17 b_1 yields a S^T:Fe ratio of about 11%, suggesting that this dispersed surface 'coat' comprised small hematite or hematite-like particulates. In contrast, the bottom spot analysis (Figure 5.17 b_2) reveals a considerably higher S^T:Fe ratio of about 33%, confirming the presence of the comparatively larger and more crystalline hydronium jarosite phase. Similarly to hematite, the negatively charged surface-active portion of the added surfactants would not be expected to adsorb strongly on these jarosite surfaces.

In general, the S^T:Fe ratios obtained from the average EDX spot analyses agree well with the chemical analyses. No hematite particulates were detected on any surfaces after 25 minutes (Test

Stellenbosch University http://scholar.sun.ac.za

FPD14), suggesting that the precipitation mechanism is primarily driven by hydronium jarosite crystal growth. This is confirmed by the XRD diffractogram in Figure 5.18 and is also in line with the GT relationship (Eq. 5.30). It is therefore not surprising that the S^T:Fe ratio obtained by EDX analysis (~39%) is slightly higher than the value obtained by chemical analysis (~35%) (Table 5.5).

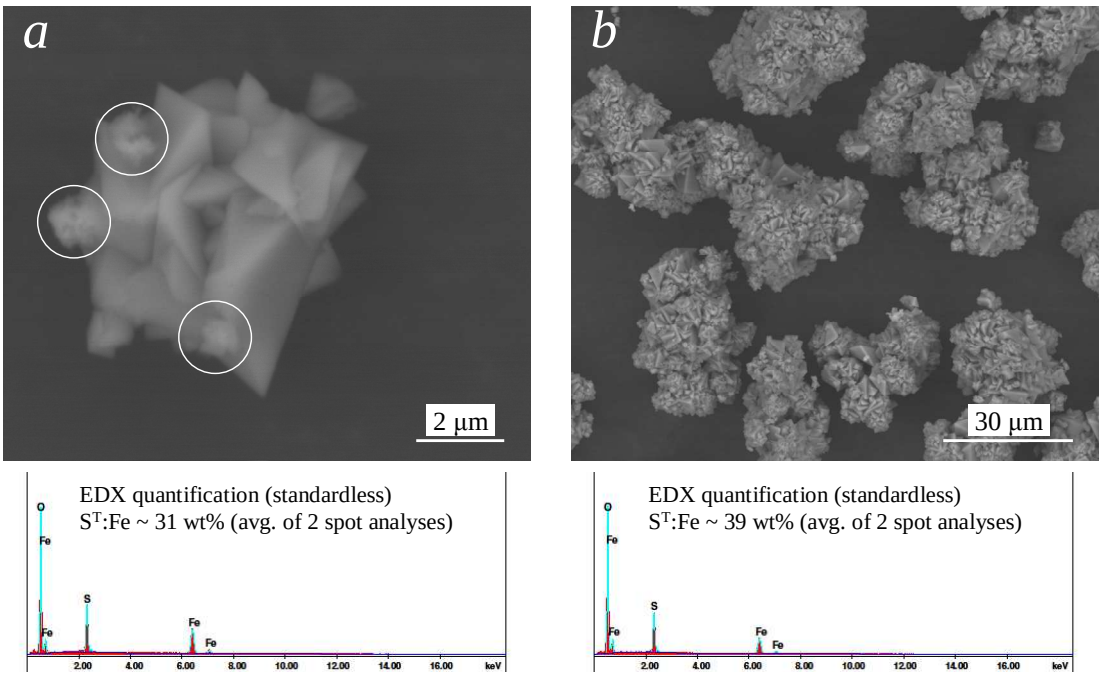

Figure 5.15
BSE images & avg. (random) EDX spot analyses of residues produced at 150ºC (1000 kPa $p_{O2}{}^o$) & 15 g/L Cu, starting with 20 g/L H_2SO_4 & 10 g/L Fe(II): *a*) After 15 min (FPD12: 4% $X_{p,Fe}$, 9% $W_{f,Hem}$); *b*) After 25 min (FPD14: 12% $X_{p,Fe}$, 6% $W_{f,Hem}$).

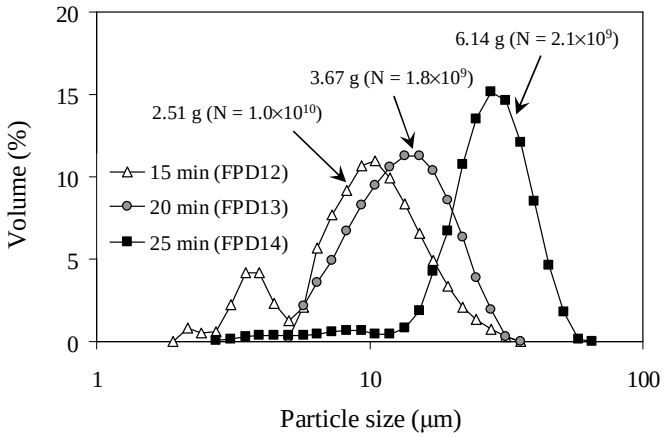

Figure 5.16
PSD, particle mass & number (in parentheses), per kg H_2O, at 150ºC (1000 kPa $p_{O2}{}^o$) & 15 g/L Cu after 15, 20 & 25 min, starting with 20 g/L H_2SO_4 & 10 g/L Fe(II).

Stellenbosch University http://scholar.sun.ac.za

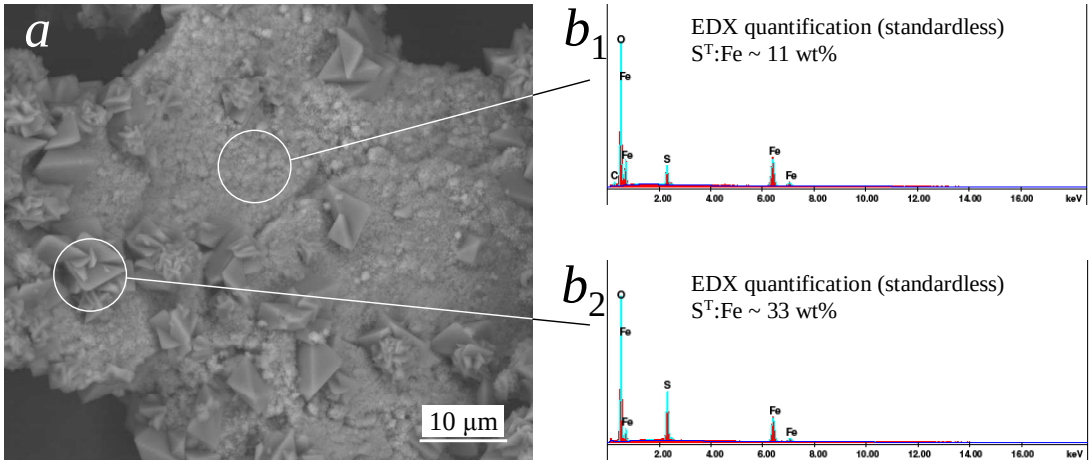

Figure 5.17
Residue produced at 150ºC (1000 kPa p_{O2}º) & 15 g/L Cu, starting with 20 g/L H_2SO_4 & 10 g/L Fe(II): *a*) BSE image after 20 min (FPD13: 11% $X_{p,Fe}$, 8% $W_{f,Hem}$); *b*) EDX spot analyses at two different particle locations.

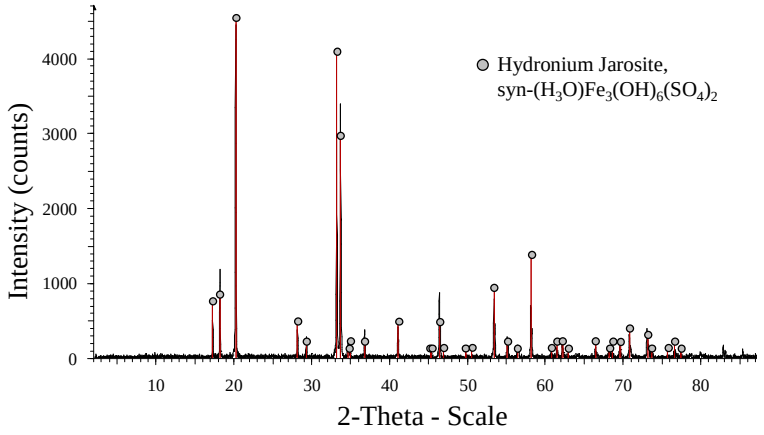

Figure 5.18
XRD pattern of residue produced after 25 min at 150ºC (1000 kPa p_{O2}º) & 15 g/L Cu, starting with 20 g/L H_2SO_4 & 10 g/L Fe(II) (FPD14).

The second series of tests (FPD2; Table 5.5) utilised starting conditions identical to Series FPD1, except for a marginally lower iron(II) concentration (9 *vs.* 10 g/L). Despite the fact that the hematite contents of these residues are about double as compared to Series FPD1, this phase still represents less than 25 % of the total residue mass. Inspection of the BSE images (Figure 5.19) again suggests that the hematite particulates are finely intermixed with the crystalline hydronium jarosite. The dull grey (low density) precipitate is low in sulfur and is assumed to be an amorphous hematite precursor phase (Rx. 5.9), which becomes more stable at these relatively high acid concentrations. This is in line with the thermodynamic expressions developed earlier (Sect. 5.2.3).

Stellenbosch University http://scholar.sun.ac.za

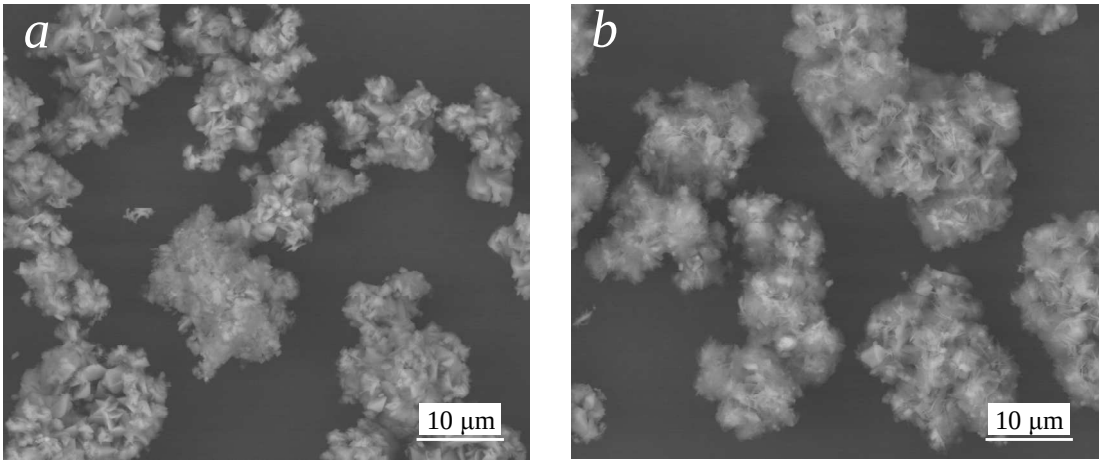

Figure 5.19
BSE images of residues produced at 150ºC (1000 kPa $p_{O2}{}^{o}$) & 15 g/L Cu, starting with 20 g/L H_2SO_4 & 9 g/L Fe(II): *a*) After 15 min (FPD21: 8% $X_{p,Fe}$, 17% $W_{f,Hem}$); b) After 30 min (FPD24: 13% $X_{p,Fe}$, 21% $W_{f,Hem}$).

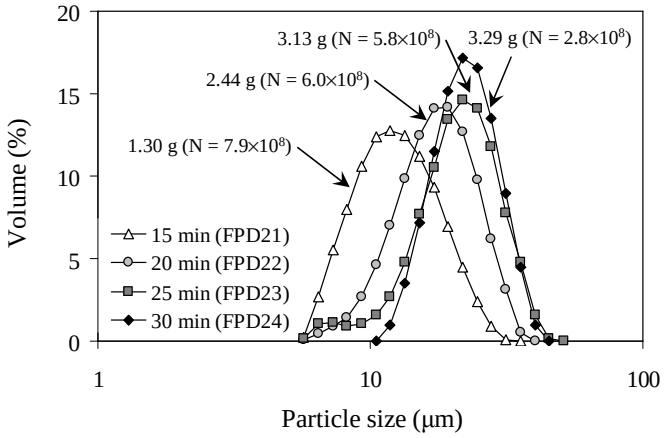

Figure 5.20
PSD, particle mass & number (in parentheses), per kg H_2O, at 150ºC (1000 kPa $p_{O2}{}^{o}$) & 15 g/L Cu after 15, 20, 25 & 30 min, starting with 20 g/L H_2SO_4 & 9 g/L Fe(II).

Figure 5.20 confirms a decrease in the number of particles after 15 minutes, despite the steady increase in precipitate mass over time. Less hydronium jarosite growth occurs under these conditions and the agglomerates appear less compact compared to Series D1 (Figure 5.15 *b*). Judging from the relatively constant hematite content over time (Table 5.5) and comparing the particle morphology (Figure 5.19 *a vs. b*), transformation of hydronium jarosite to hematite (*via* redissolution-precipitation) seems to be slow under terminal acidities of around 15 g/L H_2SO_4. This is important because these acidity conditions are lower than would be expected in a commercial continuous autoclave (Ch. 7), suggesting that the conversion reaction can be neglected in the case of the continuous precipitation model. Notwithstanding, it should be realised that the supersaturation 'path' of iron(III) is significantly different during continuous operation compared to batch operation. Besides the residue data from mineral oxidation in a continuous pilot autoclave,

Stellenbosch University http://scholar.sun.ac.za

the phenomenological model relies mostly on batch data. Batch data are transient and a description of the rates of all the reaction steps as a function of the actual supersaturation is required to simulate continuous systems based on batch data.

The next three series (FPD3, FPD4 & FPD5; Table 5.5) represent higher initial acid and iron(II) concentrations at 150ºC. These tests conditions generally promote crystalline hydronium jarosite formation (App. E.5), with varying (small) amounts of the assumed hematite precursor phase (Figure 5.21 *a*; circled). Figure 5.21 and Figure 5.22 again illustrate that the average hydronium jarosite growth rate is highly dependent on the iron(III) supersaturation level. This growth clearly results in smooth individual crystallite surfaces but many different orientations, most likely due to a twinned growth mechanism under these relatively high supersaturation conditions.

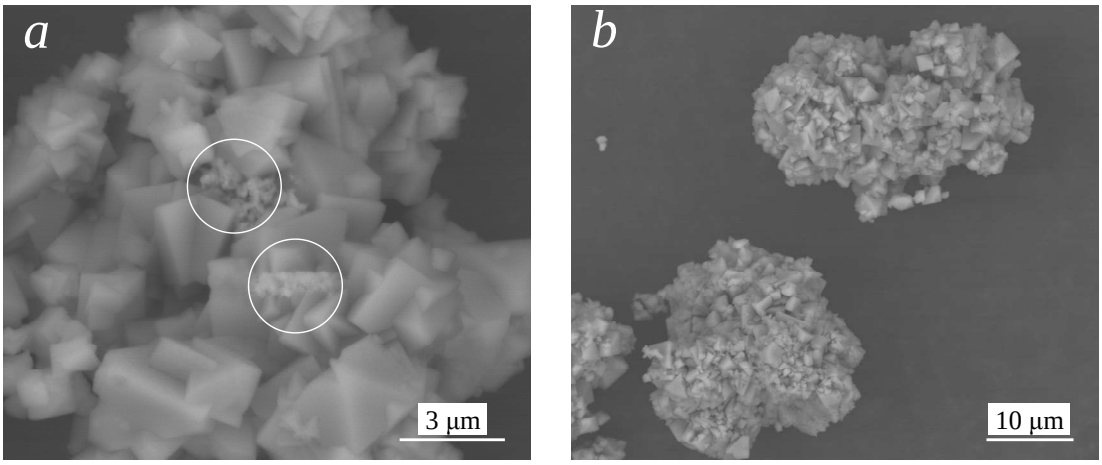

Figure 5.21
BSE images of residues produced at 150ºC (1000 kPa p_{O2}º), 15 g/L Cu & 25 g/L H_2SO_4: *a*) After 10 min, starting with 15 g/L Fe(II) (FPD31); *b*) After 60 min, starting with 12 g/L Fe(II) (FPD43).

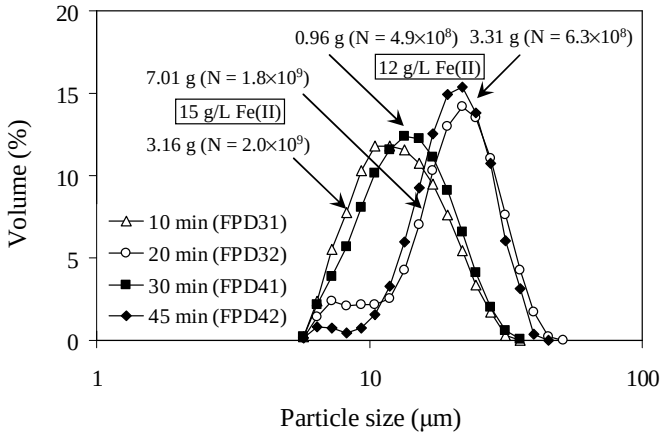

Figure 5.22
PSD, particle mass & number (in parentheses), per kg H_2O, at 150ºC (1000 kPa p_{O2}º), 15 g/L Cu & 25 g/L H_2SO_4 after 10 & 20 min, starting with 15 g/L Fe(II) (FPD31 & FPD32), compared to after 30 & 45 min, starting with 12 g/L Fe(II) (FPD41 & FPD42).

Stellenbosch University http://scholar.sun.ac.za

Comparison of the particle numbers in Figure 5.22 suggests that the initial agglomerates are established relatively early on under these higher acidity levels. Growth of crystalline hydronium jarosite then increases the agglomerate bulk density and overall size over time.

Although these polycrystalline structures are remnants of the initial (amorphous) agglomerates (next section), hydronium jarosite particle growth is accompanied by a general increase in particle mass. A topochemical reaction boundary assumption (App. F.4) is therefore the logical premise of the phenomenological model, which imposes an idealised surface area on the simulation.

Hematite precipitation at 140 ℃ (1000 kPa oxygen) in the medium-high acid (7.5-20 g/L H_2SO_4) and medium-high iron(II) (5-10 g/L Fe) concentration regimes, in copper sulfate background

This section compares the particle morphology and size and the precipitation rate in the H_2SO_4-$CuSO_4$ system at 140°C, medium-high initial acid (7.5-20 g/L) and progressively higher iron(II) (5-10 g/L) concentrations. The detailed mass balances and BSE images can be found in Appendix E.6 and the results are summarised in Table 5.6.

Table 5.6
Results of iron(III) precipitation at tests 140ºC (1000 kPa p_{O2}[o]), starting with 7.5 to 20 g/L H_2SO_4, 5 to 10 g/L Fe(II) & 15 g/L Cu.

[a] Test	Time	[b] [A, Fe]	$[H_2SO_4]$	[c] $[Fe^T]\cdot10^2$	[d] Cu	[d] Fe	[d] S^T	[e] S^T:Fe	$X_{p,Fe}$	$W_{f,Hem}$
–	(min)	(g/L)	(mol/kg)	(mol/kg)	(%)	(%)	(%)	(%)	(%)	(%)
FPE11	10	7.5, 5	0.079	6.31 (5.1)	0.87	52.5	3.5	6.6 (7)	33	82
FPE12	20	7.5, 5	0.095	5.33 (3.8)	1.57	49.8	4.3	8.7 (8)	45	74
FPE13	30	7.5, 5	0.1215	3.22 (4.0)	1.37	50.0	4.05	8.1 (9)	66	76
FPE21	10	12.5, 5.5	0.090	9.80 (3.0)	1.00	45.0	5.2	11.5 (14)	5	62
FPE22	20	12.5, 5.5	0.106	8.36 (2.8)	1.45	45.1	6.0	13.2 (15)	18	56.5
FPE23	30	12.5, 5.5	0.1215	7.05 (2.0)	0.97	45.8	5.9	12.9 (13)	31	57
FPE31	20	15, 6.5	0.117	11.32 (2.4)	1.28	42.1	7.2	17.0 (16)	7.5	44
FPE32	30	15, 6.5	0.117	10.61 (2.1)	0.87	42.3	7.7	18.2 (18)	13	40
FPE33	40	15, 6.5	0.132	9.78 (1.8)	0.89	44.7	6.8	15.1 (15)	19	49
FPE41	20	15, 7.5	0.106	12.84 (2.6)	0.62	39.9	9.1	22.8 (22)	9	28.5
FPE42	30	15, 7.5	0.116	11.72 (2.3)	0.38	38.1	10.8	28.3 (23)	15	17
FPE43	40	15, 7.5	0.127	11.04 (1.6)	0.70	42.9	10.4	24.2 (23)	21	25
FPE51	30	20, 10	0.127	17.90 (1.9)	0.05	36.5	10.3	28.2 (27)	3	16.5
FPE52	45	20, 10	0.138	16.83 (1.2)	0.10	36.0	10.6	29.4 (25)	10	14

[a] 0.05 g/L Arbo A02 (LS) & Orfom 2 (QB) added initially; [b] Initial H_2SO_4 & Fe(II), respectively; [c] Bracketed values refer to Fe(II) left in sln. (wt. % of Fe^T); [d] Wt. % in residue; [e] S^T:Fe wt. ratio (avg. from EDX spot analyses in brackets).

Stellenbosch University http://scholar.sun.ac.za

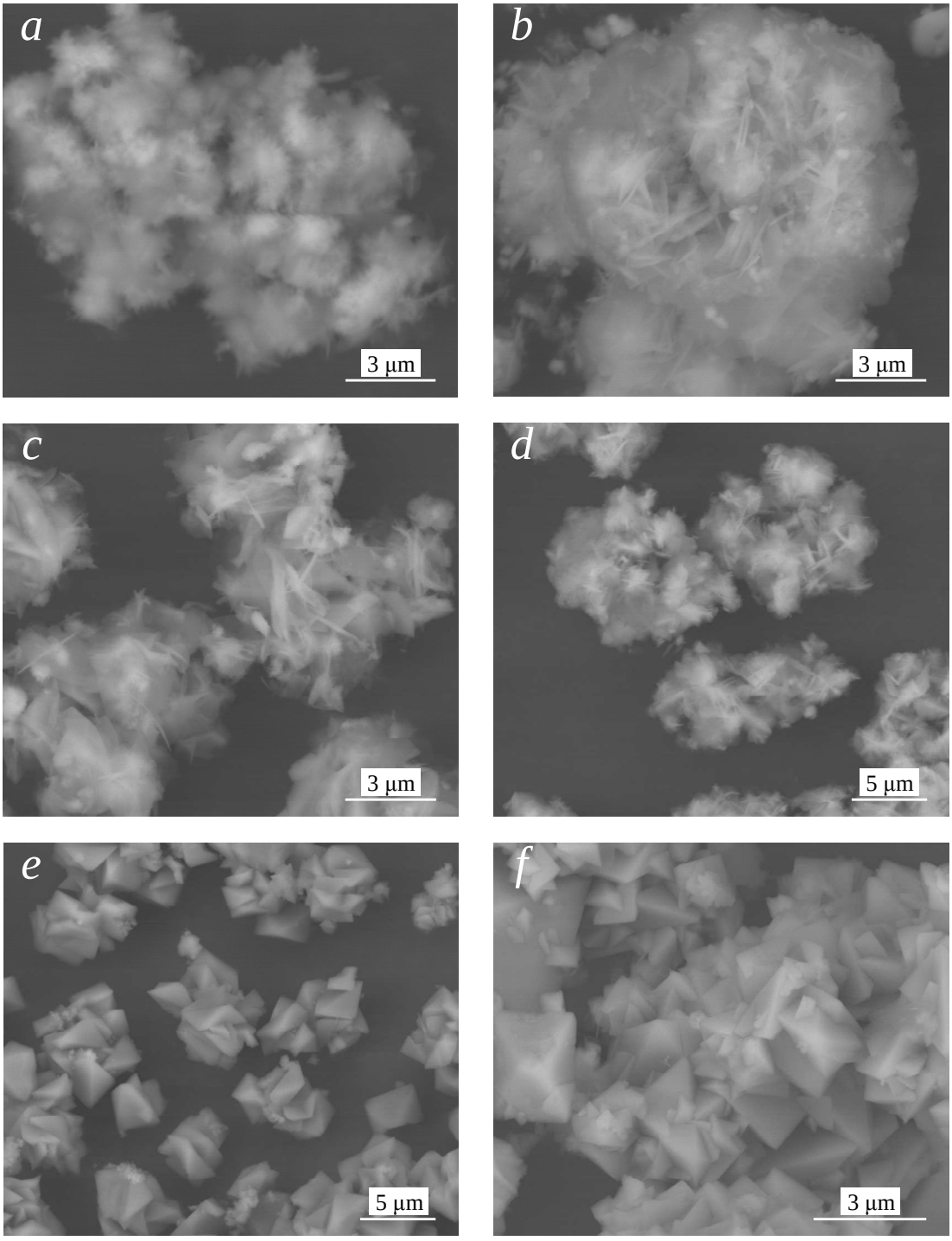

Figure 5.23
BSE images of residues produced at 140ºC (1000 kPa p_{O2}º) & 15 g/L Cu: *a*) After 10 min, starting with 7.5 g/L H_2SO_4, 5 g/L Fe(II) (FPE11; 82% $W_{f,Hem}$); *b*) After 10 min, starting with 12.5 g/L H_2SO_4, 5.5 g/L Fe(II) (FPE21; 62% $W_{f,Hem}$); *c*) After 20 min, starting with 15 g/L H_2SO_4, 6.5 g/L Fe(II) (FPE31; 44% $W_{f,Hem}$); *d*) After 20 min, starting with 15 g/L H_2SO_4, 7.5 g/L Fe(II) (FPE41; 29% $W_{f,Hem}$); Starting with 20 g/L H_2SO_4 & 10 g/L Fe(II): *e*) After 30 min (FPE51; 3% $X_{p,Fe}$, 17% $W_{f,Hem}$); *f*) After 45 min (FPE52; 10% $X_{p,Fe}$, 14% $W_{f,Hem}$).

Stellenbosch University http://scholar.sun.ac.za

The same trends are observed as at higher operating temperatures, *i.e.*, a lower overall precipitation rate with increasing initial acid concentration. Again, the BSE images (Figure 5.23) reveal that the spheroidal (comparatively brighter) hematite aggregates (Figure 5.23 *a*) consist of similar (characteristic) size particulates. The formation of these hematite nano-aggregates dominates at the lower initial acid levels, while hydronium jarosite growth dominates when higher initial acid and iron(II) concentrations are applied.

The lower acid regime (< 15 g/L H_2SO_4) first yields an amorphous-type jarosite phase (Figure 5.23 *b*, *c* & *d*), but this then becomes more crystalline at longer reaction times. Under these conditions, these polycrystalline structures are remnants of the initial (more amorphous) agglomerates. Figure 5.23 *e* and *f* clearly illustrate that hydronium jarosite precipitation is driven by preferential growth along the lowest energy axes at the higher acid initial concentration of 20 g/L H_2SO_4. This results in smooth individual crystallite surfaces, but with many different crystal orientations, again, probably *via* a twinned growth mechanism.

Figure 5.24 and Figure 5.25 present examples of these residue PSDs, illustrating that they often become relatively narrow at longer reaction times. As mentioned before, no attempt is made in this study to relate these observed PSDs to the overall iron(III) precipitation rate. The initial hematite and hydronium jarosite agglomerates (*e.g.*, Figure 5.23 *a* to *d*) act as precursor structures and influence the final PSDs in unpredictable ways. Idealised hematite and hydronium jarosite surface areas (particle sizes) are assumed adequate from the phenomenological modelling perspective.

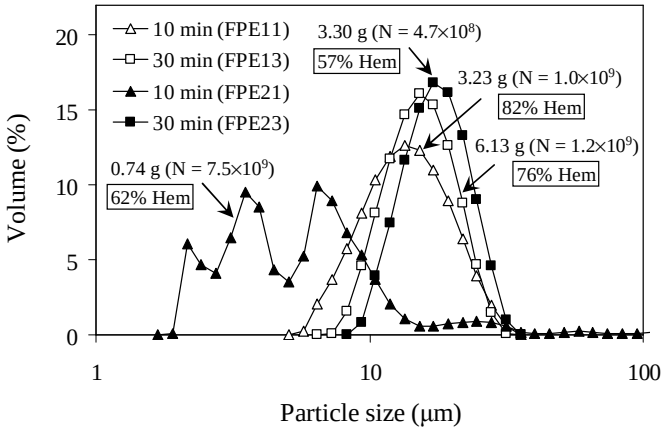

Figure 5.24
PSD, particle mass & number (in parentheses), per kg H_2O, at 140ºC (1000 kPa $p_{O2}{}^{o}$) & 15 g/L Cu, after 10 & 30 min, starting with 7.5 g/L H_2SO_4 & 5 g/L Fe(II) (FPE11 & FPE13) & starting with 12.5 g/L H_2SO_4 & 5.5 g/L Fe(II) (FPE21 & FPE23).

Stellenbosch University http://scholar.sun.ac.za

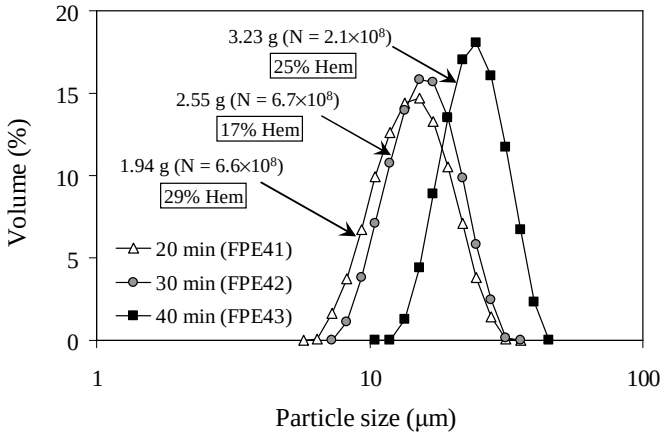

Figure 5.25
PSD, particle mass & number (in parentheses), per kg H_2O, at 140ºC (1000 kPa $p_{O2}{}^o$), 15 g/L Cu, after 20, 30 & 40 min, starting with 15 g/L H_2SO_4 & 7.5 g/L Fe(II) (FPE41, FPE42 & FPE43).

Hematite precipitation at 130 ºC (1000 kPa oxygen) in the low-medium acid (4-12.5 g/L H_2SO_4) and around low iron(II) (3.5-5.5 g/L Fe) concentration regimes, in copper sulfate background

This section compares the particle morphology and size and the precipitation rate in the H_2SO_4-$CuSO_4$ system at 130ºC. To prevent excessive hydronium jarosite formation and since these tests also aim to identify possible surface interactions between the different precipitate phases, lower initial acid and iron(II) concentration regimes were utilised, *i.e.*, 4 to 12.5 g/L H_2SO_4 and 3.5 to 5.5 g/L Fe(II). The detailed mass balances and BSE images can be found in Appendix E.7 and the results are summarised in Table 5.7.

Table 5.7
Results of iron(III) precipitation tests at 130ºC (1000 kPa $p_{O2}{}^o$), starting with 4 to 12.5 g/L H_2SO_4, 3.5 to 5.5 g/L Fe(II) & 15 g/L Cu.

[a] Test	Time	[b] [A, Fe]	$[H_2SO_4]$	[c] $[Fe^T]\cdot10^2$	[d] Cu	[d] Fe	[d] S^T	[e] S^T:Fe	$X_{p,Fe}$	$W_{f,Hem}$
–	(min)	(g/L)	(mol/kg)	(mol/kg)	(%)	(%)	(%)	(%)	(%)	(%)
FPF11	15	4, 3.5	0.063	3.03 (7.6)	2.43	48.8	3.6	7.4 (8)	53	81
FPF12	30	4, 3.5	0.074	2.55 (4.3)	0.99	52.8	2.9	5.5 (6)	63	88
FPF13	45	4, 3.5	0.084	1.72 (6.4)	2.27	47.6	2.8	5.9 (6)	74	88
FPF21	20	8.5, 4.5	0.063	7.70 (3.8)	1.11	46.3	4.9	10.6 (12)	6	66
FPF22	40	8.5, 4.5	0.084	5.58 (3.4)	0.91	47.5	4.8	10.1 (12)	33	67
FPF23	60	8.5, 4.5	0.100	4.41 (3.2)	1.12	45.1	5.05	11.2 (11)	47	63
FPF31	30	12.5, 5.5	0.101	9.83 (2.6)	1.00	44.7	6.1	13.6 (15)	9	55
FPF32	45	12.5, 5.5	0.095	9.28 (2.4)	0.93	42.3	7.3	17.2 (19)	8.5	43
FPF33	60	12.5, 5.5	0.111	8.26 (2.3)	0.73	43.7	6.3	14.4 (14)	19	52

[a] 0.05 g/L Arbo A02 (LS) & Orfom 2 (QB) added initially; [b] Initial H_2SO_4 & Fe(II), respectively; [c] Bracketed values refer to Fe(II) left in sln. (wt. % of Fe^T); [d] Wt. % in residue; [e] S^T:Fe wt. ratio (avg. from EDX spot analyses in brackets).

Stellenbosch University http://scholar.sun.ac.za

Figure 5.26 *a* illustrates that the lowest acid and iron concentrations (4 g/L H_2SO_4 & 3.5 g/L Fe(II); Series FPF1) yielded the highest hematite abundance. The phase consists of spheroidal nano-aggregates, which agglomerate into larger units. At higher acid concentrations, the individual hematite particulates become finely intermixed with the hydronium jarosite crystals (Figure 5.26 *c*). Small hematite spheroidal composites are still visible at higher acid concentrations, but their sizes are only marginally larger than the individual particulates (Figure 5.26 *c* & *d*; circled).

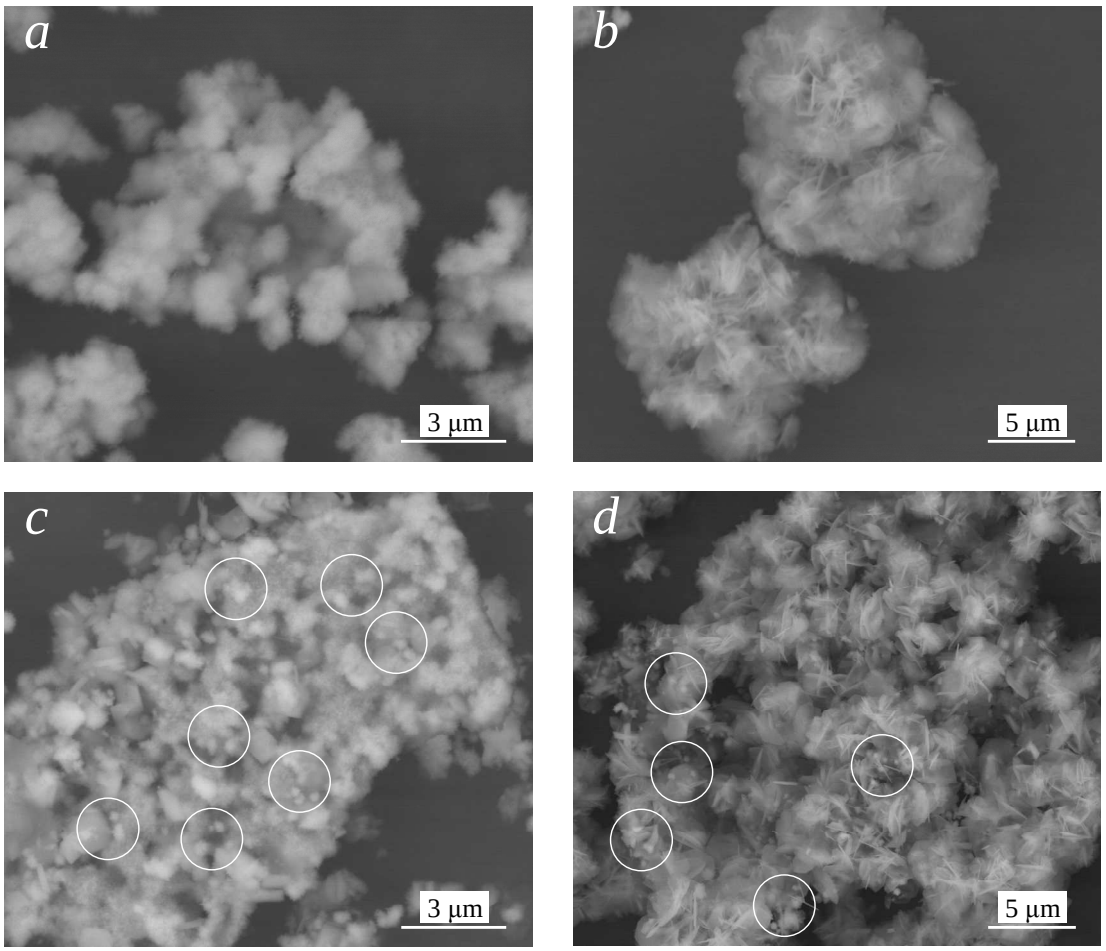

Figure 5.26
BSE images of residues produced at 130ºC (1000 kPa p_{O2}^{o}), 15 g/L Cu: *a*) After 45 min, starting with 4 g/L H_2SO_4, 3.5 g/L Fe(II) (FPF13; 88% $W_{f,Hem}$); *b*) After 60 min, starting with 8.5 g/L H_2SO_4, 4.5 g/L Fe(II) (FPF23; 63% $W_{f,Hem}$); Starting with 12.5 g/L H_2SO_4, 5.5 g/L Fe(II): *c*) After 30 min (FPF31; 55% $W_{f,Hem}$); *d*) After 45 min (FPF32; 43% $W_{f,Hem}$).

Similarly to the trends at higher temperatures, increased acid concentration results in higher hydronium jarosite content, forming agglomerates with increasingly less crystalline and smaller hematite particulates (see App. E.7). Figure 5.26 *b* illustrates that the hydronium jarosite crystal growth is constrained by hematite particulate formation in the case of Series FPF2, starting with 8.5 g/L H_2SO_4 and 4.5 g/L Fe(II). These conditions result in insignificant compositional changes over time (~65% hematite), despite a significant overall mass gain.

Stellenbosch University http://scholar.sun.ac.za

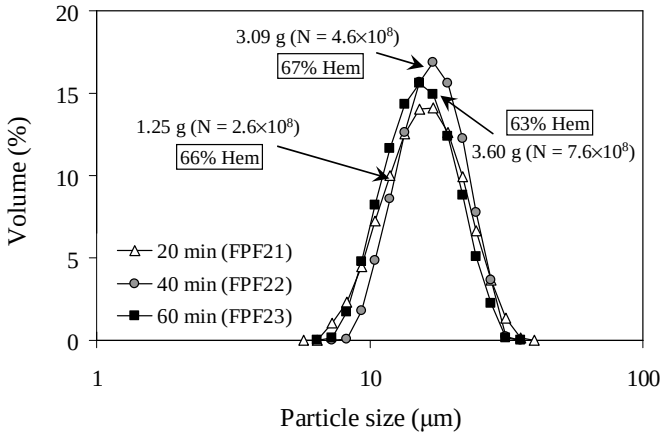

Figure 5.27
PSD, particle mass & number (in parentheses), per kg H_2O, at 130ºC (1000 kPa p_{O2}º), 15 g/L Cu, after 20, 40 & 60 min, starting with 8.5 g/L H_2SO_4 & 4.5 g/L Fe(II) (FPF21, FPF22 & FPF23).

Figure 5.27 illustrates the PSDs of these tests, confirming that agglomerate formation overshadows the individual particle growth effects. The above results confirm that the hematite and hydronium jarosite phases can be produced simultaneously and that the phenomenological model should be based on calculated (idealised) particle surface areas.

The above results support the methodology of assigning primary and secondary nucleation, accompanied by rapid and limited growth, to hematite particulate formation, while continuous growth on existing surfaces is assigned to the hydronium jarosite phase.

5.4.2 Regression of the thermodynamic model

Thermodynamics are used as the departure point to describe the rate of iron(III) precipitation (Sect. 5.2.3). The general lack of thermodynamic data, as well as the exact nature and abundance of the dominant iron(III) species at high temperatures and varying solution compositions, necessitates the simplified approach of only recognising the neutral $FeH(SO_4)_2°$ and $Fe(OH)_3°$ species. The formation of the dominant $FeH(SO_4)_2°$species is described as follows (Ch.2, Sect. 2.4.3):

$$Fe^{3+} + 2SO_4^{2-} + H^+ \Leftrightarrow FeH(SO_4)_2^o \qquad 5.41$$

The inclusion of the $Fe(OH)_3^o$ species (Sect. 5.2.3) is convenient but cognisance has to be taken of the fact that this species rather arbitrarily represents a host of possible complex species at lower acidities (< 0.15 mol/kg H_2SO_4), demanding that the dominant $FeH(SO_4)_2^o$ species assume thermodynamic values unique to this study.

For the sake of maintaining internal consistency, the thermodynamic data of all the species partaking in these iron(III) equilibria are based on the values of Liu *et al*. (2003). The Gibbs free

Stellenbosch University http://scholar.sun.ac.za

energy of formation ($\Delta G°$) value of the $FeH(SO_4)_2°$ species is treated as an adjustable parameter to best represent the hematite solubility data of Reid and Papangelakis (2006). Since no heat capacity parameters (Eq. 2.34) are available for the $FeH(SO_4)_2°$ species, and to simplify the problem, the heat capacity ($\Delta C_p°$) of Reaction 5.41 is assumed to be zero, *i.e.*, a constant reaction enthalpy ($\Delta H°$) is applied (Eq. 2.43). The detailed calculation methodology and results are summarised Appendix E.8. The standard thermodynamic values (at the reference temperature of 25°C) involving iron(III) species are summarised in Table 5.8.

Table 5.8
Standard thermodynamic values at 25°C used to obtain the iron(III) equilibrium constants.

[a] Species	$\Delta G°$ (kJ/mol)	$\Delta H°$ (kJ/mol)	[b] Kelley-a (J/mol.K)	[b] Kelley-b (J/mol.K^2)	[b] Kelley-c (J.K/mol)
H_2O	-237.18	-285.85	75.35	–	–
Fe^{3+}	-17.238	-49.58	-142.67	–	–
SO_4^{2-}	-744.46	-909.6	-269.37	–	–
$FeH(SO_4)_2°$	[c] -1529.75	[d, e] -1726.71	[e] -681.41	–	–
$Fe(OH)_3°$	-660.32	-801.17	-19.79	–	–
Fe_2O_3	-742.2	-824.2	103.85	–	–
$(H_3O)Fe_3(OH)_6(SO_4)_2$	[f] -3226.4 ± 4.6	[f] -3770.2 ± 4.6	[f] 287.2	[f] 628.1	[f] -32.86

[a] All data from Liu *et al.* (2003), unless indicated otherwise; [b] Pertaining to the Maier-Kelley equation (Eq. 2.34); [c] Regressed to hematite solubility between 0.12 & 0.75 mol/kg H_2SO_4 at 130°C, 150°C, 170 °C (*ref.* Reid & Papangelakis, 2006), using the Density function (Eq. 2.44) to extrapolate $K°_{FeIII}$ (Rx. 5.18); [d] Calc. from the data in Cifuentes *et al.* (2006) (App. E.8); [e] Assuming $\Delta C_p° = 0$ J/mol.K for Rx. 5.41; [f] Majzlan *et al.* (2004).

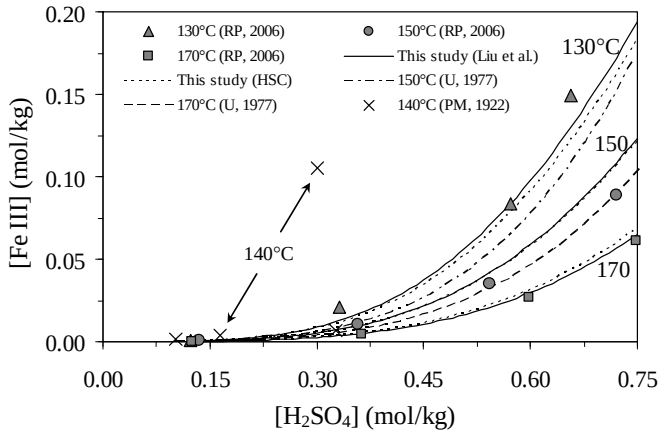

Figure 5.28
Comparison between the calculated & measured α-Fe_2O_3 solubilities. The solid lines represent the regression results of this study *ref.* Reid & Papangelakis (RP, 2006), using thermodynamic values of Liu *et al.* (2003). The data of Umetsu *et al.* (U, 1977) are presented as smooth curves, using density (Eq. 7.49) to convert to molality (Eq. 2.2). Posnjak & Merwin (PM, 1922) refer to 140°C.

Stellenbosch University http://scholar.sun.ac.za

The regression results are summarised in Figure 5.28, which highlights the considerable spread of reported solubilities, especially with regards to the data of Posnjak and Merwin (1922). The data of Umetsu *et al.* (1977) are significantly different to the values of Reid and Papangelakis at higher acid concentrations. Reid and Papangelakis (2006) ascribed this to the experimental procedure utilised by Umetsu *et al.* (1977); they did not withdraw their samples 'at temperature', but allowed the autoclave to cool to 100°C before sample retrieval, which resulted in some redissolution of the precipitated hematite. This statement is consistent with Figure 5.28, which shows that the hematite solubility increases rapidly with decreasing temperature. On the other hand, since Reid and Papangelakis (2006) did not analyse the solid phase sulfur content, the precipitation of hydronium jarosite or BFS may have influenced the solubility, which casts some doubt on the accuracy of their results at higher acidities.

The regression makes use of only one adjustable parameter, *i.e.*, $\Delta G°_{25°C}$ of the $FeH(SO_4)_2°$ species, and, considering the various assumptions made, Figure 5.29 illustrates that this model gives a good representation of the hematite solubility. This thermodynamic framework is also used to calculate the solubility of hydronium jarosite (see App. E.8). The calculated hydronium jarosite solubility value of 0.11 mol/kg Fe(III) at 140ºC and 0.3 mol/kg H_2SO_4, *i.e.*, corresponding to the ±4.6 kJ/mol uncertainty in the standard thermodynamic values of Majzlan *et al.* (2004), is close to the average measured value of Posnjak and Merwin (1922) of 0.13 mol/kg Fe(III) (Figure 5.29). Although the model underpredicts the jarosite solubility at higher acidities, no conclusions can be drawn without generating more data using modern measurement techniques. For example, Posnjak and Merwin (1922) cooled the reaction vessel before the contents were removed and filtered. This could also be the reason for the questionable hematite solubility point at 0.3 mol/kg H_2SO_4 in Figure 5.28.

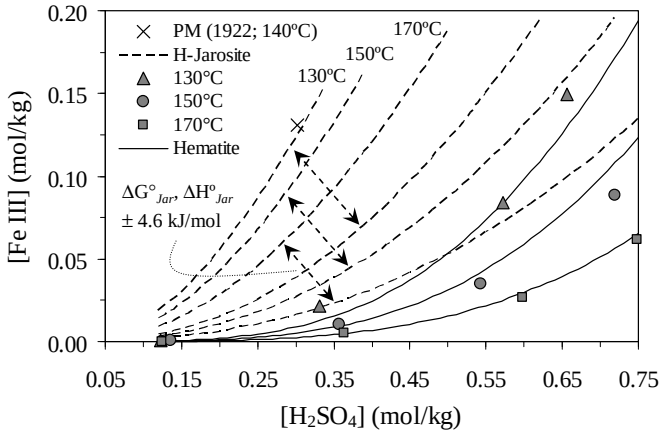

Figure 5.29
Calculated solubilities of α-Fe_2O_3 & H-Jar ($\Delta G°_{Jar}$ & $\Delta H°_{Jar}$ varied ±4.6 kJ/mol; Majzlan *et al.*, 2004). The closed symbols represent the measured Fe_2O_3 solubilities (Reid & Papangelakis, 2006) used in the regression. The open symbol is the avg. H-Jar solubility (Posnjak & Merwin, 1922).

Stellenbosch University http://scholar.sun.ac.za

Figure 5.29 suggests that hydronium jarosite is metastable in comparison to hematite, particularly under typical batch and continuous autoclave conditions (< 0.3 mol/kg H_2SO_4). However, the tendency of hydronium jarosite to form larger surfaces further decelerates (Eq. 5.30) the slow conversion of hydronium jarosite to hematite, especially above about 0.1 mol/kg H_2SO_4.

The above thermodynamic basis is therefore consistent with the general rate expression of Section 5.2.6, which is now expanded based on the experimental insights of Section 5.4.1.

5.4.3 Phenomenological modelling framework

Based on the above experimental evidence, it is reasonable to assume that hematite and hydronium jarosite precipitation are strongly interrelated, demanding a simplified approach. Different mechanisms would also be expected to come into play over the evolution of time as the degree of supersaturation varies, whether reflecting transient or continuous behaviour. The selection of one specific mechanism is therefore in itself a major simplification: the following mechanistic proposals attempt to quantify the phenomenon of iron(III) precipitation in batch and continuous MT autoclaves.

Primary formation of small hematite particles of similar (characteristic) size

Figure 5.29 reflects the general decrease in hematite solubility with decreasing acid concentration. In the low acidity range, hematite solubility decreases dramatically, *e.g.*, at 155ºC, the above thermodynamic model yields calculated solubilities of 2×10^{-4}, 1×10^{-4}, 6×10^{-5} and 6×10^{-6} mol/kg Fe(III), corresponding to 0.13, 0.11, 0.09 and 0.05 mol/kg H_2SO_4, respectively. MT chalcopyrite oxidation typically yields a significant proportion of elemental sulfur (~60%; Ch. 6), causing the initial fast iron dissolution process to be accompanied by a drop in acid concentration. This is the reason why iron(II) was utilised in the batch precipitation testwork.

Due to the high initial supersaturation and the relatively high interfacial energy, hematite nucleation is accompanied by rapid growth, which, in turn, causes the supersaturation to dissipate rapidly, leading to a large number of small particulates of similar size. The rapid growth effect is therefore combined with the nucleation term to yield particles of characteristic size, L_{Hem}, so that the iron(III) precipitation rate (mol Fe/kg.min) as primary hematite particles, $R_{FeIII,Hem(\text{prim})}$ is then:

$$R_{FeIII,Hem(\text{prim})} = \tilde{k}_{Hem} L_{Hem}^3 \cdot J_{\text{prim}} \qquad 5.42$$

The nucleation term (Eq. 5.37) may be expressed as follows, after neglecting the complex temperature dependency of the correction factor, ξ (see David & Klein, 2001), so that only two adjustable parameters essentially remain, *i.e.*, k_{prim} and $\xi\cdot\gamma^3_{Hem}$:

Stellenbosch University http://scholar.sun.ac.za

$$J_{prim} = k_{prim} \cdot exp\left(\frac{-\xi K_{Hem}}{(2\,ln S_{Hem})^2} \cdot \left(\frac{\gamma_{Hem}}{T} \right)^3 \right) \qquad 5.43$$

where the pre-exponential efficiency factor, k_{prim} (1/kg.min), is assumed to be a weak function of the temperature and K_{Hem} adopts the constant value of 1.6304×10^{13} $m^6.K^3/J^3$. The proportionality constant, $\tilde{k}_{Hem}$ (mol Fe/μm^3), translates the one-dimensional size increase into an iron(III) molal concentration decrease. This constant is obtained using an analogous approach, opposite in sign, to leaching (see Eq. F.28 & related discussions):

$$\tilde{k}_{Hem} = -\frac{3\rho_{Hem}\Phi_v \nu_{Fe,Hem}}{Mw_{Hem}\Phi_a} \qquad 5.44$$

where the stoichiometric coefficient of iron(III) in hematite, $\nu_{Fe,Hem}$, is equal to 2, yielding the value of -3.2813×10^{-14} mol Fe/μm^3_{Hem} for spherical (idealised) particles.

It should be emphasised that the above simplifications would likely collapse above a critical acid activity, *i.e.*, where primary hydronium jarosite nucleation in the bulk solution might become dominant. Since most batch and continuous tests reflect lower initial acidities (< 25 g/L H_2SO_4), the primary nucleation – rapid growth of hematite is the logical premise of this study. The experimental results in Section 5.4.1 have confirmed that these nano-sized hematite particles are typically about 0.15 µm in size.

Hydronium jarosite growth on existing surfaces

The phenomenological model assumes that each primary particle remains in contact with the surrounding solution and retains its identity, *i.e.*, agglomeration is neglected. Although not yet proven, the strong association between hematite and sulfate ion (Sect. 5.2.5) is thought to be the precursor to the (initial) formation of amorphous hydronium jarosite on hematite surfaces, as suggested by the BSE images in Section 5.4.1. This is not entirely surprising, since sulfate complexes of iron(III) are known to be strong (Ch. 2, Sect. 2.4.3; also Sect. 5.2.2). The proposal of hydronium jarosite nucleation and growth on hematite surface is not that unusual, *e.g.*, Blakey and Papangelakis (1994) concluded that hematite surfaces acted as seed for hydronium alunite, $(H_3O)Al_3(OH)_6(SO_4)_2$, growth after high temperature (230-270ºC) leaching of boehmite (AlOOH).

To summarise, the following general trends are identified regarding the presence of metastable amorphous phases, preceding the thermodynamically stable hematite phase:

- Ferrihydrite ($Fe_2O_3 \cdot 0.5H_2O$) may compete with hematite in nitrate (*e.g.*, Van der Woude *et al.*, 1983) or other media (see Cornell & Schwertmann, 2003)

Stellenbosch University http://scholar.sun.ac.za

- Akaganeite (β-FeOOH) may compete with hematite in pure chloride medium (Cornell & Schwertmann, 2003; Dutrizac & Riveros, 1999; Sugimoto *et al.*, 1998), and
- Hydronium-jarosite, or other hydroxy-sulfate salts, may compete with hematite in media containing sulfate (*e.g.*, Kandori *et al.*, 2004; Zerella *et al.*, 1983).

These trends are consistent with the concept of faster growth of the metastable phases on existing surfaces due to the lower comparative interfacial tension (Sect. 5.2.4). Hydronium jarosite precipitation is therefore often kinetically favoured above hematite precipitation under typical leaching conditions (0.15-0.30 mol/kg H_2SO_4). Preferential growth along particular crystal planes within the amorphous precursor structures leads to different initial growth phenomena. Attempting to simulate such phenomena, as well as the agglomeration effects, is not warranted in the context of a phenomenological model, since a wide range of supersaturation ratios and associated growth mechanisms could be valid over the course of a leaching-precipitation process. Furthermore, since the growth of crystalline hydronium jarosite often dominates iron(III) precipitation at longer reaction times under typical MT autoclave conditions, the topochemical boundary assumption (Sect. 5.2.6) is adopted. The rate of iron(III) precipitation (mol Fe/kg.min) as hydronium jarosite growth on existing surfaces is then as follows:

$$R_{FeIII,Jar} = \tilde{k}_{Jar} \cdot a_{Fe} \cdot G_{Jar} \qquad 5.45$$

where the proportionality constant, $\tilde{k}_{Jar}$, has a value of -8.4248×10^{-15} mol Fe/μm^3_{Jar}, assuming that the particles maintain their spherical shape as they grow, *i.e.*, comply with McCabe's (ΔL) rule (see Mersmann *et al.*, 2001b). Since the phenomenological model does not need to cater for any artificial manipulation of acid levels, *e.g.*, by pumping oxides or other neutralising agents into the downstream compartments of the continuous autoclave, the conversion to hematite at lower acidities (< 0.15 mol/kg H_2SO_4) can be dealt with phenomenologically by decreasing the value of G_{Jar}. No distinction is therefore made between growth on existing jarosite and barren hematite substrate surfaces. This assumption is based on the strong adsorption of the sulfate ion on hematite (noted earlier). It further assumes that the growth rate does not vary with particle size (McCabe's rule), so that the calculated particle size, L_{Fe} (μm), and total (spherical) surface area, a_{Fe} (μm^2/kg H_2O), of precipitated iron(III) (per unit mass water) in the batch reactor are, respectively as follows:

$$L_{Fe} = L_{Hem} + (G_{Jar} \cdot t) \qquad 5.46$$

$$a_{Fe} = \sum_{L_{Fe}} \Phi_a L_{Fe}^2 \cdot N_{Fe,L} \qquad 5.47$$

where $N_{Fe,L}$ represents the total iron(III) particle number (per unit mass water) in size class L_{Fe}.

Stellenbosch University http://scholar.sun.ac.za

Secondary formation of small hematite particles of similar (characteristic) size

Various BSE images in Section 5.4.1 suggest that secondary hematite particles may form on existing precipitate surfaces.

As emphasised in various publications, *e.g.*, Mersmann *et al*. (2001a) and Söhnel and Garside (1992), secondary nucleation mechanisms are often relevant in practical systems. Randolph and Larson (1988) indicated that the energy of contact nucleation is important and smaller particles (< 100 µm) would not be expected to be instrumental in producing secondary nuclei. A power-law rate expression is often used to describe such mechanisms, which is typically proportional to the pulp density (mass) and also related to the 'degree' of mechanical agitation. David and Klein (2001) and Söhnel and Garside (1992) indicated that secondary nucleation could become relevant during the precipitation of sparingly soluble substances when large crystals are brought into contact with a solution at lower supersaturation, either *via* the above contact-type mechanism or due to particle fracturing, *e.g.*, of dendrites. Based on the experimental evidence of this study (BSE images), these kinds of secondary nucleation mechanisms are unlikely to be prominent during iron(III) precipitation under typical autoclave leaching conditions. Therefore, the term 'secondary nucleation' in this study refers to a true surface nucleation mechanism, where hematite nuclei are formed due to solid/solution interactions and lead to new particles.

Söhnel and Garside (1992) highlighted three secondary nucleation mechanisms that may play a role during precipitation (reactive crystallisation):

- the formation of surface nuclei that grow, *e.g.*, as dendrites, on the surface of the mother crystal and subsequently break off. However, as indicated above, this mechanism should not be assigned to nucleation
- the formation of nuclei in the liquid phase adjacent to the crystal due to localised structural changes of the liquid in that position, and
- the formation of nuclei in the adsorption layer on the surface, due to the presence of crystalline molecular aggregates, from where they are washed into solution.

The latter two mechanisms are assumed to be of particular relevance to the surface nucleation of hematite in solid suspensions.

Although growth on seed particles is more likely in the case of jarosites, it is unclear at what point (in the degree of supersaturation) secondary nucleation would start to dominate over a continuous growth mechanism. The following examples of the effect of seeding on iron(III) precipitation emphasise the 'grey' area that currently exists with regard to the growth and nucleation mechanisms at high supersaturations (*ref.* Figure 5.4).

Stellenbosch University http://scholar.sun.ac.za

Dutrizac (1996) studied the effect of seeding on ammonium and sodium jarosite precipitation and confirmed the initial rate to increase linearly with mass density (g/L) of seed particles present.

Riveros and Dutrizac (1997) studied the precipitation of hematite from chloride media and found akaganeite (β-FeOOH) to precipitate more rapidly than hematite at lower temperatures (< 125°C), which then slowly transformed *via* a redissolution-crystallisation mechanism. Hematite seed was found to promote hematite formation and also improved the filterability of the product. They observed that hematite particles formed at 150°C, in the absence of seed, were very small (< 1 µm) and spheroidal, and were loosely intergrown into 10 to 20 µm aggregates. However, in the presence of 20 g/L hematite seed, the residue consisted of coarser individual particles, often several microns in size, while extensive particle agglomeration created larger aggregates. Another feature of seeding was the very fast kinetics of precipitation, which was virtually complete after heating the contents of the batch autoclave to temperature. In a follow-up study, Dutrizac and Riveros (1999) confirmed that akaganeite is metastable relative to hematite and that hematite seed promotes direct precipitation of hematite. Although the seed particles would obviously have experienced some degree of growth, it is unclear to what extent a secondary nucleation mechanism, in the presence of initial surface area, contributed to the direct precipitation of hematite.

Dutrizac and Chen (2009) investigated the conditions favouring hematite precipitation over sodium jarosite formation at 150°C in nickel sulfate-chloride solutions, and again found the presence of hematite seed to significantly suppress jarosite precipitation, while promoting hematite formation. Dutrizac and Jambor (2000) (also see Ciriello *et al.*, 1996) reviewed various studies dealing with the precipitation kinetics of different jarosites; in general, the rate of precipitation increased in a linear manner with the mass (density) of initial seed material, while any induction period was readily overcome.

Itou *et al.* (2006) studied, among other parameters, the effect of seed material on the mechanism of scorodite ($FeAsO_4.xH_2O$) precipitation. They found that the effect of seed was not to precipitate scorodite directly but rather to provide reaction sites for crystallisation. First, an amorphous scorodite phase precipitated on such reaction sites, and only later were well-crystallised single crystals observed on the seed surface.

Papangelakis *et al.* (1996) studied hematite particle morphology under acid pressure leaching conditions of limonite ore (> 240°C) and proposed that small hematite particles formed rapidly, probably due to secondary nucleation.

Stellenbosch University http://scholar.sun.ac.za

Although continuous growth may occur on existing hematite surfaces at lower supersaturations, such a mechanism is more probable in the case of hydronium jarosite due to its lower interfacial energy. The assumption is made that secondary nucleation – rapid growth of hematite is relevant when enough surface area is available at higher supersaturations, *e.g.*, at lower acidities. The overall iron(III) precipitation rate as hematite, $R_{FeIII,Hem}$ (mol Fe/kg.min), is then (see Eq. 5.42):

$$R_{FeIII,Hem} = \tilde{k}_{Hem} L_{Hem}^3 \cdot J_{Hem} = \tilde{k}_{Hem} L_{Hem}^3 \cdot (J_{prim} + J_{sec}) \qquad 5.48$$

An appropriate mathematical form of the secondary nucleation rate, J_{sec}, is dealt with in Sect. 5.4.4.

Overview of the phenomenological batch modelling framework, its assumptions and its application to the continuous reactor configuration

Three iron(III) precipitation rate regimes are adopted in this study, depending on the degree of supersaturation and the total precipitate surface area present. Figure 5.30 illustrates this modelling scheme, after assigning unity values to all the critical supersaturation ratios.

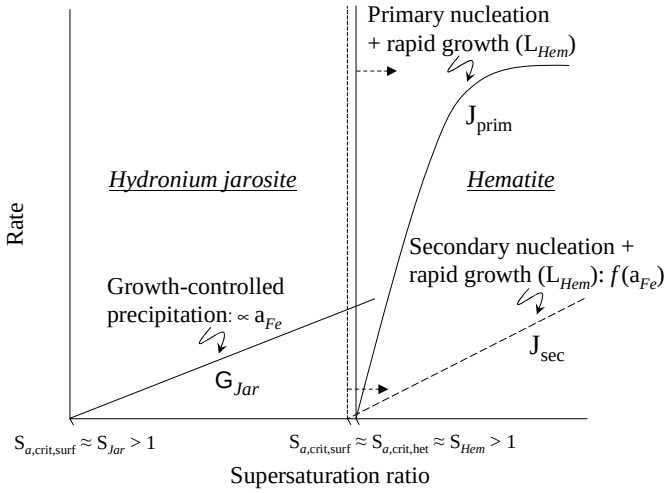

Figure 5.30
Schematic diagram of the different kinetic regimes of iron(III) precipitation (adopted from Demopoulos (2009), modified & expanded to reflect the assumptions made in this study).

This phenomenological model provides an estimate of the complex processes taking place during iron(III) precipitation in MT autoclaves. It assumes that the primary nucleation rate of hematite dominates the formation of new hydronium jarosite particles due to the higher hematite interfacial energy, and hence supersaturation, especially as the acid concentration drops during the initial stages of sulfide mineral or iron(II) oxidation. Due to the relatively high interfacial energy, the formation of these hematite nuclei is accompanied by rapid growth, which, in turn, causes the supersaturation to dissipate rapidly, leading to a large number of small particulates of similar size.
On the other hand, crystalline hydronium jarosite growth occurs under conditions of higher acid concentration, and hence lower relative supersaturation, *i.e.*, where nucleation on existing surfaces

Stellenbosch University http://scholar.sun.ac.za

leads to a continuous growth mechanism. It is assumed that this growth rate is independent of particle size, *i.e.*, complies with McCabe's rule. This assumption would not hold if the jarosite precursor particles are very small, which is in agreement with the GT relationship (Eq. 5.30). As illustrated by the BSE images in Section 5.4.1, the hydronium jarosite precursor phase generally yields particles comparatively large in size due to its low relative interfacial energy. Although this leads to different initial growth phenomena as compared to the crystalline hydronium jarosite phase, mathematical capturing of such a phenomenon is not warranted in the current context: jarosite precipitation is simply dealt with *via* an average linear topochemical growth rate expression. This spontaneous precipitation of hydronium jarosite on hematite surfaces has been confirmed experimentally (Section 5.4.1) and is thought to originate from the strong association (adsorption) of the sulfate ion with hematite surfaces, as discussed previously. As a first estimate, the model makes no distinction between the surface energies of the different polymorphic phases. The initial hydronium jarosite growth rate is therefore strongly dependent on the number of new hematite particulates, which allows simulation of the relative precipitation rates of these two phases over typical fluctuating acid levels in a batch oxidation reactor.

This modelling scheme does not cater for a classical hematite growth mechanism, *e.g.*, when hematite particles come in contact with a solution at lower supersaturation levels. In fact, it is doubtful whether such a mechanism exists in the first place for hematite precipitation under typical MT leaching conditions due to its relatively high interfacial energy. Qualitative evidence from the BSE images (Sect. 5.4.1) and literature suggests that a surface nucleation mechanism may be important in the case of hematite, but it falls in a 'grey' area that is not currently well understood (Figure 5.4). This mechanism is also assumed to be accompanied by rapid growth, yielding secondary hematite particles of similar (characteristic) size. However, this rate would also be expected to be some function of the exposed iron(III) precipitate surface area (Sect. 5.4.4).

Ostwald's step rule postulates that the precipitation of the phase with the highest solubility, *i.e.*, the least stable phase, is kinetically favoured (Stumm, 1992). This phenomenon has been confirmed by the BSE images in Section 5.4.1 for both the hematite and hydronium jarosite phases. It evolves around the precipitation of a precursor phase, followed by its transformation to the stable phase over time. It is assumed that this transformation process occurs at some reaction front that does not influence the bulk precipitation rate, which is in line with the thermodynamic framework (Sect. 5.2.3). The amorphous analogue of the stable phase is kinetically favoured because it is characterised by comparatively lower interfacial energy, forming comparatively large surfaces, probably *via* a continuous growth mechanism. This is also in line with the GT relationship (see above). Therefore, the amorphous precursor phase creates the 'driving force' for the subsequent heterogeneous precipitation of the more crystalline stable phase, *i.e.*, the interfacial energy between

Stellenbosch University http://scholar.sun.ac.za

the crystalline and amorphous precipitate is smaller than the interfacial energy between the crystalline phase and the solution (see detailed discussions in Stumm, 1992). This heterogeneous precipitation mechanism *via* 'mediation' of the amorphous precursor phase is visually most evident (see the BSE images in Sect. 5.4.1) for hematite and hydronium jarosite at higher and lower acidities, respectively. Amorphous hematite may therefore sustain the secondary hematite nucleation – rapid growth mechanism under higher acidities on crystalline jarosite surfaces, albeit at a reduced rate compared to the same mechanism on rudimentary hematite particulates at lower acidities. In the same vein, amorphous hydronium jarosite surfaces may precede crystalline jarosite particle formation under lower acidity conditions, depending on the extent to which such a crystalline phase is promoted in a particular solution environment. Table 5.9 presents a summary of the most important assumptions made in deriving this phenomenological model.

Table 5.9
The most important assumptions of the phenomenological model.

Assumptions	Rate dependency	Basis / Reason
Two neutral iron(III) species: $FeH(SO_4)_2^o$ & $Fe(OH)_3^o$.	Equilibrium rate >> precipitation rate	No experimental data to suggest otherwise.
$\Delta G^o_{x\{metastable\}} \approx \Delta G^o_{x(stable)}$ (nominal crystalline composition).	–	No thermodynamic data available for the metastable precursor phases.
S_{Hem} & S_{Jar} independent of particle size or other surface-specific properties.	–	Lack of data.
Neglect particle aggregation & agglomeration (all new particles in full contact with the solution).	–	Phenomenological model does not require quantification of these complex & variable processes.
Primary nucleation of hematite, no induction effects, $S_{crit,het} \approx S_{Hem}$.	$\propto exp\{-k\,(ln\ S_{Hem})^{-2}\}$ for $S_{Hem} > 1$	Relatively high temperatures, drop in $[H_2SO_4]$ during initial oxidation, $S_{Hem} >> S_{Jar} >> 1$.
Hematite nucleation accompanied by rapid growth to form small particles of characteristic size.	$\propto (L_{Hem})^3$	High interfacial energy ($\gamma_{Hem} > \gamma_{Jar}$), $S_{Hem} >> 1$ (especially at lower $[H_2SO_4]$), Gibbs-Thomson (GT) relationship.
Surface (secondary) nucleation of hematite, rapid growth to L_{Hem}, $S_{crit,surf} \approx S_{Hem}$.	$\propto (L_{Hem})^3$ & $\propto f(a_{Fe})$ for $S_{Hem} > 1$ (see Sect. 5.4.4)	Catalytic effect of iron(III) ppt. surface area on a molecular level (this is a 'grey area'), relatively high γ_{Hem}, $S_{Hem} >> 1$.
Growth of jarosite on (spherical) ppt. surfaces (incl. on hematite), McCabe's rule, topochemical kinetics, $S_{crit,surf} \approx S_{Jar}$.	$\propto a_{Fe}$ & $\propto \sigma^n_{Jar}$ for $S_{Jar} > 1$	Lower interfacial energy ($\gamma_{Jar} < \gamma_{Hem}$), association of SO_4 with hematite surfaces, $S_{Jar} < S_{Hem}$ but still $S_{Jar} >> 1$, first-order growth, *i.e.*, n = 1 (see Sect. 5.4.4).

Stellenbosch University http://scholar.sun.ac.za

5.4.4 Model verification and regression results

The phenomenological model developed above provides a crude estimate of the complex processes taking place during iron(III) precipitation. Nevertheless, the experimental (Section 5.4.1) and regression results (below) illustrate that the essential elements of the kinetic processes are captured by this modelling framework.

Preliminary model regression

The preliminary regression of the low pulp density precipitation results (Sect. 5.4.1) includes only the two rudimentary precipitation rate terms, *i.e.*, the primary hematite nucleation (Eq. 5.43) and hydronium jarosite continuous growth terms (Eq. 5.38 or 5.40). This model implicitly assumes that iron(III) precipitation starts when S_{Hem} and S_{Jar} exceed 1, *i.e.*, at $\sigma_{Hem} > 0$ and $\sigma_{Jar} > 0$ (Table 5.9).

The regression minimises an objective function, which, in turn, is based on the equally weighed absolute errors of the precipitation extent and weight fraction hematite at each datapoint *i*:

$$E_F = \tfrac{1}{2}\sum_i [(X_{p,Fe})^{exp} \cdot E(X_{p,Fe})]_i + \tfrac{1}{2}\sum_i [(W_{f,Hem})^{exp} \cdot E(W_{f,Hem})]_i \qquad 5.49$$

where E is the absolute relative error (see Eq. 2.72). This error function (E_F) places less emphasis on the experimental results at the lower precipitation extents, *i.e.*, where the experimental error is proportionally most significant. It also places less emphasis on hydronium jarosite growth at longer reaction times in the batch reactor, which tends to overshadow the overall iron(III) precipitation rate as the acid concentration increases over time.

The growth of new particulates is assumed to cease at the characteristic size (L_{Hem}) of 0.15 µm (see Sect. 5.4.1) and is based on a primary hematite nucleation rate expression (Eq. 5.43) only. For reasons outlined in Sections 5.2.4 and 5.2.6, estimates of the interfacial energy (γ_{Hem}) and correction factor (ξ) are difficult to obtain from first principles or phenomenological-type experimentation (Sect. 5.3). Therefore, constant interfacial energy and correction factor values of 0.5 J/m^2 (Sect. 5.2.4) and 1×10^{-3} are, respectively, selected. In any event, realistic deviations from these values have a relatively insignificant impact on the above error function value.

The regression of the low pulp density batch precipitation results is therefore focused on finding the value of k_{prim} for the rate of primary hematite particulate formation (Eq. 5.43), as well as a suitable hydronium jarosite growth rate expression and its associated constants. Interestingly, despite a suite of available growth rate models (*e.g.*, the B+S model; Eq. 5.38 & 5.39), a simple first-order dependence on the relative superstation ratio and an Arrhenius response to temperature change consistently yields the best results (*ref.* Eq. 5.40):

Stellenbosch University http://scholar.sun.ac.za

$$G_{Jar} = k_G \cdot exp\frac{-E_{a,Jar}}{R_g}\left(\frac{1}{T}-\frac{1}{T_r}\right)\cdot\sigma_{Jar} \qquad 5.50$$

The regression is therefore constrained to finding values of k_{prim}, k_G and $E_{a,Jar}$. Based on reasonable estimates of the batch precipitation rates of hematite and hydronium jarosite at low pulp densities, the overall precipitation rate in the higher pulp density continuous reactor is then dealt with *via* the time- and space-averaged PB (see App. H):

$$G_{Jar,j}\frac{\partial\psi_j}{\partial L_{Fe}}+\frac{\psi_j}{\tau_j}=\frac{\psi_{j-1}}{\tau_j}+\frac{dJ_{prim,j}}{dL_{Hem}} \qquad 5.51$$

where ψ_j and ψ_{j-1} are the particle number density distributions (1/kg.µm) exiting and entering compartment *j*, respectively, and τ is the average residence time (min).

Although reasonable batch estimates of $X_{p,Fe}$ and $W_{f,Hem}$ are obtained at low pulp densities in the medium to high acid regime, the model underpredicts $X_{p,Fe}$ in the low acid regime. It should, however, be kept in mind that the oversimplified thermodynamic description (Sect. 5.4.2), especially at lower acidities, may place unrealistic demands on the performance of the simulation.

Most importantly, despite obtaining reasonable estimates in dilute slurries (*ref.* Sect. 5.4.1), the optimised simulation consistently underestimates the precipitation rate in the batch (Ch. 7) and continuous (Ch. 8) leaching systems. No changes in the above nucleation and growth rate functions can adequately compensate for these discrepancies, which support the inclusion of a secondary hematite nucleation mechanism. Surface integration models are therefore not the appropriate modelling framework to describe the surface nucleation of hematite in uncontrolled leaching-precipitation systems. This notion is consistent with the formation of characteristically small hematite particulates over relatively wide acidity and temperature ranges (BSE images; Sect. 5.4.1).

Developing a modelling framework to quantify secondary hematite nucleation

As highlighted in Section 5.4.3, ambiguity exists between the different modes of precipitation under typical autoclave conditions because a surface nucleation mechanism that yields secondary particles is not easily differentiated from a continuous growth mechanism in sparingly soluble systems, especially when accompanied by the rapid formation of nano-aggregates and agglomerates. The above preliminary regression discussion highlights the need to improve the simulation performance of iron(III) precipitation in high pulp density leaching systems.

Assuming that secondary nuclei are formed in the surface adsorption layer or liquid phase adjacent to the surface from where they are washed into the bulk solution (Sect. 5.4.3), a surface nucleation

Stellenbosch University http://scholar.sun.ac.za

rate, J_{surf} ($1/m^2$.min), is relevant, leading to the following generic form of the secondary nucleation rate:

$$J_{sec} = f(a_{Fe}) \cdot J_{surf} \qquad 5.52$$

This equation assumes that all surface nuclei detach from the surface to become volume nuclei, which is consistent with describing the precipitation rate in terms of individual hematite particulates. Expressions of the intrinsic surface nucleation rate are typically non-linear functions of the supersaturation ratio, while also containing various other parameters (see Mersmann *et al.*, 2001a). Since experimental observations often reveal an apparent linear dependence of surface nucleation mechanisms on the existing precipitate mass (& not its area; see Sect. 5.4.3), a modified approach is followed.

It is again assumed that metastable hematite acts as a precursor phase during the surface nucleation of hematite in higher acid environments, *i.e.*, where crystalline hydronium jarosite growth is most prominent. This allows direct application of the thermodynamic expressions of Section 5.2.3. Mersmann *et al.* (2001a) have emphasised that the number of surface nucleation events rises rapidly with increasing supersaturation: a general power-function (Eq. 5.36) is adopted here, while the rate constant is assumed to follow a conventional Arrhenius dependency. Since this phenomenological model needs to account for an increased rate of hematite particulate formation in high pulp density environments, which seemingly stretches beyond a linear response in the total iron(III) precipitate surface area, the pre-exponential area function (reaction frequency) is used to capture the catalytic effect of the existing surface area on the secondary rate nucleation, *i.e.*:

$$J_{sec} = k_{sec} \cdot f(a_{Fe}) \cdot exp\frac{-E_{a,Hem}}{R_g T} \cdot \sigma_{Hem}^{n_{sec}} \qquad 5.53$$

where σ_{Hem} is the relative supersaturation of hematite ($\sigma = S_a - 1$) and the apparent activation energy is such that $E_{a,Hem} < E_{a,hom}$. The rate constant, k_{sec} ($1/m^2$.min), then becomes an adjustable parameter, while the area function incorporates a catalytic enhancement factor, κ, which results in an approximately linear response of the surface nucleation rate to the precipitate pulp density, ρ_{Fe} (kg/kg H_2O), of a typical average particle size, *i.e.*:

$$f(a_{Fe}) = \kappa a_{Fe} \propto \rho_{Fe} \qquad 5.54$$

Examples of catalytic surface effects on reaction kinetics can be found in the literature. For example, Teixeira and Tavares (1986) proposed a (semi-empirical) power-law model (see Weller, 1956) to describe the effect of ammonium jarosite seed on its precipitation rate as a heterogeneously catalysed reaction. Tamura *et al.* (1976) described the heterogeneous oxidation

Stellenbosch University http://scholar.sun.ac.za

rate of iron(II) in close to neutral solutions as an autocatalytic reaction, with an apparent first-order dependence on the precipitated mass concentration of ferric hydroxide. Sugimoto and Matijevic (1980) studied the rate of iron(II) hydroxide conversion to magnetite. Iron(III) centres on the surface of iron(II) hydroxide gave rise to the magnetite nuclei and the conversion extent followed sigmoidal profiles over time.

In chemical reaction theory, a reaction is said to have undergone autocatalysis if the reaction product itself is the catalyst for that reaction. S-shaped variation of the product concentration with time is typical of such reactions; the reaction proceeds slowly at the start, because little catalyst is present, and the rate increases progressively as the reaction proceeds, and then again slows down as the reactant concentration decreases. It is easily shown that the concentration of an autocatalytic product species follows a sigmoidal response over time (see, *e.g.*, Thomas & Thomas, 1997). The autocatalytic effect of surface area may be treated in an analogous manner. However, unlike classical autocatalysis reactions, a transition-type variation of the surface 'activity' as a function of the total available area would be expected to be governed by different processes. For example, even at high supersaturation ratios, supply limitations of hematite growth units might manifest as an apparent efficiency drop at high exposed surface areas: the following versatile transition function is therefore adopted in the phenomenological model:

$$log\ \kappa a = p_1 + p_2\left(\frac{log\ a - p_3}{p_4}\right)\left(\frac{|log\ a - p_3|}{p_4}\right)^{-p_5} \qquad 5.55$$

where p_1 to p_5 are adjustable parameters. Indicative plots of enhancement factors *vs.* surface area are compared in Figure 5.31 *a*, while Figure 5.31 *b* illustrates that this transition function can yield a relatively linear relationship (in comparison to typical sigmoidal functions) between the nucleation rate (at constant temperature & supersaturation) and typical precipitate pulp densities (1 to 5 wt%) for monosized spherical particles (in this case, hematite particulates of 0.15 µm). This linear response is seen as sufficient justification to adopt the above equation in this study, despite the fact that this expression is unrelated to the underlying surface nucleation events on a molecular level. This linearity is also maintained over limited L_{Hem} variations, *e.g.*, in the 0.12 to 0.25 µm range.

The above approach does not account for variations in the hematite particle size due to, *e.g.*, changing acid concentration or temperature. However, this constant characteristic size should be seen in the context of preventing over-parameterisation of the initial model and not as an absolute phenomenon. As shown in the next section, the simulation performance is improved by incorporating limited growth on hematite surfaces and hydronium jarosite particle shrinkage (due to its conversion to hematite) in the low acid regime.

Stellenbosch University http://scholar.sun.ac.za

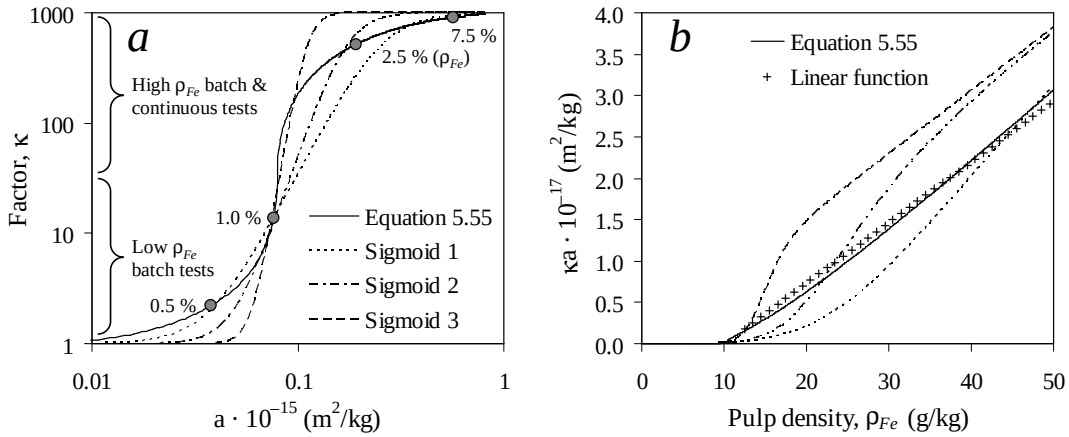

Figure 5.31
Transition functions *ref.* monosized spherical hematite particles (L_{Hem} = 0.15 µm & ρ_{Hem} = 5240 kg/m^3; Lide, 2004): *a*) κ *vs.* particle surface area; *b*) Term κa *vs.* precipitate pulp density. This sigmoidal function represents the optimised parameters from the final regression analysis (below).

Phenomenological model refinements to improve the simulation performance at low acidities

Since the hematite and hydronium jarosite precipitation rates are closely related by virtue of the above phenomenological scheme, non-linear growth rate functions (*e.g.*, the B+S model; Eq. 5.38 & 5.39) also demand higher orders from the secondary nucleation rate order, *i.e.*, $n_{sec} > 1$. Numerous permutations of these different growth rate models have been tested for n_{sec} between one and six, using exhaustive regression analyses of the low pulp density batch (Sect. 5.4.1), high pulp density continuous (Ch. 7) and high pulp density batch (Ch. 8) results. The best results are achieved by assuming a simple linear dependence on the jarosite supersaturation, *i.e.*, Equation 5.50, and an apparent reaction order, n_{sec} (Eq. 5.53) of unity. No conclusions can be drawn from this apparent linear dependence on σ_{Jar} since small changes in the thermodynamic model tend to overshadow the impact of the different growth rate models. This emphasises the need to develop more thermodynamic (including speciation) data for iron(III) in mixtures with sulfuric acid and metal(II) sulfates at typical autoclave temperatures (see Ch.2, Sect. 2.4.3, Sect. 5.2.2 & 5.2.3). The unity value of n_{sec} is also appropriate because various possible secondary nucleation mechanisms are combined and the effect of supersaturation is not derived from first principles (see above), as is the case with primary nucleation (Sect. 5.2.4).

Due to underestimation of the overall precipitation rate in the low acid regime (see above) and since the precipitation rates of the hematite and hydronium jarosite phases are dependent on each other, a new parameter is utilised, *i.e.*, the relative saturation ratio of these two phases, σ_{Fe}:

$$\sigma_{Fe} = \frac{[\mathrm{Fe\,III}]^{*}_{Jar}}{[\mathrm{Fe\,III}]^{*}_{Hem}} - 1 \qquad 5.56$$

Stellenbosch University http://scholar.sun.ac.za

Figure 5.32 illustrates that this ratio is a highly non-linear function of the hydrogen ion concentration, especially below about 0.1 mol/kg H^+ in the ternary H_2SO_4-$Fe_2(SO_4)_3$-H_2O system, *i.e.*, based on the chemistry model (Ch. 2) and thermodynamic relationships of Section 5.2.3.

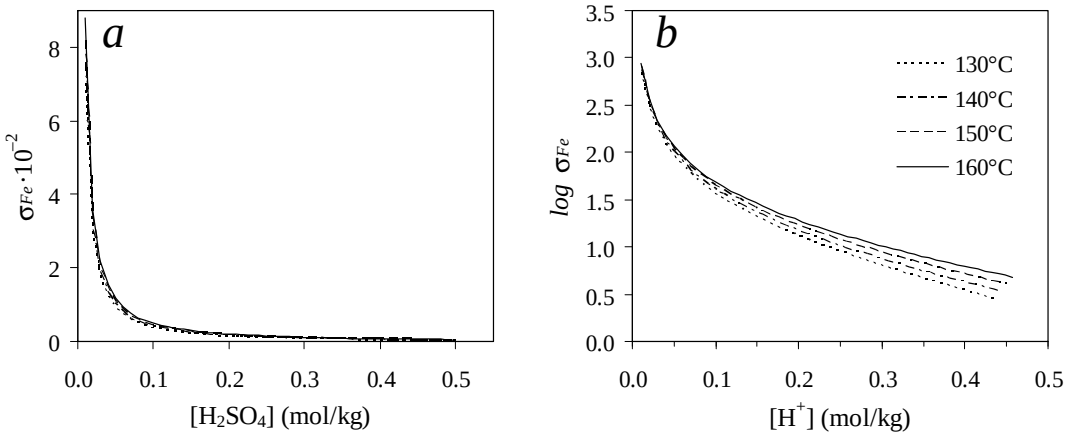

Figure 5.32
Relative saturation ratio of iron(III) *ref.* hydronium jarosite & hematite in the H_2SO_4-$Fe_2(SO_4)_3$-H_2O system: *a*) σ_{Fe} *vs.* H_2SO_4 molality; *b*) *log* σ_{Fe} *vs.* average H^+ molality 'at temperature'.

Incorporation of this ratio into Equation 5.53 provides the means to account for an increased surface nucleation rate *via* hematite-like surfaces, as compared to hydronium jarosite surface structures, *i.e.*, to cater for $S_{crit,surf} < S_{crit,het}$ (see Figure 5.33). A more consistent simulation performance at different pulp densities in the batch and continuous reactors is obtained by the following functional form of the secondary nucleation rate expression:

$$J_{sec} = k_{sec} \cdot (\kappa a_{Fe} \cdot ln\sigma_{Fe}) \cdot exp\frac{-E_{a,Hem}}{R_g}\left(\frac{1}{T} - \frac{1}{T_r}\right) \cdot \sigma_{Hem} \qquad 5.57$$

where the bracketed pre-exponential function (reaction frequency) captures the catalytic effect of the existing precipitate surface area. The higher the acid concentration due to the advancing precipitation reactions, the smaller the values of σ_{Fe} and σ_{Hem} and the comparatively less significant the role of secondary nucleation becomes. This trend is qualitatively in line with the above discussions, because the higher the driving force of hydronium jarosite growth, the lower the tendency of its precursor phases to yield secondary hematite nuclei. Equation 5.57 is therefore most dominant at lower acidities and in the presence of high iron(III) precipitate surface area.

The conversion of hydronium jarosite to hematite (Sect. 5.2.5 & 5.4.3) also needs to be accounted for at low acidities and is assumed to be driven by the relative solubility difference between the hematite and jarosite phases, *i.e.*, σ_{Fe}. The net jarosite growth rate is then as follows, assuming an Arrhenius response and a linear dependence on σ_{Fe}:

Stellenbosch University http://scholar.sun.ac.za

$$G_{Jar} = G^{+} - G^{-} = k_G \cdot exp\frac{-E_{a,Jar}}{R_g}\left(\frac{1}{T} - \frac{1}{T_r}\right)\cdot\sigma_{Jar} - k_G^{-}\cdot exp\frac{-E_{a,Jar/Hem}}{R_g}\left(\frac{1}{T} - \frac{1}{T_r}\right)\cdot ln\,\sigma_{Fe} \qquad 5.58$$

The simulation performance at artificially low acidities is improved further by assuming the hematite particulate size is a weak linear function of σ_{Fe}:

$$L_{Hem} = p_6 + p_7 \cdot \sigma_{Fe} \qquad 5.59$$

This equation is also related to the rapid conversion of hydronium jarosite to hematite at very low terminal acidities. The optimised p_6 and p_7 parameter values of 0.125 and 10^{-4} µm, respectively (Table 5.10), yield a rounded L_{Hem} value of 0.15 µm at about 0.075 mol/kg H^+ in the 130 to 160ºC range. Neither this variation of L_{Hem} nor the conversion rate expression (G^-) has a significant bearing on the simulation performance under typical sulfide mineral oxidation conditions. The premise of the above two equations is that the hydronium jarosite conversion rate is driven by the solubility difference between the two phases in the diffusion layer surrounding the hydronium jarosite surface. It assumes that the outwards diffusion of the hydrated proton is much faster than the inward diffusion of iron(III) species, which makes the consideration of any transport equations redundant. This assumption is justified on the grounds of the high diffusivity of the proton and bisulfate ions (~9.3×10^{-9} & ~1.4×10^{-9} m^2/sec, respectively; Lide, 2004), which are at least twice as high as the diffusivities of typical iron(III) species (0.2-0.6$\times10^{-9}$ m^2/sec; Casas *et al.*, 2005a).

The final form of the phenomenological model is summarised in Figure 5.33, consisting of the three major precipitation steps: 1) hematite precipitation (Eq. 5.48) as primary particulates (Eq. 5.43), 2) secondary particulates (Eq. 5.57), and 3) hydronium jarosite precipitation (Eq. 5.45) *via* continuous growth on existing surfaces (Eq. 5.58).

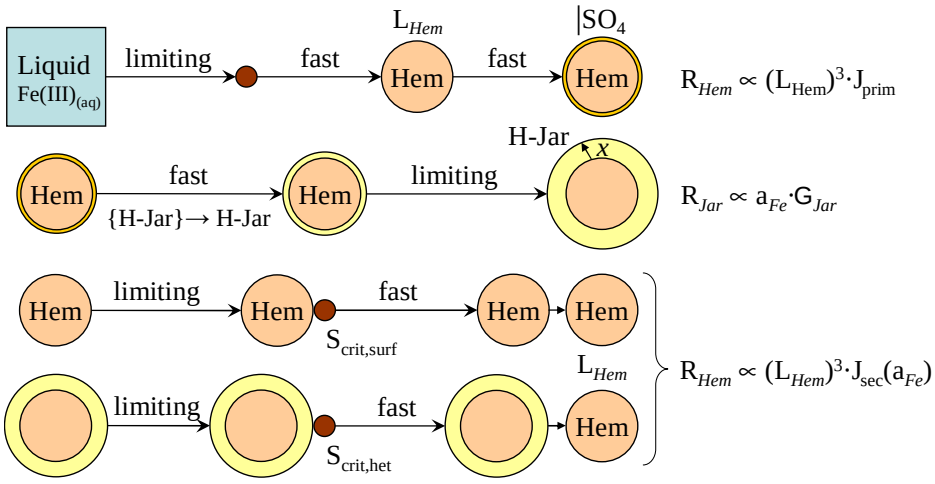

Figure 5.33
Schematic representation of the phenomenological model of iron(III) precipitation (this study).

Stellenbosch University http://scholar.sun.ac.za

Final regression incl. consideration of high pulp density batch and continuous leaching systems

The final regression utilised optimised κa_{Fe}-term parameters (Eq. 5.55; see Table 5.10 footnote) to best represent the precipitation rates in high pulp density environment in the continuous (Ch. 7) and batch (Ch. 8) reactor configurations. These optimised parameters correspond to an estimated k_{sec} value of 1×10^{-8} 1/µm^2.min. Although this expression of J_{sec} is most relevant to high pulp densities, where high iron(III) supersaturation and precipitate surface area are experienced at the same time, the bottom half of Equation 5.55 also influences the regression of the low pulp density precipitation results. With parameters p_1 to p_5 and the value of k_{sec} fixed, the other parameters are optimised, *i.e.*, k_{prim}, $E_{a,Hem}$, k_G, $E_{a,Jar}$, k^-_G and $E_{a,Jar/Hem}$.

The error function (Eq. 5.49) is relatively insensitive to the activation energy values. To simplify the regression analysis, the value of $E_{a,Jar}$ is set at 100 kJ/mol. This is the activation energy value measured for sodium jarosite (without seed) and falls within the generally high range of 70 to 106 kJ/mol reported for different jarosite compounds (Dutrizac, 1980, 1996). Van der Woude *et al.* (1983) estimated the activation energies of hematite nucleation and growth to be very similar, albeit referring to precipitation of relatively amorphous phases at lower temperatures (25-70ºC) and higher pH (> 7) in a nitrate solution environment. This justifies the use of a single activation energy term for the secondary hematite nucleation – rapid growth expression, *i.e.*, $E_{a,Hem}$.

The regression analysis consisted of choosing initial estimates of k_{prim} and k_G, while constraining Equation 5.59 to $L_{Hem} < 0.175$ µm at acid levels higher than 0.05 mol/kg H^+. The results (23 tests; Table 5.11) at low starting acidities (< 12 g/L H_2SO_4) were then used to obtain estimated values of k^-_G, $E_{a,Jar/Hem}$, p_6 and p_7, while the tests at higher acidities and temperatures other than 150ºC (T_r) (16 tests; Table 5.12) were used to obtain $E_{a,Hem}$. This is the logical reference temperature choice since the continuous pilot campaigns (Ch. 7) were also conducted at 150ºC. These optimised values of k^-_G, $E_{a,Jar/Hem}$, p_6 and p_7 were then used to obtain new estimates of k_{prim} and k_G at 150ºC, using all 24 test results at initial acidities above 12 g/L H_2SO_4 (Table 5.13). As mentioned before, the optimised values of these two parameters are highly dependant on each other, while the value of k_G also needs to be aligned with k_{sec} (1×10^{-8} 1/µm^2.min). A systematic 'scan' of k_{prim} reveals a rounded value of 1×10^{12} l/kg.min, while the final converged value of k_G is obtained by repeating the above procedure.

The optimised values are summarised in Table 5.10, while the test conditions, experimental and calculated reaction extents, as well as absolute deviations of all the tests are summarised in Table 5.11, Table 5.12 and Table 5.13.

Stellenbosch University http://scholar.sun.ac.za

Table 5.10
Optimised Fe(III) precipitation rate constants & activation energies in acidic sulfate solutions.

[a] k_{prim}	[b] k_{sec}	[c] $E_{a,Hem}$	[a] k_G	[d] $E_{a,Jar}$	[a, e] k^-_G	[c, e] $E_{a,Jar/Hem}$
(1/kg.min)	($1/\mu m^2$.min)	(kJ/mol)	(µm/min)	(kJ/mol)	(µm/min)	(kJ/mol)
1×10^{12}	(1×10^{-8})	125	3.5×10^{-5}	(100)	1×10^{-4}	[f] (50)

[a] Based on γ_{Hem} = 0.5 J/m^2, $\xi = 1 \times 10^{-3}$ (Eq. 5.43), T_r = 150°C; [b] Based on p_1 to p_5 of 15.40, 2.43, 13.90, 0.95, 0.54, respectively (Eq. 5.55), T_r = 150°C; [c] 130-150°C; [d] Literature; [e] Based on p_6 & p_7 values of 0.125 µm & 4×10^{-4} µm, respectively (Eq. 5.59); [f] Avg. optimised value (~25-75 kJ/mol): E_F (Eq. 5.49) insensitive *ref.* low pulp density results.

The calculated precipitation extents and hematite contents in the solid phase generally compare well with the experimental values. Taking the notable experimental uncertainty and the primitive nature of the thermodynamic and phenomenological models into consideration, as well as the sometimes low measured precipitation extents, these results are considered acceptable. Figure 5.34 illustrates that a mere 1 g/L Fe(II) concentration difference at the start results in a notable deviation in the measured hematite content. Experimental uncertainty is therefore a significant factor in these tests, especially at low precipitation extents. Figure 5.34 *b* and Figure 5.35 *b* suggest that experimental error is the likely reason behind the data scattering in selected tests, which often outweighs inaccuracies in the simulation framework. This may also be the reason for the apparent insensitivity of the error function to selected parameters during the regression exercise, *e.g.*, $E_{a,Jar/Hem}$ (Table 5.10). In general, however, these figures illustrate that the phenomenological model correctly simulates the increase in the precipitation extent and hydronium jarosite content with increasing iron(III) supersaturation.

The simulation performance at lower initial acid concentrations (< 12 g/L H_2SO_4) is summarised in Table 5.11. Agreement between the measured and simulated hematite contents is generally acceptable, except for the apparent underestimation of the precipitation extents and residue hematite contents at longer reaction times, despite accounting for the jarosite to hematite conversion (Eq. 5.58 & 5.59). However, relatively small adjustments of the solution thermodynamic model in this low acid regime have a significant impact on the relative hematite and hydronium jarosite precipitation rates, which outweigh the benefits offered by these empirical conversion rate expressions. The lack of accurate control of the amount of iron(II) solution pumped into the autoclave, especially at these lower initial iron(II) solution volumes, is thought to be another reason for the discrepancies in Table 5.11. These aspects also impact the iron(II) oxidation rate simulation (Ch. 4). Improvements in the thermodynamic description of the iron(III) supersaturation should therefore be a priority in future investigations, which should also include a re-evaluation of the intrinsic iron(II) oxidation rate in this low acid regime.

Stellenbosch University http://scholar.sun.ac.za

Table 5.11
Comparison between the experimental & simulated Fe(III) precipitation extents & hematite contents at various temperatures in the batch autoclave (low pulp densities), starting with low to medium initial acidities (< 12 g/L H_2SO_4) & 15 g/L Cu or Zn (regression of k_G, $E_{a,Jar/Hem}$, p_5, p_6).

Test no.	Time	Temp.	[a] [A, Fe]	System	[b] [H_2SO_4]	$X_{p,Fe}$	[c] $X_{p,Fe}$	$W_{f,Hem}$	[c] $W_{f,Hem}$
–	(min)	(°C)	(g/L)	(15 g/L)	(mol/kg)	(% meas.)	(% calc.)	(% meas.)	(% calc.)
FPF11	15	130	4, 3.5	Cu	0.063	53	44.9 (15)	81	87.8 (8)
FPF12	30	130	4, 3.5	Cu	0.074	63	58.1 (7)	88	86.5 (1)
FPF13	45	130	4, 3.5	Cu	0.084	74	66.8 (9)	88	86.9 (1)
FPF21	20	130	8.5, 4.5	Cu	0.063	6	16.1 (155)	66	69.1 (5)
FPF22	40	130	8.5, 4.5	Cu	0.084	33	27.4 (17)	67	63.4 (6)
FPF23	60	130	8.5, 4.5	Cu	0.100	47	35.3 (24)	63	62.7 (1)
FPE11	10	140	7.5, 5	Cu	0.079	33	28.3 (14)	82	62.8 (23)
FPE12	20	140	7.5, 5	Cu	0.095	45	38.6 (14)	74	55.1 (26)
FPE13	30	140	7.5, 5	Cu	0.1215	66	45.4 (31)	76	52.3 (31)
FPC11	5	150	10, 8.5	Cu	0.090	33.5	35.3 (5)	41	50.0 (21)
FPC12	7.5	150	10, 8.5	Cu	0.1105	44	40.2 (9)	38	44.6 (18)
[d] FPA12	40	155	3.5, 3.5	Zn	0.110	97	89.5 (8)	88	79.8 (9)
[e] FPA22	15	155	3.5, 3.5	Cu	0.105	93	72.5 (22)	94	78.5 (17)
FPA31	5	155	3.5, 3.5	Zn	0.090	84	53.9 (36)	90	85.9 (4)
FPA32	15	155	3.5, 3.5	Zn	0.095	95	74.4 (22)	86	78.0 (10)
FPB11	2.5	155	4, 3	Cu	0.069	59	40.7 (31)	84	90.7 (8)
FPB12	5	155	4, 3	Cu	0.080	70	53.5 (24)	92	85.5 (7)
FPB13	10	155	4, 3	Cu	0.091	81	66.9 (18)	88	80.8 (9)
FPB21	5	155	4, 4	Zn	0.1095	82	50.6 (38)	88	81.7 (7)
FPB22	10	155	4, 4	Zn	0.120	92	62.5 (32)	91	74.8 (18)
FPB23	15	155	4, 4	Zn	0.125	95	69.8 (27)	92.5	71.5 (23)
FPB42	10	155	7, 3.5	Zn	0.100	50	35.5 (29)	84	63.0 (25)
FPB43	15	155	7, 3.5	Zn	0.115	67	45.0 (33)	82.5	57.5 (30)

[a] Initial H_2SO_4 & Fe(II), resp.; [b] Final (meas.) conc.; [c] *AARD* (%) (Eq. 2.73) in brackets; [d] 350 kPa $p_{O2}{}^o$; [e] 700 kPa $p_{O2}{}^o$.

The above considerations have led to the objective function being described by Equation 5.49, rather than attempting to minimise the individual absolute average relative deviation (*AARD*) (Ch.2, Eq. 2.73) values. By definition, the *AARD* values tend to be large at the low experimental reaction extents, placing unwarranted emphasis on the results with questionable accuracy. Table 5.12 and Table 5.13 present verification that the measured reaction extents are reasonably well simulated by the phenomenological model in the higher acid regime (> 10 g/L H_2SO_4). In fact,

Stellenbosch University http://scholar.sun.ac.za

Figure 5.36 suggests that the simulation performance is acceptable over a wider acid range, stretching beyond the conditions experienced in the continuous pilot autoclave (Ch. 7). Nevertheless, the simulation of iron(III) precipitation in low acid regime is still relevant to selected high pulp density batch mineral oxidation tests at lower initial acid concentrations (Ch. 8), placing some demand on the performance of this iron(III) precipitation model, especially during the initial leaching stages.

Table 5.12
Comparison between the experimental & simulated Fe(III) precipitation extents & hematite contents at various temperatures in the batch autoclave (low pulp densities), starting with medium to high initial acidities (> 11 g/L H_2SO_4) & 15 g/L Cu (results used to regress $E_{a,Hem}$).

Test no.	Time	Temp.	[a] [A, Fe]	[b] $[H_2SO_4]$	$X_{p,Fe}$	[c] $X_{p,Fe}$	$W_{f,Hem}$	[c] $W_{f,Hem}$
–	(min)	(°C)	(g/L)	(mol/kg)	(% meas.)	(% calc.)	(% meas.)	(% calc.)
FPB31	2.5	155	12, 2.5	0.128	9	1.3 (86)	86	98.5 (14)
FPB32	5	155	12, 2.5	0.123	12.5	2.6 (79)	92	95.9 (5)
FPB33	10	155	12, 2.5	0.127	20	5.5 (72)	86	90.8 (5)
FPE21	10	140	12.5, 5.5	0.090	5	3.4 (34)	62	74.2 (20)
FPE22	20	140	12.5, 5.5	0.106	18	8.1 (56)	56.5	55.5 (2)
FPE23	30	140	12.5, 5.5	0.1215	31	13.2 (58)	57	46.9 (18)
FPE31	20	140	15, 6.5	0.117	7.5	4.8 (35)	44	56.5 (28)
FPE32	30	140	15, 6.5	0.117	13	8.2 (36)	40	45.7 (13)
FPE33	40	140	15, 6.5	0.132	19	11.8 (39)	49	39.9 (19)
FPE41	20	140	15, 7.5	0.106	9	10.2 (19)	28.5	29.8 (5)
FPE42	30	140	15, 7.5	0.116	15	16.1 (15)	17	24.9 (50)
FPE43	40	140	15, 7.5	0.127	21	20.9 (1)	25	23.1 (9)
FPE51	30	140	20, 10	0.127	3	10.4 (226)	16.5	17.8 (8)
FPE52	45	140	20, 10	0.138	10	16.2 (60)	14	15.5 (8)
FPF31	30	130	12.5, 5.5	0.101	9	7.7 (10)	55	73.1 (34)
FPF32	45	130	12.5, 5.5	0.095	8.5	11.8 (38)	43	66.6 (53)
FPF33	60	130	12.5, 5.5	0.111	19	15.6 (18)	52	63.2 (22)

[a] Initial H_2SO_4 & Fe(II), respectively; [b] Final (measured) concentration; [c] *AARD* (%) (Eq. 2.73) in brackets.

Stellenbosch University http://scholar.sun.ac.za

Table 5.13
Comparison between the experimental & simulated Fe(III) precipitation extents & hematite contents at 150ºC (T_r) in the batch autoclave (low pulp densities), starting with medium to high initial acidities (> 12 g/L H_2SO_4) & 15 g/L Cu (results used to regress k_{prim} & k_G).

Test no.	Time	[a] [A, Fe]	[b] [H_2SO_4]	$X_{p,Fe}$	[c] $X_{p,Fe}$	$W_{f,Hem}$	[c] $W_{f,Hem}$
–	(min)	(g/L)	(mol/kg)	(% meas.)	(% calc.)	(% meas.)	(% calc.)
FPC21	15	12.5, 4	0.117	13	6.3 (51)	65	73.4 (13)
FPC22	20	12.5, 4	0.127	23	8.8 (62)	68	66.9 (2)
FPC32	10	13.5, 5.5	0.111	6	4.1 (27)	52	57.9 (10)
FPC42	10	14, 6	0.111	6	4.4 (27)	38	49.7 (31)
FPC43	15	14, 6	0.126	19	8.3 (56)	57	37.7 (34)
FPC52	10	15, 7.5	0.111	5	11.1 (135)	27.5	28.2 (3)
FPC53	15	15, 7.5	0.122	17	17.8 (4)	11	22.4 (106)
FPC62	15	16, 8.5	0.1475	28	22.4 (20)	26	19.4 (26)
FPD21	15	20, 9	0.143	8	4.0 (48)	17	27.4 (65)
FPD22	20	20, 9	0.153	8	6.7 (19)	15	20.9 (40)
FPD23	25	20, 9	0.1595	11	9.6 (15)	14	17.6 (26)
FPD24	30	20, 9	0.159	13	12.5 (2)	21	15.7 (27)
FPD11	10	20, 10	0.1215	2	5.9 (185)	11	20.2 (89)
FPD12	15	20, 10	0.143	4	11.5 (113)	9	14.9 (66)
FPD13	20	20, 10	0.138	10.5	16.1 (53)	8	12.8 (62)
FPD14	25	20, 10	0.165	12	19.9 (70)	6	11.7 (111)
FPD31	10	25, 15	0.152	13	22.2 (76)	5	14.3 (171)
FPD32	20	25, 15	0.184	25	29.8 (21)	6	11.7 (110)
FPD33	30	25, 15	0.193	29	34.3 (20)	8.5	10.9 (28)
FPD41	30	25, 12	0.174	8	12.7 (67)	13.5	9.7 (28)
FPD42	45	25, 12	0.179	10	19.4 (98)	5	8.6 (75)
FPD43	60	25, 12	0.200	20	24.3 (22)	8	8.4 (11)
FPD51	45	30, 15	0.212	10	18.7 (85)	9	6.3 (26)
FPD52	60	30, 15	0.210	14	22.9 (63)	8	6.3 (17)

[a] Initial H_2SO_4 & Fe(II), respectively; [b] Final (measured) concentration; [c] *AARD* (%) (Eq. 2.73) in brackets.

In the high acid regime (> 15 g/L H_2SO_4), as would normally be expected during the pressure oxidation of chalcopyrite-pyrite concentrates, the phenomenological model performance is good, even without relying on Equations 5.58 and 5.59. It can therefore be assumed that the conversion of previously formed hydronium jarosite to hematite is insignificant under these conditions, which ties in with the discussions in Section 5.2.4 and justifies the treatment of hydronium jarosite as a

Stellenbosch University http://scholar.sun.ac.za

thermodynamically stable phase under typical MT autoclave leaching conditions (Sect. 5.2.1 & 5.2.3). Furthermore, since the acidity generally increases during the latter stages of mineral oxidation, the transformation reaction (Rx. 5.31) is unimportant in context of the integrated continuous autoclave simulation (Ch. 7 & 8).

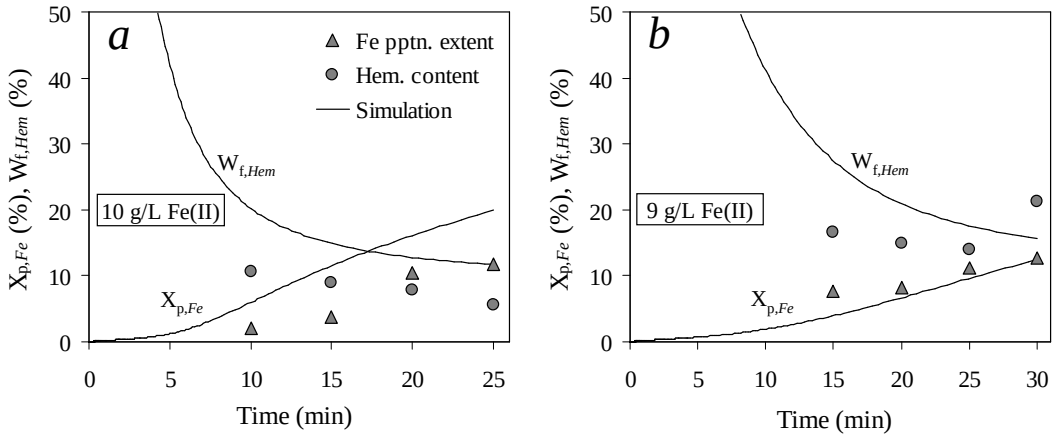

Figure 5.34
Comparison between the experimental & calculated Fe(III) precipitation extents & residue hematite contents at 150ºC (1000 kPa p_{O2}º) & 15 g/L Cu, starting with 20 g/L H_2SO_4: *a*) Series FPD1, starting with 10 g/L Fe(II); *b*) Series FPD2, starting with 9 g/L Fe(II).

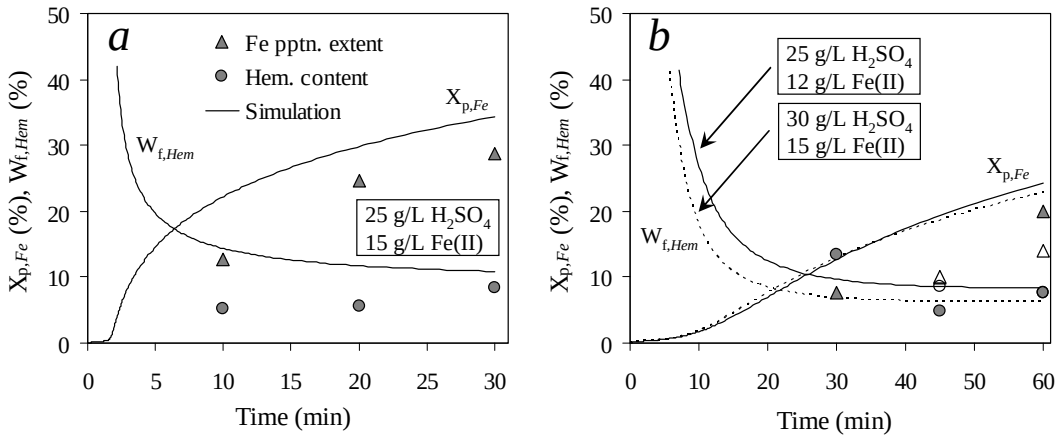

Figure 5.35
Comparison between the exp. & calc. Fe(III) precipitation extents & residue hematite contents at 150ºC (1000 kPa p_{O2}º) & 15 g/L Cu in the high acid & iron(II) conc. regimes: *a*) Series FPD3 (25 g/L H_2SO_4, 15 g/L Fe(II) initially); *b*) Series FPD4 (25 g/L H_2SO_4, 12 g/L Fe(II) initially). The open symbols & dotted lines refer to Series FPD5 (30 g/L H_2SO_4, 15 g/L Fe(II) initially).

Figure 5.36 verifies the batch model performance under different acid and iron(II) concentrations, at 150ºC (Series FPC1, FPC5 & FPD4) and lower temperatures (130-140ºC) (Series FPF1, FPF2 & FPE4). Clearly, the phenomenological model captures the essential features of the system, even

Stellenbosch University http://scholar.sun.ac.za

under those conditions (acid levels) where the solution chemistry model is unresolved. In conclusion, Table 5.14 presents a summary of the probable 'sources of errors' of this phenomenological model, which should be addressed in future investigations.

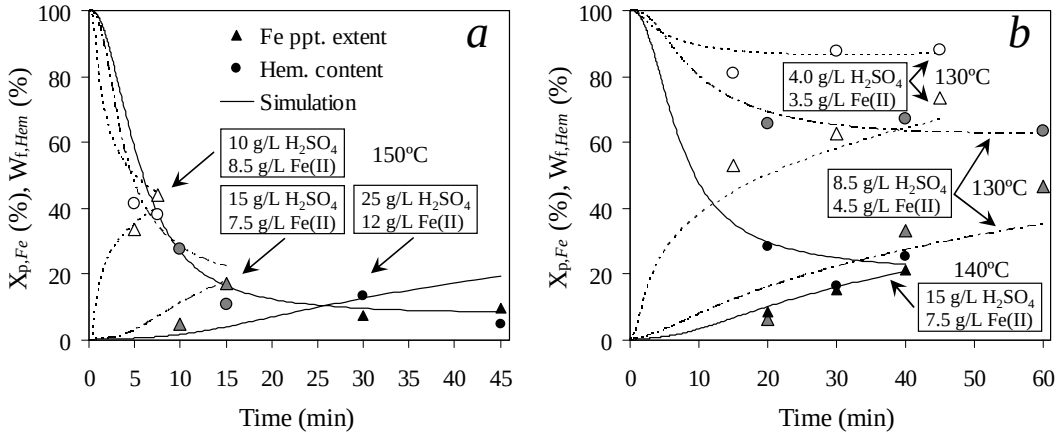

Figure 5.36
Comparison between exp. & calc. Fe(III) precipitation extents & residue hematite contents at 15 g/L Cu: *a*) 150ºC: Series FPC1 (open symbols, dotted lines), Series FPC5 (grey symbols, broken lines), Series FPD4 (black symbols, solid lines); *b*) 130ºC: Series FPF1 (open symbols, dotted lines), Series FPF2 (grey symbols, broken lines); 140ºC: Series FPE4 (black symbols, solid lines).

Table 5.14
The most likely 'sources of error' *ref.* the above optimised phenomenological model.

Errors (in order: most to least relevant *ref.* this study)	Perceived reasons.
S_{Hem} & S_{Jar} not adequately described in the lower acid regimes (< 10-15 g/L H_2SO_4).	Solution thermodynamics oversimplified in the lower acid regimes under MT autoclave conditions.
Rate of Fe(II) oxidation not adequately described in the lower acid regimes (< 10-15 g/L H_2SO_4).	Solution thermodynamics & Fe(II) oxidation rate oversimplified in the lower acid regimes.
Errors in the measured extent of Fe(III) pptn., especially in the lower acid regimes.	Inaccurate Fe(II) sln. volume pumped into autoclave 'at temperature' (suboptimal pump setup).
Measured errors in the residue composition (Hem *vs.* H-Jar content).	Inaccurate Fe & S^T analyses, as well as the presence of amorphous & unknown precipitates.
Surface area changes not adequately captured by the phenomenological model.	Aggregation & agglomeration complex, variable & difficult to capture mathematically (outside scope).
Underestimation of the hematite content in the low acid regime at lower S_{Hem} & high pulp densities.	Hematite growth not adequately described by the phenomenological model (H-Jar/Hem conversion).
Overestimation of the hematite content at increasing acid levels over time.	Hematite re-leaching not accounted for at increasing acid levels (Hem/H-Jar conversion, GT relationship).

Stellenbosch University http://scholar.sun.ac.za

5.5 Overview and recommendations

5.5.1 General

The relative thermodynamic stability of hematite *vs.* the other iron(III) precipitate phases varies greatly with temperature and hydrogen ion concentration (activity). From a thermodynamic perspective, jarosites are more stable at higher acidities, while hematite is favoured at higher temperatures. Co-precipitation of metastable hydronium jarosite is promoted by the lack of supersaturation control during the oxidation of iron-containing minerals. Although it may convert to the thermodynamically favoured phase, *i.e.*, hematite, over time, hydronium jarosite itself can be considered thermodynamically stable if retained in the mother liquor of high enough terminal acidity, at least over typical autoclave timeframes. The phenomenological model of the iron(III) precipitation rate is therefore independently based on the thermodynamics of the hematite and hydronium jarosite phases, of nominal compositions.

Hematite is the preferred product of mineral oxidation, both from an economical and environmental viewpoint, as it tends to absorb fewer metals in its structure, is compact and contains few waters of hydration, which also means that it generally settles and filters fast. The transition point between hematite and hydronium jarosite is close to the typical solution conditions experienced during MT chalcopyrite oxidation, which is one of the major drawbacks of the AA-UBC process.

5.5.2 Model validation (experimental results)

The experimental programme was designed to withdraw samples ‘at temperature’, *i.e.*, to minimise phase redissolution or transformation due to cooling. A separate test was conducted for each kinetic data point in order to generate statistically superior results. Each test was initiated ‘at temperature’, using iron(II) oxidation to drive iron(III) precipitation. Since supersaturation is difficult to control in a sparingly soluble system, the phenomenological model is also based on backscattered electron (BSE) images and qualitative energy dispersive X-ray (EDX) spot analyses. The following summary highlights the most important outcomes of this experimental programme:

- The interpretation of the experimental results demands various assumptions regarding the sulfur and iron balances. Firstly, a constant hematite sulfur content of 2% is assumed (based on the average reported literature values), due to the strong surface adsorption of sulfate on hematite. Secondly, as confirmed by the X-ray powder diffraction (XRD) analyses, the residual (chemical analysed) copper and zinc in the washed precipitates may be ascribed to antlerite and basic zinc sulfate (BZS) phases, respectively. The sulfur balance then leads to the hydronium jarosite content, while the iron balance reveals the hematite content. Since no other crystalline precipitates were identified by XRD, the formation of other iron(III) precipitates, *e.g.*, goethite, is assumed to constitute an

Stellenbosch University http://scholar.sun.ac.za

insignificant portion of the total precipitated mass. Furthermore, since the particle morphologies of the hematite and hydronium jarosite phases are quite distinct, BSE imaging, supported by the EDX spot analyses, lends qualitative support to the main assumptions of the phenomenological model. Crystalline hematite particles appear relatively bright (higher average atomic number) in these BSE images, are spheroidal and relatively small (roughly 0.5-1 µm in diameter) compared to the hydronium jarosite crystals (typically > 5 µm). Finally, although surfactants were added to simulate the leaching environment (Ch. 6-8), the strong association of sulfate ion with hematite is assumed to prevent the strong adsorption of the negatively charged surface-active moieties, similarly to hydronium jarosite surfaces

- The first few test series were conducted at higher temperature (155ºC) and lower initial acid (< 15 g/L H_2SO_4) and iron(II) (< 5 g/L Fe) concentrations in zinc or copper (15 g/L) sulfate background solution. The precipitation rate is fast and the crystalline hematite content high (> 85%) at these low acidity conditions, as confirmed by the low total sulfur-to-iron (S^T:Fe) mass ratios and XRD analyses. Since the iron(II) oxidation rate is very fast and iron(III) is highly insoluble below about 15 g/L H_2SO_4, the hematite nucleation rate appears to be dominated by the initial acid and iron(II) concentrations. This supports the use of supersaturation as the main parameter in the nucleation and growth rate expressions. Furthermore, the individual hematite particles appear (at high magnification) to consist of nano-aggregates of small spindle-like particulates. The differences in supersaturation ratios under these low acidity conditions are relatively inconsequential with regard to these particulate sizes, which are typically between 0.1 and 0.2 µm in length. Since the phenomenological model does not account for the effects of agglomeration, an average characteristic (spherical) hematite particle size of 0.15 µm is adopted, irrespective of whether it follows primary or secondary nucleation mechanisms (see below). Another feature at shorter reaction times is the appearance of an amorphous precursor phase, assumed to be $Fe_2O_3 \cdot 3H_2O$, which ties in with the thermodynamic model assumptions
- The subsequent test series were conducted at the baseline temperature of 150ºC, and utilised low to medium initial acid (10-16 g/L H_2SO_4) and iron(II) (4-8.5 g/L Fe) concentrations in a copper (15 g/L) sulfate background solution. Amorphous hydronium jarosite forms first but becomes more crystalline over time. Various examples are illustrated where spheroidal hematite aggregates are visible in the amorphous jarosite agglomerate structures and also on the surfaces of the more crystalline jarosite phase. This might suggest that hematite and jarosite precipitate independently and then agglomerate into larger structures, or, alternatively, that the hematite particulates could act as substrate surface for hydronium jarosite formation, before being swamped by the large agglomerate structures. The latter case is assumed, including the reverse scenario, *i.e.*, the secondary

Stellenbosch University http://scholar.sun.ac.za

nucleation – rapid growth of hematite particulates onto existing jarosite surfaces. It is not unreasonable to expect that the interfacial energy of secondary hematite nucleation on hydronium jarosite surfaces is lower than the high interfacial energy between hematite and the solvent during primary nucleation. It is assumed that the strong adsorption of sulfate ion on hematite is the driving force that makes these mechanisms possible. Again, iron(III) supersaturation appears to be pivotal in determining the precipitation rate and relative amount of hematite *vs.* hydronium jarosite phase. Most importantly, lower supersaturations at these intermediate acidities often produce dispersed hematite particles (not aggregated) on the jarosite surfaces. These particles are typically between 0.1 and 0.2 µm in size, again justifying the baseline characteristic size of 0.15 µm adopted in the phenomenological model. The fact that large jarosite particles evolve at longer reaction times suggests that the GT relationship is the driving force that makes crystalline hydronium jarosite more stable than nano-sized hematite particulates under these conditions, despite the fact that the thermodynamics may suggest otherwise. This highlights the complex relationship between the acid and iron(III) concentrations and the exposed surface area, justifying the assumptions of the phenomenological model

- The next few test series were also conducted at the baseline temperature, but utilising high initial acid (> 15 g/L H_2SO_4) and iron(II) (> 7.5 g/L Fe) concentration regimes in copper (15 g/L) sulfate background solution. Relatively large hydronium jarosite crystals (confirmed by XRD) form rapidly under these conditions, which then agglomerate and grow into even larger polycrystalline aggregate structures over time. Although these polycrystalline structures are often remnants of the initial (amorphous) agglomerates, hydronium jarosite particle growth is accompanied by a general increase in particle mass. A topochemical reaction boundary assumption is therefore the logical premise of the phenomenological model, which imposes an idealised surface area on the simulation. Again, layers of dispersed particulates are visible on selected jarosite surfaces. This low density precipitate is low in sulfur and is assumed to be an amorphous hematite precursor phase, which is comparatively more stable (*cf.* hematite) at these higher acidities. This is again in line with the thermodynamic framework developed for the phenomenological model. Furthermore, the transformation of hydronium jarosite to hematite (*via* redissolution-precipitation) seems to be insignificantly slow under terminal acidities of around 15 g/L H_2SO_4 and above
- The final test series reverted to the lower temperatures of 140 and 130ºC, targeting progressively lower initial acid and iron(II) concentration ranges, *i.e.*, 7.5 to 20 g/L H_2SO_4 & 5 to 10 g/L Fe and 4 to 12.5 g/L H_2SO_4 & 3.5 to 5.5 g/L Fe, respectively. The trends at these lower temperatures are consistent with the above higher operating temperatures, *i.e.*, a lower overall precipitation rate with increasing initial acid concentration. The BSE

Stellenbosch University http://scholar.sun.ac.za

images confirm that the initial amorphous hydronium jarosite structures become more crystalline over time, especially at higher initial acid concentrations, while crystalline hematite aggregates are preferentially formed at lower initial acid concentrations. Again, the polycrystalline structures are often remnants of the initial (amorphous) agglomerates. Crystalline hydronium jarosite precipitation is driven by preferential growth along the lowest energy axes at the higher acid initial concentrations, resulting in smooth individual crystallite surfaces, but many different crystal orientations, probably *via* twinned growth

- The above results provide qualitative, yet strong, support in favour of primary and secondary hematite nucleation, accompanied by rapid (but limited) growth. Hydronium jarosite precipitation, on the other hand, manifests *via* a continuous growth mechanism on existing surfaces. These results confirm further that the hematite and hydronium jarosite phases can be produced simultaneously and that the phenomenological model should be based on calculated (idealised) particle surface areas. However, the batch data are transient and a description of the rates of all the reaction steps, as a function of the supersaturation, is required to simulate the continuous systems *i.e.*, the supersaturation 'path' of iron(III) differs significantly between the continuous and batch operations.

5.5.3 Phenomenological iron(III) precipitation rate model

Current (published) theory cannot be applied without major simplifications. The assumptions are justified by keeping the objective of the phenomenological model in mind, *i.e.*, to describe the kinetics of iron(III) precipitation (reactive crystallisation) and the relative amount of the hematite *vs.* hydronium jarosite precipitation in batch and continuous autoclaves, without necessarily addressing all the fundamental questions.

For the sake of simplicity, only two polyatomic iron(III) species, $FeH(SO_4)_2^o$ and $Fe(OH)_3^o$, are explicitly recognised, with the former representing the dominant species and the latter providing the extra degree of freedom required to form a simplistic solution chemical basis. The premise of this assumption is the fact that the free ferric species (Fe^{3+}) is a highly charged entity in a relatively low dielectric solvent (at high temperature). Hence, it would tend to form strong contact ion pairs (CIPs) of neutral (or low) terminal charge, which reduces the free energy of the electrolyte system. Adopting these neutral species is also mathematically convenient in that unity single-ion activity coefficients may be assumed, *i.e.*, these species would be expected to interact only weakly with their immediate electrolyte environment. The $FeH(SO_4)_2^o$ and $Fe(OH)_3^o$ species are related by an equilibrium reaction, which, in turn, is incorporated into the thermodynamic formulations of the hematite and hydronium jarosite supersaturation ratios; these ratios form the basis of the phenomenological precipitation rate expressions. Since the $FeH(SO_4)_2^o$ and $Fe(OH)_3^o$ act as surrogate species for the different iron(III) hydroxide and sulfate species, respectively, they cannot

Stellenbosch University http://scholar.sun.ac.za

simulate all the complex chemical changes over changing temperature and solution composition. This is considered to be one of the more important weaknesses of the overall phenomenological model and should be expanded upon in future extensions of this model.

Crystallinity is closely related to the rate at which growth units are supplied to the surface: the slower the supply rate, the more ordered the precipitate, which emphasises the dependency of precipitation on both thermodynamic and kinetic aspects. The interfacial energy greatly influences the precipitation behaviour of the phase and is dependent on surface morphology, structure, waters of hydration and particle size. Although no accurate interfacial energies are available for crystalline hematite and hydronium jarosite, a higher value would be expected for hematite based on its lower solubility and higher apparent surface enthalpy compared to iron(III) hydroxide and oxyhydroxide precipitates. Significantly smaller critical nuclei sizes are therefore prevalent in the case of hematite, leading to the rapid formation of a high number of small particulates in a region of spontaneous nucleation, *i.e.*, at lower acidities. The Gibbs-Thompson (GT) relationship explains why these characteristic hematite particulates tend to remain small, whereas the continuous growth mechanism is most prevalent in the case of hydronium jarosite precipitation.

Primary nucleation and rapid growth, to yield hematite particles of characteristic small size, are combined in a single event and are assumed to precede the other precipitation steps. This assumption is supported by the significant elemental sulfur yield of chalcopyrite concentrates (~60%; Ch. 6-8), *i.e.*, the iron(III) supersaturation is the highest when the acid consumption and iron dissolution rates are the highest, yielding the following rate expression:

$$J_{prim} = k_{prim} \cdot exp\left(\frac{-\xi K_{Hem}}{(2\,ln S_{Hem})^2} \cdot \left(\frac{\gamma_{Hem}}{T} \right)^3 \right) \qquad 5.60$$

Although these particulates aggregate into particles, which, in turn, may agglomerate into larger structures, a description of these processes is not required from a phenomenological modelling perspective and they are assumed to have an insignificant impact on the overall precipitation rate. Furthermore, since iron(III) may first precipitate as an amorphous precursor phase of lower interfacial energy before being converted into hematite, the supersaturation is described in terms the $Fe_2O_3.3H_2O$ phase. This phase is assumed to dehydrate rapidly (non-rate limiting) to form crystallites of characteristic size, each treated as an individual particulate and fully exposed to the bulk solution environment.

A secondary nucleation – rapid growth expression is also required to account for the rapid formation of characteristic hematite particulates on existing iron(III) surfaces, *e.g.*, during the latter stages of batch precipitation or during high pulp density batch or continuous autoclave mineral

Stellenbosch University http://scholar.sun.ac.za

oxidation. This secondary mechanism provides the required link to simulate high pulp density leaching-precipitation systems using low pulp density batch precipitation data. Although various empirical seeding and contact-type nucleation studies have reported a linear relationship between the precipitation rate and pulp (mass) density, no clear distinction is made between surface integration growth and the formation of new particulates *via* surface nucleation. This 'grey area' is most consistent with surface nucleation in the case of sparingly soluble hematite, *i.e.*, secondary nucleation is assumed to occur in the surface adsorption layer or liquid phase adjacent to the surface, yielding secondary hematite particulates of characteristic size. The most important aspect of this mechanism is the apparent autocatalytic effect of the existing precipitate surface, while aggregation is again neglected. An enhancement factor, κ, captures the autocatalytic (S-shape) impact of existing surface area on the rate, while reflecting an apparent linear response to the pulp density above a set minimum (~1 wt% solids):

$$J_{sec} = k_{sec} \cdot (\kappa a_{Fe} \cdot ln\sigma_{Fe}) \cdot exp\frac{-E_{a,Hem}}{R_g}\left(\frac{1}{T} - \frac{1}{T_r}\right) \cdot \sigma_{Hem} \qquad 5.61$$

The total (spherical) surface area term, a_{Fe}, assumes that secondary hematite nucleation can also occur on hydronium jarosite surfaces (see below). However, the σ_{Fe} term represents the relative saturation ratio of iron(III) in equilibrium with the hematite and hydronium jarosite, and provides the means to distinguish between the higher nucleation rate on rudimentary hematite *vs.* hydronium jarosite surfaces, *i.e.*, to cater for $S_{crit,surf} < S_{crit,het}$. Although this secondary nucleation rate framework is speculative, this general formulation is justified due to the current lack of thermodynamic and mechanistic knowledge.

The above scheme does not cater for a classical hematite growth mechanism, *e.g.*, when hematite seed particles come in contact with a solution at low supersaturation levels, hence the assumption of a constant characteristic size, L_{Hem}. The overall precipitation rate of iron(III) as hematite is then:

$$R_{FeIII,Hem} = \tilde{k}_{Hem} L_{Hem}^3 \cdot (J_{prim} + J_{sec}) \qquad 5.62$$

The advantage of this approach is the mathematical consistency in treating the simultaneous precipitation of hematite and hydronium jarosite, each of which can act as a substrate surface for the other phase (see experimental verification below). However, this model underestimates the precipitation rate of hematite in the low acid regime (< 15 g/L H_2SO_4). The reason for this is thought to be the simplistic thermodynamic model, which leads to underestimated supersaturations and iron(II) oxidation rates (Ch. 4) in this regime. Two additional and (presumably) related expressions are therefore added, both expressed in terms of the relative saturation ratio. One expression captures the rapid conversion of hydronium jarosite to hematite (2nd term in Eq. 5.64), while the other increases in the characteristic hematite particle size in this regime:

Stellenbosch University http://scholar.sun.ac.za

$$L_{Hem} = 0.125 + (4\times10^{-4} \cdot \sigma_{Fe}) \qquad 5.63$$

This hydronium jarosite to hematite conversion process is assumed to occur at a reaction front that does not directly influence the bulk precipitation rate.

Observations from the literature have confirmed that hydronium jarosite usually manifests as relatively large particles (*cf.* the thermodynamically stable phase) and may transform over time *via* a redissolution-precipitation mechanism under surface chemical reaction control. However, at high enough terminal acidity, crystalline hydronium jarosite becomes stable, at least over typical autoclave reaction times. It is assumed that hydronium jarosite nucleation only occurs under conditions of higher acid concentration and, hence, lower supersaturation, *i.e.*, where surface nucleation is accompanied by a continuous growth mechanism. Therefore, the classical continuous growth mechanism is exclusively reserved for hydronium jarosite precipitation due to its lower interfacial energy, and, hence, higher solubility. Under such conditions, very limited primary nucleation of jarosite would occur and the rate of hydronium jarosite growth would be dependent on the total surface area present at that specific point in time. It is assumed that hydronium jarosite growth may originate just as readily on hematite surfaces as on existing jarosite surfaces. This phenomenon has been validated experimentally (see above) and is thought to be a result of the strong adsorption of sulfate species on hematite surface (~2% S^T). The growth rate of hydronium jarosite is simply dealt with *via* a conventional topochemical reaction, assuming the growth rate is independent of particle size, *i.e.*, complies with McCabe's (ΔL) rule. The linear growth rate (G_{Jar}) assumes a first-order dependence on the relative supersaturation and an Arrhenius-like response in temperature. This linear relationship has been verified by regression (see below) to best represent the experimental results, while the conversion term (G^-) is included to increase the hematite to jarosite ratio in the low acid regime:

$$G_{Jar} = G^+ - G^- = k_G \cdot exp\frac{-E_{a,Jar}}{R_g}\left(\frac{1}{T} - \frac{1}{T_r}\right)\cdot\sigma_{Jar} - k_G^- \cdot exp\frac{-E_{a,Jar/Hem}}{R_g}\left(\frac{1}{T} - \frac{1}{T_r}\right)\cdot ln\,\sigma_{Fe} \qquad 5.64$$

A phenomenological description of the rate of iron(III) removal *via* the hydronium jarosite growth mechanism is therefore as follows:

$$R_{FeIII,Jar} = \tilde{k}_{Jar} \cdot a_{Fe} \cdot G_{Jar} \qquad 5.65$$

Similarly to hematite (Eq. 5.62), the proportionality constant, $\tilde{k}$, translates the one-dimensional increase in particle size into an iron(III) molal concentration change, assuming a conservation of the particle shape and no impact of aggregation or agglomeration on the precipitation rate:

$$L_{Fe} = L_{Hem} + (G_{Jar} \cdot t) \qquad 5.66$$

Stellenbosch University http://scholar.sun.ac.za

In conclusion, the above phenomenological model provides an estimate of the complex processes taking place during iron(III) precipitation under typical MT autoclave conditions. Based on the current methodology, the continuous autoclave simulation is readily dealt with *via* the time- and space-averaged population balance around each compartment, using an iterative calculation scheme to simplify the population balance equation:

$$\upsilon_j \cdot \frac{\partial \psi_j}{\partial L_{Fe}} + \frac{\psi_j}{\tau_j} = \frac{\psi_{j-1}}{\tau_j} + B_{L,j} \qquad 5.67$$

where υ_j refers to the mean hydronium jarosite velocity vector (µm/min), while the formation rate of new hematite particles, $B_{L,j}$ (1/kg.µm.min) of characteristic size (L_{Hem}) is assumed to occur instantaneously on entering the reactor compartment *j*:

$$\upsilon_j = G_{Jar}(\sigma_{Jar}, \sigma_{Fe}, T)_j \quad \text{and} \quad B_{L,j} = \frac{dJ_{Hem}(S_{Hem}, a_{Fe}, \sigma_{Hem}, \sigma_{Fe}, T)_j}{dL_{Hem}(\sigma_{Fe})_j} \qquad 5.68$$

5.5.4 Model verification and quantification (regression analyses)

Thermodynamic framework

The first part of quantifying the above phenomenological model is to establish an internally consistent thermodynamic framework. Hematite solubility data from the literature between 130 and 170ºC were used as a basis to regress a Gibbs free energy value of the $FeH(SO_4)_2^o$ species. This exercise revealed that hydronium jarosite is thermodynamically metastable with respect to hematite under typical MT autoclave conditions (< 0.30 mol/kg H_2SO_4). However, literature information indicates that the transformation of the relatively large jarosite particles is slow above about 0.1 mol/kg H_2SO_4, which is in line with the GT relationship, and which allows application of its solubility in a conventional manner over typical autoclave timeframes.

Phenomenological rate model

The above experimental results and discussion highlight the complexity of the iron(III) precipitation system under MT operating conditions, which demand a phenomenological modelling approach. Firstly, the iron(II) oxidation rate model (Ch. 4) is directly utilised, without any modifications. The model assumes that the characteristic hematite particulates act as a substrate surface for jarosite nucleation and subsequent continuous growth, while secondary hematite nucleation is promoted by higher total exposed surface areas, irrespective of the precipitate surface type. This model also assumes that precipitation commences at the point where the supersaturation ratio exceeds unity. Furthermore, the regression makes use of an equally weighted error function, *i.e.*, between the precipitation reaction extent and the residue hematite content.

Stellenbosch University http://scholar.sun.ac.za

The final regression utilised optimised transition function parameters (κa_{Fe}-term) to best represent the precipitation rate at high pulp densities in the continuous and batch reactor configurations (*ref.* Ch. 7 & 8, respectively), which also impact on the low pulp density simulations (this chapter). Selected parameters, *i.e.*, k_{sec} and $E_{a,Jar}$, are best utilised by fixing their values, while regressing the others, based on the test results at low initial acidities (< 12 g/L H_2SO_4) to obtain k^{-}_{G}, $E_{a,Jar/Hem}$, p_5 and p_6 (Eq. 5.59) and also the test results at typical autoclave acidities (> 12 g/L H_2SO_4) to obtain the main parameters, k_{prim} and k_G. These different regimes are utilised in iterative fashion until no further minimisation of the objective function is achieved. The optimised parameter values are summarised in Table 5.10.

A general first-order dependency of the hydronium jarosite growth rate on the relative supersaturation gives the best representation of the experimental results. No other surface integration models, such as the birth and spread (B+S) model, are capable of yielding superior simulation results. Taking the experimental uncertainty into account, the simulation reflects most of the measured trends, *e.g.*, an increase in the hydronium jarosite content with increasing iron(III) supersaturation. Besides the experimental errors, the primitive nature of the solution thermodynamic model impacts most profoundly on the performance of the simulation. Both the supersaturation ratios and the iron(II) oxidation rate appear to be underestimated in the low acidity region. Furthermore, the above scheme does not consider the re-leaching of precipitated iron(III) phases, *e.g.*, the possible redissolution of small hematite particulates as the acid concentration increases over time (GT relationship). These aspects need to be improved upon in future investigations, as well as the comparatively large experimental errors when targeting the lower precipitation extents.

5.5.5 Achieving the overall modelling objective

This chapter presents a phenomenological model of the rate of iron(III) precipitation in batch and continuous autoclaves under medium temperature (MT) autoclave conditions. The rate expressions are based on information obtained from the literature and experimentation at low and high pulp densities. Special allowance is made for the formation of hematite surface nuclei, which appears to be promoted at higher precipitate surface area, especially in suspensions of lower terminal acidity. This leads to the formation of secondary particulates and provides the required link to simulate high pulp density leaching-precipitation systems using low pulp density batch precipitation data. In particular, the model allows direct application of the simulation to the autoclave oxidation of iron-containing copper sulfide concentrates and provides a good estimation of the relative precipitation rate of hematite, the preferred product, compared to hydronium jarosite. Some interesting mechanistic understandings of iron(III) precipitation in autoclaves are further elucidated.

Stellenbosch University http://scholar.sun.ac.za

VOLUME II

MINERAL OXIDATION REACTIONS, REACTORS & SYSTEMS

(CH. 6 TO 8)

Stellenbosch University http://scholar.sun.ac.za

CHAPTER 6. SULFIDE MINERAL OXIDATION

6.1 Introduction

This chapter focuses on the intrinsic oxidation behaviour of a disseminated chalcopyrite concentrate under medium temperature (MT) autoclave conditions, in the presence of dissolved oxygen, sulfate salts and sulfur-dispersing surfactants, *i.e.*, to simulate the intrinsic oxidation behaviour of the concentrate on a phenomenological level under Anglo American – University of British Columbia (AA-UBC) process conditions (Ch. 1, Sect. 1.1.2).

The development roadmap of this phenomenological mineral oxidation rate model is as follows:

- Reviewing the literature to identify the most important factors that may impact on the sulfide mineral oxidation rate, covering all areas, from the thermodynamic driving force (Sect. 6.3.1), to the fundamental anodic (mineral) dissolution, sulfur oxidation and rearrangement, and cathodic (oxidant) reduction mechanisms (Sect. 6.3.2), as well as the workings of the pre-selected surfactants (Sect. 6.3.3)
- Developing simplified mechanistic views and the corresponding intrinsic oxidation rate expressions of the important minerals, based on insights from the literature and preliminary quantum-level modelling of the reactive species' surface adsorption (Sect. 6.3.4 & 6.6.2)
- Relating these oxidation rate expressions on a phenomenological level (Sect. 6.3.5)
- Establishing confidence in the experimental procedure (Sect. 6.4 & 6.5.1), identifying the relevant reaction regimes (Sect. 6.5.2), quantifying the chalcopyrite oxidation response to bulk property changes on a phenomenological level (Sect. 6.5.3), and validating the oxidation chemistry and mechanism on a phenomenological level (Sect. 6.5.4), and
- Quantifying (regressing) and verifying the intrinsic oxidation rate model (Sect. 6.5.5).

6.2 AA-UBC process (context)

Section 1.1.2 presents a brief overview of some of the processes proposed to treat chalcopyrite concentrates under MT conditions. Detailed aspects of the AA-UBC process are described in the patent publication (Dempsey & Dreisinger, 2003) and Dreisinger *et al.* (2002). One of the most important aspects of this process is the use of fine grinding (typically a d_{80} of 10-15 µm, although the patent covers a wider range, *viz.* a d_{80} of 5-20 µm) to overcome the problem of chalcopyrite passivation (Sect. 6.3.2). Leaching is performed in sulfate medium at around 150°C to obtain fast oxidation kinetics and stable iron residues, while surfactants are added to disperse elemental sulfur from the unreacted sulfide surfaces to prevent liquid sulfur occlusion. Therefore, the AA-UBC process relies on a combination of fine-grinding, surfactants and temperature to increase the rate of chalcopyrite oxidation and the work presented in this chapter should be viewed within this context.

Stellenbosch University http://scholar.sun.ac.za

6.3 Review and theory

The purpose of this section is to condense the relevant literature in context of the AA-UBC process. The review and theory are presented in chronological order, from a general overview of the chemistry and thermodynamics, to the mechanisms of sulfide mineral oxidation and the detailed building blocks required to describe the oxidation process phenomenologically.

6.3.1 Reaction stoichiometries and thermodynamics: bulk perspective

The oxidation of sulfide to higher oxidation states may follow a number of different electron transfer steps, depending on the nature of the dissolved oxidant and other properties of the solution in contact with a sulfide mineral particle (see Lotens & Wesker, 1987). For now, it is assumed that sulfide is first oxidised to elemental sulfur (S°), followed by further oxidation to sulfate (S^{6+}):

$$S_{(s)}^{Y-} \rightarrow S_{(s)}^{o} \rightarrow SO_{4(aq)}^{2-} \qquad 6.1$$

Although such a sequential oxidation mechanism is unlikely (Sect. 6.3.2), the reaction stoichiometry is best dealt with in this manner. From a bulk perspective, the following oxidation reactions are most relevant to this study, *i.e.*, for chalcopyrite ($CuFeS_2$), bornite (Cu_5FeS_4), chalcocite (Cu_2S), covellite (CuS), pyrite (FeS_2), pyrrhotite (Fe_7S_8) and sphalerite ($Zn_xFe_{1-x}S$), respectively:

$$CuFeS_{2(s)} + O_{2\,(aq)} + 2H_2SO_{4(aq)} \Rightarrow CuSO_{4(aq)} + FeSO_{4(aq)} + 2H_2O + 2S_{(s)}^{o} \qquad 6.2$$

$$Cu_5FeS_{4(s)} + 3O_{2\,(aq)} + 6H_2SO_{4(aq)} \Rightarrow 5CuSO_{4(aq)} + FeSO_{4(aq)} + 6H_2O + 4S_{(s)}^{o} \qquad 6.3$$

$$Cu_2S_{(s)} + O_{2\,(aq)} + 2H_2SO_{4(aq)} \Rightarrow 2CuSO_{4(aq)} + 2H_2O + S_{(s)}^{o} \qquad 6.4$$

$$CuS_{(s)} + \tfrac{1}{2}O_{2\,(aq)} + H_2SO_{4(aq)} \Rightarrow CuSO_{4(aq)} + H_2O + S_{(s)}^{o} \qquad 6.5$$

$$FeS_{2(s)} + \tfrac{1}{2}O_{2\,(aq)} + H_2SO_{4(aq)} \Rightarrow FeSO_{4(aq)} + H_2O + 2S_{(s)}^{o} \qquad 6.6$$

$$Fe_7S_{8(s)} + \tfrac{7}{2}O_{2\,(aq)} + 7H_2SO_{4(aq)} \Rightarrow 7FeSO_{4(aq)} + 7H_2O + 8S_{(s)}^{o} \qquad 6.7$$

$$Zn_xFe_{1-x}S_{(s)} + \tfrac{1}{2}O_{2\,(aq)} + H_2SO_{4(aq)} \Rightarrow xZnSO_{4(aq)} + (1-x)FeSO_{4(aq)} + H_2O + S_{(s)}^{o} \qquad 6.8$$

The elemental sulfur is oxidised to sulfuric acid according to the following overall stoichiometry:

$$S_{(s)}^{o} + \tfrac{3}{2}O_{2\,(aq)} + H_2O \Rightarrow H_2SO_{4(aq)} \qquad 6.9$$

Since these mineral oxidation reactions differ mechanistically, their relative oxidation rates would also differ. However, it is appropriate to first discuss the driving force from a thermodynamic perspective, *i.e.*, using Pourbaix diagrams, which utilise the electromotive force (EMF) of the cell

Stellenbosch University http://scholar.sun.ac.za

(E_h), with reference to the standard hydrogen electrode (SHE), and pH as the primary variables. Although these diagrams are useful to describe hydrometallurgical systems, their applicability is often restricted to geologic time spans where kinetic factors, such as metastability and diffusion limitations, are not dominant (Peters, 1973).

Sulfur stability

Figure 6.1 presents E_h-pH diagrams of the S-H_2O and S-Fe-H_2O systems at 150°C (*HSC*, 2006).

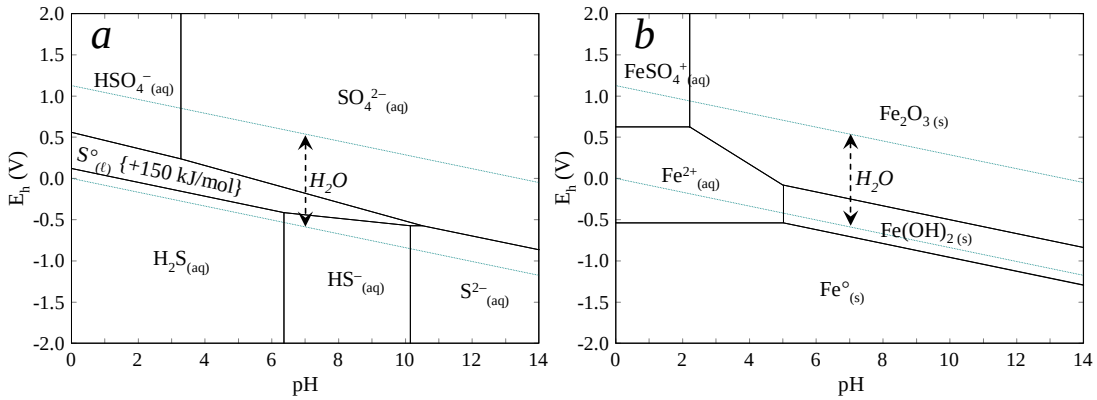

Figure 6.1
E_h-pH diagram in aqueous environment at 150°C & 1 mol/kg ionic strength: *a*) S-H_2O system at 0.5 mol/kg S; *b*) S-Fe-H_2O system (without sulfide minerals) at 0.5 mol/kg S & 0.1 mol/kg Fe.

The region of particular application to hydrometallurgical systems is the water stability region (dotted lines), *i.e.*, the region above the anodic oxidation of diatomic hydrogen:

$$2H^+_{(aq)} + 2e^- \Leftrightarrow H_{2(g)} \qquad 6.10$$

and the region below the cathodic reduction of diatomic oxygen:

$$O_{2(g)} + 4H^+_{(aq)} + 4e^- \Leftrightarrow 2H_2O \qquad 6.11$$

The stability region of liquid sulfur (rhombic sulfur data, *ref. HSC*, 2006) is unrealistically small and, hence, the Gibbs free energies (see Ch. 2) of the bisulfate and sulfate ions are artificially increased by an arbitrary amount of 150 kJ/mol (methodology adopted from Peters, 1986). Elemental sulfur is known to be relatively stable, even under MT autoclave conditions (*e.g.*, Chalkley *et al.*, 1993) and may be ascribed to the kinetic resistance of breaking the S_8 ring structure (Dreisinger, 2004; also see Sect. 6.3.2). In contrast, Figure 6.1 *a* suggests that under conditions where most of the iron is present as iron(III) species (E_h > ~600 mV, *ref.* Figure 6.1 *b*), molten elemental sulfur would not be stable. Even though the sulfur yield is affected by the acidity and oxidation temperature, only a small portion of pyritic sulfide is oxidised to elemental sulfur (< 25% at 150°C & typical leach acidities; see Papangelakis & Demopoulos, 1991). This lower sulfide yield in the case of pyrite is also reflected in Figure 6.2 *a*, where the aqueous sulfur species

Stellenbosch University http://scholar.sun.ac.za

(HSO_4^-, $FeSO_4^+$ & SO_4^{2-}) have, once again, been destabilised by 150 kJ/mol. The increased stability of hematite (Fe_2O_3) at lower pH values (*cf.* Figure 6.1 *b*) is due to this destabilisation energy. A better representation would be obtained by also including metastable hydronium jarosite (Ch. 5), which highlights the artificial nature of these diagrams. Figure 6.2 *b* presents the analogous diagram of the S-Zn-H_2O system, where the above destabilisation energy is doubled to 300 kJ/mol in order to be consistent with experimental observation. For example, in zinc pressure leaching, at least 95% of the non-pyritic sulfide is oxidised to elemental sulfur (Chalkley *et al.*, 1993). Higher destabilisation energies would also be required to mirror the observed behaviour of other minerals, like pyrrhotite (not illustrated here). Therefore, the elemental sulfur yield gives a reflection of the intrinsic oxidation mechanisms of the different minerals, rather than supporting the notion that elemental sulfur and iron(III) do not co-exist under MT autoclave conditions.

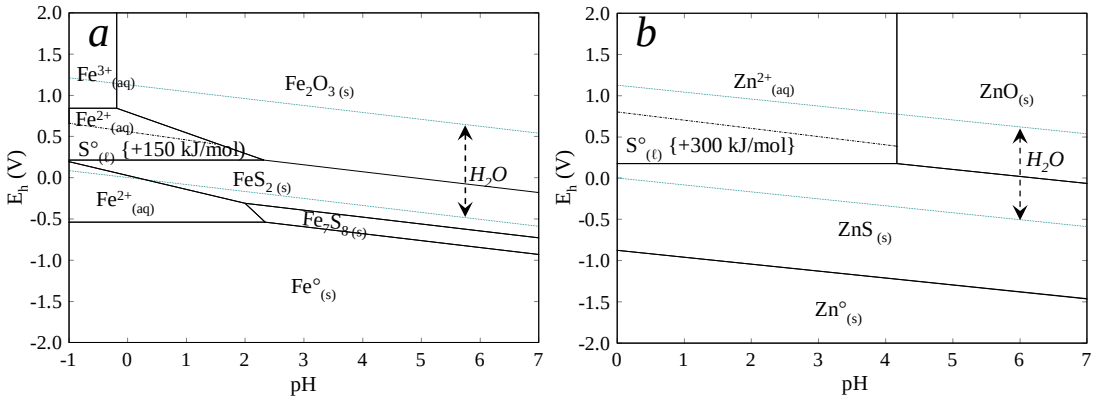

Figure 6.2
E_h-pH diagram in aqueous environment at 150°C & 1 mol/kg ionic strength: *a*) S-Fe-H_2O system at 0.5 mol/kg S & 0.1 mol/kg Fe; *b*) S-Zn-H_2O system at 0.5 mol/kg S & 0.1 mol/kg Zn.

Figure 6.3 *a* illustrates the stability diagram for the S-Cu-Fe-H_2O system, after omitting the iron sulfide minerals and using a destabilising energy of 250 kJ/mol to artificially extend the stability range of elemental sulfur. This particular arrangement emphasises the variable behaviour of sulfur, which depends, amongst other factors, on solution acidity, oxidation potential and temperature. Hackl *et al.* (1995a) list various references from the open literature, covering a wide range of recorded sulfur yields for different chalcopyrite concentrates and oxidation conditions. Hackl *et al.* themselves oxidised chalcopyrite concentrate from the Gibraltar mine (British Columbia) in sulfuric acid medium (98 g/L H_2SO_4), using acid (starting solution) to copper (concentrate) (H_2SO_4:Cu) molar ratios of around 2.25 and 100 g/L sample mass, *i.e.*, 100 g concentrate per litre solution. They reported sulfide to elemental sulfur conversions of 72% (110°C), 63% (130°C), 52% (170°C) and 0% (>200°C). Besides the obvious drop in sulfur yield with temperature, these were substantially lower than the results obtained by, *e.g.*, Vizsolyi *et al.* (1967), who oxidised Lynn Lake (Manitoba) chalcopyrite concentrate in sulfuric acid medium (95 g/L H_2SO_4) at 100 to 150°C. Despite the fact that the H_2SO_4:Cu ratio was lower (0.66, using 300 g/L concentrate), Vizsolyi *et*

Stellenbosch University http://scholar.sun.ac.za

al. obtained sulfide to elemental sulfur conversions of 85 to 90%. Although this difference in sulfur yield may be partly due to the low pyrite content in the Lynn Lake concentrate (<5%) compared to the Gibraltar concentrate (17%), the intrinsic oxidation of the Gibraltar chalcopyrite appears to have yielded significantly less elemental sulfur, despite having a significantly higher acid to copper ratio. The study of Braithwaite and Wadsworth (1976) represents an extreme example of where acid deficiency resulted in very low sulfur yields. They oxidised a relatively pure chalcopyrite specimen from Bingham Canyon mine (Utah) under highly acid deficient conditions (starting pH of 1.88) and dilute pulp densities (< 40 g/L solids). The yield of elemental sulfur was less than 10% after complete chalcopyrite oxidation at 150°C, which reflects the negative slope (over pH) of the sulfur line (Figure 6.3 *a*). These tests were conducted using a relatively coarse size fraction (+53–74 µm), which required long oxidation times (~10 hrs). This long reaction time and the presence of copper in solution could have resulted in considerable oxidation of previously formed elemental sulfur (Corriou & Kikindai, 1981; Habashi & Bauer, 1966). A more appropriate example of variable mineral behaviour can be found in the study of Yu *et al.* (1972). They used very coarse particle size fractions (geometric averages of 218 & 248 µm), very low pulp densities (< 6 g/L concentrate) and oxidation times, ranging between 2 and 4 hours. This particular concentrate, from Walker mine (California), was relatively pure and contained only about 5% pyrite. The interesting aspect of this work is the low elemental sulfur yield that was observed (< 4%), even at moderate acid concentration (0.25 mol/L H_2SO_4) and 150°C. The low sulfur yield was reflected in linear mineral oxidation kinetics (Sect. 6.3.5), without the presence of surfactants. This example confirms that thermodynamics alone cannot explain some of the observed trends and important parameters, such as the sulfur yield, are deeply imbedded within the kinetic realm, *i.e.*, the mechanism of oxidation on a particular mineral surface. These thermodynamic diagrams should therefore be interpreted in conjunction with knowledge of the kinetic limitations.

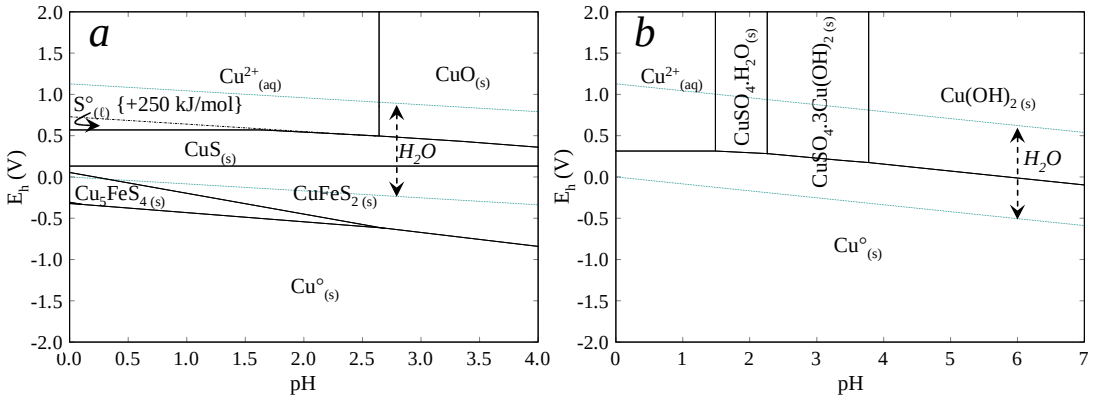

Figure 6.3
E_h-pH diagram in aqueous environment at 150°C & 1 mol/kg ionic strength: *a*) S-Cu-Fe-H_2O system at 0.6 mol/kg S, 0.5 mol/kg Cu & 0.1 mol/kg Fe (without Fe sulfide minerals); *b*) S-Cu-H_2O system at 0.5 mol/kg S & 0.5 mol/kg Cu (without sulfide minerals).

Stellenbosch University http://scholar.sun.ac.za

Formation of new mineral phases on existing surfaces

Figure 6.2 *a* suggests that pyrrhotite may oxidise to pyrite. In hydrometallurgical leaching systems however, only elemental sulfur is produced, unless the acid concentration is higher, in which case hydrogen sulfide (H_2S) gas may also be produced (*e.g.*, Dutrizac & MacDonald, 1974). As explained by Peters (1973): "evidently the nucleation and growth of new mineral phases is a process that does not take place readily at ambient (or even autoclave) conditions in the kind of time periods available for hydrometallurgy." In contrast, various studies (*e.g.*, Dutrizac & MacDonald, 1974) identified intermediate stoichiometric and non-stoichiometric compounds on the surface of original copper minerals after partial oxidation. For example, Dutrizac *et al.* (1970) noted that bornite dissolved in acidified iron(III) sulfate solution *via* the formation of non-stoichiometric bornite ($Cu_{5-x}FeS_4$) to form chalcopyrite, which then dissolved slowly. This intermediate chalcopyrite correctly occupies the region of the E_h-pH diagram through which the bornite passes upon oxidation (Figure 6.3 *a*). The cathodic reduction of chalcopyrite in copper(II) sulfate solutions, using sulfur dioxide (SO_2) gas as a reductant, was studied by Sohn and Wadsworth (1980) and an initial defect structure close to bornite was observed. The presence of covellite rims on relict chalcopyrite grains has been observed under oxidative conditions at medium to high temperatures (>130°C) (Ferron *et al.*, 2000; Jang & Wadsworth, 1993; Peters, 1976), which is correctly reflected by Figure 6.3 *a*. The anodic chalcopyrite dissolution of chalcopyrite may therefore be represented as follows:

$$CuFeS_{2(s)} \Rightarrow CuS_{(s)} + S^{o}_{(s)} + Fe^{2+}_{(aq)} + 2e^{-} \qquad 6.12$$

$$CuS_{(s)} \Rightarrow Cu^{2+}_{(aq)} + S^{o}_{(s)} + 2e^{-} \qquad 6.13$$

The proposal of covellite formation as an intermediate step in the autoclave leaching of chalcopyrite dates back many years (Dobrokhotov & Maiorova, 1962). On the other hand, it seems to be formed under less oxidising conditions at atmospheric temperatures (Córdoba *et al.*, 2008). Ferron *et al.* (2000) detected hydrogen sulfide gas in the first compartment of their continuous pilot autoclave and also fine-grained bladed crystals of covellite around the impeller. This led them to propose that covellite precipitated from aqueous cupric ions (Cu^{2+}), according to:

$$Cu^{2+}_{(aq)} + H_2S_{(aq)} \Leftrightarrow CuS_{(s)} + 2H^{+}_{(aq)} \qquad 6.14$$

The fact that the chalcopyrite concentrate (Guelb Moghrein, Mauritania) contained some pyrrhotite and the first compartment had a high acid concentration, may explain the presence of hydrogen sulfide gas (superimpose Figure 6.1 *a* onto Figure 6.2 *a*). However, since the solution redox potential was moderately high (~500 mV *vs.* Ag|AgCl), an alternative mechanism may also be proposed. For example, Figure 6.3 *a* may suggest a possible reaction between cupric ion and sulfur:

Stellenbosch University http://scholar.sun.ac.za

$$CuSO_{4(aq)} + \tfrac{4}{3}S^{o}_{(s)} + \tfrac{4}{3}H_2O \Rightarrow CuS_{(s)} + \tfrac{4}{3}H_2SO_{4(aq)} \qquad 6.15$$

This reaction would be expected to be slow at lower temperatures because copper in solution and elemental sulfur are known to coexist under conditions where sulfur is metastable (Warren & Wadsworth, 1980). However, at high temperatures elemental sulfur decomposes more rapidly in the presence of copper ions and oxygen (Corriou & Kikindai, 1981; Habashi & Bauer, 1966), which could be used in support of Reaction 6.15. Alternatively, Figure 6.3 *a* shows that chalcopyrite forms covellite *via* a simple metathesis reaction at lower solution redox potentials:

$$CuFeS_{2(s)} + Cu^{2+}{}_{(aq)} \Rightarrow 2CuS_{(s)} + Fe^{2+}{}_{(aq)} \qquad 6.16$$

This reaction has been proposed as an intermediate step in the enrichment of chalcopyrite by cupric ion in the absence of oxygen at elevated temperatures (> 100°C) (Jang & Wadsworth, 1993; Peters, 1976), and more recently under atmospheric conditions (Sequeira *et al.*, 2008). The fact that covellite was only detected by Kametani and Aoki (1985) in leach residues after oxidation (90°C) at low redox potential, may also suggest covellite formation as an intermediate species *via* non-oxidative dissolution (also see Peters, 1976):

$$CuFeS_{2(s)} + 2H^{+}{}_{(aq)} \Rightarrow CuS_{(s)} + Fe^{2+}{}_{(aq)} + H_2S_{(aq)} \qquad 6.17$$

The predominance area of the other minerals in Figure 6.3 overshadows the chalcocite region under the conditions of artificial sulfur stability, and is therefore incomplete. Chalcocite may be formed by cathodic decomposition (Hiskey & Wadsworth, 1981; Peters, 1976) or non-oxidative dissolution (Senanayake, 2009). Figure 6.3 also neglects the existence of a number of other metal-rich minerals, *e.g.*, djurleite ($Cu_{31}S_{16}$), digenite (Cu_9S_5), haycocktite ($Cu_4Fe_5S_8$), mooihoekite ($Cu_9Fe_9S_{16}$) and talnakhite($Cu_9Fe_8S_{16}$). Various studies have also discussed the role of non-stoichiometric copper sulfide compounds, such as digenite, as intermediates in the anodic oxidation of chalcocite (Hiskey & Wadsworth, 1981; Peters, 1976) or the cathodic reduction of chalcopyrite (Jang & Wadsworth, 1993), but these reactions are not elaborated upon in this study. Finally, Figure 6.3 *b* illustrates that copper-containing salts may precipitate at higher pulp densities and temperatures. The most likely candidates under the acidic conditions encountered in this study are the monohydrate sulfate salt, $CuSO_4.H_2O$, or copper hydroxy-sulfate salts (see Ch. 5).

The above predominance diagrams depict, to some extent, what has been observed in hydrometallurgical leaching systems (with the artificial inclusion of metastable phases), but fail to provide any mechanistic information. Nevertheless, the various examples support the notion that covellite may be formed as an intermediate product during chalcopyrite oxidation under MT autoclave conditions, although the exact mechanism has not yet been resolved (discussed next).

Stellenbosch University http://scholar.sun.ac.za

6.3.2 Mechanisms of sulfide mineral oxidation in acidic media

This section attempts to derive a general picture of the most prominent mechanistic proposals to date. However, the above discussions highlight the fact that it is unlikely that a single mechanism is applicable to each mineral across a wide array of solution and surface properties. The following discussions should therefore be viewed in context of this study, *i.e.*, to derive phenomenological oxidation rate expressions for the relevant sulfide minerals under typical MT autoclave conditions.

The electrochemical nature of sulfide oxidation has been recognised since early in the previous century and many pertinent studies can be found in the open literature (see introductions by Crundwell, 1988b, Hiskey, 1993 & Osseo-Asare, 1992). A detailed review of these concepts is out of context here, since no fundamental electrochemical measurements are conducted in this study. However, basic application of the mixed potential (MP) theory of metallic corrosion forms an integral part of the rate expressions derived in this chapter. The paper of Holmes and Crundwell (2000) provides an example of the application of the MP theory to derive sulfide mineral oxidation rate expressions.

Implicit in this approach is a basic understanding of semiconductor electrochemistry and solid-state electronic structure theory (discussed in detail in App. F.1). Most sulfide minerals are semiconductors because inter-atomic distances are large, meaning that the energy gap between the valence and conduction bands is greater than the thermal energy of the valence-band electrons. The mechanistic departure point is therefore imbedded within semiconductor electrochemistry and solid-state electronic structure theory. The role of impurity metals, *e.g.*, silver (Ag) is important in this regard. A metal-excess compound, such as chalcopyrite, is most likely to display *n*-type semiconducting behaviour (excess electrons), whereas compounds such as CuS, are *p*-type metallic conductors. The anodic dissolution of sulfides is usually dominated by a hole-decomposition pathway. The supply of holes may be migration-limited in *n*-type semiconductors, which explains why saturation effects are often observed during chalcopyrite dissolution at high oxidant concentrations. Due to the development of an electric field at the solid/solution interface, the transport of charge carriers across this region is usually the rate-limiting step of sulfide mineral dissolution. The presence of a high density of surface states would anchor the Fermi energy at the average energy of those states and the mineral would behave like a metal, *i.e.*, the electric potential would predominantly reside across the Helmholtz layer. This allows direct application of the MP theory to describe the rate of mineral dissolution, analogous to metal corrosion. One of the most important factors determining the rate of mineral dissolution is the adsorption or approach of the oxidant species at the mineral surface. The energy levels of these species are also important, since the intrinsic ability to accept electrons depends on the energy overlap of the empty orbitals with the

Stellenbosch University http://scholar.sun.ac.za

relevant semiconductor band. These concepts are now applied to the most important sulfide minerals encountered in this study, *i.e.*, chalcopyrite, pyrite, covellite and sphalerite.

Chalcopyrite oxidation

The above discussions emphasise the importance of basic knowledge of the electronic structure of minerals. Chalcopyrite has a zinc blende structure and its unit cell is simply constructed by doubling the ZnS unit cell in the *z*-direction and replacing zinc cations with alternating Fe and Cu cations. The optimised unit cell (bulk) structure is presented in Figure 6.4 and illustrates that each metal atom is surrounded by a sulfur atom, while each sulfur atom is surrounded by two copper and two iron atoms in tetrahedral interstices. The oxidation states of the metals are still under discussion, with opinion divided between Cu^{+}/Fe^{3+}, Cu^{2+}/Fe^{2+} or mixed states. Pearce *et al.* (2006) attempted to resolve the issue by suggesting the Cu state is neither d^{10}, d^{9}, nor mixed, but in fact a state with non-integral number of *d*-electrons between 9 and 10, since chalcopyrite is not a truly ionic solid but has a strong covalent character that results in delocalisation of the electrons (Phala, 2008). However, the formal assignment is usually given as $(Cu^{+})(Fe^{3+})(S^{2-})_2$, as suggested by chalcopyrite's anti-ferromagnetic structure (Donnay *et al.*, 1958) and supported by Mössbauer (MES) data (Boekema *et al.*, 2004). The average optimised bond lengths (in the bulk material) of Cu–S, Fe–S and S–S (0.23 nm, 0.23 nm & 0.37 nm, respectively) indicate that metal sulfide bonds are significantly covalent in nature, with no extensive covalence among the anions (also see Crundwell, 1988b).

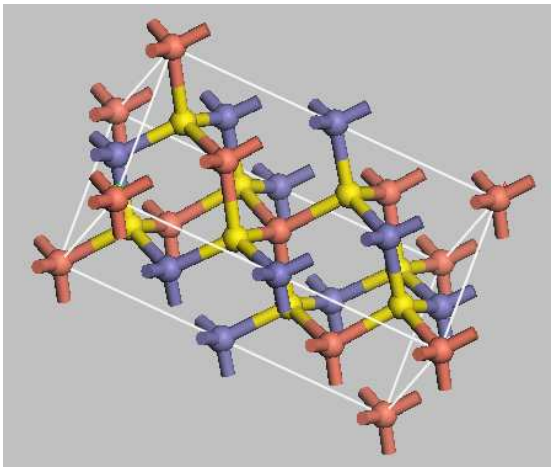

Figure 6.4
Optimised chalcopyrite unit cell (*MS*, 2008); Cu, Fe & S atoms are coloured orange, blue & yellow, respectively (space group I 42d, with experimental lattice parameters: a = b = 5.289Å & c = 10.423Å at room temperature; Absolon, 2008).

The semiconducting electronic band structure of chalcopyrite and the relative position (standard reduction potentials) of the important redox couples are schematically illustrated in Figure 6.5.

Stellenbosch University http://scholar.sun.ac.za

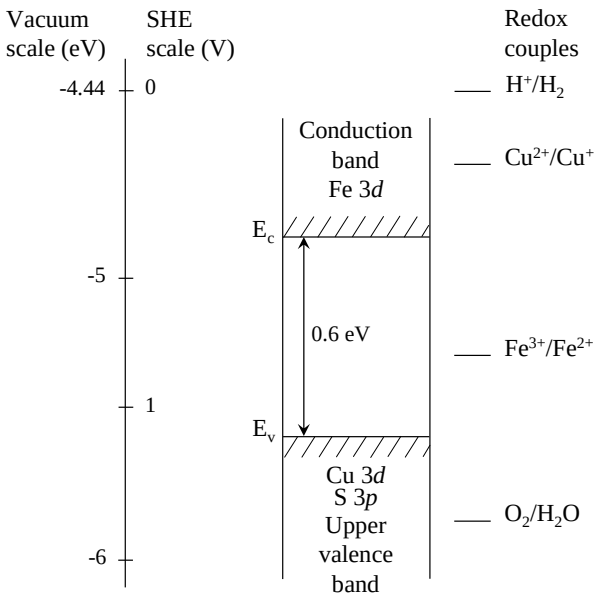

Figure 6.5
Qualitative semiconductive electronic band structure of chalcopyrite, with inclusion of the various standard reduction potentials of the important redox couples (reproduced from Crundwell, 1988a).

Chalcopyrite is a semiconductor with unusual magnetic and electrical properties and behaves like a Mott insulator (Boekema *et al.*, 2004). Yet, the band gap is relatively narrow (~0.6 eV), with the (covalent) bonding orbitals between the copper and sulfide forming the upper part of the valence band, while the lower part of the conduction band is associated with iron (3*d* orbital) (Crundwell, 1988b). In order to achieve mineral dissolution, the electrons in the copper sulfide bonding orbitals need to be exited to the conduction band or directly captured by a redox couple (hole formation in the valence band). Either way, the redox couple would have to have an energy level fluctuating within the range of the appropriate band (FEL model; App. F.1). An import factor, in the context of this study, is that temperature can induce high electron fluctuations (& frequency) (Osseo-Asare, 1992), increasing the chance of energy-level matching between the donor and acceptor sites (Phala, 2008). Parker *et al.* (1981) confirmed experimentally that the anodic dissolution of chalcopyrite can occur *via* valence- and conduction-band processes, *e.g.*, dissolution *via* hole injection by ferric ion and *via* electron capture by cupric ion, respectively. These experimental observations are in line with the qualitative picture presented in Figure 6.5. Parker *et al.* (1981) observed higher dissolution currents by hole injection compared to electron capturing, suggesting that the initial step during dissolution is the release of chalcopyritic iron (Crundwell, 1988b). This is in line with experimental observations from various chemical and electrochemical studies that have reported the preferential release of iron during the initial stages of oxidation (Biegler & Swift, 1979a; Harmer, 2002; Hiskey, 1993; Klauber, 2008; Viramontes-Gamboa *et al.*, 2007), with release ratios of iron to copper as high as 5 (Holliday & Richmond, 1990).

Stellenbosch University http://scholar.sun.ac.za

In context of the band structure of chalcopyrite, the mechanism of dissolution may be represented as follows (Crundwell, 1988b): the Fe^{3+}/Fe^{2+} redox couple is ideally placed (energetically) to capture electrons from the valence band edge (E_v) and the initial step represents hole transfer to break the chalcopyritic Fe–S bond:

$$CuFeS_{2(s)} + 3h^{+} \Rightarrow Fe^{3+}{}_{(aq)} + \cdot CuS_{2(s)} \qquad 6.18$$

The unstable radical intermediate, $\cdot CuS_2$, is then subjected to oxidation by hole transfer, which breaks the covalent Cu–S bond:

$$\cdot CuS_{2(s)} + 2h^{+} \Rightarrow Cu^{2+}{}_{(aq)} + 2S^{o}_{(s)} \qquad 6.19$$

or oxidation by electron transfer:

$$\cdot CuS_{2(s)} \Rightarrow Cu^{2+}{}_{(aq)} + 2S^{o}_{(s)} + 2e^{-} \qquad 6.20$$

or simply decomposes according to:

$$\cdot CuS_{2(s)} \Rightarrow CuS_{(s)} + S^{o}_{(s)} \qquad 6.21$$

This mechanism represents a general description of the dissolution of chalcopyrite and ties in with the anodic dissolution reactions presented earlier (Eq. 6.12 & 6.13). However, this mechanistic representation is an oversimplification, since electrochemical and chemical dissolution studies, as well as surface electron spectroscopy studies have identified complex phenomena associated with the relatively slow dissolution of intermediate surface phases compared to the original chalcopyrite phase. Figure 6.5 also suggests that reductive dissolution of chalcopyrite may occur if the energy level of the reductant (*e.g.*, Fe^{2+}) overlaps with the conduction band (Crundwell, 1988b) under low electrode potential conditions, *i.e.*, the chemical bond can also be weakened by adding additional electrons to non-bonding orbitals of interacting atoms (see Gerischer & Mindt, 1968).

Various electrochemical studies (see reviews by Crundwell, 1988b & Viramontes-Gamboa *et al.*, 2007) have observed a passive region (low sensitivity of the anodic current) during slow anodic potential scanning of chalcopyrite electrodes. Despite some valuable insights gained from these studies, the nature of the passivation layer remains unclear, the results are usually highly irreproducible, and the conclusions reached by different researchers are often conflicting (see Klauber, 2008). However, the more recent electrochemical study in acidic iron(III) sulfate solution (Viramontes-Gamboa *et al.*, 2007) has introduced techniques (slow potentiostatic polarisation) to improve experimental reproducibility, to better define the onset of passivation, and to allow the electrochemical approach to be reconciled with actual leaching results. Figure 6.6 illustrates that the critical current (j_{cc}) corresponds to the passivation potential (E_{pp}), *i.e.*, the potential defining the onset of passivation.

Stellenbosch University http://scholar.sun.ac.za

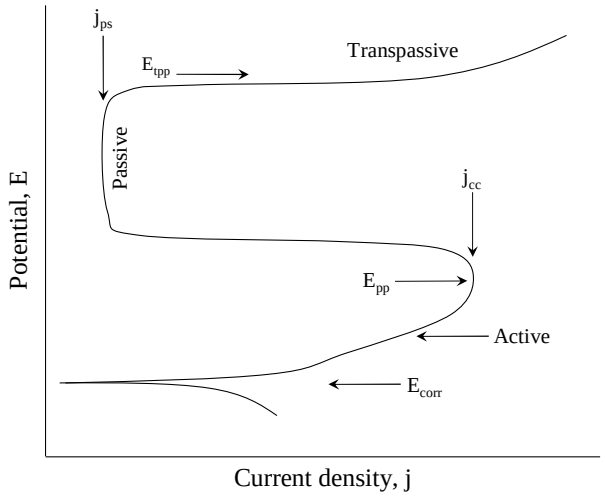

Figure 6.6
Schematic anodic polarisation curves showing active-passive behaviour, indicating the passivation potential (E_{pp}), open circuit (corrosion) potential (E_{corr}), critical current (j_{cc}), passive current (j_{ps}) & transpassive potential (E_{tpp}) (adopted from Viramontes-Gamboa *et al.*, 2007).

The important results from this work (in context of this study) may be summarised as follows:

- chalcopyrite behaviour does, in fact, resemble classical active-passive (polarisation) behaviour, even at higher solution temperatures, *e.g.*, 80°C
- increased acid concentration results in a higher oxidation current in the active window and generally a higher critical current, while the passivation potential is relatively unaffected
- acid concentration has a negligible effect on the oxidation current in the passive region
- increased temperature results in a higher oxidation current in both the active and passive regions and also higher passivation potentials, and
- the onset of the transpassive region occurs at progressively higher potentials at increased acidity and temperature.

Anodic polarisation curves at higher temperatures (98-175°C) from other studies (see Hiskey & Wadsworth, 1981) have also revealed progressively higher passivation potentials, but these were ascribed to the formation of dense sulfur layers of low conductivity. Nava and González (2006) potentiometrically scanned carbon paste electrodes of relatively pure chalcopyrite in high acid concentration solutions, characterised the remnant surface phases by cyclic voltammetry and analysed the corresponding amount of copper released into solution. At typical solution potentials of 615 to 1015 mV (*vs.* SHE), a passive $Cu_{1-r}Fe_{1-s}S_{2-t}$ non-stoichiometric polysulfide was proposed to cover the surface, inhibiting the diffusion of charged species. Klauber (2008) has questioned this proposition, since *r*, *s* and *t* have not been quantified. It would also be challenging to characterise its existence by alternative means, *e.g.*, surface electron spectroscopic techniques.

Stellenbosch University http://scholar.sun.ac.za

The study of Harmer *et al.* (2006) is a recent example in which surface analytical techniques were utilised to deduce a mechanism by which chalcopyrite oxidises in acidic solution. A feature of this mechanism is the initial formation of metal-deficient polysulfide (S_n^{2-}) species, claimed to be responsible for the passivation of chalcopyrite. The proposed reaction pathway allows for the reductive rearrangement of the amorphous long-chain polysulfide species *via* shorter chain sulfur building blocks, such as disulfide (S_2^{2-}) and sulfide (S^{2-}), while the oxidation reactions convert the rearranged sulfides to crystalline elemental sulfur. The formation extent of the initial polysulfide layer was assumed to be related to the amount of copper and iron released from the chalcopyrite matrix, which is consistent with the electrochemical test results of Viramontes-Gamboa *et al.* (2007), indicating more severe passivation (relative difference between j_{cc} & j_{ps}) at higher temperature (presumably due to higher metal release):

$$3n\mathrm{CuFeS}_{2(s)} \Rightarrow$$
$$[3(\mathrm{CuFe})^{4+} \cdot 6(\mathrm{S}_n)^{2-}]_{(s)} + (3n-3)\mathrm{Cu}^{2+}{}_{(aq)} + (3n-3)\mathrm{Fe}^{2+}{}_{(aq)} + (12n-12)\mathrm{e}^- \quad \text{where } n \geq 2 \qquad 6.22$$

Next, the mechanism relies on the reduction of the amorphous polysulfide layer to shorter chain species by iron(II) and involves adsorption of the hydrogen ion (H^+) to balance the resulting surface charge (Harmer *et al.*, 2006):

$$[3(\mathrm{CuFe})^{4+} \cdot 6(\mathrm{S}_n)^{2-}]_{(s)} + (12n-12)\mathrm{H}^+_{(aq)} + (12n-12)\mathrm{e}^- \Rightarrow$$
$$[3(\mathrm{CuFe})^{4+} \cdot (12n-12)\mathrm{H}^+ \cdot 6n(\mathrm{S}^{2-})]_{(s)} \quad \text{or} \quad [3(\mathrm{CuFe})^{4+} \cdot (6n-6)\mathrm{H}_2\mathrm{S} \cdot 6(\mathrm{S}^{2-})]_{(s)} \qquad 6.23$$

Finally, this short-chained phase is further oxidised to form crystalline elemental sulfur:

$$[3(\mathrm{CuFe})^{4+} \cdot (12n-12)\mathrm{H}^+ \cdot 6n(\mathrm{S}^{2-})]_{(s)} \Rightarrow$$
$$6n\mathrm{S}^{o}{}_{(s)} + 3\mathrm{Cu}^{2+}_{(aq)} + 3\mathrm{Fe}^{2+}_{(aq)} + (12n-12)\mathrm{H}^+_{(aq)} + (6n)\mathrm{e}^- \qquad 6.24$$

Klauber (2008) has questioned the applicability of this mechanism to iron(III) sulfate solutions, since the above study was conducted in ferric-free perchloric acid solution, which would artificially eliminate the effects of surface sulfates or jarosites. Moreover, Klauber has questioned the energy assignment of polysulfides by X-ray photoelectron spectroscopy (XPS), which is essential to the understanding of the mechanism. However, more recent references can be found in Absolon (2008), allowing for these sulfur species to be assigned with some degree of confidence.

A reduction-oxidation-type mechanism has also been proposed to explain the non-oxidative dissolution of non-stoichiometric minerals (Nicol & Scott, 1979; Thomas *et al.*, 2001). The electrochemical study of Filmer and Nicol (1980) revealed that sulfur-rich iron sulfides, such as pyrrhotite and pyrite, have to be reduced first (by applying a cathodic potential) before non-oxidative dissolution could commence. It was concluded that any metal-deficient bulk

Stellenbosch University http://scholar.sun.ac.za

stoichiometry or sulfide surface that has resulted from oxidation, dissolves non-oxidatively more slowly than a metal sulfide that contains an excess of metal at a greater than 1:1 stoichiometry. However, the non-oxidative dissolution of nickel-deficient nickel sulfides proceeded spontaneously in acid solution and did not require any induction period, contrary to the behaviour of iron-deficient iron sulfides. Scott and Nicol (1977) reported that the non-oxidative dissolution of pyrrhotite could be initiated by a cathodic pulse or by adding hydrogen sulfide (H_2S), *i.e.*, reduction of the metal-deficient non-stoichiometric mineral using hydrogen sulfide itself. Nicol and Lázaro (2003) conducted electrochemical studies and proposed that a parallel non-oxidative dissolution route should be considered when describing the dissolution of chalcopyrite, which may provide an alternative explanation for the enhanced dissolution rate at low potentials.

Besides hydrogen sulfide, thiosulfate ($S_2O_3^{2-}$) was proposed as a soluble sulfur species formed during leaching (Lázaro & Nicol, 2003, 2006). Al-Harahsheh (2006) also found evidence of an intermediate sulfur-oxy surface species and proposed that different chalcopyrite faces would exhibit different surface chemistries. They speculated on the formation of a pyrite-like structure on specific microplanes, which have more sulfur available to form S_2^{2-} dimers. These and the adjacent microplanes may not only behave like electrically connected chalcopyrite and pyrite, but may explain the formation of thiosulfate, which is normally associated with pyrite oxidation (see later in this section). This species would however be expected to rapidly oxidise under acidic MT autoclave conditions.

Absolon (2008) lists various examples from the open literature which report faster oxidation at lower solution redox potentials as compared to slower oxidation above a critical value (see, *e.g.*, Kametani & Aoki, 1985). A series of papers by Hiroyoshi (Hiroyoshi *et al.*, 2001, 2004, 2008) has identified (*via* electrochemical techniques and leaching testwork) faster oxidation rates in the presence of adequate ferrous (Fe^{2+}) and cupric ion concentrations, which supports the idea of increased oxidation *via* a pre-reduction step to form an intermediate chalcocite phase:

$$CuFeS_{2(s)} + 3Cu^{2+}_{(aq)} + 4e^- \Rightarrow 2Cu_2S_{(s)} + Fe^{2+}_{(aq)} \qquad 6.25$$

$$Cu_2S_{(s)} \Rightarrow 2Cu^{2+}_{(aq)} + S^{o}_{(s)} + 4e^- \qquad 6.26$$

This mechanism is consistent with an optimum solution potential range ('window') for chalcopyrite oxidation, as well as the apparently strong influence of cupric ion concentration. This mechanism is supported by the fact that ferrous ions suppressed chalcopyrite oxidation in the absence of cupric ions (Hiroyoshi *et al.*, 2001), although the presence of chalcocite has always been assumed and never verified by alternative means, *e.g.*, surface analytical techniques. Klauber (2008) highlights the fact that the very intense Cu(I) 2*p* emission from the underlying chalcopyrite would preclude its

Stellenbosch University http://scholar.sun.ac.za

easy identification. The anodic polarisation measurements of Hiroyoshi *et al.* (2004, 2008) apparently support the notion that active-passive behaviour is only present when cupric and ferrous ions coexist in solution, suggesting activation rather than passivation. In addition, their AC impedance spectra (Hiroyoshi *et al.*, 2004) indicate a high-resistance passive layer without cupric and/or ferrous ion. These observations are however contradicted by the recent electrochemical study of Viramontes-Gamboa *et al.* (2007). They found no change in the shape of the anodic polarisation curves, with and without coexisting cupric and ferrous ions, although the magnitude of the current density was significantly higher in the former case. This was ascribed to ferrous oxidation on the electrode surface rather than to the oxidation of chalcopyrite.

Elsherief (2002) used carbon paste electrodes to study the behaviour of chalcopyrite in sulfuric acid solutions, containing cupric and ferrous ions. Surface passivation was ascribed to the formation of an iron-deficient, copper-rich polysulfide layer. Cathodic treatment (to form chalcocite) was found to reactivate the anodically polarised surface, whilst an increase in the current with the addition of ferrous ions was also ascribed to its oxidation on the surface, which reaffirms the conductive character of the surface layers.

There is therefore general consensus that chalcopyrite passivation is caused by some sort of transformed phase or surface product, but the exact nature of this layer remains elusive. Chalcopyrite oxidation characteristics may also differ between samples with varying impurity levels (*n*- or *p*-type) and even between different crystal faces. The term 'hindered dissolution', instead of 'passivation' (Klauber, 2008), may be a more appropriate term to use in the context of chalcopyrite oxidation. Either way, Klauber (2008) has reviewed the merit of each of the four primary candidates most often proposed, *i.e.*:

- jarosites ($XFe_3(SO_4)_2(OH)_6$)
- elemental sulfur
- metal-deficient sulfides, and
- polysulfides (MS_n).

Jarosites

Although worth considering in lower temperature studies (see reviews by Absolon, 2008 & Klauber, 2008), Section 6.5 presents evidence that excludes iron precipitation products as candidates responsible for chalcopyrite passivation under MT autoclave conditions.

Stellenbosch University http://scholar.sun.ac.za

Elemental sulfur

Section 6.5 shows that the stifling role of liquid elemental sulfur should be treated as a secondary factor that may inhibit sulfide oxidation. However, this statement does not necessarily hold for the possible formation of thin layers of polymerised elemental sulfur on unreacted chalcopyrite surfaces (explored later in this section).

Metal-deficient sulfides

Metal- or iron-deficient sulfides, by definition, only refer to transformed surface phases and not to products of oxidation (Klauber, 2008). In this context, Reaction 6.29 is best represented by using the proposal of Warren *et al.* (1982):

$$CuFeS_{2(s)} \Rightarrow Cu_{1-x}Fe_{1-y}S_{2-z(s)} + xCu^{2+}{}_{(aq)} + yFe^{2+}{}_{(aq)} + zS^{o}_{(s)} + 2(x+y)e^{-} \quad \text{where } y > x \qquad 6.27$$

This remnant phase then undergoes a relatively slow solid-state transformation. Both oxidative and non-oxidative dissolution of chalcopyrite was proposed by Lázaro and Nicol (2003) to selectively dissolve iron, leaving microscopically thin copper-rich layers, which inhibit solid-state diffusion of iron and copper. In contrast, long-term flow-through experiments, where iron consistently dissolved preferentially to copper at ratios higher than 2 (see Klauber, 2008), were found not to result in any inhibitory phases. Mikhlin *et al.* (2004) used different spectroscopic techniques to characterise the metal-deficient surface layers on chalcopyrite after anodic oxidation in acid solutions. They claim that relatively thick (up to several microns) amorphous and metal-deficient surface layers of variable stoichiometry formed, which did not resemble known stable compounds of copper, iron and sulfide. Even though metal depletion was considerable, these surface layers were not inhibitory and reflected electronic structures similar to chalcopyrite. These examples suggest that non-stoichiometric metal-deficient layers are not responsible for slower chalcopyrite oxidation. Similarly, the observed reactive anodic characteristics of bornite or covellite, in a region where chalcopyrite is relatively passive (Lázaro & Nicol, 2003), make such stoichiometric phases unlikely candidates to explain the passivation behaviour of chalcopyrite, even though the thermodynamics, surface analyses (Sect. 6.3.1) and mechanistic proposals (see above & review of Harmer, 2002) may support its formation on partially leached chalcopyrite or as part of a mixed sulfide-sulfur product layer (see Ammou-Chokroum *et al.*, 1977 & McMillan *et al.* 1982).

Polysulfides

A polysulfide may be formed either by the subsequent release of copper from the disulfide (Rx 6.30) or by congruent metal release from the already metal-deficient layers (Warren *et al.*, 1982):

$$Cu_{1-x}Fe_{1-y}S_{2-z(s)} \Rightarrow (y-x)CuS_{n(s)} + (1-y)Cu^{2+}{}_{(aq)} + (1-y)Fe^{2+}{}_{(aq)} + (2+x-y-z)S^{o}_{(s)} + 2(1-y)e^{-} \qquad 6.28$$

Stellenbosch University http://scholar.sun.ac.za

This reaction is consistent with the results of Bauer *et al.* (1974), suggesting higher congruency in iron and copper release during extended leaching times and higher temperatures. Klauber (2008) presents the general class of components belonging to polysulfides (the chain length of polysulfides is usually limited to six, & oligomers may therefore be a better description) as M_2S_n ($n > 2$), where M represents a monovalent cation, like copper(I). Polysulfide layers, whether containing residual iron or not, may be reduced (*e.g.*, Rx. 6.23), oxidised (*e.g.*, Rx. 6.31) or simply decomposed (*e.g.*, Rx. 6.21) before producing more reactive phases, *i.e.*, assuming them to be relatively unreactive in the first place.

Parker *et al.* (2003) identified a sulfur entity on the surface of leached chalcopyrite with an average oxidation state of –1 and ascribed it to the sulfur dimer, S_2^{2-} (similar to bulk pyrite & covellite). This disulfide species, although not necessarily inhibitory, was assumed to play a key role in the leaching mechanism. Yin *et al.* (1995) proposed a metastable CuS_2 phase to be rate limiting in acid solutions but stated that this phase is unlikely to have a pyrite structure. Ueda *et al.* (2002) have shown, using a variety of experimental techniques, that copper in copper pyrite has a monovalent d^{10} rather than a divalent d^9 oxidation state. Absolon (2008) cited various surface studies that have identified S_2^{2-} groups on partially leached chalcopyrite surfaces. Solid-state diffusion has often been suggested to be a rate-limiting phenomenon. Mikhlin *et al.* (2004) identified S_3^{2-} and S_4^{2-} oligomers after spectroscopic characterisation of remnant chalcopyrite surfaces and suggested a reaction mechanism that depends on the role of surface charges and electronic states.

Hackl *et al.* (1995b) presented one of the few fundamental studies conducted under oxygen pressure leach conditions, although the authors suggested similar chemistry during ferric sulfate leaching at lower temperatures. They elaborated on the intrinsic rate-controlling mechanism on the basis of X-ray Auger electron spectroscopy (XAES) and XPS studies and described chalcopyrite dissolution as a two-step reaction. An intermediate disulfide phase was claimed to form first due to the preferential (faster) leaching of iron:

$$\begin{aligned} &CuFeS_{2(s)} \Rightarrow \\ &Cu_{1-x}Fe_{1-y}S_{2(s)} + xCu^{2+}{}_{(aq)} + yFe^{2+}{}_{(aq)} + 2(x+y)e^- \quad \text{where } y>>x,\ \ x+y\sim 1 \end{aligned} \qquad 6.29$$

The slow subsequent release of copper from the disulfide then produces a polysulfide:

$$Cu_{1-x}Fe_{1-y}S_{2(s)} \Rightarrow Cu_{1-x-z}S_{2(s)} + zCu^{2+}{}_{(aq)} + (1-y)Fe^{2+}{}_{(aq)} + 2(z+1-y)e^- \qquad 6.30$$

This polysulfide was claimed to be responsible for the passivation of chalcopyrite and its oxidation is characterised by a slow release of copper and polysulfide restructuring to form stable sulfur (S_8):

$$Cu_{1-x-z}S_{2(s)} \Rightarrow (1-x-z)Cu^{2+}{}_{(aq)} + 2S^{o}{}_{(s)} + 2(1-x-z)e^- \qquad 6.31$$

Stellenbosch University http://scholar.sun.ac.za

A thin passive layer, consisting of a metal-deficient copper-rich polysulfide, CuS_n with $n = 2/(1–x–z)$, *i.e.*, $n > 2$, was identified on the leach residue particles. This layer is thought to stabilise at a defined thickness (< 1 µm), limiting the transport of ions and thus controlling leaching at a slower rate compared to that of the initial chalcopyrite mineral. This hypothesis was originally introduced by Burkin (1969) and a similar two-step mechanism was proposed by Warren *et al.* (1982). Klauber (2008) has, however, questioned the binding energy (BE) assignment of Hackl *et al.* (1995b) for the S_n^{2-} species (163.0-163.5 eV) and, instead, ascribed those lines to elemental sulfur.

The role of polysulfides may be questioned, firstly because their identification is complicated (a single peak assignment is inadequate because true polysulfides have two oxidation states) and also because synthetic polysulfides were found to be highly reactive towards oxidation in acidic solutions (Klauber, 2008). However, it is unclear to what extent synthetic alkali metal polysulfide analogues represent the true polysulfide layers on chalcopyrite.

Clearly, there remains considerable disagreement on the mechanism of chalcopyrite oxidation. Nevertheless, there is overwhelming evidence that the metal cations, especially iron, are preferentially released during initial dissolution and that chalcopyrite oxidation in acidic copper sulfate solutions is intrinsically slow. The formation of thin remnant surface layers is widely accepted as playing a primary inhibiting role in the dissolution process. Therefore, in context of the above discussions and the current lack of mechanistic knowledge, as well as the phenomenological nature of this study, it is sufficient to assume that this inhibitory surface resembles a covellite-like phase under typical MT autoclave conditions (see later in this section).

Besides cathodic-reduction limitations, contributing factors may include solid-state diffusion, solid-state rearrangements to form elemental sulfur and/or inhibition due to polymeric sulfur itself. Some of the fundamental aspects of the transformation of sulfur species during charge transfer are reviewed next.

Sulfur rearrangement, transformation and oxidation

As mentioned in the previous section, hole formation in the valence band means that one of the bonding electrons has been removed and the bond weakened (Crundwell, 1988b). Hole formation can occur due to electrical current (dissolution *via* anodic polarisation) or holes can be injected by an oxidising agent (leaching mechanism of semiconductors with wide band gaps). In the case of *n*-type chalcopyrite, dissolution would be expected to be dominated by such hole-decomposition pathways. However, the band gap may be narrow enough (~0.6 eV) that dissolution can also occur *via* electron capture, especially at higher temperatures ($kT \geq E_g$; App. F.1) and also if surface

Stellenbosch University http://scholar.sun.ac.za

phenomena allow electronic states in the band gap, which, in turn, may improve energy-level matching between the oxidant and the semiconductor surface.

For the purpose of this study, it is assumed that iron leaches preferentially (discussed previously) to leave an intermediate Cu_xS phase behind, while the copper retains its monovalent oxidation state (see Mikhlin *et al.* 2004 & Ueda *et al.*, 2002). The oxidation of stoichiometric sulfide sulfur may occur *via* the following sequence (based on the discussions of Gerischer & Mindt, 1968): The electronegative part of the reactant may preferentially dissolve the more electropositive component of the semiconductor, while charge transfer occurs *via* hole injection or electron withdrawal, *i.e.*, respectively:

$$(Cu^{\delta+}S^{\delta-})_{(s)} + h^{+} \Rightarrow Cu^{+}{}_{(aq)} + \cdot S_{(s)} \qquad 6.32$$

$$(Cu^{\delta+}S^{\delta-})_{(s)} \Rightarrow Cu^{+}{}_{(aq)} + \cdot S_{(s)} + e^{-} \qquad 6.33$$

The more electronegative semiconductor component may undergo recombination, which would result in an elementary state for this component, *i.e.*, a diatomic elemental sulfur precursor:

$$\cdot S_{(s)} + \cdot S_{(s)} \Rightarrow (S\text{-}S)^{o}_{(s)} \qquad 6.34$$

or generally:

$$\cdot S_{(s)} + S_{n\text{-}1(s)} \Rightarrow S^{o}_{n(s)} \qquad 6.35$$

The ·S denotes the radical state of a surface atom, which would be expected to be highly reactive. If intermediate polysulfide formation is an intrinsic part of the oxidation mechanism (*e.g.*, Rx. 6.22 & 6.28), and adopting the notation of Harmer *et al.* (2006), sulfide oxidation may be represented as:

$$n(S^{2-})_{(s)} \Rightarrow (S_n)^{2-}_{(s)} + (2n-2)e^{-} \qquad 6.36$$

This intermediate polysulfide would represent a physically large long-chain entity and may either be relatively reactive or unreactive to further oxidation (discussed in previous section). Either way, in order to form crystalline elemental sulfur, the rearrangement of sulfur atoms would be expected to kinetically prefer a route *via* shorter chain building blocks (see surface speciation results & proposition of Hamer *et al.*, 2006). The reduction mechanism of long-chain polysulfides may be an important step in this mechanism and may follow different pathways, *e.g.*:

$$(S_n)^{2-}_{(s)} + (2n-2)H^{+}_{(aq)} + (2n-2)e^{-} \Rightarrow (2n-2)H^{+} \cdot n(S^{2-})_{(s)} \qquad 6.37$$

$$(S_n)^{2-}_{(s)} + (2n-2)H^{+}_{(aq)} + (2n-2)e^{-} \Rightarrow (n-1)H_2S \cdot (S^{2-})_{(s)} \qquad 6.38$$

Stellenbosch University http://scholar.sun.ac.za

Hydrogen ion adsorption is obviously an intrinsic part of the formation of adsorbed hydrogen sulfide, while it serves to balance the surface charge in the first case (see Rx. 6.23). The subsequent oxidation of short-chain sulfides involves a massive structural rearrangement of the surface to form crystallites of elemental sulfur (see Hamer *et al.*, 2006):

$$(2n-2)H^{+}\cdot n(S^{2-})_{(s)} \Rightarrow nS^{o}_{(s)} + (2n-2)H^{+}_{(aq)} + (2n)e^{-} \qquad 6.39$$

$$(n-1)H_2S\cdot(S^{2-})_{(s)} \Rightarrow nS^{o}_{(s)} + (2n-2)H^{+}_{(aq)} + (2n)e^{-} \qquad 6.40$$

It can be seen that there is no stoichiometric difference between these two mechanistic pathways. However, highly acidic conditions may stabilise the hydrogen sulfide entity to such an extent that it can desorb and be released into solution:

$$(n-1)H_2S\cdot(S^{2-})_{(s)} \Rightarrow S^{o}_{(s)} + (n-1)H_2S_{(aq)} + 2e^{-} \qquad 6.41$$

Depending on the nature of the solution at the mineral surface, this dissolved species may diffuse into the bulk solution, be oxidised by iron(III) to elemental sulfur or react with copper to form covellite (Rx. 6.14) on the mineral surface. Under conditions of lower terminal acidity, the long-chain polysulfides or short-chain reduced sulfides may be expected to directly oxidise to higher oxidation states; hence, the range of soluble sulfide species (*e.g.*, thiosulfate) and elemental sulfur yields claimed in different studies (Sect. 6.3.1 & 6.3.2).

A simplified reaction scheme has also been proposed by Lotens and Wesker (1987), based on the formation of higher oxidation products of sulfide, depending on the nature of the oxidant, *i.e.*, one-electron or two-electron transfer, respectively:

$$S^{2-}_{(s)} \rightarrow S^{-}_{(s)}(+e^{-}) \rightarrow S^{o}_{(s)}(+e^{-}) \rightarrow S^{+}_{(s)}(+e^{-}) \rightarrow S^{2+}_{(s)}(+e^{-}) \qquad 6.42$$

$$S^{2-}_{(s)} \rightarrow S^{o}_{(s)}(+2e^{-}) \rightarrow S^{2+}_{(s)}(+2e^{-}) \qquad 6.43$$

In the case of one-electron transfer, thiosulfurous acid ($H_2S_2O_2$) would form after hydrolysis of the S^{+}-species and may be expected to kinetically predominate to such an extent that further oxidation is prevented and that the reaction essentially occurs at the surface:

$$2S^{+}_{(s)} + 2H_2O \Rightarrow H_2S_2O_2 + 2H^{+} \qquad 6.44$$

The thiosulfurous species would rearrange and decompose rapidly in acid solution (see Lotens & Wesker, 1987) and theoretically yield 75% elemental sulfur:

$$2H_2S_2O_2 \Rightarrow \tfrac{3}{8}S^{o}_{8(s)} + H_2SO_3 + H_2O \qquad 6.45$$

or, expressed more generally:

Stellenbosch University http://scholar.sun.ac.za

$$4S^{+}_{(s)} \Rightarrow \tfrac{3}{8}S^{o}_{8(s)} + S^{4+} \qquad 6.46$$

This mechanism was actually proposed by Davies (1958) to explain the decomposition of thiosulfate in acid solution and involves a series of protonation reactions (Wackenroder scheme), with each intermediate compound reacting with another thiosulfate species to form the next compound, until eight sulfurs break off the last member, leaving sulfurous acid (H_2SO_3) behind. In the case of two-electron transfer, sulfoxylic acid (H_2SO_2) would form after hydrolysis of the S^{2+}-species (Lotens & Wesker, 1987):

$$S^{2+}_{(s)} + 2H_2O \Rightarrow H_2SO_2 + 2H^{+} \qquad 6.47$$

Once again, the sulfoxylic species disproportionates rapidly in acid solution and theoretically yields 50% elemental sulfur (Lotens & Wesker, 1987):

$$2H_2SO_2 \Rightarrow \tfrac{1}{8}S^{o}_{8(s)} + H_2SO_3 + H_2O \qquad 6.48$$

or, expressed more generally:

$$2S^{2+}_{(s)} \Rightarrow \tfrac{1}{8}S^{o}_{8(s)} + S^{4+} \qquad 6.49$$

This difference in expected elemental sulfur yields for the one-and two-electron transfer reactions is based on the assumption that the desorption of a two-electron oxidant does not take place after one electron has been transferred (see next section). This implies that the average oxidation state of sulfur depends more heavily on the nature of the oxidising agent than on the solution potential (Lotens & Wesker, 1987). This is the reason why no attempt is made in this study to relate the elemental sulfur yield to the solution potential (recorded for each leaching test in App. G, I & J).

The above mechanism was qualitatively verified (Lotens & Wesker, 1987) by oxidising sphalerite, galena (PbS) and pyrite minerals with different oxidation agents. The only mineral that behaved unexpectedly was pyrite, where virtually all the sulfide was converted to sulfate, suggesting that the mechanism of pyrite oxidation differs substantially from that of other sulfides.

Reaction between hydrogen sulfide (formed non-oxidatively) and the intermediate oxidation products (along the lines of the Wackenroder reaction) accounts for the acid sensitivity of the elemental sulfur yield. Under conditions of low acidity, sulfurous acid would be expected to rapidly oxidise to sulfate (S^{6+}):

$$S^{4+} \Rightarrow S^{6+} + 2e^{-} \qquad 6.50$$

Stellenbosch University http://scholar.sun.ac.za

At higher acidity levels, the following reactions are consistent with the mechanism proposed above:

$$2S^{+}_{(s)} + H_2S \Rightarrow \tfrac{3}{8}S^{o}_{8(s)} + 2H^{+} \qquad 6.51$$

$$S^{2+}_{(s)} + H_2S \Rightarrow \tfrac{2}{8}S^{o}_{8(s)} + 2H^{+} \qquad 6.52$$

$$S^{4+}_{(s)} + 2H_2S \Rightarrow \tfrac{3}{8}S^{o}_{8(s)} + 4H^{+} \qquad 6.53$$

The mechanism of Hamer *et al.* (2006) relies on the reduction of polysulfides to short-chain sulfides, *i.e.*, prior to oxidation to form elemental sulfur crystallites. The proposals of Lotens and Wesker (1987) depend strongly on the characteristics of electron transfer between the oxidant and the intermediary sulfur species.

An alternative mechanism was proposed by Schippers and Sand (1999) to explain the behaviour of minerals in bacterial leaching systems. Minerals such as chalcopyrite are said to oxidise to elemental sulfur under low-temperature conditions *via* intermediary polysulfides. The dissolution of metal sulfide was claimed to start *via* hydrogen ion attack to form the $H_2S^{\cdot +}$ radical:

$$S^{2-}_{(s)} + 2H^{+} \Rightarrow H_2S^{\cdot +}_{(s)} + e^{-} \qquad 6.54$$

Polysulfide formation starts with the dissociation of this (strong acid) species to form a HS· radical:

$$H_2S^{\cdot +}_{(s)} \Rightarrow H^{+} + HS^{\cdot}_{(s)} \qquad 6.55$$

Two HS· radicals may react to form a disulfide species:

$$HS^{\cdot}_{(s)} + HS^{\cdot}_{(s)} \Rightarrow H_2S_{2\,(s)} \qquad 6.56$$

The disulfide may oxidise again or react with another HS· radical:

$$H_2S_{2\,(s)} \Rightarrow H_2S_2{}^{\cdot +}_{(s)} + e^{-} \qquad 6.57$$

$$H_2S_{2\,(s)} + HS^{\cdot}_{(s)} \Rightarrow HS_2{}^{\cdot}_{(s)} + H_2S \qquad 6.58$$

Trisulfide (H_2S_3) may form by reaction of HS· with HS_2·, tetrasulfide (H_2S_4) may form *via* dimerisation of two HS_2· radicals, and so forth. This elongation of the polysulfides increases until it decomposes into S_8 rings in acidic solution (Schippers & Sand, 1999):

$$H_2S_{9\,(s)} \Rightarrow S_{8\,(s)} + H_2S \qquad 6.59$$

Schippers and Sand (1999) based the high elemental sulfur yield in atmospheric leaching systems on Reaction 6.59, with side reactions that form small amounts of thiosulfate, which would then be oxidised to sulfate:

Stellenbosch University http://scholar.sun.ac.za

$$H_2S_{n\,(s)} + 3H_2O \Rightarrow \tfrac{(n-2)}{8} S_{8\,(s)} + S_2O_3^{2-} + 8H^+ + 6e^- \qquad 6.60$$

$$S_2O_3^{2-} + 5H_2O \Rightarrow 2SO_{4(aq)}^{2-} + 10H^+ + 8e^- \qquad 6.61$$

Even for chalcopyrite, more than 90% of the sulfide was converted into elemental sulfur, *i.e.*, without the presence of sulfur-oxidising bacteria. Lotens and Wesker (1987) also conducted their tests at low temperature and over a relatively narrow temperature range (~25-60°C), *i.e.*, where the yield was insensitive to temperature changes. These models would therefore be inadequate in simulating the extent of sulfur formation under MT and, especially, total pressure oxidation (TPOX) conditions (*e.g.*, Hackl *et al.*, 1995a; also see Sect. 6.3.1). Therefore, Reaction 6.9 is introduced to account for sulfuric acid formation from a purely stoichiometric (mass balance) perspective. Furthermore, it is imperative to quantify the kinetics of elemental sulfur oxidation itself, because such mechanism could come into play during higher-temperature autoclave oxidation, *i.e.*, besides the intrinsic formation of sulfate emanating from the mineral oxidation.

Oxidation of stable elemental sulfur and the formation polymeric sulfur

Relatively few studies have been conducted to study elemental sulfur stability, most likely due to the problem of assigning surface area to sulfur particles above the melting point, and also due to the presence of different allotropic forms at higher temperatures. The two most noticeable studies have been conducted by Habashi and Bauer (1966) and Corriou and Kikindai (1981). Corriou and Kikindai reported a half-order dependency of the mean oxidation rate on the sample mass below 160°C. With a ratio of the mean and instantaneous rates close to unity over relatively 'short' initial reaction times (< 6 hrs), the changes in physical properties with temperature influenced the exposed surface area of molten sulfur in such a way that the behaviour was analogous to solid cylinder-shaped particles (below 160°C; see Corriou & Kikindai, 1981). They did, however, not investigate the effect of agitation speed on the oxidation rate and their rate expressions contained only the (sample) mass term. However, Habashi and Bauer (1966) found that the reaction rate was independent of the agitation speed between 400 and 900 rev/min. This not only confirmed that the reaction operated within the chemical reaction regime, but also suggested that the molten sulfur surface area was not greatly influenced by the degree of turbulence in the reactor. The workings of surfactants in the AA-UBC process, *i.e.*, to disperse molten sulfur from unreacted mineral surfaces, are discussed in more detail in Section 6.3.3. Even if it is assumed that all elemental sulfur is dispersed (away) from the mineral surface, the mean oxidation rates reported by Corriou and Kikindai (1981) suggest very slow oxidation (~1% S^o/hr), even under conditions that would promote sulfur oxidation (low acidity in copper(II) solution) at 150ºC, *i.e.*., 1% solids, 700 kPa O_2, 1 g/L H_2SO_4 and 1 g/L Cu(II). They reported relatively high activation energy of 119.3 kJ/mol, but did not quantify the effect of metal cations above 1 g/L. However, Habashi and Bauer (1966) found

Stellenbosch University http://scholar.sun.ac.za

the rate to be insensitive above this concentration level for all the cations tested, including cupric ion. An enhancement factor of between 3 and 4 is expected for cupric ion at 130ºC, while Corriou and Kikindai reported a smaller factor of about 2.7 at 140ºC and 1.3 at 200ºC. A smooth curve was fitted to these data (App. A.6), which presents a rough estimate of the sulfur oxidation rate below the transition temperature.

There are a large number of possible metastable sulfur allotropes, but the primary stable liquid allotropes below 200°C are S_λ (crown-shaped octagonal ring structure, S_8) and S_μ (long, polymerised chains, S_∞). Although liquid sulfur is a combination of these and other allotropes, their dynamic equilibria depend on the temperature history of a specific system (Owusu, 1993). The sulfur atoms in the eight-membered puckered rings are connected together by covalent bonds, while the rings are attached to each other by Van der Waals' forces (Habashi, 1993). S_λ is the only stable allotrope in the solid state and crystallises either as orthorombic α-S_8, monoclinic β-S_8 or monoclinic γ-S_8 (Tong, 2009). In the liquid state, the proportion of S_λ predominates (> 90%) below 160°C and makes sulfur highly fluid (the lowest dynamic viscosity is found at 157°C; Steudel, 2003). Above this temperature, the proportion of S_μ increases rapidly (> 25% at 180°) and there is also a dramatic increase in viscosity (Habashi, 1993; Steudel, 2003; Tong, 2009). However, these two factors are not related directly. This viscosity increase is likely due to the breakdown of the S_λ ring structures and the formation of a 'new type of chain-like polymer' *via* sulfenyl diradicals, which attack other sulfur rings to initiate heat-induced polymerisation (Steudel, 2003).

Figure 6.7 illustrates the effect of temperature and different soluble impurities on sulfur viscosity and highlights the sudden increase of the viscosity at the transition temperature, *i.e.*, between 159 and 160°C. The viscosity (η) of liquid sulfur increases by a factor of 2000 over a mere 25°C change. This figure also highlights the fact that the AA-UBC process operates very close to this critical point and that small amounts of particular soluble impurities may have a dramatic effect on the behaviour of liquid sulfur. For example, the increase in viscosity begins at a much lower temperature, as compared to pure sulfur, if a small amount of arsenic (As) is present. Another species that may dramatically alter the behaviour of liquid sulfur is hydrogen sulfide. If gaseous hydrogen sulfide is passed through pure liquid sulfur, while heating from 125 to 190°C within 90 minutes, no viscous state is attained (Steudel, 2003). Similarly, elemental sulfur that has formed from the microbial oxidation of hydrogen sulfide is more hydrophilic and of lower density as compared to pure hydrophobic sulfur (Klauber, 2008). Pressure exerts a negligible effect on liquid sulfur viscosity below 160°C (Doi, 1963). Another relevant property of liquid sulfur is its electrical conductivity. Although sulfur is an insulator under ambient conditions, liquid sulfur at high temperatures is a semiconductor, caused by unpaired electrons at the chain-end atoms of polymeric

Stellenbosch University http://scholar.sun.ac.za

sulfur, which are assumed to form acceptor states within the band gap (Steudel, 2003). Impurities may also increase its conductivity.

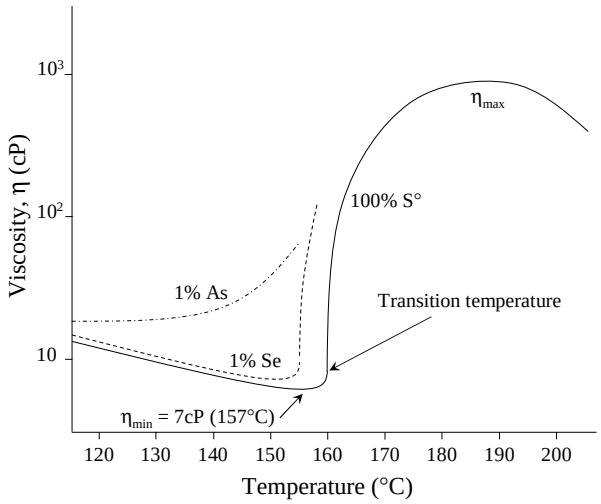

Figure 6.7
Schematic diagram showing the effects of temperature & (soluble) impurities on the viscosity of elemental sulfur (reproduced from Matsushima, 1959, Meyer, 1965 & Steudel, 2003).

Polymeric sulfur (S_μ), consisting of larger rings and/or long chains, may not be soluble in organic solvents, such as carbon disulfide (CS_2), above a certain molecular mass (Steudel, 2003). The inhibiting role of polymeric sulfur towards mineral oxidation should therefore not be underestimated (Biegler & Swift, 1979a; Klauber, 2008). Its ability to cause slow mineral oxidation may, however, be questioned in view of its relatively low abundance at temperatures below 157°C (< 3%; see Steudel, 2003). Then again, if polymerisation is possible by photo-excitation of valence-band electrons (to the conduction band) in molten sulfur, *i.e.*, below the transition temperature (see Munejiri *et al.*, 2000), surface oxidant species, *e.g.*, reactive radicals associated with pyrite surfaces (see later), may do the same, *i.e.*, at temperatures too low to allow complete elemental sulfur oxidation to higher (soluble) states, but high enough to initiate polymerisation.

In conclusion, the slow oxidation rate of elemental sulfur supports the notion that relatively low sulfur yields during chalcopyrite and pyrite oxidation are not due to a direct reaction between elemental sulfur and oxygen, *i.e.*, stable sulfur allotropes are not likely to be intermediate phases. It is more likely that the intermediate oxidation products forming on refractory mineral surfaces, such as those described above, are prone to oxidation to higher oxidation states before they can form molecular S_8 rings. This conclusion was also reached by Tributsch & Gerischer (1976). The role of the hydrogen ion is also emphasised in the sulfur rearrangement and oxidation mechanisms presented above. Another important aspect is the nature of the cathodic reaction (reviewed next).

Stellenbosch University http://scholar.sun.ac.za

Cathodic reactions

During electrochemical dissolution of a mineral phase, the anodic steps are coupled with the cathodic reduction of the oxidant. If a solvent is present to stabilise ion formation, the net half-cell reactions (applicable to this study) on a mineral surface may be represented as follows:

$$Cu^{2+}_{(aq)} + e^- \Leftrightarrow Cu^{+}_{(aq)} \qquad 6.62$$

$$Fe^{3+}_{(aq)} + e^- \Leftrightarrow Fe^{2+}_{(aq)} \qquad 6.63$$

$$O_{2(aq)} + 4H^{+}_{(aq)} + 4e^- \Leftrightarrow 2H_2O_{(aq)} \qquad 6.64$$

The standard reduction potentials ($E°_h$) of these couples are 0.153 V, 0.771 V and 1.229 V, respectively (Lide, 2004).

Copper(II) reduction

Free cuprous (Cu^+) ion is clearly less stable in the aqueous environment than the cupric ion, most likely due to a higher degree of orbital symmetry matching between the 3*d* cupric ion and water sp^3 orbitals as compared to the lesser overlap with the 4*s* orbitals of the cuprous ion. In contrast, the stability of the cuprous ion surpasses the cupric ion's stability in acetonitrile (CH_3CN). The strong solvation of the cuprous ion allows the cupric ion to act as a powerful oxidising agent. This higher thermodynamic driving force and high copper(I) solubility is the premise on which the Parker Copper process has been based (Muir, 2008). Similarly, chloride ions may stabilise the cuprous ion, despite its comparatively low salt (CuCl) solubility. This stabilisation of the reduced species enhances the ability of the cupric ion to be reduced on mineral surfaces (see, *e.g.*, Miki & Nicol, 2008), while the presence of ferric ions would ensure cupric regeneration, *i.e.*, a typical electrochemical-chemical (EC) mechanism. An important aspect of this system is the equilibrium involving both couples, *i.e.*, the combination of Equations 6.62 and 6.63:

$$Fe^{3+}_{(aq)} + Cu^{+}_{(aq)} \Leftrightarrow Cu^{2+}_{(aq)} + Fe^{2+}_{(aq)} \qquad 6.65$$

As pointed out by Miki and Nicol (2008), the absence of chloride ions would strongly favour the right-hand side of this equilibrium. In aqueous solution, the lifetime of the cuprous ion is very short (< 1 sec), unless a strong reducing agent is present without oxidant species, such as dissolved oxygen (Cotton *et al.*, 1995). The equilibrium concentration in water is, however, less than 0.01 mol/L and would be expected to be significantly lower still in systems that contain oxidant species. Yet, the reduction of copper(II) has been proposed to play an important role in the catalysis of iron(II) oxidation by oxygen in non-complexing perchlorate and sulfate media, *i.e.*, *via* the copper(I) intermediate (left-hand direction of Rx. 6.65; *e.g.*, George, 1954; Huffman & Davidson, 1956; also see Sect. 4.2.3). Similar mechanisms have been proposed in the free-radical chain

Stellenbosch University http://scholar.sun.ac.za

mechanism of copper-catalysed sulfite (SO_3^{2-}) (Barron & O'Hern, 1966) and vanadic-ion oxidation (George, 1954). However, the thermodynamic driving force for this mechanism is extremely low. Even for a relatively low ferric to ferrous activity ratio of one third (⅓), and using the standard $E°_h$ values of the two couples (Atkins & De Paula, 2006), a favourable thermodynamic stability regime ($E_h > 0$) for driving the couple towards the left requires a cuprous ion activity of less than 1.5×10^{-10} (at unit cupric ion activity). It is doubtful whether such low ion activity would translate into any meaningful catalytic activity and the workings of cuprous ion are more likely related to the reduction of dissolved oxygen.

Diatomic oxygen reduction

The reduction of this diatomic oxygen occurs in a series of consecutive one-electron transfer steps:

$$O_{2(aq)} + H^+_{(aq)} + e^- \Leftrightarrow HO_2\cdot_{(aq)} \qquad 6.66$$

$$HO_2\cdot_{(aq)} + H^+_{(aq)} + e^- \Leftrightarrow H_2O_{2(aq)} \qquad 6.67$$

$$H_2O_{2(aq)} + H^+_{(aq)} + e^- \Leftrightarrow HO\cdot_{(aq)} + H_2O_{(aq)} \qquad 6.68$$

$$HO\cdot_{(aq)} + H^+_{(aq)} + e^- \Leftrightarrow H_2O_{(aq)} \qquad 6.69$$

These reactions are an intrinsic part of oxygen electro-reduction on fuel-cell catalysts (see, *e.g.*, the recent paper of Shi *et al.*, 2006). The reduction of oxygen on mineral surfaces would be expected to proceed *via* a similar mechanism, albeit without external current. This is because single-electron transfer is energetically more favourable than multi-electron processes (Jin *et al.*, 1985). A kinetically less favourable scenario is thus represented by combining Equations 6.66 and 6.67 and Equations 6.68 and 6.69, *i.e.*, respectively:

$$O_{2(aq)} + 2H^+_{(aq)} + 2e^- \Leftrightarrow H_2O_{2(aq)} \qquad 6.70$$

$$H_2O_{2(aq)} + 2H^+_{(aq)} + 2e^- \Leftrightarrow 2H_2O_{(aq)} \qquad 6.71$$

Although these two reactions are thermodynamically favourable ($E°_h$ = 0.694 V & 1.776 V, respectively; Lide, 1991), it is highly unlikely that the oxygen molecule would simultaneously receive two electrons. Even for a highly reactive, pure metal platinum surface, most recent *ab initio* quantum-chemistry studies (Shi *et al.*, 2006) involve single-electron transfer during the initial reduction step. Also, direct chemical attack is improbable on mineral surfaces where covalency (of varying degrees) between the metal and sulfide atoms would prevent major delocalised electron density, which in turn would prevent sufficient electron wave-function overlap to overcome the bonding energy of the O=O molecule (see Tributsch & Gerischer, 1976). Tributsch and Gerischer

Stellenbosch University http://scholar.sun.ac.za

concluded that the reduction of oxygen on sulfide mineral surfaces involves a series of electrochemical steps. These reduction potentials are compared in Table 6.1:

Table 6.1
Standard single-electron reduction potentials of diatomic oxygen.

Reaction	Conditions	$E°_h$ (V)	Reference
[a] $O_{2\,(aq)} + H^+ + e^- \Leftrightarrow HO_2\cdot$	pH = 0	0.12	[b] Calculated
$HO_2\cdot + H^+ + e^- \Leftrightarrow H_2O_2$	pH = 0	1.42 – 1.49	Wardman (1989)
$H_2O_2 + H^+ + e^- \Leftrightarrow OH\cdot + H_2O$	pH = 7	0.5 – 0.8	Wardman (1989)
$OH\cdot + H^+ + e^- \Leftrightarrow H_2O$	pH = 0	2.6 – 2.9	Wardman (1989)

[a] Standard state of unit activity; [b] Value calculated from standard Gibbs free energy of $O_{2\,(aq)}$ from Wagman *et al.* (1982), *p*K value of $HO_2\cdot$ & standard reduction potential of $O_2/HO_2\cdot$ couple, as reported by Bielski *et al.* (1985).

The relatively low reduction potential of the diatomic oxygen molecule, to form the perhydroxyl radical ($HO_2\cdot$), confirms the unfavourable thermodynamic driving force for the initial step. The role of the conjugate base, *i.e.*, the superoxide radical ($O_2^{-}\cdot$), is assumed to be insignificant under the acidic conditions encountered in this study. Highly reductive conditions would be required to drive this reaction at room temperature, conditions that cannot be efficiently provided by aqueous iron(II) (low reductive power) or copper(I) (low concentration in sulfate medium, as discussed above). This is the reason why oxygen plays an insignificant cathodic role in mineral leaching systems at around room temperature. Fundamentally, this may be ascribed to the ground-state electronic configuration of the superoxide radical, with three π^* electrons (*vs.* two π^* electrons in the ground-state configuration of O_2; see Atkins & De Paula, 2006). However, this first reduction step of the diatomic oxygen molecule would increase with temperature and highlights the kinetic nature of this reaction. The unpaired electron would make the superoxide species very reactive and, depending on the prevailing conditions in the surrounding solution, it may accept another electron to form the peroxide ion (O_2^{2-}) (Rx. 6.67, which is thermodynamically strongly favourable; Table 6.1).

Alternatively, the perhydroxyl radical may be oxidised by metal species in solution to, again, liberate a diatomic oxygen molecule (see Foote *et al.*, 1995):

$$HO_2\cdot_{(aq)} \Rightarrow O_{2(aq)} + H^+_{(aq)} + e^- \qquad 6.72$$

The reduction of both Cu^{2+} and Fe^{3+} is thermodynamically favourable, with potentials (net reactions) of 0.03 V and 0.65 V, respectively. Although the thermodynamic driving force is far greater for perhydroxyl oxidation by ferric ion, the kinetics of the reaction with cupric ion is orders of magnitude faster (see Table 6.2) and again illustrates that kinetics, and not thermodynamics, may be the determining factor. Although these cited references (Table 6.2) are related to the biochemistry field, the kinetic constants are relatively independent of the type of ligand at low pH

Stellenbosch University http://scholar.sun.ac.za

(Cabelli *et al.*, 2000). This is certainly true in the case of relatively weak metal-ligand complex formation and would be expected to also apply to the sulfate system (see Ch. 2).

Table 6.2
Rate constants of single-electron transfer between oxygen, perhydroxyl, peroxide & hydroxyl species, & the relevant transition metal cations.

Reaction	Rate constant (L/mol.sec)	Conditions	Reference (see for primary references)
$O_2 + Cu^+ + H^+ \Rightarrow Cu^{2+} + HO_2\cdot$	4.6×10^5	pH = 2.1	Cabelli *et al.* (2000)
$HO_2\cdot + Fe^{3+} \Rightarrow Fe^{2+} + O_2 + H^+$	$< 1.2\times10^4$	pH = 0.4	Bielski *et al.* (1985)
	$\sim4\times10^5$	pH = 1	
$HO_2\cdot + Fe^{2+} + H^+ \Rightarrow Fe^{3+} + H_2O_2$	1.2×10^6	pH = 1	Bielski *et al.* (1985)
$HO_2\cdot + Cu^{2+} \Rightarrow Cu^+ + O_2 + H^+$	$\sim1\times10^8$	pH = 0.8-2	Bielski *et al.* (1985)
$HO_2\cdot + Cu^+ + H^+ \Rightarrow Cu^{2+} + H_2O_2$	6×10^8	pH = 2.3	Bielski *et al.* (1985)
	2.3×10^9	pH = 2.3	
[a] $H_2O_2 + Fe^{2+} + H^+ \Rightarrow Fe^{3+} + H_2O + OH\cdot$	4.2×10^1	–	Bielski & Cabelli (1995)
[a] $H_2O_2 + Cu^+ + H^+ \Rightarrow Cu^{2+} + H_2O + OH\cdot$	4.7×10^3	pH = 2.3	Cabelli *et al.* (2000)
[a] $HO\cdot + Fe^{2+} + H^+ \Rightarrow Fe^{3+} + H_2O$	2.3×10^8	–	Bielski & Cabelli (1995)
[a] $HO\cdot + Cu^+ + H^+ \Rightarrow Cu^{2+} + H_2O$	2×10^{10}	–	Bielski & Cabelli (1995)

[a] Fenton-type reactions (see, *e.g.*, Bielski & Cabelli, 1995).

Cuprous ion reacts significantly more rapidly than ferric ion with the various intermediate species, *i.e.*, the perhydroxyl radical, peroxide molecule (H_2O_2) and hydroxyl radical ($OH\cdot$). Both from a thermodynamic (Table 6.1) and kinetic viewpoint (Table 6.2), the presence of hydroxyl radicals would be expected to most benefit the oxidation of sulfide minerals. There are many possible pathways by which this species may be formed (Bielski *et al.*, 1985; Bielski & Cabelli, 1995). Firstly, its formation *via* an uncatalysed Haber-Weiss mechanism would be relatively insignificant (Bielski & Cabelli, 1995):

$$HO_2\cdot_{(aq)} + H_2O_{2(aq)} \Leftrightarrow HO\cdot_{(aq)} + H_2O_{(aq)} + O_{2(aq)} \qquad 6.73$$

In contrast, the presence of perhydroxyl and peroxide species, in the presence of copper, might provide very efficient oxidation pathways because the perhydroxyl radical could reduce cupric ion at a rapid rate and the resulting cuprous ion could then undergo Fenton-type reactions to generate the hydroxyl radical (Bielski & Cabelli, 1995). Similarly, the oxidation of sulfide mineral surfaces by oxygen is critically dependent on the catalytic properties of the surface (Tributsch & Gerischer, 1976). They considered peroxide to be the most stable intermediate in the reduction of oxygen on sulfide minerals, because the complete reduction of peroxide on pyrite required more negative potentials, as compared to oxygen.

Stellenbosch University http://scholar.sun.ac.za

Since semiconducting minerals with narrow band gaps, such as chalcopyrite and pyrite, would exhibit a high surface concentration of conducting electrons and holes, the oxidation reaction may be represented as follows (after Tributsch & Gerischer, 1976, here omitting the role of the cation):

$$S^{2-} + O_2 + 2H^+ \Rightarrow S^o + H_2O_2 \qquad 6.74$$

which may be considered to consist of the following two half-cell reactions:

$$S^{2-} + O_2 + 2H^+ \Rightarrow S^{2-} + H_2O_2 + 2h^+ \qquad 6.75$$

$$S^{2-} + 2h^+ \Rightarrow S^o \qquad 6.76$$

An important observation is the oscillatory behaviour during the cathodic reduction of peroxide in the case of the copper-containing minerals, such as chalcopyrite, whilst such effect was absent in the case of minerals such as pyrite. This led Tributsch and Gerischer (1976) to believe that surface-bound copper(I) species can act as catalytic sites for peroxide reduction. Therefore, although pyrite is known to be a catalyst for diatomic oxygen (Biegler *et al.*, 1977 & next section) and peroxide (Tributsch & Gerischer, 1976) reduction, the mechanism appears to be fundamentally different to that on copper-containing chalcopyrite surface. The electrochemical results of Biegler *et al.* (1977) also suggest that different rate-determining steps and/or mechanisms of oxygen reduction could be operating on different sulfide mineral surfaces. They observed significantly different overpotentials for oxygen reduction on different sulfide minerals and suggested (due to a lack of any observed pH dependence of the cathodic current) that the rate-limiting step on a pyrite mineral surface is the formation of the superoxide radical.

Although oxygen reduction (at the cathode) in electrolyte-based fuel cells has been studied extensively, the reaction pathways and mechanisms on different catalyst surfaces are still unclear. Oxygen may reduce all the way to water (transfer of four electrons), to peroxide followed by reduction to water (transfer of two electrons), or various combinations of these (see Shi *et al.*, 2006). Once again, the first electron transfer step (Rx. 6.66) is commonly assumed to be the rate-determining step. Anderson and Albu (1999) conducted an *ab initio* study of the four elementary oxygen reduction reactions (Rx. 6.66-6.69) on a platinum (Pt) surface and found peroxide reduction (Rx. 6.68) to have the highest activation energy, *i.e.*, energy required to break the O–O bond. This is consistent with the experimental observation of a significantly higher overpotential for peroxide compared to oxygen reduction on weakly interacting electrodes, like mercury (see reference in Anderson & Albu, 1999). This translates into preferential peroxide formation on mercury electrodes compared to electrodes with higher catalytic activity, such as platinum. The results of the study by Anderson and Albu (1999) suggest that the activation energies of the four elementary reduction steps are in the order: Reaction 6.68 > Reaction 6.66 > Reaction 6.67 > Reaction 6.69

Stellenbosch University http://scholar.sun.ac.za

and that an efficient four-electron reduction catalyst surface must activate the first and third reduction steps, without deactivating the other two steps. Anderson and Albu (2000) concluded that surface binding of the first three species to platinum resulted in stretching of the O–O bond compared to no surface bonding. The effect was largest in the order $H_2O_2 > O_2 > HO_2\cdot$, which transpired into a corresponding degree of activation energy lowering. However, the surface bonding of the $OH\cdot$ species increased the activation energy of the fourth step (Rx. 6.69). Sidik and Anderson (2002) calculated the dissociation energy of oxygen reduction when bonded to a platinum dual site and found that the first electron transfer had a smaller barrier than that of O–O dissociation. They concluded therefore that diatomic oxygen would not dissociate before the first reduction step. In contrast, the dissociation barrier for the perhydroxyl radical was found to be so low that it may easily dissociate, once formed. Another important finding from this study is that the hydrogen ion may facilitate the first electron transfer step because of the ability of its electrical field to enhance the electron-attracting capability of the surface-coordinated diatomic oxygen molecule (after Shi *et al.*, 2006).

Various *ab initio* studies, covered in the review of Shi *et al.* (2006), proposed that the first electron transfer reaction is the rate-determining step and that the dissociation tendency of oxygen is the dominant factor that determines its reactivity. Various schemes have been proposed, involving either two-fold or one-fold (end-on) adsorption on the platinum surface, either before or after proton transfer. After the first electron transfer step, the intermediate may either resemble the perhydroxyl radical or be directly split into hydroxyl radicals without major barriers, depending on the catalytic properties of the surface. The activity of an electro-catalyst is seemingly related to its ability to break the O–O bond and form the O–H bond (see Shi *et al.*, 2006).

The insightful paper of Norskov *et al.* (2004) has also demonstrated that it is not only adsorption of oxygen on the surface that is important but also the ability to exchange electrons and protons with the intermediate species, *i.e.*, the reduction of oxygen may be strongly activated (kinetically slow) due to a high adsorption tendency of the intermediate species on the surface. Similarly, at higher potential, adsorbed oxygen becomes more stable, with progressively slower proton and electron transfer. Norskov *et al.* investigated the free energy changes and the kinetics of electrochemical reduction of oxygen, and found the peroxide mechanism to dominate on the most noble metals. The mechanism of reduction on a specific surface depends on the sequence of the proton and electron transfer steps. Tsuda and Kasai (2007) suggested that the proton transfer to oxygen, adsorbed on a platinum catalyst, preferentially migrates to O_2 as compared to O, because the highest molecular orbital (HOMO) level of the Pt-O_2 system is higher than that of the Pt-O system. The associative sequence proposed by Norskov *et al.* (2004) may therefore be the preferred mechanism on a more catalytic surface:

Stellenbosch University http://scholar.sun.ac.za

$$O_{2(aq)} + {}^{*} \Leftrightarrow O_2^{*} \qquad 6.77$$

$$O_2^{*} + H^{+}_{(aq)} + e^{-} \Leftrightarrow HO_2^{*}\cdot \qquad 6.78$$

$$HO_2^{*}\cdot + H^{+}_{(aq)} + e^{-} \Leftrightarrow H_2O_{(aq)} + O^{*} \qquad 6.79$$

$$O^{*} + H^{+}_{(aq)} + e^{-} \Leftrightarrow HO^{*}\cdot \qquad 6.80$$

$$HO^{*}\cdot + H^{+}_{(aq)} + e^{-} \Leftrightarrow H_2O_{(aq)} + {}^{*} \qquad 6.81$$

where * denotes a site on the surface. An alternative to forming water in Reaction 6.79 is hydrogen peroxide, which may desorb and diffuse away from the surface. The hydrogen peroxide may also decompose with evolution of oxygen in the presence of some transition metal ions. This is a self-reduction-oxidation disproportionation reaction (Burkin *et al.*, 1981):

$$H_2O_2 \Rightarrow H_2O_{(aq)} + \tfrac{1}{2}O_{2(aq)} \qquad 6.82$$

The reaction of hydrogen peroxide with sulfide minerals might also occur *via* direct attack, *i.e.*, it might consist of substitution-type reactions (see Tributsch & Gerischer, 1976), which may not contribute to a measured current-voltage relationship. Therefore, the reaction of any of the intermediate products of the electrochemical oxygen reduction reaction at mineral surfaces or in solution might lead to higher sulfur oxidation states, which could be accounted for outside the mixed-potential framework. These reactions remain, however, highly speculative, as there is a number of possible schemes, which would vary between different minerals and oxidation conditions and may be ‘electrochemical’ or ‘chemical’ in nature (see Tributsch & Gerischer, 1976).

Iron(III) reduction

Contrary to oxygen and its intermediates, such as peroxide, iron(III) is an efficient electron acceptor, hence the steep polarisation (current-potential) relationship (App. F.2) compared to the oxygen reduction on a mineral surface (Hiskey & Wadsworth, 1981; Peters, 1984). Certainly at lower temperatures, the cathodic reduction of iron(III) would be most effective, as it would develop the highest anodic mixed potential current during leaching (Figure 6.22). Although the iron couple is thermodynamically less favourable than the oxygen couple (see above), the degenerate 3*d* orbital of the ferric ion, with five unpaired electrons (d^5), might easily accommodate another electron to form the ferrous ion (d^6). This charge transfer process (Rx. 6.63) would encounter a relatively small activation barrier and would be comparatively faster than the reduction of oxygen on a sulfide mineral surface. This is demonstrated by the fact that ferric reduction commences at a comparatively more positive potential (*cf.* diatomic oxygen), especially at lower temperatures (see Tributsch & Gerischer, 1976). Oxidation by ferric ions would also be expected to produce

Stellenbosch University http://scholar.sun.ac.za

predominantly molecular sulfur *via* hole-decomposition pathways (alignment of energy levels of aqueous species with the valence band *via* surface states, as discussed earlier).

On the other hand, the adsorption of ferric ion on mineral surfaces would be expected to be energetically less favourable (*cf.* diatomic oxygen) due to its highly negative free energy of solvation value of -4265 kJ/mol (-1840 kJ/mol for Fe^{2+}; Marcus, 1991) as compared to the small positive value for diatomic oxygen (based on Henry's law constant; App. A.4), as well as the positive mineral surface charge in an acidic environment. However, Horne and Axelrod (1964) have provided evidence that supports the hypothesis that the ferric/ferrous electron exchange reaction involves a Grotthuss-type mechanism. This mechanism is closely related to the mobility of the hydrogen ion in aqueous solution, *i.e.*, water plays a crucial role in this exchange reaction. It is assumed that the hydration shell of ferric ion would stay largely intact and that electron transfer from the mineral surface could be achieved over relatively large distances *via* a water-bridge mechanism. A similar mechanism was even proposed to account for long distance electron transfer between -SH and -S–S groups in proteins (see Horne & Axelrod, 1964). Therefore, it is assumed that water molecules could form a conductive chain between the cathodic site on a mineral surface and the solvation shell of the iron(III) species. As explained by Horne and Axelrod, valence electrons of these solvated cations are not confined to their parent sites but wander over the molecular orbital of the entire solvated cation aggregate. However, this process would be significantly slower than when an electron transfer agent, such as adsorbed chloride ion, forms a (covalent) link between the surface and the iron(III) species (see Taube, 1952).

Finally, the oxidation of a mineral usually becomes less effective at higher oxidant concentrations, *e.g.*, the oxidation of chalcopyrite (Braithwaite & Wadsworth, 1976) and pyrite (Bailey & Peters, 1976; Papangelakis & Demopoulos, 1991) reflected lower reaction order dependencies at higher oxygen overpressures, while sphalerite (Jin *et al.*, 1985), chalcocite (Hiskey & Wadsworth, 1981) and chalcopyrite (Hirato *et al.*, 1987) oxidation reflected lower reaction order dependencies at higher iron(III) concentrations. Although the decrease in reaction order with respect to the diatomic molecule has often been quantified in terms of an adsorption mechanism (Lin *et al.*, 1986), such an approach is significantly less common in the case of iron(III) (Jin *et al.*, 1985). The saturation effect of iron(III) is usually ascribed to solution properties, either on a strictly thermodynamic basis (Hiskey & Wadsworth, 1981) or in terms of the actual electro-active species (Crundwell, 1987; Hirato *et al.*, 1987). Solid-state electronic properties, especially in the case of *n*-type semiconductors such as chalcopyrite and sphalerite, might also be responsible for saturation effects at high oxidant concentrations (Crundwell, 1988b; discussed above). Now that some general aspects of sulfide mineral oxidation have been discussed, the properties of pyrite and its interaction with oxygen are dealt with in more detail.

Stellenbosch University http://scholar.sun.ac.za

Pyrite oxidation

Pyrite crystallises in the cubic system and its lattice resembles that of sodium chloride, with iron replacing the sodium and S_2^{2-} replacing the chloride. The optimised unit cell of the bulk structure is presented in Figure 6.8 and illustrates that each iron atom is surrounded by six sulfur atoms in a distorted octahedral array, while each sulfur atom has one nearest-neighbour sulfur atom and three nearest-neighbour iron atoms (Lowson, 1982).

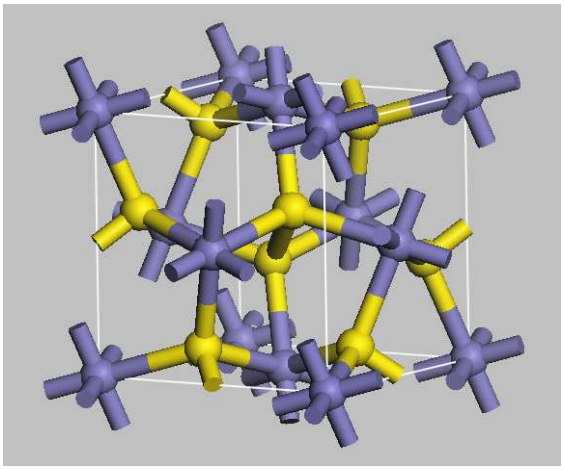

Figure 6.8
Optimised pyrite unit cell (*MS*, 2008); Fe & S atoms are coloured purple & yellow, respectively (space group Pa3, with experimental lattice parameters: a = b = c = 5.4175Å at room temperature; Lowson, 1982).

There is consensus that iron in pyrite is present as Fe^{2+} (Lowson, 1982) and has, therefore, no magnetic moment. The sulfur is present as the S_2^{2-} moiety and has no magnetic moment either; the ionic model may therefore be represented as $Fe^{2+}(S_2)^{2-}$. The strong octahedral crystal field causes a large enough energy difference (Brown, 1980) so that the $3d^6$ electrons of Fe^{2+} are paired and only occupy the triplet t_{2g} ground (low-spin) state (Lowson, 1982). These electrons form the valence band but remain non-bonding (Crundwell, 1988b). Trigonal distortion of the strong octahedral crystal field further splits the t_{2g} orbitals. The ten electrons of the sulfur moiety completely fill the 3*p* bonding (p_σ & p_π) and anti-bonding (p_π^*) orbitals. The bonding orbital band (sulfur valence band) is about 7 eV wide and occupies the region just below the t_{2g} valence band (Lowson, 1982; Crundwell, 1988b). The lower part of the conduction band is derived from the anti-bonding e_g^* doublet of the Fe^{2+} 3*d* orbitals, while the upper part is derived from its 4*s* orbital. The band gap is therefore situated between the non-bonding t_{2g} and e_g^* orbitals (Crundwell, 1988b). The inferred gap is between 0.9 and 1.2 eV (measured by different techniques) and depends on both the sulfur content and the presence of impurity metals (Lowson, 1982). Since sulfur occurs in an octahedral arrangement around the iron atom, orbital overlap is not significant and the non-bonding valence band is narrow (~1 eV; Crundwell, 1998b). The average optimised bond lengths of Fe–S and S–S

Stellenbosch University http://scholar.sun.ac.za

in the bulk material (Figure 6.8) are 0.23 nm and 0.22 nm, respectively. The electronic band structure and the relative position of the bands' edges to the relevant standard reduction potentials are illustrated in Figure 6.9.

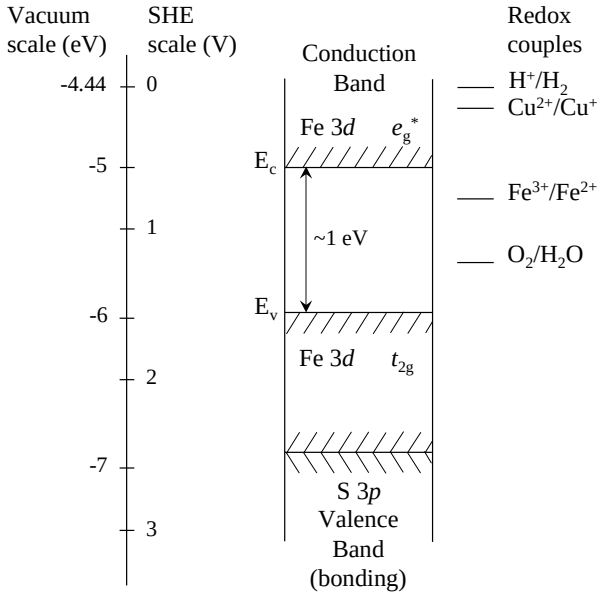

Figure 6.9
Qualitative semiconducting electronic band structure of pyrite, with inclusion of the various standard reduction potentials of the important redox couples (adopted from Crundwell, 1988a).

Clearly, energy-level matching between donor and acceptor sites during electron transfer from the bonding orbitals to these common redox couples would be poor and might be the reason for the slow dissolution behaviour of pyrite at room temperature. Lowson (1982) has covered most of the earlier mechanistic proposals, which may be divided into chemical and electrochemical reaction sequences. The chemical route (oxygen atom transfer) may be expressed *via* the following general reaction sequence, where * refers to the adsorbed species on the reacting surface:

$$FeS_{2(s)} + 2O_{2(aq)} \Rightarrow FeS_2(O_2)^* \Rightarrow Fe^{2+}_{(aq)} + SO^{2-}_{4(aq)} + S^o_{(s)} \qquad 6.83$$

Although the direct mechanism might account for some oxidation at very high temperatures, the previous section has highlighted that a series of one-electron reduction steps of oxygen would be significantly more favourable and this is therefore assumed to predominate over the temperature range encountered in this study.

Electrochemical nature of pyrite oxidation

Discussions in the next few paragraphs support the electrochemical nature of pyrite oxidation by oxygen and iron(III). The review of Holmes and Crundwell (2000), and others, is particularly useful in this regard and only the main conclusions are emphasised here. First of all, isotope studies

Stellenbosch University http://scholar.sun.ac.za

(Bailey & Peters, 1976; more recent references in Holmes & Crundwell, 2000) have shown that sulfate formed from pyritic sulfur acquires its oxygen atom from water and not diatomic oxygen (Rx. 6.85). The fact that pyrite is also known to enhance the contact dissolution of less noble minerals *via* galvanic mechanisms (Hiskey & Wadsworth, 1981; Holmes & Crundwell, 1995) supports the electrochemical route. Bailey and Peters (1976) observed that the degree of sulfate formation was relatively independent of the leaching extent, but increased with increasing oxidation potential (~60% at 0.7 V *vs.* SHE & ~90% at 1.0 V). Similar sulfur yields were obtained under constant mixed potential conditions, but under varying oxygen content, *i.e.*, pressure oxidation *vs.* (potentiostatically) imposed conditions, without oxygen present. A direct chemical mechanism (Rx. 6.83) does not support these findings. They also observed higher open-circuit (rest) potentials at increasing oxygen overpressures, confirming the electrochemical nature of pyrite oxidation, and partitioned the anodic reaction in terms of the final sulfur oxidation state:

$$FeS_{2(s)} \Rightarrow Fe^{2+}_{(aq)} + 2S^{o}_{(s)} + 2e^{-} \qquad 6.84$$

$$FeS_{2(s)} + 8H_2O \Rightarrow Fe^{2+}_{(aq)} + 2SO^{2-}_{4(aq)} + 16H^{+} + 14e^{-} \qquad 6.85$$

Despite these insights, the exact oxidation mechanism has remained under scrutiny.

The reproducible anodic polarisation curves, measured by Biegler and Swift (1979b), had a Tafel slope (App. F.2) of 0.096 V/decade, implying a transition between a semiconductor Tafel slope of 0.059 V/decade and a metal-like Tafel slope of 0.118 V/decade (Crundwell, 1988b). Just like Bailey and Peters (1976), Biegler and Swift (1979b) also observed the elemental sulfur yield to decrease linearly with increasing potential and concluded that these two pathways (Rx. 6.84 & 6.85) operate in parallel and not *via* sulfur formation. Peters (1984) has, however, pointed out that this statement only holds when referring to a stable allotrope of sulfur (see earlier discussions on intermediate sulfur species). Biegler and Swift (1979b) suggested a mechanism of adsorption of hydroxyl radicals and oxygen atoms derived from water (* denotes surface species):

$$FeS_{2(s)} + H_2O \Leftrightarrow FeS_2(OH)^{*}_{(s)} + H^{+} + e^{-} \qquad 6.86$$

$$FeS_2(OH)^{*}_{(s)} \Leftrightarrow FeS_2(O)^{*}_{(s)} + H^{+} + e^{-} \qquad 6.87$$

They proposed that the second charge transfer step is rate limiting. They also pointed out that the sulfur yield was relatively insensitive to the temperature at fixed potential, which suggests that the two pathways (Rx. 6.84 & 6.85) either happen to have similar activation energies or share the same rate-limiting step, *e.g.*, Reaction 6.87. The foremost case would be an unlikely coincidence since the free energy changes of these reactions are significantly different.

Stellenbosch University http://scholar.sun.ac.za

The possible role of polymeric sulfur

Just like chalcopyrite oxidation kinetics (discussed earlier), the stifling role of elemental sulfur should not be underestimated. Peters (1986) elaborated on the issue of sulfur morphology on pyrite surfaces. Sulfur may be expected to form a denser structure on pyrite due to a positive molar volume change, while the other sulfide minerals encountered in this study all show negative changes and would form relatively porous structures. However, some operating temperatures, where pyrite still oxidised relatively slowly (Bailey & Peters, 1976; Long & Dixon, 2004), were close to or higher than the sulfur melting point; the above arguments would therefore not hold as the surface (sulfur) structure would be able to relax. Furthermore, the intrinsic elemental sulfur yield on pyrite might be too low to passivate the surface *via* the progressive formation of dense sulfur layers. A more likely scenario is the formation of polymeric sulfur under certain surface potential conditions. Such polymeric ('plastic') sulfur surface layers were detected by Biegler and Swift (1979a) on chalcopyrite surfaces after anodic polarisation at room temperature. Steudel (2003) has emphasised that the transition from stable S_λ allotrope (see previous discussions on sulfur species) to S_μ (polymerised sulfur) cannot be considered to be a phase transformation in the normal sense, but should be viewed as a kinetically controlled equilibrium reaction. Mechanistic studies, using *ab initio* molecular dynamics (MD) simulations (Steudel, 2003), have confirmed that the S_8 ring structure may be opened either thermally or photochemically. In this context, the study of Munejiri *et al.* (2000) is of particular relevance, as their calculations have shown that once the structure was opened, the eight-atomic diradical chain did not recombine back to the original ring. Longer chains were also formed in the presence of other S_8 diradical chains, which might be important intermediates in the polymerisation of sulfur. These results suggest that the potential gradient at a mineral surface might impose changes to the sulfur structure, even below its melting point. This statement also does not necessarily imply that polymeric sulfur would be formed *via* a stable allotrope, *i.e.*, polymeric sulfur could be formed earlier on during the oxidation of a sulfide mineral (see previous mechanistic discussions).

A rapid increase in pyrite oxidation rate is usually accompanied by an increase in sulfur oxidation, which is consistent with the requirement of a large overpotential for sulfur oxidation (see Peters, 1984). This phenomenon may be viewed as something more than pure coincidence. This statement also holds for chalcopyrite (Biegler & Swift, 1979a; Lázaro & Nicol, 2003; Viramontes-Gamboa *et al.* 2007). Although Viramontes-Gamboa *et al.* observed a slight increase in the current with increasing acid concentration in the Tafel region, the transpassive potential (E_{tpp}; Figure 6.6) also increased with increasing acid concentration and temperature. The current increase in the Tafel region will be dealt with later in this study and is believed to be associated with surface states (App. F.1). The more important aspect in the current context is the increase in the transpassive

Stellenbosch University http://scholar.sun.ac.za

potential with increasing acid concentration. If passivation is indeed caused by the formation of polymeric-type sulfur, its diradical chain-ends would be prone to combining with hydrogen ion (see Steudel, 2003). The hydrogen ion would therefore be expected to play an important role in its stability, analogous to previous proposals for S_8 ring formation *via* a chain-propagation mechanism, involving polysulfides and $HS\cdot$ radicals (Eq. 6.55-6.59). Below the transition temperature (Figure 6.7), two opposing effects may be at work; the conversion of S_μ to the stable S_λ allotrope might become slower as the transition temperature is approached, but the oxidation kinetics of the intermediate sulfur phases might increase. Complete oxidation to sulfate may predominate at higher surface potentials ($> E_{tpp}$) and a sudden change in the current-potential relationship would be observed (transpassive region), while the passivation effect of the S_μ may predominate at lower surface potentials. At even lower surface potentials, the formation of a polymeric sulfur intermediate may be limited or prevented altogether. Such a layer might be thin enough to permit electron transfer and reflect Tafel-like behaviour (App. F.2), but would be sensitive to the potential and temperature conditions experienced at the surface. The current-potential (polarisation) behaviour of the cathodic reduction reaction would also be significantly different on an intermediate sulfur layer compared to a barren chalcopyrite or pyrite surface. Polarisation of the cathodic reaction could result in a lower mixed potential (Figure 6.22), which in turn, could worsen the oxidation rate before improving again in the transpassive region, where the surface layer would be completely oxidised to sulfur(VI). It is not only electrochemical experimentation that reflects his kind of behaviour, but it has also been observed in autoclave oxidation of pyrite (Long & Dixon, 2004; Papangelakis & Demopoulos, 1991). Both these research groups concluded that sulfur was at least partially responsible for the passivation of the surface. The workings of surfactants may prove to be pivotal in determining the net effect of such surface layers on the overall pyrite oxidation rate.

Pyrite surface oxidation of water

Whether the presence of surface sulfur constitutes a secondary barrier or not, it should not be confused with the primary oxidation mechanism of the barren mineral, which seemingly differs between pyrite and chalcopyrite. Biegler and Swift (1979b) found that the semiconducting properties of pyrite do not significantly influence its anodic oxidation kinetics. The most important factor is that the t_{2g} valence band is of a non-bonding character and is capable of oxidising water (see above), while it could also explain the slow dissolution behaviour of the pyrite structure (Crundwell, 1988b). A recent paper by Cohn *et al.* (2010) has confirmed that pyrite surface can generate hydroxyl radicals in water. Parker *et al.* (1981) have also illustrated that the iron(III)/iron(II) couple behaves in a similarly reversible fashion on pyrite and platinum surfaces, while a reversible surface oxidation region of water (similar to platinum) is detected on pyrite at a relatively low potential (Mishra & Osseo-Asare, 1988). Therefore, the generation of holes in the t_{2g}

Stellenbosch University http://scholar.sun.ac.za

valence band is a characteristic feature of the pyrite surface in oxidative solutions, with iron(III) concentration (see Figure 6.9) being an important factor:

$$Fe^{3+}_{(aq)} \Leftrightarrow Fe^{2+}_{(aq)} + h^{+} \qquad 6.88$$

The first reduction step of oxygen, despite being energetically unfavourable (see above), might also generate holes, but it would depend on the catalytic properties of the mineral surface at a cathodic site. These holes do not directly result in pyrite dissolution, but they can split water as follows:

$$H_2O + h^{+} \Leftrightarrow H^{+} + OH\cdot \qquad 6.89$$

Standard reduction potentials between 2.59 and 2.85 (at pH ≈ 0) have been reported for this couple, with a recommended value of 2.73 (Wardman, 1989). This potential coincides with the bonding orbitals of the sulfur (3*p*) valence band (Figure 6.9) and would be expected to form predominantly sulfate at high temperatures, *i.e.*, this hydroxyl radical could satisfy the high overpotential required for the stepwise oxidation of sulfide (Rx. 6.42). This mechanism is also consistent with the results from various isotope studies (see above), suggesting that sulfate is formed from oxygen acquired from water. It is furthermore consistent with the results of Biegler and Swift (1979b), who found no correlation between the electrochemical reduction of oxygen at the electrode and the semiconducting properties of various pyrite samples. This suggests that the splitting of water could be a rate-determining step (Crundwell, 1988b). Mishra and Osseo-Asare (1988) observed (by measuring anodic current) very slow pyrite oxidation in acetonitrile (1% H_2O) solution, but this accelerated dramatically with an increase in water concentration, confirming the importance of water in the oxidation mechanism.

Holmes and Crundwell (2000) conducted an electrochemical study and derived rate expressions based on mixed potential theory. They have shown that the experimental half-order dependence of the rate on the oxidant concentration is a direct consequence of an electrochemical mechanism, while maintaining consistency with the water-split mechanism *via* (anodic) Reaction 6.85. XPS analyses also showed that the total amount of polysulfides on the pyrite surface increased with increasing potential. However, the formation of this surface product did not limit the oxidation rate (all tests ≤ 35°C), since a constant Butler-Volmer relationship (App. F.2) was maintained over a relatively wide potential range. It should also be highlighted that the elemental sulfur yield was found to be very sensitive to the applied potential and tended to 100% at low potentials. Higher potentials would therefore result in less surface sulfur but the nature of the product layer may become more inhibiting at higher operating temperatures. The fact that almost 100% elemental sulfur yield was recorded at low potentials and relatively low temperature suggests that the sulfur(0) and sulfur(VI) final oxidation states could have been produced by independent electrochemical pathways (after Holmes & Crundwell, 2000). This conclusion is not supported by

Stellenbosch University http://scholar.sun.ac.za

some other proposals, *e.g.*, Mishra and Osseo-Asare (1988), suggesting that elemental sulfur is produced *via* decomposition of intermediate thiosulfate ($S_2O_3^{2-}$). Despite the lack of mechanistic information regarding intermediate oxy-sulfur species and associated reaction pathways, there is general agreement on the prevalence of hole generation in non-bonding orbitals and the subsequent splitting of water. Holes in *d*-orbital states of certain materials (Mishra & Osseo-Asare, 1988) are able to initiate coordination of OH-groups of water to the surface as a precondition for successive electron transfer. The completed electron transfer reaction is best represented by the following equilibrium reaction (after Mishra & Osseo-Asare, 1988), where * denotes a surface state:

$$FeS_{2(s)} + H_2O + h^+ \Leftrightarrow Fe(OH)S^*_{2(s)} + H^+ \qquad 6.90$$

The fact that higher potential is required to oxidise sulfide (*e.g.*, H_2S) to elemental sulfur on platinum (≥ ~1 V), compared to the mixed potential of pyrite during spontaneous oxidation to sulfate (Holmes & Crundwell, 2000), suggests that the 3*d* orbital of iron(II) in the pyrite surface lattice is key to this pathway. The pyrite surface is therefore more electrocatalytic towards water oxidation compared to platinum. This is further supported by the dominant formation of elemental sulfur during the oxidation of non-*d*-band sulfides, *e.g.*, sphalerite (Mishra & Osseo-Asare, 1988). They suggested that the OH-surface group is first transferred onto a S_2^{2-} site before electron transfer occurs, *i.e.*:

$$Fe(OH)S^*_{2(s)} \Leftrightarrow FeS_2(OH)^*_{(s)} \qquad 6.91$$

The complete hydroxylation of the surface to form thiosulfate may be represented as follows:

$$FeS_2(OH)^*_{(s)} + 3H_2O + 3h^+ \Rightarrow Fe(OH)_2 \cdot S_2(OH)^*_{2(s)} + 3H^+ \qquad 6.92$$

$$Fe(OH)_2 \cdot S_2(OH)^*_{2(s)} + 2h^+ \Rightarrow Fe^{2+}_{(aq)} + S_2O^{2-}_{3(aq)} + 2H^+_{(aq)} + H_2O \qquad 6.93$$

The competing reaction mechanisms on pyrite surfaces

The different proposals (covered above) are relatively consistent up to the point of surface adsorption, but differ substantially with regards to the route that sulfide follows to higher oxidation states. A general representation of the final reaction-step, *i.e.*, to form atomic sulfur, is as follows:

$$OH\cdot + HS\cdot \Rightarrow H_2O + S \qquad 6.94$$

This mechanism assumes that the proton adsorbs preferentially at the negatively charged S_2^{2-} moiety and that a transient HS· radical intermediate surface species is formed. This proposition is analogous to the bridging model of Luther (1987), but does not require direct adsorption of the ferric ion at the sulfide site. The half-cell electron-exchange reaction is then as follows:

$$HS\cdot \Leftrightarrow S + H^+ + e^- \qquad 6.95$$

Stellenbosch University http://scholar.sun.ac.za

The standard reduction potential of this couple (at pH = 0) is -1.3 V (Wardman, 1989), so that the overall thermodynamic driving force of Reaction 6.94 (Table 6.1) is highly positive, *i.e.*, 1.3+2.7 = ~4 V. Even if the subsequent oxidation of the HS· surface species occurs *via* direct interaction with aqueous ferric ion, the free energy would still be highly positive, *i.e.*, 1.3+0.8 = ~2.1 V. The first electron transfer step is therefore assumed to be the rate-limiting step.

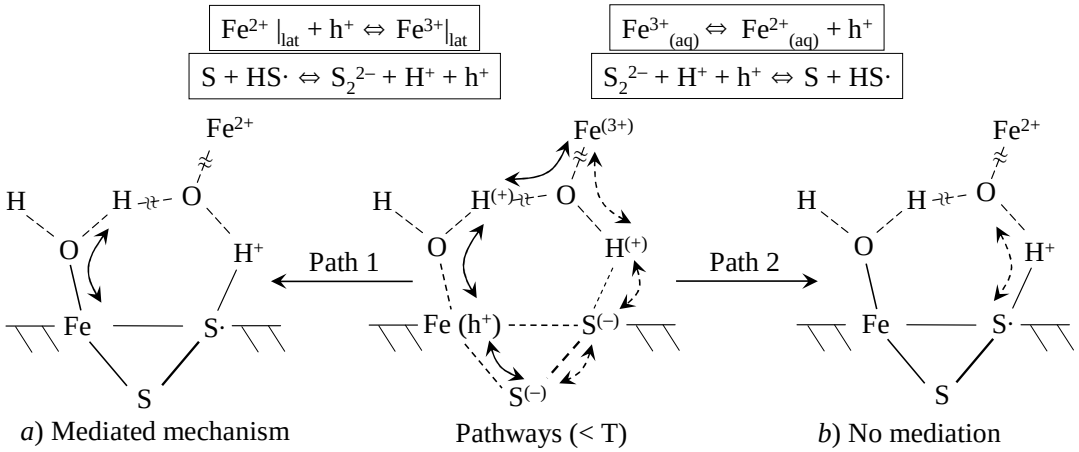

Figure 6.10
Schematic diagram of direct pyrite oxidation by ferric ion (no oxygen) in acid environment at lower temperature: *a*) Electron exchange between t_{2g} orbital of aqueous Fe(III) species & surface iron (hole creation), followed by internal electron transfer from adjacent sulfide site; *b*) Oxidation of sulfide by direct electron exchange with partially-filled t_{2g} orbital of aqueous Fe(III) species.

Figure 6.10 depicts the direct oxidation mechanism by iron(III), *i.e.*, at lower temperature and potential, where the water-split mechanism is too slow to generate the hydroxyl surface species. This model assumes that the hydrogen ion concentration is too high to allow direct adsorption of iron(III) species on sulfide sites and presumes that electron transfer may occur *via* the relatively slow Grotthuss-type conduction mechanism (discussed previously). There is no explicit recognition of the dissociation of water into hydroxyl radical species, *e.g.*, as proposed by Moses *et al.* (1987). The negative effect of higher proton concentrations on the anodic dissolution reaction (Holmes & Crundwell, 2000) is ascribed to interference of the above charge transfer process, even though the adsorbed proton would play an intrinsic part in stabilising the HS· surface species. This proposal implicitly assumes that the free energy of chemisorption of the proton at a sulfide site is lower than that of ferric ion. This is likely to be the case, even if their respective (unhydrated) binding energies are similar, since the average Gibbs free energy of hydration of the proton is -87.5 kJ/mol (per hydration water molecule) compared to -257 kJ/mol for ferric ion (values calculated from published data of Marcus, 1991). The high surface potential (overpotential) required to oxidise sulfur in acid environment (discussed earlier in this section) is thought to be related to this strong adsorption tendency of the proton. Furthermore, the hydrogen ion concentration encountered in this study is usually more than double the total iron(III) concentration.

Stellenbosch University http://scholar.sun.ac.za

There is clearly very little distinction between cathodic and anodic sites in this scheme. Depending on the particular crystal face and conditions at the surface, either the direct hole exchange (Figure 6.10 *a*) or electron transfer (Figure 6.10 *b*) mechanism might be more favourable (energetically). It is unclear whether typical iron(III) concentrations during autoclave oxidation of chalcopyrite-pyrite concentrates would be high enough, and the surface potential low enough, for such a direct oxidation mechanism to predominate. There are also other mechanisms, *e.g.*, fracturing (Todd *et al.*, 2003), which may explain the appearance of holes on the pyrite surface, not to mention the role of other oxidised species and also temperature. However, if holes are supplied at a fast rate (*cf.* its surface consumption) to the non-bonding *d* orbitals of iron in the pyrite surface-structure, the water-split mechanism could become the more dominant route.

Mishra and Osseo-Asare (1988) have proposed (see above) that the OH-group, after water splitting, is transferred to sulfur sites in the pyrite lattice where higher oxidation states of sulfur, such as thiosulfate, are produced. The formation of peroxide upon addition of pyrite to oxygen-free water has also been observed (Borda *et al.*, 2001). Borda *et al.* (2003) explained this by proposing that hydroxyl radicals might form at sulfur-deficient defect sites on pyrite surface *via* the water dissociation mechanism. These radicals could then combine to form peroxide and are therefore sequestrated in a significantly less reactive form:

$$OH\cdot + OH\cdot \Rightarrow H_2O_2 \qquad 6.96$$

Schippers and Sand (1999) have proposed that the thiosulfate route is exclusively followed during the oxidative attack of ‘acid-insoluble’ pyrite. On the other hand, minerals such as chalcopyrite might follow the polysulfide route *via* the HS· mechanism (discussed above). Nicol and Liu (2003) have proposed that the formation of elemental sulfur, during the oxidation of pyrite under pressure leaching conditions, might also follow a non-oxidative route, *i.e.*, *via* the formation of hydrogen sulfide, while sulfate might be produced by a direct oxidation mechanism. Mycroft *et al.* (1990) suggested that electrochemical oxidation of pyrite proceeds *via* at least two mechanisms, in agreement with various other researchers (*e.g.*, Bailey & Peters, 1976). Different pathways were proposed, depending on the potential, temperature and other hole-generation mechanisms, *e.g.*, radiation by laser light. Despite these different proposals, there is enough evidence to suggest that a water-split mechanism could become dominant at higher potentials.

A generalised scheme is proposed and is illustrated, in its simplest form, in Figure 6.11(*a*-*c*), *i.e.*, the splitting of adsorbed water under higher surface potential conditions, allowing hydroxyl radical species to capture electrons from surface sulfide species. This charge transfer rate accelerates with increasing temperature, while higher hydrogen ion concentrations are assumed to decrease the activation energy barrier.

Stellenbosch University http://scholar.sun.ac.za

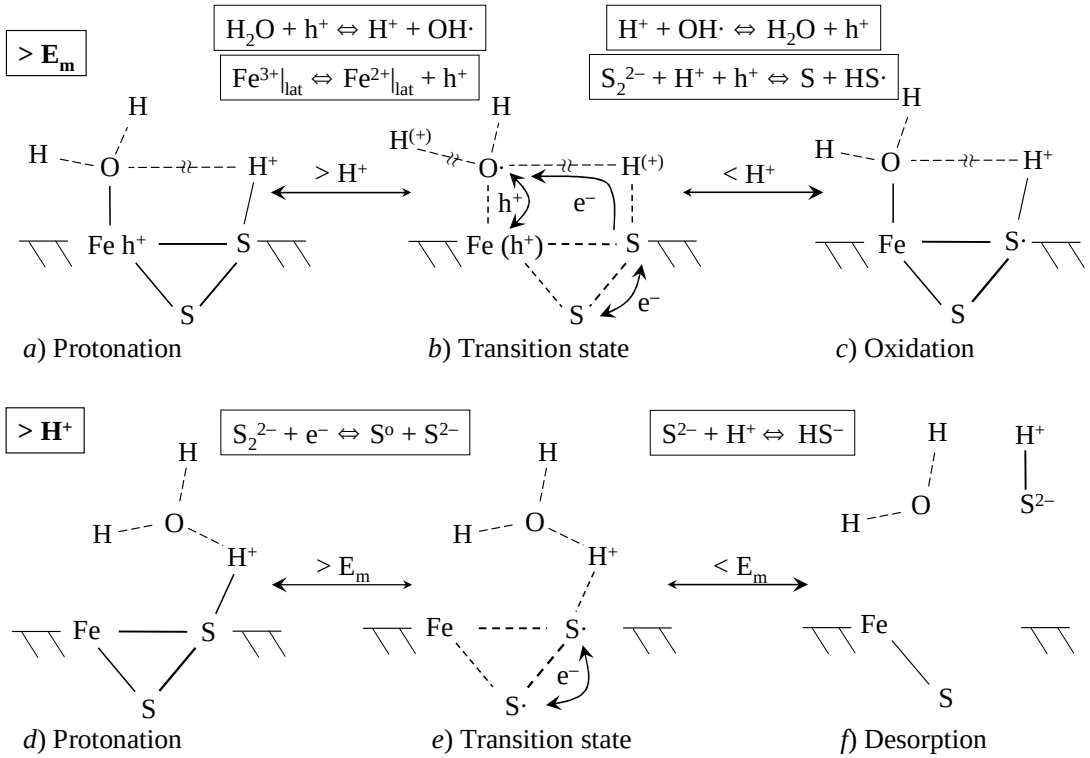

Figure 6.11
Simple mechanistic proposals of pyrite leaching; Oxidative dissolution *via* water splitting at high E_m: *a*) Protonation of surface sulfide site; *b*) Hole exchange with adsorbed water to form hydroxyl intermediate; *c*) Oxidation of nearby sulfide site; Non-oxidative dissolution at high H^+ concentration: *d*) Protonation; *e)* Reduction of surface sulfide to bisulfide species; *f*) Desorption.

In this scheme, both the combined water-split/charge transfer processes would constitute the activation energy barrier of the anodic reaction. Under low surface potential conditions, in a highly acidic environment, bisulfide species might form *via* reduction, *i.e.* the oxidation of an adjacent sulfide in the mineral lattice. These redox couples are estimated as follows:

$$HS\cdot + e^- \Leftrightarrow HS^- \qquad 6.97$$

$$\tfrac{1}{2}S_2^{2-} \Leftrightarrow S + e^- \qquad 6.98$$

The standard reduction potential of these two couples are 1.15 V (Wardman, 1989) and -0.21 V (Lide, 1991), respectively. The net potential (1.36 V) of this mechanism is highly positive and suggests that Reactions 6.97 and 6.98 may constitute a preferred non-oxidative route. This is in line with the proposal of Nicol and Liu (2003). These mechanistic proposals (oxidative and/or non-oxidative) might produce any of the observed intermediate phases, depending on the surface potential and hydrogen ion concentration. However, the non-oxidative route would be less important under high surface potential conditions, as would be expected on a pyrite surface submerged in an oxidative solution at higher temperatures.

Stellenbosch University http://scholar.sun.ac.za

The behaviour of the -Fe–S–S- entity upon oxidation may likely depend on the specific crystal face under consideration and also the nature of the oxidant. The release of a sulfate ion into solution upon the oxidation of pyrite, involves the transfer of seven electrons for each S^{-} atom (see Lotens & Wesker, 1987). Since charge transfer is likely to proceed *via* single-electron transfer steps (see above), the overall oxidation process is complex (see Rimstidt & Vaughan, 2003). Rimstidt and Vaughan have pointed out (see cited references) that, although the exact structure of the activated complex is unknown, the transfer of electrons to the oxidant likely occurs at metal sites in mineral surfaces, rather than at sulfide sites. In the case of oxygen adsorbed on the pyrite surface, this reduction process might follow Fenton-type mechanisms (Lowson, 1982). After each hole-generation step, an electron could be transferred from an anodic site which, in turn, would consume a hole. This scheme is represented in Figure 6.12 and follows a sequence similar to that proposed by Rimstidt and Vaughan (2003). The initial adsorption of oxygen may follow the Griffiths model (Shi *et al.*, 2006) and is schematically represented by Figure 6.12 *a*.

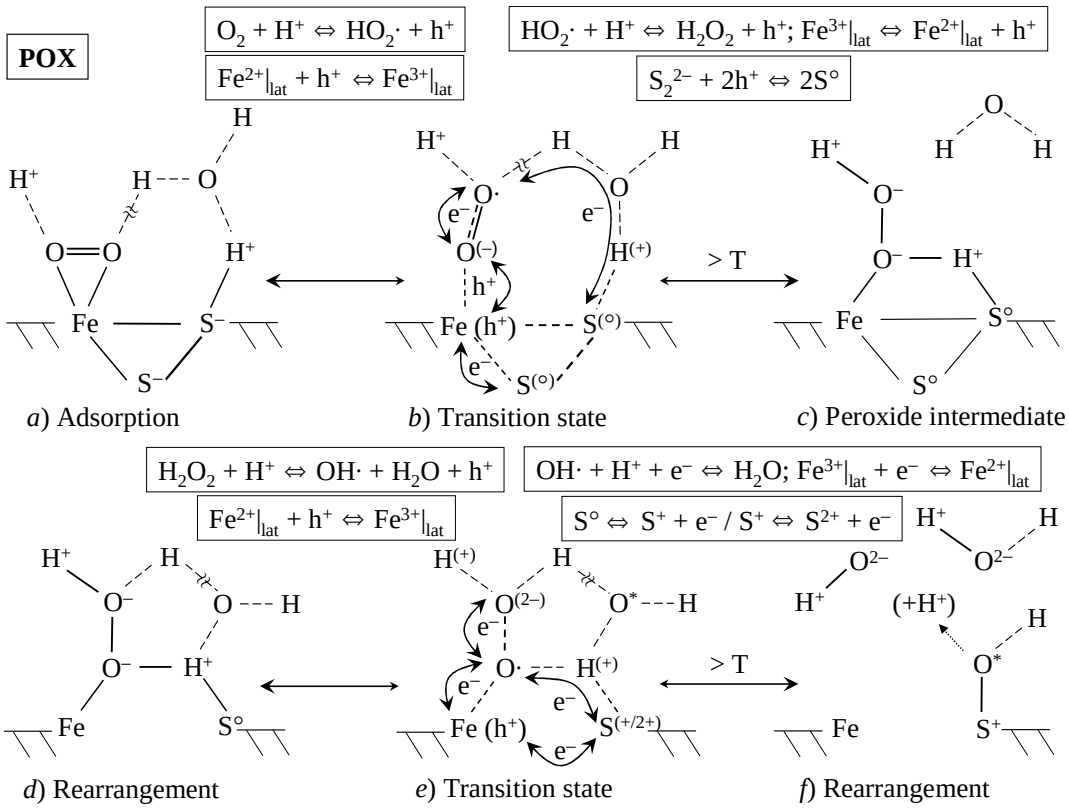

Figure 6.12
Simple mechanistic proposal of pyrite oxidation by oxygen: *a*) Adsorption of diatomic oxygen & protonation of surface sulfide sites; *b*) Hole exchange with adsorbed oxygen to form the perhydroxyl intermediate, followed by oxidation of nearby sulfide sites; *c*) Peroxide intermediate; *d*) Rearrangement of nearby water molecules; *e*) Hole exchange with peroxide to form hydroxyl intermediate, followed by oxidation of nearby sulfur sites; *f*) Nucleophilic attack of positive sulfur species by oxygen (* serves to indicate that this oxygen is derived from water).

Stellenbosch University http://scholar.sun.ac.za

At higher temperatures, the electrocatalytic role of the non-bonding t_{2g} orbital of iron and the enhanced electron-attracting capability of surface-coordinated O=O (assisted by the hydrogen ion in solution) may facilitate the first electron exchange between the mineral and diatomic oxygen (Figure 6.12 *b*). This step is associated with breakage of the first oxygen molecule bond (the illustration imitates the Pauling adsorption model at this point along the reaction coordinate; there is no scientific basis for this and, without mechanistic proof, any adsorption model may have been assumed). Once again, the free-radical states are viewed as part of the transition state that operates within conductive hydrogen-bonded water networks (Figure 6.12 *b*, *e*). Electrons may be transferred *via* a Grotthuss-type tunnelling mechanism or self-propagate from surface radical species, *i.e.*, besides electron conduction via the semiconductor surface itself. The peroxide intermediate group (Figure 6.12 *c*, *d*) is not entirely speculative and draws upon its detection during potentiostatic electrolysis in oxygen saturated solution (Ahlberg & Broo, 1996; Biegler *et al.*, 1977; also see Rand, 1977, who ascribed the loss of a four-electron limiting current to a loss of peroxide to the bulk solution). However, peroxide may also be produced after combination of two hydroxyl radicals (Rx. 6.96) in relatively neutral solutions (Borda *et al.*, 2003). Alternatively, peroxide may convert back to oxygen *via* a self-reduction-oxidation disproportionation reaction at high temperature and in the presence of transition metal ions (Rx. 6.82). In fact, the role of peroxide, as a separate entity, has often been neglected in associative sequences of oxygen reduction on more catalytic surfaces (Norskov *et al.*, 2004).

Sulfur has to pass through several oxidation states, and numerous possible mechanisms may be proposed, yielding different types of intermediate species (Druschel *et al.*, 2003; Druschel & Borda, 2006). The logic of Rimstidt and Vaughan (2003) is, once again, followed, proposing the formation of a sulfur-enriched surface, *i.e.*, preferential removal of iron, similar to the behaviour of chalcopyrite (see above). Further removal of electrons (Figure 6.12 *e*) causes the terminal sulfur to become more electropositive and the negative end of water can mount a nucleophilic attack on this electropositive sulfur (Rimstidt & Vaughan, 2003). This, and each successive oxygen (water) attachment, is associated with the release of a proton, equivalent to the number of electrons absorbed by the oxidant, *i.e.*, the number of protons released by water balances the number of electrons absorbed by oxygen which, in turn, balances the number of hydrogen ions absorbed during its reduction. This scheme is illustrated in Figure 6.12 *f*, representing the first increase in the sulfur oxidation state, *i.e.*, S° to S^+. These sequences may be generalised as follows:

$$\text{-Fe-S-S-H} + H_2O \Rightarrow \text{-Fe-S-S}^+\text{-OH} + 2H^+ + e^- \qquad 6.99$$

$$\text{-Fe-S-S}^+\text{-OH} \Rightarrow \text{-Fe-S-S}^{2+}\text{-O} + H^+ + e^- \qquad 6.100$$

$$\text{-Fe-S-S}^{2+}\text{-O} + H_2O \Rightarrow \text{-Fe-S-S}^{4+}\text{-O}_2 + 2H^+ + 2e^- \qquad 6.101$$

Stellenbosch University http://scholar.sun.ac.za

$$\text{-Fe-S}-\text{S}^{4+}\text{-O}_2+\text{H}_2\text{O} \Rightarrow \text{-Fe-S}-\text{S}^{6+}\text{-O}_3\ +2\text{H}^+ +2\text{e}^- \qquad 6.102$$

Rimstidt and Vaughan (2003) proposed that at high pH the terminal S-SO_3 entity may completely ionise, with the S–S bond becoming stronger than the Fe–S bond and releasing thiosulfate ($S_2O_3^{2-}$) into solution. At low pH, the S-SO_3 entity may retain a proton, which may facilitate the transfer of the S–S bond electrons, followed by nucleophilic attack of another water molecule:

$$\text{-Fe-S}-\text{S}^{6+}\text{-O}_3+\text{H}^+ +\text{H}_2\text{O} \Rightarrow \text{-Fe-S-H}+\text{H}_2\text{SO}_4\ +2\text{e}^- \qquad 6.103$$

The remaining sulfur may follow a similar oxidation pathway (Rx. 6.99-6.102), donating another six electrons (totalling fourteen electrons; Rx. 6.85). Various alternative routes may also be plausible during the final release of the sulfur entity into solution, but these are outside the scope of this study (see Druschel & Borda, 2006). Reedy *et al.* (1991) has also shown that significant amounts of sulfur-oxygen isotopomers may be derived from oxygen gas, suggesting more than one pathway for the formation of sulfate from pyrite oxidation in acid solution. The above description may be simplified by assuming that the formation of higher oxidation states of sulfur proceeds *via* a multistep mechanism, with diatomic elemental sulfur as an intermediate species. Rimstidt and Vaughan (2003) argue that a positive surface potential would pull the electron cloud of the S_2^{2-} dipole away from the surface at an anodic site, exposing its positive end to the electrolyte, *i.e.*, adsorbed protons would desorb and the oxygen atom from water would be adsorbed instead. However, very high proton concentrations might interfere with the approaching water molecules, while playing a central role in the reduction of long-chain polysulfides and structural rearrangements to form crystallites of elemental sulfur (S_8). Besides the electro-catalytic role of the non-bonding t_{2g} orbital of iron in electron transfer, the π^* antibonding orbital of the S_2^{2-} dipole is relatively delocalised and would be more reactive, *i.e.*, the dipole would be oxidised first and, hence, iron could be released as Fe^{2+} (Luther, 1987; Rimstidt & Vaughan, 2003).

Rimstidt and Vaughan (2003) proposed that the rate-determining step in sulfide oxidation is the transfer of electrons from the anodic site to the oxidant at the cathode site. An electrochemical description of the rate demands that the overall dissolution current be deconvoluted into its (rate-determining) half-cell reactions. Qiu *et al.* (2004) have used a quantum mechanical supercell approach to show that iron sites are energetically favoured over the sulfide dipole sites for redox interaction with electron donor or acceptor species on the pyrite surface, which explains the reversible behaviour of pyrite during cyclic voltammetry (Mishra & Osseo-Asare, 1988). The band gap of the surface was also found to be significantly smaller than that of the bulk material, confirming the reason behind the quasi-metallic electrochemical character of pyrite, *i.e.*, higher experimental Tafel slopes than would expected from a semiconductor (Crundwell, 1988b). It was concluded by Qiu *et al.* (2004) that the conductivity on pyrite surfaces is much higher than in the

Stellenbosch University http://scholar.sun.ac.za

bulk material and that the transfer of electrons between anodic and cathodic sites would not be rate limiting, and neither would the supply of holes to non-bonding orbitals. Defect states on the surface were proposed to act as mediators of electrons on both anodic and cathodic sites. This may also explain why similar Tafel slopes were found for *n*- and *p*-type pyrite in the anodic potential region (Biegler, 1976; Crundwell, 1988b). Furthermore, Biegler (1976) found no correlation between kinetic parameters for oxygen reduction and the nature of the pyrite semiconductor. Qiu *et al.* proposed that both the splitting of water (Rx. 6.89) and electron transfer to oxygen (Rx. 6.66) are the rate-limiting steps. This is consistent with the model of Mishra and Osseo-Asare (1988), suggesting Reaction 6.90 to be the rate-limiting step of the anodic process. This also explains why the effect of the proton is often found in the denominator of rate expressions for the dissolution of pyrite (see Crundwell, 1988b; Holmes & Crundwell, 2000). This reaction may therefore be viewed as a reversible charge transfer reaction (Rx. 6.89), which is consistent with the mechanistic representation of Figure 6.11(*a-c*).

A negative effect of chloride concentration on the anodic oxidation rate of pyrite at elevated temperatures (Lehmann *et al.*, 1999) may suggest interference of the charge transfer reactions at the electrocatalytic iron site. Dimitrijević *et al.* (1999) found that the chloride ion also interferes with the oxidation kinetics when using hydrogen peroxide as the oxidant. Nicol and Liu (2003) conducted electrochemical measurements at high temperatures (150-200°C) and found that the anodic oxidation of pyrite was largely unaffected by the presence of up to 4 mol/L Cl. This may suggest that the water-split mechanism becomes less important or is not affected by the presence of chloride ion at higher temperatures. On the other hand, they found that the cathodic reduction of 0.1 mol/L Fe(III) on pyrite was retarded in the presence of chloride ions, resulting in lower mixed potentials and, hence, lower mineral oxidation rates. This was ascribed to a cathodic shift in the ferric reduction half-cell reaction which, in turn, was thought to be a result of the more favourable formation of iron(III) chloro-complexes relative to iron(II). This argument was backed up by the observation of similar cathodic shifts with increasing temperature, which ties in with the tendency to increased complexation (Ch. 2) (in terms of the mixed potential, the net effect of such a cathodic shift would be offset, to a greater or lesser degree, by increased Tafel slopes with temperature). The presence of chloride ions also increased the yield of elemental sulfur, which may be ascribed to the lower surface potential and/or to reduced nucleophilic attack by water (*i.e.*, preferential adsorption of chloride ions at the disulfide sites). It may therefore be argued that the preferential adsorption of chloride anions at neutral or electropositive sites, and their negative effect on the transfer of electrons to approaching ferric ions, could become a rate-determining factor, which outweighs their role as an electron transfer agent (see Taube, 1952). The mechanism of oxidation is therefore highly dependent on the nature of the dominant oxidant species at the interface. These reaction pathways may exhibit parallel and competing steps, which would be dependent on the potential

Stellenbosch University http://scholar.sun.ac.za

conditions experienced at the mineral surface, as well as the different bonding environments on different mineral faces (after Druschel & Borda, 2006).

Simplifying the pyrite oxidation mechanism (phenomenological picture)

Despite the various insights presented above, there is still no clear picture of how the overall anodic and cathodic reactions operate in tandem, especially since the current study involves two oxidants with markedly different electron exchange mechanisms. The following arguments therefore present a simplified platform on which to base the phenomenological rate expressions (Sect. 6.3.4).

There is little doubt that ferric ion is, kinetically, a superior oxidant of pyrite at lower temperatures. Nevertheless, the mixed potential may stabilise at relatively high values in the presence of oxygen at high temperature. This positive surface potential and the relatively high hydrogen ion concentration may enforce a mechanism where the reduction of oxygen is the major contributor to the cathodic current. Ahlberg and Broo (1996) have speculated on the role of iron(II) sites as redox mediators during the reduction of oxygen on a pyrite surface. In high acid environments, the disulfide sites would be expected to be strongly protonated, as illustrated in Figure 6.12. Thus, the partially filled π^* orbitals of oxygen (lowest unoccupied molecular orbitals, LUMO) could accept an electron from the t_{2g} orbitals (highest occupied molecular orbitals, HOMO) (formally π-type orbitals; see Luther, 1987) of iron(II) in the lattice and create a hole which, in turn, may migrate to a disulfide site where sulfide is oxidised or to another iron site where water is oxidised. Direct electron exchange between the π^* orbitals of oxygen and the π^* orbitals of disulfide site is also possible but would be expected to be less favourable due to spin restrictions, *i.e.*, electron transfer from the diamagnetic disulfide group (fully spin-paired) to the paramagnetic (two unpaired electrons) oxygen molecule (see Moses *et al.*, 1987). In that sense, ferric ion would be the more reactive acceptor of an electron because there would be no loss of molecular orbital stabilisation energy (see Luther, 1987). However, it might be less likely for such a highly charged positive entity to approach a protonated surface compared to a neutral oxygen molecule. On the other hand, the water molecules surrounding a ferric ion may dampen the field (high dielectric) and facilitate electron transfer (diamagnetic molecules in hydration sphere) without a requirement of direct ferric ion adsorption onto disulfide sites (Figure 6.10; also see Moses *et al.*, 1987). An even more important factor may, however, be the high degree of ferric sulfate contact ion pair (CIP) formation at high temperature (Ch. 2), rendering ferric ion relatively ineffective as an oxidant.

The FEL concept (App. F.1) also applies here and suggests (qualitatively) that ferric ion, the perhydroxyl radical and peroxide may be most effective in generating the initial holes in the surface iron t_{2g} non-bonding orbitals. The e_g orbital of the iron is σ^* and oxygen has no vacant σ orbital of low energy. It can therefore be deduced that the first (catalytic) reduction step of

Stellenbosch University http://scholar.sun.ac.za

oxygen is either related to iron(II) t_{2g} surface states and/or is related to the attachment of a positive species, *e.g.*, a hydrogen ion, to the oxygen molecule, similar to its role in the first reduction step on a platinum surface (discussed above). Either way, the first reduction step may only become feasible at higher temperatures, where significant orbital overlap between the π orbitals of oxygen and the t_{2g} orbitals of iron(II) in the pyrite lattice is achieved. The disulfide entity could consume a newly generated hole (illustrated in Figure 6.10 & Figure 6.12; also see Luther, 1987), which would make the hole transfer route the preferred mechanism and reduce pyritic iron back to the iron(II) oxidation state. The hydroxyl radical would be thermodynamically and kinetically amenable to remove electrons from the π bonding orbital of the S_2 unit, *i.e.*, to break the diatomic unit to form sulfoxy compounds of higher oxidation states, *e.g.* the sulfate ion. This general picture also explains why anions, such as chloride, might inhibit pyrite oxidation (interfere with the electrocatalytic iron site), but not chalcopyrite oxidation (see previous discussions). Ion couples at lower redox potential, *e.g.*, the copper(II)/copper(I) couple and others (Sasaki *et al.*, 1995), would also not be expected to oxidise pyrite, as its conduction band consist predominantly of empty iron e_g^* orbitals with a relatively large gap (> 2 eV) compared to the sulfur 3*p* bonding orbitals.

Sphalerite oxidation

Most of the leaching testwork in this study utilised a disseminated chalcopyrite concentrate, with a minor (~7%) associated sphalerite fraction. This mineral represents an extreme case of a semiconductor (wide band gap) and is also the sulfide mineral with the lowest rest potential in this study. Cubic zinc sulfide is by far the most abundant zinc sulfide mineral (Farnsworth & Kline, 1973) and has a fundamental crystal structure (zinc blende) with zinc atoms at the corners and at the face centres. The optimised (pure) unit cell of the bulk material is presented in Figure 6.13.

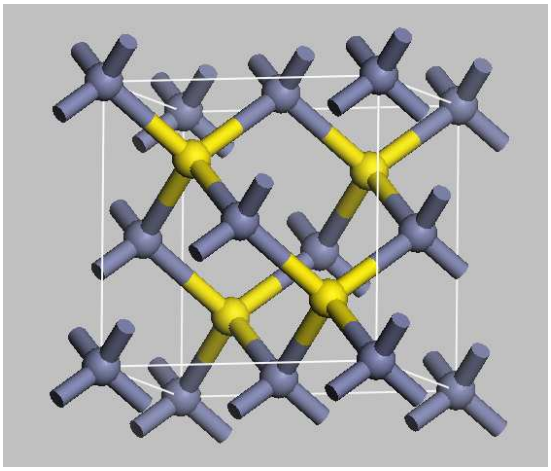

Figure 6.13
Optimised zinc blende unit cell (*MS*, 2008); Zn & S atoms are coloured blue & yellow, respectively (space group F 43m, with experimental lattice parameters: a = b = c = 5.4093Å at room temperature; Farnsworth & Kline, 1973).

Stellenbosch University http://scholar.sun.ac.za

The four sulfur atoms, within a unit cell, lie at the centre of a tetrahedron of zinc atoms, and each zinc atom at the centre of a regular sulfur tetrahedron (Crundwell, 1988a, b). Natural sphalerite adopts the zinc blende structure but contains a significant iron impurity, which would obviously affect the lattice parameters. The iron impurity could vary between 1 and 15% depending on the temperature of crystallisation during geological formation (see Farnsworth & Kline, 1973). Optical measurements have confirmed that zinc sulfide is a semiconductor with excess electrons and bonds that have both an ionic and a covalent character (Farnsworth & Kline, 1973). The band gap is in the range 3.6 to 3.9 eV, with the bottom of the conduction band derived from the zinc 4*s* orbital and the top of the valence band derived from the sulfur 3*p* orbital (Crundwell, 1988b). The electronic band structure of sphalerite and the relative positions of the (flat) bands' edges to the standard reduction potentials of some redox couples are (qualitatively) illustrated in Figure 6.14.

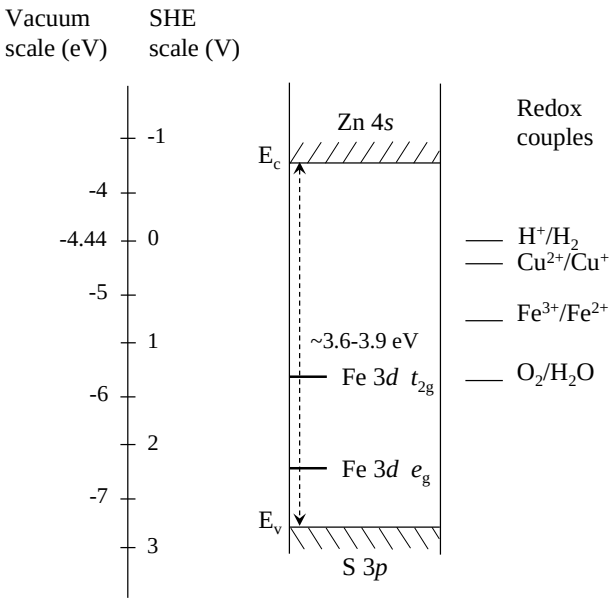

Figure 6.14
Qualitative semiconducting electronic band structure of sphalerite, with inclusion of the various standard reduction potentials of the important redox couples (adopted from Crundwell, 1988a).

The standard redox potential of the iron couple is situated approximately midway between the two bands' edges and, according to the FEL model, ferric ion would be expected to be an inefficient oxidant for sphalerite. However, the iron impurity in sphalerite has the effect of creating an impurity band within the band gap of zinc sulfide. This localised impurity band originates from the *d* orbital of iron and supplies holes for the conduction mechanism (Crundwell, 1988a, b). The transfer of electrons is therefore energetically more favourable, compared to the valence band and, since the iron *d* orbital is of bonding character, the removal of electrons from this band will result in the dissolution of the solid. In addition, a high density of mono-energetic surface states is created because of this impurity band, which has the effect of making the potential change across the space

Stellenbosch University http://scholar.sun.ac.za

charge layer independent of the solution electrochemical potential. A variation in solution potential only manifests in a potential change across the Helmholtz layer, *i.e.*, the interface assimilates metal-like behaviour. If the space-charge region is sufficiently narrow, quantum tunnelling will occur between the surface *d* orbital and the valence band. This will result in the oxidation of a sulfide atom in close proximity to form elemental sulfur and the release of zinc ion into solution (Crundwell, 1988a, b). It may therefore be assumed that ferric ion oxidises sphalerite directly and that the rate of this electron exchange reaction will also depend on the iron impurity levels in the solid structure. Both Crundwell (1988) and Palencia Perez and Dutrizac (1991) have illustrated that the rate of zinc dissolution is directly proportional to the iron impurity of the sphalerite phase in the absence of other electrically active impurities, while the activation energy was found by Palencia Perez and Dutrizac to decrease with an increase in the sphalerite iron content. The presence of the iron *d* orbital within the band gap (Figure 6.14) has therefore two consequences for charge transfer between the solid and solution, *i.e.*, it creates a narrow localised band that is energetically more favourable to exchange electrons with the ferric couple than the valence band, and it pins the Fermi level at the *d*-orbital band (after Crundwell, 1988b).

Although sphalerite may deviate from an intrinsic mechanism at high extraction due to the formation of surface layers (see, *e.g.*, Crundwell, 1987), the formation of metal-deficient polysulfide layers has also been proposed (Weisener *et al.*, 2003). The formation of copper sulfide films on sphalerite has also been suggested to have a decreasing effect on its oxidation rate in copper sulfate solutions (Kammel *et al.*, 1987).

Covellite and chalcocite oxidation

Although covellite constitutes a relatively minor phase of the concentrates used in this study, it was proposed by various authors to be formed as an intermediate phase during the oxidation of chalcopyrite (see above), copper mattes and chalcocite, especially at higher temperatures. The crystal structure is complex and the ionic model is $Cu^{2+}(Cu^{+})_2S^{2-}S_2^{2-}$, in which Cu^{2+} is in a triangular site and Cu^{+} is in a tetrahedral site (Crundwell, 1988b). This formal view of covellite has been challenged because it fails to explain the absence of copper(II) in Cu 2*p* photoelectron spectra of unoxidised material (Goh *et al.*, 2006). The calculated electronic structure suggests that the top of the partially filled valence band is predominantly Cu 3*d* in character and the conduction band is Cu 4*s* in character. Crundwell (1988b) pointed out that covellite is a *p*-type metallic conductor because the valence band is only partially filled. The upper valence band is mainly a crystal field band, similar to pyrite, and this may explain the relatively high potential required to dissolve covellite during cyclic voltammetry (Crundwell, 1988b).

Stellenbosch University http://scholar.sun.ac.za

The dissolution rate of natural and synthetic covellite is slower than that of chalcocite (Cu_2S) (Cheng & Lawson, 1989; Dutrizac & MacDonald, 1974), while the elemental sulfur yield is generally higher for chalcocite than for covellite (Cheng & Lawson, 1989), but of a more amorphous character on covellite in the pure sulfate system (Cheng & Lawson, 1991). Although the dissolution mechanism of chalcocite itself is not particularly important for this study, its gradual transformation through a series of copper-deficient phases to eventually form a covellite-like phase (Cheng & Lawson, 1991; Crundwell, 1988b; Elsherief *et al.*, 1995; Mao & Peters, 1983), is interesting. The rest potential of a thin-film synthetic chalcocite electrode increases progressively (& reversibly) during anodic polarisation, *i.e.*, as copper is removed in step-wise fashion. Crundwell (1988b) pointed out that this preferential extraction of copper is accompanied by the removal of electrons from the top of the valence band and, as a result, shifts the adsorption band to progressively higher values, *i.e.*, reflecting an increased band gap. The shift of the rest potential to progressively higher values was assumed to be due to the stronger bonding character of the electrons occupying the valence band. The fact that chalcocite leaches faster than covellite may be explained by the fact that the absolute leaching rate of synthetic covellite was found to be slower than that of covellite from chalcocite (Cheng & Lawson, 1989). The oxidation of the covellite intermediate phase, whether originating from synthetic or natural chalcocite, has been proposed to be a rate-determining factor in various studies (Ruiz *et al.*, 2007a). This rate-limiting intermediate has even been proposed during the pressure oxidation of white metal (Cu_2S produced during pyrometallurgical processing of copper concentrates) at high temperature in an autoclave (Ruiz *et al.*, 2007a). The increase of the oxidation rate with oxygen partial pressure and the low elemental sulfur yield (~10% at 110°C & ~1% at 150°C) suggest that oxygen is the main oxidising agent. This is in line with the results of Biegler *et al.* (1977), suggesting that oxygen is readily reduced on the covellite surface in acid solution, being only marginally less favourable as compared to pyrite surface. Covellite does therefore not resemble the behaviour of other binary sulfides. Cheng and Lawson (1991) have also proposed that the sulfur layer on covellite is amorphous. This proposal ties in with the suggestions of Peters (1984), ascribing the formation of amorphous sulfur under conditions of higher polarisation, *i.e.*, at forced rate, despite a 25% volume reduction of the sulfur as compared to covellite. Marsden *et al.* (2007a) reported that covellite formed predominantly sulfate, increasing to around 40% elemental sulfur yield at high acid addition, while Marsden *et al.* (2007d) reported that covellite reacted more slowly than chalcopyrite, pyrite and chalcocite.

The above mechanistic discussions have highlighted the fact that mineral oxidation rates depend heavily on the nature of the mineral surface and the properties of the mineral/solution interface. Before these intrinsic steps are captured within a mathematical framework, the inhibiting effect of molten elemental sulfur and the beneficial effect of surface active agents are briefly reviewed.

Stellenbosch University http://scholar.sun.ac.za

6.3.3 The elemental sulfur yield, its stifling role and the use of surfactants

Earlier discussions have highlighted the fact that the elemental sulfur yield varies between the different minerals. The highest yields (> 95%) are observed for minerals such as sphalerite (Chalkley *et al.*, 1993) and pyrrhotite, which are directly oxidised by iron(III), even under MT autoclave conditions. Similarly, if the acid concentration is high enough and dissolution takes place *via* a non-oxidative mechanism, the concomitant release of hydrogen sulfide would be expected to react with iron(III) to yield close to stoichiometric quantities of elemental sulfur (Verhulst, 1974).

However, the sulfur yield during chalcopyrite oxidation has been shown to vary considerably between different material sources and operating conditions, such as temperature and acid concentration (Sect. 6.3.1). Although the roles of temperature and acid concentration on the sulfur yield are discussed in detail in Sections 6.3.1 and 6.3.2, the chalcopyrite oxidation mechanism appears to affect sulfur stability at the interface. An extreme example is presented by pyrite mineral oxidation, which is associated with less elemental sulfur formation under MT oxidation conditions (see, *e.g.*, Marsden *et al.*, 2007a). Based on literature data (Papangelakis & Demopoulos, 1991), it may be assumed that no more than 25 to 30% of pyritic sulfide sulfur would be converted to elemental sulfur at 150°C at relatively dilute acid concentrations (< 25 g/L H_2SO_4).

Phenomenological mineral oxidation trends resulting from secondary sulfur passivation

From a phenomenological perspective, similar general kinetic trends have been observed for different mineral systems, even when oxidation is performed below the melting point of sulfur. Various authors have reported parabolic leaching kinetics during chalcopyrite oxidation at lower temperatures (*e.g.*, Dutrizac & MacDonald, 1974), which have been attributed to the diffusion of the oxidant, iron(III), through a constantly thickening porous product layer of elemental sulfur. Munoz *et al.* (1979) suggested that the rate-limiting process may be the transport of electrons through the elemental sulfur layer. Even during the atmospheric oxidation of sphalerite, Crundwell (1987) observed that diffusion of the oxidant through the product layer becomes the dominant mechanism during the latter stages of leaching. Hackl *et al.* (1995a) summarised the findings from earlier studies on chalcopyrite concentrate oxidation, conducted over a range of temperatures. At temperatures above the melting point of sulfur, wetting and agglomeration of the unreacted sulfide particles completely stifle the oxidation reactions. Such leaching kinetics are typically characterised by a rapid initial rate, followed by a sudden levelling off in copper dissolution over time (Hackl *et al.*, 1995b; Vizsolyi *et al.*, 1967). The results of Yu *et al.* (1972) are interesting in that only trace amounts of elemental sulfur were formed in the temperature range of 125 to 175°C, with an initial particle size of over 100 µm, using less than 6 g chalcopyrite concentrate per litre of solution and typically 0.25 mol/L H_2SO_4. Not surprisingly, the intrinsically controlled oxidation mechanism was

Stellenbosch University http://scholar.sun.ac.za

maintained up to high copper extractions, without the need to add any surfactants. The role of elemental sulfur is also clearly illustrated by the results of Bailey and Peters (1976). Sulfur interfered with the oxidation kinetics of pyrite above its melting point, even though the yield is known to be relatively low on this type of mineral. Similar trends were observed by Papangelakis and Demopoulos (1991) and Long and Dixon (2004) at even higher temperatures (140-180°C & 170-230°C, respectively), suggesting passivation of the pyrite surface by molten elemental sulfur. Although sulfur yield and morphology are also important factors when introducing the oxidant below sulfur melting point, its stifling effects would be less severe. For example, Lin *et al.* (1986) observed intrinsically controlled chalcopyrite and pyrite oxidation kinetics under various oxygen overpressures, up to high extractions (> 80%) below 100ºC.

The use and workings of surfactants under MT autoclave conditions

Besides the yield, the viscosity of molten sulfur varies considerably with temperature, especially above the transition temperature of 157°C (Figure 6.7), and also due to the presence of impurities, such as arsenic and selenium (Sect. 6.3.2). The operating range of a MT oxidation autoclave is generally limited to this transition temperature, since surfactants (more appropriate nomenclature: sulfur dispersing agents; see Tong, 2009) would not be expected to be effective in dispersing molten sulfur from mineral surfaces when the sulfur is highly viscous (due to a high degree of polymerisation). This explains the excessive prill and clinker formation observed at 170°C in a continuous pilot autoclave (Marsden *et al.*, 2007a). Surfactants were first introduced in commercial (zinc) pressure leaching to prevent occlusion of unleached sphalerite particles by liquid sulfur (Parker, 1981).

Surfactants adsorb strongly on solid surfaces, which reduces the attraction between sulfide and elemental sulfur and, thereby, inhibits sulfur coating and increases the mineral oxidation efficiency (Owusu, 1993). Owusu showed that lignosulfonate (LS) is adsorbed both physically and chemically by sphalerite. The AA-UBC process also utilises surfactants to expose unreacted chalcopyrite mineral surface (Dempsey & Dreisinger, 2003). Water-soluble LS (salts of lignosulfonic acid) are complicated polymers, produced in a chemical wood-pulping process (Owusu, 1993; Tong, 2009). Their structures and functional groups vary between different sources (Lu & Dreisinger, 2003). Since the surface-active portion of the molecule has a negative charge, it is classified as an anionic surfactant (Owusu, 1993). Owusu *et al.* (1992) have pointed out that the cation is unlikely to play a role in its behaviour because sulfonate groups lose their cations during dissolution. Xia *et al.* (1987) and Owusu (1993) reported that there is no difference between sodium and calcium LS, or the raw material type; as long as the amount of effective LS is the same, the effect would be the same. Dreisinger *et al.* (1990) and Owusu *et al.* (1992) reported that the introduction of LS lowers the interfacial tension (from 55 mN/m to as low as 20 mN/m) between the sulfur and aqueous

Stellenbosch University http://scholar.sun.ac.za

solution, *i.e.*, it promotes the dispersion of sulfur. LS also adsorbs onto the sulfide mineral surface and increases the sulfur/mineral contact angle (from 80° to as high as 155°), making it relatively less sulfophilic and more hydrophilic. The sulfur is consequently easier to disperse from the mineral surface in the presence of this surfactant, allowing leaching to proceed, *i.e.*, it significantly reduces the work of adhesion (Owusu 1993; Owusu & Dreisinger, 1996). The work of adhesion is the reversible work required to separate a unit area of liquid sulfur from a mineral surface, which implies that less agitation energy would be required to remove liquid sulfur from unreacted mineral surface in the presence of surfactants, than for a system without surfactants. This approach has been commercially applied by Sherritt Gordon Mines Ltd. in their two-stage pressure leach process for zinc concentrates (Veltman *et al.*, 1977), *e.g.*, at Hudson Bay Mining and Smelting (HBMS) Company (Ozberk *et al.*, 1995).

Quebracho (QB) is a natural wood extract, rich in tannins. Similar to LS, its structure and composition are complicated, varying between different types of wood (Lu & Dreisinger, 2003). Dreisinger *et al.* (2002) found that the LS and Quebracho (QB), in combination, promotes the kinetics of copper extraction from chalcopyrite under AA-UBC leach conditions. This combination also yielded the best results during continuous chalcopyrite oxidation (Marsden *et al.*, 2007b). LS is more effective in decreasing the sulfur/aqueous solution interfacial tension, while QB is more effective in increasing the sulfur/chalcopyrite contact angle, *i.e.*, in lowering the sulfur/chalcopyrite contact area (Lu & Dreisinger, 2003). Again, the combination of LS and QB results in a more significant decrease in the work of adhesion and therefore chalcopyrite can be more effectively oxidised (Owusu & Dreisinger, 1996).

Lu and Dreisinger (2003) also determined, using an infrared measuring technique, that both LS and QB adsorb onto the chalcopyrite surface. Doyle *et al.* (1989) pointed out that typical surfactants have a large number of polar groups and their strong adsorption at high concentrations may also decrease the surface area available for charge transfer, resulting in slower mineral oxidation rates. A large amount of QB has been found to hinder mineral oxidation (Huang & Bernal, 1984).

Doyle *et al.* (1989) and Owusu *et al.* (1995) postulated that if surfactants were oxidised during leaching they would be expected to act similarly, since the degradation products would also be strongly polar. However, the results of Dreisinger *et al.* (1990) suggest that surfactants degrade upon heating in an autoclave during zinc sulfide pressure leaching, resulting in a predominantly diffusion-controlled mechanism during the latter stages of oxidation (also see Owusu & Dreisinger, 1996). Hackl *et al.* (1995a) found that surfactants decompose even faster in copper pressure leaching, compared to zinc pressure leaching, suggesting that surfactant decomposition may be copper catalysed, a viewpoint shared by Peters (1992). Owusu *et al.* (1995) (sphalerite pressure

Stellenbosch University http://scholar.sun.ac.za

oxidation) and Hackl *et al.* (1995b) (chalcopyrite pressure oxidation) found that globules of sulfur, entrained with unreacted sulfide particles, are formed in the absence of any surfactant.

Surfactants used in this study

The initial experimental program (Sect. 6.4) used calcium LS (Norlig A, 58%) and QB (Orfom grade 2 Tannin), both obtained from Hudson Bay Mining and Smelting (HBMS) Co. Ltd. The follow-up experimental programme (Ch. 7) used ammonium LS liquid (Arbo A02, ~50%), obtained from Tembec Inc. in Quebec, Canada, while the Orfom grade 2 Tannin directly obtained from Chevron Philips Chemical Company LP (North America), contained 85 to 95% sulfited QB and 5 to 15% water. A different calcium LS (Borrepal U) from Lignotech USA Inc. was utilised under higher pulp density conditions (Ch. 8).

The above review emphasises the secondary effects of elemental sulfur and surfactants on the charge transfer reactions at the mineral/solution interface. It is clear from the various citations reviewed by Hiskey (1993), Hackl *et al.* (1995a) and Lázaro and Nicol (2003) that the formation of dense coatings of elemental sulfur often interferes with measurement when studying the fundamentals of mineral dissolution kinetics. In this context, the effects exerted by an impervious or semi-impervious sulfur product layer should not be confused with the fundamental oxidation mechanisms; these intrinsic mechanisms are phenomenologically described in the next section.

6.3.4 Simplified descriptions of the intrinsic oxidation rates of the primary sulfide minerals encountered in this study, based on preliminary quantum-level modelling results

The above detailed review highlights the complex nature of sulfide mineral oxidation and presents a suite of intrinsic rate-limiting steps for each mineral. As demanded by a phenomenological rate model, the simplest conceptualised pathways are now tabled, based on preliminary quantum-level calculations of the surface structures and species adsorption energies.

Electrochemical reaction framework

The electrochemical nature of sulfide mineral oxidation is emphasised above, even though some of the side-reactions may involve direct chemical interactions, *i.e.*, no transfer of charge between separate reaction sites. No chemical interactions are therefore assumed to be rate limiting.

The electrochemical potential of the reacting surface determines the leaching rate. The anodic oxidation rate of the mineral and the cathodic reduction rate of the oxidant govern the mineral surface potential at a specific reaction site. The driving force behind the intrinsic rates of these processes has its roots in the realm of quantum physics and varies between different minerals, crystal planes, oxidants and temperatures. These intrinsic rates are determined by activation energy

Stellenbosch University http://scholar.sun.ac.za

barriers and report to the conducting surface as (activation) polarisation, *i.e.*, they manifest as a potential energy barrier (resistance) to the charge transfer reaction. The resistance to the cathodic reduction of the oxidant may, for example, be due to a CIP (Ch. 2) adjusting its coordination shell of ligand ions or the cation adjusting its hydration shell of water molecules. Polarisation means that the surface departs from its rest potential. The rest potential is the actual potential measured when no current is produced, *i.e.*, no leaching occurs. It is different from the thermodynamic equilibrium potential, which is only indicative of the tendency of a reaction to occur in a particular direction. The thermodynamic equilibrium potential is a theoretical quantity, whilst the rest potential is a measured equilibrium potential (or extrapolated from measured potential-current density data).

The kinetics of the cathodic half-cell reaction(s) can be related to the kinetics of the anodic dissolution reaction by virtue of no charge accumulation (see, *e.g.*, Holmes & Crundwell, 2000). In order to derive the phenomenological leaching model, it is assumed that there are no mass transfer limitations, *i.e.*, no concentration polarisation. It is also assumed that there is no ohmic resistance due to, for example, the formation of non-conducting surface layers on the mineral surface or due to the limiting conduction of electrons within the semiconductor itself. The theory leading to the activation polarisation relationship, *i.e.*, the relationship between the potential difference ($\Delta\phi$) and current density (j), is summarised in Appendix F.2 (Butler-Volmer equation). The net current density of the anodic (j_A) and cathodic (j_C) reactions may be represented as follows, respectively:

$$j_A = |z_{rx}|F \cdot k_a m_{red} \cdot exp\left(\frac{\beta_A |z| F\Delta\phi}{R_g T}\right) - |z_{rx}|F \cdot k_c m_{ox} \cdot exp\left(\frac{-(1-\beta_A)|z|F\Delta\phi}{R_g T}\right) \qquad 6.104$$

$$j_C = |z_{rx}|F \cdot k_a m_{red} \cdot exp\left(\frac{\beta_C |z| F\Delta\phi}{R_g T}\right) - |z_{rx}|F \cdot k_c m_{ox} \cdot exp\left(\frac{-(1-\beta_C)|z|F\Delta\phi}{R_g T}\right) \qquad 6.105$$

The subscripts ‘a’ and ‘c’ refer to the anodic and cathodic directions, respectively. The rate constant, k, consists of various coefficients (App. F.4) and adopts the units of kg/m^2.min when using the molality scale to describe the species concentration at the solution side of the solid/liquid interface. The previous sections propose that charge transfer across the double layer would probably occur in single-electron transfer steps; hence, $|z|$ adopts unity value, while $|z_{rx}|$ takes the overall stoichiometry of the charge transfer reaction into account. The symbols β_A and β_C refer to the transfer coefficients of the net anodic and cathodic processes, respectively, and it is usually assumed that $\beta_A = \beta_C = \beta$. It lies between zero and one, and is often found (experimentally) to be about half (½) (Atkins & De Paula, 2006; Bockris & Reddy, 1970).

Since the batch autoclave oxidation results (Sect. 6.5) cannot be used to deduce the mechanism of mineral oxidation, a simplified approach is required, *i.e.*, to prevent over-parameterisation of the

Stellenbosch University http://scholar.sun.ac.za

phenomenological rate model. Quantum-level calculations are employed to generate a qualitative picture of the most likely mechanistic scenarios, which, in turn, are used to derive the intrinsic oxidation rate expressions.

Methodology used to calculate the surface structures and free energies of adsorption

A density functional theory (DFT) plane-wave pseudopotential method, *Cambridge Serial Total Energy Package* (CASTEP) (*MS*, 2008) was used to perform the quantum-level calculations of the surface structures and species adsorption energies. DFT is a computationally fast and efficient first-principles approach, where electron-correlation effects are taken into account, making it the ideal methodology for more demanding systems, such as the mineral surfaces encountered in this study (also see Sect. 2.3.2). The gradient-corrected (gradient generalised approximation, GGA) local density approximation (LDA) method was employed, as developed by Pedrew and Wang (1992) (PW), with application of the pseudopotential concept. CASTEP is based on a supercell method, wherein all studies must be performed on a periodic system, even when the periodicity is superficial. Thus, for example, a crystal surface must be represented by a finite-length slab. The system is considered to be surrounded on all sides by replicas of itself, forming an infinite macro-lattice. The surface slab must be thick enough to represent a real material (both bulk & surface atoms), and the vacuum must be large enough to prevent the slabs from interacting with each other. In order to reduce the plane-wave cut-off value, the Lin *et al.* (1993) optimization method was used to generate norm-conserving pseudopotentials in the Kleinman-Bylander representation. The Monkhorst-Pack scheme was used to perform the sampling of the Brillouin zone and the LDA exchange-correlation energy was represented by the Ceperley-Alder formula. The self-consistent ground state of the systems was determined by minimizing (conjugate gradient) the total energy with respect to the plane wave coefficients of the occupied orbitals (after Burger, 2009).

In order to minimise the (potential) error in the predicted total energy of the system, due to the truncation of the basis set at a finite energy, the cut-off energies were investigated. The cut-off energies were systematically increased until the energy converged. This step was followed by the optimisation of the bulk crystals, using the optimal cut-off energies calculated in the previous step (GGA-PW91; Perdew 1991). The optimized crystal structures were then cleaved in the most probable facets (Bayliss, 1977; Kratz & Fuess, 1989; Rabadanov *et al.*, 1997), *i.e.*, (110) for chalcopyrite (*Cpy*), (100) for pyrite (*Py*), (100) for sphalerite (*Sph*) and (100) for sulfur (S_8), followed by building of the vacuum slab. The structure of the relaxed surface was then determined by performing geometry optimisations on the periodic systems. The preferred adsorption sites of specific species onto the mineral surfaces were probed by docking the species at different locations on the surface and calculating a set on interaction energies. The highest adsorption energy was taken as the preferred site (after Burger, 2009).

Stellenbosch University http://scholar.sun.ac.za

Determining the binding energies

The binding energies were calculated by first optimising the bulk and then the surface structures (discussed above). The aqueous species were then moved (by automated increments) parallel to the mineral surface, in a two-dimensional space, to find the lowest potential energy region. The species was then moved away (by automated increments) from the mineral surface in a perpendicular direction, *i.e.*, exactly above the energetically preferred adsorption site, to find the region where no increase in energy was calculated. This position represented the sum of the individual energies of the surface structure ($|_{lat}$) and the aqueous species (X), *i.e.*, the total energy of the system before adsorption ($|_{lat} + X$). The aqueous species was then moved slightly closer to the surface to initiate the optimisation sequence. The final optimised geometric structure represented the minimum energy of the interactive system ($|_{lat}–X$), *i.e.*, the most likely adsorbed surface state of the aqueous species. The binding energy was calculated as the difference in the optimised total energy of the system, *i.e.*, before and after adsorption (see footnotes below). In the case of diatomic oxygen, this sequence was repeated using different molecular orientations at the point of initiation. Identical final orientation and calculated potential energy values signified the optimised surface structure. Direct comparison of the gas-phase binding energies of neutral diatomic oxygen on different mineral facets is justified because this molecule remains largely unhydrated. These results are summarised in Table 6.3.

Table 6.3
Binding energies of aqueous reactant species at selected (most probable) sulfide mineral facets (after Burger 2009).

Mineral	Surface	[a] H^+ (S) (eV)	[a] Fe^{3+} (S) (eV)	[a] O_2 (eV)
FeS_2	(100)	-1.884 (-1.901)[b]	-1.283	-6.041
$CuFeS_2$	(110)	-4.264 (-4.311)[b]	-5.880	-2.4555
ZnS	(100)	[c] -3.883	–	-0.4525
S_8	(100)	-1.975	–	–

[a] Binding energy of aqueous species, X, defined as the energy difference of the reaction: $|_{lat} + X \Leftrightarrow |_{lat}–X$ in vacuum & 25°C, using a pseudopotential method, CASTEP (*MS*, 2008); [b] Values in brackets generated by Dmol^3 method (*MS*, 2008; Sect. 2.3.2); [c] Refers to the ZnS (110) surface.

The high interaction energies between the surfaces and aqueous species are indicative of distinct covalent characteristics (chemisorption). Obviously, consideration of the solvated ions (COSMO methodology; Sect. 2.3.2) would have generated a superior picture of the adsorption process. However, the increase in computational effort and the qualitative nature of comparing the different binding energies did not warrant such an exercise. It also has to be realised that these adsorption characteristics would vary between different facets and only the facets of highest surface area were

Stellenbosch University http://scholar.sun.ac.za

considered here, *i.e.*, as suggested by Bayliss (1977), Kratz and Fuess (1989), and Rabadanov *et al.* (1997) for pyrite, chalcopyrite and sphalerite, respectively.

Pyrite

Figure 6.15 *a* represents the system with no interaction between the surface and proton species, *i.e.*, similar total energy values, independent of the spatial orientation of the protons (anywhere further from the surface). Figure 6.15 *b*, *c* and *d* represent the optimised geometry of the system after proton, ferric and oxygen species adsorption, respectively. It is clear that only the proton and ferric ions compete for the same surface sites (sulfide atoms), while oxygen preferentially interacts with two bonds (two-fold adsorption) on a single iron substrate atom (Griffiths model; Shi *et al.*, 2006).

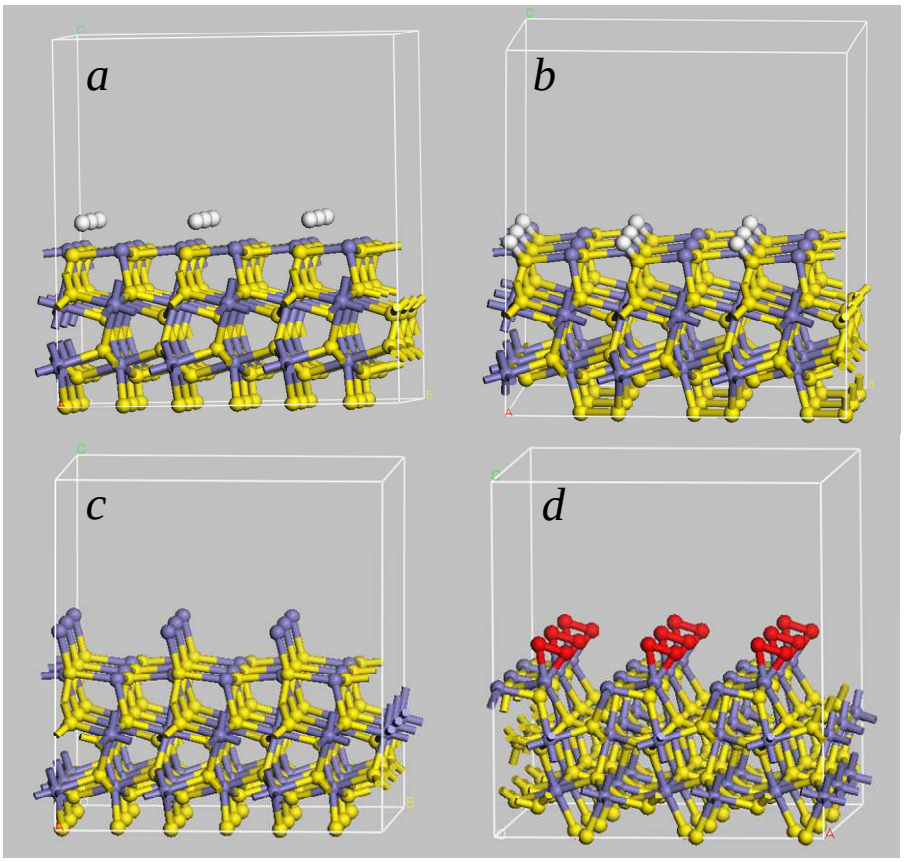

Figure 6.15
Optimised pyrite surface (100) structures (*MS*, 2008; after Burger, 2009); Fe & S atoms are coloured purple & yellow, respectively: *a*) H^+ ions before adsorption (grey colour indicates protons); *b*) After H^+ adsorption; *c*) After Fe^{3+} adsorption; *d*) After O_2 adsorption (red colour indicates diatomic oxygen).

Figure 6.10 illustrates direct oxidation scenarios that may be expected at lower temperature and mixed potential conditions, *i.e.*, without oxygen and, hence, little oxidation beyond the elemental state of sulfur. However, the surface is severely distorted after oxygen adsorption (Figure 6.15 *d*), which could make the ferric ion approach more unfavourable; the positively charged iron substrate

Stellenbosch University http://scholar.sun.ac.za

sites create narrow 'valleys', forming an electrostatic barrier to the approaching aqueous ferric species. Also, the typically low elemental sulfur yield of pyrite (< 25%; Sect. 6.3.1) is not indicative of an exclusive one-electron ferric reduction mechanism.

The simplest explanation of the preferential reaction of oxygen with the pyrite surface is that the first reduction step (Rx. 6.66) is catalysed by the non-bonding t_{2g} orbital of iron in the surface lattice (Sect. 6.3.2). The diatomic molecule may approach the surface without electrostatic interference and may therefore become the primary oxidant at higher oxidation temperatures. The electronic band structure of pyrite (Figure 6.9) also reflects a relatively narrow band gap; the thermal energy of the system may overcome this gap and the first oxygen reduction step (Rx. 6.66; E_h = 0.12 V) may be ideally placed (thermodynamically) to exchange an electron with the conduction band of pyrite. The overall rate of this hole creation mechanism may be kinetically comparable with ferric ion, especially since the iron(III) concentration would be buffered by its precipitation at higher temperatures. As a first estimate, it is therefore assumed that the reduction of oxygen on iron substrate sites are the predominant mechanism of hole generation at high temperature in an autoclave. Once a hole has formed, it may migrate to another (iron) surface site where water is adsorbed onto the surface (Sect. 6.3.2). This may result in the oxidation of water; the anodic and cathodic reactions may then be represented as follows, *i.e.*, the net reactions, in excess of any reverse exchanges (Rx. 6.72) or reactions with other species (Table 6.2) (* refers to the adsorbed species):

$$H_2O^* + h^+ \Rightarrow H^+ + OH\cdot^* \qquad 6.106$$

$$O_2^* + H^+ \Rightarrow HO_2\cdot^* + h^+ \qquad 6.107$$

Reaction 6.106 may be viewed as a transition state (Figure 6.11 *a*, *b*). Higher proton concentrations would reduce the kinetics of the net water oxidation reaction. The role of the hydrogen ion in this first oxygen reduction step is assumed to be similar to its role during the analogous reaction on a platinum surface, *i.e.*, the hydrogen ion facilitates the first charge transfer step because of the ability of its electrical field to enhance the electron-attracting capability of the surface-coordinated oxygen molecule (Sect. 6.3.2). In the same vein, aqueous ferric ion, coordinated with the adsorbed diatomic oxygen molecule, may also facilitate this charge transfer step. This proposal is revisited later in this study (Ch. 7; Sect. 7.4.2).

Either way, depending on the catalytic properties of the surface, the perhydroxyl radical may exchange electrons with other t_{2g} orbitals *via* the peroxide path (Rx. 6.66-6.69) or, *e.g.*, *via* the associative path of Norskov *et al.* (2004) (Rx. 6.78-6.81). These holes may migrate and oxidise water at anodic sites, gradually building a surface consisting of predominantly $Fe(OH)S_2$. The

Stellenbosch University http://scholar.sun.ac.za

mechanism by which pyrite may stabilise such species, is currently unknown. At lower temperature and potential these reactions may be reversible, as illustrated by the cyclic voltammetry results of Biegler and Swift (1979b) and Mishra and Osseo-Asare (1988). No removal of electrons from the bonding orbitals in the pyrite lattice has been considered up to this point, *i.e.*, no oxidation of sulfide in the pyrite structure has occurred. This oxidative pyrite surface may, however, readily exchange electrons with less noble (more reactive) minerals or (pyrite) surfaces; such possible phenomena are elaborated upon later in this section and are schematically illustrated in Figure 6.16.

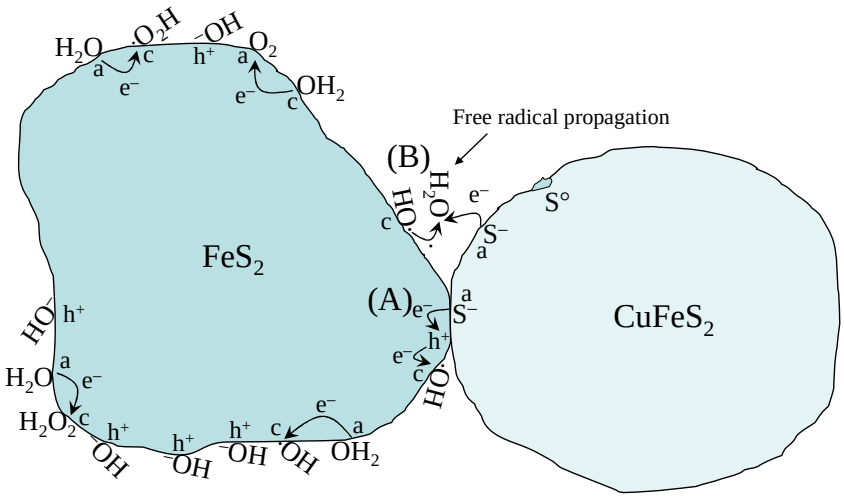

Figure 6.16
Schematic diagram of electron exchange between cathodic (c) & anodic (a) substrate sites on pyrite surface, as well as anodic reaction sites on an adjacent chalcopyrite surface.

Anodic and cathodic processes are usually depicted as local short-circuited electrochemical cells (especially in corrosion theory), where the reactions take place on spatially separate surface sites (Atkins, 1986). Even in leaching, electrochemical reactions are assumed to be spatially separate (Habashi, 1967). An anodic site on chalcopyrite (Figure 6.16) would exchange an electron with a cathodic site of highest electrochemical potential in close proximity, which is here represented by the (physical) galvanic interaction with pyrite (A). Alternatively, a surface radical species on pyrite surface, *e.g.*, surface hydroxyl species, may self-propagate *via* water to an anodic site on the chalcopyrite surface, without any physical contact between the two minerals (B). If peroxide is an intermediate species, it may be considered to be the kinetically rate-limiting step with the highest activation energy, *i.e.*, Equation 6.68 (Anderson & Albu, 1999). However, without more information to support this, the pyrite surface is assumed to lower the activation energy barrier of this step, compared to the first reduction step of oxygen. If all the non-reversible exchanges, *e.g.*, sulfide oxidation, are neglected for now, Equation 6.107 may be assumed to represent the rate-limiting cathodic reaction on pyrite surfaces. In order to satisfy the requirement of electrical neutrality, the sum of all the anodic currents must equal the sum of all the cathodic currents:

Stellenbosch University http://scholar.sun.ac.za

$$\sum a_A j_A = -\sum a_C j_C \qquad 6.108$$

The terms a_A and a_C represent the anodic and cathodic surface areas, respectively. Because both anodic and cathodic reactions are restricted to iron substrate sites, the overall stoichiometry of oxygen reduction (Rx. 6.64) results in the following current density relationship:

$$j_A = -j_C \qquad 6.109$$

The current density contribution, due to sulfide oxidation, is separately dealt with below. If it is assumed that these iron substrate sites adopt an average potential value (E_m, *i.e.*, with respect to a reference system), the MP theory is applicable (Nicol *et al.*, 1975), which validates the condition of zero net production of electrons. The anodic and cathodic current densities are easily obtained from Equations 6.104 and 6.105, respectively, assuming unit water activity, *i.e.*, assuming an insignificant impact of water activity changes to its oxidation rate (for convenience, the square bracket notation for molality is adopted here):

$$j_A = Fk_a[H^+]^{m_1} \cdot exp\frac{\beta_A FE}{R_g T} \qquad 6.110$$

$$j_C = -4Fk_c[H^+]^{n_1}[O_2] \cdot exp\frac{-(1-\beta_C)FE}{R_g T} \qquad 6.111$$

Due to its high electron affinity (discussed below), the reaction order with respect to the hydrogen ion concentration is likely negative ($m_1 < 0$) for the anodic reaction but positive ($n_1 > 0$) for the cathodic reaction (see Holmes & Crundwell, 2000). Assuming $\beta_A = \beta_C = \beta_1$ (see, *e.g.*, Hiskey & Wadsworth, 1981) and applying Equation 6.109, results in the following relationship:

$$\frac{\beta FE_m}{R_g T} = ln(k[H^+]^{(n_1-m_1)}[O_2])^{\beta_1} \qquad 6.112$$

where the anodic and cathodic reaction constants are lumped together in k. The exchange current density (j_o) is the current at the mixed potential, *i.e.*, where the net anodic and cathodic current densities are equal (see Figure 6.22). Higher oxygen concentration (increased oxygen partial pressure) would result in higher mixed potential, provided no concentration polarisation is prevalent. This, in turn, would result in a higher exchange current density and, hence, increased oxidation of water on the pyrite surface, *i.e.*, increased formation of surface oxide species, notated as $Fe(OH)S_2$. The relationship between the exchange current density and the intrinsic oxidation rate ($mol/m^2.min$) is expressed by Faraday's equation (Holmes & Crundwell, 2000):

$$r = \frac{j_o}{|z_{rx}|F} \qquad 6.113$$

Stellenbosch University http://scholar.sun.ac.za

Substitution of Equations 6.112 and 6.113 into Equation 6.110, leads to an expression for the intrinsic formation rate of oxidative pyrite surface, $r_{Fe(OH)S2}$:

$$r_{Fe(OH)S_2} = k_1 [H^+]^{m_1(1-\beta_1)+n_1\beta_1} [O_2]^{\beta_1} \qquad 6.114$$

The overall formation rate of oxidative surface (per kg H_2O), $R_{Fe(OH)S2}$, is simply related to the intrinsic rate, as follows:

$$R_{Fe(OH)S_2} = k^{\sim} \cdot [Fe(OH)S_2] = a_{Fe(OH)S_2} \cdot k_1 [H^+]^{m_1(1-\beta_1)+n_1\beta_1} [O_2]^{\beta_1} \qquad 6.115$$

The proportionality constant, $k^{\sim}$ (1/min), and the intrinsic rate constant are then combined to give an expression of the molality (mol/kg) of surface-oxide species:

$$[Fe(OH)S_2] = a_{Fe(OH)S_2} \cdot k_{Fe(OH)S_2} [H^+]^{m_1(1-\beta_1)+n_i\beta_1} [O_2]^{\beta_1} \qquad 6.116$$

where $k_{Fe(OH)S2}$ adopts the units of $kg^{m1(1-\beta1)+\beta1(n1+1)}.mol^{1-m1(1-\beta1)-\beta1(n1+1)}/m^2$ and $a_{Fe(OH)S2}$ refers to the surface area of stabilised radical oxide species in units of m^2/kg.

Under specific surface conditions, especially at higher temperature, stabilised radical oxide species may receive electrons from nearby sulfide species, *i.e.*, pyritic sulfide may start to oxidise rapidly. This scheme is discussed in Section 6.3.2 and illustrated in Figure 6.11 (*a-c*).

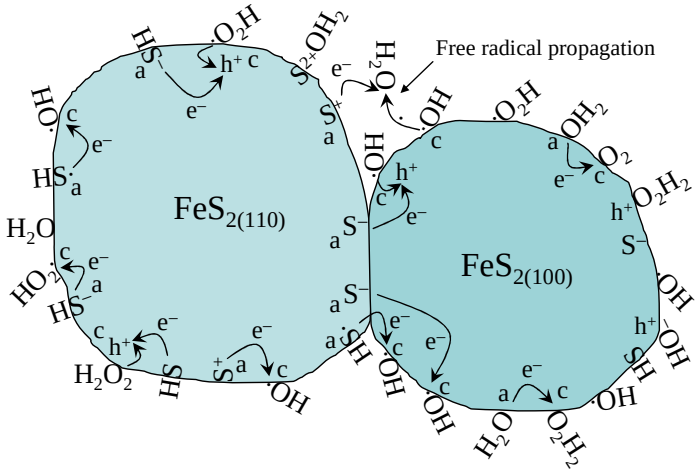

Figure 6.17
Schematic diagram of electron exchange between anodic (a) sulfur & cathodic (c) iron substrate sites on the pyrite surface (this includes interactions with less noble sites).

Figure 6.17 illustrates the scenario where two different pyrite faces are in close proximity, with one face (100) preferentially oxidising water, while the other (110) preferentially undergoes sulfide oxidation. Holes may therefore also be injected into the bonding orbitals of the (110) face by the more stable (to sulfide oxidation) (100) face *via* a range of possible mechanisms. As mentioned before, it is assumed (as a first estimate) that the role of ferric ion, although very efficient in

Stellenbosch University http://scholar.sun.ac.za

accepting electrons, is less important at high temperature in oxygenated systems, due to the predominance of adsorbed oxygen on the pyrite surface (Table 6.3), resulting in high surface potential and distorted surfaces (Figure 6.15 *d*). The solubility of iron(III) species is also relatively low at high temperatures (Ch. 5), while it would be heavily complexed as CIPs (Sect. 2.4.3), reducing its effectiveness as an oxidant. At lower oxidation temperatures, ferric ion would be more amenable to accept electrons from anodic sulfide sites and it would be expected to be the dominant oxidant, especially since the rate of oxygen reduction would start to diminish under those conditions (see Holmes & Crundwell, 2000). Depending on the surface under consideration, electron exchange may occur *via* the exchange of holes between the non-bonding t_{2g} orbitals of iron and nearby sulfide sites. In other cases, electrons may be directly transferred to the oxidant species on a nearby cathodic site; both these cases are illustrated in Figure 6.12 *b* (for perhydroxyl reduction) and also in Figure 6.12 *e* (peroxide reduction). Alternatively, the oxidant may physically migrate to an anodic sulfide site or the radical species may propagate (*via* water) to anodic dissolution sites. The non-oxidative scenario, depicted in Figure 6.11 (*d-f*), would become more favourable under very high proton concentrations and lower concentrations of oxidative surface species, *i.e.*, lower potential across the double layer. This non-oxidative mechanism would therefore not be expected to dominate at high temperatures in oxygenated systems on a pyrite surface, which has been shown to be highly catalytic towards oxygen reduction. The anodic oxidation of sulfide in a pyrite structure may then be generalised as follows:

$$S_2^{2-}|_{lat} + 8yH_2O \Rightarrow 2ySO_4^{2-} + 2(1-y)S^o + 16yH^+ + (12y+2)e^- \qquad 6.117$$

As highlighted before (Sect. 6.3.2), there are various possible dissolution mechanisms. For the sake of simplicity, the transfer of the first electron is assumed to be rate limiting, *i.e.*:

$$S_2^{2-}|_{Py} + H^+ + h^+ \Rightarrow S + HS^{\cdot *} \qquad 6.118$$

The role of the proton is not clear but may be associated with stabilising the S–HS· species, before its subsequent oxidation to form diatomic or elongated sulfur (S_x), polysulfides or higher oxidation products, *i.e.*, the value of *y* in Equation 6.117. Some of these mechanisms are discussed in Section 6.3.2 and, although increased hydrogen ion concentrations could facilitate the formation of polysulfides or polymeric sulfur on pyrite surfaces, such surfaces are assumed to be secondary, *i.e.*, time-dependent, phenomena. Figure 6.11 (*a-c*) attempts to represent the water-split mechanism as an equilibrium reaction, which could be impeded by the electro-affinity of the proton and, hence, also an increase in its concentration close to surface adsorbed water. At lower hydrogen ion concentrations, water oxidation would occur more readily, producing hydroxyl species which may, in turn, oxidise sulfide, either *via* an electron-jump mechanism, directly after migrating to a suitable anodic site, or *via* self-propagation of the radical species (Figure 6.17). In the case of oxygen reduction on a pyrite surface (Figure 6.12), the role of the proton is reversed and it may

Stellenbosch University http://scholar.sun.ac.za

play a facilitating role in the first reduction step of oxygen, which is assumed to be the rate-limiting step of the cathodic reaction (Rx. 6.107). Subsequent reduction steps can occur *via* many different mechanisms, which may include self-propagation of radicals, electron tunnelling, migration to sulfide sites, hole transfer, *etc.* No additional commentary regarding these mechanism(s) of pyrite oxidation is possible at this stage, which requires detailed quantum-level simulation. The simplest mathematical description of the pyrite oxidation rate is therefore to separate the anodic oxidation of sulfide by an oxidant at close proximity and anodic sulfide oxidation by reactive oxides on a more stable pyrite surface. The rate of oxidative surface formation (water splitting) is assumed to occur predominantly on surfaces with more exposed iron sites, *e.g.*, the pyrite (100) surface, while surfaces with higher sulfide exposure, *e.g.*, the pyrite (110) surface (Figure 6.18), may be more amenable to proton adsorption and subsequent oxidation to higher sulfur oxidation states. This is in line with the quantum-level calculations of Qiu *et al.* (2004). Despite the fact that the pyrite (100) surface has a small band gap and exhibits some metallic character, they found such surfaces to be more stable. It is therefore assumed that water and oxygen preferentially interact with iron mediator sites on the pyrite (100) surface, without necessarily resulting in rapid sulfide oxidation.

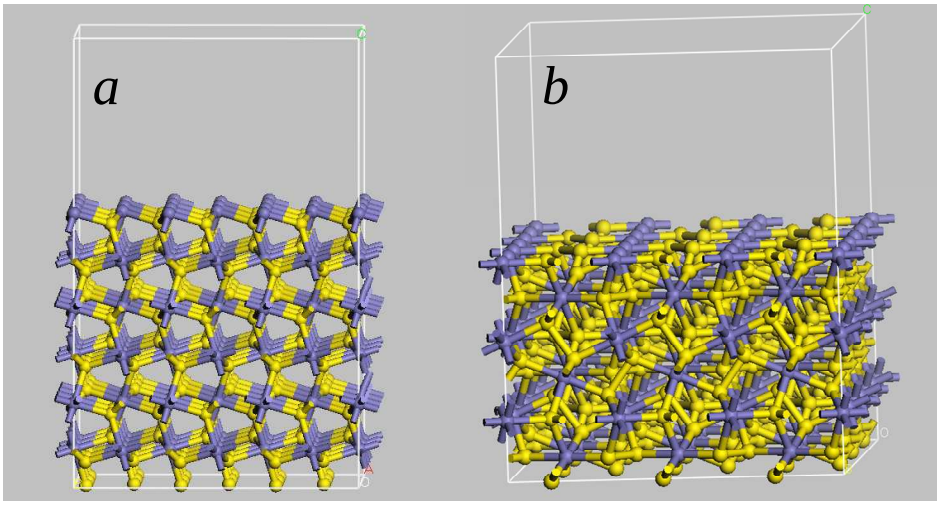

Figure 6.18
Optimised pyrite surface structures (*MS*, 2008; after Burger, 2009); Fe & S atoms are coloured purple & yellow, respectively: *a*) (100) surface; *b*) (110) surface.

It is also assumed that the sulfide atoms, undergoing oxidation, would experience different mixed potentials, depending on whether the cathodic reduction reactions occur on the same surface or on a more stable pyrite surface. This approach allows a linear combination of the two primary dissolution routes contributing to the overall anodic current density. The rate-limiting cathodic reaction is represented by Reaction 6.107, while the subsequent oxidative species is assumed to directly inject holes into the sulfur 3*p* valence-band (bonding) orbitals, *i.e.*, due to their relative position on the electronic band structure diagram (Figure 6.9). All subsequent oxidation reactions are assumed not to be rate limiting. The anodic dissolution reaction is not expected to be reversible,

Stellenbosch University http://scholar.sun.ac.za

as the original pyrite structure is unlikely to re-assemble once the HS· radical species has been formed, *i.e.*, after the first sulfide bond has been broken. The cathodic reduction reaction is analogous to Equation 6.111, so that:

$$j_{A_2} = (12y+2)Fk_{a_2} \cdot exp\frac{\beta_{A_2} FE}{R_g T} \qquad 6.119$$

$$j_{C_2} = -4Fk_{c_2}[H^+]^{n_2}[O_2] \cdot exp\frac{-(1-\beta_{C_2})FE}{R_g T} \qquad 6.120$$

The resulting mixed potential term is, again, explicitly substituted into Equation 6.119 in order to obtain the exchange current density term for the anodic dissolution of pyrite, *i.e.*, due to oxygen reduction on a nearby site, irrespective of the charge transfer mechanism:

$$j_{o_2} = (12y+2)Fk_2[H^+]^{n_2\beta_2}[O_2]^{\beta_2} \qquad 6.121$$

The reaction order, with respect to the proton (n_2), is expected to be positive due to its accelerating effect on the first oxygen reduction reaction. For the sake of simplicity, due to the restrictions associated with iron(III) sulfate CIP formation and due to the rapid oxygen reduction rate on a pyrite surface under higher operating temperatures, the dissolution current *via* iron(III) reduction is neglected in these expressions. Even if such oxidation mechanisms are prevalent at high temperatures in oxygenated systems, the highly oxidative pyrite surface would be expected to re-oxidise the resulting iron(II) species before reaching the bulk solution and the net electron balance would be unaffected. However, these rate expressions neglect the possible role of iron(III) during the first oxygen charge transfer step, as well as the negative effect that increased hydrogen ion concentration could have on the anodic dissolution rate when involving the water-split mechanism (see above) or the subsequent reduction of oxygen after the first charge transfer step. These aspects are revisited later in this study (see Sect. 7.4.2).

Besides these short-circuited cell mechanisms, sulfide oxidation by surface hydroxyl species on more stable surfaces could occur, *i.e.*, following oxygen reduction and/or water oxidation:

$$j_{A_3} = (12y+2)Fk_{a_3} \cdot exp\frac{\beta_{A_3} FE}{R_g T} \qquad 6.122$$

The cathodic reaction and corresponding current density may then be represented as follows, respectively:

$$Fe(OH)^*S_2 + H^+ \Rightarrow Fe(H_2O)^*S_2 + h^+ \qquad 6.123$$

$$j_{C_3} = -Fk_{c_3}[Fe(OH)S_2] \cdot exp\frac{-(1-\beta_{C_3})FE}{R_g T} \qquad 6.124$$

Stellenbosch University http://scholar.sun.ac.za

The explicit recognition of the hydroxyl surface species, $Fe(OH)S_2$, benefits both interpretation and mathematical manipulation. A better representation of the reality may, in fact, be depicted by an analogous representation to Figure 6.11 (*a-c*), *i.e.*, the electrochemical potential of a bonding electron in the sulfide lattice would depend on both the electro-active surface oxidant species concentration (surface potential) and the adsorbed proton concentration. The methodology of the MP theory is, once again, followed and it is assumed that a unique mixed potential would be associated with surfaces where this indirect mechanism is most prevalent. This leads to the following equation of the exchange current density due to the oxidation of a pyrite surface, in close vicinity of the more stable pyritic-oxide surface of high electron affinity:

$$j_{o_3} = (12y+2)Fk_3[Fe(OH)S_2]^{\beta_3} \qquad 6.125$$

It is assumed that the activation barrier would be exclusively associated with the anodic reaction, *i.e.*, fast reduction of the radical species after self-propagating to the reacting surface, making the charge transfer coefficient highly asymmetric and approaching unity. The potential difference across the double layer is therefore assumed to only affect the kinetics of the anodic dissolution reaction and not the cathodic reduction rate of the hydroxyl radical species on the reactive (protonated) sulfide surface at higher temperature, *i.e.*, $\beta_3 \approx 1$ (Eq. 6.104 & 6.105). Substitution of Equation 6.116 into Equation 6.125 then results in the following relationship:

$$j_{o_3} = (12y+2)Fk_3 a_{Fe(OH)S_2} \cdot k_{Fe(OH)S_2}[H^+]^{m_1(1-\beta_1)+n_1\beta_1}[O_2]^{\beta_1} \qquad 6.126$$

The overall intrinsic rate of pyrite oxidation is then obtained from Faraday's relationship:

$$r_{Py} = \frac{j_{o_2}+j_{o_3}}{|z_{rx}|F} = k_2[H^+]^{n_2\beta_2}[O_2]^{\beta_2} + k_3 a_{Fe(OH)S_2} \cdot k_{Fe(OH)S_2}[H^+]^{m_1(1-\beta_1)+n_1\beta_1}[O_2]^{\beta_1} \qquad 6.127$$

The catalytic pyrite surface (Py_c) is here represented as a fraction (θ) of the total available pyrite surface area at a specific point in time (a_{Py}), using generalised intrinsic rate constants (k_{Py} & k_{Pyc}).

The general assumption is made that the transition state of the rate-limiting electrochemical reactions, involving diatomic oxygen, is intermediate in its resemblance to the oxidised and reduced species (Atkins & De Paula, 2006), *i.e.*, the charge transfer coefficients of the anodic and cathodic processes are assumed to be half (½), resulting in the final expression of the intrinsic oxidation rate of pyrite in oxygenated solutions under typical MT autoclave conditions:

$$r_{Py} = k_{Py}[H^+]^{\frac{1}{2}n_2}[O_2]^{\frac{1}{2}} + \theta_{Py_c} a_{Py} k_{Py_c}[H^+]^{\frac{1}{2}(m_1+n_1)}[O_2]^{\frac{1}{2}} \qquad 6.128$$

Stellenbosch University http://scholar.sun.ac.za

Sphalerite

In contrast with pyrite, sphalerite has a wide band gap. However, localised iron impurity bands create surface states within the band gap, which is then energetically better positioned to exchange electrons with aqueous iron(III) species. The dissolution rate of sphalerite is therefore directly proportional to its iron impurity level (Sect. 6.3.2). The binding energy of oxygen on the sphalerite surface (100) is significantly lower compared to pyrite (Table 6.3). Other sphalerite facets (110, 111) resulted in similar (qualitative) values, which emphasises the importance of ferric ion in the leaching of sphalerite in copper-free solutions. This is also reflected by the high elemental sulfur yields observed during zinc pressure leaching of (low-pyrite) sphalerite concentrates (> 95% yield at ~150°C; Sect. 6.3.1 & 6.3.3). Previous discussions regarding the cathodic reduction of oxygen (Sect. 6.3.2) have emphasised the multi-step nature of the mechanism, yielding various radicals of high oxidation potential. With oxygen as the primary oxidant, the mixed potential would be expected to stabilise at a relatively high value and the elemental sulfur yield would be significantly lower than 95% under MT autoclave conditions.

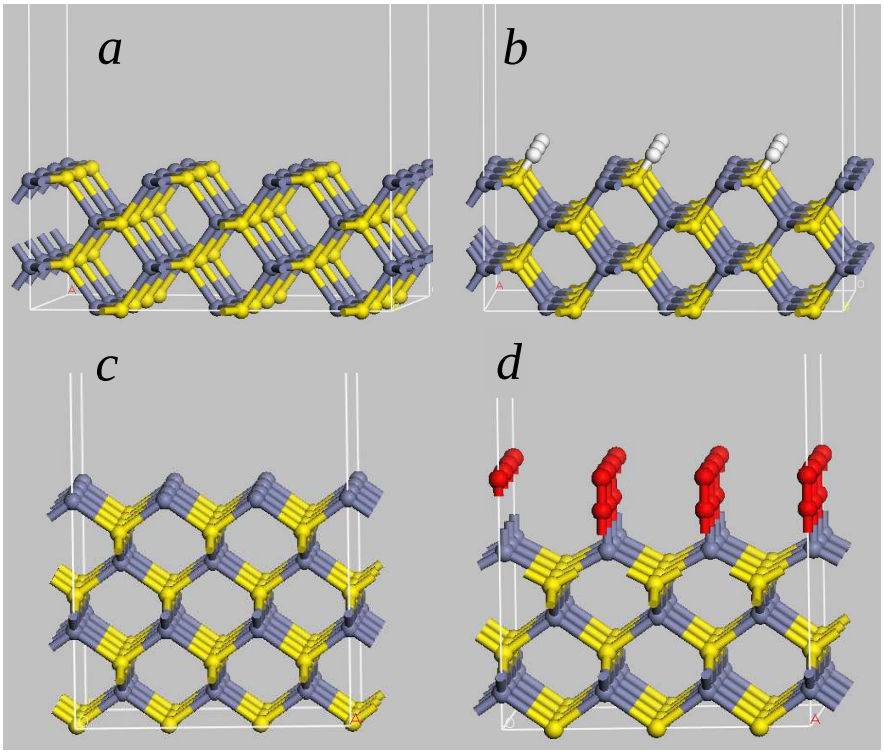

Figure 6.19
Optimised zinc sulfide surface structures (*MS*, 2008; after Burger, 2009); Zn & S atoms are coloured blue & yellow, respectively: *a*) (110) surface; *b*) (110) surface after H^+ adsorption (grey colour indicates protons); *c*) (100) surface; *d*) (100) surface after O_2 adsorption (red colour indicates diatomic oxygen).

The unfavourable adsorption characteristics of oxygen are reflected by the end-on interaction of the diatomic molecule on positively charged zinc atoms (Figure 6.19 *d*). It was not possible to calculate

Stellenbosch University http://scholar.sun.ac.za

a binding energy of the proton on the (100) surface, while it was found to bond relatively strongly to the (110) surface (Table 6.3). It is apparent from Figure 6.19 (*a*-*c*) why the (110) face is more amenable to proton adsorption compared to the (100) face. However, hydrated ferric ion may exchange electrons with the mineral surface, without physically adsorbing onto an anodic sulfide site. The anodic dissolution reaction, with ferric ion as oxidant, is represented by the reaction:

$$(Zn,Fe)S + 2h^+ \Rightarrow Zn^{2+} + Fe^{2+} + S^o \qquad 6.129$$

Iron atoms, which substitute zinc atoms in the sphalerite lattice, create 3*d*-orbital bands within the band gap. Injection of holes by ferric ion would result in electron tunnelling between the sulfur 3*p* orbitals in the valence band and holes in the surface 3*d* orbitals, followed by the concomitant release of Zn^{2+} (associated with the conduction band) and Fe^{2+} (3*d* orbitals are of bonding character) (after Crundwell, 1988b). In more general terms, the oxidation of monosulfide minerals, like sphalerite, may be represented as follows:

$$S^{2-}|_{lat} + 4yH_2O \Rightarrow ySO_4^{2-} + (1-y)S^o + 8yH^+ + (6y+2)e^- \qquad 6.130$$

The reduction of ferric ion on sphalerite surfaces involves a single-electron transfer step at lower mixed potentials, *i.e.*, the sulfide oxidation would be expected to yield elemental sulfur almost quantitatively (see above). The rate-limiting step is assumed to be the first electron transfer reaction, *i.e.*:

$$S^{2-}|_{Sph} + H^+ + h^+ \Rightarrow HS\cdot^* \qquad 6.131$$

The subsequent oxidation of radical surface species would be expected to be comparatively fast:

$$HS\cdot^* + h^+ \Rightarrow S^o + H^+ \qquad 6.132$$

The E_h of this oxidation step is 1.3 V (Wardman, 1989) and both ferric and cupric ion reduction yield highly positive EMF values, *i.e.*, 2.071 V and 1.453 V, respectively. Alternatively, this radical species may be reduced by, *e.g.*, remnant ferrous species of the first electron transfer step:

$$HS\cdot^* + e^- \Rightarrow HS^{-*} \qquad 6.133$$

The EMF of the reaction is also positive (0.379 V) but, due to the strong interaction between the proton with the sulfur atom, would be expected to result in a structure that does not resemble the original sphalerite surface; hence, the irreversible representation of Equation 6.131. This surface species may also be produced by a non-oxidative dissolution mechanism:

$$S^{2-}|_{Sph} + H^+ \Rightarrow HS^{-*} \qquad 6.134$$

At high acid concentrations and low aqueous zinc and oxidative species concentrations (low redox potential), hydrogen sulfide and zinc ion would be released into solution. In the copper system,

Stellenbosch University http://scholar.sun.ac.za

however, surface bisulfide (HS^-) species may rapidly form a covellite (*Cov*) structure on the surface. The reason for this is that the $K°_{sp}$ (Sect. 2.2.3) of covellite (*log* $K°_{sp} \approx -35.9$) is orders of magnitude lower than ZnS (*log* $K°_{sp} \approx -24.5$) (values from Monhemius, 1977). This reaction is represented as follows:

$$HS^{-*} \Rightarrow S^{2-}|_{Cov} + H^+ \qquad 6.135$$

Surface bonding with proton ions would not weaken the covellite lattice to the same extent as sphalerite, hence, the irreversible representation of this reaction. Equations 6.134 and 6.135 may be viewed as the forward and backward directions of a dynamic equilibrium, with rate constants k and k′, respectively:

$$S^{2-}|_{lat} + H^+ \Leftrightarrow HS^{-*} \qquad 6.136$$

If this dynamic equilibrium is represented by the Langmuir isotherm (Atkins & De Paula, 2006), the extent of proton coverage (θ_{H^+}) may be represented as follows:

$$\theta_{H^+} = \frac{[H^+]}{K + [H^+]} \qquad 6.137$$

where the equilibrium constant, K, represents the ratio of reverse to forward rate constants. It is assumed here that the equilibrium is insensitive to the copper concentration above a certain critical level. Since the reaction between copper ion and the surface bisulfide species would be expected to be significantly faster than the non-oxidative dissolution of sphalerite (k′ >> k), the absolute value of K should be significantly higher than $[H^+]$, and the above equation simplifies as follows:

$$\theta_{Cov} = \theta_{H^+} \propto [H^+] \qquad 6.138$$

The anodic current density, due to direct reaction with ferric ion (Rx. 6.131), may be represented as follows:

$$j_A = 2Fk_{a_1} N_{Fe} \cdot exp\frac{\beta_A FE}{R_g T} \qquad 6.139$$

where N_{Fe} is the mole ratio of iron over zinc (mol Fe/mol Zn) in substituted sphalerite lattice sites (Crundwell, 1988b, c). The cathodic reduction of ferric ions and the corresponding half-cell current density may be represented as follows, respectively:

$$Fe^{3+} \Leftrightarrow Fe^{2+} + h^+ \qquad 6.140$$

$$j_C = Fk_{a_2} N_{Fe}[Fe^{2+}] \cdot exp\left(\frac{\beta_C FE}{R_g T}\right) - Fk_c N_{Fe}[Fe^{3+}] \cdot exp\left(\frac{-(1-\beta_C)FE}{R_g T}\right) \qquad 6.141$$

Stellenbosch University http://scholar.sun.ac.za

If it is assumed that these anodic and cathodic reactions take place randomly over the particle surface where no surface covellite has formed, the total anodic and cathodic surface areas due to ferric ion reduction may be assumed to be equal. This corresponds to the corrosion mechanism on a uniform surface, first proposed by Wagner and Traud (1938). The second consequence of the iron impurity is that the Fermi level is pinned at the *d*-orbital band and the potential difference would therefore only appear across the Helmholtz layer (Crundwell, 1988b, c), *i.e.*, not also across the space-charge region. Sphalerite oxidation would therefore be expected to behave like a metal, with a one-half order dependence on the active iron(III) species concentration. This has been shown to be the case (Jin *et al.*, 1985) and it is therefore assumed that $\beta_A = \beta_C = ½$. The MP methodology is again followed (see above) to derive the current density of sphalerite oxidation by ferric ion:

$$j_{o_4} = 2Fk_{Sph}\left(\frac{k_{Fe^{3+}}[Fe^{3+}]}{1+k_{Fe^{2+}}[Fe^{2+}]}\right)^{\frac{1}{2}} \qquad 6.142$$

The dissolution of surface covellite would be expected to be significantly slower than that of sphalerite and yield less elemental sulfur (Sect. 6.3.2). Based on previous discussions, oxygen would be the primary oxidant of covellite oxidation. The oxygen reduction rate on covellite surface is comparable to that on pyrite (Biegler et al., 1977). However, the mechanism of oxygen reduction is different and would depend heavily on the presence of copper(I) surface lattice sites (Table 6.2). It is difficult to express the anodic dissolution of covellite, due to its complex crystal structure, and the sulfur valency is simply assumed to vary between 1 and 2, *i.e.*, according to the ionic model:

$$\tfrac{1}{3}(S^{2-})(S_2^{2-})|_{Cov} + H^+ + h^+ \Rightarrow HS\cdot^* \qquad 6.143$$

Alternatively, this reaction could be based on the experimental observation of Goh *et al.* (2006), suggesting predominantly copper(I) surface states. Nevertheless, no impact on the phenomenological expression transpires and the dissolution rate of covellite oxidation by oxygen is derived in analogous fashion to the methodology followed for pyrite, yielding the following exchange current density:

$$j_{o_5} = (6y+2)Fk_5[H^+]^{n_5\beta_5}[O_2]^{\beta_5} \qquad 6.144$$

The simplest treatment is to assume that the mixed potential would be different on surfaces where sphalerite is exposed (ferric ion reduction) and coated with a covellite surface (oxygen reduction). The various charge transfer coefficients are assumed to be one half (½) and the overall dissolution rate of sphalerite may then be expressed as follows:

Stellenbosch University http://scholar.sun.ac.za

$$r_{Sph} = \frac{(1-\theta_{Cov})j_{o_4}}{2F} + \frac{\theta_{Cov} j_{o_5}}{(12y+2)F}$$
$$= (1-\theta_{Cov})k_{Sph}\left(\frac{k_{Fe^{3+}}[Fe^{3+}]}{1+k_{Fe^{2+}}[Fe^{2+}]}\right)^{\frac{1}{2}} + \theta_{Cov} k_{Cov}[H^+]^{\frac{1}{2}n_5}[O_2]^{\frac{1}{2}} \quad 6.145$$

Besides possible diffusion barriers, *e.g.*, elemental sulfur, the most abundant mineral faces (see above) would determine which of these paths dominates. If the covellite mechanism is dominant under MT autoclave conditions, *i.e.*, $\theta_{Cov} \approx 1$, the above equation simplifies to:

$$r_{Sph} = k_{Cov}[H^+]^{\frac{1}{2}n_5}[O_2]^{\frac{1}{2}} \quad 6.146$$

In this study, the only disseminated concentrate which contained significant amounts of sphalerite, *i.e.*, the HBMS 777 copper concentrate (Sect. 6.4.3), contained relative small amounts of pyrite. No enhanced oxidation effect at high pulp density due to the catalytic effect of pyrite is therefore deemed necessary and Equation 6.146 represents the most simplistic representation of sphalerite dissolution in acidic copper sulfate solutions. These assumptions are revisited in Chapter 7.

A similar approach may be adopted for pyrrhotite (Fe_7S_8; *Ph*). The non-stoichiometric nature of this phase introduces some complications, but these details are not captured mathematically, due to its relatively small abundance (< 4%) in the concentrates encountered in this study. A series of publications by Thomas *et al.* (1998, 2001, 2003) provides insightful discussion on possible dissolution mechanisms. The most important aspect, for the purpose of this study, is that these types of iron sulfide minerals exhibit low relative rest potentials; E_{rest} = -0.28 for FeS *vs.* -0.24 for ZnS in 1 mol/L H_2SO_4 at 20°C (Hiskey & Wadsworth, 1981). This suggests that the proton adsorbs even more strongly on these types of iron sulfide surfaces and might weaken the lattice to such an extent that non-oxidative dissolution mechanisms could dominate. The nature of the Fe-S and S-S bonds are also important (Thomas *et al.*, 2003), so is the presence of non-stoichiometric sulfur-rich (pyrrhotite) structures, which would require a reduction step before non-oxidative dissolution can occur (Thomas *et al.*, 2001). As a first estimate, pyrrhotite oxidation is assumed to follow a similar mechanism in an acidic copper sulfate system at high temperature to that proposed for sphalerite (above), *i.e.*, preferential formation of a covellite rim on unreacted pyrrhotite, due to the presence of adsorbed bisulfide surface species, followed by oxidative dissolution *via* oxygen reduction on catalytic copper(I) sites:

$$r_{Ph} = k_{Cov}[H^+]^{\frac{1}{2}n_5}[O_2]^{\frac{1}{2}} \quad 6.147$$

The next section focuses on the dissolution rate of chalcopyrite, the most abundant mineral phase encountered in this study, which has also attracted the most controversy in the open literature.

Stellenbosch University http://scholar.sun.ac.za

Chalcopyrite surface

Figure 6.20 *a* represents the optimised chalcopyrite surface, without any interaction with the hydrogen ion species, while Figure 6.20 *b*, *c* and *d* represent the optimised geometry of the system after hydrogen ion, ferric and oxygen species adsorption, respectively. Similar to the other sulfide minerals, the hydrogen and ferric ions compete for the same surface sites (sulfide atoms). Although oxygen preferentially interacts with iron atoms, the surface lattice does not accommodate the diatomic molecule in two-fold fashion, as observed for the pyrite surface (Figure 6.15 *d*) This geometry resembles the weaker-bonded Pauling model (Shi *et al.*, 2006), which reflects modest binding energy of diatomic oxygen with chalcopyrite, with pyrite and sphalerite representing two opposite extremes (Table 6.3). Once again, the surface is severely distorted after species adsorption. However, contrary to pyrite (Figure 6.15 *d*), the same surface can accommodate both ferric ion and diatomic oxygen, and both oxidants have to be considered as possible candidates. However, the role of the hydrogen ion should not be underestimated, as its binding energy to the chalcopyrite (110) surface is even higher than that on the corresponding sphalerite surface.

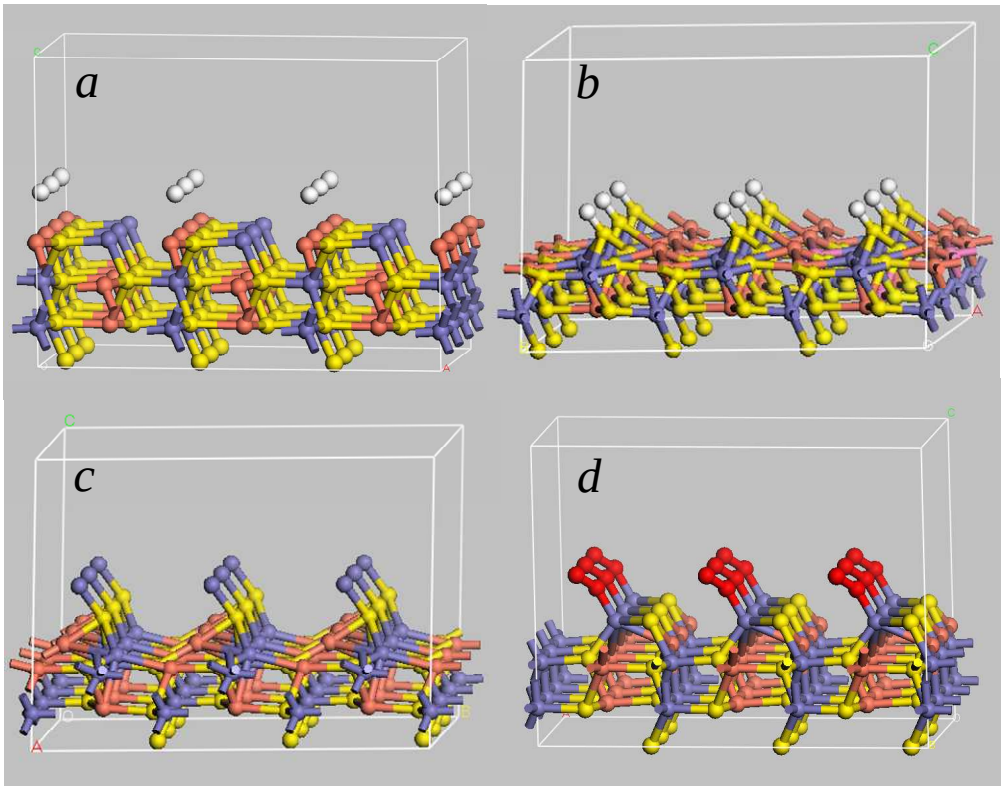

Figure 6.20
Optimised chalcopyrite surface (110) structures (*MS*, 2008; after Burger, 2009); Cu, Fe & S atoms are coloured pink, purple & yellow, respectively: *a*) H^+ ions before adsorption (grey colour indicates protons); *b*) After H^+ adsorption; *c*) After Fe^{3+} adsorption; *d*) After O_2 adsorption (red colour indicates diatomic oxygen).

Stellenbosch University http://scholar.sun.ac.za

A useful way of characterising the electronic structure of a material is by the density of states (DOS). The DOS counts the relative number of energy levels in each energy range. In a molecule, there are distinct energy Eigen values; strictly speaking, the DOS has a value of one at each of these values and a value of zero elsewhere. By contrast, the energy levels of a crystal are a continuum, with more or fewer energy values squeezed into an energy range (after Burger, 2009). The calculated DOS for bulk chalcopyrite and the (110) surface are illustrated in Figure 6.21.

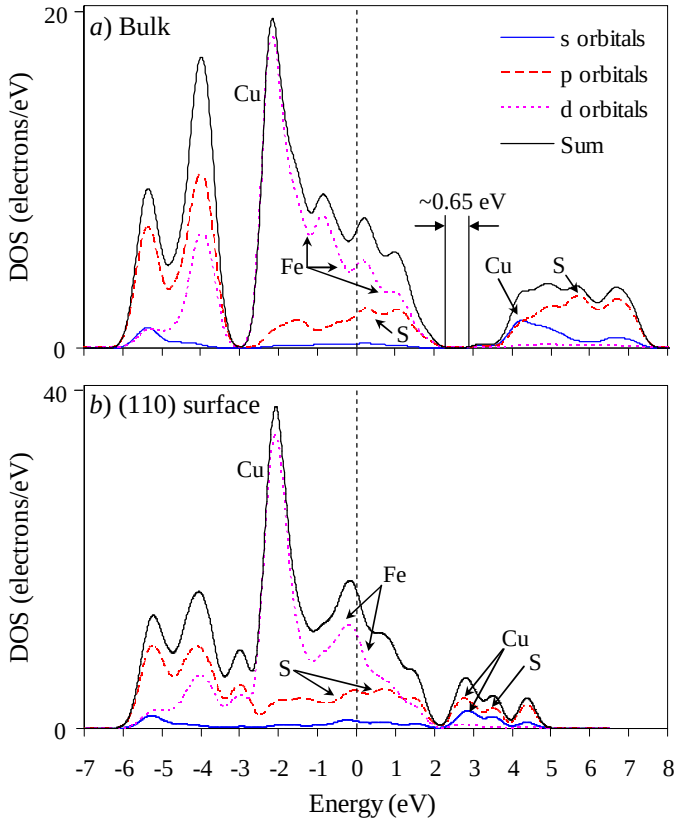

Figure 6.21
Calculated total & partial DOS of chalcopyrite crystal (*MS*, 2008; after Burger, 2009) (LDOS were used to assign the major atom-projected contributions): *a*) Bulk structure; *b*) (110) surface.

The partial density of states (PDOS) allows a semi-qualitative tool to characterize the DOS in terms of particular atomic orbitals, *s*, *p*, *d*, or *f* (omitted). The energies of these bands are plotted with respect to the Fermi level, which was assigned a value of zero. The local density of states (LDOS) shows which atoms in the system contribute electronic states to various parts of the energy spectrum. Although these states are not represented above, the major contributions were labelled accordingly. LDOS and PDOS analyses give a qualitative handle on the nature of electron hybridization in the system. Firstly, it is emphasised that the calculated band gap is of a similar magnitude as that reported in Section 6.3.2, *i.e.*, 0.6-0.7 eV. However, the valence band edge is described by Fe 3*d* and S 3*p* states, while the conduction band edge is represented by Cu *s* and *p*

Stellenbosch University http://scholar.sun.ac.za

orbital states. This finding is different from the band structure represented in Figure 6.5. Another difference is the presence of empty Fe *d* and S *p* orbitals above the Fermi level, which suggests that chalcopyrite should behave like a metal during oxidation, provided the redox couple is positioned accordingly. A surface structure also introduces a large number of states, which reduces the band gap even further (Figure 6.21 *b*). Furthermore, it is apparent from Figure 6.21 why iron leaches first during oxidative dissolution, especially if the ferric/ferrous redox couple represents the primary electron-exchange mechanism. On the other hand, the Cu–S bonding orbitals are situated at more negative energy levels, which may only be directly accessible by highly reactive oxidant species, *e.g.*, the surface perhydroxyl radical ($E_h \approx 1.5$ V). No more mechanistic conclusions can be drawn from these preliminary modelling results.

Once again, it is most appropriate to use the MP perspective to derive a generic rate expression of mineral oxidation; this scheme is illustrated in Figure 6.22.

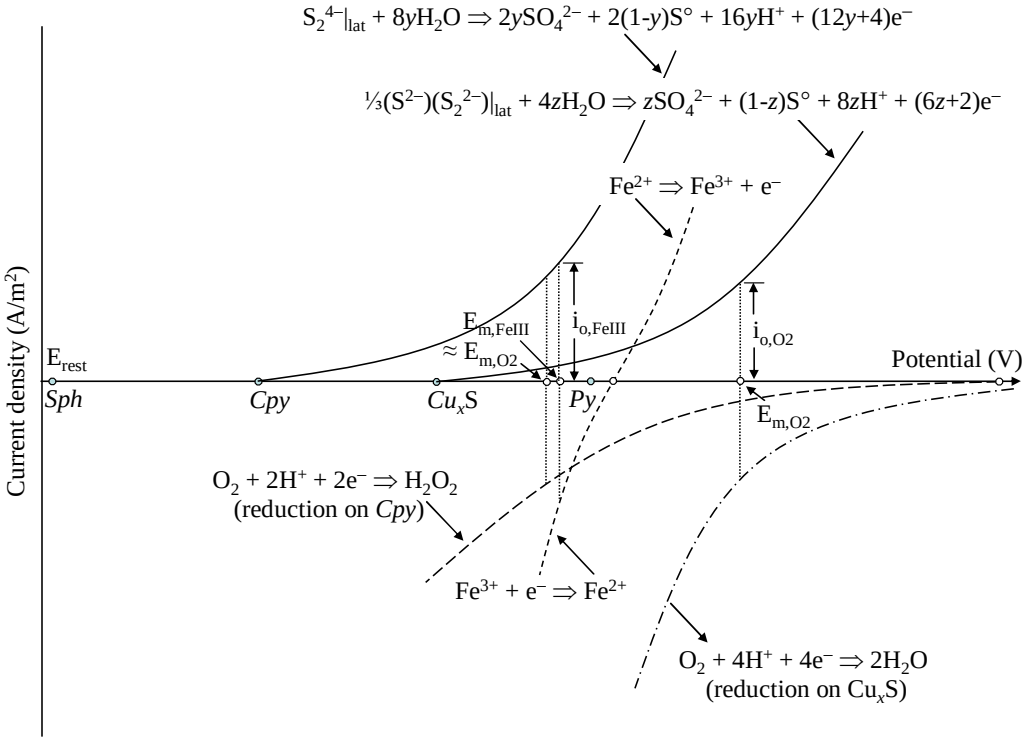

Figure 6.22
Schematic diagram applying the MP theory to the oxidation of chalcopyrite in acidic, oxygenated sulfate solutions at MT autoclave temperatures.

This figure is based on various insights obtained from the literature review (Sect. 6.3.2), despite the contradictory views regarding the surface layer on partially oxidised chalcopyrite. The preferential release of iron, observed in various experimental studies, is consistent with the quantum-level modelling results, presented above. There is also strong evidence of the formation of covellite-like

Stellenbosch University http://scholar.sun.ac.za

surface layers on chalcopyrite during pressure oxidation in acidic solutions. A high binding energy is also calculated for the proton on specific (*e.g.*, 110) chalcopyrite surfaces. It is therefore proposed that the chalcopyrite dissolution mechanism may also produce a copper sulfide surface, but the mechanism may differ from the one proposed for sphalerite (se above). This surface layer may be presented as Cu_xS, with the sulfur assumed to arrange itself in a monosulfide-disulfide ($S^{2-}S_2^{2-}$) structure, *i.e.*, according to the ionic model for covellite. If this phase contains primarily monovalent copper (Goh *et al.*, 2006; Van der Laan, 1992), the oxygen reduction mechanism would be expected to dominate on these types of surfaces. However, on some surfaces under MT autoclave conditions, a more congruent release of copper and iron atoms may occur. The number of monovalent copper states on an unaltered chalcopyrite surface is assumed to be lower than on covellite-like surface structures. Oxygen may reduce less efficiently on the chalcopyrite surface when exposed as unaltered sulfide phase (S_2^{4-}), because iron(III) may oxidise copper(I) surface states as it is released from the surface structure (Figure 6.20 & Section 6.3.2).

Figure 6.22 proposes that monovalent copper in the surface structure may catalyse the first reduction step of oxygen (to form the perhydroxyl species), but that intermediate peroxide may have to migrate to another site in order to be reduced further. Section 6.3.2 suggests that peroxide reduction may be kinetically slow on a less catalytic surface, *i.e.*, desorption may effectively result in its destruction, either *via* 'stray' reduction (*e.g.*, by ferrous ion) or *via* disproportionation (Eq. 6.82), followed by reduction of the resulting radical. As illustrated in Figure 6.22, the mixed potential would not be expected to vary significantly between the two oxidation routes, *i.e.*, hole injection by ferric ion (Eq. 6.140) or oxygen, limited by the first reduction of the diatomic molecule (Eq. 6.107). This is because barren chalcopyrite surface would be less catalytic towards oxygen reduction (*cf.* pyrite) and would not be able to produce a high density of oxidising surface species. The assumption of equal anodic and cathodic surface areas and symmetrical charge transfer coefficients allows elimination of this mixed potential term. Its back-substitution into the anodic current density term results in the following equation:

$$j_{o_6} = (12y_1 + 4)Fk_{Cpy}\left(\frac{k_{Fe^{3+}}[Fe^{3+}] + k_{O_2}[H^+]^{n_6}[O_2]}{1 + k_{Fe^{2+}}[Fe^{2+}]}\right)^{\beta_6} \qquad 6.148$$

The presence of catalytic pyrite surfaces may accelerate both unaltered chalcopyrite surface and altered, covellite-like, surface oxidation at high pulp densities; these enhancing effects are represented by the following two rate expressions (adopted from Eq. 6.126):

$$j_{o_7} = (12y_2 + 4)Fk_7\, a_{Fe(OH)S_2} \cdot k_{Fe(OH)S_2}[H^+]^{m_1(1-\beta_1)+n_1\beta_1}[O_2]^{\beta_1} \qquad 6.149$$

$$j_{o_9} = (6z_2 + 2)Fk_9\, a_{Fe(OH)S_2} \cdot k_{Fe(OH)S_2}[H^+]^{m_1(1-\beta_1)+n_1\beta_1}[O_2]^{\beta_1} \qquad 6.150$$

Stellenbosch University http://scholar.sun.ac.za

Finally, the current density due to the oxidation of the covellite-like surface by oxygen is derived in an manner analogous to the above description; however, the dissolution current, due to ferric ion reduction, is assumed to be relatively insignificant on these surfaces due to the stability of the Cu–S bond (see above), while such surfaces would also be expected to be heavily protonated:

$$j_{o_8} = (6z_1 + 2)Fk_8[H^+]^{n_8\beta_8}[O_2]^{\beta_8} \qquad 6.151$$

The overall intrinsic rate of chalcopyrite mineral oxidation is obtained from Faraday's relationship and substitution of Equations 6.148 to 6.151, to yield:

$$\begin{aligned} r_{Cpy} &= \frac{(1-\theta_{Cu_xS})}{F}\left(\frac{j_{o_6}}{(12y_1+4)}+\frac{j_{o_7}}{(12y_2+4)}\right)+\frac{\theta_{Cu_xS}}{F}\left(\frac{j_{o_8}}{(6z_1+2)}+\frac{j_{o_9}}{(6z_2+2)}\right) \\ &= (1-\theta_{Cu_xS})k_{Cpy}\left(\frac{k_{Fe^{3+}}[Fe^{3+}]+k_{O_2}[H^+]^{n_6}[O_2]}{1+k_{Fe^{2+}}[Fe^{2+}]}\right)^{\beta_6} \\ &+ (1-\theta_{Cu_xS})\theta_{Py_c}a_{Py}k_{Py_{c,1}}[H^+]^{m_1(1-\beta_1)+n_1\beta_1}[O_2]^{\beta_1} \\ &+\theta_{Cu_xS}k_{Cu_xS}[H^+]^{n_8\beta_8}[O_2]^{\beta_8} + \theta_{Cu_xS}\theta_{Py_c}a_{Py}k_{Py_{c,2}}[H^+]^{m_1(1-\beta_1)+n_1\beta_1}[O_2]^{\beta_1} \end{aligned} \qquad 6.152$$

A symmetric charge transfer coefficient is assumed for the catalytic (pyrite) surface formation reaction, *i.e.*, $\beta_1 = ½$ (see above), while the activation energy barrier of its reaction with a chalcopyrite surface is assumed to be exclusively associated with the anodic reaction. Furthermore, $k_{Pyc,1} \approx k_{Pyc,2}$ (similar rate enhancement by pyrite), resulting in the following equation:

$$\begin{aligned} r_{Cpy} &= (1-\theta_{Cu_xS})k_{Cpy}\left(\frac{k_{Fe^{3+}}[Fe^{3+}]+k_{O_2}[H^+]^{n_6}[O_2]}{1+k_{Fe^{2+}}[Fe^{2+}]}\right)^{\beta_6} \\ &+\theta_{Cu_xS}k_{Cu_xS}[H^+]^{n_8\beta_8}[O_2]^{\beta_8} + \theta_{Py_c}a_{Py}k_{Py_c}[H^+]^{\frac{1}{2}(m_1+n_1)}[O_2]^{\frac{1}{2}} \end{aligned} \qquad 6.153$$

Even if other copper sulfide surface phases are formed, this rate expression would still be applicable, as stoichiometric charge transfer changes would simply be absorbed in the various rate constants.

If additional layers, *e.g.*, elemental sulfur, are formed on top of the above surface structures, a retarded rate of electron transfer would be expected in all cases, *i.e.*, reaction routes involving iron(III), oxygen, as well as enhancement routes involving catalytic pyrite surfaces. No conclusive evidence has been presented in the open literature to support any one mechanism over another (see previous discussions), except for the observation of Cu_xS surfaces under higher oxidation temperature conditions. This is, however, an engineering study and the above propositions will remain speculative until modelled on a fundamental level and verified experimentally. This study is follows a phenomenological approach and the relevant theory is discussed next.

Stellenbosch University http://scholar.sun.ac.za

6.3.5 Phenomenological description of the intrinsic mineral oxidation rate

It is important to mathematically relate the observed oxidation phenomena (leaching experiments) to a viable electrochemical mechanism. The unreacted shrinking particle (USP) (or unreacted shrinking core, USC) model under intrinsic surface reaction control is discussed in detail in Appendix F.4. A phenomenological description of the leaching kinetics of sulfide mineral particles, displaying topochemical kinetics under approximately constant reaction conditions, is as follows:

$$1-(1-X_s)^{\frac{1}{3}} = k_s t \qquad 6.154$$

where X_s represents the fractional amount of sulfide mineral leached after time, t (min).

$$k_s = -\frac{1}{3}\frac{Mw_s}{\rho_s}\frac{\Phi_a}{\Phi_v}\frac{r_s}{L_o} \qquad 6.155$$

If the term, $1-(1-X_s)^{1/3}$ is plotted against time, and the system is under surface reaction control, a straight line should be obtained. The slope would then yield the overall observed leaching rate constant, k_s (1/min). This rate constant is a function of the initial particle size (L_o), area and volume shape factors (Φ_a & Φ_v, respectively), the sulfide mineral density and molecular weight (ρ_s & Mw_s, respectively) and the intrinsic reaction rate, r_s (mol/m^2.min).

As discussed previously, the major parameters affecting this intrinsic reaction rate are temperature, hydrogen ion concentration, and the type and concentration of the oxidation agents. Only when these parameters are kept approximately constant, can the linear rate constant (rate of particle shrinkage), k_ℓ (μm/min), be directly obtained from the above slope:

$$k_s = \frac{k_\ell}{L_o} \qquad 6.156$$

It is obvious from Equation 6.156 that a straight line would only be obtained if the particles are screened to a narrow size range, L_o. Equation 6.154 may also be rearranged to yield the following useful relationship:

$$X_s = 1-\left(1-\frac{t}{\tau_s}\right)^3 \qquad 6.157$$

where τ_s is the time constant ($1/k_s$), which gives the time (min) for complete oxidation of monosized sulfide mineral particles in a batch reactor, under controlled reaction conditions, with no diffusion limitations. Finally, the above sections emphasise that different mineral faces would be expected to oxidise at different rates and, possibly, *via* different mechanisms. This (simplified) phenomenological modelling approach averages such effects over the total particle surface area.

Stellenbosch University http://scholar.sun.ac.za

6.4 Experimental

This section describes the testwork procedures used in the primary kinetic study, utilising the HBMS 777 chalcopyrite concentrate at low pulp density, in order to obtain a phenomenological description of sulfide mineral oxidation rates under MT autoclave conditions.

6.4.1 Equipment and procedures

The 2-litre Parr autoclave was exclusively used in this part of the study, as described in detail in Section 3.3 and illustrated in Figure 3.1. Sulfuric acid and surfactants were injected into the autoclave 'at temperature', utilising the high-pressure feed bomb arrangement (Figure 6.23).

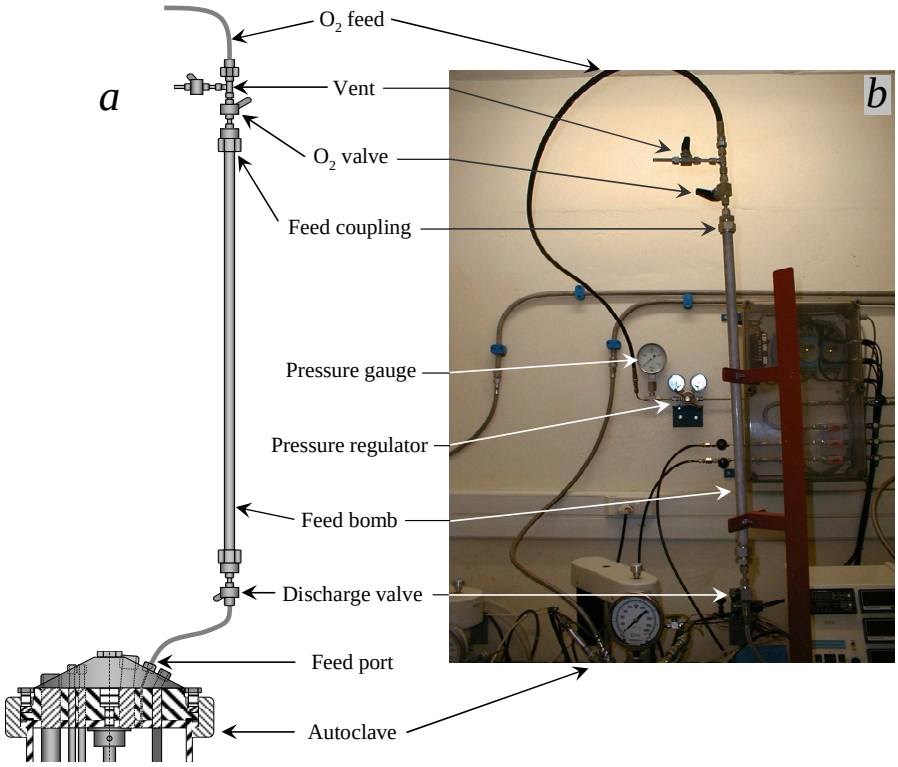

Figure 6.23
High-pressure feed bomb: *a*) Schematic diagram of the feed bomb; *b*) Photo of feed bomb & peripheral equipment.

In order to minimise temperature variations during the initial period of rapid mineral oxidation, the injection volume was kept as low as possible. For this reason, copper sulfate was added to the solid slurry and heated to temperature. Although cupric ion would be expected to cement or undergo metathesis reactions with sulfide surfaces during this heat-up period, its impact on the measured rate constants is deemed to be small compared to the temperature disturbance during initial oxidation. This method of introducing the solid concentrate into the autoclave also resembles, to

Stellenbosch University http://scholar.sun.ac.za

some extent, the conditions in the feed system (tanks & heat exchanger) of the continuous pilot autoclave (Sect. 7.3.1). The experimental procedure may be summarised as follows:

- The initial slurry was prepared by mixing the concentrate sample with a fixed amount of water and dissolving the required amount of copper sulfate salt
- The autoclave (Parr model 4522; Figure 3.1) was then heated to the setpoint temperature, with the impeller stirring slowly (all mixing aspects are discussed in detail in Ch. 3)
- The surfactants were dissolved into a predetermined amount of water, placed into the feed bomb and injected into the reactor, using 50 kPa overpressure of oxygen
- The feed bomb was then charged with the required amount of concentrated acid and this was also injected into the reactor, using a further 50 kPa increase in overpressure
- Oxidation was initiated by adjusting the oxygen overpressure and increasing the impeller speed to the respective setpoint values; this signified the start of the kinetic test
- The autoclave was continuously vented at a slow rate during the first five minutes of the test, in order to remove inert gases from the vapour space
- A predetermined amount of water was also injected into the reactor during this initial period, to purge the feed bomb and to ensure all the acid entered the reaction vessel; this brought the important species (acid, sulfate & surfactants) to their desired concentration levels and ensured the correct total slurry volume in the autoclave (see Ch. 3 for a detailed discussion of the effect of slurry volume on the interfacial gas/liquid mass transfer rate)
- A dedicated gas feed system ensured constant oxygen overpressure by regulating the total pressure of the vessel for the remainder of the test. The temperature was controlled to within 1°C by a PID controller (see Sect. 3.3 for more detail on this & other quality control aspects)
- On completion of the leach, the impeller speed was decreased to 100 rev/min, followed by rapid cooling (4-5 min) to 85°C and venting of the vapour phase
- The final slurry was filtered and the autoclave washed out with pH 2 water. The filter cake was also thoroughly washed with pH 2 water
- Metals in solution were quantified by inductively coupled plasma - optical emission spectroscopy (ICP-OES; App. B.2.1)
- Iron(II) and H_2SO_4 contents were determined by wet chemical methods (App. B.2.3)
- Solid samples were fused, dissolved in acid medium (App. B.2.1) and also analysed by ICP-OES, and
- The elemental sulfur content was determined by leaching the sample with tetrachloroethylene in an ultrasonic bath and analysing the resulting solution by high performance liquid chromatography (HPLC). The residue of this leach was then subjected

Stellenbosch University http://scholar.sun.ac.za

to a second leach with 10% Na_2CO_3 at boiling point and the resulting solution analysed by HPLC for sulfate sulfur. The final residue was analysed for sulfide sulfur, using an automated sulfur analyser (Leco). The total sulfur was also measured by Leco and then compared with the total sulfur calculated from the individual sulfur species. The sample was re-analysed if the difference was more than 5% (see App. B.2.2 for more details).

6.4.2 Data interpretation

A separate test was conducted for each kinetic data point in order to eliminate the sampling effects at high temperature and also to statistically minimise the impact of the experimental error on the measured rate constant values. Each experiment (datapoint) was scrutinised by conducting a mass balance for copper, iron, zinc and sulfur. The accountability (*AC*) of an element, *i*, is simply obtained as follows:

$$AC_i = \frac{(W_{i\,(s)} + W_{i\,(aq)})_t}{(W_{i\,(s)} + W_{i\,(aq)})_o} \times 100\% \qquad 6.158$$

where $W_{(s)}$ and $W_{(aq)}$ refer to the elemental mass in the solid and aqueous phases, respectively, and the subscripts, o and t, refer to the head and leached samples, respectively. Analyses or, in selected cases, tests were repeated if the accountability fell outside the 100 ± 10% range; this requirement was relaxed to 15% for zinc due to its low content in the HBMS 777 concentrate. Metal accountabilities (including zinc) are generally good (see detailed results in App. G) and the fractional extraction (X_i) is simply calculated as:

$$X_i = 1 - \frac{W_{i\,(s),t}}{W_{i\,(s),o}} \qquad 6.159$$

Previous discussions (Eq. 6.154) revealed that a plot of $1-(1-X_i)^{1/3}$ against time would be expected to yield a straight line for a system under surface reaction control. Solids analyses form the basis of this calculation, as this produces the most consistent results. The observed leaching rate constant, k_s (1/min) is directly obtained from the slope, provided that the intrinsic reaction rate is approximately constant. As mentioned before, this is only possible when using a sample consisting of 'monosized' particles (see next section) and keeping the solution composition approximately constant during the course of the batch experiment. Leaching tests were therefore conducted at relatively low solids' content (pulp density) of less than 2 wt%. No attempt is made to simultaneously fit a generalised model to all the leach results, since product layer diffusion played an inhibitory role in many of these tests (Sect. 6.5). Despite the above-mentioned precautions, various microscopic factors could have influenced the quality of the experimental results. The next section discusses the sample preparation and mineral and particle characterisation.

Stellenbosch University http://scholar.sun.ac.za

6.4.3 Sample preparation and characterisation

The preparation of a well-liberated sample, with low gangue mineral content, is important in order to mathematically describe the leaching behaviour of the sulfide concentrate, up to high extractions. Nevertheless, in order to avoid modelling an artificial system, it was also important to conduct this study within a commercial context.

Background information

The concentrate used in this part of the study was obtained from the Hudson Bay Mining and Smelting Co Limited (HBMS), with the overall objective of evaluating a MT autoclave (hydrometallurgical) process for possible replacement of the existing smelting operation at Flin Flon, Manitoba, Canada. The HBMS 777 ore body consists of two massive polymetallic sulfide lenses, overlying each other at approximately 4.6% Zn and 2.5% Cu. Five tonnes of this material was removed and floated, using the standard mineral processing technology at HBMS.

Particle size (head samples)

The feed material for the batch test programme was prepared by milling the concentrate for 7 minutes in a stirred-media detritor (SMD; Metso Minerals). The grinding media consisted of -2 mm carbolite material (density 2,710 kg/m^3, mass 1.908 kg & media ratio 50%). The milled sample was then split (in water medium) into different size fractions with a Warman cyclosizer. The +11/–16 µm and +16/–24 µm fractions were treated individually and repeatedly through the cyclosizer, whilst the –11 µm fraction was wet screened through a 5 µm cloth in an ultrasonic bath. The finest fraction was prepared by further milling of the +11/–16 µm sample in the SMD.

The size distributions of the final four products, referred to as (feed) Sample A, B, C and D respectively, are presented in Figure 6.24; the detailed particle size distributions (PSDs) can be found in Appendix G.1. These size distributions were measured by a Malvern MasterSizer 2000 (App. B.3.1). Table 6.4 compares the volume-median diameter (d_{50} percentile) readings to the equivalent (area) surface-mean diameter, d[3,2] and the equivalent volume-mean diameter, d[4,3]; the latter two quantities emphasise where the surface area and mass of the system of particles lie, respectively (Rawle, 1995). Both these parameters vary almost linearly with the median, *i.e.*, these head samples have approximately the same shape in the area and mass distributions, respectively. This is expected, since these samples exhibit almost symmetrical bell-shaped volume distributions (Figure 6.24). The median diameters are therefore used as a first approximation of the average particle sizes, despite the relatively large distribution span. The span is relatively smaller in the case of the two coarser distributions (Samples C & D) and these samples were therefore used in most of the batch testwork.

Stellenbosch University http://scholar.sun.ac.za

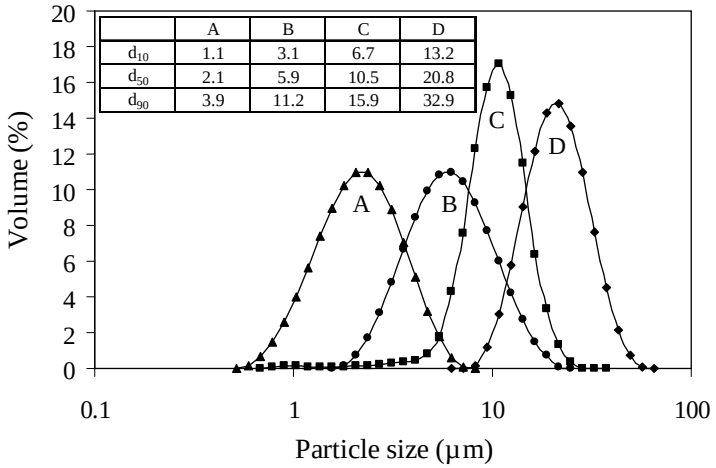

Figure 6.24
Size fractions used in the batch oxidation testwork (HBMS 777 concentrate).

Table 6.4
Comparison of various equivalent-sphere parameters for the HBMS 777 concentrate samples used in the batch oxidation testwork.

Sample	d_{50} (µm)	d[3,2] (µm)	d[4,3] (µm)	[a] Span (%)
A	2.1	1.9	2.3	133
B	5.9	4.9	6.6	137
C	10.5	9.3	11.1	88
D	20.8	19.6	22.1	95

[a] The distribution span (%) captures the width of the distribution: $(d_{90}-d_{10})/d_{50} \times 100$.

There is a relatively large discrepancy between the measured equivalent-median diameters and the mean target diameters (*ref.* the screen apertures) of Sample B and C, respectively. This may be ascribed to the irregular particle shape; the secondary electron images (SEI; App. B.3.3) on the next page illustrate typical particle geometries (Figure 6.25). The measured distributions may have corresponded better with the screen apertures and cyclosizer targets had the particles been more spherical. Nevertheless, these figures confirm that the objective of producing narrow-sized fractions was indeed met. Comparison between the milled concentrate (before sizing) and the prepared samples reveals that the sizing techniques clearly overcame the electrostatic attraction between ultrafine particles and the surfaces of the larger particles.

The most important feature of these samples is that they were approximately symmetrical and relatively narrow in size, simplifying the interpretation of experimental leaching data (Sect. 6.3.5). Nevertheless, these samples clearly did not comprise truly monosized particles and this aspect is revisited later in this chapter.

Stellenbosch University http://scholar.sun.ac.za

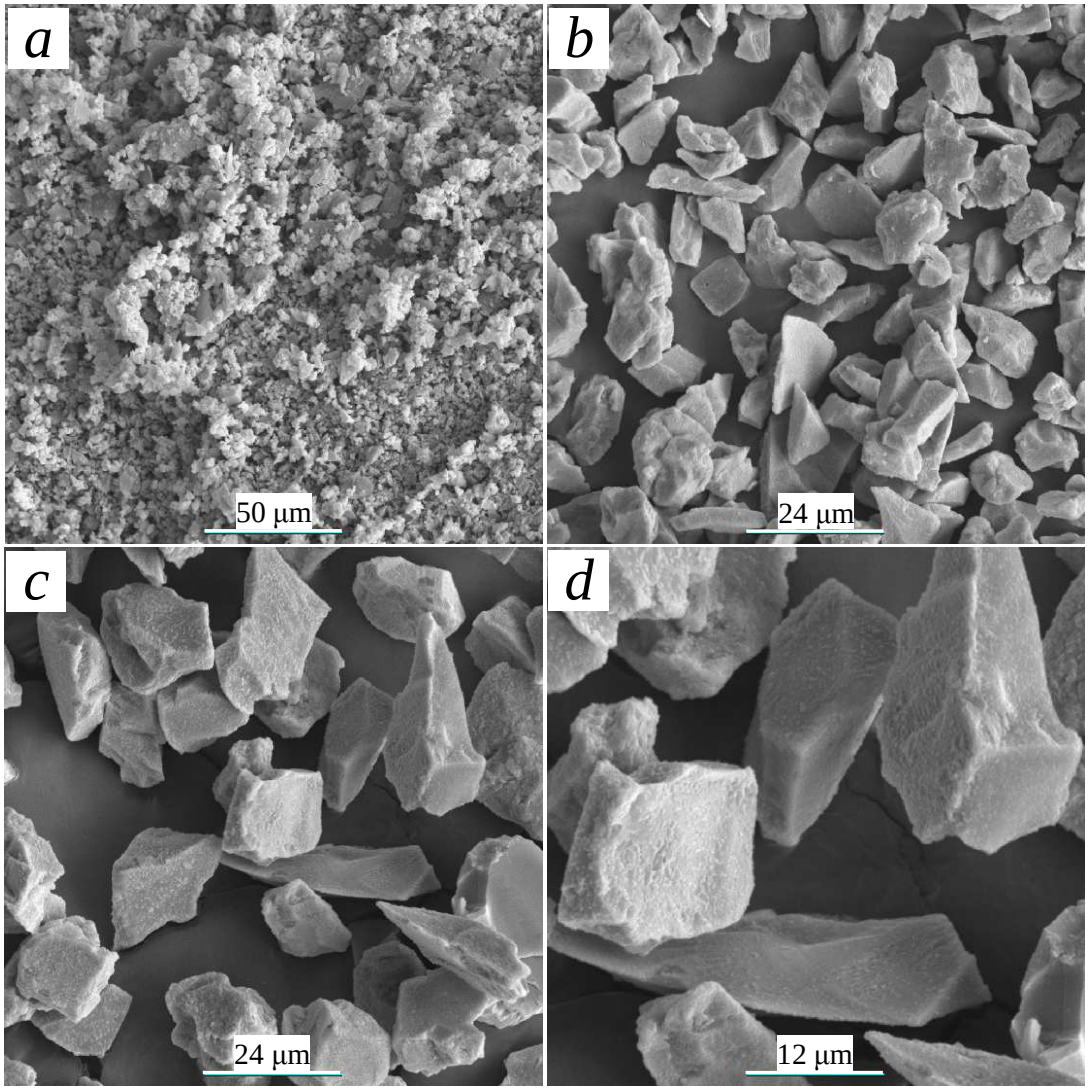

Figure 6.25
SEI of the HBMS 777 samples used in the batch oxidation testwork: *a*) Sample after 7 min milling in the SMD (500× magnification); *b*) Sample C (d_{50} 10.5 µm, 88% span, 1000× magnification); *c*) Sample D (d_{50} 20.8 µm, 95% span, 1000× magnification; d) Sample D (2000× magnification).

Mineralogical and chemical composition

Qualitative X-ray diffraction (XRD) analysis (App. B.3.2) of the HBMS 777 concentrate suggests that the major sulfide mineral phases were chalcopyrite >> pyrite > sphalerite > pyrrhotite. Galena (PbS) and arsenopyrite (FeAsS) only occurred in trace proportions. The mineralogical (bulk modal) composition was quantified with a scanning electron microscope (SEM)-based image analyser (App. B.3.2). The total sulfide mineral content was around 88 wt% for the pilot plant feed and 98 to 99 wt% for the above samples. These narrow size fractions (A, B, C & D) were thus naturally upgraded (in terms of sulfide mineral content) by successive washing, ultrasonic 'cleaning' and cyclosizing. Table 6.5 summarises the mineral breakdown of the two samples (C & D) used in most of the batch testwork; these abundances are reported as the average of two analyses, *i.e.*, average

Stellenbosch University http://scholar.sun.ac.za

results of normal-polished and perpendicular-polished sections. The mineralogical composition of the unmilled pilot plant feed (Sect. 7.3) is also presented.

Table 6.5
Detailed mineralogical abundance (bulk modal) analyses of unmilled pilot plant feed & narrow-sized (batch) head concentrate samples (HBMS 777).

Mineral	[a] Pilot plant (%)	Sample C (%)	Sample D (%)	Average (C, D) (%)
Chalcopyrite	68.51	81.54	80.86	81.2
Chalcocite/Digenite	0.01	0.01	0.01	0.0
Covellite	0.05	0.00	0.00	0.0
Sphalerite	7.64	6.52	6.38	6.5
Pyrite	10.27	8.81	9.09	9.0
Pyrrhotite	1.31	1.52	1.62	1.6
Galena	0.08	0.04	0.04	0.0
Arsenopyrite	0.03	0.03	0.04	0.0
Other sulfides	0.20	0.14	0.11	0.1
Magnetite	0.11	0.02	0.03	0.0
Hematite	0.01	0.01	0.01	0.0
Goethite	0.02	0.03	0.03	0.0
Other oxides	0.09	0.07	0.06	0.1
Carbonate	0.60	0.05	0.06	0.1
Quartz	1.92	0.16	0.19	0.2
Chlorite	0.34	0.18	0.21	0.2
Mica	0.37	0.04	0.08	0.1
Feldspar	0.29	0.02	0.03	0.0
Amphibole	1.95	0.06	0.08	0.1
Other silicates	1.10	0.69	1.05	0.9
Other	5.10	0.05	0.02	0.0
Total	100.00	99.99	100.00	100.0

[a] Composite sample collected over the course of the pilot plant campaign from unmilled material (Sect. 7.3.3).

Salts were present in the pilot plant feed material, consisting of unidentified ([Cu,Fe,Zn,Ag][As,Sb]) sulfate phases. These Cu-rich sulfate salts occur as conglomerates of very fine material and are associated with chalcopyrite. For the purpose of the mineralogical investigation, these conglomerates are broadly classified into four types; Ca(Cu,Zn,Fe,Cd) sulfate, (Cu,Zn,Fe,Cd) sulfate, (Cu,Zn,Co) sulfate and Fe-rich sulfate. The total estimated concentration of these complex conglomerates is about 5% in the pilot plant feed, but less than 0.1% in the narrow-sized fractions, suggesting that it was either water soluble or disintegrated during micro-screening.

Stellenbosch University http://scholar.sun.ac.za

Gangue minerals were identified as amphibole/pyroxene, quartz, chlorite, calcite, mica, feldspar and iron oxides. The total gangue concentration (excluding carbonate phases) is 6.2% in the pilot plant feed material and 1.5% in the narrow-sized fractions.

The copper sulfide minerals consist almost entirely of chalcopyrite, with insignificant chalcocite and covellite phases. The total base metal sulfide (BMS) minerals are well liberated (see App. B.3.2 for details on these measurement techniques). Around 93% of the total particle surface area (TPSA), *i.e.*, not the polished section area) falls within the >80 liberation class, while 78% of the chalcopyrite surface area falls within this class (Figure 6.26).

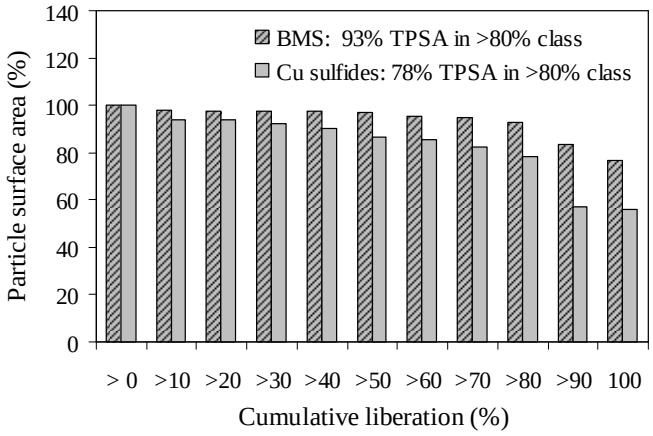

Figure 6.26
Comparison between base metal sulfide (BMS) & copper sulfide liberation (cumulative) in terms of the total particle surface area (TPSA) of narrow-sized HBMS 777 concentrate (Sample D).

These trends suggest some association between chalcopyrite and other sulfide minerals, predominantly sphalerite and pyrite, but very little association between BMS and gangue minerals. Backscatter electron (BSE) images of narrow-sized fractions C and D were produced on the SEM (App. B.3.2). These photomicrographs are presented in Figure 6.27, confirming that most mineral particles were well liberated (the apparent PSDs in these images are completely coincidental). Intergrowths of different sulfide minerals, not shown in these images, were visible but rare. Two particles of intergrown chalcopyrite and gangue minerals are highlighted by the arrows, *i.e.*, referring to narrow-sized fraction D. Although some particles may appear to have been in physical contact with each other, this is just an artefact of sample preparation and the overwhelming majority of particles was fully liberated.

Sample D represents the coarsest of the four narrow-sized fractions and mineral liberation would be expected to be even higher in the case of the finer fractions (A, B & C). Chalcopyrite is therefore well liberated, which made these samples ideal for testing the (batch) dissolution kinetics.

Stellenbosch University http://scholar.sun.ac.za

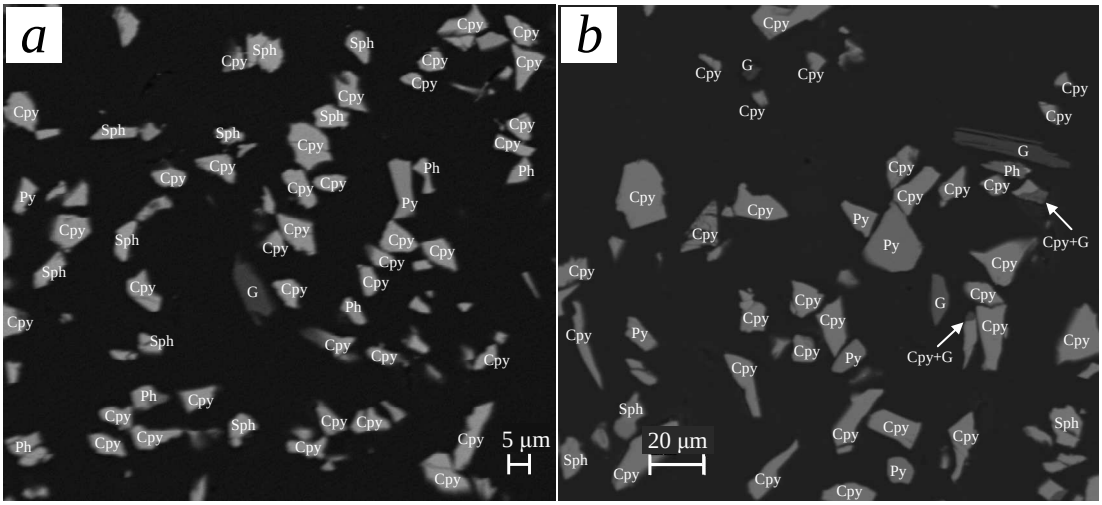

Figure 6.27
BSE images of HBMS 777 narrow-sized fractions, used in most of the batch oxidation testwork: chalcopyrite (*Cpy*), pyrite (*Py*), Pyrrhotite (*Ph*), sphalerite (*Sph*), gangue (*G*) &, intergrown chalcopyrite & gangue (*Cpy* + *G*): *a*) Sample C; *b*) Sample D.

Table 6.6 presents a summary of the chemical analysis results. The results of the pilot plant feed material are presented as the average of 27 analyses, conducted over the course of the pilot campaign. A direct comparison between the chemical assays and mineralogical analyses reveals that the latter method underestimates the proportion of copper and, especially, iron in the pilot plant feed. In all likelihood, this resulted from the unknown and variable sulfate phases in the pilot feed material. This discrepancy is not as evident for the narrow-sized fractions, where relatively little of the unknown phases were present, which further supports this argument.

Table 6.6
Chemical analyses of milled pilot plant & narrow-sized (batch) feed material (HBMS 777).

	Chemical analyses (%)					
Species	[a] Pilot plant	A	B	C	D	[b] Average
Cu	24.70	28.12	28.34	28.64	28.90	28.5
Fe	29.00	29.14	29.67	30.10	29.25	29.5
Zn	4.23	4.45	4.62	4.51	4.87	4.6
Ca	0.16	0.02	0.02	0.01	0.03	0.0
Mg	0.06	0.01	0.01	0.01	0.01	0.0
SO_4	1.81	0.12	0.17	0.09	0.06	0.1
S^{2-}	33.40	34.30	36.02	35.89	35.87	35.5
Total	93.36	96.16	98.85	99.25	98.99	98.3

[a] Average of 27 samples, analysed over the course of the pilot campaign (Sect. 7.3.3); [b] Average analyses of narrow-sized fractions, utilised in the (leaching) test mass balances (App. G).

A calculated mineralogical breakdown is also derived from these chemical assays, and assumed to yield a more accurate measure of the solid-phase composition. This is the preferred methodology of

Stellenbosch University http://scholar.sun.ac.za

reconciling the experimental rate constants with other batch and continuous data and models (Ch. 7 & 8). The average calculated composition of the four narrow-sized samples is 82.3% chalcopyrite, 7.5% pyrite, 6.9% sphalerite and 1.3% pyrrhotite, assuming all the copper and zinc were present as chalcopyrite and sphalerite, respectively, and neglecting the presence of trace sulfide species. An average molar ratio of sulfur in pyrite *vs.* all the iron-bearing phases, *i.e.*, $S_{Py}/(S_{Py}+S_{Ph})$, of about 0.9 is used in these calculations; this ratio is directly obtained from the mineralogical composition (Table 6.5). Similarly, the average composition of the pilot feed material is calculated to be 71.3% chalcopyrite, 10.9% pyrite, 6.3% sphalerite and 1.4% pyrrhotite. Both these calculated mineralogical compositions are in good agreement with the bulk modal analyses (Table 6.5). Further refinement may be introduced by including iron in solid solution with zinc sulfide (in sphalerite). This slightly improves agreement between the calculated and measured pyrite contents in the pilot plant feed material, but has the opposite effect for the (average) batch head material. This is not warranted for interpreting the batch data since the rounding error in the above-mentioned molar ratio is more than the impact of this refinement. However, for the higher pulp density testwork and models, this refinement is worth considering (see Ch. 7 & 8). The iron content in sphalerite phase, as derived from SEM-EDX (energy dispersive X-ray) scans (App. B.3.2), averages at around 7.5 wt% in the pilot feed material. No elemental sulfur was detected in any of the feed concentrate samples, while the magnesium and calcium in the pilot feed are assumed to have been present as acid-consuming carbonates, *i.e.*, stoichiometrically about 0.6% $(Ca,Mg)CO_3$.

6.5 Results and discussion

The overall objective of the batch leaching testwork program was to establish rate equations for the oxidation of the chalcopyrite concentrate, based on the bulk solution properties. Although electrochemistry is fundamental to the observed oxidation mechanisms, a phenomenological description is required in order to capture all the various aspects of the leaching chemistry.

6.5.1 Verifying the experimental procedure

The elimination of experimental start-up effects prompted the use of a high-pressure bomb to inject small volumes of reagent (solution) into the autoclave, *i.e.*, once the required test temperature had been reached. However, the water required to dissolve the copper and zinc sulfate salts, prior to injection, resulted in unwanted temperature disturbances. For this reason, the required amounts of copper and zinc sulfate were dissolved with the initial slurry, *i.e.*, before heating commenced. As mentioned before, an advantage of this approach is that this heat-up procedure resembles, to some extent, the flow through the heat exchanger of the continuous pilot autoclave (Sect. 7.3.1), albeit at lower residual acid levels (< 2.5 g/L H_2SO_4, produced during heating). Table 6.7 presents the results of two tests (PLA1 & PLA2), using Sample C, without any acid injected or applied oxygen overpressure, but with varying copper concentration (the detailed results can be found in App. G.2).

Stellenbosch University http://scholar.sun.ac.za

Clearly, a small amount of the copper(II) reacted *via* metathesis reactions with sphalerite and, probably, also pyrrhotite. Small amounts of sulfide oxidised and the appearance (colour) of the residues suggests copper-rich surface layers formed. No in-depth investigation of this mechanism is warranted since the extent of this 'premature' chalcopyrite oxidation was minimal.

Table 6.7
Tests conducted at 150°C for 30 minutes (Sample C), without initial acid & oxygen overpressure.

Test number	Reaction extent (%)				Solids (%)				Solution (g/L)		
	Cu	Zn	Fe	S^{2-}	Cu	Zn	Fe	S^{2-}	$[Fe^T]$	[Fe(II)]	$[H_2SO_4]$
Initial composition	–	–	–	–	28.5	4.6	29.5	35.5	0.0	0.0	0.0
PLA1 (35 g/L Cu)	< 0	13	5	5	29.9	4.2	29.0	35.2	0.36	0.33	2.3
PLA2 (15 g/L Cu)	< 0	18	7	8	29.9	3.95	28.1	33.9	0.27	0.26	1.7

Section 6.4.2 highlighted the importance of conducting (batch) kinetic testwork at a lower solids content. However, accuracy is sacrificed when the test evaluation is based on low mass exchange of a species against an already high electrolyte background concentration of the same species. In addition, some degree of vapour leakage was almost always present, resulting in varying final solution mass. For these reasons, the extent of mineral oxidation is based on the solid-phase analyses. The absence of elemental sulfur formation in the tests conducted by Yu *et al.* (1972; Sect. 6.3.1), at less than 0.6 wt% solids, could suggest an enhancement of some reaction mechanisms at very low pulp density, *e.g.*, due to a higher ratio of oxygen concentration to surface area or even a particular crystal face (Sect. 6.3.4). Four tests were therefore conducted at relatively low acid (15 g/L H_2SO_4) and high copper (35 g/L) concentrations at 150°C, 700 kPa oxygen (based on the vapour pressure of pure water, *i.e.*, $p_{O2}°$) and in the presence of surfactants, again using the narrow-sized Sample C, but starting with 1.5 wt% (PLB1) and 0.5 wt% (PLB2) solids, respectively (all pulp densities are based on total slurry mass). These results are presented in Table 6.8 and the detailed results can be found in Appendix G.2.

Table 6.8
The effect of solids wt% (Sample C) on selected reaction extents at 150 °C, 700 kPa $p_{O2}°$, starting with 15 g/L H_2SO_4 & 35 g/L Cu.

Time (test) (min)	[a] Initial solids (%)	Cu extraction (%)	S^{2-} oxidation (%)	[b] S° yield (%)	[Fe(III)] (PLS) (g/L)
30 (PLB12)	1.5	43	45	51	0.37
120 (PLB15)	1.5	93	90	62	0.17
30 (PLB22)	0.5	42	48	53	0.21
120 (PLB25)	0.5	95	86	58	0.18

[a] At constant lignosulfonate (0.35 g/L LS) & Quebracho (0.35 g/L QB) concentrations; [b] $S°/S^{2-}{}_{rx} \times 100\%$.

Stellenbosch University http://scholar.sun.ac.za

These tests were conducted in the presence of calcium lignosulfonate (LS) (Norlig A, 58%) and Quebracho (QB) (Orfom grade 2 Tannin) (Sect. 6.3.3). These surfactants were used without any pre-drying to prevent oxidation, *i.e.*, to preserve their surface-active properties. For the same reason, they were injected into the autoclave 'at temperature' (Sect. 6.4.1). Clearly, these two pulp densities yield similar results; the sulfide to elemental sulfur conversion is similar (within the range of experimental error), suggesting that the reaction mechanism is not severely affected by pulp-density changes in this low range. The 1.5 wt% solids' content was used in most of the testwork, presented in this chapter as it yields superior mass accountability and sufficient residue mass for chemical analyses (including repeat analyses). The similar sulfide oxidation extents after 30 minutes oxidation time also suggest insignificant interfacial oxygen mass transfer limitations at these low pulp densities.

Table 6.8 also reveals that the iron(III) concentration, during the initial oxidation period, was significantly lower for the 0.5 wt% solids test; yet, the oxidation rate appears similar to that found for the test conducted at 1.5 wt% solids and a relatively higher iron(III) concentration in solution. Firstly, it is unlikely that any oxidant, *e.g.*, iron(III), saturation effects were prevalent under such low concentrations (Sect. 6.3.2) These results suggest, therefore, that a low iron(III) concentration plays a relatively insignificant role in limiting the chalcopyrite oxidation rate. In order to verify this conclusion, a comprehensive (multipoint) evaluation of the oxidation kinetics was conducted, using narrow-sized fraction D. These two series (App. G.2) were conducted at 1.5 wt% (Series PLC1) and 1.0 wt% (Series PLC2) solids, respectively, 25 g/L H_2SO_4, 15 g/L Cu and 0.35 g/L of each of the two surfactants at 150°C and 700 kPa oxygen (p_{O2}°). Each series consisted of a number of tests at different reaction times, but conducted under otherwise identical starting conditions. An additional 1 g/L Fe(II) was initially injected, 'at temperature', for each of the 1.0 wt% tests (PLC2), *i.e.*, in order to simulate the (steady-state) 2 to 3 g/L Fe tenor during continuous reactor operation (Ch. 7). In contrast, all the aqueous iron in the case of Series PLC1 originated from the concentrate itself. The lower pulp-density series (PLC2) was actually conducted a couple of years after the continuous pilot campaigns, while the higher pulp-density series (PLC1) followed immediately after those campaigns. Unfortunately, the surfactants used during the piloting campaigns (Ch. 7) and most of the batch tests in this chapter (Norlig A & Orfom 2) had degraded to such an extent that the alternatives (Arbo A02 & Orfom 2; Sect. 6.3.3) had to be used for Series PLC2. HBMS had also changed its suppliers by then and the original surfactants could not be easily obtained. These results are compared in Figure 6.28 and Table 6.9. The copper leaching rate (USP model) is only slightly lower for the tests conducted with Arbo A02, under similar average iron(III) concentrations in solution (Figure 6.28 *b*). However, the corresponding zinc extraction rates and elemental sulfur yields are significantly lower, despite the slightly higher residual acid concentration in the pregnant leach solution (PLS). These results suggest a change in mineral behaviour when using these

Stellenbosch University http://scholar.sun.ac.za

different surfactants. Although not proven conclusively, the workings of the surfactants appear to have outweighed the more subtle effects of changing solution composition.

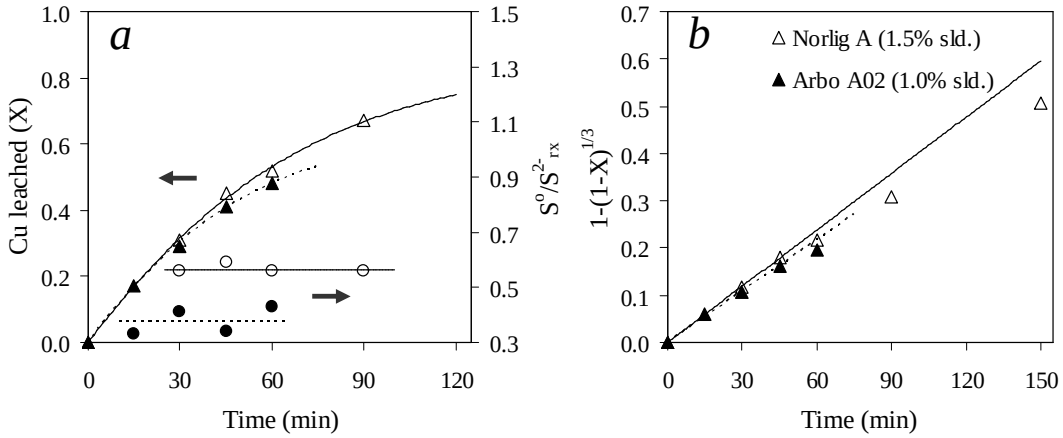

Figure 6.28
Comparison of reaction extents & rates (Sample D, 25 g/L H_2SO_4, 15 g/L Cu & 0.35 g/L LS, QB) using different iron introduction methods at 150°C (700 kPa p_{O2}°); open symbols represent 1.5 wt% solids (no initial Fe injection) & Norlig A LS; closed symbols represent 1 g/L Fe(II) injected at 1.0 wt% solids & Arbo A02 LS: *a*) Reaction extents; *b*) USP model for surface reaction control (lines represent best fits; 0 – 45 min).

Table 6.9
Effect of initial iron concentration at 150 °C (Sample D, 700 kPa p_{O2}°, 25 g/L H_2SO_4 & 15 g/L Cu) & different LS sources (0.35 g/L).

Time (test) (min)	Solids (sln Fe) (%)	Cu extr. (%)	Zn extr. (%)	S^{2-} ox. (%)	[H_2SO_4] (PLS) (g/L)	[Fe (III)] (PLS) (g/L)
30 (PLC11)	[a] 1.5 (0 g/L Fe)	31	96	45	18.8	1.67
45 (PLC12)	[a] 1.5 (0 g/L Fe)	45	99	52	17.6	2.13
60 (PLC13)	[a] 1.5 (0 g/L Fe)	52	99	58	18.4	2.50
30 (PLC22)	[b] 1.0 (1 g/L Fe)	29	66	33	23.3	1.60
45 (PLC23)	[b] 1.0 (1 g/L Fe)	41	82	43	23.3	1.55
60 (PLC24)	[b] 1.0 (1 g/L Fe)	48	86	57	22.7	3.01

[a] Using 0.35 g/L LS (Norlig A) & 0.35 g/L QB; [b] Using 0.35 g/L LS (Arbo A02) & 0.35 g/L QB.

Another possible explanation for the lower sulfur 'yield' with Arbo A02 may be the preferential formation of polymeric sulfur (Sect. 6.3.2), *i.e.*, not all elemental sulfur dissolved in the organic solvent during chemical analysis (App. B.2.2). Therefore, the elemental sulfur may have reported as unreacted sulfides; hence, the lower apparent elemental sulfur yield and sulfide oxidation rate. All results, presented in the rest of this chapter, utilised the original Norlig A and Orfom 2 surfactants, *i.e.*, allowing direct comparison with the results obtained in the continuous pilot autoclave (Ch. 7). For the sake of simplicity, no iron was originally injected in any of these tests

Stellenbosch University http://scholar.sun.ac.za

and the temperature was kept constant at 150°C; no further reference will therefore be made to the operating temperature or the pulp density of 1.5 wt% solids (slurry basis). Generally, both acid and copper concentrations were limited to between 15 and 45 g/L, as this range spans typical variations encountered in the continuous pilot campaigns (Sect. 7.4.1).

Figure 6.28 *b* illustrates an approximately constant initial chalcopyrite oxidation rate but a deviation at longer reaction times (> 45 min). In order to ascertain whether this deviation from linearity is unique to the largest size fraction, and also to determine the reproducibility of the test procedure, several tests (Series PLD1 & PLD2; App. G.2) were conducted using narrow-sized Sample C. In order to eliminate (possible) direct oxidation of elemental sulfur by oxygen, and thereby simplifying experimental interpretation, a relatively high initial acid concentration (35 g/L H_2SO_4) was used. The LS and QB concentrations were kept constant at 0.35 g/L and the oxygen partial pressure at 700 kPa (p_{O2}°); these results are illustrated in Figure 6.29.

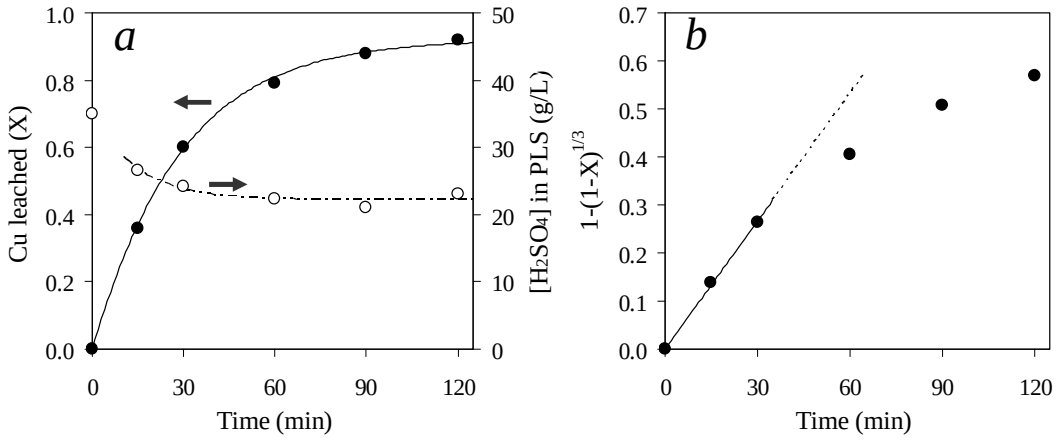

Figure 6.29
Copper leaching kinetics of Sample C (35 g/L H_2SO_4, 35 g/L Cu & 0.35 g/L LS, QB) at 700 kPa p_{O2}°: *a*) Cu leaching extent & residual acid concentration (PLS); *b*) USP model for surface reaction control (line represent best fit; 0 – 30 min).

Once again, the USP-model plot for surface reaction control (Figure 6.29 *b*) reflects initially linear leaching kinetics, but a definite deviation after about 45 minutes. The acid concentration decreased to within 15% of the final average value (~23 g/L H_2SO_4) within 15 minutes' reaction time. The reaction regime change is therefore not caused by a change in acid concentration over time and the experimental procedure is assumed to be adequate to obtain initial oxidation rate data. Since it is practically difficult to obtain rate data over the first few minutes, the linear regression is forced through the origin. This procedure essentially averages any start-up effects over the full regression, *i.e.*, an apparently rapid dissolution rate during the first few minutes, due to the presence of ultra-fine particles, reactive surface layers and higher initial acid concentration. In addition, it provides a clearer picture of sudden deviations from linear kinetics (Figure 6.29 *b*), since the reference (zero)

Stellenbosch University http://scholar.sun.ac.za

point is always fixed. In any event, the net impact of these start-up effects is expected to be relatively insignificant due to the thorough sample preparation procedure (Sect. 6.4.3).

In order to instil confidence in these results, a few of the kinetic datapoints were repeated, with additional tests at 45 and 150 minutes of oxidation time (Series PLD2; App. G.2). These repeat tests were conducted towards the end of the batch experimental program, close to five months after the initial set was completed. Figure 6.30 compares these repeat tests with the initial dataset.

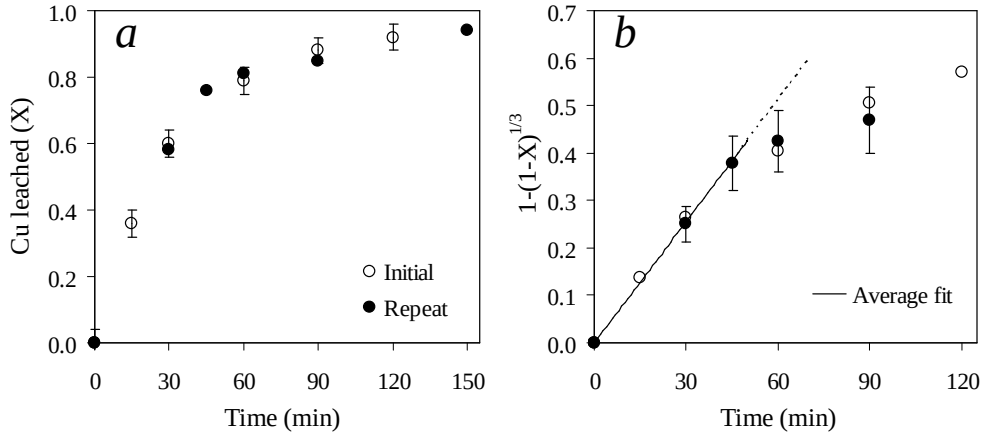

Figure 6.30
Repeatability testwork (Sample C, 35 g/L H_2SO_4, 35 g/L Cu, 0.35 g/L LS, QB) at 700 kPa p_{O2}°: *a*) Cu leach extent; *b*) USP model for surface reaction control (line represents best fit; 0 – 45 min).

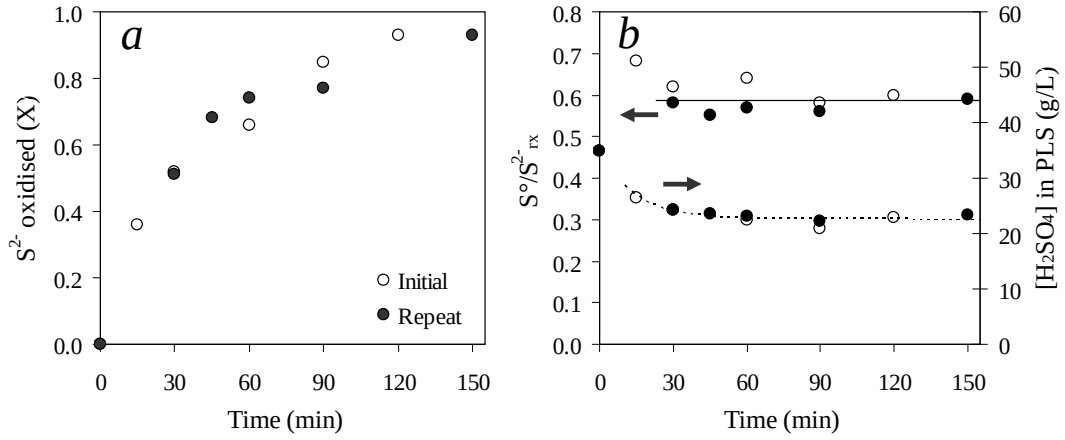

Figure 6.31
Repeatability of sulfur speciation (Sample C, 35 g/L H_2SO_4, 35 g/L Cu & 0.35 g/L LS, QB at 700 kPa p_{O2}°: *a*) Sulfide oxidation extent; *b*) Sulfur yield & residual acid concentration (PLS).

The copper extractions of the repeat tests are within 4% of the initial tests (Figure 6.30 *a*), *i.e.*, resulting in at least about 15% accuracy of the rate constant (Figure 6.30 *b*), when using data points

Stellenbosch University http://scholar.sun.ac.za

between 35 and 90% copper extraction. However, this represents a conservative estimate due to the statistical spread introduced by conducting an individual test for each kinetic data point, *i.e.*, statistically, this methodology improves the repeatability of the overall rate constant. On the other hand, solid phase sulfur speciation is relatively variable. Figure 6.31 *a* illustrates significant scattering of the sulfide oxidation extents, which would translate into inaccurate mineral oxidation rate constants, *e.g.*, if the residue sulfide assays are used to reconcile the degree of pyrite oxidation. Nevertheless, the data are assumed to be consistent enough to derive an average sulfur yield ($S°/S^{2-}_{rx}$) of 59±5%, while the PLS acid concentration (after 30 min) averages around 23 g/L H_2SO_4 (Figure 6.31 *b*) These trends suggest that no appreciable oxidation of stable elemental sulfur (to acid) occurs, once formed, *i.e.*, over these experimental timeframes.

A final test series was conducted (Series PLD3; App. G.2) at a significantly higher oxygen partial pressure, in order to determine whether the sulfur yield (related to the oxidation mechanism) deviates under relatively higher dissolved oxygen concentrations in solution. These results are presented in Figure 6.32.

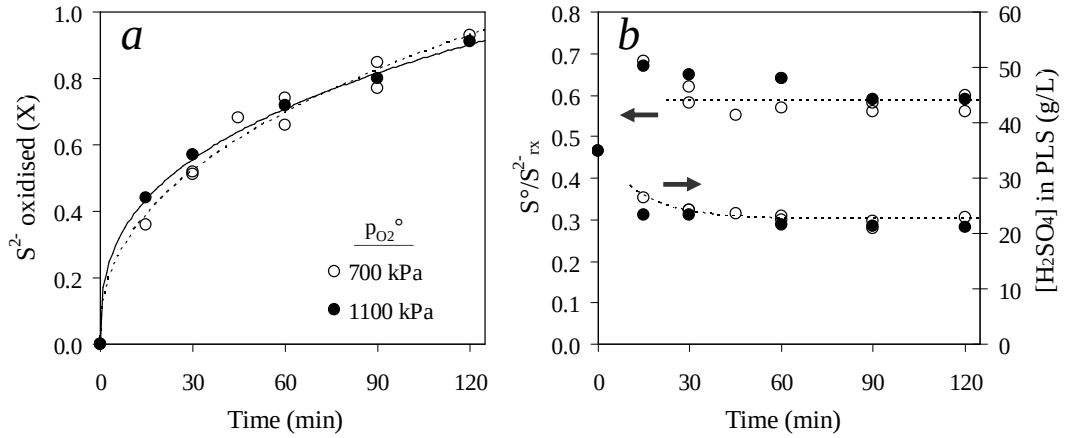

Figure 6.32
The effect of oxygen partial pressure on sulfur speciation (Sample C, 35 g/L H_2SO_4, 35 g/L Cu & 0.35 g/L LS, QB): *a*) Sulfide oxidation extent; *b*) Sulfur yield & residual acid concentration (PLS).

As expected, the initial sulfide oxidation extent increases, albeit slightly, with increasing oxygen partial pressure (Figure 6.32 *a*). Nevertheless, the elemental sulfur yield at 1100 kPa $p_{O2}°$ (after 30 min oxidation) is within, or very close, to the 59±5% average. This is also reflected by similar PLS acid concentration values for the 700 and 1100 kPa tests (Figure 6.32 *b*).

No mechanism change is therefore observed by doing testwork at low pulp densities. Neither were any interfacial oxygen mass transfer effects prevalent under these conditions. The reaction extents also respond, in a relatively consistent manner, to changes in solution composition and oxygen

Stellenbosch University http://scholar.sun.ac.za

partial pressure. However, the effect of different surfactant sources seems to have had a strong effect on the stability of sulfur forming on chalcopyrite surfaces. This testwork was therefore restricted to the same surfactants as those used during the continuous pilot campaigns (Sect. 7.4.1).

6.5.2 Reaction regimes

This section elaborates on the different reaction regimes present during the oxidation of the HBMS 777 chalcopyrite concentrate, under MT autoclave conditions. The previous section has highlighted the apparent deviation (after ~60 min) from linearity (USP model) for monosized samples under surface reaction control. Possible reasons for this include:

- Surface or product layers may form on the particles over time
- Film diffusion may become important, as the particles shrink to small sizes, and/or
- The distribution of initial particle sizes, albeit narrow, may influence the observed trends.

The first set of tests aimed to determine whether a change in the initial dosage of the surfactants would result in an extension or shortening of the linear region of the USP model plot under surface reaction control. All previous testwork utilised 0.35 g/L LS and 0.35 g/L QB. The following two series of tests used lower (0.2 g/L) and higher (0.5 g/L) surfactant concentrations, respectively, while keeping the initial solution matrix (35 g/L H_2SO_4 & 35 g/L Cu) and oxygen overpressure (700 kPa $p_{O2}°$) the same. The highest surfactant concentration (0.5 g/L) corresponds to a dosage of 4.5 kg/t (at 10 wt% solids), which could be considered relatively high (expensive) in industry. The tested range of 0.2 to 0.5 g/L is therefore adequate, *i.e.*, spanning surfactant concentrations that may be encountered in industrial operation (at typical pulp densities). The results of these tests are presented in Figure 6.33, while the detailed results can be found in Appendix G.3 (Series PLE1 & PLE2). The most interesting aspect of these results is the insensitivity of the kinetics towards the initial surfactants dosages (Figure 6.33). The regressed rate constants at these two extreme dosages (0.091 µm/min & 0.083 µm/min at 0.2 g/L & 0.5 g/L, respectively) are within 10% of the rate constant at 0.35 g/L LS and QB (0.090 µm/min). Variations of the degree of sulfide oxidation between these test series are erratic and no definite conclusion can be drawn regarding the effect of the initial surfactant concentration on any of the other mineral phases, except for sphalerite, which leached rapidly in all three cases. Although the linear region of the USP model plot (Figure 6.33 *b*) is slightly extended (up to 60 min) for the highest surfactants addition (0.5 g/L), a sudden and definite deviation from linearity prevails for all the tests at longer reaction times. The preliminary conclusion from these trends is that the surfactants became ineffective after an initial period (45-60 min) of rapid oxidation, and this is thought to be the primary reason for the sulfur blockage problems experienced in the latter compartments of the continuous autoclave during the pilot campaigns (Sect. 7.4.1). However, this deviation at higher reaction extents could also stem from the distribution of initial particle sizes, albeit narrow (Figure 6.24). Film diffusion may also

Stellenbosch University http://scholar.sun.ac.za

become more relevant as these (already small) particles shrink , *i.e.*, when reaching very low slip velocities, relative to the fluid phase.

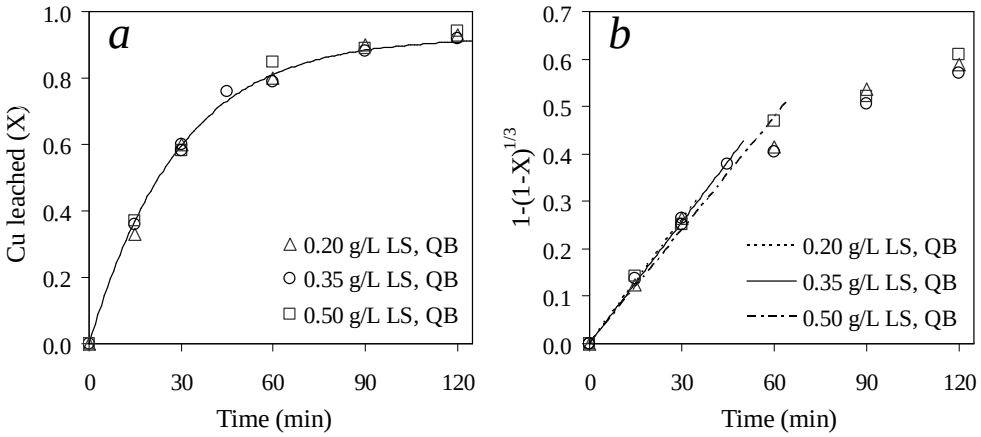

Figure 6.33
The effect of initial surfactants concentration on copper leaching extents & rates (Sample C, 35 g/L H_2SO_4 & 35 g/L Cu) at 700 kPa p_{O2}°: *a*) Cu leaching extent; b) USP model for surface reaction control (lines represent best fits; 0, 15, 30 min at 0.20 g/L; 0, 15, 30, 45 min at 0.35 g/L; 0, 30, 60 min at 0.50 g/L LS, QB).

In an attempt to establish the relative importance of film diffusion on the observed kinetics, tests were repeated (*ref.* Series PLD1 & PLD1, Figure 6.31, at 15, 45 & 150 min) at a lower agitation speed (750 rev/min), while keeping the other variables constant (35 g/L H_2SO_4, 35 g/L Cu, 0.35 g/L LS, QB & 700 kPa p_{O2}°). The outcome of these tests is compared with the 1000 rev/min series in Figure 6.34, while the detailed results can be found in Appendix G.3 (Series PLE3).

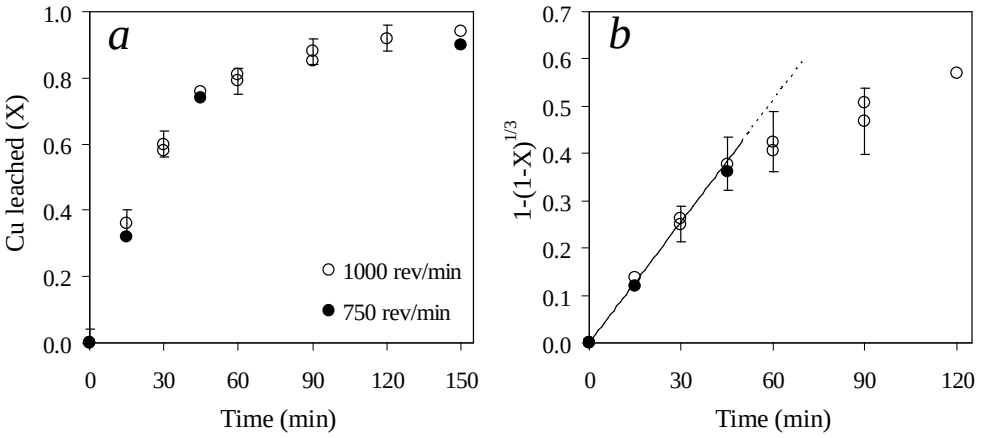

Figure 6.34
Effect of agitation speed on copper leaching extents & rate (Sample C, 35 g/L H_2SO_4, 35 g/L Cu & 0.35 g/L LS, QB) at 700 kPa p_{O2}°: *a*) Cu leaching extent; *b*) USP model plot for surface reaction control (line represent best fit of 1000 rev/min data; 0 – 45 min).

Stellenbosch University http://scholar.sun.ac.za

The reactions extents at lower agitation speed (750 rev/min) fall well within the experimental uncertainty (±4% *ref.* X_{Cu} & ±15% *ref.* k_ℓ) of the 1000 rev/min results, suggesting insignificant film diffusion limitations. With regard to oxygen mass transfer effects, the lower impeller speed represents a drop of at least 50% in the value of the mass transfer coefficient *cf.* the corresponding measured values at 1000 rev/min (Ch. 3; Table 3.9). This large difference in $k_L a$-values and the fact that the reaction extents are similar at different pulp densities (Table 6.8) is seen as sufficient proof that no mass transfer limitations were prevalent in the autoclave. Burkin (1966; pp.78), amongst others, has pointed out that the absence of an agitation speed effect may not necessarily prove that no intra-particle mass transfer limitations exist. However, the fact that the USP model plot (for chemical reaction control) shows linear behaviour over the first 45 to 60 minutes, even at low agitation speeds (Figure 6.34 *b*), proves that no such limitations were initially present. All subsequent leaching testwork was conducted at 1000 rev/min.

A follow-up test (Test PLE43; App G.3) investigated the effect of injecting additional fresh LS (0.35 g/L) and QB (0.35 g/L) at the point of deviation from linearity, *i.e.*, at 45 minutes leaching time, and recording the reaction extents after 60 minutes. Table 6.10 compares this result to the corresponding tests in which no additional surfactants were injected.

Table 6.10
Effect of additional surfactant injection on selected reaction extents (Sample C, 700 kPa p_{O2}°, 35 g/L H_2SO_4, 35 g/L Cu & 0.35 g/L LS, QB).

Time (test) (min)	[a] LS, QB (min)	Cu extraction (%)	S^{2-} oxidation (%)	S° yield (%)	$[H_2SO_4]$ (PLS) (g/L)
60 (PLD13)	0	79	66	64	22.4
60 (PLD23)	0	81	74	57	23.2
60 (PLE43)	0, [b] 45	77	62	71	23.3

[a] Initial injection time of 0.35 g/L LS & QB; [b] Injection of additional 0.35 g/L LS & QB after 45 min reaction time.

These results clearly indicate that no improvement in the rate of copper leaching is achieved by injecting additional surfactants after 45 minutes. The elemental sulfur yield appears to be higher for Test PLE43, but this may be an artefact of (an apparent) slower pyrite oxidation rate, *i.e.*, as derived from the unreacted total sulfide content. However, similar PLS acid concentrations suggest otherwise and, once again, the accuracy of the sulfur speciation results is questioned, despite good overall sulfur accountability. The residue samples at 45 minutes (before injection of fresh surfactants injection) and at 60 minutes (after injection of fresh surfactant injection) were mounted on carbon stubs and coated with Au-Pd alloy (App. B.3.3). Figure 6.35 *a* and *b* present the SEI of these two samples, respectively. EDX analyses (App. B.3.2) were conducted at two different points on the first image and are also represented. Figure 6.35 *a* clearly illustrates the formation of very small (< 20 µm) sulfur conglomerates, resulting in a decrease in total surface area of the unreacted

Stellenbosch University http://scholar.sun.ac.za

chalcopyrite mineral. EDX analyses, at two different points on Figure 6.35 *a*, also confirm that elemental sulfur can act as a 'collector' of unreacted sulfides and this clustering effect may explain the decrease in the observed reaction rate after 45 minutes in the autoclave. Fresh surfactant injection at 45 minutes results in a more rugged appearance of the conglomerates (Figure 6.35 *b*), but clearly is unable to disperse the conglomerates and no improvement of the reaction rate results. This is to be expected because these surfactants are large macro-molecules, which would diffuse with difficulty through molten sulfur (product layers) to adsorb on an unreacted sulfide mineral surface, *i.e.*, once molten sulfur has enveloped a chalcopyrite particle.

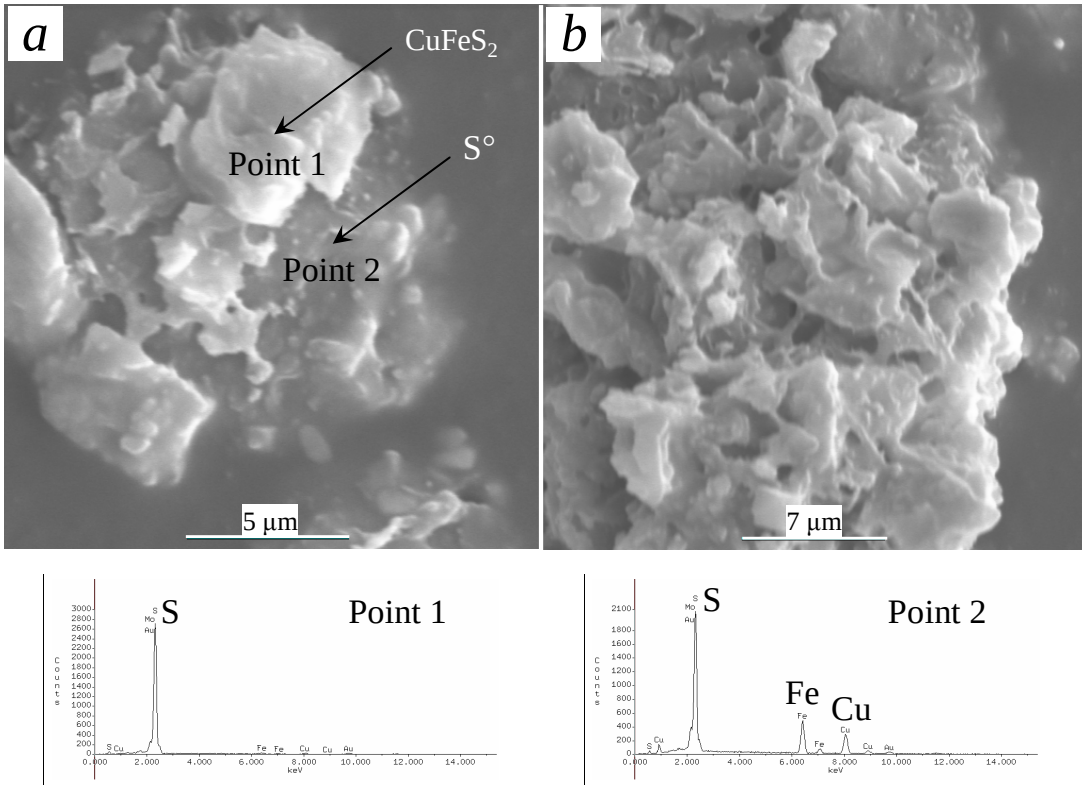

Figure 6.35
SEI & qualitative EDX analyses of selected autoclave residues (Sample C): *a*) After 45 min reaction time, with no additional surfactants (Test PLD13); *b*) After 60 min reaction time with additional surfactants injection at 45 min (Test PLE43).

Although elemental sulfur is a liquid at 150ºC, these conglomerates likely exist as kinetic entities in the autoclave, because liquid elemental sulfur and the electrolyte solution are not miscible. Rapid 'freezing' (by flushing a small sample from the autoclave at temperature) was utilised in order to obtain samples for producing these images, *i.e.*, the stirring action of the autoclave, during normal cooling, was not responsible for creating these conglomerates. The above results provide additional proof that the deviation from linearity (USP model plot, for particles under surface reaction control) is a likely result of the formation of molten elemental sulfur (product layers) around the unreacted mineral particles, *i.e.*, after a fixed oxidation time in the autoclave. No information was

Stellenbosch University http://scholar.sun.ac.za

found in the open literature regarding sulfur conglomerate formation in zinc autoclaves, *i.e.*, when oxidising sphalerite under MT conditions, in the presence of surfactants. Since the oxidation rate of sphalerite is significantly faster than the chalcopyrite oxidation rate (Sect. 7.4), no conclusions can be drawn from this lack of information.

Nevertheless, the rapid surfactant degradation could also result from the high PLS copper concentration in the case of chalcopyrite oxidation. Two series of tests were consequently conducted, starting with only 15 g/L copper (Series PLE5; App. G.3) and without any copper in the initial solution (Series PLE6; App. G.3), respectively. An additional series (PLE7; App. G.3), again investigated the effect of injecting additional fresh surfactants after 45 minutes reaction time. All these results are compared in Figure 6.36.

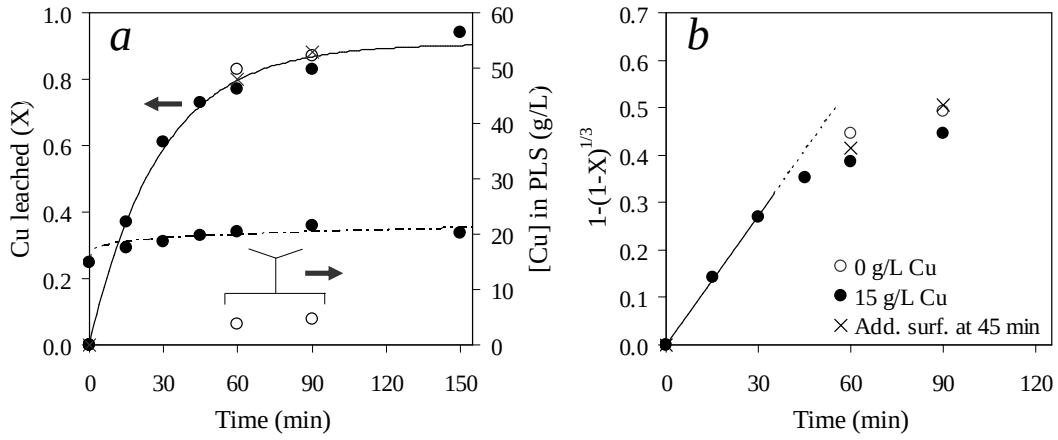

Figure 6.36
Effect of lower initial copper tenors on the extent & rate of copper dissolution (Sample C, 35 g/L H_2SO_4 & 0.35 g/L LS, QB) at 700 kPa p_{O2}°: *a*) Cu leaching extent; b) USP model plot for surface reaction control (line represents best fit of 15 g/L Cu series; 0 – 30 min).

Clearly, the deviation from the linear USP model plot is still prevalent at longer oxidation times (> 45 min), even without any initial copper in solution (Figure 6.36 *b*). The open data point at 60 minutes is somewhat closer to the straight line, suggesting an improvement in the dispersing action of the surfactants, *i.e.*, when no copper was initially present in solution. However, these results are marginal (close to experimental uncertainty) and no conclusion can be drawn regarding the relative effect of copper concentration on the degradation rate of the surfactants under MT autoclave conditions (positive oxygen pressures).

EDX analyses of the Au-Pd-coated particles (Figure 6.35) are qualitative and incapable of detecting very thin polymeric sulfur or metal-deficient polysulfide layers that could have been present (see Sect. 6.3.2). The apparent retardation in the leaching rate due to the presence of such surfaces, *i.e.*, as thin layers on the unreacted mineral surface, and the effect of the initial distribution of particle

Stellenbosch University http://scholar.sun.ac.za

sizes, albeit narrow, remained unknown. Follow-up tests, using different 'monosized' samples, hoped to address these issues and are discussed next.

6.5.3 Particle size effects at varying acid concentration

Each of the four narrow-sized fractions, *i.e.*, Sample A, B, C and D (Figure 6.24), was oxidised at 150ºC, starting with 15 g/L copper, 0.35 g/L LS and QB, and varying amounts of sulfuric acid. The detailed results of these tests can be found in Appendix G.4; Series F represents all tests with 15 g/L initial H_2SO_4 addition; Series G represents all tests (including repeats) with 25 g/L initial H_2SO_4 addition (Series PLC1, in App. G.2, represents Sample D results); Series H represents all tests with 35 g/L initial H_2SO_4 (Series PLE5, in App. G.3, represents Sample C results); and Series I represents all tests (including repeats) with 45 g/L initial H_2SO_4 addition. These results are illustrated below, after splitting the adjacent series (initial acid concentrations) between Figure 6.37 *a* and Figure 6.37 *b*, respectively. The most interesting aspect of these trends is that the higher acid concentration leads to accelerated initial copper leaching rates but shows reduced leaching rates at longer reaction times, especially for the coarser samples. Elemental sulfur is therefore more difficult to disperse at a higher acid concentration and this has a more pronounced effect on the slower-leaching, coarser particle size fractions.

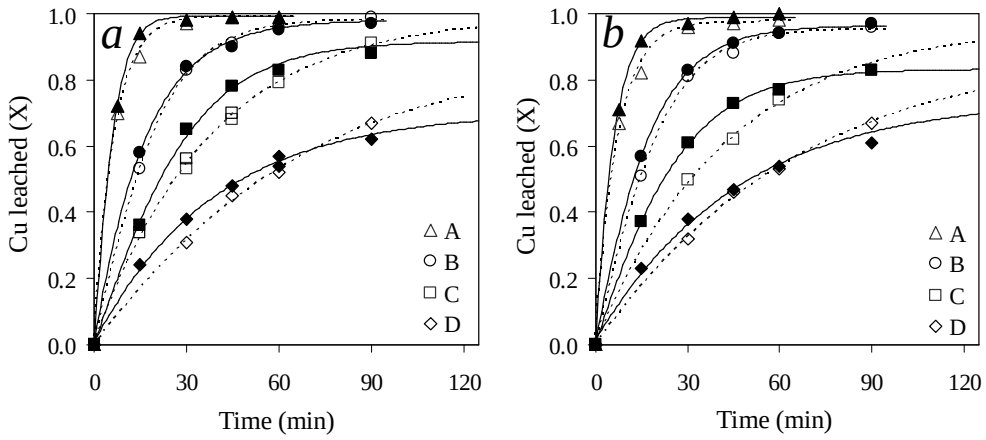

Figure 6.37
Effect of different initial (narrow) particle size fractions on the extent of copper dissolution, starting with 15 g/L Cu & 0.35 g/L LS, QB at 700 kPa p_{O2}°: *a*) 25 g/L H_2SO_4 (open symbols), 45 g/L H_2SO_4 (closed symbols); *b*) 15 g/L H_2SO_4 (open symbols), 35 g/L H_2SO_4 (closed symbols).

These results are therefore in agreement with the assumption that the deviation from linear USP model behaviour is due to inefficient sulfur dispersion after some reaction time in the autoclave.

A further test was conducted in order to illustrate the important role that elemental sulfur plays in the sulfide oxidation kinetics. This test was conducted for 30 minutes without any surfactant addition, using narrow-sized Sample B, and starting with 25 g/L H_2SO_4 and 15 g/L Cu (the detailed

Stellenbosch University http://scholar.sun.ac.za

results can be found in App. G.4; Test PLJ12). Table 6.11 compares the results of this test with those from an identical test (PLG22), conducted in the presence of 0.35 g/L LS, QB.

Table 6.11
Reaction extents with & without surfactants (Sample B, 700 kPa p_{O2}°, 25 g/L H_2SO_4, 15 g/L Cu).

Time (test) (min)	LS, QB inject (min)	Cu extraction (%)	S^{2-} oxidation (%)	S° yield (%)	$[H_2SO_4]$ (PLS) (g/L)
30 (PLG22)	[a] 0	83	88	58	17.4
30 (PLJ12)	None	61	61	55	19.7

[a] Initial injection of 0.35 g/L LS & 0.35 g/L QB.

Besides the clear drop in copper extraction for Test PLJ12, the absence of surfactants resulted in the collection of unreacted sulfides into relatively large sulfur conglomerates, varying between 0.1 and 5 mm in size. Figure 6.38 represents the SEIs of other test residues, produced under similar conditions, but without any surfactants, using narrow-sized Sample C.

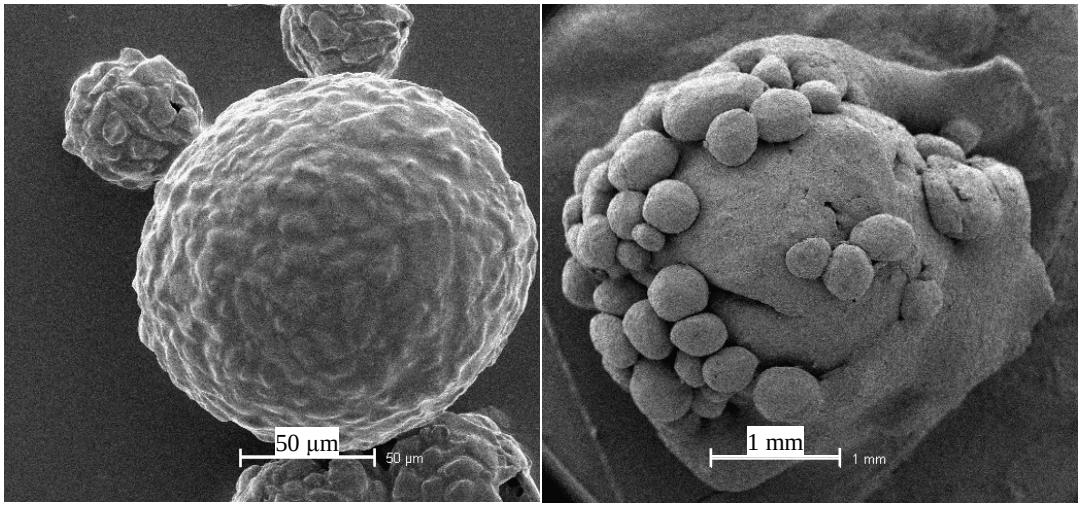

Figure 6.38
SEIs of selected residues (Sample C) after 30 minutes oxidation time, without any surfactants.

These results confirm that surfactants are indeed necessary, even for the finest particle size fractions. Nevertheless, degradation of the surfactants is responsible for an ultimate build-up of elemental sulfur around the unreacted mineral particles, which impacts more significantly on the coarser particle size fractions by virtue of their slower oxidation kinetics.

This point is further illustrated in Figure 6.39, which represents the USP model plots for the four narrow-sized fractions under surface reaction control. Although the initial leaching rates are higher at higher acid concentrations, it can be seen that stronger deviations from linearity occur later on, compared to the tests conducted at lower initial acid concentrations. The deviation from linearity for the fine particle size fractions (at high copper extractions) is probably caused by the width of

Stellenbosch University http://scholar.sun.ac.za

PSDs in the head samples, albeit narrow (Figure 6.24). Figure 6.40 compares the initial overall observed leaching rate constant, k_s (1/min), obtained from the USP model plots, against the inverse of the initial mean particle size (L_o).

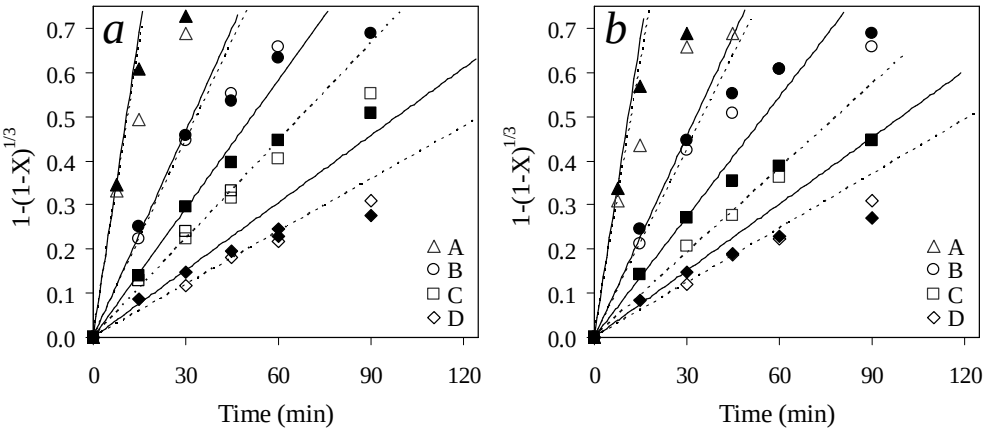

Figure 6.39
USP model plots (surface reaction control) for different narrow-sized fractions, starting with 15 g/L Cu & 0.35 g/L LS, QB at 700 kPa p_{O2}°: *a*) 25 g/L H_2SO_4 (open symbols), 45 g/L H_2SO_4 (closed symbols); *b*) 15 g/L H_2SO_4 (open symbols), 35 g/L H_2SO_4 (closed symbols).

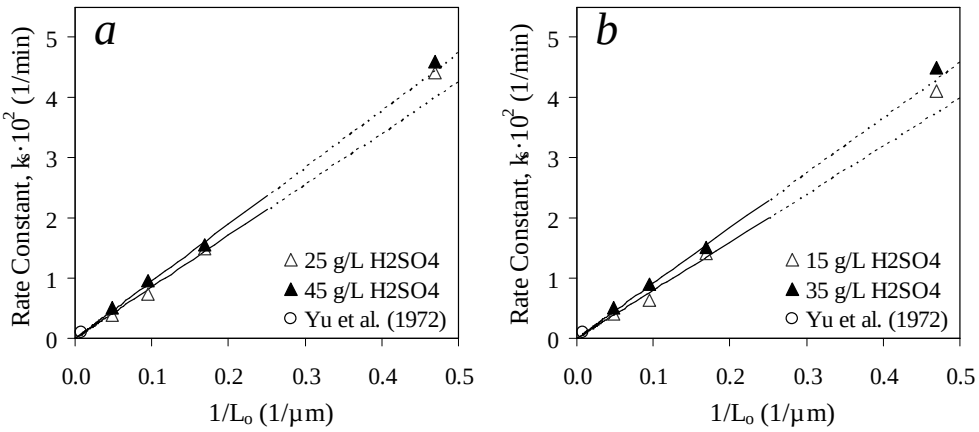

Figure 6.40
Initial overall rate constant *vs.* inverse of the mean particle size, starting with 15 g/L Cu & 0.35 g/L LS, QB at 700 kPa p_{O2}°.The lines represent linear regressions *ref.* the three coarser size fractions.

This linear relationship follows directly from Equation 6.156, where the slope yields the linear rate constants, k_ℓ (µm/min). It is interesting to note that the linear leaching rate constant measured by Yu *et al.* (1972), with very little (< 5%) elemental sulfur formation, is comparable to the initial linear rate constants obtained in this study. The trends illustrated in Figure 6.40 and the linear rate constants listed in Table 6.12, clearly illustrate an increased rate of chalcopyrite particle shrinkage with increasing acid concentration. The rate constants obtained from the finest narrow-sized

Stellenbosch University http://scholar.sun.ac.za

fraction (Sample A) are not considered particularly accurate due to the short reaction times available to obtain the kinetic data, relying in most cases on a single data point. Furthermore, this size-fraction was produced by further milling in the SMD, suggesting that mechanical activation could have resulted in an increased reaction rate (see, *e.g.*, Gerlach *et al.*, 1973).

Table 6.12
Initial linear rate constants, obtained at 700 kPa p_{O2}°, 15 g/L Cu & different acid concentrations.

Measured	$[H_2SO_4]_{to}$	[a,b] $[H_2SO_4]_t$	[a,b] $[Cu]_t$	[a,b] Density	k_ℓ (all sizes)	[b] k_ℓ (B, C, D)
–	(g/L)	(g/L)	(g/L)	(g/L)	(µm/min)	(µm/min)
This study	15	12.4	17.3	1053	0.087	0.082
This study	25	17.0	17.6	1062	0.093	0.086
This study	35	26.4	17.5	1069	0.096	0.097
This study	45	36.1	17.7	1075	0.098	0.101
Yu *et al.* (1972)	24.5	–	(<2.5)	–	[c] 0.166	–

[a] Avg. over the linear region of the USP model plot; [b] Referring to the three coarser narrow-sized fractions, *i.e.*, Samples B, C & D; [c] Using 0.5% solids, 124 µm (initial) avg. particle size & 689 kPa O_2.

The linear rate constants obtained from the three coarser fractions may be used to integrate over the initial distribution of particle sizes, *i.e.*, to establish whether the distribution of sizes, albeit narrow, caused the deviation from linear USP model behaviour. Substitution of Equation 6.156 into Equation 6.154, and integrating over varying initial particles size (L_o), yield the overall observed oxidation extent of a mineral (X_s) at any specific point in time (Sect. 7.2.4):

$$1-X_s(t) = \sum_{k_\ell t}^{L_{o,max}} \left(1 - \frac{k_\ell t}{L_{o,n}}\right)^3 W_{f,n} \qquad 6.160$$

where $W_{f,n} = W_f(L_{o,n})$ is the fractional weight of original mineral feed particles in a class *n*, with average size, $L_{o,n}$, (histogram obtained from the particle size analyser). Figure 6.41 and Figure 6.42 illustrate the leaching curves obtained for each of the narrow-sized head samples (solid lines) and also the average leaching curves, assuming no distribution of sizes, *i.e.*, using the median of the distribution (dotted lines). These results clearly illustrate that the deviations from linearity for the two finer particle size fractions (Samples A & B) were caused by the distribution of initial sizes. However, for the two coarser fractions (Samples C & D), the experimental data deviate from these models, thus confirming that a product layer diffusion mechanism was prevalent at longer reaction times. Generally, the higher the initial acid concentration, the higher the degree of deviation observed. The elemental sulfur is therefore more difficult to disperse under conditions of higher initial acid concentration. Figure 6.42 *b* also includes the result of a test (Test PLJ23) conducted for 45 minutes on a 60 minutes' residue, after removing all elemental sulfur with fresh tetrachloroethylene solution. Test PLJ23 was conducted by injecting the required amount of acid, iron(III) and iron(II) sulfate, and fresh surfactants into the pulp, resembling the solution

Stellenbosch University http://scholar.sun.ac.za

composition at 60 minutes residence time (Test PLI44). The solid sample was prepared by repeating Test PLI44 twice and removing all elemental sulfur from the combined residue (twice for 30 minutes at 80ºC). The amount of residue returned to the autoclave for Test PLJ23 resembles the amount of ore (without sulfur) left after 60 minutes, based on the residue analysis of Test PLI44. The rest of the residue sample was used for chemical analysis.

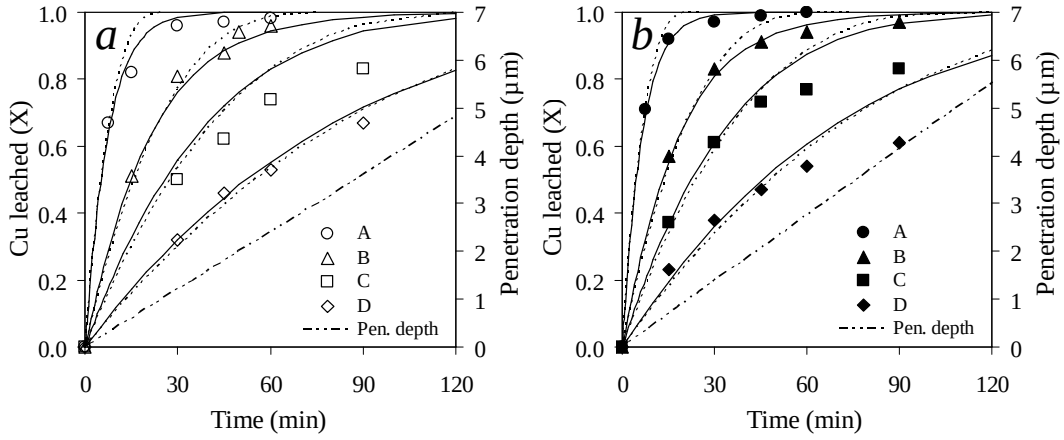

Figure 6.41
Comparison between the experimental copper extractions using narrow-sized fractions (symbols), the integrated (over particle size) USP model (solid lines) & the monosized USP model (at the median of the distribution; dotted lines), starting with 15 g/L Cu & 0.35 g/L LS, QB at 700 kPa p_{O2}°: *a*) 15 g/L H_2SO_4 (open symbols); *b*) 35 g/L H_2SO_4 (closed symbols).

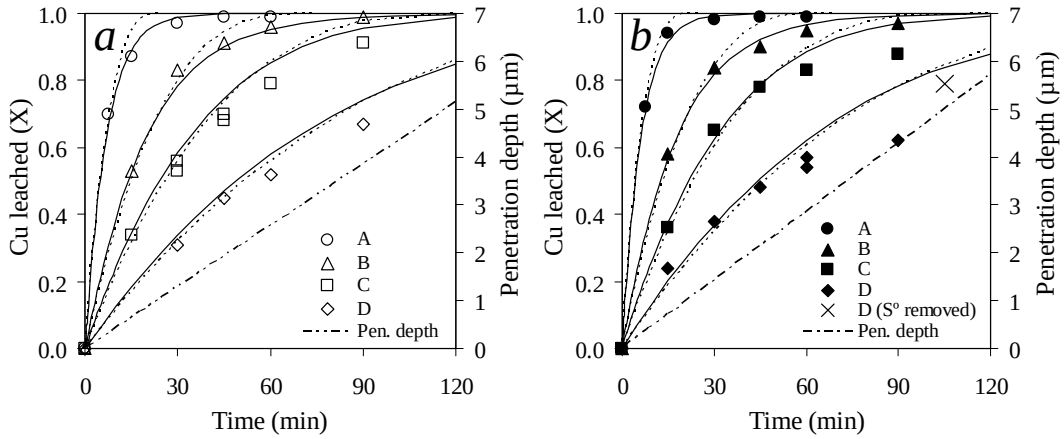

Figure 6.42
Comparison between the experimental copper extractions using narrow-sized fractions (symbols), the integrated (over particle size) USP model (solid lines) & the monosized USP model (at the median of the distribution; dotted lines), starting with 15 g/L Cu & 0.35 g/L LS, QB at 700 kPa p_{O2}°: *a*) 25 g/L H_2SO_4 (open symbols); *b*) 45 g/L H_2SO_4 (closed symbols); the open symbol (cross) represents total copper leached (after 105 min) with intermediate (60 min) S° removal.

Stellenbosch University http://scholar.sun.ac.za

Clearly (Figure 6.42 *b*), the reaction rate was re-established after elemental sulfur removal, confirming that molten elemental sulfur was responsible for stifling the oxidation reactions at longer leaching times. The above figures also include the calculated particle penetration depth (PPD) as a function of reaction time. The test conducted after the removal of the elemental sulfur translates into a PPD of just over 5 µm. This observation and the general trends presented in these figures suggest that the deviations from linearity (USP model plots in Figure 6.39) are not the result of passivation layers, but rather due to the distribution range of the initial particle sizes (at high copper extractions) and, especially, due to the formation of elemental sulfur conglomerates (at longer reaction times).

6.5.4 Validating the oxidation chemistry and mechanism on a phenomenological level

The previous sections have revealed various insights into the role of particle size and molten sulfur product layers on the kinetics of chalcopyrite oxidation under MT autoclave conditions. Nevertheless, very little information on the chemistry and mechanism of oxidation is apparent. This section attempts to reveal additional information on the chemistry (stoichiometry) and mechanism of oxidation, despite the phenomenological nature of the batch experiments.

The importance of iron(III) in the oxidation rate of sulfides is highlighted in Section 6.3.2, especially at lower temperatures. However, its relative importance in the direct oxidation of sulfide minerals in an acidic copper sulfate system under MT autoclave conditions remains unknown. The only study found to reveal some information in this regard is that of Yu *et al.* (1972), claiming a 13% increase in chalcopyrite oxidation rate with the initial addition of 1 g/L Fe(III) at 160°C. However, this marginal increase was observed under conditions of low background sulfate content, *i.e.*, a low (0.5%) solids content in the leach and no initial copper in solution. In order to quantify the importance of iron(III) as an oxidation agent, Test PLK12 (App. G.5) was conducted on a residue (Test PLE52, App. G.2; 30 min reaction time) after removing elemental sulfur with tetrachloroethylene solution. Series PLE5 (35 g/L H_2SO_4) yielded acid concentrations close to the steady-state concentration in the first two compartments of the pilot autoclave (Sect. 7.4.1) and was therefore the ideal baseline for this part of the study. The experimental procedure was similar to the sequence described in the previous section; it involved producing enough residue mass (30 min oxidation of Sample C; Test PLE52) and then resuming the pressure leach for another 30 minutes after elemental sulfur removal. The synthetic solution of the second oxidation step resembled the PLS after the first (30 min) oxidation, except that in this case, no iron was injected with the acid and fresh surfactants. Figure 6.43 *b* illustrates that the iron concentration rapidly built up to around 4 g/L Fe(III) in Series PLE5, while the USP model plot suggests a deviation from linearity after 45 minutes. The above-mentioned test (PLK12), resuming without any iron in solution, resulted in less than 1 g/L Fe(III) in the final PLS, *i.e.*, after a total oxidation time of 60 minutes. Although the rate

Stellenbosch University http://scholar.sun.ac.za

of leaching was re-established, it fell marginally short of the initial rate, suggesting some effect of iron(III) concentration in solution (Figure 6.43 *b*). However, the calculated extraction curve (solid line), based on the (initial) observed linear rate constant (0.095 µm/min; App. G.5) and integrating over the initial particle size distribution (Eq. 6.160), suggests that the chalcopyrite oxidation rate of Test PLK12 was only marginally lower than the initial leaching rate (~3% difference in total copper extraction; see Figure 6.43 *a*). This difference falls within the experimental error and it is therefore assumed that the iron(III) concentration is relatively unimportant in determining the rate of chalcopyrite oxidation at these relatively low levels.

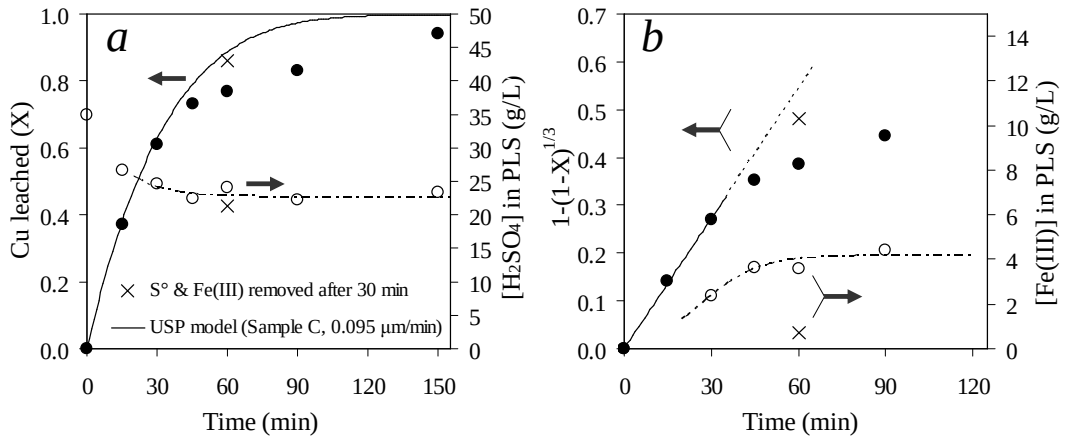

Figure 6.43
Comparison between the experimental data (symbols) & the integrated USP model (solid line), using Sample C & starting with 35 g/L H_2SO_4, 15 g/L Cu & 0.35 g/L LS, QB at 700 kPa p_{O2}°; *a*) Fraction Cu leached & [H_2SO_4] in PLS; *b*) USP model plot & [Fe(III)] in PLS. The open symbol (×) represent the reaction extents after 60 min, with intermediate (30 min) S° & Fe(III) removal.

It is, however, emphasised that this apparent insensitivity towards the iron(III) concentration is based on overall observed rates, lacking fundamental electrochemical information. As pointed out by Hiskey (1993), insensitivity of the leaching rate towards iron(III) concentration may be due to incipient surface film formation in the sulfate system.

The total reaction stoichiometry, *i.e.*, overall release of metal ions (Eq. 6.2) and sulfate ions (*e.g.*, reactions on Figure 6.22) into solution, is important from an engineering perspective and is discussed next. Previous discussions (Sect. 6.3.2) have emphasised that the exact stoichiometric relationship between the mineral oxidation extent and the oxygen consumption would be difficult to deduce from any phenomenological approach because multiple reactions occur simultaneously in these leaching systems. Nevertheless, the tests conducted using the finest particle size (Sample A) and starting with the two highest acid concentrations (35 & 45 g/L H_2SO_4), *i.e.*, Series PLH1 and PLI1, respectively, were used to gain some insight into the overall stoichiometry. Figure 6.44 *b* illustrates the behaviour of iron from a solution perspective.

Stellenbosch University http://scholar.sun.ac.za

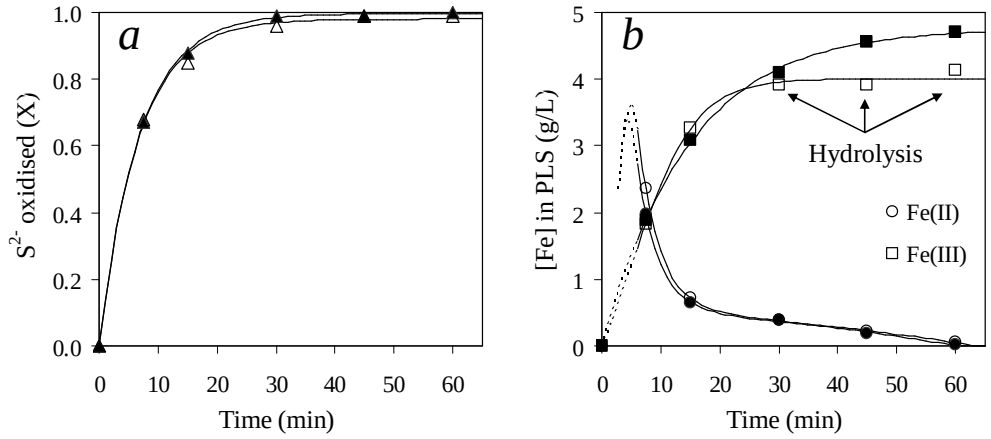

Figure 6.44
Iron transfer to the solution phase, using narrow-sized Sample A & starting with 15 g/L Cu, 0.35 g/L LS, QB at 700 kPa p_{O2}°. The open & closed symbols represent initial acid concentration of 35 g/L & 45 g/L H_2SO_4, respectively: *a*) Sulfide oxidation extent; *b*) [Fe(II)] & [Fe(III)] in PLS.

Figure 6.44 *a* illustrates the rapid rate of sulfide oxidation, while Figure 6.44 *b* points to a higher initial iron(II) concentration. In view of the apparent insensitivity of the chalcopyrite oxidation rate with respect of the iron(III) concentration (discussed above), these results suggest that most of the iron entered the solution in the reduced state. Precipitation of iron(III) started after 30 minutes for the 35 g/L H_2SO_4 series, whereas the free acid concentration for the 45 g/L H_2SO_4 series was too high to allow any precipitation. Therefore, most of the leached iron appears to have been oxidised in the bulk solution. From an engineering perspective (phenomenological modelling of the chemistry), it is necessary to check whether the preferential leaching of iron translates into non-stoichiometric ratios in the bulk solid and solution phases. The iron-to-sulfide and iron-to-copper ratios remaining in the solid phase are plotted against the total sulfide oxidation extent in Figure 6.45 *a*, *i.e.*, for all data points where neither iron precipitation nor high (> 85%) total sulfide oxidation occurred. If most of the iron remained in stoichiometric quantities in the unreacted chalcopyrite and pyrite phases, and assuming the other iron-containing phases (sphalerite & pyrrhotite) oxidised rapidly, a consistent molar ratio of around 0.5 would be expected. Clearly, most of the experimental molar ratios fell below this level, suggesting that some preferential leaching of iron may have occurred, especially at higher sulfide oxidation extents. On the other hand, the iron-to-copper molar ratios in the solids (Figure 6.45 *a*) and solution (Figure 6.45 *b*) appear random, with no consistent indication of preferential iron leaching. This apparent contradiction suggests that the trend towards lower iron-to-sulfide molar ratios in the solid phase (triangles in Figure 6.45 *a*) may be the result of sulfur speciation errors. As mentioned before, it appears that some solid samples, especially at higher oxidation extents, contained polymeric sulfur. This sulfur may not have dissolved in the organic solvent during the sulfur speciation analyses (App. B.2.2), translating into inaccurate residual sulfide levels. When the metal content in the solid

Stellenbosch University http://scholar.sun.ac.za

phase is relatively low, even a small error in the residual sulfide content would translate into a significantly lower than expected molar ratio of iron to sulfide. On the other hand, when using the residual sulfide analyses as basis, such errors would suggest a lower pyrite oxidation extent.

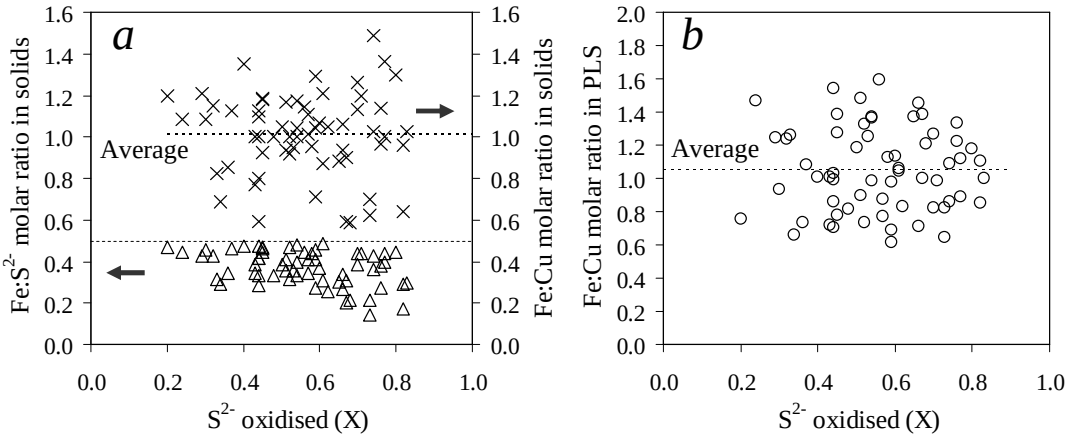

Figure 6.45
Molar ratios of iron to other species in bulk solid & solution phase, using all the leaching results where no iron precipitation occurred & where the total sulfide oxidation was below 85%: *a*) Molar ratio of Fe:S^{2-} & Fe:Cu in solid phase; *b*) Molar ratio of Fe:Cu transferred to the PLS.

The average molar ratio of iron to copper in all the leach residues, containing no iron precipitation products, is about 1.0, while the corresponding solution transfer occurs at an average molar ratio of about 1.0(5). The theoretical iron-to-copper ratio, based on the mineralogical analysis of the head material and assuming chalcopyrite and pyrite minerals leach at the same limiting rate, varies between 1.09 and 1.14, depending on the inclusion of sphaleritic iron at the expense of pyrite, or *vice versa* (see end of Sect. 6.4.3). Although these figures suggest no (little) preferential leaching of iron, *i.e.*, from a bulk property perspective, no conclusive evidence has been presented in this regard. Although such a mechanism is likely at work at the mineral surface, affecting its rate of dissolution, the engineering model requires a more accurate description than depicted in Figure 6.45. In addition, the comparative oxidation rates of chalcopyrite and pyrite are important factors that need to be quantified; these issues are revisited below.

The next two series of tests were conducted at different oxygen partial pressures in order to compare the concentrations of iron(II) in solution over time. These tests utilised Sample C, starting at relatively low acid (25 g/L H_2SO_4) and copper (15 g/L) concentrations. The detailed test results can be found in Appendix E.4 (Series PLG3 & PLG4) for the baseline condition, *i.e.*, 700 kPa oxygen ($p_{O2}°$), whereas the series conducted at the alternative pressures, *i.e.*, 250 kPa and 1500 kPa oxygen ($p_{O2}°$), are presented in Appendix E.5 (Series PLL1 & PLL2, respectively). Figure 6.46 presents these results and points to an increase in sulfide oxidation rate with increasing oxygen pressure (Figure 6.46a), confirming the importance of the cathodic reaction (see Figure 6.22).

Stellenbosch University http://scholar.sun.ac.za

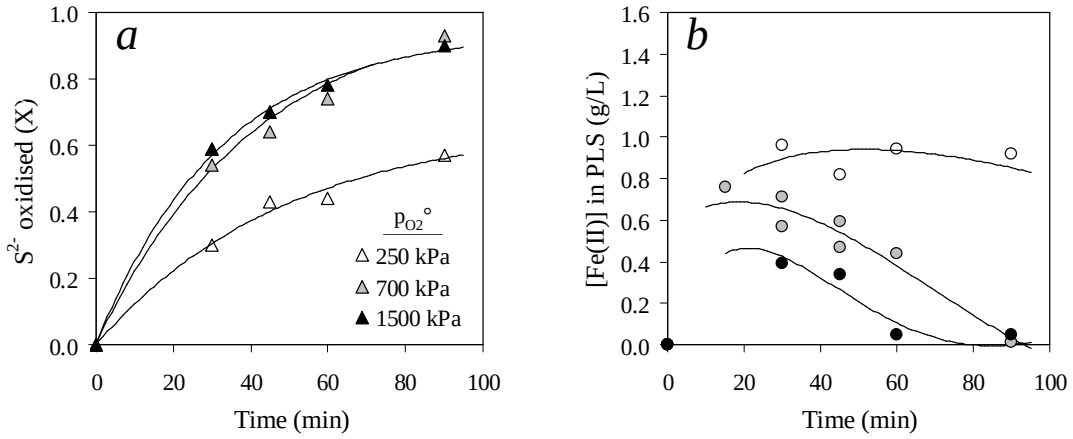

Figure 6.46
Effect of oxygen partial pressure, using narrow-sized Sample C & starting with 25 g/L H_2SO_4, 15 g/L Cu & 0.35 g/L LS, QB: *a*) Sulfide oxidation extent; *b*) [Fe(II)] in PLS.

As expected, Figure 6.46 *b* confirms that a lower applied oxygen partial pressures result in higher iron(II) concentrations in solution. As a first estimate, it is assumed that all the iron from chalcopyrite dissolution enters the solution in the reduced state, before being oxidised to iron(III) in the bulk solution (this assumption is re-evaluated in Ch. 7). In the same vein, it is assumed that copper(I) is first oxidised to the copper(II) state, before being released into solution. There is no net effect of this assumption on the overall electron balance for the chalcopyrite dissolution reaction. In the case of pyrite, it is assumed that there are so many oxidised species swamping the surface (see Figure 6.17), that all pyritic iron enters the solution in the oxidised state.

Figure 6.47 *a* presents the various copper leaching extents at different oxygen partial pressures, while Figure 6.47 *b* gives the corresponding USP model plots, suggesting that higher oxygen pressures cause a stronger deviation from linearity. It is therefore assumed that oxygen is primarily responsible for surfactant degradation, *i.e.*, the surfactants are essentially oxidised (combusted) over time. The elemental sulfur yield of each test is also presented in Figure 6.47 *a*; all three pressures give sulfur yields of 61±5%, except for a couple of (higher) points at 250 kPa. This value compares favourably with the sulfide-to-elemental sulfur conversion (59±5%) presented in Figure 6.32 *b*, also conducted at different pressures, but starting off at significantly different conditions. Therefore, despite the scattering of data (due to analytical error), the sulfur yield appears to be relatively insensitive to the solution composition and potential at 150ºC. This aspect is reviewed in more detail in the next section, with the objective of finding the stoichiometric coefficients (values for *y* or *z*; see Figure 6.22).

Stellenbosch University http://scholar.sun.ac.za

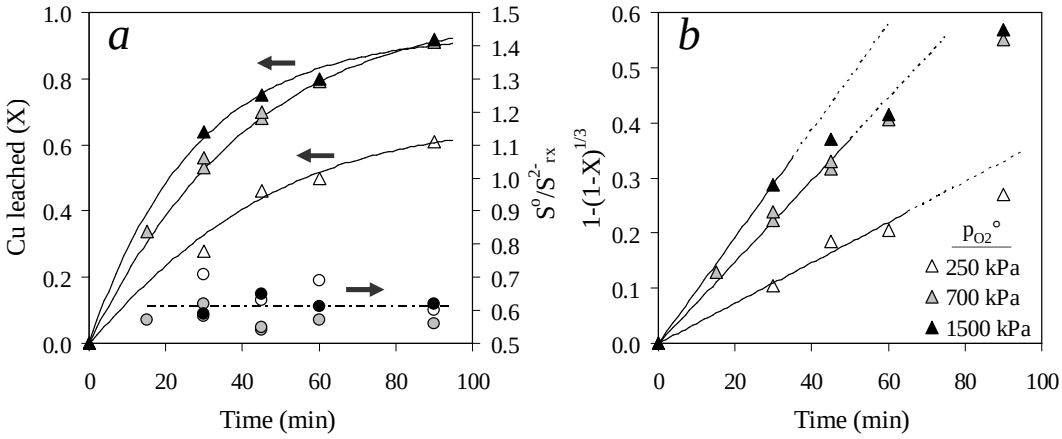

Figure 6.47
Effect of oxygen partial pressure, using narrow-sized Sample C & starting with 25 g/L H_2SO_4, 15 g/L Cu & 0.35 g/L LS, QB: *a*) Copper leaching & sulfur yield extents; *b*) USP model plots for surface reaction control (lines represent best fits; 0 – 60 min at 250 kPa & 0 – 45 min at 750 kPa & 1500 kPa).

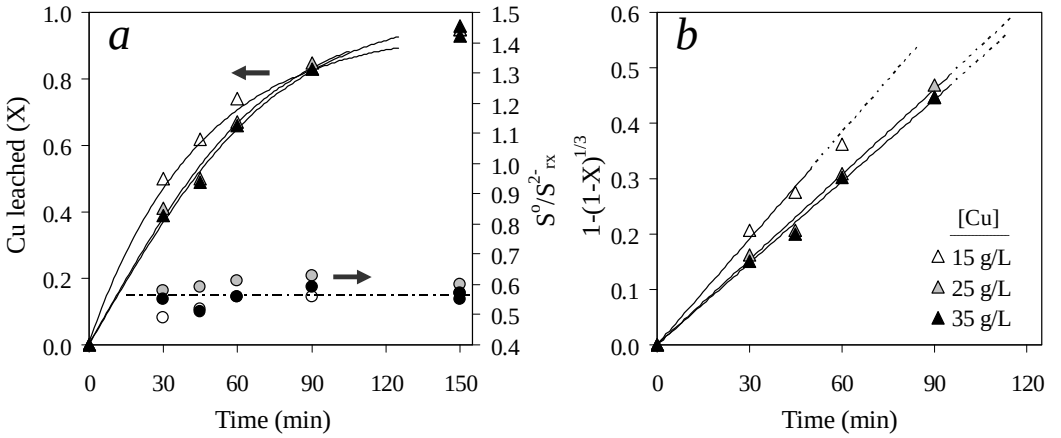

Figure 6.48
Effect of initial copper concentration on reaction extents, using narrow-sized Sample C & starting with 15 g/L H_2SO_4 & 0.35 g/L LS, QB at 700 kPa $p_{O2}°$: *a*) Copper leaching & sulfur yield extents; *b*) USP model plots for surface reaction control (lines represent best fits; 0 – 45 min at 15 g/L Cu & 0 – 90 min at 25 & 35 g/L Cu).

The final phase of the preliminary experimental programme investigated the effect of the background electrolyte composition on the rate of copper and iron leaching kinetics, and the corresponding sulfur yields. The tested ranges of salt concentration represent typical concentrations expected in the continuous integrated circuit (Sect. 7.4.1). All these tests were conducted using Sample C at 150ºC, 700 kPa oxygen ($p_{O2}°$) and 0.35 g/K LS, QB. The detailed results can be found in Appendix G.5 (Series M, N & O), whilst some results were also drawn from the other sections in Appendix G; Figure 6.48 to Figure 6.54 summarise these results.

Stellenbosch University http://scholar.sun.ac.za

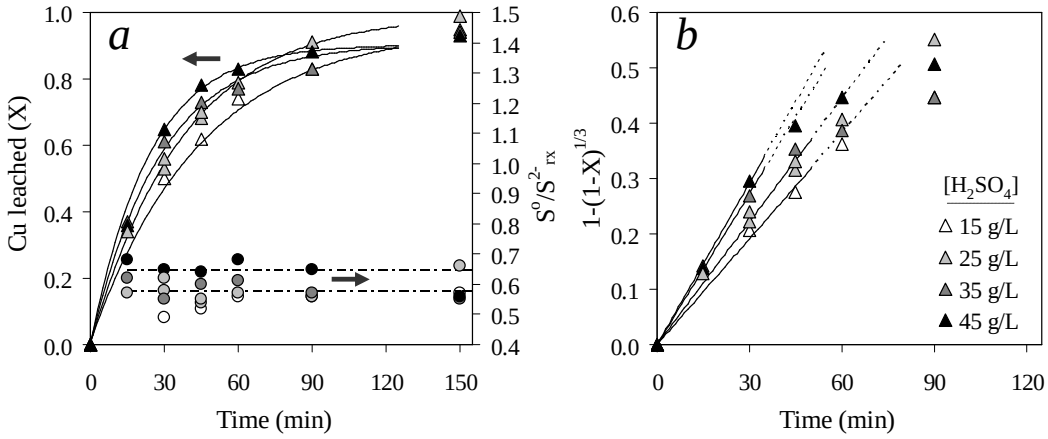

Figure 6.49
Effect of initial acid concentration on the reaction extents, using narrow-sized Sample C & starting with 15 g/L Cu & 0.35 g/L LS, QB at 700 kPa p_{O2}°: *a*) Copper leaching & sulfur-yield extents; *b*) USP model plot for surface reaction control (lines represent best fits; 0 – 30 min at 15 g/L & 25 g/L H_2SO_4, & 0 – 45 min at 35 & 45 g/L H_2SO_4).

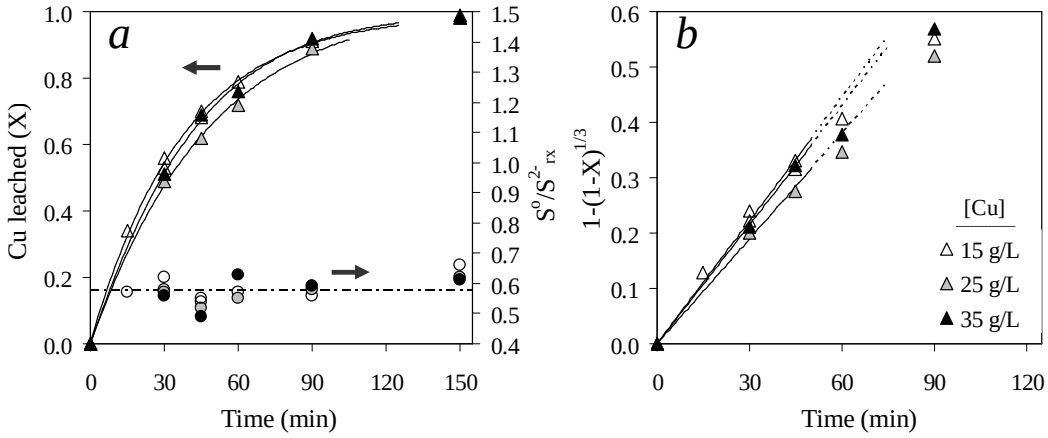

Figure 6.50
Effect of initial copper concentration on reaction extents, using narrow-sized Sample C & starting with 25 g/L H_2SO_4 & 0.35 g/L LS, QB at 700 kPa p_{O2}°: *a*) Copper leaching & sulfur-yield extents; *b*) USP model plot for surface reaction control (lines represent best fits; 0 – 45 min).

Stellenbosch University http://scholar.sun.ac.za

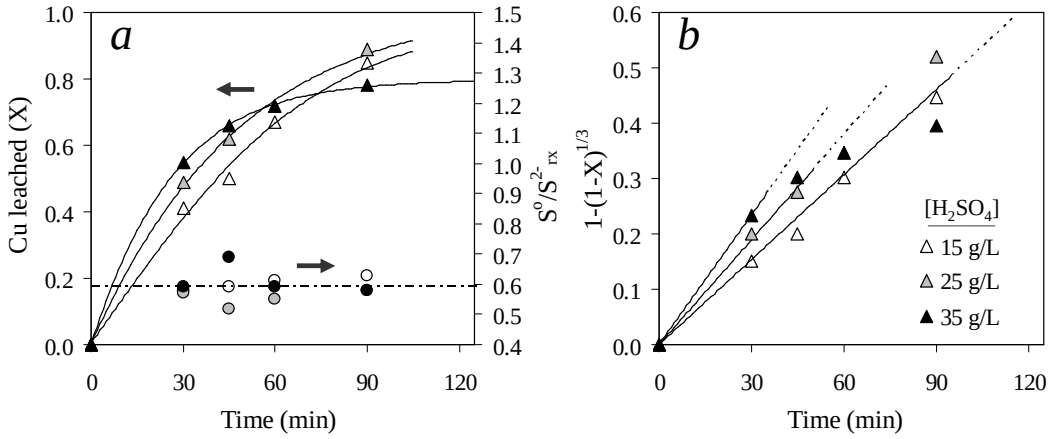

Figure 6.51
Effect of initial acid concentration on reaction extents, using narrow-sized Sample C & starting with 25 g/L Cu & 0.35 g/L LS, QB at 700 kPa p_{O2}°: *a*) Copper leaching & sulfur yield extents; *b*) USP model plot for surface reaction control (lines represent best fits; 0 – 90 min at 15 g/L H_2SO_4, 0 – 45 min at 25 g/L H_2SO_4 & 0 – 30 min at 35 g/L H_2SO_4).

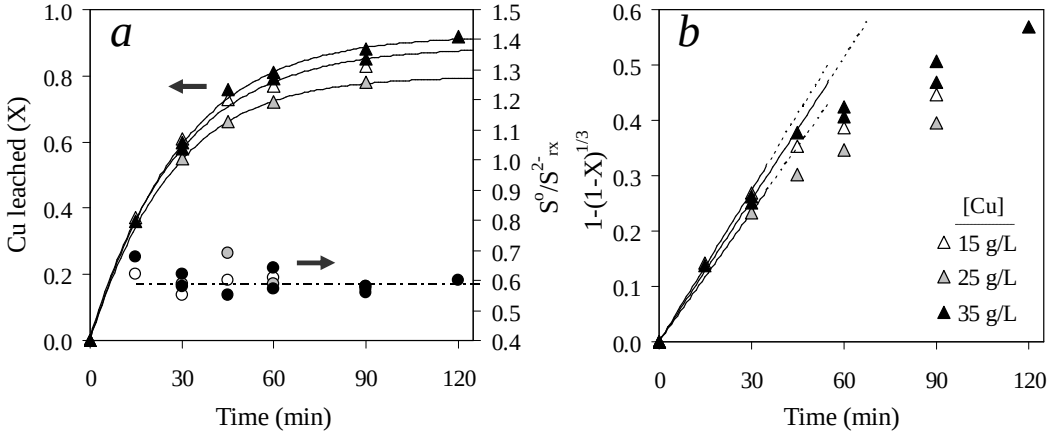

Figure 6.52
Effect of initial copper concentration on reaction extents, using narrow-sized Sample C & starting with 35 g/L H_2SO_4 & 0.35 g/L LS, QB at 700 kPa p_{O2}°: *a*) Copper leaching & sulfur yield extents; *b*) USP model plot for surface reaction control (lines represent best fits; 0 – 30 min at 15 & 25 g/L Cu & 0 – 45 min at 35 g/L Cu).

Clearly, the reaction kinetics are relatively insensitive to the background sulfate salt concentration, while increased acid concentrations consistently accelerate the oxidation rate. Another consistent trend is the apparent increase in the deviation from linear USP model behaviour at a higher acid concentration (see Figure 6.49, Figure 6.51 & also Figure 6.53), which confirms that elemental sulfur is primarily responsible for these deviations. The elemental sulfur yield is insensitive to the background electrolyte composition, except for the tests conducted at very high acid and low sulfate concentrations (45 g/L H_2SO_4, 15 g/L Cu; see Figure 6.49 *a*).

Stellenbosch University http://scholar.sun.ac.za

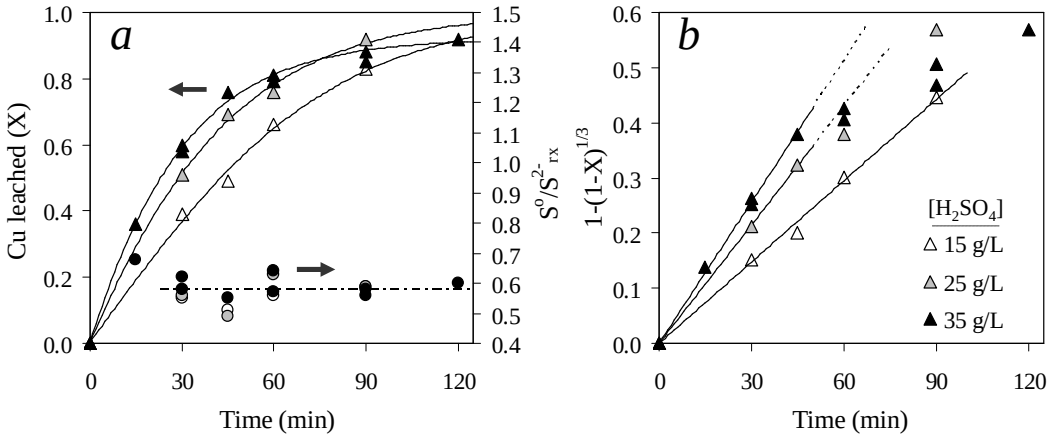

Figure 6.53
Effect of initial acid concentration on reaction extents, using narrow-sized Sample C & starting with 35 g/L Cu & 0.35 g/L LS, QB at 700 kPa p_{O2}°: *a*) Copper leaching & sulfur-yield extents; *b*) USP model plot for surface reaction control (lines represent best fits; 0 – 90 min at 15 g/L H_2SO_4, & 0 – 45 min at 25 & 35 g/L H_2SO_4).

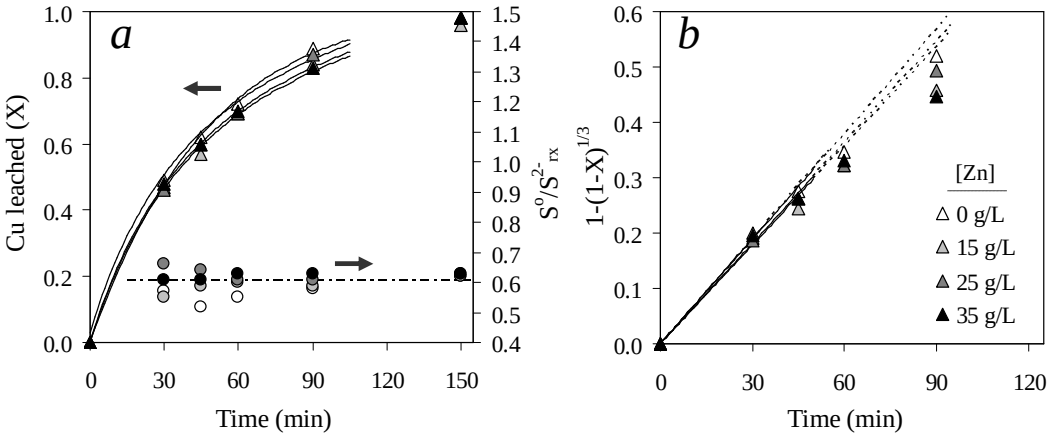

Figure 6.54
Effect of initial zinc concentration on reaction extents, using narrow-sized Sample C & starting with 25 g/L H_2SO_4, 25 g/L Cu & 0.35 g/L LS, QB at 700 kPa p_{O2}°: *a*) Copper leaching & sulfur yield extents; *b*) USP model plot for surface reaction control (lines represent best fits; 0 – 30 min at 15 g/L Zn, & 0 – 45 min at 0, 25 & 35 g/L Zn).

One of the conclusions from these results is that significant copper concentration changes (15 to 35 g/L Cu) have insignificant influence on the reaction rate, except for the low acid case (15 g/L H_2SO_4; Figure 6.48), which may be ascribed to solution phase equilibria changes affecting the free hydrogen ion concentration; this assumption is revisited later in this section. There is therefore no need to quantify the variation of θ (Cu_xS) (Eq. 6.153) with changing solution properties. An important consequence of the lack of sensitivity towards copper and iron(III) concentrations (discussed previously), is that the intrinsic rate expression (Eq. 6.153) may be simplified. With the

Stellenbosch University http://scholar.sun.ac.za

charge transfer coefficient of electron exchange on the mineral surface assumed to be one half (β_8 = ½; see Eq. 6.153), the overall dissolution rate of chalcopyrite may be expressed as follows:

$$r_{Cpy} = k_{Cpy}[H^+]^{\frac{1}{2}n_8}[O_2]^{\frac{1}{2}} + \theta_{Py_c} a_{Py} k_{Py_c}[H^+]^{\frac{1}{2}(m_1+n_1)}[O_2]^{\frac{1}{2}} \qquad 6.161$$

At low pulp densities, the second (pyrite) term would also be expected to become redundant. This rate expression is simple and relies on a high surface coverage of a covellite-like mineral, which would allow relatively fast oxygen reduction under MT autoclave conditions.

In order to test this hypothesis, three leach residues were examined, using a reflected light microscope and a mineral liberation analyser (MLA; App. B.3.2), *i.e.*, after 15 minutes (Test PLC21) and 60 minutes (Test PLC24) at 700 kPa $p_{O2}°$, and 60 minutes at 250 kPa $p_{O2}°$. Definite rims were visible around the majority of the chalcopyrite and sphalerite particles in the 15 minutes residue. Figure 6.55 indicates that these rims are only a few microns thick and also extend into the fractures of the host chalcopyrite particles.

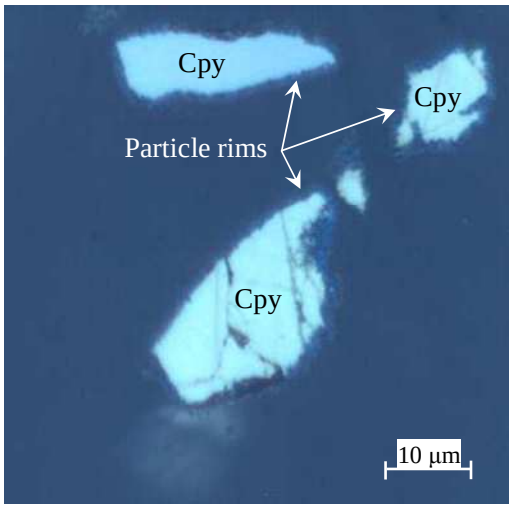

Figure 6.55
Optical microscope image of leach residue after 15 minutes oxidation; Test PLC21, Sample D, 25 g/L H_2SO_4, 15 g/L Cu & 0.35 g/L LS (Arbo A02), QB (Orfom 2) at 700 kPa $p_{O2}°$.

EDX analyses indicated that these particle rims contain of high copper and oxygen levels, with iron concentration decreasing towards the outer edge. These rims could not be analysed accurately using the BSE images. However, the clarity and detail of the field emission gun (FEG-SEM) (App. B.3.2) images, in conjunction with these optical observations, suggest that the outer rim is copper sulfate and the inner layer a discontinuous rim of covellite. The bimodal composition of the rims around a chalcopyrite particle is illustrated in Figure 6.56. The reason that the copper sulfate rim could not be distinguished by reflected light microscopy may be due to the high reflective pleochroism of covellite, masking any view of adjacent thin copper sulfate rims.

Stellenbosch University http://scholar.sun.ac.za

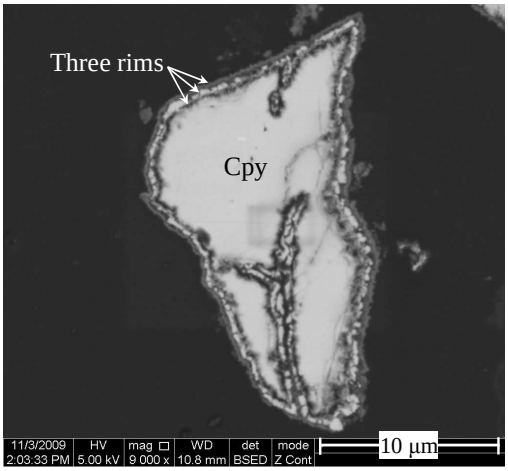

Figure 6.56
BSE image of chalcopyrite rims at lower oxygen partial pressure (250 kPa p_{O2}°) after 60 minutes oxidation; Sample D, 25 g/L H_2SO_4, 15 g/L Cu & 0.35 g/L LS (Arbo A02), QB (Orfom 2).

In the case of this residue, produced at a lower solution oxidation potential (250 kPa p_{O2}°), both the outer copper sulfate and inner covellite rims around chalcopyrite grains were distinguishable. This phenomenon was confirmed using FEG-MLA imaging, but again could not be conclusively proven by EDX analysis. It appears that even with the smaller electron-beam diameter achievable on this instrument, the rim sizes were smaller than the excitation envelope, therefore precluding its accurate analysis (Safi & Dinham, 2009). The alteration rims around the chalcopyrite host particles also appear to be discontinuous and their role in inhibiting chalcopyrite oxidation may therefore be questioned. Furthermore, residues produced over longer times at higher oxidation potentials (60 min at 700 kPa p_{O2}°) revealed no particle rims.

It is therefore concluded that these mineralogical techniques provide accurate imaging of surface phenomena, occurring in fine-grained residues, but as far as EDX analyses are concerned, these only served as a useful adjunct to X-ray photoelectron spectroscopy (XPS; App. B.3.6). The latter technique was particularly useful in comparing the surfaces of the two 60 minute residues with the head material (narrow-sized Sample D). These results are summarised in Table 6.13, while Figure 6.57 presents selected XPS spectra. In short, the head sample surface appeared to be partially oxidised to sulfate. The residue produced at a high solution potential (700 kPa p_{O2}°) contained a high concentration of copper(I), associated with monosulfide, suggesting the formation of a covellite surface (Goh *et al.*, 2006). At lower oxygen partial pressure, the surface clearly consisted of copper(II) sulfate, overlying a di-or polysulfide mineral. Both residues also contained some elemental sulfur, although no such layers were evident from mineralogical measurements and imaging (they may, however, have dissolved in the epoxy resin of the polished sections) or SEI imaging (see later). The absence of well-developed elemental sulfur product layers, even after 60 minutes oxidation, is a consistent feature when using Arbo A02 LS.

Stellenbosch University http://scholar.sun.ac.za

Table 6.13
XPS depth profile speciation data for head & 60 minute residue samples (Shackleton, 2009).

Sample (min)	Etch level (sec)	[a] Distribution (atomic percentage)	[b] Description –
Head (D)	0 (Top)	58% O, 19% S, 3% Cu {77% Cu(I)}	Mainly sulfate
	180	50% O, 27% S, 13% Cu {93% Cu(I)}	[b] Mainly sulfide (some sulfate)
	350	48% O, 31% S, 14% Cu {95% Cu(I)}	[b] Mainly sulfide (some sulfate)
[c]60 (700 kPa)	0 (Top)	15% O, 31% S, 11% Cu {99% Cu(I)}	[b] Mainly sulfide (some elem. sulfur)
	180	16% O, 37% S, 19% Cu {99% Cu(I)}	[b] Mainly sulfide (some elem. sulfur)
	350	14% O, 41% S, 20% Cu {95% Cu(I)}	[b] Mainly sulfide (some elem. sulfur)
60 (250 kPa)	0 (Top)	47% O, 4% S, 1% Cu {1% Cu(I)}	Mainly sulfate ([d] some sulfide)
	180	47% O, 12% S, 9% Cu {99% Cu(I)}	[b] Mainly sulfide (some elem. sulfur)
	350	44% O, 16% S, 13% Cu {99% Cu(I)}	[b] Mainly sulfide (some elem. sulfur)

[a] Balance mainly adventitious carbon; [b] Most likely monosulfide; [c] Test PLC24; [d] Most likely polysulfide, with some elemental sulfur.

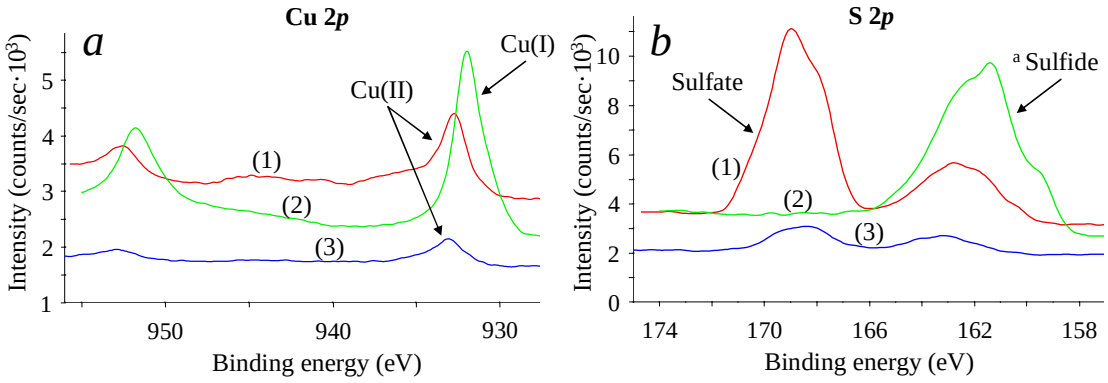

Figure 6.57
XPS spectra at etch level 0 (Shackleton, 2009), obtained from surfaces of unleached narrow-sized Sample D (line 1) & leached chalcopyrite samples (60 minutes, starting with 25 g/L H_2SO_4, 25 g/L Cu & 0.35 g/L Arbo A02 LS, QB) at 700 kPa $p_{O2}°$ (Test PLC24) (line 2) & 250 kPa $p_{O2}°$ (line 3): *a*) Cu 2*p* spectra; *b*) S 2*p* spectra ([a] predominant monosulfide peak; see Hackl *et al.*, 1995).

Although these preliminary mineralogical and XPS techniques provide no conclusive evidence of the exact nature of the sulfide surface layers on host chalcopyrite particles, the absence of iron and the abundance of copper(I) monosulfide are indicative of a covellite-like surface structure. At shorter reaction times, after rapid oxidation of the most reactive surfaces, and lower oxygen concentrations, intermediate polysulfide-sulfate surface layers formed. However, their inhibiting role is questioned, as they appeared rather discontinuous, while a deviation from linear USP kinetics usually appeared at a point in time where no such surface layers have been identified (*e.g.*, 60 min at 700 kPa $p_{O2}°$). Instead, it is proposed that the mere presence of copper(I) monosulfide

Stellenbosch University http://scholar.sun.ac.za

surface states allows oxygen reduction to be the dominant cathodic reaction at MT autoclave conditions, which, in turn, allows relatively fast mineral oxidation kinetics compared to atmospheric processes, where oxygen or iron(III) reduction would be relatively slow on such surfaces. The role of elemental sulfur, forming impervious surface structures, should also not be underestimated. However, the kinetic oxidation results (presented in this section) strongly suggest that this phenomenon is linked to surfactant degradation. Furthermore, the insensitivity of the oxidation kinetics with regard to the bulk copper concentration suggests that the covellite-like surface structure is probably a remnant of the leaching process and not of copper ions from the bulk solution, diffusing inwards to form new particle surfaces. The covellite surface coverage term (θ) may therefore be omitted from Equation 6.161.

Finally, the insensitivity of chalcopyrite oxidation kinetics to the iron(III) concentration may be a direct consequence of iron leaching rapidly from the chalcopyrite structure (previous sections), thus always allowing some iron(III) presence in the proximity of the reacting surface. In contrast, materials such as white metal contain very little iron and the absence of initial iron in solution usually results in significantly slower oxidation rates (Ruiz *et al.*, 2009). Therefore, omitting the role of iron from the above rate expression does not necessarily imply that the oxidation mechanism of chalcopyrite does not involve iron(III). However, the above results suggest that iron(III) reduction is unrelated to the rate-limiting steps during MT chalcopyrite oxidation. The reduction of iron(III) on remnant surface layers around host chalcopyrite particles may also fundamentally differ from the surface layers formed during the oxidation of white metal. This may indeed be the case, since white metal oxidation is intrinsically faster than chalcopyrite oxidation (Ruiz *et al.*, 2009), suggesting a different surface structure, associated with a different mechanism.

6.5.5 Quantification (regression) and verification of the chalcopyrite oxidation rate model

In order to verify the half-order dependency of the chalcopyrite oxidation rate on the dissolved oxygen concentration, and to determine the values of the other constants in Equation 6.161, most of the above experimental results are included in the regression (see Table 6.14). The (initial) experimental rate constants from the USP model are used in the error function (Eq. 6.162), *i.e.*, at the corresponding average solution composition (over the linear region) and mean particle size, rather than attempting to regress the leaching extents (X). The latter method would require more knowledge of the extraction curves during initial oxidation (at least three data points) and also the degree of retardation by molten elemental sulfur at longer reaction times. The regression is therefore more consistent if based on averages, rather than attempting to also integrate over particle size. However, the particle size integration method is applied in Chapter 7 (Sect. 7.4.2), utilising more (initial) datapoints from additional leaching testwork, while the residue bulk modal analysis (App. B.3.2) provides invaluable information on the relative mineral oxidation extents.

Stellenbosch University http://scholar.sun.ac.za

Table 6.14
Experimental data used to obtain the intrinsic rate expression of the oxidative leaching of HBMS 777 concentrate at 150°C, in the presence of LS (Norlig A) & QB (Orfom 2).

Series	Eval. range (min)	[a] $k_{\ell,Cpy}$ (µm/min)	P_g (kPa)	[b,c] Density (g/L)	[c] $[H_2SO_4]$ (g/L)	[c] [Cu] (g/L)	[c] [Zn] (g/L)	[c,d] [Fe(II)] (g/L)
PLC1	45	0.083	1090	1060	18.2	17.3	0.7	0.7 (2.6)
PLD1,D2	45	0.090	1090	1122	24.6	40.0	0.8	0.5 (3.4)
PLD3	30	0.104	1490	1120.5	23.4	39.5	0.8	0.5 (3.5)
PLE5	30	0.095	1090	1071	25.7	18.1	0.8	0.7 (3.0)
PLF1	7.5	0.087	1090	1057	12.4	16.5	0.4	0.1 (0.9)
PLF2	30	0.084	1090	1050	12.2	17.7	0.6	0.2 (0.6)
PLF3	45	0.067	1090	1057.5	12.8	18.2	0.8	0.0 (0.4)
PLF4	45	0.085	1090	1051.5	12.2	16.1	0.7	0.0 (1.0)
PLG1	7.5	0.093	1090	1057.5	20.4	16.5	0.4	0.7 (1.7)
PLG2	30	0.088	1090	1062	16.8	18.6	0.7	0.5 (2.1)
PLG3,G4	45	0.078	1090	1064	16.1	18.7	0.8	0.6 (2.6)
PLH1	7.5	0.095	1090	1064.5	29.6	17.0	0.4	1.2 (2.1)
PLH2	30	0.089	1090	1071.5	24.3	18.2	0.7	1.8 (3.3)
PLH3	30	0.105	1090	1065.5	29.1	16.3	0.6	0.7 (1.5)
PLI1	7.5	0.097	1090	1069.5	39.1	16.6	0.4	1.0 (1.9)
PLI2	30	0.092	1090	1077.5	35.7	18.0	0.7	1.0 (3.3)
PLI3	30	0.102	1090	1075.5	35.0	18.0	0.8	0.8 (2.8)
PLI4	30	0.106	1090	1071	37.6	17.0	0.6	0.7 (1.7)
PLL1	60	0.038	640	1063	16.6	17.5	0.8	0.9 (2.2)
PLL2	30	0.101	1890	1066	15.8	19.5	0.4	0.4 (2.7)
PLM1	90	0.054	1090	1083	12.1	32.5	0.9	0.0 (0.4)
PLM2	45	0.066	1090	1092	15.6	28.8	0.8	0.5 (2.2)
PLM3	30	0.082	1090	1098	24.2	28.0	0.8	0.6 (3.1)
PLN1	90	0.052	1090	1107	12.5	43.1	0.8	0.0 (0.3)
PLN2	45	0.075	1090	1117	16.4	43.1	0.9	0.4 (2.3)
PLO1	30	0.067	1090	1126	18.0	30.1	17.2	0.4 (2.0)
PLO2	45	0.063	1090	1144	19.2	29.1	27.4	0.2 (1.4)
PLO3	45	0.064	1090	1158	17.3	27.5	35.9	0.2 (1.7)

[a] Based on Eq.6.156 & the mean particle size (L_o); [b] 20°; [c] Avg. over the linear region (eval. range) of the USP model plot (App. G); [d] Bracketed values refer to $[Fe]^T$.

Stellenbosch University http://scholar.sun.ac.za

The error function, E_F, is defined as the absolute error between the calculated and measured rate constants for *k* tests, *i.e.*:

$$E_f = \sum_k E_k = \sum_k \left| (p_1[H^+]^{p_2}[O_2]^{p_3}) / k^{exp}_{\ell,Cpy} - 1 \right| \qquad 6.162$$

Similarly to the regressions of Chapter 2, the optimisation routines (*Matlab*, 2011) implicitly minimise the root mean square deviation, irrespective of whether the error is defined as a vector (dataset) or scalar value (sum of errors), *i.e.*, to suit the specific mathematical routine. Because the above experimental constants are based on average rate and solution composition data during initial oxidation, the oxygen concentration in solution is first assumed to be at its saturation concentration, using the correlations presented in Appendix A.4. The actual free hydrogen ion concentration 'at temperature' and the solution vapour pressure of the electrolyte solution are obtained from the solution chemistry model developed in Chapter 2. The optimisation yields the values 3.66, 0.23 and 0.59 for parameters p_1, p_2 and p_3, respectively, by equal weighting of the tests conducted at different gauge pressures, *i.e.*, ¼ for Series PLL1 (640 kPa P_g), PLD3 (1490 kPa P_g) and PLL2 (1890 kPa P_g), and (¼ × 1/25) for the other twenty five series (1090 kPa P_g). This value of p_3 is seen as sufficient confirmation of the electrochemical nature of chalcopyrite oxidation; the reaction rate expression is therefore fixed at the half-order dependency on the dissolved oxygen concentration, *i.e.*, $p_3 = 0.5$. The subsequent optimisation, using equal (1/28) weighting for all twenty eight tests, yields rounded values of 1.95 and 0.16 for p_1 and p_2, respectively. However, the interfacial gas/liquid mass transfer rate is neglected in this analysis, prompting a follow-up mathematical exercise. Firstly, an oxygen mass balance for the batch oxidation reactor is written:

$$\frac{d[O_2]}{dt} = k_L a([O_2]^* - [O_2]) - R_{O_2} W_{s,o} \frac{dX_s}{dt} \qquad 6.163$$

where R_{O2} refers to the intrinsic mineral oxygen demand (g O_2/g sulfide concentrate) and $W_{s,o}$ is the initial mass of the concentrate (g concentrate/kg water). The first term on the right follows directly from the oxygen absorption rate expression (Sect. 3.2), while the second differential can be expressed as follows (App. F.4):

$$\frac{dX_s}{dt} = \frac{3p_1}{L_o}[H^+]^{p_2}[O_2]^{\frac{1}{2}}(1-X_s)^{\frac{2}{3}} \qquad 6.164$$

These two differential equations are solved numerically. Figure 6.58 compares the two smallest size fractions at the highest acid concentration (Series PLI1 & PLI2), using a typical oxygen demand of 350 kg/t. The k_La-value used in this model (1 1/min at 25°C, corrected for the temperature and pulp density; Ch. 3) corresponds to operating mode B (Figure 3.5), as applied to all the autoclave testwork presented in this chapter (App. G).

Stellenbosch University http://scholar.sun.ac.za

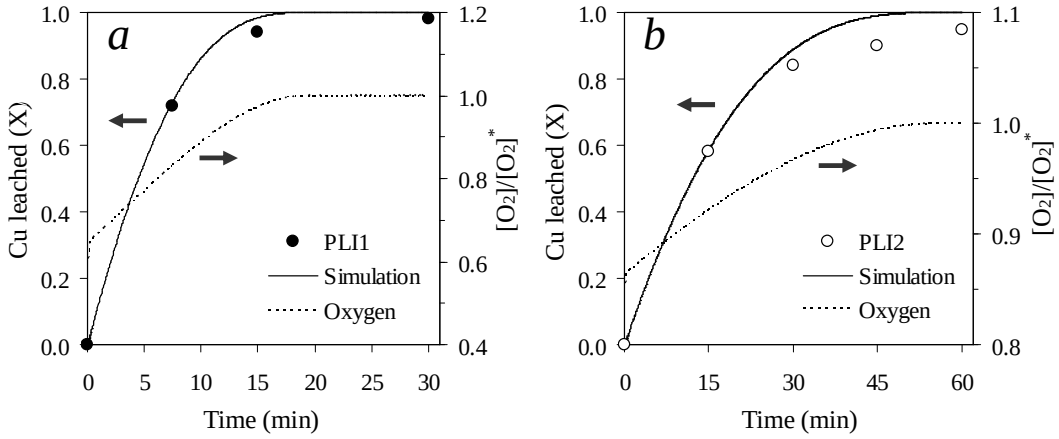

Figure 6.58
Comparison between the measured (points) & simulated (lines) Cu extraction & O_2 concentration, using narrow-sized fractions & starting with 45 g/L H_2SO_4, 15 g/L Cu & 0.35 g/L LS, QB at 700 kPa p_{O2}°: *a*) Sample A (Series PLI1); *b*) Sample B (Series PLI2) ($k_La \approx 13.5$ 1/min at 150°C).

Clearly, the test series conducted with the finest fraction (Sample A) was under notable oxygen mass transfer limitations, with only approximately 70% of saturation reached halfway to the first datapoint (7.5 min). This situation improves for narrow-sized Sample B, reaching approximately 90% of oxygen saturation halfway to its first datapoint (15 min). For narrow-sized Sample C, and obviously also for the coarsest fraction D, the oxygen concentration is always close to saturation (>90%), even when using a conservative k_La-value of 0.75 1/min (25°C) (Table 3.9). This statement does, however, not hold for cases where the autoclave slurry level dropped below the top impeller. This situation was prevented by always checking that the slurry level was above the top impeller after completing a leach test. Note that the final PLS volume (App. G) was often much lower than expected due to notable water evaporation during venting and filtration. Cellulose acetate (Sartorius Millipore) filter paper was used to capture all residues and this often resulted in slow filtration, especially if particles were leached to very fine sizes or when iron precipitation occurred (this procedure was improved for the leach tests presented in Ch. 7; Sect. 7.3).

The above assessment of the role of oxygen mass transfer prompted a re-evaluation of the parameters for the intrinsic chalcopyrite oxidation rate expression, excluding the results from narrow-sized Sample A. This resulted in similar values of p_1 and p_2, *i.e.*, 2.07 and 0.17, respectively, as obtained with the full experimental set, suggesting that experimental error overshadowed most mass transfer limitation effects. Table 6.15 summarises these optimised parameters, while Figure 6.59 compares the experimental linear rate constant values with the corresponding (calculated) values. The error introduced by using this simplistic model (9%) is of the same order of magnitude as the experimental error (5-15%).

Stellenbosch University http://scholar.sun.ac.za

Table 6.15
Optimised rate constant parameters for the intrinsic oxidation (Eq. 6.164) of HBMS 777 $CuFeS_2$ at 150°C, in the presence of LS (Norlig A) & QB (Orfom 2).

p_1	$2 \cdot p_2$	p_3	[a] *AARD*
$(\mu m/min)\cdot(kg/mol)^{2/3}$	–	–	(%)
2	⅓	½	9.00

[a] Absolute average relative deviation of $k_{\ell,Cpy}$ (µm/min) (see Eq. 2.73): $AARD\,(\%) = \frac{100}{N_k} \cdot \sum_k E_k$

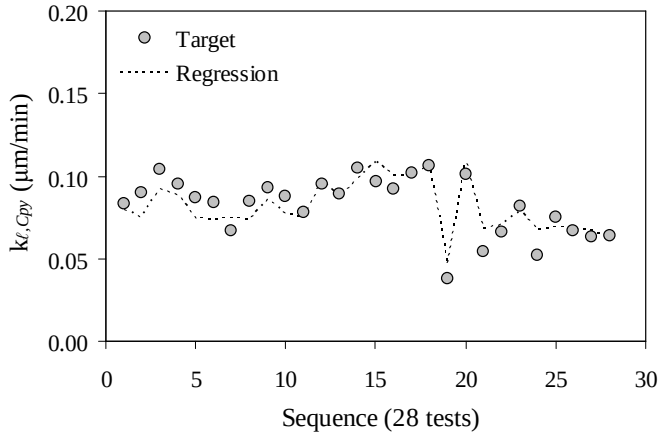

Figure 6.59
Comparison between measured (Table 6.14) & regressed values of the initial linear rate constant, $k_{\ell,Cpy}$, for HBMS 777 concentrate at 150°C, in the presence of LS (Norlig A) & QB (Orfom 2).

The derivation of an intrinsic rate expression for pyrite oxidation is attempted next, albeit representing a minor phase (< 10%) in this (HBMS 777) concentrate. No consistent trends of the relative oxidation rate of pyrite *vs.* chalcopyrite have yet been established (see discussions in the previous section regarding the relative dissolution of iron-to-copper and iron-to-sulfide ratios in the leach residues). Figure 6.60 attempts to correlate the pyrite to chalcopyrite oxidation ratio and the primary variables of the kinetic study, *i.e.*, time and acid concentration. The extent of pyrite oxidation is based on the residual sulfide content, after accounting for chalcopyrite (copper) and other sulfides (zinc) dissolution. Clearly, no relationship is obtained from these representations, prompting the use of the residual iron as the calculation basis and incorporating only the tests where no iron(III) precipitation occurred. Figure 6.61 *a* emphasises the high degree of data scattering and, again, no clear trend is distinguishable. Focussing on a (narrow) region at lower total sulfide oxidation extents and comparing the ratios based on sulfide analyses with the corresponding ratios based on iron analysis (Figure 6.61 *b*), suggested that preferential iron leaching could have occurred in some tests, *i.e.*, where higher than average residual sulfide contents

Stellenbosch University http://scholar.sun.ac.za

correspond to lower than average residual iron contents. However, no information on the relative oxidation rates of pyrite *vs.* chalcopyrite is obtained from these relationships.

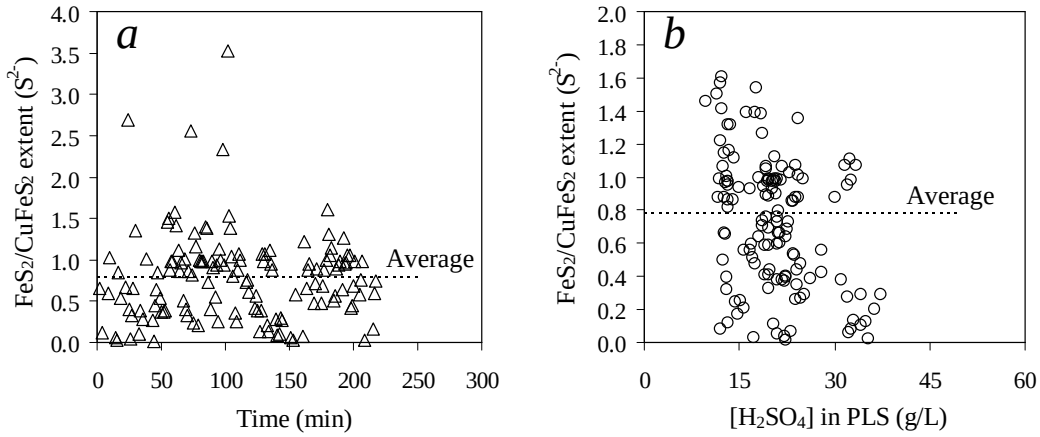

Figure 6.60
Comparison of FeS_2 to $CuFeS_2$ (oxidation) extent ratios, based on total S^{2-} & Cu analyses, respectively, with the primary variables: *a*) Time (min); *b*) $[H_2SO_4]$ (g/L) in PLS.

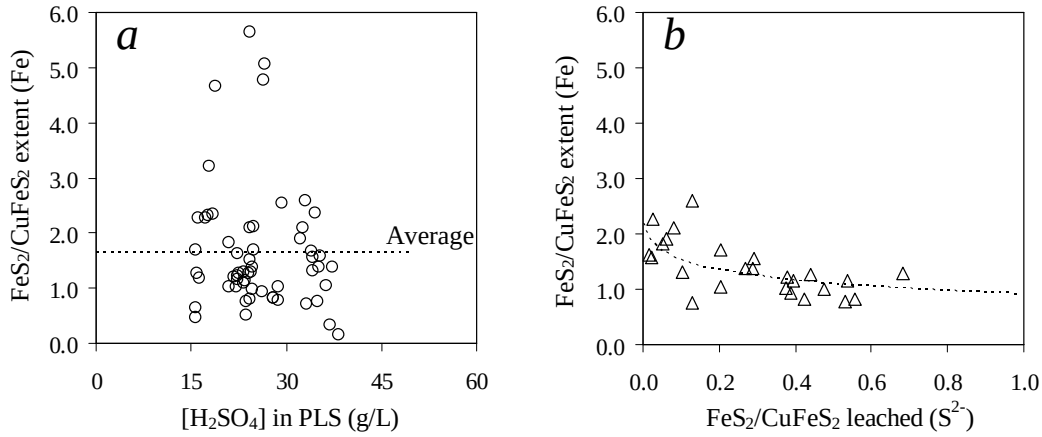

Figure 6.61
Comparison of FeS_2 to $CuFeS_2$ (oxidation) extent ratios based on Fe (& Cu) analyses, with acid concentration & the corresponding ratios based on total S^{2-} (& Cu) analyses: *a*) Ratio against H_2SO_4 concentration (g/L) in PLS; *b*) Comparison of ratios, using the different calculation bases.

The general lack of correlation between these properties highlights the impact of inaccurate chemical analyses when attempting to estimate dissolution rates of minor mineral phases. The simplest approach is therefore adopted for, *i.e.*, comparing the total copper and iron leaching extents of all the tests where no iron precipitation occurred (Figure 6.62). At first glance, comparison between the total iron and corresponding copper leaching extents (Figure 6.62 *a*) could support either argument, *i.e.*, preferential iron dissolution or relatively faster pyrite oxidation rate. However, Figure 6.62 *b* confirms that there is no indication that pyrite leached faster than

Stellenbosch University http://scholar.sun.ac.za

chalcopyrite, neither that iron leached preferentially to copper, *i.e.*, after iron dissolution from pyrrhotite and sphalerite is accounted for, using the residual zinc content as the calculation basis.

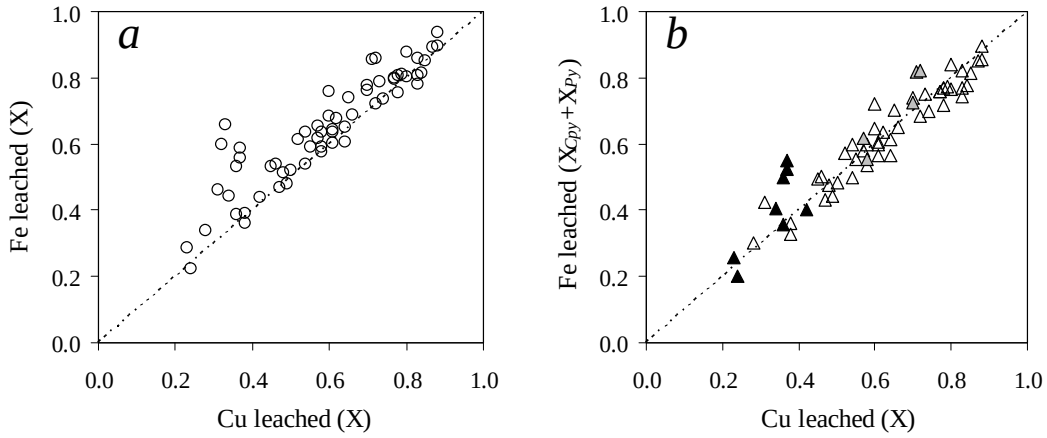

Figure 6.62
Comparison between total Fe & Cu leaching extents, using datapoints where no iron precipitation occurred: *a*) Total Fe *vs.* Cu leaching extents; *b*) Fe leached from $CuFeS_2$ & FeS_2 *vs.* Cu leaching extents. Black symbols represent the shortest reaction (time) tests in each series, while the grey symbols represent the reaction extents from the two finest fractions (Sample A & B).

Table 6.16 presents the bulk modal analyses of narrow-sized Sample D and two leach residues, containing no iron precipitates, *i.e.*, after 15 minutes (Test PLC21) and 60 minutes (Test PLC24).

Table 6.16
Mineral abundance (bulk modal) analyses of narrow-sized feed material, leach residues after 15 min (Test PLC21) & 60 min (Test PLC24), respectively, & calculated leaching extents (Sample D, 25 g/L H_2SO_4, 15 g/L Cu & 0.35 g/L Arbo A02 LS, Orfom 2 QB at 700 kPa p_{O2}°).

Mineral	[a] Sample D	[b] 15 min	[d] X (modal)	[e] X (chem.)	[f] 60 min	[d] X (modal)	[e] X (chem.)
	(%)	(%)	(%)	(%)	(%)	(%)	(%)
Chalcopyrite	79.3	81.0	16	17	91.0	47	48
Covellite	0.0	0.4	–	–	0.1	–	–
Sphalerite	6.8	5.1	38	25	0.8	95	86
Pyrite	8.6	8.7	16	–	2.8	(85)	–
Pyrrhotite	2.1	1.5	41	–	0.6	87	–
Other sulfides	[c] 0.3	[c] 0.6	–	–	[c] 2.0	–	–
Gangue minerals	2.9	2.7	–	–	2.7	–	–
Total	100.0	100.0	–	–	100.0	–	–

[a] Bulk modal analysis of Sample D (differs marginally from Table 6.5); [b] Bulk modal analysis of Test PLC21 residue (15 min); [c] Mainly other Cu sulfides; [d] Based on mineralogical analyses & measured mass loss (Series PLC2), neglecting the presence of S°; [e] Based on chemical analyses (App. G.2); [f] Bulk modal analysis of Test PLC24 residue (60 min).

No elemental sulfur was detected in any of these samples, which suggests that all finely divided sulfur dissolved in the epoxy resin of the polished sections. These residues were produced in the

Stellenbosch University http://scholar.sun.ac.za

presence of Arbo A02 LS and Orfom 2 QB. Unfortunately, no residues were analysed in this manner using Norlig A LS (in combination with Orfom 2 QB) and, therefore, these results do not truly reflect the mineral surface conditions experienced in most of the tests presented in this chapter. Nevertheless, excellent agreement is obtained between the mineral oxidation extents calculated by the bulk modal and chemical analyses, especially for chalcopyrite, and to a lesser degree for sphalerite. Once again, it is emphasised that Arbo A02 resulted in a significantly slower oxidation rate of sphalerite (also see Table 6.9), which appears to be imitated by pyrrhotite. The extent of pyrite oxidation is identical to the degree of chalcopyrite oxidation in the 15 minutes residue, but is almost double in the case of the 60 minutes residue. The suggestion of faster oxidation towards the latter stages of leaching contradicts the (passivation) behaviour normally observed for pyrite minerals, whether caused by an intrinsic surface mechanism or by the formation of molten sulfur product layers (see, *e.g.*, Long & Dixon, 2004). This apparent phenomenon is discussed in more detail in Chapter 7 (Sect. 7.4.2), based on the bulk modal analyses of oxidation residues from different concentrate samples. For now, it is assumed that pyrite oxidises at approximately the same rate as chalcopyrite under MT autoclave conditions, while a similar assumption is adopted for the pyrrhotite *vs.* sphalerite oxidation rates in the HBMS 777 concentrate. For the sake of completeness, Figure 6.63 presents the BSE images of the partially leached particles from the above two residues. Particles, in particular chalcopyrite, were preferentially attacked at particular crystal planes, which is most evident during the initial oxidation period (15 min residue). Figure 6.64 illustrates the SEI of this residue, after removing all elemental sulfur with hot tetrachloroethylene solution (for 30 min at 90°C).

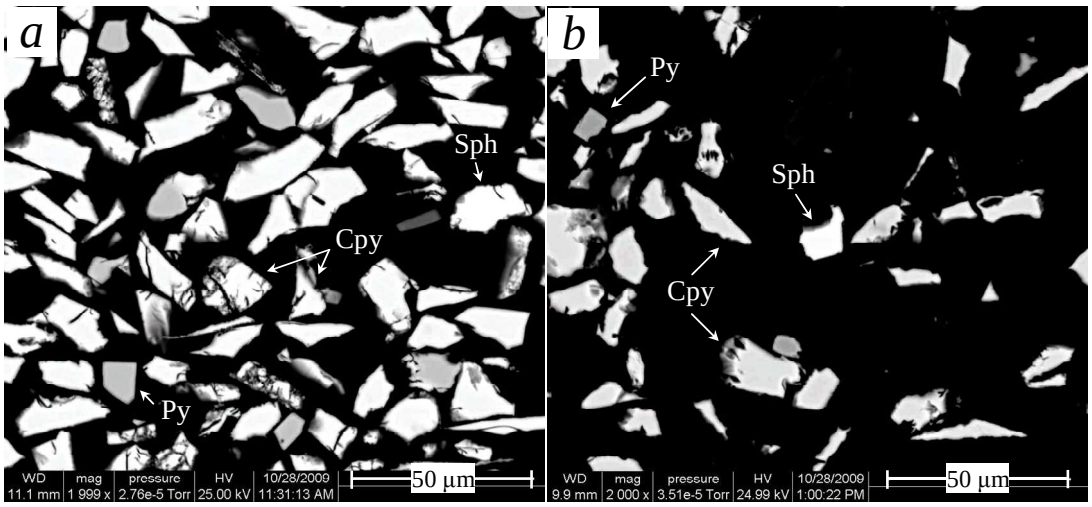

Figure 6.63
BSE images of Series PLC2 residues after oxidation (Sample D, 25 g/L H_2SO_4, 15 g/L Cu & 0.35 g/L Arbo A02 LS, Orfom 2 QB at 700 kPa p_{O2}°): chalcopyrite (Cpy), pyrite (Py), & sphalerite (Sph): *a*) Test PLC21 (after 15 min); *b*) Test PLC24 (after 60 min).

Stellenbosch University http://scholar.sun.ac.za

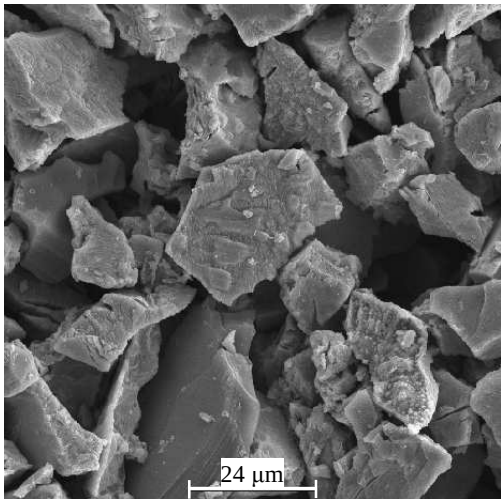

Figure 6.64
SEI of Test PLC21 residue (washed with tetrachloroethylene solution) after a 15 min oxidation: Sample D, 25 g/L H_2SO_4, 15 g/L Cu & 0.35 g/L Arbo A02 LS, Orfom 2 QB at 700 kPa $p_{O2}°$.

Most particles exhibit highly irregular and rugged shapes, compared to the head sample (see Figure 6.25 *c*). This cast some doubt on the applicability of the USP model, which relies on particles retaining their shape during shrinkage (App. G.4). Preferential oxidative attack appears to have occurred at particular crystal planes, which may explain the apparently faster initial oxidation rate in selected cases, *e.g.*, Figure 6.42 *b* (Sample D). However, such effects manifest as marginal deviations from the USP model behaviour, while the results presented in the previous section provide enough evidence to support the notion that elemental sulfur is responsible for the deviation from linear kinetics at longer reaction times. Therefore, although the above images pose some questions around the applicability of the USP model, the general leaching framework and associated rate expressions appear robust enough to be used as a phenomenological modelling tool.

Finally, the stability of elemental sulfur during mineral oxidation needs to be quantified. If the dissolved iron content of sphalerite (~4.7% Fe, *ref.* Sample D) is included, the following estimated mineralogical composition is obtained for the HBMS 777 concentrate: 82.3% $CuFeS_2$, 6.9% ZnS, 5.1% FeS_2 and 1.8% FeS. Figure 6.65 *a* is based on two extreme assumptions regarding the intrinsic sulfur yield. The one extreme (closed symbols) assumes sphalerite and pyrrhotite oxidise at similar rates, yielding 100% sulfur, while pyrite yields 25% sulfur (see Sect. 6.3.1). The other extreme (open symbols) assumes that sphalerite and pyrrhotite surfaces resemble covellite (see Sect. 6.3.4), yielding 40% sulfur (Marsden *et al.*, 2007a), while pyrite is assumed to yield no elemental sulfur. An average calculated chalcopyrite sulfur yield of 63% is then obtained (Figure 6.65a), albeit from highly scattered data. Nevertheless, this average yield bore almost no correlation with the total copper leaching extent, even at relatively long reaction times, suggesting

Stellenbosch University http://scholar.sun.ac.za

the no significant oxidation of elemental sulfur occurs after it has formed (also see App. A.6; < 0.1% S° oxidation after 30 min at 150°C, 0.2 mol/kg H^+ & 0.5 wt% sulfur)

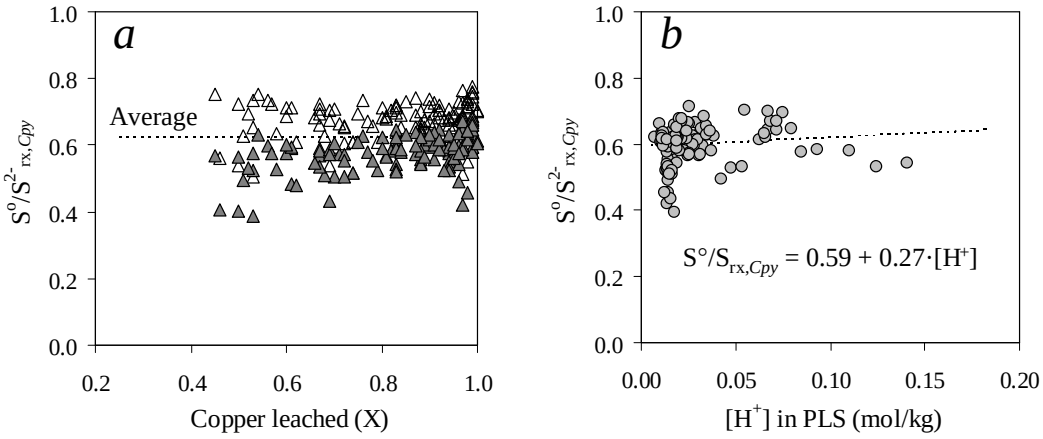

Figure 6.65
Calculated elemental sulfur yields of $CuFeS_2$ (FeS_2 oxidation extents based on sulfide in residue): *a*) Sulfur yield *vs.* Cu leaching extent (solid symbols refer to 100% yield for ZnS, FeS & 25% for FeS_2; open symbols represent 40% yield for ZnS, FeS & 0% for FeS_2; *b*) Sulfur yield *vs.* $[H^+]$ ('at temperature'), assuming 100% yield for ZnS, FeS & 1% for FeS_2 at 0.1 mol/kg H^+ (linear regression line based on the same slopes for $CuFeS_2$ & FeS_2).

Figure 6.65 *b* suggests that the elemental sulfur yield increases slightly with the free hydrogen ion concentration (based on the solution chemistry model; Ch. 2), assuming constant yields of 100% for sphalerite and pyrrhotite, and fixing the pyrite yield at 1% (Marsden *et al.*, 2007a) at 0.1 mol/kg H^+ (~0.1 mol/kg H_2SO_4). The linear correlation is obtained iteratively, after assuming that the chalcopyrite and pyrite respond in similar fashion to increased hydrogen ion concentration (same slope). These assumptions result in an average chalcopyrite elemental sulfur yield of 60%, which translates into the following general equation (y = 0.4; Figure 6.22):

$$CuFeS_{2\,(s)} + 2.2O_{2\,(aq)} + 1.2H_2SO_{4\,(aq)} \Rightarrow CuSO_{4\,(aq)} + FeSO_{4\,(aq)} + 1.2H_2O_{(aq)} + 1.2S^o_{(s)} \qquad 6.165$$

The elemental sulfur yields of chalcopyrite and pyrite are incorporated into the overall model (Ch. 7), using this (rounded) slope, *i.e.*, $0.3\times[H^+]$.

Stellenbosch University http://scholar.sun.ac.za

6.6 Overview of intrinsic mineral oxidation mechanisms and rates

This chapter presents a detailed literature review of possible oxidation mechanisms of sulfide minerals in a typical chalcopyrite concentrate, followed by batch experimental work to evaluate the response of the HBMS 777 chalcopyrite concentrate to medium temperature (MT) oxidation, according to the AA-UBC process.

6.6.1 Literature information

Thermodynamics

The first section of the literature review highlights the complexity of sulfide mineral oxidation from a thermodynamic perspective. Metastability of species such as elemental sulfur cannot be adequately captured by thermodynamics alone and no mechanistic information can be deduced from such a description. However, it is a valuable supplementary tool to confirm some observed phenomena, *e.g.*, the increased stability of elemental sulfur at lower temperatures and higher acid concentrations.

The formation of covellite-like phases has been observed during chalcopyrite oxidation in autoclaves, while higher acidity and lower redox potential appear to encourage its formation at lower oxidation temperatures. Most importantly, the formation of covellite, as an intermediate product on partially oxidised chalcopyrite, is shown to be thermodynamically possible from various perspectives, *i.e.*, the anodic dissolution of chalcopyrite, reaction between cupric ion and hydrogen sulfide or elemental sulfur, metathesis reaction of cupric ion with chalcopyrite and the non-oxidative dissolution of chalcopyrite. It should be realised that the oxidation mechanism that dominates on any given particle surface is deeply imbedded within the kinetic realm, explaining the variety of intermediate surface structures that have been proposed to form or have been detected experimentally on partially oxidised chalcopyrite.

Kinetics

Kinetic studies represent the superior methodology when attempting to gain mechanistic information, *e.g.*, in order to mathematically describe sulfide mineral oxidation rates. However, as pointed out above, it is unlikely that a single mechanism is applicable to each mineral across a wide array of solution and surface properties. The following discussion should therefore be viewed in context of this study, *i.e.*, to derive phenomenological oxidation rate expressions for the relevant sulfide minerals under typical MT autoclave conditions. Although the background theory ultimately results in simple rate laws, this level of detail is justified because it challenges our understanding of each sulfide mineral oxidation reaction step, what assumptions are made and what information is currently lacking.

Stellenbosch University http://scholar.sun.ac.za

Most sulfide minerals are semiconductors because inter-atomic distances are large, meaning that the energy gap between the valence and conduction bands is greater than the thermal energy of the valence-band electrons. The mechanistic departure point is therefore imbedded within semiconductor electrochemistry and solid-state electronic structure theory. The role of impurity metals is particularly important in this regard. A metal-excess compound, such as chalcopyrite, is most likely to display *n*-type semiconducting behaviour (excess electrons), whereas compounds such as CuS, are *p*-type metallic conductors. The anodic dissolution of sulfides is usually dominated by a hole-decomposition pathway. The supply of holes may be migration-limited in *n*-type semiconductors, which explains why saturation effects are often observed during chalcopyrite dissolution at high oxidant concentrations. Due to the development of an electric field at the solid/solution interface, the transport of charge carriers across this region is usually the rate-limiting step of sulfide mineral dissolution. The presence of a high density of surface states would anchor the Fermi energy at the average energy of those states and the mineral would behave like a metal, *i.e.*, the electric potential would predominantly reside across the Helmholtz layer. This allows direct application of the mixed potential (MP) theory to describe the rate of mineral dissolution, analogous to metal corrosion. One of the most important factors determining the rate of mineral dissolution is the adsorption or approach of the oxidant species at the mineral surface. The energy levels of these species are also important, since the intrinsic ability to accept electrons depends on the energy overlap of the empty orbitals with the relevant semiconductor band.

Chalcopyrite

In the case of chalcopyrite, the metal sulfide bonds are significantly covalent in character, constituting the upper part of the valence band, while the band gap is relatively narrow. The conclusion from this, experimentally verified in the literature, is that an increase in temperature can increase the extent of electron fluctuation between donor and acceptor states, allowing chalcopyrite dissolution to occur *via* valence- and conduction-band processes, *e.g.*, dissolution *via* hole injection by ferric (Fe^{3+}) ion and *via* electron capture by cupric (Cu^{2+}) ion, respectively.

Various studies have confirmed the preferential release of iron from the surface structure during initial chalcopyrite oxidation, suggesting that the iron-sulfide bond is energetically most prone to oxidative attack. This would result in a remnant copper sulfide surface, which is in line with numerous proposals from the literature. The central theme of all these studies is that this surface layer is more resistant (refractory) to oxidative attack, compared to the original chalcopyrite surface, and that the transition point is characterised by classical active-passive (polarisation) behaviour. More severe passivation, *i.e.*, a relative decrease in dissolution current, has been observed at increased temperatures, implying that autoclave oxidation also has to deal with passive surfaces. However, higher temperature oxidation would also be expected to differ mechanistically

Stellenbosch University http://scholar.sun.ac.za

from lower temperature (atmospheric) oxidation, besides allowing for a more efficient reaction, *i.e.*, with a higher frequency of successful activation (energy) barrier jumps. Besides the slower dissolution rate of metal-deficient surface layers, polysulfides and elemental sulfur have been proposed as possible candidates that may cause surface inhibition. Reductive rearrangement of long-chain polysulfides to shorter-chain species has been proposed to explain the common experimental observation of increased chalcopyrite dissolution at lower oxidation potentials, *i.e.*, the so-called optimum solution-potential 'window' of chalcopyrite oxidation. On the other hand, a reduction-oxidation-type mechanism could also be indicative of the non-oxidative dissolution of non-stoichiometric (sulfur-rich) minerals. The role of chalcopyrite dissolution *via* electron exchange with the conduction band (discussed above) should also not be ruled out as a possible explanation of this phenomenon. Despite these and various other proposals (Sect. 6.3.2), there is still no general consensus on the exact nature of the inhibitory surface layers on chalcopyrite and the mechanism that limits its oxidation rate. In addition, mechanisms would differ between samples with varying impurity levels (*n*- or *p*-type) and even between different crystal faces. Also, it is unlikely that these surface layers resemble known mineral structures, such as naturally occurring covellite, because such structures have been found, in the literature, to exhibit high anodic dissolution currents in potential regions where chalcopyrite is passive. This conclusion neglects, however, the possible limiting rate of the cathodic reduction reaction on such surfaces. Criticism of the postulation of inhibitory polysulfide surface layers is justified, as synthetic polysulfide substances have been shown to be reactive towards oxidation in acidic solutions.

In conclusion, there is overwhelming evidence that the metal cations, especially iron, are preferentially released during initial dissolution and the formation of thin remnant surface layers is widely accepted as playing a primary inhibiting role in the chalcopyrite dissolution process. In context of the current lack of mechanistic knowledge, as well as the phenomenological nature of this study, the general assignment of Cu_xS ($2 \geq x \geq 0.5$) is adopted in this study to describe this inhibitory surface layer (these boundaries resemble chalcocite and copper pyrite, respectively). This surface is referred to as a covellite-like phase in view of its resemblance to that mineral (see below), since it is known to be relatively refractory towards oxidation and because various researchers have claimed its formation under autoclave oxidation conditions (see above). However, it should again be emphasised that this phase could be very different from naturally occurring or synthetic covellite, despite the copper retaining its monovalent oxidation state. Besides possible cathodic reduction limitations, contributing factors could include solid-state diffusion, solid-state rearrangements and/or inhibition (primary or secondary) due to elemental sulfur itself.

Stellenbosch University http://scholar.sun.ac.za

Sulfur rearrangement, transformation and oxidation

Solid-state rearrangement of sulfur, to form short-chain building blocks, may follow various routes (Sect. 6.3.2). An important factor in all these routes appears to be the central role of the adsorbed hydrogen ion and, more specifically, the ultimate formation of surface HS··-like species. The general agreement is that sulfide is more prone to oxidation under lower acidity conditions, forming a range of soluble oxidation products, *i.e.*, with higher oxidation states than the elemental form. The chemistry is complicated and the sulfur oxidation state during its release into solution depends heavily on the nature of the oxidant.

An oxidant, such as iron(III), can exchange only a single electron and would tend to form higher elemental sulfur yields. At lower temperatures, a mechanism *via* intermediate polysulfide formation has been proposed to account for the formation of S_8 rings. The elongation of the polysulfide structure has been claimed to operate *via* various $H_xS_y\cdot$ surface radicals. Elemental sulfur yields of over 90% have been reported in the literature at lower temperatures, *i.e.*, during chalcopyrite oxidation using one-electron transfer oxidants. Under conditions where oxygen reduction is appreciable, charge transfer would occur in two-electron or four-electron sequences (next section) and may oxidise sulfide to higher oxidation states before its release into solution and the yield of elemental sulfur would be consequently lower. Conditions (higher temperature) under which these multi-electron sequences occur readily also coincide with conditions where the sulfur species are more prone to oxidative attack, *i.e.*, it would be difficult to distinguish between the nature of the oxidant and the effect of temperature under, for example, total pressure oxidation (TPOX) conditions. The same is true under conditions where elemental sulfur is stable on most sulfide minerals, *i.e.*, under atmospheric temperatures. However, minerals such as pyrite are known to yield less elemental sulfur than, for example, sphalerite under MT oxidation because of the reactive radical surface species developing naturally on pyrite (see later). Therefore, the sulfur yield does reveal qualitative information about the nature of the surface mechanism on the different sulfide mineral surfaces under MT autoclave conditions. Since the oxidation of elemental sulfur is slow under MT autoclave conditions, the lower sulfur yields on covellite and chalcopyrite are most probably also related to the intrinsic oxidation mechanisms occurring on these mineral surfaces.

Stable elemental sulfur surfaces are best viewed as a secondary factor that can inhibit mineral dissolution, especially above the sulfur melting point, and even more so, above its transition temperature (159-160°C), where its viscosity increases rapidly. This transition temperature has been found to be sensitive to small amounts of impurities, such as arsenic, which may induce polymerisation at even lower temperatures, *i.e.*, the inhibiting role of polymeric sulfur should not be underestimated, even in the presence of surfactants (see below). This is especially true for the

Stellenbosch University http://scholar.sun.ac.za

AA-UBC process because it operates close to this critical point. Minerals, such as pyrite, may also induce sulfur polymerisation due to the radical species forming naturally on these surfaces under oxidative aqueous conditions.

Cathodic reactions

In this study, the cathodic reduction reactions are limited to copper(II), iron(III) and diatomic oxygen, in order of increasing (thermodynamic) driving force for its reduction. Although the driving force of copper(II) reduction is the lowest, the cupric-cuprous couple is most favourably positioned to interact with the conduction band of chalcopyrite. However, this couple is neglected in this study, primarily due to the instability of cuprous ion in the aqueous sulfate system. On the other hand, copper(I) in a surface-bound structure could play an integral part in the reduction of adsorbed oxygen (see below).

Direct chemical attack of sulfide by diatomic oxygen is unlikely, even at high temperature in an autoclave, due to the significant covalency of the metal and sulfide atoms in a mineral lattice. Instead, the reduction of oxygen involves a series of one-electron transfer (electrochemical) steps, limited by the first and third electron transfer reactions, *i.e.*, reduction of the diatomic oxygen molecule to form the perhydroxyl radical ($HO_2\cdot$), and reduction of the peroxide molecule to form the hydroxyl radical ($OH\cdot$), respectively. These steps become more feasible at higher temperatures, highlighting the kinetic nature of these reactions. Of all the intermediate species, hydroxyl radicals on the mineral surface would oxidise sulfide most efficiently, both from a thermodynamic and kinetic perspective. Although pyrite is known to be a catalyst for oxygen reduction, the mechanism is fundamentally different from that in respect of copper sulfides, *e.g.*, chalcopyrite or covellite, where copper(I) in the surface lattice may act as catalytic sites for oxygen reduction.

An unknown factor is the extent of oxygen reduction on different surfaces, *i.e.*, only the most catalytic surfaces, such as platinum metal, would be expected to reduce oxygen all the way to water (four-electron exchange). The mechanism of reduction on a specific surface depends on the sequence of the proton and electron transfer steps. Not only has peroxide reduction been found to exhibit the highest activation energy of all the elementary steps, but it also requires the highest overpotential on more weakly interacting surfaces. Breaking of the O–O bond, to form the hydroxyl radical, presents therefore a major activation-energy barrier. In addition, peroxide may decompose back to oxygen at high temperatures, especially in the presence of transition-metal ions. A proposed alternative mechanism on highly catalytic surfaces is that the reduction of diatomic oxygen is the rate-determining step, followed by splitting of the perhydroxyl radical directly into hydroxyl radicals, *i.e.*, not *via* the peroxide intermediate; this may occur on pyrite, but would be less likely to happen on chalcopyrite or a covellite-like surface. The reduction of diatomic oxygen

Stellenbosch University http://scholar.sun.ac.za

is therefore considered to be the rate-limiting step. The role of the hydrogen ion appears to be particularly important in facilitating this step, because of the ability of its electric field to enhance the electron affinity of surface-coordinated oxygen.

Ferric ion, on the other hand, is characterised by a steep polarisation relationship, confirming a small activation barrier for charge transfer. This is due to the presence of unpaired electrons in its degenerate 3*d* orbital, while it may be ideally placed (energetically) to inject holes in the sulfide mineral surface states. As discussed previously, iron(III) would be expected to produce predominantly elemental sulfur. Another important difference with the action of oxygen is that the approach and adsorption of ferric ion would be significantly less favourable due to its structured solvation shell (surrounding water molecules), complexation (contact ion pair, CIP, formation, *i.e.*, with sulfate anion) and electrostatic (positively charged mineral surface in acidic environment) considerations. However, it has been proposed that its solvation shell may form a conductive chain, allowing electron exchange over some distance, without requiring physical adsorption of ferric ion onto the mineral surface. Assuming that this process would be relatively slow, especially when considerable sulfate CIP formation is prevalent, the accelerating effect of electron transfer agents, *e.g.*, adsorbed chloride ions, would be important. This study is, however, confined to the pure sulfate system. Diatomic oxygen, on the other hand, is not positively charged, nor strongly solvated, allowing favourable adsorption onto a suitable mineral surface site. Finally, saturation effects with regards to oxidant concentration may be due to a number of factors, *e.g.*, solution chemistry (speciation) in the case of iron(III), adsorption isotherms in the case of oxygen, and/or solid-state electronic properties of the mineral, such as hole-migration limitations.

Pyrite oxidation

Considerable effort is expended in this study to simplify the important mechanisms of pyrite interaction with oxidative solution environments, as it is the major impurity mineral in chalcopyrite concentrates and also because it represents the most ideal mineral surface for oxygen reduction.

The lower part of the conduction band of pyrite is derived from the anti-bonding e_g^* doublet of iron(II), while its $3d^6$ electrons are paired and occupy the triplet t_{2g} ground (low-spin) state. These electrons form the valence band but remain non-bonding. The ferric/ferrous couple is relatively far removed (energetically) from the bonding orbitals of the valence band, which explains why iron(III) oxidises pyrite at a slow rate under atmospheric conditions. This mineral dissolves electrochemically, even with oxygen as oxidant at high temperature. It produces predominantly sulfate, which has been shown (isotope studies) to acquire its oxygen atom from water. The adsorption of water, and its subsequent oxidation to form the hydroxyl radical, has been accepted (in the open literature) as an intrinsic part of the anodic oxidation reaction of pyrite. A peculiar

Stellenbosch University http://scholar.sun.ac.za

'coincidence' is the rapid increase in pyrite oxidation rate under conditions (temperature & potential) where sulfur oxidation also increases rapidly, *i.e.*, the role of sulfur in inhibiting pyrite surface could be underestimated. The argument of a denser sulfur structure on pyrite (*cf.* other sulfide minerals) is not valid under autoclave conditions because the melting point of sulfur is exceeded. Instead, the role of polymeric sulfur and the high overpotential required for complete sulfur oxidation to sulfate are assumed to go hand-in-hand. Cognisance is taken of the possibility that polymeric sulfur may form under conditions of high surface potential, which develops naturally on pyrite in oxidative solution environments. If such layers are indeed present, the cathodic reduction reactions (discussed above) would polarise and result in relatively slow pyrite oxidation rates. Only once such layers have been oxidised would rapid pyrite oxidation commence (transpassive region), unless the intrinsic sulfur yield is low enough. Surfactants may be pivotal in determining the net effect of such surface layers on the pyrite oxidation rate.

Whether the presence of surface sulfur constitutes a secondary barrier or not, it should not be confused with the primary oxidation mechanism on a barren pyrite surface. The most important feature of this surface is the presence of the t_{2g} valence band, which is of non-bonding character. Injection of holes into this band would not necessarily result in sulfide oxidation but is capable of oxidising water (in reversible fashion) to form hydroxyl radicals. These radicals are, in turn, energetically better positioned to inject holes into the sulfur 3*p* valence band (bonding orbitals) and are also able to satisfy the high overpotential required for the stepwise oxidation of sulfide beyond the elemental state. This mechanism is consistent with various isotope studies, suggesting that sulfate is formed from oxygen acquired from water. In fact, the pyrite surface could be considered to be even more electrocatalytic towards water oxidation than platinum metal. Similarly, the iron(III)/iron(II) couple behaves in a reversible fashion on pyrite surfaces. Different studies are cited, proposing that hole injection into the t_{2g} valence band is a possible rate-limiting step. However, various mechanistic schemes may be proposed to describe pyrite dissolution, depending on the particular crystal face and conditions at the surface, *e.g.*, temperature and the nature and concentration of different oxidative species.

If holes are supplied at a fast rate (*cf.* its surface consumption) to the non-bonding *d* orbitals of iron in the pyrite surface-structure, the water-split mechanism may become the dominant mechanistic route. The negative effect of higher proton concentrations on this anodic dissolution reaction is ascribed to its interference in this charge transfer process, *i.e.*, increasing the activation energy barrier, even though the adsorbed proton is proposed to play an intrinsic part in stabilising intermediate surface sulfide species ($HS^{\cdot}$). Under high dissolved oxygen concentration conditions at higher temperatures, the transfer of electrons may follow a Fenton-type mechanism at metal sites rather than at surface sulfide sites. The primary reason for the catalytic properties of the pyrite

Stellenbosch University http://scholar.sun.ac.za

surface towards oxygen reduction is most probably related to the strong adsorption of the diatomic molecule at the surface iron site. Once again, the non-bonding t_{2g} orbital of iron and the enhanced electron affinity of the protonated diatomic oxygen molecule are proposed to be key factors that could facilitate the first, rate-limiting, electron transfer step. This mechanistic proposal assumes that the free-radical transition state operates within conductive hydrogen-bonded water networks. Subsequent removal of electrons allows sulfur to become more electropositive, causing adsorbed protons to desorb, before the negative end of water can mount a nucleophilic attack. This sequence releases protons, equivalent to the number of electrons and protons accepted by oxygen during its reduction. Regarding the rate-limiting steps, the band gap of the pyrite surface is relatively small, explaining its quasi-metallic behaviour, *i.e.*, it has higher Tafel slopes than would be expected from a semiconductor. Its conductivity is therefore higher than the bulk material and electron transfer between anodic and cathodic sites would not be expected to be rate limiting, and neither would be the supply of holes to non-bonding orbitals.

On local short-circuited cells, where adsorbed water is exposed to a hole in the t_{2g} orbital of iron, the splitting of water and first electron transfer to oxygen are proposed as the two primary rate-limiting anodic and cathodic steps, respectively, with the former best viewed as a reversible transition state. Both rate-limiting reactions would therefore be dependent on the proton concentration and the net-positive or -negative effect would depend on the most dominant relationship. The manifestation of anodic and cathodic sites on pyrite surfaces would be dictated by the properties of a particular crystal facet, as well as by the nature of the dominant oxidant species at the interface. Direct electron exchange between oxygen and the disulfide entity would be least favourable, due to spin restrictions. In that sense, ferric ion may be a more reactive electron acceptor, because there would be no loss of molecular orbital stabilisation energy. It may be less likely for such a highly charged positive entity to approach a protonated surface compared to a neutral oxygen molecule. On the other hand, the water molecules surrounding a ferric ion may dampen the field (high dielectric) and facilitate electron transfer (diamagnetic molecules in the hydration sphere) without a requirement of direct ferric ion adsorption onto a disulfide site. An even more important factor may, however, be the high degree of iron(III) sulfate CIP formation at high temperatures, rendering ferric ion relatively ineffective as an oxidant. Therefore, charge transfer mediation of iron t_{2g} surface states, facilitated by the attachment of positive species to the oxygen molecule, *e.g.*, hydrogen or ferric ion, is assumed to promote oxygen reduction, leaving a hole in the non-bonding orbital. This hole may either migrate to an anodic site, where only water is oxidised, or it may oxidise the disulfide entity *via* a number of different possibilities. Any reaction that involves perhydroxyl and hydroxyl radicals would provide an attractive thermodynamic and kinetic pathway for hole injection into the bonding orbitals of the disulfide unit.

Stellenbosch University http://scholar.sun.ac.za

Sphalerite oxidation

Compared to pyrite, sphalerite represents the other extreme in this study, *i.e.*, in terms of its rest potential and its ability to interact with oxygen at high temperatures in an autoclave. Sphalerite has a wide band gap and would therefore be expected to behave like a semiconductor, with the ferric/ferrous couple placed (energetically) almost in the middle of the band gap. Ferric ion would also not be expected to be an efficient oxidant for sphalerite. However, iron impurities in sphalerite have the effect of creating an impurity band within the band gap of zinc sulfide. This localised impurity band originates from the *d* orbital of iron and supplies holes for the conduction mechanism. The transfer of electrons is therefore energetically more favourable, compared to the valence band, and, since the iron *d* orbital is of a bonding character, the removal of electrons from this band would result in the dissolution of the solid. In addition, a high density of mono-energetic surface states is created due to this impurity band, which has the effect of making the potential change across the space charge layer independent of the solution electrochemical potential. A variation in solution potential only manifests itself in a potential change across the Helmholtz layer, *i.e.*, the interface assimilates metal-like behaviour. If the space-charge region is sufficiently narrow, quantum tunnelling will occur between the surface *d* orbital and the valence band. This would result in the oxidation of a sulfide atom in close proximity, to form elemental sulfur with the release of zinc ion into solution. Ferric ion therefore oxidises sphalerite directly, and the rate of this reaction is dependant on the iron impurity levels in the mineral. Just like chalcopyrite, this intrinsic oxidation mechanism may be affected by surface layers, *e.g.*, the formation of copper sulfide films on sphalerite has been shown to decrease its oxidation rate in copper sulfate solutions.

Covellite oxidation

Although covellite constitutes a relatively minor phase in the concentrates used in this study, it was proposed by various authors to be formed as an intermediate phase during the oxidation of chalcopyrite, copper mattes and chalcocite, especially at higher temperatures. The crystal structure is complex, but consists predominantly of copper(I) at its surface. Covellite is a *p*-type metallic conductor, because the valence band is only partially filled. The upper valence band is mainly a crystal field band, similar to pyrite, and this may explain the relatively high potential required to dissolve covellite during cyclic voltammetry. Its elemental sulfur yield has generally been found to be relatively low (< 50%) and of amorphous character in the sulfate system. This observation also ties in with previous discussions, suggesting that polymeric sulfur may form under conditions of higher surface polarisation. Increased covellite oxidation rates with oxygen partial pressure and the low intrinsic elemental sulfur yield, especially at higher temperatures, suggested that oxygen is readily reduced on a covellite surface, similar to pyrite. However, the mechanism is fundamentally different and it is assumed to rely on the presence of copper(I) surface states, analogous to the above discussions for chalcopyrite. An important conclusion from the literature is that compounds,

Stellenbosch University http://scholar.sun.ac.za

all referred to as covellite, may oxidise at significantly different rates, depending on their history. For example, synthetic covellite may react at a different rate compared to a remnant covellite phase on a host copper sulfide mineral, while some natural covellite minerals have been found to oxidise more slowly than chalcopyrite and pyrite.

The role of surfactants above the melting point of sulfur

As mentioned above, the formation of a molten sulfur layer, irrespective of its allotropic form, should be viewed as a secondary inhibiting effect towards mineral oxidation. Surfactants (sulfur dispersing agents) are used to disperse this molten layer from the unreacted mineral surface, by lowering the sulfur/solution interfacial tension and by making the mineral less sulfophilic. The combination of lignosulfonate (LS) and Quebracho (QB) has been found to be most effective in decreasing the work of sulfur adhesion under AA-UBC leach conditions. However, these surfactants rapidly degrade at high temperatures in an oxidative autoclave, especially in the presence of copper. Without effective dispersion of elemental sulfur, mineral oxidation usually displays parabolic kinetics, attributed to the diffusion of the oxidising agent through a constantly thickening layer of elemental sulfur. Above the melting point of sulfur, this layer may completely stifle the mineral oxidation reaction.

6.6.2 Intrinsic mineral oxidation rate expressions

This section summarises how the above insights are used to derive sulfide mineral oxidation rate expressions that are simplistic enough from a phenomenological modelling perspective, while maintaining consistency with the published literature. The overall methodology is based on an electrochemical reaction framework, *i.e.*, relating the rates of the cathodic the half-cell reactions to the rates of the anodic half-cell reactions by virtue of no charge accumulation (*via* the MP theory). The departure point in deriving these rate expressions is a qualitative understanding of the species adsorption on the most probable mineral faces, using quantum-level calculations of the surface structures and species adsorption energies (these results are presented in Sect. 6.3.4).

Pyrite

Hydrogen and ferric ions compete for sulfide surface sites on pyrite (100) surface, while oxygen adsorbs strongly (two-fold bond) with a single iron substrate. This strong adsorption causes severe distortion of the pyrite surface, making the ferric ion approach highly unfavourable. The non-bonding t_{2g} orbital of surface iron is assumed to catalyse the first oxygen reduction step at high temperatures, with proton adsorption dominating at sulfide surface sites. Hole formation by oxygen is therefore assumed to be the dominant mechanism at higher temperature because of retarded iron(III) *vs.* oxygen reactivity, either due to electrostatic (Fe^{3+}), complexation (sulfate CIP formation) and/or iron(III) precipitation phenomena. Assuming that the first electron transfer step

Stellenbosch University http://scholar.sun.ac.za

is limited by the (cathodic) oxygen reduction rate, the anodic processes are divided between surfaces where sulfide oxidation would be accompanied by water oxidation on a different site and surfaces of local short-circuited cells without any water oxidation mechanism.

Attention is first focussed on the migration of holes to surface iron sites where water oxidation is most prevalent, *i.e.*, neglecting the migration of holes to sites where interaction with sulfide bonding orbitals would occur. The rate-limiting anodic and cathodic reactions are then:

$$H_2O^* + h^+ \Rightarrow H^+ + OH\cdot^* \qquad 6.166$$

$$O_2^* + H^+ \Rightarrow HO_2\cdot^* + h^+ \qquad 6.167$$

where the asterisk denotes the adsorbed species. It is assumed that these reactions would gradually build a surface consisting of predominantly $Fe(OH)S_2$. At lower temperatures and potentials these reactions may be reversible, as illustrated by cyclic voltammetry (in the literature). This surface may readily exchange electrons with less noble (*i.e.*, more reactive) minerals or (pyrite) surfaces (*e.g.*, 110), but is deliberately ignored for now. Application of the MP theory and assuming symmetrical charge transfer across the Helmholtz layer yield the following expression of the concentration (mol/kg water) of surface oxide species (see Sect. 6.3.4 for derivation & symbols):

$$[Fe(OH)S_2] = a_{Fe(OH)S_2} \cdot k_{Fe(OH)S_2} [H^+]^{m_1(1-\beta_1)+n_1\beta_1} [O_2]^{\beta_1} \qquad 6.168$$

Due to the presence of these highly oxidising species under MT autoclave conditions, non-oxidative mechanism is ignored. It is proposed that these surface hydroxyl species could self-propagate *via* water to an anodic site, *i.e.*, to oxidised sulfide, without necessarily being in physical contact with this surface. If sulfide oxidation is limited by the first charge transfer step, irrespective of whether the pathway is driven by physical migration or self-propagation of radical species, the anodic reaction may be expressed as follows:

$$S_2^{2-}|_{Py} + H^+ + h^+ \Rightarrow S + HS\cdot^* \qquad 6.169$$

The role of the proton is not clear, but is assumed to be associated with the stabilisation of the S–HS· species, before its subsequent oxidation to form diatomic or elongated sulfur (S_x), polysulfides and higher oxidation products. The simplest mathematical description of the pyrite oxidation rate is to separate the anodic oxidation of sulfide by an oxidant at close proximity from anodic sulfide oxidation by reactive oxides on a more stable pyrite surface. This leads to the following overall rate expression for pyrite oxidation:

$$r_{Py} = k_{Py} [H^+]^{\frac{1}{2}n_2} [O_2]^{\frac{1}{2}} + \theta_{Py_c} a_{Py} k_{Py_c} [H^+]^{\frac{1}{2}(m_1+n_1)} [O_2]^{\frac{1}{2}} \qquad 6.170$$

Stellenbosch University http://scholar.sun.ac.za

where θ_{Pyc} represents the fraction of catalytic pyrite surface, exhibiting a lesser tendency to dissolve and a higher tendency to oxidise water, *i.e.*, refractory pyrite. Importantly, cognisance has to be taken of the phenomenological nature of this expression. For example, under autoclave oxidation conditions and in the case of a less refractory pyrite, this so-called 'catalytic' surface could lead to its own demise, *i.e.*, the water oxidation mechanism could lead to sulfide oxidation on all surfaces and the first term in Equation 6.170 would become redundant; with $\theta_{Pyc}a_{Py}k_{Pyc} = k'_{Py}$. This scenario would be most consistent with the notion that sulfate, formed from pyritic sulfur, acquires its oxygen atom from water and not diatomic oxygen. The reality under MT autoclave conditions may, in fact, lie between these extreme scenarios, which could be dealt with, on a phenomenological level, by assuming that θ_{Pyc} remains constant over time and that the total pyrite surface area, a_{Py}, varies according to the unreacted shrinking particle (USP) model.

Sphalerite

Sphalerite surfaces show no/little tendency to reduce oxygen, which is reflected by a comparatively (*cf*. pyrite) weak binding energy of diatomic oxygen on all its surfaces. The anodic dissolution reaction, with ferric ion as the oxidant, is represented by the following rate-limiting step:

$$S^{2-}|_{Sph} + H^+ + h^+ \Rightarrow HS^{\cdot *} \qquad 6.171$$

At the relatively low mixed potential, the dissolution of particular mineral faces (*e.g.*, 110) may be driven by strong proton adsorption, followed by a non-oxidative dissolution tendency:

$$S^{2-}|_{Sph} + H^+ \Rightarrow HS^{-*} \qquad 6.172$$

In the copper system, however, the bisulfide species would rapidly form a covellite structure, before dissociating and desorbing from the surface due to the low solubility of CuS:

$$HS^{-*} \Rightarrow S^{2-}|_{Cov} + H^+ \qquad 6.173$$

This reaction would be expected to be insensitive to the copper concentration above a certain critical value. The simplest treatment is to assume that the mixed potential would be different on surfaces where sphalerite is exposed (ferric ion reduction) and surfaces coated with covellite (oxygen reduction). This results in the following dissolution rate expression for sphalerite in acidic copper sulfate solutions:

$$r_{Sph} = (1-\theta_{Cov})k_{Sph}\left(\frac{k_{Fe^{3+}}[Fe^{3+}]}{1+k_{Fe^{2+}}[Fe^{2+}]}\right)^{\frac{1}{2}} + \theta_{Cov}k_{Cov}[H^+]^{\frac{1}{2}n_5}[O_2]^{\frac{1}{2}} \qquad 6.174$$

The presence of diffusion barriers, such as prevailing surface (elemental) sulfur, and the particular mineral surface would determine which of these reaction paths dominates, *e.g.*, the (100) surface

Stellenbosch University http://scholar.sun.ac.za

would be less amenable to proton adsorption, but may exchange electrons with ferric ions *via* a surface water conduction mechanism. No catalytic effect due to the presence of pyrite surfaces is required in this expression, because the disseminated (chalcopyrite/sphalerite) HBMS 777 concentrate has relatively low pyrite content (< 10%). Since the rest potential of pyrrhotite is even lower than that of sphalerite, with strong proton adsorption characteristics, similar rate expressions are applicable for this mineral under MT autoclave conditions in acidic copper sulfate solutions.

Chalcopyrite

Diatomic oxygen exhibits modest binding energy with chalcopyrite surfaces: qualitatively almost halfway between the two extremes, *i.e.*, strong, two-fold adsorption on pyrite *vs.* weak interaction with a sphalerite surface (Sect 6.3.4; Table 6.3). The end-on adsorption of the oxygen molecule displays a lower binding energy than that of ferric ion, while the proton adsorbs even more strongly on chalcopyrite (110) compared to ZnS (110) surface. Various reaction paths may therefore dominate on the chalcopyrite surfaces, complicating the derivation of a single rate expression.

Preliminary quantum-level modelling results reveal that the valence band edge is described by the Fe 3*d* and S 3*p* states, while the conduction band edge is represented by Cu *s* and *p* orbital states. This explains why iron would leach first during oxidative dissolution and probably *via* the ferric/ferrous redox couple (energetically best positioned). The presence of empty Fe *d* and S *p* orbitals above the Fermi level suggests that chalcopyrite should behave like a metal during oxidation, provided the redox couple is positioned accordingly. Furthermore, the surface structure also introduces a large number of states, which reduces the band gap to values significantly less than 0.65 eV. Therefore, theoretically, chalcopyrite oxidation should be fast. However, the Cu–S bonding orbitals are situated at negative energy levels, which may only be directly accessible by highly reactive oxidant species, *e.g.*, the surface perhydroxyl radical ($E_h \approx 1.5$ V). There is also strong evidence of the formation of covellite-like surfaces on chalcopyrite during pressure oxidation in acidic solutions. High binding energy is also calculated for the proton on specific chalcopyrite surfaces (*e.g.*, 110). It is therefore proposed that the chalcopyrite dissolution mechanism may also produce copper sulfide surfaces, here denoted as Cu_xS, but the mechanism may differ from the one proposed for sphalerite. This phase would be expected to contain a high density of copper(I) and the oxygen reduction mechanism may dominate on this surface. The dissolution current due to iron(III) reduction would be relatively minor, due to the stability of the Cu–S bond, while surface sulfide sites would be expected to be heavily protonated.

Once again, the first reduction step of oxygen (to form the perhydroxyl species) is assumed to be rate limiting. Furthermore, peroxide reduction has been shown to be kinetically slow on less catalytic surfaces, *i.e.*, desorption may effectively result in its destruction. On some surfaces, a

Stellenbosch University http://scholar.sun.ac.za

more congruent release of copper and iron atoms could also occur, but oxygen would be expected to reduce less efficiently when exposed to an unaltered sulfide phase (S_2^{4-}). Both iron(III) and oxygen could therefore oxidise chalcopyrite at appreciable rates, depending on the prevailing surface structure, while the mixed potential is assumed to be similar for these two reaction routes, *i.e.*, hole injection by iron(III) species, or by oxygen, limited by the first reduction of the diatomic molecule.

The presence of catalytic pyrite surfaces could also accelerate chalcopyrite oxidation at high pulp densities. A symmetric charge transfer coefficient is assumed for the catalytic (pyrite) surface formation reaction, while the activation energy barrier of its reaction with a chalcopyrite surface is assumed to be exclusively associated with the anodic reaction. The following overall intrinsic rate equation of chalcopyrite mineral oxidation results:

$$r_{Cpy} = (1-\theta_{Cu_xS})k_{Cpy}\left(\frac{k_{Fe^{3+}}[Fe^{3+}]+k_{O_2}[H^+]^{n_6}[O_2]}{1+k_{Fe^{2+}}[Fe^{2+}]}\right)^{\beta_6} + \theta_{Cu_xS}k_{Cu_xS}[H^+]^{n_8\beta_8}[O_2]^{\beta_8} + \theta_{Py_c}a_{Py}k_{Py_c}[H^+]^{\frac{1}{2}(m_1+n_1)}[O_2]^{\frac{1}{2}} \quad 6.175$$

If additional layers, *e.g.*, elemental sulfur, are formed on top of the above surface structures, a retarded rate of electron transfer would be expected for all reaction routes, *i.e.*, reaction routes involving iron(III), oxygen, as well as enhancement routes involving catalytic pyrite surfaces.

No conclusive evidence has been presented in the open literature to support any one mechanism over another, except for the observation of Cu_xS surface under higher oxidation temperature conditions. This is an engineering study and the above propositions will remain speculative until modelled on a fundamental level and verified experimentally.

6.6.3 Phenomenological (experimental) rates and dependencies

Although the experimental programme was not designed to answer fundamental mechanistic questions, the unreacted shrinking particle (USP) model is used to mathematically relate the overall observed oxidation phenomena (leaching results) to the above mechanistic proposals. The experimental conditions were controlled, within practical limits, to simplify the interpretation of the leaching results. This included the development of experimental procedures to minimise external (non-intrinsic) effects, careful control of the operating conditions and solution composition, and the use of narrow-sized mineral particles of high chalcopyrite content (low gangue mineral content). In addition, each kinetic datapoint consisted of a separate leach test, which eliminates sampling effects at high temperatures and (statistically) minimises the impact of the experimental error on

Stellenbosch University http://scholar.sun.ac.za

the observed rate constant value. The testwork programme utilised four narrow-sized fractions, each obtained from the same HBMS 777 chalcopyrite concentrate. There were relatively insignificant mineralogical variations between these fractions, yielding good agreement with the average calculated composition of approximately 82% chalcopyrite, 7% sphalerite, 7.5% pyrite and 1% pyrrhotite. Very little association between the total base metal sulfide (BMS) and gangue minerals was prevalent, with only a small number of chalcopyrite particles being associated (in physical contact) with sphalerite and pyrite phases.

Although the solution redox potential is reported for each test (App G), no attempt is made to relate this potential to the elemental sulfur yield. This is because the average oxidation state of sulfur depends more heavily on the mineral surface conditions than on the solution potential. The objective of the batch leaching program was to establish phenomenological oxidation rate equations for the chalcopyrite concentrate, based on the bulk solid and solution properties. Neither electrochemical nor pure mineral sample leaching studies were therefore undertaken. The conclusions obtained from this batch test programme (Sect. 6.5) may be summarised as follows:

- A small amount of copper(II) reacts with chalcopyrite and sphalerite (metathesis reactions) during autoclave heat-up, which resembles the conditions experienced by the continuous pilot autoclave feed in the heat exchanger (Ch. 7)
- Low and variable batch test pulp densities (0.5-1.5 wt%) result in similar copper leaching extents and elemental sulfur yields, suggesting that the reaction mechanism is not affected by pulp density changes in this low range. These and other batch results also suggest insignificant interfacial gas/liquid mass transfer limitations in the 2-litre Parr autoclave, while the sulfide mineral oxidation rates appear insensitive towards the iron(III) concentration
- Different types of lignosulfonate (LS) surfactants (Norlig A & Arbo A02) result in similar chalcopyrite oxidation rates, but different sphalerite oxidation rates and elemental sulfur yields. The zinc extraction rate and elemental sulfur yield decreased in the presence of Arbo A02, even though higher initial iron(III) concentration was present, suggesting that the workings of these surfactants may alter the dominating mechanisms at the mineral surfaces in these two cases
- USP model plots under surface reaction control reflect linear initial kinetics, but deviate from this (parabolic kinetics) after about 45 minutes. This reaction regime change is not caused by a changing solution composition over time and the repeatability is excellent. In general, rate constant accuracies better than ±15% (conservative) were obtained. Sulfur speciation results were too variable to accurately determine the relative oxidation rate of pyrite *vs.* chalcopyrite, but consistent enough to suggest that no appreciable oxidation of

Stellenbosch University http://scholar.sun.ac.za

stable elemental sulfur (to acid) occurs, once it has been formed, *i.e.*, over typical experimental timeframes. In conclusion, no mechanism change is observed by doing testwork at low pulp densities, neither are any apparent oxygen mass transfer effects prevalent, at least not for the coarser narrow-sized fractions. Reaction extents respond in a relatively consistent manner to changes in the solution composition and oxygen partial pressure. However, different surfactants appear to exert a strong effect on the stability of elemental sulfur on the chalcopyrite mineral surface; the rest of this testwork programme focussed on the surfactants used during the continuous pilot campaigns (Ch. 7)

- With regard to the initial reaction regime, the chalcopyrite oxidation rate is insensitive to different surfactant concentrations, *i.e.*, over typical concentration ranges encountered in industrial operation. Again, sudden deviations from linearity prevail, even at the highest surfactant dosages. This suggests that the surfactants become ineffective after an initial period (45-60 min) of rapid oxidation, and this is thought to be the primary reason for the sulfur blockage problems experienced in the latter compartments of the continuous autoclave during piloting (Ch. 7). A test conducted at significantly (25%) lower impeller speed, representing at least a 50% drop in the k_La-value, yields a similar linear rate constant value (within experimental uncertainty) compared to the baseline test, confirming that insignificant oxygen mass transfer or film diffusion limitations were prevalent
- No improvement in the rate of copper dissolution is achieved by injecting additional surfactants at the deviation point from linearity, *i.e.*, at around 45 minutes. Secondary electron images (SEI) and qualitative energy dispersive X-ray (EDX) results confirm that elemental sulfur can act as a ‘collector’ of unreacted sulfides, resulting in a lower accessible surface area and a lower observed reaction rate. Additional surfactant addition is unable to disperse these conglomerates, which is probably due to the inability of such large macro-molecules to diffuse though molten elemental sulfur, enveloping unreacted chalcopyrite surfaces. Deviation from linear oxidation rate occurs even in cases where no initial copper was added to the leaching system. The absence of any surfactants results in substantial sulfur agglomeration, confirming that surfactants are indeed necessary, even for the finest particle size fractions.
- Higher acid concentrations accelerate the initial copper leaching rates but show reduced leaching rates at longer reaction times, especially for the coarser fractions. Elemental sulfur is therefore assumed to be more difficult to disperse at a higher acid concentration, which has a more pronounced effect on coarser particles by virtue of their slower oxidation kinetics, accompanied by surfactant degradation
- A linear relationship is obtained by plotting the observed rate constants of the three coarser size fractions against the inverse of the initial mean particle size. The finest fraction yields

Stellenbosch University http://scholar.sun.ac.za

slightly higher reaction rates but this may be due to experimental error. Furthermore, this sample was prepared by excessive milling in the Stirred-media detritor (SMD), suggesting that mechanical activation could have increased the intrinsic reaction rate

- Integration over particle size indicates that a distribution of sizes, albeit narrow, causes the deviation from linearity for the finer particle size fractions at high metal extractions. However, this effect cannot explain the apparent deviation from linearity for the two coarser fractions, confirming that surfactant degradation is responsible for the agglomeration of unreacted sulfide particles and the subsequent drop in the reaction rate. Further confirmation of this phenomenon is obtained by removing elemental sulfur from an intermediate residue with an organic solvent, before commencing with further oxidation. The reaction rate is re-established after this sulfur removal step, confirming that molten elemental sulfur is responsible for the stifling of the oxidation reactions at relatively long (> 45-60 min) reaction times
- It is important to realise that the above elemental sulfur effects are secondary to the intrinsic reaction mechanism at the mineral surface. The leaching kinetics were consistently found to be insensitive to the iron(III) concentration and a further attempt was made to reveal additional information on the chemistry (stoichiometry) and mechanism of oxidation (see proposal below), despite the phenomenological nature of the batch experiments
- The molar ratio of iron to copper in the solid and solution phases shows considerable randomness, with no conclusive evidence of any preferential iron leaching. However, most of the chalcopyritic iron appears to enter the bulk solution in the reduced form, and, in terms of the overall reaction stoichiometry, it is assumed that copper(II) is the product of the mineral dissolution reaction. On the other hand, the pyrite surface supports a high surface concentration of oxidative species and it is assumed that all pyritic iron enters the solution in the oxidised form
- Increased oxygen partial pressures result in increased sulfide mineral oxidation rates, confirming the importance of the cathodic reaction on the overall mechanism. Deviation from linear (USP) kinetics is more prevalent at higher oxygen partial pressures, while the elemental sulfur yield is relatively insensitive to such changes, suggesting that the oxygen is primarily responsible for the degradation of the surfactants
- Optical microscope, backscatter electron (BSE) and EDX analyses have confirmed the presence of rims on partially oxidised chalcopyrite particles, analysing high copper and oxygen concentrations with decreasing iron levels towards the outer surface. At lower oxygen partial pressures, these rims display bimodal composition, *i.e.*, a thin covellite-like layer, enveloped by copper sulfate rims. No accurate analyses are possible by EDX,

Stellenbosch University http://scholar.sun.ac.za

because these rim thicknesses are smaller than the excitation envelope. These alteration rims also appear to be discontinuous and their role in inhibiting chalcopyrite oxidation is therefore questioned. Furthermore, residues produced over longer times at higher oxidation potentials reveal no particle rims. It is therefore concluded that, although these mineralogical techniques provide accurate imaging of surface phenomena occurring in fine-grained residues, they can only serve as a useful adjunct to X-ray photoelectron spectroscopy (XPS)

- XPS reveals that the residue surfaces, produced at typical oxygen partial pressures (700 kPa $p_{O2}°$), contain a high concentration of copper(I), associated with monosulfide, suggesting the formation of covellite-like surface layers. At lower oxygen partial pressures, the surface consists of copper(II) sulfate, overlying a di-or polysulfide mineral. These XPS analyses also confirm the absence of well-developed elemental sulfur product layers when utilising Arbo A02 LS at low pulp densities
- Although these preliminary mineralogical and XPS techniques provide no conclusive evidence of the exact nature of the sulfide surface layer on host chalcopyrite particles, the absence of iron and the abundance of copper(I) monosulfide is indicative of a covellite-like surface structure. It is proposed that oxygen reduction would be the dominant cathodic reaction, which, in turn, would allow relatively fast mineral oxidation kinetics under MT autoclave conditions, *i.e.*, compared to atmospheric processes, where oxygen or iron(III) reduction would be relatively slow on such surfaces. The role of elemental sulfur, forming impervious surface structures, should also not be underestimated, although the above results suggest that this scenario is linked to surfactant degradation
- The reaction kinetics are relatively insensitive to the background sulfate salt composition, particularly over relatively wide copper and iron(III) concentration ranges. This simplifies the intrinsic chalcopyrite oxidation rate expression, as there is no need to express its variation with changing solution composition in terms of a covellite-like surface coverage, *i.e.*, it may be assumed that θ (Cu_xS) = 1 in Equation 6.175. Omitting the role of iron(III) from this rate expression does not necessarily imply that the oxidation mechanism of chalcopyrite does not involve iron(III). It does, however, suggest that iron(III) reduction is not related to any of the rate-limiting steps under MT autoclave conditions.

6.6.4 Quantification (regression) and verification of the chalcopyrite oxidation rate model

The final form of the phenomenological oxidation rate expression is obtained from the regression of the experimentally observed rate constants, using the initial rate data of the three coarser particle size fractions, in conjunction with the solution chemistry model (Ch. 2) to calculate the vapour pressure and free hydrogen ion concentration. The following optimised expression is obtained for

Stellenbosch University http://scholar.sun.ac.za

the intrinsic chalcopyrite oxidation rate at low pulp densities, *i.e.*, at low (catalytic) pyrite surface areas, in acidic copper sulfate solutions, at 150°C:

$$k_{\ell,Cpy} = 2[H^+]^{\frac{1}{6}}[O_2]^{\frac{1}{2}} \qquad 6.176$$

Using this relationship and simultaneously solving the intrinsic dissolution rate expression and the oxygen mass transfer rate for the test reactor (2-litre Parr autoclave; Chapter 3), reveals notable interfacial mass transfer limitations in the case of the finest narrow-sized fraction, *i.e.*, under conditions of higher total surface area.

In terms of the rate of pyrite oxidation, there is a general lack of any correlation between the relative oxidation extent of pyrite and that of chalcopyrite, which highlights the impact of inaccurate chemical analyses on our ability to calculate dissolution rates of minor mineral phases. The simplest approach is to compare the total copper and total iron leaching extents for the tests where no iron precipitation occurred. After accounting for iron dissolution from pyrrhotite and sphalerite, using residual zinc as the calculation basis, there is neither an indication that pyrite leached faster than chalcopyrite, nor that iron leached preferentially to copper. Bulk modal analyses of leach residues also suggest that chalcopyrite and pyrite oxidise at similar initial rates, while pyrrhotite oxidation closely follows the sphalerite oxidation rate. However, the pyrite oxidation rates appear to accelerate at longer reaction times, which contradict the (passivation) behaviour normally observed for refractory minerals, whether caused by an intrinsic surface mechanism or by the formation of molten sulfur product layers. As a first estimate, it is crudely assumed that pyrite oxidises at approximately the same rate as chalcopyrite (re-evaluated in Ch. 7), while a similar assumption is adopted for pyrrhotite *vs.* sphalerite oxidation rate under MT autoclave conditions.

BSE images and SEI reveal preferential attack at particular chalcopyrite crystal planes, especially during initial oxidation, casting some doubt on the applicability of the USP model to describe mineral oxidation kinetics. Nevertheless, the general USP model framework and the associated rate expressions appear robust enough to be used as a phenomenological modelling tool.

In terms of the intrinsic oxidation of sulfide to elemental sulfur, the experimental data are too variable to detect any correlation with the total copper leaching extent. However, they confirm insignificant oxidation of stable elemental sulfur over typical MT reaction times, once it has formed. By assuming rapid oxidation of sphalerite and pyrrhotite to yield 100% elemental sulfur, the chalcopyrite and pyrite sulfur yields appear to increase slightly at higher free hydrogen ion concentrations. The pyrite sulfur yield is fixed at 1% at 0.1 mol/kg H^+ (~0.1 mol/kg H_2SO_4) and assumed to respond similarly the chalcopyrite sulfur yield (same slope). The following fractional sulfur yields (valid from 0.1 mol/kg H^+) are subsequently obtained:

Stellenbosch University http://scholar.sun.ac.za

$$S^o/S_{rx,Cpy} = 0.59 + 0.3 \cdot [H^+] \qquad 6.177$$

$$S^o/S_{rx,Py} = (0.01 - 0.03) + 0.3 \cdot [H^+] \qquad 6.178$$

The rate of (molten) elemental sulfur oxidation, albeit slow, is captured in the overall model (Ch. 7) by using the rate expressions developed in Appendix A.6.

6.6.5 Qualitative picture of the chalcopyrite oxidation mechanism

The above discussions reflect current understanding of the mechanism of chalcopyrite oxidation in acidic solution environments under MT conditions. This limited information, in combination with the insights gained from the literature review, is now used to propose a qualitative and simplified mechanism of chalcopyrite oxidation by oxygen.

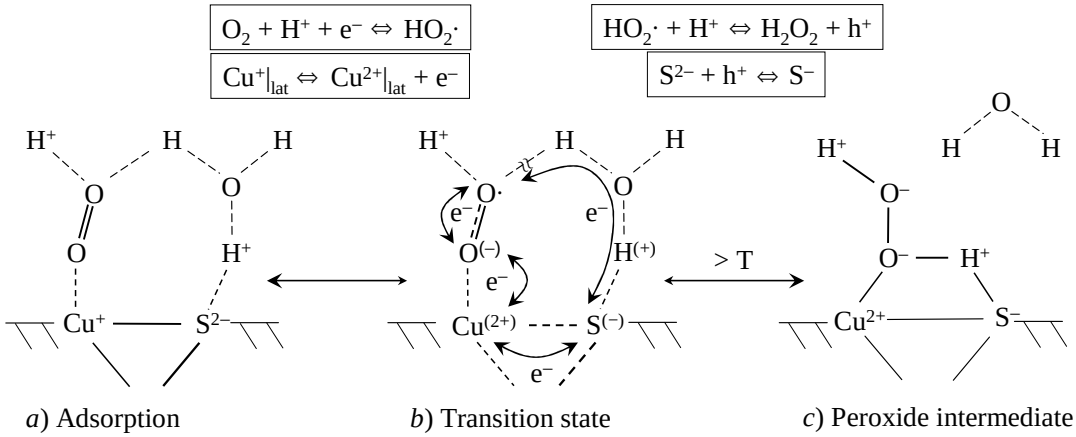

Figure 6.66
Simplistic mechanism of chalcopyrite oxidation by oxygen: *a*) Protonation of surface sulfide sites & adsorption of diatomic oxygen at Cu(I) sites; *b*) Reduction of diatomic oxygen to form the perhydroxyl intermediate, followed by oxidation of nearby sulfide sites; *c*) Peroxide intermediate.

Firstly, it is assumed that the ferric/ferrous ion couple is energetically favoured to inject holes in the iron–sulfide bonding orbitals (Figure 6.21) and to release iron from the surface structure. The reaction is assumed to be fast at autoclave temperatures, resulting in the restructuring of the structure to resemble a covellite-like surface.

It is further expected that the proton would form strong chemisorption bonds with the sulfide sites, while oxygen would preferentially adsorb at copper(I) sites and undergo reduction according to the scheme presented in Figure 6.66. The electrocatalytic role of copper(I) in the first reduction step of oxygen is thermodynamically marginal at -0.03V (based on E^o_h for Cu^{2+}/Cu^+ couple of 0.153 V from Lide, 1991, & 0.12V for diatomic oxygen from Wardman, 1989), but kinetically fast (Table 6.2). The transient HS· radical state may be produced by the reaction between the resulting

Stellenbosch University http://scholar.sun.ac.za

perhydroxyl species (Rx. 6.107) and the adjacent sulfide in the mineral lattice. This couple may be estimated as follows, with a standard reduction potential of 1.15 V (Wardman, 1989):

$$HS^- \Leftrightarrow HS\cdot + h^+ \qquad 6.179$$

The overall reaction to form the peroxide intermediate molecule is thermodynamically favourable (1.45 V – 1.15 V = 0.3 V; values from Wardman, 1989):

$$HS^- + HO_2\cdot + H^+ \Rightarrow HS\cdot + H_2O_2 \qquad 6.180$$

Elemental sulfur may be formed by the following two half-cell reactions:

$$HS\cdot + h^+ \Leftrightarrow S^o + H^+ \qquad 6.181$$

$$H_2O_2^* + H^+ \Rightarrow OH\cdot^* + H_2O + h^+ \qquad 6.182$$

The standard reduction potentials of these two couples are -1.3 V and ~0.7 V, respectively (Wardman, 1989). The net potential (+2 V) of this mechanism is highly positive and suggests that the HS· radical state may catalyse peroxide reduction to form the highly reactive, hydroxyl radical:

$$HS\cdot + H_2O_2^* \Leftrightarrow S^o + OH\cdot + H_2O \qquad 6.183$$

Subsequent oxidation of elemental sulfur may therefore be expected:

$$S^o + OH\cdot + H^+ \Rightarrow S^+ + H_2O \qquad 6.184$$

Depending on the prevailing surface conditions (species), thiosulfurous acid ($H_2S_2O_2$) or elemental sulfur may form as a result of this S^+ species (Sect. 6.3.2). Thiosulfurous species may (theoretically) yield 75% sulfur, *i.e.*, sulfur may follow the following overall route during chalcopyrite oxidation by iron(III) and oxygen:

$$2S^{2-} \Rightarrow \tfrac{7}{4}S^o + \tfrac{1}{4}S^{6+} + 10e^- \qquad 6.185$$

Theoretically this yields 87.5% elemental sulfur, which is obviously higher than the experimental yield of around 60% at 150°C (see above). The intermediate HS· species, formed after initial oxidation by iron(III), may also catalyse the reduction of the diatomic oxygen molecule (analogous to Rx. 6.183; net potential of ~1.4 V) on adjacent metal sites, with subsequent oxidation to higher sulfur oxidation states.

As indicated in Figure 6.66, electron transfer may occur *via* conduction mechanisms in the solid phase or solution phase, adjacent to the reacting surface. Sulfur chemistry is complex and highly dependent on the mineral surface conditions. An empirical approach is therefore adopted in the rest of this study. A complete representation of the mechanism of chalcopyrite oxidation may only be revealed after comprehensive quantum-level simulation, which fell outside the scope of this study.

Stellenbosch University http://scholar.sun.ac.za

CHAPTER 7. BATCH & CONTINUOUS REACTOR SIMULATION

7.1 Introduction

This chapter deals with the modelling of a continuous multi-compartment autoclave and a comparison of the model calculations with the results obtained from two integrated pilot campaigns. Furthermore, it discusses the results of supplementary batch oxidation testwork, using three copper concentrates from different locations, to shed more light on different mineral behaviour under medium temperature (MT) operating conditions. The reactor model is also extended to simulate the batch leach responses of these concentrates at low pulp densities, which, in turn, are used to regress their intrinsic rate constants and activation energies.

The initial part of this chapter focuses on modelling theory and methodology, which are then applied to develop the continuous reactor model, based on the thermodynamic and rate expressions developed earlier, *i.e.*, the solution chemistry (Ch. 2), interfacial oxygen mass transfer rate (Ch. 3), iron(II) oxidation rate (Ch. 4), iron(III) precipitation rate (Ch. 5) and the intrinsic mineral oxidation rates (Ch. 6). This model output is then compared to the actual pilot plant results at 150°C, using the HBMS 777 chalcopyrite concentrate (Sect. 6.4.3) as feed material. The second part of this chapter reports the measured low pulp density oxidation rates and activation energies of three different concentrates, which are used as primary inputs to simulate their high pulp density batch and integrated continuous autoclave leach behaviour (Ch. 8). The information generate in this chapter is also used to gain insight into the relative behaviour of the different sulfide minerals, *i.e.*, to support particular assumptions regarding the apparent mineral reaction mechanisms and stoichiometries under MT conditions (*ref.* Ch. 6).

The most important aspects covered in this chapter may be summarised as follows:

- Reviewing the literature and developing a mathematical framework to describe the interfacial gas/liquid, homogeneous and heterogeneous (particulate) processes occurring in a multi-compartment continuous reactor under steady-state conditions (Sect. 7.2)
- Comparing the output of this simulation with the results obtained from a primary autoclave pilot plant circuit (Sect. 7.4.1)
- Measuring the intrinsic leaching rate constants and activation energies of three different chalcopyrite concentrates, gaining insight into their relative responses to oxidation (Sect. 7.4.2), and
- Expanding current understanding of the primary sulfide mineral oxidation mechanisms, developed in Chapter 6, albeit from a phenomenological leaching perspective (Sect. 7.4.2).

Stellenbosch University http://scholar.sun.ac.za

7.2 Review and theory

This section summarises the results of selected modelling studies of metallurgical leaching reactors, as well as the theoretical frameworks used to mathematically describe the behaviour of continuous and batch particulate processes.

7.2.1 Principles of stirred tank leaching

The mineral oxidation mechanisms and rate expressions developed in Chapter 6 form the backbone of the reactor model, while the reaction stoichiometries are used to relate species movement between the different material phases. The interfacial gas/liquid mass transfer and homogeneous and heterogeneous processes have been discussed in detail in the previous chapters, and are directly incorporated into the overall reactor model, using rate and stoichiometric mass balance expressions. This methodology, discussed in more detail later in this section, mathematically captures the mass and heat changes of the overall system *via* a macro-model (after Peters, 1991). The micro-model, in turn, deals with changes in solid particles, *i.e.*, while they undergo leaching or precipitation. The overall reactor model is a marriage between the micro- and macro-models, related by the conversion (X), which, in turn, depends on the solution properties at the solid surface along the time dimension. The overall objective is to establish a relationship between mineral extraction and the reaction time, whether operated in batch or continuous mode, and to track changes in the solids and solution composition of the reacting slurry.

The micro-model only describes the rate at which particle size changes as a function of the solution environment (Sect. 6.3.5). Since the macro-model only accounts for bulk property changes, the overall reactor model requires a framework to calculate changes in the immediate particle environment over reaction time. In the case of a well-mixed batch reactor, no ambiguity exists around the time dimension and the reactor model simply integrates over particle size (ℓ) at each interval along the time dimension ($t+\Delta t$). However, the situation becomes more complicated in continuous reactors, where time is defined as an average, *i.e.*, the average (mean) residence time:

$$\tau_j = \frac{V_{sl,j}}{Q_{sl,j}} = \frac{V_{l,j}}{Q_{l,j}} \qquad 7.1$$

where $V_{sl,j}$ refers to the total volume of gas-free slurry in reactor compartment j 'at temperature' and $Q_{sl,j}$ is the volumetric outflow of slurry. The analogous terms, $V_{l,j}$ and $Q_{l,j}$, refer to the solids- and gas-free solution volume and volumetric outflow, respectively. The understanding of different mixing concepts is important and this is discussed first (based on Crundwell, 1994b, 1995).

Two types of extreme mixing models exist. Firstly, complete micro-mixing (Levenspiel, 1972, Ch.10) refers to total dispersion of the feed on a molecular scale and no element in the reactor is

Stellenbosch University http://scholar.sun.ac.za

considered to have an authentic history; this is known as the maximum mixedness model (Zwietering, 1959). The other extreme is represented by the dispersion of a feed stream into discrete elements on entering the reactor. These elements are small compared to the volume of the reactor and are assumed to remain intact while in the reactor, so that each element of fluid behaves like a batch reactor; this is known as the segregated flow model (Danckwerts, 1958; Levenspiel, 1972). The degree of micro-mixing would lie in between these two extremes, *i.e.*, in most commercial agitated reactors. The flow pattern in the reactor plays an important part in the overall conversion, because it determines the time that a specific fluid element, whether defined as a dispersed molecular phase (maximum mixedness) or as a discrete volume (segregated flow), stays in the reactor. In the case of a continuous stirred tank reactor (CSTR), a residence time distribution (RTD) is applicable, rather than a single value, *e.g.*, as in a perfect plug-flow reactor. Since the CSTR is most often encountered in commercial leaching operations, the RTD needs to be elaborated upon. The following extremes may be identified (Levenspiel, 1972): purely segregated flow, with micro-mixing achieved just before the fluid exits the reactor *vs.* complete micro-mixing as the fluid enters the reactor, *i.e.*, the ideal CSTR. Practical reactors present some intermediate scenario, which can only be modelled accurately once the real RTD is combined with knowledge of the degree of micro-mixing. Since the degree of micro-mixing is difficult to formulate, the question arises whether such improvement in accuracy would justify the increased computational effort, *i.e.*, by not assuming ideal mixing and flow.

The above concepts were originally developed from the homogeneous reactor perspective. In the case of heterogeneous leaching reactors, the overall rate of reaction is more complex due to the feed particle size distribution (PSD), as well as the mere fact that the reactor RTD also needs to account for a dispersed (solid) phase. Crundwell (1995) reviewed the different approaches that have been used to describe leaching in a series of CSTRs, and emphasised that these models essentially differ in their assumptions regarding the state of micro-mixing. This author also pointed out that the feed PSD needs to be taken into consideration, as a monosized particle approach would lead to large differences in the model calculation. For example, a monosized feed to an ideal CSTR would be converted into an exponential number distribution, *i.e.*, the exit distribution would reflect the RTD of the reactor. The two most prominent models applied to particulate processes are the segregated and population balance (PB) approaches. Crundwell (1995) elaborated on these, which may be summarised as follows: the segregated flow approach, as applied in various theoretical (*e.g.*, Bartlett, 1971; Ruether, 1979) and sulfide mineral pressure leaching studies (*e.g.*, Papangelakis *et al.*, 1990; Papangelakis & Demopoulos, 1992a, b, c), assumes that the reactant (*e.g.*, oxygen) concentration is constant with residence time and equal to the exit concentration; this is equivalent to assuming that the particles themselves are individual reactors. To illustrate the relationship between the segregated flow and PB models, Crundwell (1994b) treated each volume

Stellenbosch University http://scholar.sun.ac.za

element as composed of both particles, independent of their physical state, and liquid reagent. These elements were assumed to remain intact and react as batch reactors; thus, the particles in each volume element were subjected to the reactant concentration in that element only. Consequently, the reagent concentration in each volume element decreased according to the leaching rate in that element only. Crundwell (1994b) showed that the segregated flow and PB models only yield the same results when assuming that the reagent concentration is constant with residence time and equal to the exit concentration, in accordance with the references cited above. If this assumption is not made, the only other scenario where this may be true is when the leaching reaction is zero order with respect to the reagent concentration, *i.e.*, the reaction rate does not depend on its environment. This scenario is also represented when the reactant is present in such large excess that its concentration does not change significantly during the course of the reaction, *i.e.*, the reaction is pseudo zero-order; hence, the leaching rate is independent of the state of micro-mixing in the reactor.

Neither of these cases are relevant to the present study. In fact, the concentration of dissolved oxygen, the primary oxidant, is generally low and often depends on the interfacial mass transfer rate in the autoclave test reactors (Ch. 3). Since the sulfide mineral oxidation rate is typically half-order in the dissolved oxygen concentration (Ch. 6), the effects of micro-mixing are assumed to be less important. In fact, Crundwell (1995) proposed that most stirred tank reactors in the metallurgical industry operate close the limit of maximum mixedness, making the PB with the RTD of an ideal CSTR most appropriate.

7.2.2 Macroscopic population balance (PB)

This model assumes that volume elements of particles and liquid, leaving the reactor at the same time, are completely mixed. An ordinary set of (macroscopic) mass balance equations may therefore be used to account for the solution phase changes. The PB approach recognises that the evolution in time and space of the distribution of any property of interest can be represented, once the kinetics of change of that property for individual particles has been specified. The rate of particle size change is described by the unreacted shrinking particle (or core) model, *i.e.*, the micro-model (Sect. 6.3.5). The population (number) balance may be used to calculate the exit PSD, based on the feed PSD and characteristics of the micro-model. This exit PSD may, in turn, be used to calculate the leaching extent, which forms the link between solid- and solution-phase changes, *i.e.*, *via* the mass balance framework.

The macroscopic PB for a well-mixed CSTR is derived in Appendix H.1. The most important PB assumptions are summarised as follows:

Stellenbosch University http://scholar.sun.ac.za

- A Lagrangian viewpoint is taken, which means that the solution surrounding a particle moves convectively with that particle
- The reactor is assumed to be a well-mixed CSTR, which means complete micro-mixing on a molecular level and complete (uniform) suspension of the particulate phase
- There is no breakage, coalescence or agglomeration of particles during the leach, and
- The volume occupied by solids is small compared to the liquid volume, as would be the case in typical leaching suspensions.

These assumptions translate into average expressions of the external motion in the particulate system and yield the following macroscopic form of the PB:

$$\tau_j \frac{\partial(\upsilon_\ell \psi_j)}{\partial \ell} + \psi_j = \psi_{j\text{-}1} \qquad 7.2$$

where $\psi_{j\text{-}1}$ and ψ_j denote the feed and exit number density distributions, respectively, both expressed per unit mass of water flowing out of the reactor j. If the rate of core size (ℓ) change, υ_ℓ, is constant, as would be the case when no inhibiting (elemental) sulfur product surface layers are formed (Sect. 6.3.5), Equation 7.2 simplifies to:

$$(\upsilon_\ell \tau)_j \frac{\partial \psi_j}{\partial \ell} + \psi_j = \psi_{j\text{-}1} \qquad 7.3$$

This linear first-order differential equation is easily solved to yield the marginal (core size) exit distribution (see App. H.2):

$$\psi_j(\ell) = \frac{1}{\tau_j \upsilon_\ell} exp\left(\frac{-\ell}{\tau_j \upsilon_\ell}\right) \int_{\ell_{max,\,j\text{-}1}}^{\ell} exp\left(\frac{\ell'}{\tau_j \upsilon_\ell}\right) \psi_{j\text{-}1}(\ell') d\ell' \qquad 7.4$$

The symbol $\ell_{max,j\text{-}1}$ refers to the largest unreacted core size in the feed distribution to the reactor (j), while ℓ' refers to any initial unreacted core size (between ℓ & $\ell_{max,j\text{-}1}$) that yields the exit density distribution, ψ_j, at size ℓ. The PSD in the feed to the first reactor is obtained from the volume fraction distribution, as measured by a particle size analyser (App. B.3.1). This is a normalised fractional distribution: if the solids' density is relatively independent of particle size, the mass and volume fraction distributions may be assumed to be the same. In this study, the cumulative feed PSD, as reported by the particle size analyser, is differentiated to obtain the feed density distribution, $w_o(L_o)$ (units of 1/m), where L_o refers to the initial particle size.

Although various empirical representations may be used to describe this feed PSD (see, *e.g.*, Randolph & Larson, 1988), the discrete distribution is directly utilised in the numerical calculation

Stellenbosch University http://scholar.sun.ac.za

of Equation 7.4. The feed particle size density distribution to the first reactor, per unit mass of water in the exit stream, is defined as follows:

$$w_{s,o}(L_o) = \frac{M_{s,o}}{M_{w,1}} w_o(L_o) \qquad 7.5$$

where $M_{s,o}$ and $M_{w,1}$ represent the mass flowrate of leachable sulfide into and water out of the first reactor, respectively. The mass of a sulfide mineral core (defined as $\rho_s \Phi_v \ell^3$, where ρ_s is the solids density & Φ_v is the volume shape factor; see App. F.4) is used to calculate the feed particle size number density distribution, again defined per unit mass of water in the outflow:

$$\psi(\ell) = \frac{1}{\rho_s \Phi_v} \frac{w_s(\ell)}{\ell^3} \qquad 7.6$$

The cumulative number distribution of unreacted core sizes (per unit mass of water in the outflow) is then obtained by integrating Equation 7.6:

$$N(\ell) = \int_0^{\ell} \psi(\ell)\, d\ell \qquad 7.7$$

The total number of particles is then represented by $N(\ell_{max})$, which, in turn, is used to normalise this cumulative distribution. The analogous expression for the cumulative mass distribution is as follows:

$$W_s(\ell) = \int_0^{\ell} w_s(\ell)\, d\ell \qquad 7.8$$

The total mass (per unit mass of water) of unreacted sulfide cores exiting the reactor *j* is obtained as follows:

$$W_{s,j} = \int_0^{\ell_{max}} w_{s,j}(\ell)\, d\ell \qquad 7.9$$

The fractional amount of sulfide leached in the reactor, $X_{s,j}$, is obtained by substituting Equations 7.6 and 7.9 into the formal definition of extraction, *i.e.*:

$$X_{s,j} = 1 - \frac{W_{s,j}}{W_{s,j-1}} = 1 - \frac{\rho_s \Phi_v}{W_{s,j-1}} \int_0^{\ell_{max}} \ell^3 \psi(\ell)\, d\ell \qquad 7.10$$

where

$$W_{s,j-1} = \frac{M_{s,j-1}}{M_{w,j}} \qquad 7.11$$

The above equations are solved with the complete set of mass balance equations (see below), with X_s forming the link between the micro- and macro-models. Since solution compositional changes also impact on the micro-model, it needs to be solved iteratively until convergence is reached.

Stellenbosch University http://scholar.sun.ac.za

7.2.3 Mass and energy balance around CSTRs and other continuous steady-state unit operations

The general conservation equation is the obvious starting point:

$$\text{Accumulation} = \text{Input} - \text{Output} + \text{Net generation} \qquad 7.12$$

In the case of steady-state operation, the accumulation term is redundant and Equation 7.12 reduces to:

$$\text{Output} = \text{Input} + \text{Net generation} \qquad 7.13$$

leading to an expression of the molar flow rate of species *i* out of the reactor *j*, F_{ij} (mol/min):

$$F_{ij} = m_{ij\text{-}1} M_{w,j\text{-}1} + \sum_k m_{ik} M_{w,k} + \left(\sum_m \nu_{im} \frac{W_{s,j-1}}{Mw_s} X_{s,m} + \sum_n \nu_{in} R_n \tau_j \right) M_{w,j} \qquad 7.14$$

with *k* streams flowing into the reactor, each at molality m_{ik} (mol/kg) and a single stream leaving with a total gas-free water flowrate, $M_{w,j}$ (kg/min). The generation term covers *m* solid-phase leaching reactions and *n* solution-phase reactions. The symbol, ν_i, refers to the stoichiometric coefficient (negative for reagents and positive for products), while R is the reaction rate per unit mass of water (mol/kg.min). This equation illustrates the advantage of defining the inflow of the sulfide mineral particles per unit mass of water in the outflow, *i.e.*, $W_{s,j\text{-}1}$, which is consistent with the molality scale used for the solute species inside the reactor. As an example, Equation 7.14 may be used to describe the gas-phase mass balance, *e.g.*, for diatomic oxygen:

$$F_{O_2,j} = F_{O_2,j\text{-}1} + x_{O_2} F_g + R_{O_2,j} \tau_j M_{w,j} \qquad 7.15$$

where the symbol x_{O2} refers to the mole fraction of oxygen in the gas phase of the total (molar) feed rate, F_g, assuming a single feed stream to each reactor. The oxygen consumption rate from the perspective of the gas phase, $R_{O2\,(g)}$, is obtained from Equation 3.1:

$$R_{O_2(g)} = -k_L a (m^*_{O_2} - m_{O_2}) \qquad 7.16$$

where m_{O2} refers to the steady-state molality of oxygen in the solution phase and the asterisk signifies the saturation molality. To complete the set of mass balance equations, the solid and solution phases also need to be considered. For example, Equation 7.14 is again utilised to obtain the steady-state oxygen solution concentration in the reactor outflow, assuming no dissolved oxygen enters in any of the other reactor feed streams *k*:

$$m_{O_2,j} = \frac{F_{O_2,j\text{-}1}}{M_{w,j}} + \sum_m \nu_{O_2,m} W_{s,j-1} X_{s,m} + \sum_n \nu_{O_2,n} R_{O_2,n} \tau_j + k_L a (m^*_{O_2,j} - m_{O_2,j}) \tau_j \qquad 7.17$$

Clearly these mass balance equations need to be solved iteratively for each reactor compartment *j*, since the thermodynamic properties and reaction rates are dependent on the species concentrations.

Stellenbosch University http://scholar.sun.ac.za

To check the mass balance calculations, a total elemental balance is conducted for each unit operation, *j*, to within a desired tolerance. In the case of the above reactor example, the solution phase elemental balance is as follows:

$$\left| \sum_i \nu_{e(i)} F_{i\,j} - \sum_k \sum_i \nu_{e(i)} F_{i\,k} \right| \leq tol \qquad 7.18$$

The symbol $\nu_{e(i)}$, represents the stoichiometric coefficient of element *e* in component species *i*.

The above mass balance equations are used to describe the movement of matter across all three material phases. Analogous expressions are also required in order to describe the energy balance around each unit operation, *e.g.*, the leach reactor compartment, *j*. However, an added complexity is the lack of thermodynamic data, especially at higher temperatures. As summarised in Section 2.3.1, the first-estimate assumption of zero partial molal heat capacity, $C_p°$, is often made. This assumption can, however, lead to errors of several orders of magnitude (Barner & Kust, 1980). The most accurate results are usually obtained if the temperature functionality, *e.g.*, the Kelly equation coefficients (Sect. 2.3.1), are known. If not, the assumption of constant heat capacity may yield an acceptable estimate of the species enthalpy at the desired temperature; more accurate results would then obviously be obtained closer to the reference point (T_r). The equations of Section 2.3.1 provide the means to calculate the partial molal enthalpies of the aqueous species at infinite dilution. The following relationship is then used to yield the species' enthalpies in the real solution (see, *e.g.*, Zemaitis *et al.*, 1986):

$$H_i = H_i^o - R_g T \cdot \left(\frac{\partial ln \gamma_i}{\partial T} \right)_{P,n} \qquad 7.19$$

With the temperature functionality of the activity coefficient, γ_i, known, the actual partial molar enthalpy in the real solution, H_i, can be obtained. However, in view of experimental uncertainty and the general lack of data at higher temperatures, a simplification is required. In practice, the second term in Equation 7.19 is often found to be small (Zemaitis *et al.*, 1986), *i.e.*:

$$H_i^o >> - R_g T \cdot \left(\frac{\partial ln \gamma_i}{\partial T} \right)_{P,n} \qquad 7.20$$

yielding the following simplification:

$$H_{i,T} \approx H_{i,T}^o \qquad 7.21$$

The Kelley parameters of most solid species of interest to this study are listed in public databases, *e.g.*, *HSC* (2006). However, most partial molal properties of the aqueous species, including H° and $C_p°$, are only known at T_r. In this regard, different extrapolation schemes can be utilised to calculate H° 'at temperature'. The most frequently applied methods include the statistical thermodynamic

Stellenbosch University http://scholar.sun.ac.za

approach of Helgeson (*e.g.*, see original publication in Helgeson, 1967; Shock & Helgeson, 1988) and the Correspondence Principle of Criss and Cobble (1964). The *HSC* (2006) database makes extensive use of the published correlations and values of Helgeson (most of the aqueous species values are summarised in App. A.7), while the Criss-Cobble technique is usually applied where no such data are available. This study compares the continuous autoclave energy balance using data from both extrapolation techniques (Ch. 8).

A variant of the Correspondence Principle, known as Lewis linearization (Lewis, 1970), is also employed to estimate the partial molal heat capacity at higher temperatures. In short, the Correspondence Principle states that the partial molal entropy of an ion at temperature T, $S°_T$, is related to its absolute partial molal entropy at the reference temperature (25°C), $S^{o(abs)}$, by the following relationship:

$$S^{o}_{T,i} = A_T + B_T S^{o(abs)}_{25,i} \qquad 7.22$$

where the coefficients A_T and B_T are dependent on temperature and the type of ion. Criss and Cobble (1964) established values for different classes of ions by analysing available experimental data. The absolute partial molal enthalpy scale corresponds to the absolute enthalpy of H^+ (-5 cal/mol.deg), so that the absolute and conventional entropy (J/mol.K) of an ion, *i*, are related by:

$$S^{o(abs)}_{25,i} = S^{o}_{25,i} - 20.92\, z_i \qquad 7.23$$

where z_i is the ionic charge. Criss and Cobble (1964) found both coefficients to vary approximately linearly with temperature, at least up to 200°C, for the four classes of ions considered, *i.e.*, simple cations (*e.g.*, Cu^{2+}), simple anions (*e.g.*, OH^-), oxy-anions (*e.g.*, SO_4^{2-}) and acid oxy-anions (*e.g.*, HSO_4^-). Substitution of these linear coefficients into Equation 7.22 and rearranging reflects an analogous mathematical form to the Kelley b-coefficient and is therefore used to estimate the partial molal heat capacity 'at temperature':

$$C^{o}_{p,i}(T) = b_i \cdot 10^{-3} \cdot T \qquad 7.24$$

where b_i is constituted by the constants e_c and g_c, unique to each class, c, of ions and independent of temperature:

$$b_i \cdot 10^{-3} = e_c + g_c S^{o(abs)}_{25,i} \qquad 7.25$$

These constants reflect the slopes of A_T and B_T against temperature and are regressed using the data of Criss and Cobble (1964) between 25 and 200°C. The values are summarised in Table 7.1 and are obtained by fixing A_T and B_T at 0 and 1, respectively, *i.e.*, at the reference temperature of 25°C. Because the A_T-value of the H^+ species should reflect the assigned standard state entropy, it is fixed at -20.92 J/mol.K (-5 cal/mol.deg) at 25°C.

Stellenbosch University http://scholar.sun.ac.za

Table 7.1
Heat-capacity parameters for different ion classes (Lewis linearization).

Ion type	[a] $e_c \times 10^3$	[b] $g_c \times 10^3$
–	(J/mol.K^2)	(1/K)
H^+	383.5	0
Simple cations	552.5	-1.647
Simple anions	-717.1	[c] -0.102
Oxy-anions	-1602.7	5.794
Acid oxy-anions	-1674.0	11.22

[a] Fitted to Criss & Cobble (1964) data (25-200°C) & fixing A_t to 0 J/mol.K at 25°C; [b] Fitted to Criss & Cobble (1964) data (25-200°C) & fixing B_t to 1 at 25°C; [c] 60 & 100°C datapoints omitted.

The resultant Kelley b-coefficients, for the ions of interest to this study, are summarised in Appendix A.7 (Table A.11) and are applied in an analogous manner to the thermodynamic values obtained using Helgeson extrapolation. However, this Criss-Cobble method is limited to a selected few ion classes: the mass and energy balance is therefore restricted to a formal treatment of all the aqueous species, except for sulfuric acid which is treated as behaving like a monoprotic acid throughout the circuit:

$$H_2SO_{4\,(tot)} \Rightarrow H^+_{(aq)} + HSO^-_{4\,(aq)} \qquad 7.26$$

This treatment yields a good approximation of the energy balance, but is nevertheless compared to the detailed species approach (Ch. 8), using the data summarised in Appendix A.6 (Table A.10).

Whether the formal or species approach is followed, the energy balance for the autoclave reactor *j* also follows the general conservation law (Eq. 7.12). In the context of this study, the energy balance of the CSTR, or any unit operation for that matter, reduces to the steady-state adiabatic form, *i.e.*, the heat generated by the chemical reactions is contained internally. Explicit energy exchanges are, however, catered for by virtue of mechanical action (Q_{mech}) or due to natural heat losses to the environment (Q_{loss}):

$$Q_{in} + Q_{mech} = Q_{out} + Q_{loss} \qquad 7.27$$

As a first-estimate, the net heat loss is assumed to be small (*cf.* the total heat flow): the steady-state energy balance then reduces to a straight-forward enthalpy balance around compartment, *j*:

$$\sum_k \sum_i F_{i\,k} \cdot \left(H^o_{25,i} + \int_{298.15}^{T_k} C^o_{p,i}(T)\,dT \right) = \sum_i F_{i\,j} \cdot \left(H^o_{25,i} + \int_{298.15}^{T_j} C^o_{p,i}(T)\,dT \right) \qquad 7.28$$

Since the molar flow (F_k) and temperature (T_k) of the input streams (k), and the molar flow out with stream j (F_j) are known within the iterative mass and energy balance framework, the temperature,

Stellenbosch University http://scholar.sun.ac.za

T_j, becomes the only unknown variable. This output temperature is readily solved using the Newton-Raphson iteration technique until the total output and input energies match. Another scenario is presented by the case where the output temperature (T_j) is specified (isothermal operation) and the rate of external energy removal (Q_{ext}), *e.g.*, by cooling liquor, is calculated:

$$Q_{\text{ext},j} = \sum_k \sum_i F_{ik} \cdot \left(H^o_{25,i} + \int_{298.15}^{T_k} C^o_{p,i}(T)\, dT \right) - \sum_i F_{ij} \cdot \left(H^o_{25,i} + \int_{298.15}^{T_j} C^o_{p,i}(T)\, dT \right) \qquad 7.29$$

The equation is consistent with the sign convention of positive energy flow out and negative energy flow into the reactor *j* (or any unit operation). In the case of the multi-compartment continuous autoclave, the total mass flow of cooling liquid (M_{cl}) and the subsequent splits to each of the compartments are calculated by minimising $|Q_{ext,j}|$, which, in turn, impacts on the steady-state pulp density ($\rho_{s/w,j}$) in each compartment. The operating pulp density is therefore a function of the heat balance inside the continuous autoclave, which, in turn, is strongly dependent on the type and extent of the oxidation reactions. These aspects are discussed in more detail in Chapter 8.

7.2.4 Population and mass balances of a well-mixed, batch stirred tank reactor

The macroscopic PB for the batch reactor, following the unreacted shrinking particle (USP) micro-model, is discussed in detail in Appendix H.3. As in the case of the continuous reactor, the spatial-averaged PB needs to be considered for a well-mixed batch stirred tank reactor (BSTR), hence the term 'macroscopic'. With the unreacted core size number distribution, $\psi(\ell)$, defined per unit mass of water in the reactor, the first-order differential form of the macroscopic PB is represented as follows:

$$\frac{\partial[W_{H_2O} \cdot \psi(\ell, t)]}{\partial t} = -W_{H_2O} \frac{\partial[\upsilon_\ell \cdot \psi(\ell, t)]}{\partial \ell} \qquad 7.30$$

where W_{H2O} is the mass of water in the batch reactor. This equation is easily solved, to yield:

$$\psi(\ell, t)\, d\ell = \psi(L_o)\, dL_o \qquad 7.31$$

where

$$\ell = L_o + \int_0^t \upsilon_\ell\, dt \qquad 7.32$$

The sulfide oxidation extent, X_s, is then described as follows (BSTR analogy of Eq. 7.10):

$$X_s = 1 - \frac{W_s}{W_{s,o}} = 1 - \frac{\int_0^{\ell_{max}} \rho_s \Phi_v \ell^3 \psi(\ell)\, d\ell}{\int_0^{L_{o,max}} \rho_s \Phi_v L_o^3 \psi(L_o)\, dL_o} \qquad 7.33$$

A simple relationship is obtained after substituting Equation 7.31 into Equation 7.33, and simplifying (see App. H.3):

Stellenbosch University http://scholar.sun.ac.za

$$1 - X_s = \int_0^{L_{o,max}} [1 - X_{s,n}] W_{f,n} dL_o \qquad 7.34$$

where $W_{f,n}$ is the fractional weight of original mineral feed particles in a size-class *n*, with average size, $L_{o,n}$, and fractional leaching extent, $X_{s,n}$, *i.e.*, corresponding to that specific class. Equation 7.34 is further manipulated and discretised to yield the following form of the leaching extent of a multi-sized particle feed to a BSTR (App. H.3):

$$1 - X_s(t) = \sum_{-\upsilon_\ell t}^{L_{o,max}} \left(1 + \frac{\upsilon_{\ell,n}(t) \cdot t}{L_{o,n}}\right)^3 W_{f,n} \qquad 7.35$$

where $\upsilon_{\ell,n}$ refers to the rate of change of the core size in original particle size-class, *n*. The (dimensionless) fractional weight, W_f, in each size class is directly obtained from the particle size analysis histogram. If the mass density distribution, w_o (units of 1/m), is obtained by differentiating the cumulative PSD, then the following equation is applicable:

$$1 - X_s(t) = \sum_{-\upsilon_\ell t}^{L_{o,max}} \left(1 + \frac{\upsilon_{\ell,n}(t) \cdot t}{L_{o,n}}\right)^3 w_{o,n} \Delta L_{o,n} \qquad 7.36$$

where $\Delta L_{o,n}$ is the (original) particle size difference in size-class *n*. These equations confirm that the leaching extent bears no direct relation to the pulp density, except for υ_ℓ (indirectly), since it depends on the concentration of the various aqueous species (*i*) molalities, m_i. Therefore, <u>if the pulp density is low enough, the solution composition changes are small and do not dramatically affect the leaching reaction extents</u>. Furthermore, if the velocity term, $\upsilon_{\ell,n}$, is independent of the particle size and history, *i.e.*, as in the case of the classical USP model under surface reaction control, Equation 7.35 simplifies to:

$$1 - X_s(t) = \sum_{k_\ell t}^{L_{o,max}} \left(1 - \frac{k_\ell t}{L_{o,n}}\right)^3 W_{f,n} \qquad 7.37$$

This equation is directly applied in Chapter 6 (Sect. 6.5.3) to calculate the leaching extent in 'diluted' slurries. The higher the pulp density, the more significant the mass balance equations become, hence they have to be solved simultaneously with Equation 7.35, *i.e.*, along the time dimension. The analogous form of the continuous mass balance (Equation 7.14) is then applied to the batch reactor to track the molality change of species, *i*, over time step, Δt, for *m* solid-phase leaching reactions and *n* solution-phase reactions:

$$\Delta m_i = \sum_m \nu_{i\,m} \frac{W_{s,t-1}}{Mw_s} \Delta X_{s,m} + \sum_n \nu_{i\,n} R_n \Delta t \qquad 7.38$$

where

Stellenbosch University http://scholar.sun.ac.za

$$\Delta X_{s,m} = X_{s,m}(t) - X_{s,m}(t-1) \qquad 7.39$$

so that

$$m_i(t) = m_i(t-1) + \Delta m_i \qquad 7.40$$

The above expressions can be adapted to represent any heterogeneous system, *i.e.*, to account for the movement of matter over all three material phases. In the context of this study, no heat balance is required for reactor operation in batch mode.

7.3 Experimental

This section discusses the experimental setup and procedures used to measure the mineral oxidation behaviour in the continuous pilot autoclave and, at lower pulp densities, in the 2-litre batch autoclave. A summary of particle size and mineral characterisation analyses is also presented, focussing on two different cleaner concentrates, *i.e.*, from Hudson Bay Mining and Smelting Co Limited (HBMS) in Canada and Las Tortolas (LT) in Chile (Los Bronces orebody), as well as a rougher concentrate from Manto Verde (MV) in Chile.

7.3.1 Equipment and procedures

The mechanical aspects and arrangement of the reactor internals are discussed in detail in Section 3.3. The following section focuses on the operation of the pilot autoclave circuit, followed by a slightly modified experimental procedure (*ref.* Ch. 6) for the 2-litre batch autoclave.

Description of the multi-compartment continuous pilot autoclave and its integrated circuit

The six-compartment horizontal autoclave and its internals are illustrated in Figure 3.3 and 3.4, respectively (also see related discussions). The first and second compartments acted as a dual compartment (no inter-compartmental overflow weir plate) to simulate the typical configuration of a full-scale autoclave reactor. Although the autoclave was controlled isothermally on the pilot scale, using external temperature control (Sect. 3.3), the actual target conditions simulated autogenous operation, *i.e.*, as reflected by the use of this dual compartment configuration (also see Papangelakis & Demopoulos, 1992c) and the relatively low feed pulp densities (Sect. 7.4.1). Tables 3.1 and 3.9 summarise the effective volume and gas/liquid mass transfer rate in each autoclave compartment, respectively. Also included in these tables are the corresponding volumes and mass transfer rates when the upcomer arrangement, between compartments 4 and 5, blocked with sulfur conglomerates. Figure 7.1 illustrates how the slurry level inside the autoclave increased during upcomer blockage events and eventually overflowed *via* the vapour slot.

Stellenbosch University http://scholar.sun.ac.za

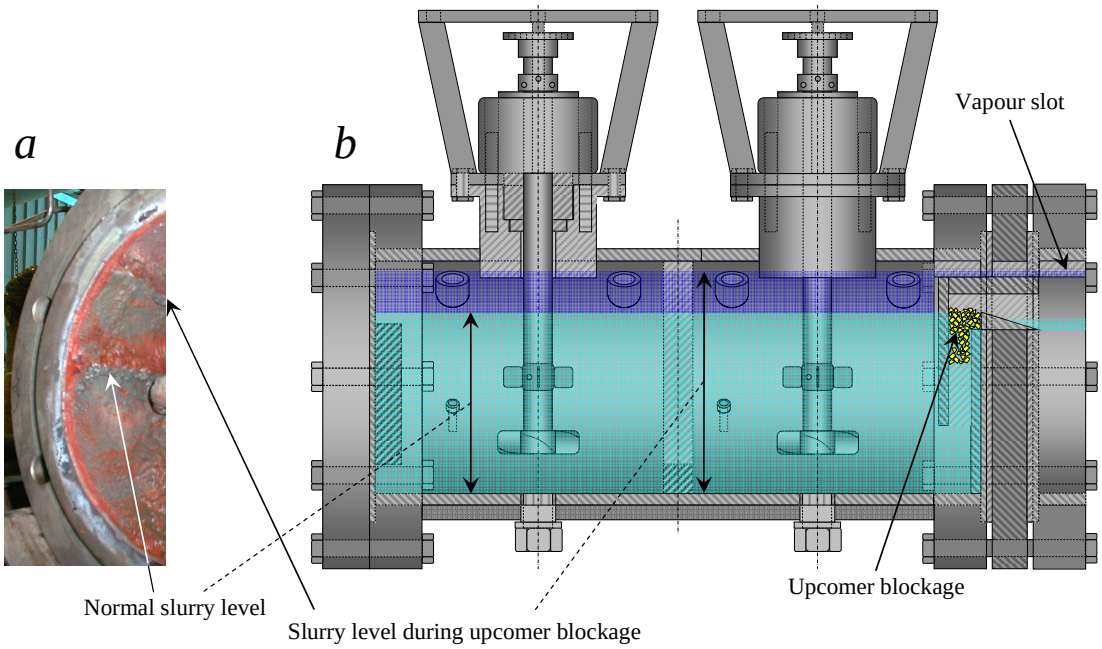

Figure 7.1
Slurry levels during 'normal' operation & after upcomer blockages: *a*) Photo of foam layers on the internal autoclave wall before & after temporary upcomer blockages; *b*) Schematic diagram of an autoclave section, consisting of two compartments.

As illustrated in Table 3.9, the higher autoclave slurry level results in significantly lower gas/liquid mass transfer rates, which, in turn, negatively affect the various oxidation reaction rates during these upcomer blockage periods. This aspect is particularly relevant to the discussions later in this chapter.

During normal operation, the autoclave was continuously fed with finely ground HBMS 777 concentrate, mixed with acid-containing solvent extraction (SX) raffinate and surfactant solution and pumped directly into the autoclave under pressure. Copper was recovered from the pregnant leach solution (PLS) by the SX–electrowinning (EW) unit operations, with the raffinate recycled back to the autoclave. This raffinate stream fulfilled the dual role of (simulated) coolant liquid and bulk carrier of acid. A raffinate bleed stream proceeded to residual copper recovery in a secondary SX operation, after which iron was removed by precipitation and filtration. The resulting solution was then neutralised to produce basic zinc sulfate (BZS), $(ZnO)_3ZnSO_4$, which was recovered by filtration, while precious metals were recovered from the washed leach residue by cyanidation.

A blockflow diagram of the piloted flowsheet is presented in Figure 7.2. This study only focuses on the primary leaching – SX circuit, but details of the other unit operations can be found in Dreisinger *et al.* (2003).

Stellenbosch University http://scholar.sun.ac.za

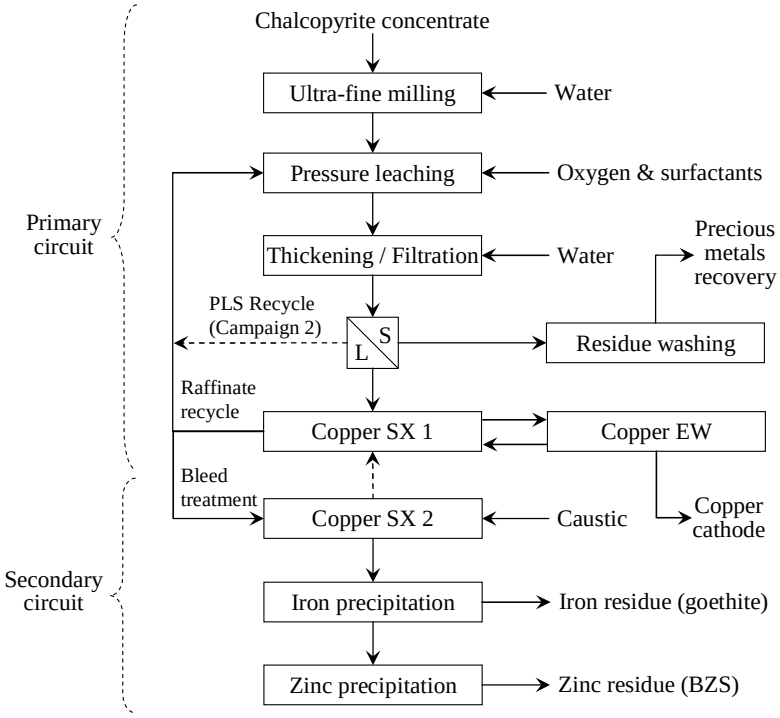

Figure 7.2
Blockflow diagram of the integrated pilot circuit, treating HBMS 777 chalcopyrite concentrate.

The purpose of the SX 1 operation is to maximise copper recovery, and hence to reduce the neutralisation (caustic soda; NaOH) requirement of the second (SX 2) operation. On the other hand, for each mole copper loaded in SX 1, one mole H_2SO_4 is transferred into the raffinate stream:

$$Cu^{2+}_{(aq)} + 2RH_{(org)} \Rightarrow CuR_{2(org)} + 2H^{+}_{(aq)} \qquad 7.41$$

where RH represents the copper extractant (Acorga M5640). The return anolyte from copper electrowinning (EW) replaces the stoichiometric equivalent of hydrogen ion of the organic during the stripping phase:

$$CuR_{2(org)} + 2H^{+}_{(aq)} \Rightarrow Cu^{2+}_{(aq)} + 2RH_{(org)} \qquad 7.42$$

The acid balance around the EW unit operation is naturally maintained by water decomposition at the Pb/Ca/Sn anode, while copper is deposited at the cathode:

$$\text{Cathode:} \quad Cu^{2+}_{(aq)} + 2e^{-} \Rightarrow Cu^{o}_{(s)} \qquad 7.43$$

$$\text{Anode:} \quad H_2O \Rightarrow 2H^{+}_{(aq)} + \tfrac{1}{2}O_{2(g)} + 2e^{-} \qquad 7.44$$

$$\text{EW balance:} \quad Cu^{2+}_{(aq)} + H_2O \Rightarrow Cu^{o}_{(s)} + 2H^{+}_{(aq)} + \tfrac{1}{2}O_{2(g)} \qquad 7.45$$

Therefore, one mole H_2SO_4 for each mole of Cu loaded in SX 1 is generated from water at the EW anode, which is then transferred, *via* the organic phase, to the raffinate stream. The raffinate recycle

Stellenbosch University http://scholar.sun.ac.za

fulfils the dual role of hydrogen ion recycle and (simulated) coolant flow to the autoclave. During the first campaign (Campaign 1), the organic flow in SX 1 was controlled to give a prescribed amount of acid recycle to the autoclave (at constant solid feed flowrate). During the second campaign (Campaign 2), the acid and 'cooling' requirements of the autoclave were partially satisfied by a PLS recycle, which allowed for separate control of SX 1. The only objective of SX 2 was to minimise copper loss in the bleed (secondary) circuit. The acid equivalent of the copper extracted (Eq. 7.41) had to be neutralised by caustic soda, and hence contributed to the operating cost of the process. These acid balance issues are discussed later in this chapter, specifically in the context of the autoclave leaching and precipitation reactions.

The autoclave was continuously fed with HBMS 777 concentrate. The concentrate was milled batch-wise in a stirred-media detritor (SMD; Metso Minerals) until the target particle size ($d_{90} \approx 10$ µm) was reached, with closed-circuit circulation between the SMD and the make-up tank (Figure 7.3 *a*). The grinding media consisted of -2 mm carbolite material (density: 2.710 g/L, mass: 1.908 kg & 50 wt% media ratio). Two-hour batches were prepared using dry concentrate and potable water to obtain the target wt% solids to the autoclave feed tanks (Figure 7.4). Figure 7.3 *b* presents the milling curves of the concentrate in the SMD, *n.b.*, they fell within the AA-UBC patent specification (Dempsey & Dreisinger, 2003). A typical feed PSD to the pilot autoclave, sampled at the delivery side of the dosing pump (Figure 7.4), is also presented in Figure 7.3 *b*.

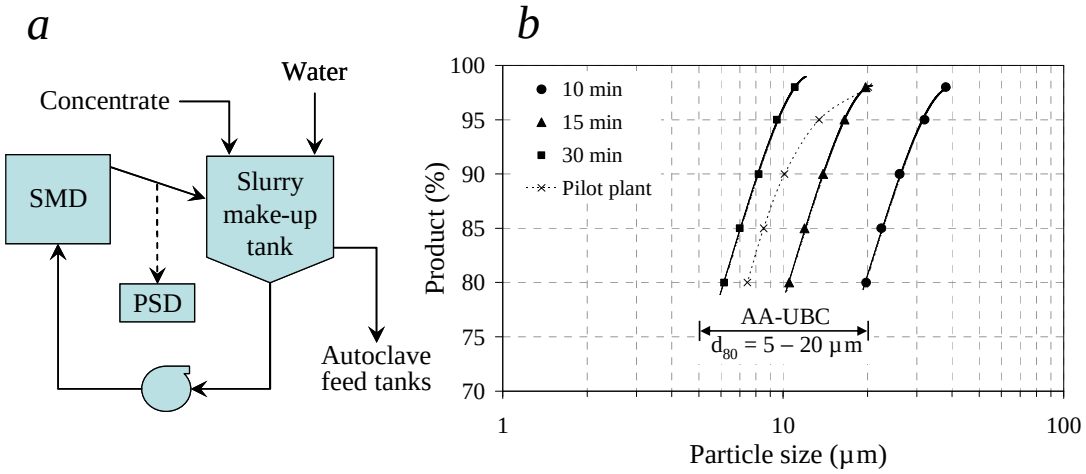

Figure 7.3
Slurry feed preparation (HBMS 777 chalcopyrite concentrate): *a*) Schematic representation of the milling circuit; *b*) Milling curves & typical pilot plant feed PSD.

The slight discrepancy towards the coarser particle size of the pilot feed compared to the milling curves, is thought to be due to the position of the sampling point: the samples were taken from the overflow of the SMD (Figure 7.3 *a*), while a slightly coarser fraction may have been retained in the

Stellenbosch University http://scholar.sun.ac.za

SMD and then could have reported to the feed preparation tanks when the SMD was drained after each feed preparation cycle.

The internal autoclave workings (mixing, volume & flow) and control (temperature & pressure) are summarised in Section 3.3. The detailed autoclave circuit arrangement is illustrated in Figure 7.4.

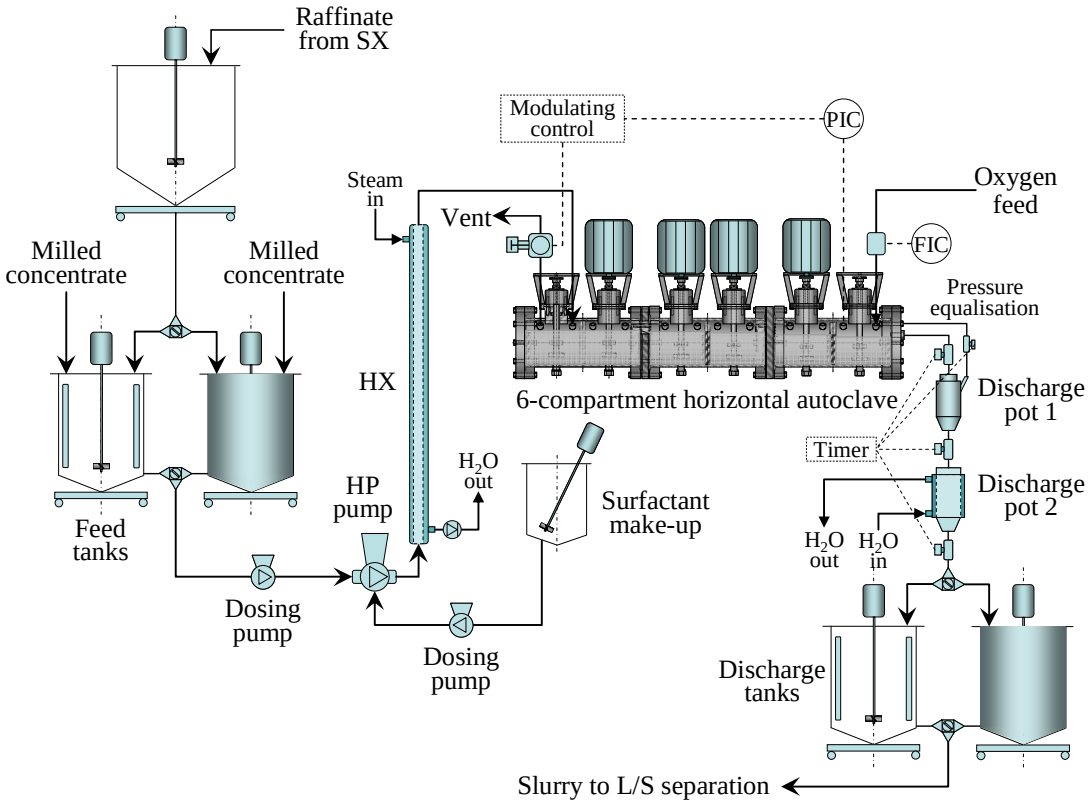

Figure 7.4
Schematic diagram of the pilot autoclave circuit.

The pilot autoclave operation may be summarised as follows: milled slurry (~44 wt% solids during Campaign 1 & ~49% during Campaign 2) was transferred to the feed tanks and mixed with the required amount of return raffinate to yield between 6.5 to 7.5 wt% solids in the autoclave feed, depending on the acid concentration and mass flow of returning raffinate. The tanks were mounted on load cells, which simplified the slurry feed preparation procedure. Each of the feed tank batches catered for 2 hour operation, *i.e.*, while the one tank was operational, the other tank was being prepared. The feed slurry was continuously metered into a high-pressure (HP) pump and transferred to the autoclave *via* the heat exchanger (HX) unit, with a target setpoint of 150°C. The purpose of this HX unit was to ensure that the operating temperature was maintained in the first two (combined) compartments. However, the HX often blocked during the commissioning phase, due to suboptimal mechanical design, and its setpoint was lowered to around 120°C; during the later periods, the HX was bypassed altogether. This posed no operational problems, as the heating

Stellenbosch University http://scholar.sun.ac.za

mantles were able to maintain the autoclave operating temperature. It was assumed that insignificant chemical reaction occurred in these heated feed lines (see Sect. 6.5.1). Fresh surfactant solution was also prepared on a two-hourly basis and dosed into the suction side of the HP pump at a constant rate, *i.e.*, 3 to 5 g calcium lignosulfonate (LS) (Norlig A, 58%) and 3 to 5 g Quebracho (QB) (Orfom grade 2 Tannin) per kg (dry) concentrate. The water used to pre-dissolve these surfactants was accounted for when preparing the feed tank pulp densities. The slurry entered the horizontal autoclave at a constant and known feed rate and cascaded down to the final compartment over ~120 min average residence time. The slurry continuously overflowed into Discharge Pot 1, which was intermittently discharged into Discharge Pot 2 (cooled). This, in turn, discharged into the two discharge tanks. Each discharge tank catered for around 2 hours of operation: one tank received discharge slurry from the autoclave, while the contents from the other tank were filtered and washed. Although this two-stage discharge system performed well mechanically, the slurry did not flash in similar fashion to a commercial autoclave discharge system. On the other hand, significant amounts of water evaporated from the comparatively small pilot discharge tanks, compared to a commercial scale. All sensor measurements were logged automatically (*via* a PLC/SCADA system).

Batch oxidation equipment and procedures

The 2-litre Parr autoclave was also used conduct the follow-up (*ref.* Ch. 6) batch leaching tests. The autoclave, internals and peripherals are discussed in detail in Section 3.3 (see Figure 3.1) and Section 6.4.1. However, the feed bomb (Figure 6.23) was replaced with two feed pumps to feed sulfate salt and surfactant solution, respectively. This pump system allowed larger volumes to be added and hence provided the means to introduce all the active reagents 'at temperature'. The initial slurry therefore only consisted of water and concentrate, which minimised the possibility of premature reactions during heat-up. The surfactants could also be added gradually over the course of a batch experiment, *i.e.*, to compensate for surfactant degradation at high temperatures. This procedure was only exercised in selected cases, towards the end of the experimental programme, but proved unsuccessful (Ch. 8).

The modified feed system is illustrated in Figure 7.5 and the experimental procedure may be summarised as follows:

- The initial slurry was prepared by mixing dry concentrate with a known amount of water
- The autoclave was then heated to a predetermined temperature (higher than the setpoint temperature), with the impeller stirring slowly (all mixing aspects are discussed in detail in Ch. 3). The initial temperature varied between 5 and 10°C higher than the setpoint temperature, depending on the operating conditions, to compensate for the sudden drop in temperature when pumping cold feed solution into the autoclave

Stellenbosch University http://scholar.sun.ac.za

- The surfactants were dissolved into a predetermined amount of water, placed into the measuring tube and pumped into the reactor, using the smaller pump (P1)
- The measuring tube of the larger pump (P2) was then charged with the required amount of electrolyte solution, consisting of water, sulfuric acid, copper sulfate and other dissolved sulfate salts (when required), which were also pumped into the reactor. The pumping typically took less than 30 seconds, and brought the autoclave temperature to within 1°C of the setpoint temperature, while the dissolved species' concentrations corresponded to their desired (calculated) levels, at 1150 g initial slurry mass (see Ch. 3 for a detailed discussion of the effect of slurry volume on the interfacial gas/liquid mass transfer rate)
- The oxygen valve was opened and autoclave vented for a few seconds in order to remove all inert gases from the vapour space. The oxygen overpressure was then adjusted to its setpoint value
- The agitation speed was then increased to its setpoint value, which signified the start of the kinetic test
- A dedicated gas feed system ensured constant oxygen overpressure by regulating the total pressure of the vessel for the remainder of the test. The temperature was controlled to within 1°C by a PID controller (see Sect. 3.3 for more detail on this and other quality control aspects). The consumption of oxygen was also continuously logged *via* a mass-flow meter and SCADA system for the tests conducted at high pulp densities
- On completion of the leach, the agitation speed was decreased to 100 rev/min, followed by rapid cooling (< 2 min) to 85°C and venting of the vapour phase
- The slurry was filtered and the autoclave washed out with a portion of the filtrate to capture all residue on the filter paper. The filter cake was then re-pulped with pH 2 water, filtered, and again washed with pH 2 water, and
- Metals in solution were quantified by inductively coupled plasma - optical emission spectroscopy (ICP-OES; App. B.2.1). Iron(II) and acid contents were determined by wet chemical methods (App. B.2.3). Solid samples were fused, dissolved in acid medium, and also analysed by ICP-OES. The elemental sulfur content was determined by leaching the sample with tetrachloroethylene in an ultrasonic bath, and analysing the resulting solution using high performance liquid chromatography (HPLC). The residue of this leach was subjected to a second leach with 10% Na_2CO_3 at boiling point, and the resulting solution analysed by HPLC for sulfate sulfur. The final residue was analysed for sulfide sulfur using an automated sulfur analyser (Leco). The total sulfur was also measured by Leco and then compared with the total sulfur calculated from the individual sulfur species. The sample was re-analysed if the difference was greater than 5% (App. B.2.2).

Stellenbosch University http://scholar.sun.ac.za

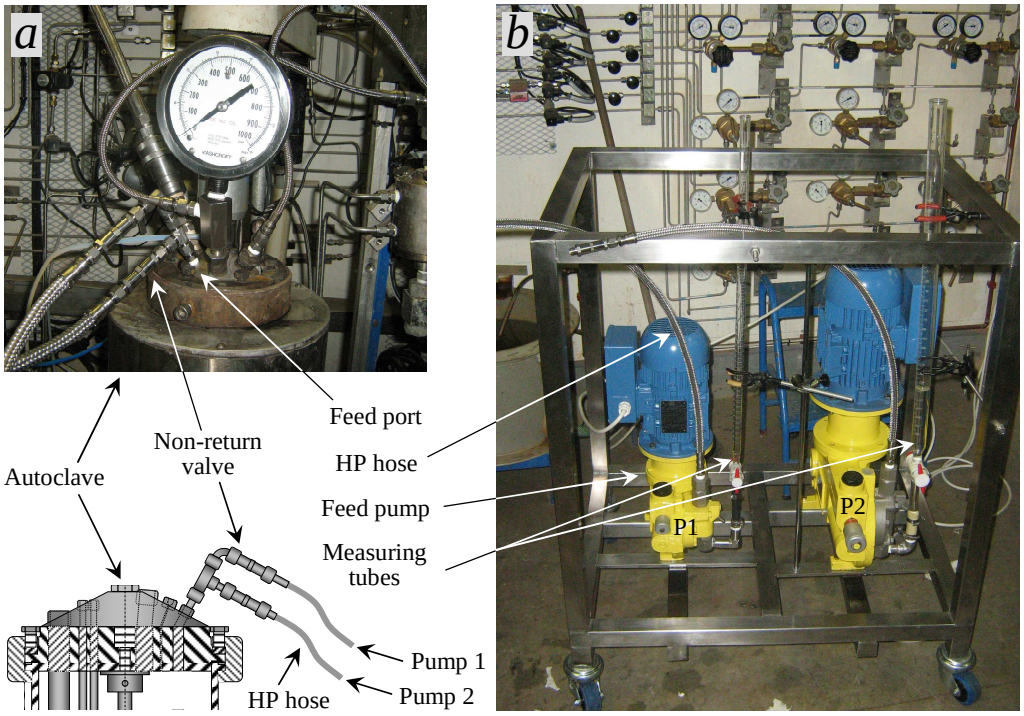

Figure 7.5
Modified feed system of the 2-litre Parr autoclave: *a*) Photo & schematic diagram of the modified autoclave peripherals; *b*) Photo of the HP feed pump system.

7.3.2 Data interpretation

The same methodology is used to obtain the rate constants from batch experimentation as described in Section 6.4.2, except that the reaction extents are based on bulk modal comparisons (App. B.3.2) of the minerals present in the leach residues compared to the head sample, *i.e.*, Equation 6.159 can be applied directly, where $W_{f,t}$ refers to the fractional weight of the residue (*cf.* the original sample) after time, t, and x_i is the corresponding mass fraction of mineral, *i*:

$$X_i = 1 - W_{f,t} \cdot \frac{x_{i,t}}{x_{i,o}} \qquad 7.46$$

The mass loss was either directly obtained by residue weighing or the silica-tie method was used in cases where silica levels were high enough, *e.g.*, in the Manto Verde (MV) rougher concentrate. This approach allows independent reaction rate constants to be obtained for each of the dominant sulfide phases.

Discrepancies between the mineralogical and chemical analyses are dealt with in a unique manner, especially with regard to sulfur speciation issues (see discussions in Sect. 6.5.1 & 7.3.3). Since elemental sulfur cannot be detected by the SEM-based image analyser (App. B.3.2), the measured total sulfur content (App. B.2.2) is assumed to be correct. Provided no iron precipitation products formed during the leach, and assuming that all sulfate phases dissolved rapidly under autoclave

Stellenbosch University http://scholar.sun.ac.za

operating conditions (next section), the elemental sulfur content is calculated (by difference), *i.e.*, if the total unreacted sulfide level is known.

The chemical and mineralogical results are reconciled using the total unreacted sulfide content of the residue sample, as obtained by the bulk modal analysis, and assuming complete dissolution of the elemental sulfur in the (resin) polished sections (App. B.3.2). Therefore, the elemental sulfur content is calculated by difference, which, in turn, is used to update the reaction extents, as based on the mineralogical results. This again yields an updated value of the total unreacted sulfide content, and the procedure is repeated. This iterative method of reconciliation produces the most consistent results (see Sect. 7.4) and is also assumed to compensate for inaccuracies in the elemental sulfur analyses, whether an artefact of polymeric sulfur (see discussions in Sect. 6.5) or due to experimental error. This is important, since the elemental sulfur yield due to mineral oxidation is sensitive to these experimental errors, especially at the relatively low elemental sulfur yields encountered in this part of the study.

7.3.3 Sample preparation and characterisation

Besides the 777 chalcopyrite concentrate from HBMS (Canada; Section 6.4.3), different samples from Chile were evaluated, *i.e.*, a cleaner concentrate from the Las Tortolas (LT) operation, which processes milled ore from the Los Bronces site, and a composite rougher concentrate from Manto Verde (MV). The following discussions only refer to the narrow-sized samples used in the low pulp density testwork presented in this chapter, *i.e.*, a freshly prepared HBMS 777 cleaner concentrate fraction (E), two LT cleaner concentrate size fractions (F & G) and a MV rougher concentrate size fraction (H).

Feed particle size

The milling procedure was identical to that described in Section 6.4.3, followed by an elaborate micro-screening treatment to produce relatively narrow-sized PSDs. These feed sample PSDs, as well as the d_{10}, d_{50} and d_{90} percentile values, are presented in Figure 7.6, while the detailed results can be found in Appendix I.1. Preparation of the two LT samples (F & G) was relatively simple, and their distribution spans are comparatively narrow, *i.e.*, 96% and 84%, respectively. In contrast, preparation of the MV sample (H) was complicated, and the micro-screening procedure appears to have produced ‘fines’ (145% distribution span). Backscattered electron (BSE) images (App. B.3.2) of two coarse fractions, produced by the high resolution (HR) scanning electron microscope (SEM) (App. B.3.4), are illustrated in Figure 7.7; clearly, the MV mineral particles appear more rugged compared to the (coarser) LT sample, which consisted predominantly of chalcopyrite particles.

Stellenbosch University http://scholar.sun.ac.za

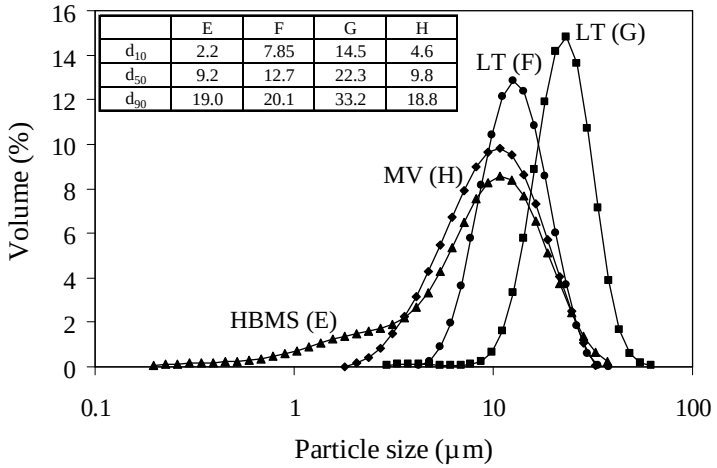

Figure 7.6
PSDs of the size fractions used in the follow-up batch oxidation testwork at low pulp densities.

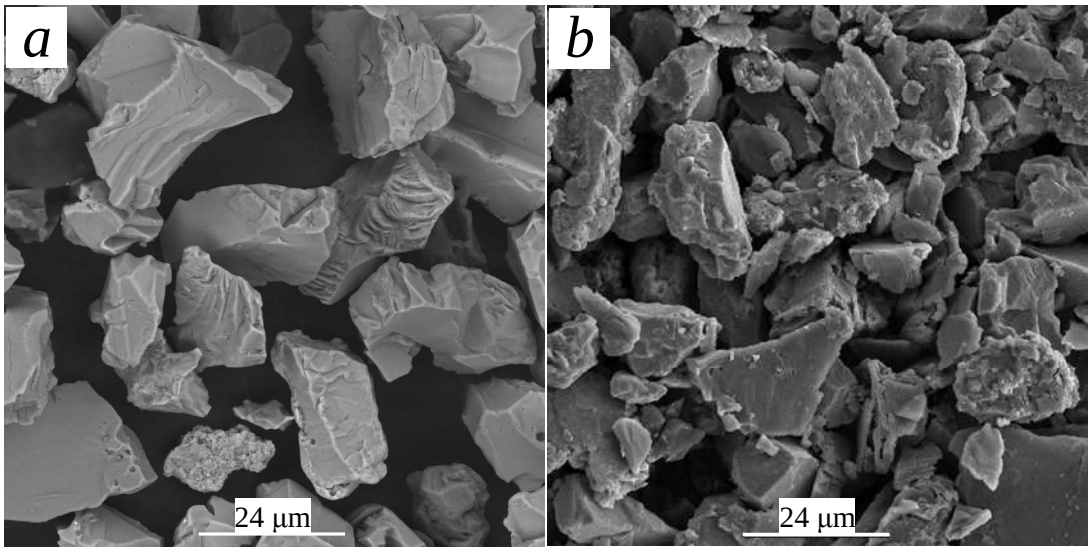

Figure 7.7
BSE images of two samples used in the follow-up batch oxidation testwork: *a*) LT (G) sample (d_{50} 22.3 µm, 84% span, 1000× magnification); *b*) MV (H) sample (d_{50} 9.8 µm, 145% span, 1000× magnification).

The substantial amount of gangue minerals in the MV sample results in a more complicated relationship between the observed sulfide oxidation rate and the feed PSD. Many of these gangue minerals appear to be relatively brittle, which suggests that the more rigid sulfide particles may have been concentrated in the coarser fraction of the size distribution. The MV sample was only included in this part of the study to provide a rough comparison of its intrinsic behaviour compared to the other concentrates at low pulp density; this material is not included in the high pulp density batch leaching testwork (Ch. 8). Furthermore, none of these head samples should be treated as truly mono-sized fractions (see Sect. 6.5.3), *i.e.*, the intrinsic rate constants are obtained in this chapter

Stellenbosch University http://scholar.sun.ac.za

by integrating the (total) discrete PSDs. In fact, the HBMS sample (E) includes a significant portion small of particles (Figure 7.6), with the objective of comparing the initial rate of particle shrinkage, k_ℓ, with the intrinsic rate at longer reaction times.

Mineralogical and chemical composition

The mineralogical bulk modal compositions of the head samples were quantified with a SEM-based image analyser (App. B.3.2) and are summarised in Table 7.2, while the analysed and corresponding calculated species concentrations are compared in Table 7.3. The unmilled pilot plant feed (HBMS) composition (briefly discussed in Sect. 6.4.3) is also discussed.

Table 7.2
Detailed mineralogical abundance (bulk modal) analyses of head material used in low pulp density batch testwork & high pulp density continuous pilot plant campaigns.

Mineral	[a] Pilot plant (%)	Sample E (%)	Sample F (%)	Sample G (%)	Average (F,G) (%)	Sample H (%)
Chalcopyrite	68.5	84.3	62.4	63.9	63.2	27.9
Chalcocite	0.0	0.1	9.2	8.5	8.9	0.3
Covellite	0.0	0.0	3.4	2.9	3.2	0.3
Bornite	0.0	0.0	4.2	3.9	4.1	0.0
Sphalerite	7.6	7.3	0.0	0.0	0.0	0.0
Pyrite	10.3	3.9	16.3	16.3	16.3	28.1
Pyrrhotite	1.3	1.7	0.2	0.1	0.1	3.1
[b] Sulfides	0.3	0.2	0.3	0.3	0.3	0.4
Sulfates	[c] 8.2	0.0	0.0	0.0	0.0	0.0
[d] Iron oxides	0.1	0.0	0.0	0.0	0.0	7.9
Carbonate	0.6	0.1	0.0	0.0	0.0	0.5
Quartz	1.9	0.2	0.7	0.9	0.8	13.4
[e] Gangue	1.2	2.2	3.3	3.2	3.2	18.1
Total	100.0	100.0	100.0	100.0	100.0	100.0

[a] Composite unmilled sample, collected over the course of the pilot campaigns; [b] Other (minor) sulfide phases, *e.g.*, arsenopyrite & galena; [c] Unidentified sulfate phase (Sect. 6.4.3), here scaled to 8.2%, using $CuSO_4/FeSO_4$ (wt) ratio of 0.4; [d] Predominantly magnetite (from qualitative XRD analysis); [e] Balance consists of other gangue minerals.

The calculated total copper and iron values in the HBMS 777 feed to the pilot autoclave are lower than the values obtained by chemical analyses. This is ascribed to the fact that this mineralogical analysis was conducted on a composite sample from the unmilled (dry) feed concentrate, while the average chemical values refer to the milled residue. The unidentified (Cu,Fe)-sulfate phase (Sect. 6.4.3) is scaled to account for these discrepancies. No such sulfate phases were identified in Sample E or the other HBMS fractions (see Table 4.6), which suggests that these unidentified agglomerate phases may have been water soluble or disintegrated during micro-screening. Either way, their

Stellenbosch University http://scholar.sun.ac.za

absence allows direct calculation of the total copper and iron content in Sample E using only the bulk modal values of the sulfide mineral phases. However, chemically analysed sulfur speciation results suggest some sulfate phases (3.6% SO_4), highlighting the difficulties in quantifying minor mineral phases that are finely dispersed within a bulk sample when using SEM-based modal analysis.

Table 7.3
Measured & calculated chemical analyses of the pilot plant feed material & head fractions used in low pulp density batch oxidation testwork.

Species	Pilot plant (HBMS)		Sample E (HBMS)		F, G (average) (LT)		Sample H (MV)	
	[a] Meas.(%)	[b] Calc.(%)	Meas.(%)	[b] Calc.(%)	Meas.(%)	[b] Calc.(%)	Meas.(%)	[b] Calc.(%)
Cu	24.7	[c] 24.7	28.8	29.3	32.8	33.6	8.7	10.1
Fe	29.0	[c,d] 29.0	29.1	[d] 29.0	28.4	27.3	28.9	29.2
Zn	4.23	[d] 4.5	4.3	[d] 4.5	0.0	0.0	0.0	0.0
Ca	(0.16)	[e] 0.2(5)	0.0	–	–	–	–	–
Mg	(0.06)	[e] 0.1	0.0	–	–	–	–	–
Si	–	–	–	–	–	–	11.3	–
CO_3	–	[e] 0.6	–	–	–	–	–	–
SO_4	1.8	[c] 4.8	3.6	0.0	0.0	0.0	0.0	0.0
S^{2-}	33.4	32.5	31.9	[f] 34.6	33.8	33.8	22.4	26.1
Total	93.3	96.4(5)	97.7	97.5	95.0	94.8	71.3	65.4

[a] Average of 27 analyses of milled solids over the course of the pilot campaigns; [b] Calc. from bulk modal analyses (Table 7.2), which excludes minor impurities; [c] $CuSO_4$ & $FeSO_4$ contents scaled (see Table 7.2) to yield analysed Cu & Fe values, respectively; [d] Assumed avg. of 7.5% Fe dissolved in sphalerite (see Sect. 6.4.3); [e] Scaled to yield 0.6% CO_3 (bulk modal value) at measured Ca/Mg ratio; [f] Assumed all Cu, Fe & Zn present as sulfide minerals only.

For the sake of simplicity, the mineralogical compositions (Table 7.2) are directly used in the continuous reactor simulation of the HBMS concentrate in the next section, assuming that these unidentified sulfate phases dissolved rapidly under autoclave operating conditions. This approach is consistent with the method used to calculate the reaction rate constants (Sect. 7.4.2), *i.e.*, by comparing the bulk mineral breakdowns in the head and leached residue sample (Sect. 7.3.2), respectively.

Excellent reconciliation between mineralogical and chemical analyses is obtained for the LT samples (F & G), as indicated by the average values in Table 7.3. On the other hand, the relatively high abundance levels of the various gangue minerals cause lower agreement in the case of the MV sample (H). These discrepancies are handled by comparing the mineralogical (bulk modal) composition of the head and corresponding residue samples. Since the oxidation rate constants (Sect. 7.4.2) are only based on the mineral oxidation behaviour over the first 30 to 45 minutes, no particle liberation studies were conducted in this part of the study.

Stellenbosch University http://scholar.sun.ac.za

7.4 Results and discussion

The experimental results are subdivided into two sections: Section 7.4.1 compares the continuous pilot campaign results and the continuous model calculations, using estimated secondary sulfide mineral oxidation and iron(III) precipitation reaction extents, while Section 7.4.2 summarises the batch oxidation results, generated at low pulp densities and varying oxidation temperatures. The final results of the continuous simulation are then presented, *i.e.*, after incorporating the additional sulfide mineral oxidation rate information, as obtained from the batch experimental programme, as well as the optimised iron(III) precipitation rate expressions (*ref.* Ch. 5).

7.4.1 Continuous pilot autoclave results and preliminary model calculations

The detailed mass balances of the continuous pilot campaigns are presented elsewhere (ATS internal reports; also see Dreisinger *et al.*, 2003). Four periods at substantially different operating conditions are selected to test the reactor model; the most relevant data are summarised below.

Results at selected periods of the 'steady-state' continuous pilot autoclave operation

The performance of the continuous autoclave simulation, within the context of the primary circuit operation (Figure 7.2), is tested at selected periods, here denoted Period 1 (P1), Period 2 (P2), Period 3 (P3) and Period 4 (P4) (see Figure 7.8).

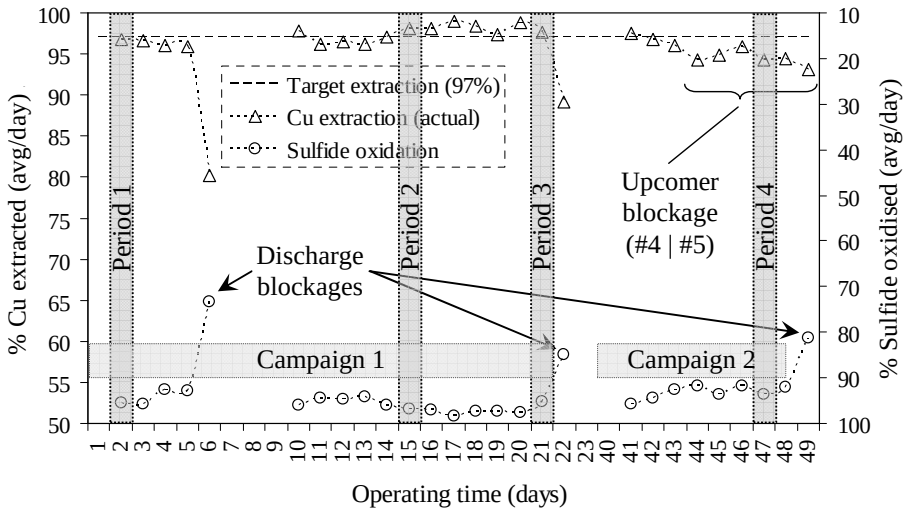

Figure 7.8
Pilot autoclave performance & selected periods (P1-P4) used to evaluate the continuous simulation.

Figure 7.8 highlights the most significant events that occurred during the two campaigns, which were dominated by three major blockages of the autoclave discharge pipe (Figure 7.4) by a sulfur/sulfide/hematite phase (confirmed by chemical & XRD analyses). As mentioned, these blockages are associated with the long average residence times and suboptimal design of the

Stellenbosch University http://scholar.sun.ac.za

autoclave internals (Figure 7.1). The latter three periods (P2, P3 & P4) represent significantly different autoclave operating conditions, falling within stages of relative steady-state operation for which good mass accounting and autoclave profile data were obtained. The target pulp densities were based on ideal adiabatic reactor behaviour (Sect. 7.2.3). Since the actual energy balance around the pilot autoclave was dominated by heat losses to the environment, the calculated return (stage-wise coolant) streams were all mixed up-front (feed make-up tanks). This was an operational simplification, but obviously did not represent full-scale reality.

To summarise, (Period) P1 was preceded by two days of commissioning and although the autoclave operated close to steady state, the primary circuit had not yet reached constant solution tenor values, *e.g.*, the autoclave feed solution contained a relatively low acid concentration (~30 g/L H_2SO_4). A finer feed grind ($d_{90} \approx 7.0$ µm) and a 6.9 wt% pulp density (from the SMD) were also utilised during this period. P2 was preceded by five days of steady-state operation, targeting a 'normal' feed grind ($d_{90} \approx 10$ µm) and slightly lower pulp density (6.6 wt% solids), while the feed acid concentration was higher (45 g/L H_2SO_4). P3 was preceded by five days of steady-state operation at a similar grind, but at a slightly higher pulp density (7.5-7.7 wt% solids). It is important to note that the autoclave profile samples during this period were taken towards the end of P3, *i.e.*, when autoclave discharge blockage problems were experienced (Figure 7.8). All three of these periods (P1, P2 & P3) fell within Campaign 1, *i.e.*, without any PLS recycle. P4, on the other hand, represents conditions towards the end of Campaign 2 (Figure 7.2), when a fraction of the PLS (~15%) was recycled to the autoclave feed make-up tanks. The target (d_{90}) grind was maintained at 10 µm, the feed acid concentration and pulp density were slightly lower (~37 g/L H_2SO_4 & 6.9-7.0 wt% solids, respectively), while the feed copper tenor was higher due to the PLS recycle. Most importantly, the upcomer arrangement between autoclave sections two and three, *i.e.*, between compartments 4 and 5 (C #4 & C #5; Figure 3.3), was blocked (Figure 7.1) during this period, and the gas/liquid mass transfer coefficient was 85 to 95% lower (see Table 3.9 & related discussions). This lower rate of interfacial mass transfer of the (primary) oxidant was the reason behind the drop in the copper extraction and sulfide oxidation during this period (Figure 7.8).

The most important measured parameters, flowrates and concentrations of these four periods are summarised in Table 7.4. The measured inflows and outflows refer mostly to averages over 24- and 12-hour periods, respectively, just before any profile samples were taken. The autoclave profile results (Table 7.9 & Table 7.10) are therefore relatively closely aligned to the feed and discharge stream properties around each period, with less emphasis on total mass and elemental balancing. This is because the feed and discharge streams were accumulated in semi-batch fashion (Sect. 7.3.1), with normal operational variation, which might not necessarily reflect ideal continuous flow behaviour.

Stellenbosch University http://scholar.sun.ac.za

Table 7.4
Measured parameters, flowrates & concentrations at steady-state operation (12-24 hr averages).

Measured (average)	Period	Dry solids (g/hr)	Solids (%)	Cu (%)	Zn (%)	Fe (%)	–	S^{2-} (%)	S° (%)	SO_4 (%)	S^T (%)
[a,b] Mill feed	P1	1092	44.0	24.7	4.2	29.0	–	33.4	–	1.8	–
	P2	1160	44.0	24.7	4.2	29.0	–	33.4	–	1.8	–
	P3	1175	48.8	24.7	4.2	29.0	–	33.4	–	1.8	–
	P4	1189	48.8	24.7	4.2	29.0	–	33.4	–	1.8	–
[c] Pulp density	P1	–	6.8(5)								
	P2	–	6.6								
	P3	–	7.4(5)								
	P4	–	6.9								
[d] Solid discharge	P1	895	5.3(5)	1.1	0.1	38.9	–	2.1	26.2	7.0	30.7
	P2	957	5.6	0.9	0.0(6)	34.4	–	1.3	27.5	17.4	34.0
	P3	990	6.3	2.2	0.3(5)	33.6	–	4.6	22.5	16.8	32.6
	P4	968	6.0	1.4	0.0(6)	37.2	–	3.1	24.0	19.9	34.2

Measured (average)	Period	Flowrate (g/hr)	Dens. (g/L)	Cu (g/L)	Zn (g/L)	Fe (g/L)	Fe(II) (g/L)	H_2SO_4 (g/L)
Raffinate return	[e] P1	12446	1065	1.4	5.8	6.1	0.2	37.3
	P2	13935	1114	4.2	10.3	13.7	0.4	53.1
	P3	11779	1089	2.7	11.6	6.9	0.1	44.7
	P4	10926	1095	7.4	11.9	3.5	0.1	52.7
[b] Surfactant	P1	958	–					
	P2	917	–					
	P3	1000	–					
	P4	917	–					
[b] PLS recycle	P4	2806	1.127	28.9	11.9	3.4	0.5	22.6
[b,f] Feed solution	P1	13872	–	2.4	5.6	6.6	6.0	30.5
	P2	15482	–	4.2	13.3	12.0	5.2	45.1
	P3	13605	–	4.2	12.8	8.5	6.2	42.7
	P4	15159	–	12.2	10.1	4.2	4.0	36.5
[d] Sln. discharge	P1	15838	1090	20.0	7.7	2.7	0.4	22.9
	P2	16089	1136	23.3	15.5	10.0	0.5	27.6
	P3	14829	1143	25.4	16.0	6.6	1.3	27.4
	P4	15344	1130	31.5	13.6	2.9	0.5	26.3

[a] Avg. of 27 chemical milled solids analyses (meas. over both campaigns); [b] Avg. (24 hrs) after sample removal; [c] Avg. solids wt% (24 hrs) in slurry feed to autoclave (incl. surfactant stream); [d] Avg. (12 hrs) before sample removal; [e] Not at steady-state flow & composition; [f] Avg. (24 hrs) before surfactant (water) addition point.

Stellenbosch University http://scholar.sun.ac.za

Obviously, the longer the evaluation time span, the closer the recorded values would represent steady-state flow. However, this could not be done here because various aqueous species concentrations, in particular the copper and acid concentrations, drifted over the course of Campaign 1 due to suboptimal integration between the leaching and SX unit operations. For the sake of completeness, the mass balances over the four extended evaluation times, associated with Periods P1, P2, P3 and P4, respectively, are summarised in Table 7.5. Other operating parameters are also presented, including the estimated autoclave residence times, using the average measured slurry densities (between in- & outflow), solid-phase mass losses, and the amount of LS and QB added (details of these surfactants are summarised in Sect. 6.3.3).

Table 7.5
Overall mass balances & some important (avg.) values, measured over extended time spans around each evaluation period.

[a] Period	[b] Span (days)	[c] Water in (kg/day)	Solids in (kg/day)	Solution in (kg/day)	Total in (kg/day)	[d] Surfactants (kg/t)	[e] τ (avg.) (min)
P1	3	22.7	26.4(5)	340.8(5)	390.0	5.8	[f] 127
P2	6	22.0	27.8	371.3	421.1	3.1	[g] 116
P3	5	21.2	28.3	346.4	395.9	4.0	[g] 127
P4	5	22.4	27.8	347.4	397.6(5)	4.3	[g] 124
[a] Period	[b] Span (days)	Samples out (kg/day)	Solids out (kg/day)	Solution out (kg/day)	Total out (kg/day)	[h] Mass loss (%)	Accountability (%)
P1	3	4.0	20.0(5)	390.8	414.9	26	106
P2	6	3.0	21.2	364.2	388.4	22	92
P3	5	1.2	21.9	372.1	395.2	22	100
P4	5	2.8	22.8	379.9	405.5	19	102

[a] Period (Figure 7.8), falling within a particular time span; [b] Extended time span (days) over which each mass balance is conducted; [c] Water used to pre-dissolve surfactants; [d] 58% Norlig A (LS) & Orfom 2 (QB); [e] Avg. autoclave residence time, based on the reactor volume (Table 3.1) & avg. slurry density 'at temperature'; [f] Agitation speed maintained at 1000 rev/min in all compartments; [g] Agitation speed increased to 1200 rev/min in C #1-5; [h] Solid-phase mass loss, based on avg. pulp density changes over the autoclave.

The total mass flow accountabilities are good, taking into consideration the various challenges experienced during Campaign 1 in integrating the autoclave and SX unit operations. The calculated solids mass loss varies between 19 and 26%, and is closely correlated to the amount of hydronium jarosite *vs.* hematite formed (discussed below). For completeness, the elemental mass balances over these extended time spans are presented in Table 7.6. Excellent mass accountabilities are obtained for all the elements, except for iron during P2 (highlighted in bold). Overall copper extractions were close to the 97% target, except during the latter part of P4 (see Figure 7.8). Subtle variations in the iron precipitation behaviour are noticed, especially when comparing the feed acid concentrations (Table 7.4) with the average solid-phase mass losses (Table 7.5) and total iron

Stellenbosch University http://scholar.sun.ac.za

extractions (Table 7.6). Table 7.7 explores these aspects further, as well as the acid balance and sulfur yields across the autoclave.

Table 7.6
Avg. elemental extractions & mass balances over selected time spans around each eval. period.

[a] Period	Elem.	[b] Solids in (kg/day)	Solution in (kg/day)	Samples out (kg/day)	Solids out (kg/day)	Solution out (kg/day)	[c] Extract (acc.) (%)
P1 (3)	Cu	6.53	0.73	0.06	0.25	6.94	96 (100)
	Zn	1.12	1.73	0.02	0.03	2.91	97 (104)
	Fe^T	7.67	2.09	0.08	8.04	1.03	<0 (94)
	S^T	8.83	5.57	0.13	6.26	8.42	(103)
P2 (6)	Cu	6.73	0.92	0.05	0.16	6.77	98 (91)
	Zn	1.15	3.53	0.03	0.04	4.38	96 (95)
	Fe^T	7.91	3.28	0.07	6.84	2.88	14 (**87**)
	S^T	9.10	9.39	0.13	6.92	10.88	(97)
P3 (5)	Cu	6.99	1.29	0.03	0.29	7.90	96 (99)
	Zn	1.20	4.00	0.02	0.04	5.05	96 (98)
	Fe^T	8.21	3.25	0.03	8.16	2.49	1 (93)
	S^T	9.44	9.36	0.05	7.18	11.63	(100)
P4 (5)	Cu	6.87	3.72	0.08	0.36	10.62	95 (104)
	Zn	1.18	3.20	0.03	0.02	4.53	99 (104)
	Fe^T	8.40	1.42	0.06	8.78	0.90	<0 (99)
	S^T	9.29	8.06	0.13	7.78	10.45	(106)

[a] Period (Figure 7.8) & extended time span (days) in brackets; [b] Avg. of 27 chem. analyses of solids (measured over both campaigns); [c] Elem. extractions based on solid-phase flow (accountabilities in brackets).

Table 7.7
The behaviour of Fe & S in the autoclave over selected time spans around each eval. period.

[a] Period	[b] Fe in (g/L) (FeII)	[b] Fe out (g/L) (FeII)	[c] $W_{f,Jar}$ (% H-Jar)	[c] $W_{f,Hem}$ (% Hem)	[d] Mass loss (%) (Cu)	[b] Acid in (g/L)	Acid out (g/L)	[e] S° yield (%) (S^{2-})
P1 (3)	6.1 (5.5)	2.9 (0.4)	13 (9.0)	87	26 (1.25)	25.8	22.6	57 (2.6)
P2 (6)	10.0 (5.0)	8.9 (0.6)	45 (21.8)	55	22 (0.8)	39.4	27.3	61 (1.7)
P3 (5)	8.7 (5.7)	7.6 (1.0)	32 (15.8)	68	22 (1.3)	38.3	29.0	62 (2.5)
P4 (5)	4.1 (4.1)	2.5 (0.4)	38 (19.85)	62	19 (1.6)	32.3	24.0	60 (3.2)

[a] Period (Figure 7.8) & extended time span (days) in brackets; [b] Concentrations corrected for surfactant (water) flow ([FeII] in brackets); [c] Calc. wt% Fe ppt. as particular phase, based on residue SO_4 content (in brackets) & 2 wt% S^T in hematite (Ch.5); [d] Solid-phase mass loss, based on avg. pulp density changes over autoclave (residual % Cu in brackets); [e] S° yield, *i.e.*, $S°/S^{2-}{}_{rx}\times 100\%$, based on solid flows & analyses (residual wt% S^{2-} in brackets).

The marginal improvement in the observed elemental sulfur yield with increasing feed acid concentration cannot explain the apparent buffering action exerted on the exit acid concentration.

Stellenbosch University http://scholar.sun.ac.za

Instead, the sulfate content of the residue, which is clearly not related to the residual copper content (or other base metal sulfate salts), suggests substantial formation of hydronium jarosite phase. X-ray powder diffraction (XRD; App. B.3.2) and Mössbauer-effect spectroscopy (MES; App. B.3.7) were employed to ascertain the relative abundance of the different residue phases. Two residues were removed after discharge blockages from the bottom of the combined first compartment (C #1+2): one after Period 1 (here referred to P1s) and the other after Period 3 (P3s). These samples were then subjected to XRD analyses. To compare the relative XRD peak heights, an internal standard (20% quartz) was added to these samples. Nevertheless, it is difficult to quantify the jarosite content, since the major peaks of jarosite overlap with the lesser peaks of sulfur. Furthermore, the iron precipitation products are poorly crystalline, and the secondary peak of jarosite is hardly distinguishable from the background noise. The advantage of using MES is that it provides an effective method to analyse the poorly crystalline materials (App. B.3.7).

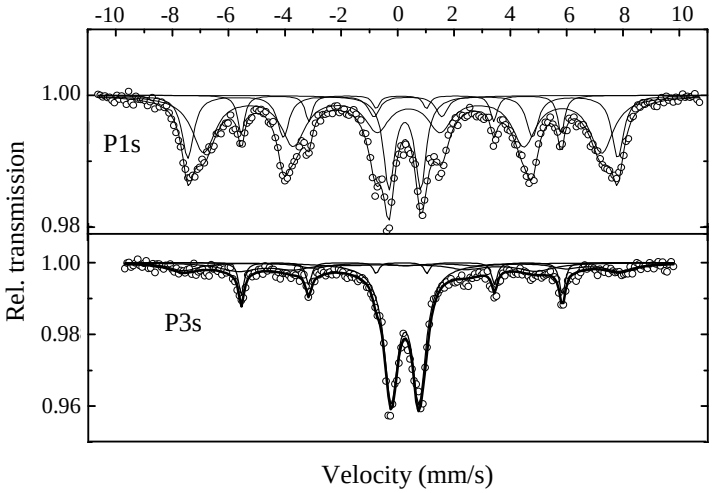

Figure 7.9
Mössbauer spectra of pilot autoclave residues, taken after Period 1 (P1s) & Period 3 (P3s), respectively; solid lines represent theoretical fits to the data (circles). All spectra were composed of a sextet representing near-crystalline hematite, a broad sextet which likely corresponded to poorly crystalline hematite, another sextet for chalcopyrite & a doublet corresponding to jarosite.

Table 7.8
Relative Fe-phase abundances from MES in autoclave residues after Periods 1 (P1s) & 3 (P3s).

[a] Period	[b] Sample name	Hematite [c] (%)	[d] Hematite-like [c] (%)	Chalcopyrite [c] (%)	[e] Jarosite/Pyrite [c] (%)
P1	P1s	23	52	9	16
P3	P3s	14	17	11	[f] ~58

[a] Period (Figure 7.8); [b] From C #1+2, following autoclave blockages; [c] Typical relative errors ~10%; [d] Amorphous hematite & possibly nano-phase hematite; [e] Difficult to distinguish between jarosite & pyrite since the central doublet, representing these two phases, exhibit low abundance (<10%) & overlap with central sextet lines; [f] Qualitative estimate, based on 11% phase abundance of $CuFeS_2$ & 31% crystalline, amorphous & nano-phase Fe_2O_3 .

Stellenbosch University http://scholar.sun.ac.za

The Mössbauer spectra of these two residue samples are presented in Figure 7.9, while the relative abundances are listed in Table 7.8. The following discussion is based on the MES analyses (WITS) and is not the author's interpretation: each spectrum was fitted with a minimum number of sub-components to obtain the best overall fit to the data, *viz*, three sextets and a doublet. The three sextets represent hematite, an unknown iron(III) phase (with parameters similar to those of hematite) and chalcopyrite. The doublet represents jarosite and/or a pyrite phase, which are difficult to distinguish between because of the low abundance (<10%) and overlapping with the central lines of the sextets. The broad line widths of the hematite-like phase indicate a likely distribution of Fe^{3+} local environments, *i.e.*, in the number of Zn/Ni/Cu near neighbours, and/or that this phase is poorly crystalline (amorphous). Both the hematite and hematite-like subspectra have magnetic hyperfine fields (B_{hf} less than that expected for bulk crystalline hematite; see App. B.3.7). This suggests a possible distribution of ultra-fine particles down to the ~10 nm range. Sample P3s is dominated by a central doublet and has broad resonances in the wings of the spectrum, with a bowing baseline. These are typical features of super-paramagnetic relaxation, indicative of nano-phase (or amorphous) iron oxides; this is the reason why this sample is not easily discerned in the XRD spectrum. Part, or all, of the central doublet may be a collapsed sextet representing the proportion of smallest particles (<10 nm). Superimposed on the bowing featureless baseline are the sharp features of the chalcopyrite sextet, whose abundance is close to 11%. This is the only phase abundance that can be identified with certainty in this sample. Iron oxides (likely hematite) exist in amorphous, poorly crystalline or nano-phase form, with an abundance of about 31%, allowing an estimated value of 58% for the jarosite/pyrite phase.

This discussion highlights the complexities of using MES to quantify the relative abundance of precipitated iron phases in a complex mixture of unreacted iron-containing sulfides. Nevertheless, this information, coupled with knowledge of the total sulfate content (Table 7.7), is sufficient evidence of more substantial hydronium jarosite formation during the latter periods compared to Period 1. This argument can be substantiated by the comparatively lower solid-phase mass loss over these latter periods (Table 7.7). Hydronium jarosite formation is therefore assumed to be the intrinsic mechanism by which an excessive acid concentration was buffered in the primary circuit.

In the rest of this study, the extent of jarosite *vs.* hematite formation is simply quantified by using the chemically analysed total sulfate content in the autoclave residue, provided no other sulfate-containing salts precipitated and assuming that 2 wt% sulfur is associated with hematite (see Ch.5).

To evaluate the efficiency of the leaching operation, profile samples were taken *via* jacketed (cooled) sampling bombs, similar to those described in Section 4.3.1. The results, including the calculated reaction extents, are summarised in Table 7.9 and Table 7.10.

Stellenbosch University http://scholar.sun.ac.za

Table 7.9
Autoclave profile results & calculated reaction extents for evaluation Periods P1 & P2.

[a] **P1** (Solids)	Cu (%)	Zn (%)	Fe (%)	S^{2-} (%)	SO_4 (%)	[b,c,d] Fe ppt. (% H-Jar)	[c,d] Fe ppt. (% Hem)	[e] Mass loss (%)
C #1+2	6.9	0.4(2)	24.4	16.4(5)	6.6	19	81	20.4
C #3	3.1	0.1(6)	24.7(5)	7.3	8.6	21	79	19.1
C #4	1.6	0.0(9)	25.5	7.0	8.4(5)	19	81	20.0
C #5	1.0	0.0(6)	25.7(5)	2.7(5)	8.6	18	82	19.4
C #6	0.7	0.0(1)	27.2	2.7	8.7(5)	17	83	18.3
[a] **P1** (Solutions)	Cu (g/L)	Zn (g/L)	Fe (g/L)	Fe(II) (g/L)	H_2SO_4 (g/L)	[d] Cu extr. (%)	[d] Zn extr. (%)	[d] S^{2-} oxid. (%)
C #1+2	12.3	7.0	4.5	1.9	18.0	77.8	93.0	71.9
C #3	15.9	7.7(5)	3.3	1.1	21.2	90.0	97.3	84.8
C #4	17.1	7.8	2.6	0.6	21.7	94.7	98.5	88.6
C #5	17.0	7.5	2.1	0.3	21.7	96.8	99.0	91.9
C #6	17.4	7.6	2.0	0.3	21.0	97.7	99.8	92.6
[a] **P2** (Solids)	Cu (%)	Zn (%)	Fe (%)	S^{2-} (%)	SO_4 (%)	[b,c,d] Fe ppt. (% H-Jar)	[c,d] Fe ppt. (% Hem)	[e] Mass loss (%)
C #1+2	8.7	0.7(1)	29.3	15.3	11.1	61	39	22.6
C #3	4.0(5)	0.5(0)	32.5	4.9	14.6	56	44	19.5
C #4	2.3	0.3(3)	30.0	3.2	15.8	54	46	17.8
C #5	1.9	0.2(6)	32.7	2.3	15.3	46	54	15.6
C #6	1.5	0.2(1)	34.6	2.0	16.9	51	49	14.1
[a] **P2** (Solutions)	Cu (g/L)	Zn (g/L)	Fe (g/L)	[f] Fe(II) (g/L)	[g] H_2SO_4 (g/L)	[d] Cu extr. (%)	[d] Zn extr. (%)	[d] S^{2-} oxid. (%)
C #1+2	16.8	15.1	15.4	–	22	72.8	88.4	68.5
C #3	18.6	15.6	13.6	–	25	86.8	91.5	83.1
C #4	20.1	15.6	12.6	–	26	92.2	94.3	87.9
C #5	20.7	15.3	10.8	–	24	93.4	95.4	89.2
C #6	22.4(5)	14.9(5)	10.8(5)	–	28	94.6	96.2	90.3

[a] Profile samples taken during each period (Figure 7.8); [b] Calc. wt% Fe precipitated as hydronium jarosite, based on sample SO_4 contents & assuming 2 wt% S^T in hematite; [c] Fe(III) precipitation extent calc. from bulk mineralogy (Table 7.2), consolidated composition (Table 7.3) & feed stream properties (Table 7.4; ρ = 1.1 & 1.14 kg/L for P1 & P2, respectively); [d] All reaction extents obtained in iterative fashion, using calc. mass loss; [e] Mass loss iterated with mineral oxidation extents (assuming $r_{Ph} = r_{Sph}$ & X_{Py} from S^{2-} balance), estimated S° yields (Sect. 6.5.5) & hematite *vs.* jarosite precipitation extents[(see b, c)]; [f] No reliable Fe(II) tenors; [g] Acid tenors uncertain due to high Fe(III) levels.

Stellenbosch University http://scholar.sun.ac.za

Table 7.10
Autoclave profile results & calculated reaction extents for evaluation Periods P3 & P4.

[a] **P3** (Solids)	Cu (%)	Zn (%)	Fe (%)	S^{2-} (%)	SO_4 (%)	[b,c,d] Fe ppt. (% H-Jar)	[c,d] Fe ppt. (% Hem)	[e] Mass loss (%)
[f] C #1+2	8.7	0.6(6)	28.9	12.6	[g] 15.6	89	11	15.9
[f] C #3	3.0	0.5(3)	30.1	4.1	16.5(5)	61	39	17.3
[f] C #4	2.6	0.4(6)	32.5	2.8	17.2	56	44	13.4
[f,h] C #5+6	2.0(5)	0.4(4)	33.3	3.2	17.2(5)	56	44	14.4
[a] **P3** (Solutions)	Cu (g/L)	Zn (g/L)	Fe (g/L)	[i] Fe(II) (g/L)	[j] H_2SO_4 (g/L)	[d] Cu extr. (%)	[d] Zn extr. (%)	[d] S^{2-} oxid. (%)
C #1+2	21.0(5)	15.9	12.2(5)	–	19	70.4	88.4	67.4
C #3	23.2	15.2	10.2	–	27	89.9	90.8	85.6
C #4	25.5	15.5	7.9	–	27	90.7	91.6	86.7
[h] C #5+6	25.4	16.2(5)	8.3	–	28	92.9	92.1	88.2
[a] **P4** (Solids)	Cu (%)	Zn (%)	Fe (%)	S^{2-} (%)	SO_4 (%)	[b,c,d] Fe ppt. (% H-Jar)	[c,d] Fe ppt. (% Hem)	[e] Mass loss (%)
[k] C #1+2	11.6(5)	1.0(1)	29.9(5)	18.8(5)	7.2	36	64	19.8
[k,l] C #3+4	3.8	0.7(5)	33.4	5.5	11.7	38	62	19.4
C #5	2.5	0.7(6)	[m] 34.7	4.5	[n] 20 (13)	[n] 64 (38)	[n] 36 (62)	[n] 8 (17)
C #6	2.2	0.6(8)	[m] 34.3	3.4(5)	[n] 22 (13)	[n] 71 (38)	[n] 29 (62)	[n] 6 (18)
[a] **P4** (Solutions)	Cu (g/L)	Zn (g/L)	Fe (g/L)	Fe(II) (g/L)	H_2SO_4 (g/L)	[d] Cu extr. (%)	[d] Zn extr. (%)	[d] S^{2-} oxid. (%)
[k] C #1+2	24.5(5)	13.0	5.6	2.4	18.5	62.2	83.0	58.7
[k,l] C #3+4	29.9	14.0	4.2(5)	2.2	24.2	87.6	87.3	83.0
C #5	30.1(5)	14.2	2.8	0.3	26.7	[n] 91 (92)	[n] 85 (87)	[n] 85 (86)
C #6	31.6	14.4	3.1	0.3	[m] 26.4	[n] 92 (93)	[n] 87 (88)	[n] 86 (88)

[a] Profile samples taken during each period (Figure 7.8); [b] Calc. wt% of Fe precipitated as hydronium jarosite, based on sample SO_4 content & assuming 2 wt% S^T in hematite; [c] Fe(III) precipitation extent calc. from bulk mineralogy (Table 7.2), consolidated composition (Table 7.3) & feed stream properties (Table 7.4; assumed liquid ρ = 1.15 kg/L); [d] Reaction extents obtained in iterative fashion, using calc. mass loss; [e] Mass loss iterated with mineral oxidation extents (assuming $r_{Ph} = r_{Sph}$ & X_{Py} from S^{2-} balance), estimated elemental S° yields (Sect. 6.5.5) & Hematite *vs.* H-Jarosite precipitation extents[(see b,c)]; [f] Avg. of chem. & mineralogical analyses; [g] Value corrected for the presence of 2% Cu, assumed to be present as $Cu_3(SO_4)(OH)_4$ (Ch. 5); [h] Autoclave discharge pipe partially blocked, causing slurry level to rise ~0.5 L in (short-circuited) C #5+6 (combined volume ~10.1 L); [i] No reliable Fe(II) tenors; [j] Acid tenors uncertain due to high Fe(III) levels; [k] Blockage of upcomer between C #4 & C #5 caused slurry to overflow *via* vapour slot (Figure 7.1) & short-circuiting between C #3 & C #4; [l] Solutions and solids analyses from C #3 & C #4, respectively; [m] Adopted from avg. profile sample analyses prior to & after period P4; [n] Bracketed values correspond to adjusted SO_4 residue levels of 13%, *i.e.*, to be consistent with the estimated H-jarosite precipitation extent (32-38%) (*ref.* Table 7.7) .

The elemental sulfur yields are not calculated over these profiles, due to considerable sulfur speciation uncertainty; this is thought to be due to sampling effects, since fine sulfur particles

Stellenbosch University http://scholar.sun.ac.za

tended to float, while heavier conglomerates tended to sink to the autoclave bottom. Furthermore, since the quartz levels were low (see Table 7.2), the silica-tie method could not be used. There is therefore considerable doubt regarding the accuracy of the residue sulfate contents, which has a large impact on these calculations. The uncertainty in the calculated extent of iron precipitated as hematite (*vs.* jarosite) is as high as ±15%. In the same vein, the residual sulfide content is highly suspicious, which, in turn, significantly impacts the calculated pyrite oxidation extent.

Calculation methodology

The following methodology is used to calculate the various reaction extents: the mass loss is first estimated and all the reaction extents calculated. The ratio of iron precipitated as hydronium jarosite *vs*. hematite is based on the residue sulfate content (after accounting for 2 wt% sulfur in hematite; Ch. 5), the amount of iron leached and the iron concentration in the autoclave feed (Table 7.4), while elemental sulfur yields are assumed for each of the minerals, *i.e.*, 60% for chalcopyrite, 95% for iron-containing (7.5% Fe) sphalerite and pyrrhotite and 0% for pyrite (Sect. 6.5.5). The chalcopyrite oxidation extent is directly obtained from the residue copper content after accounting for (Cu,Fe)-sulfate phases (Sect. 7.3.3), while the sphalerite oxidation extent is calculated from the residual zinc content. The rate of pyrrhotite oxidation is assumed to closely follow the rate of sphalerite oxidation, while the extent of pyrite oxidation is obtained from the residual sulfide content (after accounting for the remaining chalcopyrite, sphalerite & pyrrhotite). Labile minerals, such as (Ca,Mg) carbonate and (Cu,Fe) sulfate, are assumed to dissolve immediately on entering the autoclave. After taking the pulp and (assumed) liquid densities into account (Table 7.4), the mass loss is calculated in each compartment and the above calculation repeated. This iterative procedure yields the reaction extents summarised in Table 7.9 and Table 7.10.

The autoclave profile results for P1 are relatively consistent with the average recorded reaction extents (Table 7.4 & Table 7.7) and MES results (Table 7.8). However, the profile samples from P2 and P3 show some discrepancies, especially with regard to the high extent of hydronium jarosite formation. As mentioned, the sulfate analyses are uncertain for these periods, especially since the corresponding calculated mass losses are lower than the measured averages (Table 7.7).

A counter-argument, which supports a higher degree of jarosite formation, is based on higher iron and acid feed tenors during P2 and P3 (Table 7.7), backed by the MES analyses of the first compartment residue, *i.e.*, referring to P3 (Table 7.8). The formation extents of hydronium jarosite in C #5 and C #6 during P4 and the corresponding mass losses, also contradict each other. Nevertheless, as indicated (bracketed values in Table 7.10; footnote [n]), adjustment of the sulfate values has a relatively insignificant impact on the calculated oxidation extents. Therefore, the hydronium jarosite formation extent (wt% split of total Fe precipitated) is a major unknown factor

Stellenbosch University http://scholar.sun.ac.za

and appears to have swung between 40 and 60%, with the balance consisting of hematite, during higher iron and acid feed tenors. This aspect is investigated in more detail later, since the calculated acid tenors in the various autoclave compartments are sensitive to the extent of this reaction, which, in turn, impacts the intrinsic mineral oxidation rates as calculated by the micro-model.

It is also worth noticing that about 2% Cu was detected by SEM-EDX analysis in the C #1+2 residue (after P3; footnote [g] in Table 7.10). The exact phase was not identified by this analysis, but it appears to be associated with hydronium jarosite. Chapter 5 elaborates on this aspect: the presence of copper during iron(III) precipitation is associated with the formation of (metastable) antlerite, $Cu_3(SO_4)(OH)_4$. Similarly, the lower than expected 'sphalerite' dissolution during P2, P3 and P4, *i.e.*, based on the zinc content of the compartmental residues, may be related to the formation of basic zinc sulfate, $ZnSO_4.2Zn(OH)_2$ (see Ch. 5) at a high zinc tenor (~15 g/L Zn during P2, P3 & P4 *vs.* ~7 g/L Zn during P1). This argument is further supported by SEM-based modal analyses of P3 profile residues, which detected less than 0.025% sphalerite in C #4 to C #6. This mineralogical investigation is discussed further, since significant amounts of the iron precipitates exhibited low crystallinity and could not be quantified by XRD. An added uncertainty with regard to the above reaction extents is the efficiency with which these metastable salts redissolved during sample preparation, *i.e.*, washing with pH 2 water (at room temperature). Correction of the sulfate content, due to the presence of this phase, is not warranted due to its compositional uncertainty. The acid concentrations in these continuous tests were also substantially higher than the conditions found to yield such phases during batch precipitation (Ch. 5). Therefore, to summarise, there is general uncertainty with regards to the hematite *vs.* jarosite content and a conservative uncertainty of ±15% in iron(III) precipitation extent as jarosite is adopted, assuming that the base metal sulfate phases were present as simple sulfate salts (at maximum 1% Cu & Zn), *i.e.*, as high as a 10% variation in the hematite ratio ($W_{f,Hem}$; see definition in Ch. 5).

With regard to the operation of the autoclave, P1 treated finer milled concentrate ($d_{90} \approx 7.0$ µm), while P2, P3 and P4 treated a 'normal' feed grind ($d_{90} \approx 10$ µm) (see Figure 7.10 below). Blockage problems were experienced during P3; this resulted in an increase in slurry volume of about 0.5 litres, causing some short-circuiting between C #5 and C #6. A more significant blockage occurred during P4, when the upcomer between C #4 and C #5 blocked completely and the slurry level in C #1 to C #4 increased up to the vapour slot height (see Figure 7.1). The autoclave therefore essentially consisted of four stages, *i.e.*, the combined C #1+2, C #3+4 (due to short-circuiting; Figure 3.3), C #5 and C #6. The high slurry levels in C #1+2 and C #3+4 resulted in a significant reduction in the gas/liquid mass transfer rate (Table 3.9); hence the slower sulfide mineral oxidation rates in the initial compartments during P4 (Table 7.10).

Stellenbosch University http://scholar.sun.ac.za

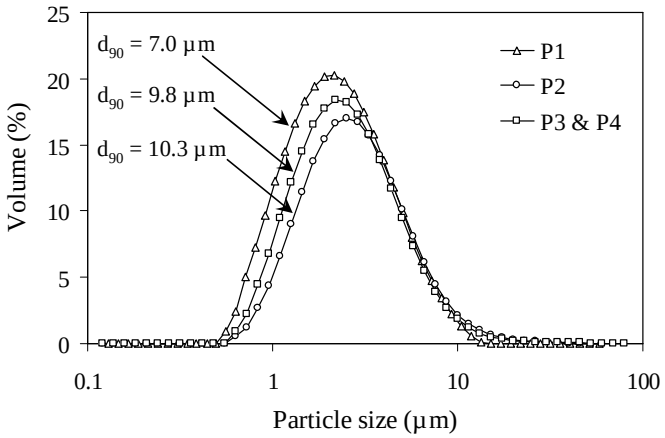

Figure 7.10
PSDs of the milled HBMS feed slurry into the pilot autoclave during Periods P1 to P4.

Comparing the continuous simulation and the measured pilot plant results

This section presents a comparison between the continuous reactor model and the measured results. Due to uncertainty of the sulfate (*e.g.*, hydronium jarosite & antlerite) formation rates and the sulfur speciation results in the various autoclave compartments, the precipitation reaction extents are manually adjusted in this section. Furthermore, to evaluate the consistency of the pilot plant results, the raffinate composition of each period (summarised in Table 7.4) is adjusted slightly to reflect the measured composition of the feed solution to the autoclave. The raffinate composition is therefore fixed for the primary circuit mass balance iteration, but relaxed later on (Ch. 8). In addition, various assumptions are made regarding the behaviour of sulfide minerals other than chalcopyrite. These assumptions are revisited later in this chapter, after incorporating the updated sulfide oxidation rate and optimised iron(III) precipitation rate expressions.

Before the PB (Sect. 7.2.2) and mass balance (Sect. 7.2.3) frameworks can be applied, the following outstanding issues need to be addressed. Firstly, to apply the macroscopic PB (Eq. 7.4), the assumption of a well-mixed reactor needs to be tested. Secondly, to calculate the average residence time and also to allow a direct comparison between the simulation output and analysed species tenors, the liquid density needs to be dynamically adjusted according to changes in the molality matrix.

Evaluating the degree of mixing (solids suspension)

With regard to mixing, the degree of solids suspension is assumed to be a good indicator of how closely the agitated slurry system approached an idealised (well-mixed) scenario. Various impeller designs and configurations were tested in the different autoclave compartments prior to the continuous campaigns. The worst-case scenario is represented by mixing in the final compartment

Stellenbosch University http://scholar.sun.ac.za

(C #6), where the agitation speed was maintained at 1000 rev/min (*vs.* 1200 rev/min in the other compartments) and the distance (h) between the impeller (diameter, d) and the autoclave bottom was the smallest (Figure 3.3; h ≈ ⅓d), *i.e.*, the effectiveness of the impeller to suspend the solids was worse than in the other compartments (*e.g.*, in C #1, where h ≈ d). Furthermore, an effective (gas-free) slurry volume (V_{sl}) of 5.6 litres was used in these tests, which was about 1 litre more than the actual effective volume in C #6 during steady-state operation at 1000 rev/min (Table 3.1).

A simple wash-out test was conducted by charging the reactor compartment (similar to the setup illustrated in Figure 3.4) with about 1.6 kg HBMS pilot feed material (d_{90} ≈ 10 µm), to yield a starting pulp density ($\rho_{s/w}$) of about 30 wt%. The impeller speed was then increased to 1000 rev/min and water was continuously pumped into the reactor at constant rate of about ~250 mL/min. The slurry that exited the vessel *via* the overflow pipe (Figure 3.4) was collected over different time intervals, weighed and filtered. The dried filter cake, corresponding to each interval, was also weighed. At the completion of the test (~120 min), the autoclave was properly washed, the wash water filtered and the cake dried; this represented the solid material that remained in the reactor at the completion of the test (∞). These results are summarised in Table 7.11.

The solid-phase mass balance for this test is straightforward and can be presented as follows:

$$\frac{d\rho_{sl}}{dt} \cdot V_{sl} = -\rho_{sl} Q_{sl} \qquad 7.47$$

where ρ_{sl} represents the pulp density, defined as the mass of solids (W) per unit volume (gas-free) slurry. Note that V_{sl} refers to the effective (gas-free) slurry volume at 1000 rev/min impeller speed, *i.e.*, at the overflow level used in this wash-out test. This equation is easily integrated to yield:

$$\frac{\rho_{sl}(t)}{\rho_{sl,o}} = \frac{W(t)}{W_o} = exp(-t\frac{Q_{sl}}{V_{sl}}) = exp(\frac{-t}{\tau}) \qquad 7.48$$

where τ is the average residence time of the slurry in the reactor. The comparison between this (ideal) mixing curve and the measured data is illustrated in Figure 7.11.

Clearly, the assumption of ideal mixing is, for all practical purposes, true. It should, however, be pointed out that the liquid density at 150°C is about 10% less than at room temperature and the degree of particle suspension may have been less ideal ‘at temperature’, than depicted below. However, the liquid density of the actual solution is higher (typically 10-15%) than pure water and it is assumed that these two opposing factors cancelled each other out. Considering the generally fine PSDs encountered in this study, it is reasonable to assume that uniform slurry suspensions prevailed in the pilot autoclave.

Stellenbosch University http://scholar.sun.ac.za

Table 7.11
Results of wash-out tests, using HBMS pilot feed material, in a single autoclave compartment at 25°C &1000 rev/min (resembling C #6 at a high slurry level).

Time (t) (min)	Slurry out (g)	Cum. Solids (g) (dry)	[a] τ (min)	W(t) (g)	W/W_o (actual) (%)	[b] *exp*(-t/τ) (%)
0	0	0	–	1572	100	100
9	2477	468	24.0	1104	70	69
13	1098	633	23.7	939	60	58
18	1307	799	24.3	773	49	48
23	1287	934	24.2	638	41	39
28	1281	1046	24.0	526	33	31
58	7430	1411	23.5	161	10	9
88	7308	1523	23.3	49	3	2
118	7132	1556	23.7	16	1	1
∞	–	1572	–	0	0	0

[a] ρ_s = 3.78 kg/L (est. solids density) & V_{sl} = 5.6 L (overflow) of test apparatus at 1000 rev/min; [b] Ideal mixing data.

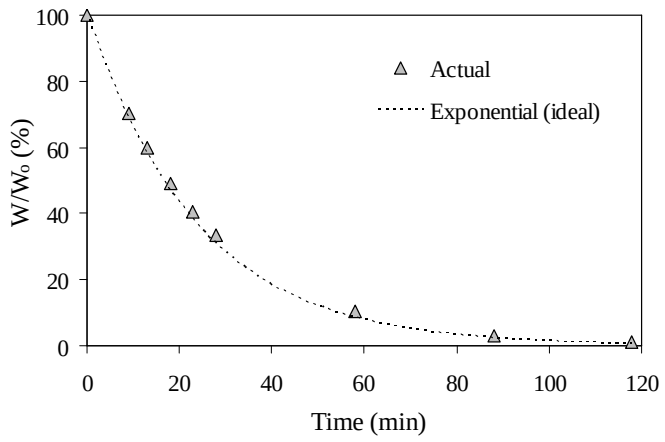

Figure 7.11
Comparison between the actual & ideal mixing curves for C #6, using HBMS pilot feed material ($d_{90} \approx 10$ µm) in water at 1000 rev/min & 25°C.

Evaluating the liquid-phase density

To implicitly calculate the actual residence time in the autoclave 'at temperature', an algorithm of the solution density is required. Density data (at 20°C) from all the experimental programmes conducted in this study were collated (565 points) and a three-dimensional robust plane surface was fitted (illustrated in Figure 7.12). The experimental data cover a wide range of solution compositions, from binary H_2SO_4-H_2O and $Me(II)SO_4$-H_2O mixtures to ternary H_2SO_4-$Me(II)SO_4$-H_2O mixtures and also datapoints from quaternary mixtures, containing iron(III).

Stellenbosch University http://scholar.sun.ac.za

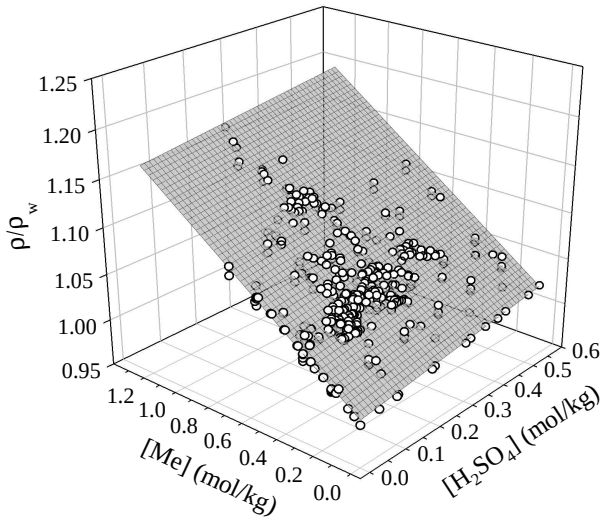

Figure 7.12
Comparison between the measured densities (at 20°C), as the ratio ρ/ρ_w from various experimental datapoints (this study) & the regressed surface (Eq. 7.49).

As illustrated in Figure 7.12, the following equation gives an acceptable representation of the data over a relatively wide composition range, based only on the total acid and metal cation (Me) molalities:

$$\frac{\rho}{\rho_w} = 1 + \tfrac{1}{19}[H_2SO_4] + \tfrac{1}{7}[Me] \qquad 7.49$$

The major assumption underlying this approach is that the ratio, ρ/ρ_w, remains approximately constant over the temperature ranges encountered in this study. In any event, small deviations would not impact greatly on the reactor simulation since this equation is mainly relied upon to estimate the compartmental residence time 'at temperature'. Alternatively, more complicated literature correlations, such as the equation of Laliberté and Cooper (2004), can be used to estimate the solution density. To maintain internal consistency, Equation 7.49 is used throughout this study, especially where no experimental densities are available. This calculated density is also used to compare the simulated and measured pilot plant solution tenors, *i.e.*, to convert the molality (m) to the molarity (M) scale, which follows directly from Equation 2.2:

$$M_i = \frac{m_i \rho}{1000 + \sum_i m_i Mw_i} \qquad 7.50$$

A consistent modelling basis is therefore established, because all the rate processes discussed in the previous chapters are also based on the molality scale. Finally, the density of molten sulfur is correlated with temperature, using the correlation of Espeau and Céolin (2007).

Stellenbosch University http://scholar.sun.ac.za

Preliminary continuous autoclave simulation

The feed PSDs illustrated in Figure 7.10 are the primary inputs to the autoclave PB, imbedded within the steady-state mass and energy balance of the primary circuit. This PB and the other kinetic modules interact iteratively with the rest of the model, *i.e.*, within the framework of conserving mass and energy. This scheme is illustrated in Figure 7.13, which is applied to each of the unit operations in the primary circuit until convergence is reached. Mass flow convergence is evaluated using a selected recycle stream as point of reference, *i.e.*, covering all the species contributing to the total flow in that stream. Control of recycling coolant flow to the various autoclave compartments (for autothermal operation) is not the objective here, and the model is configured to only reflect the pilot operation, *i.e.*, the total raffinate return solution is mixed with the feed concentrate (Sect. 7.3.1). The raffinate compositions are modified slightly to approximately match the feed solution composition to the autoclave (Table 7.4) during each period.

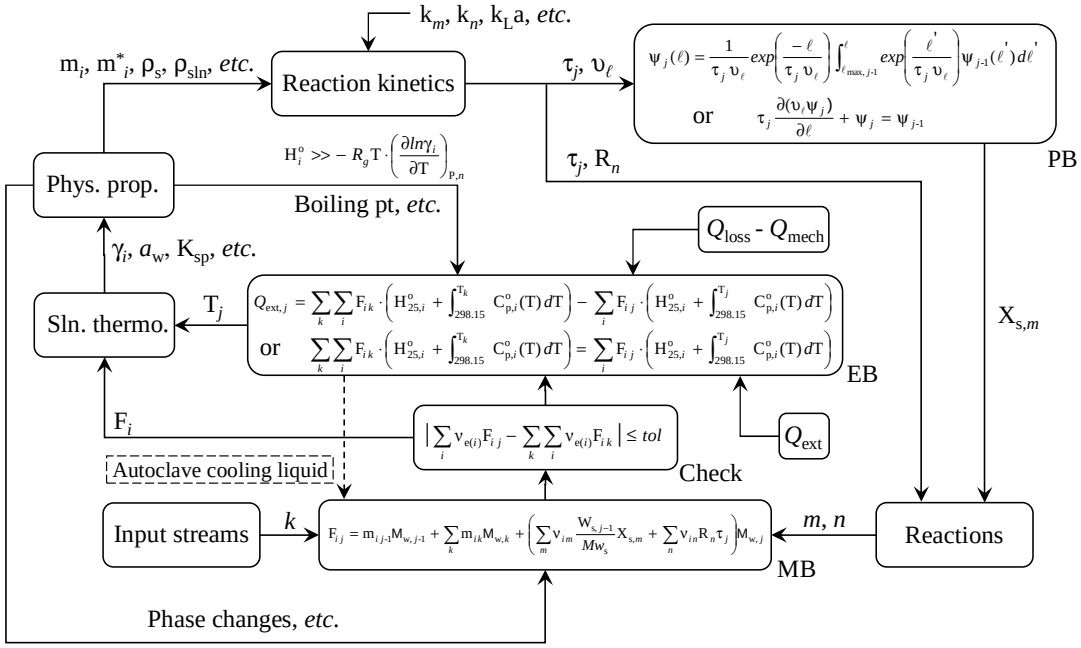

Figure 7.13
Iterative scheme (logic flow) used in the continuous steady-state model of the primary circuit.

The model is iterated until convergence is reached, based on the pilot plant solids and solution flows into the autoclave. These calculated feed stream properties and the corresponding model outputs for each of the four periods are summarised in Table 7.12 and Table 7.13. The differential form of the macroscopic PB is used in these calculations because the velocity term, υ_ℓ, needs to be variable when describing the rate of mineral oxidation in the latter compartments, *i.e.*, where surfactant degradation was prevalent. The hematite and jarosite precipitation extents are estimated so as to yield realistic compartmental acid and iron(III) profiles (*ref.* Table 6.9 & 6.10).

Stellenbosch University http://scholar.sun.ac.za

Table 7.12
Simulation output at fixed raffinate & mill feed flows for evaluation periods P1 & P2.

P1 Simulation	Flowrate (g/hr)	[a] Sln. dens. (g/L)	Cu (g/L)	Zn (g/L)	Fe(II) (g/L)	Fe(III) (g/L)	H_2SO_4 (g/L)	[b] Solids. (%) (S^{2-})
Mill prod.	2482	997	–	–	–	–	–	44.0 (32.5)
Raffinate	12446	1045	1.4	5.8	0.2	4.3	35.0	–
[c] Feed	15881	1046	1.9	6.1	5.0	0.6	28.5	[d] 6.2 (34.7)
[e] Discharge	15726	1084	20.6	8.6	0.3	2.1	24.6	[f] 5.4 (3.5)
P1 Simulation	[g] Fe(II) (g/L)	[h] Fe(III) (g/L)	H_2SO_4 (g/L)	[h] Fe ppt. (% Hem)	Mass loss (%)	[i] Cu extr. (%)	[j1] S^{2-} oxid. (%)	[k] S° yield (%)
C #1+2	1.8	2.6	19.7	85.0	16.0	77.5	69.6	65.7
C #3	0.9	2.0	21.8	84.5	15.6	91.1	82.3	64.4
C #4	0.6	1.8	22.9	83.4	15.3	96.0	87.6	63.4
C #5	0.4	1.7	23.7	82.0	14.4	97.9	90.2	62.7
C #6	0.3	1.6	24.4	80.6	13.3	98.6	91.6	62.2
P2 Simulation	Flowrate (g/hr)	[a] Sln. dens (g/L)	Cu (g/L)	Zn (g/L)	Fe(II) (g/L)	Fe(III) (g/L)	H_2SO_4 (g/L)	[b] Solids. (%) (S^{2-})
Mill prod.	2636	997	–	–	–	–	–	44.0 (32.5)
Raffinate	13935	1094	4.2	13.3	0.4	10.3	50.0	–
[c] Feed	17483	1087	4.3	12.4	5.0	5.9	41.4	[d] 6.0 (34.8)
[e] Discharge	16792	1132	23.1	15.8	0.5	9.9	30.7	[f] 5.6 (4.1)
P2 Simulation	[g] Fe(II) (g/L)	[h] Fe(III) (g/L)	H_2SO_4 (g/L)	[h] Fe ppt. (% Hem)	Mass loss (%)	[i] Cu extr. (%)	[j2] S^{2-} oxid. (%)	[k] S° yield (%)
C #1+2	1.8	13.7	19.6	65.0	25.0	64.6	62.7	62.5
C #3	1.1	12.4	22.0	64.3	21.7	80.4	77.1	61.5
C #4	0.8	11.1	24.4	62.6	17.8	88.3	84.3	61.0
C #5	0.6	9.8	26.8	60.1	13.1	92.2	87.9	60.8
C #6	0.4	8.6	29.1	57.9	8.4	94.1	89.7	60.6

[a] Calc. sln. density at 25°C; [b] Wt% solids (bracketed values refer to residual sulfide content); [c] After surfactant (water) addition point; [d] After 35% ZnS & Fe_7S_8 oxidised by iron(III) in feed mixing tanks; [e] After autoclave discharge tank; [f] Assuming 1.5% hematite & 4.5% H-jarosite redissolved in discharge tank & fixing pulp density (by adding water) to simulate pilot conditions (Table 7.4); [g] Based on the assumption that leaching yields 3 mol Fe(II)/mol $CuFeS_2$, 2 mol Fe(II)/mol ZnS, 21 mol Fe(II)/mol Fe_7S_8 & 1 mol Fe(III)/mol FeS_2 oxidised; [h] Estimated Fe precipitation & hematite formation extents (%Fe ppt. as hematite); [i] Cumulative extraction (*ref.* mill feed) from PB (differential form; $k_{\upsilon,Cpy}$, = 2, *ref.* Ch.6), assuming 10× reduction of $CuFeS_2$ oxidation rate constant at 4.5 µm PPD (due to surfactant degradation); [j] Cumulative oxidation (*ref.* mill feed), assuming FeS_2 oxidation (rate constant) is [(j1)]10× or [(j2)]2× slower *cf.* $CuFeS_2$ oxidation (additional 10× reduction at 1 µm PPD), while ZnS & Fe_7S_8 oxidation rates estimated ~2× faster *cf.* $CuFeS_2$ oxidation; [k] S° yield, *i.e.*, $S°/S^{2-}_{rx}$×100% *ref.* mill feed, using Eq. 7.59 & assuming baseline yield of 65% for $CuFeS_2$, while ZnS (& Fe_7S_8) & FeS_2 oxidation is assumed to yield constant 95% & 1% S°, respectively.

Stellenbosch University http://scholar.sun.ac.za

Table 7.13
Simulation output at fixed raffinate & mill feed flows for evaluation periods P3 & P4.

P3 Simulation	Flowrate (g/hr)	[a] Sln. dens. (g/L)	Cu (g/L)	Zn (g/L)	Fe(II) (g/L)	Fe(III) (g/L)	H_2SO_4 (g/L)	[b] Solids. (%) (S^{2-})
Mill prod.	2408	997	–	–	–	–	–	48.8 (32.5)
Raffinate	11779	1072	1.8	10.7	0.4	6.9	48.5	–
[c] Feed	15182	1070	2.4	10.3	5.7	2.5	39.5	[d1] 7.0 (34.8)
[e] Discharge	14324	1127	24.7	14.2	0.5	8.8	27.1	[f] 6.0 (4.1)
P3 Simulation	[g] Fe(II) (g/L)	[h] Fe(III) (g/L)	H_2SO_4 (g/L)	[h] Fe ppt. (% Hem)	Mass loss (%)	[i] Cu extr. (%)	[j] S^{2-} oxid. (%)	[k] S° yield (%)
C #1+2	1.8	10.7	17.3	75.0	25.1	69.6	67.3	61.9
C #3	1.0	9.2	21.0	74.4	22.8	84.6	81.2	61.0
C #4	0.7	7.1	25.7	73.5	18.4	91.3	87.4	60.6
[l] C #5+6	0.4	7.4	25.2	71.5	18.1	94.8	90.9	60.2
P4 Simulation	Flowrate (g/hr)	[a] Sln. dens (g/L)	Cu (g/L)	Zn (g/L)	Fe(II) (g/L)	Fe(III) (g/L)	H_2SO_4 (g/L)	[b] Solids. (%) (S^{2-})
Mill prod.	2436	997	–	–	–	–	–	48.8 (32.5)
Raffinate	10926	1076	7.4	11.9	0.1	3.0	47.5	–
PLS recyc.	2806	1107	28.9	11.9	0.5	2.9	22.6	–
[c] Feed	17080	1079	10.8	10.9	3.6	0.9	35.6	[d2] 6.4 (34.9)
[e] Discharge	16068	1130	31.8	15.3	0.5	3.0	27.5	[f] 5.8 (4.0)
P4 Simulation	[g] Fe(II) (g/L)	[h] Fe(III) (g/L)	H_2SO_4 (g/L)	[h] Fe ppt. (% Hem)	Mass loss (%)	[i] Cu extr. (%)	[j] S^{2-} oxid. (%)	[k] S° yield (%)
C #1+2	2.6	2.9	23.3	66.7	15.0	64.4	62.2	62.5
[m] C #3+4	0.9	3.3	22.9	66.7	15.5	87.6	84.0	61.0
C #5	0.6	2.8	24.2	66.5	13.9	92.2	88.3	60.7
C #6	0.4	2.2	25.6	66.5	12.3	94.3	90.3	60.5

[a] Calc. sln. density at 25°C; [b] Wt% solids (bracketed values refer to residual sulfide content); [c] After surfactant (water) addition point; [d] After [(d1)]35%,[(d2)]20% ZnS & Fe_7S_8 oxidised by iron(III) in feed mixing tanks; [e] After autoclave discharge tank; [f] Assuming 1.5% hematite & 4.5% H-jarosite redissolved in the discharge tank & fixing pulp density (by adding water) to simulate pilot conditions (Table 7.4); [g] Based on the assumption that mineral oxidation yielded 3 mol Fe(II)/mol $CuFeS_2$, 2 mol Fe(II)/mol ZnS, 21 mol Fe(II)/mol Fe_7S_8 & 1 mol Fe(III)/mol FeS_2 oxidised; [h] Estimated Fe precipitation & hematite formation extents (%Fe ppt. as hematite); [i] Cumulative extraction (*ref.* mill feed) from PB (differential form; $k_{\upsilon,Cpy}$, = 2, *ref.* Ch.6), assuming 10× reduction of $CuFeS_2$ oxidation rate constant at 4.5 µm PPD (due to surfactant degradation); [j] Cumulative oxidation (*ref.* mill feed), assuming FeS_2 oxidation (rate constant) is 2× slower *cf.* $CuFeS_2$ oxidation (additional 10× reduction at 1 µm PPD), while ZnS & Fe_7S_8 oxidation rates estimated ~2× faster *cf.* $CuFeS_2$ oxidation; [k] S° yield, *i.e.*, $S°/S^{2-}{}_{rx}$×100% *ref.* mill feed, using Eq. 7.59 & assuming baseline yield of 65% for $CuFeS_2$, while ZnS (& Fe_7S_8) & FeS_2 oxidation is assumed to yield constant 95% & 1% S°, respectively; [l] Autoclave discharge pipe partially blocked, causing slurry level to rise ~0.5 L in (short-circuited) C #5+6 (combined vol. ~10.1 L); [m] Upcomer blockage between C #4 & C #5, causing slurry to overflow *via* vapour slot (Figure 7.1), *i.e.*, short-circuiting between C #3 & C #4.

Stellenbosch University http://scholar.sun.ac.za

The regime change in the intrinsic rate is therefore treated on the basis of particle penetration depth (PPD), with reference to the original particle. This approach allows the diminishing rate in the latter compartments to be averaged over all particles within the PB framework. Although this is an over-simplification, the added complexity of accounting for changing surface area due to sulfur agglomeration effects cannot be justified in context of this study. The well-known Euler numerical method is therefore applied to the differential form of the PB (Eq. 7.2), and incorporated into the continuous steady-state simulation (Figure 7.13). The boundary conditions are selected at some particle size, L_∞, which is larger than the maximum size (L_{max}) in the feed distribution, so that $\psi(\ell, L) \rightarrow 0$ as $\ell \rightarrow L_\infty$. The marginal distribution, $\psi(\ell)$, of unreacted mineral particles is then extracted from the two-dimensional distribution (Crundwell, 1995):

$$\psi(\ell) = \int_{\ell}^{L_\infty} \psi(\ell, L)\, dL \qquad 7.51$$

Reaction stoichiometries and extents

The return raffinate solution (see compositions in the above tables) contained appreciable amounts of iron(III), which would react with the less refractory sulfide minerals, *e.g.*, Zn(Fe)S and Fe_7S_8, in the feed mixing tanks. The reaction extents are assumed to be the same for these types of minerals and, based on the amount of iron(II) in the autoclave feed solution, are estimated to be 35% for P1 to P3 and 20% for P4. The reaction stoichiometry is assumed as follows:

$$S^{2-}|_{lat} + Fe_2(SO_4)_{3(aq)} \Rightarrow S^o + 2FeSO_{4(aq)} + SO_{4(aq)}^{2-} \qquad 7.52$$

At the other end of the autoclave, *i.e.*, the discharge tanks, a proportion of the iron(III) precipitation products redissolved. Average redissolution extents of 1.5% hematite and 4.5% hydronium jarosite yield reasonable agreement with the acid and iron(III) discharge solution tenors, *i.e.*, between the simulated and pilot results during all four evaluation periods. In terms of the rate of release and oxidation state of iron in solution, various assumptions are made. For the less refractory sulfides (sphalerite & pyrrhotite), the iron(III) reduction mechanism (Eq. 7.52) is assumed to dominate, resulting in all mineral iron entering the solution in the reduced state. For example, the reaction of pyrrhotite is assumed to follow the following stoichiometry:

$$5Fe^{2+}|_{lat} + 2Fe^{3+}|_{lat} + 8S^{2-}|_{lat} + 7Fe_2(SO_4)_{3(aq)} \Rightarrow 8S^o + 14FeSO_{4(aq)} + 7Fe_{(aq)}^{2+} + 7SO_{4(aq)}^{2-} \qquad 7.53$$

In contrast, no iron(III) is assumed to reduce on the pyrite surface and all iron in the lattice is assumed to enter the solution in the oxidised state (Sect. 6.3.4). Assumptions regarding chalcopyrite behaviour are uncertain, since many aspects have not yet been adequately addressed in the open literature (see Sect. 6.3.4). The assumption is made that only two electrons are exchanged with iron(III) species on the solution-side of the interface, which is consistent with the formation of an intermediate covellite-like surface:

Stellenbosch University http://scholar.sun.ac.za

$$3Cu^{+}|_{lat} + 3Fe^{3+}|_{lat} + 3S_2^{4-}|_{lat} + 3Fe_2(SO_4)_{3(aq)} \Rightarrow Cu^{2+}(Cu^{+})_2S^{2-}S_2^{2-}|_{surf} + 6FeSO_{4(aq)} + 3Fe^{2+}_{(aq)} + 3SO^{2-}_{4(aq)} \quad 7.54$$

Further oxidation of this covellite-like surface layer is assumed to proceed *via* a direct diatomic oxygen reduction reaction, catalysed by the presence of copper(I) in the surface lattice (Sect. 6.3.4). This is assumed to be the rate-limiting step, as the oxidation rate was found to be insensitive to the iron(III) tenor in solution (Sect. 6.5.4). With regard to the formation of elemental sulfur, there is no simple way of predicting the yield and the model treats the extent of sulfate formation as originating from oxygen reduction only. This assumption is in line with the discussions of Section 6.3.2. The stoichiometric reactions are therefore treated from a bulk phenomenological perspective, *e.g.*, for chalcopyrite, pyrite, sphalerite and pyrrhotite, the following reactions apply, respectively:

$$CuFeS_{2(s)} + (3y+1)O_{2(aq)} + 2(1-y)H_2SO_{4(aq)} \Rightarrow 2(1-y)S^{o} + CuSO_{4(aq)} + FeSO_{4(aq)} + 2(1-y)H_2O \quad 7.55$$

$$FeS_{2(s)} + (3y+\tfrac{1}{2})O_{2(aq)} + (2y-1)H_2O \Rightarrow 2(1-y)S^{o} + FeSO_{4(aq)} + (2y-1)H_2SO_{4(aq)} \quad 7.56$$

$$ZnS_{(s)} + (\tfrac{3}{2}y+\tfrac{1}{2})O_{2(aq)} + (1-y)H_2SO_{4(aq)} \Rightarrow (1-y)S^{o} + ZnSO_{4(aq)} + (1-y)H_2O \quad 7.57$$

$$Fe_7S_{8(s)} + (12y+\tfrac{7}{2})O_{2(aq)} + (7-8y)H_2SO_{4(aq)} \Rightarrow 8(1-y)S^{o} + 7FeSO_{4(aq)} + (7-8y)H_2O \quad 7.58$$

These stoichiometries are derived using the various half-cell reactions and empirically accounting for the degree of sulfate formation (y). Although the elemental sulfur yield ($1–y$) for chalcopyrite is determined in batch experimentation to be around 62% at 0.1 mol/kg H^{+}, a baseline value of 65% yields more realistic acid tenors, *i.e.*, Equation 6.177 is adjusted as follows:

$$S^{o}/S_{rx,Cpy} = 0.65 + 0.3\cdot[H^{+}] \quad 7.59$$

The less refractory minerals are assumed to yield 95% elemental sulfur, while the pyrite sulfur yield is fixed at 1%. Besides being influenced by the sulfur yield, the acid balance is sensitive to the degree of iron(III) precipitation and the relative amount of hydronium jarosite formation (*cf.* hematite). Since the above phenomenological stoichiometries (Rx. 7.55-7.58) assume by default, that all the iron enters the solution in the reduced state, R^{F}_{FeII}, a revised expression is required to calculate the net iron(II) oxidation rate, $R_{FeII,net}$. This equation is important because it influences the degree of supersaturation in each of the autoclave compartments, which, in turn, impacts strongly on the iron(III) precipitation rate (incorporated later, *ref.* Table 7.21 & Table 7.22; also Ch. 5):

$$R_{FeII,net} = R_{FeII,sln} + R_{FeIII,surf} - R_{FeIII,red} \quad 7.60$$

Stellenbosch University http://scholar.sun.ac.za

where $R_{FeII,sln}$ refers to the rate of homogeneous iron(II) oxidation in the bulk solution (Ch. 4), $R_{FeIII,surf}$ is the rate at which oxidised iron exits the mineral lattice, *e.g.*, on a pyrite surface, and $R_{FeIII,red}$ is the rate at which iron(III) reduces on mineral surfaces, *e.g.*, on a sphalerite surface. If $R_{FeII,net} > 0$, the sequential conversion extent of iron(II), $X_{FeII,ox}$, is obtained for reactor *j*:

$$X_{FeII,ox} = \frac{R_{FeII,net} \cdot M_{w,j}}{F_{FeII,j-1} + R^{F}_{FeII} \cdot M_{w,j}} \qquad 7.61$$

Again, the lack of knowledge around the chalcopyrite oxidation mechanism necessitates the assumptions highlighted by Reaction 7.54, *i.e.*, 2 mol Fe(III) are reduced for every mol S_2^{4-} oxidised to produce a covellite-like surface layer, while all lattice iron exits the surface in the reduced state. In contrast, all iron exits pyrite in the oxidised state, with no appreciable iron(III) reduction occurring on the solution side of the interface. The oxidation of iron(II) and other sulfide minerals, in close proximity to pyrite, could also be possible (see discussions in Ch. 4, 6 & 7).

Comparison between the measured and simulated reaction extents

Figure 7.14 compares the pilot plant results and the steady-state continuous simulation for P1. Good agreement between the measured and simulated results is clearly obtained, using the previously determined rate expression of chalcopyrite shrinkage (Eq. 6.176) and assuming a 10× reduction in the intrinsic constant after 4.5 µm PPD, *i.e.*, 0.2 (µm/min) (kg/mol)^{⅔}, due to the build-up of molten sulfur on the reacting surfaces.

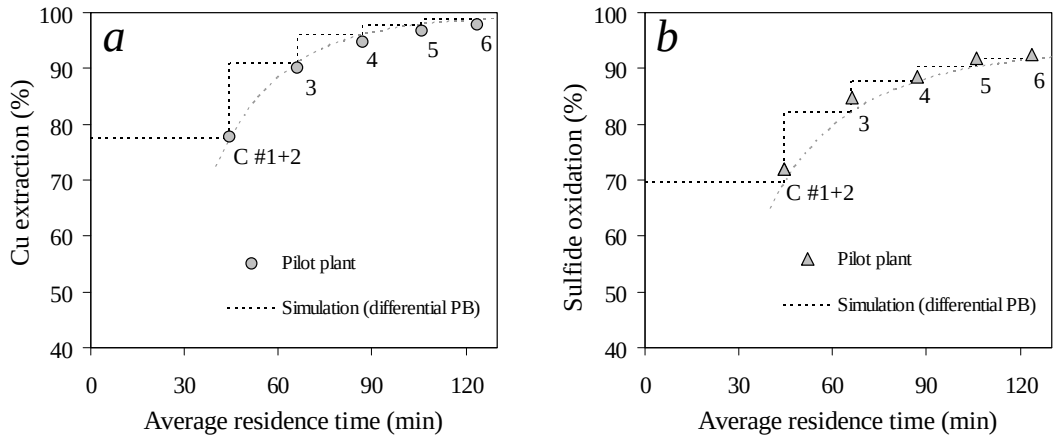

Figure 7.14
Comparison between continuous pilot autoclave reaction extents (HBMS 777 concentrate) & the compartmental simulation for P1, using the two-dimensional (differential) form of the PB & fixing the input stream compositions & flows to reflect the pilot operation: *a*) Copper extractions, assuming a 10× reduction in the $CuFeS_2$ oxidation rate at 4.5 µm PPD; *b*) Sulfide oxidation extents, assuming 10× slower oxidation of FeS_2 (*cf.* $CuFeS_2$) & a regime change (10× reduction) at 1 µm PPD. The oxidation rates of the less refractory minerals are assumed to be double that of $CuFeS_2$.

Stellenbosch University http://scholar.sun.ac.za

A 10× reduction of the rate constant of pyrite (*cf.* chalcopyrite) is also assumed and a regime change at 1 µm PPD is used, while the less refractory sulfides are assumed to oxidise at double the rate of chalcopyrite Again, these assumptions are arbitrarily chosen, and can only be resolved by conducting follow-up batch testing and a more accurate description of the rate of iron(III) precipitation (see later in Sect. 7.4.2).

Figure 7.15 compares the simulation outputs for P1 using both the integral and differential methods, which highlights the insignificant effect of a regime change on the calculated results for this fine feed PSD (Figure 7.10). Figure 7.15 *a* also illustrates that using the mass loss calculations of the simulation (Table 7.12), instead of the estimated values from the pilot plant (Table 7.9), has an insignificant influence on the calculated reaction extents. A comparison of Table 7.4 and Table 7.12 also reveals good agreement of the simulated exit flow rates and species concentrations, while the calculated iron(II) profile closely agrees with the measured values (Table 7.9).

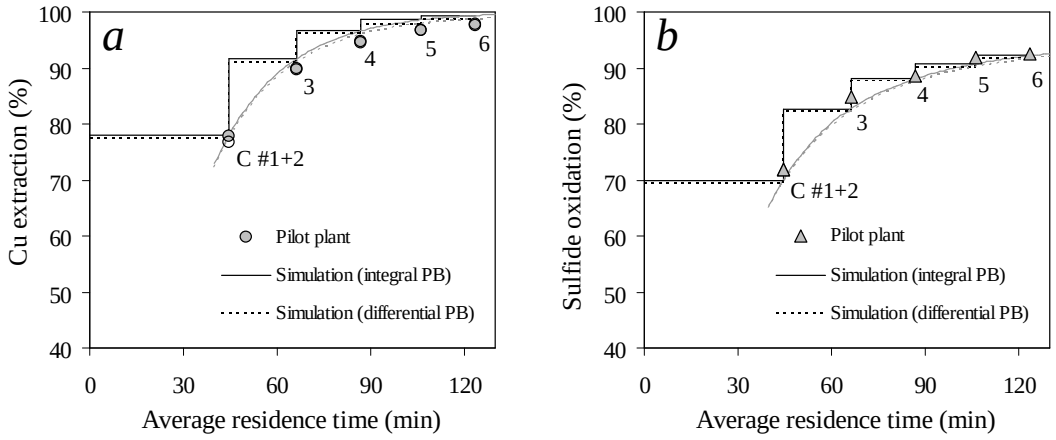

Figure 7.15
Comparison between the integral & two-dimensional (differential) PB calculations for P1, using fixed & variable rate constants, respectively; the open symbols represent pilot results, based on solid-phase mass loss calculations from the PB model: *a*) Copper extractions, assuming a 10× reduction in the $CuFeS_2$ oxidation rate at 4.5 µm PPD (two-dimensional PB); *b*) Sulfide oxidation extents, assuming 10× slower oxidation of FeS_2 (*cf.* $CuFeS_2$) & regime change (10× reduction) at 1 µm PPD (two-dimensional PB). The oxidation rates of the less refractory minerals are assumed to be double that of $CuFeS_2$.

Unusual conditions were experienced inside the autoclave during P2 and P3, as the raffinate return acid and iron concentrations were artificially high. The primary reason for this was the lower than expected overall elemental sulfur yield, which resulted in the uncontrolled build-up of acid in the primary circuit. The high acid concentration in the system was buffered by an increase in the precipitation rate of hydronium jarosite *vs.* hematite, which, in turn, resulted in an increase in iron solubility. The solution conditions inside the autoclave therefore extended beyond the regression

Stellenbosch University http://scholar.sun.ac.za

range of the thermodynamic model, as well as the various kinetic expressions, *e.g.*, the sulfide mineral and iron(II) oxidation rates. These simulations are compared to the measured data in Figure 7.16 and Figure 7.17 for P2 and P3, respectively.

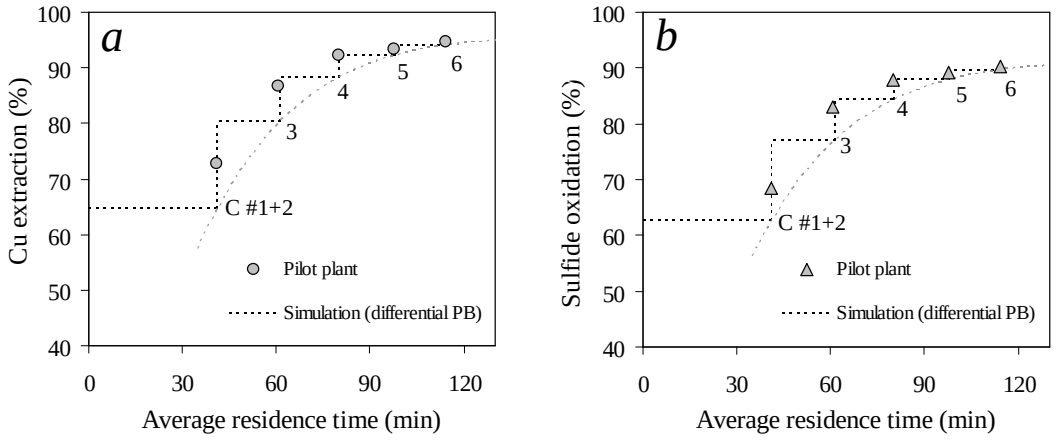

Figure 7.16
Comparison between continuous pilot autoclave reaction extents (HBMS 777 concentrate) & the compartmental model calculations for P2, using the two-dimensional (differential) form of the PB & fixing the input stream compositions & flows to reflect the pilot operation: *a*) Copper extractions, assuming a 10× reduction in the $CuFeS_2$ oxidation rate at 4.5 µm PPD; *b*) Sulfide oxidation extents, assuming 2× slower oxidation of FeS_2 (*cf.* $CuFeS_2$) & a regime change (10× reduction) at 1 µm PPD. The oxidation rates of the less refractory minerals are assumed to be double that of $CuFeS_2$.

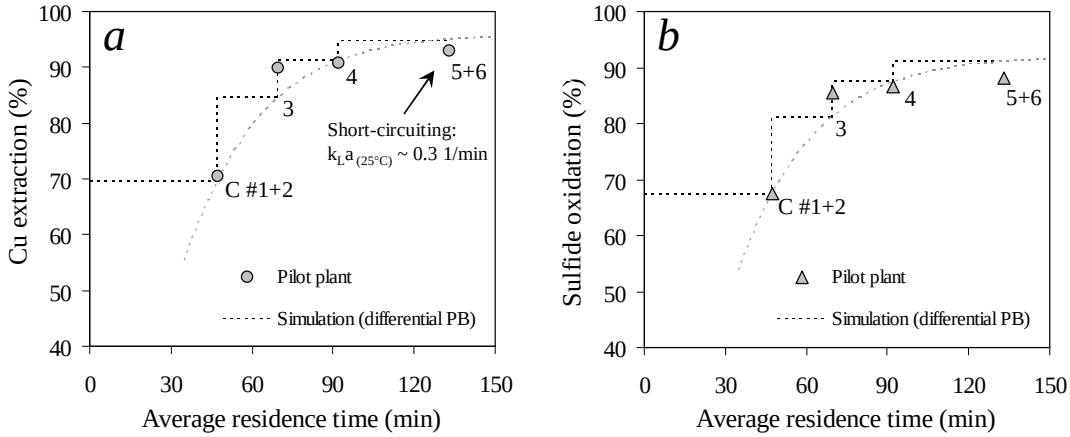

Figure 7.17
Comparison between continuous pilot autoclave reaction extents (HBMS 777 concentrate) & the compartmental model calculations for P3, using the two-dimensional (differential) form of the PB & fixing the input stream compositions & flows to reflect the pilot operation: *a*) Copper extractions, assuming a 10× reduction in the $CuFeS_2$ oxidation rate at 4.5 µm PPD; *b*) Sulfide oxidation extents, assuming 2× slower oxidation of FeS_2 (*cf.* $CuFeS_2$) & a regime change (10× reduction) at 1 µm PPD. The oxidation rates of the less refractory minerals are assumed to be double that of $CuFeS_2$.

Stellenbosch University http://scholar.sun.ac.za

Agreement between the simulated and measured oxidation extents is relatively poor in the case of P2, which emphasises the importance of establishing confidence in the iron precipitation rate, the oxidation rates of the secondary sulfide minerals and the intrinsic mineral sulfur yields. Notwithstanding, agreement improves between the simulated and the measured results during P3, casting some doubt on the accuracy of the measured data for P2. Despite the high iron(III) tenors in the various autoclave compartments, the calculated oxidation extents are relatively close to the measured data (as compared between Table 7.10 & Table 7.13). Reasonable agreement is also achieved between the calculated and exit stream properties (as compared between Table 7.4, Table 7.7 & Table 7.13). As mentioned, a partial blocking of the discharge pipe resulted in a rise in the slurry volume in the last two compartments, causing significant short-circuiting. This rise in slurry volume also caused a significant (order-of-magnitude) reduction of the gas/liquid mass transfer coefficient (Table 3.9) in the combined C #5+6. However, mineral oxidation and other oxygen-consuming reactions are relatively slow in these latter compartments and are not greatly affected by this diminishing mass transfer rate.

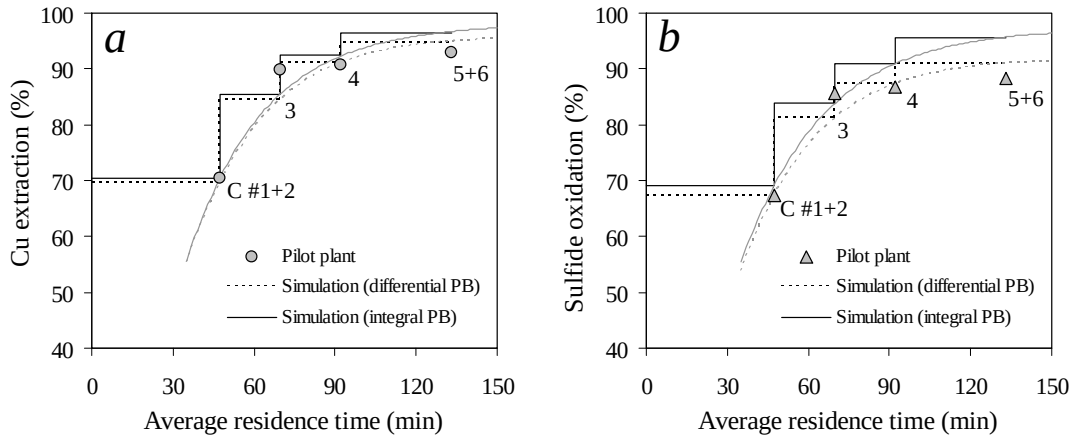

Figure 7.18
Comparison between the integral & two-dimensional (differential) PB calculations for P3, using fixed & variable rate constants, respectively: *a*) Copper extractions, assuming a 10× reduction in the $CuFeS_2$ oxidation rate at 4.5 µm PPD (two-dimensional PB); *b*) Sulfide oxidation extents, assuming 2× slower oxidation of FeS_2 (*cf.* $CuFeS_2$) & regime change (10× reduction) at 1 µm PPD (two-dimensional PB). The oxidation rates of the less refractory minerals are assumed to be double that of $CuFeS_2$.

A more important factor is the agglomeration of unreacted sulfides by elemental sulfur in the latter autoclave compartments. This is illustrated in Figure 7.18, where the simulation of the PB integral, at constant mineral shrinkage rates, is compared with the two-dimensional differential PB calculation at variable shrinkage rates, *i.e.*, as a function of the (imaginary) PPDs. The PB integral can also be solved for variable shrinkage rates, but such regime changes have to be confined to compartmental residence times.

Stellenbosch University http://scholar.sun.ac.za

Finally, the calculated values for P4 are compared with the continuous pilot autoclave results in Figure 7.19, while a more detailed evaluation is obtained by comparing Table 7.13 with Table 7.4 and Table 7.7 (exit stream properties) and Table 7.10 (profile properties). The recycling of PLS solution to the autoclave, at the expense of returning raffinate, resulted in less acid flow into the autoclave, while the copper tenor increased somewhat (as would have been expected). Besides these and other minor changes in the operation of the primary circuit, this period (P4) was characterised by the complete blockage of the upcomer weir between C #4 and C #5. As mentioned (Figure 7.1 & related discussions), this resulted in a rise in the slurry volume of the first 'two' compartments, *i.e.*, the combined C #1+2 and the short-circuited C #3+4. An order-of-magnitude reduction in the baseline k_La-value (~3 1/min; see Table 3.9) is selected here, and this results in excellent agreement between the simulated and measured results. Further optimisation of the k_La-value within experimental uncertainty could be utilised to improve the simulation even further. This would however be an arbitrary exercise with little scientific significance.

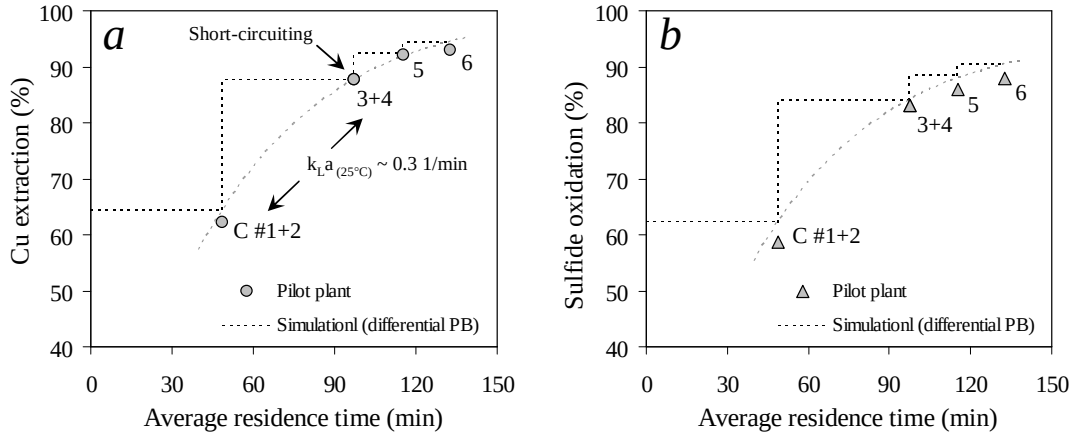

Figure 7.19
Comparison between continuous pilot autoclave reaction extents (HBMS 777 concentrate) & the compartmental simulation for P4, using the two-dimensional (differential) form of the PB & fixing the input stream compositions & flows to reflect the pilot operation: *a*) Copper extractions, assuming a 10× reduction in the $CuFeS_2$ oxidation rate at 4.5 µm PPD; *b)* Sulfide oxidation extents, assuming 2× slower oxidation of FeS_2 (*cf.* $CuFeS_2$) & a regime change (10× reduction) at 1 µm PPD. The oxidation rates of the less refractory minerals are assumed to be double that of $CuFeS_2$.

The most important conclusion from this preliminary autoclave simulation, imbedded within the steady-state mass balance of the primary circuit, is that more information is required regarding the oxidation rates of the other sulfide minerals in a chalcopyrite concentrate. These reaction rates, as well as incorporation of the iron precipitation module, are important factors that could clarify some acid balance uncertainties in the primary circuit and hence improve the performance of the overall simulation. These aspects are discussed in the following section.

Stellenbosch University http://scholar.sun.ac.za

7.4.2 Intrinsic sulfide mineral oxidation rates at low pulp density (batch) conditions and re-evaluation of the continuous pilot autoclave simulation

A similar test methodology was followed as described in Section 6.4.2, except that the oxidation extents are based on the bulk modal composition (App. B.3.2) of the various minerals present (App. I.3, calculating the residual elemental sulfur contents iteratively rather than relying on chemically analysed values; Sect. 7.3.1 & 7.3.2). The pulp densities of all these tests were low enough to prevent the iron(III) precipitation. The HBMS 777 concentrate (Sample D & E; Sect. 7.3.3) was tested first, as it formed the basis of the detailed testwork results presented in Chapter 6.

Batch oxidation of HBMS 777 cleaner concentrate (Samples D & E)

The detailed mass and energy balances of these tests can be found in Appendix I.4. These tests intended to quantify the effect of a lower surfactant concentration (Test PLP13) and varying temperature (145, 150 & 155ºC, corresponding to Series PLQ1, PLQ2 & PLQ3, respectively) on the rate of mineral oxidation in the HBMS 777 cleaner concentrate to obtain the intrinsic rate constants and activation energies. These constants are then used as primary inputs to the continuous and batch reactor models at higher pulp densities (Ch. 8).

Test PLP13 repeated test PLC23 (see Figure 6.28 in Sect. 6.5.1 & related discussions), but using lower (0.1 g/L, instead of 0.35 g/L) surfactant concentrations (Arbo A02 and Orfom 2; see Sect. 6.3.3), a slightly lower pulp density (~0.9% instead of 1% solids) and a higher initial slurry mass (1150 g). These results are compared in Figure 7.20, suggesting marginal improvement of the copper extraction and sulfide oxidation rates with lower Arbo A02 additions.

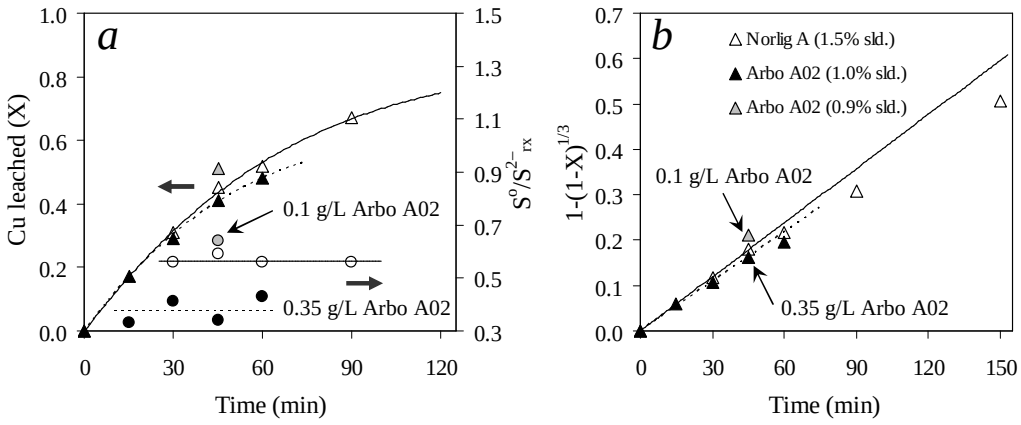

Figure 7.20
Comparison of Cu leaching extents & rates (Sample D, 25 g/L H_2SO_4, 15 g/L Cu) using different surfactants & dosages at 150°C (700 kPa p_{O2}°); open symbols represent 1.5 wt% solids, 0.35 g/L Norlig A LS, Orfom 2 QB; closed symbols represent 1.0 wt% solids, 0.35 g/L Arbo A02 LS, Orfom 2 QB & 1 g/L Fe(II); grey symbols represent ~0.9 wt% solids, 0.1 g/L Arbo A02 LS, Orfom 2 QB: *a*) Reaction extents; b) USP model for surface reaction control (solid & broken lines represent best 0 – 45 min fits of the original datasets, *i.e.*, Series PLC1, PLC2, respectively).

Stellenbosch University http://scholar.sun.ac.za

However, the elemental sulfur yields are substantially higher than observed for Series PLC2, showing better agreement with the tests conducted using Norlig A LS (Series PLC1). It was therefore decided to use less Arbo A02 LS, *i.e.*, 0.15 g/L, for the rest of this testwork programme, although the fundamental reasons for this effect were not pursued in this study; it is simply accepted that an 'over-addition' of Arbo A02 (kg LS/t mineral) results in a higher intrinsic oxidation rate of sulfur on the mineral surfaces. That the sulfide oxidation extents (based on chemical analyses; Table 6.9) are comparatively lower when using 0.35 g/L Arbo A02 could support the polymeric sulfur argument (Sect. 6.5.1). Either way, all subsequent testwork used Arbo A02 at limited dosages, *i.e.*, below 20 kg/t.

The next three series of tests (PLQ1, PLQ2 & PLQ3) focussed on the effect of temperature and the relative oxidation rates of the primary minerals in the HBMS 777 concentrate, using Sample E (detailed results in App. I.3). This feed sample exhibits a relatively wide PSD (Figure 7.6) so as to compare the initial oxidation rate (dominated by finer particles) to the rate at longer reaction times (dominated by coarser particles). The chalcopyrite oxidation extents and unreacted shrinking particle (USP) model plots are presented in Figure 7.21 *a* and *b*, respectively.

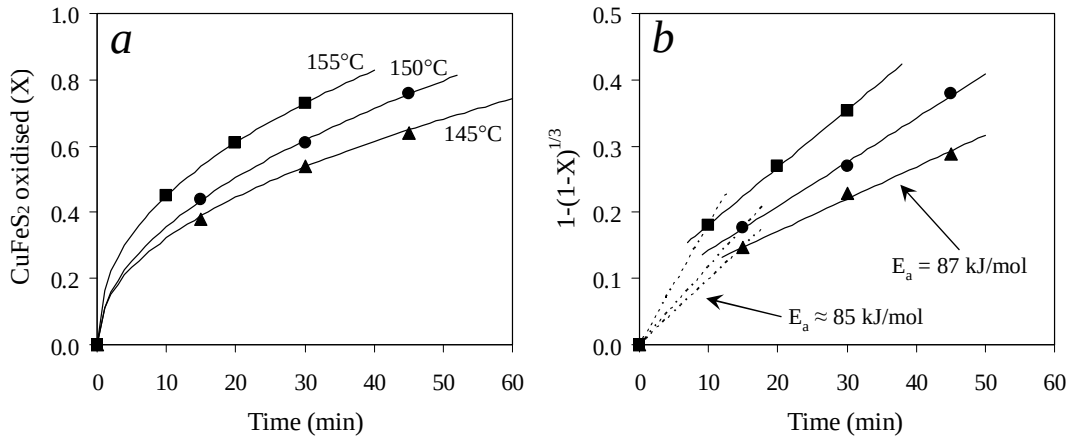

Figure 7.21
$CuFeS_2$ oxidation reaction extents & rates (Sample E, 25 g/L H_2SO_4, 15 g/L Cu, 0.15 g/L Arbo A02 LS, Orfom 2 QB) at different oxidation temperatures (700 kPa p_{O2}°): *a*) Reaction extents; *b*) USP model for surface reaction control (broken & solid lines represent best linear fits of the initial & final rates, respectively, while the activation energies are obtained from Arrhenius plots).

The effect of temperature on the oxidation rate of chalcopyrite is consistent with the theory of reaction activation (energy barrier), *i.e.*, higher observed rates are observed at higher temperatures. The observed rate constants, $k_{s,Cpy}$, and activation energies, calculated using the Arrhenius relationship, are summarised in Table 7.14. The constants obtained from the initial period are less accurate compared to the constants determined from the final period (see R^2 values). Nevertheless, these similar activation energies suggest that the same rate-determining step(s) were prevalent and

Stellenbosch University http://scholar.sun.ac.za

that no fundamental change in the oxidation mechanism occurred during the first 45 minutes, *i.e.*, the intrinsic linear rate constant is likely independent of particle size (Sect. 6.5.3).

Table 7.14
USP & Arrhenius plot results of $CuFeS_2$ oxidation, using Sample E at 25 g/L H_2SO_4, 15 g/L Cu, 0.15 g/L Arbo A02 LS, Orfom 2 QB & different oxidation temperatures (700 kPa p_{O2}°).

Test series	Temperature	[a] $k_{s,Cpy}\cdot10^2$ (init.)	R^2	[b] $k_{s,Cpy}\cdot10^3$ (fin)	R^2
–	(ºC)	(1/min)	–	(1/min)	–
PLQ1	145	~2.5	–	4.8(5)	0.992
PLQ2	150	~2.9	–	6.6(5)	0.998
PLQ3	155	~4.5	–	8.7	0.999
$E_{a,Cpy}$	145–155ºC	~85 kJ/mol	0.922	87 kJ/mol	0.998

[a] *Ref.* origin; [b] Regression of each series fixed at first datapoint, *i.e.*, at 15 min for PLQ1, PLQ2 & 10 min for PLQ3.

The activation energy of 87 kJ/mol is also in qualitative agreement with other chalcopyrite oxidation studies under MT and low pulp density conditions, *e.g.*, Yu *et al.* (1972) proposed experimental activation energies of between 37 and 141 kJ/mol (avg. ~89 kJ/mol), in the 125 to 175ºC temperature range, with the lower and higher boundaries relating to the predominance of the mineral surface reaction and oxygen adsorption/reduction mechanisms, respectively. More recently, the study of Padilla *et al.* (2008) reported an activation energy of about 94 kJ/mol for the oxidative leaching of sulfidised chalcopyrite, between 125 and 150ºC. The earlier study of Warren (1958) reported an experimental activation energy of about 96 kJ/mol in the 120 to 180ºC temperature range, while Dobrokhotov and Maiorova (1962) reported a lower value of about 30 kJ/mol between 125 and 175ºC. Jang and Wadsworth (1993) oxidised chalcopyrite between 170 and 200ºC and found an experimental activation energy of about 59 kJ/mol. Many atmospheric studies of chalcopyrite oxidation by iron(III) sulfate have also been reported, *e.g.*, Dutrizac *et al.* (1969), Munoz *et al.*, (1979), Hirato *et al.* (1987), *etc.* (see also references in Dutrizac, 1981); most activation energies fell in the range of about 40 to 90 kJ/mol. However, recently Cordoba *et al.* (2008a) reported a higher value of about 131 kJ/mol when leaching chalcopyrite with iron(III) between 35 and 68ºC.

The mineralogical make-up of a particular chalcopyrite concentrate is also important, *e.g.*, the presence of more and less refractory minerals, such as pyrite and pyrrhotite, respectively. In terms of lower temperature oxidation by oxygen, the studies of Peters (Majima & Peters, 1966; Peters & Loewan, 1968) between 105 and 130ºC revealed activation energies of about 46 and 67 kJ/mol, corresponding to predominantly sulfur and sulfate formation pathways, respectively. This raises the question of whether the diffusion of oxygen through elemental sulfur product layers could explain the wide range of observed activation energies. If the acceleration of the observed rate at increasing

Stellenbosch University http://scholar.sun.ac.za

temperature is directly related to the rate-limiting step, various possible mechanisms could be important. It would be naïve to assume that a single rate-limiting step would be valid over a wide temperature range and long reaction times, hence the narrow temperature range (145-155ºC) and relatively short reaction times (< 45 min) selected for this study. For example, during initial oxidation of a chalcopyrite surface, the rate could be limited by the breaking of bonds in the solid mineral structure. At longer residence times, surface layers (molten sulfur or other minerals, *e.g.*, a covellite-like surface; Ch. 6) may be formed, resulting in the slow reduction of oxygen. The activation energy may then assimilate the reduction rate of oxygen. At even longer residence times, the surfactants may degrade to such an extent that the transport of diatomic oxygen through molten sulfur becomes rate limiting, reflecting the lower activation energy associated with diffusion-controlled processes. As mentioned, the fact that the observed activation energies of the initial and subsequent reaction periods are very similar for the relatively pure chalcopyrite concentrate (Sample E) suggests that there is no major regime change over the course of the measurement. This is also reflected by the BSE and superimposed X-ray images (App. B.3.4) of selected residues (Series PLQ2) in Figure 7.22 *a* and *b*, respectively.

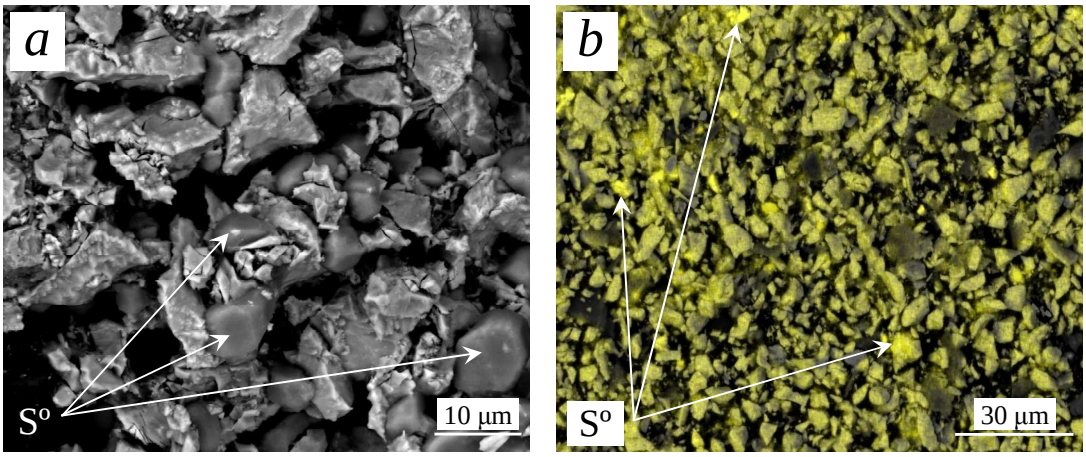

Figure 7.22
Images of autoclave residues (Sample E) after 30 min oxidation (700 kPa p_{O2}°) at 145ºC, starting with 25 g/L H_2SO_4, 15 g/L Cu & 0.15 g/L Arbo A02 LS, Orfom 2 QB (Test PLQ12): *a*) BSE (HR SEM) image; *b*) XRD map of Sº, superimposed on the BSE image.

Smooth sulfur globules are clearly visible (highlighted) between the relatively more rugged and brighter sulfide particles (Figure 7.22 *a*). Although this BSE image suggests that most sulfide particles were fully exposed to the solution environment, Figure 7.22 *b* indicates that nearly all sulfide surfaces also emitted an elemental sulfur fingerprint (coloured yellow). Despite the lower relative intensity (yellow) on these particles compared with the (highlighted, bright yellow) sulfur globules, it does suggest that thin elemental sulfur layers are present on all the sulfide residue particles, even with the surfactants still effective.

Stellenbosch University http://scholar.sun.ac.za

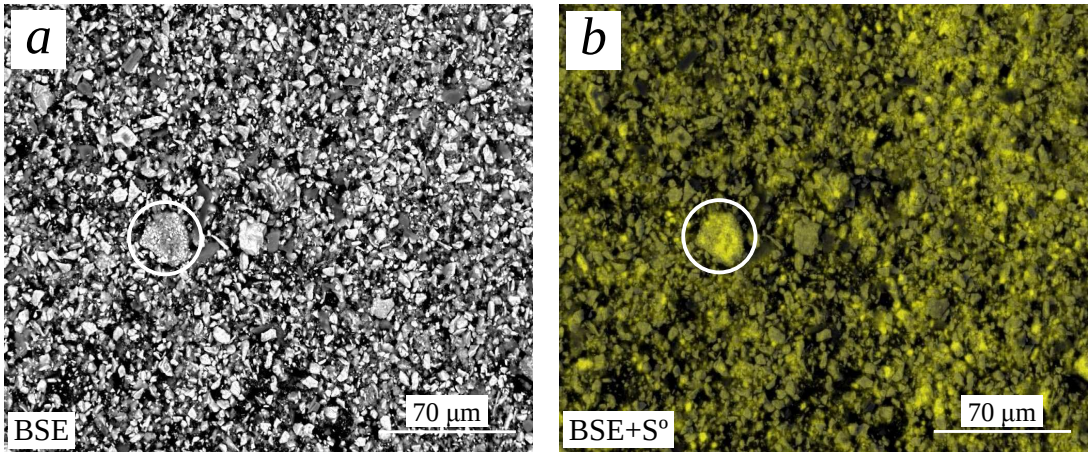

Figure 7.23
Images of autoclave residues (Sample E) after 45 min oxidation (700 kPa p_{O2}°) at 150ºC, starting with 25 g/L H_2SO_4, 15 g/L Cu & 0.15 g/L Arbo A02 LS, Orfom 2 QB (Test PLQ23): *a*) BSE image; *b*) XRD map of Sº superimposed on the BSE image.

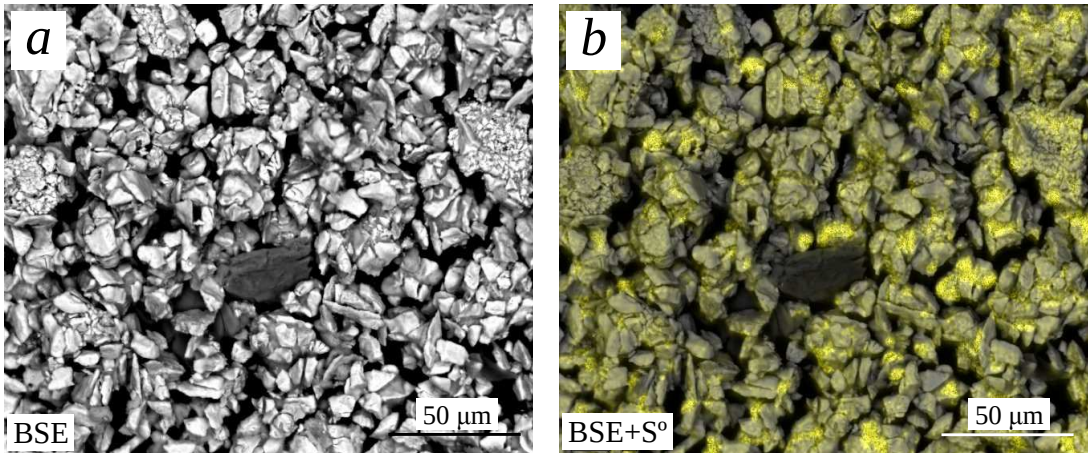

Figure 7.24
Images of autoclave residues (Sample D) after 45 min oxidation (700 kPa p_{O2}°) at 150ºC, starting with 25 g/L H_2SO_4, 15 g/L Cu & 0.1 g/L Arbo A02 LS, Orfom 2 QB (Test PLP13): *a*) BSE image; *b*) XRD map of Sº, superimposed on the BSE image.

It is assumed that the thickness of these surface sulfur layers is restricted by the workings of the surfactants. After the surfactants have degraded (45-60 min; see Sect. 6.5), particle agglomeration becomes more prevalent, as can be seen in Figure 7.23 and Figure 7.24 (also see Figures 6.35 & 6.38). Clearly, at a lower surfactant concentration (0.1 g/L LS, QB; PLP13), the agglomeration point was reached somewhat earlier than in the corresponding test at a higher concentration (0.15 g/L LS, QB; PLQ23). However, the average particle size at the higher surfactant concentration (PLQ23; $d_{50} \approx 9$ µm, SSA ≈ 1.3 m^2/g) is less than half the size found at the lower concentration (PLP13; $d_{50} \approx 20$ µm, SSA ≈ 0.3 m^2/g), which translates into a greater than fourfold increase in the measured specific surface area (SSA). This may suggest that a larger particle size affects the

Stellenbosch University http://scholar.sun.ac.za

dispersion efficiency of surfactants in a negative manner, despite its relatively lower SSA. Nevertheless, despite the prevalence of agglomerates in the Test PLP13 (45 min) residue, no effect on its USP kinetics is observed (Figure 7.20 *b*). Therefore, these agglomerates formed just prior to 45 minutes, *i.e.*, diffusion limitations had not yet transpired into the reduced oxidation rate observed at longer reaction times.

In terms of the amount of sulfide oxidised and elemental sulfur formed, Figure 7.25 presents the comparative reaction extents for Series PLQ1, PLQ2 and PLQ3.

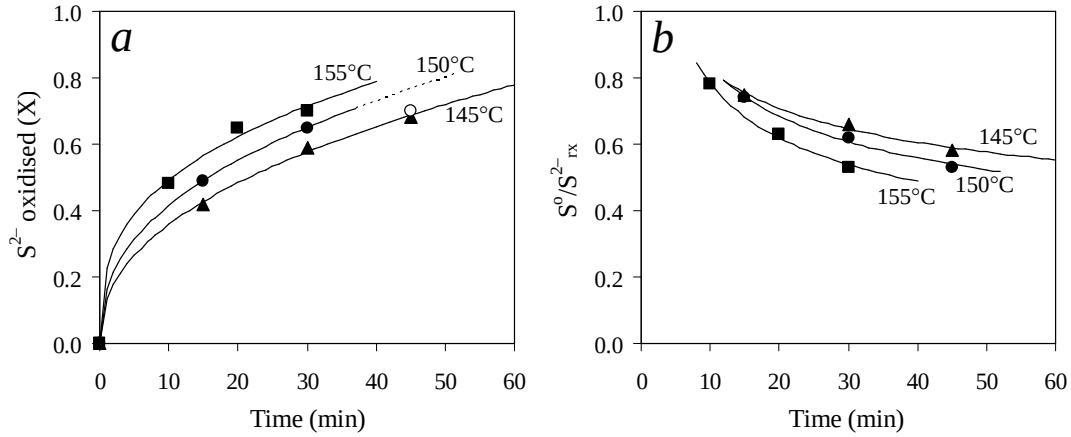

Figure 7.25
Comparison of sulfide oxidation extents & elemental sulfur yields (Sample E, starting with 25 g/L H_2SO_4, 15 g/L Cu, 0.15 g/L Arbo A02 LS, Orfom 2 QB) at different oxidation temperatures (700 kPa p_{O2}°): *a*) Sulfide oxidation extents; *b*) Elemental sulfur yields.

Although a decrease in elemental sulfur with increasing temperature is expected, the systematic drop during the first 45 minutes (Figure 7.25 *b*) is different from the relatively constant yields reported in Chapter 6 (Sect. 6.5) when using Norlig A LS. Since the chalcopyrite sample used here (Sample E) was relatively pure (Table 7.2), these results suggest that the Arbo A02 LS was comparatively more active in dispersing sulfur and exposing it to oxidation. These aspects are revisited in Chapter 8, when using higher pulp densities and different surfactants.

Since pyrite was the only other refractory mineral present in the HBMS 777 concentrate, the results from the bulk modal analysis are used to assess its relative oxidation rate. These results are summarised in Figure 7.26, but are considered relatively inaccurate, since Sample E contained only a small amount of pyrite (~4%). Furthermore, small amounts of iron(III) precipitated at the longer reaction times at 150ºC (45 min; PLQ23) and 155ºC (30 min; PLQ33), which interfered with the bulk modal (pyrite) analyses. The BSE images of Test PLQ23 residue again suggest that sulfur started to form agglomerates with unreacted sulfide particles after about 45 minutes (Figure 7.27 *a*). At higher magnification (Figure 7.27 *b*), small (amorphous) hematite or goethite and larger

Stellenbosch University http://scholar.sun.ac.za

hydronium jarosite particles (see Ch. 5) are visible on the mineral surfaces. The calculated activation energy of about 90 kJ/mol, based on these modal analyses, is therefore only indicative. Most importantly, the pyrite seems to have experienced an initial induction period, followed by a comparatively fast (*cf.* chalcopyrite) observed oxidation rate, *e.g.*, ~0.025 1/min for FeS_2 *vs.* ~0.009 1/min for $CuFeS_2$ at 155ºC & ~0.015 1/min for FeS_2 *vs.* ~0.005 1/min for $CuFeS_2$ at 145ºC.

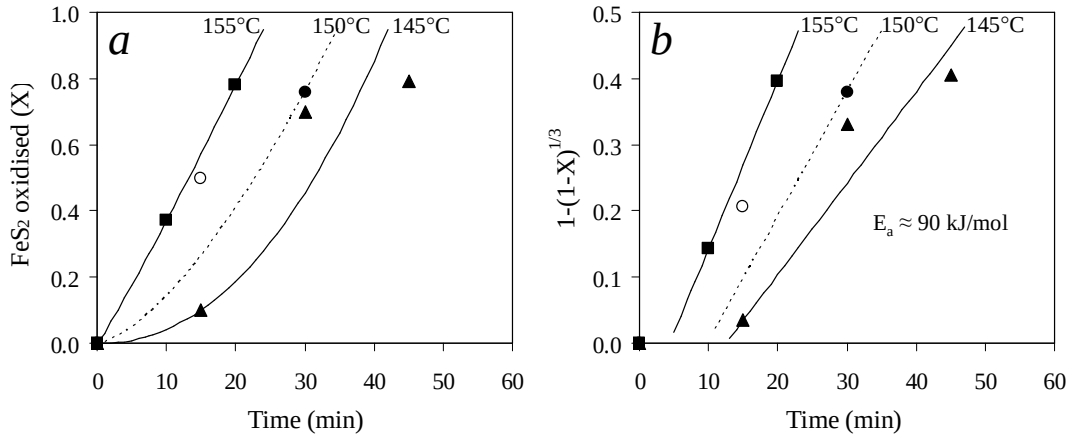

Figure 7.26
FeS_2 oxidation reaction extents & rates (Sample E, 25 g/L H_2SO_4, 15 g/L Cu, 0.15 g/L Arbo A02 LS, Orfom 2 QB) at different oxidation temperatures (700 kPa p_{O2}°): *a*) Reaction extents; *b*) USP model plot for surface reaction control. The solid lines represent the best linear fits of the final oxidation rates, from which the activation energy is obtained in Arrhenius coordinates (the dotted line is derived from the 30 min datapoint & calculated activation energy).

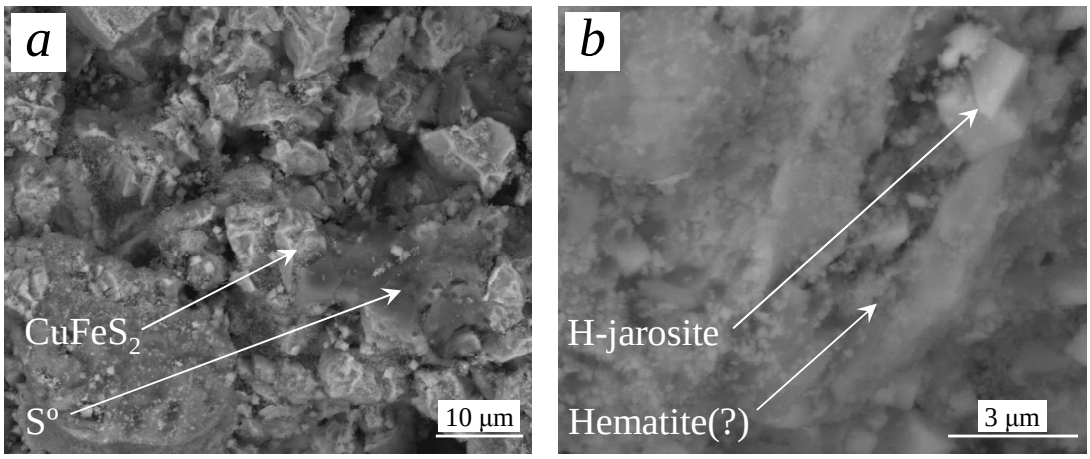

Figure 7.27
Images of autoclave residues (Sample E) after 45 min oxidation (700 kPa p_{O2}°) at 150ºC, starting with 25 g/L H_2SO_4, 15 g/L Cu & 0.15 g/L Arbo A02 LS, Orfom 2 QB (Test PLQ13): *a*) BSE image at 5000x magnification; *b*) BSE image at 25000x magnification.

Stellenbosch University http://scholar.sun.ac.za

Batch oxidation of the LT cleaner concentrate (Samples F & G)

Measurement of the mineral oxidation rates in the Las Tortolas (LT) cleaner concentrate followed a similar procedure to that discussed above. The silica content is too low to be used as solid-phase tie element and the mass loss over each test is based on the actual measured residue mass. Detailed results can be found in Appendix I.5. Since the mineralogical composition of this concentrate, especially with regards to the copper-containing minerals (Table 7.2), is more complicated than for the HBMS concentrate, the bulk model analyses (App. I.3) are essential in deriving the various reaction rates. The oxidation of the primary sulfide minerals, *i.e.*, chalcopyrite and pyrite, is most important in context of this study and is discussed first.

Figure 7.28 and Table 7.15 present summaries of the oxidation rates of chalcopyrite at different temperatures.

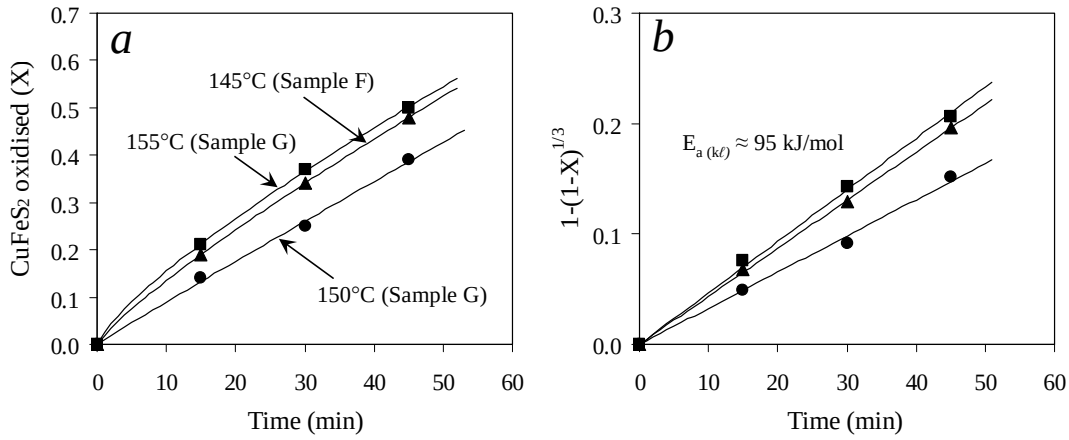

Figure 7.28
$CuFeS_2$ oxidation reaction extents & rates (Samples F & G, 25 g/L H_2SO_4, 15 g/L Cu, 0.15 g/L Arbo A02 LS, Orfom 2 QB) at different oxidation temperatures (700 kPa p_{O2}°): *a*) Reaction extents; *b*) USP model for surface reaction control (solid lines represent best linear fits of the oxidation rates, while activation energy is obtained from k_ℓ values within Arrhenius coordinates).

Table 7.15
USP & Arrhenius plot results of $CuFeS_2$ oxidation, using Sample F & G at 25 g/L H_2SO_4, 15 g/L Cu, 0.15 g/L Arbo A02 LS, Orfom 2 QB & different oxidation temperatures (700 kPa p_{O2}°).

Test series	Temperature	[a] $k_{s,Cpy}\cdot10^3$	R^2	d_{50}	[b] $k_{\ell,Cpy}\cdot10^2$
–	(ºC)	(1/min)	–	(µm)	(µm/min)
PLR1	145	4.3(5)	0.9996	12.67	5.5
PLR2	150	3.3	0.995	22.34(5)	7.3
PLR3	155	4.7	0.998	22.34(5)	10.4
$E_{a,Cpy}$	145–155ºC	–	0.995	–	94.7 kJ/mol

[a] Regressed through origin; [b] Based on d_{50} of sample PSD.

Stellenbosch University http://scholar.sun.ac.za

Good consistency and correlation (see R^2 values of the USP model plots) are evident from these results for the chalcopyrite mineral. Both the linear rate constant, $k_{\ell,Cpy}$ and the activation energy are comparable to the corresponding values obtained for the HBMS concentrate (see, *e.g.*, Table 6.14). All the intrinsic constants, ultimately used in the continuous and high pulp density batch models (Ch. 8), are obtained (regressed) by integrating over the feed PSD (see later). Again, the oxidation behaviour of pyrite is found to be more complex and uncertain. Figure 7.29 *a* and *b* illustrate the rates and USP model plots for pyrite, respectively, while the regressed rate constants are summarised in Table 7.16 (bracketed values).

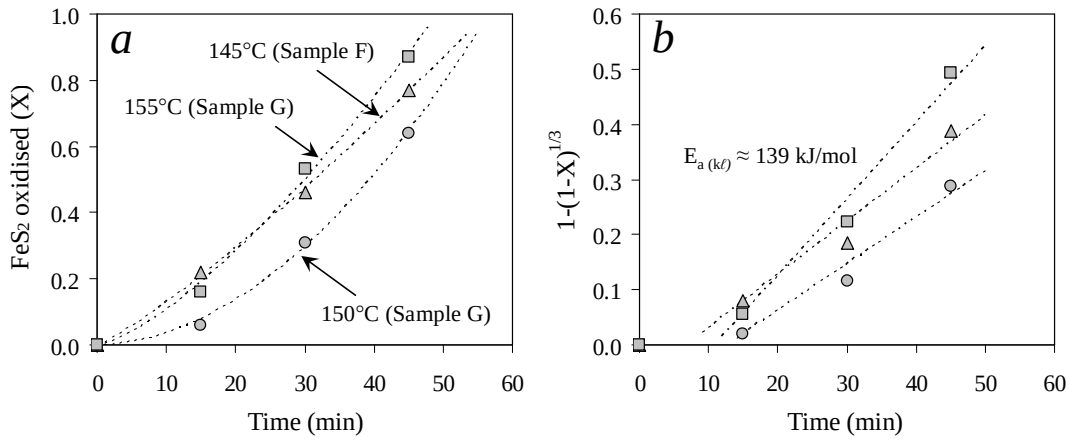

Figure 7.29
FeS_2 oxidation reaction extents & rates from the modal analyses (Samples F & G, 25 g/L H_2SO_4, 15 g/L Cu, 0.15 g/L Arbo A02 LS & Orfom 2 QB) at different oxidation temperatures (700 kPa p_{O2}°): *a*) Reaction extents; *b*) USP model for surface reaction control. Dotted lines represent best linear fits of the oxidation rates, fixed at the corresponding 15 min datapoints, while activation energy is obtained from k_ℓ values within Arrhenius coordinates.

Table 7.16
USP model & Arrhenius plot results for FeS_2 oxidation, using Sample F & G at 25 g/L H_2SO_4, 15 g/L Cu, 0.15 g/L Arbo A02 LS, Orfom 2 QB & different oxidation temperatures (700 kPa p_{O2}°).

Test series	Temperature	[a,b] $k_{s,Py}\cdot10^3$	[b] R^2	d_{50}	[b,c] $k_{\ell,Cpy}\cdot10^1$
–	(ºC)	(1/min)	–	(µm)	(µm/min)
PLR1	145	12.4 (9.6)	0.928 (0.963)	12.67	16.1 (12.2)
PLR2	150	9.4 (8.4)	0.926 (0.968)	22.34(5)	21.1 (18.8)
PLR3	155	11.9 (14.9)	0.999 (0.977)	22.34(5)	26.65 (31.0)
$E_{a,Py}$	145–155ºC	–	0.999 (0.998)	–	75 (139) kJ/mol

[a] Regression of each series fixed at first datapoint, *i.e.*, at the 15 min; [b] Un-bracketed values based on the iron balance, $CuFeS_2$ & Cu_5FeS_4 mineral contents (see below). All bracketed values based on residue pyrite contents, as directly obtained from the bulk modal analyses; [c] Based on d_{50} of sample PSD.

Stellenbosch University http://scholar.sun.ac.za

Figure 7.29 illustrates that the initial lag period (for pyrite), as previously observed for the HBMS concentrate, is also prevalent in the case of the LT concentrate. The apparent pyrite activation energy of 139 kJ/mol is significantly higher than for the HBMS concentrate (~90 kJ/mol), as well as reported values in the open literature, *e.g.*, Warren (1956) measured an activation energy of about 84 kJ/mol in the 130 to 190ºC range, while McKay and Halpern (1958) reported an activation energy of about 56 kJ/mol in the 100 to 130ºC range, which is similar to the value of about 51 kJ/mol reported by Bailey and Peters (1976) between 85 and 130ºC and the values of 69 to 77 kJ/mol proposed by Cornelius and Woodcock (1958) between 130 and 165ºC. Other earlier studies (see references in Bailey & Peters, 1976; Lowson, 1982) proposed values between about 40 and 55 kJ/mol in sulfate media. More recently, Papangelakis and Demopoulos (1991) measured values of about 46 kJ/mol between 140 and 160ºC, and 110.5 kJ/mol between 160 and 180ºC in sulfuric acid medium. This shift (increase) in the activation energy may have been related to the impact of complete sulfide to sulfate oxidation, commencing above about 170ºC, *i.e.*, due to the progressive removal of (potentially stifling) molten sulfur surface layers with increasing temperature, albeit at low overall yield. This argument is supported by the recent measurements of Long and Dixon (2004), who proposed a significantly lower value of about 33 kJ/mol with respect to dissolved oxygen concentration in a high temperature region (170-230ºC), where no elemental sulfur would have been expected.

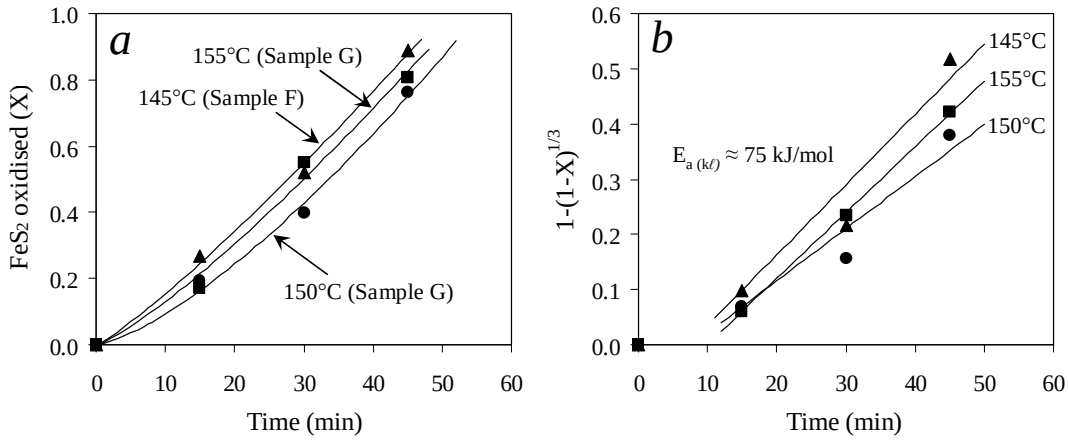

Figure 7.30
FeS_2 oxidation reaction extents & rates, using a revised procedure to determine residual pyrite contents (Samples F & G, 25 g/L H_2SO_4, 15 g/L Cu, 0.15 g/L Arbo A02 LS, Orfom 2 QB) at different oxidation temperatures (700 kPa p_{O2}°): *a*) Reaction extents; *b*) USP model for surface reaction control. Lines represent best linear fits of the oxidation rates, fixed at the corresponding 15 min datapoints, while activation energy is obtained from k_ℓ values within Arrhenius coordinates.

The residual pyrite content may also be based on the total iron dissolution extents calculated from chemical analyses and the total iron content calculated from the head mineralogical breakdown, after which the labile iron contributions from the other iron-containing phases, *i.e.*, chalcopyrite

Stellenbosch University http://scholar.sun.ac.za

and bornite (modal analyses), are subtracted. These values are summarised in Table 7.16 (un-bracketed values), while Figure 7.30 *a* and *b* present the rate and USP model plots, based on this revised procedure, respectively. Although the R^2 values are only marginally different from those obtained before, the re-calculated pyrite activation energy of about 75 kJ/mol is more in line with the above literature values. These revised pyrite oxidation extents and rates (for the LT concentrate) are therefore adopted in the rest of this study. The higher proportion of pyrite mineral in the LT (*cf.* HBMS) concentrate, and the associated lag period, result in the relatively linear response of the total sulfide oxidation extent over time (illustrated in Figure 7.31 *a*).

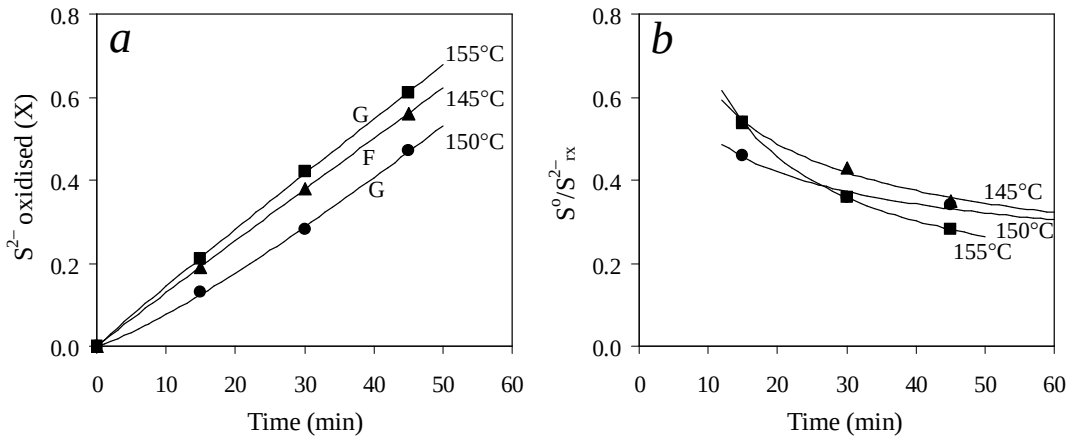

Figure 7.31
Total sulfide oxidation extents & elemental sulfur yields of the LT concentrate (Sample F & G, starting with 25 g/L H_2SO_4, 15 g/L Cu, 0.15 g/L Arbo A02 LS, Orfom 2 QB) at different oxidation temperatures (700 kPa p_{O2}°): *a*) Sulfide oxidation extents; *b*) Elemental sulfur yields.

Figure 7.31 *b* also highlights the significantly lower elemental sulfur yields compared to the HBMS concentrate (see Figure 7.25 *b*). The high pyrite content, with its low intrinsic sulfur yield, is likely a major contributing factor to this low overall yield. As described earlier, the workings of the Arbo A02 surfactant at low pulp density may also have resulted in a higher proportion of oxidation of sulfide to sulfate. The drop in sulfur yield over time may also be linked to the faster initial oxidation of minerals that tend to form sulfur (*e.g.* sphalerite in the case of HBMS, and bornite & chalcocite for the LT concentrate), *i.e.*, while the pyrite lag period is prevalent. The sudden increase in pyrite oxidation then presents as an overall drop in the overall sulfur yield. The comparatively low sulfur yield of the LT concentrate is also confirmed by the BSE images and XRD maps of elemental sulfur (at 150ºC) in Figure 7.32 *a* and *b*, respectively. Some sulfur globules are visible in Figure 7.32 *a*, suggesting that most of the sulfur was dispersed from the mineral surface at a shorter reaction time (30 min), unless trapped within cavities (circled). Bare mineral surfaces are clearly visible, exposing multiple hillocks on particular facets. On the other hand, agglomeration of unreacted sulfide particles by the cementing action of sulfur was prevalent after 45 minutes (Figure 7.32 *b*), even at these relatively low sulfur yields.

Stellenbosch University http://scholar.sun.ac.za

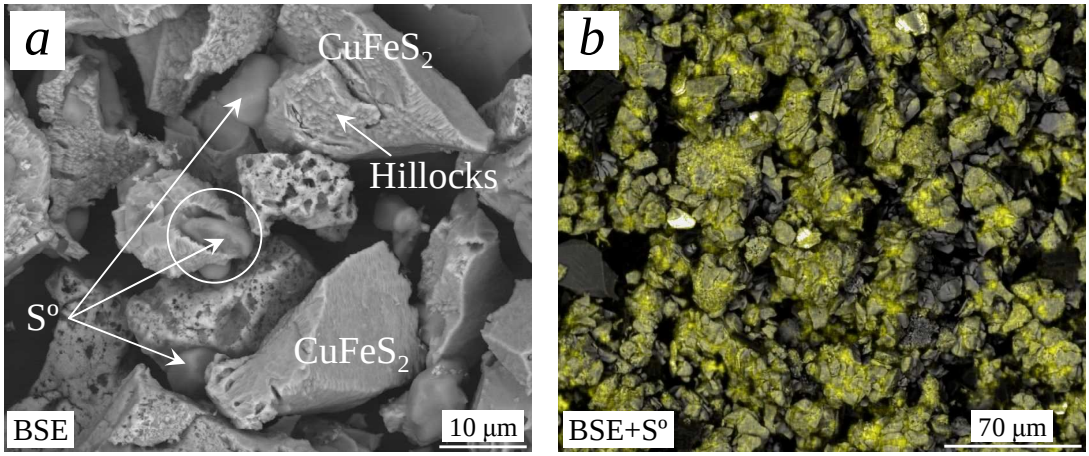

Figure 7.32
Images of autoclave residues (Sample G) at 150ºC (700 kPa p_{O2}°), starting with 25 g/L H_2SO_4, 15 g/L Cu & 0.15 g/L Arbo A02 LS, Orfom 2 QB: *a*) BSE image after 30 min (Test PLR22); *b*) XRD map of Sº, superimposed on the BSE image (at lower magnification) after 45 min (Test PLR23).

Finally, with regard to the oxidation rate of the minor copper sulfide minerals (*cf.* chalcopyrite) in the LT concentrate, some interesting trends are summarised in Table 7.17. Firstly, the fast dissolution rate of bornite (Cu_5Fe_S4) is reminiscent of a mineral phase where no refractory surface layers formed, similar to sphalerite in the HBMS concentrate. The reduction reaction of iron(III) species on the bornite surface can therefore be simplified as follows:

$$5Cu^{+}|_{lat} + Fe^{3+}|_{lat} + 4S^{2-}|_{lat} + 6Fe_2(SO_4)_{3(aq)} \Rightarrow 4S^{o} + 12FeSO_{4(aq)} + 5Cu^{2+}_{(aq)} + Fe^{2+}_{(aq)} + 6SO^{2-}_{4(aq)} \qquad 7.62$$

Table 7.17
Calculated mineral oxidation extents from bulk modal analyses, using Sample F, G at 25 g/L H_2SO_4, 15 g/L Cu, 0.15 g/L Arbo A02 LS, Orfom 2 QB & different oxidation temperatures (700 kPa p_{O2}°).

Test series	Temperature	Time	[a] $CuFeS_2$	[a] Cu_2S	[a] CuS	[a] Cu_5FeS_4
–	(ºC)	(min)	(%)	(%)	(%)	(%)
PLR1	145	15	19	62	–67	93
PLR1	150	30	34	59	17	97
PLR1	155	34	48	67	29	98
PLR2	145	15	14	69	–39	90
PLR2	150	30	25	68	–2	97
PLR2	155	45	39	74	35	99
PLR3	145	15	21	70	–25	93
PLR3	150	30	37	73	2	95
PLR3	155	45	50	82	40	97

[a] All the reaction extents are based on the measured residue masses (*cf.* original sample mass) & bulk modal compositions, after correcting (estimating) the Sº content (Sect. 7.3.2).

Stellenbosch University http://scholar.sun.ac.za

Similar to the approach used to describe the oxidation of the primary mineral phases (Sect. 7.4.1), the overall reaction stoichiometry can be simplified as follows:

$$Cu_5FeS_{4\,(s)} + (6y+3)O_2 + 2(3-2y)H_2SO_{4\,(aq)} \Rightarrow 4(1-y)S^o + 5CuSO_{4\,(aq)} + FeSO_{4\,(aq)} + 2(3-2y)H_2O \qquad 7.63$$

where the sulfur yield (1–y) is expected to be similar to or higher than for the chalcopyrite phase.

Chalcocite (Cu_2S) also reacts rapidly at the beginning (~60-70% in 15 min), but then suddenly slows down. It appears to be converted into covellite (CuS), which is in line with the discussions of Sect. 6.3.2, hence the negative oxidation rate of covellite over the initial oxidation period (15-30 minutes). It is assumed that iron(III) initially reacts with chalcocite, until a rate-limiting and impervious covellite surface structure formed:

$$6Cu^+|_{lat} + 3S^{2-}|_{lat} + 3Fe_2(SO_4)_{3\,(aq)} \Rightarrow Cu^{2+}(Cu^+)_2S^{2-}S_2^{2-}|_{surf} + 6FeSO_{4\,(aq)} + 3Cu^{2+}_{(aq)} + 3SO^{2-}_{4\,(aq)} \qquad 7.64$$

Again, provided the net oxidation rate of iron(II) is faster than the reduction rate of iron(III) on the chalcocite mineral surface, the following overall reaction stoichiometry is adopted for the initial reaction rate:

$$Cu_2S_{(s)} + \tfrac{1}{2}O_2 + H_2SO_{4(aq)} \Rightarrow CuS_{(s)} + CuSO_{4\,(aq)} + H_2O \qquad 7.65$$

Consistent with earlier assumptions, covellite oxidation is assumed to proceed *via* direct interaction with diatomic oxygen, catalysed by the presence of Cu(I) in the surface lattice:

$$CuS_{(s)} + (\tfrac{3}{2}y + \tfrac{1}{2})O_{2\,(aq)} + (1-y)H_2SO_{4\,(aq)} \Rightarrow (1-y)S^o + CuSO_{4\,(aq)} + (1-y)H_2O \qquad 7.66$$

As mentioned (Sect. 6.3.2), covellite is expected to oxidise more slowly than the other minerals in these concentrates, while the elemental sulfur yield is known to be relatively low (< 50%; see, *e.g.*, Marsden *et al.*, 2007d). No attempt is made to conduct a detailed evaluation of these reaction rates in this section, as it would deter from the main focus of this study, *i.e.*, the relative oxidation of chalcopyrite-pyrite concentrates under MT conditions. Rough estimates of these reaction rates and their activation energies are, however, obtained *via* the phenomenological regression analysis, as reported later in this section.

Batch oxidation of MV rougher concentrate (Sample H)

The Manto Verde (MV) rougher concentrate consisted predominantly of chalcopyrite, pyrite and quartz, while the minor phases were the iron minerals, magnetite (Fe_3O_4) and pyrrhotite (Table 7.2). The high silica content allows the tie method to be used to give a more accurate estimate of the solid-phase mass loss over time. With regard to the iron oxide phases, only magnetite was

Stellenbosch University http://scholar.sun.ac.za

detected by XRD analysis, with less than 10 vol% material present as amorphous phases. According to the bulk modal analyses (see App. I.6), a portion (~24-45%, *i.e.*, roughly a third) of the magnetite phase appears to be soluble. Since the kinetics of this dissolution reaction are fast, no stoichiometric or kinetic expressions are derived from these results. With the objective of developing a phenomenological model, the dissolution reaction is assumed to occur instantaneously on entering the reactor and according to the following overall stoichiometry:

$$Fe_3O_{4(s)} + H_2SO_{4(aq)} \Rightarrow Fe_2O_{3(s)} + FeSO_{4(aq)} + H_2O \qquad 7.67$$

The only purpose of this reaction is to provide a crude estimate of the associated acid consumption and iron(II) dissolution. The 'transformation' of magnetite into a hematite phase is artificial and the use of this equation is re-evaluated later in this chapter (see regression analyses).

All the detailed oxidation results can be found in Appendix I.6. Bulk model analyses (App. I.3) are essential to interpret the various mineral reaction rates. The oxidation extents and USP model plots for chalcopyrite and pyrite at different temperatures are summarised in Figure 7.33 and Figure 7.34, respectively, while the activation energy and observed rate constants are summarised in Table 7.18.

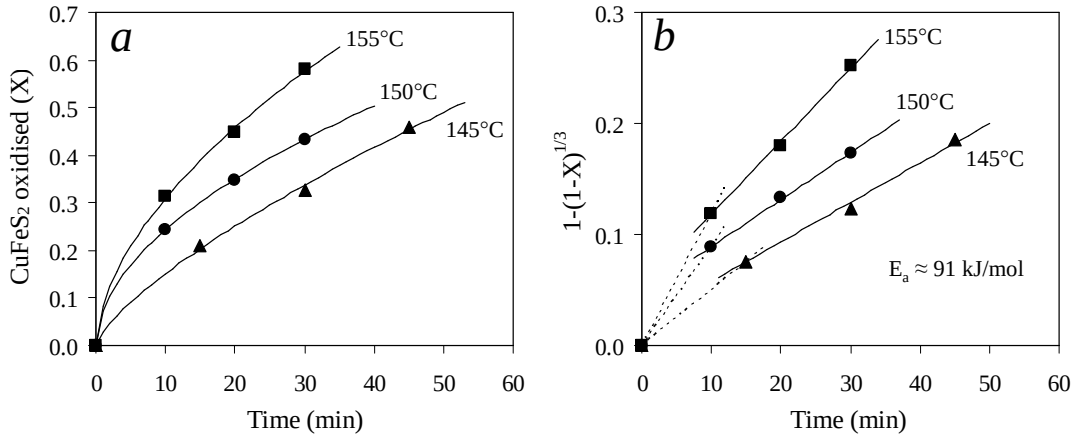

Figure 7.33
$CuFeS_2$ oxidation reaction extents & rates (Samples H, 25 g/L H_2SO_4, 15 g/L Cu, 0.15 g/L Arbo A02 LS, Orfom 2 QB) at different temperatures (700 kPa p_{O2}°): *a*) Reaction extents; *b*) USP model for surface reaction control (solid lines represent best linear fits of the oxidation rates, while activation energy is obtained from k_ℓ values within Arrhenius coordinates).

The presence of small particles (due to the relatively wide distribution of Sample H; see Figure 7.6) results in a faster initial chalcopyrite oxidation rate, similar to the trends observed for the HBMS concentrate (Figure 7.21 *b*). The USP model plots, based on the first kinetic datapoints of each set, are however relatively linear (Figure 7.33 *b*).

Stellenbosch University http://scholar.sun.ac.za

Table 7.18
USP model & Arrhenius plot results of $CuFeS_2$ oxidation, using Sample H at 25 g/L H_2SO_4, 15 g/L Cu, 0.15 g/L Arbo A02 LS, Orfom 2 QB & different oxidation temperatures (700 kPa p_{O2}°).

Test series	Temperature	[a] $k_{s,Cpy}\cdot10^3$ (fin)	R^2	[a,b] $k_{s,Py}\cdot10^3$ (fin)	R^2
–	(ºC)	(1/min)	–	(1/min)	–
PLS1	145	3.5(6)	0.993	10.7	0.954
PLS2	150	4.2	0.999	12.4	0.940
PLS3	155	6.5(5)	0.997	17.3	0.940
E_a	145–155ºC	~91 kJ/mol	0.937	~71 kJ/mol	0.945

[a] Regression of each series fixed at first datapoint; [b] Values based on the Fe balance (from chem. analyses), $CuFeS_2$, Fe_7S_8 & Fe_3O_4 mineral contents (from bulk modal analyses) & calc. Fe content (head mineralogy).

Despite the relatively poor representation of the observed rate constants in Arrhenius coordinates, the activation energy of about 91 kJ/mol is comparable to the values obtained for chalcopyrite in the LT (~95 kJ/mol) and HBMS (~85 kJ/mol) concentrates. However, the linear rate constant ($k_{\ell,Cpy}$) value of ~0.04 µm/min (at 150ºC), assuming a d_{50} of about 9.8 µm, is significantly lower than the observed value for the LT concentrate (~0.07 µm/min). Although there are some discrepancies between the MV copper extractions, *i.e.*, as calculated from the bulk modal and chemical analyses (App. I.6), similar relatively low rate constants result. This suggests that the MV concentrate is more resistant to oxidative attack, compared to the other two concentrates. However, to make a more accurate assessment of these relative reaction rates, these constants should rather be obtained by integrating over particle size (see next section).

The extent of pyrite oxidation is determined similarly to the method used for the LT concentrate, *i.e.*, the total iron dissolution extent is calculated first (from chemical analysis & the measured solids mass loss), after which the labile iron contribution from the other iron-containing phases (chalcopyrite, pyrrhotite & magnetite, based on bulk modal analysis & the silica-tie method) is subtracted from the calculated head iron content. This procedure reveals the residual pyrite content, which, in turn, is used to obtain the results illustrated in Figure 7.34. Although the USP model and Arrhenius regressions yield relatively poor results (see R^2 values in Table 7.18), the proposed pyrite activation energy of about 71 kJ/mol is comparable to the LT concentrate value of about 75 kJ/mol, determined on a similar basis. The linear rate constant ($k_{\ell,Py}$) value of ~0.12 µm/min, based on the assumed average particle size of 9.8 µm, is approximately 43% lower than the corresponding value observed for the LT concentrate (~0.21 µm/min). The lag period in pyrite dissolution is again prevalent (Figure 7.34 *b*) and clearly contributed to these USP model plots being relatively poor. As mentioned, it is important to interpret the mineral oxidation rates and activation energies in terms of the complete PSD, which would help to elucidate the reasons behind these observed phenomena.

Stellenbosch University http://scholar.sun.ac.za

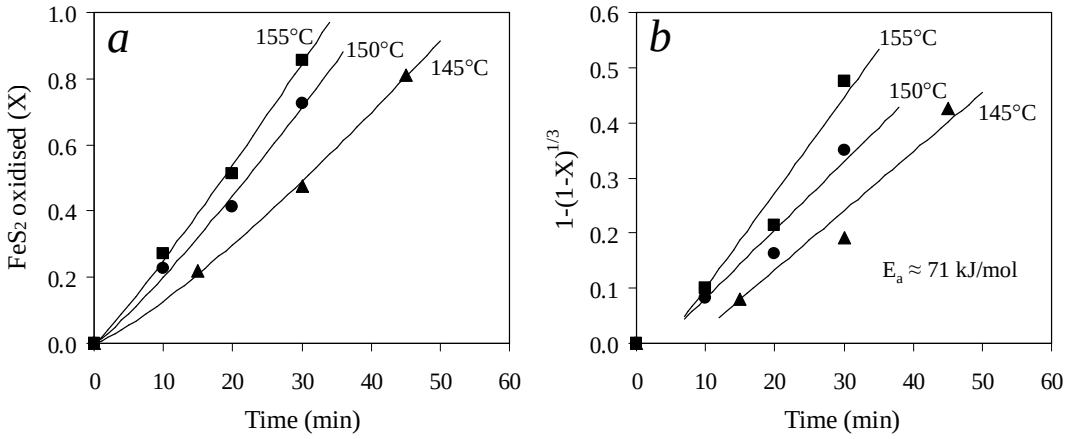

Figure 7.34
FeS_2 oxidation reaction extents & rates, using the revised procedure (to determine residual pyrite contents) (Sample H, 25 g/L H_2SO_4, 15 g/L Cu, 0.15 g/L Arbo A02 LS, Orfom 2 QB) at different oxidation temperatures (700 kPa p_{O2}°): *a*) Reaction extents; *b*) USP model for surface reaction control. Lines represent best linear fits of the oxidation rates (intersecting the first datapoints), while activation energy is obtained within Arrhenius coordinates.

The reason for the slower oxidation of the MV concentrate is not clear, but could have been related to liberation issues, due to the relatively high gangue mineral content (Table 7.2). However, the fact that these rates are obtained from initial dissolution data and most of the (relatively brighter) sulfide particles appear well liberated from the (relatively darker) gangue minerals (Figure 7.35; highlighted areas show some association) cannot account for the close to 40% reduction in the rate constant. The absolute oxidation rates, after integrating over particle size, are evaluated in more detail in the following section.

Figure 7.36 *b* illustrates that the higher pyrite content of the MV concentrate results in a significantly lower overall sulfur yield compared to the HBMS concentrate. That the chalcopyrite and pyrite contents were almost equal (Table 7.2) and the intrinsic rate of pyrite oxidation was at least double that of chalcopyrite (after the initial lag period; Table 7.18), explain why the overall yield of elemental sulfur approaches such low final levels. This also confirms that the intrinsic yield of sulfur on pyrite surfaces is very low.

The detailed mineral oxidation results (App. I) suggest that the sphalerite (in HBMS) and pyrrhotite (in HBMS & MV) phases oxidised very fast and at similar rates. Wide activation energy ranges have been observed in the literature, *e.g.*, Souza *et al.* (2007) reported a low activation energy of about 28 kJ/mol in the 40 to 90ºC range in acidic iron(III) sulfate medium, while Palencia Perez and Dutrizac (1991) reported values between about 40 and 70 kJ/mol in the 50 to 90ºC range. The activation energy appeared to decrease with increasing iron content in the sphalerite (elaborated upon in Sect. 6.3.2). Various other investigations reported values of generally between 30 and 60

Stellenbosch University http://scholar.sun.ac.za

kJ/mol (*e.g.*, Souza *et al.* 2007). An average value of 50 kJ/mol is therefore assumed for this study for both sphalerite and pyrrhotite, emphasising that these minerals require less activation by higher temperature, compared to the more refractory chalcopyrite and pyrite minerals.

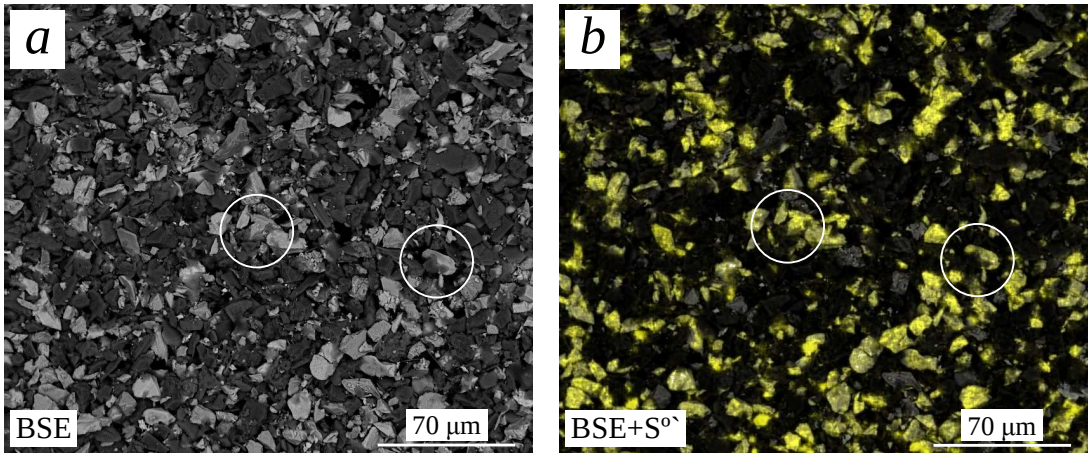

Figure 7.35
Images of autoclave residues (Sample E) after 20 min oxidation (700 kPa p_{O2}°) at 155ºC, starting with 25 g/L H_2SO_4, 15 g/L Cu & 0.1 g/L Arbo A02 LS, Orfom 2 QB (Test PLS32): *a*) BSE image; *b*) XRD map of S°, superimposed on the BSE image.

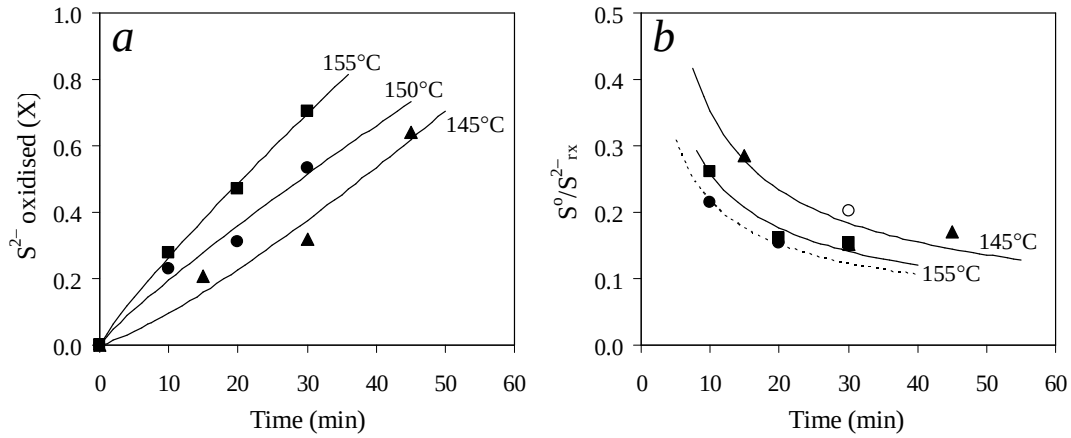

Figure 7.36
Comparing the sulfide oxidation extents & elemental sulfur yields of the MV concentrate (Sample H, starting with 25 g/L H_2SO_4, 15 g/L Cu, 0.15 g/L Arbo A02 LS, Orfom 2 QB) at different oxidation temperatures (700 kPa p_{O2}°): *a*) Sulfide oxidation extents; *b*) Elemental sulfur yields.

Regression of the low pulp density batch data to obtain the intrinsic rate constants and activation energies of the primary minerals in the HBMS 777 concentrate

The above kinetic results are now used to regress the intrinsic rate constants and activation energies over the feed PSD. The batch model (Sect. 7.2.4) is solved for each time step and the sum of the differences between the calculated and measured reaction extents is used to obtain the optimised k_ℓ

Stellenbosch University http://scholar.sun.ac.za

and E_a values. The error function, E_F, is defined as an equally weighed absolute error of the oxidation extents for *m* minerals, *e.g.*, for the HBMS concentrate, the following function is used:

$$\mathsf{E}_F = \sum_m y_{F,m}\mathsf{E}_m = \tfrac{1}{4}\mathsf{E}_{Cpy} + \tfrac{1}{4}\mathsf{E}_{Sph} + \tfrac{1}{4}\mathsf{E}_{Py} + \tfrac{1}{4}\mathsf{E}_{Ph} \qquad 7.68$$

where y_F is the weighed error function coefficient so that $\sum y_{F,k} = 1$ and E represents the absolute relative error of the relevant mineral over time, t:

$$\mathsf{E}_m = \sum_t \left| (1 - W_{m,t} W_{H_2O,t} / W_{m,o} W_{H_2O,o})^{calc} - (X_{m,t})^{exp} \right| \qquad 7.69$$

The previous mineral abbreviations (Ch. 6) are also used here, *i.e.*, *Cpy* (chalcopyrite), *Sph* (sphalerite), *Chc* (Chalcocite), *Cov* (covellite), *Bor* (bornite), *Py* (pyrite) and *Ph* (pyrrhotite). The results for the HBMS concentrate (Sample E) are summarised in Table 7.19.

Table 7.19
Optimised linear rate & activation energy constants for the primary minerals in the HBMS 777 concentrate (Sample E), using the experimental results of Series PLQ1, PLQ2 & PLQ3.

Sample	[a,c] $k_{\upsilon,Cpy}$	[b,c] $E_{a,Cpy}$		[a,d] $k_{\upsilon,Sph/Ph}$	[b,d] $E_{a,Sph/Ph}$		[a,e] $k_{\upsilon,Py}$	[b,e] $E_{a,Py}$	
	(µm/min)·(kg/mol)^{⅔}	(kJ/mol)		(µm/min)	(kJ/mol)		(µm/min)·(kg/mol)^{⅔}	(kJ/mol)	
HBMS	[f] 1.9 (1.9)	[f] 84 (87.5)		[f] 37 (15)	(50)		[f] 2.8 (2.9)	(90)	
Series	$X_{Cpy}^{(calc)}$	[g] $X_{Cpy}^{(exp)}$	[h] *AARD*	$X_{Sph}^{(calc)}$	[g] $X_{Sph}^{(exp)}$	[h,i] *AARD*	$X_{Py}^{(calc)}$	$X_{Py}^{(modal)}$	[h] *AARD*
–	(%)	(%)	(%)	(%)	(%)	(%)	(%)	(%)	(%)
PLQ1	37, 55, 67	41, 55, 67	3.8	93,100,100	99, 99, 100	2.3 (2.7)	28, 57, 72	10, 70, 79	68.6
PLQ2	45, 64, 76	45, 64, 78	1.0	99,100,100	94, 99, 100	2.5 (0.9)	41, 69, 83	–, 76, –	9.0
PLQ3	42, 61, 73	45, 61, 72	2.6	95,100,100	88, 99, 100	2.9 (1.5)	37, 66, 80	37, 78, –	8.3

[a] T_r = 150ºC (Eq. 7.70); [b] Range: 145-155ºC; [c] Assumed Fe(III) reduced according to Eq. 7.54, *i.e.*, $N_{FeIII,Cpy}$ = 2; [d] Assumed equal oxidation rates & activation energies for *Sph* & *Ph*, $N_{FeII,Sph}$ = 2, $N_{FeII,Ph}$ = 14, $\theta_{(Cov)}$ = 0 (Eq. 6.174) & $E_{a,Sph/Ph}$ fixed at 50 kJ/mol; [e] Slow oxidation regime of 0.035 µm /min up to 0.01 µm PPD, $E_{a,Py}$ fixed at 90 kJ/mol, & $N_{FeIII,Py}$ = –1; [f] Values in brackets refer to exclusive O_2 reduction on *Cpy*, *Sph* & *Ph* ($N_{FeIII,Cpy}$ = $N_{FeIII,Sph}$ = $N_{FeIII,Ph}$ = 0, $\theta_{(Cov)}$ = 1, $S°/S^{2-}{}_{rx}$ ($y_{Sph/Ph}$) = 0.6); [g] Avg. of bulk modal & chem. analyses (App. I.4) over reaction time; [h] Absolute avg. relative deviation between calc. & exp. oxidation extents (see Eq. 2.73); [i] Bracketed values refer to *Ph*.

The mineral oxidation rate expressions, developed in Chapter 6 (see Sect. 6.6), form the fundamental basis of this batch leach model. However, the optimisation exercise and the general lack of datapoints demand further mechanistic simplifications.

Chalcopyrite oxidation

Since the experimental data of chalcopyrite oxidation are considered most accurate, the intrinsic rate constant ($k_{\upsilon,Cpy}$; see below) and activation energy ($E_{a,Cpy}$) are optimised simultaneously, assuming that only two electrons are exchanged between the unaltered chalcopyrite surface and iron(III) species (energetically best positioned) at the solution-side of the interface, *i.e.*, according to Equation 7.54 ($N_{FeIII,Cpy}$ = 2). This initial reaction, which is postulated to form an intermediate

Stellenbosch University http://scholar.sun.ac.za

covellite-like surface (see earlier discussions), is also assumed to be fast and not rate limiting. This leads to the assumption of complete surface coverage of the surface, *i.e.*, $\theta(Cu_xS) = 1$ (Sect. 6.6). Furthermore, since the total catalytic pyrite surface area is too low to accelerate the chalcopyrite oxidation rate, the following expression is adopted from Chapter 6 (Eq. 6.176) and modified to include an Arrhenius response to changing oxidation temperature:

$$k_{\ell,Cpy} = -\upsilon_{\ell,Cpy} = k_{\upsilon,Cpy} \cdot exp\frac{-E_{a,Cpy}}{R_g}\left(\frac{1}{T} - \frac{1}{T_r}\right) \cdot [H^+]^{\frac{1}{6}}[O_2]^{\frac{1}{2}} \qquad 7.70$$

where the velocity term, $\upsilon_{\ell,Cpy}$, is consistent with the macroscopic population balance for the batch reactor (Sect. 7.2.4) and $k_{\upsilon,Cpy}$ refers to the intrinsic constant, assuming no deviation in the shrinkage rate over varying particle size. The oxidation of a covellite-like surface layer by diatomic oxygen is assumed to be rate limiting, as the oxidation rate was found to be insensitive to the iron(III) solution tenor (Sect. 6.5.4). Oxygen reduction on the unaltered chalcopyrite surface may also occur, *i.e.*, without appreciable iron(III) concentration initially. The half-order dependency of the rate on the dissolved oxygen concentration originates from electrochemical considerations and assumes symmetrical charge transfer across the Helmholtz layer (Sect. 6.3.4). However, this assumption cannot be substantiated because the experimental data conducted at different oxygen partial pressures (Sect. 6.5.4) are not sufficiently extensive. Some studies (Dobrokhotov & Maiorova, 1962; Jang & Wadsworth, 1993) suggested half-order dependency of the oxidation rate on the oxygen partial pressure, while others (Yu *et al.*, 1972) reported varying dependencies, *i.e.*, first-order at low overpressures and approaching zero-order at very high pressures. To be consistent with the electrochemical reaction framework, while keeping the phenomenological nature of the model in mind, a half-order dependency on the dissolved oxygen concentration is the logical premise for this study.

The overall chalcopyrite oxidation rate, R_{Cpy}, is thus described by the following relationship:

$$R_{Cpy} = \tilde{k}_{Cpy} \cdot a_{Cpy} \cdot k_{\ell,Cpy} \qquad 7.71$$

where the proportionality constant, $\tilde{k}_{Cpy}$, is represented as follows (App. F.4):

$$\tilde{k}_{Cpy} = -\frac{3\rho_{Cpy}\Phi_v}{Mw_{Cpy}\Phi_a} \qquad 7.72$$

Judging from the *AARD* values listed in Table 7.19, this mathematical description gives a good representation of the oxidation rate of chalcopyrite. The only other study found in the open literature to comment on the rate of chalcopyrite oxidation under MT conditions is that of Yu *et al.* (1972); they observed only a weak variation (~13%) in the rate when adding about 1 g/L Fe(III) ions. However, taking experimental error and solution speciation phenomena into account, this

Stellenbosch University http://scholar.sun.ac.za

variation is too marginal to warrant its inclusion in the phenomenological model. The regressed rate constant, $k_{\upsilon,Cpy}$, of 1.9 (µm/min)·(kg/mol)^{⅔} is close to the value of 2 obtained in Chapter 6 (Table 6.15) for the HBMS 777 concentrate, albeit using different surfactants and feed sample PSDs. These results are illustrated in Figure 7.37.

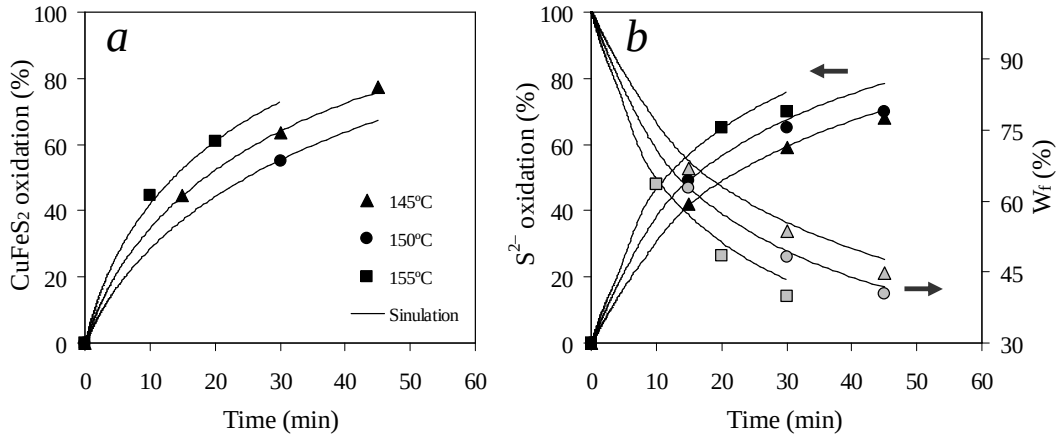

Figure 7.37
Comparison between the simulated & experimental $CuFeS_2$ oxidation, sulfide oxidation & mass loss extents for HBMS (Sample E, starting with 25 g/L H_2SO_4, 15 g/L Cu, 0.15 g/L Arbo A02 LS, Orfom 2 QB) at different oxidation temperatures (700 kPa p_{O2}°): *a*) $CuFeS_2$ oxidation extents; *b*) Total sulfide oxidation extents & residue mass as % of initial head solids mass (W_f).

Sphalerite and pyrrhotite oxidation

The oxidation rate of the minerals with a lower tendency to reduce oxygen, *i.e.*, sphalerite and pyrrhotite, is very fast and the above experimental data provide no insight into possible reaction mechanisms. Therefore, the reaction rate expression proposed in Chapter 6 (Eq. 6.174) needs further simplification. This lack of experimental data and the fact that this study is confined to high background copper concentrations make the distinction between the exposed sphalerite surfaces and covellite-like (*Cov*) surfaces largely redundant. Despite the likely formation of such surfaces, either of these mechanisms may be adopted to account for sphalerite and pyrrhotite dissolution kinetics. Both these scenarios are tested and the response of the sphalerite oxidation extent and the corresponding acid concentration are illustrated in Figure 7.38 *a* and *b*, respectively, *i.e.*, for θ_{Cov} = 0 and 1. Furthermore, since the iron(II) concentration is generally very low under most test conditions (see below), the rate constant for the cathodic direction of the anodic half-cell reaction (see Eq. 6.174), is discarded, *i.e.*, it is assumed that $k_{Fe2+}\cdot[Fe(II)^T] << 1$. Either of the following two rate expressions may therefore be adopted to describe the sphalerite oxidation rate (& analogous expressions for pyrrhotite):

$$k_{\ell,Sph} = -\upsilon_{\ell,Sph} = k_{\upsilon,Sph}\cdot exp\frac{-E_{a,Sph}}{R_g}\left(\frac{1}{T}-\frac{1}{T_r}\right)\cdot[FeIII]^{\frac{1}{2}} \qquad 7.73$$

Stellenbosch University http://scholar.sun.ac.za

$$k_{\ell,Sph} = -\upsilon_{\ell,Sph} = k_{\upsilon,Sph} \cdot exp\frac{-E_{a,Sph}}{R_g}\left(\frac{1}{T} - \frac{1}{T_r}\right) \cdot [H^+]^{\frac{1}{6}}[O_2]^{\frac{1}{2}} \qquad 7.74$$

The yield of elemental sulfur on barren sphalerite (& pyrrhotite) surfaces is assumed to be high (y_{Sph} = y_{Ph} = 0.05) and independent of increasing acid concentration. The shrinkage rate of covellite-covered surfaces is assumed to show a similar weak response to a changing acid concentration as measured for chalcopyrite (1/6th order *ref*. H^+ molality), while sulfur is assumed to be similar to the expected yield on a covellite surface (Sect. 6.3.2):

$$S^o/S_{rx,Sph} = S^o/S_{rx,Ph} = 0.4 + 0.3 \cdot [H^+] \qquad 7.75$$

The solid lines in Figure 7.38 *a* represent the iron(III) reduction mechanism, while the dotted lines refer to the direct oxygen reduction scenario. Differences in the acid concentration are relatively minor (Figure 7.38 *b*) and have a relatively small impact on the chalcopyrite and pyrite oxidation rates (Table 7.19). These results illustrate that either mechanism would suffice from a phenomenological modelling perspective under the conditions encountered in this study, at least until more data become available for the initial reaction rate. The overall rate of dissolution is captured by the following equation, with a proportionality constant analogous to Equation 7.72:

$$R_{Sph} = k^{\sim}_{Sph} \cdot a_{Sph} \cdot k_{\ell,Sph} \qquad 7.76$$

Analogous equations are also adopted for the pyrrhotite mineral phase.

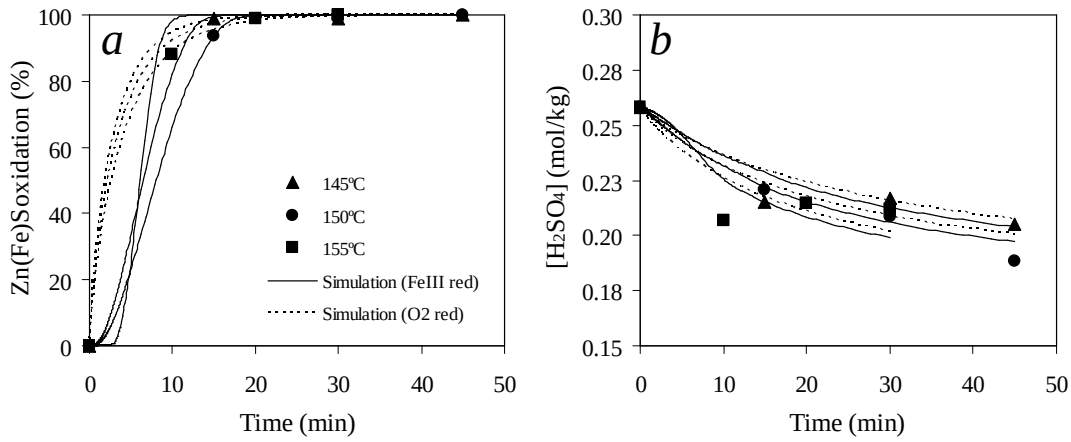

Figure 7.38
Comparison between the simulated & experimental Zn(Fe)S oxidation extent & H_2SO_4 concentration for HBMS (Sample E, starting with 25 g/L H_2SO_4, 15 g/L Cu, 0.15 g/L Arbo A02 LS, Orfom 2 QB) at different oxidation temperatures (700 kPa p_{O2}°): *a*) *Sph* oxidation extents; *b*) Acid concentration. The solid lines refer to barren (θ_{Cov} = 0) *Sph* & *Ph* surfaces (y_{Sph} = y_{Ph} = 0.05, $N_{FeIII,Sph}$ = 2, $N_{FeIII,Ph}$ = 14), & limited Fe(III) interaction with *Cpy* surface ($N_{FeIII,Cpy}$ = 2). The dotted lines refer to completer covellite-like surface coverage (θ_{Cov} = 1 & $N_{FeIII,Sph}$ = $N_{FeIII,Ph}$ = 0) & no Fe(III) interaction with *Cpy* surface ($N_{FeIII,Cpy}$ = 0).

Stellenbosch University http://scholar.sun.ac.za

The extent of iron(III) reduction on chalcopyrite, sphalerite and pyrrhotite surfaces

The assumptions regarding iron(III) reduction on the chalcopyrite surface have a significant impact on the oxidation state of iron, as illustrated in Figure 7.39. Cognisance has to be taken of the low iron concentration levels, which cast some doubt on the accuracy of these test results. Nevertheless, these results do suggest that little or no iron(III) reduces on chalcopyrite. Alternatively, if substantial iron(III) reduction does occur, most of it is re-oxidised by oxygen species on the surface, *i.e.*, the iron(II)/iron(III) couple may operate in true catalytic fashion without impacting significantly on the bulk iron oxidation state. The assumption of an initial transfer of two electrons from the unaltered chalcopyrite surface is still valid, and the above chalcopyrite oxidation rate expressions are therefore retained. The value of $N_{FeIII,Cpy}$ may therefore vary between –1 and 2; the value of –1 refers to a scenario where the mineral surface is so oxidising that all iron, including iron from the mineral lattice, exits the diffusion layer (towards the bulk solution) in the oxidised state.

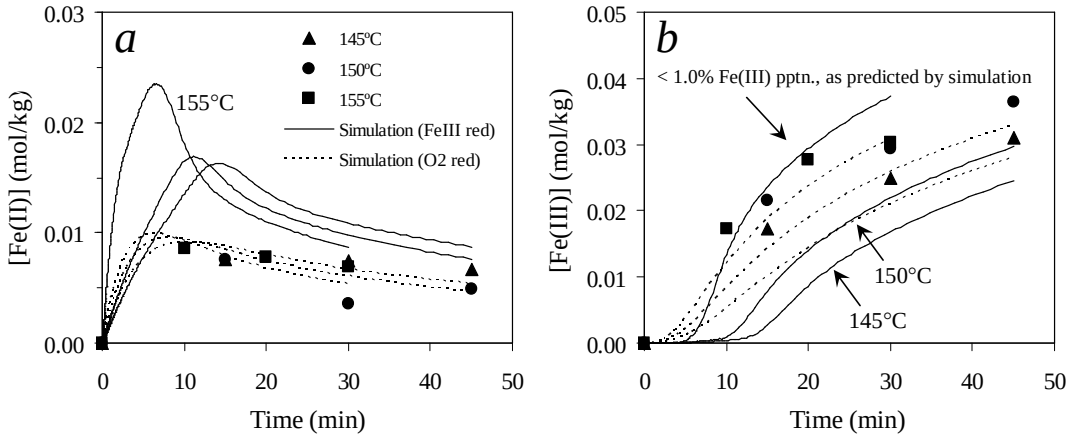

Figure 7.39
Comparison between the simulated & experimental Fe concentrations during oxidation of HBMS concentrate (Sample E, starting with 25 g/L H_2SO_4, 15 g/L Cu, 0.15 g/L Arbo A02 LS, Orfom 2 QB) at different oxidation temperatures (700 kPa p_{O2}°): *a*) [Fe(II)]; *b*) [Fe(III)]. The solid lines refer to predominantly Fe(III) reduction on minerals ($N_{FeIII,Cpy}$ = 2, $N_{FeIII,Sph}$ = 2, $N_{FeIII,Ph}$ = 14). The dotted lines refer to only O_2 reduction on minerals ($N_{FeIII,Cpy}$ = 0, $N_{FeIII,Sph}$ = $N_{FeIII,Ph}$ = 0).

The ultimate value of $N_{FeIII,Cpy}$ also hinges on the assumptions regarding the sphalerite and pyrrhotite phases. The fact that these phases oxidise so rapidly in the copper system strongly suggests that the covellite-like surface layer on sphalerite does not resemble covellite at all and that iron(III) reduction is the primary dissolution mechanism. This assumption, although it remains unresolved, is adopted for the rest of this study, while $N_{FeIII,Cpy}$ yields the best results when confined to values between –1 and 0. Equation 7.73 is therefore adopted for sphalerite and pyrrhotite, while the assumption is made that the surface, even if coated with a copper sulfide layer, is not refractory and promotes iron(III), rather than oxygen, reduction. Furthermore, since electrons would then be

Stellenbosch University http://scholar.sun.ac.za

primarily transferred in one-electron steps, the sulfur yield is expected to be high, and it is assumed that $y_{Sph} = y_{Ph} = 0.05$. The surface is also expected to be less oxidising, assuming that $N_{FeIII,Sph} = 2$ and $N_{FeIII,Ph} = 14$, while all iron in these mineral lattices is assumed to enter the bulk solution in the reduced state. Most importantly, the dissolution rate of chalcopyrite is relatively insensitive to these assumptions regarding sphalerite and pyrrhotite.

A re-evaluation of the pyrite oxidation rate expression

Finally, the pyrite oxidation mechanism requires elaboration as its oxidation rate has a significant bearing on the sulfur balance. The characteristic lag period during initial oxidation (see previous section) is particularly important in this regard. Figure 7.40 illustrates the kinetics of pyrite and pyrrhotite oxidation, respectively, after incorporating the above assumption regarding sphalerite and pyrrhotite reduction by iron(III) and assuming $N_{FeIII,Cpy} = 0$. The initial oxidation rate of pyrite is fixed at 0.035 µm/min, up to 0.01 µm PPD, after which the regressed value of $k_{\upsilon,Py} = 2.8$ (µm/min)·(kg/mol)^{⅔} is utilised.

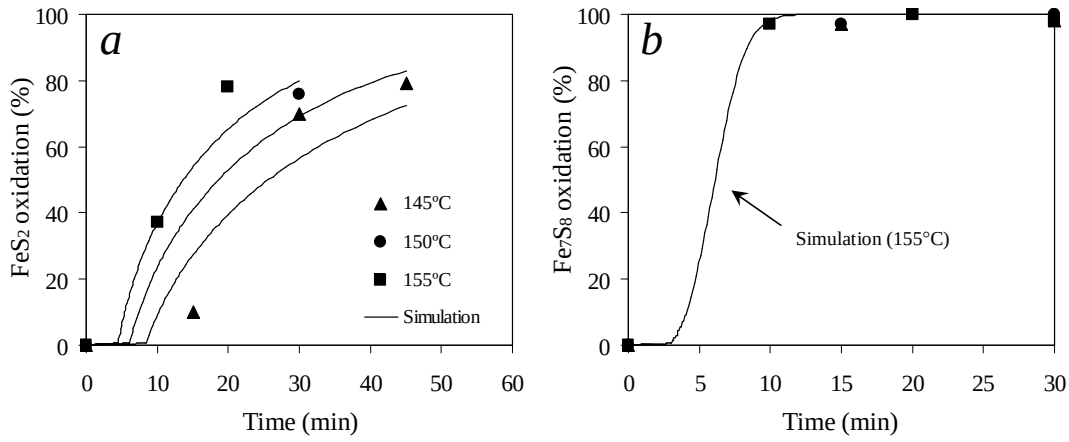

Figure 7.40
Comparison between the simulated & experimental FeS_2 & Fe_7S_8 oxidation extents for HBMS concentrate (Sample E, starting with 25 g/L H_2SO_4, 15 g/L Cu, 0.15 g/L Arbo A02 LS, Orfom 2 QB) at different oxidation temperatures (700 kPa p_{O2}°): *a*) FeS_2 oxidation extents; *b*) Fe_7S_8 oxidation extents. The lines represent the simulation, assuming $N_{FeIII,Cpy} = 0$, $N_{FeIII,Sph} = 2$, $N_{FeIII,Ph} = 14$ ($y_{Sph} = y_{Ph} = 0.05$) & fixing $k_{\upsilon,Py}$ at 0.035 & 2.8 before & after 0.01 µm PPD, respectively.

Although this PPD approach can be used to account for the initial lag period, the transition is sharp and the experimental data not adequately represented. The reason for this initial inhibition period is open to debate. Firstly, refractory oxide surface layers are not expected. The concentrate sample was ultra-fine milled (Sect. 7.3.3), reducing the possibility of passivation by flotation reagents. Secondly, the sample was stored in an inert environment, preventing the formation of oxide layers - not that such layers would be expected to inhibit dissolution in acidic environments. A different mechanism was therefore likely at play on the pyrite surface. Such mechanisms could include the

Stellenbosch University http://scholar.sun.ac.za

precipitation of iron(III) on pyrite surfaces, *e.g.*, as hydronium jarosite, and the galvanic protection of pyrite by minerals such as chalcopyrite. It is assumed that the characteristic S-shape oxidation kinetics of pyrite are related to a rate dependency on the iron(III) concentration, similar to sphalerite and pyrrhotite minerals (see the shape of the pyrrhotite oxidation simulation in Figure 7.40 *b*). Section 6.3.4 proposed direct oxygen interaction with the pyrite surface due to its strong adsorption tendency, while the approach of positively charged ferric ion is expected to be less important in acidic solution due to the heavily protonated surface. Detailed arguments are presented in support of this mechanism. Although the equations derived in Section 6.3.4 are still valid, the above results suggest that the iron(III) reduction mechanism on pyrite should not be ignored under MT autoclave conditions. The mechanistic proposals of Chapter 6 need further refinement.

For the sake of simplicity, it is assumed that only the transfer of the first electron is worth considering in context of the phenomenological model. The rate-limiting cathodic and anodic reactions may therefore be represented as follows, respectively (the asterisk* refers to adsorbed species; see Sect. 6.3.3):

$$Fe^{3+} \Leftrightarrow Fe^{2+} + h^{+} \qquad 7.77$$

$$S_2^{2-}|_{Py} + H^{+} + h^{+} \Rightarrow S + HS\cdot^{*} \qquad 7.78$$

The assumption is made that iron(III) species could approach the heavily protonated pyrite surface due to the buffering action of the inner- and outer-sphere complexing anions and solvation molecules. Thus, even at relatively low iron(III) concentrations, as experienced in most batch and continuous leaching systems, the iron could inject holes into the non-bonding t_{2g} orbital of iron in the surface lattice or directly into the bonding orbitals of the S_2^{2-} species. The water splitting mechanism (Eq. 6.106) is also still relevant and could create highly oxidised surface species. It was previously assumed that the t_{2g} orbital of lattice iron could catalyse the first reduction step of oxygen. In view of the apparent dependency of the pyrite oxidation on iron(III) concentration and the low characteristic yield of sulfur on its surface, different sequences of electron transfer events are proposed. For example, a series of relatively fast electron transfer reactions, evolving around the water splitting mechanism, could catalyse the weakening of the bonding orbitals, *i.e.*, *via* the surface-stabilised hydroxyl ($OH\cdot^{*}$) and bisulfide ($HS\cdot^{*}$) radical species:

$$OH\cdot^{*} + H^{+} \Rightarrow H_2O^{*} + h^{+} \qquad 7.79$$

$$S_2^{2-}|_{Py} + H^{+} + h^{+} \Rightarrow S + HS\cdot^{*} \qquad 7.80$$

$$HS\cdot^{*} + h^{+} \Rightarrow S^{o} + H^{+} \qquad 7.81$$

$$O_2^{*} + H^{+} \Rightarrow HO_2\cdot^{*} + h^{+} \qquad 7.82$$

Stellenbosch University http://scholar.sun.ac.za

The last two reactions would be very favourable as the net electromotive force (EMF) of that cell is about 1.42 V (see standard reduction potentials of the various half cells in Ch. 6). An alternative scheme is now proposed, according to which the iron(III) species does not have to adsorb onto the pyrite surface, which is shown in Section 6.3.3 (Figure 6.15 & related discussions) to be unfavourable. Instead, the diatomic oxygen molecule is proposed to complex with iron in the surface lattice, as well as with iron(III) in solution. This scheme, illustrated in Figure 7.41, emphasises the catalytic role of aqueous iron(III).

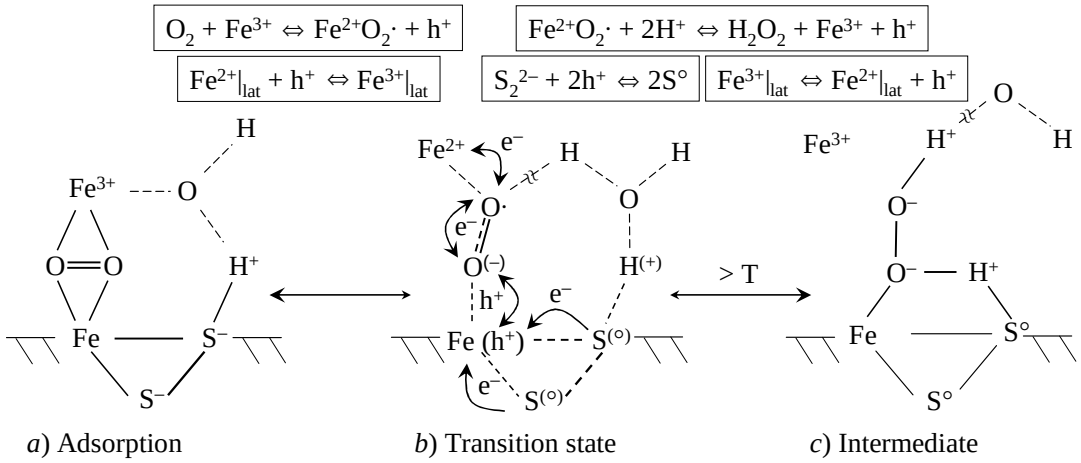

Figure 7.41
Simple mechanistic proposal of pyrite oxidation by oxygen, catalysed by its complexation with both lattice iron & aqueous iron(III): *a*) Adsorption of diatomic oxygen onto lattice iron, complexation with aqueous iron(III) & protonation of surface sulfide sites; *b*) Hole exchange with aqueous iron(III) *via* adsorbed oxygen, forming the perhydroxyl intermediate, followed by oxidation of nearby sulfide sites; *c*) Peroxide intermediate & iron(III) release into aqueous solution.

The overall scheme of strong oxygen interaction with the pyrite surface, its low intrinsic elemental sulfur yield, and the catalytic role of aqueous iron(III) are all combined in this scheme, without detracting from the concepts presented in Chapter 6. The same logic as presented in Section 6.3.4 is therefore followed to derive the cathodic and anodic current density contributions, with only one important difference, *i.e.*, that the reduction of iron(III) could become a rate-limiting prerequisite in the overall scheme at very low aqueous concentrations. Application of the mixed potential theory then leads to an analogous expression to Equation 6.170, except for the role of the iron(III)/iron(II) couple:

$$r_{Py} = k_1[H^+]^n \left(\frac{k_{Fe^{3+}}[Fe^{3+}]}{k_2[H^+]^n + k_{Fe^{2+}}[Fe^{2+}]} \right)^{\frac{1}{2}} \qquad 7.83$$

The contribution of catalytic pyrite surface is ignored in this equation because of the low pyrite content and pulp densities used. The anodic dissolution reaction is also assumed to be dependent on the hydronium ion concentration, based on the electrochemical study of Holmes and Crundwell

Stellenbosch University http://scholar.sun.ac.za

(2000), albeit conducted at temperatures below 40ºC. They found the reaction order with respect to this species (n) to be –½, although the reason for the dependency was unknown. The above experimental data are not extensive enough to derive this reaction order under the conditions of this study, however various other studies (see Holmes & Crundwell, 2000) also observed similar reaction orders with respect to the hydronium ion concentration, which justifies its inclusion in this rate expression. Besides the uncertainties associated with the extent of pyrite oxidation and the extent of iron(III) reduction on minerals such as chalcopyrite, neither the inclusion of the first and/or the second denominator terms significantly improves the overall regression (see also discussions in Chapter 8; Section 8.3.1). To reduce the number of adjustable parameters, this equation is simplified by assuming $k_2[H^+]^n + k_{Fe2+}[Fe^{2+}] \approx$ constant, while the final rate expression is extended to include the Arrhenius response to temperature:

$$k_{\ell,Py} = -\upsilon_{\ell,Py} = k_{\upsilon,Py} \cdot exp\frac{-E_{a,Py}}{R_g}\left(\frac{1}{T} - \frac{1}{T_r}\right) \cdot [H^+]^{-\frac{1}{2}}[FeIII]^{\frac{1}{2}} \qquad 7.84$$

The overall rate of pyrite oxidation is determined by the following relationship:

$$R_{Py} = \tilde{k}_{Py} \cdot a_{Py} \cdot k_{\ell,Py} \qquad 7.85$$

where the proportionality constant is analogous to Equation 7.72. Although this simplified treatment may compromise the ability of the model to predict the pyrite oxidation rate outside of the experimental conditions of this study, it constitutes a minor phase in chalcopyrite cleaner concentrates. Nevertheless, it is recommended that future studies focus on the mechanism of pyrite oxidation under MT autoclave conditions using pure mineral samples.

Finally, the sulfur yield on the pyrite surface is assumed to be very low under MT autoclave conditions due to the strong interaction with oxygen (Sect. 6.6.4):

$$S^o/S_{rx,Py} = 0.01 + 0.3 \cdot [H^+] \qquad 7.86$$

Final regression results of the HBMS 777 chalcopyrite concentrate

The above scheme suggests that iron(III) behaves as the ideal catalyst on pyrite surfaces, while pyritic lattice iron would be expected to enter the solution in the oxidised state, *i.e.*, yielding (overall) $N_{FeIII,Py} = -1$. Based on all these assumptions, the phenomenological model was re-regressed for the two remaining scenarios, *i.e.*, $N_{FeIII,Cpy} = -1$ and $N_{FeIII,Cpy} = 0$ (see above). Figure 7.42 compares the effect of these two scenarios on the experimental oxidation extent of pyrite and the iron(II) concentration, respectively. The model performance is clearly more consistent with the observed pyrite inhibition period and the final iron(II) concentration when assuming $N_{FeIII,Cpy} = 0$. On the other hand, the initial iron(II) concentration (Figure 7.42 *b*) is more adequately described by assuming $N_{FeIII,Cpy} = -1$. Since the S-shape kinetic oxidation curves are better represented by the

Stellenbosch University http://scholar.sun.ac.za

$N_{FeIII,Cpy}$ = 0 assumption, the rest of the low pulp density simulations (below) assumed that chalcopyritic iron entered the bulk solution in the reduced state. This assumption is consistent with the notion that the bonds involving lattice iron are broken first, allowing it to be reduced, before diffusing into the bulk solution, *i.e.*, the chalcopyrite surface is not oxidising enough to allow re-oxidation of lattice iron on its diffusion path. This proposal is also in line with the experimental observations of Section 6.5.4. The two aqueous iron(III) species partaking in the oxidation mechanism at the solution-side of the interface are, however, assumed to be prone to re-oxidation by the adsorbed oxygen molecule. More work, outside the scope of this study, is required to clarify this mechanism.

For the time being, it is assumed that, similar to the pyrite oxidation mechanistic proposal (Figure 7.41), the catalytic role of iron(III) is related to the initial electron transfer steps in association with diatomic oxygen and no net contribution to the bulk iron(II) concentration results. However, contrary to the pyrite case, this electron exchange is not rate limiting, as the chalcopyrite oxidation rate was found to be insensitive to the bulk iron(III) concentration (Sect. 6.5.4).

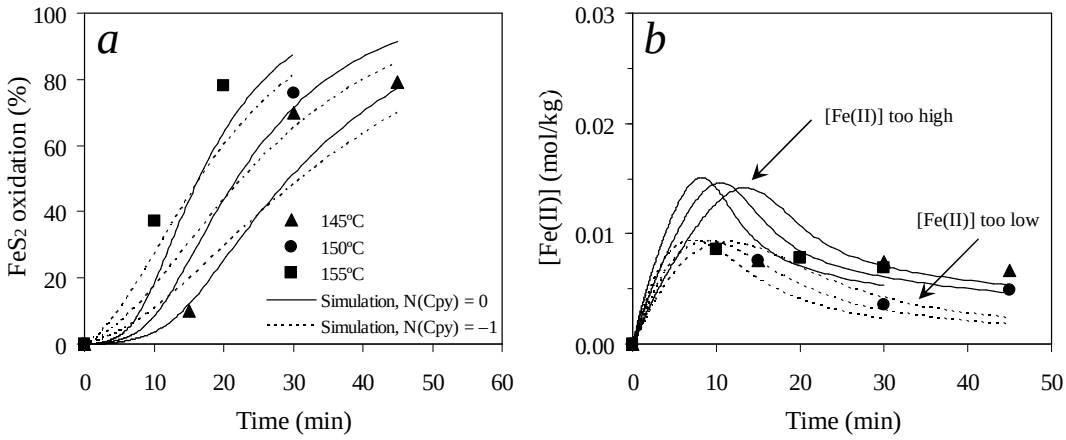

Figure 7.42
Comparison between the simulated & experimental FeS_2 oxidation extents & iron(II) concentrations for HBMS concentrate (Sample E, starting with 25 g/L H_2SO_4, 15 g/L Cu, 0.15 g/L Arbo A02 LS, Orfom 2 QB) at different oxidation temperatures (700 kPa p_{O2}°): *a*) FeS_2 oxidation extent; *b*) [Iron (II)]. The solid lines refer to $N_{FeIII,Cpy}$ = 0, $N_{FeIII,Sph}$ = 2, $N_{FeIII,Ph}$ = 14 & $N_{FeIII,Py}$ = –1. The dotted lines refer $N_{FeIII,Cpy}$ = –1, $N_{FeIII,Sph}$ = $N_{FeIII,Ph}$ = 0 & $N_{FeIII,Py}$ = –1.

The optimised rate constants and activation energies are listed in Table 7.20, together with the calculated reaction extents and *AARD* values for both the scenarios discussed above. Generally, this simulation gives an excellent representation of reaction extent, solution tenor and residue mass. These rate constants are also applied to the continuous reactor simulation, after incorporating the detailed iron(III) precipitation module (Ch. 5). These aspects are discussed in the next section.

Stellenbosch University http://scholar.sun.ac.za

Table 7.20
Linear rate & activation energy constants used in the batch & CSTR models for the primary minerals, & comparison with the experimental results of Series PLQ1, PLQ2 & PLQ3 (HBMS).

Sample	[a] $k_{\upsilon,Cpy}$	[b] $E_{a,Cpy}$		[a] $k_{\upsilon,Sph/Ph}$	[b] $E_{a,Sph/Ph}$		[a] $k_{\upsilon,Py}$	[b] $E_{a,Py}$	
	$(\mu m/min)\cdot(kg/mol)^{2/3}$	(kJ/mol)		$(\mu m/min)\cdot(kg/mol)^{1/2}$	(kJ/mol)		(μm/min)	(kJ/mol)	
E	1.9 (1.9)	89 (89)		20 (7.5)	50		0.23 (0.15)	90	
Series	$X_{Cpy}^{(calc)}$	[c] $X_{Cpy}^{(exp)}$	*AARD*	$X_{Sph}^{(calc)}$	[c] $X_{Sph}^{(exp)}$	[d] *AARD*	$X_{Py}^{(calc)}$	$X_{Py}^{(modal)}$	*AARD*
–	(%)	(%)	(%)	(%)	(%)	(%)	(%)	(%)	(%)
PLQ1	37, 55, 67	41, 55, 67	3 (3)	85,100,100	99,99,100	5.0 (5.4)	12, 51, 77	10, 70, 79	16 (46)
PLQ2	45, 64, 76	45, 64, 78	1 (1)	98,100,100	98,100,100	1.8 (0.2)	25, 71, 91	–, 76, –	0 (14)
PLQ3	42, 61, 73	44, 61, 72	2 (2)	90,100,100	88, 99, 100	2.9 (1.0)	18, 63, 87	37, 78, –	34 (25)
Series	$X_{S2-}^{(calc)}$	[e] $X_{S2-}^{(exp)}$	*AARD*	$X_{S^o/Srx}^{(calc)}$	[e] $X_{S^o/Srx}^{(exp)}$	*AARD*	$W_f^{(calc)}$	$W_f^{(exp)}$	*AARD*
–	(%)	(%)	(%)	(%)	(%)	(%)	(%)	(%)	(%)
PLQ1	40, 59, 71	42, 59, 68	3 (2)	71, 68, 66	75, 66, 58	7 (8)	70, 56, 48	67, 54, 45	5 (6)
PLQ2	48, 68, 79	49, 65, 70	6 (6)	70, 66, 65	74, 62, 53	12 (12)	63, 49, 41	63, 48, 40	2 (3)
PLQ3	45, 65, 77	48, 65, 70	5 (5)	70, 66, 65	78, 63, 53	13 (14)	67, 51, 43	64, 49, 40	5 (6)
Series	$[Acid]^{(calc)}$	$[Acid]^{(exp)}$	*AARD*	$[FeII]^{(calc)}$	$[FeII]^{(exp)}$	*AARD*	$[FeIII]^{(calc)}$	$[FeIII]^{(exp)}$	*AARD*
–	$(m\cdot10)$	$(m\cdot10)$	(%)	$(m\cdot10^2)$	$(m\cdot10^2)$	(%)	$(m\cdot10^2)$	$(m\cdot10^2)$	(%)
PLQ1	2.3,2.1,2.0	2.2,2.2,2.1	3 (3)	1.4,0.7,0.5	0.8,0.7,0.7	36 (41)	0.4,2.0,2.8	1.7,2.5,3.1	34 (17)
PLQ2	2.2,2.0,1.9	2.2,2.1,1.9	2 (2)	1.2,0.6,0.5	0.8,0.4,0.5	42 (27)	1.0,2.6,3.3	2.2,2.9,3.7	24 (12)
PLQ3	2.2,2.1,2.0	2.1,2.2,2.2	6 (6)	1.4,0.7,0.5	0.9,0.8,0.7	33 (38)	0.7,2.4,3.1	1.7,2.8,3.0	27 (15)

All values refer to $N_{FeIII,Cpy} = 0$, $N_{FeIII,Sph} = 2$, $N_{FeIII,Ph} = 14$ & $N_{FeIII,Py} = -1$, except bracketed values which refer to $N_{FeIII,Cpy} = -1$, $N_{FeIII,Sph} = N_{FeIII,Ph} = 0$, $N_{FeIII,Py} = -1$. Equal k_υ & E_a (50 kJ/mol) for *Sph* & *Ph*, $S^o/S^{2-}{}_{rx}$ ($y_{Sph/Ph}$) = 0.05. $E_{a,Py}$ = 90 kJ/mol & $S^o/S^{2-}{}_{rx}$ (y_{Py}) = 0.99 – 0.3·[H^+]. [a] T_r = 150ºC; [b] Range: 145-155ºC; [c] Avg. of bulk modal & chem. analyses (App.I.4); [d] Bracketed values refer to *Ph*; [e] Chem. analysis (App.I.4).

Comparison between the continuous model calculations and the measured results for the HBMS 777 concentrate after incorporating the iron(III) precipitation rate model and revised mineral oxidation rate expressions

The modelling results for the multi-compartment continuous autoclave pilot Periods P1 and P2, and P3 and P4, are summarised in Table 7.21 and Table 7.22, respectively. This simulation includes the detailed iron(II) oxidation (Ch. 4) and iron(III) precipitation modules (Ch. 5), as well as the updated intrinsic linear oxidation rate expressions of the various minerals in the HBMS concentrate (discussed above). The optimised parameters (Table 5.10 footnotes) of the enhancement factor κ (Eq. 5.55, Figure 5.31) give a reasonable estimate of the iron(III) precipitation behaviour under these high pulp density conditions (see below; also see Sect. 8.3.1). Although further optimisation of these parameters could have been embarked upon, the quality of the continuous pilot results, especially with regard to iron(III) precipitation and the quantitative amount of elemental sulfur and hematite formed (see Sect. 7.4.1; as high as 10% uncertainty in hematite content, $W_{f,Hem}$), did not warrant further optimisation. Correlations were used to simulate the sulfur yield on chalcopyrite

Stellenbosch University http://scholar.sun.ac.za

and pyrite surfaces as a function of the unassociated hydrogen ion molality (see Sect. 8.3.1). Most importantly, the simulation adequately captures the general oxidation and precipitation trends observed during the continuous pilot campaigns.

Table 7.21
Simulation output (updated) at fixed raffinate & mill feed flows for evaluation periods P1 & P2.

P1 Simulation	Flowrate (g/hr)	[a] Sln. dens. (g/L)	Cu (g/L)	Zn (g/L)	Fe(II) (g/L)	Fe(III) (g/L)	H_2SO_4 (g/L)	[b] Solids. (%) (S^{2-})
Mill prod.	2482	997	–	–	–	–	–	44.0 (32.5)
Raffinate	12446	1042 ([e] 45)	1.4	5.8	0.2	4.3	30, [e] 35	–
[c] Feed	15881	1044 ([e] 46)	1.9	6.1	5.0	0.6	24.4, [e] 28.5	[d] 6.2 (34.7)
[e] **P1** Simulation	[f] Fe(II) (g/L)	Fe(III) (g/L)	H_2SO_4 (g/L)	[g] $W_{f,Hem}$ (% Hem)	Mass loss (%)	[h] Cu extr. (%)	[i] S^{2-} oxid. (%)	[j] S° yield (%)
C #1+2	1.3 (1.1)	3.8 (4.0)	18.4 (19.1)	69.4 (66.6)	16.9 (15.7)	74.2 (73.8)	77.9 (73.0)	60.6 (63.8)
C #3	0.7 (0.7)	2.9 (3.2)	20.6 (20.8)	71.5 (68.1)	16.6 (15.8)	88.3 (88.0)	89.8 (85.6)	60.8 (63.3)
C #4	0.5 (0.5)	2.1 (2.5)	22.4 (22.6)	72.6 (69.1)	15.7 (15.1)	94.3 (94.1)	94.9 (91.0)	61.0 (63.2)
C #5	0.3 (0.4)	1.3 (1.6)	24.4 (24.6)	72.8 (69.3)	14.1 (13.4)	97.0 (96.8)	97.1 (93.4)	61.0 (63.1)
C #6	0.3 (0.3)	0.4 (0.7)	26.6 (26.9)	72.9 (69.4)	12.0 (11.2)	98.1 (98.0)	98.0 (94.5)	61.0 (63.1)
P2 Simulation	Flowrate (g/hr)	[a] Sln. dens (g/L)	Cu (g/L)	Zn (g/L)	Fe(II) (g/L)	Fe(III) (g/L)	H_2SO_4 (g/L)	[b] Solids. (%) (S^{2-})
Mill prod.	2636	997	–	–	–	–	–	44.0 (32.5)
Raffinate	13935	1094	4.2	13.3	0.4	10.3	50.0	–
[c] Feed	17483	1087	4.3	12.4	5.0	5.9	41.4	[d] 6.0 (34.8)
[e] **P2** Simulation	[f] Fe(II) (g/L)	Fe(III) (g/L)	H_2SO_4 (g/L)	[g] $W_{f,Hem}$ (% Hem)	Mass loss (%)	[h] Cu extr. (%)	[i] S^{2-} oxid. (%)	[j] S° yield (%)
C #1+2str	1.1 (1.3)	10.9 (10.1)	28.0 (27.2)	45.9 (47.0)	14.4 (12.9)	67.1 (67.4)	72.1 (67.6)	61.4 (64.4)
C #3	0.6 (0.6)	9.3 (8.7)	30.5 (29.5)	46.3 (47.4)	10.2 (9.2)	81.7 (81.9)	84.5 (80.3)	61.7 (64.1)
C #4	0.5 (0.5)	8.0 (7.5)	32.6 (31.7)	47.1 (48.4)	7.3 (6.6)	88.9 (89.1)	90.5 (86.4)	61.9 (64.0)
C #5	0.4 (0.4)	6.9 (6.5)	34.8 (33.9)	48.3 (49.6)	5.2 (4.5)	92.4 (92.5)	93.5 (89.4)	62.0 (64.0)
C #6	0.3 (0.3)	5.9 (5.5)	37.1 (36.2)	48.9 (50.2)	2.6 (2.0)	94.1 (94.2)	94.9 (90.9)	62.0 (63.9)

[a] Calc. sln. density at 25°C; [b] Wt% solids (bracketed values refer to residual sulfide content); [c] After surfactant (water) addition point; [d] After 35% ZnS & Fe_7S_8 oxidised by iron(III) in feed mixing tanks; [e] All bracketed values refer to simulated results, based on slower pyrite oxidation rate (10× reduction in $k_{\upsilon,Py}$ to better simulate pilot sulfide oxidation extents) & 35 g/L H_2SO_4 in raffinate feed (*ref.* P1; better representation of autoclave feed sln. *ref.* Table 7.4); [f] Based on the assumption that mineral oxidation yield 1 mol Fe(II)/mol $CuFeS_2$, 2 mol Fe(II)/mol ZnS, 21 mol Fe(II)/mol Fe_7S_8, & 1 mol Fe(III)/mol FeS_2 oxidised; [g] %Hematite (the balance consists of H-jarosite); [h] Cumulative extraction (*ref.* mill feed) from PB (differential form), assuming 10× reduction of $CuFeS_2$ oxidation rate constant at 4.5 µm PPD (due to surfactant degradation); [i] Cumulative oxidation (*ref.* mill feed), assuming 10× reduction of FeS_2 oxidation rate constant at 1 µm PPD (due to surfactant degradation); [j] S° yield, *i.e.*, $S°/S^{2-}{}_{rx}\times 100\%$ *ref.* mill feed, using Eq. 8.3 (Sect. 8.3.1) & assuming baseline yields of 70% & 20% for $CuFeS_2$ & FeS_2, respectively, while ZnS (& Fe_7S_8) oxidation is assumed to yield a constant 95% S°.

Stellenbosch University http://scholar.sun.ac.za

Table 7.22
Simulation output (updated) at fixed raffinate & mill feed flows for evaluation periods P3 & P4.

P3 Simulation	Flowrate (g/hr)	[a] Sln. dens. (g/L)	Cu (g/L)	Zn (g/L)	Fe(II) (g/L)	Fe(III) (g/L)	H_2SO_4 (g/L)	[b] Solids. (%) (S^{2-})
Mill prod.	2408	997	–	–	–	–	–	48.8 (32.5)
Raffinate	11779	1072	1.8	10.7	0.4	6.9	48.5	–
–	–	–	–	–	–	–	–	–
[c] Feed	15182	1070	2.4	10.3	5.7	2.5	39.5	[d1] 7.0 (34.8)
[e] **P3** Simulation	[f] Fe(II) (g/L)	Fe(III) (g/L)	H_2SO_4 (g/L)	[g] $W_{f,Hem}$ (% Hem)	Mass loss (%)	[h] Cu extr. (%)	[i] S^{2-} oxid. (%)	[j] S° yield (%)
C #1+2	1.4 (1.2)	8.0 (7.4)	25.4 (24.5)	54.1 (55.8)	16.6 (15.0)	71.9 (71.7)	76.0 (71.3)	61.3 (64.1)
C #3	0.7 (0.6)	6.6 (6.0)	27.8 (27.2)	54.9 (56.5)	14.1 (12.8)	85.7 (85.4)	87.7 (83.3)	61.6 (63.7)
C #4	0.4 (0.4)	5.5 (4.9)	30.2 (29.5)	56.9 (58.5)	12.7 (11.6)	91.6 (91.4)	92.6 (88.5)	61.7 (63.7)
[k] C #5+6	0.3 (0.3)	4.2 (3.7)	33.4 (32.5)	58.1 (59.7)	10.3 (9.6)	94.7 (94.6)	95.3 (91.5)	61.8 (63.6)
P4 Simulation	Flowrate (g/hr)	[a] Sln. dens (g/L)	Cu (g/L)	Zn (g/L)	Fe(II) (g/L)	Fe(III) (g/L)	H_2SO_4 (g/L)	[b] Solids. (%) (S^{2-})
Mill prod.	2436	997	–	–	–	–	–	48.8 (32.5)
Raffinate	10926	1076	7.4	11.9	0.1	3.0	47.5	–
PLS recyc.	2806	1103	28.9	11.9	0.5	2.9	22.6	–
[c] Feed	17080	1079	10.8	10.9	3.6	0.9	35.6	[d2] 6.4 (34.9)
[e] **P4** Simulation	[f] Fe(II) (g/L)	Fe(III) (g/L)	H_2SO_4 (g/L)	[g] $W_{f,Hem}$ (% Hem)	Mass loss (%)	[h] Cu extr. (%)	[i] S^{2-} oxid. (%)	[j] S° yield (%)
C #1+2	1.5 (1.7)	5.1 (4.5)	22.3 (21.2)	60.5 (62.2)	19.9 (18.8)	65.7 (65.7)	71.0 (66.4)	62.0 (65.0)
[l] C #3+4	0.6 (0.8)	3.7 (3.3)	25.2 (24.1)	66.5 (68.5)	19.5 (19.1)	86.8 (86.8)	88.7 (84.6)	62.5 (64.5)
C #5	0.4 (0.5)	2.4 (2.1)	28.2 (26.9)	67.2 (69.2)	17.1 (16.9)	91.6 (91.5)	92.6 (88.6)	62.6 (64.5)
C #6	0.3 (0.3)	1.7 (1.4)	30.0 (28.7)	67.5 (69.5)	15.5 (15.4)	93.8 (93.7)	94.4 (90.5)	62.7 (64.4)

[a] Calc. sln. density at 25°C; [b] Wt% solids (bracketed values refer to residual sulfide content); [c] After surfactant (water) addition point; [d] After [(d1)]35%,[(d2)]20% ZnS & Fe_7S_8 oxidised by iron(III) in feed mixing tanks; [e] All bracketed values refer to simulated results, based on slower pyrite oxidation rate (10× reduction in $k_{\upsilon,Py}$ to better simulate pilot sulfide oxidation extents); [f] Based on the assumption that mineral oxidation yielded 1 mol Fe(II)/mol $CuFeS_2$, 2 mol Fe(II)/mol ZnS, 21 mol Fe(II)/mol Fe_7S_8 & 1 mol Fe(III)/mol FeS_2 oxidised; [g] % Hematite (the balance consists of H-jarosite); [h] Cumulative extraction (*ref.* mill feed) from PB (differential form), assuming 10× reduction of $CuFeS_2$ oxidation rate constant at 4.5 µm PPD (due to surfactant degradation); [i] Cumulative oxidation (*ref.* mill feed), assuming 10× reduction of FeS_2 oxidation rate constant at 1 µm PPD (due to surfactant degradation); [j] S° yield, *i.e.*, $S°/S^{2-}{}_{rx}\times100\%$ *ref.* mill feed, using Eq. 8.3 (Sect. 8.3.1) & assuming baseline yields of 70% & 20% for $CuFeS_2$ & FeS_2, respectively, while ZnS (& Fe_7S_8) oxidation is assumed to yield a constant 95% S°; [k] Autoclave discharge pipe partially blocked, causing slurry level to rise ~0.5 L in (short-circuited) C #5+6 (combined vol. ~10.1 L); [l] Upcomer blockage between C #4 & #5 caused slurry to overflow *via* vapour slot (Figure 7.1), *i.e.*, short-circuiting between C #3 & C #4.

During (period) P1, the acid concentration was lower and the amount of iron precipitated as hematite increased. However, as highlighted in Table 7.4, this period was not at steady-state

Stellenbosch University http://scholar.sun.ac.za

operation, as the feed acidity increased steadily over the first campaign. In addition, the observed pyrite oxidation rate was significantly lower compared to the rates suggested by low pulp density batch experimentation. This was thought to be due the less efficient Norlig A LS used in the pilot campaigns, which were characterised by sulfur conglomerate formation after the first two compartments. The pyrite oxidation rate appears to be particularly sensitive to the sulfur dispersion efficiency (see Figure 7.43 *a*). This aspect is revisited in Chapter 8 (Sect. 8.3.1). The simulated chalcopyrite oxidation extents are only marginally lower than the observed extents, primarily due to the lower value of 1.9 (µm/min)·(kg/mol)$^{2/3}$, compared to the value of 2.0 used previously. Figure 7.43 *b* illustrates that a mere 5 g/L change in the raffinate acid concentration results in a notable shift in the hematite formation extent and highlights the sensitivity of the residue hematite content to the operating conditions, feed mineral and solution compositions and oxidation reaction extents.

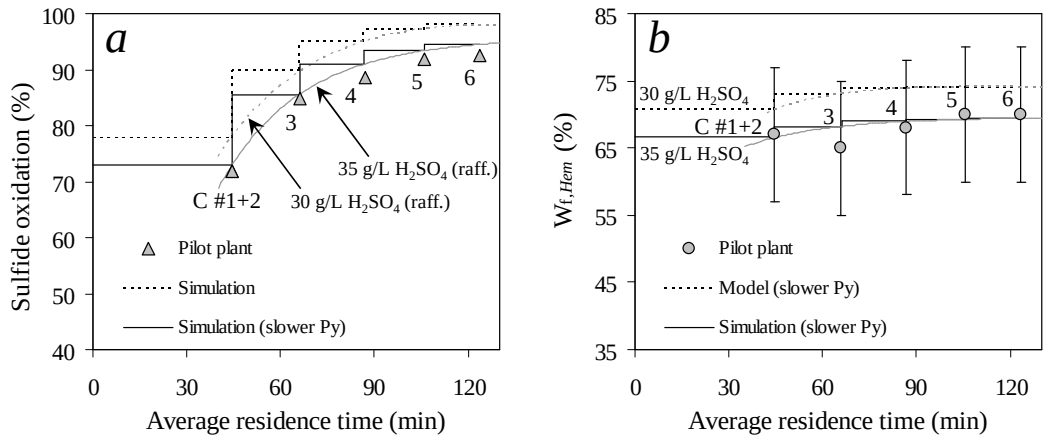

Figure 7.43
Comparison between continuous pilot autoclave reaction extents (HBMS 777 concentrate) & the compartmental simulation for P1, using the two-dimensional (differential) form of the PB & fixing the input stream compositions & flows to reflect pilot operation at two raffinate acid tenors, *i.e.*, 30 g/L & 35 g/L H_2SO_4. 'Slower Py' refers to 10× reduction in $k_{υ,Py}$: *a*) Sulfide oxidation extents, assuming 10× reduction in $CuFeS_2$ & FeS_2 oxidation rates at 4.5 µm & 1 µm PPDs, respectively (surfactant degradation); *b*) Hematite contents ($W_{f,Hem}$) at slower assumed pyrite oxidation rate.

Hydronium jarosite phase became more dominant during P2 and P3 due to the high raffinate acid and iron(III) tenors, as illustrated in Table 7.21 and Table 7.22, respectively. Under these conditions, the simulated copper dissolution extents are almost identical to that observed on the pilot plant (compare these results to Table 7.9 & Table 7.10, respectively). However, the calculated acid and iron(III) tenors and percentage mass losses are somewhat different from the measured results. The reason for this is probably related to the redissolution of the iron precipitates during sampling. The compartmental profile samples were taken *via* jacketed (cooled) sampling bombs, which would have allowed some redissolution of the precipitates under these high acidity conditions. The iron(III) precipitation rate constants, on the other hand, were obtained using a more refined (batch) testing procedure (Sect. 5.3), hence the higher calculated acid and lower iron(III)

Stellenbosch University http://scholar.sun.ac.za

concentration and solids mass loss, especially for P2. At lower hydrogen ion activity, *e.g.*, during P4 (with a portion of PLS solution recycled to the feed make-up tanks), the simulated and measured solution tenors and mass losses are similar, while good agreement between most of the reaction extents is again obtained. The slightly higher calculated iron(III) tenors in the first autoclave compartment during this period suggests that the simulated precipitation rate is too slow under the lower acidity conditions, in line with the discussions in Chapter 8 (see Sect. 8.3.1).

Between about 50 and 70% hematite ($W_{f,Hem}$), with the balance being hydronium jarosite, was produced during P4 (Figure 7.44). Since the operation was the closest to steady state during this period, the closed-circuit simulation (30% raff. Bleed, 90% Cu extr. in SX 1 & adding 4 kg filter water/kg solids (dry); Figure 7.2) yields good agreement with the measured results. The closed-circuit response to changing operating conditions is discussed in more detail in Section 8.3.2.

In conclusion, these results confirm that the iron(III) precipitation model of Chapter 5 is consistent with experimental observation at high pulp densities and that the enhancement factor κ (see Figure 5.31, Table 5.10, as well as the batch simulations in Sect. 8.3.1) is adequate for the purpose of this study, *i.e.*, allowing the low pulp density batch constants to be incorporated into the higher pulp density continuous simulation.

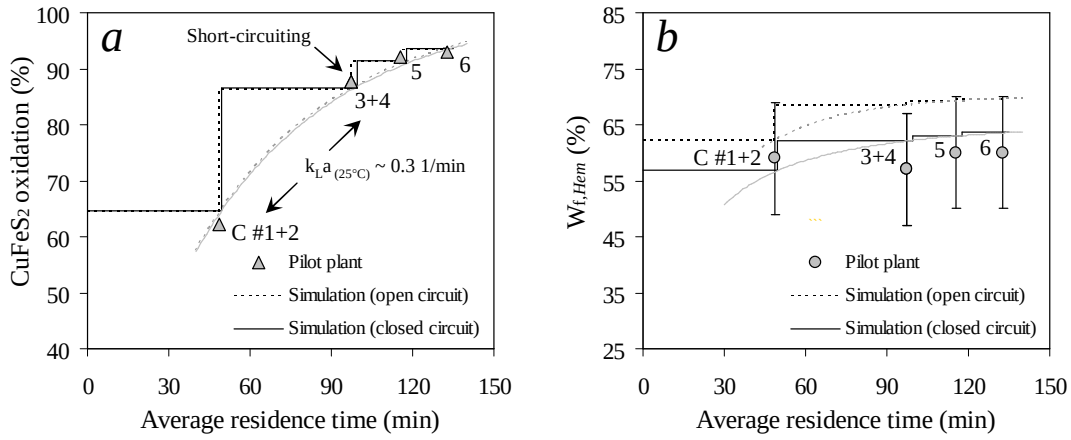

Figure 7.44
Comparison between continuous pilot autoclave reaction extents (HBMS 777 concentrate) & the compartmental simulation calculations (using 10× reduced $k_{υ,Py}$ value) for P4, using the two-dimensional (differential) form of the PB & fixing the input stream compositions & flows to reflect pilot operation (open circuit simulation). The closed-circuit simulation implements the pilot plant targets of 30% raff. Bleed, 90% Cu extr. in SX1, & adding 4 kg H_2O/kg solids (dry) during residue washing: *a*) $CuFeS_2$ oxidation extent, assuming 10× reduction in $CuFeS_2$ & FeS_2 oxidation rates at 4.5 µm & 1 µm PPDs, respectively (surfactant degradation); *b*) Hematite contents ($W_{f,Hem}$).

The weak point of the overall model is its inability to accurately account for the overall sulfur yield and to capture its effect on the oxidation rates of the sulfide minerals, especially pyrite. Variation in

Stellenbosch University http://scholar.sun.ac.za

the effectiveness of the different surfactants and the effects of aging appear to impact strongly on the pyrite oxidation rate, while the effects of a regime change after their degradation (45-60 min) are difficult to accurately quantify. These aspects should be expanded upon in future studies under MT operating temperatures. For the time being, the approach of enforcing a regime change at a fixed PPD is no more empirical than the current alternatives offered in the open literature (*e.g.*, Long & Dixon, 2004). The final section deals with the regression of the primary sulfide minerals in the South American chalcopyrite concentrates.

Regression of the low pulp density batch data to obtain the intrinsic rate constants and activation energies of the primary sulfide minerals in the two South American chalcopyrite concentrates

Detailed discussions of the oxidation rate of the primary sulfide minerals in the two South American concentrates have been presented earlier in this section. A multiple regression analysis was conducted by accounting for the feed PSD, using algorithms analogous to those used for the HBMS concentrate (Eq. 7.69). The detailed results for the LT cleaner concentrate are presented in Table 7.23. Note that two different PSDs were used, *i.e.*, Samples F and G (Figure 7.6), which explains the apparently anomalous behaviour at 150ºC. However, the corresponding *AARD* values confirm that the different mineral oxidation rates are reasonably well described by the mathematical model (also see Figure 7.45 & Figure 7.46 *a*), despite the complex mineralogy of this concentrate (Sect. 7.3.3).

The above rate expressions (Eq. 7.70 & 7.84) were used to simulate the oxidation rates of the chalcopyrite and pyrite minerals, respectively. Again, it is assumed that chalcopyritic iron entered the bulk solution in the reduced state and that aqueous iron(III), although a possible oxidant, diffuses back into the bulk solution in the oxidised state, *i.e.*, $N_{FeIII,Cpy} = 0$. It is also interesting to note that $k_{\upsilon,Cpy}$, is slightly lower (~16%) for the LT concentrate compared to the HBMS concentrate. Although aqueous iron(III) is proposed to be a true catalyst with respect to the surface reactions on these refractory minerals, its activity appears to play a rate-limiting role in the case of pyrite oxidation (Figure 7.41). The typically high surface potential of pyrite is seen as justification to assume that pyritic iron enters the bulk solution in the oxidised state, *i.e.*, $N_{FeIII,Py} = -1$. The bulk iron concentrations and oxidations states (Figure 7.46 *b*) confirm that these assumptions are correct. However, cognisance has to be taken of the fact that elemental sulfur formation, albeit at low yield on the pyrite surface, may interfere with the mineral surface potential. The above assumptions may therefore only be valid during initial leaching and then change over time. Despite the relatively slower oxidation rate of chalcopyrite (*cf.* HBMS), the value of $k_{\upsilon,Py}$, is over 100% higher for the LT material, which may have been related to its lower overall sulfur yield (Table 7.23). Elemental sulfur rapidly collects unreacted sulfides, especially when the surfactants are less effective: this could explain the low pyrite oxidation rate observed in the continuous pilot oxidation

Stellenbosch University http://scholar.sun.ac.za

of the HBMS concentrate (previous section). Interestingly, although the regressed activation energy of chalcopyrite is very similar between these two concentrates, the activation energy of pyrite in the LT concentrate is significantly lower, which agrees with various other studies from the literature (see earlier discussions & Figure 7.30).

Table 7.23
Linear rate constants & activation energies of the primary minerals in the LT concentrates, as obtained by the multiple regression analyses, including the comparison between the experimental & simulated values (Series PLR1, PLR2 & PLR3).

Sample		[a] $k_{\upsilon,Cpy}$	[b] $E_{a,Cpy}$			[a] $k_{\upsilon,Py}$	[b] $E_{a,Py}$	
		(µm/min)·(kg/mol)$^{2/3}$	(kJ/mol)			(µm/min)	(kJ/mol)	
F, G		1.6	95.7			0.5(3)	56.0	
Series	$X_{Cpy}^{(calc)}$	[e] $X_{Cpy}^{(exp)}$	*AARD*			$X_{Py}^{(calc)}$	$X_{Py}^{(Fe,modal)}$	*AARD*
–	(%)	(%)	(%)			(%)	(%)	(%)
PLR1	19, 34, 46	19, 34, 48	1.5			18, 60, 89	27, 52, 89	17.1
PLR2	16, 29, 39	14, 25, 39	9.3			10, 40, 71	19, 40, 76	18.1
PLR3	21, 37, 50	21, 37, 50	0.5			17, 57, 87	17, 55, 81	5.0
	[a] $k_{\upsilon,Bor}$	[b] $E_{a,Bor}$	[a,d] $k_{\upsilon,Chc}$	[c,d] $E_{a,Chc}$		[a,d] $k_{\upsilon,Cov}$	[b,d] $E_{a,Cov}$	
(µm/min)·(kg/mol)$^{2/3}$		(kJ/mol)	(µm/min)·(kg/mol)$^{2/3}$	(kJ/mol)		(µm/min)·(kg/mol)$^{2/3}$	(kJ/mol)	
F, G	16.6	55.1	6.9	(55)		3.6	75.1	
Series	$X_{Bor}^{(calc)}$	[e] $X_{Bor}^{(exp)}$	*AARD*	[d] $X_{Chc}^{(calc)}$	[e] $X_{Chc}^{(exp)}$	*AARD*	[d] $X_{Cov}^{(calc)}$	[e] $X_{Cov}^{(exp)}$	*AARD*
–	(%)	(%)	(%)	(%)	(%)	(%)	(%)	(%)	(%)
PLR1	96,100,100	93, 97, 98	2.7	68, 85, 92	62, 59, 67	30.9	–41, 3, 39	–67, 17, 20	52.3
PLR2	88, 99, 100	90, 97, 99	1.8	54, 71, 82	69, 68, 74	12.1	–39,–13,13	–39, –2, 35	204
PLR3	93,100,100	93, 95, 97	2.7	61, 78, 87	70, 73, 82	9.1	–33, 2, 34	–25, 2, 40	22.6
Series	$X_{S2-}^{(calc)}$	[f] $X_{S2-}^{(exp)}$	*AARD*	$X_{S°/Srx}^{(calc)}$	[f] $X_{S°/Srx}^{(exp)}$	*AARD*	$W_f^{(calc)}$	$W_f^{(exp)}$	*AARD*
–	(%)	(%)	(%)	(%)	(%)	(%)	(%)	(%)	(%)
PLR1	22, 44, 61	19, 38, 56	13.4	53, 43, 41	54, 43, 35	6.7	80, 63, 51	80, 65, 51	1.2
PLR2	17, 34, 50	13, 28, 47	20.0	56, 47, 42	46, 36, 34	26.0	84, 71, 59	83, 71, 57	1.9
PLR3	22, 45, 62	21, 42, 61	5.7	54, 45, 42	54, 36, 28	25.2	79, 62, 50	78, 61, 46	4.4
Series	$[Acid]^{(calc)}$	$[Acid]^{(exp)}$	*AARD*	$[FeII]^{(calc)}$	$[FeII]^{(exp)}$	*AARD*	$[FeIII]^{(calc)}$	$[FeIII]^{(exp)}$	*AARD*
–	(m×10)	(m×10)	(%)	(m×10^2)	(m×10^2)	(%)	(m×10^2)	(m×10^2)	(%)
PLR1	2.4,2.3,2.3	2.5,2.4,2.2	2.9	0.5,0.6,0.5	0.2,0.6,0.7	72.7	0.4,1.4,2.2	0.4,0.9,2.1	26.3
PLR2	2.4,2.4,2.3	2.2,2.4,2.3	4.6	0.4,0.5,0.4	0.4,0.4,0.7	19.3	0.3,1.0,1.8	0.5,1.0,1.6	20.5
PLR3	2.4,2.3,2.3	2.5,2.4,2.2	2.3	0.5,0.5,0.4	0.4,0.6,0.6	24.0	0.5,1.5,2.4	0.7,1.5,2.9	16.6

All calcs. based on $N_{FeIII,Cpy} = N_{FeIII,Bor} = N_{FeIII,Chc} = N_{FeIII,Cov} = 0$ & $N_{FeIII,Py} = -1$. $S°/S^{2-}{}_{rx}$ (y_{Cpy}) = 0.35 – 0.3·[H^+], $S°/S^{2-}{}_{rx}$ (y_{Cov}) = 0.6 – 0.3·[H^+], $S°/S^{2-}{}_{rx}$ (y_{Bor}) = 0.25 – 0.3·[H^+], $S°/S^{2-}{}_{rx}$ (y_{Py}) = 0.99 – 0.3·[H^+]; [a] T_r = 150ºC; [b] Range: 145-155ºC; [c] Assume $E_{a,Chc} \approx E_{a,Bor}$; [d] Regime change adopted at fixed product-layer thickness (Eq. 7.87); [e] From bulk modal analyses (App. I.5); [f] From chem. analyses (App. I.5).

Stellenbosch University http://scholar.sun.ac.za

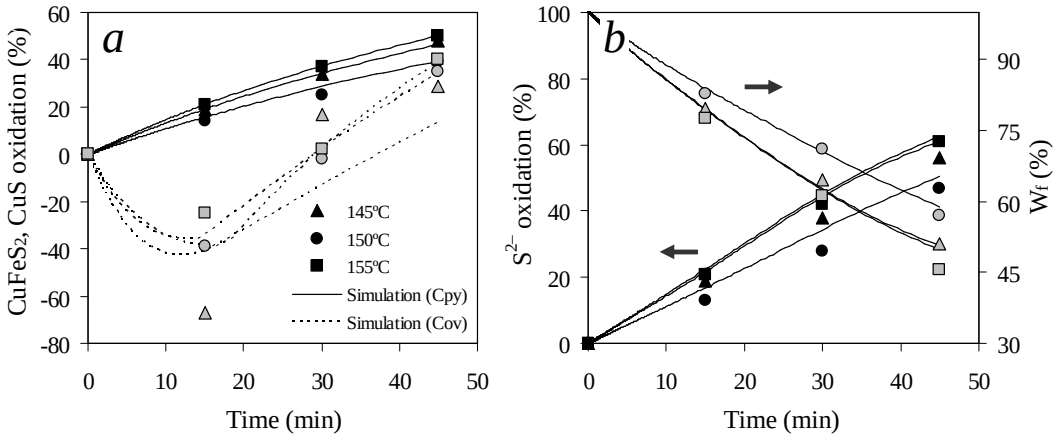

Figure 7.45
Comparison between the simulated & experimental $CuFeS_2$, CuS & total sulfide oxidation & mass-loss extents for LT concentrate (Samples F & G, starting with 25 g/L H_2SO_4, 15 g/L Cu, 0.15 g/L Arbo A02 LS, Orfom 2 QB) at different oxidation temperatures (700 kPa p_{O2}°): *a*) $CuFeS_2$ & CuS oxidation extents; *b*) Total sulfide oxidation extents & residue mass, W_f (% of head solids mass).

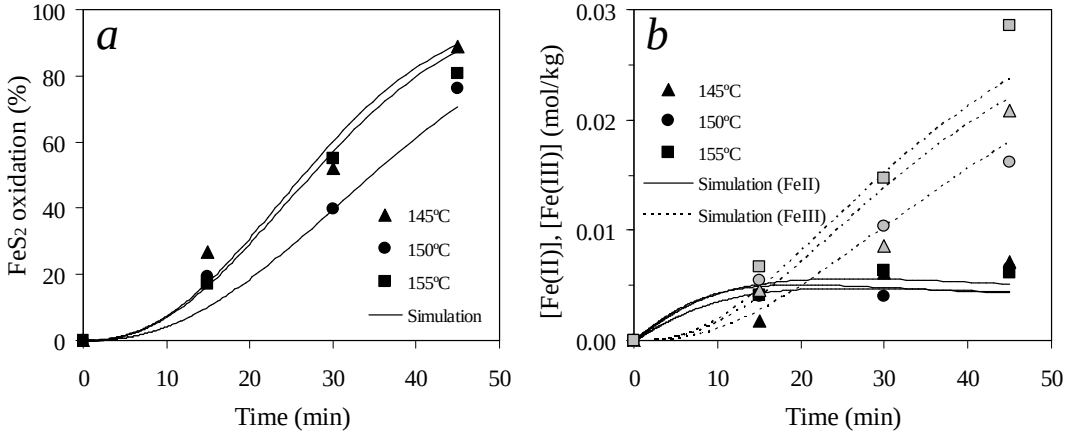

Figure 7.46
Comparison between the simulated & experimental FeS_2 oxidation extent & iron concentration for LT concentrate (Samples F & G, starting with 25 g/L H_2SO_4, 15 g/L Cu, 0.15 g/L Arbo A02 LS, Orfom 2 QB) at different oxidation temperatures (700 kPa p_{O2}°): *a*) FeS_2 oxidation extent; *b*) [Fe(II)] & [Fe(III)] (mol/kg).

Figure 7.47 *a* illustrates that the oxidation rate and activation energy of bornite are comparable to those of sphalerite in the HBMS concentrate. As is the case with sphalerite (& pyrrhotite), the lack of experimental data during initial oxidation prevents any assumptions regarding the oxidation mechanism. Again, either oxygen or iron(III) reduction may be used in the phenomenological model to describe its oxidation kinetics. For the sake of simplicity, the oxidation rate expression of chalcopyrite was adopted for both bornite and chalcocite, assuming that the activation energy of the latter mineral is similar to bornite. Although the reduction of iron(III) is likely prevalent on both

Stellenbosch University http://scholar.sun.ac.za

these surfaces (Eq. 7.62 & 7.64, respectively), the presence of Cu(I) in the surface lattices of these minerals is assumed to also catalyse the reduction of diatomic oxygen at high temperatures. Although the reduction of iron(III) would be the kinetically superior oxidant, the presence of copper and highly oxidised surface species is assumed to rapidly re-oxidise iron(II) on the surface, allowing the overall stoichiometries to be used in the phenomenological model, *i.e.*, according to Equations 7.63 and 7.65, respectively. This is the premise for the assumption that $N_{FeIII,Bor}$ = $N_{FeIII,Chc}$ = 0 (Table 7.23 footnotes).

The yield of elemental sulfur on the chalcopyrite and pyrite surfaces is assumed to be the same as for the HBMS concentrate. The yield on the bornite surface is assumed to be relatively high (y_{Bor} = 0.25), *i.e.*, to be consistent with mostly iron(III) reduction taking place on the surface, while the covellite mineral and the covellite-like phase forming on the chalcocite surface are assumed to interact predominantly with diatomic oxygen. The yield is therefore assumed to be relatively low (y_{Cov} = 0.6 *ref.* Eq. 7.63; Sect. 6.3.2) and, again, the assumption is made that no net reduction of iron(III) occurs on this mineral, *i.e.*, $N_{FeIII,Cov}$ = 0.

These assumptions result in reasonable estimates of the overall observed elemental sulfur yields (Table 7.23). The overall sulfur yields again dropped at longer reaction times, primarily due to the presence of pyrite and its tendency to produce acid rather than elemental sulfur. Figure 7.47 *b* illustrates that this simulation also gives a relatively good representation of the terminal acid concentration over time, which is considered enough justification to adopt these mineral-specific sulfur yields in the rest of this study.

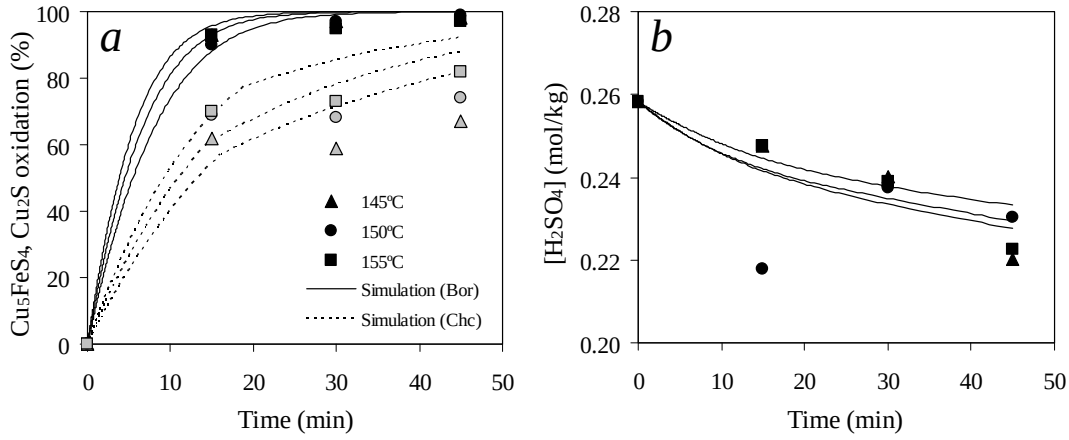

Figure 7.47
Comparison between the simulated & experimental Cu_5FeS_4 & Cu_2S oxidation rates & H_2SO_4 concentration for the LT concentrate (Sample E, starting with 25 g/L H_2SO_4, 15 g/L Cu, 0.15 g/L Arbo A02 LS, Orfom 2 QB) at different oxidation temperatures (700 kPa p_{O2}°): *a*) Cu_5FeS_4 & Cu_2S oxidation extents; *b*) [H_2SO_4] (mol/kg).

Stellenbosch University http://scholar.sun.ac.za

The functional form of the chalcopyrite rate expression (Eq. 7.70) is therefore adopted to describe the oxidation rate of all three secondary copper minerals, *i.e.*, bornite, chalcocite and covellite. This assumption is justified due to the relatively high experimental (modal analyses) uncertainty associated with these minor mineral phases. By adopting the same functional forms of the rate expressions for the different copper minerals in the phenomenological model, a quantitative comparison is also readily made between their intrinsic reaction rate constants. As mentioned, bornite oxidised an order of magnitude (10×) faster than chalcopyrite, while chalcocite initially reacted more than four times faster than chalcopyrite. Figure 7.45 *a* clearly illustrates that chalcocite was converted into a covellite phase, which is in line with earlier discussions and the literature (see Sect. 6.3.2). Since an accurate and detailed model of this mechanism is beyond the scope of this study, this phenomenon is simply accounted for by adopting the slower (~half) oxidation rate regime for the unreacted shrinking core, *i.e.*, chalcocite, above a fixed product layer (covellite) thickness. This parameter was optimised, resulting in the following condition:

$$k_{\upsilon,Chc} = k_{\upsilon,Cov} \text{ for } L_{Cov} - \ell_{Chc} > 2.5\,\mu m \qquad 7.87$$

This regime change accounts for an apparent reduction in chalcocite oxidation rate after about 15 minutes (Figure 7.47 *a*), which coincides with an inversion in the covellite oxidation extent (Figure 7.45 *a*). It is important to note that the oxidation rate of covellite after this point was more than double that of chalcopyrite, suggesting that this mineral was different from the refractory surface structure on partially oxidised chalcopyrite. The above rate constants and activation energies are directly utilised in the high pulp density simulation (Ch. 8). Although these parameters were obtained using crude experimental techniques and rate expressions that are based on many assumptions, this does not detract from the fact that higher rate constant values correspond to lower activation energy values. This is consistent with the fundamentals of chemical reaction theory.

The regression results of the MV rougher concentrate are summarised in Table 7.24, following the same methodology as applied in the regression of the HBMS and LT concentrates. Equation 7.67 yields lower iron(III) concentration values during the initial oxidation, which, in turn, underestimate the oxidation rates of the pyrite and pyrrhotite mineral phases. This is illustrated in Figure 7.48, suggesting that Equation 7.67 is not consistent with the observed trends; the soluble (⅓) fraction of the ‘magnetite’ phase is therefore assumed to rather consist of a stoichiometric amount of hematite, despite the fact that no such phase was identified by XRD. Assuming that phase was amorphous and part of an ‘apparent‘ magnetite phase, as identified by the bulk modal analysis, the following equation is used to account for the initial surge of iron(III) into solution, *i.e.*, following acid injection into the autoclave:

$$Fe_2O_{3(s)} + 3H_2SO_{4(aq)} \Rightarrow Fe_2(SO_4)_{3(aq)} + 3H_2O \qquad 7.88$$

Stellenbosch University http://scholar.sun.ac.za

The calculated terminal acid concentration is also consistently lower than the measured results, prompting the inclusion of an artificial magnesia (MgO) phase (4.4 wt%) to account for this additional acid consumption:

$$MgO_{(s)} + H_2SO_{4\,(aq)} \Rightarrow MgSO_{4\,(aq)} + H_2O \qquad 7.89$$

This 'extra' consumption of acid, albeit small (~1 g/L), was most likely due to the abundance of gangue minerals. Since a more detailed analysis of these digestion extents is outside the scope of this study, the magnesia approach is adequate in context of the phenomenological model.

Table 7.24
Regressed linear rate constants & activation energies of the primary minerals in the MV (rougher) concentrates, including a comparison between the experimental & simulated values (Series PLS1, PLS2 & PLS3).

Sample	[a] $k_{\upsilon,Cpy}$	[b] $E_{a,Cp}$		[a] $k_{\upsilon,Py}$	[b] $E_{a,Py}$		[a] $k_{\upsilon,Ph}$	[b] $E_{a,Ph}$	
	$(\mu m/min)\cdot(kg/mol)^{2/3}$	(kJ/mol)		$(\mu m/min)$	(kJ/mol)		$(\mu m/min)\cdot(kg/mol)^{1/2}$	(kJ/mol)	
H	1.6	111		0.3	74.7		[c] (20)	[c] (50)	
Series	$X_{Cpy}^{(calc)}$	[d] $X_{Cpy}^{(exp)}$	*AARD*	$X_{Py}^{(calc)}$	[e] $X_{Py}^{(Fe,modal)}$	*AARD*	$X_{Ph}^{(calc)}$	[e] $X_{Ph}^{(exp)}$	*AARD*
–	(%)	(%)	(%)	(%)	(%)	(%)	(%)	(%)	(%)
PLS1	22, 38, 50	26, 36, 50	8	22, 54, 74	22, 47, 81	8	89, 90, 90	85, 89, 86	4
PLS2	22, 38, 50	30, 38, 45	13	18, 47, 68	23, 41, 73	14	88, 90, 90	87, 88, 94	2
PLS3	30, 49, 62	34, 47, 62	7	27, 61, 80	27, 51, 77	8	89, 90, 90	91, 90, 89	1
Series	$X_{S2-}^{(calc)}$	[f] $X_{S2-}^{(exp)}$	*AARD*	$X_{S°/Srx}^{(calc)}$	[f] $X_{S°/Srx}^{(exp)}$	*AARD*	$W_f^{(calc)}$	[g] $W_f^{(exp)}$	*AARD*
–	(%)	(%)	(%)	(%)	(%)	(%)	(%)	(%)	(%)
PLS1	25, 50, 66	21, 32, 64	26	39, 29, 27	29, 15, 17	64	81, 69, 62	78, 71, 57	5
PLS2	23, 45, 62	23, 31, 53	21	42, 31, 28	22, 15, 20	82	82, 71, 63	79, 74, 62	3
PLS3	31, 58, 73	28, 47, 70	13	38, 27, 28	26, 16, 15	73	78, 64, 57	74, 66, 53	5
Series	$[Acid]^{(calc)}$	$[Acid]^{(exp)}$	*AARD*	$[FeII]^{(calc)}$	$[FeII]^{(exp)}$	*AARD*	$[FeIII]^{(calc)}$	$[FeIII]^{(exp)}$	*AARD*
–	$(m\cdot10)$	$(m\cdot10)$	(%)	$(m\cdot10^2)$	$(m\cdot10^2)$	(%)	$(m\cdot10^2)$	$(m\cdot10^2)$	(%)
PLS1	2.4,2.4,2.4	2.4,2.3,2.3	2	0.6,0.5,0.4	0.6,0.7,0.8	28	0.8,1.8,2.5	1.2,1.4,2.5	21
PLS2	2.4,2.4,2.4	2.2,2.3,2.4	4	0.7,0.5,0.4	0.6,0.65,0.8	24	0.6,1.6,2.4	1.0,1.5,2.1	21
PLS3	2.4,2.4,2.4	2.2,2.4,2.4	4	0.7,0.5,0.4	0.6,0.8,0.7	28	0.9,2.1,2.8	1.4,1.7,2.8	21

All calcs. based on $N_{FeIII,Cpy} = 0$, $N_{FeIII,Py} = -1$ & $N_{FeIII,Ph} = 14$. $S°/S^{2-}{}_{rx}$ (y_{Cpy}) = 0.35 – 0.3·[H^+], $S°/S^{2-}{}_{rx}$ (y_{Py}) = 0.99 – 0.3·[H^+] & $S°/S^{2-}{}_{rx}$ (y_{Ph}) = 0.05. Simulation incl. soluble oxides, *i.e.*, 2.7% Fe_2O_3 & 4.4% MgO; [a] T_r = 150ºC; [b] Range: 145-155ºC; [c] Rate constant & activation energy adopted (HBMS regression); [d] Avg. of bulk modal & chem. analyses (App. I.6); [e] From bulk modal analyses (App. I.6); [f] From chem. analyses (App. I.6); [g] Avg. of Si tie & weighed values.

Figure 7.49 *a* compares the measured and simulated dissolution kinetics of the pyrrhotite phase, using the adopted rate constant and activation energy values from the HBMS analysis. Clearly the lack of experimental data at short reaction times does not justify further regression and the values used are deemed adequate for this study. More importantly, a fraction of this phase appears to be

Stellenbosch University http://scholar.sun.ac.za

inaccessible to oxidation, probably due to the abundance of the gangue material (Figure 7.35). It is therefore assumed that approximately 10% of the other sulfides, *i.e.*, chalcopyrite and pyrite, are also not accessible to oxidation. Figure 7.49 *b* illustrates that the assumption of about 4.4 wt% magnesia (Eq. 7.89) yields acceptable acid tenors, despite some scattering of the experimental data.

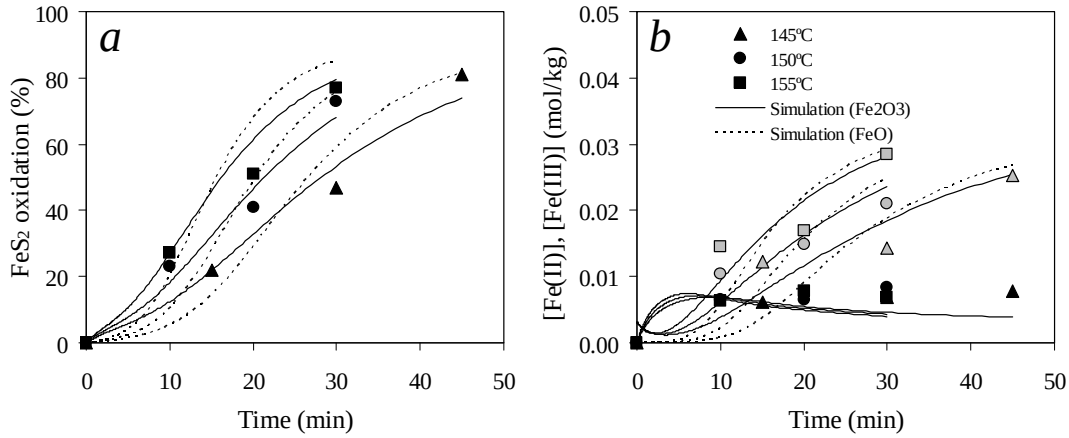

Figure 7.48
Comparison between the simulated & experimental FeS_2 oxidation extents & iron concentrations during oxidation of the MV concentrate (Sample H, starting with 25 g/L H_2SO_4, 15 g/L Cu, 0.15 g/L Arbo A02 LS, Orfom 2 QB) at different oxidation temperatures (700 kPa p_{O2}°) & different assumptions regarding the solubility of the apparent 'magnetite;' phase: *a*) FeS_2 oxidation extent; b) [Fe (II)] & [Fe(III)] (mol/kg).

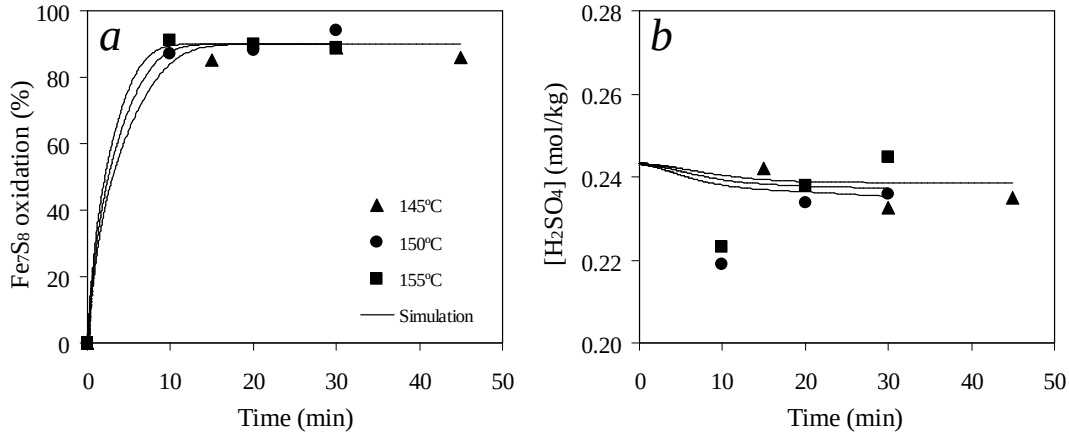

Figure 7.49
Comparison between the simulated & experimental Fe_7S_8 oxidation extents & H_2SO_4 concentration for the MV concentrate (Sample H, starting with 25 g/L H_2SO_4, 15 g/L Cu, 0.15 g/L Arbo A02 LS, Orfom 2 QB) at different oxidation temperatures (700 kPa p_{O2}°): *a*) Fe_7S_8 oxidation extents; *b*) [H_2SO_4] (mol/kg).

Stellenbosch University http://scholar.sun.ac.za

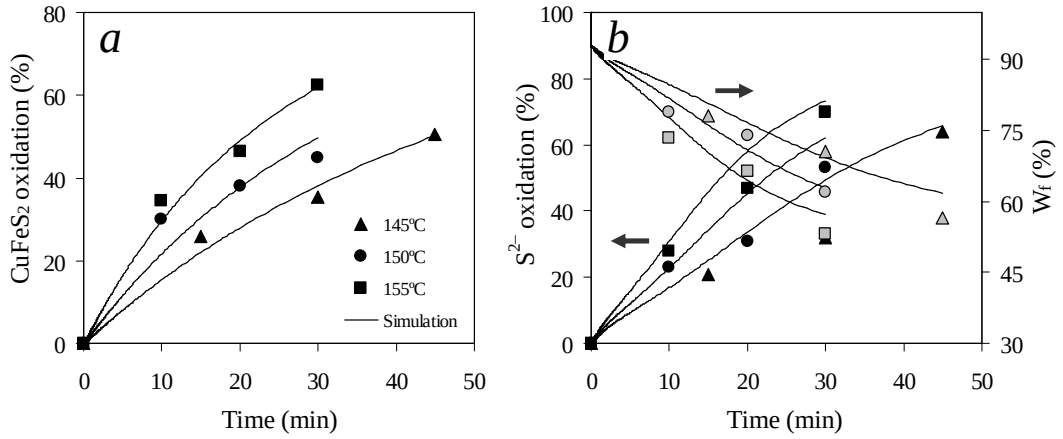

Figure 7.50
Comparison between the simulated & experimental $CuFeS_2$ & total sulfide oxidation extents, & (solids) mass loss for the MV concentrate (Sample H, starting with 25 g/L H_2SO_4, 15 g/L Cu, 0.15 g/L Arbo A02 LS, Orfom 2 QB) at different oxidation temperatures (700 kPa p_{O2}°): *a*) $CuFeS_2$ oxidation extents; *b*) Total sulfide oxidation extents & residue mass, W_f (% of head solids mass).

Figure 7.50 *a* compares the experimental and simulated chalcopyrite oxidation extents, suggesting a slightly higher than expected initial oxidation rate. The reason for this is unknown; due to experimental uncertainty no attempt is made to account for this effect and the apparently higher initial consumption of acid (Figure 7.49 *b*). This experimental uncertainty is also apparent in Figure 7.50 *b*. Despite accurate simulation of the residue mass, the (total) measured sulfide oxidation extents are relatively inconsistent with the measured chalcopyrite and pyrite mineral oxidation extents. These experimental inconsistencies may also be partly responsible for the differences between the measured and simulated elemental sulfur yields (Table 7.24). However, as observed for the HBMS and LT concentrates, the drop in sulfur yield towards longer reaction times may be associated with the strong dispersion characteristics of the Arbo A02 LS. The chalcopyrite oxidation rate constants are similar for the LT and MV concentrates under these low pulp density conditions, although the MV concentrate contained almost double the pyrite content (Table 7.2). The role of pyrite in accelerating the initial chalcopyrite oxidation rate should, however, not be disregarded; these aspects are revisited in Chapter 8 under higher pulp density conditions.

The intrinsic rate constants and activation energies of the sulfide minerals in all three concentrates are summarised in Figure 7.51. A correlation exists between the rate constant and the activation energy values, which is consistent with chemical reaction theory, *i.e.*, a lower activation energy is associated with a kinetically faster reaction. No further conclusions should be drawn from the absolute values of these constants, as they are only meaningful in context of the phenomenological model.

Stellenbosch University http://scholar.sun.ac.za

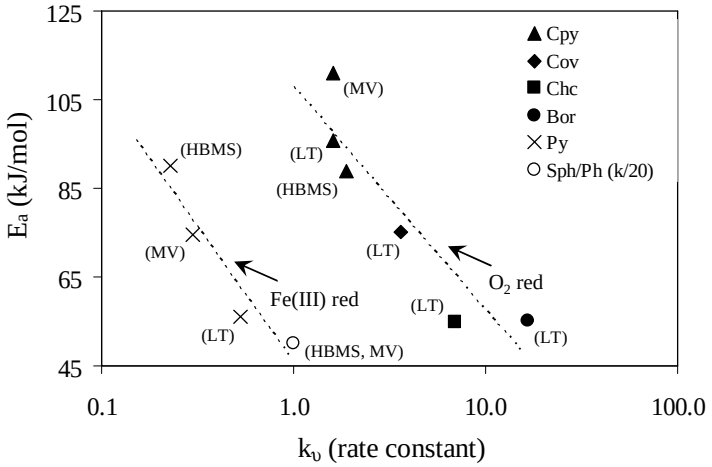

Figure 7.51
Comparison between the simulated reaction rate constants & activation energies of the various sulfide minerals in different concentrates. The closed symbols represent all constants based on the oxygen reduction mechanism, while the open symbols represent the constants based on a limiting iron(III) reduction mechanism.

7.5 Overview and recommendations

A clear distinction is made between the micro- and macro-models, *i.e.*, the micro-model only describes the rate at which particle size changes as a function of its solution environment (Ch. 6), while the macro-model accounts primarily for bulk property changes. The overall reactor model is a marriage between the micro- and macro-models, related by reaction extent, which, in turn, depends on the time-dependent solution properties at the mineral surface. Whereas no ambiguity exists in the case of a batch reactor, the continuous modelling framework demands simplification around the time dimension. The two extreme scenarios are discussed, *i.e.*, the maximum mixedness and segregated flow models, which drew primarily from the insights of Crundwell (1994b & 1995) for the heterogeneous case. The population balance (PB) for an ideal continuous stirred tank reactor (CSTR) is the most appropriate model and the relevant equations are derived from fundamental considerations.

The macro-model equations were derived using the mass conservation equation across all three material phases, while the elemental balance was used as a check. Analogous expressions were also derived to describe the energy balance around unit operations in the continuous, integrated autoclave circuit. An added complexity is the lack of thermodynamic data at the high temperatures of this study. Several simplifications are made: firstly, it was assumed that the term containing the temperature derivative of the species activity coefficient is significantly smaller than the partial molal enthalpy of that species in the actual solution. This allows all species enthalpies to be approximated by their standard partial molal enthalpies at the solution temperature. This approximation requires the well-known Maier-Kelley heat capacity parameters for each relevant

Stellenbosch University http://scholar.sun.ac.za

species. Although these are mostly available for the solid- and solution-phase species, this is not the case for most aqueous species, and further assumptions were required. Lewis linearization is employed to estimate the partial molal heat capacity at higher temperatures, *i.e.*, to obtain the Kelly b-parameters for the ions of interest. This method demands all aqueous species, except for the bisulfate ion, be considered from the formal concentration perspective. However, the thermodynamic data derived in Chapter 2 also allow an actual species approach; the results of these two methods are briefly compared in Chapter 8.

In terms of energy conservation, the steady-state adiabatic form is applied to the overall reactor model, and, after neglecting heat losses to the environment, reduces to an enthalpy balance around each reactor compartment. This calculation is configured to yield either the exit temperature or the heat duty (energy added or removed) at a specified exit temperature of the unit operation. Analogous number- and mass-conservation equations were also derived for the batch stirred tank reactor (BSTR), *i.e.*, to derive the intrinsic rate constants and activation energies from low pulp density leaching testwork (see below).

The experimental equipment and test procedures are discussed in detail. Three concentrates were tested, *i.e.*, cleaner concentrates from Hudson Bay Mining and Smelting Co Limited (HBMS) in Canada and Las Tortolas (LT) in Chile, and a rougher concentrate from Manto Verde (MV) in Chile. The HBMS concentrate was used to generate 'steady-state' continuous data during two integrated piloting campaigns, while detailed batch investigations followed in the 2-litre Parr autoclave at low pulp densities, utilising all three concentrates.

Detailed aspects of the pilot equipment, the operation of the integrated primary circuit and the continuous results are presented. The first campaign was characterised by a set acid recycle to the autoclave, *i.e.*, from the first solvent extraction operation (SX1). In reality, the recycle acid (& copper) concentration varied in the primary circuit, and true steady-state operation was never achieved. The reason for this was the lower than expected acid consumption of the HBMS concentrate, which is buffered by the ever-increasing extent of hydronium jarosite formation. During the second campaign, part of the pregnant leach solution (PLS) was recycled to the autoclave, to partially decouple the acid and (simulated) cooling requirements of the pilot autoclave from the SX1 unit operation.

Four periods of operation were selected to evaluate the overall continuous reactor simulation, *i.e.*, Periods 1 (P1), 2 (P2) and 3 (P3) in Campaign 2, characterised by varying acid concentration conditions, and Period 4 (P4) in Campaign 2, characterised by partial (~15%) PLS recycle. The particle size distributions (PSDs) also varied during Campaign 1: the finest grind (d_{90} of 7.0 µm)

Stellenbosch University http://scholar.sun.ac.za

was obtained during P1, while the PSDs during the other three periods were closer to the target d_{90} grind of 10 µm. The feed pulp densities were based on heat balance calculations, to give steady-state operation at 150ºC (during full-scale operation), despite the fact that isothermal operation, without external heating, was unattainable at pilot scale, due to excessive heat losses to the environment. The average autoclave residence time was in the region of 2 hours. Norlig A lignosulfonate (LS) and Orfom 2 Quebracho (QB) surfactants were tested during the two campaigns. The most significant upsets during the campaigns were caused by blockages of the inter-compartmental upcomer arrangements and the discharge pipe. This resulted in an increase in the autoclave slurry level in the preceding compartments and 85 to 95% reduction in the interfacial gas/liquid mass transfer coefficient. This, in turn, resulted in a sharp drop in the copper leaching and total sulfide oxidation extents during these events.

In general, the mass accountabilities of the primary elements are good, although some degree of uncertainty exists concerning the relative amounts of hydronium jarosite *vs.* hematite formed. Different analytical techniques were utilised to ascertain the relative abundances of these phases, *i.e.*, X-ray powder diffraction (XRD), Mössbauer-effect spectroscopy (MES), sulfate speciation, and assessment of the overall solid-phase mass losses. Despite these efforts, the amount of iron precipitated, *e.g.*, as hematite, is not exactly known and the residue sulfate content, after subtracting the 2 wt% sulfur associated with hematite phase (Ch. 5), is used to quantify this ratio. Autoclave profile samples are utilised as the primary source of this information, but, due to considerable sulfur speciation uncertainties and the presence of precipitated sulfate phases (*e.g.*, antlerite, $Cu_3(SO_4)(OH)_4$), the estimated extent of iron precipitated as hydronium jarosite may have varied up to ±15%. Despite these uncertainties, the relative amount of hematite (with the balance being jarosite) appears to have decreased from an initial level, higher than 70% during P1 to less than 50% during P2 and P3, while P4 was again characterised by improved hematite formation extents (60-70%).

Comparison between the measured and simulated results is first based on assumed iron precipitation extents, *i.e.*, without the inclusion of precipitation rate expressions, to focus attention on the behaviour of the different sulfide minerals in the multi-compartment pilot autoclave. The model is based on the assumption of a well-mixed reactor. This assumption was first tested by conducting simple wash-out tests, using HBMS pilot-plant feed material. Although this procedure only reveals that the slurry was well suspended, the conditions inside each autoclave compartment were so vigorous and the particle size distribution (PSD) so fine that the ideal CSTR methodology may be assumed under medium temperature (MT) autoclave conditions, *i.e.*, complete (uniform) suspension of the particulate phase

Stellenbosch University http://scholar.sun.ac.za

To correctly simulate the average residence time in the pilot autoclave, while maintaining consistency with all rate expressions (from batch data), a liquid density correlation is derived, using information from all the batch tests conducted in this study. Mass flow convergence is evaluated using one selected recycle stream as point of reference and by including all the species contributing to the total flow in that stream. Control of recycling coolant flow to the various autoclave compartments (to maintain autothermal operation) was not the objective here and the model is configured to only reflect pilot operation, *i.e.*, the total raffinate return was mixed with the feed concentrate and fed to the combined first two compartments (C #1+2). The raffinate compositions are modified slightly to approximately match the feed solution composition to the autoclave during each evaluation period.

An added complexity is the change in sulfide particle shrinkage behaviour due to the prevalence of sulfur agglomeration in the latter autoclave compartments due to surfactant degradation. Since particle shrinkage varies linearly over time (in a constant solution environment), while surface area changes, due to agglomeration, are difficult to account for, the reaction regime change is dealt with phenomenologically by considering reduced particle shrinkage rates after reaching fixed particle penetration depths (PPDs). The differential form of the PB is utilised for this purpose and solved numerically. This approach is no more empirical than the alternatives offered in the open literature.

After incorporating estimated pre- and post-leach reaction extents, the autoclave model is solved iteratively for each of the evaluation periods. Various assumptions are made, as only the intrinsic expression of chalcopyrite oxidation is available for the HBMS concentrate (Ch. 6). These assumptions (Sect. 7.4.1) evolve primarily around the relative dissolution rates, reaction stoichiometries and intrinsic elemental sulfur yields for each of the sulfide minerals in the HBMS concentrate. These aspects are summarised below after conducting follow-up batch tests, utilising improved experimental procedures and analysis methods. The preliminary continuous simulation yields the same results for the differential and integral methods during P1, when chalcopyrite oxidised rapidly due to the fine feed PSD. During the later periods, the reaction regime change approach (at estimated PPD) allows a qualitative simulation of the mineral dissolution behaviour and this approach is adopted in the rest of this study. Most importantly, the simulation successfully accounts for the effects of the reduced interfacial gas/liquid mass transfer rate due to autoclave blockages during P3 and P4. Furthermore, this preliminary modelling exercise emphasises the need to generate more detail around the relative mineral oxidation rates and their unique reaction stoichiometries, especially with regards to iron, as well as the intrinsic behaviour of sulfur on their surfaces. The apparent anomalous behaviour of pyrite under high pulp densities in the continuous autoclave is also noted, prompting a revisit of its intrinsic oxidation in the batch tests (below).

Stellenbosch University http://scholar.sun.ac.za

The batch testing equipment and procedure were similar to those utilised in other parts of this study (Ch 6), except that feed pumps were used to add the reagents 'at temperature'. This prevented premature oxidation of the sulfides, while the surfactants could be added batch-wise at the start of a kinetic test or over time, *i.e.*, in semi-batch fashion. The different mineral oxidation extents are quantified using bulk modal analyses of the autoclave residues at different reaction times. Due to the uncertainties regarding sulfur speciation in partially leached residues, an iterative calculation scheme is followed to obtain the elemental sulfur contents (Sect. 7.3.2). This produces more consistent results, but relies heavily on the bulk modal analyses of the head and residue samples, as well as the corresponding measured mass losses. Three different concentrates (HBMS, LT & MV) were tested using this procedure, with the objective of generating more information on the specific behaviour of the primary sulfide minerals.

A multiple-regression technique was employed to obtain the intrinsic rate constants and activation energies of the sulfide minerals, by integrating over the PSD of each head sample. The results from the bulk modal and chemical analyses are reconciled for the concentrates with relatively simple mineralogy and the objective function utilises average reaction extent values. In the case of the more complex mineral compositions, *e.g.*, the LT concentrate, the objective function only utilises the experimental results derived from the bulk modal analyses. The LS used in Chapter 6 and in the continuous pilot campaigns, Norlig A, had degraded at this point in time and a different surfactant (Arbo A02) had to be used. Although the intrinsic chalcopyrite oxidation rate is only marginally affected by this change, the elemental sulfur yield is significantly lower at high LS concentration levels (0.35 g/L). It is concluded that the dispersion characteristics of Arbo A02 are probably better than those of the Norlig A LS. Alternatively, the nature of the resulting elemental sulfur, when using Arbo A02, is such that its detection was problematic, *e.g.*, due to the formation of polymeric sulfur. However, at lower LS concentration levels (0.15 g/L), the results are very similar, and the rest of the study utilised dosages below 20 kg/t.

The main outcomes from this experimental programme are summarised below:

- The HBMS concentrate was prepared to include a wider PSD, skewed towards the smaller size fraction to assess the effect of particle size on the apparent activation energies. Similar activation energies are obtained during initial oxidation and at longer reaction times, suggesting that the same rate-limiting step exists between different particle sizes in the head material and that no fundamental change in the oxidation mechanism occurs
- To limit the number of rate-limiting steps that can influence the observed activation energy, a narrow temperature range of 145 to 155ºC was chosen. The observed activation energy of chalcopyrite in the HBMS concentrate is typical of the values reported in the open literature. Nevertheless, X-ray maps superimposed on backscatter electron (BSE)

Stellenbosch University http://scholar.sun.ac.za

images of partially leached material reveal that elemental sulfur layers are present on all particles, even in the presence of the highly effective Arbo A02 LS. The kinetic oxidation curves suggest that reactant diffusion through these layers only becomes restrictive at a point where surfactant degradation is prevalent and substantial particle agglomeration occurs. This is usually detected at reaction times longer than 45 to 60 minutes, based on the BSE images and the unreacted shrinking particle (USP) model plots

- A systematic drop in the overall elemental sulfur yield with increasing reaction times is observed in the case of the Arbo A02, while the yield is relatively constant in the case of Norlig A LS. This confirms that the former additive is more efficient in dispersing elemental sulfur, thereby exposing it to further oxidation to sulfate
- With regard to the behaviour of the different sulfide minerals, based on residue modal analyses, an induction (lag) period is observed during pyrite oxidation. On completion of this period (5-15 min), the pyrite oxidises at a relatively high rate compared to chalcopyrite. This lag period is prevalent, to a greater or lesser degree, for pyrite in all three concentrates. However, the residual pyrite content, based on bulk modal analyses alone, is suspicious, as the activation energy is significantly higher for the LT concentrate than most values published in the open literature. A revised analysis procedure, using the extent of total iron dissolution from chemical analysis and subtracting the other mineral oxidation extents, using the bulk modal results, yields a more realistic value of the activation energy. Notwithstanding, the observed lag period is still prevalent at all three oxidation temperatures, *i.e.*, at 145. 150 and 155ºC
- The fast oxidation rate of bornite in the LT concentrate is comparable to the oxidation rates of the sphalerite and pyrrhotite phases in the HBMS concentrate. The chalcocite phase also initially reacts fast, but then slows significantly at a point that coincides with the formation of covellite phase. This is seen as conclusive proof that chalcocite converts into a covellite phase over time, forming an impervious surface layer that oxidises at a significantly slower relative rate. Overall reaction stoichiometries are derived for each of these phases, which are subsequently adopted in the batch and continuous reactor models
- The bulk modal analyses are also essential in interpreting the sulfide mineral oxidation rates of the MV rougher concentrate. The initial USP model plots suggest a slower intrinsic oxidation rate of chalcopyrite compared to the LT and HBMS concentrates. However, the regression analysis, integrating over the full PSD, yields similar rate constants for the LT and MV concentrates. With regard to the dissolution rate of the pyrite phase, the lag period is less pronounced than for the HBMS and LT concentrates, but still prevalent. The low overall elemental sulfur yield (< 30%) is attributed to the high pyrite content, although the

Stellenbosch University http://scholar.sun.ac.za

strong dispersion characteristics of the Arbo A02 LS also play a role. The oxidation rate of the pyrrhotite phase is comparable to its corresponding rate in the HBMS concentrate

- The detailed regression analyses first focussed on the HBMS concentrate, *i.e.*, to re-evaluate the continuous pilot simulation, including the iron oxidation (Ch. 4) and precipitation (Ch. 5) modules. The intrinsic rate constant value of 1.9 $(\mu m/min)\cdot(kg/mol)^{2/3}$ is only marginally lower than the corresponding value of 2.0, derived in Chapter 6. The same rate expression is utilised in this part of the study, after incorporating an Arrhenius response to temperature. The default assumption is that the transfer of the first two electrons (per mole $CuFeS_2$ oxidised) occurs rapidly and is not related to the rate-limiting step. The fact that the dissolution rate of chalcopyrite is insensitive to the aqueous iron(III) concentration is seen as justification to assume that the oxygen reduction reaction is the limiting cathodic reaction during chalcopyrite oxidation, *i.e.*, once the refractory covellite-like surface has formed (see Ch. 6). Comparison between the measured and simulated iron(II) and iron(III) concentrations over time reveals that little, if any, net iron(III) reduces on chalcopyrite surface. Alternatively, if iron(III) is reduced at an appreciable rate, its re-oxidation by oxidising surface species is assumed to be part of the intrinsic surface mechanism. Inclusion of an iron(III) concentration term is therefore deemed redundant and, for all practical purposes, it is assumed that no net reduction of iron(III) occurs on chalcopyrite surface. As a first estimate, chalcopyritic lattice iron is assumed to enter the bulk solution in the reduced state (see below)
- Experimental sphalerite and pyrrhotite dissolution data, especially for the initial oxidation reaction, is limited, and either the iron(III) or oxygen reduction mechanism may be adopted in the phenomenological model. The latter mechanism becomes plausible if covellite surface layers form rapidly *via* the interaction of aqueous copper(II) with a relatively reducing sulfide surface (see Ch. 6). However, since the observed sphalerite (& pyrrhotite) oxidation reaction is so fast, it is unlikely to involve a refractory covellite surface layer, which makes the irreversible iron(III) reduction reaction the logical choice for this study. Since bonding electrons in the mineral surface would be exchanged with individual iron(III) ions, in one-electron transfer steps, a high elemental sulfur yield of 95% is adopted for these phases. Since the surfaces of these minerals are assumed to be more reducing compared to pyrite, iron from their mineral lattices is proposed to enter the bulk solution in the reduced state
- Comparison between the measured and simulated reaction rates of pyrite in the HBMS concentrate reveals that a step change of its rate constant value cannot adequately describe the initial lag period followed by an increased oxidation rate. Instead, the iron(III) reduction mechanism gives a better representation of the observed S-shape kinetics. Since

Stellenbosch University http://scholar.sun.ac.za

the presence of refractory oxide layers and possible passivation by flotation reagents are both ruled out as possible causes of this initial lag period, the iron(III) reduction mechanism is adopted and assumed to partake in the rate-limiting step. This demands a revisit of the mechanistic proposals of Chapter 6 (see Sect. 6.3.4). Whereas the t_{2g} orbital of the lattice iron was previously assumed to directly catalyse the reduction of adsorbed diatomic oxygen, the complexation of aqueous iron(III), on the solution side of the interface, also needs to be considered. This is the only mechanism perceived to be consistent with the apparent dependency of the reaction rate on the iron(III) concentration, as well as the low (< 5%) observed sulfur yield. Although no fundamental basis is presented to support such mechanism, the strong interaction of diatomic oxygen with the pyrite surface, as well as its complexation with aqueous iron(III), is assumed to lower the activation energy of the first oxygen reduction step. Diatomic oxygen is therefore proposed to be a suitable electron transfer agent, catalysed by its complexation with both lattice iron and aqueous iron(III) species. Only the first electron transfer step is considered to be rate limiting and the resulting rate expression is analogous to the direct iron(III) reduction mechanism, under limiting iron(III) tenor. The pyrite oxidation rate expression for oxidation by iron(III), as proposed by Holmes and Crundwell (2000) *via* a detailed electrochemical study, is also adopted in this study. However, there is no need to consider the reversible surface oxidation of iron(II) from a phenomenological modelling perspective, whilst the exact reaction order with respect to the hydrogen ion concentration (anodic dissolution reaction) has an insignificant impact on the overall regression results. Uncertainties related to the pyrite oxidation and iron(III) reduction extents on different minerals justify the use of a simplified pyrite reaction rate expression, with a minimum number of adjustable parameters. This simple rate expression is only expanded to include an Arrhenius response to temperature change. Due to the oxidative nature of the pyrite surface (see discussions in text, Sect. 6.3.2 & 6.3.4), all pyritic iron is assumed to enter the bulk solution in the oxidised state. Although this revised picture of the pyrite oxidation mechanism provides the methodology to simulate the pyrite oxidation kinetics under low pulp densities, other possibilities should not be ruled out. Alternative mechanisms could include the precipitation of iron(III) on pyrite surfaces, *e.g.*, as hydronium jarosite, and the galvanic protection of pyrite by minerals such as chalcopyrite. It is recommended that future studies focus on the mechanism of pyrite oxidation under MT autoclave conditions using pure mineral samples

- All the above assumptions were incorporated into the overall phenomenological model, after which the rate constants and activation energies of sulfide minerals in the HBMS concentrate were re-regressed. The S-shape pyrite oxidation curves are best represented by the assumption that chalcopyritic iron enters the bulk solution in the reduced state; this

Stellenbosch University http://scholar.sun.ac.za

premise is also applied in the rest of this study. These intrinsic constants were incorporated into the CSTR model, including the iron(II) oxidation (Ch. 4) and iron(III) precipitation (Ch. 5) modules. The estimated variation in the value of the enhancement factor (κ; Figure 5.31; see high pulp density batch simulations in Ch. 8, Sect. 8.3.1), yields realistic estimates of the hematite precipitation rates in the continuous pilot autoclave

- Overall, the simulated results are in good agreement with the pilot results, except for the extent of pyrite oxidation. The pyrite oxidation rate appears to be particularly sensitive to the sulfur dispersion efficiency of the surfactants. The lower than expected oxidation rate of pyrite in the pilot campaigns was ascribed to the inefficient dispersion of elemental sulfur by Norlig A LS at longer reaction times and higher pulp densities compared to the efficient dispersion of sulfur by Arbo A02 LS during low pulp density batch experimentation; this assumption is revisited in Ch. 8 (Sect. 8.3.1). After reducing the simulated pyrite oxidation rate and increasing the raffinate acid concentration by a mere 5 g/L during P1 (better simulating the autoclave feed acidity), the calculated hematite content ($W_{f,Hem}$) is in closer agreement with the measured results. The phenomenological model responds in a manner consistent with the observed continuous pilot results and highlights the sensitivity of the hematite content to the operating conditions, feed mineral and solution compositions and oxidation reaction extents. Periods P2 and P3 during the first campaign were characterised by higher and varying hydronium jarosite contents, reaffirming its buffering action on the excess acid concentration in the primary leaching-SX circuit. Besides the fact that the high primary circuit acidity during these periods does not resemble typical industrial operation, some redissolution of the iron precipitates occurred during sampling. This complicates a direct comparison between the simulated and pilot results. Excellent agreement between the simulated and pilot results are obtained for P4 (Campaign 2), operated under more realistic raffinate acid concentrations and allowing partial (15 wt%) PLS recycle. The calculated residue hematite content is in particularly good agreement with the measured results when simulated in closed-circuit configuration, using the (pilot) target parameters of 90% copper extraction (SX1) and 30% raffinate bleed from the primary circuit, as well as 4 kg water per kg dry solids addition during washing of the final residue cake. The weak point in the overall model is, without doubt, its inability to accurately capture the extent of elemental sulfur formation and its effect on the oxidation rate of sulfide minerals, especially pyrite. Variation in the effectiveness of the different surfactants and the effects of aging appear to impact more strongly on the pyrite oxidation rate, while the regime change after surfactant degradation (45-60 min) is difficult to quantify accurately. Nevertheless, the approach of enforcing a regime change at a fixed PPD is no more empirical than the current alternatives offered in the open literature

Stellenbosch University http://scholar.sun.ac.za

- The regression of the oxidation rates of the LT cleaner and MV rougher concentrates followed the same methodology as discussed above for the HBMS concentrate. The yields of elemental sulfur on chalcopyrite and pyrite surfaces are assumed to be the same as for the HBMS concentrate. Comparison between the calculated and measured iron(II) and iron(III) concentrations over time re-affirms the above assumptions with regard to chalcopyrite and pyrite reaction stoichiometries and iron oxidation states. The regressed intrinsic chalcopyrite rate constants for the LT and MV concentrates are only marginally lower (~16%) than those for the HBMS concentrate, while the activation energies are slightly higher, but within the typical literature range. The reaction rate constant of pyrite varies substantially between these three concentrates and is very sensitive to the calculated iron(III) concentration at each point in time. Although there is considerable uncertainty with regard to the absolute values of the pyrite rate constants due to the presence of molten elemental sulfur, the highest rates correspond to the lowest activation energies, which is consistent with chemical reaction theory. The other copper minerals in the LT concentrate, *i.e.*, chalcocite, covellite and bornite, are simulated in analogous fashion to chalcopyrite. The presence of copper(I) in the surface lattices of these minerals is assumed to catalyse the reduction of diatomic oxygen at high temperatures. Although the reduction of iron(III) may be the primary (relatively faster) oxidation mechanism, the presence of copper and highly oxidised surface species are assumed to rapidly re-oxidise iron(II) on these surfaces, allowing the use of the overall oxygen reduction reaction, and its associated rate expressions, in the phenomenological model. The yield on the bornite surface is assumed to be relatively high (~75%), *i.e.*, to be consistent with mostly iron(III) reduction taking place on the surface, while the covellite mineral and the covellite-like phase forming on the chalcocite surface are assumed to interact predominantly with diatomic oxygen. The sulfur yield is therefore assumed to be relatively low (~40%). These assumptions result in reasonable estimates of the overall observed elemental sulfur yields and terminal acid concentration over time, which justifies adopting these characteristic sulfur yields in the rest of this study
- By adopting the same functional forms of the rate expressions for the different copper minerals in the phenomenological modal, a quantitative comparison is made between their intrinsic reaction rate constant values. Bornite oxidises an order of magnitude (10×) faster than chalcopyrite, while chalcocite initially reacts more than four times faster that chalcopyrite. Conclusive proof is presented that chalcocite converts into a covellite phase, which is in line with the literature (Sect. 6.3.2). This phenomenon is simply accounted for by adopting a relatively slower (~half) oxidation rate regime for the unreacted shrinking particle core, *i.e.*, for chalcocite, above a fixed product layer (covellite) thickness.

Stellenbosch University http://scholar.sun.ac.za

The oxidation rate of covellite after this point is still more than double that of chalcopyrite, suggesting that this mineral is different from the refractory surface structure on partially leached chalcopyrite

- Bulk modal analyses and residual acid tenors suggest that acid-soluble oxide fractions are present in the MV rougher concentrate. These are accounted for by assuming total dissolution of 4.4 wt% magnesia and 2.7 wt% amorphous hematite, with the latter species accounting for an apparently soluble 'magnetite' phase, *i.e.*, according to the bulk modal analysis. Furthermore, not all sulfides are liberated, since about 10 wt% pyrrhotite phase remains intact after rapid initial oxidation. This locked fraction is also assumed to apply proportionally to the other sulfide minerals in this rougher concentrate, yielding a chalcopyrite reaction rate constant comparable to that of the LT concentrate. However, the initial oxidation rate of the chalcopyrite appears to be slightly faster than anticipated from the PSD of the MV concentrate, which is also reflected by a temporary drop in the initial acid concentration. This could have been due to the catalytic effect of the relatively abundant pyrite phase in this concentrate (Sect. 6.3.4) (which is explored further in Ch. 8)
- The intrinsic rate constants and activation energies of the sulfide minerals in all three concentrates are compared. Lower activation energy values are associated with the kinetically faster reactions, which is consistent with chemical reaction theory. All the regressed intrinsic rate constant and activation energy (rounded) values are summarised below. Since these values are based on a limited number of experimental datapoints and many assumptions, they are only meaningful in context of this phenomenological model.

Table 7.25
Linear rate constants & activation energies of sulfide minerals in HBMS, LT & MV concentrates.

Concentrate	[a] $k_{\upsilon,Cpy}$	[b] $E_{a,Cpy}$	[a] $k_{\upsilon,Cov}$	[b] $E_{a,Cov}$	[a] $k_{\upsilon,Bor}$	[b] $E_{a,Bor}$	[a] $k_{\upsilon,Chc}$	[b] $E_{a,Chc}$
HBMS	1.9	89	–	–	–	–	–	–
LT	1.6	96	3.6	75	16.6	55	6.9	(55)
MV	1.6	111	–	–	–	–	–	–
Concentrate	[c] $k_{\upsilon,Py}$	[b] $E_{a,Py}$	[d] $k_{\upsilon,Sph}$	[b] $E_{a,Sph}$	[d] $k_{\upsilon,Ph}$	[b] $E_{a,Ph}$	–	–
HBMS	0.2_3	90	20	(50)	20	(50)	–	–
LT	0.5_3	56	–	–	–	–	–	–
MV	0.3	75	(20)	(50)	20	(50)	–	–

Bracketed values are assumed (not regressed). [a] T_r = 150ºC & units of (µm/min)·(kg/mol)^{⅔}; [b] E_a in units of kJ/mol, over the 145-155ºC range; [c] T_r = 150ºC & units of (µm/min); [d] T_r = 150ºC & units of (µm/min)·(kg/mol)^{½}.

Stellenbosch University http://scholar.sun.ac.za

CHAPTER 8. MODEL APPLICATION

8.1 Introduction

This chapter focuses on the application of the overall model to high pulp density oxidation in batch and continuous reactor configurations. The overall model comprises the modules presented in the previous chapters and therefore no additional theory is presented here. The testwork is limited to high pulp density oxidation in a stand-alone batch reactor, while the continuous model investigates sensitivities of the most important reaction extents to changes in the key control parameters of the integrated process flowsheet.

The most important aspects covered in this chapter may be summarised as follows:

- Measuring and validating the mineral oxidation response at high pulp density conditions under typical medium temperature (MT) autoclave acidities, as well as under conditions where high copper extraction and hematite stability overlap, *i.e.*, at finer (feed) particle size distributions (PSDs) and lower head solution acidities (Sect. 8.2 & 8.3.1)
- Verifying the overall simulation performance under these high pulp density batch autoclave conditions and relatively wide operating parameter space, where necessary modifying the relevant rate expressions and/or stoichiometric coefficients (Sect. 8.3.1)
- Developing a phenomenological picture of the mineral oxidation mechanisms, as well as insights into the overall leaching-precipitation system behaviour under high pulp density conditions in batch and continuous autoclaves (Sect. 8.3.1 & 8.3.2), and
- Conducting continuous autoclave simulations under autothermal operation in an integrated primary flowsheet, and studying the sensitivities of selected reaction extents, solution species concentrations and circuit properties to step-changes in important operating parameters, *e.g.*, feed mineralogy, PSD and autoclave temperature (Sect. 8.3.2).

8.2 Experimental

This section briefly discusses the experimental procedures used to measure the important reaction extents in the 2-litre batch autoclave. A summary of the PSDs, chemical and mineralogical compositions is also presented, focussing on the cleaner concentrates from Hudson Bay Mining and Smelting Co Limited (HBMS) in Canada and Las Tortolas (LT) in Chile (Los Bronces orebody).

8.2.1 Equipment and procedures

The 2-litre Parr autoclave was used to conduct these batch leaching experiments. The autoclave, internals and peripherals are discussed in detail in Chapter 3 (Sect. 3.3; Figure 3.1) and Chapter 6 (Sect. 6.4.1). The feed pump system was used to add relatively large solution volumes of the active

Stellenbosch University http://scholar.sun.ac.za

reagents 'at temperature' (see Sect. 7.3.1 for details of this setup & the associated experimental procedures). The only additional feature of this testwork was the use of higher pulp densities, while, in selected cases, the cumulative consumption of oxygen was measured and recorded by a Bronkhorst digital mass-flow meter.

With regard to the interpretation of data, no bulk modal analyses of residue minerals (Sect. 7.3.1) were conducted, because all these tests were accompanied by simultaneous iron(III) precipitation. Only chemical analyses are therefore utilised to derive the various reaction extents, using the analysed residue and solution values from two different laboratories, *i.e.*, Anglo American Technical Solutions (Research) (ATS) and SGS South Africa Pty Ltd. Average values are used, except in exceptional cases where discrepancies are notable and significantly better mass accountability or consistency is achieved by using either the one or the other laboratory result. As explained in Section 6.4.2, solids residue analyses are most important in determining the overall oxidation and leaching extents (also see Sect. 7.3.1). ATS and SGS used inductively coupled plasma – optical emission spectroscopy (ICP-OES) and X-ray fluorescence (XRF) methods (App. B.2.1), respectively, to determine the solid-phase metal concentrations. Due to the problems associated with obtaining accurate residue sulfur speciation analyses (Sect. 7.3.1), only the conventional total sulfur and sulfate sulfur analysis methods (App. B.2.2) are assumed accurate. Sulfide sulfur values were determined after extending the leaching time, in hot (> 90ºC) tetra-chloroethylene solution (App. B.2.2), to more than 5 hours. The actual elemental sulfur values were then calculated by difference, *i.e.*, after subtracting these sulfide and sulfate sulfur values from the total sulfur values.

8.2.2 Data interpretation

In view of the previous experimental observations, reported in Chapter 6 and 7, the intrinsic mineral oxidation rates rely heavily on the effective use of sulfur-dispersing agents (surfactants). Most oxidation testwork was conducted in the presence of both Arbo A02 lignosulfonate (LS) and Orfom 2 Quebracho (QB), while selected tests only utilised Borrepal LS (see Sect. 6.3.3). As in previous chapters, each kinetic datapoint was obtained by conducting a separate test. Solid-phase mass loss over time ($W_{f,t}$) was directly obtained by residue weighing and the important reaction extents were calculated in the normal manner (Sect. 7.3.2). Due to the complex mineralogical breakdown of the LT concentrate, the relative mineral oxidation extents cannot be derived from the overall extents of metal dissolution. However, in the case of HBMS concentrate, the chalcopyrite mineral oxidation rate is directly related to the overall copper extraction rate, while the sphalerite oxidation rate corresponds to the total zinc extraction rate. Furthermore, the assumption is made that the pyrrhotite mineral phase, as well as sphaleritic iron, dissolve at the same rate as zinc, which allows the unreacted pyrite content to be estimated from the total residue sulfide content, *i.e.*, from

Stellenbosch University http://scholar.sun.ac.za

the difference between the total unreacted sulfide content and the residual sulfide remaining in the chalcopyrite, sphalerite and pyrrhotite minerals.

Finally, the hematite and hydronium jarosite contents are calculated iteratively, based on the total iron and sulfate contents in the residue. Firstly, the total iron remaining in chalcopyrite, pyrite, sphalerite, pyrrhotite and estimated hydronium jarosite phase, is subtracted from the total residual iron content to obtain the amount of hematite present (other possible iron(III) polymorphic phases are ignored). The sulfate adsorbed onto hematite (assuming 2 wt% S^T; Sect. 5.3.3) is then subtracted from the total residual sulfate content, to obtain an updated value of the hydronium jarosite content (no other sulfate phases are assumed to be present in the washed residue). This calculation is repeated until a converged hematite content ($W_{f,Hem}$; normalised to the total hematite plus hydronium jarosite mass) is obtained.

8.2.3 Sample preparation and characterisation

The following discussions refer to the head samples used in the experimental batch programme, *i.e.*, freshly milled HBMS 777 cleaner concentrate of different PSDs (unscreened), namely Samples I, J and K, and two LT cleaner concentrate samples, namely Sample G (pre-screened & relatively coarse; Sect. 7.3.3) and the fine-milled Sample L.

Feed particle size

The milling procedure was identical to that described in Section 6.4.3. Except for Sample G, no micro-screening was employed, hence the relatively wide PSDs. These results are summarised in Figure 8.1 (including the d_{10}, d_{50} & d_{90} percentile values; see detailed results in App. J.1).

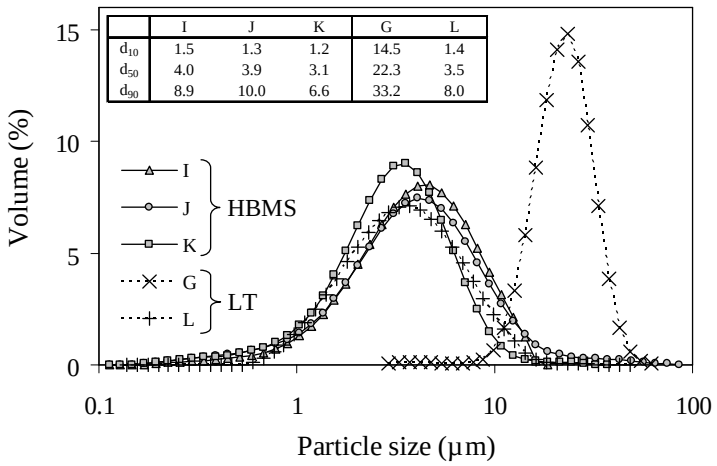

Figure 8.1
Size fractions used in the high pulp density batch oxidation testwork (the solid & open symbols refer to the HBMS & LT concentrates, respectively).

Stellenbosch University http://scholar.sun.ac.za

The PSDs of the three HBMS concentrate samples are comparable to the feed material used in the continuous pilot campaigns (Figure 7.10). Despite measuring the response of the relatively narrow-sized and coarse LT sample (G) under low pulp density conditions (Sect. 7.4.2), the impact of higher pulp density on the oxidation rate of minerals like pyrite and the copper leaching rate are of interest here. The PSD of the milled LT sample (L), on the other hand, is in qualitative agreement with the HBMS samples (I, J & K) and is also illustrated in Figure 8.1.

Mineralogical and chemical composition

Good comparison was previously obtained between the measured mineralogical (bulk modal) composition of the head samples and the corresponding calculated values (from chemical analyses) (Sect. 7.3.3). This justifies the use of the latter approach in this chapter, as accurate bulk-modal analyses of the residues could not be obtained under these higher pulp density conditions, due to the presence of precipitated iron(III) phases. These calculated mineral abundances (Table 8.1) are also similar to the values used in the (overall) simulation of the primary leach (Sect. 8.3.2). Since the differences between the calculated mineral abundances of the three HBMS samples are less than the typical variation due to analytical error, only the geometric average values are used (Table 8.1). Preliminary bulk modal analyses revealed qualitative agreement with these calculated values. However, indicative Scanning electron microscope (SEM) – Energy dispersive X-ray (EDX) scans (App. B.3.2) suggested slightly lower iron content in the sphalerite phase (~5%), compared to the values reported for the pilot feed material (Sect. 6.4.3). This mineral substitution is simplified by treating it as a pure FeS phase, and using the rounded value of 7.5 wt% (*ref*. total sphalerite-phase abundance), while the pyrrhotite content of the concentrate is assumed to be similar to that of the pilot plant feed (~1.3 wt%; Table 6.5). Uncertainty with regard to the unidentified sulfate phase (Sect. 6.4.3) justifies the simplified approach of assuming a (Cu,Fe)SO_4 mineral at a rounded mass ratio of 2:1 $FeSO_4$:$CuSO_4$. The relative abundances of $CuSO_4$ and $FeSO_4$ are therefore calculated (iteratively) to be consistent with the total measured sulfate content of 1.4%. The magnesium and calcium species are assumed to be present as acid-consuming carbonates, using a rounded mass ratio of 2:1 $CaCO_3$:$MgCO_3$. The abundance of magnesium carbonate is obtained from the stoichiometric average amount of magnesium leached (App. J), which, in turn, is used to estimate the leachable calcium carbonate content. The abundances of chalcopyrite and sphalerite are directly calculated from the total copper (excluding $CuSO_4$) and zinc contents, respectively. The pyrite content is calculated as the difference between the total analysed sulfide content and the sulfide in the other mineral phases.

In the case of the relatively complex LT concentrate samples (G & L), no unique mineral composition can be derived from only using the chemical analyses. As a first estimate, the relative abundance of the sulfide minerals in Sample L is scaled to the (chemically analysed) total copper

Stellenbosch University http://scholar.sun.ac.za

and iron contents, using the relative chemical and mineral compositions of Sample G as basis, *i.e.*, as determined by the bulk modal analysis (Sect. 7.3.3). Assumptions similar to those described above are made regarding the sulfate and carbonate phases in the LT concentrate, despite the lack of mineralogical evidence. Nevertheless, these assumptions result in relatively good agreement between the chemically analysed and calculated (formal) species concentrations (see Table 8.2).

Table 8.1
Mineralogical abundance of the head samples used in the high pulp density batch simulations.

Mineral	[a] Samples I, J, K (HBMS) (%)	[e] Sample G (LT) (%)	[f] Sample L (LT) (%)
$CuFeS_2$	74.22	63.20	56.80
Cu_2S	0.00	8.90	8.00
CuS	0.00	3.20	2.88
Cu_5FeS_4	0.00	4.10	3.69
ZnS	6.26	0.00	0.00
FeS	0.51	0.00	0.00
Fe_7S_8	1.30	0.04	0.03
FeS_2	8.62	16.30	14.75
[b] $CuSO_4$	0.75	0.00	0.16
[b] $FeSO_4$	1.50	0.00	0.32
[c] $MgCO_3$	0.29	0.42	0.41
[c] $CaCO_3$	0.58	0.85	0.82
[d] Inert	5.97	2.99	12.15
Total	100.00	100.00	100.00

[a] Geometric avg. of three HBMS samples; [b] Unidentified (Cu,Fe) sulfate phase, assuming $FeSO_4$:$CuSO_4$ (wt) ratio of 2; [c] Carbonates assumed to be proportional to leachable Mg content (App. J), based on $MgCO_3$:$CaCO_3$ (wt) ratio of 2; [d] Balance assumed to consist of inert phases; [e] From bulk modal analysis (Sect. 7.3.3); [f] Estimated, using comparative chem. analyses of Sample G & L, & Sample G mineralogical breakdown.

These calculated chemical and mineralogical compositions are directly applied in the batch reactor simulations (next section), assuming that the sulfate and carbonate phases dissolved rapidly under MT autoclave operating conditions. It is also worth noticing that the two LT samples contain almost twice the average pyrite content compared to the HBMS samples (Table 8.1).

With regard to the degree of liberation (App. B.3.2) of the LT copper sulfide minerals, a relatively minor degree of (physical) particle association was detected, even in the case of coarser fraction (Sample G). Figure 8.2 illustrates that 92% of the total particle surface area (TPSA, *i.e.*, not the polished section area) of the copper sulfide minerals fall within the >80% liberation class, while an average of 88% and 69% fall in the >90% and 100% liberation classes, respectively.

Stellenbosch University http://scholar.sun.ac.za

Table 8.2
Measured & calculated chemical analyses of the head materials used in the high pulp density batch oxidation testwork.

Species	Samples I, J & K (HBMS)		Sample G (LT)		Sample L (LT)	
	[a] Meas. (%)	[b] Calc. (%)	Meas. (%)	[b] Calc. (%)	Meas. (%)	[d] Calc. (%)
Cu	26.0	26.0	32.8	33.6	30.2	30.4
Fe	28.7	28.3	28.4	27.3	24.7	24.7
Zn	4.2	4.2	0.0	0.0	0.0	0.0
Ca	–	0.17	–	0.34	–	0.34
Mg	–	[c] 0.06	–	[c] 0.12	–	[c] 0.12
CO_3	–	0.4	–	0.8	–	0.8
SO_4	1.4	1.4	0.0	0.0	0.3	0.3
S^{2-}	33.3	33.3	33.8	34.7	30.7	31.3
Total	–	93.8	–	97.0	–	88.0

[a] Geometric avg. of the three HBMS samples; [b] Back-calculated from mineralogical composition; [c] Leachable fraction (App. J); [d] Consolidated chemical composition, using estimated mineralogical breakdown (Table 8.1).

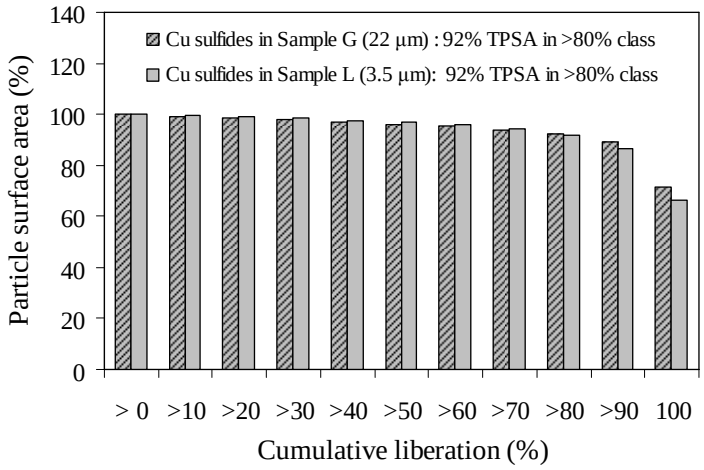

Figure 8.2
Comparison of the degree of total copper sulfide mineral liberation (cumulative) in the coarser (G) & finer (L) LT concentrate samples, expressed in terms of the total particle surface area (TPSA).

The mineral association results summarised in Table 8.3 confirm that the copper sulfide minerals are poorly associated with the other sulfides (mainly pyrite). Accelerated chalcopyrite oxidation by classical (mineral-mineral) galvanic contact with pyrite is therefore expected to be insignificant. Most importantly, there is hardly any difference in copper sulfide mineral association between the coarser (G; $d_{50} \approx 22$ µm) and finer (L; $d_{50} \approx 3.5$ µm) samples. This is an important observation, since Section 8.3.1 elaborates on possible reasons for the apparent enhanced copper leaching rate from this coarser sample.

Stellenbosch University http://scholar.sun.ac.za

Table 8.3
Association of the copper sulfide minerals (TPSA) in the LT concentrate samples.

Sample	[a] Liberated Cu (%)	[b] Free Cu/G (%)	[c] Free Cu/Py (%)	[d] Free Cu/(Py) (%)	[e] Locked Cu (%)
G	71.5	24.8	2.8	0.9	0.0
L	66.1	22.8	10.4	0.7	0.0

[a] Fully liberated (100% TPSA); [b] Partially liberated (<100% TPSA) & associated with gangue minerals; [c] Partially liberated (<100% TPSA) & associated with 'surface-exposed' pyrite; [d] Partially liberated (<100% TPSA) & associated with 'locked' pyrite; [e] Not liberated (0% TPSA).

8.3 Results and discussion

The experimental and simulated results are subdivided into two sections. Section 8.3.1 compares the high pulp density batch experimental results with the simulated output. This information is then used to modify selected rate expressions and to generate additional information, aiming to improve the performance of the generalised model. Section 8.3.2 elaborates on the continuous autoclave simulation, imbedded within the primary hydrometallurgical circuit. This simulation was used to conduct sensitivity analyses of the important reaction extents, species concentrations and other circuit properties with respect to changes in selected key control parameters.

8.3.1 Simulating the high pulp density batch oxidation of the HBMS and LT concentrates

The batch oxidation tests were conducted at different initial acid and iron concentrations, while fixing the initial copper concentration at 5 g/L and, in the case of the HBMS concentrate, a constant initial zinc concentration of 5 g/L. The first five series of tests (PLT1-PLT5; App. J.2) utilised moderate initial acid (& iron) concentrations of 30 g/L H_2SO_4, 5 g/L Fe(II) and 5 g/L Fe(III), using HBMS Sample I ($d_{90} \approx 9$ µm), different surfactants and surfactant concentrations. These simulations utilise the rate constant and activation energy values in Table 7.25 (Ch. 7).

Figure 8.3 *a* compares the chalcopyrite and pyrite simulations for Series PLT1, while Figure 8.3 *b* presents the comparative overall sulfur yields and corresponding acid concentrations. Despite achieving reasonably accurate chalcopyrite oxidation extents, the simulated pyrite oxidation rate is clearly too high when the rate expression is based on the iron(III) concentration, as derived from the low pulp density testwork in Section 7.4.2 (see Eq. 7.84). Even with the inclusion of the (reverse) surface oxidation of iron(II) (Eq. 7.83), no significant improvement of the simulation is observed. Approximately a ten times (10×) reduction in the intrinsic rate constant value (*ref.* Table 7.25) is required to correctly simulate the pyrite oxidation extent over time. This is exactly in line with the observations from the continuous pilot plant simulation (Sect. 7.4.2), also applied to relatively high pulp densities. This phenomenon was previously ascribed to the relatively inefficient Norlig A LS, used in the pilot campaigns, compared to the Arbo A02 LS, used in the low pulp density batch oxidation tests (Sect. 7.4.2). These tests also utilised (~6 kg/t) Arbo A02

Stellenbosch University http://scholar.sun.ac.za

LS, while the measured oxidation extents are clearly much lower than anticipated, even after 15 minutes. This discrepancy in the pyrite oxidation rate is therefore not due to surfactant degradation.

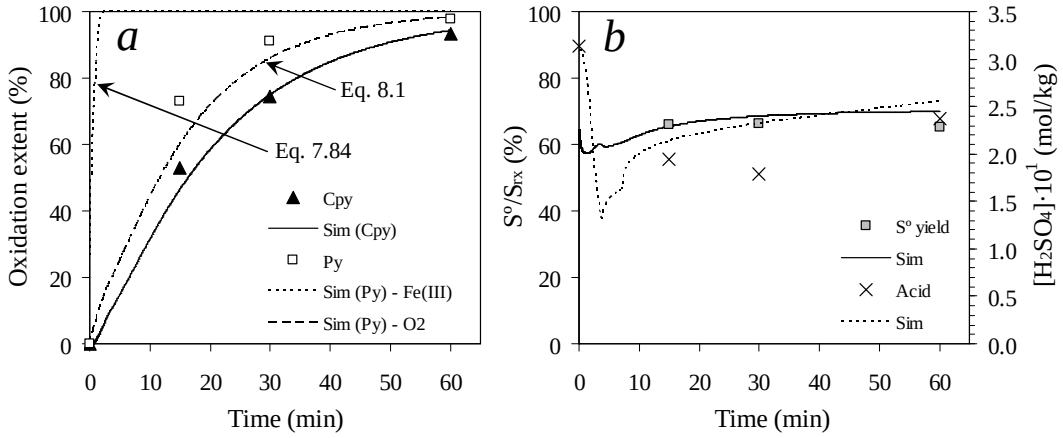

Figure 8.3
Comparison between the experimental & simulated reaction extents of Series PLT1 (HBMS 777 concentrate; 8.85 wt% Sample I) at 150ºC (700 kPa p_{O2}º), starting with medium acidity of 30 g/L H_2SO_4 (5 g/L Cu, Zn), 5 g/L Fe(II) & 5 g/L Fe(III), using optimised mineral rate constant values (Table 7.25) & elemental sulfur yields (see below): *a*) Comparative $CuFeS_2$ & FeS_2 oxidation extents; *b*) Comparative elemental sulfur yields & terminal acid concentrations.

The parallel oxygen and iron(III) reduction pathways, as proposed by Holmes and Crundwell (2000), also cannot account for these observed inconsistencies between the low and high pulp density conditions. It is therefore proposed that both iron(III) and dissolved oxygen are intrinsic elements of the rate-limiting step of pyrite oxidation, which is in line with the proposals of Chapter 7 (Figure 7.41). That the dissolved oxygen concentration during initial oxidation is significantly lower under these higher pulp density conditions (*cf.* low pulp density oxidation; see below), suggests that the slow supply of diatomic oxygen may be limiting to the overall rate in this case. On the other hand, pyrite often exhibits relatively long lag periods at lower pulp densities (~1 wt% solids) and without iron(III) in the initial solution (Sect. 7.4.2 & 7.4.3), despite undergoing relatively rapid oxygenation. This suggests that the contributions of both of iron(III) and diatomic oxygen are important. Figure 8.3 *a* illustrates that under high pulp density conditions, the pyrite oxidation rate is phenomenologically better described by the original rate expression (Sect. 6.6.2):

$$k_{\ell,Py} = -\upsilon_{\ell,Py} = k_{\upsilon,Py} \cdot exp\frac{-E_{a,Py}}{R_g}\left(\frac{1}{T} - \frac{1}{T_r}\right) \cdot [H^+]^{\frac{1}{6}}[O_2]^{\frac{1}{2}} \qquad 8.1$$

with $k_{\upsilon,Py}$ adopting the value of 2.8 (µm/min)·(kg/mol)^{⅔} (Table 6.19). To summarise, the above experimental observations are in agreement with the continuous simulation (Table 7.21 & 6.22), which demands a significant reduction in pyrite oxidation rate. Equation 8.1 is therefore adopted in the rest of the study, despite lacking deep fundamental understanding of the pyrite oxidation mechanism in oxygenated iron(III) solution environments under MT conditions.

Stellenbosch University http://scholar.sun.ac.za

The intrinsic yield of elemental sulfur on different sulfide minerals is also important, as it directly affects the terminal acid concentration, which, in turn, influences the various oxidation and precipitation rate expressions. Section 7.4.1 has highlighted the dependency of the elemental sulfur yield on the unassociated hydrogen ion concentration (*e.g.*, Eq. 7.59). Section 7.4.2 has attempted to derive the degree of sulfur oxidation by following the step-wise oxidation of sulfide in the chalcopyrite surface lattice. Due to the various reaction (pathway) complexities and multiple mechanistic possibilities, such attempts were unsuccessful, hence the empirical approach followed in this study. Various high pulp density oxidation tests were conducted at lower acidities (see later) and these results are used to derive a more appropriate algorithm to describe the intrinsic yield of elemental sulfur on chalcopyrite and pyrite surfaces. Since there is a significant drop in the observed elemental sulfur yield at lower starting acidities (see later), an empirical algorithm is adopted for this purpose.

Simulating the elemental sulfur yield

The baseline yield of elemental sulfur on a chalcopyrite surface is expected to be close to 75%, as this is most consistent with the proposals of Section 6.6.5 and 7.4.1. The first two electron-exchange steps are assumed to be associated with the release of iron from the chalcopyrite lattice, while the next four electron-exchange steps are assumed to be dominated by direct oxygen reduction, catalysed by the presence of copper(I) surface species. The resulting overall reaction may therefore be represented as follows, assuming that the thiosulfurous species (S^{+}) rearranges and decomposes rapidly in acid solution to theoretically yield 75% elemental sulfur (Sect. 6.3.2), *i.e.*, 2 mol Fe(III) and 1 mol O_2 are reduced per mol $CuFeS_2$ oxidised, to yield 25% sulfate:

$$S_2^{4-} \Rightarrow S_2^{2-} + 2e^{-}(2Fe^{3+}) \Rightarrow 2S^{+} + 4e^{-}(O_2) \Rightarrow \tfrac{3}{16}S_8 + \tfrac{1}{2}S^{(4+)} \qquad 8.2$$

The regressed baseline value turns out to be close to 80% for the tests conducted with Arbo A02 LS at 150ºC (App. J). The correlation adopts the following functional form, emphasising the roles of both the hydrogen ion and dissolved oxygen concentrations in the sulfide oxidation mechanism:

$$S^{o}/S_{rx,Cpy} = \left(0.8 - 0.005 \cdot (T - T_r) - \frac{1}{F_H}\frac{[O_2]}{[H^{+}]} \right) \times 100\% \qquad 8.3$$

where the empirical acidity factor, F_H, is estimated to be close to 7.5, based on the testwork results at lower acidities (later in this section), and the baseline yield is assumed to vary by 5% for every 10ºC change in the solution temperature. Clearly, the behaviour of sulfur is not well understood and rather unpredictable, as is illustrated by the need to increase this baseline yield by 5%, *i.e.*, to 85%, when using the Borrepal LS (see later), whereas the over-addition of surfactants in the continuous campaigns (Table 7.21 & 7.22) and low pulp density tests (Sect. 7.4.2) demands lower baseline values.

Stellenbosch University http://scholar.sun.ac.za

The lack of accurate experimental data regarding the extent of pyrite oxidation and sulfur speciation, the prevalence of complicated surface mechanisms (*e.g.*, the water splitting mechanism; Sect. 6.3.2 & 6.3.4) and the associated high surface potential, make the baseline sulfur yield on a pyrite surface relatively arbitrary. A value of 30% sulfur yield is adopted, based on the discussions of Chapter 6 (Section 6.3.1), while this value is assumed to be more sensitive to changing acidity on pyrite surface, *i.e.*, F_H, is assumed to be 5. These indicative sulfur yield trends, at different (constant) dissolved oxygen concentrations and temperatures, are illustrated in Figure 8.4 *a* and *b* for chalcopyrite and pyrite surfaces, respectively.

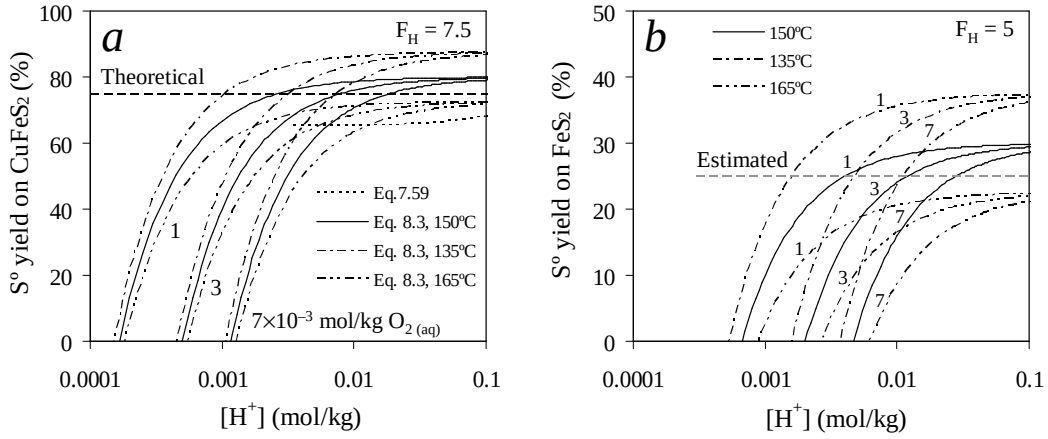

Figure 8.4
Indicative elemental sulfur yields on the refractory sulfide minerals, as a function of the hydrogen ion & dissolved oxygen concentrations & temperature (Eq. 8.3): *a*) $CuFeS_2$ surface, with regressed values: F_H = 7.5 & 80% baseline yield; *b*) FeS_2 surface, assuming F_H = 5 & 30% baseline yield. The linear correlation refers to the low pulp density testwork results (Ch. 7. Eq. 7.59).

Since the linear correlation in Chapter 7 (Eq. 7.59; see dotted line in Figure 8.4 *a*) was derived without considering changes in the dissolved oxygen concentration, temperature and an initial acidity drop during mineral oxidation under MT conditions, the above correlations are more relevant to the high pulp density conditions investigated in this chapter. However, cognisance has to be taken of the experimentally observed drop in the baseline yield at higher surfactant-to-surface area ratios, *i.e.*, referring to the low pulp density conditions in Chapters 6 and 7. For the sake of simplicity, changing temperature, acidity and dissolved oxygen concentrations are assumed to have an insignificant effect on the yield of sulfur on sphalerite and pyrrhotite mineral surfaces under MT conditions. These elemental sulfur yields are therefore kept constant at 95%, which is in line with the mechanistic considerations of Section 7.4.2, *i.e.*, iron(III) reduction ($N_{FeIII,Sph}$ = 2 & $N_{FeIII,Ph}$ = 14) is likely dominant on these minerals (see Sect. 7.5). With regard to the net rate of iron(III) reduction on the minerals in the HBMS concentrate, assumptions have to be made regarding the effects of chalcopyrite and pyrite surface potential, specifically under high pulp density conditions.

Stellenbosch University http://scholar.sun.ac.za

Simulating the rate of iron(III) reduction on the different sulfide minerals

Firstly, it would be naïve to assume that a rounded mole-number of electrons is exchanged for each $CuFeS_2$ and FeS_2 unit cell oxidised, *e.g.*, as represented by Equation 8.2. Detailed discussions in Chapter 6 (Sect. 6.3.2 & 6.6.2) have highlighted that surface sulfurs move through many different oxidation states and intermediate radical species, while some species may become more mobile and desorb from the surface, before taking part in further oxidation. Furthermore, adjacent reaction sites are not electrochemically isolated from each other, which makes these reactions complex and renders them highly dependent on the prevailing mineral surface conditions. These conditions are not necessarily the same for minerals in different concentrates, not even on different crystal faces of the same mineral, while the effect of sulfur product layers, however thin, may result in changing conditions over time (diffusion limitations).

For the sake of simplicity, it is assumed that there is a strong relationship between the sulfur yield and the surface potential, which, in turn, depends on whether mineral oxidation is driven by multi-electron oxygen reduction or one-electron iron(III) reduction mechanisms, or, in the case of pyrite, is accompanied by a water splitting mechanism. These mechanisms are summarised in Section 6.6, insinuating the following: the higher the prevalence of highly oxidised surface species, the lower the intrinsic sulfur yield and the lower the net degree of iron(III) surface reduction. In the case of chalcopyrite, such conditions would prevail during HT oxidation. However, under MT conditions, elemental sulfur surface layers are more prevalent, even in the presence of surfactants (see, *e.g.*, Figure 7.22 *b*), and the prevailing surface conditions would be more variable. In general, it is expected that a higher surface potential would transpire during initial oxidation at lower pulp densities, where the ratio of surfactant concentration to mineral surface area is higher. Under such conditions, the net amount of iron(III) reduction on the mineral surface would be lower, while the situation might be reversed at longer reaction times (see, *e.g.*, Figure 7.42 *b*). As a first estimate, the assumptions of Section 7.4.2 are retained for the HBMS concentrate, as they accurately account for the acid and iron behaviour in the continuous pilot plant, *i.e.*, $N_{FeIII,Cpy} = 0$ and $N_{FeIII,Py} = -1$.

Verifying the batch reactor simulation under typical MT autoclave acidity conditions

Incorporation of the above pyrite oxidation rate expression and the sulfur yield correlations generally results in acceptable agreement between the experimental and simulated reaction extents (see below). Taking into consideration the various assumptions made in this study, Figure 8.5 and Figure 8.6 illustrate that the reaction extents and solution tenors are well described by the phenomenological batch reactor model. Figure 8.6 also illustrates the consistent performance of the iron(III) precipitation model, using the optimised enhancement factor (κ) parameters in Chapter 5 (Table 5.10 footnotes). The initial drop in acid concentration clearly coincides with the

Stellenbosch University http://scholar.sun.ac.za

precipitation of iron(III), *i.e.*, the initial low acid environment creates high supersaturation conditions which, in turn, create new hematite particles *via* primary nucleation (accompanied by rapid but limited growth). However, these high supersaturation conditions also promote hydronium jarosite surface nucleation (on existing hematite substrate surface) and subsequent growth, resulting in its dominance during the initial mineral oxidation period. The increase in the total iron(III) precipitate surface area with time then results in secondary hematite nucleation (accompanied by rapid but limited growth), at the expense of jarosite growth, which translates into a gradual increase in the predominance of the hematite phase, $W_{f,Hem}$.

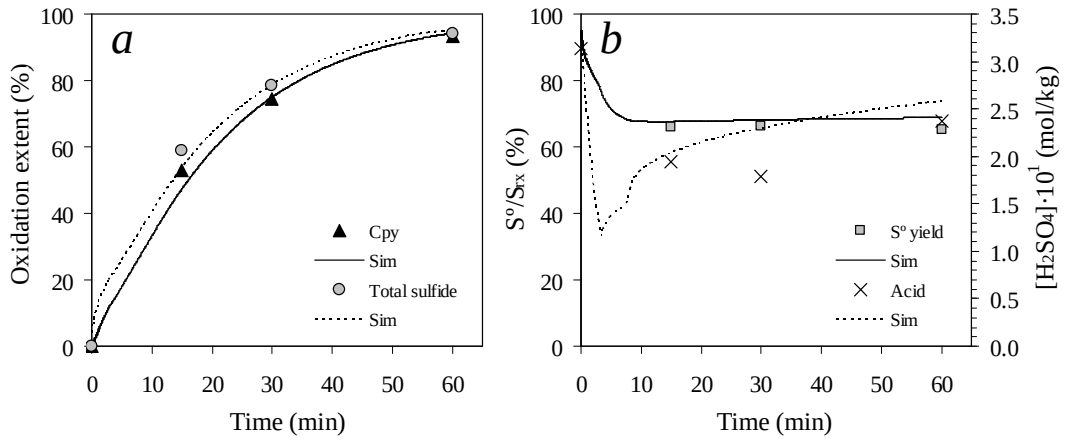

Figure 8.5
Comparison between experimental & simulated reaction extents of Series PLT1 (HBMS; 8.85% Sample I) at 150ºC (700 kPa p_{O2}º), after incorporating the revised FeS_2 oxidation rate expression (Eq. 8.1), starting with 0.5 g/L LS (Arbo A02), QB at medium acidity of 30 g/L H_2SO_4 (5 g/L Cu, Zn), 5 g/L Fe(II) & 5 g/L Fe(III: *a*) Comparative $CuFeS_2$ & total sulfide oxidation extents; *b*) Comparative elemental sulfur yields & terminal acid concentrations.

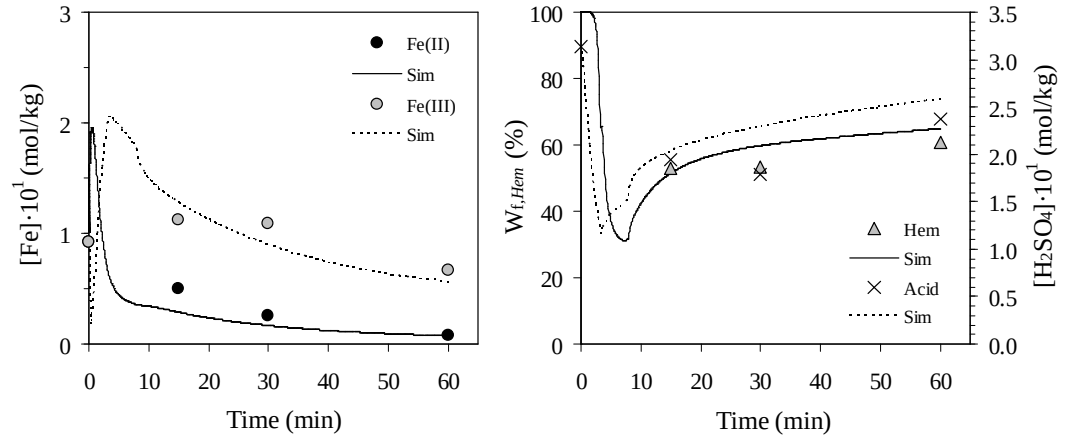

Figure 8.6
Comparison between the experimental & simulated reaction extents of Series PLT1 (8.85 wt% of Sample I) at 150ºC (700 kPa p_{O2}º), starting with 0.5 g/L LS (Arbo A02), QB at medium acidity of 30 g/L H_2SO_4 (5 g/L Cu, Zn), 5 g/L Fe(II) & 5 g/L Fe(III): *a*) Comparative iron(II) & iron(III) concentrations; *b*) Comparative Fe_2O_3 formation extents & terminal acid concentrations.

Stellenbosch University http://scholar.sun.ac.za

The accurate representation of the iron concentration and oxidation states with time (Figure 8.6 *a*), also pays testimony to the relevance of the (above) average iron(III) reduction extents on the primary sulfide minerals. Despite the relatively high pulp density of ~8.85 wt% solids (per unit mass water), the initial addition of 0.5 g/L LS (Arbo A02) and QB (Orfom 2) appears to have sufficiently dispersed molten sulfur, as the simulation closely follows the measured chalcopyrite oxidation extent over the first 60 minutes (Figure 8.5 *a*).

Using the simulation to assess the influence of different surfactants on the reaction rates

The following two test series (T2 & T3) investigated the effects of using an alternative LS, *i.e.*, Borrepal U (Sect. 8.2.1), at concentrations of 0.15 g/L and 0.5 g/L, respectively, without the addition of any QB. Comparison between the experimental and simulated results is presented in Figure 8.7, which illustrates that the lower addition of LS results in a slight drop in chalcopyrite and total sulfide oxidation extents at 60 minutes (Figure 8.7 *a*). This example also illustrates how the generalised phenomenological model may be used to quantify the response of the system to a changing variable - in this case, a new (different) surfactant at different concentrations.

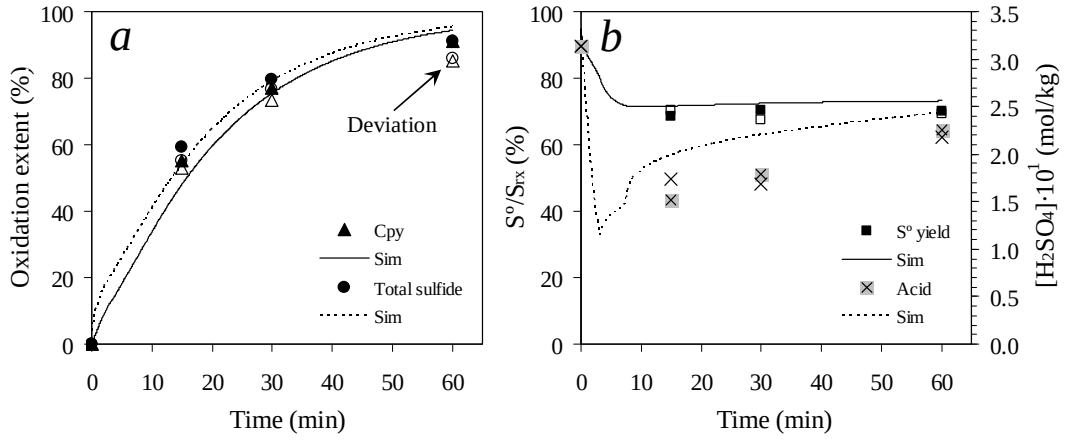

Figure 8.7
Comparison between the experimental & simulated reaction extents of Series PLT2 & PLT3 (8.85 wt% Sample I) at 150ºC (700 kPa p_{O2}º), starting with 0.15 & 0.5 g/L LS (Borrepal U; no Quebracho), respectively, at medium acidity of 30 g/L H_2SO_4 (5 g/L Cu, Zn), 5 g/L Fe(II) & 5 g/L Fe(III): *a*) Comparative $CuFeS_2$ & total sulfide oxidation extents; *b*) Comparative elemental sulfur yields & terminal acid concentrations (85% & 35% baseline sulfur yields assumed for $CuFeS_2$ & FeS_2, respectively). The open & closed symbols refer to 0.15 & 0.5 g/L Borrepal, respectively.

Good agreement between the observed and simulated iron(II) and iron(III) concentrations are again obtained (Figure 8.8 *a*), while the simulated residue hematite contents ($W_{f,Hem}$) are most consistent with the measured results of Series PLT2 (Figure 8.8 *b*). The corresponding total solid-phase mass loss ($W_{f,tot}$) is presented in Figure 8.9 *b* (also see the terminal acid concentrations & sulfur yields in Figure 8.7 *b*). These results are consistent with an over-estimated hematite content (~10% *ref.* $W_{f,Hem}$) in the case of Series PLT3, which illustrates the sensitivity of the relative hematite and

Stellenbosch University http://scholar.sun.ac.za

hydronium jarosite precipitation rates to slight changes in the feed solution composition during batch experimentation (see discussions in Ch. 5; Sect. 5.4.4). Alternatively, these results could suggest that these relative precipitation rates are influenced by the surfactants. These issues will only be resolved once the iron(III) precipitation mechanisms and the behaviour of elemental sulfur on the different mineral surfaces are better understood, *i.e.*, by improving the experimentation and analyses methods to accurately record changes in the residue sulfur and jarosite contents over reaction time in a leaching reactor.

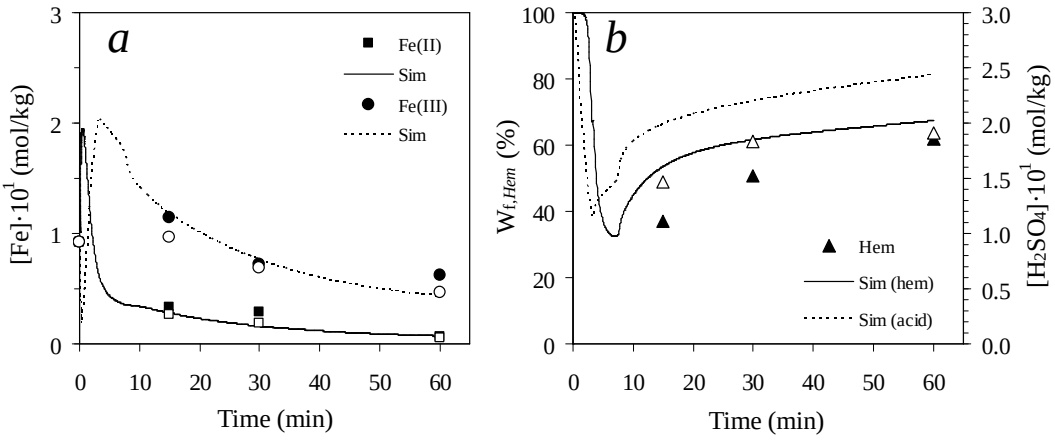

Figure 8.8
Comparison between the experimental & simulated reaction extents of Series PLT3 (8.85 wt% of Sample I) at 150ºC (700 kPa p_{O2}º), starting with 0.5 g/L LS (Borrepal U) at medium acidity of 30 g/L H_2SO_4 (5 g/L Cu, Zn), 5 g/L Fe(II) & 5 g/L Fe(III): *a*) Comparative iron(II) & iron(III) concentrations; *b*) Comparative Fe_2O_3 formation extents & terminal acid concentrations. The open & closed symbols refer to 0.15 & 0.5 g/L Borrepal, respectively.

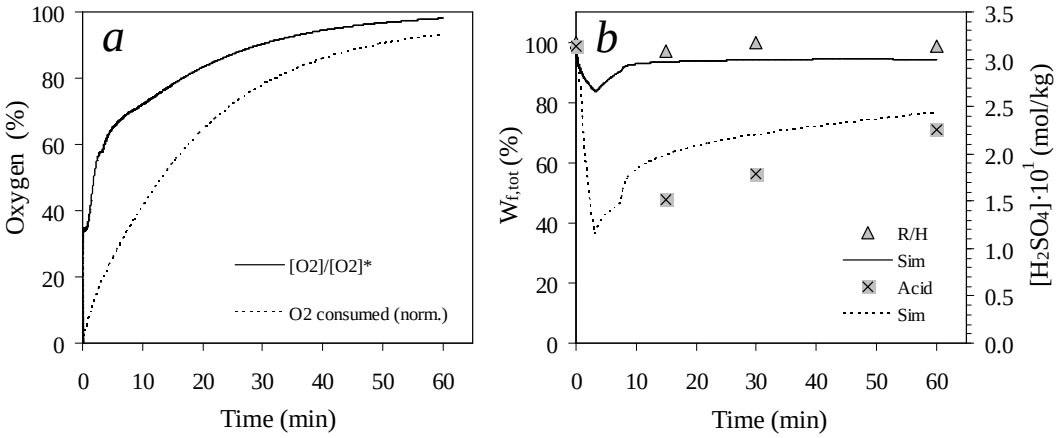

Figure 8.9
Comparison between the experimental & simulated reaction extents of Series PLT3 (8.85 wt% of Sample I) at 150ºC (700 kPa p_{O2}º), starting with 0.5 g/L LS (Borrepal U) at medium acidity of 30 g/L H_2SO_4 (5 g/L Cu, Zn), 5 g/L Fe(II) & 5 g/L Fe(III): *a*) Normalised O_2 saturation & consumption curves; *b*) Comparative total solid-phase mass loss & terminal acid concentrations.

Stellenbosch University http://scholar.sun.ac.za

Figure 8.9 *a* (solid line) emphasises the fact that the oxygen concentration is relatively far removed from its saturation level during the initial oxidation period (0-10 min) and only approaches saturation after about 60 minutes. The dotted line represents the calculated cumulative oxygen consumption, normalised to its theoretical consumption after complete oxidation. These theoretical consumption curves are only compared to the measured curves in selected tests (see later) because the mass flow meter was slightly undersized and, although it produced sensitive consumption data during the latter oxidation stages, it could not always adequately deal with the high consumption of oxygen during initial oxidation in the batch reactor.

The following two tests (PLT43 & PLT44) measured the effect of surfactant addition over time, *i.e.*, 50% of total addition at the start and then 25% after 30 and 45 minutes, respectively. Although the 60 minutes' result is similar to that obtained before, large sulfur conglomerates were prevalent after 90 minutes (see App. J.2). The addition of fresh surfactants during the latter oxidation stages is therefore unsuccessful in breaking up the sulfur-sulfide conglomerates, which is consistent with the conclusions of Section 6.5.2 (see Figure 6.35 & related discussions).

The final test series, using HBMS Sample I (Series T5), investigated the effect of a slightly higher temperature on the various reaction extents (see Table 8.4). Agreement between the simulated and experimental hematite contents ($W_{f,Hem}$) is excellent, while a small offset in acid concentration is again apparent despite a good simulation of the iron(II) and iron(III) concentrations.

Table 8.4
Comparison between the experimental & simulated reaction extents of Series PLT5 (8.85 wt% of Sample I) at 155ºC, starting with 0.5 g/L LS (Arbo A02), QB at medium acidity of 30 g/L H_2SO_4 (5 g/L Cu, Zn) & iron concentration of 5 g/L Fe(II) & 5 g/L Fe(III).

Time	$X_{Cpy}^{(sim)}$	$X_{Cpy}^{(exp)}$	$X_{Py}^{(sim)}$	[a] $X_{Py}^{(exp)}$	[b] $X_{Sph}^{(sim)}$	[b] $X_{Sph}^{(exp)}$
(min)	(%)	(%)	(%)	(%)	(%)	(%)
30	84	80	93	86	100	92
60	98	96	99	100	100	92
Time	$X_{S2-}^{(sim)}$	$X_{S2-}^{(exp)}$	$X_{S^o/Srx}^{(sim)}$	$X_{S^o/Srx}^{(exp)}$	$W_f^{(sim)}$	$W_f^{(exp)}$
(min)	(%)	(%)	(%)	(%)	(%)	(%)
30	87	81	66	71	92	97
60	98	96	67	66	92	103
Time	$[Acid]^{(sim)}$	$[Acid]^{(exp)}$	$[Fe(III)]^{(sim)}$	$[Fe(III)]^{(exp)}$	$W_{f,Hem}^{(sim)}$	$W_{f,Hem}^{(exp)}$
(min)	(mol/kg)	(mol/kg)	(mol/kg)	(mol/kg)	(mol/kg)	(mol/kg)
30	0.25	0.20	0.08	0.09	61	61
60	0.29	0.23	0.04(5)	0.04	66	66

[a] Calc. from the residual sulfide content (chem. analyses); [b] *Sph* & *Ph* assumed to oxidise at same rate.

Stellenbosch University http://scholar.sun.ac.za

Again, taking the various assumptions and inaccuracies of the experimental techniques (Sect. 8.2) and the uncertain behaviour of elemental sulfur (Eq. 8.3) into account, the agreement between the simulation and experimental results is deemed acceptable. The various rate expressions can therefore be directly incorporated into the continuous reactor simulation, *i.e.*, under typical MT autoclave acidity environments (see Sect. 8.3.2).

Verifying the batch reactor simulation under high acidity conditions

The next two series of tests (PLU1 & PLU2; App. J.3) utilised the HBMS Sample J ($d_{90} \approx 10$ µm) at a higher initial acidity of 40 g/L H_2SO_4 at 145ºC, using 0.5 g/L Arbo A02 (in addition to 0.5 g/L Orfom 2 QB) and 0.5 g/L Borrepal U LS, respectively. These test results are illustrated in Figure 8.10 and Figure 8.11, which confirm that the batch reactor simulation replicates most of the observed trends under these higher autoclave acidity conditions. For example, the higher feed acid concentration results in a higher hydronium jarosite content, compared to Series T, which commenced at a lower initial acidity of 30 g/L H_2SO_4. The higher acid concentration environment appears to be buffered by an increase in the rate of hydronium jarosite phase formation, which mirrors the results obtained in the continuous pilot campaigns (Sect. 7.4.1). These figures also highlight the uncertainty in the sulfur speciation results, which does not justify the use of different baseline sulfur yields in the simulation. The standard values of 80% on chalcopyrite (*ref.* Eq. 8.3) and 30% on pyrite are used here, as well as for the rest of the batch simulations in this section. Unfortunately, no reliable residue modal analyses could be obtained and the chemically analysed results cannot therefore be fully reconciled with the various reaction extents.

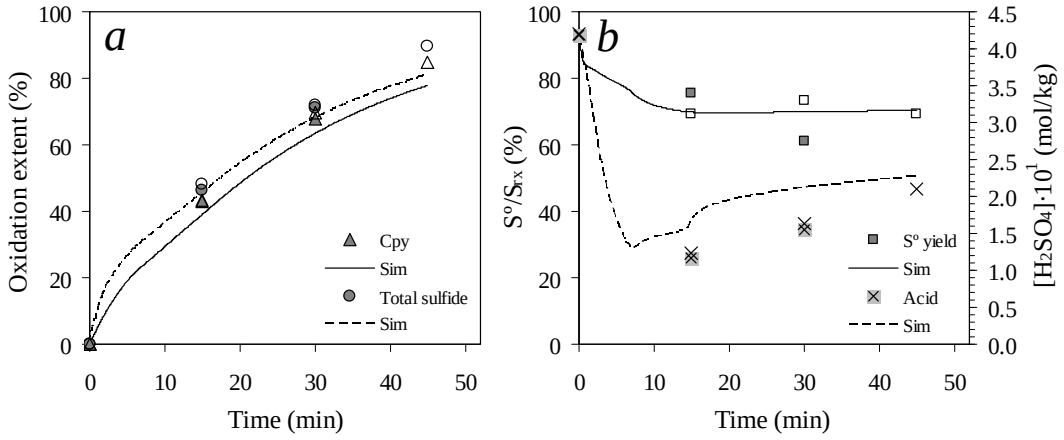

Figure 8.10
Comparison between the experimental & simulated reaction extents of Series PLU1 & PLU2 (8.85 wt% Sample J) at 145ºC (700 kPa p_{O2}º), starting with 0.5 g/L Arbo A02 (0.5 g/L QB) & 0.5 g/L Borrepal U (0 g/L QB) LS, respectively, at a higher acidity of 40 g/L H_2SO_4 (5 g/L Cu, Zn), 5 g/L Fe(II) & 2.5 g/L Fe(III): *a*) Comparative $CuFeS_2$ & total sulfide oxidation extents; *b*) Comparative elemental sulfur yields & terminal acid concentrations (80% & 30% baseline yields for $CuFeS_2$ & FeS_2, respectively). The open & closed symbols refer to Arbo A02 & Borrepal U LS, respectively.

Stellenbosch University http://scholar.sun.ac.za

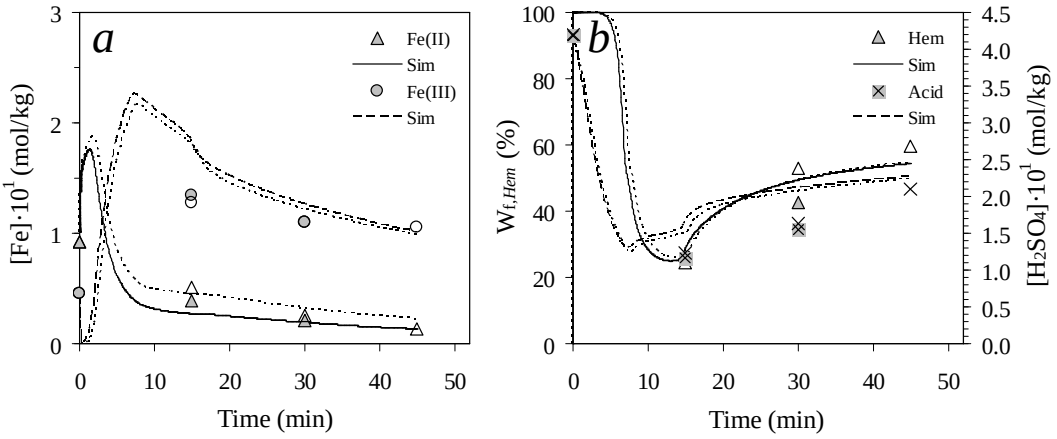

Figure 8.11
Comparison between the experimental & simulated reaction extents of Series PLU1 & PLU2 (8.85 wt% Sample J) at 145ºC (700 kPa p_{O2}º), starting with 0.5 g/L Arbo A02 (0.5 g/L QB) & 0.5 g/L Borrepal U (0 g/L QB), respectively, at a higher acidity of 40 g/L H_2SO_4 (5 g/L Cu, Zn), 5 g/L Fe(II) & 2.5 g/L Fe(III): *a*) Comparative iron tenors; *b*) Comparative Fe_2O_3 formation extents & terminal acid concentrations. The open & closed symbols refer to Arbo A02 & Borrepal U LS, respectively. The dotted line represents the simulated output, assuming $N_{FeIII,Cpy} = 2$.

Considerable variations in the experimental sulfur yield (±10%; Figure 8.10 *b*) and hematite content (±10%; Figure 8.11 *b*) are most likely related to experimental and chemical analysis errors. The reason behind the slightly higher experimental chalcopyrite and total sulfide oxidation extents at longer reaction times (Figure 8.10 *a*) is also not known. Although a slight improvement in the calculated iron(II) and iron(III) concentrations is obtained by increasing the extent of iron(III) reduction on the chalcopyrite surface ($N_{FeIII,Cpy}$ = 2; dotted lines in Figure 8.11), the mineral oxidation rates are largely unaffected. Further experimental work of improved accuracy would be required in order to clarify the reasons behind these (relatively minor) discrepancies.

Verifying the batch reactor simulation under low acidity conditions

HBMS 777 concentrate

The next two series of tests (PLU3 & PLU4; App. J.3) focussed on a significantly lower initial acidity of 20 g/L H_2SO_4 and varying amounts of iron, *i.e.*, 2.5 g/L Fe(III) (7.5 g/L Fe^T) and 0.5 g/L Fe(III) (2.5 g/L Fe^T), respectively. These results are compared in Figure 8.12 and Figure 8.13.

These lower acidity environments result in a significantly higher hematite content (> 70% after 60 min), with relatively good agreement between the simulated and experimental values (Figure 8.13 *b*). The deviation is somewhat more notable at longer reaction times, which may be due the redissolution of metastable jarosite as the acid concentration increases, particularly during autoclave cooling after completing a test. This statement is in line with the discussions around the

Stellenbosch University http://scholar.sun.ac.za

performance of the continuous autoclave and its simulation (Ch. 7; Sect. 7.4.2) and needs to be explored further in future investigations under these leaching conditions.

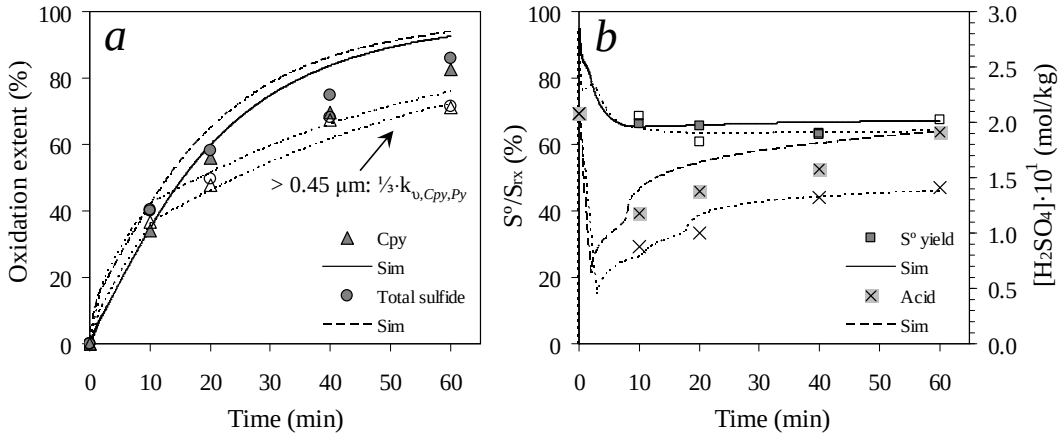

Figure 8.12
Comparison between the experimental & simulated reaction extents of Series PLU3 & PLU4 (Sample J; 8.7 wt% & 8.55 wt%, respectively) at 150ºC (700 kPa p_{O2}º), starting with 0.5 g/L Arbo A02 (0.5 g/L QB) at a lower acidity of 20 g/L H_2SO_4 (5 g/L Cu, Zn) & different Fe tenors: *a*) Comparative $CuFeS_2$ & total sulfide oxidation extents; *b*) Comparative elemental sulfur yields & terminal acid concentrations. The open symbols refer to 0.5 g/L Fe(III) & 2.0 g/L Fe(II) initially, while the closed symbols refer to 2.5 g/L Fe(III) & 5 g/L Fe(II) initially. The dotted lines correspond to the open symbols (PLU4) & represent the simulation at the lower iron tenors, utilising reduced $CuFeS_2$ & FeS_2 rate constants (⅓·k_υ) after 0.45 µm PPD.

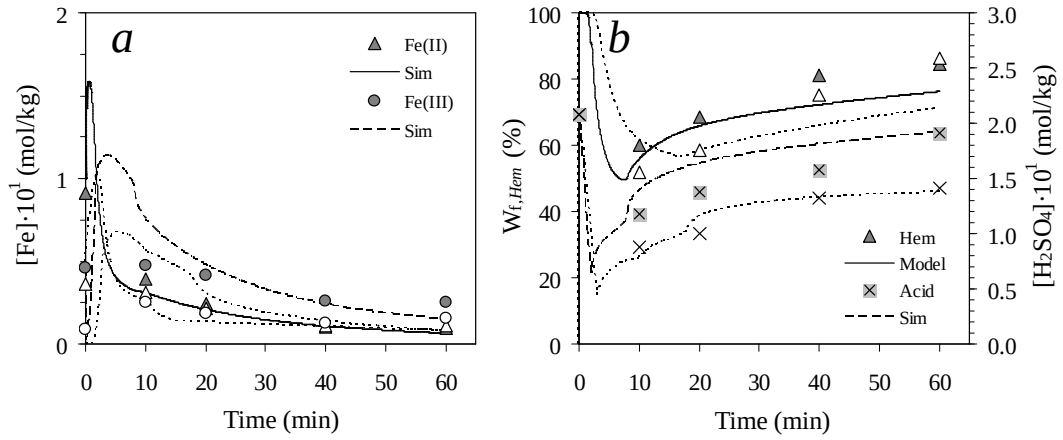

Figure 8.13
Comparison between the experimental & simulated reaction extents of Series PLU3 & PLU4 (Sample J; 8.7 wt% & 8.55 wt%, respectively) at 150ºC (700 kPa p_{O2}º), starting with 0.5 g/L Arbo A02 (0.5 g/L QB) at a lower acidity of 20 g/L H_2SO_4 (5 g/L Cu, Zn) & different Fe tenors: *a*) Comparative iron(II) & iron(III) concentrations; *b*) Comparative Fe_2O_3 formation extents & terminal acid concentrations. The open symbols refer to 0.5 g/L Fe(III) & 2.0 g/L Fe(II) initially, while the closed symbols refer to 2.5 g/L Fe(III) & 5 g/L Fe(II) initially. The dotted lines correspond to the open symbols (PLU4) & represent the simulation at the lower iron tenors, utilising reduced $CuFeS_2$ & FeS_2 rate constants (⅓·k_υ) after 0.45 µm PPD.

Stellenbosch University http://scholar.sun.ac.za

Agreement between the sulfur yields and terminal acid concentrations is generally good (Figure 8.12 *b*), and, as expected, the lower initial iron concentration results in a lower terminal acidity concentration environment. The corresponding iron(II) and iron(III) tenors are also in reasonable agreement (Figure 8.13 *a*), considering the number of simplifications incorporated into the phenomenological model. Nevertheless, the simulation underpredicts the initial rate of iron(III) precipitation, *i.e.*, in the low acid region (< 15 g/L H_2SO_4) during the acid initial consumption. This observation is in line with the conclusions in Chapter 5 (Sect. 5.4.4) and 6 (Sect. 6.4.2).

An important observation from these tests is the good agreement between the simulated and experimental chalcopyrite and total sulfide oxidation extents during initial oxidation, but the substantial negative deviation of the experimental extents at longer reaction times (Figure 8.12 *a*). The oxygen consumption curves of Series PLU4, as well as the corresponding total solid-phase mass losses, are illustrated in Figure 8.14 *a* and *b*, respectively.

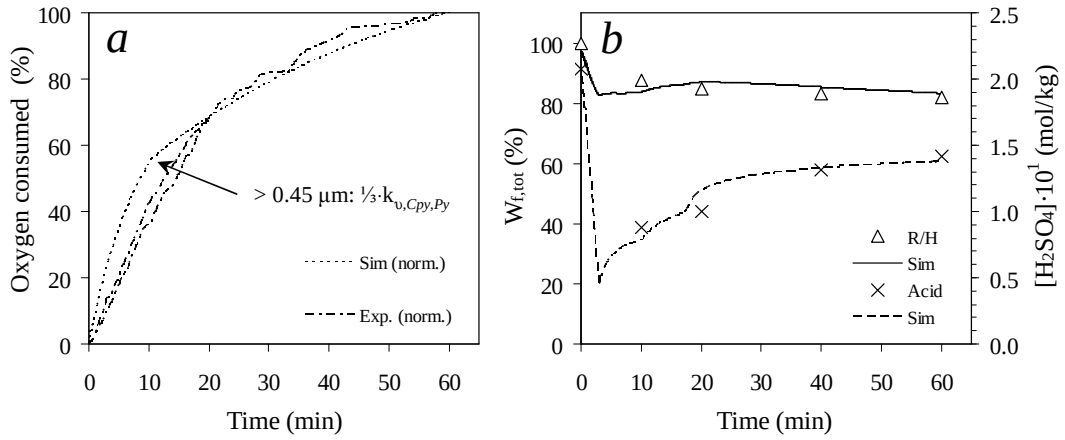

Figure 8.14
Comparison between the experimental & simulated reaction extents of Series PLU4 (8.55 wt% of Sample J) at 150ºC (700 kPa p_{O2}), starting with 0.5 g/L Arbo A02 (0.5 g/L QB) at a lower acidity of 20 g/L H_2SO_4 (5 g/L Cu, Zn) & lower initial Fe tenors of 0.5 g/L Fe(III) & 2.0 g/L Fe(II): *a*) Normalised O_2 saturation & consumption curves; *b*) Comparative total solid-phase mass losses & terminal acid concentrations. The simulation utilised reduced $CuFeS_2$ & FeS_2 rate constants ($⅓·k_υ$) after 0.45 µm PPD.

As illustrated in Figure 8.12 and Figure 8.14, the chalcopyrite and pyrite oxidation rate constants have to be reduced significantly ($⅓·k_υ$) at an 'imaginary' particle penetration depth (PPD) of 0.45 µm in order to account for the apparent reduction in mineral reactivity. These surprising deviations may be related to reagent diffusion limitations through the thin molten sulfur product layers, which have been shown (Ch. 7; Figure 7.22) to develop relatively rapidly on the unreacted chalcopyrite surface, even in the presence of surfactants. Since a lower initial iron concentration results in lower terminal acid levels, a decrease in the oxidation rate of chalcopyrite would be expected (Sect. 6.6.2), especially if diffusion limitations through a molten sulfur product layer become relevant.

Stellenbosch University http://scholar.sun.ac.za

However, a counter-argument could be made that changing speciation phenomena, associated with a lower iron(III) concentration, would tend to buffer the unassociated proton concentration (Sect. 2.4.3), notwithstanding the fact that the diffusion limitations of the other reactants would overshadow any transport limitations of the hydrated proton (high relative diffusivity). The two more likely scenarios are therefore postulated to be the following:

- oxygen diffusion limitations could be highly dependent on the nature of the prevailing surface layers, which, in turn, could be sensitive to the free acidity, or
- diffusion limitations of iron(III) could transpire into lower chalcopyrite oxidation rates.

The latter scenario suggests that the oxidative role of iron(III) could be a mechanistic prerequisite, similar to its proposed role in the pyrite oxidation mechanism (discussed above). However, Section 6.5.4 and especially Section 7.4.2 have clearly illustrated the insensitivity of the chalcopyrite oxidation rate to the iron(III) concentration in a higher acidity environment. On the other hand, the chalcopyrite oxidation mechanism could become more reliant on the role of iron(III) at lower acidities, such as those conditions experienced in the above tests. The characteristic 60 to 65% elemental sulfur yield (Figure 8.12 *b*) suggests that the oxygen reduction reaction is still relevant at the chalcopyrite mineral surface.

The following series of tests (PLU5) were therefore conducted at similarly low initial iron concentrations of 2 g/L Fe(II) and 0.5 g/L Fe(III), but utilising a higher oxygen overpressure (1000 kPa) and higher surfactant concentrations. The detailed experimental results can be found in Appendix J.3 and they are compared with the simulated results in Figure 8.15 and Figure 8.16.

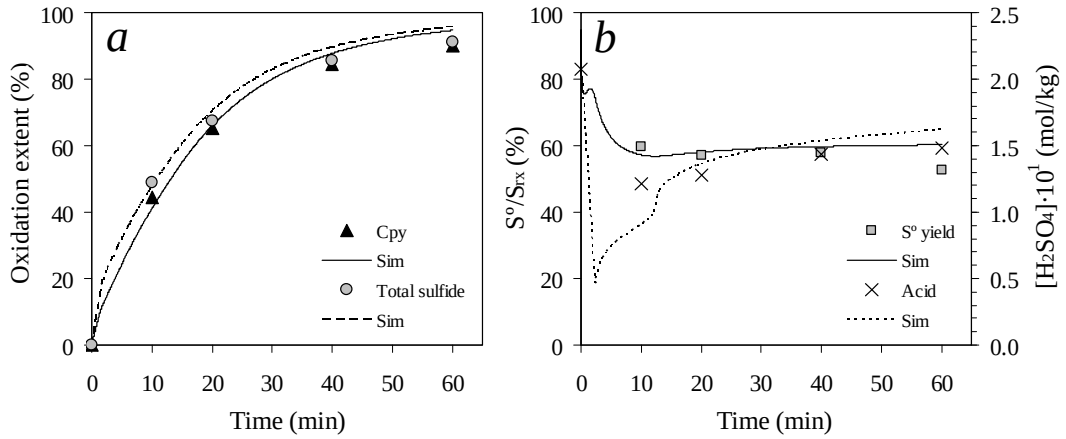

Figure 8.15
Comparison between the experimental & simulated reaction extents of Series PLU5 (8.56 wt% of Sample J) at 150°C & higher overpressure of 1000 kPa p_{O2}°, starting with 0.6 g/L Arbo A02 (0.6 g/L QB), 20 g/L H_2SO_4 (5 g/L Cu, Zn), 2 g/L Fe(II) & 0.5 g/L Fe(III): *a*) Comparative $CuFeS_2$ & total sulfide oxidation extents; *b*) Comparative elemental sulfur yields & terminal acid concentrations.

Stellenbosch University http://scholar.sun.ac.za

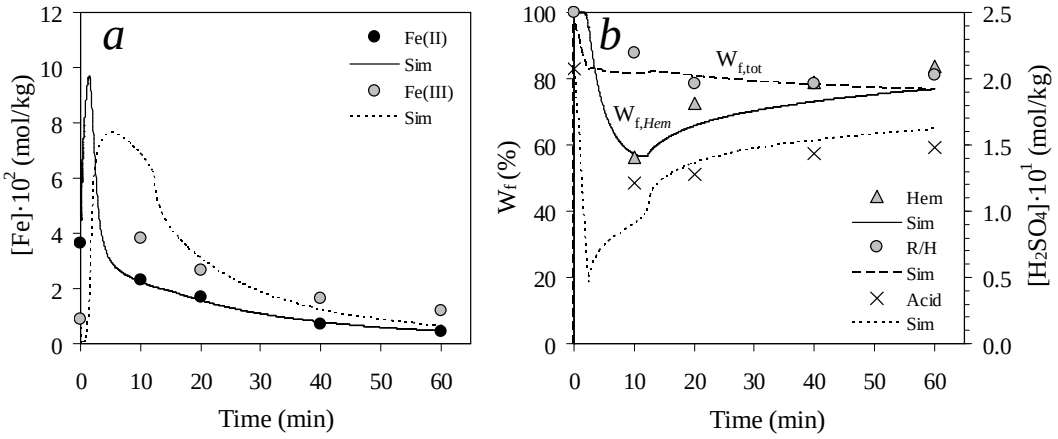

Figure 8.16
Comparison between the experimental & simulated reaction extents of Series PLU5 (8.56 wt% of Sample J) at 150ºC & higher overpressure of 1000 kPa p_{O2}º, starting with 0.6 g/L Arbo A02 (0.6 g/L QB), 20 g/L H_2SO_4 (5 g/L Cu, Zn), 2 g/L Fe(II) & 0.5 g/L Fe(III): *a*) Comparative iron(II) & iron(III) concentrations; *b*) Comparative Fe_2O_3 formation extents, solid-phase mass losses & terminal acid concentrations.

Clearly, the higher oxygen overpressure and surfactant concentrations result in better agreement between the experimental and simulated chalcopyrite and sulfide oxidation extents (Figure 8.15 *a*). Similarly, the calculated iron(II) and iron(III) tenors are in relatively good agreement with the measured values (Figure 8.16 *a*), considering the primitive nature of the overall phenomenological model. Nevertheless, the precipitation rate of iron(III) is, again, slightly underestimated in the low acid regime, while some redissolution of the iron(III) precipitated might have occurred as the acid concentration started to increase again. A more accurate description of the solution thermodynamics in the low acid regime should be considered in future studies in order to account for this rapid iron(III) precipitation rate (see Sect. 5.4.4), whereas the redissolution reactions should be investigated *via* more expansive experimental programmes, *e.g.*, by focussing on the redissolution rate of hematite in high acid environments. In addition, improved experimental procedures need to ensure minimum redissolution hydronium jarosite during sampling (cooling).

In conclusion, the above results suggest that some restriction imposed on the primary oxidant, diatomic oxygen, caused the diminishing of the rates at low acidity. The primary reason for this apparent phenomenon, *e.g.*, due to the formation of denser or polymeric-type sulfur and/or iron(III) precipitate surface layers in low acidity environment, cannot be determined from this testwork and no further conclusions regarding the mechanism of chalcopyrite oxidation are possible; this requires more fundamental work.

The final series of tests, using HBMS concentrate (PLV1, PLV2 & PLV3; App. J.4), was conducted using a higher surfactant addition (0.6 g/L), but at a finer grind (Sample K; d_{90} = 6.6

Stellenbosch University http://scholar.sun.ac.za

µm), at varying pulp densities, temperatures and oxygen partial pressures. Although the phenomenological model results in reasonable estimates of the initial reaction extents, the measured chalcopyrite and total sulfide oxidation extents, again, deviate in a negative direction at longer reaction times in the low acid regime. Again, the chalcopyrite and pyrite oxidation rate constants are reduced at 'imaginary' PPDs to account for this apparent reduction in mineral reactivity. These comparative results are illustrated in Figure 8.17.

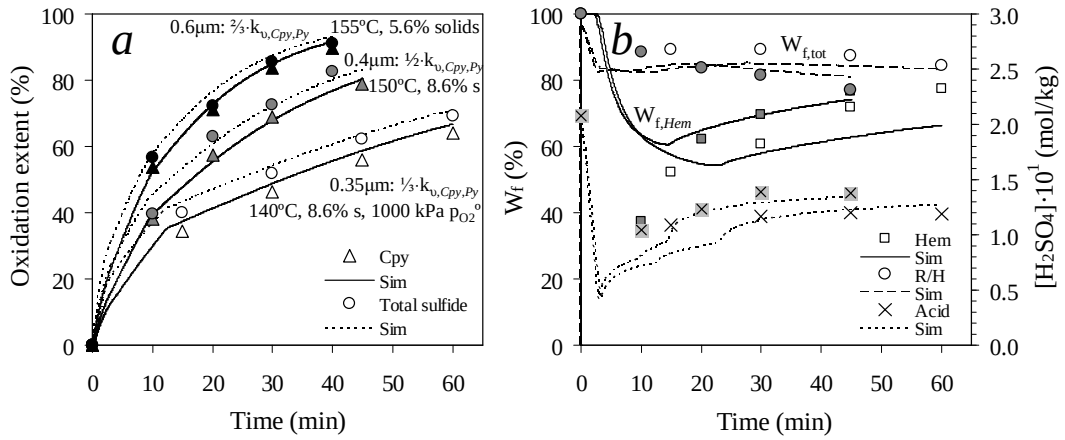

Figure 8.17
Comparison between the experimental & simulated reaction extents of Series PLV1, PLV2 & PLV3 (Sample K; 5.55, 8.55 & 8.55 wt% solids, respectively) at 155, 150 & 140ºC, respectively, & overpressures of 700, 700 & 1000 kPa p_{O2}º, respectively, starting with 0.6 g/L Arbo A02 (0.6 g/L QB), 20 g/L H_2SO_4 (5 g/L Cu, Zn), 2 g/L Fe(II) & 0.5 g/L Fe(III): *a*) Comparative $CuFeS_2$ & total sulfide oxidation extents; *b*) Comparative Fe_2O_3 formation extents, solid-phase mass losses & terminal acid concentrations. The white, grey & black symbols refer to the tests conducted at 140, 150 & 155ºC, respectively. The simulations utilised different adjustments (as highlighted).

These rate 'adjustments' are similar to the approach followed in the case of the continuous pilot autoclave (Sect. 7.4.1). Various modifications to the intrinsic chalcopyrite and pyrite oxidation rate expressions may be considered, but no simple functionality in hydrogen ion, iron(III) or dissolved oxygen concentration adequately accounts for these deviations at higher pH conditions. Also, since possible reactant transport limitations across thin molten sulfur and/or iron(III) precipitate surface layers fall outside the classical porous product layer diffusion case, decreasing the intrinsic rate constants, after a certain cut-off PPD, appears to be the simplest and most practical approach.

These results suggest that molten elemental sulfur layers are at least partly responsible for the reduced mineral oxidation kinetics at longer reaction times, and that low surfactant concentration per unit particle surface area exacerbates the problem, *i.e.*, when using fine grinds, such as for Sample K. Series PLV1 (155ºC, 700 kPa p_{O2}º), conducted at a lower pulp density of 5.55 wt% (solids/kg water), requires less (~33%) reduction of the intrinsic rate constants of chalcopyrite and pyrite minerals. The other two series (PLV2 & PLV3), conducted at 8.55 wt% solids, require about

Stellenbosch University http://scholar.sun.ac.za

50% and 66% reduction, *i.e.*, at 150 (700 kPa p_{O2}^{o}) and 140ºC (1000 kPa p_{O2}^{o}), respectively. The most striking aspect of these deviations is the low apparent 'cut-off' PPD (0.5, 0.25 & 0.25 µm for Series PLV1, PLV2 & PLV3, respectively) compared to the continuous pilot campaigns (Sect. 7.4.2) of 4.5 µm, operated at a significantly higher terminal acid concentration. This observation suggests that different surface layers, *e.g.*, polymeric sulfur and/or hydronium jarosite, form under these low terminal acid concentrations and that the conditions are especially inhibitory to sulfide oxidation at lower operating temperatures. Although further testwork would be required to characterise these surface layers, it is assumed that lower temperature oxidation, under conditions of low acidity, is not ideal for achieving fast chalcopyrite oxidation rates, especially when a high initial particle surface area is exposed to the feed solution. The surfactant concentration per unit mineral surface area may be particularly important in this regard, and further studies should be conducted to determine whether such surface layers can be efficiently dispersed.

LT concentrate

The final three series of tests (PLW1, PLX1 & PLX2; App. J.5 & J.6) were conducted using the LT samples, varying grind (Samples G & L) and temperature, under similarly low acid conditions. Unfortunately, due to its complicated nature, no unique mineral composition can be derived from the residue chemical analysis alone (Sect. 8.2.3). Therefore, the accuracy of these results cannot be verified, while the relative proportions of elemental and sulfide sulfur often appear suspicious. The reason for this is again thought to be the formation of more inhibitory surface layers under lower acidities, which cannot be accurately determined by chemical analysis (Sect. 6.5.1), while no residue modal analyses are available to reconcile the abundance of the different sulfur species (see Sect. 7.3.2). Future investigations should also utilise different analysis techniques, *e.g.*, sublimation under vacuum or thermogravimetry, to determine the elemental sulfur content of the residues.

Nevertheless, Figure 8.18 and Figure 8.19 compare the experimental and simulated results for Series PLW1, using Sample G ($d_{50} \approx 22$ µm; 5.5 wt% solids) at 145ºC, and Series PLX1 and PLX2, using Sample L ($d_{50} = 3.5$ µm; 8.45 wt% solids) at 150 and 155 ºC, respectively. All these tests utilised 20 g/L H_2SO_4, 5 g/L Cu, 2 g/L Fe(II), 0.5 g/L Fe(III), 0.6 g/L LS (Arbo A02) and 0.6 g/L QB (Orfom 2), while a constant overpressure of 700 kPa p_{O2}^{o} was maintained. The rate constants of the other copper mineral phases, chalcocite, covellite and bornite, are directly obtained from the low pulp density testwork in Chapter 7 (Table 7.25 in Sect. 7.5), while the rate constant of pyrite is estimated to be $k_{\upsilon,Py} = 6.4(5)$ (µm/min)·(kg/mol)^{⅔} (based on Eq. 8.1). The intrinsic elemental sulfur yields on chalcopyrite and pyrite surfaces are assumed the same as for the HBMS concentrate (see above), while a baseline sulfur yield of 40% is assumed for covellite (*ref.* Eq. 8.3) and constant yields for bornite (85%) and pyrrhotite (95%) are assumed. As a first estimate, similar extents of iron(III) reduction are assumed for all the copper sulfide minerals, as reported in Section 7.4.2, *i.e.*,

Stellenbosch University http://scholar.sun.ac.za

$N_{FeIII,Cpy}$ = $N_{FeIII,Chc}$ = $N_{FeIII,Cov}$ = $N_{FeIII,Bor}$ = 0 and $N_{FeIII,Py}$ = –1 (Table 6.23). However, significant discrepancies are again noted between the initial experimental and simulated iron(II) and iron(III) concentrations. Moderate improvement is obtained after assuming that less oxidising conditions (preferential iron(III) reduction mechanisms) prevail at higher pulp densities on the less refractory minerals, *i.e.*, $N_{FeIII,Chc}$ = 2, $N_{FeIII,Bor}$ = 12 and $N_{FeIII,Ph}$ = 14 (Sect. 7.4.1 & 7.4.2). However, Figure 8.18 *a* illustrates that, even with these assumptions, the initial calculated iron(III) concentrations (< 20 min) are higher than the experimental values, while, again, some iron(III) redissolution seems to have occurred during sampling (at higher bulk acid concentrations). Despite the reasonable agreement between the simulated and experimental elemental sulfur yields and residual acid concentrations (Figure 8.18 *b*), the experimental trends suggest increased oxidation of sulfide to sulfate at longer reaction times, *i.e.*, at higher relative oxygen concentrations and at higher relative prevalence of the more refractory (to iron(III) oxidation) chalcopyrite and pyrite minerals. It should also be kept in mind that the assumption of a constant surface oxidation mechanism may not necessarily hold, especially during batch oxidation in a low acidity environment.

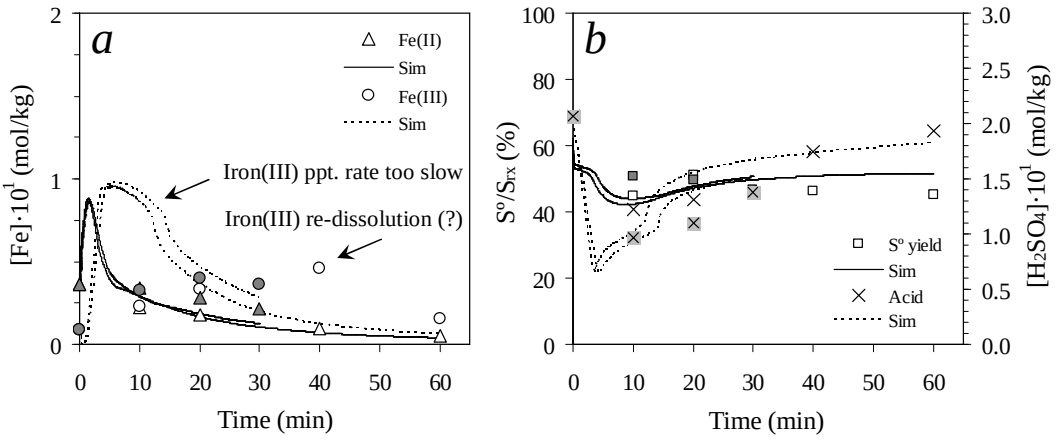

Figure 8.18
Comparison between the experimental & simulated reaction extents of Series PLX1 & PLX2 (Sample L; 8.45 wt% solids) at 150 & 155 ºC (700 kPa p_{O2}º), starting with 0.6 g/L Arbo A02 (0.6 g/L QB), 20 g/L H_2SO_4 (5 g/L Cu), 2 g/L Fe(II) & 0.5 g/L Fe(III): *a*) Comparative iron(II) & iron(III) concentrations; *b*) Comparative elemental sulfur yields & terminal acid concentrations. The open & closed symbols refer to the tests at 155 & 150ºC, respectively. The simulations (lines) refer to $N_{FeIII,Py}$ = –1, $N_{FeIII,Cpy}$ = $N_{FeIII,Cov}$ = 0, $N_{FeIII,Chc}$ = 2, $N_{FeIII,Bor}$ = 12 & $N_{FeIII,Ph}$ = 14.

Figure 8.19 *a* illustrates that the simulation is in reasonable agreement with the measured copper leaching extents for the finely milled Sample L (d_{50} ≈ 3.5 µm), *i.e.*, Series PLX1 and PLX2. The calculated solid-phase mass losses ($W_{f,tot}$) and residue sulfate contents are also acceptable (Figure 8.19 *b*). On the other hand, Series PLW1 (Sample G; d_{50} ≈ 22 µm) exhibits significant acceleration of the initial oxidation rate, *i.e.*, up to about 3.5 µm PPD (0-20 min), which translates into a roughly five times (5×) increase in the intrinsic rate constants of chalcopyrite, covellite and bornite minerals during this period.

Stellenbosch University http://scholar.sun.ac.za

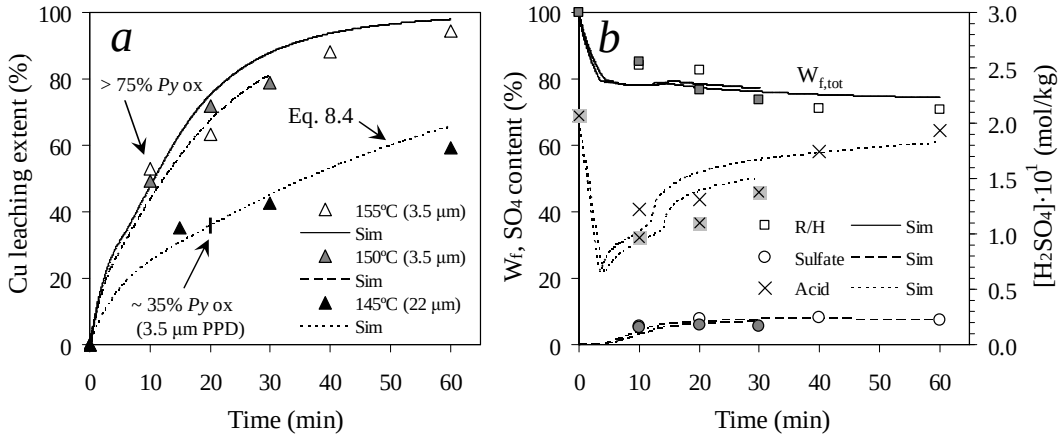

Figure 8.19
Comparison between the experimental & simulated reaction extents of Series PLW1 (Sample G; 5.5 wt% solids), PLX1 & PLX2 (Sample L; 8.45 wt% solids) at 145, 150 & 155 ºC (700 kPa p_{O2}º), respectively, starting with 0.6 g/L Arbo A02 (0.6 g/L QB), 20 g/L H_2SO_4 (5 g/L Cu), 2 g/L Fe(II) & 0.5 g/L Fe(III): *a*) Comparative copper leaching extents; *b*) Comparative solid-phase mass losses, residue sulfate contents & terminal acid concentrations. The open, grey & closed symbols refer to the tests conducted at 155 (PLX2), 150 (PLX1) & 145ºC (PLW1), respectively. The simulation of Series PLW1 includes the accelerated oxidation of the *Cpy*, *Cov* & *Bor* minerals due the presence of catalytic *Py* surfaces (Eq. 8.4).

This apparent acceleration of the initial oxidation rates strongly supports the discussions of Sections 6.3.2 and 6.3.4, regarding catalytic pyrite (Py_c) surfaces. Figure 8.19 *a* also confirms why this accelerating effect is not observed for Series PLX1 and PLX2, *i.e.*, the bulk (> 75%) of the pyrite mineral was already oxidised after the first 10 minutes. Series PLW1, on the other hand, utilised a slightly lower temperature (145ºC) and significantly coarser material (Sample G), and resulted in only ~35% pyrite oxidation after the first 20 minutes, *i.e.*, corresponding to a 3.5 µm 'imaginary' PPD. Significantly more catalytic pyrite surface area was therefore available in the case of Series PLW1, resulting in accelerated oxidation of the copper sulfide minerals over the first 20 minutes. Table 8.3 illustrates that the pyrite and copper sulfide minerals are very weakly associated and, more importantly, notably less association is prevalent in Sample G compared to Sample L. The copper sulfide minerals are therefore not expected to have experienced any accelerated oxidation by classical (mineral-mineral) galvanic contact, especially not in the case of the coarser sample (G). Instead, these observations provide evidence of the promotion of the sulfide oxidation rate by pyrite-generated radical species. This proposal is in line with recent experimental confirmation (Cohn *et al.*, 2010) and the discussion of Section 6.3.4, rather than supporting a classical pyrite – copper sulfide galvanic mechanism (Dixon *et al.*, 2008; Dixon & Tshilombo, 2005; Hiskey & Wadsworth, 1981; Holmes & Crundwell, 1995; Javad Koleini *et al.*, 2011). Although it could be argued that the above acceleration resulted from particle-particle contact in the slurry suspension, the presence of insulating elemental sulfur surface layers (*e.g.*, Figure 7.32) and the low pyrite-to-copper sulfide mass ratio (~1:5; Table 8.1), at only 5.5 wt% solids, is

Stellenbosch University http://scholar.sun.ac.za

consistent with the propagation of radical species, *e.g.*, hydroxyl radicals (Cohn *et al.*, 2010). Claims of chalcopyrite leaching enhancement by pyrite (Dixon, 2007; Dixon *et al.*, 2008; Dixon & Tshilombo, 2005; Javad Koleini *et al.*, 2011) typically require a pyrite-to-chalcopyrite mass ratio of at least 1:1 in the pulp, before the galvanic effect becomes notable. This approach is based on accelerated reduction of the iron(III) on the pyrite surface, which then enhances the oxidation of the copper sulfide minerals *via* electrochemical contact with pyrite. To put this into perspective, the above experimental results, under conditions of a relatively high oxygen concentration and low acidity (Figure 8.19 *a*), indicate a roughly five times (5×) improvement in the initial rate, at a mass ratio of only 0.2:1 (pyrite:chalcopyrite).

The dominant copper sulfide oxidation mechanism appears, therefore, to be fundamentally different; this could open up alternative processing options at lower oxidation temperatures. Commercial low temperature (LT; Figure 1.1) processing of chalcopyrite concentrates could even become a reality, provided enough oxygen radical species could be formed under such conditions, *i.e.*, if the interaction of diatomic oxygen with pyrite surface is still fast enough, while the inhibiting effect of elemental sulfur could be managed below its melting point.

With these insights in mind, the simulation of Series PLW1 (Figure 8.19) includes the catalytic pyrite surface area term in the rate expressions of the slower leaching copper minerals. Assuming that the catalysed and uncatalysed reaction routes follow similar respective rate dependencies on the hydrogen ion and dissolved oxygen concentrations, and that the total pyrite surface area is catalytically 'active', *i.e.*, that $\theta_{Pyc} = 1$ (Eq. 6.175), the following (simplified) velocity term expression (µm/min) is obtained:

$$\upsilon_{\ell,x}^{Py_c} = \upsilon_{\ell,x}\left(1 + k_{Py_c} a_{Py}\right) \qquad 8.4$$

for each of the slower-leaching copper minerals, *i.e.*, for x = *Cpy*, *Cov* or *Bor*. For illustrative purposes, the rate constant, k_{Pyc}, assumed the same value for all three of these copper sulfide minerals, *i.e.*, 5×10^{-11} kg/µm^2, with the total pyrite surface area, a_{Py}, expressed in units of µm^2/kg (water). As illustrated in Figure 8.19 *a*, this rate expression gives a good representation of the enhanced leaching rate of copper, which only starts to dissipate once a significant portion of the pyrite (surface area) has been oxidised. It is nevertheless recommended that more work be conducted to determine if the S-shaped oxidation kinetics of pyrite (Ch. 7; Sect. 7.4.2) are also present under these high pulp density conditions. If not the case, this would provide additional proof of the absence of a classical galvanic mechanism (galvanic protection of pyrite by, *e.g.*, chalcopyrite; see Sect. 7.5).

Stellenbosch University http://scholar.sun.ac.za

8.3.2 Continuous autoclave and integrated circuit performance, varying key control parameters and monitoring the effects on important reaction extents and reagent consumptions

This section is devoted to the overall phenomenological model, *i.e.*, to gain insight into the effects of the key control parameters on the important reaction extents, species concentrations and reagent consumptions. Based on the above results and discussions, the behaviour of the chalcopyrite oxidation system under typical MT autoclave oxidation conditions is adequately described by the phenomenological model, especially at medium to higher terminal acid concentrations (> 15 g/L H_2SO_4). The following sensitivity analyses are limited to pulp densities above 5 wt% solids to avoid the artificial lowering of the average sulfur yield, due to a high surfactant concentration per unit mineral surface area (compare the low & higher pulp density test results in Sect 7.4.2 & 8.3.1, respectively). In any event, the steady-state pulp density is determined by the autoclave heat balance (Sect. 7.4.1, Figure 7.13 & below), and economical processing (capital & operating expenditure) would obviously favour operation at higher pulp densities.

The following discussions are limited to a few examples, using HBMS concentrate as basis, while the circuit (unit operation) integration does not necessarily reflect any technology or economical optimum. Only the primary flowsheet is therefore included in this analysis, while controlling the mass flow and reagent concentrations within specified limits. This flowsheet arrangement is illustrated in Figure 8.20, summarising all the control parameters utilised during these analyses.

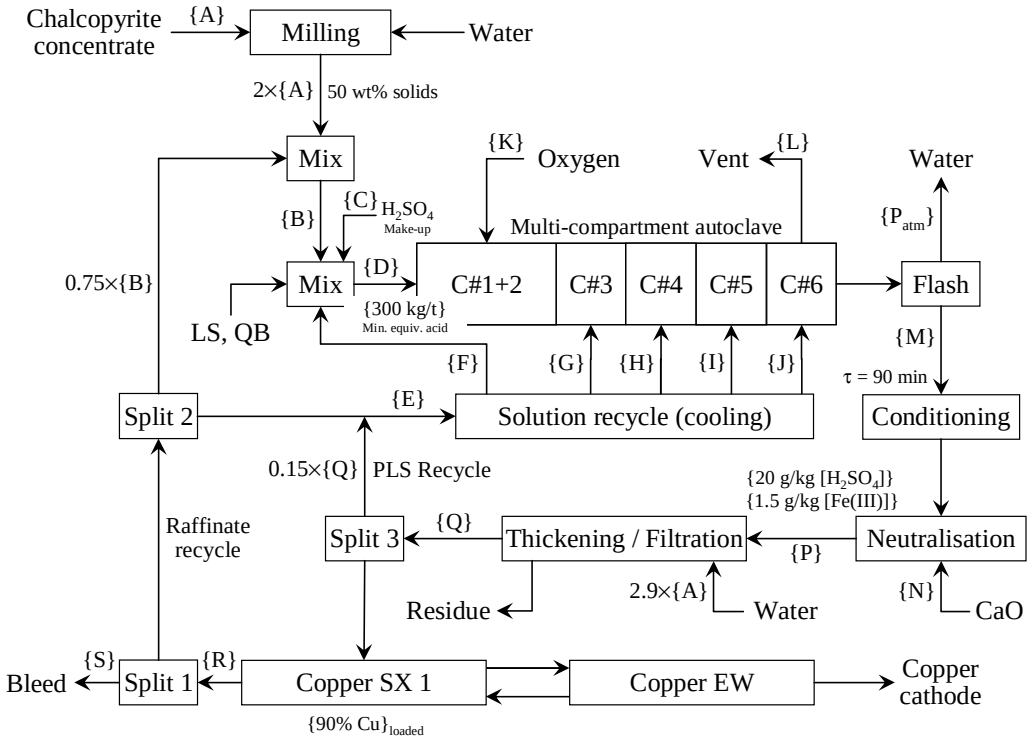

Figure 8.20
Primary flowsheet & control parameters used to conduct the various trend analyses.

Stellenbosch University http://scholar.sun.ac.za

As indicated above, the (ultra-fine) milled concentrate {A} is assumed to carry 50 wt% water into the circuit, which is then mixed with the bulk of the return raffinate to increase the slurry mass three times (3×). This resulting slurry {B} is then mixed with the surfactants, make-up acid {C} (if required) and cooling liquid {F}, to yield the autoclave feed slurry {D}. The cooling liquid flow {F} is controlled to give autothermal operation in the first combined autoclave compartment (C #1+2), while the minimum equivalent acid flow in this feed stream is set at 300 kg/t, *i.e.*, 300 kg ($H_2SO_{4\,(aq)}$ + acid as iron(III)$_{(aq)\rightarrow Hem}$), per tonne dry concentrate feed. The cooling liquid flow {E} comprises 15 wt% recycled pregnant leach solution (PLS) and the rest of the return raffinate solution. This cooling liquid contains a slightly lower acid concentration and is distributed to achieve autothermal operation in all the downstream compartments, *i.e.*, C #3 {G}, C #4 {H}, C #5 {I} and C #6 {J}. The autoclave discharge solution is then subjected to an adiabatic flash calculation, *i.e.*, to atmospheric pressure, before proceeding {M} to the conditioning tank.

Some redissolution of the iron(III) precipitates was observed during the pilot campaigns (Sect. 7.4.1). The extents of these redissolution reactions are not exactly known, due to temperature fluctuations in the semi-batch discharge tanks, in addition to the uncertain and variable hematite and jarosite contents of the discharge slurry. Since conditioning in a full-scale plant would expose the autoclave discharge slurry to higher temperatures and average residence times, these reaction extents are assumed to be higher than experienced during the pilot campaigns, especially in the case of the hydronium jarosite phase. The following correlations are used to estimate the acid dependence of the hematite and jarosite time constants (App. F.4), τ_{Hem} and τ_{Jar} (min), respectively:

$$\tau_{Hem} \cdot 10^{-3} = 15 - [H^+] \qquad 8.5$$

$$\tau_{Jar} \cdot 10^{-3} = 5 - 50 \cdot [H^+] \qquad 8.6$$

where the concentration term refers to the unassociated hydronium ion molality, at the temperature of the conditioning process. A detailed experimental study would be required to establish an accurate mathematical framework to simulate these redissolution reactions, but this was beyond the scope of this study. A relatively large intercept and small negative slope are selected for hematite to account for the inhibitory surface phenomena expected on dissolving iron(III) oxide surfaces (Eq. 8.5). On the other hand, hydronium jarosite is expected to be more prone to redissolution (Sect. 7.4.1), hence the relatively smaller intercept, while the larger slope tries to account for the increased sensitivity to changing solution acidity (Eq. 8.6). The USP model (App. F.4) is applied to both phases, albeit that it is most relevant to the redissolution of the hydronium jarosite phase:

$$X_{Jar} = 1 - \left(1 - \frac{\tau}{\tau_{Jar}}\right)^3 \qquad 8.7$$

Stellenbosch University http://scholar.sun.ac.za

This approach implicitly assumes that the average residence time, τ, is short enough, that the redissolution of these iron(III) precipitates is uninhibited. The effects of other surface equilibria, *e.g.*, precipitation of metastable or thermodynamic phases, are therefore neglected in this simplified approach. An average residence time of 90 minutes is selected and typically yields about 2% hematite redissolution, while the extent of hydronium jarosite redissolution varies between 10 and 20%, depending on the discharge solution acidity. The resulting slurry is neutralised with lime (CaO, {N}) to yield 20 g H_2SO_4/kg (water) and 1.5 g Fe(III)/kg (precipitated as $Fe(OH)_3$ phase). These values are arbitrarily chosen to control the build-up of acid in the primary circuit. The slurry is then thickened and filtered using a fixed washwater addition of 2.9 kg water per kg dry chalcopyrite concentrate feed. This typically translates into 1.5 to 2.0 kg water added per tonne of dry residue. A portion (15 wt%) of the resulting PLS solution {Q} is recycled to the autoclave, while the rest proceeds to the first solvent extraction unit operation (SX 1). The extent of copper loading is fixed at 90%, resulting in raffinate solution {R} of relatively high acidity. Between 10 and 25% of this solution is typically split off, depending on the PLS recycle mass, which represents the only bleed {S} from the primary circuit. The rest of the raffinate solution is recycled, in order to satisfy the total autoclave cooling requirement {E} (discussed above).

This primary flowsheet arrangement is simulated using the mass and energy balance framework developed in Chapter 7. The overall routine minimises the 'excess' energy in the autoclave, *i.e.*, to maintain isothermal operation in each autoclave compartment. Before any trend is generated, the thermodynamic basis for the solution-phase enthalpy calculation needs to be clarified.

Evaluation of the enthalpy calculation bases

Formal and speciated solution calculation bases may used to generate comparative optimisations. The (baseline) formal calculations utilise the standard thermodynamic values of the *HSC* (2006) database (incl. the bisulfate, HSO_4^-, species), while the speciated approach includes all the complex species explicitly recognised in this study (Ch. 2). A summary of all the thermodynamic parameters can be found in Appendix A.7. A comparative formal calculation is also conducted using the standard formal species values from the NBS database (Wagman *et al.*, 1982), but using Lewis linearization (LL) to obtain the Kelly b-parameters (Sect. 7.2.3 & Table A.11 in App. A.7).

The comparative impact on the autoclave and primary circuit performance of using these different calculations and databases is summarised in Table 8.5. The feed PSD is the same as Periods P3 and P4 during the second pilot campaign (Figure 7.10), *i.e.*, d_{90} = 9.8 µm. Calculation of the different mineral phase distributions follows the same methodology as described in Section 8.2.3, using the following chemical composition: 24.7% Cu, 4.5% Zn, 29.0% Fe, 0.25% Ca, 0.09% Mg, 0.6% CO_3, and 3.4% SO_4. After assuming 33.4% S^T, the following baseline mineralogical composition is

Stellenbosch University http://scholar.sun.ac.za

obtained: 68.5% $CuFeS_2$, 6.7% ZnS, 0.9% FeS, 0.1% Fe_3O_4, 1.3% Fe_7S_8, 12.0% FeS_2, 0.6% $CaCO_3$, 0.3% $MgCO_3$, 2.5% $CuSO_4$, 3.1% $FeSO_4$ and 4.0% SiO_2. The baseline sulfur yields on the chalcopyrite and pyrite surfaces (Eq. 8.3) are set at 75% and 25%, respectively. Finally, the compartmental volumes are adjusted to give around 100 minutes total average residence time. These volumes are distributed as follows: 38% C #1&2, 18% C #3, 16.5% C #4, 15% C #5 and 12.5% C #6. The different mineral rate expressions and assumed reaction stoichiometries are identical to those used in the previous section for the HBMS concentrate, *i.e.*, to simulate the batch system under high pulp density conditions. Since the higher steady-state acidities of the continuous operation result in less severe deviation (regime change) from USP kinetics (*cf.* batch operation, at a lower relative acidity), higher PPD values are relevant to chalcopyrite and pyrite. The same methodology utilised in Section 7.4.2, is also adopted here, *i.e.*, a ten times (10×) reduction in the intrinsic rate constants after 4.5 µm PPD.

Table 8.5
Effect of using different solution thermodynamic calculation bases & different databases on the performance of the primary circuit, at autothermal autoclave temperature of 150ºC, 700 kPa $p_{O2}{}^{o}$ & d_{90} ~ 9.8 µm (PSD of pilot feed), during P3 & P4 of the second campaign (Sect. 7.4.1).

[a] Sln. basis	Pulp dens.	Cooling	Compartmental pulp densities (% cooling distribution in brackets)				
–	Feed {D}	{E/A}	C#1,2 {F/E}	C#3 {G/E}	C#4 {H/E}	C#5 {I/E}	C#6 {J/E}
–	[b] (%)	[c] (kg/kg)	[d] %Sld (Split)	[d] %Sld (Split)	[d] %Sld (Split)	[d] %Sld (Split)	[d] %Sld (Split)
[f1] FS (*HSC*)	9.9	4.4	7.7 (35)	6.0 (40)	5.4 (17)	5.3 (7)	5.3 (1)
[f2] FS (NBS, LL)	10.2	3.9	7.9 (33)	6.2 (42)	5.6 (18)	5.6 (6)	5.6 (1)
[g] Actual species	10.5	3.6	8.1 (28)	6.4 (44)	5.8 (19)	5.7 (8)	5.7 (1)
[a] Sln. basis	Bleed	$O_{2,rx}$	[e] Cumulative average residence time ([c] Cu extraction in brackets)				
–	{S/R}	{K-L}	C#1,2	C#3	C#4	C#5	C#6
–	(%)	[c] (kg/t)	min (% Cu)	Min (% Cu)	min (% Cu)	min (% Cu	min (% Cu)
[f1] FS (*HSC*)	17.4	344	43 (69)	59.5 (82)	74 (88)	87 (91.5)	98 (93.2)
[f2] FS (NBS, LL)	18.5	345	44 (69.5)	61 (83)	76.5 (89)	90 (92)	101 (93.7)
[g] Actual species	19.7	346	45.5 (70)	63 (83)	79 (89)	93 (92)	104 (93.8)

[a] All incl. HSO_4^- species; [b] kg solids/kg slurry; [c] *Ref.* dry feed concentrate; [d] kg solids/kg water (exit); [e] 'At temperature'; [f1] Formal species (*HSC* 2006; Table A.10); [f2] Formal species (NBS database; Table A.11); [g] This study (Table A.10).

The most striking aspect of these preliminary calculations is that only slight variations (< 10%) in the calculated pulp densities result due to the different solution enthalpy bases, which translate into relatively small changes in the corresponding average residence times. Despite these variations, the calculated copper extractions are within 1% of each other. Nevertheless, in terms of the process economics, the formal species (thermodynamic) values from the *HSC* database yield the most conservative results, *i.e.*, the lowest pulp densities, justifying its use in the following (indicative) trend analyses.

Stellenbosch University http://scholar.sun.ac.za

The effect of the chalcopyrite sulfur yield on the autoclave and primary circuit performance

The first stepwise variation aims at quantifying the effect of the baseline chalcopyrite sulfur yield. Although this variation refers predominantly to an intrinsic mineral property, it is important to ascertain its impact on particular reaction extents and the (primary) circuit performance. All the above input and control specifications are retained, except for the baseline chalcopyrite sulfur yield, which is adjusted from 85% to 60% in 5% decrements, and the oxygen partial pressure of 1000 kPa p_{O2}^{o}. As indicated above, total feed sulfide content is fixed at 33.4%, yielding 12.0% FeS_2. These results are summarised in Figure 8.21.

The most obvious impact of decreasing the chalcopyrite sulfur yield is the decrease in the pulp density under autothermal autoclave conditions, which, in turn, results in a shorter average residence time and a lower corresponding copper extraction (Figure 8.21 *a*). This response to a change in the average residence time is, however, relatively insensitive in this case, due to the slow leaching kinetics in the latter autoclave stages (10× reduction in the intrinsic rate constants after 4.5 µm PPD; see above). Nevertheless, in economical terms this negative impact would be exacerbated by the notable increase in the overall oxygen consumption, as illustrated in Figure 8.21 *a*.

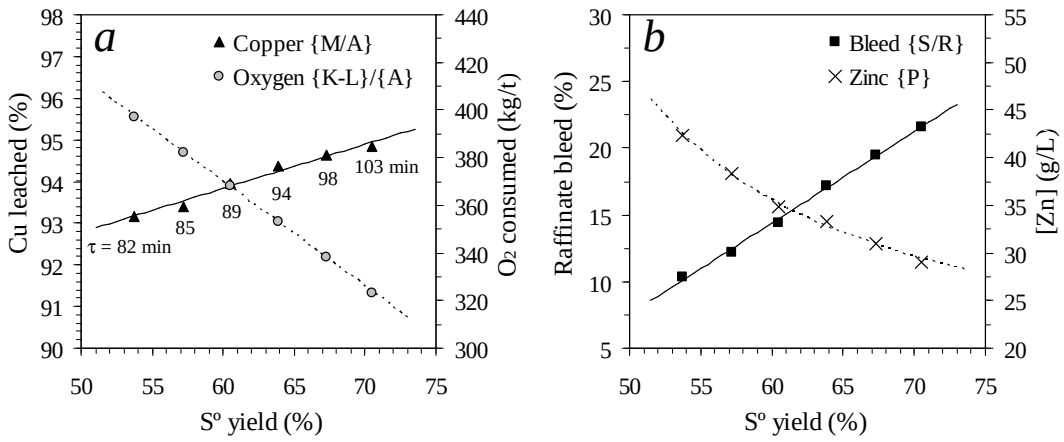

Figure 8.21
The impact of changing the baseline chalcopyrite sulfur yield on selected reaction extents & the primary circuit performance at 150ºC, 1000 kPa p_{O2}^{o} & d_{90} = 9.8 µm (PSD of pilot feed, *ref.* P3 & P4): *a*) Cu leaching extent & O_2 consumption {K-L}/{A} *vs.* overall sulfur yield; *b*) Comparative raffinate bleed ratio {S/R} & [Zn] in neutralised PLS {P} *vs.* overall sulfur yield.

The increased autoclave cooling requirement also demands a lower bleed ratio, which results in a higher zinc tenor in the primary circuit (Figure 8.21 *b*). This tenor refers to a point in the circuit where zinc would be most likely to precipitate (besides in the autoclave itself), *i.e.*, after PLS neutralisation and before the washwater addition point (*ref.* {P} in Figure 8.20). Since the precipitation of hydroxy-sulfate species, *e.g.*, $ZnSO_4.2Zn(OH)_2$, is not incorporated into this analysis, the accurate impact of using lower bleed ratios still has to be quantified for this

Stellenbosch University http://scholar.sun.ac.za

disseminated sulfide concentrate. In practice, an uncontrolled zinc tenor in the primary circuit could result in value losses during filtration, especially if PLS neutralisation is driven excessively.

Figure 8.22 *a* illustrates the dramatic increase in the total equivalent acid concentration (terminal acid, as well as acid locked in as soluble iron(III) species) with the decreasing sulfur yield. It also emphasises the buffering action exerted by the dissolved iron(III) tenor, resulting in relatively weak free acidity changes until most iron(III) has precipitated. Figure 8.22 *b* illustrates that the hydronium jarosite phase also acts as a buffering agent, mirrored by a drop in the hematite fraction, $W_{f,Hem}$, with the decreasing sulfur yield. This is in line with the experimental observations of Section 8.3.1 and Chapter 7 (Sect. 7.4.1). Despite these buffering phenomena, the total neutralisation (CaO) requirement responds almost linearly to the drop in the overall sulfur yield.

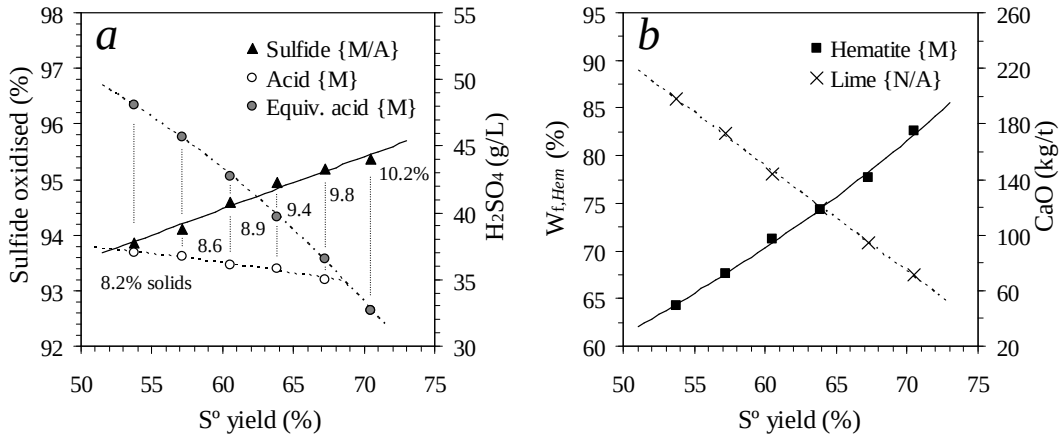

Figure 8.22
The impact of changing the baseline chalcopyrite sulfur yield on selected reaction extents & the primary circuit performance at 150ºC, 1000 kPa $p_{O2}{}^{o}$ & d_{90} = 9.8 µm (PSD of pilot feed *ref.* P3 & P4): *a*) Sulfide oxidation extent & terminal H_2SO_4 concentration {M} *vs.* overall sulfur yield (incl. total equiv. acid, assuming 1.5 mol H_2SO_4 released/mol Fe(III) precipitated); *b*) Fractional (normalised) hematite content {M} & CaO requirement {N/A} *vs.* overall sulfur yield (equiv. CaO to yield 20 g/kg H_2SO_4, 1.5 g/kg Fe(III) & neutralise the total hydronium jarosite phase {P}). The labels refer to the pulp density (kg solids/kg slurry) in the autoclave feed {D}.

The effect of pyrite-to-chalcopyrite feed ratio on the autoclave and primary circuit performance

The following analysis follows on from the above trends, but instead of manipulating the intrinsic sulfur yield, the pyrite (Py)-to-chalcopyrite (Cpy) mass ratio is varied. Again, the feed composition and PSD are kept the same (see above), while the feed mineralogy is calculated to yield a constant 32.5% total sulfide content. The chalcopyrite content is systematically lowered, which results in an increasing pyrite content. The copper content of 24.7% is kept constant by increasing the corresponding relative abundance of the $CuSO_4$ phase. The total iron content of 29% is also kept constant by varying the prevalence of the $FeSO_4$ phase, except at the highest pyrite content (30.6% Py/Cpy), where the total iron content is slightly lower (28%) in order to yield a realistic, *i.e.*,

Stellenbosch University http://scholar.sun.ac.za

positive, gangue SiO_2 content. The other mineral abundances remain constant and the baseline sulfur yield on chalcopyrite surface is fixed at 75%. These results are illustrated in Figure 8.23 and Figure 8.24, and are in agreement with the above trends, albeit less accentuated.

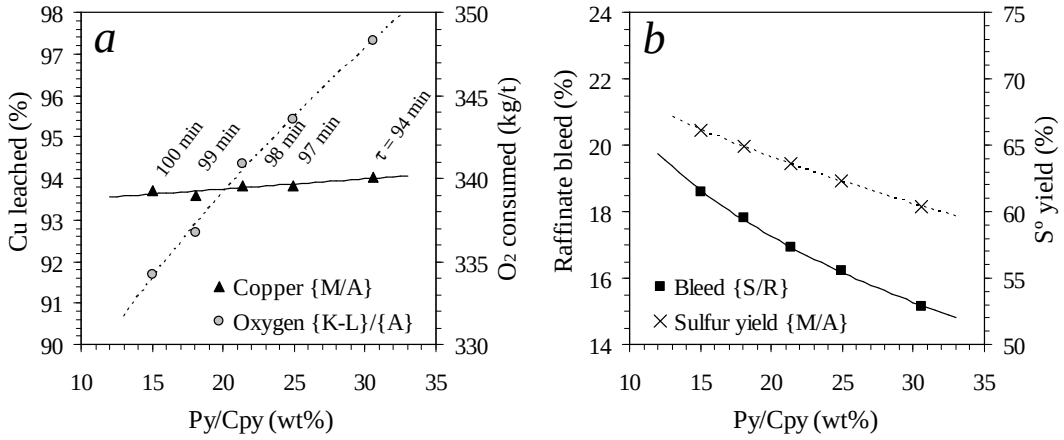

Figure 8.23
The impact of changing the relative pyrite (Py)-to-chalcopyrite (Cpy) abundance in the feed {A} on selected reaction extents & the primary circuit performance at 150ºC, 700 kPa p_{O2}° & d_{90} = 9.8 µm (PSD of pilot feed *ref.* P3 & P4): *a*) Cu leaching extent & O_2 consumed {K-L}/{A} *vs.* Py/Cpy ratio; *b*) Comparative raffinate bleed ratio {S/R} & overall sulfur yield {M/A} *vs.* Py/Cpy ratio.

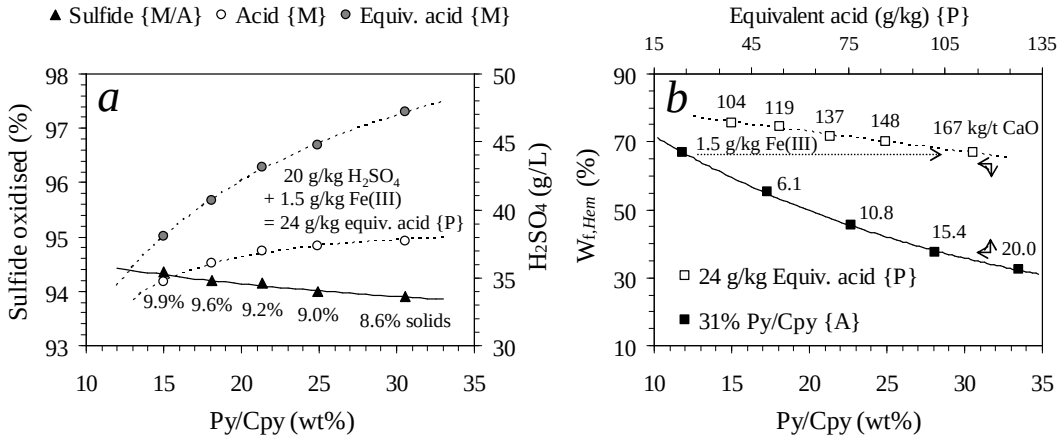

Figure 8.24
The impact of changing the relative pyrite (Py)-to-chalcopyrite (Cpy) abundance in the feed {A} on selected reaction extents & the primary circuit performance at 150ºC, 700 kPa p_{O2}° & d_{90} = 9.8 µm (PSD of pilot feed *ref.* P3 & P4): *a*) Sulfide oxidation extent & terminal H_2SO_4 concentration {M} *vs.* Py/Cpy ratio (incl. total equiv. acid, assuming 1.5 mol H_2SO_4 released/mol Fe(III) precipitated); The labels refer to the pulp density (kg solids/kg slurry) in the autoclave feed {D}; *b*) Fractional (normalised) hematite content {M} *vs.* Py/Cpy ratio (open symbols; the labels refer to the equiv. CaO {N/A} to yield 20 g/kg H_2SO_4, 1.5 g/kg Fe(III) & neutralise the total hydronium jarosite phase {P}). The closed symbols illustrate the response of $W_{f,Hem}$ to varying neutralisation extents (residual equiv. acid) at 31% Py/Cpy ratio (the labels refer to the residual Fe(III) molalities {P}).

Stellenbosch University http://scholar.sun.ac.za

A contradictory (*ref.* the previous trends) increase in the copper extraction with decreasing residence time (higher pyrite content) is apparent in Figure 8.23 *a*. However, this trend is somewhat artificial, because the copper content of the feed material is kept constant by increasing the relative abundance of the $CuSO_4$ phase. This phase is assumed to dissolve immediately on entering the reactor hence the apparent increase in copper extraction rate. A steady drop in total sulfide oxidation extent with increasing pyrite content (Figure 8.24 *a*), is more typical of what would be expected in practice. No catalytic effect of pyrite on the oxidation rates of sulfide minerals is included in this analysis, since the feed PSD is smaller and the steady-state autoclave acidity significantly higher compared to the conditions where such effects have been observed during batch experimentation (Figure 8.19).

These trends confirm that the primary reason for the negative (economical) impact of an increased pyrite content in the autoclave feed is related to the low intrinsic yield of elemental sulfur on its surface (Figure 8.23 *b*). This translates into an increased oxygen consumption (Figure 8.23 *a*), while the excess acid either has to be neutralised or the system will buffer itself by producing more hydronium jarosite (Figure 8.24 *b*). Besides these aspects, an increased pyrite content (per kg water) releases additional heat into the system, primarily due to its low intrinsic sulfur yield (see pulp densities in Figure 8.23 *a*). This becomes apparent after comparing the relative energies released by the primary oxidation reactions (Table 8.6). Although the energy released per mole elemental sulfur produced increases in the order pyrite < chalcopyrite < sphalerite, the respective intrinsic yield of sulfate decreases dramatically. Since the oxidation of elemental sulfur to form acid (last reaction in Table 8.6) is most exothermic, pyrite mineral oxidation releases about 60% and 160% more energy than chalcopyrite and sphalerite oxidation, respectively (based on 95%, 25% and 5% sulfate yields, $y_{(SO4)}$, on pyrite, chalcopyrite & sphalerite, respectively). It is therefore clear that control of the pyrite content in the autoclave feed is important to ensure maximum pulp density under MT oxidation conditions, especially if a target copper extraction is to be maintained in a commercial autoclave that operates close to its maximum (volume) capacity.

Table 8.6
Intrinsic heat regenerated by the primary oxidation reactions at 150ºC.

Oxidation reaction –	[a] $\Delta H_{rx,150ºC}$ (kJ/mol Sº)	$y_{(SO4)}$ (%)	$\Delta H_{rx,150ºC}$ (kJ/mol S_{rx})
$FeS_2 + ¾O_2 \Rightarrow ½Fe_2O_3 + 2Sº$	-114	95	-727
$CuFeS_2 + H^+ + HSO_4^- + 1¼O_2 \Rightarrow Cu^{2+} + SO_4^{2-} + ½Fe_2O_3 + 2Sº + H_2O$	-226	35	-452
$ZnS + H^+ + HSO_4^- + ½O_2 \Rightarrow Zn^{2+} + SO_4^{2-} + Sº + H_2O$	-248	5	-280
$Sº + 1½O_2 + H_2O \Rightarrow H^+ + HSO_4^-$	–	100	-645

[a] Solid-phase & liquid sulfur enthalpy & Kelley parameters from *HSC* (2006) (Table A.10). Solution-phase enthalpy values from NBS tables (Wagman *et al.*, 1982) (Kelly b-values derived using Lewis linearization; Table A.11).

Stellenbosch University http://scholar.sun.ac.za

The effect of the feed PSD on the autoclave and primary circuit performance

The next important operating parameter is the PSD of the feed concentrate. The above trends are based on the feed PSD of P3 and P4 during the second pilot campaign. (Figure 7.10, *i.e.*, d_{90} = 9.8 µm). The following analysis trend evaluates the effect of shifting this PSD in coarser and finer directions, without changing the shape of the distribution, while an additional calculation focuses on the autoclave performance after 'removing' the coarsest particles (> 11.5 µm). These PSDs are illustrated in Figure 8.25.

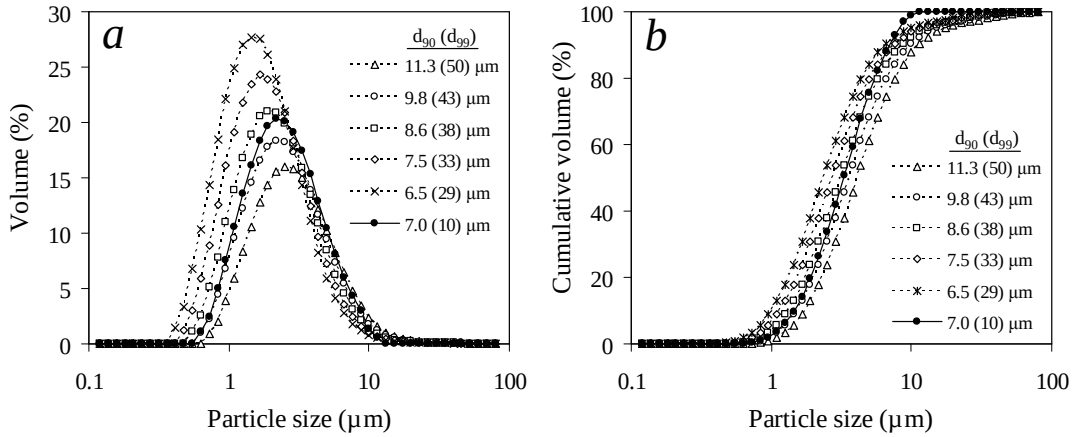

Figure 8.25
Feed particle size distributions (PSDs) used in the trend analysis: *a*) Particle density distributions; *b*) Cumulative distributions (d_{99} in brackets). The open symbols represent the same 'shape' PSDs of varying (grind) size, while the closed symbols represent the PSD without the coarser particle fraction (100% < 11.5 µm, yielding d_{99} = 10 µm & d_{90} = 7.0 µm).

These feed PSDs are each subjected to an iterative mass and energy balance calculation, again using the constant baseline mineralogy (68.5% $CuFeS_2$, 12.0% FeS_2, *etc.*, to give 33.4% total sulfide content) and sulfur yields (75% & 25%, respectively). The resulting trends are illustrated in Figure 8.26 and Figure 8.27.

As expected, the finer PSDs result in a higher overall copper extraction. Figure 8.26 *a* illustrates that the overall oxygen consumption closely follows the copper leaching extent, provided the overall sulfur yield remains relatively constant (Figure 8.26 *b*). This analysis ignores the possible effects of varying surfactant concentration per unit particle surface area (see Sect. 8.3.1). Nevertheless, the higher oxidation extents of the finer PSDs result in more heat generation per unit mass water, which, in turn, increases the raffinate recycle (lower bleed ratio) and results in a shorter average residence time. The most important result from this analysis is the improvement (indicated by the arrow in Figure 8.26 *a*) in the copper leaching extent (~97%), after the coarse particles have been 'removed'. This feed material (d_{99} = 10 µm) is 'generated' by subtracting the coarse particles (> 11.5 µm) from the baseline PSD (d_{90} = 9.8 µm) and replacing the equivalent

Stellenbosch University http://scholar.sun.ac.za

mass, proportionally using the remaining distribution (see Figure 8.25 *b*). This methodology could find particular use in industrial applications, *e.g.*, by using a cyclone to 'cut' the PSD at some maximum particle size, improving the copper extraction with a minimum (milling) energy penalty. Figure 8.27 *a* illustrates that these different PSDs would not be expected to significantly change the free or total (equivalent) acidity of the autoclave, which is mirrored by similar hematite contents and overall neutralisation requirements (Figure 8.27 *b*).

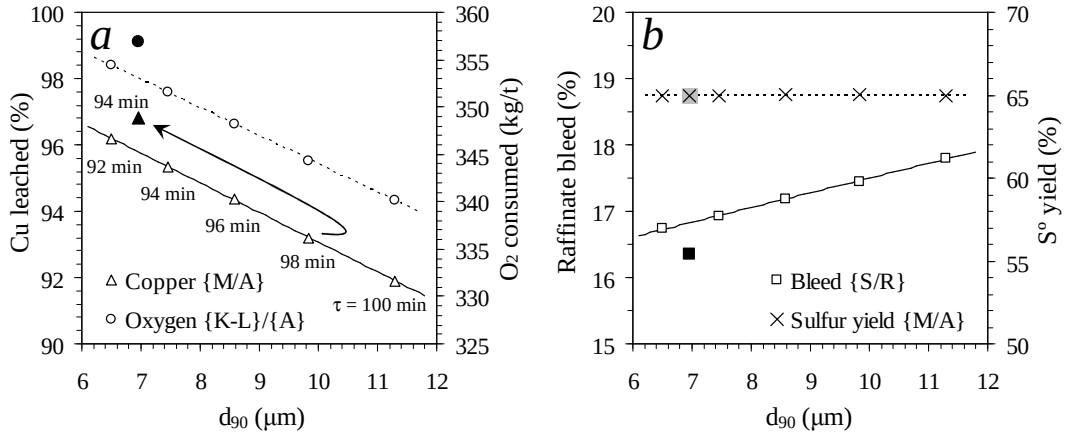

Figure 8.26
The impact of different feed PSDs on selected reaction extents & primary circuit performance at 150ºC & 700 kPa p_{O2}º: *a*) Cu leaching extent & O_2 consumed {K-L}/{A} *vs.* d_{90}; *b*) Comparative raffinate bleed ratio {S/R} & overall sulfur yield {M/A} *vs.* d_{90}. The closed symbols represent the results of the feed PSD, without the coarser segment (100% < 11.5 µm, yielding d_{90} = 7.0 µm).

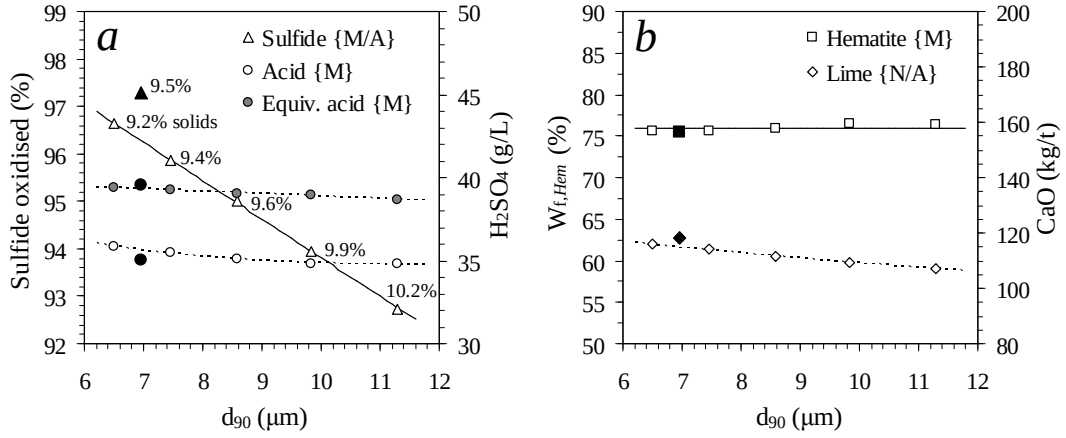

Figure 8.27
The impact of different feed PSDs on selected reaction extents & the primary circuit performance at 150ºC & 700 kPa p_{O2}º: *a*) Sulfide oxidation extent & terminal H_2SO_4 concentration {M} *vs.* d_{90} (incl. total equiv. acid, assuming 1.5 mol H_2SO_4 released/mol Fe(III) precipitated); *b*) Fractional (normalised) hematite content {M} & CaO requirement {N/A} *vs.* d_{90} (equiv. CaO to yield 20 g/kg H_2SO_4, 1.5 g/kg Fe(III) & neutralise total hydronium jarosite phase {P}). The labels refer to the pulp density (kg solids/kg slurry) in the autoclave feed {D}. The closed symbols represent the results of the feed PSD, without the coarser segment (100% < 11.5 µm, yielding d_{90} = 7.0 µm).

Stellenbosch University http://scholar.sun.ac.za

The effect of the operating temperature on the autoclave and primary circuit performance

The autoclave temperature is the final variable included in these preliminary trend analyses and is illustrated in Figure 8.28 and Figure 8.29. This exercise is not elaborated upon in much detail here, because of the uncertainties associated with changes in the kinetics of iron(III) precipitation at high precipitate area, as well as due to the changes in the intrinsic elemental sulfur yield with varying temperature (discussed previously). Furthermore, significant changes in mineral oxidation rates complicate a direct comparison of the autoclave performance at different oxidation temperatures. This is because a lower copper leaching extent, at a lower oxidation temperature, strongly impacts on the acid balance in the primary circuit, primarily due to a lower copper concentration in the feed to SX 1 {Q}. In order to prevent abnormally low autoclave acidities at the lower temperature end, the PLS acid control {P} is varied to give an approximately constant concentration (~42 g/L equiv. H_2SO_4) exiting the autoclave flash {M}, while (artificially) maintaining the 1.5 g/kg Fe(III) target in {P}.

As a first estimate, the activation energy of the secondary hematite precipitation mechanism, $E_{a,Hem}$, is adopted from Chapter 5 (125 kJ/mol; Table 5.10), while the average literature activation energy value for jarosite growth (100 kJ/mol) is also retained. This results in a marginal increase in the hematite content, $W_{f,Hem}$, with increasing temperature (see below; Figure 8.29 *b*). An increased temperature accelerates the oxidation of chalcopyrite and pyrite minerals, as well as of iron(II). The resulting (high) iron(III) supersaturation levels particularly favour hydronium jarosite growth, G_{Jar}, at autoclave acidity levels above about 20 g/L H_2SO_4, which explains the reason behind the strong buffering action exerted by this precipitate. If the elemental sulfur yield decreases more than depicted by Equation 8.3 (over the 140-160ºC range), even this high hematite activation energy (of 125 kJ/mol) would not prevent an increase in the hydronium jarosite content with temperature. As illustrated in Chapter 5 (Figure 5.2), significantly higher temperatures would then be required to drive the hematite phase, provided the acidity is still low enough to prevent basic ferric sulfate (BFS) phase formation. Therefore, under MT autoclave conditions, control of the autoclave acidity rather than the temperature is required to ensure that a high-hematite residue is produced. Depending on the mineralogical composition of the feed concentrate, this may require more or less post-leach neutralisation. Interestingly, the batch simulation (previous section) is also not significantly affected by a high $E_{a,Hem}$ value, even at 140ºC (Figure 8.17 *b*). This is because a high iron(III) supersaturation is usually associated with the initial batch leaching period, when the iron(III) precipitate surface area is still relatively low and hydronium jarosite growth dominates the precipitation mechanism. Then, during the latter leaching stages, when significant iron(III) precipitate surface area has accumulated, the supersaturation level has decreased to such an extent that the overall hematite content becomes less sensitive to this activation energy value.

Stellenbosch University http://scholar.sun.ac.za

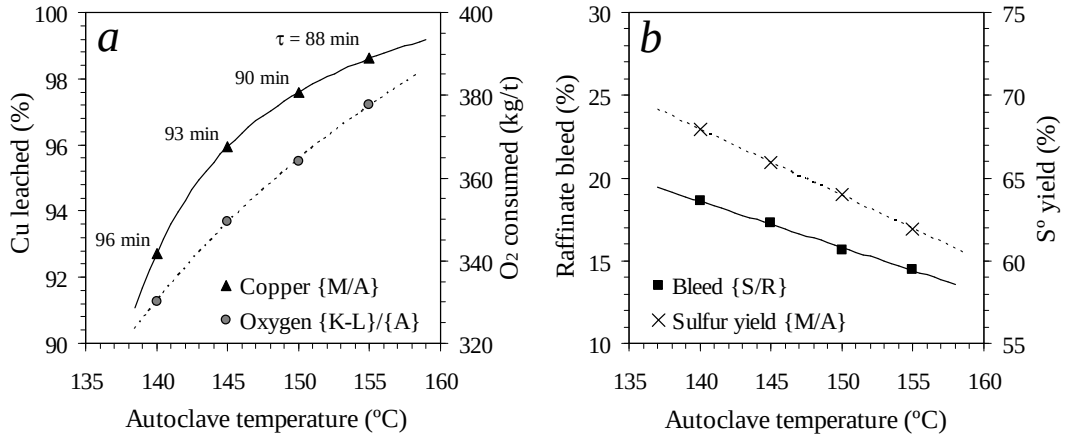

Figure 8.28
The effect of the autothermal autoclave temperature on selected reaction extents & the primary circuit performance at 1000 kPa p_{O2}º, using the feed PSD without the coarser segment (100% < 11.5 µm, yielding d_{90} = 7.0 µm) & controlling the PLS acid in {P} to give constant equiv. acidity (~42 g/L) exiting the autoclave {M}: *a*) Cu leaching extent & O_2 consumed {K-L}/{A} *vs.* temp.; *b*) Comparative raffinate bleed ratio {S/R} & overall sulfur yield {M/A} *vs.* temp.

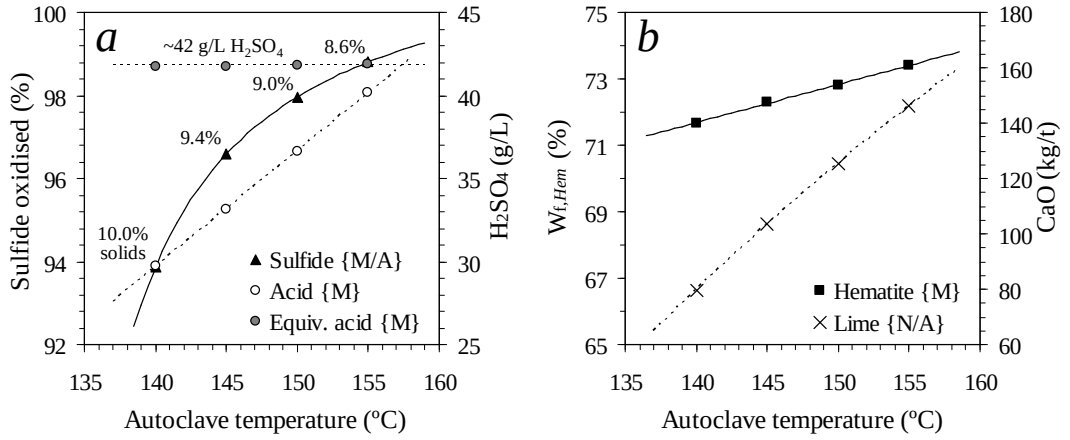

Figure 8.29
The effect of different autothermal autoclave temperatures on selected reaction extents & primary circuit performance at 1000 kPa p_{O2}º, using the feed PSD without the coarser segment (100% < 11.5 µm, yielding d_{90} = 7.0 µm) & controlling the PLS acid in {P} to give constant equiv. acidity (~42 g/L) exiting the autoclave {M}: *a*) Sulfide oxidation extent & terminal H_2SO_4 concentration {M} *vs.* temp. (incl. total equiv. acid, assuming 1.5 mol H_2SO_4 released/mol Fe(III) precipitated); *b*) Fractional (normalised) hematite content {M} & CaO requirement {N/A} *vs.* temp. (equiv. CaO to yield varying H_2SO_4, 1.5 g/kg Fe(III) & neutralise total hydronium jarosite phase {P}). The labels refer to the pulp density (kg solids/kg slurry) in the autoclave feed {D}.

These simulations utilise the feed PSD, without the coarser size fraction (100% < 11.5 µm, yielding d_{90} = 7.0 µm; Figure 8.26) and the same mineralogical composition as before (see above). The oxygen partial pressure is arbitrarily set at 1000 kPa p_{O2}º. The equivalent acid in the recycle (post-neutralisation) PLS stream {P} is adjusted (increased) to account for the increase in the elemental

Stellenbosch University http://scholar.sun.ac.za

sulfur yield and the decrease in the copper leaching extent with decreasing temperature, while the raffinate bleed ratio also mirrors this change in the intrinsic elemental sulfur yield (Figure 8.28 *b*). Despite the smaller bleed ratio, the average residence time (at autothermal operation) decreases with increasing oxidation temperature, while the oxygen consumption follows the overall copper leaching extent by virtue of the drop in the intrinsic elemental sulfur yield (Figure 8.28 *a*). Figure 8.29 *a* illustrates that a higher free acidity level, but approximately constant total (equivalent) acid quantity (~42 g/L H_2SO_4), exits the autoclave over increasing operating temperature. Figure 8.29 *b* illustrates that the kinetics of hydronium jarosite precipitation dominate under these relatively high autoclave acidities, and that significant lime additions would be required to prevent excessive jarosite formation, even at a relatively high operating temperature (*e.g.*, 155ºC). It is therefore imperative to control the acidity in the feed to the autoclave, unless the mineralogy of the concentrate intrinsically yields more elemental sulfur (Figure 8.22 *b*).

No further conclusions are drawn from these trends due to the uncertainties associated with the relative activation energies of the different iron(III) precipitates, different precipitation mechanisms at lower iron(III) supersaturation levels, complicated sulfide mineral oxidation mechanisms, and uncertain intrinsic elemental sulfur yields on these mineral surfaces, especially at lower acidity levels. Nevertheless, a powerful phenomenological simulation has been developed and various insightful conclusions are drawn, not only regarding possible oxidation and precipitation mechanisms, but also regarding the important process control variables.

8.4 Overview and recommendations

This chapter is devoted to the application of the overall model to describe high pulp density chalcopyrite concentrate oxidation in batch and continuous reactor configurations. The batch simulation performance is compared with the experimental response at high pulp density conditions, using different head solution acidities, oxidation temperatures and oxygen overpressures. Where necessary, these observations are used to improve the most important mineral oxidation rate expressions, after which these are incorporated into the continuous reactor simulation. This simulation is imbedded within the integrated (primary flowsheet) mass and energy balance (*ref.* Chapter 7), which is then used to study the sensitivities of selected reaction extents and other primary circuit properties to step changes in the important operating parameters.

8.4.1 Simulating the batch autoclave under high pulp density conditions

The (batch) experimental programme investigated two concentrates, namely HBMS (Hudson Bay Mining and Smelting) and LT (Las Tortolas) cleaner concentrates, utilising the same equipment and similar procedures as those described in the previous chapters. Unfortunately, due to the prevalence of iron(III) precipitation at these high pulp densities, no bulk modal information could

Stellenbosch University http://scholar.sun.ac.za

be generated to determine the relative oxidation rates of the different minerals. Therefore, this chapter solely relies upon average chemical analyses, from two different laboratories, to obtain the relative mineral oxidation rates and total elemental sulfur yields. A number of simplifying assumptions are adopted for this purpose, *e.g.*, the copper and zinc extraction rates are directly related to the oxidation rates of the chalcopyrite and sphalerite minerals, respectively, the pyrrhotite oxidation rate is assumed the same as the sphalerite phase, while the unaccounted sulfide content in the residue as assumed to correspond to the pyrite mineral. The solid-phase mass loss is directly measured, while the hematite *vs.* hydronium jarosite ratio is obtained iteratively from the residual iron and sulfate contents. The particle size distributions (PSDs) of all the head samples are known and serve as input to the batch simulations. The mineralogical compositions of these head samples are also based on the chemical analyses and closely follow the measured composition, as obtained from selected bulk modal analyses. Unfortunately, the mineralogical composition of the LT concentrate is too complex to rely on chemical analysis alone. The relative abundance of the sulfide minerals is therefore scaled to the (chemically analysed) total copper and iron contents, using the chemical and bulk modal analyses of a LT reference sample. Good agreement between the chemically analysed and calculated elemental contents is obtained in this manner.

A liberation study of the LT samples reveals only minor physical association between the chalcopyrite and pyrite minerals, especially for the coarser sample. This is an important observation since the discussions below elaborate on the possible reasons for an apparent enhanced copper leaching rate from this coarser sample, which support the argument for the catalytic workings of pyrite rather than classical (mineral-mineral) galvanic contact. In fact, comparison between the simulated and experimental high pulp density batch leach tests reveals various insights, which may be summarised as follows:

- The chalcopyrite oxidation rate expression and constants derived under low pulp density conditions (Sect. 7.4.2) perform relatively well in the high pulp density batch simulation. However, the pyrite mineral oxidation rate expression, based on the dissolved iron(III) concentration (Eq. 7.84), significantly overestimates the oxidation rate. No significant improvement can be obtained by introducing the anodic half-cell contribution, *i.e.*, the iron(II) surface oxidation reaction, to the cathodic reduction of iron(III). Initial indications are that around a ten times (10×) reduction in the intrinsic rate constant value is required to correctly describe the pyrite oxidation rate. This is in line with previous observations (Ch. 7), which demanded a similar reduced pyrite rate constant when simulating the continuous pilot autoclave, also conducted at high pulp density conditions. Although this phenomenon was previously (Sect. 7.4.2) ascribed to the inefficiency of the sulfur dispersing agent (surfactant), *i.e.*, Norlig A lignosulfonate (LS), these high pulp density batch results utilised relatively high concentrations of an alternative and fresh LS, *i.e.*, Arbo A02. These

Stellenbosch University http://scholar.sun.ac.za

discrepancies are therefore not due to surfactant degradation. Instead, it is speculated that either or both the iron(III) and dissolved diatomic oxygen could be rate-limiting, depending on mineral surface and solution conditions. It is proposed that both iron(III) and dissolved oxygen are intrinsic elements of the rate-limiting step during pyrite oxidation, which is in line with the proposals of Chapter 7 (Figure 7.41). This proposal is also supported by the fact that the original pyrite oxidation rate equation, expressed in terms of the dissolved oxygen concentration (Sect. 6.6.2 & Eq. 8.1), is more successful under these high pulp density conditions and in the presence of a notable initial iron(III) concentration

- The elemental sulfur yield on the primary minerals, chalcopyrite and pyrite, also needs some elaboration, since a significant drop in the observed elemental sulfur yield is observed at lower starting acidities. Besides the various reaction (pathway) complexities and different mechanistic possibilities, the behaviour of sulfur appears rather unpredictable. Various tests were conducted at lower acidities in order to derive empirical dependencies of these sulfur yields on the unassociated hydrogen ion concentration. A baseline (theoretical) chalcopyrite sulfur yield of 75% is expected, *i.e.*, after the first two electrons have been transferred to the iron(III) species, releasing chalcopyritic iron, followed by oxygen reduction, sulfur species rearrangement and decomposition. This mechanism, albeit vague, is consistent with the discussions of Section 6.3.2 and the regressed baseline value of 80%, which turns out to be close to this theoretical yield, forms the departure point of the empirical algorithm. This sulfur yield algorithm accounts for the stabilising and destabilising effects of the hydrogen ion and dissolved oxygen concentrations, respectively. A similar algorithm is also adopted for pyrite the mineral surface, but cannot be regressed due to the lack of accurate experimental data with regard to the extent of pyrite oxidation, as well as its complicated oxidation mechanism. An arbitrary baseline yield of 30% is selected, based on the high surface potential expected for this mineral. Cognisance should also taken of an apparent drop in the overall sulfur yield when conducting testwork at low pulp densities, *i.e.*, under conditions of higher surfactant concentration *vs.* total particle surface area. The elemental sulfur yields on sphalerite and pyrrhotite are assumed to be constant at 95%, which is consistent with a predominantly iron(III) reduction mechanism
- Not only the sulfur chemistry, but also the type and surface concentration of the oxidants would influence the reaction stoichiometries. For example, surface sulfur moves through many different oxidation states and intermediate radical species, while some species may become more mobile and desorb from the surface, before taking part in further oxidation. Adjacent reaction sites are also not be electrochemically isolated from each other, which makes these reactions complex and renders them highly dependent on the prevailing mineral surface conditions. These conditions are not necessarily the same for minerals in different concentrates, not even on different crystal faces of the same mineral, while the

Stellenbosch University http://scholar.sun.ac.za

effect of sulfur product layers, however thin (see, *e.g.*, Figure 7.22 *b*), may result in changing conditions over time (diffusion limitations). For the sake of simplicity, it is assumed that there is a strong relationship between the sulfur yield and the surface potential, which, in turn, depends on whether mineral oxidation is driven by multi-electron oxygen reduction or one-electron iron(III) reduction mechanisms, or, in the case of pyrite, is accompanied by a water splitting mechanism. In general, it is expected that a higher surface potential would transpire during initial oxidation at lower pulp densities, where the ratio of surfactant concentration to mineral surface area is higher. Under such conditions, the net amount of iron(III) reduction on the mineral surface would be lower, while the situation may be reversed at longer reaction times. As a first estimate, the assumptions of Section 7.4.2 are retained for the HBMS concentrate, as they accurately account for the acid and iron behaviour in the continuous pilot plant, *i.e.*, $N_{FeIII,Cpy} = 0$ and $N_{FeIII,Py} = -1$

- The above assumptions are incorporated into the high pulp density batch simulations, yielding good agreement with the experimental reaction extents, at least over the first 60 minutes, especially with regard to pyrite oxidation, the overall elemental sulfur yield and the (associated) terminal acid concentration. Considering the various assumptions made with regard to the oxidation and precipitation mechanisms (Ch. 4-7), the oxidation and precipitation behaviours of iron are relatively well described by the simulation. The initial drop in acid concentration due to the fast-reacting sulfides, coincides with the precipitation of iron(III), *i.e.*, the initial low acid environment creates high supersaturation conditions which, in turn, create new hematite particles *via* primary nucleation (accompanied by rapid but limited growth). However, these high supersaturation conditions also promote hydronium jarosite surface nucleation (on existing hematite substrate surface) and subsequent growth, resulting in its dominance during the initial mineral oxidation period. The increase in the total iron(III) precipitate surface area with time then results in secondary hematite nucleation (accompanied by rapid but limited growth), at the expense of jarosite growth, which translates into a gradual increase in the predominance of the hematite phase. Therefore, to a large extent, the prevailing solution acidity (with time) determines which phase dominates overall, *i.e.*, hematite *vs.* hydronium jarosite. In accordance with the continuous pilot plant simulation results (Ch. 6), hydronium jarosite is also shown to buffer increased solution acidity, *i.e.*, at the expense of the hematite phase
- Based on the consistent performance of the overall phenomenological model, it may also be used to quantify the response of the system to a changing variable, *e.g.*, a new (different) surfactant at different concentrations Experimental results, using 0.15 and 0.5 g/L Borrepal LS, reveal that only the lower surfactant addition caused a deviation from the simulated total sulfide oxidation and copper extraction extents, and only after 60 minutes' reaction time. This confirms that this surfactant is a suitable alternative to the Arbo A02 LS

Stellenbosch University http://scholar.sun.ac.za

and Orfom 2 QB, provided high enough addition is initially made (*e.g.*, 6 kg/t). The simulation is also used to assess the effect of adding the same amount of surfactant, but more gradually over time. Large sulfur conglomerates appeared after 90 minutes, confirming the conclusions of Section 6.5.2 (see Figure 6.35 & related discussions), *i.e.*, additional surfactant addition is unable to disperse sulfur conglomerates, once formed. Based on the k_La-value of the test autoclave (Ch. 3), the simulation also illustrates that the oxygen concentration is far removed from its saturation level during the initial oxidation period at these high pulp densities and, typically, only approaches saturation after about one hour

- In summary, taking the various assumptions and inaccuracies of the experimental techniques and the uncertain behaviour of elemental sulfur into account, the agreement between the batch simulation and experimental results is deemed acceptable. The various rate expressions can therefore be directly incorporated into the continuous reactor simulation, *i.e.*, under typical MT autoclave acidity environments (> 15 g/L H_2SO_4)
- In view of the above discussions, the rest of the experimental programme focussed on generating high pulp density data in the low acid regime (< 15 g/L H_2SO_4). This lower acidity environments result in significantly higher hematite content (generally > 70%), with relatively good agreement between the simulated and experimental iron concentration values. The iron(III) precipitation rate only appears to be underestimated during the initial reaction, *i.e.*, under very low terminal acid concentrations during initial mineral oxidation, which is in line with the conclusions of Chapter 5, suggesting that a more accurate description of the solution thermodynamics is required in the low acid regime
- In general, most reaction extents are reasonably well simulated in the low acid regime, except for the sulfide mineral oxidation rates. Although agreement is good between the simulated and experimental chalcopyrite and total sulfide oxidation extents during initial oxidation, substantial negative deviation of the experimental extents occurs at longer reaction times. These deviations may be related to reagent diffusion limitations through the thin molten sulfur product layers, which have been shown (Ch. 7; Figure 7.22) to develop relatively rapidly on the unreacted mineral surfaces, even in the presence of surfactants. Iron(III) precipitation on these mineral surfaces may also explain why these surface layers appear to become more inhibitory under lower acidity conditions
- Since the tests conducted at lower initial iron(III) concentrations show even more substantial negative deviations, the mechanistic role of iron(III) at lower acidities may also have to be considered. This may point to a mechanistic shift, since tests conducted at higher acidities have confirmed the general insensitivity of the chalcopyrite oxidation rate to the iron(III) concentration (Sect. 6.5.4 & 7.4.2). However, the characteristic 60 to 65%

Stellenbosch University http://scholar.sun.ac.za

elemental sulfur yield, in addition to a better agreement between the simulation and experimental results when using higher oxygen partial pressures, suggests that the oxygen reduction reaction is still the more relevant rate-limiting step on the chalcopyrite surface. Notwithstanding, the primary reason for this apparent phenomenon, *e.g.*, due to denser or polymeric-type sulfur (Sect. 6.3.2) and/or iron(III) precipitation on these mineral surfaces in low acidity environment, cannot be determined from this testwork. No conclusions regarding the mechanism of chalcopyrite oxidation are therefore possible, without conducting more fundamental work

- The final three series of tests, using the finest HBMS ground concentrate, were conducted at different temperatures and oxygen partial pressures. Deviation between the experimental chalcopyrite oxidation and simulated extents is again observed, which appears to be most prevalent at lower oxidation temperatures. Similarly to the pilot autoclave simulation, the intrinsic rate constants are decreased after an 'imaginary' particle penetration depth (PPD) (Sect. 7.4.1; *ref.* unreacted shrinking particle, USP model). Various modifications to the intrinsic chalcopyrite and pyrite oxidation rate expressions have been considered, but no simple functionality in hydrogen ion, iron(III) or dissolved oxygen concentration adequately accounts for these deviations at higher pH conditions. Also, since possible reactant transport limitations across thin molten sulfur and/or iron(III) precipitate surface layers fall outside the classical porous product layer diffusion case, decreasing the intrinsic rate constants, after a certain cut-off PPD, appears to be the simplest and most practical approach
- These results suggest that molten elemental sulfur layers are at least partially responsible for the reduced mineral oxidation rates observed under higher pH conditions, and that low surfactant concentration per unit particle surface area exacerbates the problem, *e.g.*, when utilising finer grinds. The most striking aspect of these deviations is the low apparent cut-off PPD (0.25-0.5 µm) compared to the continuous pilot plant simulations (4.5 µm; Sect. 7.4.2), conducted at higher terminal acid concentrations. This suggests that the surface layers, whether consisting of pure elemental sulfur or mixed with, *e.g.*, hydronium jarosite, are more difficult to disperse at these low terminal acid concentrations and that the conditions are especially inhibitory to sulfide oxidation at lower operating temperatures. Although further testwork would be required to characterise these surface structures, lower temperature oxidation, under conditions of low acidity, does not appear ideal for achieving fast chalcopyrite oxidation, especially when a high initial particle surface area is exposed to the feed solution. The surfactant concentration per unit mineral surface area may be particularly important in this regard, and further studies should be conducted to determine whether molten sulfur could be efficiently dispersed under such conditions

Stellenbosch University http://scholar.sun.ac.za

- Three series of confirmatory high pulp density tests were also conducted on the LT cleaner concentrate, using significantly different PSDs. As mentioned above, the interpretation of the leaching results is more complicated, due to the relatively complex mineralogy, in addition to the sulfur speciation inaccuracies. It is proposed that different analysis techniques be employed in future studies, *e.g.*, thermogravimetry, in order to determine the total elemental sulfur content of the residues. As a first estimate, the simulation assumes a baseline sulfur yield of 40% on covellite, using the correlation developed for chalcopyrite, and constant yields for bornite (85%) and pyrrhotite (95%). It is also assumed that the surface potentials of the various copper minerals are high enough to assume $N_{FeIII} = 0$. However, comparison between the oxidation states of the simulated and calculated iron species in solution is relatively poor. A moderate improvement is achieved when assuming that less oxidising surface conditions prevail at higher pulp densities on the less refractory minerals, *i.e.*, preferential iron(III) reduction mechanisms, to yield $N_{FeIII,Chc} = 2$, $N_{FeIII,Bor} = 12$ and $N_{FeIII,Ph} = 14$. These results suggest that the assumption of a constant surface oxidation mechanism may not hold, especially during batch oxidation in a low acidity environment. However, the relative oxidation rates of the different iron-containing minerals are not known accurately enough to assign a N_{FeIII}-value for each mineral as a function of the (changing) solution properties with time. In general, the lower the temperature, the more significant the direct iron(III) oxidation mechanism would be expected to become. Besides all these complexities, the simulation performs reasonably well and good agreement between the calculated and experimental total sulfide, copper leaching, and mass loss extents, as well as the residue sulfate contents, is achieved for the finely milled LT samples ($d_{50} \approx 3.5$ µm)
- With regard to the tests conducted using the coarser LT material ($d_{50} \approx 22$ µm), the simulation requires roughly around five times (5×) increase in the intrinsic rate constants of the chalcopyrite, covellite and bornite minerals over the initial leaching period (< 20 min) to accurately simulate the experimental copper leaching extent. This suggests that pyrite accelerated the oxidation of these copper minerals. This phenomenon is thought to be a direct result of the relatively coarse grind used, since significant oxidation (> 75%) of the pyrite mineral itself occurs over the first 10 minutes reaction time in the case of the finer LT sample ($d_{50} \approx 3.5$ µm). The fact that the pyrite and copper sulfide minerals are weakly associated (see above), suggests that no accelerated oxidation by classical (mineral-mineral) galvanic contact occurred. Instead, these observations provide evidence of the promotion of the sulfide oxidation rate by pyrite-generated radical species, which is in line with recent publications in the open literature, as well as the discussions in Section 6.3.4

Stellenbosch University http://scholar.sun.ac.za

- Although it could be argued that this acceleration resulted from particle-particle contact in the slurry suspension, the presence of insulating elemental sulfur surface layers and the low pyrite-to-copper sulfide mass ratio (0.2:1) is consistent with the propagation of radical species, *e.g.*, hydroxyl radicals (see Cohn *et al.*, 2010). The dominant copper sulfide oxidation mechanism appears therefore to have been fundamentally different, and this could open up alternative processing options at lower oxidation temperatures
- In terms of the simulation, it is assumed that the catalysed and uncatalysed reaction routes follow similar respective rate dependencies on the hydrogen ion and dissolved oxygen concentrations, and that the total pyrite surface area is catalytically 'active', *i.e.*, that $\theta_{Pyc} = 1$ (Eq. 6.175). Simplified velocity term expressions (µm/min) are then derived (based the discussions in Sect. 6.6.2) for the chalcopyrite covellite and bornite minerals, yielding a good representation of the enhanced leaching rate of copper, which only starts to dissipate once a significant portion of the pyrite (surface area) has been oxidised, and
- It is nevertheless recommended that more work be conducted to determine if the S-shaped oxidation kinetics of pyrite observed under low pulp densities (Ch. 7; Sect. 7.4.2) are also present under these high pulp density conditions. If not the case, this would provide additional proof of the absence of a classical galvanic mechanism, *i.e.*, initial galvanic protection of pyrite by the other sulfide minerals, *e.g.*, chalcopyrite.

8.4.2 Using the phenomenological model to simulate the performance of a continuous MT oxidative autoclave and the integrated circuit to changes in key operating parameters

Based on the above results and discussions, the behaviour of the chalcopyrite oxidation system under typical MT autoclave oxidation conditions is adequately described by the phenomenological model, especially at medium to higher terminal acid concentrations (> 15 g/L H_2SO_4). The final section is devoted to the overall phenomenological model, *i.e.*, to gain insight into the performance of a continuous MT autoclave and to quantify the effects of selected key control parameters on the important reaction extents, species concentrations and reagent consumptions.

The primary leaching – solvent extraction (SX) circuit is configured to conduct trend analyses, without reflecting any technological or economical optimum. Stringent mass flow and reagent concentration controls are implemented to simplify the interpretation of the simulated results, while varying specific control parameters. Most importantly, the autoclave is simulated as a steady-state reactor, operated autothermally by controlling the recycle of SX raffinate and some proportion (15 wt%) of the PLS (cooling) solution to each of the autoclave compartments. The moisture content of the milled concentrate is fixed at 50 wt%, while a minimum acid requirement is set in the feed to the autoclave. The exit slurry is flashed adiabatically, before proceeding to a conditioning tank. Since some of the precipitated hematite and hydronium jarosite redissolved in the pilot campaigns

Stellenbosch University http://scholar.sun.ac.za

(Sect. 7.4.1), estimated time-constant values (USP model) are adopted for these phases. The hydronium jarosite phase is most susceptible to redissolution, especially under conditions of higher free acidity in the discharge slurry. This resulting slurry is then subjected to acid and iron(III) concentration control, using lime as the neutralising agent. Finally, the extent of copper loading during SX is fixed at 90%, while a portion of the raffinate solution is bled from the primary circuit. This bleed ratio is the primary energy balance control, allowing autothermal operation in each of the autoclave compartments (see Figure 8.20). The key outcomes of these trend (sensitivity) analyses may be summarised as follows:

- Firstly, clarification is required on the thermodynamic basis used to calculate the solution-phase enthalpy, *i.e.*, determining the impact of using a formal *vs.* speciated approach on the pulp density and important reaction extents in the autoclave. The formal calculations utilise two sources, namely, the *HSC* (2006) and NBS (Wagman *et al.*, 1982) databases, with the latter relying on the Lewis linearization technique to obtain the Kelly b-parameters (Sect. 7.2.3). The speciated approach relies on the solution thermodynamic model (Ch. 2) and thermodynamic information used in the rest of this study (App. A.7). These different calculation bases only result in slight (< 10%) variation in the calculated pulp densities, which have a relatively small impact on the average residence time and overall copper extraction (< 1%). Nevertheless, the formal species approach, using the *HSC* database, yields the most conservative results and is therefore used to generate the various trends
- In order to test the response of the primary circuit to different chalcopyrite baseline sulfur yields (Eq. 8.3; *ref.* sulfur yield correlation), this value is incrementally lowered from 85% to 60%, while maintaining the pyrite baseline yield at 25% and a constant yield of 95% on the sphalerite and pyrrhotite surfaces. The feed PSD is the same as for Periods P3 and P4 during the second pilot campaign (d_{90} = 9.8 µm; Fig 7.10), while the mineralogical breakdown resembles the HBMS pilot plant feed material. Since the feed acidity is never allowed to drop below a minimum acidity value (300 kg/t acid, as free H_2SO_4 plus the equivalent amount in iron(III)), the kinetic mineral oxidation regime is well described by the various rate expressions developed in this study. Expectedly, the higher the total sulfur yield, the higher the autoclave pulp density, the longer the average residence time and the higher the overall copper leaching extent. This response to the change in the average residence time is, however, relatively insensitive in this case, due to the slow leaching kinetics in the latter autoclave stages, caused by surfactant degradation. Nevertheless, in economical terms the negative impact of a lower sulfur yield is exacerbated by the notable increase in the overall oxygen consumption. In addition, the lower the sulfur yield, the higher the equivalent acid concentration, the lower the relative hematite content (*vs.* hydronium jarosite) and the higher the overall lime requirement. A less obvious negative

Stellenbosch University http://scholar.sun.ac.za

impact of a lower elemental sulfur yield is the build-up of valuable metals, *e.g.*, zinc, in the primary circuit, due to the high relative cooling requirements of the autoclave. Although the precipitation of hydroxy-sulfate species is not included in this simulation, formation of such phases, especially during post-leach neutralisation, could potentially result in some loss of revenue

- Besides the baseline sulfur yield on the chalcopyrite surface, variation of the pyrite-to-chalcopyrite ratio is found to result in similar trends, albeit less accentuated. Different concentrate pyrite-to-chalcopyrite ratios of between 15 and 30 wt% are simulated, while keeping the total sulfide, copper and iron contents of the feed material constant. This trend analysis emphasises the negative impact that increased feed pyrite content would have on the process economics. The low intrinsic yield of elemental sulfur on the pyrite surface is shown to be the primary reason for the excessive generation of heat and acid, as well as increased oxygen consumption. Control of the pyrite content in the milled feed would therefore be of paramount importance to the economical viability of this processing route, making MT or HT oxidation of rougher concentrates (*e.g.*, Sample H; Table 7.2) unfavourable, unless an economical 'acid sink', *e.g.*, a synergistic oxide ore, is available
- The PSD of the feed material is the next important operating parameter that is varied incrementally. As expected, the smaller PSDs result in a higher overall copper extraction, but a slightly lower pulp density, due to the increased rate of heat generation. However, this analysis ignores the (potential) effects of changing surface area on the 'ability' of the surfactants to efficiently disperse sulfur. It also assumes that changes in the surfactant concentration per unit surface area do not affect the overall sulfur yield. The most important indication from this analysis is the impact of physical manipulation of the feed PSD on the overall copper extraction efficiency, *e.g.*, by 'cutting' the PSD at some coarser maximum, the autoclave residence time is utilised more efficiently. The top-size specification, *e.g.*, d_{99}, is particularly important in this regard. However, the practical means to achieve this (*e.g.*, by cycloning) is outside the scope of this study and not elaborated upon
- Finally, the autothermal autoclave temperature is varied in order to illustrate the typical sensitivities of the process to such changes. This exercise is however more complicated, because of the uncertainties associated with the kinetics of iron(III) precipitation at high precipitate surface area, as well as due to the changes in the intrinsic elemental sulfur yield with varying temperature. Furthermore, significant changes in mineral oxidation rate complicate a direct comparison of the autoclave performance at different oxidation temperatures. This is because a lower copper leaching extent at lower oxidation temperature strongly impacts on the acid balance in the primary circuit, primarily due to a

Stellenbosch University http://scholar.sun.ac.za

lower copper concentration in the feed to SX 1. By incorporating sufficient acid control in the primary circuit and using estimated hematite and hydronium jarosite activation energies (Ch. 5), a marginal increase in the hematite content with increasing temperature is noted. The increased temperature also accelerates the oxidation of chalcopyrite and pyrite minerals, as well as of iron(II). The resulting (high) iron(III) supersaturation levels are found to particularly favour hydronium jarosite growth at autoclave acidity levels above about 20 g/L H_2SO_4, which explain the reason behind the strong buffering action exerted by this phase. Therefore, under MT autoclave conditions, control of the autoclave acidity and/or the mineralogical composition of the feed material (overall sulfur yield) would be most important in ensuring that a high-hematite residue is produced. Alternatively, the HT oxidation region could be employed to produce hematite, provided a cheap neutralising agent is available to prevent the acidity of the primary circuit driving the autoclave into the basic ferric sulfate (BFS) regime.

No further conclusions could be drawn from these trends. Better understanding of the fundamental oxidation and precipitation mechanisms, as well as more comprehensive continuous pilot plant data, would allow further improvement of this research and process design tool. In particular, improved understanding of the behaviour of elemental sulfur and iron(III) precipitation on the different sulfide mineral surfaces and their quantitative impact on the mineral oxidation kinetics is required, especially at lower acidity levels. More information is also required on the precipitation rate of iron(III) and of other phases, *e.g.* antlerite, at lower autoclave acidities, while knowing the redissolution rates of the precipitates during slurry conditioning would improve the overall performance of the simulation. With regard to the behaviour of different chalcopyrite concentrates, impurities, *e.g.*, silver (Ag), are known to play important roles in accelerating the oxidation rate. Such variables have not been elaborated upon in this study because they are best viewed as intrinsic mineral properties and not as economically controllable parameters.

8.4.3 Achieving the overall modelling objective (overview)

This chapter presents a detailed assessment of the batch and continuous autoclave reactor simulations developed in Chapter 6, utilising constants obtained from predominantly batch experimentation. In general, these modelling frameworks give excellent representation of the oxidation and precipitation reaction kinetics under typical MT autoclave acidities (> 15 g/L H_2SO_4). A powerful phenomenological simulation has been developed and various insightful conclusions are drawn, not only regarding possible oxidation and precipitation mechanisms, but also regarding the important process control variables

Stellenbosch University http://scholar.sun.ac.za

VOLUME III

STUDY OVERVIEW & KEY OUTCOMES (CH. 9)

REFERENCES

APPENDICES

Stellenbosch University http://scholar.sun.ac.za

CHAPTER 9. STUDY OVERVIEW AND KEY OUTCOMES

9.1 General overview

The major advantage of operating chalcopyrite leaching at typical medium (MT) temperatures (140-155ºC) is that fast sulfide mineral oxidation kinetics is accompanied by notable elemental sulfur yields and a reasonably stable hematite precipitation zone, which is the preferred hydrometallurgical process residue. However, the economically ideal operating window is relatively small and is highly dependent on the mineralogical make-up of the concentrate and, hence, the primary circuit acid balance. If no relatively cheap copper oxide ore or other neutralising source is available, the cost associated with higher operating temperatures (> 180ºC) may be prohibitive. On the other hand, the relatively slow chalcopyrite oxidation kinetics under MT operating temperatures require ultra-fine grinding and higher acid concentrations, which may, to a greater or lesser degree overlap with metastable hydronium jarosite formation. The higher the total elemental sulfur yield, the higher the autothermal pulp density, the lower the oxygen consumption and the more favourable the overall process economics. However, the stifling effect of liquid elemental sulfur is highly dependent on the effectiveness of the surfactants and also places strict requirements on the top size (coarse) fraction in the autoclave feed. The discussions below give a concise summary of the key outcomes of each chapter, the original contributions to the understanding of MT mineral oxidation systems and the capturing of all this knowledge in an internally consistent mathematical framework.

9.2 Solution chemistry

The solution thermodynamics form the departure point of some important reaction kinetic descriptions in this study, *e.g.*, the rate of iron(III) precipitation. Besides quantifying the important speciation trends, the solution vapour pressure is readily obtained from this model, which is important because it influences the oxygen partial pressure, *viz.*, the aqueous concentration of the primary oxidant. Although the Pitzer ion-interaction framework is widely used to capture such thermodynamic properties, an excessive number of interaction parameters are required in mixed electrolyte systems, especially when explicitly recognising the important inner-sphere complexes, *i.e.*, the contact ion pairs (CIPs), that most influence the rates of the various reactions.

The study introduces a unique simplification of the complicated H_2SO_4-$CuSO_4$-$FeSO_4$-$Fe_2(SO_4)_3$-$ZnSO_4$-$MgSO_4$-H_2O mixture by treating the system as H_2SO_4-M(II)-M(III)-SO_4-H_2O. Iron(III) sulfate CIP formation under typical MT autoclave conditions is most likely to form neutrally charged polynuclear clusters because of its trivalent nature and due to a significant drop in the dielectric constant of the solvent (water) compared to room temperature. This complexation is,

Stellenbosch University http://scholar.sun.ac.za

according to the literature, accompanied by a reduction in the acidity *via* the formation of the $FeH(SO_4)_2^o$ species. Although the existence of this species has yet to be convincingly proven, its net zero charge is convenient in that its interaction with the surrounding solute species would be relatively unimportant, justifying its unity activity coefficient and reducing its impact on the electrolyte system to a stoichiometric lowering of the free solution acidity, 'H_2SO_4'. It is further assumed that the $FeH(SO_4)_2^o$ species lowers the water activity in a similar (stoichiometric) fashion to a metal(II) sulfate salt. The overall thermodynamic description is then treated in an internally consistent manner by adopting magnesium as a surrogate salt, reducing the above complicated mixture to the ternary 'H_2SO_4'-'$MgSO_4$'-H_2O system and explicitly recognising only the most important CIPs that may impact on the reaction kinetics.

Although this methodology only provides an estimate of the salt solubilities, solution vapour pressure and speciation changes over changing solution composition and temperature, the complicated nature of the above mixture and the general lack of experimental data justify these simplifications. This unique approach not only prevents over-parameterisation of the model using existing thermodynamic and speciation data, but infers the speciation behaviour at higher temperatures where no quantitative information is currently available. A semi-quantitative interpretation of the quantum-level chemistry is used as a complementary tool to add more confidence to the ambiguous nature of the thermodynamic data in the literature and highlights the differences in the complexation of the different divalent metal sulfate CIPs. Fortunately, such differences can be absorbed in the rate constants of the relevant kinetic expressions, while the CIP formation extents in ternary acid mixtures are low enough, and the divalent metal cation activity coefficients similar enough, to justify this surrogate salt approach. All-in-all, the thermodynamic simulation module contributes to current knowledge in an original manner, not only by mathematically capturing the essential speciation trends in complicated electrolyte mixtures, but also allowing the interpretation and simulation of the various rate processes, *e.g.*, the iron(II) oxidation (Ch. 4), iron(III) precipitation (Ch. 5) and sulfide mineral oxidation (Ch. 6) rates.

Future investigations should focus on generating thermodynamic data at higher temperatures in quaternary mixtures with sulfuric acid and on generating more experimental information around the specific nature and formation extents of the CIPs. Elaborative *ab initio* quantum mechanical – molecular dynamics simulations would be a powerful complementary tool in this quest.

9.3 Interfacial oxygen mass transfer

This part of the study deals with the interfacial oxygen mass transfer rate between the gas and bulk liquid phase, assuming well-mixed stirred tank reactors and using two different methods of

Stellenbosch University http://scholar.sun.ac.za

determining the k_La value, *i.e.*, the indirect chemical (sulfite oxidation) and direct (oxygen) electrode methods.

Besides quantifying the effects of the most important system variables, *e.g.*, temperature and pulp density, on the k_La-values of the reactors used in this study, slurry volume changes are shown to have a potentially critical effect on the overall gas absorption rate. Relatively small variations in the distance between the top impeller and the slurry level can dramatically affect the k_La value, especially in the dual-agitation 2-litre Parr autoclave, used to conduct most kinetic testwork in this study, as well as the continuous pilot autoclave. A mere 20% increase in the overflow level of the pilot reactor, due to the blocking of the inter-compartmental upcomer assembly, reduces the k_La-value by as much as 85 to 95%, while a similar effect (~75% reduction) is observed when the slurry level drops below the top impeller in the 2-litre batch autoclave due to sampling. This highlights the drawback of conducting testwork in small-scale reactors, where the interfacial mass transfer rate relies on the entrainment of gas bubbles *via* the gas phase, as compared to the sparging assemblies used in large-scale equipment.

Oxygen mass transfer testwork in the 2-litre autoclave utilises both the indirect (chemical) and direct (oxygen electrode) methods, yielding conservative upper and lower k_La-value estimates, respectively. A particularly interesting observation, not recorded previously, is the effect of the sulfur-dispersing surfactants (*ref.* Ch. 6) on the k_La-values, with and without the presence of sulfide mineral particles. It is shown that these surfactants, at commercial concentrations and typical mineral pulp densities, do not significantly alter the interfacial mass transfer rate. On the other hand, they dramatically reduce the oxygen absorption rate in solids-free sulfite solutions. Importantly, this retardation of the k_La-value dissipates as the surfactants degrade over time. The retardation period is dependent of the initial surfactant concentrations. For the first time, unequivocal proof is presented to show that these surfactants are degraded by dissolved oxygen and that the degradation products seemingly have no influence on the physical absorption process.

Although some of the experimental observations in this chapter are of peripheral importance to the overall study objectives, the impact on the sulfide mineral and iron(II) oxidation kinetics in the copper system is potentially critical. For example, reactor volume changes can either lead to erroneous intrinsic oxidation rate constant values (*ref.* Ch. 4, 5 & 6), *e.g.*, due to sampling, or can impose significant retardation effects on the oxidation rate during pilot testing at typical (commercial) pulp densities, *e.g.*, due to inter-compartmental blockages (*ref.* Ch. 7). The general framework developed in this chapter is used in other parts of this study to mathematically capture the dissolved oxygen concentration over time, with special consideration of the equipment and testing procedures. No other kinetic studies of chalcopyrite mineral or iron(II) oxidation in copper

Stellenbosch University http://scholar.sun.ac.za

solutions have verified the intrinsic rate constant values by quantitative consideration of both the interfacial mass transfer rate, as a function of the operating environment, and the rates of the oxidation reactions.

9.4 Iron(II) oxidation rate

This chapter presents a phenomenological model of the rate of iron(II) oxidation under typical MT autoclave leach conditions. In order to prevent over-parameterisation of the rate model, various assumptions are made, based on literature information and scrutinised using experimental observation. During the course of this model development, interesting insights are gained, while various mechanistic proposals are tabled from a phenomenological reaction rate perspective. The regression analysis is then used to simplify and verify the rate model, while maintaining consistency with the main proposals of this study.

There is considerable evidence in the literature to suggest that the iron(II) sulfate CIPs oxidise faster than unassociated ferrous ion, which explains the beneficial effect of adding 'inert' sulfate salts on the overall oxidation rate. A clear distinction is therefore made between the sulfate-independent (SI) and sulfate-dependent (SD) reaction pathways. Although the background salt matrix and temperature differed significantly between the different studies in the open literature, the trends are in qualitative agreement with the relative abundance of the metal(II)-sulfate CIPs as a function of acid, sulfate and temperature (*ref.* Ch. 2). In fact, many of the apparent reaction order 'anomalies' reported for the sulfate system can either be ascribed to such speciation changes or to interfacial mass transfer limitations, especially at high iron(II) concentrations in the presence of copper. Various studies in the literature also contradict the fact that the SD and copper-catalysed pathways exhibit faster kinetics compared to the SI pathway, *i.e.*, higher or mutual activation energies are assigned to these pathways, despite the fact that comparatively lower activation energy barriers would be expected at their respective transition states.

The catalytic role of copper in accelerating the oxidation rate is shown to be truly catalytic in nature, and not merely related to speciation changes, as is the case for the other metal(II) sulfate salts, *e.g.*, zinc sulfate. The relatively low apparent activation energy value, compared to the copper-free sulfate system, is also consistent with a catalysed reaction pathway. Based on the rate constants obtained at different oxygen partial pressures and high reaction extents (no interfacial mass transfer limitations), a first-order dependence of the oxidation rate on the saturated oxygen concentration in the copper system is validated. Its catalytic efficiency is mimicked, to some extent, by the relative abundance of the metal(II) sulfate CIPs, *i.e.*, again according to the solution chemistry model (Ch. 2). This supports the proposal of this study that the copper(II) sulfate CIPs are most effective in catalysing the oxidation of unassociated ferrous ions, as well as itself acting in

Stellenbosch University http://scholar.sun.ac.za

first-order fashion. This approach is also consistent with the diminished copper activity in low complexation media, *e.g.*, in perchlorate solutions and at atmospheric temperatures (according to the literature), while explaining why the second-order dependence of the oxidation rate is maintained down to lower terminal iron(II) concentration levels in copper sulfate solutions than in the equivalent zinc sulfate background. These unique insights provide the mathematical methodology to simulate the iron(II) oxidation rate in copper sulfate solutions, without changing the fundamental form of the rate expression.

The importance of the oxygen mass transfer rate in the copper system is highlighted in this chapter, *i.e.*, to account for the interfacial mass transfer limitations during the regression. The rate constants at low terminal iron(II) concentrations (no mass transfer limitations) reveal that insignificant iron(II) oxidation occurs in the interfacial layer. This justifies the methodology of simultaneously considering the intrinsic oxidation and interfacial mass transfer rate expressions in a conventional manner. Besides these mass transfer effects, the overall simulation takes the solution speciation effects into consideration at each time step, instead of relying on average concentration values. The oxidation rate exhibits Arrhenius-like behaviour, yielding lower apparent activation energies in high sulfate and copper solutions, which justify assigning distinct activation energy values to the each pathway. The best regressions are obtained without any explicit hydrogen ion concentration terms. The overall oxidation rate is therefore insensitive to the hydronium ion concentration, other than that accounted for by the solution chemistry model (Ch. 2).

With knowledge of the k_La-values under the different operating conditions, the phenomenological rate expression gives a reasonable representation of the experimental results not used in the regression. Since the activation energy of the iron(II) oxidation reaction is higher than the interfacial diffusion of diatomic oxygen, insignificant mass transfer limitations are prevalent at lower temperatures (90-105ºC), even in the presence of copper. However, significant deviations from the second-order rate dependence on the iron(II) concentration occur at these temperatures. Therefore, as the temperature decreases, other effects, whether kinetic or speciation related, appear to come into play and the simulation becomes less accurate. It should, however, be noted that this model makes use of a limited number of adjustable parameters and it would be unrealistic to expect an accurate extrapolation outside the regressed parameter space, at least without a more elaborate description of the solution speciation. It is therefore recommended that more data be generated in future work to improve the solution thermodynamic model, especially in more complicated metal sulfate salt mixtures over a relatively wide acid concentration range.

Stellenbosch University http://scholar.sun.ac.za

9.5 Iron(III) precipitation

The objective of this chapter is to describe the kinetics of iron(III) precipitation and the relative amounts of hematite *vs.* hydronium jarosite precipitation. Current knowledge has not yet revealed sufficient mechanistic and kinetic information about this sparingly soluble salt system. In fact, very few simulations of the kinetics of iron(III) precipitation are found in the open literature, and none under MT autoclave conditions. This study provides, therefore, a unique contribution to the understanding of iron(III) precipitation behaviour in the H_2SO_4-M(II)SO_4-H_2O system, especially in context of the MT oxidation of iron-containing sulfide concentrates. The rate expressions are based on literature information and experimental observations at low pulp density conditions, in particular backscatter electron (BSE) images and qualitative energy dispersive X-ray (EDX) spot analyses of the precipitates, complemented by the iron(III) precipitation behaviour under high pulp density leaching systems (Ch. 7 & 8). The final regression encapsulates all the experimental results, *i.e.*, obtained in both the batch and continuous reactor configurations, and provides an estimate of the complex processes taking place during iron(III) precipitation in autoclave leaching systems.

The phenomenological model developed in this study assumes that the primary nucleation rate of hematite dominates the formation of new hydronium jarosite particles, due to the higher hematite interfacial energy, and hence supersaturation, especially as the acid concentration drops during the initial stages of sulfide mineral oxidation. Due to the relatively high interfacial energy, the formation of these hematite nuclei is accompanied by rapid growth, which, in turn, causes the supersaturation to dissipate rapidly, leading to a large number of small particulates of similar size. On the other hand, crystalline hydronium jarosite growth occurs under conditions of higher acid concentration, and hence lower relative supersaturation, *i.e.*, where nucleation on existing surfaces leads to a continuous growth mechanism. The overall hydronium jarosite growth rate is strongly dependent on the number of hematite particulates, which allows simulation of the relative precipitation rates of these two phases over typical fluctuating acid concentrations during chalcopyrite oxidation in batch and continuous autoclaves.

The formation of secondary hematite nuclei appears to be promoted at a higher precipitate surface area, especially in suspensions of lower terminal acidity. This surface nucleation, accompanied by rapid growth, leads to the formation of secondary hematite particulates, and provides the required link to simulate high pulp density leaching-precipitation systems *via* the time- and space-averaged population balance, using low pulp density batch precipitation data.

This modelling exercise has helped to elucidate some interesting mechanistic understandings of iron(III) precipitation in MT autoclaves. More experimental data of the thermodynamics, speciation

Stellenbosch University http://scholar.sun.ac.za

and precipitation rate of iron(III) in mixtures with sulfuric acid and metal(II) sulfates are required to expand our understanding of this sparingly soluble salt system. It should also be emphasised that the overall model includes various reactions that impact on the net oxidation and precipitation rate of iron. For example, although the homogeneous oxidation of iron(II) is accurately simulated (Ch. 4), the extent of iron(III) reduction on each of the mineral surfaces is unknown and may not even be constant over time (see below). It also does not consider the re-leaching of precipitated iron(III) phases, *e.g.*, the possible re-dissolution of small hematite particulates as the acid concentration increases over time. These aspects, including a more elaborate solution thermodynamic framework, especially in the low acid regime (< 15 g/L H_2SO_4), would need to be addressed in future modelling exercises.

9.6 Sulfide mineral oxidation

This part of the study relies heavily on published mechanistic information of sulfide mineral oxidation. Distinct surface phenomena are prevalent on the different minerals, while secondary surface layers become increasingly important at longer reaction times. Important insights are highlighted and these are used to formulate generic mineral oxidation rate expressions, while leaching experiments are used to simplify these expressions into a set of pragmatic algorithms. The detailed mechanistic discussions not only provide a summary of the most important kinetic considerations, but also contextualise the various simplifying assumptions.

The unreacted shrinking particle (USP) model and electrochemical mixed potential (MP) theory are used to mathematically relate the overall observed oxidation rate phenomena to the perceived mechanisms. The testwork programme has yielded the most elaborate, meticulously planned and experimentally well-controlled autoclave results to date, which contribute to the understanding of chalcopyrite concentrate oxidation under MT autoclave conditions. Neither mechanism changes nor interfacial gas/liquid mass transfer limitations are observed by doing testwork at low pulp densities (< 2 wt% solids), provided narrow-sized (screened) particles are used. However, the final simulation elegantly reveals that relatively ‘wide’ particle size distributions (PSDs) can create apparent anomalies in the USP model performance, while very fine (fast reacting) particles may cause a mass transfer regime change, even at these low pulp densities.

Different surfactants are shown to have a significant effect on the stability of elemental sulfur at low pulp densities, *i.e.*, at high surfactant to surface area ratios. Even under these conditions, the surfactants are shown to become ineffective after about 45 to 60 minutes; this is the primary reason for the sulfur blockage problems experienced during continuous autoclave pilot testing (Ch. 7). It is also shown that no improvements in the rate of copper dissolution can be achieved by injecting

Stellenbosch University http://scholar.sun.ac.za

additional surfactants at the deviation point from USP kinetics, due to the inability of these large surfactant macro-molecules to diffuse though molten elemental sulfur.

In terms of developing the phenomenological model, the batch autoclave test results reveal that the chalcopyrite oxidation rate is relatively insensitive to the background sulfate salt composition and that there is no need to recognise the role of iron(III) in the intrinsic rate description. X-ray photoelectron spectroscopy (XPS) surface analyses of partially oxidised residues confirm a high concentration of copper(I) at typical oxygen partial pressures (700 kPa). Although these results provide no conclusive evidence of the exact nature of the sulfide surface layer on host chalcopyrite particles, the absence of iron and the abundance of copper(I) monosulfide is indicative of a covellite-like surface structure. A strong argument for the direct reduction of oxygen is tabled, while the role of the adsorbed proton in weakening these surfaces is highlighted (see below). Elemental sulfur yields above 90% have been observed in the literature at lower temperatures, *i.e.*, during chalcopyrite oxidation using one-electron transfer oxidants, like iron(III). Under conditions where oxygen reduction is appreciable, charge transfer would occur in two-electron or four-electron sequences and may oxidise sulfide to higher oxidation states, before its release into solution; the yield of elemental sulfur would be consequently lower. In this study, sulfur yields in the order of 60% are observed, suggesting (qualitatively) that both iron(III) and oxygen reduction are prevalent under MT autoclave conditions.

The insensitivity of the chalcopyrite oxidation rate to the initial iron(III) concentration, in addition to the assembled knowledge of possible cathodic reductions reactions and sulfur rearrangements, lead to a proposition of the chalcopyrite oxidation mechanism under MT autoclave conditions. This proposition is supported by qualitative quantum-level calculations, revealing the nature of electron hybridization in the system. The iron(III)/iron(II) couple is energetically favoured to inject holes in the iron–sulfide bonding orbitals, first releasing iron during oxidative dissolution, followed by surface restructuring to leave behind a $Cu^{+}S_2^{2-}$ (covellite-like) surface. Based on these preliminary modelling results, the strong chemisorption bonds between the sulfide sites and the proton would be expected to remain intact during this surface rearrangement process, while oxygen would preferentially adsorb at copper(I) sites. The electrocatalytic role of copper(I) in the first reduction step of oxygen is shown to be thermodynamically marginal, but kinetically fast, while a transient $HS\cdot$ radical state is likely to be produced by the reaction of the subsequent perhydroxyl species with the adjacent sulfide species in the mineral lattice. The subsequent reactions are also shown to be thermodynamically plausible, leading to the reduction of the oxygen intermediate, peroxide, or a diatomic oxygen molecule on an adjacent metal site and yielding higher oxidation states of sulfur, the extents of which depend on the prevailing mineral surface conditions (oxidation potential).

Stellenbosch University http://scholar.sun.ac.za

Besides justifying the empirical approach in dealing with the sulfur yield on these surfaces, this qualitative mechanistic picture also opens up alternative iron(III) reduction rate permutations, *i.e.*, the possibility of variable iron(III) reduction extents over time (net mole Fe(III) reduction/mole sulfide oxidised; Ch. 7 & 8). In view of the complex and often conflicting arguments tabled in the open literature, these insights provide a basic outline of the chalcopyrite oxidation mechanism that is most consistent with current knowledge.

Although the phenomenological (regressed) sulfide oxidation rate equations are relatively simple, it is the theoretical mechanistic and electrochemistry backdrop that give substance to the general forms of these expressions, while the catalytic effect of pyrite surfaces at high pulp densities (Ch. 8) is uniquely catered for, again utilising insights obtained from the literature. The use of quantum-level calculations of surface structures and species adsorption energies, complemented by the above-mentioned experimental results, is, in itself, a unique approach in obtaining relatively simple oxidation rate expressions for polysulfide concentrates. For example, hydrogen and ferric ions are found to compete for sulfide-surface sites on pyrite (100) surface, while oxygen adsorbs strongly (two-fold bond) on a single iron substrate. The non-bonding t_{2g} orbital of surface iron is assumed to catalyse the first oxygen reduction step at high temperatures, with proton adsorption dominating at sulfide surface sites. Where the pyrite lattice is not broken down, highly oxidised surfaces are formed, in which case pyrite can catalyse the oxidation of the less noble sulfide minerals, without any physical contact between the particles. Sphalerite represents the other extreme in this study, *i.e.*, in terms of its rest potential and its ability to interact with oxygen at high temperatures in an autoclave. However, just like chalcopyrite, its intrinsic oxidation mechanism may be affected by surface layers. Detailed arguments are presented that support the formation of copper sulfide films on sphalerite, which, for the first time, are experimentally shown (see below) to cause a decrease of its oxidation rate in copper sulfate solutions.

The resulting phenomenological rate model for chalcopyrite, pyrite, and sphalerite, as well as for the other sulfides, therefore caters for different scenarios; the final forms of these expressions, as well as the apparent rate constants, are regressed using the high pulp density leach data obtained in the batch and continuous autoclaves (Ch. 7 & 8).

9.7 Batch and continuous reactor simulation

This part of the study deals with the architecture and details of the batch and continuous reactor models, as well as the integrated mass and energy balance simulation of the primary circuit (autoclave leaching, thickening-filtration and solvent extraction (SX) – electrowinning). Besides the particular contributions of this part of the study, it is emphasised that these batch and continuous reactor models, imbedded within the solution thermodynamic (Ch. 2), interfacial

Stellenbosch University http://scholar.sun.ac.za

oxygen mass transfer (Ch. 3) and population, mass and energy balance frameworks (Ch. 7), represent the most comprehensive autoclave simulation of the chalcopyrite oxidation system to date. For the first time, the dynamics of the various oxidation and precipitation reactions (Ch. 4, 5 & 6) can be studied, while simultaneously accounting for changes in the accompanying slurry environment. It is not only these insights that are unique, but also the questions that arise as the overall model description becomes more complete, *i.e.*, as the degrees of freedom of the total system start to diminish.

The most important illustration of the power of the integrated continuous reactor simulation is the accurate account of the drop in the copper leaching and total sulfide oxidation extents caused by blockages of the inter-compartmental upcomer assemblies. Knowledge of the increase in slurry volume and accompanying reduction in the gas/liquid mass transfer coefficients is all that is required to account for these deviations. In general, variations in the iron(III) precipitation rate and relative amount of hydronium jarosite *vs.* hematite formed in the continuous pilot autoclave, due to the changing circuit acidity, are accurately accounted for by the phenomenological model.

A particularly challenging complexity of the overall reaction system is the change in sulfide particle shrinkage behaviour due to the prevalence of sulfur agglomeration in the latter autoclave compartments, due to surfactant degradation. Since particle surface area changes due to agglomeration are difficult to account for, the reaction regime change is dealt with phenomenologically by considering reduced particle shrinkage rates after reaching fixed particle penetration depths (PPDs). In this regard, the behaviour of sulfur, especially on particular mineral surfaces, *e.g.*, pyrite, is singled out as an important area towards which to direct future research, *i.e.*, the role of polymeric sulfur in inhibiting mineral oxidation is, in the author's opinion, underestimated.

Another major contribution of this chapter is the extensive mineral oxidation rate results, using bulk model analyses: in particular, using these measurements to assess the various assumptions made in deriving the intrinsic mechanisms (*ref.* Ch. 6). Various proposals are tabled, which are mostly related to the oxidation of chalcopyrite and pyrite, the relative interaction of these minerals with the different oxidants and the oxidation state of the resulting iron and sulfur. Although iron(III) may reduce at appreciable rates on chalcopyrite surfaces, the evolving iron(II)-to-iron(III) concentration ratio in solution suggests that iron(II) is rapidly re-oxidised on its surfaces, allowing the direct use of the overall oxygen reduction reaction, and its associated rate expressions, in the phenomenological model. Although uncertainty exists regarding the oxidation state of chalcopyritic lattice iron on its release into solution, the insensitivity of the chalcopyrite oxidation rate to the iron(III) concentration is indicative of its unimportant role from a phenomenological modelling

Stellenbosch University http://scholar.sun.ac.za

perspective. It is proposed that diatomic oxygen surface adsorption and reduction play an important role in this mechanism under MT autoclave temperatures. Similar assumptions are also made for the other copper sulfide minerals, *e.g.*, bornite and covellite, with oxygen reduction *via* copper(I) surface states mostly reserved for the latter mineral phase. It is only the fast-oxidising sphalerite and pyrrhotite minerals that are more indicative of high net iron(III) reduction rate and elemental sulfur yield.

Conclusive proof is also presented that chalcocite oxidation produces a covellite surface layer, but that the oxidation rate of this covellite surface is still more than double that of the covellite-like surface structure forming on partially oxidised chalcopyrite.

The pyrite oxidation rate is shown to exhibit characteristic S-shaped kinetics for all three of the concentrates examined, probably due to the initial absence of iron(III) in solution. It is therefore proposed that the iron(III) reduction mechanism partakes in the rate-limiting step, which demands a revisit of the mechanistic proposals of Chapter 6. Whereas the t_{2g} orbital of the lattice iron was previously assumed to directly catalyse the reduction of adsorbed diatomic oxygen, the complexation of aqueous iron(III), on the solution-side of the interface, also needs to be considered. This is the only mechanism perceived to be consistent with the apparent dependency of the reaction rate on the iron(III) concentration, as well as the low observed sulfur yield. Although no fundamental basis is presented to support such a mechanism, the strong interaction of diatomic oxygen with the pyrite surface, as well as its complexation with aqueous iron(III), are assumed to lower the activation energy of the first oxygen reduction step. Diatomic oxygen is therefore proposed to be a suitable electron transfer agent, catalysed by its complexation with both lattice iron and aqueous iron(III) species. Only the first electron transfer step is considered to be rate limiting and the resulting rate expression is analogous to the direct iron(III) reduction mechanism under limiting iron(III) tenor. Due to the oxidative nature of the pyrite surface, all pyritic iron is assumed to enter the bulk solution in the oxidised state and results in very low intrinsic sulfur yields (< 5%), with the role of adsorbed iron(III) being purely catalytic in nature.

All these assumptions are incorporated into the phenomenological model and subjected to multiple regression, allowing a direct comparison between the intrinsic rate constants and activation energies of all the sulfide minerals in all the concentrates. It appears that the lower activation energy values are associated with the kinetically faster reactions, which is consistent with chemical reaction theory. These optimised rate constant and activation energy values are used to verify the overall simulation under high pulp conditions in the continuous and batch (Ch. 8) reactor configurations.

Stellenbosch University http://scholar.sun.ac.za

9.8 Model application

The final section of this work presents a comparison between the batch simulation and the experimental results of two different chalcopyrite concentrates, but conducted at higher pulp densities. The aim is to verify the accuracy of the batch model, in particular the iron(III) precipitation kinetics at high precipitate surface area, as well as recording changes in the intrinsic mineral oxidation rates at high pulp densities and over relatively wide acidity (pH) ranges. Only once the batch simulation performs satisfactorily, or at least the parameter space is validated where it performs satisfactorily, can the full-scale continuous reactor simulation be utilised with confidence.

Two of the concentrates tested in Chapter 7 were therefore subjected to high pulp density oxidation, utilising a range of different initial test conditions. Most importantly, the chalcopyrite oxidation rate behaviour under typical MT autoclave acidities is relatively well represented by the rate expressions derived under low pulp density conditions. On the other hand, apparent anomalies are again observed in the case of pyrite oxidation. Similarly to the conclusion derived from simulating the continuous pilot plant autoclave, an approximate order of magnitude reduction in the intrinsic rate constant value is required to correctly describe the pyrite oxidation rate, *i.e.*, when utilising the rate model and constants based on the iron(III) concentration, as obtained from the accurate low pulp density testwork (Sect. 7.4.2). Since the original pyrite oxidation rate expression, *i.e.*, in terms of the dissolved oxygen concentration (Ch. 6), gives a better representation of the behaviour of pyrite in both the continuous pilot and high pulp density batch autoclaves, it is concluded that either oxygen or iron(III) could be rate limiting. Most importantly, this viewpoint is still consistent with the mechanistic picture presented in Chapter 7 (Figure 7.41), which proposes that adsorbed diatomic oxygen acts as an electron transfer agent, catalysed by its complexation with both lattice iron and aqueous iron(III) species. It is proposed that focused quantum-level modelling studies be conducted to verify this proposal, supplemented by follow-up autoclave kinetic studies under low and high pulp density conditions.

Another conclusion from the high pulp density batch testwork results, as well as the continuous pilot plant results in Chapter 7, is the importance of the sulfur dispersion efficiency in the case of the slower leaching chalcopyrite and pyrite minerals. For chalcopyrite oxidation, the negative influence of lower acidity levels (< 0.15 mol/kg H_2SO_4) stretches beyond the ‘normal’ rate model (*ref.* Eq. 6.176). The thin molten sulfur diffusion barrier appears to be more inhibiting under these lower, albeit artificial, acidity conditions, especially at lower temperatures, while a low surfactant concentration per unit particle surface area (finer grind) exacerbates the problem. The prevalence of these thin surface sulfur layers is also not constant over time, which seemingly influences the

Stellenbosch University http://scholar.sun.ac.za

degree of iron(III) reduction on the chalcopyrite surface. The higher the prevalence of highly oxidised surface species, the lower the intrinsic sulfur yield and the lower the net degree of iron(III) surface reduction.

In general, it is expected that higher surface potentials would transpire on the chalcopyrite surface during initial oxidation and at lower pulp densities, where the ratio of surfactant concentration to the mineral surface is higher. Under such conditions, the net rate of iron(III) reduction is lower, while the situation may be reversed at longer reaction times. Clearly, further studies are required to determine the exact role of molten sulfur in these mineral oxidation mechanisms, as well as the net reduction rate of iron(III) under changing surface potential conditions.

A final result worth noticing is the apparent acceleration of chalcopyrite oxidation when using a relatively coarse grind. Whereas pyrite itself is rapidly oxidised when using very fine grinds, catalytic pyrite surfaces appear to accelerate the oxidation of the copper sulfides, even though these minerals are very weakly physically associated. The accelerated oxidation cannot, therefore, be ascribed to classical (mineral-mineral) galvanic contact. Instead, these observations provide evidence of the promotion of oxidation by pyrite-generated radical species; this is in line with recent publications in the open literature, as well as the discussions in Section 6.3.4. Although it could be argued that this acceleration results from particle-particle contact in the slurry suspension, the presence of insulating elemental sulfur surface layers, and the low pyrite-to-copper sulfide mass ratio, support an oxidation mechanism *via* the propagation of radical species, *e.g.*, hydroxyl radicals, rather than an electrochemical contact scenario.

Armed with this new information, the continuous autoclave simulation is refined and expanded to include energy optimisation around the autoclave, *i.e.*, to maintain isothermal operation, as well as its integration in the primary leach-SX flowsheet in closed-circuit fashion. A number of sensitivity analyses are also conducted to illustrate its power as a process design tool. Several operating parameters and intrinsic properties are systematically varied, while recording the responses of the autoclave and primary circuit.

Details of these sensitivity analyses yield insights into the behaviour of the primary circuit. For example, an increased temperature accelerates the oxidation of chalcopyrite and pyrite minerals, as well as of iron(II). The resulting high iron(III) supersaturation levels are found to particularly favour hydronium jarosite growth at autoclave acidity levels above about 20 g/L H_2SO_4, which explains the reason behind the strong buffering action exerted by this precipitate phase. Therefore, under MT autoclave conditions, control of the autoclave acidity and/or the mineralogical composition of the feed material (overall sulfur yield) would be most important in ensuring that a

Stellenbosch University http://scholar.sun.ac.za

high-hematite residue is produced. Alternatively, a high temperature (>180ºC; Sect. 1.1.1) oxidation region could be employed to produce hematite, provided enough cheap neutralising agent is available to prevent the acidity of the primary circuit driving the autoclave into the basic ferric sulfate (BFS) regime.

Another example is the beneficial effect of finer PSDs on the overall copper extraction. However, due to the increased rate of heat generation, a slightly lower autoclave pulp density results. The most important insight from this analysis is the impact of a physical manipulation of the feed PSD on the overall copper extraction efficiency, *e.g.*, by 'cutting' the PSD at some coarser maximum (*e.g.*, 100% < 11.5 µm), the autoclave residence time is most efficiently utilised. The top-size specification, *e.g.*, the d_{99}, is particularly important in this regard.

9.9 Meeting the overall research objective

The overall objective of this study was to develop a modelling framework to simulate MT batch and continuous chalcopyrite oxidation, as well as the integration of the latter into the primary (leach-SX) circuit, and, in so doing, to quantify the effects of the key control parameters on the most important AA-UBC process variables. This objective has been met, resulting in a unique combination of thermodynamics, mineral and iron(II) oxidation and iron(III) precipitation kinetics, all imbedded within the laws of mass and energy conservation. The end product is not only unique to MT chalcopyrite oxidation process development but also to autoclave sulfide mineral oxidation, in general. Most importantly, this modelling exercise has highlighted the areas where important knowledge is lacking, only some of which have been experimentally addressed in this study.

Stellenbosch University http://scholar.sun.ac.za

REFERENCES

Absolon, V.J. (2008) *A Comparison of Biological and Chemically Induced Leaching Mechanisms of Chalcopyrite*, Ph.D. Dissertation, Ian Wark Research Institute, ARC Special Research Centre for Particle and Material Interfaces, Univ. of South Australia, Adelaide.

Aebi, H. (1974) Catalase, In: H.U. Bergmeyer (ed.), *Methods of Enzymatic Analysis*, 2nd Edition, Academic Press, New York, vol.2, pp.673-684.

Ahlberg, E. and Broo, A.E. (1996) Oxygen reduction at sulphide minerals. 3. The effect of surface pre-treatment on the oxygen reduction at pyrite, *Int. J. Miner. Process.*, vol.47, pp.46-60.

Ahrland, S. (1972) How to distinguish between inner and outer sphere complexes in aqueous solution. Thermodynamic and other criteria, *Coordin. Chem. Rev.*, vol.8, pp.21-29.

Akilan, C., Rohman, N., Hefter, G. and Buchner, R. (2006a) Temperature effects on ion association and hydration in $MgSO_4$ by dielectric spectroscopy, *Eur. J. Chem. Phys. Phys. Chem.*, vol.7, pp.2319-2330.

Akilan, C., Hefter, G., Rohman, N. and Buchner, R. (2006b) Ion association and hydration in aqueous solutions of copper(II) sulfate from 5 to 65ºC by dielectric spectroscopy, *J. Phys. Chem. B*, vol.110, pp.14961-14970.

Albright, J.G., Rard, J.A., Serna, S., Summers, E.E. and Yang, M.C. (2000) Isopiestic determination of the osmotic and activity coefficients of $ZnSO_4$(aq) at T = 298.15 K, and the standard potential of the electrochemical cell $ZnHg_x$(two phase) | $ZnSO_4$(aq) | $PbSO_4$(s) | $PbHg_x$(two phase), *J. Chem. Thermodyn.*, vol.32, pp.1447-1487.

Al-Harahsheh, M., Kingmans, S., Rutten, F. and Briggs, D. (2006) ToF-DIMS and SEM study on the preferential oxidation of chalcopyrite, *Int. J. Miner. Process.*, vol.80, pp.205-214.

Ammou-Chokroum, M., Cambazoglu, M. and Steinmetz, D. (1977) Soft oxidation of chalcopyrite in acid solution: kinetic study of reactions. I. Chemical models, *Bull. Soc. Fr. Mineral. Cristallogr.*, vol.100, pp.149-161.

Anderson, C.G. (1999) The treatment of chalcopyrite concentrates with nitrogen species catalyzed oxidative pressure leaching, In: S.K. Young, D.B. Dreisinger, R.P. Hackl, and D.G. Dixon (eds.), *COPPER 99*, Hydrometallurgy of Copper, vol.IV, TMS, Warrendale, PA, pp.139-149.

Anderson, A.B. and Albu, T.V. (1999) Ab initio approach to calculating activation energies as functions of electrode potential. Trial application to four-electron reduction of oxygen, *Electrochem. Commun.*, vol.1, pp.203-206.

Anderson, A.B. and Albu, T.V. (2000) Catalytic effect of platinum on oxygen reduction. An ab initio model including electrode potential dependence, *J. Electrochem. Soc.*, vol.147, no.11, pp.4229-4238.

Anderson, G.M., Castet, S., Schott, J. and Mesmer, R.E. (1991) The density model for estimation of thermodynamic parameters of reactions at high temperatures and pressures, *Geochim. Cosmochim. Acta*, vol.55, pp.1769-1779.

Andzelm, J., Kölmel, Ch. and Klamt, A. (1995) Incorporation of solvent effects into the density functional calculations of molecular energies and geometries, *J. Chem. Phys.*, vol.103, pp.9312-9320.

Stellenbosch University http://scholar.sun.ac.za

Archer, D.G. and Rard, J.A. (1998) Isopiestic investigation of the osmotic and activity coefficients of aqueous $MgSO_4$ and the solubility of $MgSO_4.7H_2O$(cr) at 298.15 K: Thermodynamic properties of the $MgSO_4 + H_2O$ system to 440 K, *J. Chem. Eng. Data*, vol.43, pp.791-806.

Archer, D.G. and Wood, R.H. (1985) Chemical equilibrium model applied to aqueous magnesium sulfate solutions, *J. Solution Chem.*, vol.14, no.11, pp.757-780.

Arrouvel, C., Viossat, V. and Minot, C. (2005) Theoretical study of hydrated sulfuric acid: Clusters and periodic modeling, *J. Mol. Struc.-Theochem.*, vol.718, pp.71-76.

Astanina, A.N. and Rudenko, A.P. (1971) Mechanism of the oxidation of iron(II) by molecular oxygen in aqueous solution, *Russ. J. Phys. Chem.*, vol.45, no.2, pp.191-194.

Atkins, P.W. (1986) *Physical Chemistry*, 3d Edition, Oxford Univ. Press, Oxford.

Atkins, P.W. (1994) *Physical Chemistry*, 5th Edition, Oxford Univ. Press, Oxford.

Atkins, P. and De Paula, J. (2006) *Atkins' Physical Chemistry*, 8th Edition, Oxford Univ. Press, Oxford.

Atkinson, G. and Petrucci, S. (1966) Ion association of magnesium sulfate in water at 25ºC, *J. Phys. Chem.*, vol.70, no.10, pp.3122-3128.

Awakura, Y., Iwai, M. and Majima, H. (1986) Oxidation of Fe(II) in HCl and H_2SO_4 solutions with dissolved molecular oxygen in the presence and absence of a cupric catalyst, In: J.E. Dutrizac and A.J. Monhemius (eds.), *Iron Control in Hydrometallurgy*, Ellis Horwood Ltd., Chichester, pp.202-222.

Awakura, Y., Koyama, K., Takegawa, Y. and Majima, H. (1990) Determination of the association constant of sulfuric acid, *Metall. Mater. Trans. B*, vol.21B, pp.689-695.

Babcan, J. (1971) Die synthese von jarosit $KFe_3(SO_4)_2(OH)_6$, *Geologicky Zbornik - Geologica Carpathica*, vol.22, no.2, pp.299-304.

Baghalha, M. and Papangelakis, V.G. (1998) Pressure acid leaching of laterites at 250ºC: A solution chemical model and its applications, *Metall. Mater. Trans. B*, vol.29B, pp.945-952.

Baghalha, M. and Papangelakis, V.G. (2000) High-temperature conductivity measurements for industrial applications. 2. H_2SO_4−$Al_2(SO4)_3$ solutions, *Ind. Eng. Chem. Res.*, vol.39, pp.3646-3652.

Bailey, L.K. and Peters, E. (1976) Decomposition of pyrite in acids by pressure leaching and anodization: the case for an electrochemical mechanism, *Can. Metall. Quart.*, vol.15, no.4, pp.333-344.

Balasubramanian, G., Murad, S., Kappiyoor, R. and Puri, I.K. (2011) Structure of aqueous $MgSO_4$ solution: Dilute to concentrated, *Phys. Chem. Lett.*, vol.508, pp.38-42.

Baldwin, S.A., Demopoulos, G.P. and Papangelakis, V.G. (1995) Mathematical modeling of the zinc pressure leach process, *Metall. Mater. Trans. B*, vol.26B, pp.1035-1047.

Bale, C.W., Pelton, A.D. and Thompson, W.T. (1991) Facility for the Analysis of Chemical Thermodynamics (FACT), Thermofact Ltd. & McGill Univ., Montreal.

Stellenbosch University http://scholar.sun.ac.za

Barner, H.E. and Kust, R.N. (1980) Application of thermodynamics in hydrometallurgy, In: A. Newman, H.E. Barnes, M. Klein and S.I. Sandler (eds.), *Thermodynamics of Aqueous Systems with Industrial Application*, ACS Symposium Series 133, ACS, Washington, DC, pp.625-641.

Barron, C.H. and O'Hern, H.A. (1966) Reaction kinetics of sodium sulfite oxidation by the rapid-mixing method, *Chem. Eng. Sci.*, vol.21, pp.397-404.

Bartlett, R.W. (1971) Conversion and extraction efficiencies for ground particles in heterogeneous process reactors, *Metall. Trans. B*, vol.2B, pp.2999-3006.

Bauer, J.P., Gibbs, H.L. and Wadsworth, M.E. (1974) Initial state of sulfuric acid leaching kinetics of chalcopyrite using radiochemical techniques, *US Bureau of Mines*, RI 7823, pp.1-37.

Baxter, K.G., Pavlides, A.G. and Dixon, D.G. (2004) Testing and modelling a novel iron control concept in a two-stage ferric leach/pressure oxidation process for the Sepon Copper Project, In: M.J. Collins and V.G. Papangelakis (eds.), *Pressure Hydrometallurgy 2004*, CIM, Montreal, pp.57-76.

Bayliss, P. (1977) Crystal structure refinement of a weakly anisotropic pyrite, *Am. Mineral.*, vol.62, pp.1168-1172.

Beck and Andreassen (2010) Spherulitic growth of calcium carbonate, *Cryst. Growth Des.*, vol.10, no.7, pp.2934-2947.

Becke, A.D. (1988) A multicenter numerical integration scheme for polyatomic molecules, *J. Chem. Phys.*, vol.88, pp.2547-2553.

Beek, W.J. and Muttzall, K.M.K. (1991) *Transport Phenomena*, John Wiley & Sons Inc., Chichester.

Bell, R.P. (1959) *The Proton in Chemistry*, Methuen, London.

Bešter Rogač, M., Babič, V., Perger, T.M., Neueder, R. and Barthel, J. (2005) Conductometric study of ion association of divalent symmetric electrolytes: I. $CoSO_4$, $NiSO_4$, $CuSO_4$ and $ZnSO_4$ in water, *J. Mol. Liq.*, vol.118, pp.111-118.

Berezowsky, R. and Trytten, L. (2002) Commercialization of the acid pressure leaching of chalcopyrite, *ALTA 2002*, Copper-7 Forum, ALTA Metallurgical Services, Melbourne, 40pp.

Biegler, T. (1976) Oxygen reduction on sulphide minerals. Part II. Relation between activity and semiconducting properties of pyrite electrodes, *J. Electroanal. Chem.*, vol.70, pp.265-275.

Biegler, T. and Swift, D.A. (1979a) Anodic electrochemistry of chalcopyrite, *J. Appl. Electrochem.*, vol.9, pp.545-554.

Biegler, T. and Swift, D.A. (1979b) Anodic behaviour of pyrite in acid solutions, *Electrochim. Acta*, vol.24, pp.415-420.

Biegler, T., Rand, D.A.J. and Woods, R. (1977) Oxygen reduction on sulphide minerals, In: J.O'M. Bockris, D.A.J. Rand and B.J. Welch (eds.), *Trends in Electrochemistry*, Plenum Press, New York and London, pp.291-302.

Bielski, B.H.J. and Cabelli, D.E. (1995) Superoxide and hydroxyl radical chemistry in aqueous solution, In: C.S. Foote, J.S. Valentine, A. Greenberg and J.F. Liebman (eds.), *Active Oxygen in Chemistry*, Chapman & Hall, London, pp.66-104.

Stellenbosch University http://scholar.sun.ac.za

Bielski, B.H.J., Cabelli, D.E., Arudi, R.L. and Ross, A.B. (1985) Reactivity of HO_2/O_2^- radicals in aqueous solution, *J. Phys. Chem. Ref. Data*, vol.14, no.4, pp.1041-1100.

Blakey, B.C. and Papangelakis, V.G. (1994) On the synthesis and solubility of hydronium alunite, In: G. Warren (ed.), *EPD Congress 1994*, TMS, Warrendale, PA, pp.3-19.

Blakey, B.C. and Papangelakis, V.G. (1996) A study of solid-aqueous equilibria by the speciation approach in the hydronium alunite - sulfuric acid - water system at high temperatures, *Metall. Mater. Trans. B*, vol.27B, pp.555-566.

Blesa, M.E. and Matijevic, E. (1989) Phase transformation of iron oxides, oxyhydroxides, and hydrous oxides in aqueous media, *Adv. Coll. Interf. Sci.*, vol.29, pp.173-221.

Bockris, J.O'M and Khan, S.U.M. (1993) *Surface Electrochemistry: A Molecular Level Approach*, Plenum Press, New York, pp.490-495.

Bockris, J.O'M. and Reddy, A.K.N. (1970) *Modern Electrochemistry*, vol.1-2, Plenum Press, New York.

Boekema, C., Krupski, A.M., Varasteh, M., Parvin, K., Van Til, F., Van der Woude, F. and Sawatsky, G.A. (2004) Cu and Fe valence states in $CuFeS_2$, *J. Magn. Magn. Mater.*, vol.272-276, pp.559-561.

Borda, M., Elsetinow, A., Schoonen, M. and Strongin, D. (2001) Pyrite-induced hydrogen peroxide formation as a driving force in the evolution of photosynthetic organisms on an early Earth, *Astrobiology*, vol.1, no.3, pp.283-288.

Borda, M.J., Elsetinow, A.R., Strongin, D.R. and Schoonen, M.A. (2003) A mechanism for the production of hydroxyl radical at surface defect sites on pyrite, *Geochim. Cosmochim. Acta*, vol.67, no.5, pp.935-939.

Bouboukas, G., Gaunand, A. and Renon, H. (1987) Oxidation of Fe(II) by oxygen in concentrated NaCl solutions: Prediction of stirred gas-liquid reactor performance from homogeneous kinetic data, *Hydrometallurgy*, vol.19, pp.25-35.

Bradley, D.J. and Pitzer, K.S. (1979) Thermodynamics of electrolytes. 12. Dielectric properties of water and Debye-Hückel parameters to 350ºC and 1 kbar, *J. Phys. Chem.*, vol.83, no.12, pp.1599-1603.

Braithwaite, J.W. and Wadsworth, M.E. (1976) Oxidation of chalcopyrite under simulated conditions of deep solution mining, In: J.C. Yannopoulos and J.C. Agarwal (eds.), *Extractive Metallurgy of Copper*, vol.II, AIME, New York, pp.752-775.

Brown, G.I. (1980) *A New Guide to Modern Valency Theory*, 4th Editions, Longmans Group, London.

Buchner, R., Chen, T. and Hefter, G. (2004) Complexity in "simple" electrolyte solutions: Ion pairing in $MgSO_4$(aq), *J. Phys. Chem. B*, vol.108, pp.2365-2375.

Burger, M. (2009) The mechanism of chemical chalcopyrite leaching, *Personal Communication*, Anglo American Technical Solutions (Research), South Africa.

Burkin, A.R. (1966) *The Chemistry of Hydrometallurgical Processes*, E.&F.N. Spon Ltd., London.

Burkin, A.R. (1969) Solid-state transformations during leaching, *Min. Sci. Eng.*, vol.1, pp.4-14.

Stellenbosch University http://scholar.sun.ac.za

Burkin, A.R., Manning, G.D. and Monhemius, A.J. (1981) Applications of hydrogen peroxide and peroxysulphuric acids in hydrometallurgy, In: *Hydrometallurgy 81*, SCI, London, Paper B5, pp.1-11.

Butler, J.N. and Roy, R.N. (1991) Experimental methods: potentiometric, In: K.S. Pitzer (ed.), *Activity Coefficients in Electrolyte Solutions*, 2nd Edition, CRC Press, Boca Raton, pp.155-208.

Cabelli, D.E., Riley, D., Rodriguez, J.A., Valentine, J.S. and Zhu, H. (2000) Models of superoxide dismutases, In: B. Meunier (ed.), *Biomimetic Oxidations Catalyzed by Transition Metal Complexes*, Imperial College Press, London, pp.461-508.

Calderbank, P.H. and Moo-Young, M.B. (1961) The continuous phase heat and mass-transfer properties of dispersions, *Chem. Eng. Sci.*, vol.16, pp.39-54.

Cannon, W.R., Pettitt, B.M. and McCammon, J.A. (1994) Sulfate anion in water: Model structural, thermodynamic, and dynamic properties, *J. Phys. Chem.*, vol.98, pp.6225-6230.

Casas, J.M., Crisóstomo, G. and Cifuentes, L. (2005a) Speciation of the Fe(II)-Fe(III)-H_2SO_4-H_2O system at 25 and 50ºC, *Hydrometallurgy*, vol.80, pp.254-264.

Casas, J.M., Papangelakis, V.G. and Liu, H. (2005b) Performance of three chemical models on the high-temperature aqueous $Al_2(SO4)_3$-$MgSO_4$-H_2SO_4-H_2O system, *Ind. Eng. Chem. Res.*, vol.44, pp.2931-2941.

Casas, J.M., Paipa, C., Godoy, I. and Vargas, T. (2007) Solubility of sodium-jarosite and solution speciation in the system Fe(III)-Na-H_2SO_4-H_2O at 70°C, *J. Geochem. Explor.*, vol.92, pp.111-119.

Chaudhari, R.V., Gholap, R.V., Emig, G. and Hofmann, H. (1987) Gas-liquid mass transfer in "dead-end" autoclave reactors, *Can. J. Chem. Eng.*, vol.65, pp.744-751.

Chalkley, M.E., Collins, M.J. and Ozberk, E. (1993) The behaviour of sulphur in the Sherritt Zinc Pressure Leach Process, In: I. Matthew (ed.), *World Zinc '93*, AusIMM, Parkville, Victoria, pp.325-331.

Chen, H. and Irish, D.E. (1971) A Raman spectral study of bisulfate-sulfate systems. III. Salt effects, *J. Phys. Chem.*, vol.75, no.17, pp.2681-2684.

Chen, T., Hefter, G. and Buchner, R. (2005) Ion association and hydration in aqueous solutions of nickel(II) and cobalt(II) sulfate, *J. Solution Chem.*, vol.34, no.9, pp.1045-1065.

Cheng, T.C.-M., and Demopoulos, G.P. (1997) Analysis of the hematite precipitation process from a crystallisation point of view, In: B. Mishra (ed.), *EPD Congress 1997*, TMS, Warrendale, PA, pp.599-617.

Cheng, C.Y. and Lawson, F. (1989) The leaching of synthetic chalcocite and covellite in oxygenated acidic sulphate-chloride solutions, *Non-ferrous Smelting Symposium*, AusIMM., Parkville, Australia, pp.167-174.

Cheng, C.Y. and Lawson, F. (1991) The kinetics of leaching covellite in acidic oxygenated sulphate-chloride solutions, *Hydrometallurgy*, vol.27, pp.269-284.

Chmielewski, T. and Charewicz, W.A. (1984) The oxidation of Fe(II) in aqueous sulphuric acid under oxygen pressure, *Hydrometallurgy*, vol.12, pp.21-30.

Stellenbosch University http://scholar.sun.ac.za

Christomir, C. (2004) Pitzer ion-interaction parameters for Fe(II) and Fe(III) in the quinary {Na + K + Mg + Cl + SO_4 + H_2O} system at T = 298 K, *J. Chem. Thermodyn.*, vol.36, pp.223-235.

Ciavatta, L., De Tommaso, G. and Iuliano, M. (2002) Hydroxo sulfate complexes of iron(III) in solution, *Ann. Chim.*, vol.92, pp.669-675.

Cifuentes, L., Casas, J.M. and Simpson, J. (2006) Temperature dependence of the speciation of copper and iron in acidic electrolytes, *Chem. Eng. Res. Des.*, vol.84 (A10), pp.965-969.

Ciriello, C. Synnott, J.A., and Pye, J. (1996) The effect of process parameters on the precipitation of sodium jarosite at Kidd, In: J.E. Dutrizac and G.B. Harris (eds.), *Iron Control and Disposal*, CIM, Montreal, Part 2, pp.117-134.

Clegg, S.L. and Brimblecombe, P. (1995) Application of a multicomponent thermodynamic model to activities and thermal properties of 0-40 mol kg^{-1} aqueous sulfuric acid from <200 to 328 K, *J. Chem. Eng. Data*, vol.40, pp.43-64.

Clegg, S.L. and Whitfield, M. (1991) Activity coefficients in natural waters, In: K.S. Pitzer (ed.), *Activity Coefficients in Electrolyte Solutions*, 2nd Edition, CRC Press, Boca Raton, pp.279-434.

Clegg, S.L., Rard, J.A. and Pitzer, K.S. (1994) Thermodynamic properties of 0-6 mol/kg^{-1} aqueous sulfuric acid from 273.15 to 328.15 K, *J. Chem. Soc., Faraday Trans.*, vol.90, pp.1875-1894.

Cohn, C.A., Fisher, S.C., Brownawell, B.J. and Schoonen, M.A.A. (2010). Adenine oxidation by pyrite-generated hydroxyl radicals, *Geochem. Trans.*, vol.11, pp.1-8.

Cooper, J.R. and Le Fevre, E.J. (1982) *Thermophysical Properties of Water Substance*, Edward Arnold Publishers Ltd., London, pp.1-12.

Córdoba, E.M., Muňoz, J.A., Blázquez, M.L., González, F. and Ballester, A. (2008a) Leaching of chalcopyrite with ferric ion. Part I: General aspects, *Hydrometallurgy*, vol.93, pp.81-87.

Córdoba, E.M., Muňoz, J.A., Blázquez, M.L., González, F. and Ballester, A. (2008b) Leaching of chalcopyrite with ferric ion. Part II: Effect of redox potential, *Hydrometallurgy*, vol.93, pp.88-96.

Cornell, R.M. and Schwertmann, U. (2003) *The Iron Oxides*, 2nd Edition, Wiley-VCH Verlag GmbH & Co., Weinheim.

Cornelius, R.J. and Woodcock, J.T. (1958) Pressure leaching of a manganese ore, Part 1: Kinetic aspects, *Proc. Austr. Inst. Min. Met.*, no.185, pp.65-107.

Corrans, I.J. and Angove, J.E. (1993) *Activation of a Mineral Species*, US Patent 5,232,491.

Corriou, J. and Kikindai, T. (1981) The aqueous oxidation of elemental sulfur and different chemical properties of the allotropic forms S_λ and S_μ, *J. Inorg. Nucl. Chem.*, vol.43, pp.9-15.

Cotton, F.A., Wilkinson, G. and Gaus, P.L. (1995) *Basic Inorganic Chemistry*, 3d Edition, John Wiley & Sons Inc., New York, Ch.24.

Covington, A.K., Dobson, J.V. and Wynne-Jones, L. (1965) Stoichiometric activity coefficients of sulphuric acid and the standard potentials of the lead dioxide/lead sulphate and mercury/mercurous sulphate electrodes at 25°C, *Trans. Faraday Soc.*, vol.61, pp.2050-2056.

Stellenbosch University http://scholar.sun.ac.za

Criss, C.M. and Cobble, J.W. (1964) The thermodynamic properties of high temperature aqueous solution. IV. Entropies and the ions up to 200° and the Correspondence Principle, *J. Am. Chem. Soc.*, vol.86, pp.5383-5390.

Crundwell, F.K. (1987) Kinetics and mechanism of the oxidative dissolution of zinc sulphide concentrate in ferric sulphate solutions, *Hydrometallurgy*, vol.19, pp.227-242.

Crundwell, F.K. (1988a) *The Role of Charge-transfer Mechanisms in the Oxidative and Non-oxidative Dissolution of Sphalerite*, Ph.D. Dissertation, Faculty of Eng., Univ. of the Witwatersrand, Johannesburg.

Crundwell, F.K. (1988b) The influence of the electronic structure of solids on the anodic dissolution and leaching of semiconducting sulphide minerals, *Hydrometallurgy*, vol.21, pp.155-190.

Crundwell, F.K. (1988c) Effect of iron impurity in zinc sulfide concentrates on the rate of dissolution, *AIChE J*., vol.34, no.7, pp.1128-1134.

Crundwell, F.K. (1994a) The modelling of leaching reactions and leaching reactors, *School Hydrometallurgy*, SAIMM, Johannesburg, pp.1-29.

Crundwell, F.K. (1994b) Micro-mixing in continuous particulate reactors, *Chem. Eng. Sci.*, vol.49, no.23, pp.3887-3896.

Crundwell, F.K. (1995) Progress in mathematical modelling of leaching reactors, *Hydrometallurgy*, vol.39, pp.321-335.

Crundwell, F.K. (2003) *Leaching Operation and Practice*, Short course notes, CM Solutions, Johannesburg.

Crundwell, F.K. and Bryson, A.W. (1992) The modelling of particulate reactors - the population balance approach, *Hydrometallurgy*, vol.29, pp.275-295.

Dalton, R.F. (1991) Cuprex metal extraction process, *JOM*, vol.43, pp.51-56.

Danckwerts, P.V. (1958) The effect of incomplete mixing on homogeneous reactions, *Chem. Eng. Sci.*, vol.8, pp.93-102.

Danckwerts, P.V. (1970) *Gas-Liquid Reactions*, McGraw-Hill, New York.

David, R. and Klein, J.P. (2001) Reaction crystallization, In: A. Mersmann (ed.), *Crystallization Technology Handbook*, Marcel Dekker Inc., New York, pp.513-561.

Davies, R.E. (1958) Displacement reactions at the sulfur atom. I. An interpretation of the decomposition of acidified thiosulfate, *J. Am. Chem. Soc.*, vol.80, pp.3565–3569.

Davies, C.W., Jones, H.W. and Monk, C.B. (1952) E.M.F. studies of electrolyte dissociation. Part I. Sulfuric acid in water, *Trans. Faraday Soc.*, vol.48, pp.921-928.

Delley, B. (1990) An all-electron numerical method for solving the local density functional for polyatomic molecules, *J. Chem. Phys.*, vol.92, pp.508-517.

Demopoulos, G.P. (2009) Aqueous precipitation and crystallization for the production of particulate solids with desired properties, *Hydrometallurgy*, vol.96, pp.199-214.

Stellenbosch University http://scholar.sun.ac.za

Dempsey, P. and Dreisinger, D.B. (2003) *Process for the Extraction of Copper*, US Patent 6,503,293.

Derksen, J.J., Buist, K., Van Weert, G. and Reuter, M.A. (2000) Oxygen transfer in agitated silica and pyrite slurries, *Miner. Eng.*, vol.13, no.1, pp.25-36.

Dew, D. and Batty, J. (2003) Biotechnology in mining. Development of the BIOCOP Process, Short course notes, *Hydro 2003*, CIM, Montreal.

Diakonov, I., Khodakovshy, I., Schott, J. and Sergeeva, E. (1994) Thermodynamic properties of iron oxides and hydroxides. I. Surface and bulk thermodynamic properties of goethite (α-FeOOH) up to 500K, *Eur. J. Min.*, vol.6, pp.967-983.

Dickson, A.G., Wesolowski, D.J., Palmer, D.A. and Mesmer, R.E. (1990) Dissociation constant of bisulfate ion in aqueous sodium chloride solutions to 250°C, *J. Phys. Chem.*, vol.94, pp.7978-7985.

Dimitrijević, M., Antonijević, M.M. and Dimitrijević, V. (1999) Investigation of the kinetics of pyrite oxidation by hydrogen peroxide in hydrochloric acid solutions, *Miner. Eng.*, vol.12, no.2, pp.165-174.

Dixon, D.G. (2007) Galvanox, A novel process for the treatment of copper concentrates, Short course notes, *Copper 2007*, CIM, Montreal.

Dixon, D.G. and Tshilombo, A.F. (2005) *Leaching Process for Copper Concentrates*, US Patent 2005/0269208 A1.

Dixon, D.G., Mayne, D.D. and Baxter, K.G. (2008) Galvanox™ – a novel galvanically-assisted atmospheric leaching technology for copper concentrate, *Can. Metall. Quart.*, vol.47, pp.327-336.

Dobrokhotov, G.N. and Maiorova, E.V. (1962) Kinetics of autoclave leaching of chalcopyrite, *J. Appl. Chem.-USSR*, vol.35, no.8, pp.1702-1709.

Doi, T. (1963) Physico-chemical properties of sulfur. 1. Pressure effects on viscosity of liquid sulfur, *Rev. Phys. Chem. Japan*, vol.33, no.2, pp.41-51.

Donnay, G., Corliss, L.M., Donnay, J.D.H., Elliott, N. and Hastings, J.M. (1958) Symmetry of magnetic structures: Magnetic structure of chalcopyrite, *Phys. Rev.*, vol.112, no.6, pp.1917-1923.

Downes, C.J. and Pitzer, K.S. (1976) Thermodynamics of electrolytes. Binary mixtures formed from aqueous NaCl, Na_2SO_4, $CuCl_2$ and $CuSO_4$ at 25ºC, *J. Solution Chem.*, vol.5, no.6, pp.389-398.

Doyle, F.M., Arauco, H., and Feng, L.M. (1989) Iron removal during oxidative, acid pressure leaching of a zinc sulphide concentrate, *Int. J. Min. Proc.*, vol.25, pp.241-260.

Dreisinger, D. (2003) New developments in the leaching of base and precious metal ores and concentrates, In: L. Lorenzen, and D.J. Bradshaw (eds.), Proceedings of the XXII International Mineral Processing Congress, SAIMM, Johannesburg, pp.70-80.

Dreisinger, D. (2004) Sulfur chemistry: Reaction pathways and hydrometallurgical processing, *Personal Communication*, Univ. of British Columbia, Vancouver.

Stellenbosch University http://scholar.sun.ac.za

Dreisinger, D. (2006) Copper leaching from primary sulfides: Options for biological and chemical extraction of copper, *Hydrometallurgy*, vol.83, pp.10-20.

Dreisinger, D.B. and Peters, E. (1989) The oxidation of ferrous sulphate by molecular oxygen under zinc pressure-leach conditions, *Hydrometallurgy*, vol.22, pp.101-119.

Dreisinger, D.B., Peters, E., Talaba, M., DeGraaf, K.B., Owusu, G. and Swiniarski, R. (1990) The kinetics of the Sherrit Gordon Zinc Pressure Leach Process, In: T.S. Mackay and R.D. Prengaman (eds.), *Lead-Zinc '90*, TMS, Warrendale, PA, pp.313-330.

Dreisinger, D., Marsh, J. and Dempsey, P. (2002) The Anglo American Corporation/University of British Columbia (AAC/UBC) chalcopyrite copper hydrometallurgical process, *ALTA 2002*, Copper-7 Forum, ALTA Metallurgical Services, Melbourne, pp.1-25.

Dreisinger, D.B., Steyl, J.D.T., Sole, K.C., Gnoinski, J. and Dempsey, P. (2003) The Anglo American Corporation/University of British Columbia (AAC/UBC) process: An integrated pilot-plant evaluation, In: P.A. Riveros, D.G. Dixon, D.B. Dreisinger and J.M. Menacho (eds.), *Copper 2003*, CIME, Santiago, Chile, vol.VI, pp.223-238.

Drouet, C. and Navrotsky, A. (2003) Synthesis, characterization, and thermochemistry of K-Na-H_3O jarosites, *Geochim. Cosmochim. Acta*, vol.67, no.11, pp.2063-2067.

Druschel, G.K., Hamers, R.J. and Banfield, J.F. (2003) Kinetics and mechanism of polythionate oxidation to sulfate at low pH by O_2 and Fe^{3+}, *Geochim. Cosmochim. Acta*, vol.63, no.23, pp.4457-4469.

Druschel, G. and Borda, M. (2006) Comment on "Pyrite dissolution in acidic media" by M. Descostes, P. Vitorge, and C. Beaucaire, *Geochim. Cosmochim. Acta*, vol.70, pp.5246-5250.

Dutrizac, J.E. (1980) The physical chemistry of iron precipitation in the zinc industry, In: J.M. Cigan, T.S. Mackay and T.J. O'Keefe (eds.), *Lead-Zinc-Tin '80*, TMS-AIME, Warrendale, PA, pp.532-564.

Dutrizac, J.E. (1981) The dissolution of chalcopyrite in ferric sulfate and ferric chloride media, *Metall. Trans. B*, vol.12B, pp.371-378.

Dutrizac, J.E. (1984) The behaviour of impurities during jarosite precipitation, In: R.G. Bautista (ed.), *Hydrometallurgical Process Fundamentals*, Plenum Press, New York, pp.125-169.

Dutrizac, J.E. (1996) The effect of seeding on the rate of precipitation of ammonium jarosite and sodium jarosite, *Hydrometallurgy*, vol.42, pp.293-312.

Dutrizac, J.E. and Chen, T.T. (2009) Factors affecting the precipitation of hematite rather than jarosite in nickel sulphate-chloride solutions, In: J.J. Budac, R. Fraser, I. Mihaylov, V.G. Papangelakis and D.J. Robinson (eds.), *Hydrometallurgy of Nickel and Cobalt 2009*, CIM, Montreal, pp.295-319.

Dutrizac, J.E. and Jambor, J.L. (2000) Jarosites and their application in hydrometallurgy, *Rev. Mineral Geochem.*, vol.40, pp.405-452.

Dutrizac, J.E. and MacDonald, R.J.C. (1974) Ferric ion as a leaching medium, *Min. Sci. Eng.*, vol.6, no.2, pp.59-100.

Dutrizac, J.E. and Riveros, P.A. (1999) The precipitation of hematite from ferric chloride media at atmospheric pressure, *Metall. Trans. B*, vol.30B, pp.993-1001.

Stellenbosch University http://scholar.sun.ac.za

Dutrizac, J.E., MacDonald, R.J.C. and Ingraham, T.R. (1969) The kinetics of dissolution of synthetic chalcopyrite in aqueous acidic ferric sulphate solutions, *Trans. Metall. Soc. AIME*, vol.245, pp.955-959.

Dutrizac, J.E., MacDonald, R.J.C. and Ingraham, T.R. (1970) The kinetics of dissolution of bornite in acidified ferric sulphate solutions, *Metall. Trans.*, vol.1, pp.225-231.

El Azher, N., Gourich, B., Vial, C., Belhaj Soulami, M. and Ziyad, M. (2008) Study of ferrous iron oxidation in Morocco drinking water in an airlift reactor, *Chem. Eng. Process.*, vol.47, no.9-10, pp.1877-1886.

Elgersma, F., Witkamp, G.J. and Van Rosmalen, G.M. (1993) Simultaneous dissolution of zinc ferrite and precipitation of ammonium jarosite, *Hydrometallurgy*, vol.34, pp.23-47.

Elsherief, A.E. (2002) The influence of cathodic reduction, Fe^{2+} and Cu^{2+} ions on the electrochemical dissolution of chalcopyrite in acidic solution, *Miner. Eng.*, vol.15, pp.215-223.

Elsherief, A.E., Saba, A.E. and Afifi, S.E. (1995) Anodic leaching of chalcocite with periodic cathodic reduction, *Miner. Eng.*, vol.8, no.9, pp.967-978.

Erdey-Grúz, T. (1972) *Kinetics of Electrode Processes*, Adam Hilger Ltd., London.

Espeau, P. and Céolin, R. (2007) Density of molten sulfur in the 334-508 K range, *Thermochim. Acta*, vol.459, pp.127-129.

Farnsworth, M. and Kline, C.H. (1973) *Zinc Chemicals*, 1st Edition, Zinc Development Association, London and Zinc Institute Inc., New York.

Fedorov, V.A., Chernikova, G.E., Kuznechikhina, M.A. and Mironov, V.E. (1973) Effect of the ionic medium and temperature on the formation of sulphato-complexes of zinc and cadmium and calculations of their thermodynamic stability constants, *Russ. J. Inorg. Chem.*, vol.18, no.3, pp.337-340.

Ferron, C.J., Dymov, I., McKay-Davison, N. and Butcher, D. (2000) Kinetics and mechanisms of high temperature pressure leaching of Guelb Moghrein chalcopyrite concentrate, In: P.R. Taylor (ed.), *EPD Congress 2000*, TMS, Warrendale, PA, pp.579-595.

Filippou, D., Papangelakis, V.G. and Demopoulos, G.P. (1995) Hydrogen ion activities and species distribution in mixed metal sulfate aqueous systems, *AIChE J.*, vol.41, no.1, pp.171-184.

Filippou, D., Cheng, T.C. and Demopoulos, G.P. (2000) Gas-liquid mass-transfer; from fundamentals to application in hydrometallurgical systems, *Min. Proc. Ext. Met. Rev.*, vol.20, pp.447-502.

Filmer, A.O. and Nicol, M.J. (1980) The non-oxidative dissolution of nickel sulphides in aqueous acidic solutions, *J. S. Afr. Inst. Min. Metall.*, no.12, pp.415-424.

Gao, B. and Liu, Z.-F. (2004) A first principles study on the solvation and structure of $SO_4^{2-}(H2O)_n$, n=6-12, *J. Chem. Phys.*, vol.121, no.17, pp.8299-8306.

George, P. (1954) The oxidation of ferrous perchlorate by molecular oxygen, *Chem. Soc. J.*, pp.4349-4359.

Gerischer, H. and Mindt, W. (1968) The mechanisms of the decomposition of semiconductors by electrochemical oxidation and reduction, *Electrochim. Acta*, vol.13, pp.1329-1341.

Stellenbosch University http://scholar.sun.ac.za

Gerlach, J.K., Gock, E.D. and Ghosh, S.K. (1973) Activation and leaching of chalcopyrite concentrates by dilute solutions of sulphuric acid, In: D.J.I. Evans and R.S. Shoemaker (eds.), *International Symposium on Hydrometallurgy*, AIME, New York, pp.87-94.

Goh, S.W., Buckley, A.N. and Lamb, R.N. (2006) Copper(II) sulfide?, *Min. Eng.*, vol.19, pp.204-208.

Guendouzi, M.EL., Mounir, A., and Dinane, A. (2003) Water activity, osmotic and activity coefficients of aqueous solutions of Li_2SO_4, Na_2SO_4, K_2SO_4, $(NH_4)_2SO_4$, $MgSO_4$, $MnSO_4$, $NiSO_4$, $CuSO_4$, and $ZnSO_4$ at T = 298.15 K, *J. Chem. Thermodyn.*, vol.35, pp.209-220.

Guerra, E. and Bestetti, M. (2006) Physicochemical properties of $ZnSO_4$-H_2SO_4-H_2O electrolytes of relevance to zinc electrowinning, *J. Chem. Eng. Data*, vol.51, pp.1491-1497.

Habashi, F. (1967) Kinetics and mechanism of gold and silver dissolution in cyanide solutions, *Bureau of Mines and Geology Bulletin*, no.59, pp.1-42.

Habashi, F. (1993) *A Textbook of Hydrometallurgy*, 1st Edition, Métallurgie Extractive Québec Enr., Sainte Foy, Quebec.

Habashi, F. and Bauer, E.L. (1966) Aqueous oxidation of elemental sulfur, In: R.L. Pigford (ed.), *I&EC Fundamentals*, vol.5, ACS, Washington, DC, pp.469-471.

Hackl, R.P., Dreisinger, D.B. and King, J.A. (1995a) Effect of sulfur-dispersing surfactants on the oxygen pressure leaching of chalcopyrite, In: W.C. Cooper, D.B. Dreisinger, J.E. Dutrizac, H. Hein and G. Ugarte (eds.), *Copper 95*, CIM, Montreal, vol.III, pp.559-578.

Hackl, R.P, Dreisinger, D.B., Peters E. and King, J.A. (1995b) Passivation of chalcopyrite during oxidative leaching in sulfate media, *Hydrometallurgy*, vol.39, pp.25-48.

Haghtalab, A., Papangelakis, V.G. and Zhu. X. (2004) The electrolyte NRTL model and speciation approach as applied to multicomponent aqueous solutions of H_2SO_4, $Fe_2(SO_4)_3$, $MgSO_4$ and $Al_2(SO_4)_3$ at 230-270ºC, *Fluid Phase Equilibr.*, vol.220, pp.199-209.

Hallett, C.J., Monhemius, A.J. and Robertson, D.G.C. (1981) Oxygen mass transfer in Pachuca tanks, In: *Extraction Metallurgy '81*, IMM, London, pp.308-320.

Hamer, W.J. (1959) The electromotive force method of determining ionization constants: Ionization of the bisulfate ion, In: W.J. Hamer (ed), *The Structure of Electrolyte Solutions*, John Wiley & Sons Inc., New York, Ch.15.

Hancock, R. (1976) Metal ions in solution, *Hydrometallurgy: Theory and Practice*, Vacation School, SAIMM, Johannesburg, vol.1, pp.1-27.

Harmer, S.L. (2002) *The Extraction of Copper from Chalcopyrite*, Ph.D. Dissertation, Ian Wark Research Institute, ARC Special Research Centre for Particle and Material Interfaces, Univ. of South Australia, Adelaide.

Harmer, S.L., Thomas, J.E., Fornasiero, D. and Gerson, A.R. (2006) The evolution of surface layers formed during chalcopyrite leaching, *Geochim. Cosmochim. Acta*, vol.70, no.17, pp.4392-4402.

Harned, H.S. and Owen, B.B. (1958) *The Physical Chemistry of Electrolyte Solutions*, 3d Edition, Reinhold Publishing Corporation Inc., New York.

Stellenbosch University http://scholar.sun.ac.za

Hefter, G. (2006) When spectroscopy fails: The measurement of ion pairing, *Pure Appl. Chem.*, vol.78, pp.1571-1586.

Helgeson, H.C. (1967) Thermodynamics of complex dissociation in aqueous solution at elevated temperatures, *J. Phys. Chem.*, vol.71, no.10, pp.3121-3136.

Herbst, J.A. (1979) Rate processes in multiparticle metallurgical systems, In: H.Y. Sohn and M.E. Wadsworth (eds), *Rate Processes of Extractive Metallurgy*, Plenum Press, New York, pp.53-112.

Hermann, C., Dewes, I. and Schumpe, A. (1993) The estimation of gas solubilities in salt solutions, *Chem. Eng. Sci.*, vol.50, pp.1673-1675.

Hirato, T., Majima, H. and Awakura, Y. (1987) The leaching of chalcopyrite with ferric sulfate, *Metall. Trans. B*, vol.18B, pp.489-496.

Hiroyoshi, N., Miki, H., Hirajima, T. and Tsunekawa, M. (2001) Enhancement of chalcopyrite leaching by ferrous ions in acidic ferric sulfate solutions, *Hydrometallurgy*, vol.60, pp.185-197.

Hiroyoshi, N., Kuroiwa, S., Miki, H., Tsunekawa, M. and Hirajima, T. (2004) Synergistic effect of cupric and ferrous ions on active-passive behaviour in anodic dissolution of chalcopyrite in sulfuric acid solutions, *Hydrometallurgy*, vol.74, pp.103-116.

Hiroyoshi, N., Kitagawa, H. and Tsunekawa, M. (2008) Effect of solution composition on the optimum redox potential for chalcopyrite leaching in sulfuric acid solutions, *Hydrometallurgy*, vol.91, pp.144-149.

Hiskey, J.B. (1993) Chalcopyrite semiconductor electrochemistry and dissolution, In: R.G. Reddy and R.N. Weizenbach (eds.), *Extractive Metallurgy of Copper, Nickel and Cobalt*, vol.I, TMS, Warrendale, PA, pp.949-969.

Hiskey, J.B. and Wadsworth, M.E. (1981) Electrochemical processes in the leaching of metal sulfides and oxides, In: M.C. Kuhn (ed.), *Process and Fundamental Considerations of Selected Hydrometallurgical Systems*, SME-AIME, New York, pp.304-325.

Högfeldt, E. (1982) *Stability Constants of Metal-Ion Complexes. Part A: Inorganic Ligands*, IUPAC Chemical Data Series No.21, Pergamon Press, Oxford.

Holliday, R.I. and Richmond, W.R. (1990) An electrochemical study of the oxidation of chalcopyrite in acidic solution, *J. Electroanal. Chem.*, vol.39, pp.353-375.

Holmes, P.R. and Crundwell, F.K. (1995) Kinetic aspects of galvanic interactions between minerals during dissolution, *Hydrometallurgy*, vol.39, pp.353-375.

Holmes, P.R. and Crundwell, F.K. (2000) The kinetics of the oxidation of pyrite by ferric ions and dissolved oxygen: An electrochemical study, *Geochim. Cosmochim. Acta*, vol.64, no.2, pp.263-274.

Holmes, H.F. and Mesmer, R.E. (1983) Isopiestic studies of aqueous solutions at elevated temperatures. VII. $MgSO_4$ and $NiSO_4$, *J. Chem. Thermodyn.*, vol.15, pp.709-719.

Holmes, H.F. and Mesmer, R.E. (1992) Isopiestic studies of H_2SO_4(aq) at elevated temperatures. Thermodynamic properties, *J. Chem. Thermodyn.*, vol.24, pp.317-328.

Hood, G.C. and Reilly, C.A. (1957) Ionization of strong electrolytes. V. Proton magnetic resonance in sulfuric acid, *J. Chem. Phys.*, vol.27, no.5, pp.1126-1128.

Stellenbosch University http://scholar.sun.ac.za

Horvath, A.L. (1985) *Handbook of Aqueous Electrolyte Solutions*, 1st Edition, Ellis Horwood Ltd., Chichester.

Horn, R.A. and Axelrod, E.H. (1964) Proton mobility and electron exchange in aqueous media, *J. Chem. Phys.*, vol.40, no.6, pp.1518-1522.

Hourn, M.M., Turner, D.W. and Holzberger, I.R. (1999) *Atmospheric Mineral Leach Process*, US Patent 5,993,635.

Hovey, J.K., Pitzer, K.S. and Rard, J.A. (1993) Thermodynamics of Na_2SO_4(aq) at temperatures from 273 K to 373 K and of {(1-y)H_2SO_4 + yNa_2SO_4}(aq) at T = 298.15 K, *J. Chem. Thermodyn.*, vol.25, pp.173-192.

Huffman, R.E. and Davidson, N. (1956) Kinetics of the ferrous iron-oxygen reaction in sulfuric acid solution, *J. Am. Chem. Soc.*, vol.78, pp.4836-4842.

Huang, H.H. and Bernal, J.H. (1984) Kinetic study on direct leaching of sphalerite in sulfuric acid solution using ferrous sulfate as the catalyst, In: P.E. Richardson, S. Srinivasan and R. Woods (eds.), *Electrochemistry in Mineral and Metal Processing*, ECS, Pennington, NJ, pp.469-485.

Hwang, H.J. and Stenstrom, M.K. (1979) The effect of surface active agents on oxygen transfer, Water Resources Program Report, School of Engineering and Applied Sciences, Univ. California, Los Angeles, pp.1-57.

Hyvärinen, O. and Hämäläinen, M. (2005) Hydrocopper – A new technology producing copper directly from concentrate, *Hydrometallurgy*, vol.77, pp.61-65.

I, T.P. and Nancollas, G.H. (1972). Equil - A general computational method for the calculation of solution equilibria, *Anal. Chem.*, vol.44, no.12, pp.1940-1950.

Itou, H., Takasu, T., Nakamura, T., Shibata, E., and Tateiwa, H. (2006) Mechanism of scorodite formation at ambient temperature as determined by TEM analysis, In: J.E. Dutrizac and P.A. Riveros (eds.), *Iron Control Technologies*, CIM, Montreal, Part 1, pp.897-909.

Iwai, M., Majima, H. and Izak, T. (1979). A kinetic study on the oxidation of ferrous ion with dissolved molecular oxygen, *Denki Kagaku*, vol.47, no.7, pp.409-414.

Iwai, M., Majima, H., and Awakura, Y. (1982) Oxidation of Fe(II) in sulfuric acid solutions with dissolved molecular oxygen, *Metall. Trans. B*, vol.13B, pp.311-318.

Izatt, R.M., Eatough, D., Christensen, J.J. and Bartholomew, C.H. (1969) Calorimetrically determined Log K, ΔH^o and ΔS^o values for the interaction of sulphate ion with several bi-and tervalent metal ions, *J. Chem. Soc. A*, pp.45-53.

Jang, J.H. and Wadsworth, M.E. (1993) Hydrothermal conversion of chalcopyrite under controlled E_h and pH, In: R.G. Reddy and R.N. Weizenbach (eds.), *Extractive Metallurgy of Copper, Nickel and Cobalt*, vol.I, TMS, Warrendale, PA, pp.689-707.

Jansen, M. and Taylor, A. (2000) Key elements in the selection of sulphide leach, *ALTA 2002*, Copper-7 Forum, ALTA Metallurgical Services, Melbourne, 24pp.

Jaskula, M. and Hotloś, J. (1992) Mean thermodynamic activity coefficient of $CuSO_4$ in the ternary system $CuSO_4$-H_2SO_4-H_2O at 60°C, *Hydrometallurgy*, vol.31, pp.233-242.

Javad Koleini, S.M., Aghazadeh, V. and Sandström, A. (2011) Acidic sulphate leaching of chalcopyrite concentrates in presence of pyrite, *Miner. Eng.*, vol.24, pp.381-386.

Stellenbosch University http://scholar.sun.ac.za

Ji, J. and King, J. (2004) Measurement of oxygen transfer rate with an EKATO gassing agitator in a 5 m^3 pressure vessel, In: M.J. Collins and V.G. Papangelakis (eds.), *Pressure Hydrometallurgy 2004*, CIM, Montreal, pp.339-349.

Jin, Z., Warren, G.W. and Henein, H. (1985) Reaction kinetics and electrochemical model for the ferric chloride leaching of sphalerite, In: K. Tozawa (ed.), *Zinc'85, Proceedings of the International Symposium on Extractive Metallurgy of Zinc*, MMIJ, Tokyo, pp.111-125.

Jones, M.W., Papangelakis, V.G. and Steyl, J.D.T. (2008) Chemical modelling of $MgSO_4$ solubility in atmospheric chloride leaching of laterites, In: C.A. Young, P.R. Taylor, C.G. Anderson and Y. Choi (eds.), *Hydrometallurgy 2008*, SME., Littleton, CO, pp.561-569.

Kammel, R., Pawlek, F., Simon, M. and Xi-Ming, L. (1987) Oxidizing leaching of sphalerite under atmospheric pressure, *Metall.*, vol.41, no.2, pp.158-161.

Kametani, H. and Aoki, A. (1985) Effect of suspension potential on the oxidation rate of copper concentrate in a sulfuric acid solution, *Metallurgical Transactions B*, vol.16B, pp.695-705.

Kandori, K., Shigetomi, T. and Ishikawa, T. (2004) Study on forced hydrolysis reaction of acidic $Fe_2(SO_4)_3$ solution – structure and properties of precipitates, *Colloids and Surf. A: Physicochem. Eng. Aspects*, vol.232, pp.19-28.

Kawase, Y., Araki, T., Shimizu, K. and Miura, H. (1997) Gas-liquid mass transfer in three-phase stirred tank reactors: Newtonian and non-Newtonian fluids, *Can. J. Chem. Eng.*, vol.75, pp.1159-1164.

Kazansky, V. and Solkan, V. (2003) Proton solvation and self-dissociation of 100% sulfuric acid: The quantum-chemical analysis, *Phys. Chem. Chem. Phys.*, vol.5, pp.31-35.

Keenen, E.A. (1969) *Bacterial Beneficiation of Uranium Metals*, Ph.D. Thesis, Univ. of New South Wales.

Kittel, C. (1996) *Introduction to Solid State Physics*, 7th Edition, John Wiley & Sons Inc., New York.

Klamt, A., and Schüürmann, G. (1993) COSMO: A new approach to dielectric screening in solvents with explicit expressions for the screening energy and its gradient, *J. Chem. Soc., Perkin Trans. 2*, pp.799-805.

Klauber, C. (2008) A critical review of the surface chemistry of acidic ferric sulphate dissolution of chalcopyrite with regards to hindered dissolution, *Int. J. Miner. Process.*, vol.86, pp.1-17.

Kobe, K.A. and Dickey, W. (1945) Oxidation of ferrous sulfate solutions with oxygen, *Ind. Eng. Chem.*, vol.37, no.5, pp.429-431.

Kobylin, P., Kaskiala, T. and Salminen, J. (2007) Modeling of H_2SO_4-$FeSO_4$-H_2O and H_2SO_4-$Fe_2(SO_4)_3$-H_2O systems for metallurgical applications, *Ind. Eng. Chem. Res.*, vol.46, pp.2601-2608.

Kohn, W. and Sham, L.J. (1965) Self-consistent equations including exchange and correlation effects, *Phys. Rev. A*, vol.140, pp.1133-1138.

Kratz, T. and Fuess, H. (1989) Simultane strukturbestimmung von kupferkies und bornit an einem kristall, *Z. Kristallogr.*, vol.186, pp.167-169.

Stellenbosch University http://scholar.sun.ac.za

Kuhn, M.C., Arbiter, N. and Kling, H. (1975) Physical and chemical separations via the Arbiter Process, *Proceedings of the XI International Mineral Processing Congress, Cagliari*, pp.831-848.

Laliberté, M. and Cooper, W.E. (2004) Model for calculating the density of aqueous electrolyte solutions, *J. Chem. Eng. Data*, vol.49, no.5, pp.1141-1151.

Lamb, A.B. and Elder, L.W. (1931) The electromotive activation of oxygen, *J. Am. Chem. Soc.*, vol.53, pp.137-163.

Larson, J.W. (1970) Thermodynamics of divalent metal sulphate dissociation and the structure of the solvated metal sulfate ion pair, *J. Phys. Chem.*, vol.74, no.18, pp.3392-3396.

Lahtinen, M., Svens, K. and Lehtinen, L. (2006) Hematite versus jarosite precipitation in zinc production, In: J.E. Dutrizac and P.A. Riveros (eds.), *Iron Control Technologies*, CIM, Montreal, Part 1, pp.93-107.

Lázaro, I. and Nicol, M.J. (2003) The mechanism of the dissolution and passivation of chalcopyrite: An electrochemical study, In: C.A. Young, A.M. Alfantazi, C.G. Anderson, D.B. Dreisinger, B. Harris, and A. James (eds.), *Hydrometallurgy 2003*, TMS, Warrendale, PA, vol.1, pp.405-417.

Lázaro, I. and Nicol, M.J. (2006) A rotating ring-disk study of the initial stages of the anodic dissolution of chalcopyrite in acidic solutions, *J. Appl. Electrochem.*, vol.36, pp.425-431.

Lehmann, M.N., Stichnoth, M. and Bailey, S.I. (1999) Electrochemistry of iron sulfide minerals at elevated temperatures and pressures in acid media, 217th ACS National Meeting, ACS, Washington, DC.

Lee, C.K. and Tavlarides, L.L. (1985) Ionic equilibria in ferric sulfate-sulfuric acid solutions, *Polyhedron*, vol.4, no.1, pp.47-51.

Lepin, L.K. and Matseevskii, B.P. (1967) Mechanism of the oxidation of cations of lower valence by oxygen in aqueous solutions, *Akad. Nauk. SSSR. Dokl. Chem. Sect.*, vol.173, pp.1336-1338.

Levenspiel, O. (1972) *Chemical Reaction Engineering*, 2nd Edition, John Wiley & Sons Inc., New York.

Levenspiel, O. and Godfrey, J.H. (1974) A gradientless contactor for experimental study of interphase mass transfer with/without reaction, *Chem. Eng. Sci.*, vol.29., pp.1723-1730.

Lewis, D. (1970) Studies of redox equilibria at elevated temperature. I. The estimation of equilibrium constants and standard potentials for aqueous systems up to 374°C, *Arkiv för Kemi*, vol.32, no.32, pp.385-404.

Lewis, A. (2011) Understanding crystallization and precipitation processes, *Personal Communication*, Univ. Cape Town, Cape Town.

Liddel, K.C. and Bautista, R.G. (1981) A partial equilibrium chemical model for the dump leaching of chalcopyrite, *Metall. Trans. B*, vol.12B, pp.627-637.

Lide, D.R. (1991) *Handbook of Chemistry and Physics*, 71st Edition, CRC Press, Boca Raton, FL.

Lide, D.R. (2004) *Handbook of Chemistry and Physics*, 85th Edition, CRC Press, Boca Raton, FL.

Stellenbosch University http://scholar.sun.ac.za

Lietzke, M.H., Stoughton, R.W. and Young, T.F. (1961) The bisulfate acid constant from 25 to 225ºC as computed from solubility data, *J. Phys. Chem.*, vol.65, pp.2247-2249.

Lin, H.K., Sohn, H.Y. and Wadsworth, M.E. (1986) The kinetics of leaching of chalcopyrite and pyrite grains in primary copper ore by dissolved oxygen, In: R.G. Bautista, R.J. Wesely and G.W. Warren (eds.) *Hydrometallurgical Reactor Design and Kinetics*, TMS-AIME, Warrendale, PA, pp.149-168.

Lin, J.S., Qteish, A., Payne, M.C. and Heine, V. (1993) Optimized and transferable nonlocal separable ab initio pseudopotentials, *Phys. Rev. B*, vol.47, pp.4174-4180.

Lindstrom, R.E. and Wirth, H.E. (1969) Estimation of the bisulfate ion dissociation in solutions of sulfuric acid and sodium bisulfate, *J. Phys. Chem.*, vol.73, no.1, pp.218-223.

Linek, V. and Vacek, V. (1981) Chemical engineering use of catalyzed sulfite oxidation kinetics for the determination of mass transfer characteristics of gas-liquid contractors, *Chem. Eng. Sci.*, vol.36, no.11, pp.1747-1768.

Linek, V., Vacek, V. and Beneš, P. (1987) A critical review and experimental verification of the correct use of the dynamic method for the determination of oxygen transfer in aerated agitated vessels to water, electrolyte solution and viscous liquids, *Chem. Eng. J.*, vol.34, pp.11-34.

Linek, V., Beneš, P. and Sinkule, J. (1990) Critical assessment of the steady-state Na_2SO_3 feeding method for k_La measurement in fermentors, *Biotechnol. BioEng.*, vol.35, pp.766-770.

Linke, W.F. and Seidell, A. (1958, vol.1 and 1965, vol.2) *Solubilities of Inorganic and Metal-Organic Compounds*, 4th Edition, ACS, Washington, DC.

Lindsay, W.T. (1980) Estimation of concentration quotients for ionic equilibria in high temperature water: The model substance approach, *Proceedings of the 41st International Water Conference*, ESWP, Pittsburgh, PA, pp.284-294.

Lister, M.W. and Rivington, D.E. (1955) Ferric sulphate complexes and ternary complexes with thiocyanate ions, *Can. J. Chem.*, vol.33, pp.1591-1602.

Littlejohn, P.O.L. and Dixon, D.G. (2008) The enhancing effect of pyrite on ferrous oxidation by dissolved oxygen, In: C.A. Young, P.R. Taylor, C.G. Anderson and Y. Choi (eds.), *Hydrometallurgy 2008*, SME., Littleton, CO, pp.1098-1109.

Liu, H. and Papangelakis, V.G. (2005a) Chemical modeling of high temperature aqueous processes, *Hydrometallurgy*, vol.79, pp.48-61.

Liu, H. and Papangelakis, V.G. (2005b) Thermodynamic equilibrium of the O_2-$ZnSO_4$-H_2SO_4-H_2O system from 25 to 250ºC, *Fluid Phase Equilibr.*, vol.234, pp.122-130.

Liu, H., Papangelakis, V.G., Alam, M.S. and Singh, G. (2003) Solubility of hematite in H_2SO_4 solution at 230-270°C, *Can. Metall. Quart.*, vol.42, no.2, pp.199-208.

Liu, H., Wei, Y., Li, P., Zhang, Y. and Sun, Y. (2007) Catalytic synthesis of nanosized hematite particles in solution, *Mater. Chem. Phys.*, vol.102, pp.1-6.

Long, H. and Dixon, D.G. (2004) Pressure oxidation of pyrite in sulfuric acid media: a kinetic study, *Hydrometallurgy*, vol.73, pp.335-349.

Lotens, J.P. and Wesker, E. (1987) The behaviour of sulphur in the oxidative leaching of sulphidic minerals, *Hydrometallurgy*, vol.18, pp.39-54.

Stellenbosch University http://scholar.sun.ac.za

Lowson, R.T. (1982) Aqueous oxidation of pyrite by molecular oxygen, *Chem. Rev.*, vol.82, no.5, pp.461-497.

Lu, J. and Dreisinger, D. (2003) The role of surfactants in the leaching of chalcopyrite in the AAC/UBC Copper Process, Unpublished, 28pp.

Lu, J., Chen, D. and Jiao, X. (2006) Fabrication, characterization, and formation mechanism of hollow spindle-like hematite via a solvothermal process, *J. Colloid Interface Sci.*, vol.303, pp.437-443.

Luther, G.W. (1987) Pyrite oxidation and reduction: Molecular orbital theory considerations, *Geochim. Cosmochim. Acta*, vol.51, pp.3193-3199.

Magini, M. (1979) Solute structuring in aqueous iron(III) sulphate solutions. Evidence for the formation of iron(III)-sulphate complexes, *J. Chem. Phys.*, vol.70, no.1, pp.317-324.

Majima, H. and Awakura, Y. (1988) Water and solute activities of the solution systems of H_2SO_4-$CuSO_4$-H_2O and HCl-$CuCl_2$-H_2O, *Metall. Trans. B*, vol.19, pp.347-354.

Majima, H. and Peters, E. (1966) Oxidation rates of sulphide minerals by aqueous oxidation at elevated temperatures, *Trans. Met. Soc. AIME*, vol.26, pp.1409-1413.

Majima, H., Awakura, Y. and Kawasaki, Y. (1988) *Activities of Water and Solutes in the Aqueous Solution Systems H_2SO_4–$M_x(SO_4)_y$ and HCl–MCl_x*, Agne Shofu Publishing Inc., Tokyo.

Majzlan, J., Stevens, R., Boerio-Goates, J., Woodfiled, B.F., Navrotsky, A., Burns, P.C., Crawford, M.K. and Amos, T.G. (2004) Thermodynamic properties, low-temperature heat-capacity anomalies, and single-crystal X-ray refinement of hydronium jarosite, $(H_3O)Fe_3(SO_4)_2(OH)_6$, *Phys. Chem. Miner.*, vol.31, pp.518-531.

Mao, M.H. and Peters, E. (1983) Acid pressure leaching of chalcocite, In: K. Osseo-Asare and J.D. Miller (eds.), *Hydrometallurgy - Research, Development and Plant Practice*, SME-AIME, Warrendale, PA, pp.243-260.

Marchand, P. and Rancourt, D.G. (2009) General model for the aqueous precipitation of rough-surface nanocrystals and application to ferrihydrite genesis, *Am. Mineral.*, vol.94, pp.1428-1439.

Marcus, Y. (1987) The thermodynamics of solvation of ions. Part 2. The enthalpy of hydration at 298.15 K, *J. Chem. Soc., Faraday Trans.*, vol.83, pp.339-349.

Marcus, Y. (1991) Thermodynamics of solvation of ions. Part 5. Gibbs free energy of hydration at 298.15 K, *J. Chem. Soc., Faraday Trans.*, vol.87, no.18, pp.2995-2999.

Margolis, E.J. (1966) *Chemical Principles in Calculations of Ionic Equilibria*, The MacMillean Company, New York.

Marsden J.O., Wilmot, J.C. and Hazen, N. (2007a) Medium-temperature pressure leaching of copper concentrates. Part I: Chemistry and initial process development, *Miner. Metall. Proc.*, vol.24, no.4, pp.193-204.

Marsden J.O., Wilmot, J.C. and Hazen, N. (2007b) Medium-temperature pressure leaching of copper concentrates. Part II: Development of direct electrowinning and an acid-autogenous process, *Miner. Metall. Proc.*, vol.24, no.4, pp.205-217.

Stellenbosch University http://scholar.sun.ac.za

Marsden J.O., Wilmot, J.C. and Hazen, N. (2007c) Medium-temperature pressure leaching of copper concentrates. Part III: Commercial demonstration at Bagdad, Arizona, *Miner. Metall. Proc.*, vol.24, no.4, pp.218-225.

Marsden J.O., Wilmot, J.C. and Hazen, N. (2007c) Medium-temperature pressure leaching of copper concentrates. Part IV: Application at Morenci, Arizona, *Miner. Metall. Proc.*, vol.24, no.4, pp.226-236.

Marshall, W.L. and Jones, E.V. (1966) Second dissociation constant of sulfuric acid from 25 to 350°C. Evaluated from solubilities of calcium sulfate in sulfuric acid solutions, *J. Phys. Chem.*, vol.70, pp.4028-4040.

Marshall, W.L. and Slusher, R. (1965) Aqueous systems at high temperature. XV. Solubility and hydrolytic instability of magnesium sulfate in sulfuric acid-water and deuterosulfuric acid-deuterium oxide solutions, 200º to 350ºC, *J. Chem. Eng. Data*, vol.10, no.4, pp.353-358.

Marx, D., Tuckerman, M.E., Hutter, J. and Parrinello, M. (1999) The nature of the hydrated excess proton in water, *Nature*, vol.397, pp.601-604.

Matijevic, E., Sapieszko, R.S. and Melville, J.B. (1975) Ferric hydrous oxide sols: I. Monodispersed basic iron(III) sulfate particles, *J. Colloid Interface Sci.*, vol.50, pp.567-581.

Mathews, C.T. and Robins, R.G. (1972) The oxidation of aqueous ferrous sulphate solutions by molecular oxygen, *Proc. Aust. Inst. Min. Met.*, no.242, pp.47-56.

Matsushima, T (1959) The viscosity of liquid sulfur, *Science Reports of the Research Institutes, Tohoku Univ., Japan, Ser. A, Physics, Chemistry and Metallurgy*, pp.474-481.

McAndrew, R.T., Wang, S.S., and Brown, W.R. (1975) Precipitation of iron compounds from sulphuric acid leach solutions, *CIM Bull.*, pp.101-110.

McDonald, R.G. and Muir, D.M. (2007) Pressure oxidation leaching of chalcopyrite Part II: Comparison of medium temperature kinetics and products and effect of chloride ion, *Hydrometallurgy*, vol.86, pp.206-220.

McKay, D.R. and Halpern, J. (1958) A kinetic study of the oxidation of pyrite in aqueous suspension, *Trans. Metall. Soc. AIME*, vol.6, pp.301-309.

McMillan, R.S., MacKinnon, D.J. and Dutrizac, J.E. (1982) Anodic dissolution of n-type and p-type chalcopyrite, *J. Appl. Electrochem.*, vol.12, pp.743-757.

McNamara, J.H., Ahrens, W.A. and Franek, J.G. (1978) A hydrometallurgical process for the extraction of copper, *Proceedings of the 107th TMS-AIME Annual Meeting*, Denver, CO.

Mellor, J.W. (1935) *A Comprehensive Treatise on Inorganic and Theoretical Chemistry*, Vol.XIV, Fe (Part 3) – Cobalt, Longmans, Green and Co. Ltd., New York.

Méndez De Leo, L.P., Bianchi, H.L. and Fernández-Prini, R. (2005) Ion pair formation in copper sulfate solutions at high temperatures, *J. Chem. Thermodyn.*, vol.37, pp.499-511.

Mersmann, A. (2001) Quality of crystalline products, In: A. Mersmann (ed.), *Crystallization Technology Handbook*, Marcel Dekker Inc., New York, pp.285-322.

Mersmann, A. and Braun, B. (2001) Agglomeration, In: A. Mersmann (ed.), *Crystallization Technology Handbook*, Marcel Dekker Inc., New York, pp.235-284.

Stellenbosch University http://scholar.sun.ac.za

Mersmann, A., Heyer, C. and Eble, A. (2001a) Activated nucleation, In: A. Mersmann (ed.), *Crystallization Technology Handbook*, Marcel Dekker Inc., New York, pp.45-79.

Mersmann, A., Eble, A. and Heyer, C. (2001b) Crystal growth, In: A. Mersmann (ed.), *Crystallization Technology Handbook*, Marcel Dekker Inc., New York, pp.81-143.

Meyer, B. (1965) *Elemental Sulphur, Chemistry and Physics*, Interscience, New York.

Mikhlin, Y.L., Tomashevich, Y.V., Asanov, I.P., Okotrub, A.V., Varnek, V.A. and Vyalikh, D.V. (2004) Spectroscopic and electrochemical characterization of the surface layers of chalcopyrite ($CuFeS_2$) reacted in acidic solutions, *Appl. Surf. Sci.*, vol.225, pp.395-409.

Miki, H and Nicol, M. (2008) Synergism in the oxidation of covellite and pyrite by iron(III) and copper(II) ions in chloride solutions, In: C.A. Young, P.R. Taylor, C.G. Anderson and Y. Choi (eds.), *Hydrometallurgy 2008*, SME., Littleton, CO., pp.646-652.

Miladinović, J., Todorović, M. and Ninković, R. (2002) Osmotic coefficient of the $ZnSO_4$(aq) at T = 298.15 K, *J. Chem. Thermodyn.*, vol.34, pp.1769-1776.

Miller, J.D. (1986) An analysis of innovative process technology in hydrometallurgy, In: D.R. Gaskell, J.P. Hager, J.E. Hoffmann and P.J. Mackey (eds.), *Proceedings of the Reinhardt Schumann International Symposium on Innovative Technology and Reactor Design in Extractive Metallurgy*, TMS-AIME, New York, pp.3-24.

Mills, D.B., Bar, R. and Kirwan, D.J. (1987) Effect of solids on oxygen transfer in agitated three-phase systems, *AIChE J.*, vol.33, no.9, pp.1542-1549.

Mironov, V.E., Makashev, Yu.A., Mavrina, I.Ya. and Kryzhanovskii, M.M. (1970) Outer-sphere and inner-sphere complexes of cobalt(II), nickel(II), and copper(II), *Russ. J. Inorg. Chem.*, vol.15, no.5, pp.668-669.

Mishra, K.K. and Osseo-Asare, K. (1988) Aspects of the interfacial electrochemistry of semiconductor pyrite (FeS_2), *J. Electrochem. Soc.*, vol.135, no.10, pp.2502-2509.

Mishra, K.K. and Osseo-Asare, K. (1992) Electroreduction of Fe^{3+}, O_2, and $Fe(CN)_6^{3-}$ at the n-pyrite (FeS_2) surface, *J. Electrochem. Soc.*, vol.139, no.11, pp.3116-3120.

Monhemius, A.J. (1977) Precipitation diagrams for metal hydroxides, sulphides, arsenates and phosphates, *Trans. Inst. Min. Met.*, vol.86, pp.C202–C206.

Moses, C.O., Nordstrom, D.K., Herman, J.S. and Mills, A.L. (1987) Aqueous pyrite oxidation by dissolved oxygen and by ferric iron, *Geochim. Cosmochim. Acta*, vol.51, pp.1561-1571.

Moyes, J., Sammut, D. and Houllis, F. (2002) The Intec copper process: superior and sustainable metals production, *ALTA 2002, Copper-7 Forum*, ALTA Metallurgical Services, Melbourne.

Muir, D. (2008) The Parker copper process – a new approach ahead of its time, In: C.A. Young, P.R. Taylor, C.G. Anderson and Y. Choi (eds.), *Hydrometallurgy 2008*, SME, Littleton, CO, pp.685-694.

Munejiri, S., Shimojo, F. and Hoshino, K. (2000) Photo-induced structural change in liquid sulphur, *J. Phys.-Condens. Mat.*, vol.12, pp.7999-8008.

Munoz, P.B., Miller, J.D. and Wadsworth, M.E. (1979) Reaction mechanism for the acid ferric sulfate leaching of chalcopyrite, *Metall. Trans. B*, vol.10B, pp.149-158.

Stellenbosch University http://scholar.sun.ac.za

Mycroft, J.R., Bancroft, G.M., McIntyre, N.S., Lorimer, J.W. and Hill, I.R. (1990) Detection of sulphur and polysulphides on electrochemically oxidized pyrite surfaces by X-ray photoelectron spectroscopy and Raman spectroscopy, *J. Electroanal. Chem.*, vol.292, pp.139-152.

Nair, V.S.K. and Nancollas, G.H. (1958) Thermodynamics of ion association. Part IV. Magnesium and zinc sulphates, *J. Chem. Soc.*, pp.3706-3710.

Nair, V.S.K. and Nancollas, G.H. (1959) Thermodynamics of ion association. Part VI. Some transition-metal sulphates, *J. Chem. Soc.*, pp.3934-3939.

Nanthakumar, B., Arinaitwe, E. and Pawlek, M. (2010) Adsorption of sodium lignosulfonates on hematite, *Adsorption*, vol.16, pp.447-455.

Narita, E., Lawson, F. and Han, K.N. (1983) Solubility of oxygen in aqueous electrolyte solutions, *Hydrometallurgy*, vol.10, pp.21-37.

Nava, D. and González, I. (2006) Electrochemical characterization of chemical species formed during the electrochemical treatment of chalcopyrite in sulfuric acid, *Electrochim. Acta*, vol.51, pp.5295-5303.

Navrotsky, A., Mazeina, L. and Majzlan, J. (2008) Size-driven structural and thermodynamic complexity in iron oxides, *Science*, vol.319, pp.1635-1638.

Nicol, M.J. and Lázaro, I. (2003) The role of non-oxidative processes in the leaching of chalcopyrite, In: P.A. Riveros, D. Dixon, D.B. Dreisinger and J. Menacho (eds.), *Copper 2003*, MetSoc, Montreal, vol.VI (Book 1), pp.367-381.

Nicol, M.J. and Liu, J.Q. (2003) The effect of chloride ions on the oxidation of pyrite under pressure oxidation conditions, In: C.A. Young, A.M. Alfantazi, C.G. Anderson, D.B. Dreisinger, B. Harris and A. James (eds.), *Hydrometallurgy 2003*, TMS, Warrendale, PA, vol.1, pp.591-601.

Nicol, M.J. and Scott, P.D. (1979) The kinetics and mechanism of the non-oxidative dissolution of some iron sulphides in aqueous acidic solutions, *J. S. Afr. Inst. Min. Metall.*, pp.298-305.

Nicol, M.J., Needes, C.S.R. and Finkelstein, N.P. (1975) Electrochemical model for the leaching of uranium dioxide, In: A.R. Burkin (ed.), *Leaching and Reduction in Hydrometallurgy*, IMM, London, pp.1-11.

Nicolella, C., Van Loosdrecht, M.C.M., Van Der Lans, R.G.J.M. and Heijnen, J.J. (1998) Hydrodynamic characteristics and gas-liquid mass transfer in a biofilm airlift suspension reactor, *Biotechnol. BioEng.*, vol.60, no.5, pp.627-635.

Norskov, J.K., Rossmeisl, J., Logadóttir, A., Lindqvist, L., Kitchin, J.R., Bligaard, T. and Jónsson, H. (2004) Origin of the overpotential for oxygen reduction at a fuel-cell cathode, *J. Phys. Chem. B*, vol.108, pp.17886-17892.

Oba, Y. and Poulson, S.R. (2009) Oxygen isotope fractionation of dissolved oxygen during reduction by ferrous iron, *Geochim. Cosmochim. Acta*, vol.73, pp.13-24.

Oblad, A.E. (1975) *Simulation of Mine Water Neutralization*, M.Sc. Thesis, Univ. of Utah, Salt Lake City, UT.

Oguz, H., Brehm, A. and Deckwer, W.D. (1987) Gas/liquid mass-transfer in sparged agitated slurries, *Chem. Eng. Sci.*, vol.42, pp.1815-1822.

Stellenbosch University http://scholar.sun.ac.za

Oscarson, J.L., Izatt, R.M., Brown, P.R., Pawlak, Z., Gillespie, S.E. and Christensen, J.J. (1988) Thermodynamic quantities for the interaction of SO_4^{2-} with H^+ and Na^+ in aqueous solution from 150 to 320ºC, *J. Solution Chem.*, vol.17, no.9, pp.841-863.

Osseo-Asare, K. (1992) Semiconductor electrochemistry and hydrometallurgical dissolution process, *Hydrometallurgy*, vol.29, pp.61-90.

Owusu, G. (1993) *The Role of Surfactants in the Leaching of Zinc Sulphide Minerals at Temperature Above the Melting Point of Sulphur*, Ph.D. Dissertation, Department of Materials Engineering, Univ. of British Columbia, Vancouver.

Owusu, G. and Dreisinger D.B. (1996) Interfacial properties determinations in liquid sulfur, aqueous zinc sulfate and zinc sulfide systems, *Hydrometallurgy*, vol.43, pp.207-218.

Owusu, G., Peters, E. and Dreisinger, D.B. (1992) Surface tensions and contact angles due to lignin sulphonates in the system: liquid sulphur, aqueous zinc sulphate and zinc sulphide, *Can. J. Chem. Eng.*, vol.70, pp.173-180.

Owusu, G., Dreisinger, D.B., and Peters, E. (1995) Effect of surfactants on zinc and iron dissolution rates during oxidative leaching of sphalerite, *Hydrometallurgy*, vol.38, pp.315-324.

Oykova, T.G. and Balarew, C. (1974) Thermodynamic study of magnesium sulphate-ferrosulfate-water system at 25ºC, *Comptes`Rendus de l'Academie Bulgare des Sciences*, vol.27, pp.1211-1214.

Ozberk, E., Jankola, W.A., Vecchiarelli, M. and Krysa, B.D. Commercial operations of the Sherritt zinc pressure leach process, *Hydrometallurgy*, vol.39, pp.49-52.

Pabalan, R.T. and Pitzer, K.S. (1987) Thermodynamics of concentrated electrolyte mixtures and the prediction of mineral solubilities to high temperatures for mixtures in the system Na-K-Mg-Cl-SO_4-OH-H_2O, *Geochim. Cosmochim. Acta*, vol.51, pp.2429-2443.

Pabalan, R.T. and Pitzer, K.S. (1988) Heat capacity and other thermodynamic properties of Na_2SO_4(aq) in hydrothermal solutions and the solubilities of sodium sulfate minerals in the system Na-Cl-SO_4-OH-H_2O to 300°C, *Geochim. Cosmochim. Acta*, vol.52, pp.2393-2404.

Pabalan, R.T. and Pitzer, K.S. (1991) Mineral solubilities in electrolyte solutions, In: K.S. Pitzer (ed.), *Activity Coefficients in Electrolyte Solutions*, 2nd Edition, CRC Press, Boca Raton, pp.435-490.

Padilla, R., Pavez, P. and Ruiz, M.C. (2008) Kinetics of copper dissolution from sulfidized chalcopyrite at high temperatures in H_2SO_4-O_2, *Hydrometallurgy*, vol.91, pp.113-120.

Palencia Perez, I. and Dutrizac, G.E. (1991) The effect of the iron content of sphalerite on its rate of dissolution in ferric sulphate and ferric chloride media, *Hydrometallurgy*, vol.26, pp.211-232.

Papangelakis, V.G. (2004) High temperature aqueous chemistry, Short course notes, *Autoclave Chemistry and Engineering Conference*, CIM, Montreal, Ch.1, pp.1-58.

Papangelakis, V.G. and Demopoulos, G.P. (1990) Acid pressure oxidation of arsenopyrite: Part I, Reaction chemistry, *Can. Metall. Quart.*, vol.29, no.1, pp.1-12.

Papangelakis, V.G. and Demopoulos, G.P. (1991) Acid pressure oxidation of pyrite: Reaction kinetics, *Hydrometallurgy*, vol.26, pp.309-325.

Stellenbosch University http://scholar.sun.ac.za

Papangelakis, V.G. and Demopoulos, G.P. (1992a) Reactor models for a series of CSTRs with a gas-liquid-solid leaching system: Part I. Surface reaction control, *Metall. Trans. B*, vol.23A, pp.847-856.

Papangelakis, V.G. and Demopoulos, G.P. (1992b) Reactor models for a series of CSTRs with a gas-liquid-solid leaching system: Part II. Gas transfer control, *Metall. Trans. B*, vol.23A, pp.857-864.

Papangelakis, V.G. and Demopoulos, G.P. (1992c) Reactor models for a series of CSTRs with a gas-liquid-solid leaching system: Part III. Model application, *Metall. Trans. B*, vol.23A, pp.865-877.

Papangelakis, V.G., Berk, D. and Demopoulos, G.P. (1990) Mathematical modelling of an exothermic leaching reaction system: Pressure oxidation of wide size arsenopyrite particles, *Metall. Trans. B*, vol.2B, pp.827-837.

Papangelakis, V.G., Blakey, B.C. and Liao, H. (1994) Hematite solubility in sulphate process solutions. In: *Hydrometallurgy '94*, IMM & SCI, Chapman & Hall, London, pp.159-175.

Papangelakis, V.G., Georgiou, D. and Rubisov, D.H. (1996) Control of iron during the sulphuric acid pressure leaching of limonitic laterites, In: J.E. Dutrizac and G.B. Harris (eds.), *Iron Control and Disposal*, CIM, Montreal, Part 4, pp.263-274.

Parker, E.G. (1981) Oxidative pressure leaching of zinc concentrates, *CIM Bull.*, vol.74, pp.145-150.

Parker, A.J., Paul, R.L. and Power, G.P. (1981) Electrochemistry of the oxidative leaching of copper from chalcopyrite, *J. Electroanal. Chem.*, vol.118, pp.305-316.

Parker, A., Klauber, C., Kougianos, A., Watling, H.R. and Van Bronswijk, W. (2003) An X-ray photoelectron spectroscopy study of the mechanism of oxidative dissolution of chalcopyrite, *Hydrometallurgy*, vol.71, pp.265-276.

Pearce, C.I., Patrick, R.A.D., Vaughan, D.J., Henderson, C.M.B. and Van der Laan, G. (2006) Copper oxidation state in chalcopyrite: Mixed Cu d^9 and d^{10} characteristics, *Geochim. Cosmochim. Acta*, vol.70, pp.4635-4642.

Perdew, J.P. (1991) Electronic structure of solids, In: P. Ziesche and H. Eschrig (eds.), *Electronic Structure of Solids '91*, Akademie Verlag, Berlin, pp.11-20.

Perdew, J.P. and Wang, Y. (1992) Accurate and simple analytic representation of the electron-gas correlation energy, *Phys. Rev. B*, vol.45, pp.13244-13249.

Perrin, D.D. (1982) *Ionisation Constants of Inorganic Acids and Basis in Aqueous Solution*, 2nd Edition, IUPAC Chemical Data Series No.29, Pergamon Press, Oxford.

Peters, E. (1973) The physical chemistry of hydrometallurgy, In: D.J.I. Evans and R.S. Shoemaker (eds.), *International Symposium on Hydrometallurgy*, AIME, New York, pp.205-228.

Peters, E. (1976) Direct leaching of sulphides: chemistry and applications, *Metall. Trans. B*, vol.7B, pp.505-517.

Peters, E. (1984) Electrochemical mechanisms for decomposing sulphide minerals, In: P.E. Richardson, S. Srinivasan and R. Woods (eds.), *Electrochemistry in Mineral and Metal Processing*, ECS, Pennington, NJ, pp.343-361.

Stellenbosch University http://scholar.sun.ac.za

Peters, E. (1986) Leaching of sulfides, In: P. Somasundaran (ed.), *Advances in Mineral Processing*, SME, Littleton, CO, pp.445-462.

Peters, E. (1991) The mathematical modelling of leaching systems, *JOM*, vol.43, no.2, pp.20-26.

Peters, E. (1992) Hydrometallurgical process innovation, *Hydrometallurgy*, vol.29, pp.431-459.

Peters, E. and Loewan, F. (1968) Pressure leaching of copper minerals in perchloric acid solutions, *Pamphlet A68-33*, Metsoc of AIME, New York, pp.1-40.

Phala, N. (2008) Atmospheric dissolution of chalcopyrite, *Personal Communication*, Anglo American Technical Solutions (Research), Johannesburg.

Pham, A.N. and Waite, T.D. (2008) Oxygenation of Fe(II) in natural waters revisited: Kinetic modeling approaches, rate constant estimation and the importance of various reaction pathways, *Geochim. Cosmochim. Acta*, vol.72, pp.3616-3630.

Phillips, D.H. and Johnson, M.J. (1959) Oxygen transfer in agitated vessels, *Ind. Eng. Chem.*, vol.51, no.1, pp.83-88.

Phutela, R.C. and Pitzer, K.S. (1986) Heat capacity and other thermodynamic properties of aqueous magnesium sulfate to 473 K, *J. Phys. Chem.*, vol.90, pp.895-901.

Pitzer, K.S. (1972) Thermodynamic properties of aqueous solutions of bivalent sulphates, *J. Chem. Soc., Faraday Trans. (II)*, vol.68, pp.101-113.

Pitzer, K.S. (1991) Ion interaction approach: Theory and data, In: K.S. Pitzer (ed.), *Activity Coefficients in Electrolyte Solutions*, 2nd Edition, CRC Press, Boca Raton, pp.75-153.

Pitzer, K.S. and Mayorga, G. (1974) Thermodynamics of electrolytes. III. Activity and osmotic coefficients for 2-2 electrolytes, *J. Solution Chem.*, vol.3, no.7, pp.539-546.

Pitzer, K.S, Roy, R.N. and Silvester, L.F. (1977) Thermodynamics of electrolytes. 7. Sulfuric acid, *J. Am. Chem. Soc.*, vol.99, pp.4930-4936.

Posnjak, E. and Merwin, H.E. (1922) The system, Fe_2O_3-SO_3-H_2O, *J. Am. Chem. Soc.*, vol.44, no.2, pp.1965-1994.

Powell, H.K.J. (1973) Entropy titrations: A reassessment of data for the reaction of the sulphate ions with protons and with bivalent metal ions, *J. Chem. Soc., Dalton Trans. (III)*, pp.1947-1951.

Prue, J.E. (1966) Ion association and solvation, In: B.E. Conway and R.G. Barradas (eds.), *Chemical Physics of Ionic Solutions*, John Wiley & Sons Inc., New York, pp.163-173.

Pye, C.C. and Rudolph, W.W. (1998) An ab initio and Raman investigation of magnesium(II) hydration, *J. Phys. Chem. A*, vol.102, pp.9933-9943.

Pye, C.C. and Rudolph, W.W. (2001) An ab initio and Raman investigation of sulfate ion hydration, *J. Phys. Chem. A*, vol.105, pp.905-912.

Qiu, G., Xiao, Q., Hu, Y., Qin, W. and Wang, D. (2004) Theoretical study of the surface energy and electronic structure of pyrite FeS_2 (100) using a total-energy pseudopotential method, CASTEP, *J. Colloid Interf. Sci.*, vol.270, pp.127-132.

Stellenbosch University http://scholar.sun.ac.za

Rabadanov, M.Kh., Loshmanov, A.A. and Shaldin, Yu.V. (1997) Anharmonic thermal vibrations of atoms in crystals with sphalerite structure-GaP, ZnS, ZnSe, and ZnTe: High-temperature x-ray structure studies, *Kristallografiya*, vol.42, pp.649-659.

Rand, D.A.J. (1977) Oxygen reduction of sulphide minerals. Part III. Comparison of activities of various copper, iron, lead and nickel mineral electrodes, *J. Electroanal. Chem.*, vol.83, pp.19-32.

Randolph, A.D. and Larson, M.A. (1988) *Theory of Particulate Processes. Analysis and Techniques of Continuous Crystallisation*, 2nd Edition, Academic Press Inc., London.

Rao, N.R. (1940) Electrolyte dissociation in sulfuric acid, as studied by Raman effect, *Indian J. Phys.*, vol.XIV, part II, pp.143-151.

Rard, J.A. and Clegg, S.L. (1999) Isopiestic determination of the osmotic and activity coefficients of $\{zH_2SO_4 + (1-z)MgSO_4\}(aq)$ at T = 298.15 K. II. Results for z = (0.43040, 0.28758, and 0.14399) and analysis with Pitzer's model, *J. Chem. Thermodyn.*, vol.31, pp.399-429.

Rard, J.A. and Miller, D.G. (1981) Isopiestic determination of the osmotic coefficient of aqueous Na_2SO_4, $MgSO_4$, and Na_2SO_4-$MgSO_4$ at 25ºC, *J. Chem. Eng. Data*, vol.26, pp.33-38.

Rard, J.A. and Platford, R.F. (1991) Experimental methods: isopiestic, In: K.S. Pitzer (ed.), *Activity Coefficients in Electrolyte Solutions*, 2nd Edition, CRC Press, Boca Raton, pp.209-277.

Rard, J.A., Habenschuss, A. and Spedding, F.H. (1976) A review of the osmotic coefficients of aqueous H_2SO_4 at 25ºC, *J. Chem. Eng. Data*, vol.21, no.3, pp.374-379.

Rawle, A. (1995) The importance of particle size and zeta potential in the mining and minerals industry, *Chem. Technol.*, November/December, pp.31-35.

Reardon, E.J. and Beckie, R.D. (1987) Modelling chemical equilibria of acid mine-drainage: The $FeSO_4$-H_2SO_4-H_2O system, *Geochim. Cosmochim. Acta*, vol.51, no.9, pp.2355-2368.

Reedy, B.J., Beattie, J.K. and Lowson, R.T. (1991) A vibrational spectroscopic ^{18}O tracer study of pyrite oxidation, *Geochim. Cosmochim. Acta*, vol.55, pp.1609-1614.

Reid, M. and Papangelakis, V.G. (2006) New data on hematite solubility in sulphuric acid solutions from 130 to 270°C, In: J.E. Dutrizac and P.A. Riveros (eds.), *Iron Control Technologies*, CIM, Montreal, Part 7, pp.673-686.

Remsungnen, T. and Rode, B.M. (2004) Molecular dynamics simulation of the hydration of transition metal ions: The role of non-additive effects in the hydration shells of Fe^{2+} and Fe^{3+} ions, *Chem. Phys. Lett.*, vol.385, pp.491-497.

Rimstidt, J.D. and Vaughan, D.J. (2003) Pyrite oxidation: A state-of-the-art assessment of the reaction mechanism, *Geochim. Cosmochim. Acta*, vol.67, no.5, pp.873-880.

Riveros, P.A. and Dutrizac, J.E. (1997) The precipitation of hematite from ferric chloride media, *Hydrometallurgy*, vol.46, pp.85-104.

Roberts, W.L., Campbell, T.J. and Rapp, G.R. (1990) *Encyclopedia of Minerals*, 2nd Edition, Van Nostrand Reinhold, New York.

Robinson, R.A. and Stokes, R.H. (1959) *Electrolyte Solutions*, 2nd Edition, Academic Press, New York.

Stellenbosch University http://scholar.sun.ac.za

Rönnholm, M.R., Wärnå, J., Salmi, T., Turunen, I. and Luoma, M. (1999) Kinetics of oxidation of ferrous sulfate with molecular oxygen, *Chem. Eng. Sci.*, vol.54, pp.4223-4232.

Rubisov, D.H. and Papangelakis, V.G. (1999) The effect of acidity 'at temperature' on the morphology of precipitates and scale during sulphuric acid pressure leaching of laterites, In: G.B. Harris and S.J. Omelon (eds.), *Solid/Liquid Separation*, CIM, Montreal, pp.185-203.

Rubisov, D.H. and Papangelakis, V.G. (2000) Sulphuric acid pressure leaching of laterites – speciation and prediction of metal solubilities "at temperature", *Hydrometallurgy*, vol.58, pp.13-26.

Rudolph, W. (1996) Structure and dissociation of the hydrogen sulphate ion in aqueous solution over a broad temperature range: A Raman study, *Z. Phys. Chem.*, vol.194, pp.73-95.

Rudolph, W.W. (1998) Hydration and water-ligand replacement in aqueous cadmium(II) sulfate solution: A Raman and infrared study, *J. Chem. Soc., Faraday Trans.*, vol.94, no.4, pp.489-499.

Rudolph, W., Brooker, M.H. and Tremaine, P.R. (1997) Raman spectroscopic investigation of aqueous $FeSO_4$ in neutral and acidic solutions from 25ºC to 303ºC: Inner- and outer-sphere complexes, *J. Solution Chem.*, vol.26, no.8, pp.757-777.

Rudolph, W., Brooker, M.H. and Tremaine, P. (1999a) Raman- and infrared spectroscopic investigation of aqueous $ZnSO_4$ solutions from 8ºC to 165ºC: Inner- and outer-sphere complexes, *Z. Phys. Chem.*, vol.209, pp.181-207.

Rudolph, W., Brooker, M.H. and Tremaine, P.R. (1999b) Raman spectroscopy of aqueous $ZnSO_4$ solutions under hydrothermal conditions: Solubility, hydrolysis, and sulfate ion pairing, *J. Solution Chem.*, vol.28, no.5, pp.621-630.

Rudolph, W.W., Irmer, G. and Hefter, G.T. (2003) Raman spectroscopic investigation of speciation in $MgSO_4$(aq), *Phys. Chem. Chem. Phys.*, vol.5, pp.5253-5261.

Ruether, J.A. (1979) Reaction in a cascade of continuous stirred tank reactors of particles following the shrinking core model, *Can. J. Chem. Eng.*, vol.57, pp.242-245.

Ruiz, M.C., Abarzúa, E. and Padilla, R. (2007a) Oxygen pressure leaching of white metal, *Hydrometallurgy*, vol.86, pp.131-139.

Ruiz, M.C., Zapata, J. and Padilla, R. (2007b) Effect of variables on the quality of hematite precipitated from sulfate solutions, *Hydrometallurgy*, vol.89, pp.32-39.

Ruiz, M.C., Gallardo, E. and Padilla, R. (2009) Copper extraction from white metal by pressure leaching in H_2SO_4-$FeSO_4$-O_2, *Hydrometallurgy*, vol.100, pp.50-55.

Rull, F., Balarew, Ch., Alvarez, J.L., Sobron, F. and Rodriguez, A. (1994) Raman spectroscopic study of ion association in aqueous magnesium sulphate solutions, *J. Raman Spectrosc.*, vol.25, pp.933-941.

Rumyantsev, A.V., Hagemann, S. and Moog, H.C. (2004) Isopiestic investigation of the systems $Fe_2(SO_4)_3$-H_2SO_4-H_2O, $FeCl_3$-H_2O, and Fe(III)-(Na, K, Mg, Ca)Cl_n-H_2O at 298.15 K, *Z. Phys. Chem.*, vol.218, pp.1089-1127.

Safi, M. and Dinham, P. (2009) Chalcopyrite leaching, *Personal Communication*, Anglo American Technical Solutions (Research), Johannesburg.

Stellenbosch University http://scholar.sun.ac.za

Sánchez, O., Michaud, S., Escudié, R., Delgenès, J-P. and Bernet, N. (2005) Liquid mixing and gas-liquid mass transfer in a three-phase inverse turbulent bed reactor, *Chem. Eng. J.*, vol.114, pp.1-7.

Sasaki, K., Ootsuka, K. and Tozawa, K. (1993) Equilibrium diagram, in the system Fe_2O_3-SO_3-H_2O, at elevated temperatures – Hydrometallurgical studies on hydrolysis of ferric sulphate solutions at elevated temperatures, *Sigen-to-Sozai*, vol.109, pp.871-877.

Sasaki, K., Tsunekawa, M., Hasebe, K. and Konno, H. (1995) Effect of anionic ligands on the reactivity of pyrite with Fe(III) ions in acid solutions, *Colloid. Surface A*, vol.101, pp.39-49.

Sasaki, N., Murakami, Y., Shindo, D. and Sugimoto, T. (1999) Computer simulation for the growth process of peanut-type hematite particles, *J. Colloid Interface Sci.*, vol.213, pp.121-125.

Schippers, A. and Sand, W. (1999) Bacterial leaching of metal sulfides proceeds by two indirect mechanisms via thiosulfate or via polysulfides and sulfur, *Appl. Environ Microb.*, vol.65, no.1, pp.319-321.

Schumpe, A., Quicker, G. and Deckwer, W.-D. (1982) Gas solubilities in microbial culture media, *Adv. Biochem. Eng*., vol.24, pp.1-38.

Schweitzer, F.W. and Livingstone, R. (1982) Duval's Clear hydrometallurgical process, In: P.D. Parker (ed.), *Chloride Electrometallurgy*, AIME, New York, pp.221-228.

Scott, P.D. and Nicol, M.J. (1977) The kinetics and mechanisms of the non-oxidative dissolution of metal sulphides, In: J.O'M Bockris, D.A.J. Rand and B.J. Welsh (eds.), *Trends in Electrochemistry*, Plenum Press, New York.

Senanayake, G. (2009) A review of chloride assisted copper sulfide leaching by oxygenated sulfuric acid and mechanistic considerations, *Hydrometallurgy*, vol.98, pp.21-32.

Senanayake, G. and Muir, D.M. (1988) Speciation and reduction potentials of metal ions in concentrated chloride and sulfate solutions relevant to processing base metal sulfides, *Metall. Trans. B*, vol.19B, pp.37-45.

Seneviratne, D.S., Papangelakis, V.G., Zhou, X.Y. and Lvov, S.N. (2003) Potentiometric pH measurements in acidic sulphate solutions at 250ºC relevant to pressure leaching, *Hydrometallurgy*, vol.68, pp.131-139.

Sepulveda, J.E. and Herbst, J.A. (1993) A population balance approach to the modelling of multistage continuous leaching systems, In: V.G. Papangelakis and G.P. Demopoulos (eds.), *Proceedings of the International Symposium on Modelling, Simulation and Control in Hydrometallurgical Processes*, CIM, Montreal, pp.41-65.

Sequeira, C.A.C., Santos, D.M.F., Chen, Y. and Anastassakis, G. (2008), Chemical metathesis of chalcopyrite in acidic solutions, *Hydrometallurgy*, vol.92, pp.135-140.

Shackleton, N.J. (2009) Chalcopyrite leaching – Surface analysis results, *Personal Communication*, Anglo American Technical Solutions (Research), Johannesburg.

Shang, Y. and Van Weert, G. (1993) Iron control in nitrate hydrometallurgy by autoclave hydrolysis of iron(III) nitrate, *Hydrometallurgy*, vol.33, pp.273-290.

Sharma, M.M. and Danckwerts, P.V. (1970) Chemical methods of measuring interfacial area and mass-transfer coefficients in two-fluid systems, *Brit. Chem. Eng.*, vol.15, pp.522-528.

Stellenbosch University http://scholar.sun.ac.za

Shi, Z., Zhang, J., Liu, Z.-S., Wang, H. and Wilkinson, D.P. (2006) Current status of ab initio quantum chemistry study for oxygen electroreduction, on fuel cell catalysts, *Electrochim. Acta*, vol.51, pp.1905-1916.

Shin, S.K., Kim, K.-K., and Kim, K. (1995) Oxygen transfer in pressurized batch fermentor, *J. Ind. Eng. Chem.*, vol.1, no.1, pp.6-10.

Shock, E.L. and Helgeson, H.C. (1988) Calculation of the thermodynamic and transport properties of aqueous species at high pressures and temperatures: Correlation algorithms for ionic species and equation of state predictions to 5 kb and 1000ºC, *Geochim. Cosmochim. Acta*, vol.52, pp.2009-2036.

Sidik R.A. and Anderson A.B. (2002) Density functional theory study of O_2 electroreduction when bonded to a Pt dual site, *J. Electroanal. Chem.*, vol.528, no.1, pp.69-76.

Sillen, L.G. and Martel, A.E. (1964) *Stability Constants of Metal-ion Complexes*, Special Publication No.17, The Chemical Society, Metcalfe & Cooper Ltd., London.

Sillen, L.G. and Martell, A.E. (1971) *Stability Constants of Metal-ion Complexes*, Special Publication No.25, The Chemical Society, Alden & Mowbray Ltd., Oxford.

Smith, R.M. and Martell, A.E. (1989) *Critical Stability Constants*, vol.6, Plenum Press, New York.

Smith, J.M. and Van Ness, H.C. (1987) *Introduction to Chemical Engineering Thermodynamics*, International Edition, McGraw-Hill, New York.

Snipes, H.P., Manly, C. and Ensor, D.D. (1975) Heats of dilution of aqueous electrolytes, *J. Chem. Eng. Data*, vol.20, no.3, pp.287-291.

Sohn H.J. and Wadsworth, M.E. (1980) Reduction of chalcopyrite with SO_2 in the presence of cupric ions, *JOM*, vol.32, pp.18-22.

Söhnel, O. and Garside, J. (1992) *Precipitation. Basic Principles and Industrial Applications*, Butterworth-Heinemann Ltd., Oxford.

Souza, A.D., Pina, P.S., Leão, V.A., Silva, C.A. and Siqueira, P.F. (2007) The leaching kinetics of a zinc sulphide concentrate in acid ferric sulphate, *Hydrometallurgy*, vol.89, pp.72-81.

Stenstrom, M.K. and Gilbert, R.G. (1981) Effects of alpha, beta and theta factor upon the design, specification and operation of aeration systems, *Water Res.*, vol.15, pp.643-654.

Sterzel, M. and Autschbach, J. (2006) Toward an accurate determination of ^{195}Pt chemical shifts by density functional computations, *Inorg. Chem.*, vol.45, no.8, pp.3316-3324.

Steudel, R. (2003) Liquid sulfur, *Top. Curr. Chem.*, vol.230, pp.81-116.

Steyl, J.D.T. (2004) The effect of surfactants on the behaviour of sulphur in the oxidation of chalcopyrite at medium temperature, In: M.J. Collins and V.G. Papangelakis (eds.), *Pressure Hydrometallurgy 2004*, CIM, Montreal, pp.101-117.

Stipp, S.L. (1990) Speciation in the Fe(II)-Fe(III)-SO_4-H_2O system at 25°C and low pH: Sensitivity of an equilibrium model to uncertainties, *Environ. Sci. Technol.*, vol.24, pp.699-706.

Stoffregen, R.E., Alpers, C.N. and Jambor, J.L. (2000) Alunite-jarosite crystallography, thermodynamics, and geochronology, *Rev. Mineral Geochem.*, vol.40, pp.454-479.

Stellenbosch University http://scholar.sun.ac.za

Stokes, R.H. (1991) Thermodynamics of solutions, In: K.S. Pitzer (ed.), *Activity Coefficients in Electrolyte Solutions*, 2nd Edition, CRC Press, Boca Raton, pp.1-28.

Stumm W. (1992) *Chemistry of the Solid-Water Interface*, John Wiley & Sons Inc., New York.

Sugimoto, T. and Matijevic, E. (1980) Formation of uniform spherical magnetite particles by crystallization from ferrous hydroxide gels, *J. Colloid Interface Sci.*, vol.74, no.1, pp.227-243.

Sugimoto, T. and Wang, Y. (1998) Mechanism of the shape and structure control of monodispersed α-Fe_2O_3 particles by sulfate ions, *J. Colloid Interface Sci.*, vol.207, pp.137-149.

Sugimoto, T., Wang, Y., Itoh, H. and Muramatsu, A. (1998) Systematic control of size, shape and internal structure of monodisperse α-Fe_2O_3 particles, *Colloids Surf A*, vol.134, pp.265-279.

Sweeton, F.H., Mesmer, R.E. and Baes, C.F. (1974) Acidity measurements at elevated temperatures. VII. Dissociation of water, *J. Solution Chem.*, vol.3, no.3, pp.191-214.

Sylva, R.N. (1972) The hydrolysis of iron(III), *Rev. Pure Appl. Chem.*, vol.22, pp.115-132.

Tamura, H., Gato, K. and Nagayama, M. (1976) The effect of ferric hydroxide on the oxygenation of ferrous ions in neutral solutions, *Corros. Sci.*, vol.16, no.4, pp.197-207.

Tartar, H.V. and Ness, A.T. (1941) A thermodynamic study of the system zinc sulfate-sulfuric acid-water at 25ºC, *J. Am. Chem. Soc.*, vol.63, pp.28-36.

Taube, H. (1952) Rates and mechanisms of substitution in inorganic complexes in solution, *Chem. Rev.*, vol.50, pp.69–126.

Teixeira, L.A. and Tavares, L.Y. (1986) Precipitation of jarosite from manganese sulphate solutions, In: J.E. Dutrizac and A.J. Monhemius (eds.), *Iron Control in Hydrometallurgy*, CIM, Ellis Horwood Ltd., Chichester, pp.431-453.

Thomas, J.M. and Thomas, W.J. (1997) *Principles and Practice of Heterogeneous Catalysis*, VCH Verlagsgesellschaft, Weinhein.

Thomas, J.E., Jones, C.F., Skinner, W.M. and Smart, R.St.C. (1998) The role of sulfur species in the inhibition of pyrrhotite dissolution in acid conditions, *Geochim. Cosmochim. Acta*, vol.62, no.9, pp.1555-1565.

Thomas, J.E., Skinner, W.M. and Smart, RSt.C. (2001) A mechanism to explain sudden changes in rates and products for pyrrhotite dissolution in acid solution, *Geochim. Cosmochim. Acta*, vol.65, no.1, pp.1-12.

Thomas, J.E., Skinner, W.M. and Smart, R.St.C. (2003) A comparison of the dissolution behaviour of triolite with other iron(II) sulfide; implications of structure, *Geochim. Cosmochim. Acta*, vol.67, no.5, pp.831-843.

Todd, E.C., Sherman, D.M. and Purton, J.A. (2003) Surface oxidation of pyrite under ambient atmospheric and aqueous (pH=2 to 10) conditions: Electronic structure and mineralogy from X-ray absorption spectroscopy, *Geochim. Cosmochim. Acta*, vol.67, no.5, pp.881-893.

Tong, L. (2009) *Sulfur Dispersing Agents for Nickel Sulfide Leaching Above the Melting Point of Sulfur*, Ph.D. Dissertation, Department of Materials Engineering, Univ. of British Columbia, Vancouver.

Stellenbosch University http://scholar.sun.ac.za

Tosawa, K. and Sasaki, K. (1986) Effect of coexisting sulphates on precipitation of ferric oxide from ferric sulphate solutions at elevated temperatures, In: J.E. Dutrizac and A.J. Monhemius (eds.), *Iron Control in Hydrometallurgy*, CIM, Ellis Horwood Ltd., Chichester, pp.454-476.

Trasatti, S. (1986) The absolute electrode potential: An explanatory note (recommendations 1986), International Union of Pure and Applied Chemistry, *Pure Appl. Chem.*, vol.58, no.7, pp.955-966.

Tremaine, P.R., Trevani, L.N. and Rudolph, W.W. (2004) Acid-base ionization and metal complexation under hydrothermal conditions by UV-visible and Raman spectroscopy, In: M.J. Collins and V.G. Papangelakis (eds.), *Pressure Hydrometallurgy 2004*, CIM, Montreal, pp.545-560.

Tributsch, H. and Bennet, J.C. (1981) Semiconductor-electrochemical aspects of bacterial leaching. I. Oxidation of metal sulphides with large energy gaps, *J. Chem. Tech. Biotechnol.*, vol.31, pp.565-557.

Tributsch, H. and Gerischer, H. (1976) The oxidation and self-heating of metal sulfides as an electrochemical corrosion phenomenon, *J. Appl. Chem. Biotechnol.*, vol.26, pp.747-761.

Tromans, D. (1998a) Temperature and pressure dependent solubility of oxygen in water: a thermodynamic analysis, *Hydrometallurgy*, vol.50, pp.327-342.

Tromans, D. (1998b) Oxygen solubility modelling in inorganic solutions: concentration, temperature and pressure effects, *Hydrometallurgy*, vol.50, pp.279-296.

Tsuda, M and Kasai, H. (2007) Proton transfer to oxygen adsorbed on Pt: How to initiate oxygen reduction reaction, *J. Phys. Soc. Jpn.*, vol.76, no.2, 4pp.

Ueda, H., Nohara, M., Kitazawa, K. and Takagi, H. (2002) Copper pyrites CuS_2 and $CuSe_2$ as anion conductors, *Phys. Rev. B*, vol.65, pp.155104-(1-5).

Umetsu, Y., Tozawa, K. and Sasaki, K. (1977) The hydrolysis of ferric sulphate solution at elevated temperatures, *Trans. Metall. Soc.*, CIM, Montreal, pp.111-117.

Van Der Laan, G., Pattrick, R.A.D, Henderson, C.M.B. and Vaughan, D.J. (1992) Oxidation state variations in copper minerals studied with Cu 2*p* X-ray absorption spectroscopy, *J. Phys. Chem. Solids*, vol.53, no.9, pp.1185-1190.

Van Der Woude, J.H.A., Verhees, P. and De Bruyn, P.L. (1983) Formation of colloidal dispersions from supersaturated iron(III) nitrate solution. II. Kinetics of growth at elevated temperatures, *Corros. Sci.*, vol.8, no.4, pp.79-92.

Van't Riet, K. (1979) Review of measuring methods and results in nonviscous gas-liquid mass transfer in stirred vessels, *Ind. Eng. Chem., Process Des. Dev.*, vol.18, no.3, pp.357-364.

Vchirawongkwin, V., Rode, B.M. and Persson, I. (2007) Structure and dynamics of sulfate ion in aqueous solution: An *ab initio* QMCF MD simulation and large angle X-ray scattering study, *J. Phys. Chem. B*, vol.111, pp.4150-4155.

Velázquez-Rivera, M., Palmer, D.A. and Kettler, R.M. (2006) Isopiestic measurement of the osmotic coefficients of aqueous $\{XH_2SO_4 + (1\text{-}X)Fe_2(SO_4)_3\}$ solutions at 298.15 to 323.15 K, *J. Solution Chem.*, vol.35, pp.1699-1730.

Veltman, H., James, G., Mould, J. and Kawulka, P. (1977) *Two-stage Pressure Leaching Process for Zinc and Iron Bearing Mineral Sulphides*, US Patent 4,004,991.

Stellenbosch University http://scholar.sun.ac.za

Verbaan, B. and Crundwell, F.K. (1986) An electrochemical model for the leaching of a sphalerite concentrate, *Hydrometallurgy*, vol.16, pp.345-359.

Verhulst, D. (1974) *The Kinetics of Oxidation of Hydrogen Sulfide and Zinc Sulfide by Ferric Iron in Sulfuric Acid Solution*, Ph.D. Dissertation, School of Engineering and Applied Science, Columbia Univ., New York.

Viramontes-Gamboa, G., Rivera-Vásquez, B.F. and Dixon, D.G. (2007) The active-passive behavior of chalcopyrite. Comparative study between electrochemical and leaching responses, *J. Electrochem. Soc.*, vol.154, no.6, pp.C299-C311.

Vizsolyi, A., Veltman, H., Warren, I.H. and Mackiw, V.N. (1967) Copper and elemental sulphur from chalcopyrite by pressure leaching, *JOM*, vol.19, no.10, pp.52-58.

Vogel, A.I. (1961) *Quantitative Inorganic Analysis*, 3^{d} Edition, Longmans, Green and Co. Ltd., London.

Vosko, S. J., Wilk, L. and Nusair, M. (1980). Accurate spin-dependent electron liquid correlation energies for local spin density calculations: A critical analysis, *Can. J. Phys.*, vol.58, pp.1200-1211.

Vračar, R.Ž. and Cerović, K.P. (1997) Kinetics of oxidation of Fe(II) ions by gaseous oxygen at high temperatures in an autoclave, *Hydrometallurgy*, vol.44, pp.113-124.

Wadsworth, M.E. and Miller, J.D. (1979) Hydrometallurgical processes, In: H.Y. Sohn and M.E. Wadsworth (eds), *Rate Processes of Extractive Metallurgy*, Plenum Press, New York, pp.133-244.

Wagman, D.D., Evans, W.H., Parker, V.B., Schumm, R.H., Halow, I., Bailey, S.M., Churney, K.L. and Nuttall, R.L. (1982) The NBS tables of chemical thermodynamic properties, selected values for inorganic and C1 and C2 organic substances in SI units, *J. Phys. Chem. Ref. Data*, vol.11, Supplement no.2, Published by ACS & AIP for the National Bureau of Standards.

Wagner, C.W. and Traud, W. (1938) Über die deutung von korrosionsvorgängen durch überlagerung von electrochemischen teilvorgängen und über die potentialbildung an mischelektroden, *Z. Electrochem.*, vol.44, no.7, pp.391-402.

Walrafen, G.E., Yang, W.-H., Chu, Y.C. and Hokmabadi, M.S. (2000) Structures of concentrated sulfuric acid determined form density, conductivity, viscosity and Raman spectroscopic data, *J. Solution Chem.*, vol.29, no.10, pp.905-936.

Walrafen, G.E., Yang, W.-H. and Chu, Y.C. (2002) High-temperature Raman investigation of concentrated sulfuric acid mixtures: Measurement of H-bond ΔH values between H_3O^+ or $H_5O_2^+$ and HSO_4^-, *J. Phys. Chem. A*, vol.106, pp.10162-10173.

Walter-Lévy, L. and Quéméneur, E. (1964) Sur l'hydrolyse du sulfate ferrique à 100°, *C.R. Acad. Sc. Paris*, vol.258, pp.3028-3031.

Wang, X.-B., Nicholas, J.B. and Wang, L.-S. (2000). Electronic instability of isolated SO_4^{2-} and its solvation stabilization, *J. Chem. Phys.*, vol.113, no.24, pp.10837-10840.

Wang, P., Anderko, A., Springer, R.D. and Young, R.D. (2006) Modeling phase equilibria and speciation in mixed-solvent electrolyte systems: II. Liquid-liquid equilibria and properties of associating electrolyte solutions, *J. Mol. Liq.*, vol.125, pp.37-44.

Stellenbosch University http://scholar.sun.ac.za

Wardman, P. (1989) Reduction potentials of one-electron couples involving free radicals in aqueous solution, *J. Phys. Chem. Ref. Data*, vol.18, no.14, pp.1637-1755.

Warren, I.H. (1956) The generation of sulphuric acid from pyrite by pressure leaching, *Austr. J. Appl. Sci.*, vol.7, pp.346-358.

Warren, I.H. (1958) A study of the acid pressure leaching of chalcopyrite, chalcocite and covellite, *Austr. J. Appl. Sci.*, vol.9, pp.36-51.

Warren, G.W. and Wadsworth, M.E. (1980) Hydrometallurgical processing of fine mineral particles, In: P. Somasundaran (ed.), *Fine Particles Processing*, AIME, New York, pp.1390-1417.

Warren, G.W., Wadsworth, M.E. and El-Raghy, S.M. (1982) Passive and transpassive anodic behaviour of chalcopyrite in acid solutions, *Metall. Trans. B*, vol.13B, pp.571-579.

Watanabe, H., Gutleben, C.D. and Seto, J. (1994) Sulfate ions on the surface of maghemite and hematite, *Solid State Ionics*, vol.69, pp.29-35.

Weisenberger, S. and Schumpe, A. (1996) Estimation of gas solubilities in salt solutions at temperatures from 273 K to 363 K, *AIChE J.*, vol.42, no.1, pp.298-300.

Weisener, C.G., Smart, R.St.C. and Gerson, A.R. (2003) Kinetics and mechanisms of the leaching of low Fe sphalerite, *Geochim. Cosmochim. Acta*, vol.67, no.5, pp.823-830.

Weiss, J. (1935) Electron transition process in the mechanism of oxidation- and reduction reactions in solutions, *Naturwissenschaften*, vol.23, pp.64-69.

Weiss, J (1953) The auto-oxidation of ferrous ions in aqueous solutions, *Experientia*, vol.9, pp.61-62.

Weller, S. (1956) Analysis of kinetic data for heterogeneous reactions, *AIChE J.*, vol.2, no.1, pp.59-61.

Xia, G-X., Li, J.-J., Shi, H-J., Yu, K-N. and Cao, C-L. (1987) Preliminary studies on the physical chemistry of the acid pressure leaching of ZnS concentrates, In: G.A. Davies (ed.), *Separation Processes in Hydrometallurgy*, Ellis Horwood Ltd., Chichester, pp.125-132.

Xiang, T., Johnston, K.P., Wofford, W.T. and Gloyna, E.F. (1996) Spectroscopic measurments of pH in aqueous sulfuric acid and ammonia from sub- to supercritical conditions, *Ind. Eng. Chem. Res.*, vol.35, no.12, pp.4788-4795.

Yatsimirskii, K.B. and Vasil'ev, V.P. (1960) *Instability Constants of Complex Compounds* (Translated from Russian), Consultants Bureau, New York.

Yoshida, F. and Arakawa, S.-I. (1968) Pressure dependence of liquid mass-transfer coefficients, *AIChE J.*, vol.14, pp.962-963.

Young, T.F. and Blatz, L.A. (1949) The variations of the properties of electrolyte solution with degrees of dissociation, *Chem. Rev.*, vol.44, no.1, pp.93-115.

Young, T.F., Maranville, L.F. and Smith, H.M. (1959) Raman spectral investigations of ionic equilibria in solutions of strong electrolytes, In: W.J. Hamer (ed), *The Structure of Electrolyte Solutions*, John Wiley & Sons Inc., New York, pp.35-63.

Stellenbosch University http://scholar.sun.ac.za

Yu, P.H., Hansen, C.K. and Wadsworth, M.E. (1972) A kinetic study of the leaching of chalcopyrite at elevated temperatures, In: D.I.J. Evans and R. Shoemaker (eds.), *Proceedings of the International Symposium on Hydrometallurgy*, AIME, New York, pp.375-402.

Yin, Q., Kelsall, G.H., Vaughan, D.J. and England, K.E.R. (1995) Atmospheric and electrochemical oxidation of the surface of chalcopyrite ($CuFeS_2$), *Geochim. Cosmochim. Acta*, vol.59, no.6, pp.1091-1100.

Zemaitis, J.F., Clark, D.M., Rafal, M. and Scrivner, N.C. (1986) *Handbook of Aqueous Electrolytic Thermodynamics*, Design Institute for Physical Property Data (DIPPR), AIChE Publications, New York.

Zerella, P.J., Randolph, A.D. and Headington, T.A. (1983) Kinetics of the jarosite/hematite crystal transition in a size classified crystalliser, In: K. Osseo-Asare and J.D. Miller (eds.), *Hydrometallurgy - Research, Development and Plant Practice*, SME-AIME, Warrendale, PA, pp.807-821.

Zhang, X., Zhang, Y. and Li, Q. (2002) Ab initio studies on the chain of contact ion pairs of magnesium sulfate in supersaturated state of aqueous solution, *J. Mol. Struc.-Theochem.*, vol.594, pp.19-30.

Ziegler, T. and Autschbach, J. (2005) Theoretical methods of potential use for studies of inorganic reaction mechanisms, *Chem. Rev.*, vol.105, pp.2695-2722.

Zuidervaart, E., Reuter, M.A., Heerema, R.H., Van der Lans, R.G.J.M. and Derksen, J.J. (2000) Effect of dissolved metal sulphates on gas-liquid oxygen transfer in agitated quartz and pyrite slurries, *Miner. Eng.*, vol.13, no.14-15, pp.1555-1564.

Zwietering, T.N. (1959) The degree of mixing in continuous flow systems, *Chem. Eng. Sci.*, vol.11, pp.1-15.

SOFTWARE REFERENCES

Materials Studio (*MS*, 2008) Accelrys Software Inc., San Diego, Release 4.2.

HSC Chemistry (*HSC*, 2006) Chemical Reaction and Equilibrium Software with Thermochemical Database, Outokumpu Research, Pori, Finland, Release 6.0.

Inorganic Crystal Structure Database (*ICSD*, 2008) Fachinformationzetrum, Karlruhe, Germany and US Department of Commerce, Release 1.4.4.

Matlab (2011), The MathWorks Inc., Natick, MA, Release 2011b.

OLI Systems Inc. (*OLI*, 2007) Morris Plains, MJ, Stream Analyzer 2.0, Release 2.0.46.

Stellenbosch University http://scholar.sun.ac.za

ABBREVIATIONS OF INSTITUTIONS

American Chemical Society	ACS
American Institute of Mining, Metallurgical and Petroleum Engineers	AIME
American Institute of Physics	AIP
Anglo American Technical Solutions (Research)	ATS
Australasian Institute of Mining and Metallurgy	AusIMM
Canadian Institute of Mining, Metallurgy and Petroleum	CIM
Chilean Institute of Mining Engineers	CIME
Electrochemical Society	ECS
Extraction and Processing Division	EPD
Engineers Society of Western Pennsylvania	ESWP
Institution of Mining and Metallurgy (UK)	IMM
Metallurgical Society of the Canadian Institute of Mining, Metallurgy and Petroleum	MetSoc
Mining and Metallurgical Institute of Japan	MMIJ
National Bureau of Standards	NBS
Report of Investigations (US Bureau of Mines)	RI
Southern African Institute of Mining and Metallurgy	SAIMM
Society of Chemical Industry (UK)	SCI
Society for Mining, Metallurgy and Exploration	SME
The Minerals, Metals and Materials Society	TMS
University of Cape Town	UCT
University of the Witwatersrand	WITS

Stellenbosch University http://scholar.sun.ac.za

APPENDIX A. CONSTANTS, EMPIRICAL CORRELATIONS AND THERMODYNAMIC RELATIONSHIPS AND DATA

This appendix summarises the fundamental constants, empirical correlations and thermodynamic relationships and data used in this study. All the relevant references are included.

A.1 Constants

The following table lists the values of the fundamental constants used in this study.

Table A.1
Fundamental constants (Atkins & De Paula, 2006).

Property	Symbol	Value	Units
Avogadro's constant	N_a	6.0221×10^{23}	1/mol
Boltzmann constant	k_b	1.38065×10^{-23}	J/K
Faraday constant	F	9.6485×10^{4}	C/mol
Gravitational acceleration	g	[a] 9.7904	m/sec^2
Gas constant	R_g	8.3145	J/K.mol
Planck's constant	h	6.6261×10^{-34}	J.sec
Vacuum permittivity	ε_o	8.8542×10^{-12}	$C^2/J.m$

[a] Value at 26° latitude (Atkins, 1986).

The atmospheric pressure at the location of this study (Crown Mines, South Africa) was measured with a barometer. The measured value varied with the humidity, but was generally found to lie between the values of 633 and 643 Torr. This translates into an average value of 85.06 kPa for P_{atm}.

The standard atomic weights of the elements relevant to this study are summarised in Table A.2.

Table A.2
Standard atomic weights (CRC Handbook: Lide, 2004).

Element	g/mol	Element	g/mol	Element	g/mol
H	1.00795	Cu	63.5463	Mg	24.3050
O	15.9994	Zn	[a] 65.380	Ca	[a] 40.080
S	[a] 32.060	Fe	[a] 55.847	Si	28.0855
C	12.0108	–	–	Al	26.9815
N	14.0067	–	–	–	–

[a] Values adopted from *HSC* (2006), *i.e.*, to be consistent with thermodynamic data from the same source.

Stellenbosch University http://scholar.sun.ac.za

A.2 Thermodynamic equilibrium constants

A.2.1 Dickson correlation for the bisulfate ion formation reaction

Dickson *et al.* (1990) measured (potentiometrically) the dissociation constant of bisulfate ion (HSO_4^-) in sodium chloride background solution. The following correlation of the thermodynamic association constant (molality scale & valid up to 250°C) for the bisulfate ion formation reaction (K^o_B) is incorporated into the phenomenological model (Sect. 2.3.3):

$$log\ K_1^o = -\left(p_1 + \frac{p_2}{T} + p_3 \cdot ln\,T + p_4 T + p_5 T^2 \right) \qquad \text{A.1}$$

Table A.3
Parameter values of Equation A.1 (Dickson *et al.*, 1990).

p_1	562.7097	p_2	-13273.75	p_3	-102.5154	p_4	0.2477538	p_5	-1.117033×10^{-4}

A.2.2 Experimental data (literature) for the bisulfate ion formation reaction

Table A.4 summarises the data obtained from a detailed review of the literature, utilising over fifteen databases. A discussion of the different methods used and the individual merits of these constant are omitted from this table. For example, various researchers have in the past used the thermodynamic values of Marshall and Jones (1966). They determined the equilibrium constant from solubility measurements of calcium sulfate in sulfuric acid solution (< 1 mol/kg) from 25 to 350°C. However, their results have been criticised by various authors (*e.g.*, Shock & Helgeson, 1988; Dickson *et al.*, 1990) because they ignored the presence of the neutral aqueous species, $CaSO_4°$ and $H_2SO_4°$, which may exist in significant amounts, especially at high temperatures.

Table A.4
Thermodynamic literature data for the bisulfate ion formation reaction ($K°_B$).

Temp. °C	$K°_B$	$\Delta G°$ kJ/mol	$\Delta H°$ kJ/mol	$\Delta S°$ J/mol.K	$\Delta C_p°$ J/mol.K	Reference
18	79.4		7.45			Sillen & Martell (1964)
18	81.3					Sillen & Martell (1964)
20	83.2					Sillen & Martell (1971)
20	87.1					Hogfeldt (1982)
20	100					Sillen & Martell (1964)
25	13.2					Yatsimirskii & Vasil'ev (1960)
25	69.2					Hogfeldt (1982)
25	75.9					Sillen & Martell (1971)
25	76.2±7		20.5±1.3			Izatt *et al.* (1969)
25	77.6					Izatt *et al.* (1969)
25	79.43					Margolis (1966)

Stellenbosch University http://scholar.sun.ac.za

Temp. °C	$K°_B$	ΔG° kJ/mol	ΔH° kJ/mol	ΔS° J/mol.K	$\Delta C_p°$ J/mol.K	Reference
25	81.3		23.4	114.22		Izatt *et al.* (1969)
25	83.18		21.8	110.04		Izatt *et al.* (1969)
25	83.2		9.33			Sillen & Martell (1964)
25	87.1					Sillen & Martell (1964)
25	89.1					Hogfeldt (1982)
25	89.13		23.85	117.2		Izatt *et al.* (1969)
25	91.2		23.4	115.9		Sillen & Martell (1964)
25	92.15±4.45		22.8±0.8	114±2	275±17	Dickson *et al.* (1990)
25	93.3		21.74±0.08			Powel (1973)
25	93.3		20.5	106.7		Hogfeldt (1982)
25	93.55±6.45		20.5±0.84	106.7±2.5		Izatt *et al.* (1969)
25	95.31±2.2					Pitzer *et al.* (1977)
25	95.5					Hogfeldt (1982)
25	91.2 to 100					Hogfeldt (1982)
25	95.6±4.4		22.6	114	300	Dickson *et al.* (1990)
25	96.98	-11.34	24.02	118.83		Ahrland (1972)
25	97					Sillen & Martell (1971)
25	97.27	-11.34	16.11	92.05	238.49	Marshall & Jones (1966)
25	97.3		21.8			Hogfeldt (1982)
25	97.32±1.9					Marshall & Jones (1966)
25	97.5					Perrin (1982)
25	97.7		24.3			Sillen & Martell (1964)
25	97.7		21.8	110.9		Sillen & Martell (1964)
25	97.7		18.83	101.25		Izatt *et al.* (1969)
25	97.7		20.5	107.11		Izatt *et al.* (1969)
25	97.7		22.2	112.6		Izatt *et al.* (1969)
25	97.7		16.1	92.1		Izatt *et al.* (1969)
25	97.7		16.1	92		Sillen & Martell (1971)
25	97.7±1		22.6±0.84	113		Smith & Martell (1989)
25	98.58					Zemaitis *et al.* (1986)
25	95.5 to 102.3					Sillen & Martell (1971)
25	100					Sillen & Martell (1964)
25	100.69					Hamer (1959)
25	109.6					Sillen & Martell (1964)
25	140.6					Perrin (1982)
25	158.5		17.2	99.2		Izatt *et al.* (1969)
25					262±5	Dickson *et al.* (1990)

Stellenbosch University http://scholar.sun.ac.za

Temp. °C	$K°_B$	ΔG° kJ/mol	ΔH° kJ/mol	ΔS° J/mol.K	$\Delta C_p°$ J/mol.K	Reference
25					280±5	Dickson *et al.* (1990)
27	97.7					Sillen & Martell (1971)
27.5	125.9					Hogfeldt (1982)
30	89.1		11.26			Sillen & Martell (1964)
30	106.2±2.5					Marshall & Jones (1966)
30	107.2					Perrin (1982)
30	134.9					Sillen & Martell (1964)
35	107.2					Sillen & Martell (1971)
35	120.2					Hogfeldt (1982)
35	123					Sillen & Martell (1964)
35	125.9					Sillen & Martell (1964)
35	126.26±4.36					Dickson *et al.* (1990)
35	128.8		21.3			Sillen & Martell (1964)
35	129.45±2.98					Pitzer *et al.* (1977)
35	131.8		23.4	117.2		Sillen & Martell (1964)
35	147.9					Sillen & Martell (1964)
40	102.3		15.36			Sillen & Martell (1964)
40	138					Perrin (1982)
40	141.2					Hogfeldt (1982)
40	142.5±1.5					Marshall & Jones (1966)
40	166					Sillen & Martell (1964)
40					234±15	Dickson *et al.* (1990)
40					250±13	Dickson *et al.* (1990)
45	150.2±0.2					Marshall & Jones (1966)
45	151.4					Perrin (1982)
45	166					Sillen & Martell (1964)
45	177.8		25.5	123.4		Sillen & Martell (1964)
50	125.9		19.67			Sillen & Martell (1964)
50	162.2					Sillen & Martell (1971)
50	176.2	-13.9	22.2	111.7	246.9	Marshall & Jones (1966)
50	177.8					Sillen & Martell (1971)
50	186.2					Perrin (1982)
50	188.3±1.4					Marshall & Jones (1966)
50	190.6					Sillen & Martell (1964)
50	195		24.4			Sillen & Martell (1964)
50	198.21±4.57					Pitzer *et al.* (1977)
50	204.2					Hogfeldt (1982)

Stellenbosch University http://scholar.sun.ac.za

Temp. °C	$K°_B$	ΔG° kJ/mol	ΔH° kJ/mol	ΔS° J/mol.K	$\Delta C_p°$ J/mol.K	Reference
50	207.09±5.72					Dickson *et al.* (1990)
50	213.8					Hogfeldt (1982)
50	234.4					Sillen & Martell (1964)
55	245.5		27.6	129.3		Sillen & Martell (1964)
55					224±15	Dickson *et al.* (1990)
55					231±11	Dickson *et al.* (1990)
60	166		24.3			Sillen & Martell (1964)
60	229.1					Perrin (1982)
60	231.9±1					Marshall & Jones (1966)
60	234.42					Oblad (1975)
60	251.2					Hogfeldt (1982)
75	345.94	-16.9	28.4	130.1	251	Marshall & Jones (1966)
75	501.2					Sillen & Martell (1964)
80	467.7					Hogfeldt (1982)
100	398					Sillen & Martell (1971)
100	716.14	-20.28	34.8	148.5	259.4	Marshall & Jones (1966)
100	724.44					Oblad (1975)
100	851.1					Hogfeldt (1982)
100	871					Sillen & Martell (1971)
100	977.2					Hogfeldt (1982)
100	1023.3					Sillen & Martell (1964)
100	1096.5					Sillen & Martell (1971)
100	1174.9					Hogfeldt (1982)
100	1202.3					Perrin (1982)
100	1513.6					Sillen & Martell (1971)
100	1584.9					Sillen & Martell (1971)
117	2169.70		50.8			Rudolph (1996)
150	3630.78		57.36	204	264	Oscarson *et al.* (1988)
150	3758.37					Davies *et al.* (1952)
150	4875.28		52.22			Lietzke *et al.* (1961)
158	11844.04		66.3			Rudolph (1996)
175	9549.93		64.97	221	349	Oscarson *et al.* (1988)
175	12218.00		52.22			Lietzke *et al.* (1961)
193	49980.43		80.8			Rudolph (1996)
200	25703.96		75.05	243	462	Oscarson *et al.* (1988)
200	30831.88		52.22			Lietzke *et al.* (1961)

Stellenbosch University http://scholar.sun.ac.za

A.2.3 Temperature extrapolation of the overall association constant of magnesium sulfate

Figure A.1 compares the overall association constant, *i.e.*, the solvent-separated ion pairs (SSIPs) plus the contact ion pairs (CIPs) (Sect. 2.3.3), derived from experimentation at lower temperatures and the extrapolations at higher temperatures. The open data points represent the models of Baghalha and Papangelakis (1998) and Casas *et al.* (2005b), using Helgeson extrapolation (Sect. 2.3.1), and the model of Liu and Papangelakis (2005a), using the Density function (Eq. 2.44). The lines represent the Density function calculations of this study, based on the reference data ($\Delta H°$ & $\Delta C_p°$) obtained from different spectroscopic studies. This figure exemplifies the importance of the reference data when extrapolating to higher temperatures (lines).

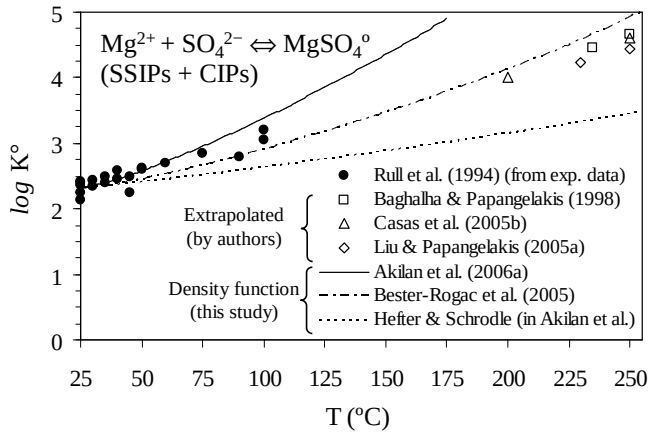

Figure A.1
Experimental data *vs.* extrapolated values of the overall thermodynamic association constant of magnesium sulfate, $K°_{(tot)}$, as a function of the solution temperature.

A.2.4 Deriving the association constant of M(II)$SO_4°$ in context of an ion-interaction framework

To be consistent with the ion-interaction modelling framework, the CIP formation reaction needs to be described in terms of the actual free hydrated ions and all the SSIPs (see Sect. 2.3.1):

$$(\tfrac{z}{y})\{M^{2+}+SO_4^{2-}\}+(1-\tfrac{z}{y})M(OH_2)_nSO_4^o \Leftrightarrow MSO_4^o+n(1-\tfrac{z}{y})H_2O \qquad A.2$$

where y represents the apparent unassociated moles of ions (molality, m) and z is the true unassociated moles of ions (m'). This thermodynamic constant cannot be obtained by extrapolating the experimental constants to infinite dilution due to the stepwise Eigen mechanism (Sect. 2.3.3). If α_C and m_C represent the mole fraction and molality of the CIP, M(II)$SO_4°$, respectively, then:

$$y=\frac{m}{m^{st}}=1-\frac{m_C}{m^{st}}=1-\alpha_C \qquad A.3$$

$$z=\frac{m'}{m^{st}}=1-\frac{(m_{SSIPs}+m_C)}{m^{st}} \qquad A.4$$

Stellenbosch University http://scholar.sun.ac.za

By adopting the notation of a step-wise reaction (Eq. 2.30) by virtue of the ion-interaction framework, the experimental constant (Rx. A.2) of the CIP, K_C (as obtained by Raman Spectroscopy (RS); see Hefter, 2006), may be related to Equation A.3 as follows:

$$K_C = \frac{\alpha_C}{(1-\alpha_C)^2 m^{st}} = K_C^o \cdot \frac{\gamma_{M^{2+}} \cdot \gamma_{SO_4^{2-}}}{\gamma_C} \qquad A.5$$

The relationship between the stoichiometric mean activity coefficient ($\gamma_{\pm}^{st}$) and the individual ion activity coefficients follows directly from Equations 2.22, 2.23 and A.3:

$$\gamma_{Mg^{2+}} \cdot \gamma_{SO_4^{2-}} = \frac{(\gamma_{\pm}^{st})^2}{(1-\alpha_C)^2} \qquad A.6$$

Equations A.5 and A.6 then yield the following expression of the thermodynamic constant:

$$K_C^o = \frac{\gamma_C}{(\gamma_{\pm}^{st})^2} \cdot \frac{\alpha_C}{m^{st}} \qquad A.7$$

This equation is used in Section 2.3.3 (Table 2.9) to derive K^o_C values from the published RS data.

A.2.5 Temperature extrapolation of the solubility product of kieserite

Figure A.2 compares the temperature extrapolation of *log* K^o_{sp} of kieserite using the Density function (Eq. 2.44) and the *HSC* (2006) database, with the values reported in other studies based on Helgeson extrapolation and alternative reference data values (see Sect. 2.3.1). Baghalha and Papangelakis (1998) and Casas *et al.* (2005b) used Helgeson extrapolation, whereas Liu and Papangelakis (2005a) calculated slightly larger values using the Density function.

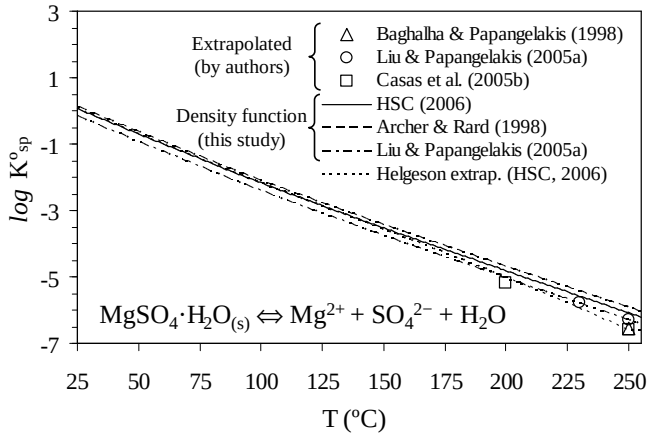

Figure A.2
Temperature extrapolation of *log* K^o_{sp} for kieserite using thermodynamic data (at 25ºC) from different sources. The datapoints represent extrapolated values reported in the literature.

Stellenbosch University http://scholar.sun.ac.za

A.3 Computational method used to iteratively determine the aqueous species molalities

A Newton-Raphson numerical routine, similar to the one proposed by I and Nancollas (1972), is adopted by the phenomenological model (Sect. 2.4) to solve the system of mass balance equations and unknown species molalities within the ion-interaction (Pitzer) framework. All four equilibrium constants (K_B, K_N, K_C & K_T) are expressed in terms of the key component molalities (Filippou *et al.*, 1995), *i.e.*, m_H, m_M and m_S, referring to the (apparent) unassociated hydrogen, metal(II) and sulfate ion molalities, respectively. The resulting mass balance equations are then expressed in terms of the residual functionals, F, of each key component:

$$F_H = (m_H + K_B m_H m_S + 2K_B K_N m_H^2 m_S) - m_H^{st} \quad \text{A.8}$$

$$F_M = (m_M + K_C m_M m_S + K_C K_T m_M m_S^2) - m_M^{st} \quad \text{A.9}$$

$$F_S = (m_S + K_B m_H m_S + K_B K_N m_H^2 m_S + K_C m_M m_S + 2K_C K_T m_M m_S^2) - m_S^{st} \quad \text{A.10}$$

A first-order Taylor expansion is used to calculate the vector of residual function values, $\boldsymbol{F}$:

$$\boldsymbol{F}(m+h) = \boldsymbol{F}(m) + \mathbf{J}(m)\cdot\mathbf{h} \quad \text{A.11}$$

The symbol **J** refers to the square Jacobian matrix, *i.e.*, the partial derivatives of each function with respect to their key component molalities. An element of this matrix is thus expressed as:

$$J_{ij} = \frac{\partial F_i}{\partial m_j} \quad \text{A.12}$$

The step-size vector between successive old and new estimates of the (variable) molality vector, **m**, is given by **h**, where the subscript *k* represents the step number:

$$\mathbf{h} = \mathbf{m}_{k+1} - \mathbf{m}_k \quad \text{A.13}$$

A converging solution is achieved in an iterative manner by choosing the step-size vector such that:

$$\boldsymbol{F}(m+h) = 0 \quad \text{A.14}$$

Equations A.11 and A.14 are combined to yield the following relationship:

$$\mathbf{h} = -\mathbf{J}^{-1}(m)\cdot\boldsymbol{F}(m) \quad \text{A.15}$$

Equation A.13 is substituted into Equation A.15 to yield a new estimate of the key component molality vector:

$$\mathbf{m}_{k+1} = \mathbf{m}_k - \mathbf{J}_k^{-1}(m)\cdot\boldsymbol{F}_k(m) \quad \text{A.16}$$

This routine continues until a specified tolerance is achieved, with the species activity coefficients (Eq. 2.3 & 2.4) and solution ionic strength (Eq. 2.9) being updated after each iteration step. Obviously, the converged species molalities also need to fulfil the condition of electrical neutrality

Stellenbosch University http://scholar.sun.ac.za

(Eq. 2.27). The converged molality and species activity coefficients are then used to calculate the thermodynamic properties of the system.

A.4 Oxygen solubility in water and electrolyte solutions

Equation A.17 presents the empirical equation of Tromans (1998a) for Henry's law constant (mol/kg.atm) of diatomic oxygen in equilibrium with water, valid up to 343ºC and 60 atm (the parameter values are listed in Table A.5):

$$ln\,K_{H,w}\cdot(8.3144T) = p_1T^2 + p_2T\cdot ln(T/298) - (p_3 + p_4T)(T-298) - p_5 \qquad \text{A.17}$$

Table A.5
Parameter values (molality scale) of Equation A.17 (Tromans, 1998a).

Parameter	Value	Parameter	Value
p_1	0.046	p_4	0.092
p_2	203.35	p_5	20591
p_3	299.378		

Equation A.18 represents the empirical equation of Tromans (1998b) for Henry's law constant (mol/kg.atm) of diatomic oxygen in equilibrium with an electrolyte mixture, valid up to (at least) 200ºC:

$$K_H = K_{H,w}\cdot\left(\frac{1}{1+\kappa_1 m_1^{\,y_1}}\right)^{\eta_1}\left\{\prod_{i=2}^{j}\left(\frac{1}{1+\kappa_i m_i^{\,y_i}}\right)^{\eta_i}\right\}^{q} \qquad \text{A.18}$$

Table A.6 lists the salt-specific parameters of this equation. The coefficient κ and the exponents y and η are solute-specific empirical parameters. An average value for parameter q of 0.8 was found, following the regression of 21 solutes (Tromans, 1998b).

Table A.6
Solute-specific parameter values (molality scale) of Equation A.18 (Tromans, 1998b).

Salt	κ	y	η
H_2SO_4	2.01628	1.253475	0.168954
Na_2SO_4	0.629498	0.911841	1.440175
$MgSO_4$	0.119674	1.107738	5.455537
$ZnSO_4$	0.232671	1.010428	2.655655
$CuSO_4$	2.23207	1.115617	0.222794
$Al_2(SO_4)_3$	0.641163	0.954719	3.033594

Stellenbosch University http://scholar.sun.ac.za

A.5 Water vapour pressure of the pure solvent and sodium sulfate solutions

A 4th-order power series was used to correlate the reported vapour pressure data of Cooper and Le Fevre (1982) between 20°C and 200°C:

$$p_w^o = \sum_{i=1}^{5} p_i \cdot (T_d/T_o)^{i-1} \qquad \text{A.19}$$

The parameter values ($1-R^2 < 1\times10^{-6}$), listed in Table A.7, yield $p_w°$ values within 0.1 kPa of the reported data below 100°C and within 0.5 kPa of the reported data above 100°C. The reference temperature (T_r) is 293.15 K, while T_o refers to unit temperature, *i.e.*, 1 K.

Table A.7
Parameter values of Equation A.19.

Parameter	$T_c < 100°C$ (kPa)	$T_c \geq 100°C$ (kPa)
p_1	2.38786034×10^{0}	4.380950265×10^{0}
p_2	1.2414042×10^{-1}	-1.04341940×10^{-1}
p_3	5.62410×10^{-3}	1.2401293×10^{-2}
p_4	8.32×10^{-6}	-6.8974×10^{-5}
p_5	1.19×10^{-6}	1.495×10^{-6}

The vapour pressure of water in equilibrium with mixed sodium sulfate and sulfite solutions is required to interpret the oxygen mass transfer results of the indirect test method (Ch. 3, Sect. 3.5). Since the vapour pressure of aqueous sulfite solutions is unavailable in the open literature, its behaviour is assumed identical to sodium sulfate solutions at the same concentration. This assumption artificially reduces the ternary Na_2SO_3-Na_2SO_4-H_2O electrolyte system to the binary Na_2SO_4-H_2O system. Osmotic coefficient data for aqueous sodium sulfate solutions, as reported by Pabalan and Pitzer (1988), are directly related to the water activity by Equation 2.7 (Ch. 2). The vapour pressure of the solution is then related to the water activity, assuming ideal gas phase behaviour (Eq. 2.79). For practical reasons, empirical equations were fitted to these calculated vapour pressures as a function of the temperature (25-175ºC) and salt concentration (0.1-1.5 mol/kg Na_2SO_4). Equation A.19 was used to constrain the regression at infinite dilution, yielding the following relationships:

$$t < 100^oC: \quad ln\, p_w = p_1 + p_2 \cdot (T_c/T_o)^{\frac{1}{2}} + p_3 \cdot [Na_2SO_4] \qquad \text{A.20}$$

$$t \geq 100^oC: \quad ln\, p_w = p_1 + 2\,p_2 \cdot ln\,(T_c/T_o) + p_3 \cdot [Na_2SO_4] \qquad \text{A.21}$$

The parameter values ($1-R^2 < 1\times10^{-4}$), listed in Table A.8, yield p_w values to within 0.5 kPa below 100°C and to within 2 kPa above 100°C (T_o refers to unit temperature, *i.e.*, 1°C). The error in the

Stellenbosch University http://scholar.sun.ac.za

calculated oxygen solubility, using these elementary equations, is less than 0.1 mg/kg at the operating conditions used in this study.

Table A.8
Parameter values of Equations A.20 & A.21.

Parameter	$T_c < 100°C$ (kPa)	$T_c \geq 100°C$ (kPa)
p_1	-2.6031×10^{0}	-3.8878×10^{0}
p_2	7.221×10^{-1}	4.004×10^{-1}
p_3	-3.48×10^{-2}	-3.02×10^{-2}

A.6 Rate of molten elemental sulfur oxidation by oxygen below 160°C

The expression of Corriou and Kikindai (1981) is modified to describe the instantaneous rate of molten elemental sulfur oxidation by oxygen below the transition temperature (< 160°C):

$$R = k\rho_{s/w}^{\frac{1}{2}} \cdot \frac{p_1[O_2]^{\frac{1}{2}}}{1+p_1[O_2]^{\frac{1}{2}}} \cdot \frac{1}{1+p_2[H^+]^T} \cdot exp\left(\frac{-E_a}{R_g T}\right) \qquad A.22$$

where the rate (R) is redefined in mol/min of elemental sulfur oxidised per unit mass (kg) water, and the solution species are expressed in the molality scale. Corriou and Kikindai (1981) reported a relatively high activation energy of 119.3 kJ/mol, while the surface area was implicitly taken into account by the half-order dependence on the pulp density, $\rho_{s/w}$ (g S°/kg H_2O). The surface area is assumed to be independent of the impeller speed (Sect. 6.3.2). The cupric ion acceleration factor is assumed to be insensitive above 1 g/L Cu (Habashi & Bauer, 1966) and is crudely fitted to the published data at different temperatures, *i.e.*, 3.5 at 130ºC (Habashi & Bauer, 1966), 2.7 at 140ºC and 1.3 at 200ºC (Corriou & Kikindai, 1981) (T_o refers to unit temperature, *i.e.*, 1°C):

$$k = \frac{p_3}{p_4 + p_5 ln(T_c/T_o)} \qquad A.23$$

Table A.9
Parameter values of Equations A.22 & A.23.

Parameter	$130°C < T_c < 160°C$	Units
p_1	[a] 6.1×10^{0}	$(kg/mol)^{0.5}$
p_2	[b] 6.1×10^{1}	kg/mol
p_3	1.66×10^{10}	mol/g.min
p_4	-5.204×10^{0}	–
p_5	1.128×10^{0}	–

[a] Value refers to 140°C (Corriou & Kikindai, 1981), but assumed constant over 130-160°C range; [b] Value of 57 (Corriou & Kikindai, 1981) adjusted to the molality scale, based on an estimated avg. sln. density of 1.1 kg/L.

Stellenbosch University http://scholar.sun.ac.za

A.7 Thermodynamic data used in reactor and integrated circuit modelling (energy balance)

The following table presents a summary of the species and their thermodynamic values used in the modelling of the continuous autoclave reactor and the integrated primary circuit (Ch. 8).

Table A.10
Thermodynamic values used in the autoclave & primary circuit energy balance.

[a] Species (sld.)	$H°_{Tr}$	T_r	[b] Kelley-a	[b] Kelley-b	[b] Kelley-c	[b] Kelley-d
–	(kJ/mol)	(K)	(J/mol.K)	(J/mol.K^2)	(J.K/mol)	(J/mol.K^3)
S°	0	298.15	7.835	79.793	-0.207	-97.893
(transf.)	0.401	368.3	968.639	-3355.340	-223.772	3368.169
Cu°	0	298.15	30.578	-11.325	-3.284	9.800
CuS {Cu(II)S}	-56.000	298.15	43.671	20.136	-2.102	-0.005
[c] Cu_2S {chalcocite}	-79.496	298.15	53.438	76.459	-0.117	2.456
Cu_5FeS_4 {bornite}	-380.326	298.15	208.196	146.775	-5.648	–
$CuFeS_2$ {chalcopyrite}	-185.991	298.15	86.985	53.555	-5.607	–
$CuSO_4$	-771.400	298.15	38.676	252.380	-1.588	-148.155
ZnS {sphalerite}	-203.000	298.15	48.676	5.760	-4.119	0.003
[d] FeS {triolite}	-101.671	298.15	-273.270	779.182	81.241	0.000
[e] Fe_7S_8 {pyrrhotite}	-736.384	298.15	398.568	–	–	–
FeS_2 {pyrite}	-171.500	298.15	72.387	8.850	-11.428	0.001
$FeSO_4$	-928.848	298.15	202.581	-296.367	-40.839	363.381
Fe_2O_3 {hematite}	-823.000	298.15	143.566	-36.323	-31.433	71.792
Fe_3O_4 {magnetite}	-1115.50	298.15	475.215	-873.665	-120.520	800.730
[e,g] $(H_3O)Fe_3(SO_4)_2(OH)_6$	-3770.20	298.15	287.20	628.10	-32.860	–
$Fe(OH)_3$	-832.6	298.15	162.477	11.916	-43.581	-0.035
$Al_2O_3.H_2O$ {diaspore}	-1999.115	298.15	95.844	34.808	-0.034	0.267
[c] $Al_2O_3.3H_2O$ {gibbsite}	-2586.55	298.15	69.705	381.581	–	–
[e] $(H_3O)Al_3(SO_4)_2(OH)_6$	[h] -5256	298.15	[i] 198	[i] 848.8	[i] -13.56	[i] -180
SiO_2 {quartz}	-910.7	298.15	-61.084	378.239	17.076	-296.898
$Mg_3(Si_2O_5)(OH)_4$ {serp.}	-4365.608	298.15	317.231	132.214	-73.555	–
$Ca_3(Si_2O_4)(OH)_6$	-4782.31	298.15	341.163	188.698	-61.379	–
Na_2SiO_3	-1561.43	298.15	112.789	76.665	-19.708	-17.968
[f] $NaFe_3(SO_4)_2(OH)_6$	[j] -3783.4	298.15	616.390	91.210	-203.760	–
[f] $NaAl_3(SO_4)_2(OH)_6$	-5131.970	298.15	641.500	-7.870	-234.120	–
$MgCO_3$ {magnesite}	-1111.396	298.15	82.555	52.463	-19.866	–
$CaCO_3$ {calcite}	-1206.60	298.15	99.544	27.136	-21.479	0.002
$CaSO_4.2H_2O$ {gypsum}	-2022.629	298.15	91.379	317.984	–	–
–	–	–	–	–	–	–
–	–	–	–	–	–	–

Table continues

Stellenbosch University http://scholar.sun.ac.za

[a] Species (liq.)	$H°_{Tr}$	T_r	[b] Kelley-a	[b] Kelley-b	[b] Kelley-c	[b] Kelley-d
–	(kJ/mol)	(K)	(J/mol.K)	(J/mol.K^2)	(J.K/mol)	(J/mol.K^3)
H_2O	-285.830	298.15	186.884	-464.247	-19.565	548.631
H_2SO_4	-788.335	298.15	153.868	38.202	-22.740	-8.643
S°	0.922	298.15	-8691.86	28084	2467.29	-25321.1
(transf.)	–	428.15	-2806919	8688672	867400	-7562393
(transf.)	–	432.25	-2959.565	7880.76	1295.64	-5843.22
[a] Species (aq.)	$H°_{298.15}$	$S°_{298.15}$	[b] Kelley-a	[b] Kelley-b	[b] Kelley-c	[b] Kelley-d
–	(kJ/mol)	(J/mol.K)	(J/mol.K)	(J/mol.K^2)	(J.K/mol)	(J/mol.K^3)
H^+	0	0	0	0	0	0
OH^-	-230.024	-10.711	40928.517	-169401.06	-7180.118	197089.62
(>60°C)	–	–	-1918.448	8830.259	182.977	-11628.816
Na^+	-240.3	58.409	11370.863	-46769.459	-1983.674	54484.673
(>60°C)	–	–	-197.031	1400.587	-0.272	-1981.956
Cu^{2+}	64.900	-98.000	19652.9	-81020.65	-3428.10	93946.45
(>60°C)	–	–	-2011.88	8870.89	315.067	-11066.35
Zn^{2+}	-153.385	-109.621	19327.2	-79748.3	-3374.235	92469.4
(>60°C)	–	–	-2003.99	8757.90	311.408	-10923.7
Fe^{2+}	-92.257	-105.855	20393.0	-84181.1	-3562.71	97657.9
(>60°C)	–	–	-1943.79	8530.47	293.747	-10685.0
Fe^{3+}	-49.580	-277.399	31340.6	-129433.5	-5474.49	149975
(>60°C)	–	–	-3668.35	15752.4	580.732	-19551.3
Mg^{2+}	-467.000	-137.000	25031.0	-103282	-4373.19	119927
(>60°C)	–	–	-1965.48	8845.75	281.066	-11190.4
Al^{3+}	-538.763	-325.000	7706.68	-28394.9	-1690.98	28600.0
(>70°C)	–	–	-2190.39	10655.0	197.009	-14764.9
(>130°C)	–	–	-5900.86	22965.3	1199.29	-26264.9
SO_4^{2-}	-909.602	18.828	71609.55	-296485	-12565.4	344883
(>60°C)	–	–	-3610.89	16366.4	364.885	-21432.5
[a] Complex species (aq.)	$H°_{Tr}$	T_r	[b] Kelley-a	[b] Kelley-b	[b] Kelley-c	[b] Kelley-d
–	(kJ/mol)	(K)	(J/mol.K)	(J/mol.K^2)	(J.K/mol)	(J/mol.K^3)
HSO_4^-	-886.900	131.700	10331.0	-42424.3	-1791.35	48997.4
(>60°C)	–	–	-1734.79	7506.41	305.075	-9183.63
[k] $H_2SO_4°$	-866.423	423.15	[l] -23985.4	[l] 31512.8	[l] 16386.9	[l] 9183.6
[m] $MeSO_4°$ (*e.g.* Cu)	-834.702	298.15	91592.5	-377505	-15993.5	438829
(>60°C)	–	333.15	-5292.77	25237.3	679.951	-32498.9
[n] $Me(SO_4)_2^{2-}$ (*e.g.* Cu)	-1695.30	298.15	163202	-673990	-28559.0	783712
(>60°C)	–	333.15	-8903.66	41603.65	1044.84	-53931.4

Table continues

Stellenbosch University http://scholar.sun.ac.za

[a] Complex species (aq.)	$H°_{Tr}$	T_r	[b] Kelley-a	[b] Kelley-b	[b] Kelley-c	[b] Kelley-d
–	(kJ/mol)	(K)	(J/mol.K)	($J/mol.K^2$)	(J.K/mol)	($J/mol.K^3$)
$FeH(SO_4)_2°$	[o] -1726.7	298.15	[p] 174559.7	[p] -722403	[p] -30605.3	[p] 839741.1
(>60°C)	–	333.15	[p] -10890.1	[p] 48868.8	[p] 1310.50	[p] -62416.3
[a] Species (g)	$H°_{Tr}$	T_r	[b] Kelley-a	[b] Kelley-b	[b] Kelley-c	[b] Kelley-d
	(kJ/mol)	(K)	(J/mol.K)	($J/mol.K^2$)	(J.K/mol)	($J/mol.K^3$)
H_2O	-241.826	298.15	28.408	12.477	1.284	0.360
O_2	0	298.15	22.060	20.887	1.621	-8.207
CO_2	-393.505	298.15	29.314	39.970	-2.484	-14.783
N_2	0	298.15	29.298	-1.567	-0.007	3.419
(>76.85°C)	–	350	27.753	0.605	0.728	4.960

[a] Values from *HSC* (2006), unless indicated otherwise; [b] Eq. 2.34; [c] Valid < 100°C; [d] Valid < 150°C; [e] Valid < 130°C; [f] Valid < 30°C; [g] Majzlan *et al.* (2004); [h] Scaled to $H°_{298.15}$ of H-jarosite [(g)], using avg. alunite/jarosite $H°_{298.15}$ ratio (1.394), *i.e.*, K-alunite/K-jarosite & Na-jarosite/Na-alunite (*HSC*, 2006); [i] Estimated, assuming $\Delta C_p°_{rx}$ = 0 J/mol.K for solid-state reaction: $(H_3O)Fe_3(SO_4)_2(OH)_{6(s)} + 1.5Al_2O_{3(s)} \Leftrightarrow (H_3O)Al_3(SO_4)_2(OH)_{6(s)} + 1.5Fe_2O_{3(s)}$; [j] Drouet & Navrotsky (2003); [k] $\Delta H°_{rx}$ & $\Delta C_p°_{rx}$ data (T_r = 150°C) of Oscarson *et al.* (1988) for second proton association reaction: $H^+ + HSO_4^- \Leftrightarrow H_2SO_4°_{(aq)}$ (other species data from *HSC*, 2006); [l] Valid > 150°C; [m] $\Delta H°_{Tr}$ = 10 kJ/mol & $\Delta C_p°_{rx}$ = 330 J/mol.K (assumed constant) for $M^{2+} + SO_4^{2-} \Leftrightarrow M(II)SO_4°_{(aq)}$, from this study (Table 2.10 & 2.14; other species data from *HSC*, 2006); [n] $\Delta H°_{rx}$ = 49 kJ/mol & $\Delta C_p°_{rx}$ = 0 J/mol.K (assumed constant) for $MeSO_4° + SO_4^{2-} \Leftrightarrow Me(SO_4)_2^{2-}$ from this study (Table 2.10 & 2.14; other species data from *HSC*, 2006); [o] Derived using the data of Cifuentes *et al.* (2006); [p] Assumed $\Delta C_p°_{rx}$ = 0 J/mol.K for the reaction: $Fe^{3+} + H^+ + 2SO_4° \Leftrightarrow FeH(SO_4)_2°$.

Table A.11 presents a summary of the thermodynamic values (NBS Tables; Wagman *et al.*, 1982) and Kelley b-coefficients, obtained using Lewis linearization (Sect. 7.2.3), and used in the modelling of the continuous autoclave reactor and the integrated primary circuit (Ch. 8).

Table A.11
Enthalpy values & Kelley-b parameters (using Lewis linearization) of the aqueous species used in the autoclave & primary circuit energy balance.

Species	[a] $H°_{298.15}$	[a,b] Kelley-b	Species	[a] $H°_{298.15}$	[a,b] Kelley-b
–	(kJ/mol)	($J/mol.K^2$)	–	(kJ/mol)	($J/mol.K^2$)
H^+	0	383.53	–	–	–
Na^+	-240.12	489.76	Fe^{3+}	-48.5	1176.08
Cu^{2+}	64.77	785.4	Al^{3+}	-531	1185.63
Zn^{2+}	-153.89	805.99	OH^-	-229.994	-718.14
Fe^{2+}	-89.1	848.15	HSO_4^-	-887.34	40.08
Mg^{2+}	-466.85	848.81	SO_4^{2-}	-909.27	-1243.79

[a] Enthalpy & entropy values from NBS Tables (Wagman *et al.*, 1982); [b] Eq. 7.25 (applied to Eq. 2.34).

Stellenbosch University http://scholar.sun.ac.za

APPENDIX B. QUANTIFYING SUBSTANCE, ANALYSES METHODS AND SPECTROSCOPIC TECHNIQUES

This appendix summarises the experimental techniques and methods used to quantify substance amount, substance characteristics and species abundance (concentration). A section is also devoted to the methods employed to identify and quantify the predominant mineral phases and species present in the concentrates and leach residues.

B.1 Quantifying substance

Throughout the experimental program, mass and volume had to be quantified to mathematically relate the observed phenomenon to the relevant species concentrations in the solid and solution phase.

B.1.1 Quantifying mass

The amount of mass was quantified gravimetrically, *i.e.*, by weighing the substance on an electronic analytical balance. Masses higher than 4 kg were weighed on a Mettler Toledo Viper SW 60 Toploader weighing scale. Masses up to 30 kg were readable in 10 g units, while the 30 to 60 kg range was readable in 20 g units. The scale was calibrated (certified) at regular intervals, using calibration weights. Intermediate masses (0.1-4.1 kg) were weighed on a Mettler Toledo PB4002-S/FACT Toploader balance and were readable in 0.01 g graduations. This balance was housed in a closed area, free of excessive air movement. The motorised internal calibration feature performed regular automatic calibrations. Accuracy was also occasionally verified with external (certified) calibration weights. When weighing hot material, care was taken to minimise the conduction of heat to the balance surface. Masses less than 100 g were weighed using the Mettler Toledo XS204/FACT (Delta Range) high precision balance. This instrument was also equipped with an automated internal calibration system. A draught guard with sliding door allowed readability to 0.1 mg.

B.1.2 Quantifying volume

The amount of material was usually quantified using mass rather than volume. However, to close the overall mass balance, *e.g.*, when conducting mineral oxidation testwork, the species concentration was reported (analysed) in grams per litre (g/L) and the solution volume had to be quantified. Volume measurements were conducted using analytical grade measuring cylinders (varying sizes) at room temperature. These measuring cylinders were properly cleaned with deionised water and dried before use.

Stellenbosch University http://scholar.sun.ac.za

Standard stock solutions were prepared using analytical grade pipettes and volumetric flasks. Liquid samples and diluent (water) were always kept close to 20°C, using a water bath with heating (Julabo F12-SL HighTech Series) or refrigeration (Julabo F12-ED) control when required. The volumetric flasks were regularly cleaned with soap and water. After every dilution, the flasks were properly rinsed with deionised water and dried. Pipettes were left overnight in chromic acid. This procedure prevented drops from clinging to the glass surface while pipetting. This chromic acid solution was prepared by dissolving 100 g sodium dichromate ($Na_2Cr_2O_7.2H_2O$) in 500 mL water and then adding 800 mL of concentrated sulfuric acid (98% H_2SO_4); fresh chromic acid was only prepared when the solution started to turn green. Consistency was maintained by always using the recommended pipetting time (reported on the specific pipette). Because of the relatively large volumes required for analysis and large variation in dilution requirements, pipettes and volumetric flasks were used instead of an auto-diluter. No differences in accuracy between the two methods were observed, although dilution by hand was more time consuming.

B.1.3 Solution density measurement

Solution density was measured at room temperature with an Anton Paar DMA 35N hand-held digital density meter. The actual measurement temperature was also recorded (built-in feature of the meter) to ensure that the recorded density value always referred to 20±1°C. The meter was calibrated on a daily basis prior to measurement using distilled water. Sample measurement commenced only once the theoretical and measured values agreed to within 0.0005 kg/L. The sample was introduced by depressing the piston of the hand pump, inserting the meter tube into the liquid sample and releasing the piston. Care was taken to ensure that the sample filled the U-tube without any air bubbles present. The measured value was then recorded, after which the U-tube was flushed with distilled water a few times, before measuring the next sample.

B.2 Chemical analyses methods

This section is divided into three subsections, *i.e.*, total metal concentration, sulfur speciation and wet chemistry methods.

B.2.1 Total metal concentration

Inductively coupled plasma – optical emission spectroscopy (ICP-OES)

The Analytical Service Division of Anglo American Technical Solutions (ATS) used this method to quantify metal species concentrations in the solid and solution phase. The method relies upon the preliminary fusion and acid dissolution (in the case of solid samples) and determinations of specified elements by ICP-OES. During the analysis process, the sample is nebulised and then transferred to the argon plasma. It is decomposed, atomised and ionized whereby atoms and ions are excited. Each element emits light of certain intensity (depending on its concentration) at

Stellenbosch University http://scholar.sun.ac.za

characteristic wavelengths as it returns to a lower energy state and these were quantitatively measured after calibration. The concentration of metal species initially in the solid or solution sample could then be determined by back-calculation, knowing the initial amount of material present and the dilution factors used.

In the case of the solid samples, aliquots were weighed into zirconium crucibles and mixed with sodium peroxide (oxidising agent). This mixture was then fused on a gas burner until the melt appeared homogeneous. The crucibles were allowed to cool and then transferred to a Teflon beaker. The contents were dissolved in 20 mL nitric acid, transferred to a 200 mL volumetric flask and made up to the mark to give a final solution matrix containing around 10% nitric acid. The sample was then analysed by ICP-OES using a matrix-matched standard for calibration. Yttrium was used as an internal standard. All standard solutions were prepared using Spec-pure metals (99.9999%). A suite of 16 elements (incl. Cu, Fe, Zn, Mg & Si) was covered with this method, with lower limits of determinations (LLDs) less than 0.05% for all elements. For the solution samples, the method also involved the preliminary dilution of the samples with 10% nitric acid and multi-element determination using matrix-matched standards for calibration. The calibration standard concentration levels were 2.5 to 500 mg/L for copper and iron, 2.5 to 250 mg/L for magnesium, and 2.5 to 50 mg/L for zinc and silica. At ten times dilution, all elements were reported with LLDs less than 1 mg/L (Mg was reported with LLD less than 5 mg/L).

Borate fusion, followed by X-ray fluorescence (XRF)

X-ray fluorescence (XRF) was used to quantify the elemental concentrations in solid samples. Fused glass discs were prepared for analysis on an AXIOS X-ray fluorescence spectrometer (XRFS), using flux and sample material. The fusion method involved the fusion of a prepared sample, milled to at least 90% passing 75 µm and mixed with the appropriate flux, at temperatures between 1000ºC and 1200ºC, in a 95% Pt 5% Au crucible. Sample to flux ratios ranged from 0.5 to 1, with flux mass added to make up to a constant total mass, which varied according to the sample type. The borate fusion was done using an automatic fusion unit (Katanax K automatic fluxer). Flat glass discs were produced using a consistent casting procedure. By using a fused disc, the sample was homogenized and particle size effects were eliminated. The cooled glass discs were then subjected to measurement in the XRFS.

B.2.2 Sulfur speciation

Due to the relatively high solution potentials encountered in this study, sulfur in the solution phase was present as the sulfate (SO_4^{2-}) species and was directly analysed by high performance liquid chromatography (HPLC) by the Analytical Service Division of ATS. Sulfur species in solid samples were subjected to a more complicated experimental procedure: total sulfur was determined

Stellenbosch University http://scholar.sun.ac.za

by infra red (IR) measurement on the original sample and the final residue, *i.e.*, after successively using tetrachloroethylene and carbonate solution to respectively leach elemental and sulfate sulfur. Therefore, this method relies on the solubility differences of these two species in these solutions. This method was checked against sulfide ore mill tailings reference materials (RTS-1 & RTS-2), as characterised by the Canadian Certified Reference Materials Project (CCRMP). Results were only reported if the certified and measured values of these reference materials agreed within 5%. These measurement procedures are now discussed in more detail.

Total sulfur, S^T

The total sulfur content was determined by combustion and IR measurement, using an automated sulfur analyser, *i.e.*, the Leco IR232 microprocessor-based instrument. The sample or reference material was weighed into a crucible and the sample mass entered into the instrument. An accelerator (Cu) was added to the sample. The crucible was then ignited in the furnace of the instrument and the sulfur level measured. Concentration levels between 0.01 and 100% S^T could be determined in this way, although requiring dilution towards the higher end.

Elemental sulfur, S^o

The elemental sulfur content was determined by leaching a sample of known mass with tetrachloroethylene solution in an ultrasonic bath at 90°C for an hour and analysing the resulting solution by HPLC. Concentrations between 0.1 and 100% S^o could be determined in this way.

Sulfate sulfur, S(VI)

The residue of the above leach was dried and weighed, before being subjected to a second leach with carbonate solution (10% Na_2CO_3) at boiling point. The resulting solution was again analysed by HPLC to determine the sulfate content (0.5-50%) of the sample.

Sulfide sulfur, S^{Y-}

The remaining residue was washed and dried. The sample was weighed and analysed for total sulfur with the automated sulfur analyser (IR spectroscopy), as described above. The total sulfide sulfur content, S^{Y-}, was calculated from the original sample mass and the residue mass after elemental and sulfate sulfur removal.

Sulfur balance

It is emphasised that none of the above species were calculated by difference. The total measured sulfur content was compared with the total calculated sulfur content from the individual species analyses, as described above. Any particular sample was re-analysed if the total measured and calculated sulfur content varied by more than 5%.

Stellenbosch University http://scholar.sun.ac.za

B.2.3 Wet chemistry methods

All of these methods determine the solution species concentrations by titration. The advantage of these methods is the short time required for analysis. These methods were therefore particularly useful in determining the concentration of solution species that are not stable, such as iron(II) and sulfite (SO_3^{2-}) ion.

Preparation of stock solutions and standardisation

Analytical (AR) grade and deionised (triple) distilled water was used in all solution preparations. All the material was weighed on calibrated high precision balances (Sect. B.1.1) and the volumes were quantified using analytical grade volumetric flasks and pipettes (Sect. B.1.2). The following stock solutions were prepared (most of the recipes are based on the suggestions of Vogel, 1961):

Dichromate solution (0.1 N)

- Anhydrous $K_2Cr_2O_7$ crystals (certified at minimum 99.5% purity) were dried overnight in an oven at 90°C and then allowed to cool in a dessicator
- A mass of 9.8588 g was accurately weighed, dissolved and diluted to the 2-litre mark of the volumetric flask
- A standard ferrous nitrate solution was prepared by dissolving 10.0000 g Spec-pure (99.9999%) iron metal wire in a nitric acid solution
- After dissolving overnight, the solution was diluted to the 1 litre mark of the volumetric flask. The excess acid (approximately 1 N HNO_3) served to prevent precipitation and minimise adsorption of iron on the container surface
- The ferrous nitrate solution was then used to standardise the dichromate solution. The accurate dichromate content was determined after back-calculation (the titration procedure is presented in the next section). The stoichiometry of the ferrous oxidation reaction may be represented as follows (Vogel, 1961):

$$Cr_2O_7^{2-} + 6Fe^{2+} + 14H^+ \Rightarrow 2Cr^{3+} + 6Fe^{3+} + 7H_2O \qquad \text{B.1}$$

Hydroxide solution (0.1 N)

- A standard ampoule of 0.1 N sodium hydroxide was standardised using three accurately weighed (4 decimals) portions of approximately 0.1 g potassium hydrogen phthalate (PHT) crystals ($KHC_8H_4O_4$), each dissolved in 40 mL distilled water
- These samples were then titrated potentiometrically to a fixed pH using a Mettler Toledo DL50 Version 2.4 auto-titrator instrument and the sodium hydroxide solution as the titrant

Stellenbosch University http://scholar.sun.ac.za

- The average titration number of the three solutions was used to back-calculate the hydroxide concentration. The reaction stoichiometry was straight forward, *i.e.*, one mole of hydroxide reacted with one mole of weak acid (PHT) added.

Iodine solution (0.2 N)

- Approximately 40 g of iodate-free potassium iodide (KI) was dissolved in 20 mL water in a 1-litre glass-stoppered flask
- A mass of approximately 25.5 g resublimed iodine (I_2) (certified at minimum 99.5% purity) was weighed and then transferred into the potassium iodide solution
- The glass stopper was inserted and the flask shaken until all the iodine crystals had dissolved (Eq. B.4)
- The solution was allowed to acquire room temperature and then diluted to the 1-litre mark with distilled water
- The solution was stored in a cool, dark place. This procedure resulted in a concentration of approximately 0.1 mol/kg I_2 or rather, I_3^- (see Eq. B.4)
- Because of the volatility of the solid iodine crystals, it was necessary to standardise the solution with (already standardised) thiosulfate stock solution (see below)
- A 10 mL volume of the iodine solution was pipetted into a 500 mL flask and 50 mL distilled water was added
- The solution was titrated with the standardised thiosulfate solution until a light yellow colour appeared
- Approximately 1 mL starch indicator (see below) was added (solution turned dark blue) and the titration was continued until the solution was almost colourless
- The end point was recorded and the iodine concentration was calculated using the following stoichiometry (follows from Eq. B.4 and B.5):

$$2S_2O_3^{2-} + I_2 \Rightarrow S_4O_6^{2-} + 2I^- \qquad \text{B.2}$$

Mixed (Spekker) acid

- The mixed acid was prepared by slowly adding 400 mL concentrated sulfuric acid (98%) to 600 mL orthophosphoric acid (85%)
- Great care was taken when mixing these chemicals due to the high heat of dilution.

Diphenylamine indicator

- This indicator was prepared by dissolving 0.15 g sodium diphenylamine sulphonate in 50 mL water

Stellenbosch University http://scholar.sun.ac.za

- The solution was stored in a dark container. Nevertheless, it biodegraded with time and fresh solution had to be prepared on a weekly basis.

Starch indicator

- A paste of 1 g soluble starch, $(C_6H_{10}O_5)_n$, was prepared by adding a small amount of water
- Distilled water (100 mL) was boiled and the starch paste was slowly added to the boiling water while constantly stirring
- This solution was boiled for another minute (until it became clear) and allowed to cool
- Potassium iodide (2 to 3 g) was added to preserve the indicator
- The solution was stored in a cool dark place.

Thiosulfate solution (0.1 N)

- A mass of approximately 24.94 g sodium thiosulfate pentahydrate crystals ($Na_2S_2O_3.5H_2O$) (certified at minimum 99.5% purity) was weighed and dissolved in previously boiled and cooled water
- Approximately 0.1 g sodium carbonate was then added (to retard bacterial activity) and the volumetric flask was filled to the 1-litre mark with the previously boiled and cooled water
- This resulted in a concentration of approximately 0.1 mol/kg thiosulfate, which was stored in a dark container
- The concentration of the thiosulfate solution had to be determined independently by titration because of the efflorescent nature of the salt, in addition to its chemical and bacterial decomposition with time. The standardisation was conducted on a weekly basis, using a known amount of dichromate
- Three accurately weighed (4 decimals) portions of approximately 0.1 g previously dried $K_2Cr_2O_7$ crystals were each dissolved in 50 mL distilled water
- Freshly prepared solutions (3 batches), each containing 2 g KI, 2 mL HCl (32%) and 50 mL distilled water, were then added to each of the dichromate solutions
- These three solutions were swirled gently, closed to the atmosphere and left to stand in a dark place for about 10 minutes. This allowed the following two reaction to take place (Vogel, 1961):

$$Cr_2O_7^{2-} + 6I^- + 14H^+ \Rightarrow 2Cr^{3+} + 7H_2O + 3I_2 \qquad \text{B.3}$$

$$3I_2 + 3I^- \Leftrightarrow 3I_3^- \qquad \text{B.4}$$

- Titration of the tri-iodide ion (I_3^-) with the thiosulfate solution followed until the dark yellow-orange colour had almost disappeared

Stellenbosch University http://scholar.sun.ac.za

- Approximately 2 mL starch indicator was added and the titration was continued until the deep purple colour of the starch-tri-iodide complex changed to a light blue colour. The reaction between the thiosulfate and tri-iodide ion has the following stoichiometry (Vogel, 1961):

$$6S_2O_3^{2-} + 3I_3^- \Rightarrow 3S_4O_6^{2-} + 9I^- \qquad \text{B.5}$$

- The average endpoint of the three solutions was then used to back-calculate the thiosulfate concentration. The overall reaction stoichiometry is easily deduced from Equations B.3, B.4 and B.5:

$$Cr_2O_7^{2-} + 6S_2O_3^{2-} + 14H^+ \Rightarrow 2Cr^{3+} + 3S_4O_6^{2-} + 7H_2O \qquad \text{B.6}$$

Titration procedures

The following procedures describe the methods of titration for solution species (most recipes have been based on the suggestions of Vogel, 1961):

Iron(II) titration

- An equivalent volume of mixed acid was added to the aliquot volume analysed (usually 10 mL mixed acid with 10 mL aliquot)
- About 10 drops of sodium diphenylamine indicator and 30 mL of deionised water were added and the solution was allowed to cool
- The standardised 0.1 N dichromate solution was used as the titrant, while stirring the solution constantly. The solution first turned green and near the endpoint assumed a greyish-blue colour
- The endpoint was obtained by adding the titrant drop-wise to an intense purple coloration
- The concentration of ferrous ion in the sample was easily calculated using the stoichiometric equation reported earlier (Eq. B.1)
- No significant interference of copper or zinc ion in the background matrix was observed.

Duplicate samples were occasionally analysed by the Analytical Service Division of ATS in order to provide the necessary quality control. This potentiometric titration method may be summarised as follows:

- Samples containing between 0.5 and 100 g/L Fe(II) were analysed potentiometrically using a Mettler Toledo DL50 Version 2.4 auto-titrator instrument and standard 0.1 N potassium dichromate as the titrant
- The electrodes of the auto-titrator were first rinsed with deionised water and 40 mL Spekker acid was added to the titration cup

Stellenbosch University http://scholar.sun.ac.za

- The electrodes were immersed into the Spekker acid and the sample aliquot was added
- The titration was conducted automatically to the endpoint potential
- Three checks were conducted for quality control prior to analysing the actual sample, *i.e.*, using 5, 20 and 100 g/L ferrous ammonium sulfate standard solutions
- The electrodes were stored in 3 mol/kg KCl solution when not in use and regularly checked against standard solutions of known potential.

Free acid titration

- This method relies on the preliminary complexation of hydrolysable ions, *e.g.*, of Cu(II) and iron(III), with potassium oxalate solution (280 g/L)
- The electrode was first calibrated with pH 4 and 7 buffer solutions until a calibration slope of between 55 and 60 mV was obtained
- A known volume of sample aliquot and 50 mL water were added to the titration cup
- The stirrer and pH probe were inserted and the test sample titrated potentiometrically to a fixed pH using a Mettler Toledo DL50 Version 2.4 auto-titrator instrument and standardised 0.1 N sodium hydroxide solution as the titrant
- The total acid concentration was easily obtained with the knowledge that one mole H^+ ion reacted with one mole OH^- ion.

Sulfite (SO_3^{2-}) titration

The titration of sulfite ion was used to determine the rate of interfacial oxygen mass transfer between the gas and solution phase in a reaction vessel (Ch. 3). This section describes the iodometric back-titration method used to determine the residual sulfite concentration in a stirred reactor over time.

- A 250 mL conical flask was filled with 50 mL standardised 0.2 N iodine solution and 10 mL acid solution (2 mol/kg HCl)
- The sulfite sample aliquot (4 mL) was then added to the (excess) iodine solution, swirled gently and left to stand in a dark place for about 10 minutes. This allowed complete oxidation of sulfite ion (Vogel, 1961):

$$SO_3^{2-} + I_2 + H_2O \Rightarrow SO_4^{2-} + 2H^+ + 2I^- \qquad \text{B.7}$$

- The iodine that remained in the flask was then titrated against standardised 0.1 N thiosulfate solution (Eq. B.5) until the dark yellow-orange colour of the tri-iodide ion had almost disappeared
- At this point about 3 mL starch solution was added, which caused the solution to darken to the deep purple colour of the starch-tri-iodide complex

Stellenbosch University http://scholar.sun.ac.za

- Titration was continued until the solution changed to an almost colourless form
- The end-point was recorded and the overall reaction stoichiometry (Eq. B.2) was used to calculate the amount of iodine that had reacted with the sulfite aliquot. This value was, in turn, used to calculate the concentration of sulfite ion that was initially present in the sample from the reactor (Eq. B.7).

B.3 Measuring particle size, mineralogy and surface properties

This section presents the experimental methods used to measure particle size, quantify the mineralogical composition, and study particle surface properties and morphology.

B.3.1 Particle size distribution (PSD)

A Malvern MasterSizer 2000 was used to measure the PSD of various samples. The instrument makes use of a diffraction technique called Low Angle Laser Light Scattering (LALLS) and is based on the principle of laser ensemble light scattering. In short, a monochromatic beam of light (Helium-Neon laser) is passed through the measurement chamber (cell) where the sample is introduced. Solid particles scatter the light beam and a series of detectors (at different angles) measures the intensity (energy) of the scattered light. A series of detectors are required because small particles scatter light at higher angles and large particles at lower angles. Every particle of a specific size produces light with unique intensity, characteristic with the angle of detection. During measurement, the detector unit integrates the scattering of all the particles simultaneously. This is then related by (least squares) regression to generate the relative volume distribution of the particles the sample. It is important to note that because particles are never spherical, there will always be a discrepancy between the measured size distribution and the distribution obtained from screening with a series of sieves. The laser scattering technique deduces the particle size from the light energy measurement, assuming all particles are spherical. The orientation of an irregular particle at the instant of measurement (projected area) may give a 'false' impression of its real size. This error is reduced by averaging the integral scattering from various readings.

Measurement procedure

Sufficient laser intensity readings (> 50%) were obtained by proper alignment and clean cell windows. This measurement technique is absolute and no calibration was therefore required. However, a series of reference materials (from Malvern Instruments Ltd.) were used to verify the condition of the instrument on a regular (~monthly) basis over the course of this study. Measured values (avg. of three readings each) of the d_{10}, d_{50} and d_{90} percentiles were compared against the standards, allowing for tolerances of 3%, 2% and 3%, respectively. After pre-inspection of the instrument and peripherals, the following measurement procedure was used:

Stellenbosch University http://scholar.sun.ac.za

- Background scattering of the dispersant (water) was first measured to ensure no contamination in the dispersing system or entrained gas bubbles. Built-in ultrasonic agitation and an admixture (Calgon) were used to help disperse cohesive particles. Stirrer and (re-circulating) pump speeds were adjusted to ensure proper transport and de-aggregation of particles, but no entrainment of gas bubbles
- The homogeneous solid sample was then added to the preparation tank until a stable obscuration reading (measure of the laser light obscuration by the sample), in the range of 3 to 20%, was obtained. If too much solid sample was added, multiple scattering of the particles interfered with the measurement
- Once a stable signal was obtained, the particle size distribution was measured as an average of multiple sweeps. Measurements were repeated until excellent reproducibility was obtained, *i.e.*, less that 1% variation in the percentile (d_{10}, d_{50} & d_{90}) readings.

B.3.2 Mineralogy

The mineralogical analyses were conducted by the Mineralogy Division of ATS. These consisted of X-ray powder diffraction (XRD) and microbeam analysis techniques. Condensed summaries of these techniques are presented below.

X-ray powder diffraction (XRD)

XRD analyses were conducted on various samples, pulverised in a Siebtechnik mill. This qualitative technique was usually utilised in the beginning of the experimental program to identify the major (20-100%), minor (5-20%) and trace (< 5%) amount of different mineral phases in concentrate, residue and precipitate samples. A Siemens D-500 X-ray diffractometer was employed using Cu-Kα radiation and a step size of 0.02° 2θ with a counting time of 1 second per step. The sample was scanned over a range of 4° to 76° 2θ. This configuration gave a detection limit of approximately 3 to 4 volume % of the crystalline phases present in the sample.

Backscattered electron (BSE) imaging

A representative sub-sample was mounted in epoxy resin, polished and coated with carbon to increase the surface conductivity. BSE images were captured on a scanning electron microscope (SEM; see below). BSE images are essentially average atomic number contrast images. Minerals with different chemical compositions have different grey levels based upon the average atomic number, with heavier particles, *e.g.*, base metal sulfides, having higher BSE brightness levels than less dense gangue mineral phases. These BSE images were not only used to produce two-dimensional views (photomicrographs) of head and residue particles, but also formed the fundamental basis of the bulk modal and mineral liberation analyses.

Stellenbosch University http://scholar.sun.ac.za

Bulk modal analysis

SEM-based image analysis was used to determine the modal composition (proportions of different minerals) of the various head samples used in this study. Various sub-samples were mounted in epoxy resin and polished sections were prepared. These sections were then carbon coated to enhance the surface conductivity. The QEMSCAN™ system was used, consisting of a Leo 1450 SEM, Bruker X-ray detectors, Intellection QEMSEM integrated control hardware and Intellection iDiscover™ analytic software suite. The QEMSCAN technique uses point analyses and trace mineral search (TMS) measurements for the bulk modal and base metal sulfide (BMS) liberation analyses (see below). BSE images from the SEM were used as input to the image analyser. As mentioned above, the TMS measurement detects particles with a BSE image intensity using set grey levels (sulfide minerals appear as bright grains & are easily identified in mixtures of much darker silicate phases). Phase discrimination was based on both BSE intensity and X-ray spectral signatures; the software database contained BSE intensity window (grey level window) and typical X-ray analysis values for every mineral phase. The relative proportions of every mineral phase were determined by the automated counting of the number of pixels. The number of pixels, calculated as a percentage of the total number of pixels (area percentage), was assumed equal to the bulk volume percentage of that phase based on previous stereological studies. This volume percentage was converted into a mass percentage by multiplication of a mineral-specific density (also stored in the iDiscover database). Some minerals have similar average atomic numbers and consequently, displayed similar BSE intensities and this is where X-ray analysis proved invaluable in differentiating these types of phases. Chemical analysis, using energy dispersive X-ray (EDX) spectroscopy, was additionally used to identify the mineral phase to which a specific pixel belonged. The mass percentage of the most important BMS and gangue minerals were determined in this way. Around 30 000 particles were measured per sample at 2 μm beam stepping intervals. 1000 X-ray counts were requested per analysis point and were compared to the library of mineral identification rules (SIP lists). On average, 950 000 analysis points were obtained per sample, at about 7 micro-seconds per point.

Mineral liberation analysis

Liberation analyses were calculated using the iDiscover™ software suite and are based on area percent liberation classes. For instance, if a particle contains 10 area % of a mineral of interest, it is said to be 10% liberated. For simplification, similar minerals were grouped together in what are known as secondary lists. For instance, chalcopyrite, chalcocite/digenite, covellite and bornite were grouped under copper sulfides. Similarly, pyrite and pyrrhotite were grouped under iron sulfides. In addition, all sulfides were combined in a single category and treated as a single entity.

Stellenbosch University http://scholar.sun.ac.za

Mineral liberation analyzer (MLA)

Polished sections of the samples were prepared and examined using a mineral liberation analyzer (MLA). This is an automated analysis system that can identify mineral phases in polished sections of particulate (or lump) materials by combining BSE image analysis and X-ray mineral identification. It is used to quantify a wide range of particle characteristics, such as abundance, composition, grain size, liberation and association. It consists of a SEM (MLA 600F) and multiple high-speed energy EDX spectrometers, with advanced automated purpose-written software (developed by the scientific instruments company, FEI & its partner JKTech). Selected leach residue samples were analysed using a field emission gun (FEG-SEM) system. The FEG produces an electron beam which is smaller in diameter, more coherent and with up to three orders of magnitude greater current density or brightness than can be achieved with conventional tungsten filaments. The result is significantly improved signal-to-noise ratio and spatial resolution, and greatly increased emitter life and reliability compared with tungsten devices. It should be noted that the SEM-EDX analysis technique, utilised by both the MLA 600F and FEG-SEM, is not standardised and all results are normalised. The detection limit of the technique is about 0.3 wt%. The presence of oxygen can be detected but not hydrogen; hydroxides and hydrated compounds cannot therefore be distinguished from oxides. Another feature influencing analysis results is the 'excitation envelope' generated around the incident beam at the point of analysis. Although the spot size of the incident beam is theoretically of the order of nanometres, in very fine-grained samples the effect of the excitation envelope results in X-rays from adjacent areas being collected. The effect is dependant on a number of factors, including the density of the analysed components but would be significant in the case of analysis of thin alteration rims around particles mounted in epoxy resin.

B.3.3 Secondary electron imaging (SEI)

In order to study the surface morphology of concentrate and leach residue particles, secondary electron images (SEI) were produced using a Jeol 840A SEM, with a Noran Vantage Microanalysis system (imaging & analysis). Particles were first grain-mounted and then coated with Au-Pd alloy. This was done to improve surface conductivity and, hence, to produce higher resolution images.

B.3.4 High resolution (HR) imaging

High resolution (HR) images of selected leach residue and iron(III) precipitate samples were produced using a FEI NovaNano SEM200, fitted with an EDX system for X-Ray analysis. The instrument was fitted with Everhart-Thornley detector for SEI imaging and the backscatter secondary electron detector for BSE imaging. The samples were mounted on an aluminium stub using double-sided carbon tape for analysis on the SEM. The instrument parameters (kV, spot size,

Stellenbosch University http://scholar.sun.ac.za

detector, magnification, WD) were set and indicated on the image data bar. All these images were generated at Mintek (South Africa).

B.3.5 X-ray mapping

In order to visually determine the distribution of elemental sulfur, and other elements, in a residue sample (of different particles), an X-ray mapping technique was employed. Each sample was surface mounted on a stub and carbon coated in preparation for observation. The instrument used was a Zeiss EVO® MA15 SEM equipped with a Bruker EDX spectrometer and Quantax® software. An accelerating voltage of 20 kV was employed with a detector count rate of approximately 28000 c/sec. X-ray mapping of, *e.g.*, sulfur, was performed by raster scanning the sample. This X-ray map was then superimposed on a BSE image, to show the distribution of sulfur in the sample. The relative intensity, *e.g.*, yellow in the case of sulfur, on the image indicated the relative abundance of the element in the sample at the specific location. All these images were generated at Mintek (South Africa).

B.3.6 X-ray photoelectron spectroscopy (XPS)

All XPS analyses were carried out by the Mineralogy Division of ATS with an Escalab 250, using a monochromatic Al-Kα source (15 kV, 150 W). The instrument work function was calibrated to give a binding energy (BE) of 368.3 eV for the Ag $5d_{5/2}$ line for silver and the spectrometer dispersion was adjusted to give a BE of 932.62 eV for the Cu $2p_{3/2}$ line of metallic copper. Binding energy accuracy is ±0.025 eV. The Escalab charge neutraliser system was used on all specimens. Survey spectra were collected with a pass energy of 150 eV and an analysis area of 500 μm. High resolution spectra (region scans) were obtained using 40 eV pass energy and an analysis area of 500 μm. Spectra were analysed using Thermo Avantage software (ver. 4.30). Charge compensation was used. It should be noted that in the C1*s* spectra for each sample surface, the charge compensation can be different. The C1*s* peak was referenced to a BE for uncharged hydrocarbon at 284.8 eV and BEs in all other spectra for the sample corrected for this shift. The samples were analysed by depth profiling, which is a process whereby a series of spectra are acquired at different physical levels within a sample by alternating data acquisition with sample layer removal. A profile of the sample is built up over time which represents the composition of the sample at and below the surface of the original sample. Layer removal was carried out by an argon ion gun source.

B.3.7 Mössbauer-effect spectroscopy (MES)

^{57}Fe Mössbauer spectroscopy measurements were conducted in the Mössbauer Laboratory of the School of Physics at WITS in Johannesburg. Mössbauer-effect spectroscopy (MES) only detects iron-bearing phases and is a (nuclear) γ-radiation resonance technique, involving the recoil-free emission of probing radiation by the source and the subsequent recoil-free absorption of this γ-

Stellenbosch University http://scholar.sun.ac.za

radiation by ^{57}Fe nuclei in the absorber, *i.e.*, sample of interest. As such, it is extremely sensitive to the local surroundings of ^{57}Fe atoms; these have a 2% natural abundance and are therefore present in all iron-bearing compounds. The local surroundings of the iron nuclei are primarily constituted by the electronic structure of the iron atom, the compositional make-up of neighbouring atoms and by neighbouring defect structures. Therefore, in the case of iron-bearing compounds the local-probe nature of the technique makes it a powerful non-destructive analytical tool for establishing the oxidation state of iron, *e.g.*, iron(II) or iron(III), quantifying the relative abundance of different iron compounds within the same sample, *i.e.*, phase analysis, and establishing the overall crystal chemistry when used in conjunction with complementary techniques, *e.g.*, XRD and SEM. Typically iron-phase abundances to as low as 5% may be detected with high accuracy. Moreover, as an atomic-scale local probe, it is equally effective in the analysis of poorly crystallised or amorphous materials where conventional macroscopic-type probes, like XRD, have considerable limitations.

The spectral parameters, that serve as fingerprints in conventional transmission MES, are the isomer shift, δ, quadrupole splitting ,QS, magnetic hyperfine field, B_{hf}, and linewidth, Γ, all of which serve to characterize the chemical state of iron in the solid phase. ^{57}Fe Mössbauer spectra measurements are recorded in the normal transmission geometry. A WISSEL constant acceleration motor was used to scan the velocity range of interest, with a ^{57}Co(Rh) source (~50 mCi) at room temperature. The absorbers (samples of interest) were thoroughly mixed with an inorganic buffer to form a homogeneous disk of uniform thickness in copper powder clamp sample holders, with sample thicknesses between 30 and 50 mg/cm^2, depending on the iron concentration. Each spectrum was measured for about 24 hours. Velocity calibration was obtained by measuring the spectrum of a 25 µm thick iron foil at room temperature (this gave a linewidth of Γ= 0.26mm/sec). Each spectrum was recorded in 1024 channels to ensure at least 10^5 counts in each channel. Prior to fitting, each spectrum was folded to remove geometrical baseline curvature. Each spectrum, comprising 512 channels, was analysed using the non-linear least-squares fitting program NORMOS-90 (distributed by Wissenschaftliche Elektronik GmbH-Germany). The nuclear hyperfine interaction parameters, comprising the isomer shift, quadrupole splitting, magnetic hyperfine field and linewidth, were extracted from the least-squares fits of the data. Each spectrum comprised a superposition of sub-spectra (sextets & doublets), which represented different iron-bearing phases in the sample. Each spectrum was fitted with three sextets and a doublet, and the integrated area under each sub-spectrum then yielded the abundance of that particular phase of iron.

Stellenbosch University http://scholar.sun.ac.za

APPENDIX C. DETAILED MASS TRANSFER TEST RESULTS

This appendix summarises the detailed oxygen mass transfer test results in sequential order, as discussed in Section 3.5 (Ch. 3). The tests conducted in the 1-gallon autoclave (App. C.2, C.3 & C.4) aimed to identify the correct physical absorption regime when using the indirect (chemical) method and also to quantify the effect of temperature and slurry pulp density, using sphalerite concentrate. These series are then followed by the tests conducted in the 2-litre autoclave (App. C.5 & C.6) to assess its k_La-value at different reactor volumes and temperatures. The k_La-value is also quantified in each of the continuous pilot autoclave compartments, at different overflow levels (App. C.7). The next test series were conducted in the 7-litre glass reaction vessel (App. C.8, C.9 & C.10) and focused on the effect of the reactor volume, oxygen partial pressure, surfactants and slurry pulp density (using chalcopyrite concentrate) on the k_La-value. Finally, direct oxygen electrode measurements were used to measure the k_La-value in the 2-litre autoclave at various operating volumes and slurry pulp densities (using chalcopyrite & hematite particles) (App. C.11 & C.12). The important experimental data and regressed k_La-values of each test are summarised in figure format at the end of each section. The detailed experimental procedures are summarised below (the equipment is described in Sect. 3.4.1).

C.1 Detailed experimental procedures

C.1.1 Indirect (chemical) method

The experimental procedure was virtually the same for all the reactors used in this study:

- The reaction vessel was charged with sodium sulfite solution, in excess of 1 mol/kg SO_3^{2-}
- The required amount of cobalt catalyst, additives and/or solids were then added
- The vessel contents were heated to the target temperature, with the impeller stirring slowly
- The vessel was then subjected to the required pressure and gas composition by continuously cycling (feeding & venting) excess gas *via* the vapour phase. The gas flowrate was set using a Bronkhorst High-Tech B.V. mass-flow meter and controller
- The agitation speed was then increased to the required setpoint value
- The reaction was allowed to proceed for a few minutes, after which two ‘time zero’ samples were taken and the clock started
- Regular (10-20 mL) samples were taken over time, as determined by the extent of the oxidation reaction. A ‘dead’ sample of similar volume preceded each actual sample, to clear any stagnant solution that may have occupied the dip tube, sampling bomb or its connection lines
- Each sample was cooled to approximately room temperature in an ice bath, immediately after being taken from the reactor

Stellenbosch University http://scholar.sun.ac.za

- An accurate volume (4 mL) was then transferred *via* a pipette from the cooled sample to a pre-prepared iodine solution and kept in a dark place before being analysed, and
- Each sample was subjected to an iodometric back-titration procedure (App. B.2.3) to determine the residual sulfite concentration remaining in the reactor, which, in turn, yielded the amount of oxygen reacted (Rx. 3.5) over time.

C.1.2 Direct (oxygen electrode) method

This experimental procedure may be summarised as follows (see Figure 3.5 & 3.6):

- Two electrodes, *i.e.*, a Mettler Toledo InLab 605 and an InPro 6800, were used in tandem to add more confidence to the results. The output from the InLab 605 electrode was recorded manually at 5 sec intervals, using a hand-held transmitter. The signal from the InPro 6800 electrode was used as the primary source of data and was logged automatically (at 0.1 sec intervals) by an Agilent 34970A data acquisition unit, connected to a Mettler Toledo 4100 transmitter
- Prior to conducting a new series of tests, the probe internals were cleaned and the membrane on each electrode replaced. The InLab 605 electrode was left overnight in water, while the InPro 6800 electrode was polarized with a Mettler Toledo Sensor-Master for a 24 hr period
- Both electrodes were then subjected to a two-point calibration, *i.e.*, first in vapour-saturated air (inside a closed bottle at 1 cm above the water surface) and then in an oxygen-free (0.25 mol/kg Na_2SO_3) solution
- The reaction vessel was charged with electrolyte solution and heated to the required operating temperature by circulating hot water (Julabo F12-SL HighTech Series bath & heating circulator) through the internal autoclave coil
- The vessel contents were then deoxygenated by adding a known amount of sodium sulfite salt and 10 mg/kg Co(II) catalyst, while continuously stirring the solution at a low agitation speed and circulating solution through the down-flow pipe (Figure 3.5) back to the vessel
- The calibrated electrodes were then inserted into the down-flow pipe. The plug ensured that the electrode membrane was fully submerged in the circulating electrolyte solution. The function of this down-flow pipe was to dislodge most oxygen bubbles from solution, before coming in contact with the electrode membrane and also to ensure relatively smooth (laminar) flow over the membrane
- The circulating flow was then increased to maximum speed, which reduced the time lag between the reactor contents and the solution in contact with the electrode to less than 3 sec
- The vapour phase was then purged with pure oxygen at a controlled and excess flowrate (Bronkhorst High-Tech B.V. mass-flow meter), while closely monitoring the output of the

Stellenbosch University http://scholar.sun.ac.za

two oxygen electrodes (this induction period was very short in cases where the initial dissolved oxygen was not removed by adding small amounts of sulfite salt)

- The data acquisition unit started recording when the dissolved oxygen (DO) concentration deviated upwards and the variable (overhead) drive was immediately adjusted to the required setpoint agitation speed (also checked with a digital tachometer), and
- The electrodes responses were recorded until their outputs stabilised, *i.e.*, at the point where the oxygen concentration in solution reached its equilibrium value.

The electrode response time was recorded by conducting the following procedure:

- The electrode was kept in deoxygenated solution (0.25 mol/kg Na_2SO_3) until a stable and zero DO reading was obtained
- Oxygen-saturated water was prepared by vigorously stirring the reaction vessel for a prolonged period, while continuously purging the vapour phase with pure oxygen
- Both the data acquisition unit and circulating pump were then switched on
- The electrode was rapidly transferred from the oxygen-free solution and placed inside the down-flow pipe, and
- The electrode response was continuously logged until the output reading stabilised.

C.2 Identifying the physical absorption regime (indirect method) in the 1-gallon autoclave

These tests aimed at identifying the interfacial mass transfer regime in the 1-gallon autoclave (AC).

MTA1	Temp.	Imp. speed	P_g	Feed gas	Mass	[Co(II)]
1-gallon AC	(°C)	(rev/min)	(kPa)	(% O_2)	(g)	(mg/L)
	~80	500	100	100	2250	0.1
[SO_3^{2-}]	Sulfite vol.	[Iodine]	Iodine vol.	[Thiosulfate]	% Solids	[LS, QB]
(mol/L)	(mL)	(N)	(mL)	(N)	(kg/kg H_2O)	(g/L ea.)
~1.2	4	0.201	50	0.099	None	None
Time	Temp.	Thiosulfate	Density	[SO_3^{2-}] left	O_2 reacted	$[O_2]^*$
(min)	(°C)	(mL)	(g/L)	(mol/kg)	(mg/kg)	(mg/kg)
0	81	5.0	1128	1.222	0	15.3
5	82	9.2	1129	1.170	844	15.0
10	81	17.6	1130	1.064	2535	15.3
15	80	22.5	1131	1.002	3522	15.5
20	80	30.3	1131	0.904	5096	15.5
30	80	44.1	1133	0.730	7884	15.5
40	80	55.4	1134	0.586	10172	15.5
50	80	65.2	1135	0.462	12160	15.5

Stellenbosch University http://scholar.sun.ac.za

MTA2	Temp.	Imp. speed	P_g	Feed gas	Mass	[Co(II)]
1-gallon AC	(°C)	(rev/min)	(kPa)	(% O_2)	(g)	(mg/L)
	~80	500	100	100	2251	5.0
$[SO_3^{2-}]$	Sulfite vol.	[Iodine]	Iodine vol.	[Thiosulfate]	% Solids	[LS, QB]
(mol/L)	(mL)	(N)	(mL)	(N)	(kg/kg H_2O)	(g/L ea.)
~1.2	4	0.201	50	0.099	None	None
Time	Temp.	Thiosulfate	Density	$[SO_3^{2-}]$ left	O_2 reacted	$[O_2]^*$
(min)	(°C)	(mL)	(g/L)	(mol/kg)	(mg/kg)	(mg/kg)
0	82	5.1	1128	1.221	0	15.0
5	83	10.7	1129	1.151	1126	14.8
10	83	19.1	1130	1.045	2817	14.8
15	82	25.2	1131	0.968	4047	15.0
20	81	35.8	1132	0.834	6186	15.3
30	81	54.1	1134	0.603	9889	15.3
40	80	70.2	1136	0.399	13156	15.5
50	80	86.4	1138	0.193	16452	15.5

MTA3	Temp.	Imp. speed	P_g	Feed gas	Mass	[Co(II)]
1-gallon AC	(°C)	(rev/min)	(kPa)	(% O_2)	(g)	(mg/L)
	~80	500	250	21	2252	0.1
$[SO_3^{2-}]$	Sulfite vol.	[Iodine]	Iodine vol.	[Thiosulfate]	% Solids	[LS, QB]
(mol/L)	(mL)	(N)	(mL)	(N)	(kg/kg H_2O)	(g/L ea.)
~1.2	4	0.199	50	0.099	None	None
Time	Temp.	Thiosulfate	Density	$[SO_3^{2-}]$ left	O_2 reacted	$[O_2]^*$
(min)	(°C)	(mL)	(g/L)	(mol/kg)	(mg/kg)	(mg/kg)
0	81	4.1	1129	1.221	0	6.7
15	81	7.4	1129	1.179	663	6.7
30	81	10.8	1129	1.137	1347	6.7
60	80	19.9	1130	1.022	3180	6.8
90	80	29.8	1131	0.897	5176	6.8
120	80	38.5	1132	0.788	6934	6.8

Stellenbosch University http://scholar.sun.ac.za

MTA4	Temp.	Imp. speed	P_g	Feed gas	Mass	[Co(II)]
1-gallon AC	(°C)	(rev/min)	(kPa)	(% O_2)	(g)	(mg/L)
	~80	500	250	21	2250	5.0
[SO_3^{2-}]	Sulfite vol.	[Iodine]	Iodine vol.	[Thiosulfate]	% Solids	[LS, QB]
(mol/L)	(mL)	(N)	(mL)	(N)	(kg/kg H_2O)	(g/L ea.)
~1.2	4	0.199	50	0.098	None	None
Time	Temp.	Thiosulfate	Density	[SO_3^{2-}] left	O_2 reacted	[O_2]*
(min)	(°C)	(mL)	(g/L)	(mol/kg)	(mg/kg)	(mg/kg)
0	81	4.0	1128	1.223	0	6.7
15	81	6.9	1129	1.187	577	6.7
30	81	11.3	1129	1.132	1453	6.7
60	81	19.4	1130	1.031	3068	6.7
90	80	28.7	1131	0.915	4924	6.8
120	80	38.8	1132	0.789	6944	6.8

MTA5	Temp.	Imp. speed	P_g	Feed gas	Mass	[Co(II)]
1-gallon AC	(°C)	(rev/min)	(kPa)	(% O_2)	(g)	(mg/L)
	~80	500	50	100	2251	5.0
[SO_3^{2-}]	Sulfite vol.	[Iodine]	Iodine vol.	[Thiosulfate]	% Solids	[LS, QB]
(mol/L)	(mL)	(N)	(mL)	(N)	(kg/kg H_2O)	(g/L ea.)
~1.2	4	0.199	50	0.098	None	None
Time	Temp.	Thiosulfate	Density	[SO_3^{2-}] left	O_2 reacted	[O_2]*
(min)	(°C)	(mL)	(g/L)	(mol/kg)	(mg/kg)	(mg/kg)
0	81	4.5	1129	1.216	0	9.7
15	81	10.3	1129	1.144	1155	9.7
30	80	17.2	1130	1.058	2530	10.0
60	80	33.1	1132	0.860	5704	10.0
90	80	47.9	1134	0.675	8666	10.0
120	80	64.7	1135	0.464	12038	10.0
150	80	75.7	1137	0.326	14251	10.0

Stellenbosch University http://scholar.sun.ac.za

MTA6	Temp.	Imp. speed	P_g	Feed gas	Mass	[Co(II)]
1-gallon AC	(°C)	(rev/min)	(kPa)	(% O_2)	(g)	(mg/L)
	~80	500	75	100	2250	5.0
$[SO_3^{2-}]$	Sulfite vol.	[Iodine]	Iodine vol.	[Thiosulfate]	% Solids	[LS, QB]
(mol/L)	(mL)	(N)	(mL)	(N)	(kg/kg H_2O)	(g/L ea.)
~1.2	4	0.202	50	0.098	None	None
Time	Temp.	Thiosulfate	Density	$[SO_3^{2-}]$ left	O_2 reacted	$[O_2]^*$
(min)	(°C)	(mL)	(g/L)	(mol/kg)	(mg/kg)	(mg/kg)
0	81	5.2	1128	1.227	19	12.5
5	82	8.0	1129	1.192	577	12.3
10	83	12.1	1129	1.141	1393	12.0
15	82	16.6	1130	1.085	2290	12.3
20	81	20.6	1130	1.035	3087	12.5
30	80	29.8	1131	0.920	4923	12.8
40	80	38.8	1132	0.808	6723	12.8
50	80	48.0	1133	0.693	8564	12.8

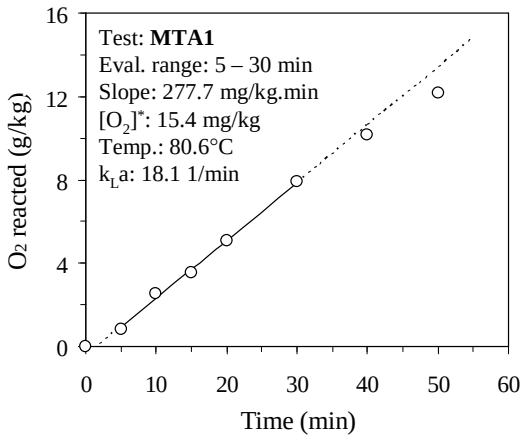

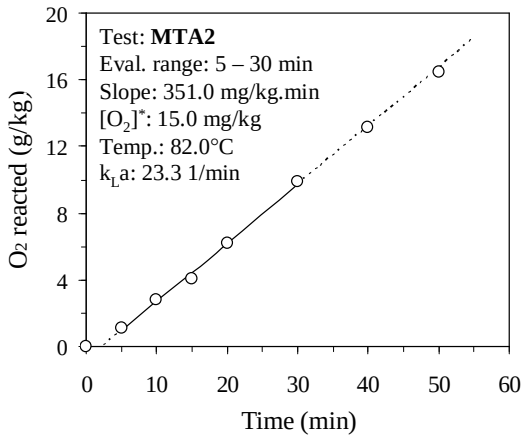

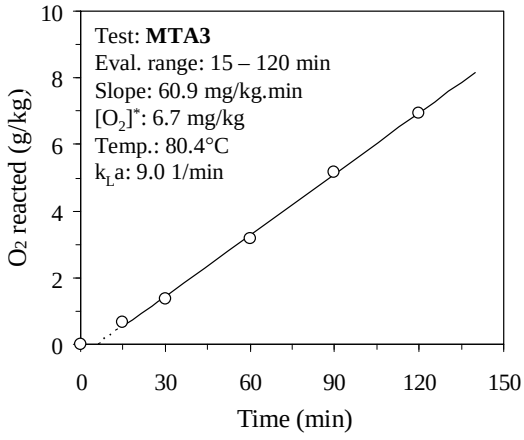

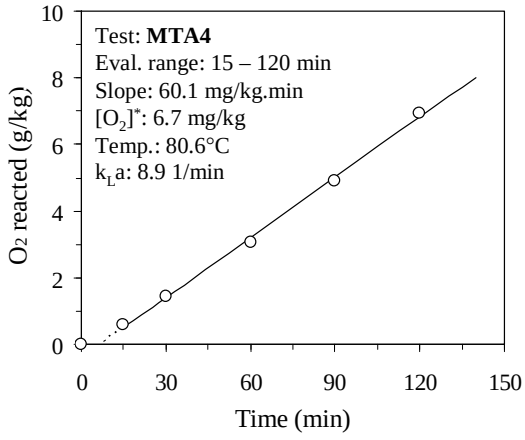

Stellenbosch University http://scholar.sun.ac.za

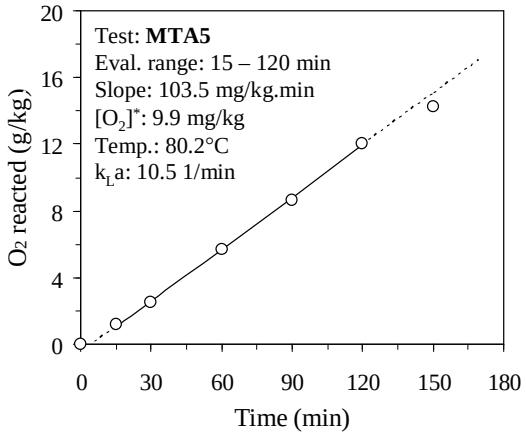

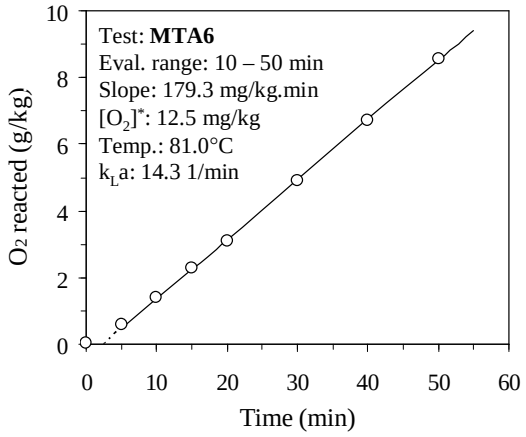

C.3 The effect of temperature on the k_La-value (1-gallon autoclave)

These tests aimed at quantifying the effect of temperature on the k_La-value (indirect method).

MTB1	Temp.	Imp. speed	P_g	Feed gas	Mass	[Co(II)]
1-gallon AC	(°C)	(rev/min)	(kPa)	(% O_2)	(g)	(mg/L)
	40	500	250	21	2300	0.1
$[SO_3^{2-}]$	Sulfite vol.	[Iodine]	Iodine vol.	[Thiosulfate]	% Solids	[LS, QB]
(mol/L)	(mL)	(N)	(mL)	(N)	(kg/kg H_2O)	(g/L ea.)
~1.2	4	0.198	50	0.102	None	None
Time	Temp.	Thiosulfate	Density	$[SO_3^{2-}]$ left	O_2 reacted	$[O_2]^*$
(min)	(°C)	(mL)	(g/L)	(mol/kg)	(mg/kg)	(mg/kg)
0	40	4.6	1129	1.207	344	10.0
15	40	7.6	1129	1.168	965	10.0
30	40	10.5	1129	1.130	1566	10.0
60	40	16.4	1130	1.054	2790	10.0
90	40	21.9	1131	0.982	3932	10.0
120	40	29.1	1132	0.889	5429	10.0
150	40	35.4	1132	0.807	6740	10.0
180	40	42.6	1133	0.713	8240	10.0
210	40	47.1	1134	0.654	9178	10.0
240	40	53.7	1135	0.568	10556	10.0

Stellenbosch University http://scholar.sun.ac.za

MTB2	Temp.	Imp. speed	P_g	Feed gas	Mass	[Co(II)]
1-gallon AC	(°C)	(rev/min)	(kPa)	(% O_2)	(g)	(mg/L)
	60	500	250	21	2280	0.1
$[SO_3^{2-}]$	Sulfite vol.	[Iodine]	Iodine vol.	[Thiosulfate]	% Solids	[LS, QB]
(mol/L)	(mL)	(N)	(mL)	(N)	(kg/kg H_2O)	(g/L ea.)
~1.2	4	0.198	50	0.102	None	None
Time	Temp.	Thiosulfate	Density	$[SO_3^{2-}]$ left	O_2 reacted	$[O_2]^*$
(min)	(°C)	(mL)	(g/L)	(mol/kg)	(mg/kg)	(mg/kg)
0	60	4.9	1129	1.203	406	8.0
15	60	10.3	1129	1.133	1525	8.0
30	60	13.4	1130	1.093	2168	8.0
60	60	21.8	1131	0.984	3911	8.0
90	60	29.7	1132	0.881	5553	8.0
120	60	36.8	1132	0.789	7031	8.0
150	60	44.6	1133	0.687	8657	8.0

MTB3	Temp.	Imp. speed	P_g	Feed gas	Mass	[Co(II)]
1-gallon AC	(°C)	(rev/min)	(kPa)	(% O_2)	(g)	(mg/L)
	100	500	250	21	2220	0.1
$[SO_3^{2-}]$	Sulfite vol.	[Iodine]	Iodine vol.	[Thiosulfate]	% Solids	[LS, QB]
(mol/L)	(mL)	(N)	(mL)	(N)	(kg/kg H_2O)	(g/L ea.)
~1.2	4	0.198	50	0.102	None	None
Time	Temp.	Thiosulfate	Density	$[SO_3^{2-}]$ left	O_2 reacted	$[O_2]^*$
(min)	(°C)	(mL)	(g/L)	(mol/kg)	(mg/kg)	(mg/kg)
0	100	7.8	1129	1.165	1006	5.5
15	100	16.1	1130	1.058	2728	5.5
30	100	20.9	1131	0.995	3724	5.5
60	100	34.7	1132	0.816	6594	5.5
90	100	46.7	1134	0.660	9095	5.5
120	100	58.9	1135	0.500	11643	5.5

Stellenbosch University http://scholar.sun.ac.za

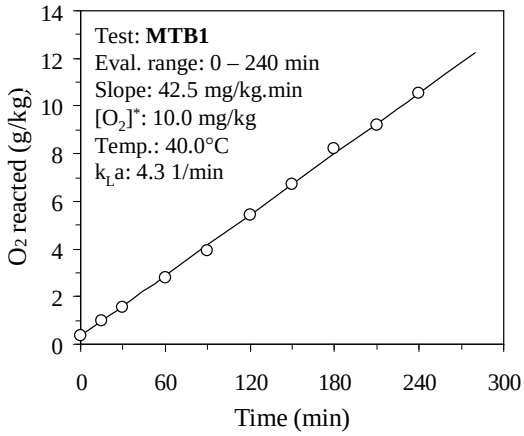

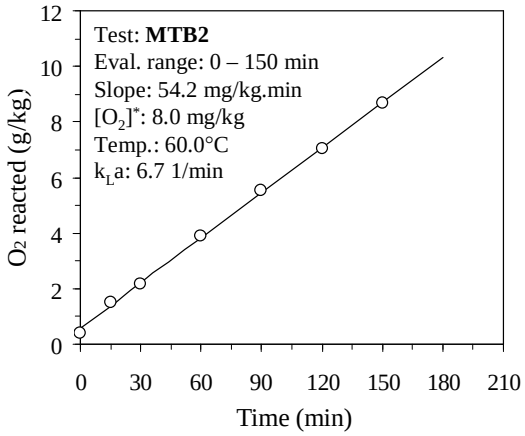

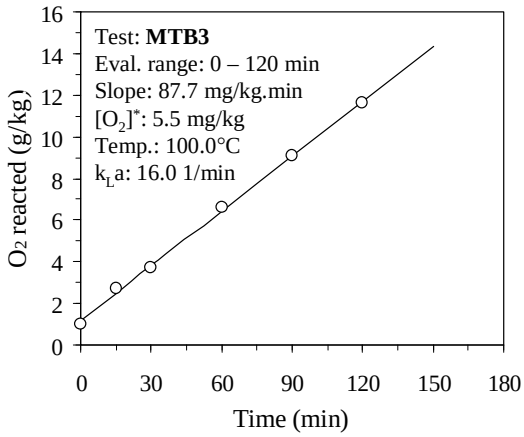

Stellenbosch University http://scholar.sun.ac.za

C.4 The effect of sulfide concentrate pulp density on the k_La-value (1-gallon autoclave)

These tests aimed at quantifying the effect of sulfide mineral particles on the k_La-value (indirect method). The concentrate (34% S^{Y-}) consisted predominantly of sphalerite (54% Zn, 7% Fe), with minor amounts of pyrite and pyrrhotite (3% Fe) and trace amount of chalcopyrite (1% Cu). The particle size distribution (PSD) was as follows: d_{10} = 15 µm, d_{50} = 36 µm and d_{90} = 92 µm.

MTC1	Temp.	Imp. speed	P_g	Feed gas	Mass	[Co(II)]
1-gallon AC	(°C)	(rev/min)	(kPa)	(% O_2)	(g)	(mg/L)
	~80	500	250	21	2250	0.1
$[SO_3^{2-}]$	Sulfite vol.	[Iodine]	Iodine vol.	[Thiosulfate]	% Solids	[LS, QB]
(mol/L)	(mL)	(N)	(mL)	(N)	(kg/kg H_2O)	(g/L ea.)
~1.2	4	0.192	50	0.102	2.9	None
Time	Temp.	Thiosulfate	Density	$[SO_3^{2-}]$ left	O_2 reacted	$[O_2]^*$
(min)	(°C)	(mL)	(g/L)	(mol/kg)	(mg/kg)	(mg/kg)
0	80	5.9	1129	1.152	1222	6.8
15	81	11.4	1130	1.080	2363	6.7
30	80	15.4	1130	1.028	3193	6.8
60	80	24.8	1131	0.906	5146	6.8
90	80	33.4	1132	0.795	6936	6.8
120	80	43.7	1134	0.660	9083	6.8
150	80	52.4	1135	0.547	10899	6.8

MTC2	Temp.	Imp. speed	P_g	Feed gas	Mass	[Co(II)]
1-gallon AC	(°C)	(rev/min)	(kPa)	(% O_2)	(g)	(mg/L)
	80	500	250	21	2240	0.1
$[SO_3^{2-}]$	Sulfite vol.	[Iodine]	Iodine vol.	[Thiosulfate]	% Solids	[LS, QB]
(mol/L)	(mL)	(N)	(mL)	(N)	(kg/kg H_2O)	(g/L ea.)
~1.2	4	0.192	50	0.097	8.7	None
Time	Temp.	Thiosulfate	Density	$[SO_3^{2-}]$ left	O_2 reacted	$[O_2]^*$
(min)	(°C)	(mL)	(g/L)	(mol/kg)	(mg/kg)	(mg/kg)
0	80	5.7	1129	1.157	1131	6.8
15	80	10.5	1130	1.098	2084	6.8
30	80	14.7	1130	1.046	2918	6.8
60	80	23.2	1131	0.940	4605	6.8
90	80	32.5	1132	0.825	6451	6.8
120	80	41.5	1133	0.713	8238	6.8
150	80	50.7	1134	0.599	10064	6.8

Stellenbosch University http://scholar.sun.ac.za

MTC3	Temp.	Imp. speed	P_g	Feed gas	Mass	[Co(II)]
1-gallon AC	(°C)	(rev/min)	(kPa)	(% O_2)	(g)	(mg/L)
	80	500	250	21	2215	0.1
$[SO_3^{2-}]$	Sulfite vol.	[Iodine]	Iodine vol.	[Thiosulfate]	% Solids	[LS, QB]
(mol/L)	(mL)	(N)	(mL)	(N)	(kg/kg H_2O)	(g/L ea.)
~1.2	4	0.192	50	0.097	17.7	None
Time	Temp.	Thiosulfate	Density	$[SO_3^{2-}]$ left	O_2 reacted	$[O_2]^*$
(min)	(°C)	(mL)	(g/L)	(mol/kg)	(mg/kg)	(mg/kg)
0	80	4.9	1129	1.167	973	6.8
15	80	9.3	1129	1.113	1846	6.8
30	80	12.8	1130	1.069	2541	6.8
60	80	21.1	1131	0.966	4188	6.8
90	80	29.2	1132	0.866	5796	6.8
120	80	38.5	1133	0.750	7642	6.8
150	80	47.5	1134	0.639	9429	6.8

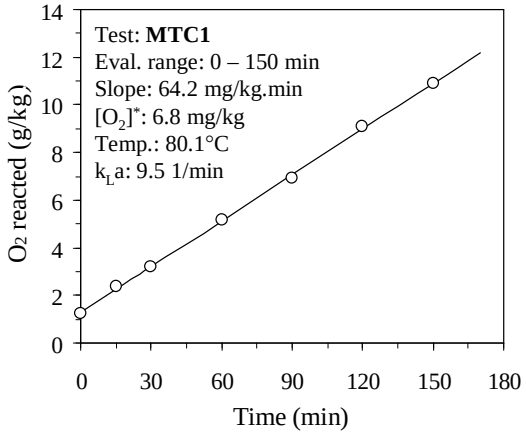

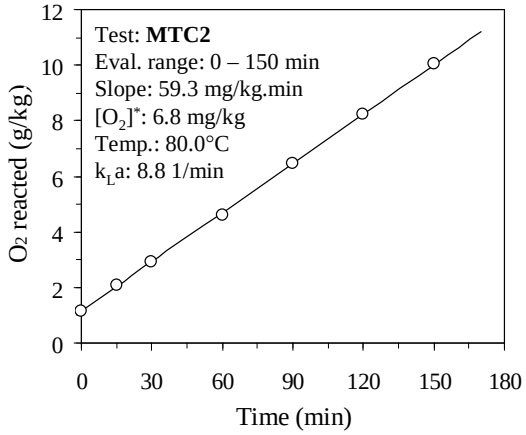

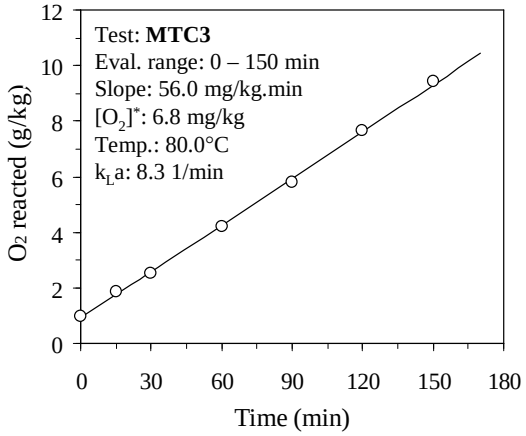

Stellenbosch University http://scholar.sun.ac.za

C.5 Identifying the physical absorption regime and determining the effect of the solution volume on the k_La-value (2-litre autoclave).

Identifying the physical absorption regime and determining the effect of volume (indirect method).

MTD1	Temp.	Imp. speed	P_g	Feed gas	Mass	[Co(II)]
2-litre AC	(°C)	(rev/min)	(kPa)	(% O_2)	(g)	(mg/L)
Imp. conf. (A)	100	1000	100	100	1300	0.1
[SO_3^{2-}]	Sulfite vol.	[Iodine]	Iodine vol.	[Thiosulfate]	% Solids	[LS, QB]
(mol/L)	(mL)	(N)	(mL)	(N)	(kg/kg H_2O)	(g/L ea.)
~1.3	4	0.205	50	0.093	None	None
Time	Temp.	Thiosulfate	Density	[SO_3^{2-}] left	O_2 reacted	$[O_2]^*$
(min)	(°C)	(mL)	(g/L)	(mol/kg)	(mg/kg)	(mg/kg)
0	100	12.4	1141	1.167	2650	9.3
5	100	14.4	1141	1.144	3029	9.3
20	100	20.2	1141	1.075	4128	9.3
40	100	30.6	1142	0.952	6102	9.3
60	100	38.6	1143	0.857	7623	9.3
80	100	48.4	1144	0.740	9488	9.3
100	100	58.0	1145	0.626	11319	9.3
120	100	68.2	1146	0.504	13267	9.3
140	100	75.6	1147	0.415	14682	9.3
160	100	80.2	1148	0.360	15563	9.3
180	100	83.4	1148	0.322	16176	9.3

MTD2	Temp.	Imp. speed	P_g	Feed gas	Mass	[Co(II)]
2-litre AC	(°C)	(rev/min)	(kPa)	(% O_2)	(g)	(mg/L)
Imp. conf. (A)	150	1000 (A)	550	21	1301	5.0
[SO_3^{2-}]	Sulfite vol.	[Iodine]	Iodine vol.	[Thiosulfate]	% Solids	[LS, QB]
(mol/L)	(mL)	(N)	(mL)	(N)	(kg/kg H_2O)	(g/L ea.)
~1.3	4	0.205	50	0.093	None	None
Time	Temp.	Thiosulfate	Density	[SO_3^{2-}] left	O_2 reacted	$[O_2]^*$
(min)	(°C)	(mL)	(g/L)	(mol/kg)	(mg/kg)	(mg/kg)
0	150	6.2	1140	1.241	1477	4.7
40	150	16.6	1141	1.118	3446	4.7
60	150	30.4	1142	0.954	6064	4.7
80	150	45.6	1144	0.773	8955	4.7
100	150	68.4	1146	0.501	13305	4.7
120	150	80.6	1148	0.355	15640	4.7

Stellenbosch University http://scholar.sun.ac.za

MTD3	Temp.	Imp. speed	P_g	Feed gas	Mass	[Co(II)]
2-litre AC	(°C)	(rev/min)	(kPa)	(% O_2)	(g)	(mg/L)
Imp. conf. (A)	150	1000	500	21	1300	1.0
$[SO_3^{2-}]$	Sulfite vol.	[Iodine]	Iodine vol.	[Thiosulfate]	% Solids	[LS, QB]
(mol/L)	(mL)	(N)	(mL)	(N)	(kg/kg H_2O)	(g/L ea.)
~1.3	4	0.204	50	0.095	None	None
Time	Temp.	Thiosulfate	Density	$[SO_3^{2-}]$ left	O_2 reacted	$[O_2]^*$
(min)	(°C)	(mL)	(g/L)	(mol/kg)	(mg/kg)	(mg/kg)
0	150	3.4	1140	1.267	1063	3.4
30	150	9.4	1140	1.194	2223	3.4
60	150	19.5	1141	1.072	4177	3.4
90	150	32.1	1143	0.919	6620	3.4
120	150	47.8	1144	0.728	9672	3.4
150	150	62.6	1146	0.548	12557	3.4

MTD4	Temp.	Imp. speed	P_g	Feed gas	Mass	[Co(II)]
2-litre AC	(°C)	(rev/min)	(kPa)	(% O_2)	(g)	(mg/L)
Low level (A)	150	1000	500	10	950	0.1
$[SO_3^{2-}]$	Sulfite vol.	[Iodine]	Iodine vol.	[Thiosulfate]	% Solids	[LS, QB]
(mol/L)	(mL)	(N)	(mL)	(N)	(kg/kg H_2O)	(g/L ea.)
~1.3	4	0.204	50	0.095	None	None
Time	Temp.	Thiosulfate	Density	$[SO_3^{2-}]$ left	O_2 reacted	$[O_2]^*$
(min)	(°C)	(mL)	(g/L)	(mol/kg)	(mg/kg)	(mg/kg)
0	150	7.1	1140	1.222	1778	1.6
5	150	10.1	1140	1.186	2358	1.6
20	150	12.2	1141	1.160	2764	1.6
40	150	13.4	1141	1.146	2996	1.6
60	150	17.6	1141	1.095	3809	1.6
80	150	18.8	1141	1.080	4042	1.6
100	150	23.1	1142	1.028	4875	1.6
120	150	26.9	1142	0.982	5611	1.6
140	150	31.8	1143	0.923	6562	1.6

Stellenbosch University http://scholar.sun.ac.za

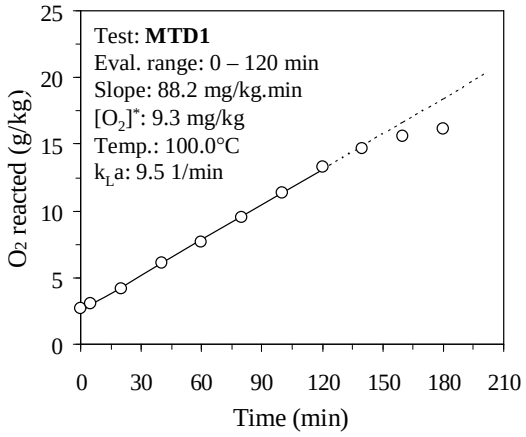

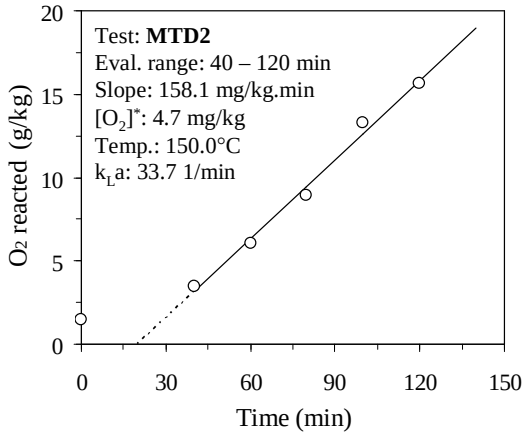

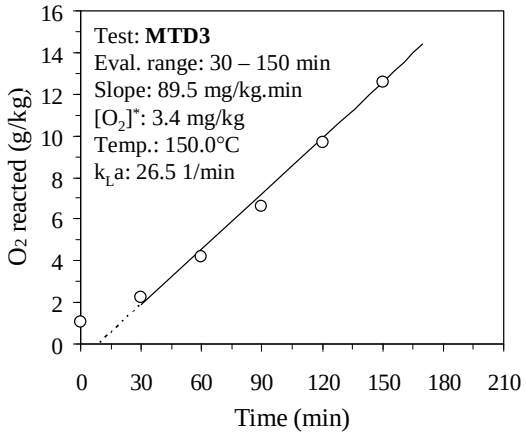

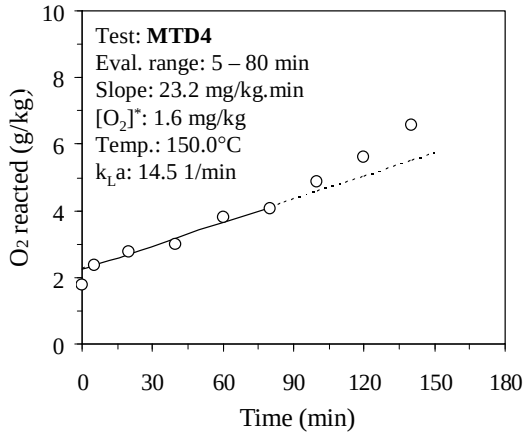

Stellenbosch University http://scholar.sun.ac.za

C.6 The effect of temperature on the k_La-value (2-litre autoclave)

These tests aimed at quantifying the effect of temperature on the k_La-value in the 2-litre autoclave (indirect method).

MTE1	Temp.	Imp. speed	P_g	Feed gas	Mass	[Co(II)]
2-litre AC	(°C)	(rev/min)	(kPa)	(% O_2)	(g)	(mg/L)
Imp. conf. (A)	80	1000	300	21	1300	1.0
[SO_3^{2-}]	Sulfite vol.	[Iodine]	Iodine vol.	[Thiosulfate]	% Solids	[LS, QB]
(mol/L)	(mL)	(N)	(mL)	(N)	(kg/kg H_2O)	(g/L ea.)
~1.3	4	0.204	50	0.105	None	None
Time	Temp.	Thiosulfate	Density	[SO_3^{2-}] left	O_2 reacted	$[O_2]^*$
(min)	(°C)	(mL)	(g/L)	(mol/kg)	(mg/kg)	(mg/kg)
0	80	2.8	1140	1.270	1004	7.6
5	80	5.2	1140	1.238	1516	7.6
20	80	10.0	1140	1.174	2542	7.6
40	80	19.0	1142	1.054	4468	7.6
60	80	25.0	1142	0.973	5753	7.6
80	80	31.5	1143	0.886	7148	7.6
100	80	35.6	1143	0.831	8028	7.6
120	80	43.6	1144	0.724	9748	7.6
140	80	48.0	1145	0.665	10695	7.6
160	80	55.8	1146	0.559	12376	7.6
180	80	61.2	1146	0.487	13541	7.6

Stellenbosch University http://scholar.sun.ac.za

MTE2	Temp.	Imp. speed	P_g	Feed gas	Mass	[Co(II)]
2-litre AC	(°C)	(rev/min)	(kPa)	(% O_2)	(g)	(mg/L)
Imp. conf. (A)	100	1000	350	21	1300	1.0
[SO_3^{2-}]	Sulfite vol.	[Iodine]	Iodine vol.	[Thiosulfate]	% Solids	[LS, QB]
(mol/L)	(mL)	(N)	(mL)	(N)	(kg/kg H_2O)	(g/L ea.)
~1.3	4	0.201	50	0.105	None	None
Time	Temp.	Thiosulfate	Density	[SO_3^{2-}] left	O_2 reacted	$[O_2]^*$
(min)	(°C)	(mL)	(g/L)	(mol/kg)	(mg/kg)	(mg/kg)
0	100	2.2	1140	1.259	1181	7.4
5	100	2.6	1140	1.254	1266	7.4
20	100	5.2	1140	1.219	1822	7.4
40	100	11.8	1141	1.131	3233	7.4
60	100	18.8	1142	1.037	4731	7.4
80	100	25.6	1142	0.946	6188	7.4
100	100	33.4	1143	0.842	7863	7.4
120	100	40.6	1144	0.745	9410	7.4
140	100	48.6	1145	0.637	11132	7.4
160	100	57.2	1146	0.521	12986	7.4
180	100	65.4	1147	0.411	14757	7.4
200	100	71.8	1148	0.324	16141	7.4

MTE3	Temp.	Imp. speed	P_g	Feed gas	Mass	[Co(II)]
2-litre AC	(°C)	(rev/min)	(kPa)	(% O_2)	(g)	(mg/L)
Imp. conf. (A)	120	1000	350	21	1300	0.1
[SO_3^{2-}]	Sulfite vol.	[Iodine]	Iodine vol.	[Thiosulfate]	% Solids	[LS, QB]
(mol/L)	(mL)	(N)	(mL)	(N)	(kg/kg H_2O)	(g/L ea.)
~1.3	4	0.201	50	0.098	None	None
Time	Temp.	Thiosulfate	Density	[SO_3^{2-}] left	O_2 reacted	$[O_2]^*$
(min)	(°C)	(mL)	(g/L)	(mol/kg)	(mg/kg)	(mg/kg)
0	120	3.0	1140	1.251	1309	5.6
5	120	3.2	1140	1.249	1349	5.6
20	120	9.8	1141	1.166	2665	5.6
40	120	18.0	1141	1.064	4303	5.6
60	120	24.8	1142	0.979	5662	5.6
80	120	34.2	1143	0.861	7545	5.6
100	120	40.8	1144	0.779	8868	5.6
120	120	50.2	1145	0.661	10756	5.6
140	120	60.8	1146	0.527	12888	5.6
160	120	69.6	1147	0.417	14662	5.6

Stellenbosch University http://scholar.sun.ac.za

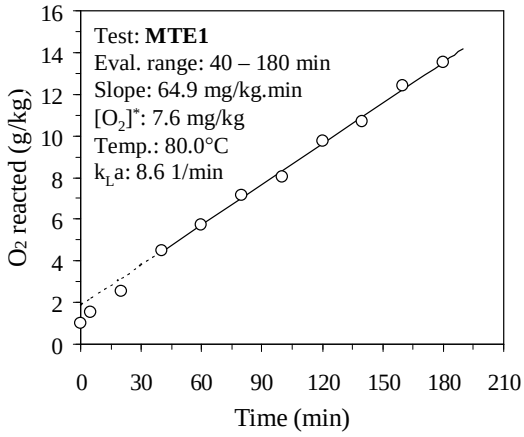

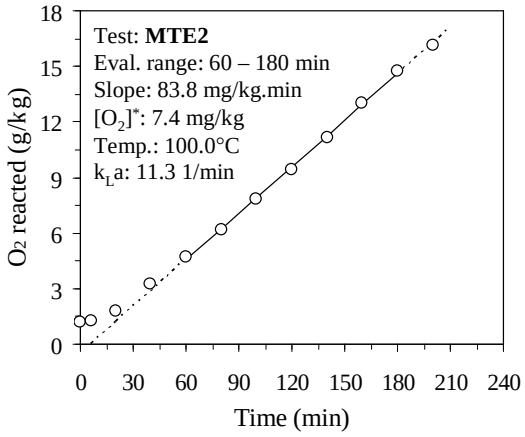

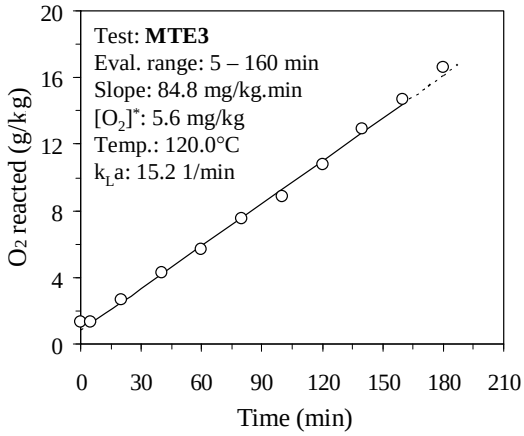

Stellenbosch University http://scholar.sun.ac.za

C.7 Effect of the overflow level on the k_La-value in different pilot autoclave compartments

These tests aimed at quantifying the effect of the overflow level on the k_La-value in the various compartments of the continuous pilot autoclave (Figure 3.3), utilising the indirect method.

MTF1	Temp.	Imp. speed	P_g	Feed gas	Mass	[Co(II)]
Pilot AC	(°C)	(rev/min)	(kPa)	(% O_2)	(g)	(mg/L)
C #1 normal	~80	1000	500	21	6500	1.0
$[SO_3^{2-}]$	Sulfite vol.	[Iodine]	Iodine vol.	[Thiosulfate]	% Solids	[LS, QB]
(mol/L)	(mL)	(N)	(mL)	(N)	(kg/kg H_2O)	(g/L ea.)
~1.3	4	0.198	50	0.098	None	None
Time	Temp.	Thiosulfate	Density	$[SO_3^{2-}]$ left	O_2 reacted	$[O_2]^*$
(min)	(°C)	(mL)	(g/L)	(mol/kg)	(mg/kg)	(mg/kg)
0	80	0.0	1140	1.269	1016	12.0
5	83	0.3	1140	1.266	1076	11.8
20	82	7.1	1140	1.181	2432	11.9
30	83	12.2	1141	1.117	3450	11.8
45	82	20.3	1142	1.016	5068	11.9
60	82	30.5	1143	0.889	7100	11.9

MTF2	Temp.	Imp. speed	P_g	Feed gas	Mass	[Co(II)]
Pilot AC	(°C)	(rev/min)	(kPa)	(% O_2)	(g)	(mg/L)
C #1+2 norm.	~80	1000	100	21	13000	1.0
$[SO_3^{2-}]$	Sulfite vol.	[Iodine]	Iodine vol.	[Thiosulfate]	% Solids	[LS, QB]
(mol/L)	(mL)	(N)	(mL)	(N)	(kg/kg H_2O)	(g/L ea.)
~1.3	4	0.198	50	0.098	None	None
Time	Temp.	Thiosulfate	Density	$[SO_3^{2-}]$ left	O_2 reacted	$[O_2]^*$
(min)	(°C)	(mL)	(g/L)	(mol/kg)	(mg/kg)	(mg/kg)
0	80	0.1	1140	1.268	1036	3.1
15	81	1.2	1140	1.255	1255	3.1
30	80	3.4	1140	1.227	1694	3.1
60	80	6.8	1140	1.185	2372	3.1
90	80	12.4	1141	1.115	3490	3.1
120	80	15.3	1141	1.078	4077	3.1

Stellenbosch University http://scholar.sun.ac.za

MTF3	Temp.	Imp. speed	P_g	Feed gas	Mass	[Co(II)]
Pilot AC	(°C)	(rev/min)	(kPa)	(% O_2)	(g)	(mg/L)
C #1+2 high	~150	1200	650	21	14000	1.0
[SO_3^{2-}]	Sulfite vol.	[Iodine]	Iodine vol.	[Thiosulfate]	% Solids	[LS, QB]
(mol/L)	(mL)	(N)	(mL)	(N)	(kg/kg H_2O)	(g/L ea.)
~1.3	4	0.200	50	0.098	None	None
Time	Temp.	Thiosulfate	Density	[SO_3^{2-}] left	O_2 reacted	$[O_2]^*$
(min)	(°C)	(mL)	(g/L)	(mol/kg)	(mg/kg)	(mg/kg)
0	160	3.5	1140	1.239	1510	4.0
5	160	7.0	1140	1.195	2208	4.0
15	155	10.1	1141	1.157	2817	5.8
30	157	13.6	1141	1.113	3526	5.1
53	155	15.4	1141	1.090	3885	5.8
75	156	20.2	1142	1.030	4844	5.5

MTF4	Temp.	Imp. speed	P_g	Feed gas	Mass	[Co(II)]
Pilot AC	(°C)	(rev/min)	(kPa)	(% O_2)	(g)	(mg/L)
C #4 normal	~150	1200	650	21	5500	1.0
[SO_3^{2-}]	Sulfite vol.	[Iodine]	Iodine vol.	[Thiosulfate]	% Solids	[LS, QB]
(mol/L)	(mL)	(N)	(mL)	(N)	(kg/kg H_2O)	(g/L ea.)
~1.3	4	0.200	50	0.098	None	None
Time	Temp.	Thiosulfate	Density	[SO_3^{2-}] left	O_2 reacted	$[O_2]^*$
(min)	(°C)	(mL)	(g/L)	(mol/kg)	(mg/kg)	(mg/kg)
0	152	13.1	1141	1.119	3426	6.7
5	154	14.2	1141	1.105	3645	6.1
10	153	29.6	1143	0.913	6725	6.4
20	152	48.2	1145	0.679	10457	6.7
30	152	58.9	1146	0.545	12609	6.7
40	151	69.9	1147	0.406	14825	7.0

Stellenbosch University http://scholar.sun.ac.za

MTF5	Temp.	Imp. speed	P_g	Feed gas	Mass	[Co(II)]
Pilot AC	(°C)	(rev/min)	(kPa)	(% O_2)	(g)	(mg/L)
C #4 high	~80	1200	100	21	7500	1.0
[SO_3^{2-}]	Sulfite vol.	[Iodine]	Iodine vol.	[Thiosulfate]	% Solids	[LS, QB]
(mol/L)	(mL)	(N)	(mL)	(N)	(kg/kg H_2O)	(g/L ea.)
~1.3	4	0.200	50	0.095	None	None
Time	Temp.	Thiosulfate	Density	[SO_3^{2-}] left	O_2 reacted	$[O_2]^*$
(min)	(°C)	(mL)	(g/L)	(mol/kg)	(mg/kg)	(mg/kg)
0	80	0.4	1140	1.277	890	3.1
15	81	1.1	1140	1.269	1025	3.1
60	81	2.6	1140	1.251	1315	3.1
120	81	4.2	1140	1.231	1624	3.1
180	81	6.1	1140	1.209	1992	3.1
240	81	8.0	1140	1.186	2359	3.1

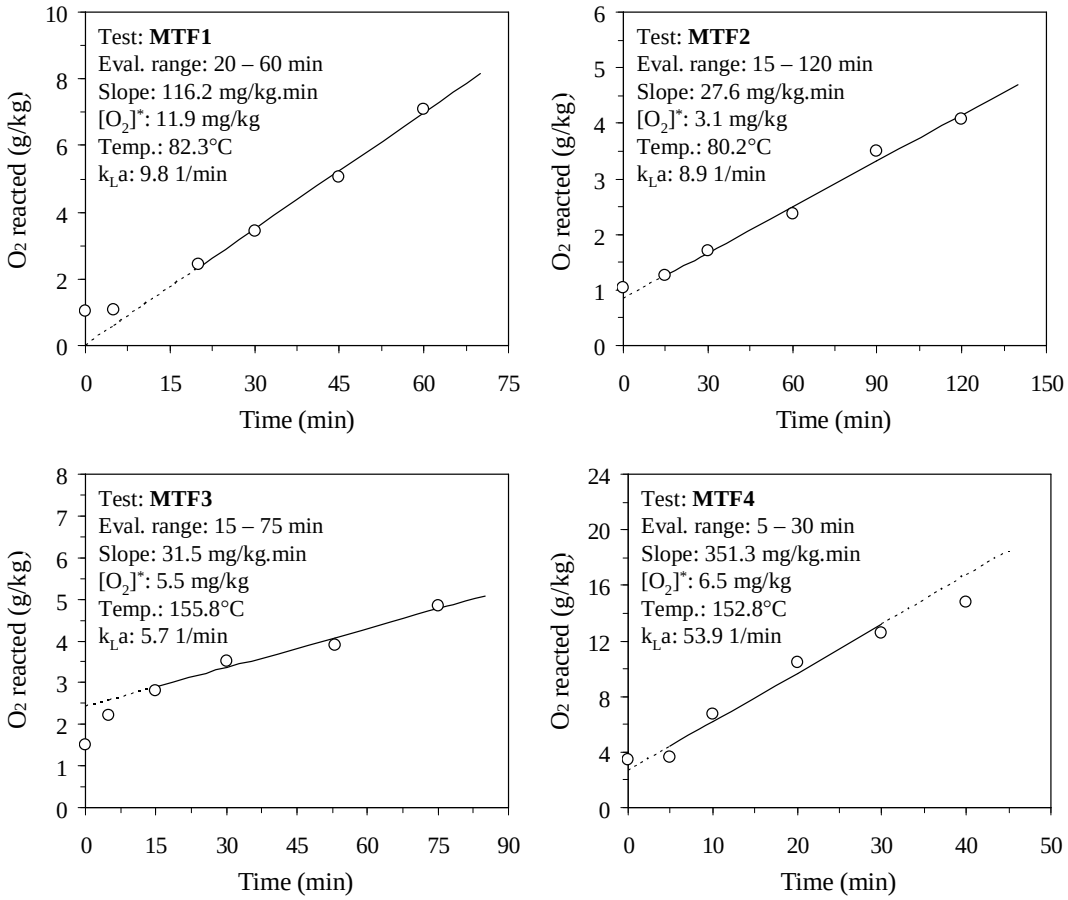

Stellenbosch University http://scholar.sun.ac.za

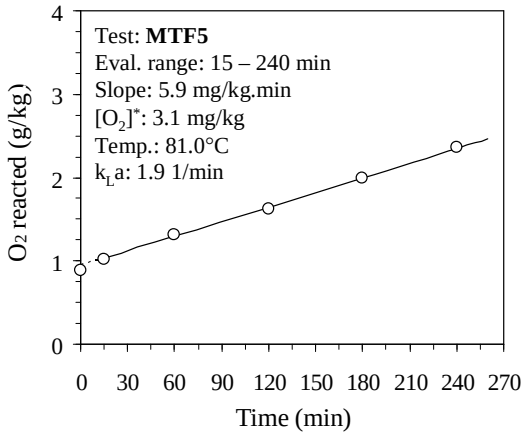

C.8 The effect of reactor volume on the k_La-value (7-litre glass reactor).

These tests aimed at quantifying the effect of reactor volume on the k_La-value in the 7-litre glass reaction vessel and also to test the repeatability of the titration (indirect) method.

MTG1	Temp.	Imp. speed	P_g	Feed gas	Mass	[Co(II)]
7-litre vessel	(°C)	(rev/min)	(kPa)	(% O_2)	(g)	(mg/L)
Low level	~50	1000	0	21	6800	0.0
$[SO_3^{2-}]$	Sulfite vol.	[Iodine]	Iodine vol.	[Thiosulfate]	% Solids	[LS, QB]
(mol/L)	(mL)	(N)	(mL)	(N)	(kg/kg H_2O)	(g/L ea.)
~1.1	4	0.199	50	0.105	None	None
Time	Temp.	Thiosulfate	Density	$[SO_3^{2-}]$ left	O_2 reacted	$[O_2]^*$
(min)	(°C)	(mL)	(g/L)	(mol/kg)	(mg/kg)	(mg/kg)
0	45	14.6	1119	1.074	776	2.3
15	46	17.8	1119	1.032	1458	2.3
30	45	19.0	1119	1.016	1713	2.3
45	45	21.3	1120	0.985	2204	2.3
60	45	22.7	1120	0.967	2502	2.3
120	45	31.3	1121	0.852	4337	2.3
180	44	37.1	1121	0.774	5576	2.3

Stellenbosch University http://scholar.sun.ac.za

MTG2	Temp.	Imp. speed	P_g	Feed gas	Mass	[Co(II)]
7-litre vessel	(°C)	(rev/min)	(kPa)	(% O_2)	(g)	(mg/L)
Normal level	~50	1000	0	21	7358	0.0
[SO_3^{2-}]	Sulfite vol.	[Iodine]	Iodine vol.	[Thiosulfate]	% Solids	[LS, QB]
(mol/L)	(mL)	(N)	(mL)	(N)	(kg/kg H_2O)	(g/L ea.)
~1.1	4	0.199	50	0.105	None	None
Time	Temp.	Thiosulfate	Density	[SO_3^{2-}] left	O_2 reacted	$[O_2]^*$
(min)	(°C)	(mL)	(g/L)	(mol/kg)	(mg/kg)	(mg/kg)
0	50	14.4	1119	1.077	734	2.1
15	52	17.2	1119	1.040	1330	2.0
30	53	19.1	1119	1.014	1735	2.0
45	53	21.3	1120	0.985	2204	2.0
60	53	23.1	1120	0.961	2587	2.0
120	51	33.5	1121	0.822	4807	2.1

MTG3	Temp.	Imp. speed	P_g	Feed gas	Mass	[Co(II)]
7-litre vessel	(°C)	(rev/min)	(kPa)	(% O_2)	(g)	(mg/L)
High level	~50	1000	0	21	7925	0.0
[SO_3^{2-}]	Sulfite vol.	[Iodine]	Iodine vol.	[Thiosulfate]	% Solids	[LS, QB]
(mol/L)	(mL)	(N)	(mL)	(N)	(kg/kg H_2O)	(g/L ea.)
~1.1	4	0.199	50	0.105	None	None
Time	Temp.	Thiosulfate	Density	[SO_3^{2-}] left	O_2 reacted	$[O_2]^*$
(min)	(°C)	(mL)	(g/L)	(mol/kg)	(mg/kg)	(mg/kg)
0	50	14.8	1119	1.072	819	2.1
15	49	16.6	1119	1.048	1202	2.2
30	50	19.9	1119	1.004	1905	2.1
45	50	21.0	1119	0.989	2140	2.1
60	49	22.8	1120	0.965	2523	2.2
120	47	31.4	1121	0.850	4358	2.2
180	46	37.6	1122	0.768	5683	2.3

Stellenbosch University http://scholar.sun.ac.za

MTG4	Temp.	Imp. speed	P_g	Feed gas	Mass	[Co(II)]
7-litre vessel	(°C)	(rev/min)	(kPa)	(% O_2)	(g)	(mg/L)
Normal level	~80	1000	0	21	7100	0.0001
$[SO_3^{2-}]$	Sulfite vol.	[Iodine]	Iodine vol.	[Thiosulfate]	% Solids	[LS, QB]
(mol/L)	(mL)	(N)	(mL)	(N)	(kg/kg H_2O)	(g/L ea.)
~1.1	4	0.198	50	0.105	None	None
Time	Temp.	Thiosulfate	Density	$[SO_3^{2-}]$ left	O_2 reacted	$[O_2]^*$
(min)	(°C)	(mL)	(g/L)	(mol/kg)	(mg/kg)	(mg/kg)
0	83	14.9	1119	1.064	942	0.8
15	83	17.6	1119	1.028	1517	0.8
30	82	18.4	1119	1.017	1687	0.9
45	81	21.3	1120	0.979	2305	0.9
60	81	22.8	1120	0.959	2625	0.9
120	80	30.2	1121	0.860	4204	1.0
181	80	36.7	1121	0.773	5593	1.0
240	80	44.2	1122	0.673	7197	1.0

MTG5	Temp.	Imp. speed	P_g	Feed gas	Mass	[Co(II)]
7-litre vessel	(°C)	(rev/min)	(kPa)	(% O_2)	(g)	(mg/L)
Repeat	~80	1000	0	21	7100	0.0001
$[SO_3^{2-}]$	Sulfite vol.	[Iodine]	Iodine vol.	[Thiosulfate]	% Solids	[LS, QB]
(mol/L)	(mL)	(N)	(mL)	(N)	(kg/kg H_2O)	(g/L ea.)
~1.1	4	0.200	50	0.096	None	None
Time	Temp.	Thiosulfate	Density	$[SO_3^{2-}]$ left	O_2 reacted	$[O_2]^*$
(min)	(°C)	(mL)	(g/L)	(mol/kg)	(mg/kg)	(mg/kg)
0	81	14.4	1118	1.100	360	0.9
15	77	15.0	1119	1.093	486	1.1
30	78	17.0	1119	1.068	878	1.0
45	80	21.4	1119	1.015	1723	1.0
60	80	22.1	1119	1.007	1859	1.0
120	80	30.7	1120	0.902	3540	1.0
180	80	39.0	1121	0.801	5156	1.0
240	81	48.6	1122	0.683	7045	0.9

Stellenbosch University http://scholar.sun.ac.za

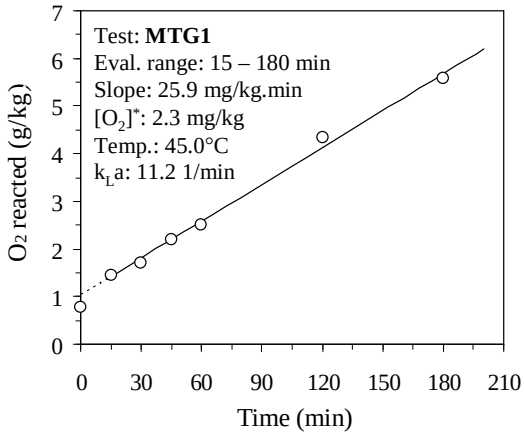

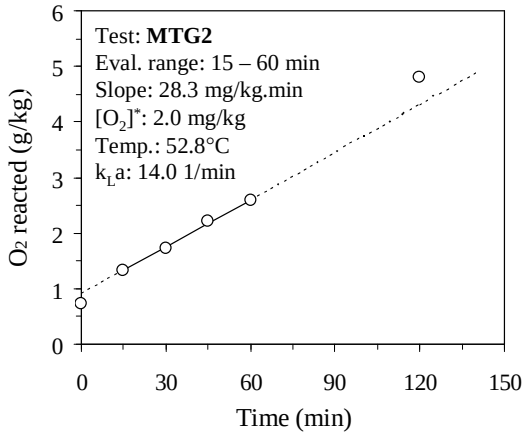

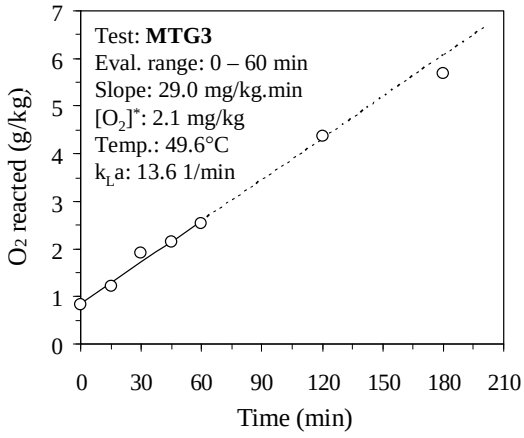

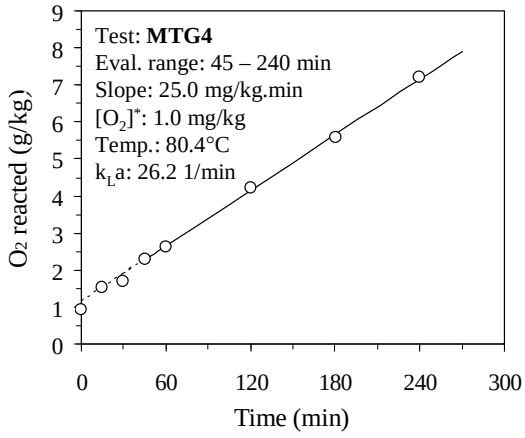

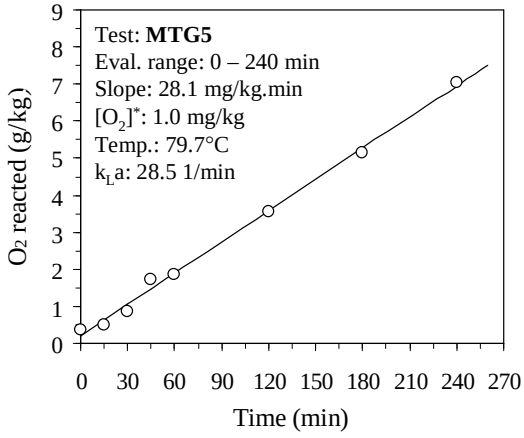

Stellenbosch University http://scholar.sun.ac.za

C.9 The effect of oxygen partial pressure on the k_La-value (7-litre reactor)

These tests aimed at quantifying the effect of the oxygen partial pressure at low catalyst levels on the k_La-value in the 7-litre glass reaction vessel (indirect method).

MTG6	Temp.	Imp. speed	P_g	Feed gas	Mass	[Co(II)]
7-litre vessel	(°C)	(rev/min)	(kPa)	(% O_2)	(g)	(mg/L)
	~80	1000	0	100	7100	0.0001
$[SO_3^{2-}]$	Sulfite vol.	[Iodine]	Iodine vol.	[Thiosulfate]	% Solids	[LS, QB]
(mol/L)	(mL)	(N)	(mL)	(N)	(kg/kg H_2O)	(g/L ea.)
~1.1	4	0.200	50	0.096	None	None
Time	Temp.	Thiosulfate	Density	$[SO_3^{2-}]$ left	O_2 reacted	$[O_2]^*$
(min)	(°C)	(mL)	(g/L)	(mol/kg)	(mg/kg)	(mg/kg)
0	79	13.9	1118	1.106	272	4.7
15	81	31.3	1120	0.894	3663	4.4
30	83	45.6	1122	0.719	6456	4.0
45	86	59.5	1124	0.549	9178	3.2
60	87	76.1	1125	0.346	12435	2.9

MTG7	Temp.	Imp. speed	P_g	Feed gas	Mass	[Co(II)]
7-litre vessel	(°C)	(rev/min)	(kPa)	(% O_2)	(g)	(mg/L)
	~80	1000	0	20	7100	0.001
$[SO_3^{2-}]$	Sulfite vol.	[Iodine]	Iodine vol.	[Thiosulfate]	% Solids	[LS, QB]
(mol/L)	(mL)	(N)	(mL)	(N)	(kg/kg H_2O)	(g/L ea.)
~1.1	4	0.197	50	0.096	None	None
Time	Temp.	Thiosulfate	Density	$[SO_3^{2-}]$ left	O_2 reacted	$[O_2]^*$
(min)	(°C)	(mL)	(g/L)	(mol/kg)	(mg/kg)	(mg/kg)
0	82	13.2	1118	1.096	430	0.9
30	82	16.0	1119	1.062	975	0.8
60	82	18.8	1119	1.027	1530	0.8
90	83	21.9	1119	0.990	2131	0.8
120	83	24.8	1120	0.955	2690	0.8
150	84	28.2	1120	0.913	3353	0.7
180	83	31.3	1121	0.876	3958	0.8
210	84	33.8	1121	0.845	4446	0.8
240	84	36.4	1121	0.812	4969	0.8
270	84	39.5	1121	0.775	5559	0.7

Stellenbosch University http://scholar.sun.ac.za

MTG8	Temp.	Imp. speed	P_g	Feed gas	Mass	[Co(II)]
7-litre vessel	(°C)	(rev/min)	(kPa)	(% O_2)	(g)	(mg/L)
	~80	1000	0	10	7100	0.001
$[SO_3^{2-}]$	Sulfite vol.	[Iodine]	Iodine vol.	[Thiosulfate]	% Solids	[LS, QB]
(mol/L)	(mL)	(N)	(mL)	(N)	(kg/kg H_2O)	(g/L ea.)
~1.1	4	0.197	50	0.096	None	None
Time	Temp.	Thiosulfate	Density	$[SO_3^{2-}]$ left	O_2 reacted	$[O_2]^*$
(min)	(°C)	(mL)	(g/L)	(mol/kg)	(mg/kg)	(mg/kg)
0	81	14.2	1119	1.083	631	0.4
60	81	18.2	1119	1.035	1404	0.4
120	79	21.8	1119	0.991	2105	0.5
180	80	26.1	1120	0.939	2943	0.5
240	81	30.2	1120	0.888	3755	0.4

MTG9	Temp.	Imp. speed	P_g	Feed gas	Mass	[Co(II)]
7-litre vessel	(°C)	(rev/min)	(kPa)	(% O_2)	(g)	(mg/L)
	~80	1000	0	21	7100	0.001
$[SO_3^{2-}]$	Sulfite vol.	[Iodine]	Iodine vol.	[Thiosulfate]	% Solids	[LS, QB]
(mol/L)	(mL)	(N)	(mL)	(N)	(kg/kg H_2O)	(g/L ea.)
~1.1	4	0.198	50	0.099	None	None
Time	Temp.	Thiosulfate	Density	$[SO_3^{2-}]$ left	O_2 reacted	$[O_2]^*$
(min)	(°C)	(mL)	(g/L)	(mol/kg)	(mg/kg)	(mg/kg)
0	78	15.9	1119	1.062	967	1.1
60	80	24.7	1120	0.952	2735	1.0
120	77	33.3	1121	0.845	4450	1.1
180	77	42.3	1122	0.731	6265	1.1
240	78	52.4	1123	0.603	8314	1.1

Stellenbosch University http://scholar.sun.ac.za

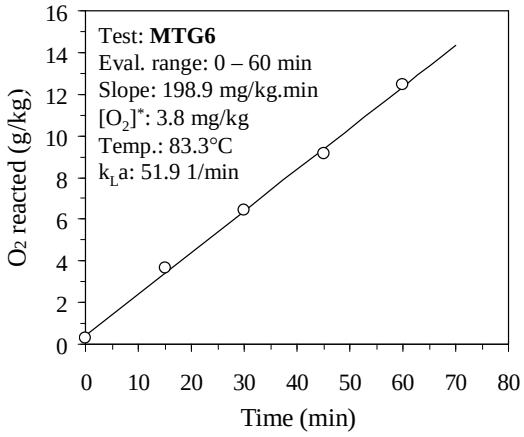

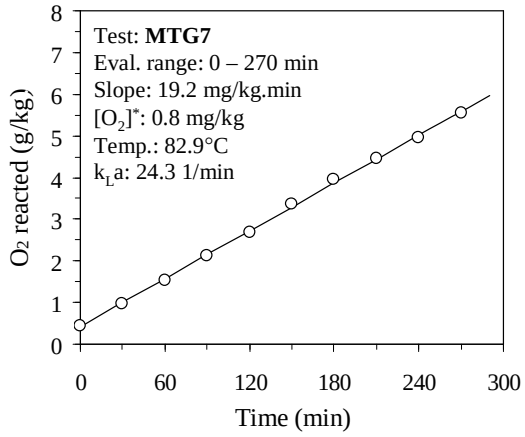

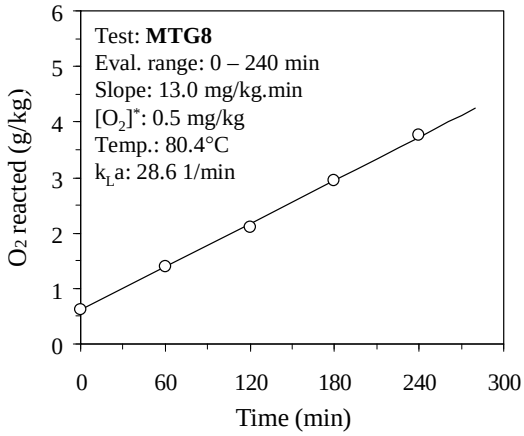

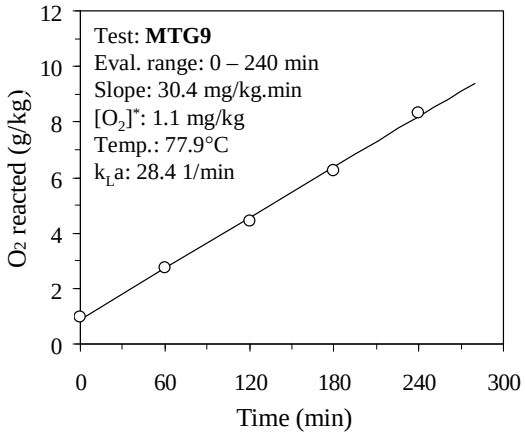

Stellenbosch University http://scholar.sun.ac.za

C.10 The effect of surfactants and sulfide pulp density on the k_La-value (7-litre reactor)

These tests aimed at quantifying the effects of the sulfur-dispersing surfactants, lignosulfonate (LS) and Quebracho (QB), and the chalcopyrite concentrate pulp density on the k_La-value in the 7-litre glass reaction vessel (indirect method). The mineral composition and PSD of this concentrate was similar to the standard feed material used in the continuous pilot autoclave campaigns (Sect. 7.4.1).

MTG10	Temp.	Imp. speed	P_g	Feed gas	Mass	[Co(II)]
7-litre vessel	(°C)	(rev/min)	(kPa)	(% O_2)	(g)	(mg/L)
	~80	1000	0	21	7100	0.001
$[SO_3^{2-}]$	Sulfite vol.	[Iodine]	Iodine vol.	[Thiosulfate]	% Solids	[a] [LS, QB]
(mol/L)	(mL)	(N)	(mL)	(N)	(kg/kg H_2O)	(g/L ea.)
~1.1	4	0.198	50	0.099	None	0.35
Time	Temp.	Thiosulfate	Density	$[SO_3^{2-}]$ left	O_2 reacted	$[O_2]^*$
(min)	(°C)	(mL)	(g/L)	(mol/kg)	(mg/kg)	(mg/kg)
0	79	15.2	1119	1.072	821	1.0
30	81	17.2	1119	1.047	1222	0.9
60	78	19.7	1119	1.015	1724	1.1
90	79	23.7	1120	0.965	2528	1.0
120	80	27.9	1120	0.912	3375	1.0
180	81	37.0	1121	0.798	5205	0.9
240	83	47.1	1122	0.670	7242	0.8

[a] Norlig A, Orfom 2 (no pre-drying).

MTG11	Temp.	Imp. speed	P_g	Feed gas	Mass	[Co(II)]
7-litre vessel	(°C)	(rev/min)	(kPa)	(% O_2)	(g)	(mg/L)
	~80	1000	0	21	7100	0.001
$[SO_3^{2-}]$	Sulfite vol.	[Iodine]	Iodine vol.	[Thiosulfate]	% Solids	[a] [LS, QB]
(mol/L)	(mL)	(N)	(mL)	(N)	(kg/kg H_2O)	(g/L ea.)
~1.1	4	0.198	50	0.099	None	0.50
Time	Temp.	Thiosulfate	Density	$[SO_3^{2-}]$ left	O_2 reacted	$[O_2]^*$
(min)	(°C)	(mL)	(g/L)	(mol/kg)	(mg/kg)	(mg/kg)
0	77	15.7	1119	1.066	915	1.1
30	80	15.8	1119	1.064	941	1.0
60	81	17.5	1119	1.043	1272	0.9
90	81	19.1	1119	1.023	1604	0.9
120	78	21.4	1119	0.993	2072	1.0
180	79	26.5	1120	0.930	3091	1.0
240	80	33.8	1121	0.838	4560	1.0

[a] Norlig A, Orfom 2 (no pre-drying).

Stellenbosch University http://scholar.sun.ac.za

MTG12	Temp.	Imp. speed	P_g	Feed gas	Mass	[Co(II)]
7-litre vessel	(°C)	(rev/min)	(kPa)	(% O_2)	(g)	(mg/L)
	~80	1000	0	21	7050	0
$[SO_3^{2-}]$	Sulfite vol.	[Iodine]	Iodine vol.	[Thiosulfate]	% Solids	[LS, QB]
(mol/L)	(mL)	(N)	(mL)	(N)	(kg/kg H_2O)	(g/L ea.)
~1.1	4	0.197	50	0.099	3.5	0
Time	Temp.	Thiosulfate	Density	$[SO_3^{2-}]$ left	O_2 reacted	$[O_2]^*$
(min)	(°C)	(mL)	(g/L)	(mol/kg)	(mg/kg)	(mg/kg)
0	78	17.7	1119	1.033	1432	1.1
30	81	23.7	1120	0.959	2626	0.9
60	82	29.2	1120	0.890	3726	0.9
90	81	36.0	1121	0.804	5105	0.9
120	79	41.2	1122	0.738	6153	1.0
180	80	53.8	1123	0.579	8701	1.0
240	82	67.6	1125	0.405	11488	0.9

MTG13	Temp.	Imp. speed	P_g	Feed gas	Mass	[Co(II)]
7-litre vessel	(°C)	(rev/min)	(kPa)	(% O_2)	(g)	(mg/L)
	~80	1000	0	21	7000	0
$[SO_3^{2-}]$	Sulfite vol.	[Iodine]	Iodine vol.	[Thiosulfate]	% Solids	[LS, QB]
(mol/L)	(mL)	(N)	(mL)	(N)	(kg/kg H_2O)	(g/L ea.)
~1.1	4	0.197	50	0.098	7.0	0
Time	Temp.	Thiosulfate	Density	$[SO_3^{2-}]$ left	O_2 reacted	$[O_2]^*$
(min)	(°C)	(mL)	(g/L)	(mol/kg)	(mg/kg)	(mg/kg)
0	79	15.4	1119	1.065	927	1.0
30	79	22.6	1120	0.975	2363	1.0
60	80	28.0	1120	0.908	3438	1.0
90	81	35.6	1121	0.814	4942	0.9
120	82	40.3	1122	0.755	5890	0.9
180	83	52.1	1123	0.607	8247	0.8
240	84	62.5	1124	0.477	10328	0.8

Stellenbosch University http://scholar.sun.ac.za

MTG14	Temp.	Imp. speed	P_g	Feed gas	Mass	[Co(II)]
7-litre vessel	(°C)	(rev/min)	(kPa)	(% O_2)	(g)	(mg/L)
	~80	1000	0	21	6850	0
$[SO_3^{2-}]$	Sulfite vol.	[Iodine]	Iodine vol.	[Thiosulfate]	% Solids	[LS, QB]
(mol/L)	(mL)	(N)	(mL)	(N)	(kg/kg H_2O)	(g/L ea.)
~1.1	4	0.198	50	0.098	15.0	0
Time	Temp.	Thiosulfate	Density	$[SO_3^{2-}]$ left	O_2 reacted	$[O_2]^*$
(min)	(°C)	(mL)	(g/L)	(mol/kg)	(mg/kg)	(mg/kg)
0	83	15.6	1119	1.069	869	0.8
30	80	20.7	1119	1.006	1873	1.0
60	78	25.9	1120	0.941	2918	1.0
90	79	31.0	1120	0.877	3934	1.0
120	80	37.8	1121	0.792	5289	1.0
180	82	47.9	1122	0.666	7305	0.9
240	83	60.0	1124	0.516	9715	0.8

MTG15	Temp.	Imp. speed	P_g	Feed gas	Mass	[Co(II)]
7-litre vessel	(°C)	(rev/min)	(kPa)	(% O_2)	(g)	(mg/L)
	~80	1000	0	21	7000	0
$[SO_3^{2-}]$	Sulfite vol.	[Iodine]	Iodine vol.	[Thiosulfate]	% Solids	[a] [LS, QB]
(mol/L)	(mL)	(N)	(mL)	(N)	(kg/kg H_2O)	(g/L ea.)
~1.1	4	0.198	50	0.098	7.0	0.5
Time	Temp.	Thiosulfate	Density	$[SO_3^{2-}]$ left	O_2 reacted	$[O_2]^*$
(min)	(°C)	(mL)	(g/L)	(mol/kg)	(mg/kg)	(mg/kg)
0	78	15.1	1119	1.075	770	1.1
30	78	20.7	1119	1.005	1883	1.1
60	80	27.7	1120	0.918	3276	1.0
90	81	32.7	1121	0.856	4272	0.9
120	81	38.4	1121	0.785	5409	0.9
180	81	51.0	1123	0.628	7925	0.9
240	81	63.0	1124	0.478	10326	0.9

[a] Norlig A, Orfom 2 (no pre-drying).

Stellenbosch University http://scholar.sun.ac.za

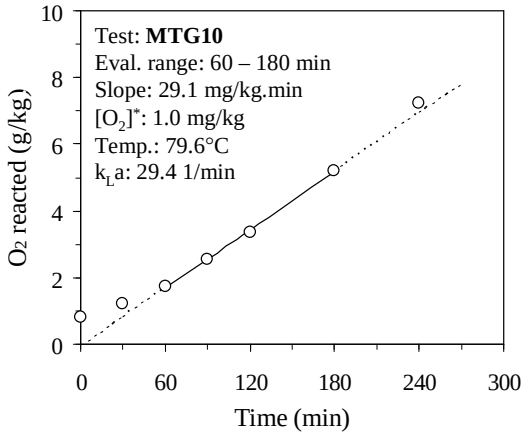

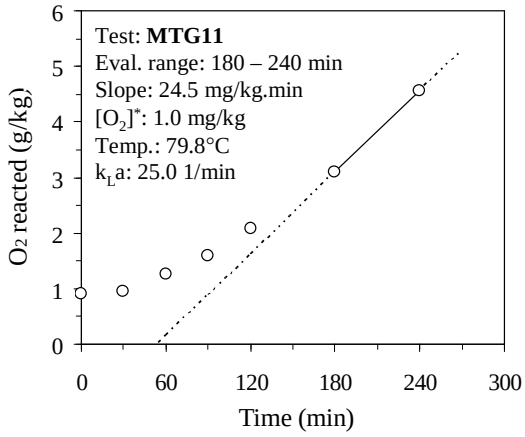

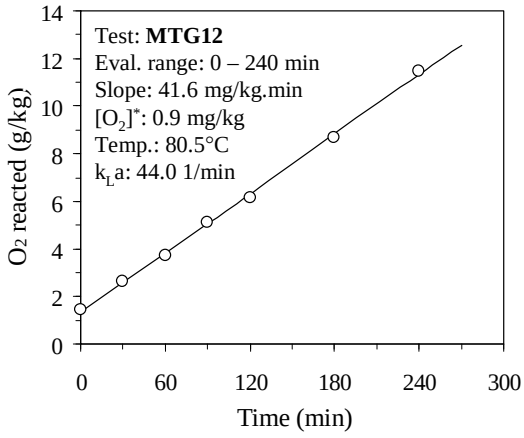

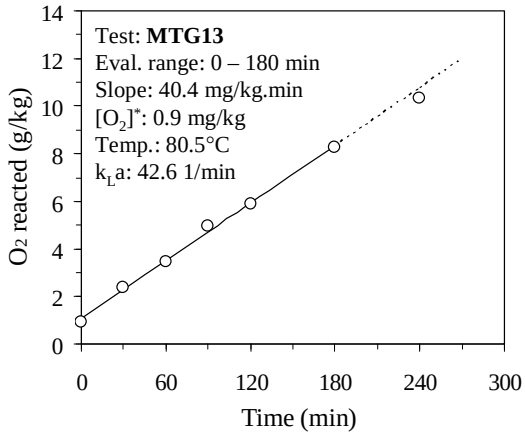

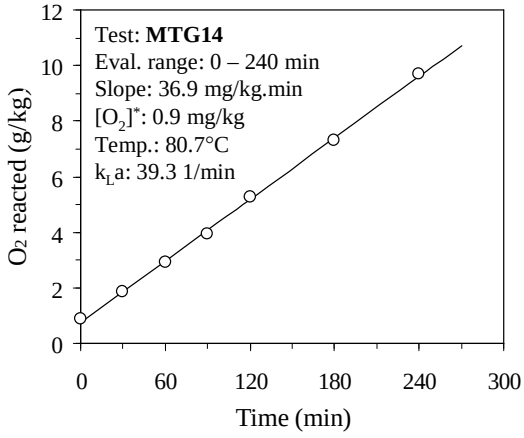

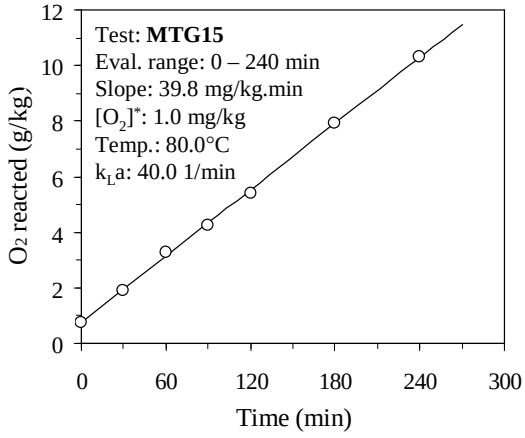

Stellenbosch University http://scholar.sun.ac.za

C.11 The effect of various operating parameters on the k_La-value (2-litre AC), based on direct oxygen electrode measurements

These tests were conducted in the 2-litre autoclave with polypropylene lid and laboratory mixing system (Figure 3.5), using direct oxygen electrode measurements (the experimental procedures are summarised in Sect. 3.4.1). They aimed at quantifying the effect of various operating parameters on the k_La-value, *e.g.*, electrolyte composition and temperature at different agitation speeds and impeller arrangements. Except for the final two tests (Tests OPB1 & OPB2), the initial dissolved oxygen was not removed by a reductant (sulfite). Data values were recorded at 0.1 sec intervals but are only reported at 5 sec intervals, and in some cases representing an average of the two electrodes used, *i.e.*, the InLab 605 and InPro 6800. The response time of these two electrodes to a step change in the dissolved oxygen concentration are summarised in the first two columns.

Test	**OP1**	**OP2**	**OPA1**	**OPA2**	**OPA3**	**OPA4**	**OPB1**	**OPB2**
(2-litre AC)	InLab $_{650}$	InPro $_{6800}$	Double	Double	Double	Double	Double	Double
–	response	response	impeller	impeller	impeller	impeller	impeller	Impeller
Imp.conf. (Fig 3.5)	–	–	A	A	A	A	**B**	**B**
[$MgSO_4$] (mol/kg)	0.00	0.50	**0.50**	**0.25**	0.00	0.50	0.50	0.50
[Na_2SO_4] (mol/kg)	0.25	0.00	0.00	0.00	**1.30**	0.00	0.00	0.00
% sld. (kg/kg H_2O)	–	–	0.0	0.0	0.0	0.0	0.0	0.0
Temp. (avg.) (°C)	31.0	46.0	22.0	39.2	42.9	42.0	44.0	51.0
Vol. (static) (L)	–	–	1.2	1.2	1.2	1.2	1.2	1.2
Imp. spd. (rev/min)	–	–	1000	1000	1000	**1100**	1000	**850**
Reductant (SO_3^{2-})	–	–	0	0	0	0	0.5×stoic.	1.5×stoic.
k_La (1/min)	**–**	**–**	**1.33**	**1.74**	**2.05**	**2.53**	**1.24**	**0.67**
AARD (%)	–	–	2.67	3.65	3.00	2.10	5.12	4.75
Time	$[O_2]/[O_2]^*$	$[O_2]/[O_2]^*$	$[O_2]/[O_2]^*$	$[O_2]/[O_2]^*$	$[O_2]/[O_2]^*$	$[O_2]/[O_2]^*$	$[O_2]/[O_2]^*$	$[O_2]/[O_2]^*$
(sec)	–	–	–	–	–	–	–	–
0	0.01	0.00	0.41	0.54	0.67	0.63	0.12	0.00
5	0.09	0.08	0.48	0.60	0.72	0.70	0.18	0.04
10	0.38	0.38	0.53	0.66	0.78	0.76	0.23	0.09
15	0.60	0.63	0.59	0.71	0.80	0.80	0.28	0.13
20	0.76	0.78	0.62	0.75	0.84	0.83	0.33	0.17
25	0.87	0.88	0.65	0.79	0.86	0.87	0.41	0.21
30	0.93	0.94	0.69	0.81	0.88	0.90	0.49	0.24
35	0.96	0.97	0.72	0.84	0.90	0.92	0.55	0.28
40	0.98	0.98	0.75	0.86	0.92	0.93	0.60	0.31
45	0.99	1.00	0.77	0.88	0.93	0.95	0.63	0.34
50	0.99	1.00	0.79	0.89	0.94	0.96	0.68	0.38

Stellenbosch University http://scholar.sun.ac.za

Time (sec)	OP1	OP2	OPA1	OPA2	OPA3	OPA4	OPB1	OPB2
55	0.99	1.00	0.83	0.90	0.95	0.97	0.72	0.41
60	1.00	1.01	0.84	0.91	0.96	0.97	0.75	0.44
65	1.00	1.00	0.86	0.92	0.95	0.98	0.77	0.47
70	1.00	1.00	0.88	0.93	0.98	0.98	0.79	0.50
75	1.00	1.00	0.89	0.94	0.99	0.99	0.82	0.53
80	1.00	1.00	0.90	0.95	0.99	0.99	0.85	0.56
85	1.00	1.00	0.92	0.96	0.99	0.99	0.86	0.59
90	1.00	1.00	0.92	0.96	1.00	0.99	0.88	0.61
95	1.00	1.00	0.94	0.97	1.00	1.00	0.88	0.63
100	1.00	1.00	0.95	0.97	0.99	1.00	0.90	0.65
105	1.00	1.00	0.95	0.98	1.00	1.00	0.91	0.68
110	1.00	1.00	0.96	0.99	1.00	1.00	0.92	0.70
115	1.00	1.00	0.96	0.99	1.00	1.00	0.93	0.72
120	1.00	1.00	0.96	1.00	1.00	1.00	0.94	0.74
125	1.00	1.00	0.96	1.00	1.00	1.00	0.95	0.75
130	1.00	1.00	0.97	1.00	0.99	1.00	1.03	0.77
135	1.00	1.00	0.98	1.00	1.00	1.00	0.99	0.78
140	1.00	1.00	0.98	1.00	1.00	1.00	0.98	0.79
145	1.00	1.00	0.99	1.00	1.01	1.00	0.99	0.81
150	1.00	1.00	0.99	1.00	1.01	1.00	0.99	0.82
155	1.00	1.00	1.00	1.00	1.01	1.00	1.00	0.83
160	1.00	1.00	0.99	1.00	1.00	1.00	1.00	0.84
165	1.00	1.00	1.00	1.00	1.00	1.00	1.00	0.86
170	1.00	1.00	1.00	1.00	1.00	1.00	1.00	0.87
175	1.00	1.00	1.00	1.00	1.00	1.00	1.05	0.88
180	1.00	1.00	0.99	1.00	1.00	1.00	1.01	0.89
185	1.00	1.00	1.00	1.00	1.00	1.00	1.00	0.89
190	1.00	1.00	1.00	1.00	1.00	1.00	1.00	0.90
195	1.00	1.00	1.00	1.00	1.00	1.00	1.00	0.91
200	1.00	1.00	1.00	1.00	1.00	1.00	0.99	0.91
205	1.00	1.00	1.00	1.00	1.00	1.00	0.99	0.92
210	1.00	1.00	1.00	1.00	1.00	1.00	1.00	0.92
215	1.00	1.00	1.00	1.00	1.00	1.00	0.99	0.93
220	1.00	1.00	1.00	1.00	1.00	1.00	0.99	0.93
225	1.00	1.00	1.00	1.00	1.00	1.00	1.00	0.94
230	1.00	1.00	1.00	1.00	1.00	1.00	1.00	0.94
235	1.00	1.00	1.00	1.00	1.00	1.00	1.00	0.94
240	1.00	1.00	1.00	1.00	1.00	1.00	1.00	0.95

Stellenbosch University http://scholar.sun.ac.za

Time (sec)	OP1	OP2	OPA1	OPA2	OPA3	OPA4	OPB1	OPB2
245	1.00	1.00	1.00	1.00	1.00	1.00	1.00	0.95
250	1.00	1.00	1.00	1.00	1.00	1.00	1.00	0.96
255	1.00	1.00	1.00	1.00	1.00	1.00	1.00	0.96
260	1.00	1.00	1.00	1.00	1.00	1.00	1.00	0.96
265	1.00	1.00	1.00	1.00	1.00	1.00	1.00	0.96
270	1.00	1.00	1.00	1.00	1.00	1.00	1.00	0.97
275	1.00	1.00	1.00	1.00	1.00	1.00	1.00	0.97
280	1.00	1.00	1.00	1.00	1.00	1.00	1.00	0.97
285	1.00	1.00	1.00	1.00	1.00	1.00	1.00	0.97
290	1.00	1.00	1.00	1.00	1.00	1.00	1.00	0.97
295	1.00	1.00	1.00	1.00	1.00	1.00	1.00	0.97
300	1.00	1.00	1.00	1.00	1.00	1.00	1.00	0.98
305	1.00	1.00	1.00	1.00	1.00	1.00	1.00	0.98
310	1.00	1.00	1.00	1.00	1.00	1.00	1.00	0.98
315	1.00	1.00	1.00	1.00	1.00	1.00	1.00	0.98
320	1.00	1.00	1.00	1.00	1.00	1.00	1.00	0.99
325	1.00	1.00	1.00	1.00	1.00	1.00	1.00	0.99
330	1.00	1.00	1.00	1.00	1.00	1.00	1.00	0.99
335	1.00	1.00	1.00	1.00	1.00	1.00	1.00	0.99
340	1.00	1.00	1.00	1.00	1.00	1.00	1.00	0.99
345	1.00	1.00	1.00	1.00	1.00	1.00	1.00	0.99
350	1.00	1.00	1.00	1.00	1.00	1.00	1.00	0.99
355	1.00	1.00	1.00	1.00	1.00	1.00	1.00	0.99
360	1.00	1.00	1.00	1.00	1.00	1.00	1.00	0.99
365	1.00	1.00	1.00	1.00	1.00	1.00	1.00	0.99
370	1.00	1.00	1.00	1.00	1.00	1.00	1.00	0.99
375	1.00	1.00	1.00	1.00	1.00	1.00	1.00	0.99
380	1.00	1.00	1.00	1.00	1.00	1.00	1.00	1.00
385	1.00	1.00	1.00	1.00	1.00	1.00	1.00	1.00
390	1.00	1.00	1.00	1.00	1.00	1.00	1.00	1.00
395	1.00	1.00	1.00	1.00	1.00	1.00	1.00	0.99
400	1.00	1.00	1.00	1.00	1.00	1.00	1.00	0.99
405	1.00	1.00	1.00	1.00	1.00	1.00	1.00	0.99
410	1.00	1.00	1.00	1.00	1.00	1.00	1.00	1.00
415	1.00	1.00	1.00	1.00	1.00	1.00	1.00	1.00
420	1.00	1.00	1.00	1.00	1.00	1.00	1.00	1.00
425	1.00	1.00	1.00	1.00	1.00	1.00	1.00	1.00
430	1.00	1.00	1.00	1.00	1.00	1.00	1.00	1.00

Stellenbosch University http://scholar.sun.ac.za

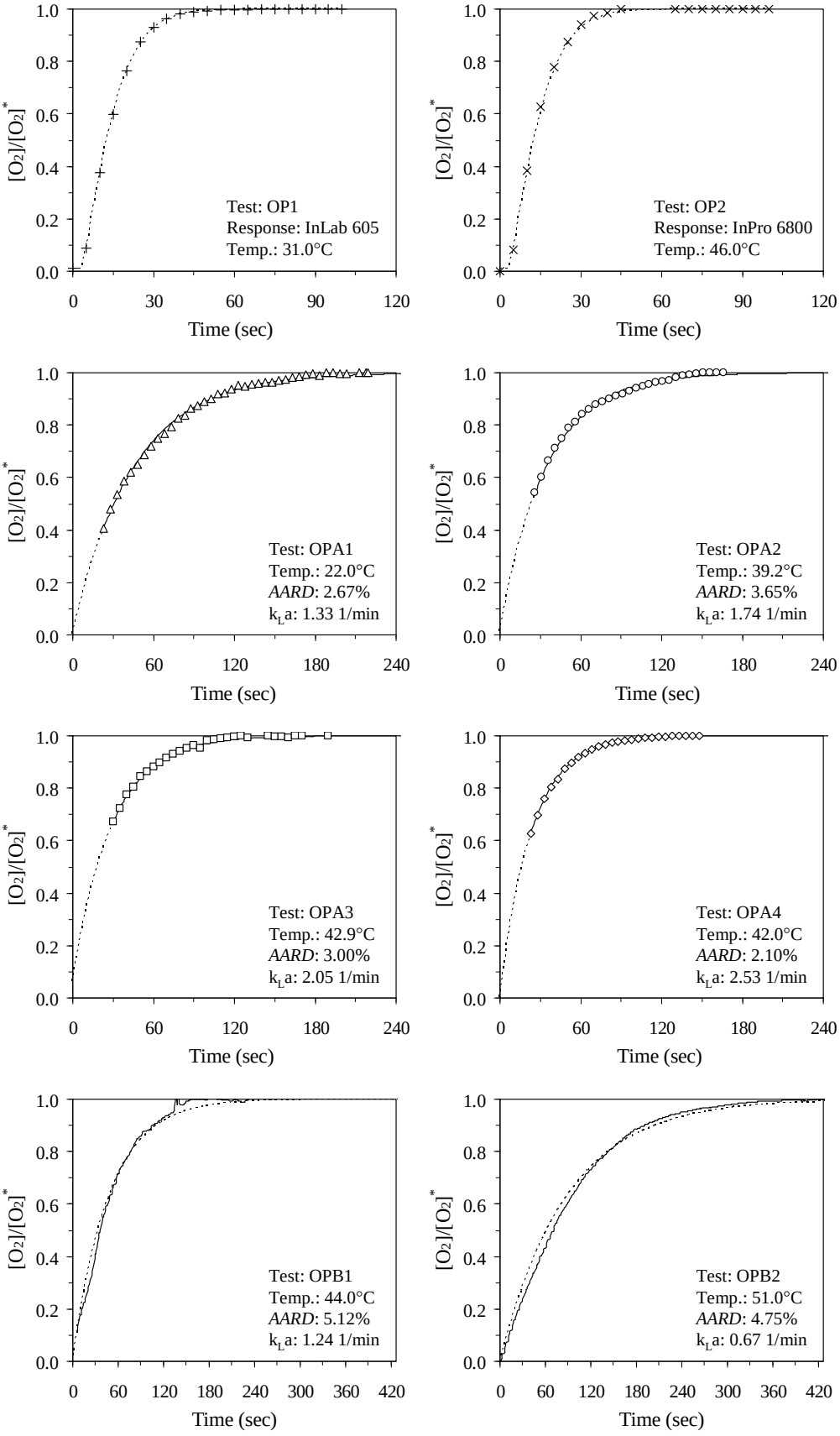

Stellenbosch University http://scholar.sun.ac.za

C.12 The effect of various parameters on the k_La-value (2-litre AC), based on direct oxygen electrode measurements at lower mass transfer rates and low initial oxygen concentrations

These tests were conducted in the 2-litre autoclave with polypropylene lid and laboratory mixing system (Figure 3.5) using direct oxygen electrode measurements (see Sect. 3.4.1). The effects of various parameters on the k_La-value were recorded, *e.g.*, different slurry pulp densities and impeller configurations. The initial dissolved oxygen was removed by adding a small amount of sulfite salt. Both the oxygen electrodes were also mounted on a pneumatic vibration system to help dislodge gas bubbles from the membrane surface. Data values were recorded at 0.1 sec intervals but are only reported at 5 sec intervals, and in some cases representing an average of the two electrodes used. The chalcopyrite (Cpy) sample was, again, similar to the standard pilot autoclave feed material (Sect. 7.4.1), while the hematite (Hem) sample (97% pure) was obtained from a chemical supplier.

Test	**OPC1**	**OPC2**	**OPC3**	**OPC4**	**OPD1**	**OPD2**	**OPD3**	**OPD4**
(2-litre AC)	**Single**	Single	Single	Single	**Double**	**Single**	Single	Single
–	impeller	impeller	impeller	impeller	impeller	impeller	impeller	impeller
Imp.conf. (Fig 3.5)	**B**	B	B	B	**A**	A	A	A
[$MgSO_4$] (mol/kg)	0.50	0.50	0.50	0.50	0.50	0.50	0.50	0.50
[Na_2SO_4] (mol/kg)	0.00	0.00	0.00	0.00	0.00	0.00	0.00	0.00
% sld. (kg/kg H_2O)	0.0	**1.0 Cpy**	**7.5 Cpy**	**7.5 Hem**	**0.0**	**0.0**	**15.0 Hem**	**7.5 Cpy**
Temp. (avg.) (°C)	46.7	40.5	43.3	42.8	41.8	43.7	41.2	39.0
Vol. (static) (L)	1.2	1.2	1.2	1.2	1.2	**0.9**	0.9	0.9
Imp. spd. (rev/min)	1000	1000	1000	1000	1000	1000	1000	1000
Reductant (SO_3^{2-})	1.1×stoic.	1.5×stoic.	0.5×stoic.	1.5×stoic.	1.1×stoic.	1.5×stoic.	1.5×stoic.	1.1×stoic.
k_La (1/min)	**0.41**	**0.36**	**0.37**	**0.35**	**1.88**	**0.46**	**0.40**	**0.39**
AARD (%)	3.80	2.07	0.88	1.47	0.21	0.31	0.69	3.77
Time	$[O_2]/[O_2]^*$	$[O_2]/[O_2]^*$	$[O_2]/[O_2]^*$	$[O_2]/[O_2]^*$	$[O_2]/[O_2]^*$	$[O_2]/[O_2]^*$	$[O_2]/[O_2]^*$	$[O_2]/[O_2]^*$
(sec)	–	–	–	–	–	–	–	–
0	0.04	0.00	0.20	0.00	0.03	0.00	0.00	0.02
5	0.06	0.04	0.23	0.03	0.09	0.04	0.02	0.04
10	0.08	0.07	0.25	0.06	0.17	0.07	0.05	0.07
15	0.10	0.11	0.27	0.09	0.29	0.11	0.08	0.10
20	0.13	0.13	0.29	0.11	0.42	0.14	0.11	0.12
25	0.15	0.16	0.32	0.14	0.52	0.17	0.14	0.15
30	0.18	0.19	0.34	0.17	0.61	0.20	0.17	0.17
35	0.20	0.21	0.36	0.19	0.68	0.23	0.20	0.19
40	0.23	0.23	0.38	0.22	0.74	0.26	0.23	0.22
45	0.25	0.26	0.40	0.24	0.78	0.28	0.26	0.24
50	0.27	0.28	0.41	0.26	0.82	0.31	0.29	0.26

Stellenbosch University http://scholar.sun.ac.za

Time (sec)	OPC1	OPC2	OPC3	OPC4	OPD1	OPD2	OPD3	OPD4
55	0.30	0.30	0.43	0.28	0.84	0.34	0.31	0.28
60	0.32	0.31	0.45	0.30	0.87	0.36	0.34	0.30
65	0.34	0.33	0.46	0.33	0.89	0.39	0.36	0.32
70	0.37	0.35	0.48	0.34	0.90	0.41	0.38	0.34
75	0.39	0.36	0.49	0.36	0.91	0.44	0.40	0.36
80	0.41	0.38	0.51	0.38	0.92	0.46	0.43	0.38
85	0.43	0.39	0.52	0.40	0.93	0.48	0.45	0.40
90	0.45	0.41	0.54	0.42	0.94	0.50	0.46	0.42
95	0.47	0.42	0.55	0.43	0.95	0.52	0.48	0.43
100	0.49	0.44	0.57	0.45	0.95	0.54	0.50	0.45
105	0.51	0.45	0.57	0.47	0.96	0.55	0.52	0.47
110	0.53	0.47	0.59	0.48	0.96	0.57	0.53	0.49
115	0.55	0.48	0.60	0.50	0.97	0.59	0.55	0.50
120	0.55	0.49	0.61	0.51	0.97	0.60	0.56	0.52
125	0.57	0.51	0.62	0.53	0.98	0.62	0.58	0.53
130	0.59	0.52	0.63	0.54	0.98	0.63	0.59	0.55
135	0.60	0.53	0.64	0.56	0.98	0.65	0.60	0.56
140	0.61	0.55	0.65	0.57	0.98	0.66	0.62	0.58
145	0.63	0.56	0.67	0.58	0.98	0.67	0.63	0.59
150	0.64	0.57	0.68	0.59	0.99	0.69	0.64	0.60
155	0.66	0.58	0.69	0.60	0.99	0.70	0.65	0.62
160	0.66	0.60	0.70	0.62	0.99	0.71	0.66	0.63
165	0.68	0.61	0.71	0.63	0.99	0.72	0.67	0.64
170	0.69	0.62	0.71	0.64	0.99	0.73	0.68	0.65
175	0.71	0.63	0.72	0.65	0.99	0.74	0.69	0.67
180	0.72	0.64	0.73	0.66	0.99	0.75	0.70	0.68
185	0.72	0.65	0.74	0.67	0.99	0.76	0.71	0.69
190	0.74	0.66	0.74	0.67	0.99	0.77	0.72	0.70
195	0.74	0.67	0.75	0.68	1.00	0.78	0.73	0.71
200	0.76	0.68	0.76	0.69	1.00	0.79	0.74	0.72
205	0.76	0.69	0.76	0.70	1.00	0.79	0.75	0.73
210	0.77	0.70	0.77	0.71	1.00	0.80	0.75	0.74
215	0.78	0.71	0.78	0.71	1.00	0.81	0.76	0.75
220	0.79	0.72	0.79	0.72	1.00	0.82	0.77	0.76
225	0.80	0.73	0.79	0.73	1.00	0.82	0.78	0.77
230	0.81	0.74	0.80	0.73	1.00	0.83	0.78	0.78
235	0.81	0.75	0.81	0.74	1.00	0.84	0.79	0.79
240	0.81	0.76	0.81	0.75	1.00	0.84	0.80	0.79

Stellenbosch University http://scholar.sun.ac.za

Time (sec)	OPC1	OPC2	OPC3	OPC4	OPD1	OPD2	OPD3	OPD4
245	0.82	0.76	0.82	0.75	1.00	0.85	0.80	0.80
250	0.83	0.77	0.82	0.76	1.00	0.86	0.81	0.81
255	0.84	0.78	0.83	0.76	1.00	0.86	0.82	0.82
260	0.84	0.78	0.83	0.77	1.00	0.87	0.82	0.83
265	0.85	0.79	0.84	0.78	1.00	0.87	0.83	0.83
270	0.85	0.80	0.84	0.78	1.00	0.88	0.83	0.84
275	0.85	0.80	0.85	0.79	1.00	0.88	0.84	0.85
280	0.87	0.81	0.85	0.79	1.00	0.89	0.84	0.85
285	0.87	0.82	0.85	0.80	1.00	0.89	0.85	0.86
290	0.88	0.82	0.86	0.81	1.00	0.90	0.85	0.87
295	0.88	0.83	0.87	0.81	1.00	0.90	0.86	0.87
300	0.88	0.83	0.88	0.82	1.00	0.90	0.86	0.88
305	0.90	0.84	0.88	0.82	1.00	0.91	0.87	0.88
310	0.90	0.84	0.88	0.83	1.00	0.91	0.87	0.89
315	0.90	0.85	0.89	0.83	1.00	0.91	0.87	0.89
320	0.90	0.85	0.89	0.84	1.00	0.92	0.88	0.90
325	0.91	0.86	0.89	0.84	1.00	0.92	0.88	0.90
330	0.91	0.86	0.90	0.85	1.00	0.92	0.89	0.91
335	0.92	0.87	0.90	0.85	1.00	0.93	0.89	0.91
340	0.92	0.87	0.90	0.86	1.00	0.93	0.89	0.92
345	0.93	0.88	0.91	0.86	1.00	0.93	0.90	0.92
350	0.94	0.88	0.91	0.86	1.00	0.93	0.90	0.93
355	0.94	0.89	0.91	0.87	1.00	0.94	0.90	0.93
360	0.94	0.89	0.91	0.87	1.00	0.94	0.91	0.93
365	0.94	0.90	0.92	0.87	1.00	0.94	0.91	0.94
370	0.94	0.90	0.92	0.88	1.00	0.94	0.91	0.94
375	0.94	0.90	0.92	0.88	1.00	0.95	0.92	0.95
380	0.95	0.91	0.92	0.88	1.00	0.95	0.92	0.95
385	0.94	0.91	0.92	0.89	1.00	0.95	0.92	0.95
390	0.95	0.92	0.93	0.89	1.00	0.95	0.92	0.95
395	0.95	0.92	0.93	0.89	1.00	0.95	0.93	0.96
400	0.96	0.92	0.93	0.89	1.00	0.96	0.93	0.96
405	0.96	0.93	0.93	0.89	1.00	0.96	0.93	0.96
410	0.95	0.93	0.92	0.90	1.00	0.96	0.93	0.97
415	0.96	0.93	0.92	0.90	1.00	0.96	0.94	0.97
420	0.96	0.93	0.92	0.90	1.00	0.96	0.94	0.97
425	0.96	0.94	0.93	0.90	1.00	0.96	0.94	0.97
430	0.97	0.94	0.93	0.91	1.00	0.97	0.94	0.98

Stellenbosch University http://scholar.sun.ac.za

Time (sec)	OPC1	OPC2	OPC3	OPC4	OPD1	OPD2	OPD3	OPD4
435	0.97	0.94	0.94	0.91	1.00	0.97	0.94	0.98
440	0.97	0.94	0.94	0.91	1.00	0.97	0.95	0.98
445	0.97	0.95	0.94	0.91	1.00	0.97	0.95	0.98
450	0.97	0.95	0.95	0.91	1.00	0.97	0.95	0.98
455	0.97	0.95	0.95	0.92	1.00	0.97	0.95	0.98
460	0.98	0.95	0.96	0.92	1.00	0.98	0.95	0.99
465	0.98	0.95	0.96	0.92	1.00	0.98	0.96	0.99
470	0.98	0.95	0.98	0.93	1.00	0.98	0.96	0.99
475	0.98	0.96	0.97	0.93	1.00	0.98	0.96	0.99
480	0.98	0.96	0.97	0.93	1.00	0.98	0.96	0.99
485	0.98	0.96	0.97	0.93	1.00	0.98	0.96	0.99
490	0.99	0.96	0.96	0.94	1.00	0.98	0.96	0.99
495	0.98	0.96	0.93	0.94	1.00	0.99	0.96	0.99
500	0.97	0.96	0.93	0.94	1.00	0.99	0.97	1.00
505	0.98	0.96	0.94	0.95	1.00	0.99	0.97	1.00
510	0.98	0.96	0.95	0.95	1.00	0.99	0.97	1.00
515	0.98	0.96	0.96	0.95	1.00	0.99	0.97	1.00
520	0.98	0.96	0.96	0.95	1.00	0.99	0.97	1.00
525	0.98	0.97	0.97	0.96	1.00	0.99	0.97	1.00
530	0.98	0.97	0.98	0.96	1.00	0.99	0.97	1.00
535	0.99	0.97	0.98	0.96	1.00	0.99	0.97	1.00
540	0.98	0.97	0.98	0.96	1.00	0.99	0.98	1.00
545	0.99	0.97	0.98	0.97	1.00	0.99	0.98	1.00
550	0.99	0.97	0.99	0.97	1.00	1.00	0.98	1.00
555	0.99	0.97	0.99	0.97	1.00	1.00	0.98	1.00
560	0.99	0.97	0.99	0.97	1.00	1.00	0.98	1.00
565	1.00	0.97	1.00	0.98	1.00	1.00	0.98	1.00
570	1.00	0.97	1.00	0.98	1.00	1.00	0.98	1.00
575	0.99	0.97	1.00	0.98	1.00	1.00	0.98	1.00
580	0.99	0.97	0.99	0.98	1.00	1.00	0.98	1.00
585	0.99	0.98	0.99	0.98	1.00	1.00	0.98	1.00
590	1.00	0.98	0.99	0.98	1.00	1.00	0.98	1.00
595	0.99	0.98	0.99	0.98	1.00	1.00	0.98	1.00
600	1.00	0.98	1.00	0.99	1.00	1.00	0.98	1.00

Stellenbosch University http://scholar.sun.ac.za

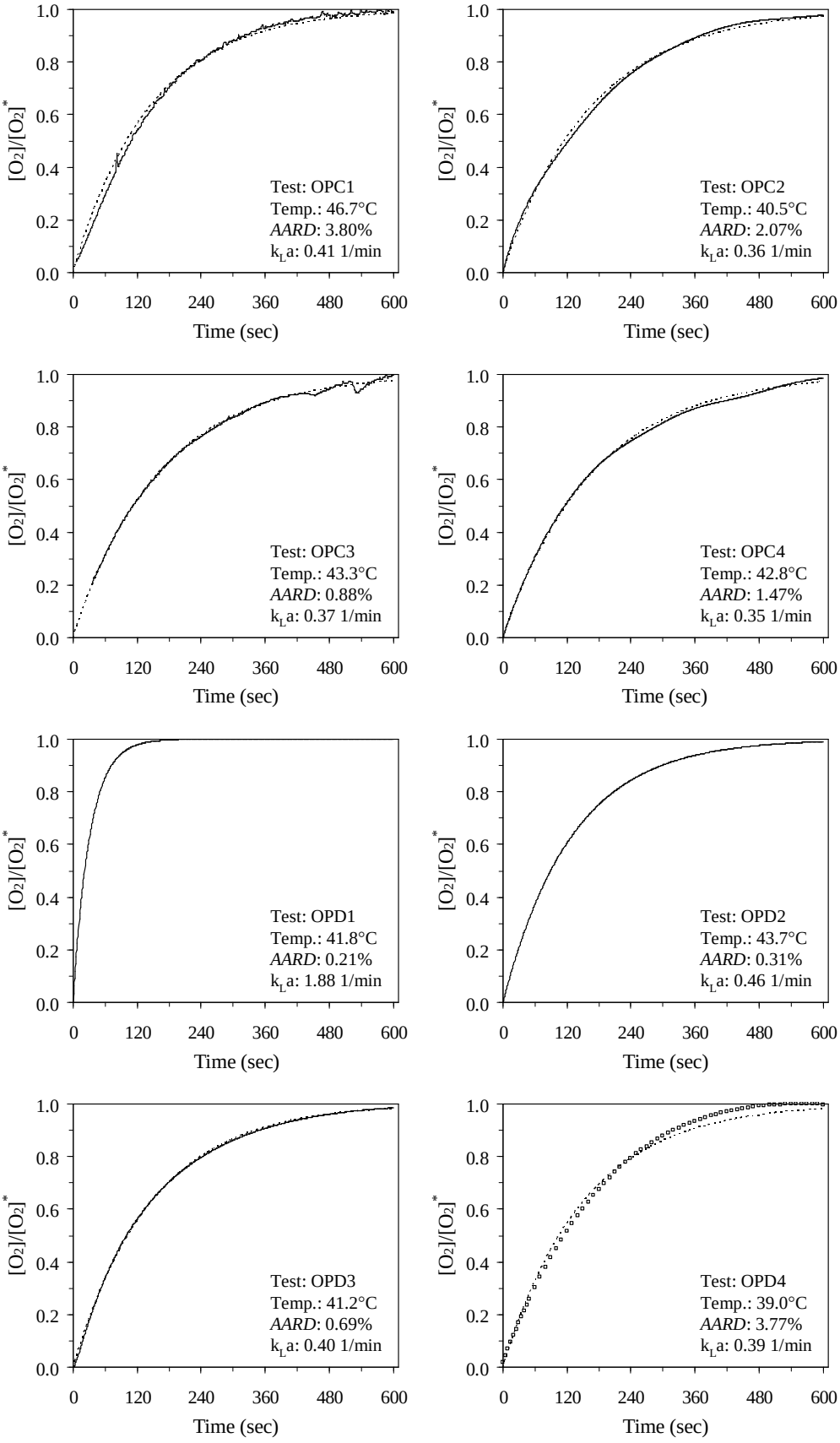

Stellenbosch University http://scholar.sun.ac.za

APPENDIX D. DETAILED IRON(II) OXIDATION TEST RESULTS

This appendix presents the detailed iron(II) oxidation test results (*ref.* Ch. 4, Sect. 4.4) obtained in the 2-litre Parr autoclave, using impeller configuration A (Ch. 3, Figure 3.5) and the 7-litre glass reactor (Sect. 3.3). The detailed experimental procedure is presented below (*ref.* Sect. 4.3.2).

The first test series aimed to develop an appropriate experimental procedure to identify the different reaction regimes, *i.e.*, to establish the role of interfacial gas/liquid mass transfer limitations and also to assess the impact of the reaction 'product', iron(III) (App. D.2). The effects of the dissolved oxygen and acid concentration were then evaluated, *i.e.*, to determine the apparent reaction orders without copper catalyst (App. D.3), as well as the activation energy (App. D.4) in low and high (zinc) sulfate solution environments. The next series of tests (App. D.5) varied the oxygen concentration and temperature in the presence of copper (catalyst), and also evaluated the rates at different copper concentrations. The final series of tests (App. D.6) was conducted under atmospheric conditions in the 7-litre glass reaction vessel and aimed to generate accurate oxidation rate data at 90°C, *i.e.*, to verify the phenomenological rate model under atmospheric conditions.

Besides the tabled data, each kinetic test and its second-order dependency, considering the 0.0005 to 0.001 mol/kg error variation in the Fe(II) concentration (see discussion in Sect. 4.3.3), is summarised in figure format. Detailed comparisons of the oxidation rates are also presented at the end of each section.

D.1 Detailed experimental procedure

The experimental setup is presented in Figure 4.3 (Sect. 4.3.1) and the procedure was as follows:

- The reaction vessel was charged with the required amount of water and varying amounts of background salts, *i.e.*, sulfuric acid, copper, iron(III), zinc and magnesium sulfate
- The reactor contents were then heated to the required operating temperature, with the impeller stirring slowly, and applying about 100 kPa oxygen overpressure (to reduce corrosion of the autoclave internals, *i.e.*, when no Fe(III) or Cu was present)
- Once the required operating temperature was reached, the overpressure was increased to the target gauge pressure, using pure oxygen. In contrast, the 7-litre glass reactor operated with pure oxygen under atmospheric pressure conditions
- The impeller speed was then increased to the setpoint value of 1000 rev/min, while the vapour phase was slowly vented for five minutes to remove inert gas from the head space. The vapour space of the 7-litre glass reactor was replaced at a rate of 300 mL/min over the

Stellenbosch University http://scholar.sun.ac.za

duration of the experiment to ensure a consistent oxygen partial pressure, *i.e.*, excess oxygen flow was maintained in the head space to prevent air inflow from the surroundings

- The feed bomb (Ch. 6, Sect. 6.4) was then charged with the required amount of iron(II) sulfate solution and injected into the autoclave, *i.e.*, to initiate the oxidation reaction at 5 g/L Fe(II), corresponding to 1000 g or 1200 g starting mass in the autoclave. The clock was started when the feed bomb discharge valve was opened (Figure 6.24). In the case of the 7-litre reactor, the test commenced by adding concentrated iron(II) sulfate solution to yield around 6.5 L starting volume (at room temperature) in the reactor
- The oxidation reaction proceeded for a predetermined time, with samples removed at regular intervals *via* the sampling bomb (Figure 4.3 *b*). A 'dead' volume of around 15 mL was taken first in order to prevent contamination of the actual sample by stagnant solution in the dip and connection tubes, *i.e.*, in the tubing on the autoclave side of the sampling valve. In the case of the 7-litre reactor, the sampling procedure was simple, could be executed in relatively short time and did not require 'dead' sample volumes; the samples were simply withdrawn using a suction tube and pro-pipette
- In the case of the autoclave reactor (Figure 4.3 *a*), cooling water from a chiller unit was continuously passed through the sampling bomb jacket. The discharge, vent and oxygen feed valves were first closed, after which the sampling valve was slowly opened. Once the pressure had equalised, the sampling valve was closed and the contents rapidly cooled (< 30 sec). The vent (needle) valve was then slowly opened until atmospheric pressure was reached. The discharge valve was then opened, the sample (~15 mL) collected, after which the oxygen feed valve was opened again. It was assumed that iron(II) oxidation ceased almost instantaneously (< 15 sec) after entering the sampling bomb. The above procedure was therefore initiated about 15 sec before the sample was due, and
- The glass sample holder was immediately covered and placed in a waterbath, which was controlled at 20°C. An accurate 10 mL volume was then pipetted into a volumetric flask (see Appendix B.1.2) and titrated against a standardised (0.05 or 0.1 N) potassium dichromate solution. The detailed titration procedure can be found in Appendix B.2.3. Selected samples were also titrated potentiometrically (App. B.2.3) for quality control. The acid concentration closely followed the iron(II) oxidation extent and was calculated, rather than relying on a free acid titration value.

D.2 Verifying the experimental procedure and identifying the intrinsic reaction regime

These tests aimed at verifying the experimental procedure and identifying the intrinsic oxidation regime in the 2-litre Parr autoclave (AC), *i.e.*, to establish the role of interfacial gas/liquid mass transfer limitations, and also to assess the impact of the reaction 'product', iron(III).

Stellenbosch University http://scholar.sun.ac.za

FOA1	Temp.	Imp. speed	Sln. mass	P_g.	$p_{O2}°$
2-litre AC	(°C)	(rev/min)	(g)	(kPa)	(kPa)
Config. A	150	1000	1000	890	500
[Dichromate]	$[H_2SO_4]$	[Cu]	[Zn]	[Fe(III)]	[a] Density
(N)	(g/L)	(g/L)	(g/L)	(g/L)	(g/L)
0.1	25	25	0	0	1087
Time	[b] Titrant	Colorimetric	Potentiometric	$[Fe(II)]_{avg}\cdot 10^2$	[c] *CV*
(min)	(mL)	[Fe(II)] (g/L)	[Fe(II)] (g/L)	(mol/kg)	(%)
0	–	5.00	–	9.08	–
1.5	3.40	1.90	–	3.45	–
3.8	1.50	0.84	–	1.53	–
4.8	1.15	0.64	–	1.16	–
6.0	1.00	0.56	–	1.01	–
7.3	0.90	0.50	–	0.91	–
8.5	0.80	0.45	–	0.81	–
9.5	0.55	0.31	–	0.56	–
11.0	0.35	0.20	–	0.36	–

[a] 20°C; [b] 10 mL sample ; [c] $\{\sum(x_i - x_{avg})^2\}^{0.5}/x_{avg}$.

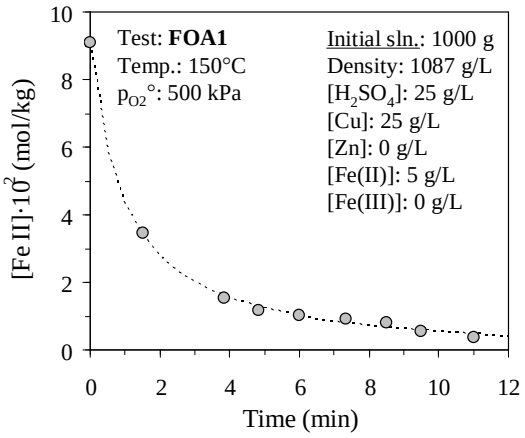

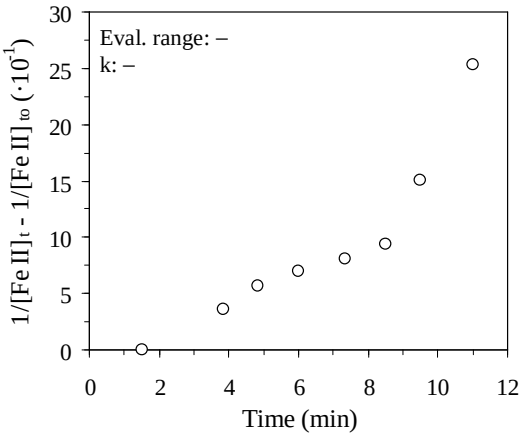

Stellenbosch University http://scholar.sun.ac.za

FOA2	Temp.	Imp. speed	Sln. mass	P_g.	$p_{O2}°$
2-litre AC	(°C)	(rev/min)	(g)	(kPa)	(kPa)
Config. A	150	1000	1000	840	450
[Dichromate]	[H_2SO_4]	[Cu]	[Zn]	[Fe(III)]	[a] Density
(N)	(g/L)	(g/L)	(g/L)	(g/L)	(g/L)
0.1	25	25	0	0	1087
Time	[b] Titrant	Colorimetric	Potentiometric	$[Fe(II)]_{avg}\cdot 10^2$	[c] *CV*
(min)	(mL)	[Fe(II)] (g/L)	[Fe(II)] (g/L)	(mol/kg)	(%)
0	–	5.00	–	9.08	–
2.0	3.40	1.90	–	3.45	–
5.0	1.45	0.81	–	1.47	–
7.5	1.25	0.70	–	1.27	–
10.0	0.95	0.53	–	0.96	–
12.5	0.75	0.42	–	0.76	–

[a] 20°C; [b] 10 mL sample ; [c] $\{\sum(x_i - x_{avg})^2\}^{0.5}/x_{avg}$.

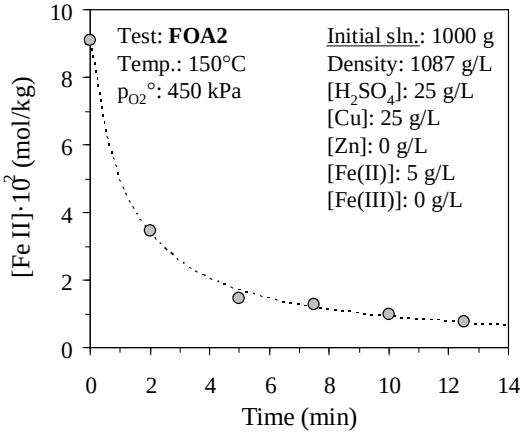

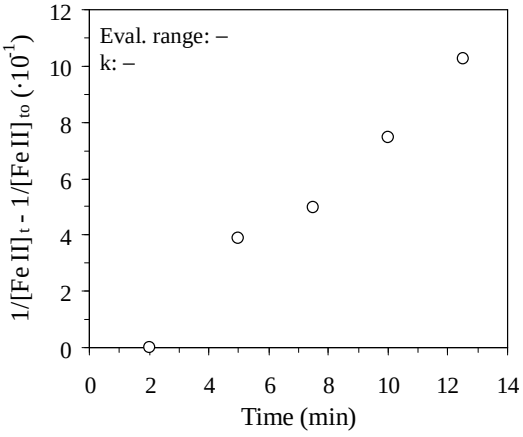

Stellenbosch University http://scholar.sun.ac.za

FOA3	Temp.	Imp. speed	Sln. mass	P_g.	$p_{O2}°$
2-litre AC	(°C)	(rev/min)	(g)	(kPa)	(kPa)
Config. A	150	1000	1000	440	50
[Dichromate]	$[H_2SO_4]$	[Cu]	[Zn]	[Fe(III)]	[a] Density
(N)	(g/L)	(g/L)	(g/L)	(g/L)	(g/L)
0.1	25	25	0	0	1087
Time	[b] Titrant	Colorimetric	Potentiometric	$[Fe(II)]_{avg}\cdot 10^2$	[c] *CV*
(min)	(mL)	[Fe(II)] (g/L)	[Fe(II)] (g/L)	(mol/kg)	(%)
0	–	5.00	–	9.08	–
2.0	5.75	3.21	–	5.83	–
5.0	5.00	2.79	–	5.07	–
7.5	4.60	2.57	–	4.67	–
10.0	4.30	2.40	–	4.36	–
12.5	3.70	2.07	–	3.75	–
15.0	3.00	1.68	–	3.04	–
20.0	2.00	1.12	–	2.03	–
30.0	0.95	0.53	–	0.96	–

[a] 20°C; [b] 10 mL sample ; [c] $\{\sum(x_i - x_{avg})^2\}^{0.5}/x_{avg}$.

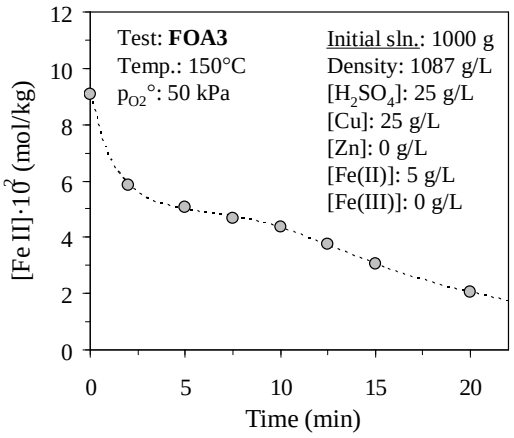

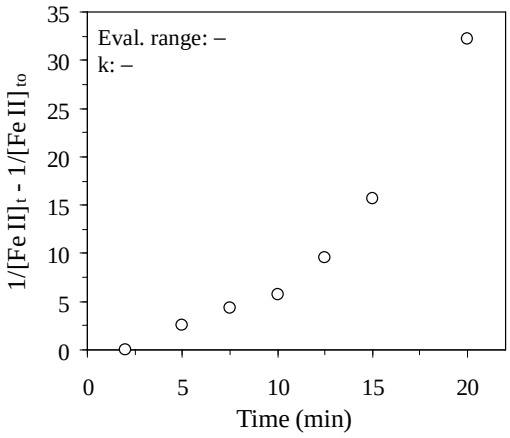

Stellenbosch University http://scholar.sun.ac.za

FOA4	Temp.	Imp. speed	Sln. mass	P_g.	$p_{O2}°$
2-litre AC	(°C)	(rev/min)	(g)	(kPa)	(kPa)
Config. A	150	1000	1000	890	500
[Dichromate]	$[H_2SO_4]$	[Cu]	[Zn]	[Fe(III)]	[a] Density
(N)	(g/L)	(g/L)	(g/L)	(g/L)	(g/L)
0.1	25	0	0	0	1023
Time	[b] Titrant	Colorimetric	Potentiometric	$[Fe(II)]_{avg}\cdot 10^2$	[c] *CV*
(min)	(mL)	[Fe(II)] (g/L)	[Fe(II)] (g/L)	(mol/kg)	(%)
0	–	5.00	–	9.09	–
3.8	6.40	3.57	–	6.50	–
5.2	5.90	3.29	–	5.99	–
6.5	5.50	3.07	–	5.58	–
8.0	5.05	2.82	–	5.13	–
10.0	4.65	2.60	–	4.72	–
11.5	4.30	2.40	–	4.37	–
13.3	4.10	2.29	–	4.17	–
15.0	3.80	2.12	–	3.86	–
17.5	3.55	1.98	–	3.61	–
20.0	3.20	1.79	–	3.25	–

[a] 20°C; [b] 10 mL sample ; [c] $\{\sum(x_i - x_{avg})^2\}^{0.5}/x_{avg}$.

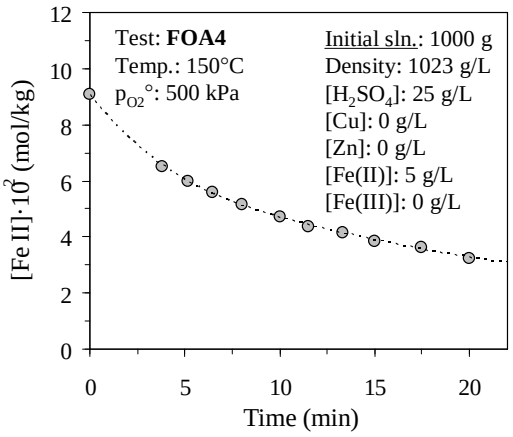

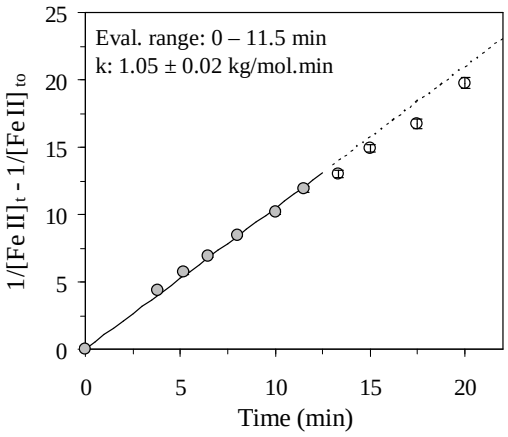

Stellenbosch University http://scholar.sun.ac.za

FOB1	Temp.	Imp. speed	[a] Sln. mass	P_g.	$p_{O2}°$
2-litre AC	(°C)	(rev/min)	(g)	(kPa)	(kPa)
Config. A	150	1000	1000	1040	650
[Dichromate]	$[H_2SO_4]$	[Cu]	[Zn]	[Fe(III)]	[b] Density
(N)	(g/L)	(g/L)	(g/L)	(g/L)	(g/L)
0.1	25	0	0	0	1023
Time	[c] Titrant	Colorimetric	Potentiometric	$[Fe(II)]_{avg}\cdot 10^2$	[d] *CV*
(min)	(mL)	[Fe(II)] (g/L)	[Fe(II)] (g/L)	(mol/kg)	(%)
0	–	5.00	5.00	9.09	–
3.3	6.50	3.63	3.84	6.79	<15
8.5	4.65	2.60	2.70	4.82	<15
10	4.15	2.32	2.40	4.29	<15
15	3.50	1.96	2.09	3.68	<15
20	3.00	1.68	1.79	3.15	<15
25	2.75	1.54	1.49	2.75	<15
45	2.20	1.23	1.28	2.28	<15
90	1.25	0.70	0.87	1.43	**16**

[a] Feed sln. preheated to ~130°C; [b] 20°C; [c] 10 mL sample ; [d] $\{\sum(x_i - x_{avg})^2\}^{0.5}/x_{avg}$.

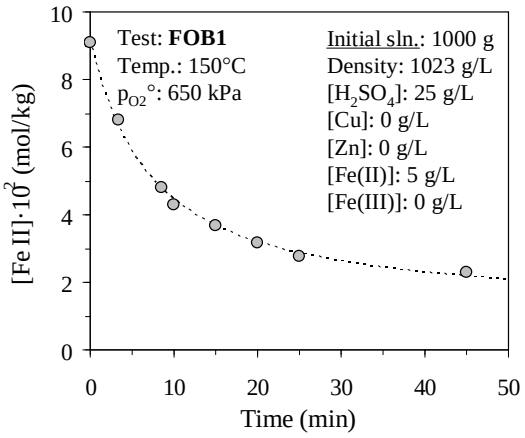

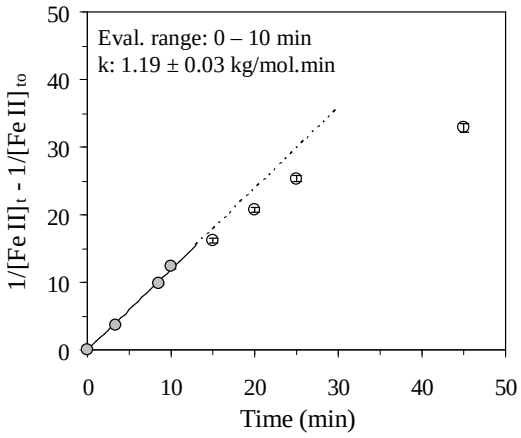

Stellenbosch University http://scholar.sun.ac.za

FOB2	Temp.	Imp. speed	Sln. mass	P_g.	$p_{O2}°$
2-litre AC	(°C)	(rev/min)	(g)	(kPa)	(kPa)
Config. A	150	1000	1200	1040	650
[Dichromate]	$[H_2SO_4]$	[Cu]	[Zn]	[Fe(III)]	[a] Density
(N)	(g/L)	(g/L)	(g/L)	(g/L)	(g/L)
0.1	25	0	0	0	1023
Time	[b] Titrant	Colorimetric	Potentiometric	$[Fe(II)]_{avg}\cdot10^2$	[c] *CV*
(min)	(mL)	[Fe(II)] (g/L)	[Fe(II)] (g/L)	(mol/kg)	(%)
0	–	5.00	5.00	9.09	–
3.0	8.90	4.97	4.47	8.59	<15
7.5	5.70	3.18	3.48	6.06	<15
10	4.50	2.51	2.77	4.80	<15
15	3.40	1.90	2.22	3.75	<15
20	2.90	1.62	1.83	3.14	<15
25	2.60	1.45	1.48	2.66	<15
30	2.35	1.31	1.27	2.35	<15
60	1.55	0.87	0.80	1.51	<15
90	1.00	0.56	0.55	1.01	<15

[a] 20°C; [b] 10 mL sample ; [c] $\{\sum(x_i - x_{avg})^2\}^{0.5}/x_{avg}$.

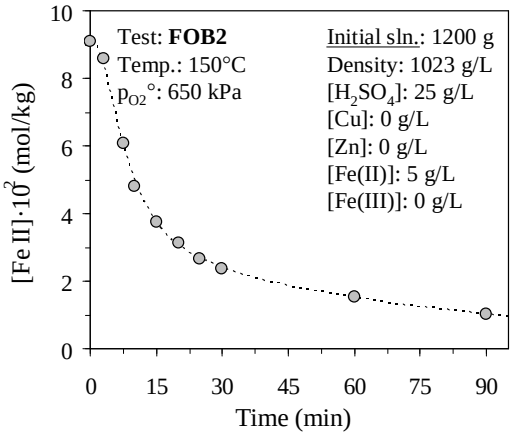

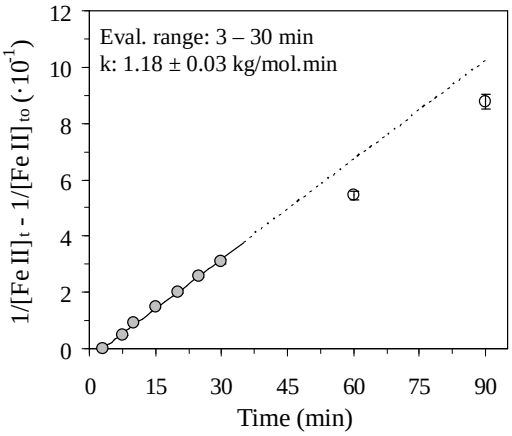

Stellenbosch University http://scholar.sun.ac.za

FOC1	Temp.	Imp. speed	Sln. mass	P_g.	$p_{O2}°$
2-litre AC	(°C)	(rev/min)	(g)	(kPa)	(kPa)
Config. A	130	1000	1200	1185	1000
[Dichromate]	$[H_2SO_4]$	[Cu]	[Zn]	[Fe(III)]	[a] Density
(N)	(g/L)	(g/L)	(g/L)	(g/L)	(g/L)
0.1	25	0	0	0	1023
Time	[b] Titrant	Colorimetric	Potentiometric	$[Fe(II)]_{avg}\cdot 10^2$	[c] *CV*
(min)	(mL)	[Fe(II)] (g/L)	[Fe(II)] (g/L)	(mol/kg)	(%)
0	–	5.00	5.00	9.09	–
3.0	8.00	4.47	4.52	8.18	<15
7.5	6.20	3.46	3.44	6.28	<15
15	3.60	2.01	2.68	4.27	**20**
20	3.10	1.73	2.29	3.66	**20**
30	2.80	1.56	1.60	2.88	<15
60	2.00	1.12	1.86	1.80	**18**
90	1.60	0.89	0.69	1.44	**18**
120	1.40	0.78	0.63	1.28	**15**

[a] 20°C; [b] 10 mL sample ; [c] $\{\sum(x_i - x_{avg})^2\}^{0.5}/x_{avg}$.

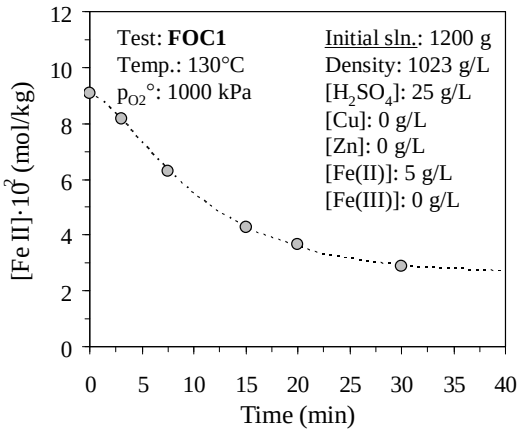

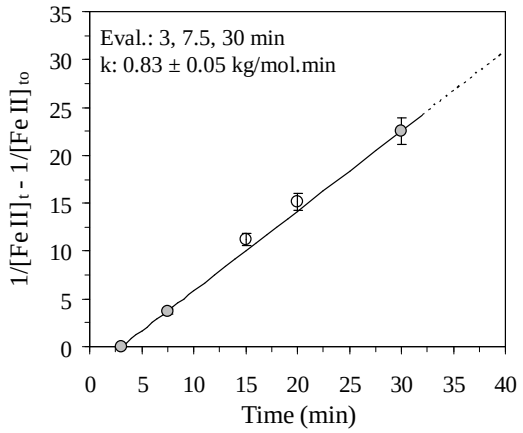

Stellenbosch University http://scholar.sun.ac.za

FOC2	Temp.	Imp. speed	Sln. mass	P_g.	$p_{O2}°$
2-litre AC	(°C)	(rev/min)	(g)	(kPa)	(kPa)
Config. A	130	1000	1200	1185	1000
[Dichromate]	$[H_2SO_4]$	[Cu]	[Zn]	[Fe(III)]	[a] Density
(N)	(g/L)	(g/L)	(g/L)	(g/L)	(g/L)
0.05	25	0	0	0	1023
Time	[b] Titrant	Colorimetric	Potentiometric	$[Fe(II)]_{avg}\cdot 10^2$	[c] *CV*
(min)	(mL)	[Fe(II)] (g/L)	[Fe(II)] (g/L)	(mol/kg)	(%)
0	–	5.00	–	9.09	–
1.0	17.80	4.97	–	9.04	–
3.0	15.90	4.44	–	8.08	–
5.0	14.10	3.94	–	7.16	–
7.5	12.20	3.41	–	6.20	–
10.0	10.50	2.93	–	5.33	–
12.5	9.60	2.68	–	4.88	–
20	6.90	1.93	–	3.50	–
25	6.10	1.70	–	3.10	–
30	5.50	1.54	–	2.79	–
45	4.30	1.20	–	2.18	–
60	3.50	0.98	–	1.78	–
75	3.00	0.84	–	1.52	–
90	2.60	0.73	–	1.32	–

[a] 20°C; [b] 10 mL sample ; [c] $\{\sum(x_i - x_{avg})^2\}^{0.5}/x_{avg}$.

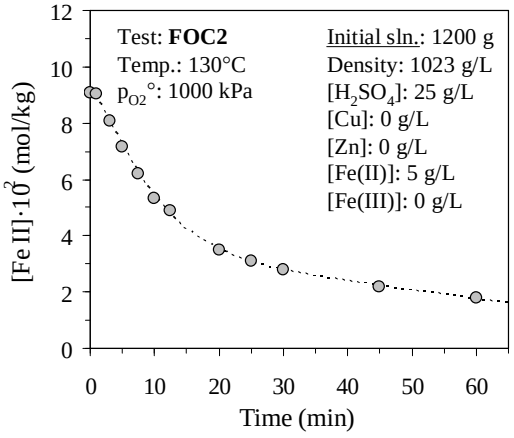

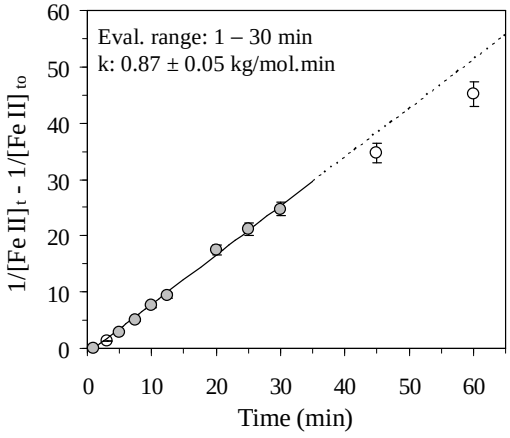

Stellenbosch University http://scholar.sun.ac.za

FOC3	Temp.	Imp. speed	Sln. mass	P_g.	$p_{O2}°$
2-litre AC	(°C)	(rev/min)	(g)	(kPa)	(kPa)
Config. A	130	1000	1200	2185	2000
[Dichromate]	$[H_2SO_4]$	[Cu]	[Zn]	[Fe(III)]	[a] Density
(N)	(g/L)	(g/L)	(g/L)	(g/L)	(g/L)
0.1	25	0	0	10	1063
Time	[b] Titrant	Colorimetric	Potentiometric	$[Fe(II)]_{avg}·10^2$	[c] *CV*
(min)	(mL)	[Fe(II)] (g/L)	[Fe(II)] (g/L)	(mol/kg)	(%)
0	–	5.00	–	9.06	–
2.0	7.80	4.36	–	7.89	–
5.0	5.60	3.13	–	5.66	–
7.5	4.50	2.51	–	4.55	–
10.0	3.90	2.18	–	3.94	–
12.5	3.40	1.90	–	3.44	–
15	2.90	1.62	–	2.93	–
20	2.30	1.28	–	2.33	–
30	1.70	0.95	–	1.72	–
45	1.30	0.73	–	1.31	–

[a] 20°C; [b] 10 mL sample ; [c] $\{\sum(x_i - x_{avg})^2\}^{0.5}/x_{avg}$.

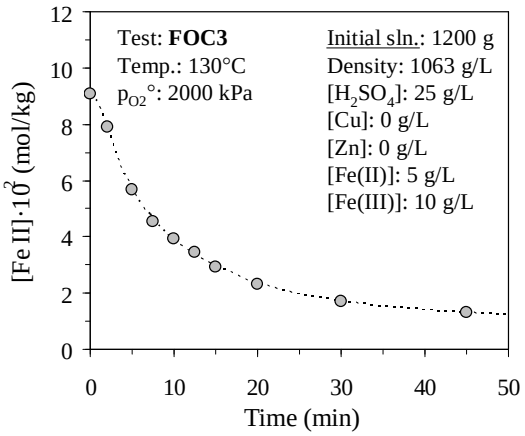

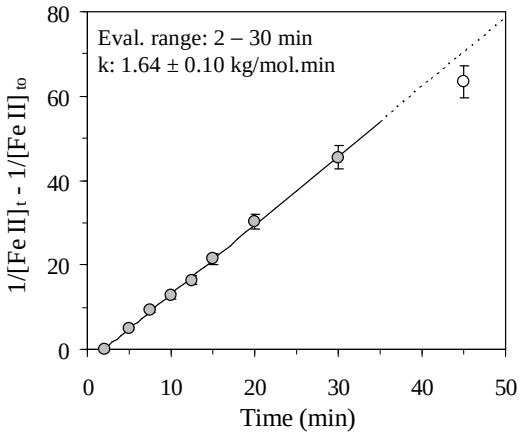

Stellenbosch University http://scholar.sun.ac.za

D.3 Reaction orders without copper (catalyst)

These tests aimed to determine the various reaction order dependencies of the iron(II) oxidation rate on the primary variables in low and high (zinc) sulfate solution environments, without any copper (catalyst).

FOD1	Temp.	Imp. speed	Sln. mass	P_g.	p_{O2}°
2-litre AC	(°C)	(rev/min)	(g)	(kPa)	(kPa)
Config. A	130	1000	1200	1685	1500
[Dichromate]	$[H_2SO_4]$	[Cu]	[Zn]	[Fe(III)]	[a] Density
(N)	(g/L)	(g/L)	(g/L)	(g/L)	(g/L)
0.1	25	0	0	0	1023
Time	[b] Titrant	Colorimetric	Potentiometric	$[Fe(II)]_{avg}\cdot 10^2$	[c] *CV*
(min)	(mL)	[Fe(II)] (g/L)	[Fe(II)] (g/L)	(mol/kg)	(%)
0	–	5.00	5.00	9.09	–
3.0	7.00	3.91	4.20	7.38	<15
7.5	5.05	2.82	3.14	5.42	<15
10	4.35	2.43	2.75	4.71	<15
20	2.80	1.56	1.93	3.18	<15
30	2.35	1.31	1.37	2.44	<15
60	1.55	0.87	0.88	1.59	<15
90	1.30	0.73	0.51	1.12	**25**

[a] 20°C; [b] 10 mL sample ; [c] $\{\sum(x_i - x_{avg})^2\}^{0.5}/x_{avg}$.

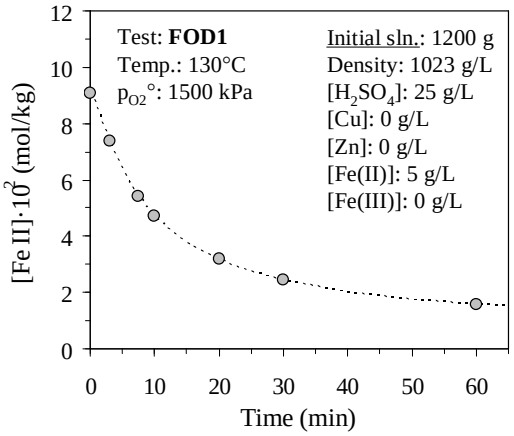

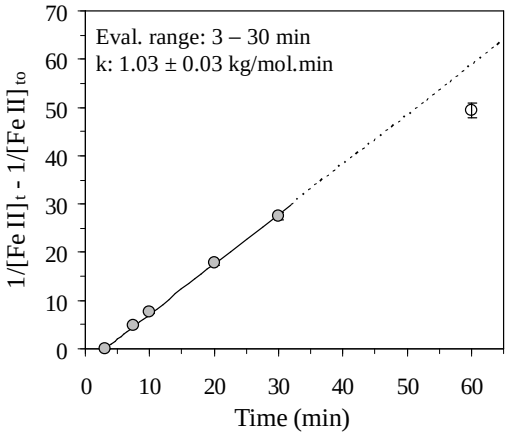

Stellenbosch University http://scholar.sun.ac.za

FOD2	Temp.	Imp. speed	Sln. mass	P_g.	$p_{O2}°$
2-litre AC	(°C)	(rev/min)	(g)	(kPa)	(kPa)
Config. A	130	1000	1200	2185	2000
[Dichromate]	$[H_2SO_4]$	[Cu]	[Zn]	[Fe(III)]	[a] Density
(N)	(g/L)	(g/L)	(g/L)	(g/L)	(g/L)
0.1	25	0	0	0	1023
Time	[b] Titrant	Colorimetric	Potentiometric	$[Fe(II)]_{avg}\cdot10^2$	[c] *CV*
(min)	(mL)	[Fe(II)] (g/L)	[Fe(II)] (g/L)	(mol/kg)	(%)
0	–	5.00	5.00	9.09	–
3.0	7.00	3.91	4.08	7.27	<15
7.5	4.40	2.46	2.71	4.70	<15
11	3.80	2.12	2.04	3.79	<15
20	2.60	1.45	1.35	2.55	<15
30	1.85	1.03	1.08	1.92	<15
45	1.40	0.78	0.75	1.39	<15
60	1.05	0.59	0.60	1.08	<15

[a] 20°C; [b] 10 mL sample ; [c] $\{\sum(x_i - x_{avg})^2\}^{0.5}/x_{avg}$.

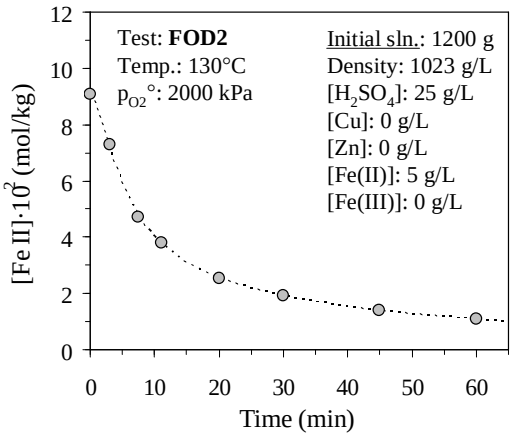

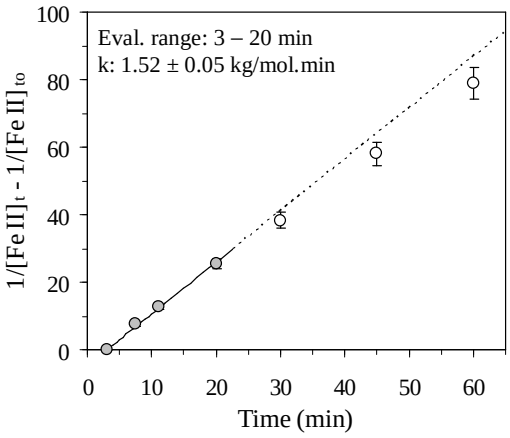

Stellenbosch University http://scholar.sun.ac.za

FOD3	Temp.	Imp. speed	Sln. mass	P_g.	$p_{O2}°$
2-litre AC	(°C)	(rev/min)	(g)	(kPa)	(kPa)
Config. A	130	1000	1200	2685	2500
[Dichromate]	$[H_2SO_4]$	[Cu]	[Zn]	[Fe(III)]	[a] Density
(N)	(g/L)	(g/L)	(g/L)	(g/L)	(g/L)
0.1	25	0	0	0	1023
Time	[b] Titrant	Colorimetric	Potentiometric	$[Fe(II)]_{avg}·10^2$	[c] *CV*
(min)	(mL)	[Fe(II)] (g/L)	[Fe(II)] (g/L)	(mol/kg)	(%)
0	–	5.00	5.00	9.09	–
3.0	6.00	3.35	3.91	6.60	<15
5.0	5.20	2.90	2.94	5.32	<15
7.5	4.00	2.23	2.26	4.09	<15
10.0	3.60	2.01	1.96	3.61	<15
12.5	3.00	1.68	1.68	3.05	<15
15	2.60	1.45	1.39	2.58	<15
30	1.80	1.01	0.80	1.64	**16**

[a] 20°C; [b] 10 mL sample ; [c] $\{\sum(x_i - x_{avg})^2\}^{0.5}/x_{avg}$.

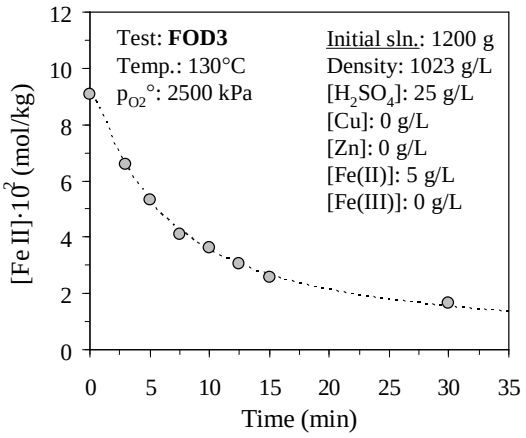

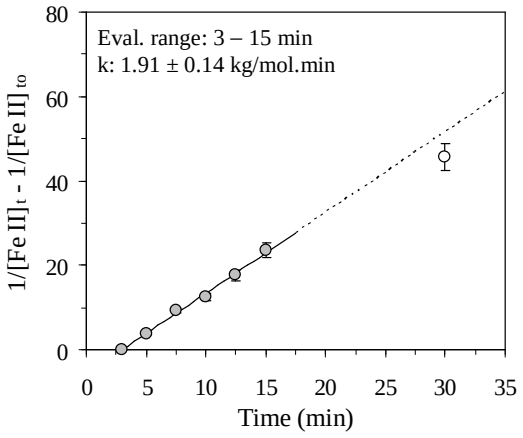

Stellenbosch University http://scholar.sun.ac.za

FOE1	Temp.	Imp. speed	Sln. mass	P_g.	$p_{O2}°$
2-litre AC	(°C)	(rev/min)	(g)	(kPa)	(kPa)
Config. A	130	1000	1200	1685	1500
[Dichromate]	$[H_2SO_4]$	[Cu]	[Zn]	[Fe(III)]	[a] Density
(N)	(g/L)	(g/L)	(g/L)	(g/L)	(g/L)
0.1	10	0	0	0	1019
Time	[b] Titrant	Colorimetric	Potentiometric	$[Fe(II)]_{avg}\cdot 10^2$	[c] *CV*
(min)	(mL)	[Fe(II)] (g/L)	[Fe(II)] (g/L)	(mol/kg)	(%)
0	–	5.00	5.00	8.99	–
3.0	6.50	3.63	3.76	6.65	<15
7.5	3.30	1.84	2.24	3.67	<15
10	2.80	1.56	1.54	2.79	<15
15	1.90	1.06	1.06	1.91	<15
30	1.20	0.67	0.63	1.17	<15
45	0.80	0.45	0.45	0.81	<15

[a] 20°C; [b] 10 mL sample ; [c] $\{\sum(x_i - x_{avg})^2\}^{0.5}/x_{avg}$.

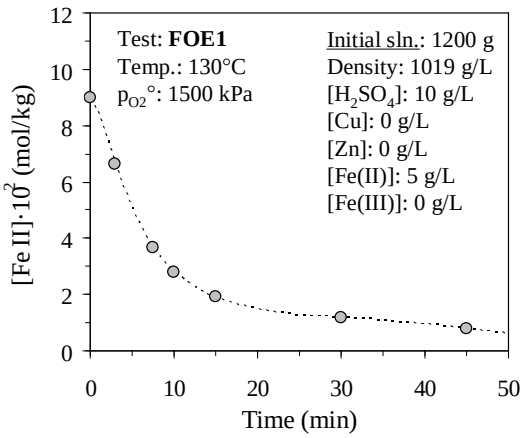

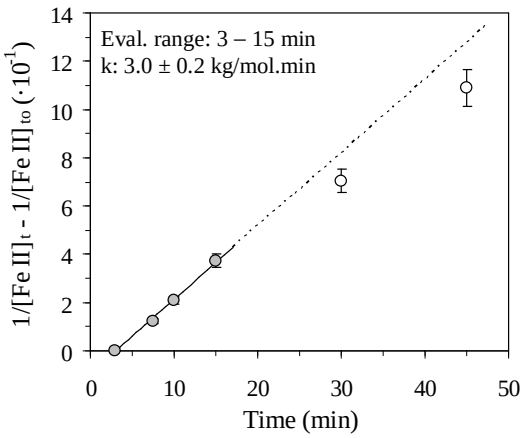

Stellenbosch University http://scholar.sun.ac.za

FOE2	Temp.	Imp. speed	Sln. mass	P_g.	$p_{O2}°$
2-litre AC	(°C)	(rev/min)	(g)	(kPa)	(kPa)
Config. A	130	1000	1200	1685	1500
[Dichromate]	$[H_2SO_4]$	[Cu]	[Zn]	[Fe(III)]	[a] Density
(N)	(g/L)	(g/L)	(g/L)	(g/L)	(g/L)
0.1	35	0	0	0	1029
Time	[b] Titrant	Colorimetric	Potentiometric	$[Fe(II)]_{avg}\cdot 10^2$	[c] *CV*
(min)	(mL)	[Fe(II)] (g/L)	[Fe(II)] (g/L)	(mol/kg)	(%)
0	–	5.00	5.00	9.13	–
3.0	7.60	4.24	4.23	7.74	<15
10	4.80	2.68	2.69	4.90	<15
20	3.30	1.84	1.74	3.27	<15
30	2.50	1.40	1.30	2.46	<15
60	1.40	0.78	0.82	1.46	<15
90	1.10	0.61	–	1.12	–
120	0.80	0.45	–	0.82	–

[a] 20°C; [b] 10 mL sample ; [c] $\{\sum(x_i - x_{avg})^2\}^{0.5}/x_{avg}$.

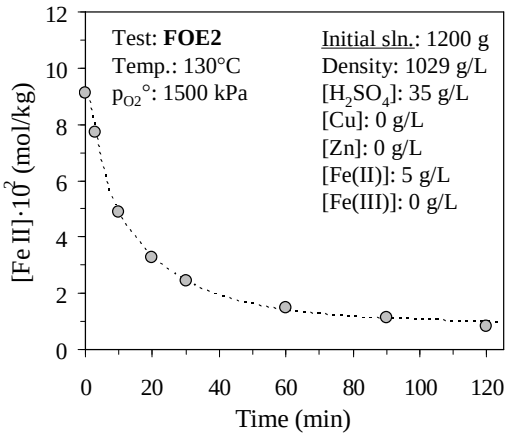

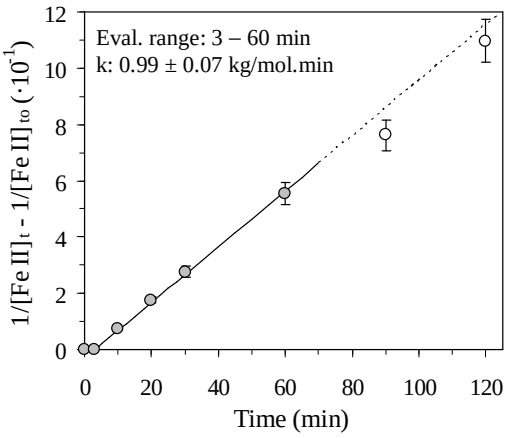

Stellenbosch University http://scholar.sun.ac.za

FOE3	Temp.	Imp. speed	Sln. mass	P_g.	$p_{O2}°$
2-litre AC	(°C)	(rev/min)	(g)	(kPa)	(kPa)
Config. A	130	1000	1200	1685	1500
[Dichromate]	$[H_2SO_4]$	[Cu]	[Zn]	[Fe(III)]	[a] Density
(N)	(g/L)	(g/L)	(g/L)	(g/L)	(g/L)
0.1	45	0	0	0	1036
Time	[b] Titrant	Colorimetric	Potentiometric	$[Fe(II)]_{avg}\cdot 10^2$	[c] *CV*
(min)	(mL)	[Fe(II)] (g/L)	[Fe(II)] (g/L)	(mol/kg)	(%)
0	–	5.00	5.00	9.16	–
3.0	7.90	4.41	4.48	8.15	<15
10	5.70	3.18	3.23	5.87	<15
20	3.70	2.07	2.16	3.87	<15
30	2.90	1.62	1.72	3.06	<15
60	1.70	0.95	0.89	1.68	<15
90	1.20	0.67	0.60	1.16	<15
120	0.90	0.50	–	0.92	–

[a] 20°C; [b] 10 mL sample ; [c] $\{\sum(x_i - x_{avg})^2\}^{0.5}/x_{avg}$.

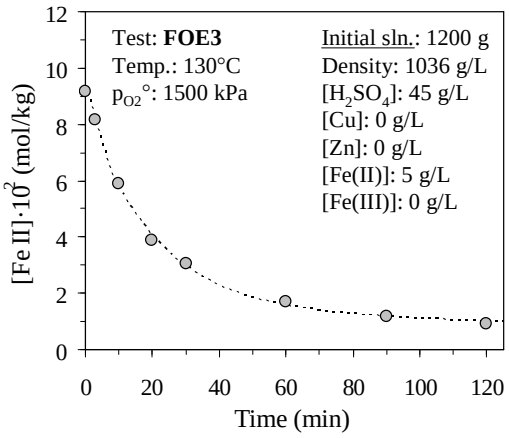

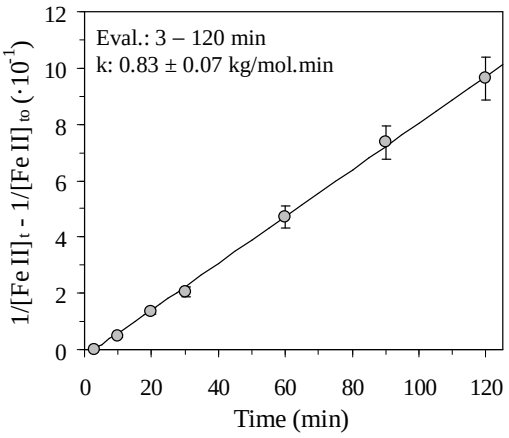

Stellenbosch University http://scholar.sun.ac.za

FOF1	Temp.	Imp. speed	Sln. mass	P_g.	$p_{O2}°$
2-litre AC	(°C)	(rev/min)	(g)	(kPa)	(kPa)
Config. A	130	1000	1200	1185	1000
[Dichromate]	$[H_2SO_4]$	[Cu]	[Zn]	[Fe(III)]	[a] Density
(N)	(g/L)	(g/L)	(g/L)	(g/L)	(g/L)
0.05	25	0	15	0	1063
Time	[b] Titrant	Colorimetric	Potentiometric	$[Fe(II)]_{avg}\cdot 10^2$	[c] *CV*
(min)	(mL)	[Fe(II)] (g/L)	[Fe(II)] (g/L)	(mol/kg)	(%)
0	–	5.00	–	9.07	–
2.0	12.20	3.41	–	6.18	–
5.0	8.50	2.37	–	4.30	–
7.5	6.20	1.73	–	3.14	–
10.0	5.20	1.45	–	2.63	–
12.5	4.40	1.23	–	2.23	–
15	3.80	1.06	–	1.92	–
20	3.00	0.84	–	1.52	–
30	2.20	0.61	–	1.11	–
45	1.60	0.45	–	0.81	–
60	1.20	0.34	–	0.61	–

[a] 20°C; [b] 10 mL sample ; [c] $\{\sum(x_i - x_{avg})^2\}^{0.5}/x_{avg}$.

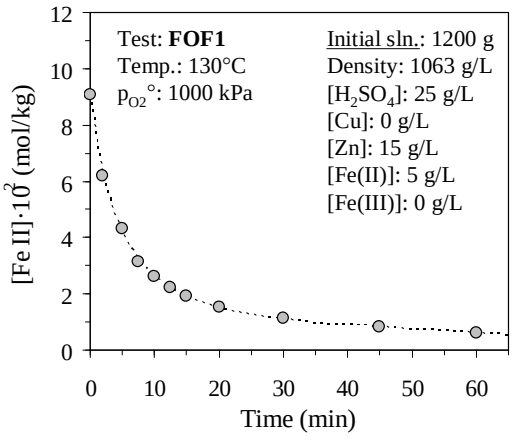

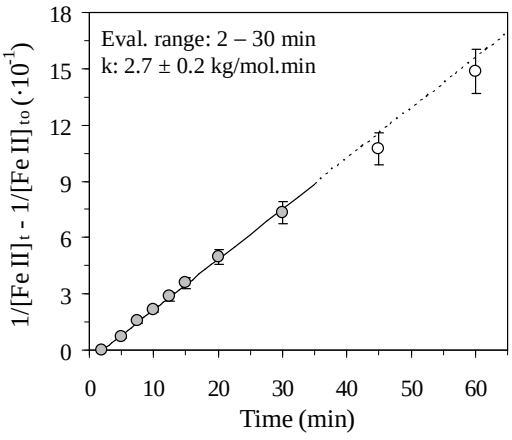

Stellenbosch University http://scholar.sun.ac.za

FOF2	Temp.	Imp. speed	Sln. mass	P_g.	$p_{O2}°$
2-litre AC	(°C)	(rev/min)	(g)	(kPa)	(kPa)
Config. A	130	1000	1200	1685	1500
[Dichromate]	$[H_2SO_4]$	[Cu]	[Zn]	[Fe(III)]	[a] Density
(N)	(g/L)	(g/L)	(g/L)	(g/L)	(g/L)
0.05	25	0	15	0	1063
Time	[b] Titrant	Colorimetric	Potentiometric	$[Fe(II)]_{avg}\cdot 10^2$	[c] *CV*
(min)	(mL)	[Fe(II)] (g/L)	[Fe(II)] (g/L)	(mol/kg)	(%)
0	–	5.00	–	9.07	–
2.0	10.20	2.85	–	5.16	–
5.0	6.20	1.73	–	3.14	–
7.5	4.80	1.34	–	2.43	–
10.0	4.00	1.12	–	2.03	–
12.5	3.20	0.89	–	1.62	–
15	2.70	0.75	–	1.37	–
20	2.00	0.56	–	1.01	–
30	1.40	0.39	–	0.71	–
45	0.90	0.25	–	0.46	–

[a] 20°C; [b] 10 mL sample ; [c] $\{\sum(x_i - x_{avg})^2\}^{0.5}/x_{avg}$.

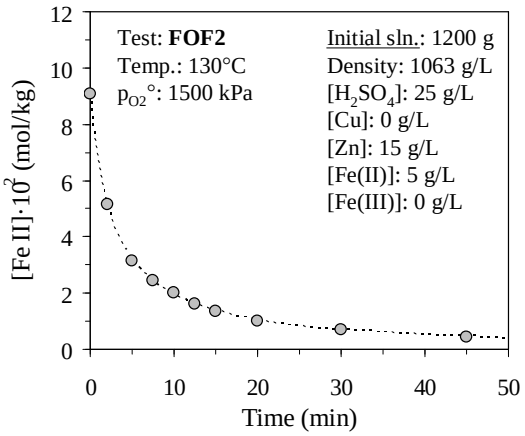

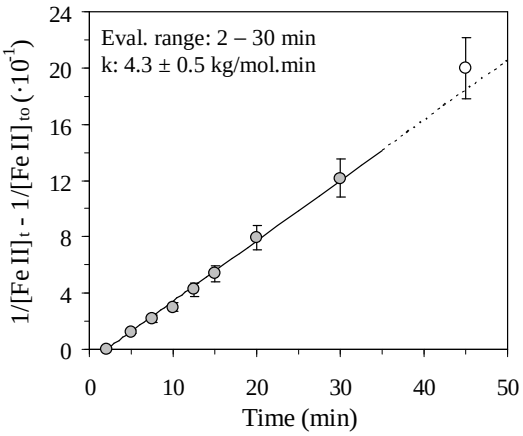

Stellenbosch University http://scholar.sun.ac.za

FOF3	Temp.	Imp. speed	Sln. mass	P_g.	$p_{O2}°$
2-litre AC	(°C)	(rev/min)	(g)	(kPa)	(kPa)
Config. A	130	1000	1200	2185	2000
[Dichromate]	$[H_2SO_4]$	[Cu]	[Zn]	[Fe(III)]	[a] Density
(N)	(g/L)	(g/L)	(g/L)	(g/L)	(g/L)
0.05	25	0	15	0	1063
Time	[b] Titrant	Colorimetric	Potentiometric	$[Fe(II)]_{avg}\cdot 10^2$	[c] *CV*
(min)	(mL)	[Fe(II)] (g/L)	[Fe(II)] (g/L)	(mol/kg)	(%)
0	–	5.00	–	9.07	–
2.0	11.60	3.24	–	5.87	–
5.0	6.00	1.68	–	3.04	–
7.5	4.20	1.17	–	2.13	–
10.0	3.20	0.89	–	1.62	–
12.5	2.40	0.67	–	1.22	–
15	2.10	0.59	–	1.06	–
20	1.70	0.47	–	0.86	–
30	1.10	0.31	–	0.56	–
45	0.70	0.20	–	0.35	–

[a] 20°C; [b] 10 mL sample ; [c] $\{\sum(x_i - x_{avg})^2\}^{0.5}/x_{avg}$.

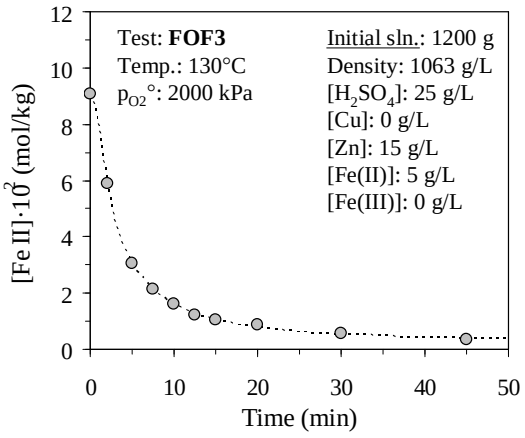

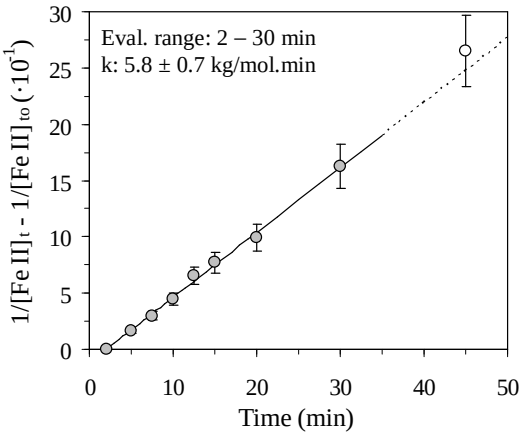

Stellenbosch University http://scholar.sun.ac.za

FOF4	Temp.	Imp. speed	Sln. mass	P_g.	$p_{O2}°$
2-litre AC	(°C)	(rev/min)	(g)	(kPa)	(kPa)
Config. A	130	1000	1200	2685	2500
[Dichromate]	$[H_2SO_4]$	[Cu]	[Zn]	[Fe(III)]	[a] Density
(N)	(g/L)	(g/L)	(g/L)	(g/L)	(g/L)
0.05	25	0	15	0	1063
Time	[b] Titrant	Colorimetric	Potentiometric	$[Fe(II)]_{avg}\cdot 10^2$	[c] *CV*
(min)	(mL)	[Fe(II)] (g/L)	[Fe(II)] (g/L)	(mol/kg)	(%)
0	–	5.00	–	9.07	–
2.0	13.60	3.80	–	6.89	–
5.0	5.90	1.65	–	2.99	–
7.5	3.90	1.09	–	1.97	–
10.0	3.00	0.84	–	1.52	–
12.5	2.40	0.67	–	1.22	–
15	2.00	0.56	–	1.01	–
20	1.50	0.42	–	0.76	–
30	1.10	0.31	–	0.56	–
45	0.80	0.22	–	0.41	–

[a] 20°C; [b] 10 mL sample ; [c] $\{\sum(x_i - x_{avg})^2\}^{0.5}/x_{avg}$.

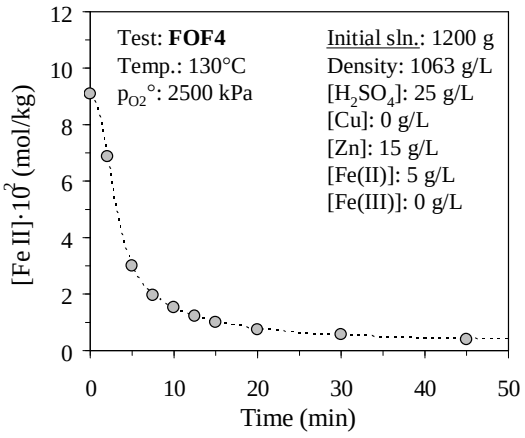

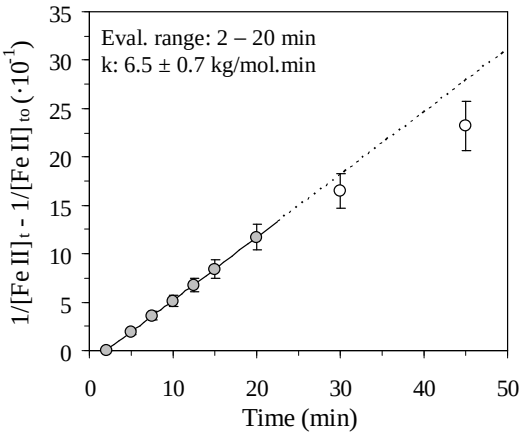

Stellenbosch University http://scholar.sun.ac.za

FOG1	Temp.	Imp. speed	Sln. mass	P_g.	$p_{O2}°$
2-litre AC	(°C)	(rev/min)	(g)	(kPa)	(kPa)
Config. A	130	1000	1000	1185	1000
[Dichromate]	$[H_2SO_4]$	[Cu]	[Zn]	[Fe(III)]	[a] Density
(N)	(g/L)	(g/L)	(g/L)	(g/L)	(g/L)
0.05	25	0	25	0	1070
Time	[b] Titrant	Colorimetric	Potentiometric	$[Fe(II)]_{avg}\cdot 10^2$	[c] *CV*
(min)	(mL)	[Fe(II)] (g/L)	[Fe(II)] (g/L)	(mol/kg)	(%)
0	–	5.00	–	9.23	–
1.0	10.20	2.85	–	5.26	–
3.0	7.40	2.07	–	3.82	–
5.0	6.40	1.79	–	3.30	–
7.5	5.20	1.45	–	2.68	–
10.0	4.20	1.17	–	2.17	–
12.5	3.50	0.98	–	1.80	–
15	3.20	0.89	–	1.65	–
20	2.40	0.67	–	1.24	–
25	2.10	0.59	–	1.08	–
30	1.70	0.47	–	0.88	–
45	1.20	0.34	–	0.62	–

[a] 20°C; [b] 10 mL sample ; [c] $\{\sum(x_i - x_{avg})^2\}^{0.5}/x_{avg}$.

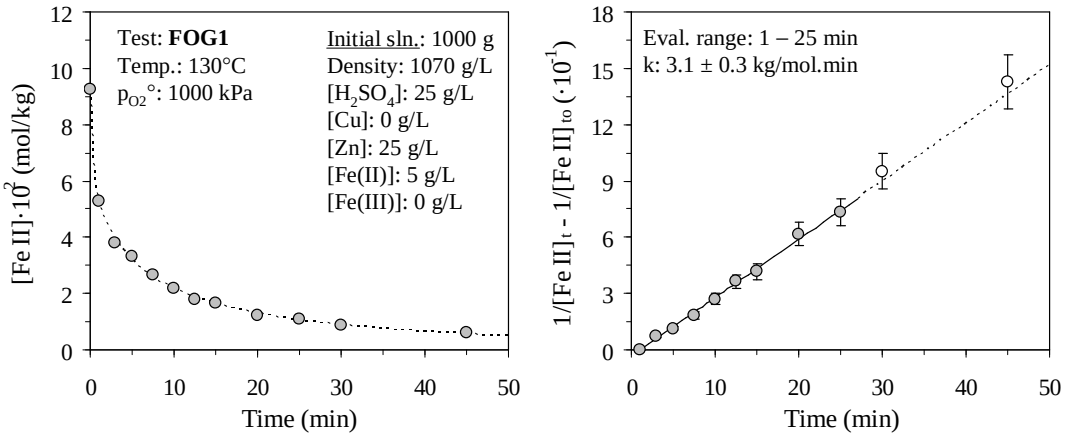

Stellenbosch University http://scholar.sun.ac.za

FOG2	Temp.	Imp. speed	Sln. mass	P_g.	$p_{O2}°$
2-litre AC	(°C)	(rev/min)	(g)	(kPa)	(kPa)
Config. A	130	1000	1200	1185	1000
[Dichromate]	$[H_2SO_4]$	[Cu]	[Zn]	[Fe(III)]	[a] Density
(N)	(g/L)	(g/L)	(g/L)	(g/L)	(g/L)
0.05	25	0	35	0	1104
Time	[b] Titrant	Colorimetric	Potentiometric	$[Fe(II)]_{avg}\cdot 10^2$	[c] *CV*
(min)	(mL)	[Fe(II)] (g/L)	[Fe(II)] (g/L)	(mol/kg)	(%)
0	–	5.00	–	9.15	–
1.0	8.00	2.23	–	4.09	–
3.0	6.00	1.68	–	3.06	–
5.0	4.80	1.34	–	2.45	–
7.5	3.80	1.06	–	1.94	–
10.0	3.30	0.92	–	1.69	–
12.5	2.60	0.73	–	1.33	–
15	2.30	0.64	–	1.17	–
20	2.00	0.56	–	1.02	–
25	1.70	0.47	–	0.87	–
30	1.30	0.36	–	0.66	–
45	1.10	0.31	–	0.56	–

[a] 20°C; [b] 10 mL sample ; [c] $\{\sum(x_i - x_{avg})^2\}^{0.5}/x_{avg}$.

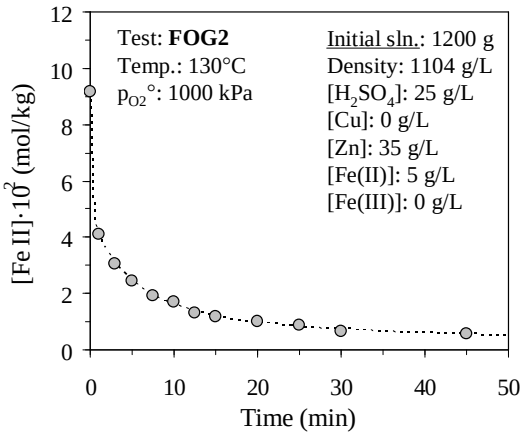

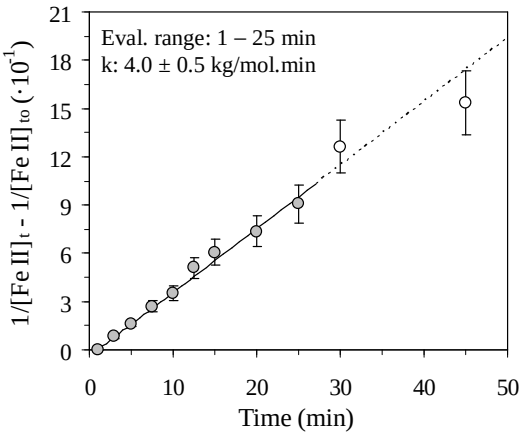

Stellenbosch University http://scholar.sun.ac.za

FOG3	Temp.	Imp. speed	Sln. mass	P_g.	$p_{O2}°$
2-litre AC	(°C)	(rev/min)	(g)	(kPa)	(kPa)
Config. A	130	1000	1200	1185	1000
[Dichromate]	$[H_2SO_4]$	[Cu]	[Zn]	[Fe(III)]	[a] Density
(N)	(g/L)	(g/L)	(g/L)	(g/L)	(g/L)
0.05	25	0	35	0	1104
Time	[b] Titrant	Colorimetric	Potentiometric	$[Fe(II)]_{avg}\cdot 10^2$	[c] *CV*
(min)	(mL)	[Fe(II)] (g/L)	[Fe(II)] (g/L)	(mol/kg)	(%)
0	–	5.00	–	9.15	–
1.0	7.90	2.21	–	4.03	–
3.0	5.90	1.65	–	3.01	–
5.0	4.55	1.27	–	2.32	–
7.5	3.95	1.10	–	2.02	–
10.0	3.20	0.89	–	1.63	–
12.5	2.70	0.75	–	1.38	–
15	2.30	0.64	–	1.17	–
20	1.90	0.53	–	0.97	–
25	1.60	0.45	–	0.82	–
30	1.30	0.36	–	0.77	–
45	0.90	0.25	–	0.54	–

[a] 20°C; [b] 10 mL sample ; [c] $\{\sum(x_i - x_{avg})^2\}^{0.5}/x_{avg}$.

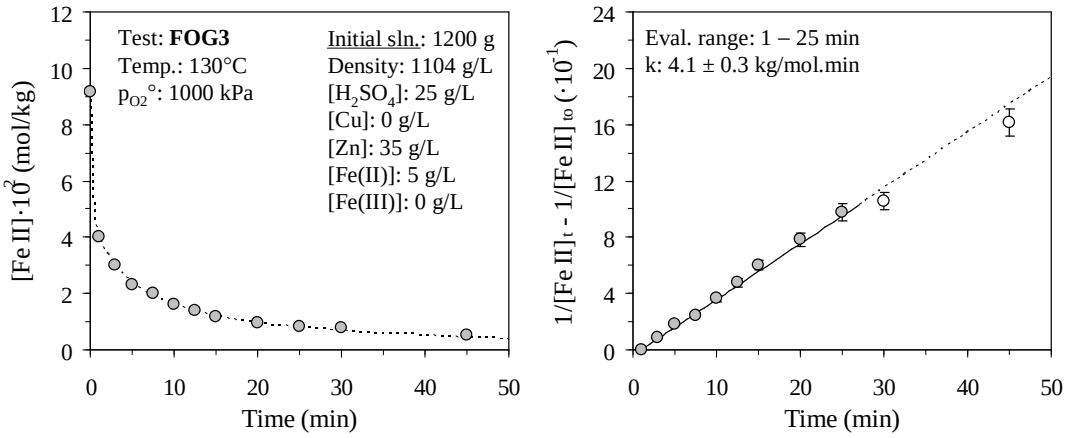

Stellenbosch University http://scholar.sun.ac.za

D.3.1 Detailed oxidation rate comparisons

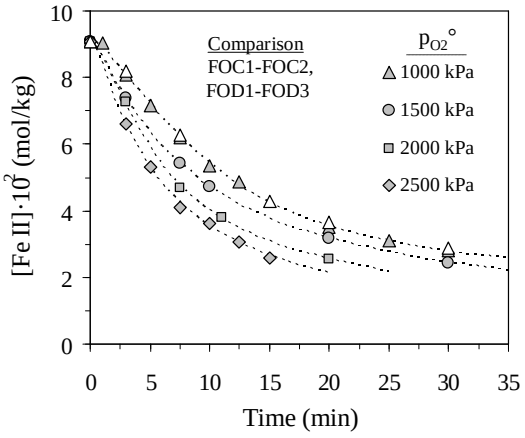

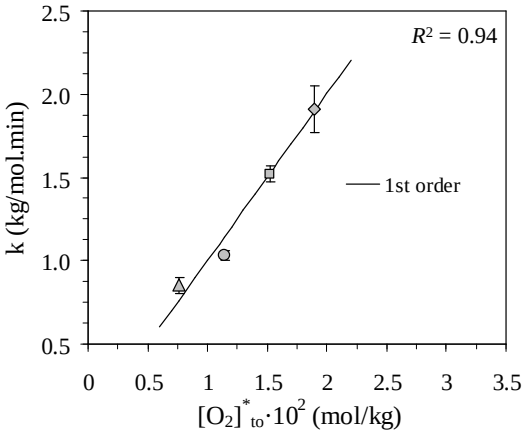

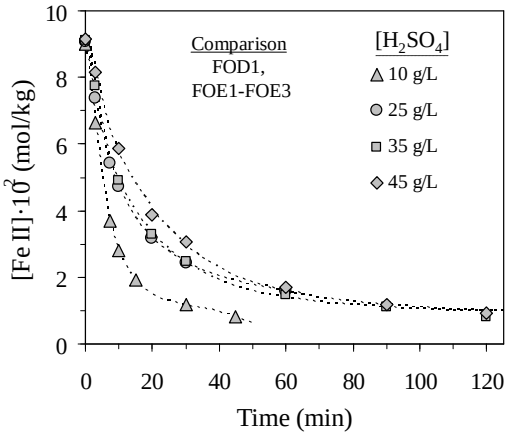

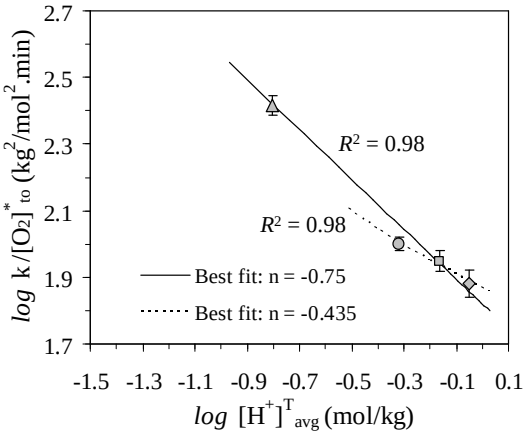

Stellenbosch University http://scholar.sun.ac.za

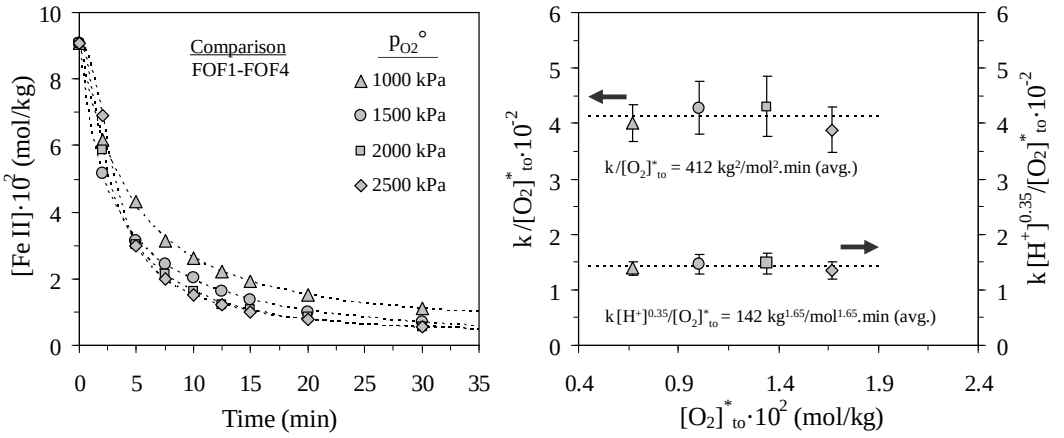

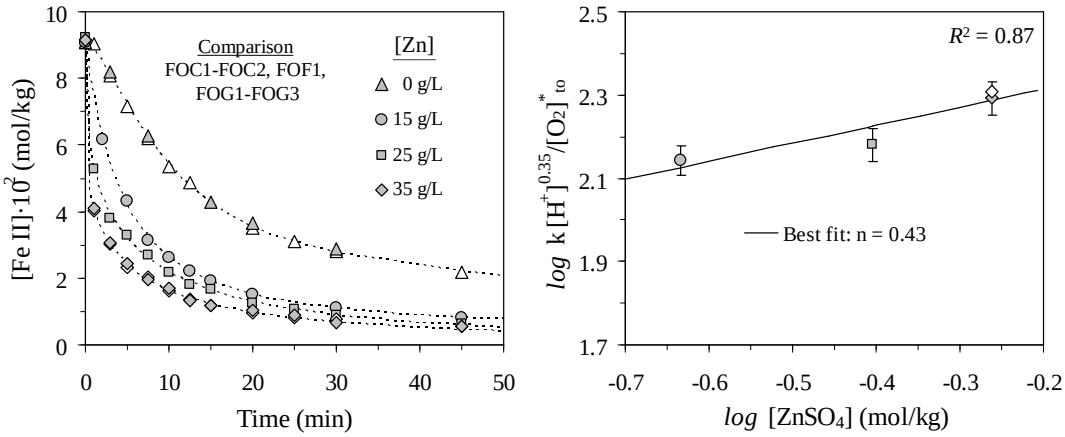

Stellenbosch University http://scholar.sun.ac.za

D.4 Activation energy without copper (catalyst)

These tests aimed to determine the apparent activation energy of the iron(II) oxidation reaction in low and high (zinc) sulfate solution environments, without any copper (catalyst).

FOH1 **2-litre AC**	Temp. (°C)	Imp. speed (rev/min)	Sln. mass (g)	P_g. (kPa)	$p_{O2}°$ (kPa)
Config. A	105	1000	1200	1035	1000
[Dichromate] (N)	[H_2SO_4] (g/L)	[Cu] (g/L)	[Zn] (g/L)	[Fe(III)] (g/L)	[a] Density (g/L)
0.1	25	0	0	0	1023
Time (min)	[b] Titrant (mL)	Colorimetric [Fe(II)] (g/L)	Potentiometric [Fe(II)] (g/L)	$[Fe(II)]_{avg}\cdot10^2$ (mol/kg)	[c] *CV* (%)
0	–	5.00	5.00	9.09	–
3.0	8.60	4.80	4.77	8.71	<15
10	7.20	4.02	4.14	7.42	<15
30	5.30	2.96	3.18	5.58	<15
60	3.60	2.01	2.41	4.02	<15
90	2.80	1.56	1.85	3.10	<15
120	2.30	1.28	1.50	2.53	<15
150	2.00	1.12	1.26	2.16	<15
180	1.80	1.00	1.12	1.93	<15

[a] 20°C; [b] 10 mL sample ; [c] $\{\sum(x_i - x_{avg})^2\}^{0.5}/x_{avg}$.

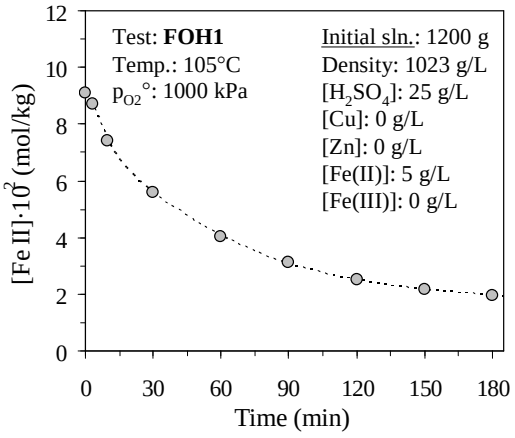

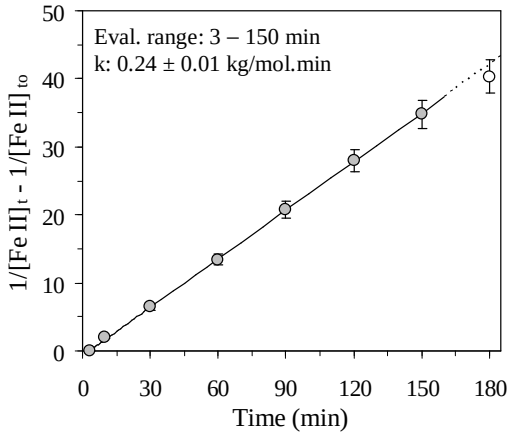

Stellenbosch University http://scholar.sun.ac.za

FOH2	Temp.	Imp. speed	Sln. mass	P_g.	$p_{O2}°$
2-litre AC	(°C)	(rev/min)	(g)	(kPa)	(kPa)
Config. A	150	1000	1200	1390	1000
[Dichromate]	$[H_2SO_4]$	[Cu]	[Zn]	[Fe(III)]	[a] Density
(N)	(g/L)	(g/L)	(g/L)	(g/L)	(g/L)
0.1	25	0	0	0	1023
Time	[b] Titrant	Colorimetric	Potentiometric	$[Fe(II)]_{avg}\cdot 10^2$	[c] *CV*
(min)	(mL)	[Fe(II)] (g/L)	[Fe(II)] (g/L)	(mol/kg)	(%)
0	–	5.00	5.00	9.09	–
3.0	6.40	3.57	3.63	6.55	<15
7.5	4.10	2.29	2.34	4.21	<15
10	3.30	1.84	1.94	3.44	<15
15	2.55	1.42	1.39	2.56	<15
20	1.85	1.03	1.26	2.09	<15
30	1.55	0.87	0.87	1.58	<15
45	1.20	0.67	0.61	1.16	<15
60	0.90	0.50	0.52	0.93	<15
90	0.60	0.34	–	0.61	–

[a] 20°C; [b] 10 mL sample ; [c] $\{\sum(x_i - x_{avg})^2\}^{0.5}/x_{avg}$.

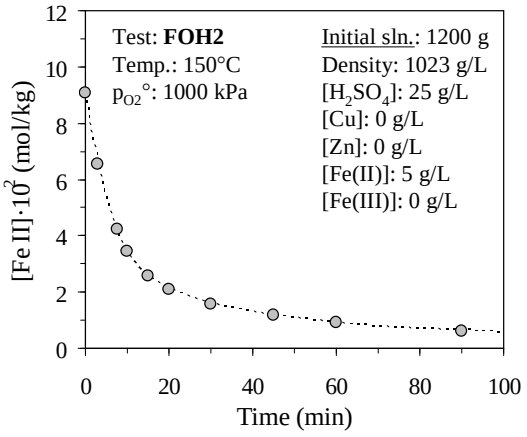

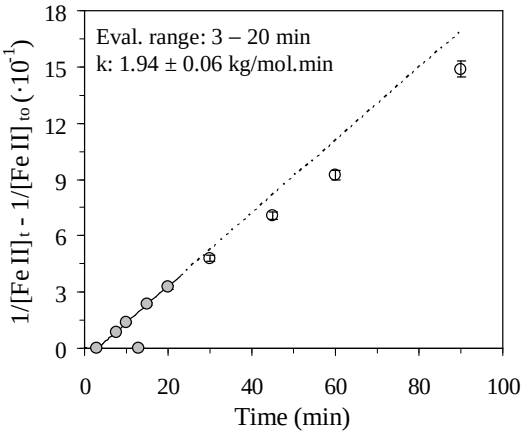

Stellenbosch University http://scholar.sun.ac.za

FOH3	Temp.	Imp. speed	Sln. mass	P_g.	$p_{O2}°$
2-litre AC	(°C)	(rev/min)	(g)	(kPa)	(kPa)
Config. A	180	1000	1200	1915	1000
[Dichromate]	$[H_2SO_4]$	[Cu]	[Zn]	[Fe(III)]	[a] Density
(N)	(g/L)	(g/L)	(g/L)	(g/L)	(g/L)
0.1	25	0	0	0	1023
Time	[b] Titrant	Colorimetric	Potentiometric	$[Fe(II)]_{avg}\cdot 10^2$	[c] *CV*
(min)	(mL)	[Fe(II)] (g/L)	[Fe(II)] (g/L)	(mol/kg)	(%)
0	–	5.00	5.00	9.09	–
3.0	4.05	2.26	2.43	4.27	<15
7.5	2.05	1.15	1.11	2.05	<15
10	1.60	0.89	0.90	1.63	<15
14	1.25	0.70	0.58	1.16	<15
20	0.80	0.45	–	0.81	–
25	0.60	0.34	–	0.61	–
30	0.45	0.25	–	0.46	–

[a] 20°C; [b] 10 mL sample ; [c] $\{\sum(x_i - x_{avg})^2\}^{0.5}/x_{avg}$.

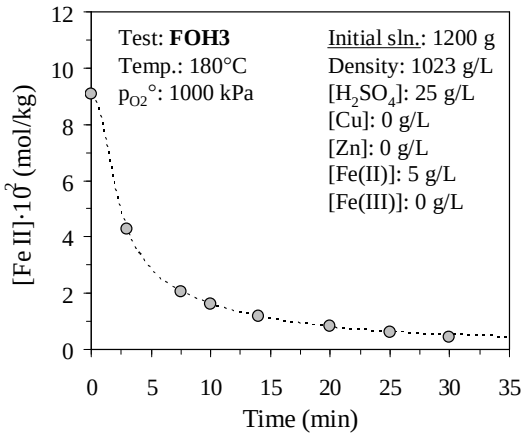

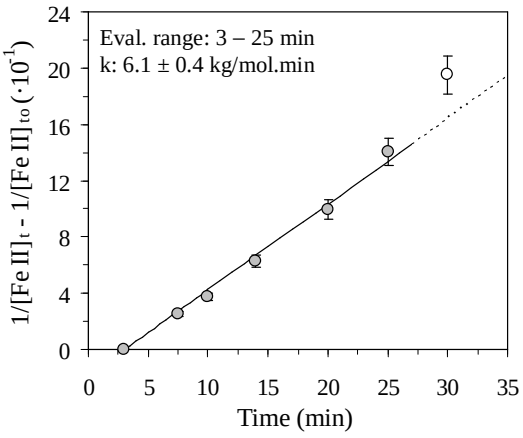

Stellenbosch University http://scholar.sun.ac.za

FOI1	Temp.	Imp. speed	Sln. mass	P_g.	$p_{O2}°$
2-litre AC	(°C)	(rev/min)	(g)	(kPa)	(kPa)
Config. A	105	1000	1200	1035	1000
[Dichromate]	$[H_2SO_4]$	[Cu]	[Zn]	[Fe(III)]	[a] Density
(N)	(g/L)	(g/L)	(g/L)	(g/L)	(g/L)
0.1	25	0	15	0	1063
Time	[b] Titrant	Colorimetric	Potentiometric	$[Fe(II)]_{avg}\cdot 10^2$	[c] *CV*
(min)	(mL)	[Fe(II)] (g/L)	[Fe(II)] (g/L)	(mol/kg)	(%)
0	–	5.00	–	9.07	–
2.0	7.40	4.13	–	7.49	–
6.0	5.80	3.24	–	5.87	–
9.0	5.00	2.79	–	5.06	–
15	4.00	2.23	–	4.05	–
30	2.80	1.56	–	2.84	–
45	2.40	1.34	–	2.43	–
60	2.00	1.12	–	2.03	–

[a] 20°C; [b] 10 mL sample ; [c] $\{\sum(x_i - x_{avg})^2\}^{0.5}/x_{avg}$.

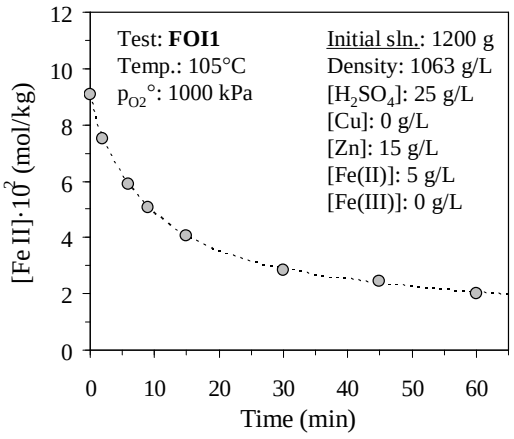

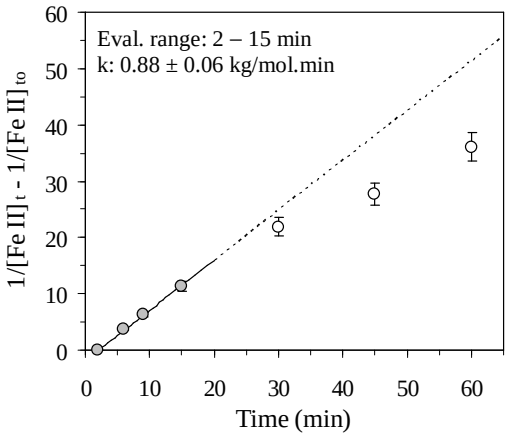

Stellenbosch University http://scholar.sun.ac.za

FOI2	Temp.	Imp. speed	Sln. mass	P_g.	$p_{O2}°$
2-litre AC	(°C)	(rev/min)	(g)	(kPa)	(kPa)
Config. A	150	1000	1200	1040	650
[Dichromate]	$[H_2SO_4]$	[Cu]	[Zn]	[Fe(III)]	[a] Density
(N)	(g/L)	(g/L)	(g/L)	(g/L)	(g/L)
0.1	25	0	15	0	1063
Time	[b] Titrant	Colorimetric	Potentiometric	$[Fe(II)]_{avg}\cdot10^2$	[c] *CV*
(min)	(mL)	[Fe(II)] (g/L)	[Fe(II)] (g/L)	(mol/kg)	(%)
0	–	5.00	–	9.07	–
2.5	6.25	3.49	–	6.33	–
5.0	3.35	1.87	–	3.39	–
7.5	2.50	1.40	–	2.53	–
12.5	1.70	0.95	–	1.72	–
17.0	1.25	0.70	–	1.27	–
21.5	1.00	0.56	–	1.01	–
25	0.80	0.45	–	0.81	–
40	0.60	0.34	–	0.61	–
60	0.40	0.22	–	0.41	–

[a] 20°C; [b] 10 mL sample ; [c] $\{\sum(x_i - x_{avg})^2\}^{0.5}/x_{avg}$.

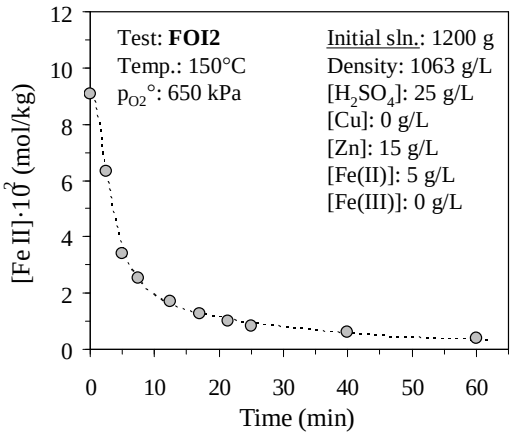

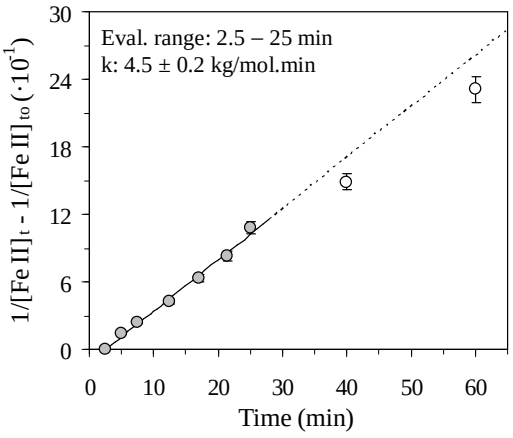

Stellenbosch University http://scholar.sun.ac.za

FOJ1	Temp.	Imp. speed	Sln. mass	P_g.	$p_{O2}°$
2-litre AC	(°C)	(rev/min)	(g)	(kPa)	(kPa)
Config. A	150	1000	1200	2390	2000
[Dichromate]	$[H_2SO_4]$	[Cu]	[Zn]	[Fe(III)]	[a] Density
(N)	(g/L)	(g/L)	(g/L)	(g/L)	(g/L)
0.1	25	0	0	10	1063
Time	[b] Titrant	Colorimetric	Potentiometric	$[Fe(II)]_{avg}\cdot 10^2$	[c] *CV*
(min)	(mL)	[Fe(II)] (g/L)	[Fe(II)] (g/L)	(mol/kg)	(%)
0	–	5.00	–	9.06	–
2.0	7.50	4.19	–	7.59	–
5.0	4.20	2.35	–	4.25	–
7.5	2.90	1.62	–	2.93	–
10.0	2.10	1.17	–	2.12	–
12.5	1.90	1.06	–	1.92	–
15	1.65	0.92	–	1.67	–
20	1.20	0.67		1.21	
30	0.90	0.50		0.91	
45	0.65	0.36	–	0.66	–

[a] 20°C; [b] 10 mL sample ; [c] $\{\sum(x_i - x_{avg})^2\}^{0.5}/x_{avg}$.

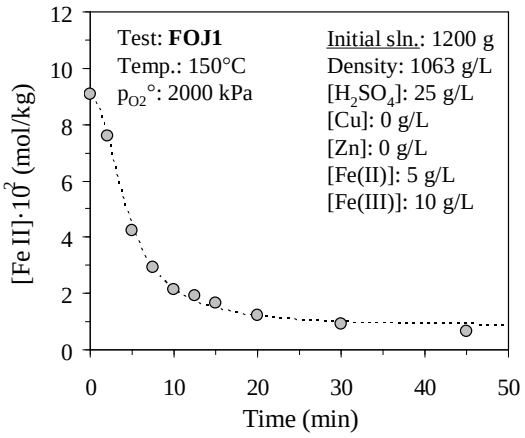

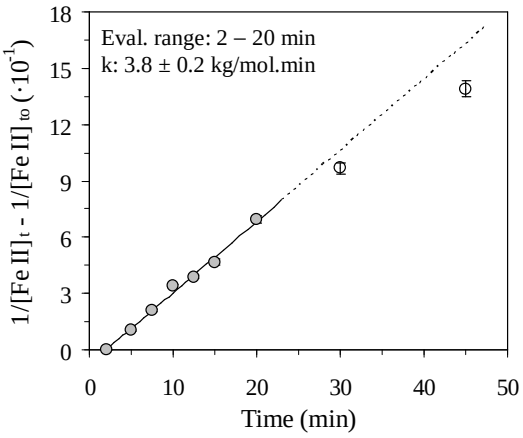

Stellenbosch University http://scholar.sun.ac.za

D.4.1 Detailed oxidation rate comparisons

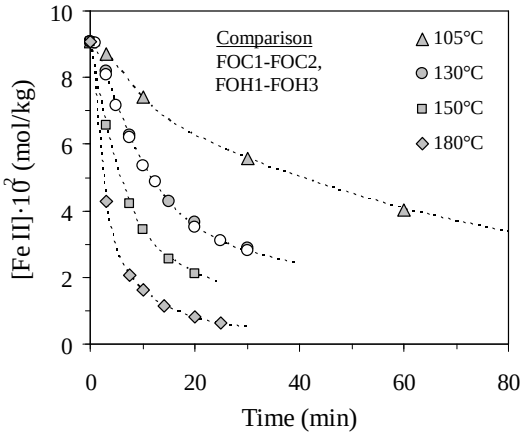

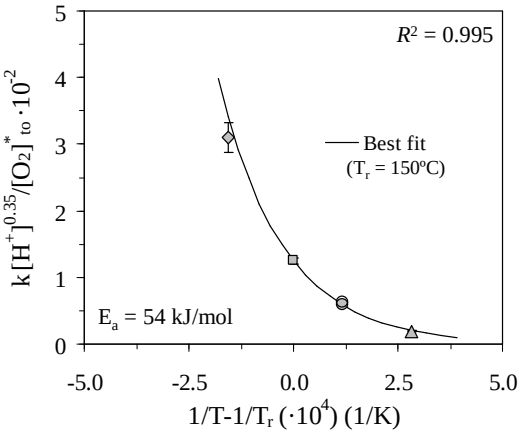

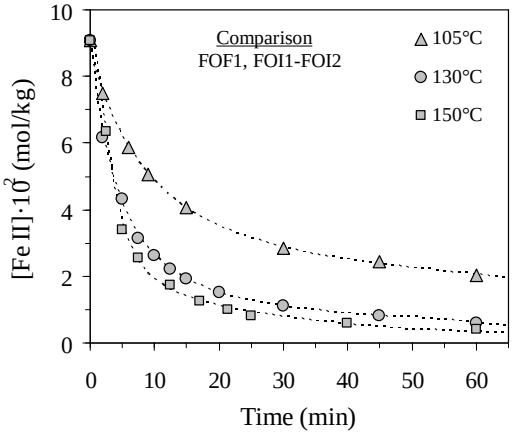

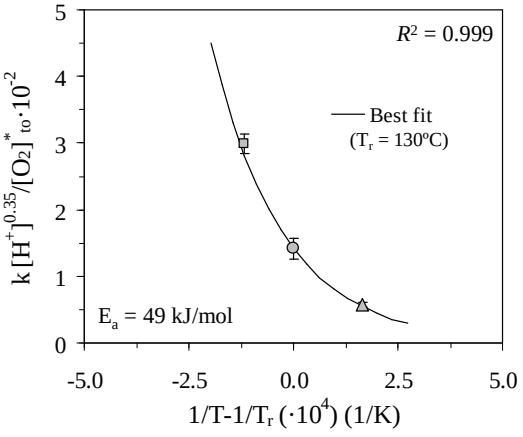

Stellenbosch University http://scholar.sun.ac.za

D.5 Reaction orders and activation energy in the presence of copper (catalyst)

These tests aimed to determine the apparent reaction orders with respect to the iron(II) and dissolved oxygen concentrations, as well as the apparent activation energy, in the presence of copper (catalyst).

FOK1	Temp.	Imp. speed	Sln. mass	P_g.	$p_{O2}°$
2-litre AC	(°C)	(rev/min)	(g)	(kPa)	(kPa)
Config. A	130	1000	1000	685	500
[Dichromate]	$[H_2SO_4]$	[Cu]	[Zn]	[Fe(III)]	[a] Density
(N)	(g/L)	(g/L)	(g/L)	(g/L)	(g/L)
0.1	25	15	0	0	1061
Time	[b] Titrant	Colorimetric	Potentiometric	$[Fe(II)]_{avg}\cdot10^2$	[c] *CV*
(min)	(mL)	[Fe(II)] (g/L)	[Fe(II)] (g/L)	(mol/kg)	(%)
0	–	5.00	–	9.09	–
2.0	3.40	1.90	–	3.45	–
5.0	2.40	1.34	–	2.44	–
7.5	2.10	1.17	–	2.13	–
10.0	1.60	0.89	–	1.62	–
12.5	1.20	0.67	–	1.22	–
15	1.00	0.56	–	1.02	–
20	0.80	0.45	–	0.76	–
25	0.60	0.34	–	0.61	–
30	0.50	0.28	–	0.51	–
45	0.40	0.22	–	0.41	–

[a] 20°C; [b] 10 mL sample ; [c] $\{\sum(x_i - x_{avg})^2\}^{0.5}/x_{avg}$.

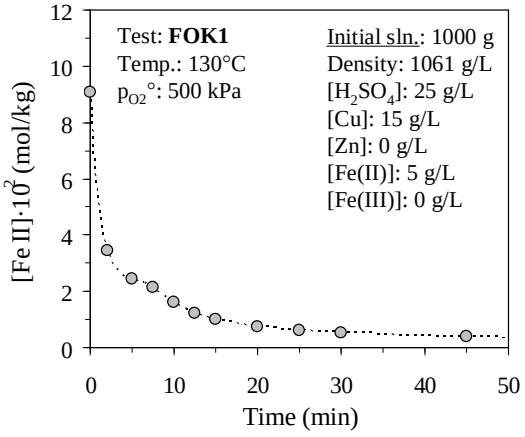

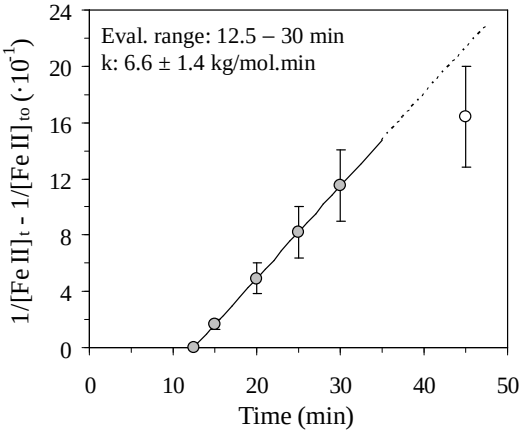

Stellenbosch University http://scholar.sun.ac.za

FOK2	Temp.	Imp. speed	Sln. mass	P_g.	$p_{O2}°$
2-litre AC	(°C)	(rev/min)	(g)	(kPa)	(kPa)
Config. A	130	1000	950	935	750
[Dichromate]	$[H_2SO_4]$	[Cu]	[Zn]	[Fe(III)]	[a] Density
(N)	(g/L)	(g/L)	(g/L)	(g/L)	(g/L)
0.1	25	15	0	0	1061
Time	[b] Titrant	Colorimetric	Potentiometric	$[Fe(II)]_{avg}\cdot 10^2$	[c] *CV*
(min)	(mL)	[Fe(II)] (g/L)	[Fe(II)] (g/L)	(mol/kg)	(%)
0	–	5.00	–	9.09	–
2.0	6.80	3.80	–	6.91	–
5.0	3.10	1.73	–	3.15	–
7.5	2.10	1.17	–	2.13	–
10.0	1.60	0.89	–	1.62	–
12.5	1.40	0.78	–	1.42	–
15	1.00	0.56	–	1.02	–
20	0.70	0.39	–	0.71	–
30	0.45	0.25	–	0.46	–
45	0.30	0.17	–	0.30	–

[a] 20°C; [b] 10 mL sample ; [c] $\{\sum(x_i - x_{avg})^2\}^{0.5}/x_{avg}$.

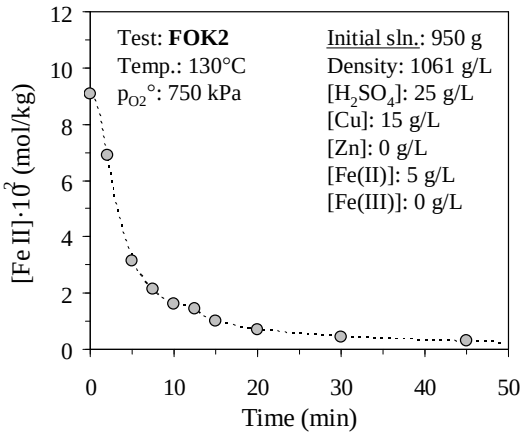

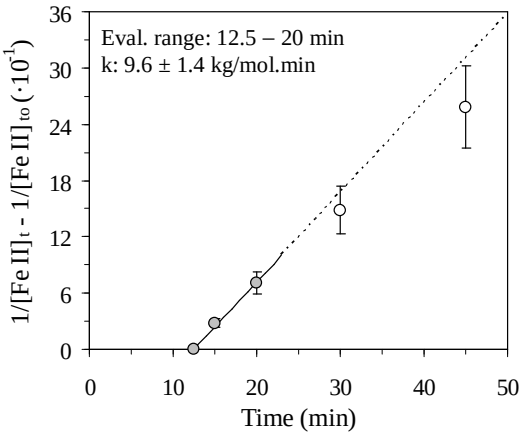

Stellenbosch University http://scholar.sun.ac.za

FOK3	Temp.	Imp. speed	Sln. mass	P_g.	$p_{O2}°$
2-litre AC	(°C)	(rev/min)	(g)	(kPa)	(kPa)
Config. A	130	1000	1000	1185	1000
[Dichromate]	$[H_2SO_4]$	[Cu]	[Zn]	[Fe(III)]	[a] Density
(N)	(g/L)	(g/L)	(g/L)	(g/L)	(g/L)
0.1	25	15	0	0	1061
Time	[b] Titrant	Colorimetric	Potentiometric	$[Fe(II)]_{avg}\cdot 10^2$	[c] *CV*
(min)	(mL)	[Fe(II)] (g/L)	[Fe(II)] (g/L)	(mol/kg)	(%)
0	–	5.00	–	9.09	–
2.0	2.30	1.28	–	2.33	–
5.0	1.40	0.78	–	1.42	–
7.5	1.20	0.67	–	1.22	–
10.0	0.80	0.45	–	0.81	–
12.5	0.65	0.36	–	0.66	–
15	0.55	0.31	–	0.56	–
20	0.40	0.22	–	0.41	–
30	0.30	0.17	–	0.30	–
45	0.20	0.11	–	0.20	–

[a] 20°C; [b] 10 mL sample ; [c] $\{\sum(x_i - x_{avg})^2\}^{0.5}/x_{avg}$.

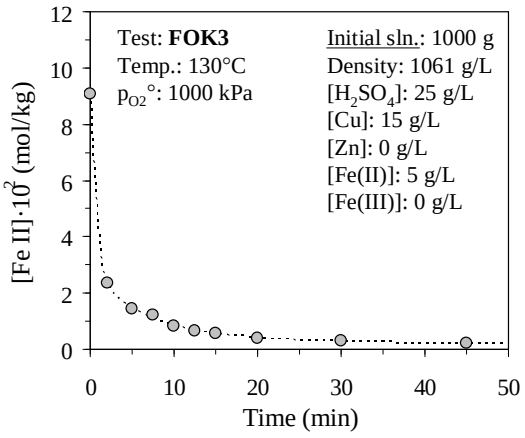

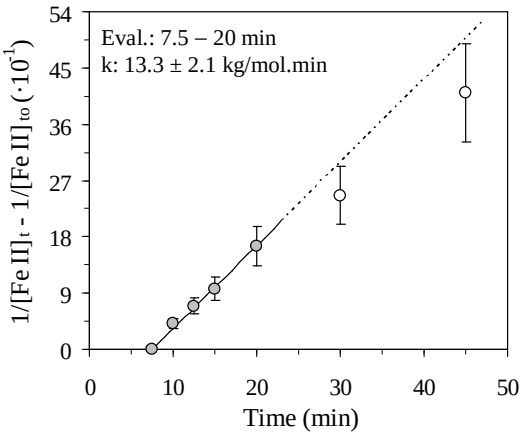

Stellenbosch University http://scholar.sun.ac.za

FOL1	Temp.	Imp. speed	Sln. mass	P_g.	$p_{O2}°$
2-litre AC	(°C)	(rev/min)	(g)	(kPa)	(kPa)
Config. A	130	1000	1200	1185	1000
[Dichromate]	$[H_2SO_4]$	[Cu]	[Zn]	[Fe(III)]	[a] Density
(N)	(g/L)	(g/L)	(g/L)	(g/L)	(g/L)
0.1	25	15	0	0	1061
Time	[b] Titrant	Colorimetric	Potentiometric	$[Fe(II)]_{avg}\cdot 10^2$	[c] *CV*
(min)	(mL)	[Fe(II)] (g/L)	[Fe(II)] (g/L)	(mol/kg)	(%)
0	–	5.00	–	9.09	–
1	3.80	2.12	–	3.86	–
3	2.20	1.23	–	2.23	–
6	1.20	0.67	–	1.22	–
10	0.80	0.45	–	0.81	–
15	0.60	0.34	–	0.61	–
25	0.45	0.25	–	0.46	–

[a] 20°C; [b] 10 mL sample ; [c] $\{\sum(x_i - x_{avg})^2\}^{0.5}/x_{avg}$.

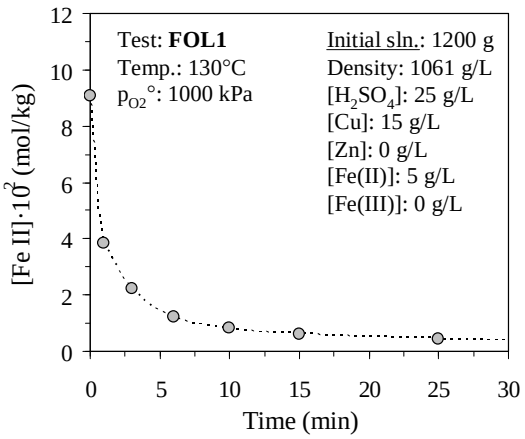

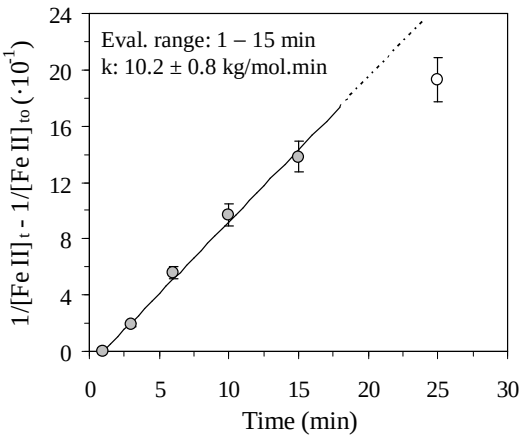

Stellenbosch University http://scholar.sun.ac.za

FOL2	Temp.	Imp. speed	Sln. mass	P_g.	$p_{O2}°$
2-litre AC	(°C)	(rev/min)	(g)	(kPa)	(kPa)
Config. A	130	1000	1200	2685	2500
[Dichromate]	$[H_2SO_4]$	[Cu]	[Zn]	[Fe(III)]	[a] Density
(N)	(g/L)	(g/L)	(g/L)	(g/L)	(g/L)
0.1	25	15	0	0	1061
Time	[b] Titrant	Colorimetric	Potentiometric	$[Fe(II)]_{avg}\cdot 10^2$	[c] *CV*
(min)	(mL)	[Fe(II)] (g/L)	[Fe(II)] (g/L)	(mol/kg)	(%)
0	–	5.00	–	9.09	–
2.0	2.30	1.28	–	2.33	–
5.0	0.80	0.45	–	0.81	–
7.5	0.55	0.31	–	0.56	–
10.0	0.45	0.25	–	0.46	–
12.5	0.35	0.20	–	0.36	–
15	0.30	0.17	–	0.30	–
20	0.25	0.14	–	0.25	–
30	0.20	0.11	–	0.20	–
45	0.15	0.08	–	0.15	–

[a] 20°C; [b] 10 mL sample ; [c] $\{\sum(x_i - x_{avg})^2\}^{0.5}/x_{avg}$.

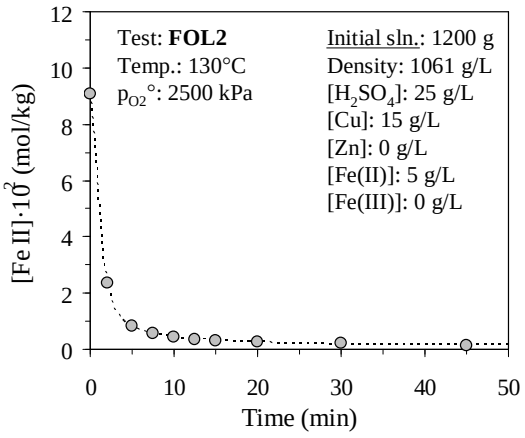

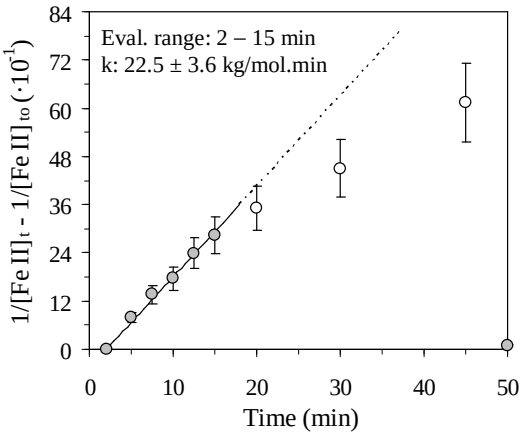

Stellenbosch University http://scholar.sun.ac.za

FOM1	Temp.	Imp. speed	Sln. mass	P_g.	$p_{O2}°$
2-litre AC	(°C)	(rev/min)	(g)	(kPa)	(kPa)
Config. A	130	1000	1200	1185	1000
[Dichromate]	$[H_2SO_4]$	[Cu]	[Zn]	[Fe(III)]	[a] Density
(N)	(g/L)	(g/L)	(g/L)	(g/L)	(g/L)
0.05	25	25	0	0	1087
Time	[b] Titrant	Colorimetric	Potentiometric	$[Fe(II)]_{avg}\cdot 10^2$	[c] *CV*
(min)	(mL)	[Fe(II)] (g/L)	[Fe(II)] (g/L)	(mol/kg)	(%)
0	–	5.00	–	9.08	–
1.0	7.40	2.07	–	3.75	–
3.0	3.50	0.98	–	1.78	–
5.0	2.30	0.64	–	1.17	–
7.5	1.60	0.45	–	0.81	–
10.0	1.40	0.39	–	0.71	–
12.5	1.00	0.28	–	0.51	–
15	0.90	0.25	–	0.46	–
20	0.75	0.21	–	0.38	–
25	0.60	0.17	–	0.30	–
30	0.40	0.11	–	0.20	–
45	0.30	0.08	–	0.15	–

[a] 20°C; [b] 10 mL sample ; [c] $\{\sum(x_i - x_{avg})^2\}^{0.5}/x_{avg}$.

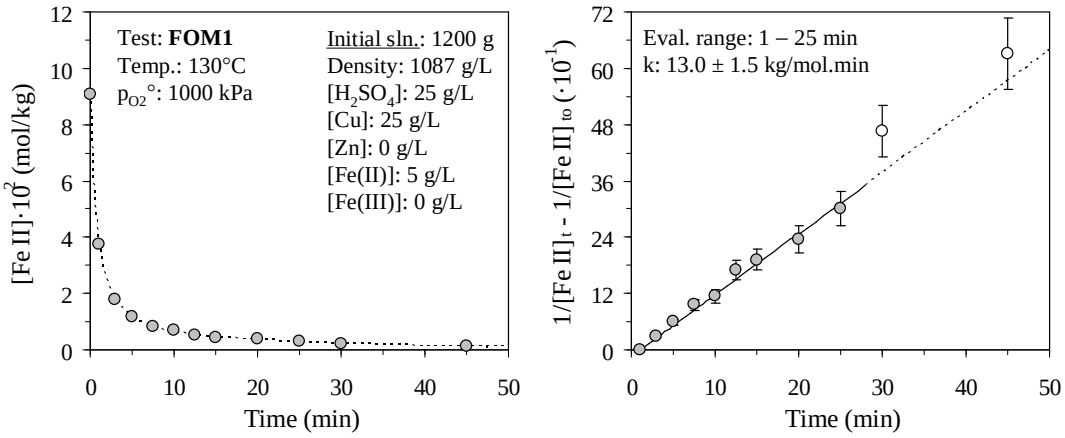

Stellenbosch University http://scholar.sun.ac.za

FOM2	Temp.	Imp. speed	Sln. mass	P_g.	$p_{O2}°$
2-litre AC	(°C)	(rev/min)	(g)	(kPa)	(kPa)
Config. A	130	1000	1200	1185	1000
[Dichromate]	$[H_2SO_4]$	[Cu]	[Zn]	[Fe(III)]	[a] Density
(N)	(g/L)	(g/L)	(g/L)	(g/L)	(g/L)
0.05	25	35	0	0	1109
Time	[b] Titrant	Colorimetric	Potentiometric	$[Fe(II)]_{avg}\cdot 10^2$	[c] *CV*
(min)	(mL)	[Fe(II)] (g/L)	[Fe(II)] (g/L)	(mol/kg)	(%)
0	–	5.00	–	9.11	–
1.0	7.90	2.21	–	4.02	–
3.0	3.00	0.84	–	1.53	–
5.0	2.00	0.56	–	1.02	–
7.5	1.50	0.42	–	0.76	–
10.0	1.20	0.34	–	0.61	–
12.5	1.00	0.28	–	0.51	–
15	0.75	0.21	–	0.38	–
20	0.50	0.14	–	0.25	–
25	0.40	0.11	–	0.20	–
30	0.40	0.11	–	0.20	–
45	0.25	0.07	–	0.13	–

[a] 20°C; [b] 10 mL sample ; [c] $\{\sum(x_i - x_{avg})^2\}^{0.5}/x_{avg}$.

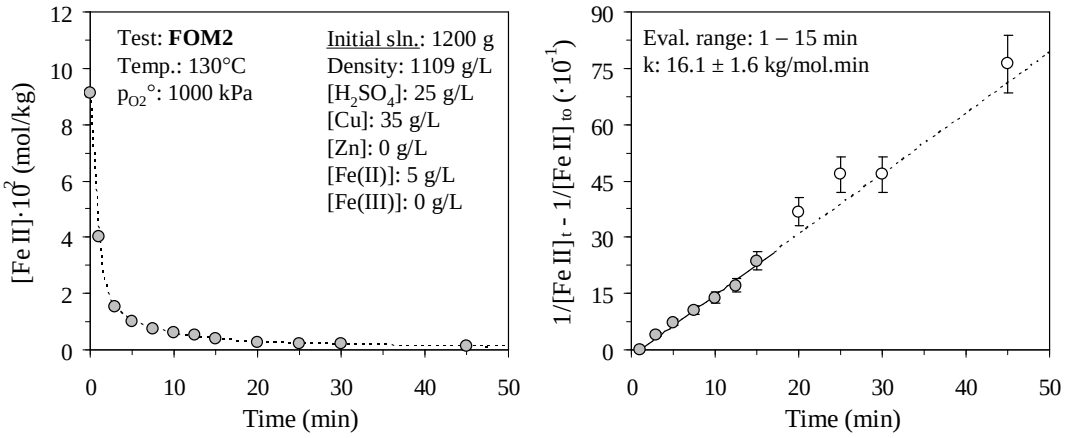

Stellenbosch University http://scholar.sun.ac.za

FON1	Temp.	Imp. speed	Sln. mass	P_g.	$p_{O2}°$
2-litre AC	(°C)	(rev/min)	(g)	(kPa)	(kPa)
Config. A	105	1000	1200	1035	1000
[Dichromate]	$[H_2SO_4]$	[Cu]	[Zn]	[Fe(III)]	[a] Density
(N)	(g/L)	(g/L)	(g/L)	(g/L)	(g/L)
0.1	25	15	0	0	1061
Time	[b] Titrant	Colorimetric	Potentiometric	$[Fe(II)]_{avg}\cdot 10^2$	[c] *CV*
(min)	(mL)	[Fe(II)] (g/L)	[Fe(II)] (g/L)	(mol/kg)	(%)
0	–	5.00	–	9.09	–
3.0	4.80	2.68	–	4.87	–
9.0	2.35	1.31	–	2.39	–
12	1.85	1.03	–	1.88	–
15	1.55	0.87	–	1.57	–
20	1.35	0.75	–	1.37	–
30	1.10	0.61	–	1.12	–
45	0.90	0.50	–	0.91	–

[a] 20°C; [b] 10 mL sample ; [c] $\{\sum(x_i - x_{avg})^2\}^{0.5}/x_{avg}$.

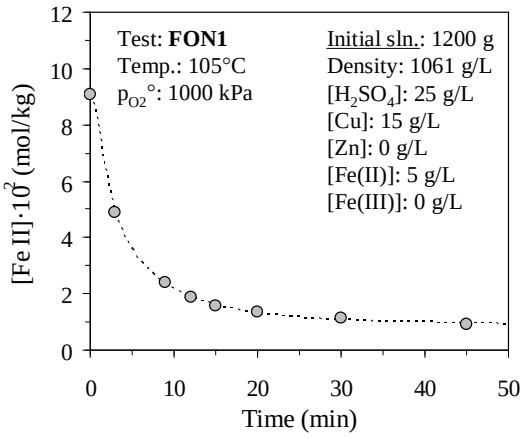

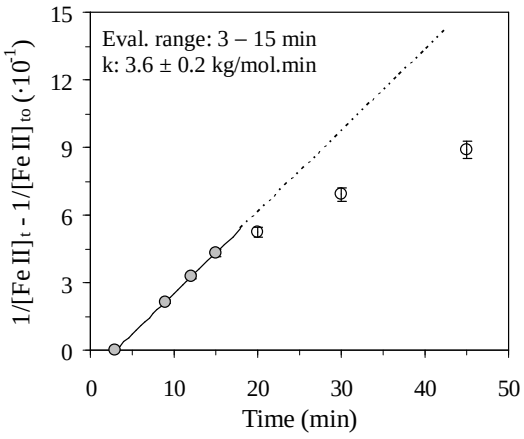

Stellenbosch University http://scholar.sun.ac.za

FON2	Temp.	Imp. speed	Sln. mass	P_g.	$p_{O2}°$
2-litre AC	(°C)	(rev/min)	(g)	(kPa)	(kPa)
Config. A	150	1000	1200	1040	650
[Dichromate]	$[H_2SO_4]$	[Cu]	[Zn]	[Fe(III)]	[a] Density
(N)	(g/L)	(g/L)	(g/L)	(g/L)	(g/L)
0.1	25	10	0	0	1051
Time	[b] Titrant	Colorimetric	Potentiometric	$[Fe(II)]_{avg}\cdot10^2$	[c] *CV*
(min)	(mL)	[Fe(II)] (g/L)	[Fe(II)] (g/L)	(mol/kg)	(%)
0	–	5.00	–	9.07	–
2.0	4.25	2.37	–	4.30	–
5.0	2.15	1.20	–	2.18	–
7.5	1.45	0.81	–	1.47	–
12.5	0.95	0.53	–	0.96	–
15.0	0.80	0.45	–	0.81	–
20.0	0.60	0.34	–	0.61	–
30	0.40	0.22	–	0.41	–
45	0.30	0.17	–	0.30	–

[a] 20°C; [b] 10 mL sample ; [c] $\{\sum(x_i - x_{avg})^2\}^{0.5}/x_{avg}$.

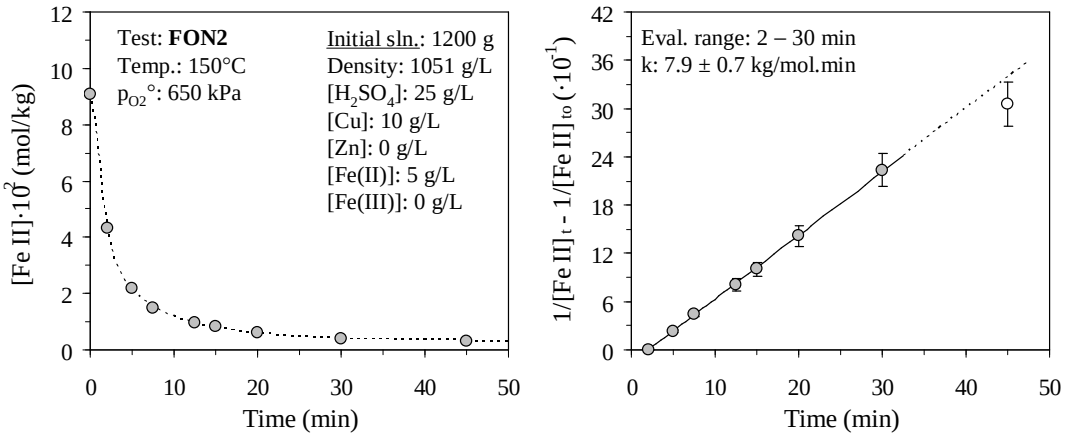

Stellenbosch University http://scholar.sun.ac.za

D.5.1 Detailed oxidation rate comparisons

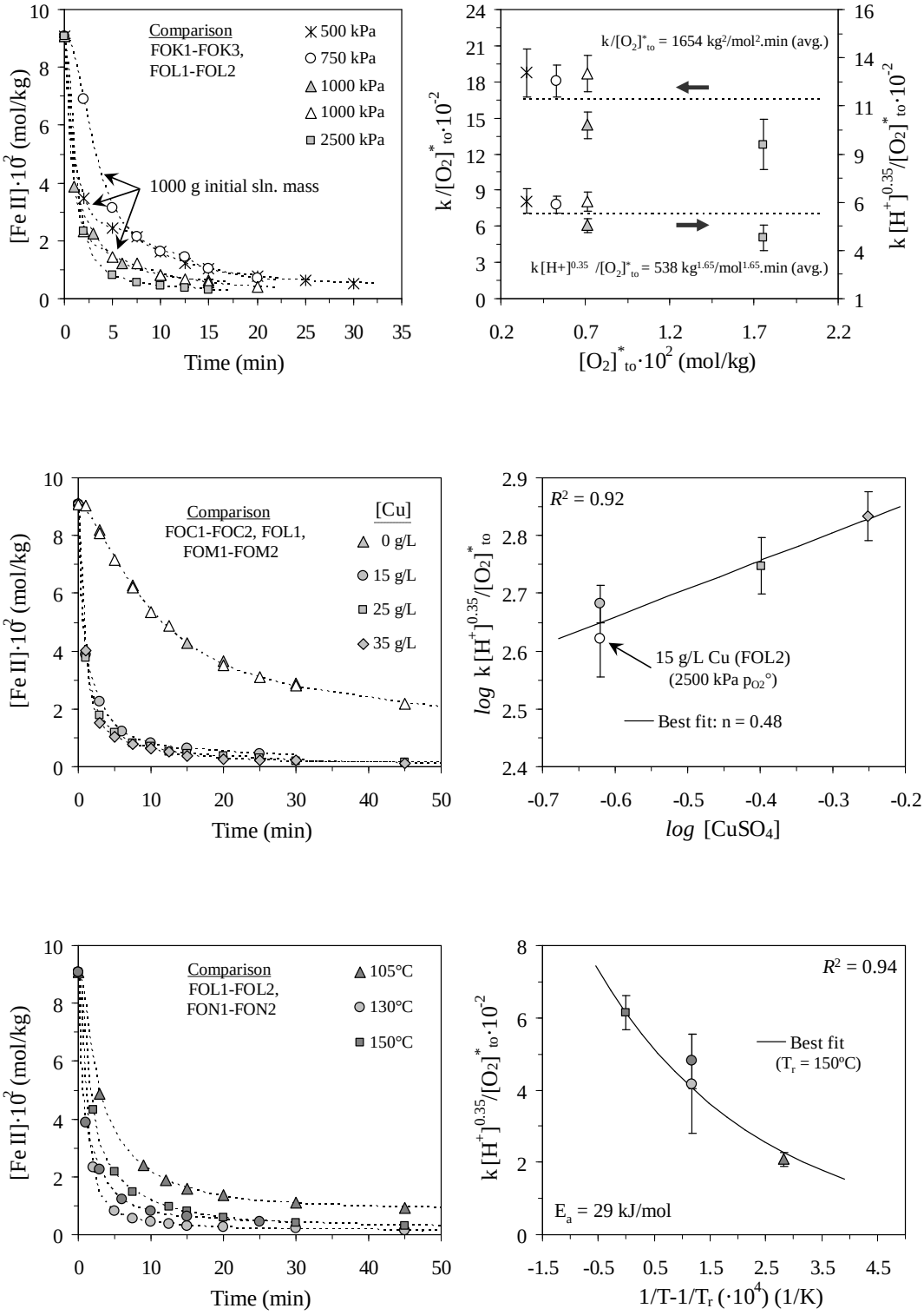

Stellenbosch University http://scholar.sun.ac.za

D.6 Reaction rate under atmospheric conditions

These tests aimed to verify the phenomenological oxidation rate model under atmospheric conditions and at high interfacial gas/liquid mass transfer rates.

FOO1 **7-litre vessel**	Temp. (°C)	Imp. speed (rev/min)	Sln. mass (g)	P_g. (kPa)	p_{O2}° (kPa)
	90	1000	7092	–	16.1
[Dichromate] (N)	[H_2SO_4] (g/L)	[Cu] (g/L)	[Zn] (g/L)	[Fe(III)] (g/L)	[a] Density (g/L)
0.1	0.25	0.4	0	0	1090
Time (min)	[b] Titrant (mL)	Colorimetric [Fe(II)] (g/L)	Potentiometric [Fe(II)] (g/L)	$[Fe(II)]_{avg}\cdot 10^2$ (mol/kg)	[c] *CV* (%)
[d] 0	8.30	4.64	–	8.40	–
5	7.90	4.41	–	8.00	–
10	7.80	4.36	–	7.89	–
15	7.60	4.24	–	7.69	–
20	7.55	4.22	–	7.64	–
25	7.30	4.08	–	7.38	–
30	7.15	3.99	–	7.23	–
35	7.05	3.94	–	7.14	–
40	6.85	3.83	–	6.94	–
45	6.80	3.80	–	6.88	–
50	6.70	3.74	–	6.78	–
55	6.65	3.71	–	6.73	–
60	6.50	3.63	–	6.57	–
75	6.20	3.46	–	6.27	–
90	6.00	3.35	–	6.07	–
105	5.80	3.24	–	5.87	–
120	5.60	3.13	–	5.66	–
150	5.30	2.96	–	5.36	–
180	4.95	2.76	–	5.01	–

[a] 20°C; [b] 10 mL sample ; [c] $\{\sum(x_i - x_{avg})^2\}^{0.5}/x_{avg}$; [d] After few min. pre-oxidation.

Stellenbosch University http://scholar.sun.ac.za

FOO2	Temp.	Imp. speed	Sln. mass	P_g.	$p_{O2}°$
7-litre vessel	(°C)	(rev/min)	(g)	(kPa)	(kPa)
	90	1000	6741	–	15.5
[Dichromate]	$[H_2SO_4]$	[Cu]	[Zn]	[Fe(III)]	[a] Density
(N)	(g/L)	(g/L)	(g/L)	(g/L)	(g/L)
0.1	0.125	0.1	0	0	1037
Time	[b] Titrant	Colorimetric	Potentiometric	$[Fe(II)]_{avg}\cdot 10^2$	[c] *CV*
(min)	(mL)	[Fe(II)] (g/L)	[Fe(II)] (g/L)	(mol/kg)	(%)
0	9.00	5.03	–	9.06	–
5	8.95	5.00	–	9.00	–
10	8.90	4.97	–	8.95	–
15	8.80	4.91	–	8.85	–
20	8.65	4.83	–	8.70	–
25	8.50	4.75	–	8.55	–
30	8.45	4.72	–	8.50	–
35	8.40	4.69	–	8.45	–
40	8.30	4.64	–	8.35	–
45	8.15	4.55	–	8.20	–
50	8.05	4.50	–	8.10	–
55	7.95	4.44	–	8.00	–
60	7.90	4.41	–	7.95	–
75	7.65	4.27	–	7.70	–
90	7.50	4.19	–	7.55	–
105	7.25	4.05	–	7.29	–
120	7.20	4.02	–	7.24	–
150	6.90	3.85	–	6.94	–
180	6.65	3.71	–	6.69	–

[a] 20°C; [b] 10 mL sample ; [c] $\{\sum(x_i - x_{avg})^2\}^{0.5}/x_{avg}$.

Stellenbosch University http://scholar.sun.ac.za

FOO3	Temp.	Imp. speed	Sln. mass	P_g.	$p_{O2}°$
7-litre vessel	(°C)	(rev/min)	(g)	(kPa)	(kPa)
	90	1000	6962	–	15.8
[Dichromate]	$[H_2SO_4]$	[Cu]	[Mg]	[Fe(III)]	[a] Density
(N)	(g/L)	(g/L)	(g/L)	(g/L)	(g/L)
0.1	0.125	0.1	0.3	0	1071
Time	[b] Titrant	Colorimetric	Potentiometric	$[Fe(II)]_{avg}·10^2$	[c] *CV*
(min)	(mL)	[Fe(II)] (g/L)	[Fe(II)] (g/L)	(mol/kg)	(%)
0	9.95	5.56	–	10.03	–
5	9.30	5.19	–	9.37	–
10	8.95	5.00	–	9.02	–
15	8.75	4.89	–	8.82	–
20	8.50	4.75	–	8.57	–
25	8.40	4.69	–	8.47	–
30	8.15	4.55	–	8.21	–
35	8.00	4.47	–	8.06	–
40	7.90	4.41	–	7.96	–
45	7.85	4.38	–	7.91	–
50	7.65	4.27	–	7.71	–
55	7.55	4.22	–	7.61	–
60	7.35	4.10	–	7.41	–
75	7.10	3.97	–	7.16	–
90	6.80	3.80	–	6.85	–
105	6.55	3.66	–	6.60	–
120	6.35	3.55	–	6.40	–
150	6.05	3.38	–	6.10	–
180	5.80	3.24	–	5.85	–

[a] 20°C; [b] 10 mL sample ; [c] $\{\sum(x_i - x_{avg})^2\}^{0.5}/x_{avg}$.

Stellenbosch University http://scholar.sun.ac.za

FOO4	Temp.	Imp. speed	Sln. mass	P_g.	$p_{O2}°$
7-litre vessel	(°C)	(rev/min)	(g)	(kPa)	(kPa)
	90	1000	7040	–	15.8
[Dichromate]	$[H_2SO_4]$	[Cu]	[Zn]	[Fe(III)]	[a] Density
(N)	(g/L)	(g/L)	(g/L)	(g/L)	(g/L)
0.1	0.125	0.1	0.3	0	1083
Time	[b] Titrant	Colorimetric	Potentiometric	$[Fe(II)]_{avg}\cdot 10^2$	[c] *CV*
(min)	(mL)	[Fe(II)] (g/L)	[Fe(II)] (g/L)	(mol/kg)	(%)
0	9.50	5.31	–	9.58	–
5	9.25	5.17	–	9.33	–
10	9.15	5.11	–	9.22	–
15	8.90	4.97	–	8.97	–
20	8.65	4.83	–	8.72	–
25	8.55	4.77	–	8.62	–
30	8.40	4.69	–	8.47	–
35	8.35	4.66	–	8.42	–
40	8.25	4.61	–	8.32	–
45	8.20	4.58	–	8.27	–
50	8.05	4.50	–	8.12	–
55	7.80	4.36	–	7.86	–
60	7.75	4.33	–	7.81	–
75	7.65	4.27	–	7.71	–
90	7.20	4.02	–	7.26	–
105	7.00	3.91	–	7.06	–
120	6.80	3.80	–	6.86	–
150	6.45	3.60	–	6.50	–
180	6.20	3.46	–	6.25	–

[a] 20°C; [b] 10 mL sample ; [c] $\{\sum(x_i - x_{avg})^2\}^{0.5}/x_{avg}$.

Stellenbosch University http://scholar.sun.ac.za

FOO5	Temp.	Imp. speed	Sln. mass	P_g.	$p_{O2}°$
7-litre vessel	(°C)	(rev/min)	(g)	(kPa)	(kPa)
	90	1000	7170	–	16.7
[Dichromate]	$[H_2SO_4]$	[Cu]	[Zn]	[Fe(III)]	[a] Density
(N)	(g/L)	(g/L)	(g/L)	(g/L)	(g/L)
0.1	0.5	0.1	0.3	0	1103
Time	[b] Titrant	Colorimetric	Potentiometric	$[Fe(II)]_{avg}\cdot 10^2$	[c] *CV*
(min)	(mL)	[Fe(II)] (g/L)	[Fe(II)] (g/L)	(mol/kg)	(%)
0	8.85	4.94	–	9.06	–
5	8.60	4.80	–	8.80	–
10	8.45	4.72	–	8.65	–
15	8.30	4.64	–	8.49	–
20	8.15	4.55	–	8.34	–
25	8.00	4.47	–	8.19	–
30	7.85	4.38	–	8.03	–
35	7.70	4.30	–	7.88	–
40	7.55	4.22	–	7.33	–
45	7.50	4.19	–	7.67	–
50	7.40	4.13	–	7.57	–
55	7.25	4.05	–	7.42	–
60	7.20	4.02	–	7.37	–
75	6.85	3.83	–	7.01	–
90	6.55	3.66	–	6.7	–
105	6.25	3.49	–	6.4	–
120	6.15	3.43	–	6.29	–
150	5.85	3.27	–	5.99	–
180	5.60	3.13	–	5.73	–

[a] 20°C; [b] 10 mL sample ; [c] $\{\sum(x_i - x_{avg})^2\}^{0.5}/x_{avg}$.

Stellenbosch University http://scholar.sun.ac.za

FOO6	Temp.	Imp. speed	Sln. mass	P_g.	$p_{O2}°$
7-litre vessel	(°C)	(rev/min)	(g)	(kPa)	(kPa)
	90	1000	6884	–	16.4
[Dichromate]	$[H_2SO_4]$	[Cu]	[Zn]	[Fe(III)]	[a] Density
(N)	(g/L)	(g/L)	(g/L)	(g/L)	(g/L)
0.1	0.5	0.1	0	0	1059
Time	[b] Titrant	Colorimetric	Potentiometric	$[Fe(II)]_{avg}\cdot 10^2$	[c] *CV*
(min)	(mL)	[Fe(II)] (g/L)	[Fe(II)] (g/L)	(mol/kg)	(%)
0	9.00	5.03	–	9.18	–
5	8.70	4.86	–	8.87	–
10	8.50	4.75	–	8.67	–
15	8.35	4.66	–	8.52	–
20	8.20	4.58	–	8.36	–
25	8.15	4.55	–	8.31	–
30	8.10	4.52	–	8.26	–
35	7.85	4.38	–	8.01	–
40	7.80	4.36	–	7.96	–
45	7.60	4.24	–	7.75	–
50	7.55	4.22	–	7.70	–
55	7.40	4.13	–	7.55	–
60	7.35	4.10	–	7.50	–
75	7.20	4.02	–	7.34	–
90	7.00	3.91	–	7.14	–
105	6.80	3.80	–	6.94	–
120	6.70	3.74	–	6.83	–
150	6.40	3.57	–	6.53	–
180	6.20	3.46	–	6.32	–

[a] 20°C; [b] 10 mL sample ; [c] $\{\sum(x_i - x_{avg})^2\}^{0.5}/x_{avg}$.

Stellenbosch University http://scholar.sun.ac.za

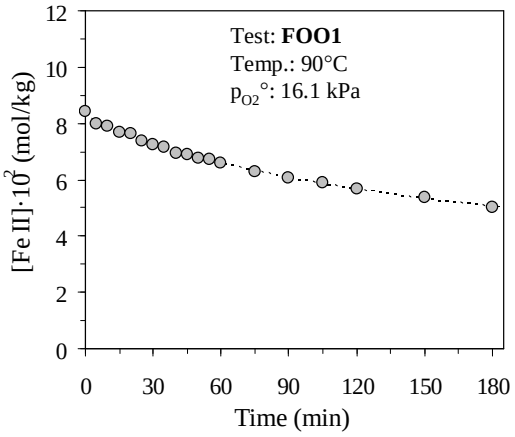

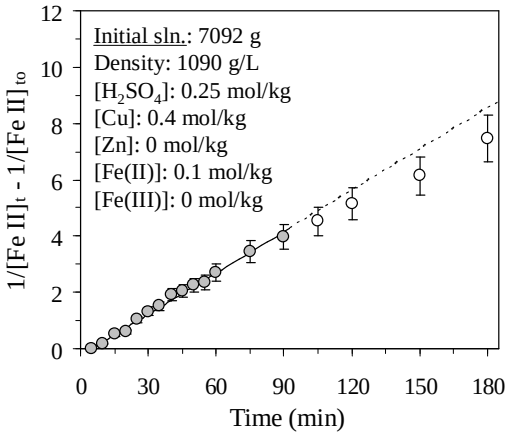

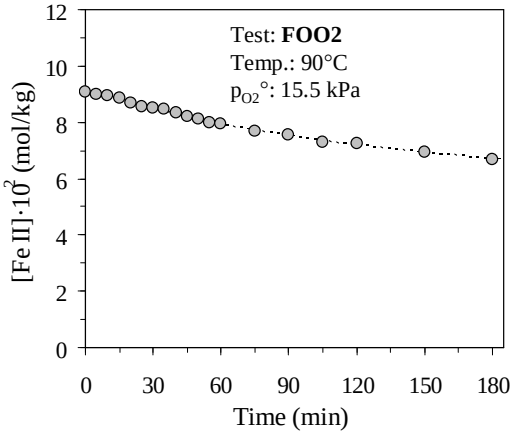

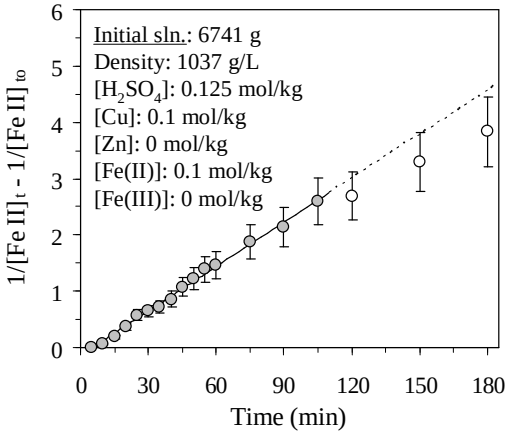

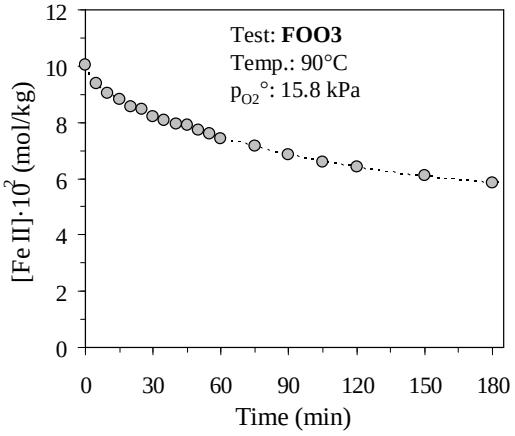

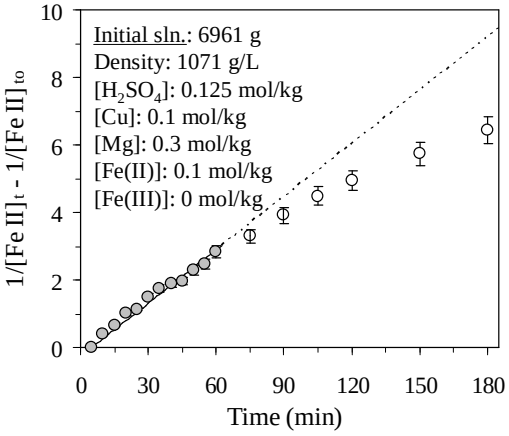

Stellenbosch University http://scholar.sun.ac.za

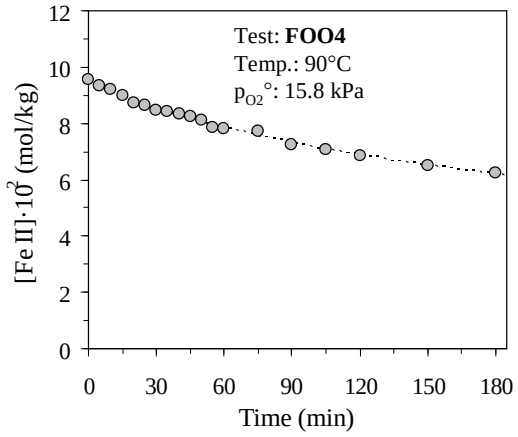

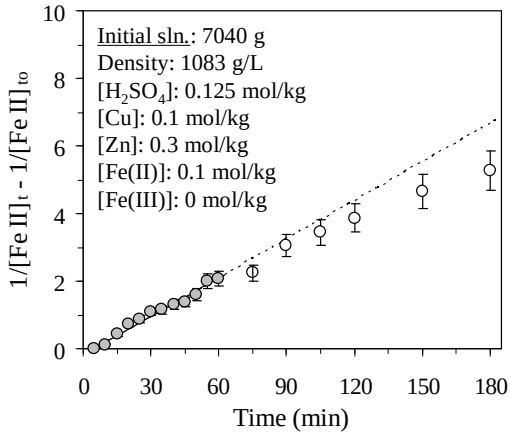

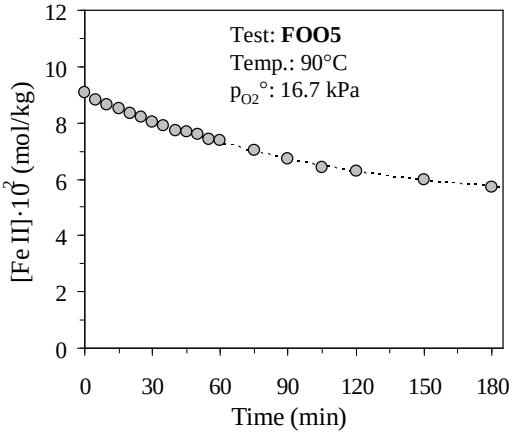

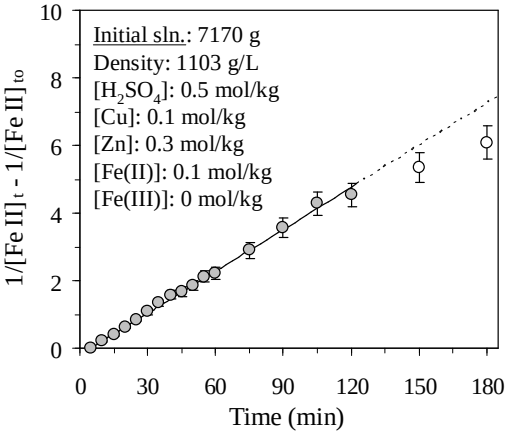

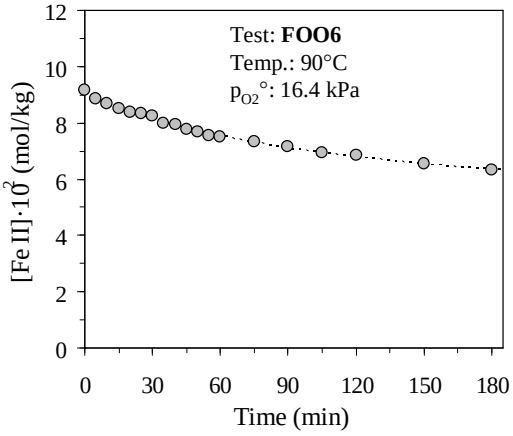

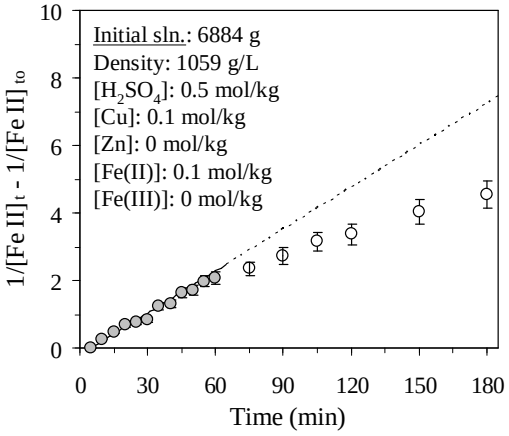

Stellenbosch University http://scholar.sun.ac.za

APPENDIX E. DETAILED IRON(III) PRECIPITATION RESULTS

This appendix summarises the detailed iron(III) precipitation testwork results (Ch. 5, Sect. 5.4) obtained in the 2-litre Parr autoclave (Ch. 3, Sect. 3.3), using impeller configuration A (Figure 3.5). The experimental procedure is presented below (also see Sect. 5.3). Each dataset is accompanied by backscatter electron (BSE) images, revealing typical particle morphologies and sizes, as well as qualitative energy dispersive X-ray (EDX) results, conducted at random points on each image (App. B.3.4). Section E.8 summarises the detailed iron(III) solubility calculations used to develop a thermodynamic basis (Sect. 5.4.2) for the phenomenological iron(III) precipitation model.

E.1 Detailed experimental procedure

The experimental setup is presented in Figure 5.5 (Sect. 5.3.1) and the procedure was as follows:

- The autoclave was charged with the required amount of water, sulfuric acid, copper (or zinc) sulfate and surfactants. In the case of the zinc system, some of the acid was pumped in with the iron(II) sulfate to reduce corrosion of the autoclave internals
- The reactor contents were then heated to the predetermined temperature, with the impeller stirring slowly. This temperature was always higher than the setpoint temperature, to account for a drop in temperature when feeding the cold iron(II) sulfate solution
- The measuring tube of the feed pump (Ch. 6, Figure 6.5) was then charged with the required amount of dissolved iron(II) sulfate (& most of the sulfuric acid, in the case of the zinc sulfate system) and pumped into the autoclave. The pumping of the cold solution typically took less than 30 sec and brought the autoclave temperature to within 1°C of the setpoint temperature. After pumping the feed solution, the dissolved species' concentrations corresponded to their desired (calculated) levels at 1200 g solution mass (see Ch. 3 for the effect of solution volume on the gas/liquid mass transfer rate)
- The oxygen valve was then opened and the autoclave vented for a few seconds to remove inert gas from the vapour space. The oxygen overpressure was then adjusted to the setpoint value and the impeller speed increased to 1000 rev/min, signifying the start of the kinetic test
- A dedicated gas feed system ensured constant oxygen overpressure by regulating the total pressure of the vessel for the remainder of the test. The temperature was controlled to within 1°C by the controller (see Sect. 3.3 for more detail on this & other quality control aspects)
- Iron(III) hydrolysis and precipitation were therefore driven by the rate of iron(II) oxidation, which is quantitatively known (Ch. 4). These reactions were allowed to proceed over a

Stellenbosch University http://scholar.sun.ac.za

predetermined reaction time, after which the autoclave contents were directly discharged (flashed) over the pressure filtration unit

- A separate test was conducted for each kinetic data point, and the same sample discharge procedure was always followed at the completion of a test: the oxygen feed valves were first closed, after which the sample valve (Fig. 5.5) was slowly opened. This commenced 30 to 60 sec before the sample was actually due
- The autoclave slurry was allowed to flash directly over the pressure filtration unit, fitted with a 0.4 µm polycarbonate (90 mm) membrane from Millipore (in some cases, 0.5 µm PTFE membranes were used, with no obvious difference), while the filtrate was continuously collected over a short period (1 to 2 min), which typically yielded filtrate volumes in the 500 to 1000 mL range. No visible solid particles passed through the membrane filter, which suggests that the cake itself also functioned as a filter medium
- The membrane and filter cake (after primary filtration) were immediately weighed, transferred to a secondary (atmospheric) flask and washed (twice) with 98% propanol (propan-2-ol or iso-propanol) solution
- In the meantime, the impeller speed was decreased to 100 rev/min and the autoclave allowed to cool to ~85°C, before the vessel was vented to atmospheric pressure. The final slurry (autoclave bucket) was then weighed. The autoclave internals were also washed with a (known) portion of the primary filtrate, *i.e.*, to collect any solid mass left in the autoclave
- The primary filtrate (not used to wash the autoclave) was cooled to room temperature and analysed by ICP-OES (App. B.2.1) for total iron and copper (or zinc), while the acid and iron(II) concentrations were determined by wet-chemical methods (App. B.2.1)
- The wet filter cake was then split into three parts: one part was dried in an oven at 40°C and subjected to chemical analysis by ICP-OES (after fusion & acid digestion; App. B.2.1) to determine the total iron and copper (or zinc) levels, while the total sulfur content was determined with a Leco analyser (App. B.2.2). The second part of the solid sample was subjected to PSD measurement (App. B.3.1), while the third part was dried in the atmosphere to produce the BSE images of the precipitated particles (App. B.3.4). EDX spectroscopy was used to estimate the sulfur/iron (S^T:Fe) mass ratio, *i.e.*, to qualitatively identify the dominant iron precipitate phases. Selected samples were also subjected to X-ray powder diffraction (XRD) analysis (App. B.3.2) to identify the major phases present.

E.2 Hematite precipitation at 155°C and different oxygen partial pressures, in the low acid (< 5 g/L H_2SO_4) and low iron(II) (< 5 g/L Fe) concentration regimes in zinc sulfate background

The first series of tests focused on determining the characteristic hematite particle morphology and size and the precipitation rate in the H_2SO_4-$ZnSO_4$ system at low acidities, *i.e.*, after injecting small

Stellenbosch University http://scholar.sun.ac.za

amounts of sulfuric acid and iron(II) sulfate 'at temperature'. These tests were conducted at 155ºC, applying progressively higher oxygen partial pressures.

FPA1	Temp.	Imp. Speed	Sln. pumped	Sln. mass	P_g	p_{O2}°
2-litre AC (A)	155ºC	1000 rev/min	Acid & Fe(II)	1200 g	890 kPa	350 kPa
FEED	[a] H_2O	$[H_2SO_4]$	[Zn]	[Fe(II)]	[b] [LS, QB]	[c] Density
A11 to A12	1141.3 g	3.5 g/L	15 g/L	3.5 g/L	0.05 g/L ea.	1043 g/L
FINAL	[d] Slurry	Filtrate	Solids (meas)	[e] Solids (calc)	[f] H_2O (evap)	[c] Density
min (test)	(g)	(g)	(g dry) (g wet)	(g dry)	(g)	(g/L)
20 (A11)	609.0	506.8	0.3 (0.6)	0.6	83.7	1051
40 (A12)	550.6	503.3	3.1 (8.1)	6.4	138.0	1048
Filtrate	$[H_2O]$	$[H_2SO_4]$	[Zn]	$[Fe(II)]\cdot10^2$	$[Fe(III)]\cdot10^2$	$[SO_4^{2-}]^{calc.}$
min (test)	(g/L)	(mol/kg)	(mol/kg)	(mol/kg)	(mol/kg)	(mol/kg)
20 (A11)	–	–	–	–	–	–
40 (A12)	992.0	0.110	0.280	0.05	0.16	0.393
Residue	$X_{p,Fe}$	$W_{f,Hem}$	[g] Zn	[g] Fe	[h] S^T:Fe	[g] S^T
min (test)	(%)	(%)	(%)	(%)	(%)	(%)
20 (A11)	–	–	–	–	– (6)	–
40 (A12)	97	88	1.35 (107)	56.7 (93)	5.6 (4)	3.2 (106)

[a] Incl. H_2O in reagents; [b] Arbo A02, Orfom 2 (no pre-drying); [c] Sln. dens. (20ºC); [d] Remaining (not filtered); [e] Total dry mass calc. from solid:slurry wt. ratio & final mass (incl. flashed H_2O); [f] Based on total mass loss; [g] Accountability in brackets; [h] S^T:Fe wt. ratio (avg. ratio from EDX spot analyses in brackets).

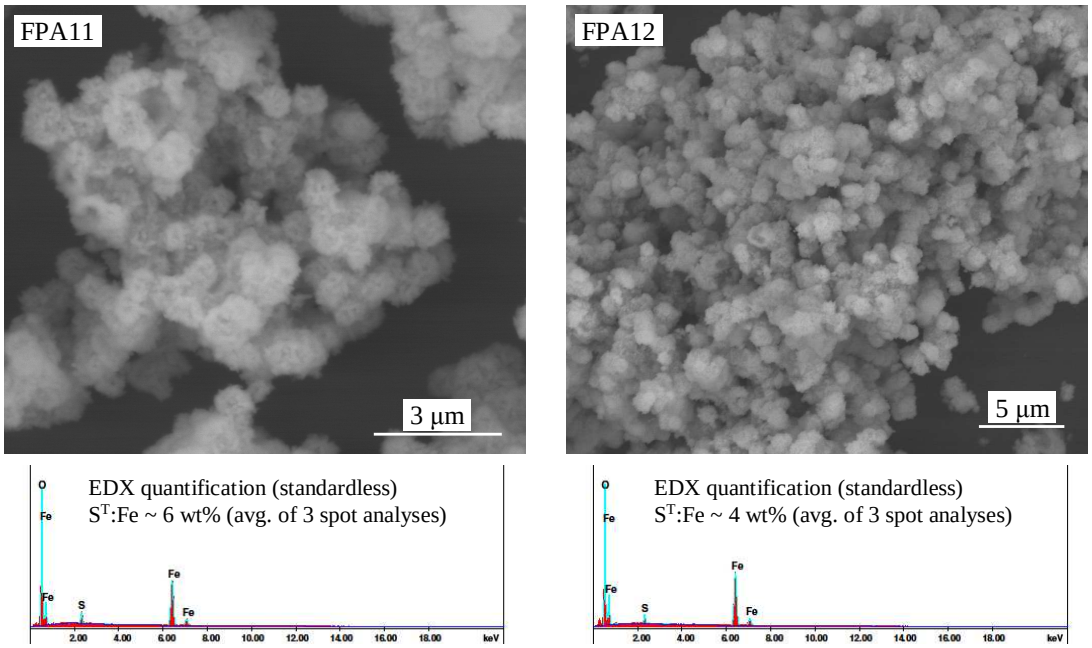

Stellenbosch University http://scholar.sun.ac.za

FPA2	Temp.	Imp. speed	Sln. pumped	Sln. mass	P_g	p_{O2}°
2-litre AC (A)	155ºC	1000 rev/min	Acid & Fe(II)	1200 g	1158 kPa	700 kPa
FEED	[a] H_2O	$[H_2SO_4]$	[Zn]	[Fe(II)]	[b] [LS, QB]	[c] Density
A21 to A22	1141.3 g	3.5 g/L	15 g/L	3.5 g/L	0.05 g/L ea.	1043 g/L
FINAL	[d] Slurry	Filtrate	Solids (meas)	[e] Solids (calc)	[f] H_2O (evap)	[c] Density
min (test)	(g)	(g)	g dry (g wet)	(g dry)	(g)	(g/L)
5 (A21)	440.2	702.0	0.1 (0.5)	0.2	57.4	1048
15 (A22)	525.2	606.8	4.0 (8.0)	7.4	60.0	1046
Filtrate	$[H_2O]$	$[H_2SO_4]$	[Zn]	$[Fe(II)]\cdot10^2$	$[Fe(III)]\cdot10^2$	$[SO_4^{2-}]^{calc.}$
min (test)	(g/L)	(mol/kg)	(mol/kg)	(mol/kg)	(mol/kg)	(mol/kg)
5 (A21)	–	–	–	–	–	–
15 (A22)	993.9	0.105	0.257	0.38	0.11	0.367
Residue	$X_{p,Fe}$	$W_{f,Hem}$	[g] Zn	[g] Fe	[h] S^T:Fe	[g] S^T
min (test)	(%)	(%)	(%)	(%)	(%)	(%)
5 (A21)	–	–	–	–	– (5)	–
15 (A22)	93	94	0.76 (105)	56.0 (110)	4.1 (4)	2.3 (107)

[a] Incl. H_2O in reagents; [b] Arbo A02, Orfom 2 (no pre-drying); [c] Sln. dens.(20ºC); [d] Remaining (not filtered); [e] Total dry mass calc. from solid:slurry wt. ratio & final mass (incl. flashed H_2O); [f] Based on total mass loss; [g] Accountability in brackets; [h] S^T:Fe wt. ratio (avg. ratio from EDX spot analyses in brackets).

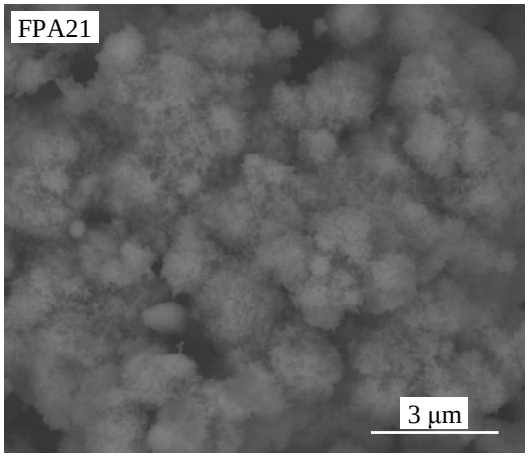

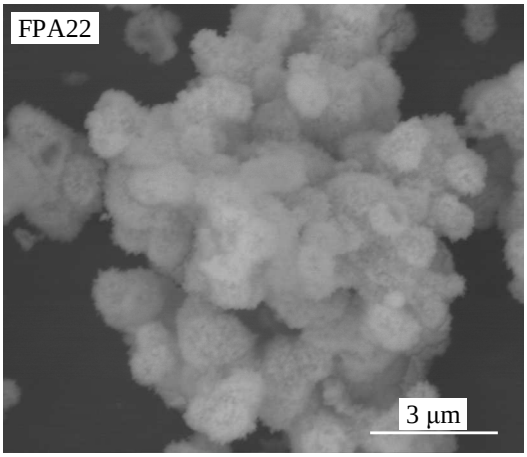

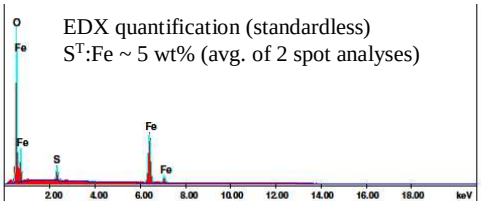

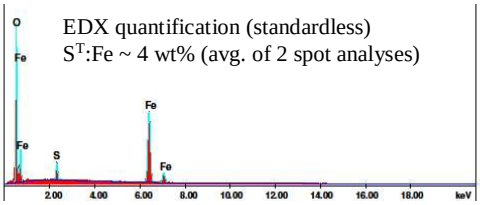

Stellenbosch University http://scholar.sun.ac.za

FPA3	Temp.	Imp. speed	Sln. pumped	Sln. mass	P_g	p_{O2}°
2-litre AC (A)	155ºC	1000 rev/min	Acid & Fe(II)	1200 g	1458 kPa	1000 kPa
FEED	[a] H_2O	$[H_2SO_4]$	[Zn]	[Fe(II)]	[b] [LS, QB]	[c] Density
A31 to A32	1141.3 g	3.5 g/L	15 g/L	3.5 g/L	0.05 g/L ea.	1043 g/L
FINAL	[d] Slurry	Filtrate	Solids (meas)	[e] Solids (calc)	[f] H_2O (evap)	[c] Density
min (test)	(g)	(g)	(g dry) (g wet)	(g dry)	(g)	(g/L)
5 (A31)	614.2	502.0	3.3 (8.7)	7.2	75.1	1046
15 (A32)	600.2	532.1	4.0 (9.3)	8.4	58.4	1045
Filtrate	$[H_2O]$	$[H_2SO_4]$	[Zn]	$[Fe(II)]\cdot10^2$	$[Fe(III)]\cdot10^2$	$[SO_4^{2-}]^{calc.}$
min (test)	(g/L)	(mol/kg)	(mol/kg)	(mol/kg)	(mol/kg)	(mol/kg)
5 (A31)	996.8	0.090	0.241	0.56	0.51	0.344
15 (A32)	996.0	0.095	0.244	0.18	0.13	0.342
Residue	$X_{p,Fe}$	$W_{f,Hem}$	[g] Zn	[g] Fe	[h] S^T:Fe	[g] S^T
min (test)	(%)	(%)	(%)	(%)	(%)	(%)
5 (A31)	84	90	1.15 (98)	53.3 (111)	5.1 (8)	2.7 (99)
15 (A32)	95	86	1.09 (101)	53.6 (116)	5.8 (5)	3.1 (100)

[a] Incl. H_2O in reagents; [b] Arbo A02, Orfom 2 (no pre-drying); [c] Sln. dens.(20ºC); [d] Remaining (not filtered); [e] Total dry mass calc. from solid:slurry wt. ratio & final mass (incl. flashed H_2O); [f] Based on total mass loss; [g] Accountability in brackets; [h] S^T:Fe wt. ratio (avg. ratio from EDX spot analyses in brackets).

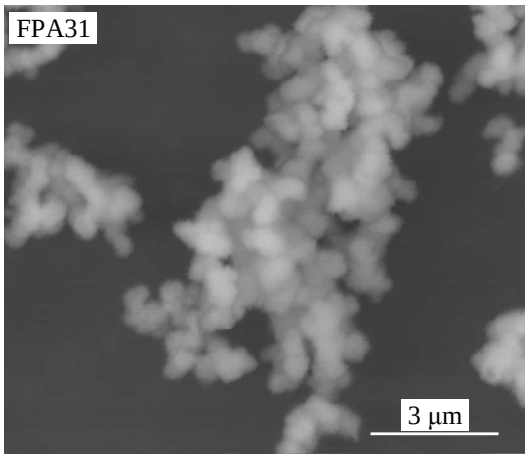

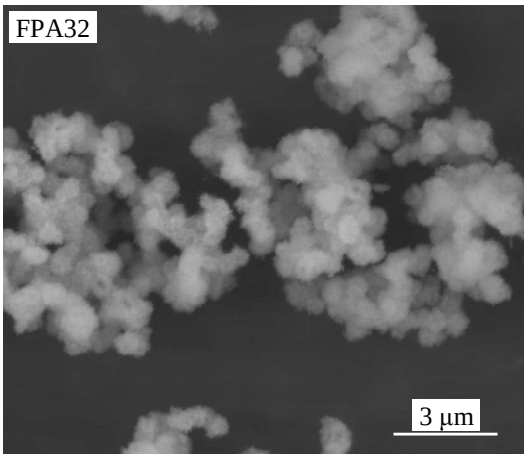

Stellenbosch University http://scholar.sun.ac.za

E.3 Hematite precipitation at 155°C (1000 kPa p_{O2}°) in the low-medium acid (4-12 g/L H_2SO_4) and low iron(II) (< 5 g/L Fe) concentration regimes in zinc and copper sulfate backgrounds

The second series of tests focused on comparing the particle morphology and size and the precipitation rate in the H_2SO_4-$ZnSO_4$ and H_2SO_4-$CuSO_4$ systems, at slightly higher acid concentrations (4-12 g/L H_2SO_4) and at a high oxygen partial pressure (1000 kPa p_{O2}°). Besides the speciation changes between these two chemical systems, copper in solution greatly enhances the oxidation rate of iron(II) (Ch. 4), which, in turn, affects the iron(III) supersaturation level. The initial iron(II) concentration was therefore reduced from 3.5 to 4 g/L Fe(II) in the case of the zinc system, to 2.5 to 3 g/L Fe(II) in the copper system. All these tests were conducted at 155ºC. Iron(II) sulfate and most of the acid was pumped into the autoclave ('at temperature') in the case of the zinc system, while only the iron(II) sulfate was injected into the autoclave in the case of the copper system (copper(II) protects the autoclave internals against corrosion in an oxygen-deficient environment during heat-up, allowing all the acid to be added upfront).

FPB1	Temp.	Imp. speed	Sln. pumped	Sln. mass	P_g	p_{O2}°
2-litre AC (A)	155ºC	1000 rev/min	Fe(II)	1200 g	1458 kPa	1000 kPa
FEED	[a] H_2O	$[H_2SO_4]$	[Cu]	[Fe(II)]	[b] [LS, QB]	[c] Density
B11 to B13	1141.8 g	4 g/L	15 g/L	3 g/L	0.05 g/L ea.	1045 g/L
FINAL	[d] Slurry	Filtrate	Solids [(meas)]	[e] Solids [(calc)]	[f] H_2O [evap]	[c] Density
min (test)	(g)	(g)	(g dry) (g wet)	(g dry)	(g)	(g/L)
2.5 (B11)	81.9	997.1	2.2 (5.3)	2.4	115.7	1049
5 (B12)	61.2	1038.2	3.0 (5.8)	3.2	94.8	1048
10 (B13)	59.4	1019.0	4.0 (5.0)	4.2	116.7	1050
Filtrate	$[H_2O]$	$[H_2SO_4]$	[Cu]	$[Fe(II)]\cdot10^2$	$[Fe(III)]\cdot10^2$	$[SO_4^{2-}]^{calc.}$
min (test)	(g/L)	(mol/kg)	(mol/kg)	(mol/kg)	(mol/kg)	(mol/kg)
2.5 (B11)	934.5	0.069	0.2785	0.22	2.24	0.383
5 (B12)	932.7	0.080	0.281	0.06	1.70	0.387
10 (B13)	930.4	0.091	0.293	0.07	1.06	0.400
Residue	$X_{p,Fe}$	$W_{f,Hem}$	[g] Cu	[g] Fe	[h] S^T:Fe	[g] S^T
min (test)	(%)	(%)	(%)	(%)	(%)	(%)
2.5 (B11)	59	84	1.44 (106)	52.9 (78)	6.4 (9)	3.4 (104)
5 (B12)	70	92	0.78 (109)	55.7 (82)	4.6 (7)	2.5 (107)
10 (B13)	81	88	0.74 (111)	54.3 (85)	5.3 (6)	2.9 (109)

[a] Incl. H_2O in reagents; [b] Arbo A02, Orfom 2 (no pre-drying); [c] Sln. dens.(20ºC); [d] Remaining (not filtered); [e] Total dry mass calc. from solid:slurry wt. ratio & final mass (incl. flashed H_2O); [f] Based on total mass loss; [g] Accountability in brackets; [h] S^T:Fe wt. ratio (avg. ratio from EDX spot analyses in brackets).

Stellenbosch University http://scholar.sun.ac.za

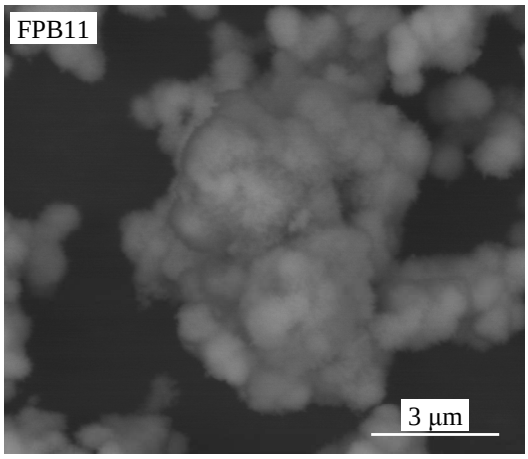

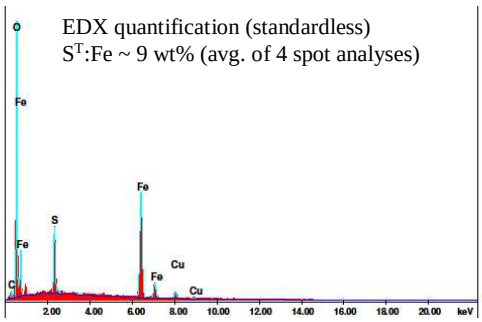

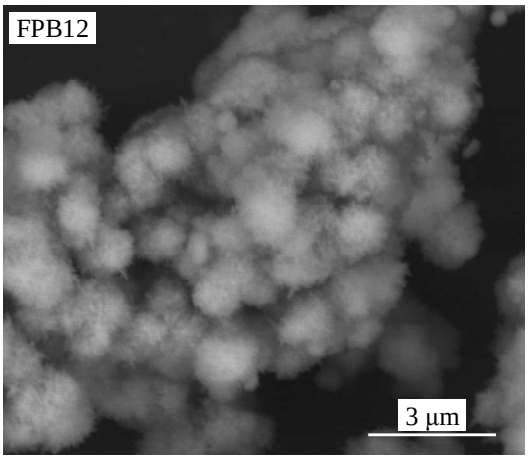

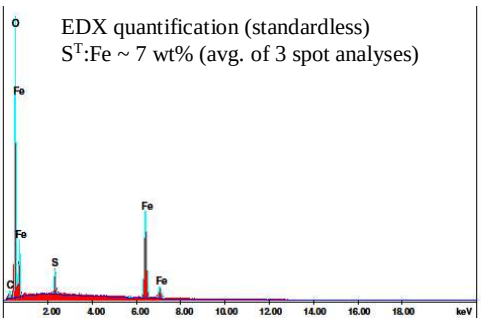

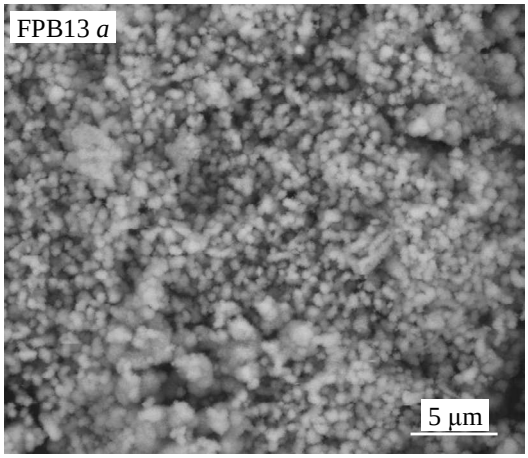

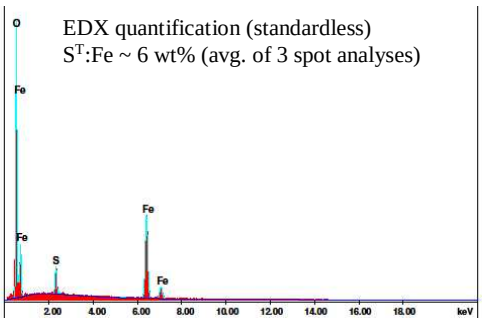

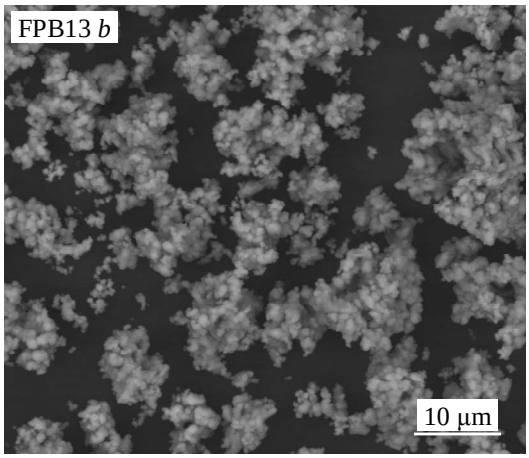

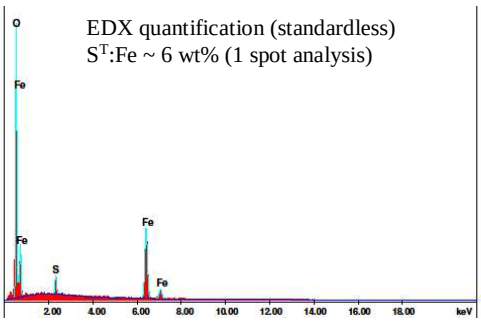

Stellenbosch University http://scholar.sun.ac.za

FPB2	Temp.	Imp. speed	Sln. pumped	Sln. mass	P_g	p_{O2}°
2-litre AC (A)	155ºC	1000 rev/min	Acid & Fe(II)	1200 g	1458 kPa	1000 kPa
FEED	[a] H_2O	$[H_2SO_4]$	[Zn]	[Fe(II)]	[b] [LS, QB]	[c] Density
B21 to B23	1139.4 g	4 g/L	15 g/L	4 g/L	0.05 g/L ea.	1047 g/L
FINAL	[d] Slurry	Filtrate	Solids (meas)	[e] Solids (calc)	[f] H_2O (evap)	[c] Density
min (test)	(g)	(g)	(g dry) (g wet)	(g dry)	(g)	(g/L)
5 (B21)	667.9	490.0	2.1 (5.1)	4.9	37.0	1048
10 (B22)	590.8	517.1	2.5 (6.7)	5.4	85.5	1048
15 (B23)	516.0	599.1	4.5 (10.5)	7.8	74.4	1048
Filtrate	$[H_2O]$	$[H_2SO_4]$	[Zn]	$[Fe(II)]\cdot10^2$	$[Fe(III)]\cdot10^2$	$[SO_4^{2-}]^{calc.}$
min (test)	(g/L)	(mol/kg)	(mol/kg)	(mol/kg)	(mol/kg)	(mol/kg)
5 (B21)	996.4	0.1095	0.242	0.61	0.72	0.368
10 (B22)	995.2	0.120	0.250	0.24	0.39	0.378
15 (B23)	995.5	0.125	0.248	0.15	0.23	0.377
Residue	$X_{p,Fe}$	$W_{f,Hem}$	[g] Zn	[g] Fe	[h] S^T:Fe	[g] S^T
min (test)	(%)	(%)	(%)	(%)	(%)	(%)
5 (B21)	82	88	0.56 (102)	53.4 (75)	5.3 (5)	2.8 (105)
10 (B22)	92	91	0.53 (100)	55.7 (75)	4.7 (5)	2.6 (103)
15 (B23)	95	92.5	0.51 (101)	56.0 (106)	4.4 (4)	2.45 (104)

[a] Incl. H_2O in reagents; [b] Arbo A02, Orfom 2 (no pre-drying); [c] Sln. dens.(20ºC); [d] Remaining (not filtered); [e] Total dry mass calc. from solid:slurry wt. ratio & final mass (incl. flashed H_2O); [f] Based on total mass loss; [g] Accountability in brackets; [h] S^T:Fe wt. ratio (avg. ratio from EDX spot analyses in brackets).

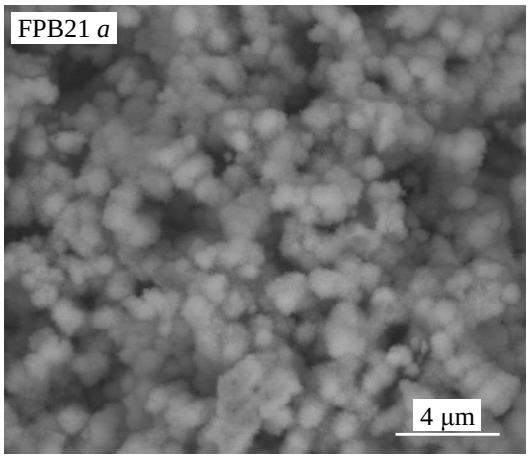

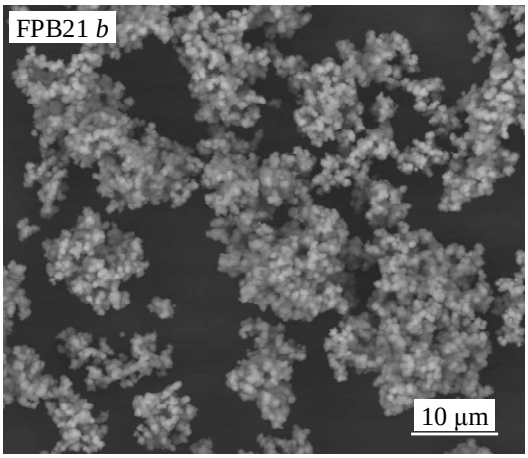

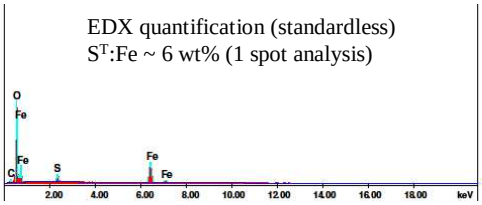

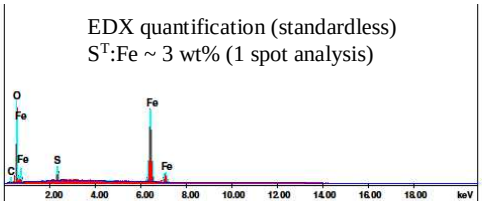

Stellenbosch University http://scholar.sun.ac.za

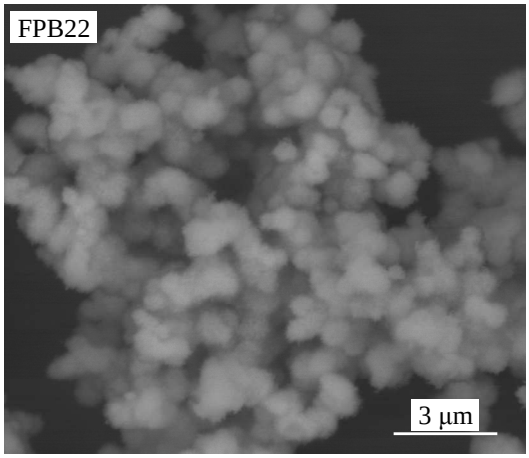

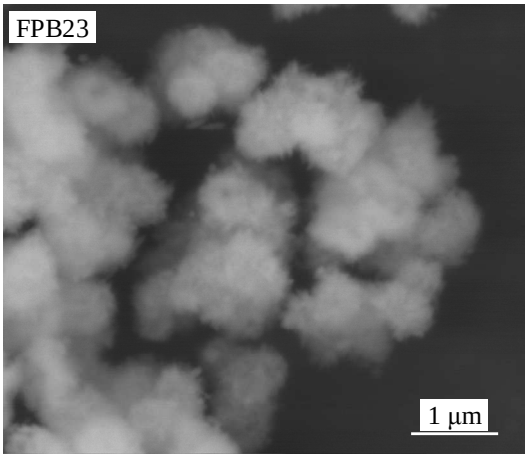

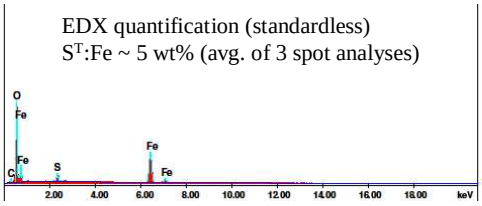

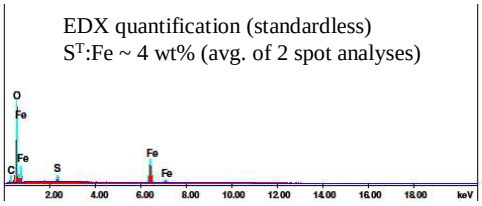

FPB3	Temp.	Imp. speed	Sln. pumped	Sln. mass	P_g	p_{O2}°
2-litre AC (A)	155ºC	1000 rev/min	Fe(II)	1200 g	1458 kPa	1000 kPa
FEED	[b] H_2O	$[H_2SO_4]$	[Cu]	[Fe(II)]	[c] [LS, QB]	[d] Density
[a] B31 to B33	1134.4 g	12 g/L	15 g/L	2.5 g/L	0.05 g/L ea.	1048 g/L
FINAL	[e] Slurry	Filtrate	Solids (meas)	[f] Solids (calc)	[g] H_2O (evap)	[d] Density
min (test)	(g)	(g)	(g dry) (g wet)	(g dry)	(g)	(g/L)
2.5 (B31)	63.9	987.9	0.4 (1.7)	0.4	146.5	1056
5 (B32)	62.4	1012.5	0.5 (1.8)	0.6	123.3	1058
10 (B33)	62.3	1033.4	0.7 (1.8)	0.8	102.6	1058
Filtrate	$[H_2O]$	$[H_2SO_4]$	[Cu]	$[Fe(II)]\cdot10^2$	$[Fe(III)]\cdot10^2$	$[SO_4^{2-}]^{calc.}$
min (test)	(g/L)	(mol/kg)	(mol/kg)	(mol/kg)	(mol/kg)	(mol/kg)
2.5 (B31)	927.0	0.128	0.296	0.44	4.27	0.493
5 (B32)	928.3	0.123	0.300	0.23	4.21	0.489
10 (B33)	934.7	0.127	0.2815	0.17	3.82	0.468
Residue	$X_{p,Fe}$	$W_{f,Hem}$	[h] Cu	[h] Fe	[i] S^T:Fe	[h] S^T
min (test)	(%)	(%)	(%)	(%)	(%)	(%)
2.5 (B31)	9	86	1.11 (108)	53.3 (99)	5.9 (8)	3.1 (106)
5 (B32)	12.5	92	0.90 (112)	55.3 (99)	4.7 (8)	2.6 (107)
10 (B33)	20	86	0.70 (108)	54.35 (95)	5.7 (10)	3.1 (105)

[a] All sets were repeated in order to generate enough solid sample for chemical analyses (reported values are averages); [b] Incl. H_2O in reagents; [c] Arbo A02, Orfom 2 (no pre-drying); [d] Sln. dens.(20ºC); [e] Remaining (not filtered); [f] Total dry mass calc. from solid:slurry wt. ratio & final mass (incl. flashed H_2O); [g] Based on total mass loss; [h] Accountability in brackets; [i] S^T:Fe wt. ratio (avg. ratio from EDX spot analyses in brackets).

Stellenbosch University http://scholar.sun.ac.za

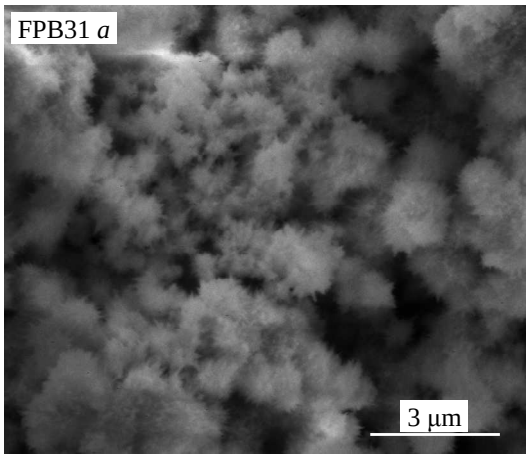

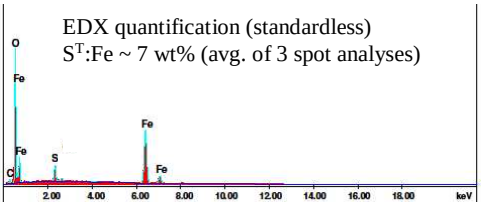

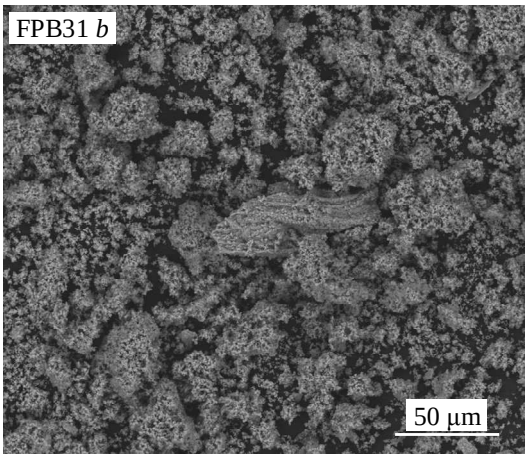

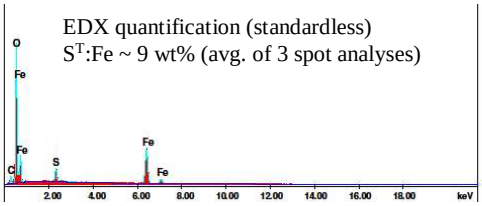

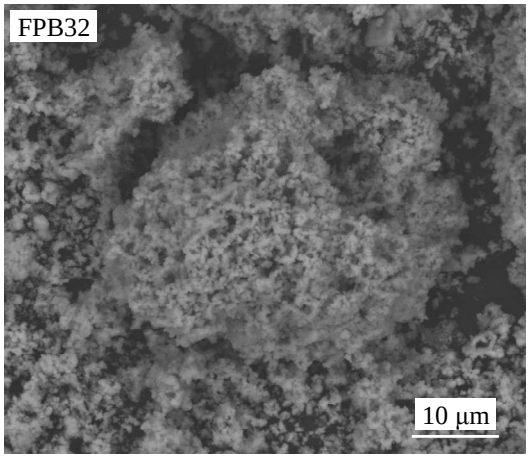

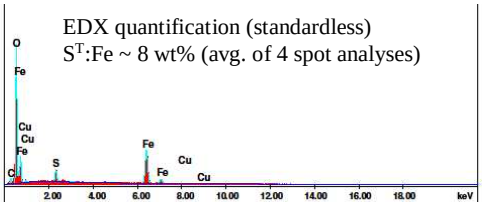

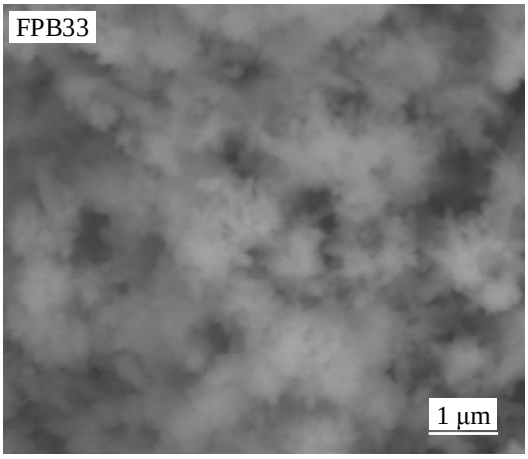

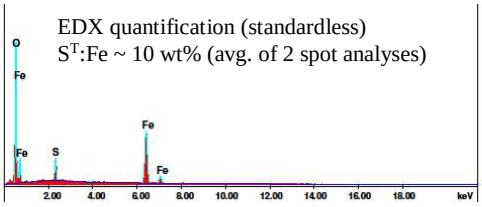

Stellenbosch University http://scholar.sun.ac.za

FPB4	Temp.	Imp. speed	Sln. pumped	Sln. mass	Gauge press.	p_{O2}°
2-litre AC (A)	155ºC	1000 rev/min	Acid & Fe(II)	1200 g	1458 kPa	1000 kPa
FEED	[a] H_2O	$[H_2SO_4]$	[Zn]	[Fe(II)]	[b] [LS, QB]	[c] Density
B41 to B43	1137.5 g	7 g/L	15 g/L	3.5 g/L	0.05 g/L ea.	1047 g/L
FINAL	[d] Slurry	Filtrate	Solids (meas)	[e] Solids (calc)	[f] H_2O (evap)	[c] Density
min (test)	(g)	(g)	(g dry) (g wet)	(g dry)	(g)	(g/L)
5 (B41)	595.0	511.2	0.8 (1.3)	1.7	92.5	1051
10 (B42)	518.1	581.1	1.3 (3.6)	2.5	97.1	1051
15 (B43)	442.0	621.2	1.7 (4.9)	3.0	131.9	1052
Filtrate	$[H_2O]$	$[H_2SO_4]$	[Zn]	$[Fe(II)]\cdot10^2$	$[Fe(III)]\cdot10^2$	$[SO_4^{2-}]^{calc.}$
min (test)	(g/L)	(mol/kg)	(mol/kg)	(mol/kg)	(mol/kg)	(mol/kg)
5 (B41)	–	–	–	–	–	–
10 (B42)	995.0	0.100	0.256	0.32	3.12	0.405
15 (B43)	994.7	0.115	0.265	0.19	2.15	0.414
Residue	$X_{p,Fe}$	$W_{f,Hem}$	[g] Zn	[g] Fe	[h] S^T:Fe	[g] S^T
min (test)	(%)	(%)	(%)	(%)	(%)	(%)
5 (B41)	–	–	–	–	–	–
10 (B42)	50	84	0.57 (101)	56.7 (85)	6.2 (5)	3.5 (102)
15 (B43)	67	82.5	0.91 (101)	55.2 (73)	6.5 (5)	3.6 (101)

[a] Incl. H_2O in reagents; [b] Arbo A02, Orfom 2 (no pre-drying); [c] Sln. dens.(20ºC); [d] Remaining (not filtered); [e] Total dry mass calc. from solid:slurry wt. ratio & final mass (incl. flashed H_2O); [f] Based on total mass loss; [g] Accountability in brackets; [h] S^T:Fe wt. ratio (avg. ratio from EDX spot analyses in brackets).

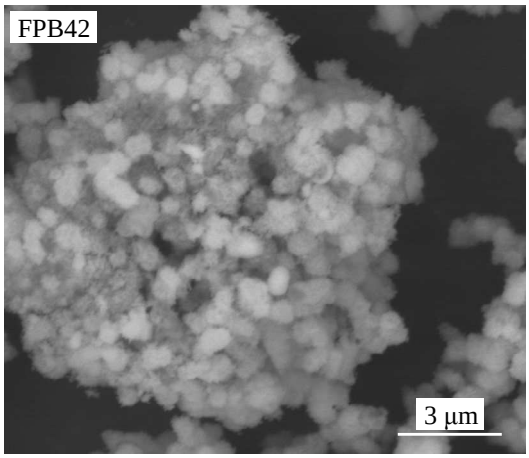

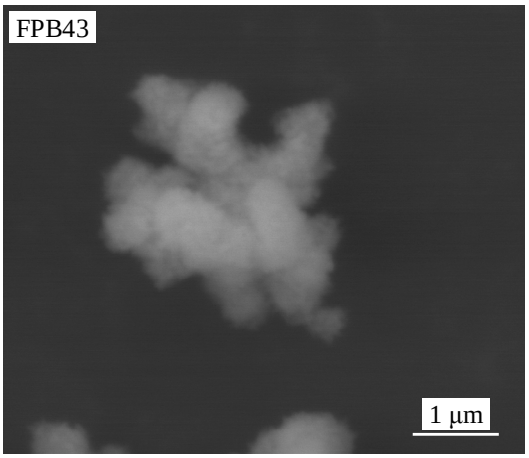

Stellenbosch University http://scholar.sun.ac.za

E.4 Iron(III) precipitation at 150°C (1000 kPa p_{O2}°) in the medium-high acid (10-16 g/L H_2SO_4) and medium iron(II) (4-8.5 g/L) concentration regimes in copper sulfate background

The third series of tests focused on comparing the particle morphology and size, and the precipitation rate in the H_2SO_4-$CuSO_4$ system, using increased acid (10-16 g/L H_2SO_4) and varying iron(II) (4-8.5 g/L) concentrations, *i.e.*, to measure the impact of different iron(III) supersaturation levels, as well as identifying possible surface interactions between the different precipitate phases. All these tests were conducted at the baseline temperature of 150ºC and, again, using the relatively high oxygen partial pressure of 1000 kPa p_{O2}º. Only iron(II) sulfate was pumped into the autoclave ('at temperature'), with all the other reagents added upfront.

FPC1	Temp.	Imp. speed	Sln. pumped	Sln. mass	P_g	p_{O2}°
2-litre AC (A)	150ºC	1000 rev/min	Fe(II)	1200 g	1391 kPa	1000 kPa
FEED	[a] H_2O	$[H_2SO_4]$	[Cu]	[Fe(II)]	[b] [LS, QB]	[c] Density
C11 to C12	1118.8 g	10 g/L	15 g/L	8.5 g/L	0.05 g/L ea.	1063 g/L
FINAL	[d] Slurry	Filtrate	Solids (meas)	[e] Solids (calc)	[f] H_2O (evap)	[c] Density
min (test)	(g)	(g)	(g dry) (g wet)	(g dry)	(g)	(g/L)
5 (C11)	61.2	1084.8	5.6 (10.7)	5.9	43.3	1062
7.5 (C12)	60.3	1068.4	6.8 (12.9)	7.1	58.5	1063
Filtrate	$[H_2O]$	$[H_2SO_4]$	[Cu]	$[Fe(II)]\cdot10^2$	$[Fe(III)]\cdot10^2$	$[SO_4^{2-}]^{calc.}$
min (test)	(g/L)	(mol/kg)	(mol/kg)	(mol/kg)	(mol/kg)	(mol/kg)
5 (C11)	939.8	0.090	0.261	0.47	10.15	0.508
7.5 (C12)	942.7	0.1105	0.256	0.34	8.74	0.508
Residue	$X_{p,Fe}$	$W_{f,Hem}$	[g] Cu	[g] Fe	[h] S^T:Fe	[g] S^T
min (test)	(%)	(%)	(%)	(%)	(%)	(%)
5 (C11)	33.5	41	0.42 (106)	43.6 (93)	17.7 (14)	7.7 (101)
7.5 (C12)	44	38	0.44 (102)	44.8 (89)	18.9 (21)	8.5 (99)

[a] Incl. H_2O in reagents; [b] Arbo A02, Orfom 2 (no pre-drying); [c] Sln. dens.(20ºC); [d] Remaining (not filtered); [e] Total dry mass calc. from solid:slurry wt. ratio & final mass (incl. flashed H_2O); [f] Based on total mass loss; [g] Accountability in brackets; [h] S^T:Fe wt. ratio (avg. ratio from EDX spot analyses in brackets).

Stellenbosch University http://scholar.sun.ac.za

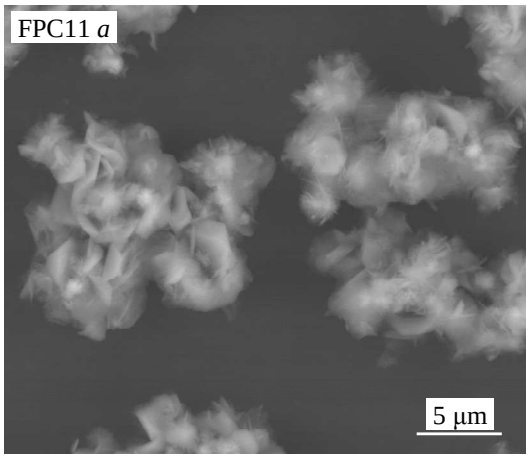

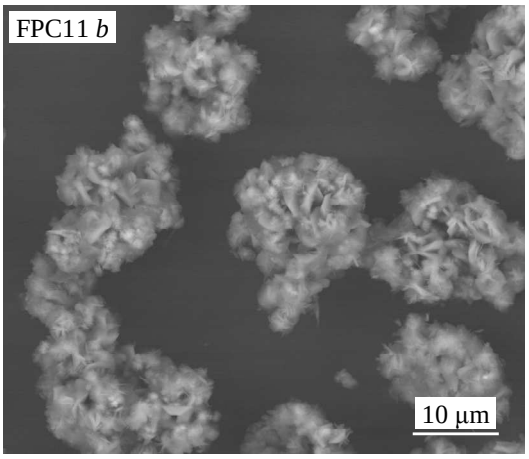

EDX quantification (standardless)
S^T:Fe ~ 13 wt% (avg. of 4 spot analyses)

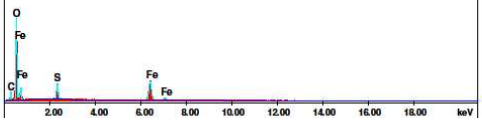

EDX quantification (standardless)
S^T:Fe ~ 14 wt% (avg. of 4 spot analyses)

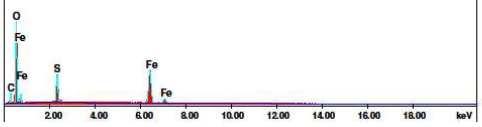

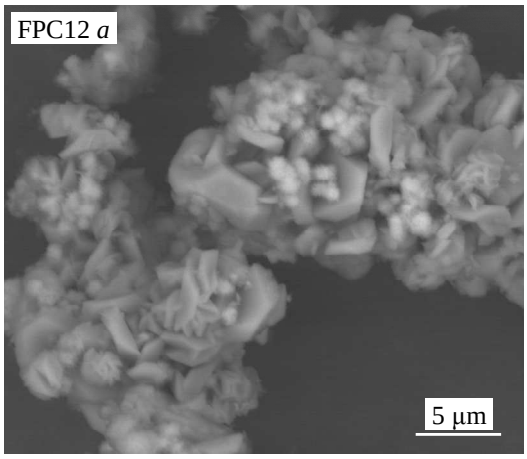

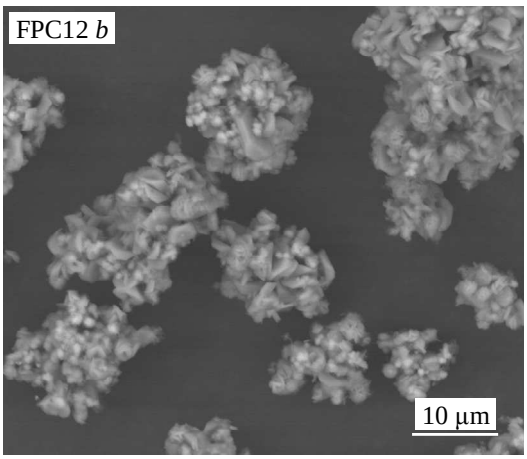

EDX quantification (standardless)
S^T:Fe ~ 18 wt% (avg. of 3 spot analyses)

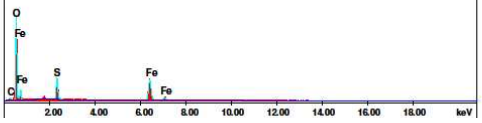

EDX quantification (standardless)
S^T:Fe ~ 24 wt% (avg. of 3 spot analyses)

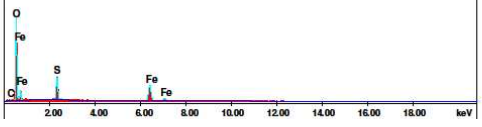

Stellenbosch University http://scholar.sun.ac.za

FPC2	Temp.	Imp. speed	Sln. pumped	Sln. mass	P_g	p_{O2}°
2-litre AC (A)	150ºC	1000 rev/min	Fe(II)	1200 g	1391 kPa	1000 kPa
FEED	[b] H_2O	$[H_2SO_4]$	[Cu]	[Fe(II)]	[c] [LS, QB]	[d] Density
[a] C21 to C22	1129.5 g	12.5 g/L	15 g/L	4.0 g/L	0.05 g/L ea.	1054 g/L
FINAL	[e] Slurry	Filtrate	Solids (meas)	[f] Solids (calc)	[g] H_2O (evap)	[d] Density
min (test)	(g)	(g)	(g dry) (g wet)	(g dry)	(g)	(g/L)
15 (C21)	62.7	1071.7	0.8 (3.0)	0.8	62.5	1060
20 (C22)	68.2	1045.6	2.7 (8.5)	2.9	77.6	1061
Filtrate	$[H_2O]$	$[H_2SO_4]$	[Cu]	$[Fe(II)]\cdot10^2$	$[Fe(III)]\cdot10^2$	$[SO_4^{2-}]^{calc.}$
min (test)	(g/L)	(mol/kg)	(mol/kg)	(mol/kg)	(mol/kg)	(mol/kg)
15 (C21)	934.5	0.117	0.280	0.19	6.48	0.496
20 (C22)	937.5	0.127	0.274	0.16	5.78	0.489
Residue	$X_{p,Fe}$	$W_{f,Hem}$	[h] Cu	[h] Fe	[i] S^T:Fe	[h] S^T
min (test)	(%)	(%)	(%)	(%)	(%)	(%)
15 (C21)	13	65	0.9 (111)	49.2 (96)	10.6 (11)	5.2 (107)
20 (C22)	23	68	1.0 (107)	47.2 (107)	9.8 (13)	4.6 (105)

[a] Test C21 was repeated in order to generate enough solid sample for chemical analyses (reported values are averages); [b] Incl. H_2O in reagents; [c] Arbo A02, Orfom 2 (no pre-drying); [d] Sln. dens.(20ºC); [e] Remaining (not filtered); [f] Total dry mass calc. from solid:slurry wt. ratio & final mass (incl. flashed H_2O); [g] Based on total mass loss; [h] Accountability in brackets; [i] S^T:Fe wt. ratio (avg. ratio from EDX spot analyses in brackets).

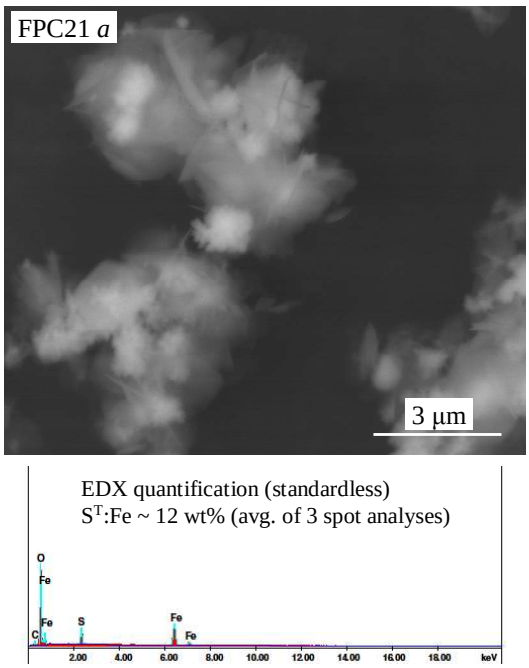

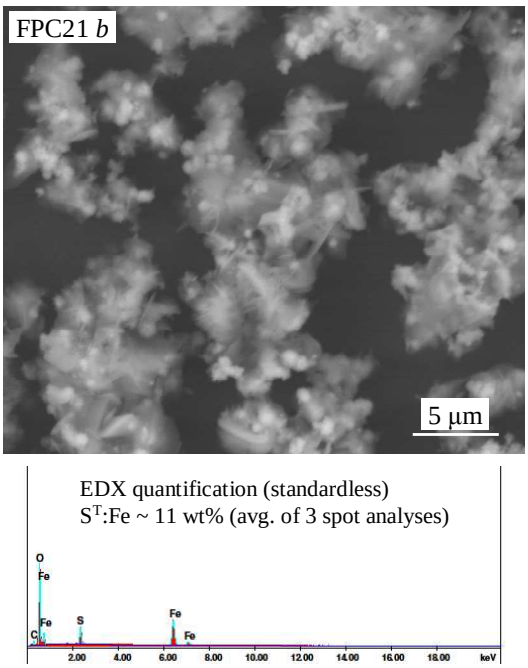

Stellenbosch University http://scholar.sun.ac.za

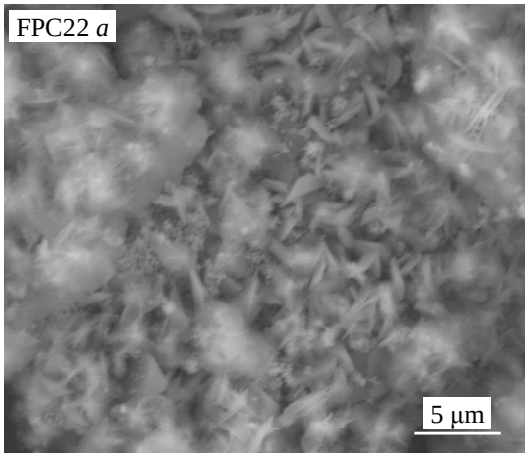

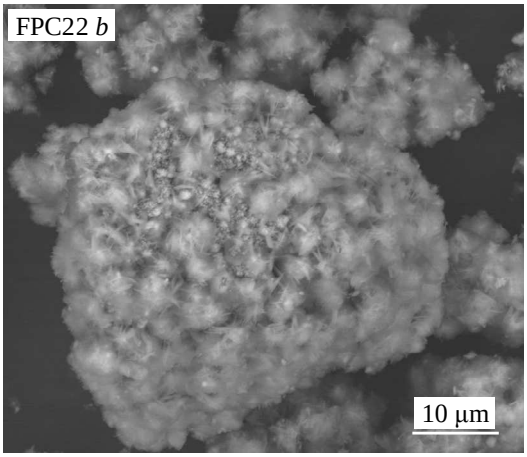

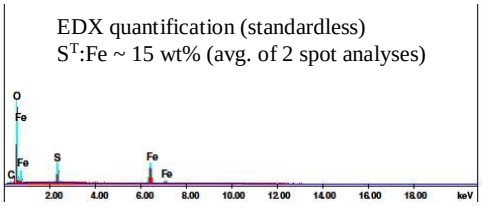

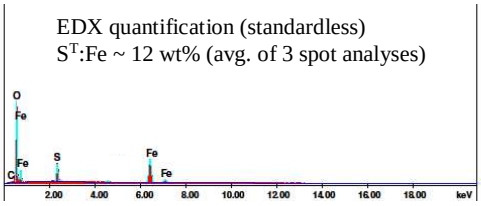

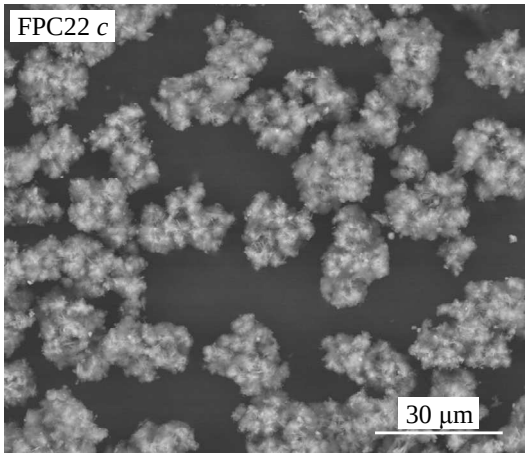

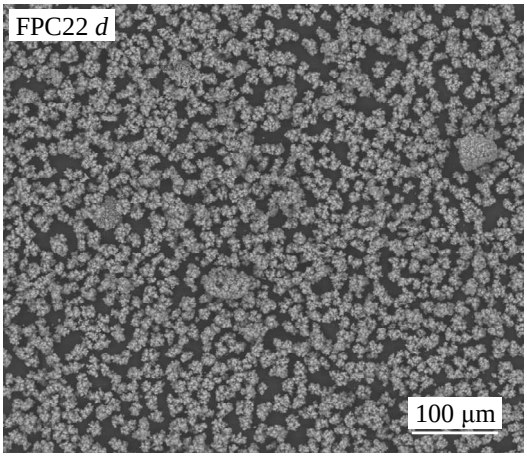

Stellenbosch University http://scholar.sun.ac.za

FPC3	Temp.	Imp. speed	Sln. pumped	Sln. mass	P_g	$p_{O2}°$
2-litre AC (A)	150ºC	1000 rev/min	Fe(II)	1200 g	1391 kPa	1000 kPa
FEED	[b] H_2O	$[H_2SO_4]$	[Cu]	[Fe(II)]	[c] [LS, QB]	[d] Density
[a] C31 to C32	1123.9 g	13.5 g/L	15 g/L	5.5 g/L	0.05 g/L ea.	1058 g/L
FINAL	[e] Slurry	Filtrate	Solids [(meas)]	[f] Solids [(calc)]	[g] H_2O [(evap)]	[d] Density
min (test)	(g)	(g)	(g dry) (g wet)	(g dry)	(g)	(g/L)
5 (C31)	57.7	1069.2	0	0	73.1	1061
10 (C32)	327.1	794.9	0.7 (2.4)	2.9	75.6	1065
Filtrate	$[H_2O]$	$[H_2SO_4]$	[Cu]	$[Fe(II)]\cdot10^2$	$[Fe(III)]\cdot10^2$	$[SO_4^{2-}]^{calc.}$
min (test)	(g/L)	(mol/kg)	(mol/kg)	(mol/kg)	(mol/kg)	(mol/kg)
5 (C31)	–	–	–	–	–	–
10 (C32)	941.6	0.111	0.261	0.29	9.76	0.521
Residue	$X_{p,Fe}$	$W_{f,Hem}$	[h] Cu	[h] Fe	[i] S^T:Fe	[h] S^T
min (test)	(%)	(%)	(%)	(%)	(%)	(%)
5 (C31)	0	–	–	–	–	–
10 (C32)	6	52	0.9 (102)	47.7 (102)	14.2 (17)	6.8 (102)

[a] Test C32 was repeated in order to generate enough solid sample for chemical analyses (reported values are averages); [b] Incl. H_2O in reagents; [c] Arbo A02, Orfom 2 (no pre-drying); [d] Sln. dens.(20ºC); [e] Remaining (not filtered); [f] Total dry mass calc. from solid:slurry wt. ratio & final mass (incl. flashed H_2O); [g] Based on total mass loss; [h] Accountability in brackets; [i] S^T:Fe wt. ratio (avg. ratio from EDX spot analyses in brackets).

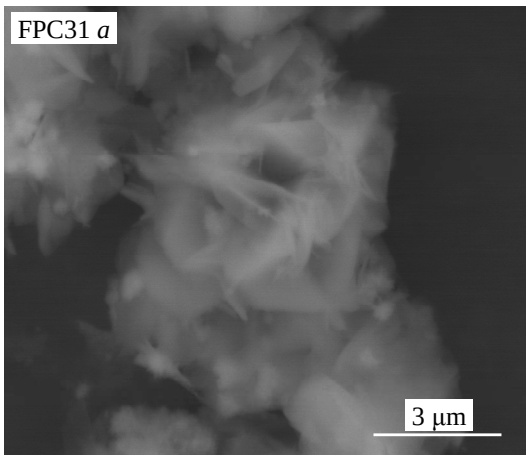

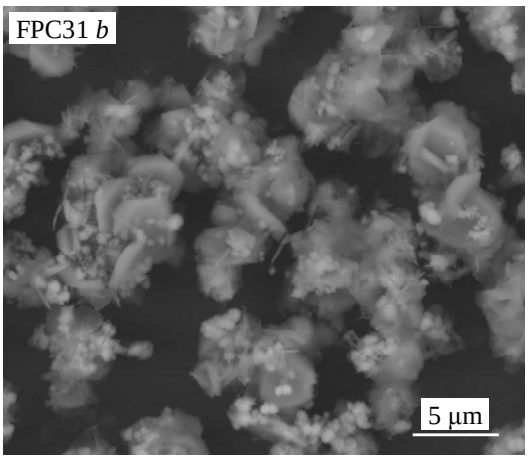

Stellenbosch University http://scholar.sun.ac.za

FPC4	Temp.	Imp. speed	Sln. pumped	Sln. mass	P_g	p_{O2}°
2-litre AC (A)	150ºC	1000 rev/min	Fe(II)	1200 g	1391 kPa	1000 kPa
FEED	[a] H_2O	$[H_2SO_4]$	[Cu]	[Fe(II)]	[b] [LS, QB]	[c] Density
C41 to C43	1121.9 g	14 g/L	15 g/L	6 g/L	0.05 g/L ea.	1060 g/L
FINAL	[d] Slurry	Filtrate	Solids (meas)	[e] Solids (calc)	[f] H_2O (evap)	[c] Density
min (test)	(g)	(g)	(g dry) (g wet)	(g dry)	(g)	(g/L)
5 (C41)	65.2	1048.6	0	0	86.2	1063
10 (C42)	61.6	1084.6	0.9 (3.8)	0.9	46.0	1063
15 (C43)	62.3	1061.8	2.0 (7.1)	2.1	68.6	1065
Filtrate	$[H_2O]$	$[H_2SO_4]$	[Cu]	$[Fe(II)]\cdot10^2$	$[Fe(III)]\cdot10^2$	$[SO_4^{2-}]^{calc.}$
min (test)	(g/L)	(mol/kg)	(mol/kg)	(mol/kg)	(mol/kg)	(mol/kg)
5 (C41)	–	–	–	–	–	–
10 (C42)	937.2	0.111	0.266	0.29	10.38	0.536
15 (C43)	942.8	0.126	0.256	0.19	9.18	0.522
Residue	$X_{p,Fe}$	$W_{f,Hem}$	[g] Cu	[g] Fe	[h] S^T:Fe	[g] S^T
min (test)	(%)	(%)	(%)	(%)	(%)	(%)
5 (C41)	–	–	–	–	–	–
10 (C42)	6	38	0.90 (107)	41.6 (100)	19.2 (19)	8.0 (105)
15 (C43)	19	57	0.67 (101)	47.3 (96)	12.7 (12)	6.0 (101)

[a] Incl. H_2O in reagents; [b] Arbo A02, Orfom 2 (no pre-drying); [c] Sln. dens.(20ºC); [d] Remaining (not filtered); [e] Total dry mass calc. from solid:slurry wt. ratio & final mass (incl. flashed H_2O); [f] Based on total mass loss; [g] Accountability in brackets; [h] S^T:Fe wt. ratio (avg. ratio from EDX spot analyses in brackets).

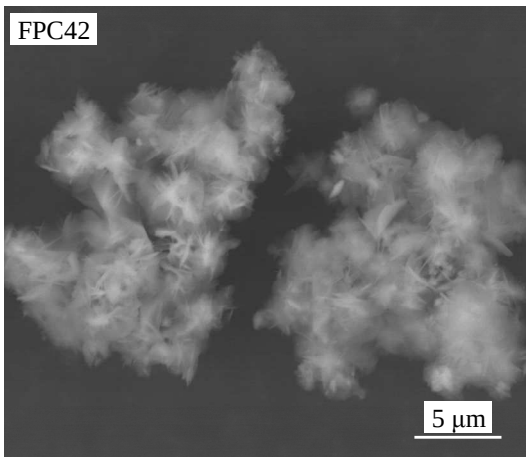

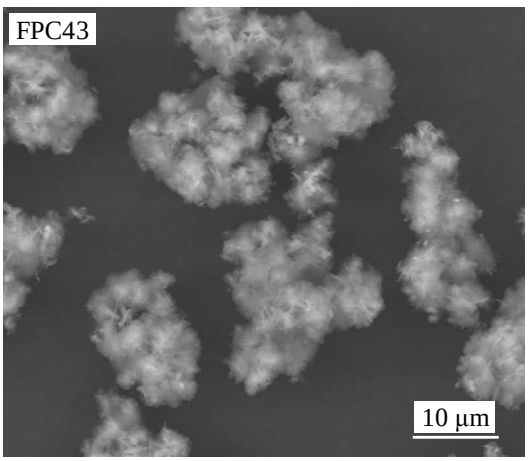

Stellenbosch University http://scholar.sun.ac.za

FPC5	Temp.	Imp. speed	Sln. pumped	Sln. mass	P_g	p_{O2}°
2-litre AC (A)	150ºC	1000 rev/min	Fe(II)	1200 g	1391 kPa	1000 kPa
FEED	[a] H_2O	$[H_2SO_4]$	[Cu]	[Fe(II)]	[b] [LS, QB]	[c] Density
C51 to C53	1116.4 g	15 g/L	15 g/L	7.5 g/L	0.05 g/L ea.	1064 g/L
FINAL	[d] Slurry	Filtrate	Solids (meas)	[e] Solids (calc)	[f] H_2O (evap)	[c] Density
min (test)	(g)	(g)	(g dry) (g wet)	(g dry)	(g)	(g/L)
5 (C51)	59.5	1055.3	– (1.0)	0	84.2	1070
10 (C52)	62.7	1077.7	2.4 (5.1)	2.5	49.5	1067
15 (C53)	59.2	1067.7	4.3 (8.7)	4.5	64.4	1068
Filtrate	$[H_2O]$	$[H_2SO_4]$	[Cu]	$[Fe(II)]\cdot10^2$	$[Fe(III)]\cdot10^2$	$[SO_4^{2-}]^{calc.}$
min (test)	(g/L)	(mol/kg)	(mol/kg)	(mol/kg)	(mol/kg)	(mol/kg)
5 (C51)	–	–	–	–	–	–
10 (C52)	938.9	0.111	0.260	0.30	13.29	0.574
15 (C53)	936.3	0.122	0.2745	0.15	11.77	0.575
Residue	$X_{p,Fe}$	$W_{f,Hem}$	[g] Cu	[g] Fe	[h] S^T:Fe	[g] S^T
min (test)	(%)	(%)	(%)	(%)	(%)	(%)
5 (C51)	–	–	–	–	–	–
10 (C52)	5	27.5	0.57 (104)	40.5 (107)	23.2 (21)	9.4 (104)
15 (C53)	17	11	0.30 (109)	36.9 (102)	31.4 (35)	11.6 (105)

[a] Incl. H_2O in reagents; [b] Arbo A02, Orfom 2 (no pre-drying); [c] Sln. dens.(20ºC); [d] Remaining (not filtered); [e] Total dry mass calc. from solid:slurry wt. ratio & final mass (incl. flashed H_2O); [f] Based on total mass loss; [g] Accountability in brackets; [h] S^T:Fe wt. ratio (avg. ratio from EDX spot analyses in brackets).

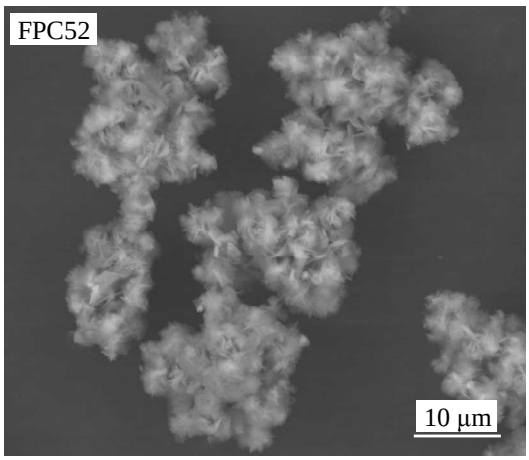

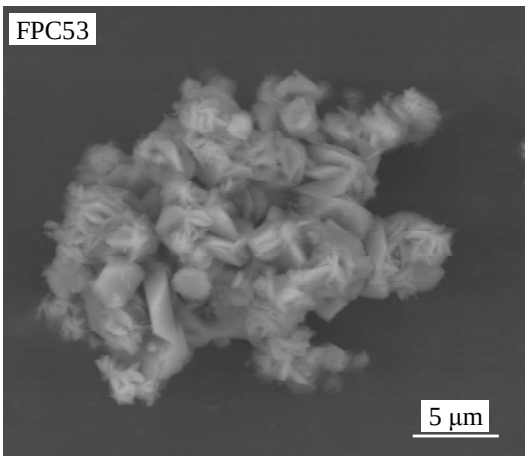

Stellenbosch University http://scholar.sun.ac.za

FPC6	Temp.	Imp. speed	Sln. pumped	Sln. mass	P_g	p_{O2}°
2-litre AC (A)	150ºC	1000 rev/min	Fe(II)	1200 g	1391 kPa	1000 kPa
FEED	[a] H_2O	$[H_2SO_4]$	[Cu]	[Fe(II)]	[b] [LS, QB]	[c] Density
C61 to C62	1112.4 g	16 g/L	15 g/L	8.5/L	0.05 g/L ea.	1067g/L
FINAL	[d] Slurry	Filtrate	Solids (meas)	[e] Solids (calc)	[f] H_2O (evap)	[c] Density
min (test)	(g)	(g)	(g dry) (g wet)	(g dry)	(g)	(g/L)
5 (C61)	57.5	1057.4	– (0.1)	0	85.1	1069
15 (C62)	62.8	1055.4	6.1 (12.8)	6.5	69.0	1073
Filtrate	$[H_2O]$	$[H_2SO_4]$	[Cu]	$[Fe(II)]\cdot10^2$	$[Fe(III)]\cdot10^2$	$[SO_4^{2-}]^{calc.}$
min (test)	(g/L)	(mol/kg)	(mol/kg)	(mol/kg)	(mol/kg)	(mol/kg)
5 (C61)	–	–	–	–	–	–
15 (C62)	941.4	0.1475	0.2665	0.22	11.60	0.590
Residue	$X_{p,Fe}$	$W_{f,Hem}$	[g] Cu	[g] Fe	[h] S^T:/Fe	[g] S^T
min (test)	(%)	(%)	(%)	(%)	(%)	(%)
5 (C61)	–	–	–	–	–	–
15 (C62)	28	26	0.57 (105)	40.9 (100)	23.7 (18)	9.7 (102)

[a] Incl. H_2O in reagents; [b] Arbo A02, Orfom 2 (no pre-drying); [c] Sln. dens.(20ºC); [d] Remaining (not filtered); [e] Total dry mass calc. from solid:slurry wt. ratio & final mass (incl. flashed H_2O); [f] Based on total mass loss; [g] Accountability in brackets; [h] S^T:Fe wt. ratio (avg. ratio from EDX spot analyses in brackets).

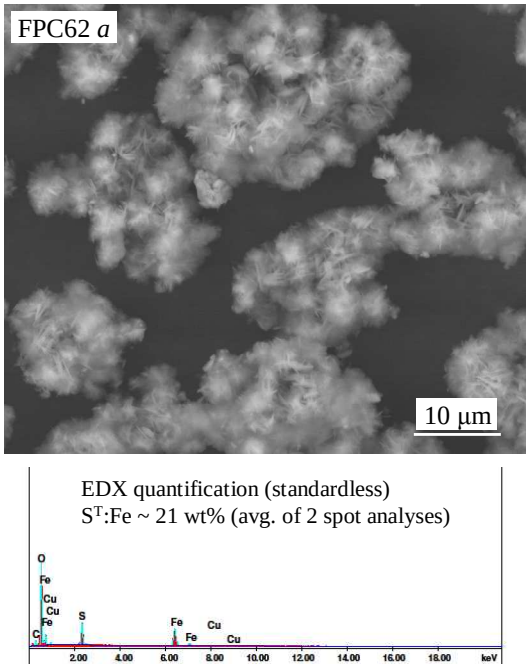

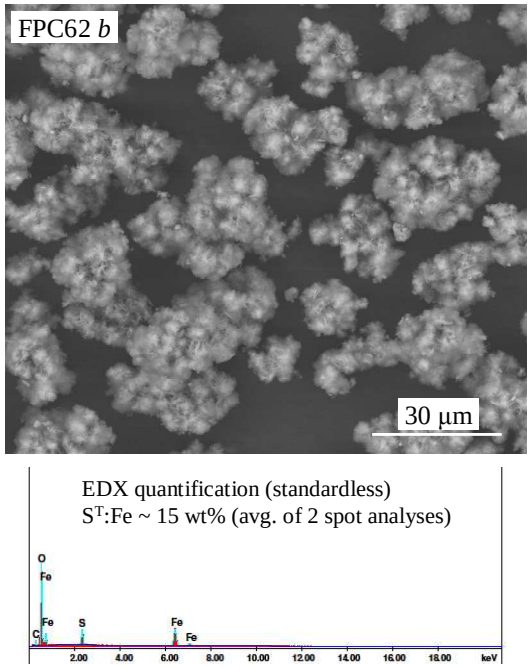

Stellenbosch University http://scholar.sun.ac.za

E.5 Iron(III) precipitation at 150°C (1000 kPa p_{O_2}°) in the high acid (> 15 g/L H_2SO_4) and high iron(II) (> 7.5 g/L Fe) concentration regimes in copper sulfate background

The fourth series of tests focused on determining the particle morphology and size and the precipitation rate in the H_2SO_4-$CuSO_4$ system, using higher initial acid (20-30 g/L) and iron(II) (9-15 g/L) concentrations. All these tests were conducted at the baseline temperature of 150ºC and, again, using the relatively high oxygen partial pressure of 1000 kPa p_{O_2}°. Only iron(II) sulfate was pumped into the autoclave ('at temperature'), with all the other reagents added upfront. In terms of the overall mass balance, these tests may be considered more accurate because larger volumes were added, *i.e.*, the percentage error due to the normal pump volume 'variation' was smaller. Under these conditions, hydronium jarosite growth is most prevalent (see below).

FPD1	Temp.	Imp. speed	Sln. pumped	Sln. mass	P_g	p_{O_2}°
2-litre AC (A)	150ºC	1000 rev/min	Fe(II)	1200 g	1391 kPa	1000 kPa
FEED	[a] H_2O	$[H_2SO_4]$	[Cu]	[Fe(II)]	[b] [LS, QB]	[c] Density
D11 to D14	1103.9 g	20 g/L	15 g/L	10 g/L	0.05 g/L ea.	1075 g/L
FINAL	[d] Slurry	Filtrate	Solids (meas)	[e] Solids (calc)	[f] H_2O (evap)	[c] Density
min (test)	(g)	(g)	(g dry) (g wet)	(g dry)	(g)	(g/L)
10 (D11)	70.5	1069.0	0.8 (2.6)	0.9	57.9	1078
15 (D12)	70.2	1056.4	2.5 (4.8)	2.6	68.1	1079
20 (D13)	70.3	1027.5	3.5 (5.6)	3.7	96.6	1077
25 (D14)	70.4	1010.0	5.7 (9.2)	6.1	110.5	1080
Filtrate	$[H_2O]$	$[H_2SO_4]$	[Cu]	$[Fe(II)]\cdot10^2$	$[Fe(III)]\cdot10^2$	$[SO_4^{2-}]^{calc.}$
min (test)	(g/L)	(mol/kg)	(mol/kg)	(mol/kg)	(mol/kg)	(mol/kg)
10 (D11)	939.2	0.1215	0.267	0.52	18.19	0.666
15 (D12)	934.0	0.143	0.280	0.38	18.21	0.701
20 (D13)	934.2	0.138	0.279	0.31	17.45	0.682
25 (D14)	933.7	0.165	0.282	0.26	17.51	0.712
Residue	$X_{p,Fe}$	$W_{f,Hem}$	[g] Cu	[g] Fe	[h] S^T:Fe	[g] S^T
min (test)	(%)	(%)	(%)	(%)	(%)	(%)
10 (D11)	2	11	0.14 (106)	35.6 (101)	31.5 (30)	11.2 (101)
15 (D12)	4	9	0.15 (110)	36.3 (105)	32.5 (31)	11.8 (106)
20 (D13)	10.5	8	0.15 (107)	35.9 (101)	33.1 (33)	11.9 (101)
25 (D14)	12	6	0.24 (106)	35.5 (108)	34.6 (39)	12.3 (106)

[a] Incl. H_2O in reagents; [b] Arbo A02, Orfom 2 (no pre-drying); [c] Sln. dens.(20ºC); [d] Remaining (not filtered); [e] Total dry mass calc. from solid:slurry wt. ratio & final mass (incl. flashed H_2O); [f] Based on total mass loss; [g] Accountability in brackets; [h] S^T:Fe wt. ratio (avg. ratio from EDX spot analyses in brackets).

Stellenbosch University http://scholar.sun.ac.za

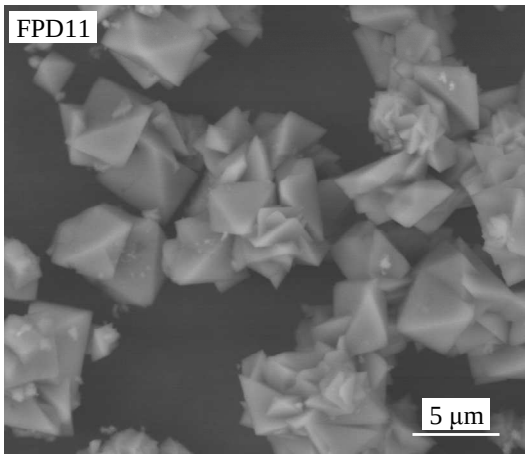

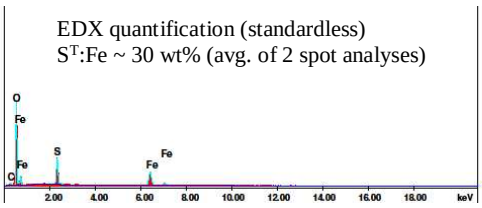

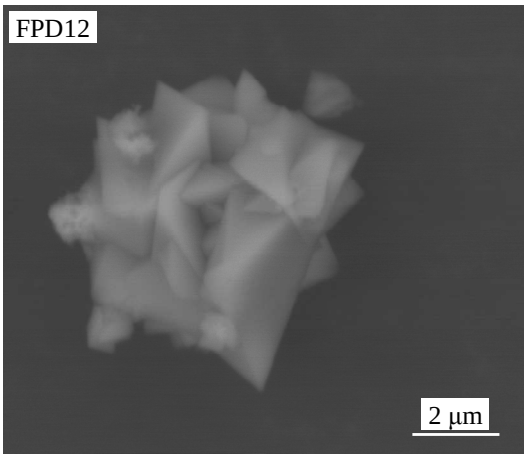

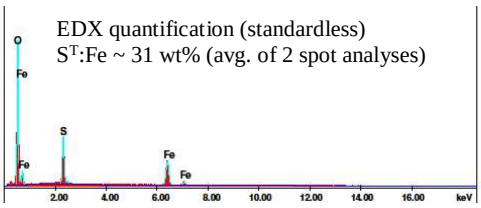

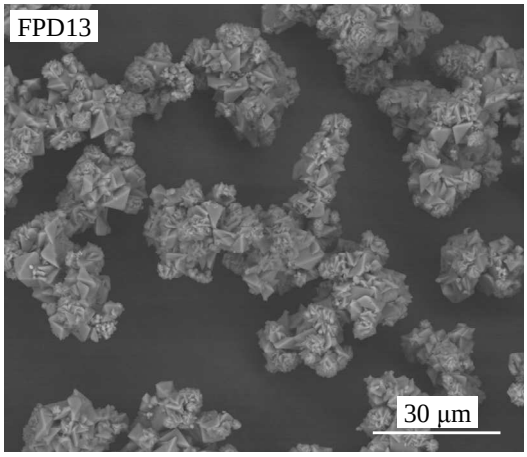

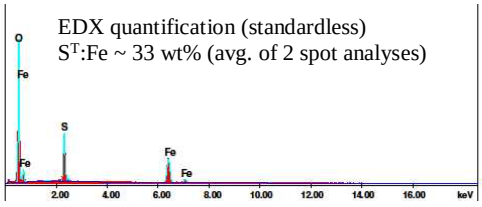

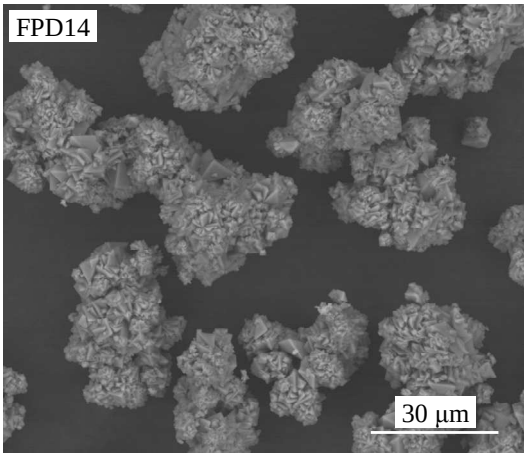

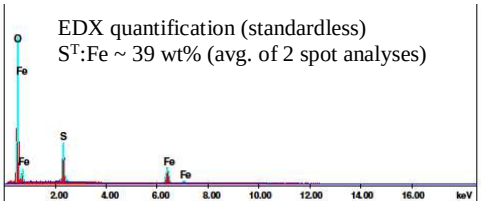

Stellenbosch University http://scholar.sun.ac.za

FPD2	Temp.	Imp. speed	Sln. pumped	Sln. mass	P_g	$p_{O2}°$
2-litre AC (A)	150ºC	1000 rev/min	Fe(II)	1200 g	1391 kPa	1000 kPa
FEED	[a] H_2O	$[H_2SO_4]$	[Cu]	[Fe(II)]	[b] [LS, QB]	[c] Density
D21 to D24	1106.6 g	20 g/L	15 g/L	9 g/L	0.05 g/L ea.	1070 g/L
FINAL	[d] Slurry	Filtrate	Solids (meas)	[e] Solids (calc)	[f] H_2O (evap)	[c] Density
min (test)	(g)	(g)	(g dry) (g wet)	(g dry)	(g)	(g/L)
15 (D21)	60.3	1101.5	1.4 (3.9)	1.4	34.3	1075
20 (D22)	67.3	1087.0	2.5 (5.5)	2.6	40.1	1077
25 (D23)	174.9	934.3	2.7 (6.0)	3.2	84.8	1075
30 (D24)	65.3	1084.3	3.3 (6.7)	3.5	43.7	1078
Filtrate	$[H_2O]$	$[H_2SO_4]$	[Cu]	$[Fe(II)]\cdot10^2$	$[Fe(III)]\cdot10^2$	$[SO_4^{2-}]^{calc.}$
min (test)	(g/L)	(mol/kg)	(mol/kg)	(mol/kg)	(mol/kg)	(mol/kg)
15 (D21)	935.8	0.143	0.276	0.38	15.19	0.651
20 (D22)	939.5	0.153	0.268	0.31	15.25	0.653
25 (D23)	932.8	0.1595	0.280	0.30	15.40	0.674
30 (D24)	937.9	0.159	0.276	0.20	14.64	0.657
Residue	$X_{p,Fe}$	$W_{f,Hem}$	[g] Cu	[g] Fe	[h] S^T:Fe	[g] S^T
min (test)	(%)	(%)	(%)	(%)	(%)	(%)
15 (D21)	8	17	0.18 (112)	37.2 (98)	28.2 (33)	10.5 (104)
20 (D22)	8	15	0.27 (108)	37.4(102)	29.1 (32)	10.9 (105)
25 (D23)	11	14	0.19 (108)	36.4 (100)	29.7 (31)	10.8 (104)
30 (D24)	13	21	0.29 (111)	38.6 (101)	25.9 (28)	10.0 (105)

[a] Incl. H_2O in reagents; [b] Arbo A02, Orfom 2 (no pre-drying); [c] Sln. dens.(20ºC); [d] Remaining (not filtered); [e] Total dry mass calc. from solid:slurry wt. ratio & final mass (incl. flashed H_2O); [f] Based on total mass loss; [g] Accountability in brackets; [h] S^T:Fe wt. ratio (avg. ratio from EDX spot analyses in brackets).

Stellenbosch University http://scholar.sun.ac.za

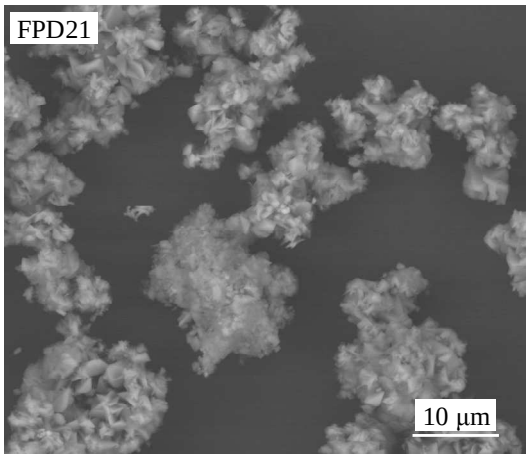

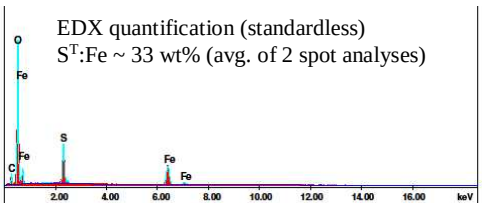

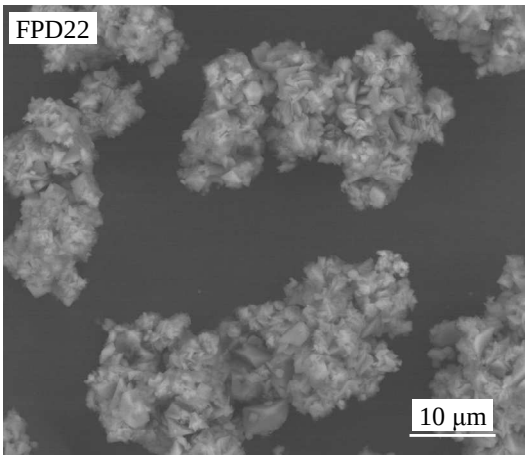

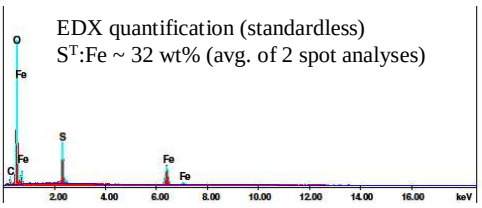

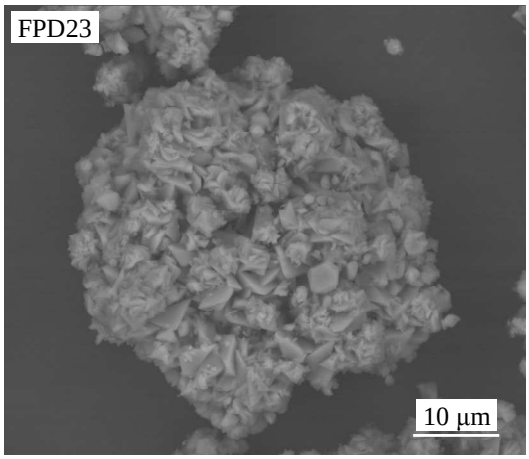

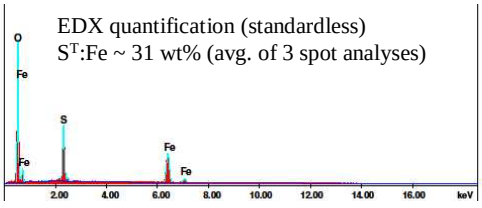

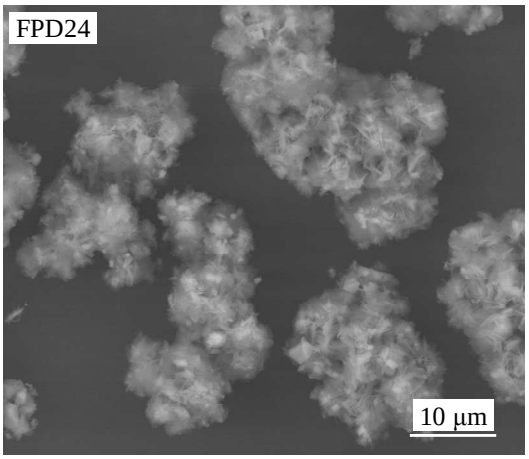

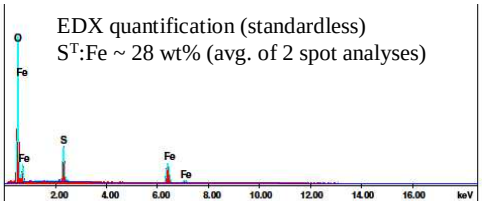

Stellenbosch University http://scholar.sun.ac.za

FPD3	Temp.	Imp. speed	Sln. pumped	Sln. mass	P_g	p_{O2}°
2-litre AC (A)	150ºC	1000 rev/min	Fe(II)	1200 g	1391 kPa	1000 kPa
FEED	[a] H_2O	$[H_2SO_4]$	[Cu]	[Fe(II)]	[b] [LS, QB]	[c] Density
D31 to D33	1084.5 g	25 g/L	15 g/L	15 g/L	0.05 g/L ea.	1090 g/L
FINAL	[d] Slurry	Filtrate	Solids (meas)	[e] Solids (calc)	[f] H_2O (evap)	[c] Density
min (test)	(g)	(g)	(g dry) (g wet)	(g dry)	(g)	(g/L)
10 (D31)	64.5	1086.4	3.1 (6.5)	3.3	42.6	1092
20 (D32)	70.2	1074.2	6.9 (11.2)	7.3	43.9	1094
30 (D33)	64.2	1072.7	9.4 (15.5)	10.0	47.7	1095
Filtrate	$[H_2O]$	$[H_2SO_4]$	[Cu]	$[Fe(II)]\cdot10^2$	$[Fe(III)]\cdot10^2$	$[SO_4^{2-}]^{calc.}$
min (test)	(g/L)	(mol/kg)	(mol/kg)	(mol/kg)	(mol/kg)	(mol/kg)
10 (D31)	945.7	0.152	0.254	0.76	24.03	0.774
20 (D32)	944.4	0.184	0.268	0.42	20.97	0.771
30 (D33)	950.5	0.193	0.254	0.29	20.06	0.751
Residue	$X_{p,Fe}$	$W_{f,Hem}$	[g] Cu	[g] Fe	[h] S^T:Fe	[g] S^T
min (test)	(%)	(%)	(%)	(%)	(%)	(%)
10 (D31)	13	5	0.10 (102)	35.4 (94)	34.7 (36)	12.3 (98)
20 (D32)	25	6	0.06 (107)	35.6 (91)	34.6 (36)	12.3 (99)
30 (D33)	29	8.5	0.09 (101)	35.4 (93)	32.8 (31)	11.6 (97)

[a] Incl. H_2O in reagents; [b] Arbo A02, Orfom 2 (no pre-drying); [c] Sln. dens.(20ºC); [d] Remaining (not filtered); [e] Total dry mass calc. from solid:slurry wt. ratio & final mass (incl. flashed H_2O); [f] Based on total mass loss; [g] Accountability in brackets; [h] S^T:Fe wt. ratio (avg. ratio from EDX spot analyses in brackets).

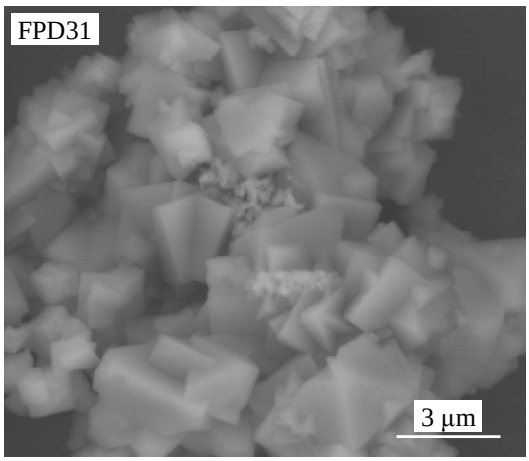

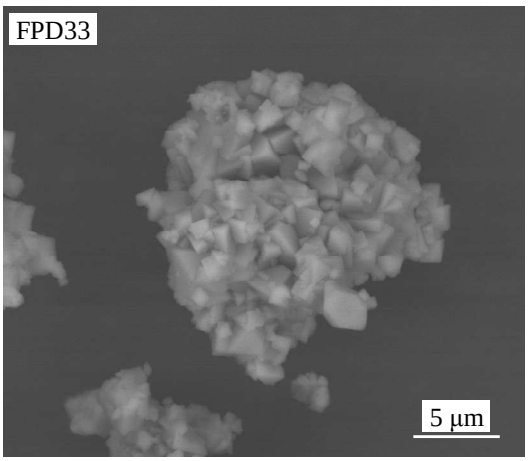

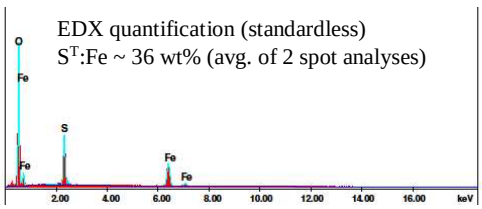

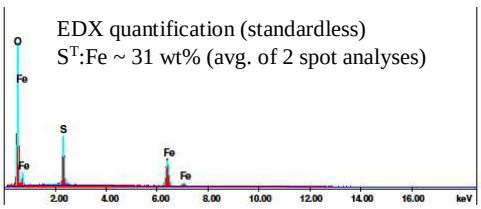

Stellenbosch University http://scholar.sun.ac.za

FPD4	Temp.	Imp. speed	Sln. pumped	Sln. mass	P_g	p_{O2}°
2-litre AC (A)	150ºC	1000 rev/min	Fe(II)	1200 g	1391 kPa	1000 kPa
FEED	[a] H_2O	$[H_2SO_4]$	[Cu]	[Fe(II)]	[b] [LS, QB]	[c] Density
D41 to D43	1093.0 g	25 g/L	15 g/L	12 g/L	0.05 g/L ea.	1084 g/L
FINAL	[d] Slurry	Filtrate	Solids (meas)	[e] Solids (calc)	[f] H_2O (evap)	[c] Density
min (test)	(g)	(g)	(g dry) (g wet)	(g dry)	(g)	(g/L)
30 (D41)	68.2	1073.4	0.9 (2.3)	1.0	56.0	1089
45 (D42)	69.3	1088.1	3.3 (5.8)	3.5	36.8	1090
60 (D43)	66.8	1072.4	5.7 (8.4)	6.0	51.5	1090
Filtrate	$[H_2O]$	$[H_2SO_4]$	[Cu]	$[Fe(II)]\cdot10^2$	$[Fe(III)]\cdot10^2$	$[SO_4^{2-}]^{calc.}$
min (test)	(g/L)	(mol/kg)	(mol/kg)	(mol/kg)	(mol/kg)	(mol/kg)
30 (D41)	941.4	0.174	0.267	0.26	20.93	0.758
45 (D42)	940.9	0.179	0.273	0.20	20.11	0.756
60 (D43)	944.3	0.200	0.2655	0.16	18.14	0.739
Residue	$X_{p,Fe}$	$W_{f,Hem}$	[g] Cu	[g] Fe	[h] S^T:Fe	[g] S^T
min (test)	(%)	(%)	(%)	(%)	(%)	(%)
30 (D41)	8	13.5	0.14 (106)	36.8 (95)	29.9 (31)	11.0 (101)
45 (D42)	10	5	0.10 (110)	36.0 (100)	35.0 (35)	12.6 (104)
60 (D43)	20	8	0.15 (106)	35.7 (96)	33.3 (32)	11.9 (101)

[a] Incl. H_2O in reagents; [b] Arbo A02, Orfom 2 (no pre-drying); [c] Sln. dens.(20ºC); [d] Remaining (not filtered); [e] Total dry mass calc. from solid:slurry wt. ratio & final mass (incl. flashed H_2O); [f] Based on total mass loss; [g] Accountability in brackets; [h] S^T:Fe wt. ratio (avg. ratio from EDX spot analyses in brackets).

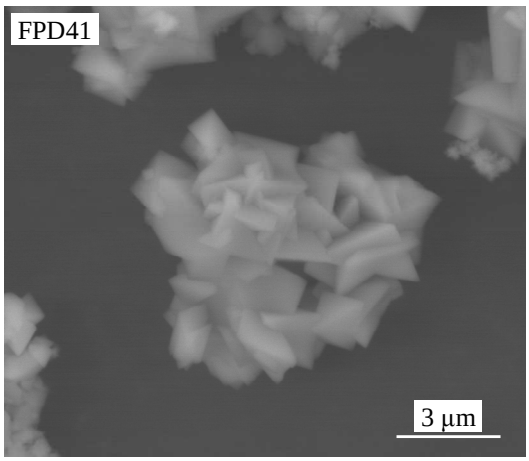

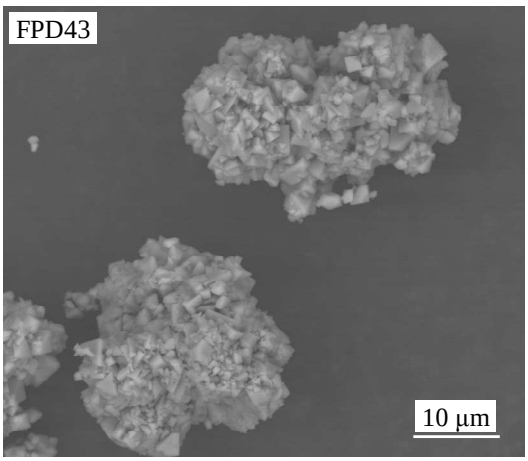

Stellenbosch University http://scholar.sun.ac.za

FPD5	Temp.	Imp. speed	Sln. pumped	Sln. mass	P_g	p_{O2}°
2-litre AC (A)	150ºC	1000 rev/min	Fe(II)	1200 g	1391 kPa	1000 kPa
FEED	[a] H_2O	$[H_2SO_4]$	[Cu]	[Fe(II)]	[b] [LS, QB]	[c] Density
D51 to D52	1079.2 g	30 g/L	15 g/L	15 g/L	0.05 g/L ea.	1092 g/L
FINAL	[d] Slurry	Filtrate	Solids (meas)	[e] Solids (calc)	[f] H_2O (evap)	[c] Density
min (test)	(g)	(g)	(g dry) (g wet)	(g dry)	(g)	(g/L)
45 (D51)	89.2	1036.0	2.8 (7.2)	3.0	67.6	1096
60 (D52)	70.7	1108.5	3.7 (4.7)	4.0	16.2	1097
Filtrate	$[H_2O]$	$[H_2SO_4]$	[Cu]	$[Fe(II)]\cdot10^2$	$[Fe(III)]\cdot10^2$	$[SO_4^{2-}]^{calc.}$
min (test)	(g/L)	(mol/kg)	(mol/kg)	(mol/kg)	(mol/kg)	(mol/kg)
45 (D51)	935.8	0.212	0.275	0.25	25.99	0.879
60 (D52)	943.2	0.210	0.264	0.19	23.68	0.831
Residue	$X_{p,Fe}$	$W_{f,Hem}$	[g] Cu	[g] Fe	[h] S^T:Fe	[g] S^T
min (test)	(%)	(%)	(%)	(%)	(%)	(%)
45 (D51)	10	9	0.07 (107)	36.4 (97)	32.7 (32)	11.9 (101)
60 (D52)	14	8	0.06 (108)	35.5 (94)	33.2 (36)	11.8 (101)

[a] Incl. H_2O in reagents; [b] Arbo A02, Orfom 2 (no pre-drying); [c] Sln. dens.(20ºC); [d] Remaining (not filtered); [e] Total dry mass calc. from solid:slurry wt. ratio & final mass (incl. flashed H_2O); [f] Based on total mass loss; [g] Accountability in brackets; [h] S^T:Fe wt. ratio (avg. ratio from EDX spot analyses in brackets).

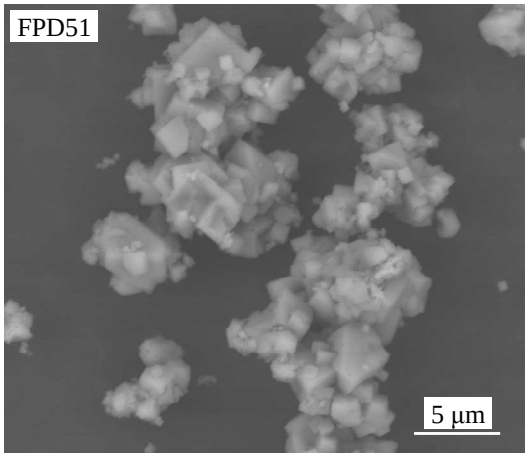

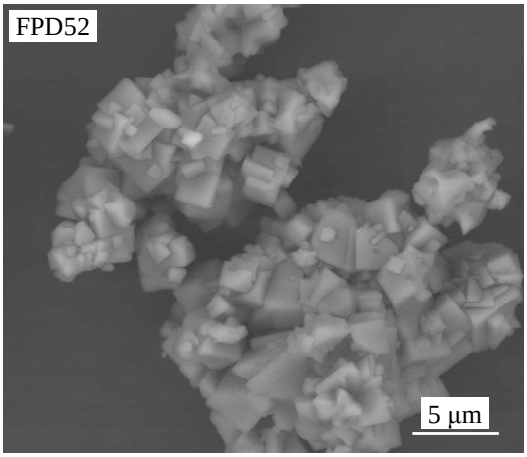

Stellenbosch University http://scholar.sun.ac.za

E.6 Hematite precipitation at 140°C (1000 kPa p_{O2}°) in the medium-high acid (7.5-20 g/L H_2SO_4) and iron(II) (5-10 g/L) concentration regimes in copper sulfate background

The fifth series of tests focused on comparing the particle morphology and size and the precipitation rate in the H_2SO_4-$CuSO_4$ system at 140ºC, again using the relatively high oxygen partial pressure of 1000 kPa p_{O2}°. Besides the impact of different iron(III) supersaturation levels, this test series also tried to identify possible surface interactions between the different precipitate phases. The initial acidity levels were limited to the medium-high (7.5-20 g/L H_2SO_4) concentration range to decrease the rate of hydronium jarosite precipitation, *i.e.*, to prevent it from dominating the overall precipitation kinetics. The iron(II) concentration was progressively increased within the 5 to 10 g/L range. It was pumped into the autoclave 'at temperature', while all the other reagents were added upfront.

FPE1	Temp.	Imp. speed	Sln. pumped	Sln. mass	P_g	p_{O2}°
2-litre AC (A)	140ºC	1000 rev/min	Fe(II)	1200 g	1276 kPa	1000 kPa
FEED	[a] H_2O	$[H_2SO_4]$	[Cu]	[Fe(II)]	[b] [LS, QB]	[c] Density
E11 to E13	1131.9 g	7.5 g/L	15 g/L	5 g/L	0.05 g/L ea.	1052 g/L
FINAL	[d] Slurry	Filtrate	Solids (meas)	[e] Solids (calc)	[f] H_2O (evap)	[c] Density
min (test)	(g)	(g)	(g dry) (g wet)	(g dry)	(g)	(g/L)
10 (E11)	61.6	1084.4	3.3 (7.2)	3.5	46.8	1054
20 (E12)	67.7	1048.2	4.1 (7.7)	4.4	76.4	1054
30 (E13)	64.2	1070.2	6.2 (11.6)	6.6	54.0	1053
Filtrate	$[H_2O]$	$[H_2SO_4]$	[Cu]	$[Fe(II)]\cdot10^2$	$[Fe(III)]\cdot10^2$	$[SO_4^{2-}]^{calc.}$
min (test)	(g/L)	(mol/kg)	(mol/kg)	(mol/kg)	(mol/kg)	(mol/kg)
10 (E11)	940.1	0.079	0.258	0.32	5.99	0.430
20 (E12)	938.6	0.095	0.262	0.20	5.13	0.446
30 (E13)	939.3	0.1215	0.259	0.13	3.09	0.428
Residue	$X_{p,Fe}$	$W_{f,Hem}$	[g] Cu	[g] Fe	[h] S^T:Fe	[g] S^T
min (test)	(%)	(%)	(%)	(%)	(%)	(%)
10 (E11)	33	82	0.87 (104)	52.5 (99)	6.6 (7)	3.5 (103)
20 (E12)	45	74	1.57 (103)	49.8 (94)	8.7 (8)	4.3 (102)
30 (E13)	66	76	1.37 (104)	50.0 (92)	8.1 (9)	4.05 (102)

[a] Incl. H_2O in reagents; [b] Arbo A02, Orfom 2 (no pre-drying); [c] Sln. dens.(20ºC); [d] Remaining (not filtered); [e] Total dry mass calc. from solid:slurry wt. ratio & final mass (incl. flashed H_2O); [f] Based on total mass loss; [g] Accountability in brackets; [h] S^T:Fe wt. ratio (avg. ratio from EDX spot analyses in brackets).

Stellenbosch University http://scholar.sun.ac.za

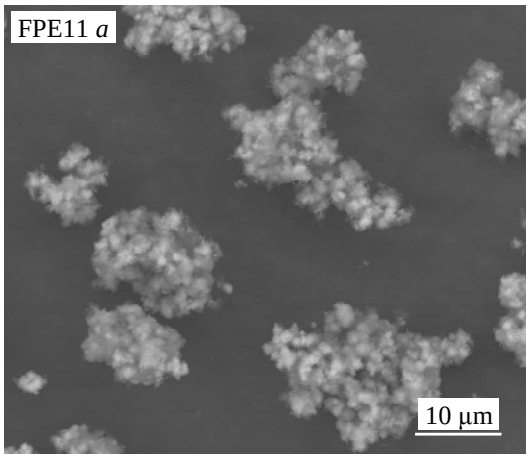

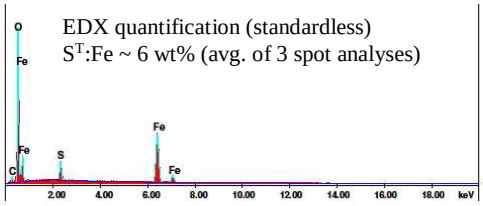

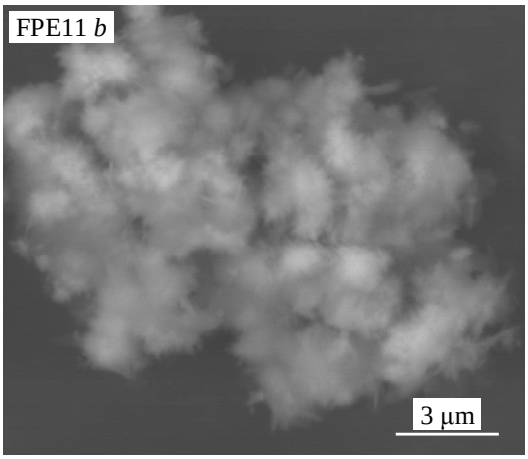

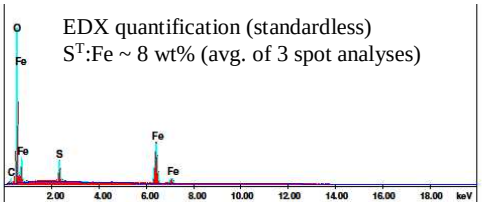

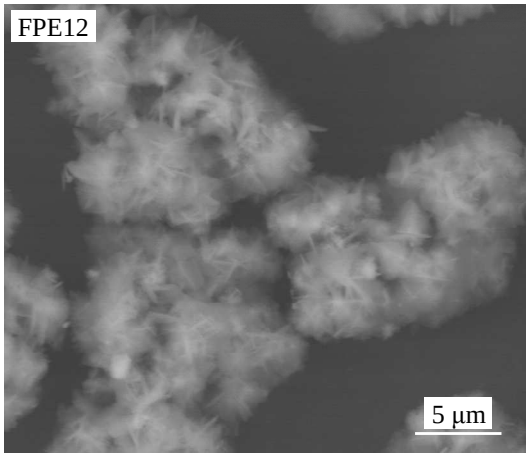

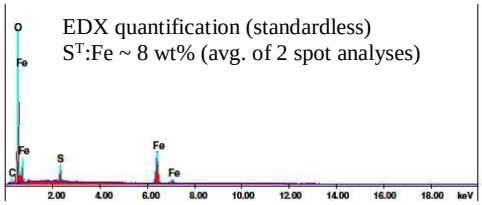

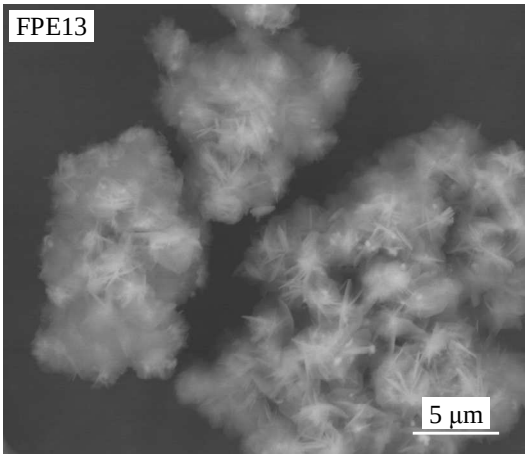

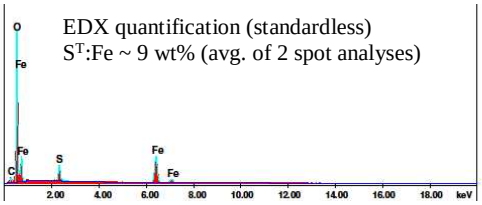

Stellenbosch University http://scholar.sun.ac.za

FPE2	Temp.	Imp. speed	Sln. pumped	Sln. mass	P_g	p_{O2}°
2-litre AC (A)	140ºC	1000 rev/min	Fe(II)	1200 g	1276 kPa	1000 kPa
FEED	[a] H_2O	$[H_2SO_4]$	[Cu]	[Fe(II)]	[b] [LS, QB]	[c] Density
E21 to E23	1124.8 g	12.5 g/L	15 g/L	5.5 g/L	0.05 g/L ea.	1055 g/L
FINAL	[d] Slurry	Filtrate	Solids (meas)	[e] Solids (calc)	[f] H_2O (evap)	[c] Density
min (test)	(g)	(g)	(g dry) (g wet)	(g dry)	(g)	(g/L)
10 (E21)	60.3	1098.3	0.7 (1.7)	0.8	39.6	1059
20 (E22)	62.4	1099.8	3.1 (7.6)	3.3	30.3	1059
30 (E23)	61.6	1096.4	3.4 (8.9)	3.6	33.2	1060
Filtrate	$[H_2O]$	$[H_2SO_4]$	[Cu]	$[Fe(II)]\cdot10^2$	$[Fe(III)]\cdot10^2$	$[SO_4^{2-}]^{calc.}$
min (test)	(g/L)	(mol/kg)	(mol/kg)	(mol/kg)	(mol/kg)	(mol/kg)
10 (E21)	939.0	0.090	0.259	0.29	9.51	0.494
20 (E22)	934.9	0.106	0.272	0.23	8.13	0.503
30 (E23)	939.1	0.1215	0.2635	0.14	6.91	0.490
Residue	$X_{p,Fe}$	$W_{f,Hem}$	[g] Cu	[g] Fe^T	[h] S/Fe	[g] S^T
min (test)	(%)	(%)	(%)	(%)	(%)	(%)
10 (E21)	5	62	1.00 (105)	45.0 (101)	11.5 (14)	5.2 (102)
20 (E22)	18	56.5	1.45 (111)	45.1 (105)	13.2 (15)	6.0 (106)
30 (E23)	31	57	0.97 (107)	45.8 (95)	12.9 (13)	5.9 (103)

[a] Incl. H_2O in reagents; [b] Arbo A02, Orfom 2 (no pre-drying); [c] Sln. dens.(20ºC); [d] Remaining (not filtered); [e] Total dry mass calc. from solid:slurry wt. ratio & final mass (incl. flashed H_2O); [f] Based on total mass loss; [g] Accountability in brackets; [h] S^T:Fe wt. ratio (avg. ratio from EDX spot analyses in brackets).

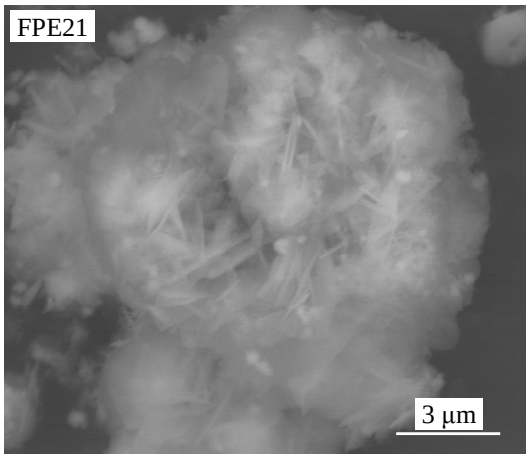

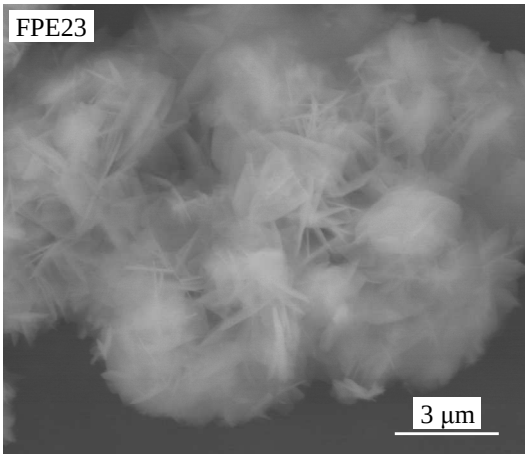

Stellenbosch University http://scholar.sun.ac.za

FPE3	Temp.	Imp. speed	Sln. pumped	Sln. mass	P_g	p_{O2}°
2-litre AC (A)	140ºC	1000 rev/min	Fe(II)	1200 g	1276 kPa	1000 kPa
FEED	[a] H_2O	$[H_2SO_4]$	[Cu]	[Fe(II)]	[b] [LS, QB]	[c] Density
E31 to E33	1119.0 g	15 g/L	15 g/L	6.5 g/L	0.05 g/L ea.	1058 g/L
FINAL	[d] Slurry	Filtrate	Solids (meas)	[e] Solids (calc)	[f] H_2O (evap)	[c] Density
min (test)	(g)	(g)	(g dry) (g wet)	(g dry)	(g)	(g/L)
20 (E31)	62.3	1094.7	1.0 (2.6)	1.1	40.4	1063
30 (E32)	61.4	1101.5	1.2 (3.2)	1.3	34.0	1062
40 (E33)	62.9	1098.9	3.5 (8.7)	3.7	29.6	1063
Filtrate	$[H_2O]$	$[H_2SO_4]$	[Cu]	$[Fe(II)]\cdot10^2$	$[Fe(III)]\cdot10^2$	$[SO_4^{2-}]^{calc}$
min (test)	(g/L)	(mol/kg)	(mol/kg)	(mol/kg)	(mol/kg)	(mol/kg)
20 (E31)	935.9	0.117	0.266	0.27	11.05	0.551
30 (E32)	932.5	0.117	0.276	0.22	10.39	0.551
40 (E33)	939.5	0.132	0.257	0.18	9.60	0.535
Residue	$X_{p,Fe}$	$W_{f,Hem}$	[g] Cu	[g] Fe	[h] S^T:Fe	[g] S^T
min (test)	(%)	(%)	(%)	(%)	(%)	(%)
20 (E31)	7.5	44	1.28 (107)	42.1 (99)	17.0 (16)	7.2 (104)
30 (E32)	13	40	0.87 (112)	42.3 (95)	18.2 (18)	7.7 (105)
40 (E33)	19	49	0.89 (105)	44.7 (103)	15.1 (15)	6.8 (103)

[a] Incl. H_2O in reagents; [b] Arbo A02, Orfom 2 (no pre-drying); [c] Sln. dens.(20ºC); [d] Remaining (not filtered); [e] Total dry mass calc. from solid:slurry wt. ratio & final mass (incl. flashed H_2O); [f] Based on total mass loss; [g] Accountability in brackets; [h] S^T:Fe wt. ratio (avg. ratio from EDX spot analyses in brackets).

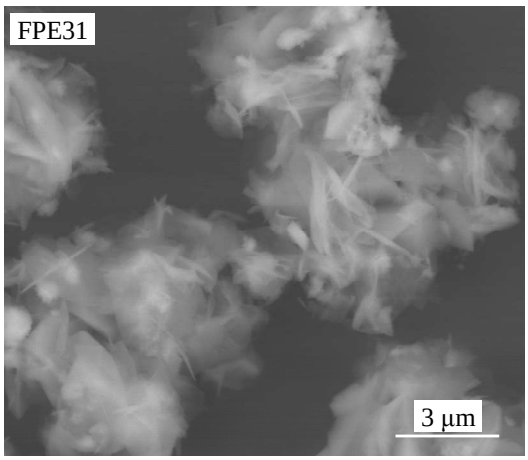

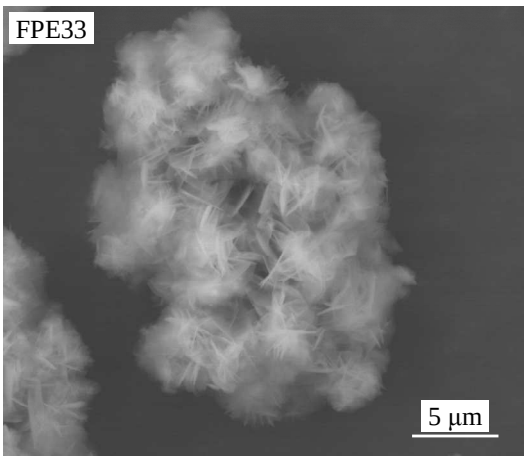

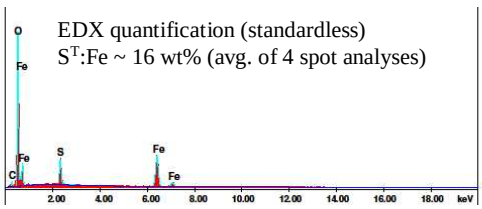

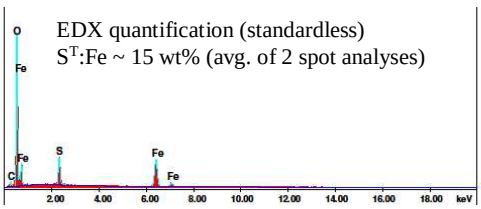

Stellenbosch University http://scholar.sun.ac.za

FPE4	Temp.	Imp. speed	Sln. pumped	Sln. mass	P_g	p_{O2}°
2-litre AC (A)	140ºC	1000 rev/min	Fe(II)	1200 g	1276 kPa	1000 kPa
FEED	[a] H_2O	$[H_2SO_4]$	[Cu]	[Fe(II)]	[b] [LS, QB]	[c] Density
E41 to E43	1116.2 g	15 g/L	15 g/L	7.5 g/L	0.05 g/L ea.	1062 g/L
FINAL	[d] Slurry	Filtrate	Solids [(meas)]	[e] Solids [(tot)]	[f] H_2O [(evap)]	[c] Density
min (test)	(g)	(g)	(g dry) (g wet)	(g dry)	(g)	(g/L)
20 (E41)	63.9	1095.5	2.0 (5.0)	2.1	35.6	1064
30 (E42)	65.6	1110.2	2.6 (4.5)	2.8	19.7	1066
40 (E43)	57.6	1103.4	3.3 (5.7)	3.5	33.3	1066
Filtrate	$[H_2O]$	$[H_2SO_4]$	[Cu]	$[Fe(II)]\cdot10^2$	$[Fe(III)]\cdot10^2$	$[SO_4^{2-}]^{calc.}$
min (test)	(g/L)	(mol/kg)	(mol/kg)	(mol/kg)	(mol/kg)	(mol/kg)
20 (E41)	937.7	0.106	0.260	0.33	12.51	0.557
30 (E42)	941.4	0.116	0.256	0.27	11.45	0.547
40 (E43)	939.3	0.127	0.262	0.18	10.86	0.554
Residue	$X_{p,Fe}$	$W_{f,Hem}$	[g] Cu	[g] Fe	[h] S^T:Fe	[g] S^T
min (test)	(%)	(%)	(%)	(%)	(%)	(%)
20 (E41)	9	28.5	0.62 (106)	39.9 (102)	22.8 (22)	9.1 (103)
30 (E42)	15	17	0.38 (105)	38.1 (97)	28.3 (23)	10.8 (103)
40 (E43)	21	25	0.70 (107)	42.9 (96)	24.2 (23)	10.4 (103)

[a] Incl. H_2O in reagents; [b] Arbo A02, Orfom 2 (no pre-drying); [c] Sln. dens.(20ºC); [d] Remaining (not filtered); [e] Total dry mass calc. from solid:slurry wt. ratio & final mass (incl. flashed H_2O); [f] Based on total mass loss; [g] Accountability in brackets; [h] S^T:Fe wt. ratio (avg. ratio from EDX spot analyses in brackets).

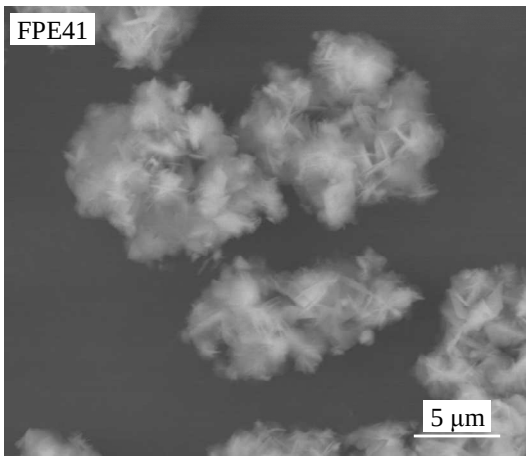

EDX quantification (standardless)
S^T:Fe ~ 22 wt% (avg. of 3 spot analyses)

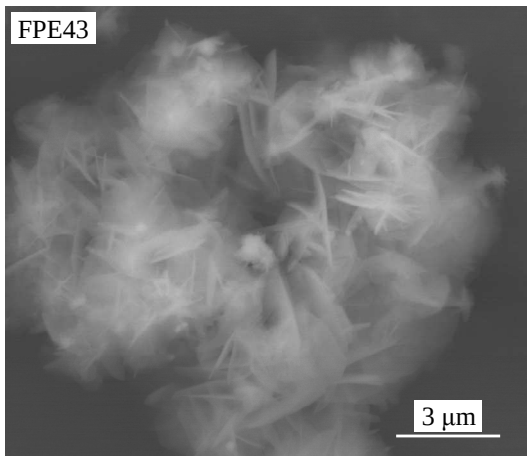

EDX quantification (standardless)
S^T:Fe ~ 23 wt% (avg. of 2 spot analyses)

Stellenbosch University http://scholar.sun.ac.za

FPE5	Temp.	Imp. speed	Sln. pumped	Sln. mass	P_g	p_{O2}°
2-litre AC (A)	140ºC	1000 rev/min	Fe(II)	1200 g	1276 kPa	1000 kPa
FEED	[a] H_2O	$[H_2SO_4]$	[Cu]	[Fe(II)]	[b] [LS, QB]	[c] Density
E51 to E52	1103.5 g	20 g/L	15 g/L	10 g/L	0.05 g/L ea.	1070 g/L
FINAL	[d] Slurry	Filtrate	Solids (meas)	[e] Solids (calc)	[f] H_2O (evap)	[c] Density
min (test)	(g)	(g)	(g dry) (g wet)	(g dry)	(g)	(g/L)
30 (E51)	62.7	1118.2	0.9 (1.8)	1.0	17.3	1075
45 (E52)	61.4	1102.7	3.0 (5.2)	3.2	30.8	1074
Filtrate	$[H_2O]$	$[H_2SO_4]$	[Cu]	$[Fe(II)]\cdot10^2$	$[Fe(III)]\cdot10^2$	$[SO_4^{2-}]^{calc.}$
min (test)	(g/L)	(mol/kg)	(mol/kg)	(mol/kg)	(mol/kg)	(mol/kg)
30 (E51)	940.2	0.127	0.258	0.34	17.56	0.651
45 (E52)	937.3	0.138	0.265	0.21	16.62	0.654
Residue	$X_{p,Fe}$	$W_{f,Hem}$	[g] Cu	[g] Fe	[h] S^T:Fe	[g] S^T
min (test)	(%)	(%)	(%)	(%)	(%)	(%)
30 (E51)	3	16.5	0.05 (106)	36.5 (100)	28.2 (27)	10.3 (102)
45 (E52)	10	14	0.10 (107)	36.0 (100)	29.4 (25)	10.6 (103)

[a] Incl. H_2O in reagents; [b] Arbo A02, Orfom 2 (no pre-drying); [c] Sln. dens.(20ºC); [d] Remaining (not filtered); [e] Total dry mass calc. from solid:slurry wt. ratio & final mass (incl. flashed H_2O); [f] Based on total mass loss; [g] Accountability in brackets; [h] S^T:Fe wt. ratio (avg. ratio from EDX spot analyses in brackets).

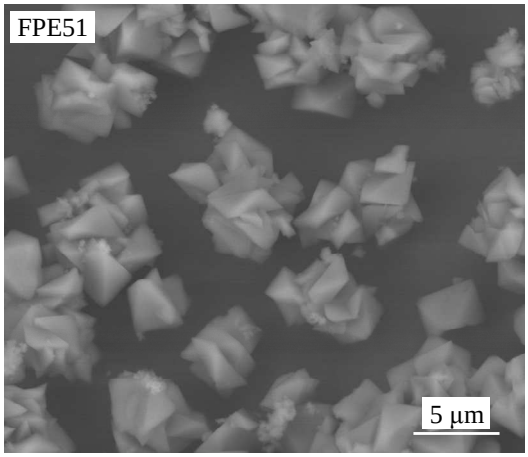

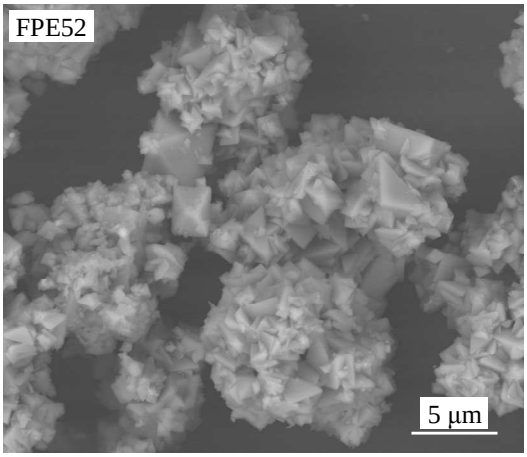

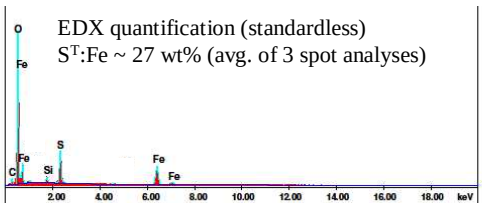

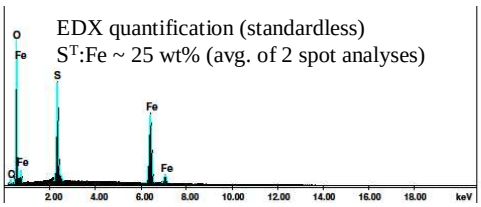

Stellenbosch University http://scholar.sun.ac.za

E.7 Hematite precipitation at 130°C (1000 kPa p_{O2}°) in the low-medium acid (4-12.5 g/L H_2SO_4) and low iron(II) (3.5-5.5 g/L Fe) concentration regimes in copper sulfate background

The final series of tests focused on comparing the particle morphology and size and the precipitation rate in the H_2SO_4-$CuSO_4$ system at 130ºC, again using the relatively high oxygen partial pressure of 1000 kPa p_{O2}°. Besides the impact of different iron(III) supersaturation levels, this test series also aimed to identify possible surface interactions between the different precipitate phases. The initial acidity levels were limited to the low-medium (4-12.5 g/L H_2SO_4) concentration range to decrease the rate of hydronium jarosite precipitation rate. The iron(II) concentration was progressively increased within the 3.5 to 5.5 g/L range. It was pumped into the autoclave 'at temperature', while all the other reagents were added upfront.

FPF1	Temp.	Imp. speed	Sln. pumped	Sln. mass	P_g	p_{O2}°
2-litre AC (A)	130ºC	1000 rev/min	Fe(II)	1200 g	1185 kPa	1000 kPa
FEED	[a] H_2O	$[H_2SO_4]$	[Cu]	[Fe(II)]	[b] [LS, QB]	[c] Density
F11 to F13	1140.2 g	4 g/L	15 g/L	3.5 g/L	0.05 g/L ea.	1045 g/L
FINAL	[d] Slurry	Filtrate	Solids (meas)	[e] Solids (calc)	[f] H_2O (evap)	[c] Density
min (test)	(g)	(g)	(g dry) (g wet)	(g dry)	(g)	(g/L)
15 (F11)	56.8	1111.4	3.6 (8.8)	3.8	23.0	1048
30 (F12)	90.5	1011.0	3.6 (7.5)	4.0	91.0	1047
45 (F13)	89.7	1060.7	4.5 (10.7)	4.9	38.9	1047
Filtrate	$[H_2O]$	$[H_2SO_4]$	[Cu]	$[Fe(II)]\cdot10^2$	$[Fe(III)]\cdot10^2$	$[SO_4^{2-}]^{calc.}$
min (test)	(g/L)	(mol/kg)	(mol/kg)	(mol/kg)	(mol/kg)	(mol/kg)
15 (F11)	941.7	0.063	0.254	0.23	2.80	0.361
30 (F12)	936.8	0.074	0.265	0.11	2.44	0.376
45 (F13)	940.3	0.084	0.255	0.11	1.61	0.364
Residue	$X_{p,Fe}$	$W_{f,Hem}$	[g] Cu	[g] Fe	[h] S^T:Fe	[g] S^T
min (test)	(%)	(%)	(%)	(%)	(%)	(%)
15 (F11)	53	81	2.43 (105)	48.8 (93)	7.4 (8)	3.6 (105)
30 (F12)	63	88	0.99 (103)	52.8 (89)	5.5 (6)	2.9 (102)
45 (F13)	74	88	2.27 (104)	47.6 (84)	5.9 (6)	2.8 (104)

[a] Incl. H_2O in reagents; [b] Arbo A02, Orfom 2 (no pre-drying); [c] Sln. dens.(20ºC); [d] Remaining (not filtered); [e] Total dry mass calc. from solid:slurry wt. ratio & final mass (incl. flashed H_2O); [f] Based on total mass loss; [g] Accountability in brackets; [h] S^T:Fe wt. ratio (avg. ratio from EDX spot analyses in brackets).

Stellenbosch University http://scholar.sun.ac.za

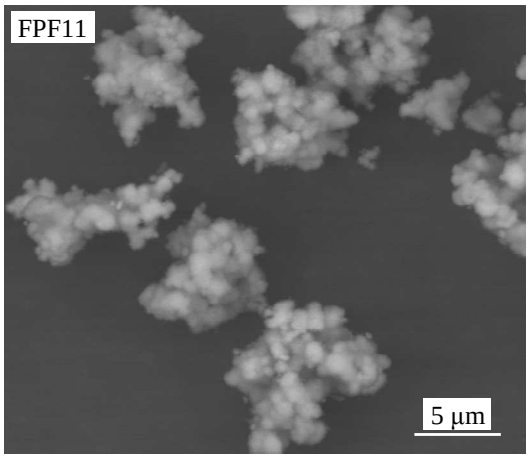

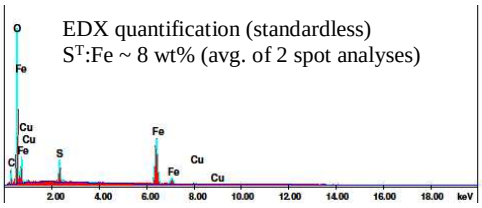

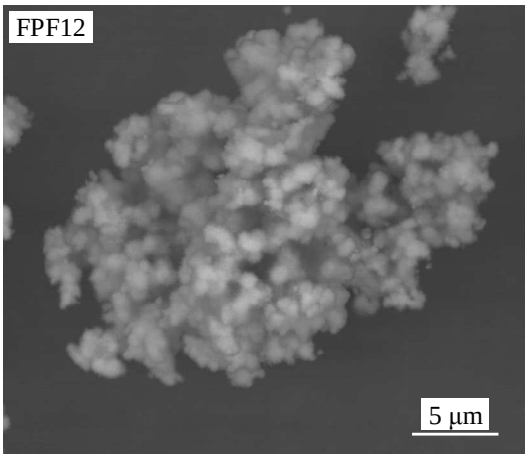

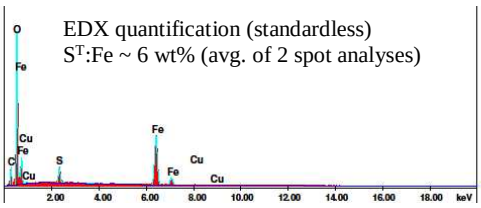

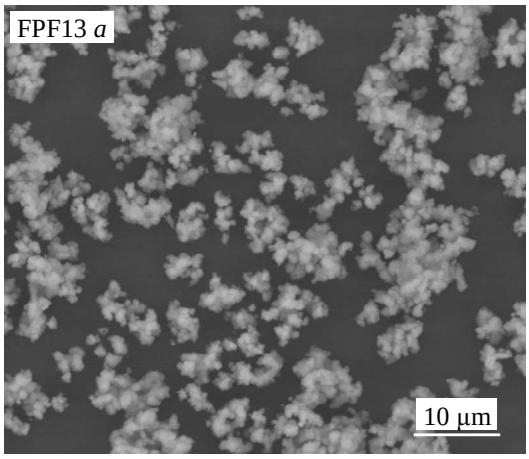

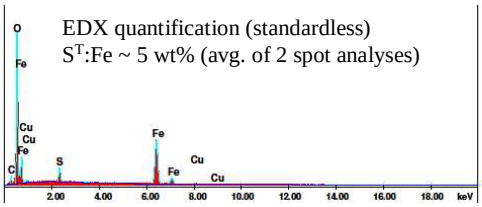

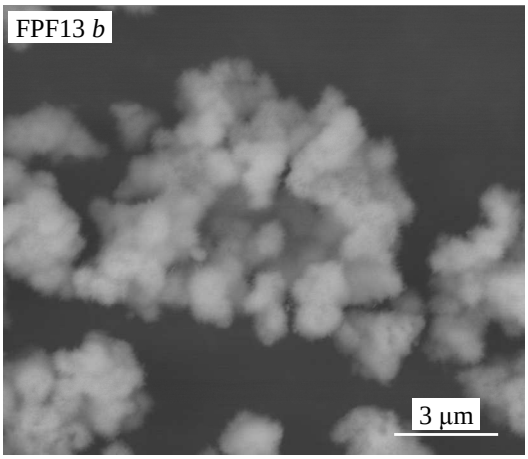

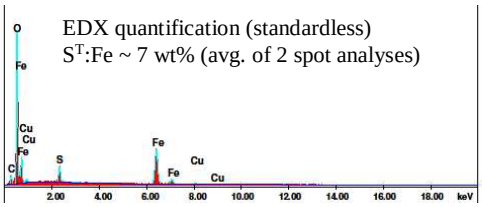

Stellenbosch University http://scholar.sun.ac.za

FPF2	Temp.	Imp. speed	Sln. pumped	Sln. mass	P_g	p_{O2}°
2-litre AC (A)	130ºC	1000 rev/min	Fe(II)	1200 g	1185 kPa	1000 kPa
FEED	[a] H_2O	$[H_2SO_4]$	[Cu]	[Fe(II)]	[b] [LS, QB]	[c] Density
F21 to F23	1132.3 g	8.5 g/L	15 g/L	4.5 g/L	0.05 g/L ea.	1051 g/L
FINAL	[d] Slurry	Filtrate	Solids (meas)	[e] Solids (calc)	[f] H_2O (evap)	[c] Density
min (test)	(g)	(g)	(g dry) (g wet)	(g dry)	(g)	(g/L)
20 (F21)	57.1	1127.3	1.4 (4.0)	1.4	11.6	1056
40 (F22)	60.3	1101.8	3.2 (7.9)	3.4	30.0	1055
60 (F23)	60.7	1110.0	3.8 (8.7)	4.0	20.6	1054
Filtrate	$[H_2O]$	$[H_2SO_4]$	[Cu]	$[Fe(II)]\cdot10^2$	$[Fe(III)]\cdot10^2$	$[SO_4^{2-}]^{calc.}$
min (test)	(g/L)	(mol/kg)	(mol/kg)	(mol/kg)	(mol/kg)	(mol/kg)
20 (F21)	941.7	0.063	0.257	0.29	7.41	0.434
40 (F22)	943.5	0.084	0.252	0.19	5.39	0.419
60 (F23)	942.9	0.100	0.252	0.14	4.27	0.417
Residue	$X_{p,Fe}$	$W_{f,Hem}$	[g] Cu	[g] Fe	[h] S^T:Fe	[g] S^T
min (test)	(%)	(%)	(%)	(%)	(%)	(%)
20 (F21)	6	66	1.11 (107)	46.3 (107)	10.6 (12)	4.9 (106)
40 (F22)	33	67	0.91(103)	47.5 (98)	10.1 (12)	4.8 (101)
60 (F23)	47	63	1.12 (104)	45.1 (88)	11.2 (11)	5.05 (102)

[a] Incl. H_2O in reagents; [b] Arbo A02, Orfom 2 (no pre-drying); [c] Sln. dens.(20ºC); [d] Remaining (not filtered); [e] Total dry mass calc. from solid:slurry wt. ratio & final mass (incl. flashed H_2O); [f] Based on total mass loss; [g] Accountability in brackets; [h] S^T:Fe wt. ratio (avg. ratio from EDX spot analyses in brackets).

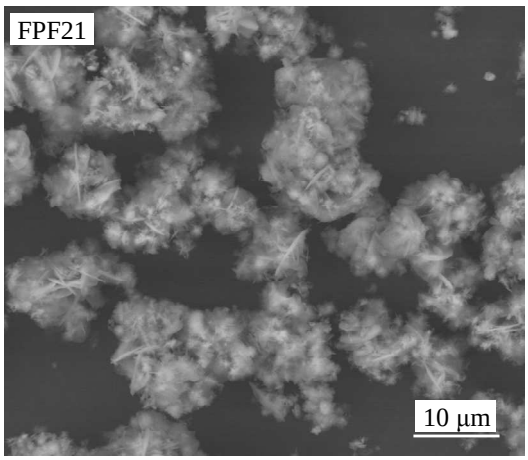

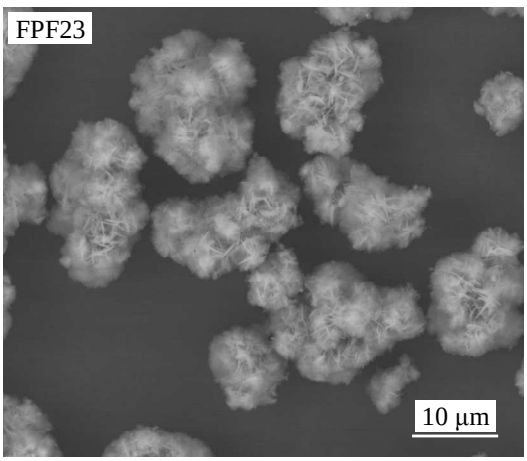

Stellenbosch University http://scholar.sun.ac.za

FPF3	Temp.	Imp. speed	Sln. pumped	Sln. mass	P_g	p_{O2}°
2-litre AC (A)	130ºC	1000 rev/min	Fe(II)	1200 g	1185 kPa	1000 kPa
FEED	[a] H_2O	$[H_2SO_4]$	[Cu]	[Fe(II)]	[b] [LS, QB]	[c] Density
F31 to F33	1124.8 g	12.5 g/L	15 g/L	5.5 g/L	0.05 g/L ea.	1055 g/L
FINAL	[d] Slurry	Filtrate	Solids (meas)	[e] Solids (calc)	[f] H_2O (evap)	[c] Density
min (test)	(g)	(g)	(g dry) (g wet)	(g dry)	(g)	(g/L)
30 (F31)	62.7	1052.4	0.9 (1.8)	1.0	83.1	1059
45 (F32)	60.4	1116.5	1.3 (3.5)	1.4	19.6	1058
60 (F33)	60.9	1105.1	2.5 (6.2)	2.6	27.8	1058
Filtrate	$[H_2O]$	$[H_2SO_4]$	[Cu]	$[Fe(II)]\cdot10^2$	$[Fe(III)]\cdot10^2$	$[SO_4^{2-}]^{calc.}$
min (test)	(g/L)	(mol/kg)	(mol/kg)	(mol/kg)	(mol/kg)	(mol/kg)
30 (F31)	931.6	0.101	0.278	0.26	9.57	0.525
45 (F32)	939.1	0.095	0.256	0.22	9.06	0.489
60 (F33)	940.4	0.111	0.2525	0.19	8.07	0.486
Residue	$X_{p,Fe}$	$W_{f,Hem}$	[g] Cu	[g] Fe	[h] S^T:Fe	[g] S^T
min (test)	(%)	(%)	(%)	(%)	(%)	(%)
30 (F31)	9	55	1.00 (108)	44.7 (98)	13.6 (15)	6.1 (104)
45 (F32)	8.5	43	0.93(106)	42.3 (101)	17.2 (19)	7.3 (104)
60 (F33)	19	52	0.73 (103)	43.7 (99)	14.4 (14)	6.3 (102)

[a] Incl. H_2O in reagents; [b] Arbo A02, Orfom 2 (no pre-drying); [c] Sln. dens.(20ºC); [d] Remaining (not filtered); [e] Total dry mass calc. from solid:slurry wt. ratio & final mass (incl. flashed H_2O); [f] Based on total mass loss; [g] Accountability in brackets; [h] S^T:Fe wt. ratio (avg. ratio from EDX spot analyses in brackets).

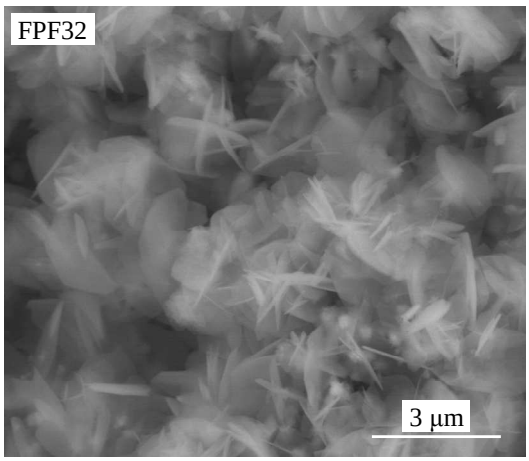

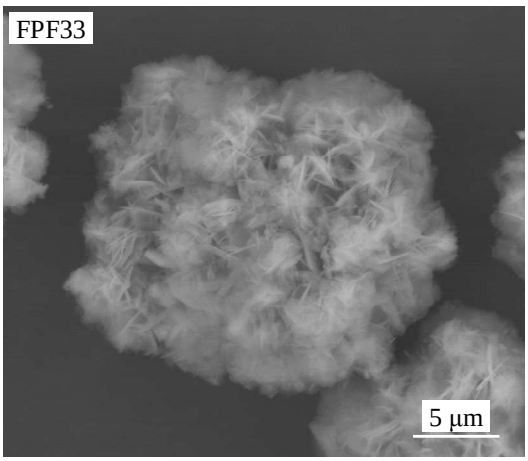

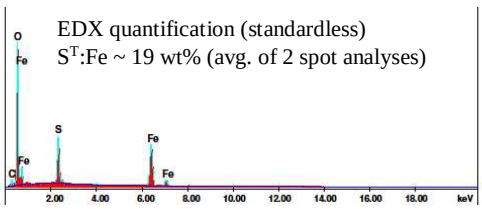

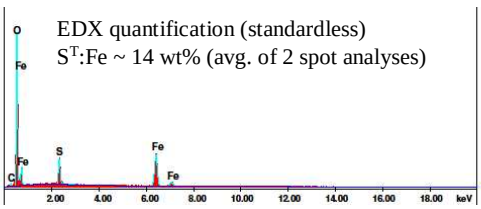

Stellenbosch University http://scholar.sun.ac.za

E.8 Thermodynamics of the iron(III) aqueous surrogate species and solubility products

The thermodynamic basis of the two surrogate iron(III) aqueous species, $FeH(SO_4)_2°$ and $Fe(OH)_3°$ (Ch. 5, Sect. 5.2.3), needs to be defined at the transcendent condition of infinite dilution. The formation of the dominant $FeH(SO_4)_2°$species is described as follows (Ch. 2, Sect. 2.4.3):

$$Fe^{3+} + 2SO_4^{2-} + H^+ \Rightarrow FeH(SO_4)_2^o \qquad \text{E.1}$$

Section 2.4.3 elaborates on this species, which is based on the work of Casas *et al.* (2005a). In general, this equilibrium constant increases with temperature and dominates the other iron(III) species in acidic solutions at higher temperatures (*log* K° = 8.1 at 25°C; Cifuentes *et al.*, 2006). The thermodynamic values published in Papangelakis *et al.* (1994) yield a *log* K° value of 3.6.

Speciation changes affecting iron(III) precipitation at lower acidity demand the explicit recognition of another iron(III) species, *i.e.*, $Fe(OH)_3°$:

$$Fe(OH)_3^o + 2SO_4^{2-} + 4H^+ \Leftrightarrow FeH(SO_4)_2^o + 3H_2O \qquad \text{E.2}$$

In principle, any species, *e.g.*, $Fe(OH)SO_4°$, $Fe(OH)_2(SO_4)^-$ or $Fe(SO_4)_2^{2-}$ (Sect. 2.5.2), could be utilised for this purpose. The $Fe(OH)_3°$ species is most convenient (Sect. 5.2.3) but cognisance has to be taken of the fact that this surrogate species represents a host of possible complex species at lower acidities (< 0.15 mol/kg H_2SO_4), demanding that the dominant $FeH(SO_4)_2°$ species to assume thermodynamic values unique to this study.

Since no heat capacity parameters (Eq. 2.34) are available for the $FeH(SO_4)_2°$ species and to simplify the problem, the heat capacity ($\Delta C_p°$) of Reaction E.1 is assumed to be zero, *i.e.*, a constant reaction enthalpy ($\Delta H°$) is applied (Eq. 2.43). This value is directly obtained from the data published by Casas *et al.* (2005a, 2005b, 2007), most of which is summarised in Cifuentes *et al.* (2006). Figure E.1 *a* illustrates that the first four points are used to obtain the slope, which, in turn, yields the $FeH(SO_4)_2°$ species enthalpy of -1726.7 kJ/mol. Thermodynamic data for the $Fe(OH)_3°$ species is obtained from Liu *et al.* (2003), based on a different partial molal heat capacity value of the ferric ion (Fe^{3+}) from the one suggested by the *HSC* (2006) database. As illustrated in Figure E.1 *a*, the Gibbs free energy of formation ($\Delta G°$) of the $FeH(SO_4)_2°$ species yields a value close to that of Papangelakis *et al.* (1994), based on the hematite solubility data of Reid and Papangelakis (2006) (Sect. 5.4.2). The partial molal heat capacity ($C_p°$) of this species is obtained after assuming a constant enthalpy change for Reaction E.1 (above), which mirrors the linear variation of *log* K° with the inverse temperature. This translates into a slightly positive deviation of *log* K° for Reaction E.2 at higher temperatures (Figure E.1 *b*), based on the Density function extrapolation technique (Eq. 2.44).

Stellenbosch University http://scholar.sun.ac.za

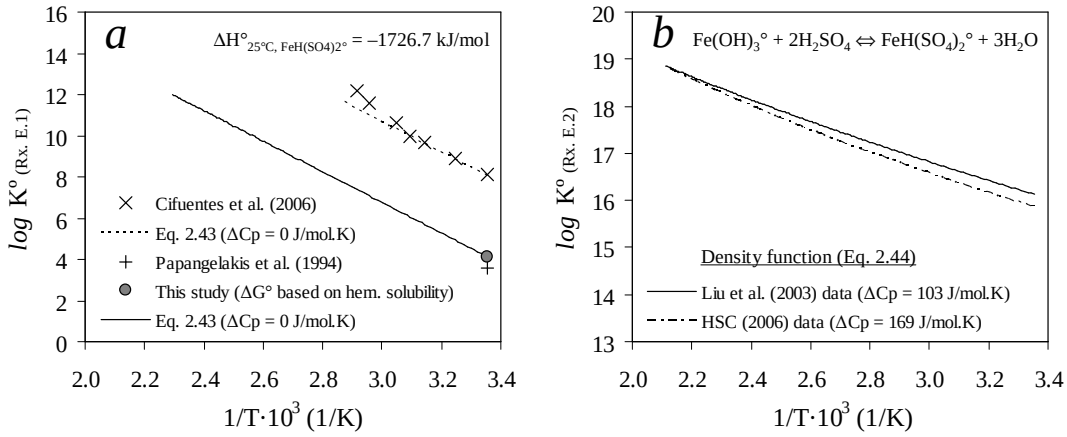

Figure E.1
Extrapolation of the $FeH(SO_4)_2°$ association constants, using the regressed $\Delta G°_{25°C}$ value of this species (based on the Fe_2O_3 solubility data of Reid & Papangelakis, 2006): *a*) Rx. E.1, assuming $\Delta C_p° = 0$ J/mol.K; *b*) Rx. E.2, using the Density function.

This $C_p°$ value of ferric ion of -142.7 J/mol.K gives a better representation of hematite solubility at high temperatures, with an added benefit of being consistent with the $Fe(OH)_3°$ species and hematite data of Liu *et al.* (2003) (Sect. 5.4.2). The resulting thermodynamic solubility product ($K°_{sp}$) values of hematite are illustrated in Figure E.2, again using the Density function to extrapolate to higher temperatures. This figure illustrates that the solubility product, as well as its temperature dependence, are highly dependent on the aqueous iron(III) species selected as basis. The extrapolated $K°_{sp}$ value of -9.7 (based on ferric ion) at 230°C is close to the value of -10.1 calculated by Liu and Papangelakis (2005a), using Helgeson extrapolation for the aqueous species and integration of the Maier-Kelley equation (Eq. 2.34) for the solid hematite phase.

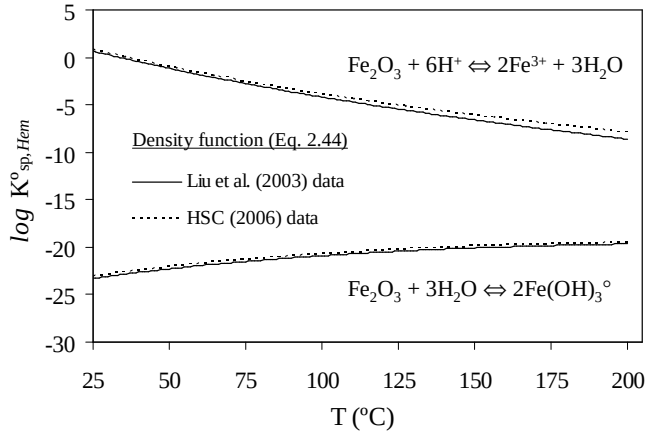

Figure E.2
Extrapolation of the Fe_2O_3 solubility constant, using the Density function (the standard thermodynamic values at the reference temperature of 25°C are summarised in Table 5.8).

Stellenbosch University http://scholar.sun.ac.za

The regressed ΔG° value of $FeH(SO_4)_2°$ of -1529.75 kJ/mol (Table 5.8) is also used as the basis to calculate the hydronium jarosite solubility product. Figure E.3 *a* presents the extrapolated thermodynamic solubility products, while Figure E.3 *b* compares the calculated iron(III) solubility with the data of Posnjak and Merwin (1922) at 140°C. The ΔG° and ΔH° values of the solid hydronium jarosite phase were adjusted by +4.6 and -4.6 kJ/mol, respectively (Table 5.8), in order to achieve better agreement with the data of Posnjak and Merwin. Although agreement at the more realistic (autoclave) acidity of 0.3 mol/kg H_2SO_4 is reasonable, the calculated solubilities are lower than the measured data at higher acidities. However, the experimental techniques utilised by Posnjak and Merwin (1922) were not ideal. The reaction vessel was cooled before the contents were removed and filtered. This could also be the reason for the questionable hematite solubility point at 0.3 mol/kg H_2SO_4 (140°C) in Figure 5.28. The steep increase in iron(III) solubility above about 0.4 mol/kg H_2SO_4 may also be due to a transition to the basic ferric sulfate (BFS) phase, *i.e.*, these data points may not necessarily reflect the hydronium jarosite equilibrium (also see Figure 5.2 in Ch. 5).

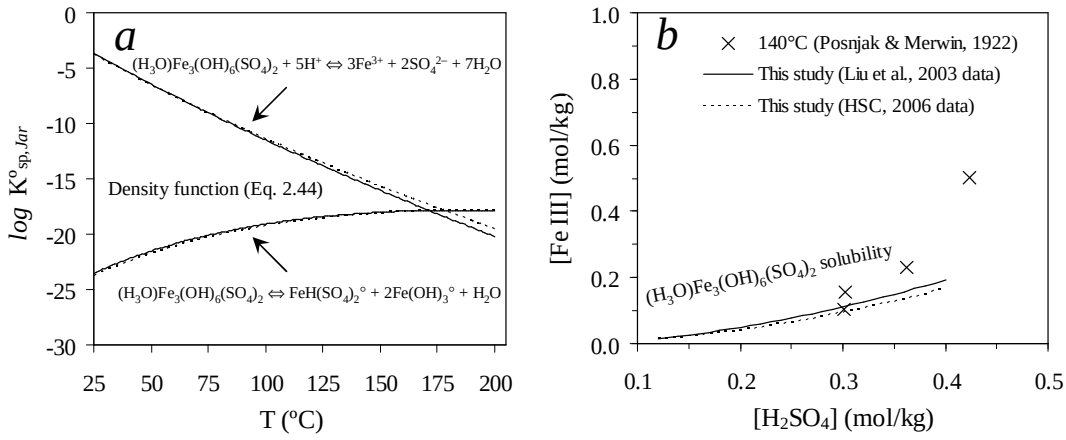

Figure E.3
Hydronium jarosite solubility calculations (this study): *a*) Solubility product extrapolation, using the Density function & standard thermodynamic values at 25°C (Table 5.8); *b*) Iron(III) solubility comparison with published data at 140°C & typical autoclave acidities ($\Delta G°_{25}$ & $\Delta H°_{25}$ values of the solid phase were increased & reduced by 4.6 kJ/mol, respectively; Majzlan *et al.*, 2004).

Stellenbosch University http://scholar.sun.ac.za

APPENDIX F. INTRINSIC AND PHENOMENOLOGICAL ACCOUNT OF SULFIDE MINERAL OXIDATION KINETICS (MICRO-MODEL)

This appendix focuses on the detailed information regarding the intrinsic oxidation kinetics of sulfide mineral particles, *i.e.*, considering no mass transfer limitations. The discussions and derivations are grounded in the fundamentals of semi-conductor and electrochemistry theory. Most of the concepts originate from Atkins and De Paula (2006), Bockris and Reddy (1970) and Wadsworth and Miller (1979), with some minor conceptual and mathematical manipulation.

F.1 Electronic structure of semiconductors

All the minerals encountered in this study are semiconductors and the interactions at the solid/solution interface need to be interpreted from that perspective. A concise review of the basic concepts can be found in Bockris and Reddy (1970), but requires some basic knowledge of atomic and molecular orbital theory (*e.g.*, Brown, 1980). Most importantly, valence electrons are involved in covalent bonding between atoms. The energy level of this molecular bonding orbital is always lower than that of the atomic orbitals from which it is derived. Conversely, the anti-bonding molecular orbital (denoted by *) is at a higher energy level than the corresponding atomic orbitals (Brown, 1980) and contains unoccupied energy states. When atoms are brought together within close proximity, as in a sulfide mineral lattice, these molecular orbitals overlap to create continuous bands of energy levels (Bockris & Reddy, 1970; Hiskey, 1993). The figure below illustrates that there is an overlap between the valence band and the conduction band (partially filled or empty anti-bonding orbitals) in metals, which increases the mobility of the charge carriers (increased conductivity). The other extreme is represented by materials where the inter-atomic distance is large and the energy gap (E_g) between the two bands, *i.e.*, forbidden energies, is significantly higher than the thermal energy of the electrons, kT. These materials are known as insulators.

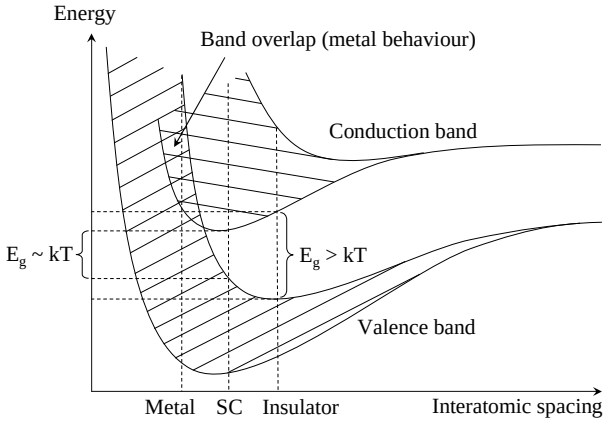

Schematic diagram of the band model of a metal, semiconductor (SC) & insulator (based on the discussions of Bockris & Reddy, 1970).

Stellenbosch University http://scholar.sun.ac.za

The intermediate scenario is represented by semiconductor (SC) materials where the band energy gap is somewhat greater than the thermal energy of the electrons. However, excitation of electrons (from the valence to the conduction band) would facilitate the motion of charge *via* electron movement in the conduction band and the movement of holes in the opposite direction in the valence band (Bockris & Reddy, 1970). If the energy difference (E_g) between the lowest molecular orbital of the conduction band (E_c) and the uppermost molecular orbital in the valence band (E_v) is more than 2 eV, the material may be classified as an insulator (Osseo-Asare, 1992). Although ZnS has a band gap in the range 3.6 to 3.9 eV (Crundwell, 1988b), natural sphalerite contains impurities, which have pronounced effects on its electrical properties. Impurities, such as iron, introduce localised bands within the ZnS band gap that are energetically more favourable for electron transfer (see Crundwell, 1988b). In general, a semiconductor impurity that releases electrons into the material (conduction band) results in *n*-type semiconductor behaviour, whereas an impurity that creates holes (by capturing electrons) in the valence band results in *p*-type semiconducting behaviour (Hiskey, 1993). A metal-excess compound, such as chalcopyrite, is more likely to display *n*-type semiconducting behaviour, while compounds such as CuS are *p*-type metallic conductors (Crundwell, 1988b). Anodic dissolution of a semiconductor with a wide band gap (> 1 eV; after Crundwell, 1988b) would be dominated by a hole-decomposition pathway (see Osseo-Asare, 1992). In the case of *n*-type semiconductors, the concentration of holes is low and saturation current may arise when charge transfer occurs *via* valence-band processes. This is because the supply of holes may be migration-limited (see examples in Crundwell, 1988b).

Another important factor is the presence of surface states at the semiconductor/electrolyte interface. A space-charge region develops adjacent to the interface where charge carriers have diffused away, *e.g.*, during spontaneous mineral oxidation, or have been forced away by an electric field. This space-charge region is analogous to the diffuse layer in a dilute electrolyte (Bockris & Reddy, 1970). The charge density on the mineral surface arises due to the change in the electron potential associated with the crystal termination (Tamm or Shockley states; Crundwell, 1988a) and exerts an electric field on the ions in the electrolyte. Similarly, the sheet of charge (adsorbed ions) on the outer Helmholtz plane exerts an electric field on the charge carriers in the semiconductor (Bockris & Reddy, 1970). Due to this net field, there is a potential drop in the semiconductor, which decays exponentially from the surface into the bulk of the semiconductor material (see calculations in Bockris & Reddy, 1970). The end result is that the energy bands near the mineral surface would bend up or down, depending on the relative potential difference, *i.e.*, the natural potential difference between the surface and the electrolyte during leaching, or the imposed potential when polarising the electrode externally. The rate-limiting step may be the transport of charge carriers across the space-charge and interfacial regions especially when the electrical field, that would develop naturally, opposes this charge transport process normal to the interface. However, the

Stellenbosch University http://scholar.sun.ac.za

presence of particular surface states at the solid surface may dominate semiconductor behaviour, *i.e.*, particular surface states, associated with the formation of adsorbed species, can trap the charge carriers at energy levels different to those provided by the bulk semiconductor material (see Bockris & Reddy, 1970).

The energy distribution of electrons determines which of the states are filled and which are empty. This distribution is described by Fermi-Dirac statistics (see, *e.g.*, Atkins & De Paula, 2006) and the Fermi energy (level) is the energy at which the probability of a state being occupied is 0.5. The position of the Fermi level, relative to the band structure, determines the density of electrons and holes. If there is a high density of mono-energetic surface states (10^{13} states per cm^2; Crundwell, 1988b), the Fermi level will be anchored ('pinned') at the energy of these surface states, and the material will behave like a metal, *i.e.*, no space-charge region exists, with the electrode potential residing across the Helmholtz layer (Bockris & Reddy, 1970; Crundwell, 1988a). Surface-state mechanisms have been proposed for the dissolution of large band-gap sulfides, such as sphalerite and cadmium sulfide (Crundwell, 1988b; Tributch & Bennet, 1981), and also for pyrite (Mishra & Osseo-Asare, 1992). Besides contact adsorption, it has been proposed that structural defects (Mishra & Osseo-Asare, 1992) and impurities (Crundwell, 1988b) may induce surface states. When the Fermi level overlaps with one of the energy bands, the semiconductor is degenerate and would act like a metal. Surface degeneracy may also be induced by an externally applied potential, forcing the Fermi level into one of the bands (Crundwell, 1988a).

Finally, in order to achieve electron transfer, the exchange at the instant of charge transfer must occur with minimal energy loss. The fluctuating energy-level (FEL) model (*e.g.*, in Crundwell, 1988a) states that the energy levels of ions in solution are distributed as a result of the thermal fluctuations of the dipoles in the solvation sheath surrounding the ion (see Ch. 2). This is the essential feature that allows the rate of charge transfer to be conceptualised as proportional to the probability that the energy level of the oxidising agent has fluctuated to the energy level of a surface state. In terms of the FEL model, charge transfer can only occur with an ion whose energy level has a significant probability of overlapping with the relevant semiconductor band.

F.2 Potential-current relationships

Based on the above discussions, it can be assumed that the charge transfer reaction occurs predominantly across the Helmholtz double layer. The Helmholtz model supposes that the solvated ions arrange themselves along the surface of the electrode, and are held away from it by the presence of their hydration spheres. The plane running through the solvated ions is known as the outer Helmholtz plane (OHP) (see above), and the charge on the electrode (reacting particle), as the inner Helmholtz plane (IHP) (Atkins & De Paula, 2006). The above discussions give good insight

Stellenbosch University http://scholar.sun.ac.za

into the processes leading to the potential difference across the double layer. Essentially, a potential difference is established because electrons and ions are continuously exchanged on the breaking of bonds (solid phase) and formation of bonds (solution phase). This leads to an upset in the electro-neutrality across the double layer, which creates the electrical field. The current density (current per unit area of electrode surface) gives a measure of the rate at which electrons are discharged, *i.e.*, the rate of oxidation. The flows of current towards and away from the electrode are equal when the potential difference has its equilibrium value. The net current depends on the potential difference of the actual potential and this equilibrium value, *i.e.*, the net current depends on the overpotential.

The theory of reaction dynamics, and more specifically the activated complex theory (see Atkins & De Paula, 2006), recognises an exponential relationship between the chemical rate constant and the Gibbs free energy of activation ($\Delta^{\ddagger}G$), required to overcome the potential energy barrier for a reaction to take place. Both anodic and cathodic directions of the charge transfer reaction are activated. Solvated ions have to discard their hydration and coordination shells before charge transfer can take place. Likewise, an ion at the surface has to detach and migrate into the bulk solution (Atkins, 1986). A first-order rate law can be expected for an intrinsic charge transfer reaction (Atkins & De Paula, 2006) and may be represented as follows (moles reacted per unit electrode surface area per unit time, *e.g.*, mol/m^2.min):

$$r = k \cdot m \qquad \text{F.1}$$

The molality (mol/kg) refers to the concentration of ions at the double layer where the charge transfer reaction takes place. The rate constant, k, is expressed in units of kg/m^2.min and encapsulates the above-mentioned exponential relationship:

$$k = \tilde{k}\left(\frac{k_b T}{h} \cdot exp\frac{-\Delta^{\ddagger}G^{o}}{R_g T}\right) \qquad \text{F.2}$$

The term in brackets gives the frequency (1/min) of successful jumps over the activation barrier. The proportional constant, $\tilde{k}$ (units of m·kg/m^3), assigns the desired units to the intrinsic rate constant (the proportionality constant is simply expressed in units of meter, m, if Eq. F.1 is based on the molarity scale). The Gibbs free energy of activation can be dismantled into the chemical free energy of activation (because of the processes mentioned above) and the contribution of the electrical field across the double layer.

The schematic representations of Wadsworth and Miller (1979) and Atkins (1986) illustrate the effect of an electrical field on the free energy of activation (a condensed interpretation is presented here; also see Bockris & Reddy, 1970). The direction of the field, assumed to vary linearly between the inner and outer plane, and the position of the summit of the energy barrier in the double layer

Stellenbosch University http://scholar.sun.ac.za

are of primary importance. The position of the summit is quantified by the transfer coefficient, β, *i.e.*, the ratio of the distance to the summit relative to the whole distance across the double layer, and varies between 0 and 1. Only single-electron charge transfer is usually assumed in the rate-determining step, even though more electrons may be required to complete an electrochemical reaction. This is because single-electron transfer is energetically more favourable than multi-electron processes (see references in Jin *et al.*, 1985). The general symbol z denotes the charge number, *i.e.*, z = –1 for single-electron transfer. The direction of the field is important and depends on whether an oxidation or reduction reaction is under consideration. In the case of oxidative leaching, the electrode reacts anodically, *i.e.*, the electrode surface (IHP) is positively charged relative to the solution (OHP). Thus, for the reduction process (cathodic reaction), the movement of the oxidant (*e.g.*, a cation towards the OHP) and an electron (towards the IHP) would be against the field. The total free energy will be increased, *i.e.*, the total work required to bring the oxidant to its transition state is higher. The magnitude of this increase is equal to $|z|F(\beta\Delta\phi)$, *i.e.*:

$$\Delta^{\ddagger}G = \Delta^{\ddagger}G_c + \beta|z|F\Delta\phi \qquad \text{F.3}$$

For the anodic direction, the opposite is true, *i.e.*:

$$\Delta^{\ddagger}G = \Delta^{\ddagger}G_a - (1-\beta)|z|F\Delta\phi \qquad \text{F.4}$$

The subscripts ‘a’ and ‘c’ refer to the anodic and cathodic directions of the half-cell reaction, respectively. Substitution of Equation F.3 and Equation F.4 into Equations F.1 and F.2, respectively, and rearranging results in the cathodic and anodic rate expressions:

$$r_c = k_c m_{ox} \cdot exp\frac{-\beta|z|F\Delta\phi}{R_g T} \qquad \text{F.5}$$

$$r_a = k_a m_{red} \cdot exp\frac{(1-\beta)|z|F\Delta\phi}{R_g T} \qquad \text{F.6}$$

where m_{ox} and m_{red} refer to the molalities of the oxidised and reduced species, respectively. The respective rate constants are given by the following two expressions:

$$k_c = k^{\sim}\left(\frac{k_b T}{h} \cdot exp\frac{-\Delta^{\ddagger}G_c^{o}}{R_g T}\right) \qquad \text{F.7}$$

$$k_a = k^{\sim}\left(\frac{k_b T}{h} \cdot exp\frac{-\Delta^{\ddagger}G_a^{o}}{R_g T}\right) \qquad \text{F.8}$$

The Gibbs free energy terms refer to the half-cell reactions at equilibrium. By setting Equations F.5 and F.6 equal and simplifying, yields the following relationship (when written as a reduction reaction):

Stellenbosch University http://scholar.sun.ac.za

$$\Delta\phi = \Delta\phi^{o} + \frac{R_g \mathrm{T}}{|\mathrm{z}|F} \cdot ln \frac{\mathrm{m}_{ox}}{\mathrm{m}_{red}} \qquad \text{F.9}$$

where $\Delta\phi^{\circ}$ refers to the electric potential at the standard state:

$$\Delta\phi^{o} = \frac{R_g \mathrm{T}}{|\mathrm{z}|F} \cdot ln \frac{\mathrm{k}_c}{\mathrm{k}_a} \qquad \text{F.10}$$

Equation F.10 is obtained by setting the molality ratio (m_{ox}/m_{red}) in Equation F.9 equal to one, *i.e.*, the electron acceptor (oxidant) to electron donor (reductant) molality ratio is normalised to one (Bockris & Reddy, 1970). Had one started with a more rigorous derivation using activity rather than molality, Equation F.9 would have yielded the more classical form of the well-known Nernst equation (for convenience, the reduced species refers here to the pure metal, *i.e.*, $a_{red} = 1$):

$$\Delta\phi = \Delta\phi^{o} + \frac{R_g \mathrm{T}}{|\mathrm{z}|F} \cdot ln\, a_{M^{z+}} \qquad \text{F.11}$$

It can now be seen that the standard state not only refers back to a unity activity ratio, but also to unity activity, and, hence, to the imaginary standard state of unit molality of each of the species contributing to the redox couple, which ties in with the discussions of Section 2.2.1 (also see Bockris & Reddy, 1970, for a derivation of the Nernst equation from basic thermodynamics).

According to Faraday's Law, the rate, r (mol/m^2.min), of an electrochemical reaction is related to the current density, j (A/m^2), as follows:

$$\mathrm{r} = \frac{\mathrm{j}}{|\mathrm{z}_{rx}|F} \qquad \text{F.12}$$

The stoichiometric number of charges taking part in the reaction is represented by z_{rx}. Equation F.12 may be inserted into Equations F.5 and F.6 to give the current densities of the anodic and cathodic directions, *i.e.*, j_a and j_c, respectively. The net current density of the cathodic process (undergoing reduction) is the difference between the individual cathodic and anodic current densities:

$$\mathrm{j}_C = |\mathrm{z}_{rx}|F \cdot \mathrm{k}_a \mathrm{m}_{red} \cdot exp\left(\frac{(1-\beta)|\mathrm{z}|F\Delta\phi}{R_g \mathrm{T}}\right) - |\mathrm{z}_{rx}|F \cdot \mathrm{k}_c \mathrm{m}_{ox} \cdot exp\left(\frac{-\beta|\mathrm{z}|F\Delta\phi}{R_g \mathrm{T}}\right) \qquad \text{F.13}$$

In order to be consistent with the sign convention used in most references (see Erdey-Grúz, 1972), the transfer coefficient of the net cathodic process (β_C) is such that $\beta = 1-\beta_C$. Equation F.13 is then transformed into the following form:

Stellenbosch University http://scholar.sun.ac.za

$$j_C = |z_{rx}|F \cdot k_a m_{red} \cdot exp\left(\frac{\beta_C |z| F\Delta\phi}{R_g T}\right) - |z_{rx}|F \cdot k_c m_{ox} \cdot exp\left(\frac{-(1-\beta_C)|z|F\Delta\phi}{R_g T}\right) \qquad \text{F.14}$$

Similarly, the net current density of the anodic process (undergoing oxidation) is given by:

$$j_A = |z_{rx}|F \cdot k_a m_{red} \cdot exp\left(\frac{\beta_A |z| F\Delta\phi}{R_g T}\right) - |z_{rx}|F \cdot k_c m_{ox} \cdot exp\left(\frac{-(1-\beta_A)|z|F\Delta\phi}{R_g T}\right) \qquad \text{F.15}$$

where β_A refers to the transfer coefficient of the net anodic process. The above equations represent the Butler-Volmer relationship between the current density and potential across the double layer. The oxidative leaching reaction is essentially irreversible, so that the second term in Equation F.15 can be ignored. Usually it is also assumed that $\beta_A = \beta_C = \beta$. β lies in the range 0 to 1 and is often found (experimentally) to be about ½ (Atkins & De Paula, 2006).

Based on the general description of an electrochemical reaction, the equilibrium situation can be represented as follows:

$$j_o = |z_{rx}|F \cdot k_a m_{red} \cdot exp\frac{\beta |z| F\Delta\phi^e}{R_g T} = |z_{rx}|F \cdot k_c m_{ox} \cdot exp\frac{-(1-\beta)|z|F\Delta\phi^e}{R_g T} \qquad \text{F.16}$$

where j_o is known as the exchange current density at the equilibrium potential, $\Delta\phi^e$. The overpotential, η, simply defines the difference between the actual and equilibrium potential, *i.e.*:

$$\eta = \Delta\phi - \Delta\phi^e \qquad \text{F.17}$$

Substitution of Equations F.16 and F.17 into any of the above Butler-Volmer relationships reveals the more general form:

$$j = j_o \cdot exp\left(\frac{\beta |z| F\eta}{R_g T}\right) - j_o \cdot exp\left(\frac{-(1-\beta)|z|F\eta}{R_g T}\right) \qquad \text{F.18}$$

If the overpotential is significant, any one of the half-cell reactions may predominate and a plot of *ln* j *vs.* η (or E) would yield the Tafel slope, *i.e.*, the slope expressed as $R_g T/(\beta|z|F)$ in units of V/decade. For a single-electron transfer reaction and a transfer coefficient of one-half (metal-like behaviour), the theoretical Tafel slope has a value of 0.118 V/decade. The current-voltage behaviour of an ideal semiconductor/solution interface implies a transfer coefficient of one (1) and a Tafel slope of 0.059 V/decade (see Crundwell, 1988b).

F.3 Effect of temperature on the intrinsic reaction rate

The activated complex theory was used as a starting point in the above section. The general form of the rate constant is represented by Equation F.2. The Gibbs free energy term can be broken down

Stellenbosch University http://scholar.sun.ac.za

into the molar enthalpy of activation ($\Delta^{\ddagger}H$) and molar entropy of activation ($\Delta^{\ddagger}S$) contributions, using classical thermodynamics (Atkins & De Paula, 2006):

$$\Delta^{\ddagger}G^{o} = \Delta^{\ddagger}H^{o} - T \cdot \Delta^{\ddagger}S^{o} \qquad \text{F.19}$$

The activation energy, E_a, represents the kinetic energy (J/mol) required for the electron transfer reaction to occur (crossing of the activation barrier; see previous section). The activation energy of charge transfer across the Helmholtz layer adopts its formal definition for reactions occurring in the solution phase (see Atkins & De Paula, 2006), *i.e.*:

$$E_a = \Delta^{\ddagger}H^{o} + R_g T \qquad \text{F.20}$$

Substitution of Equations F.19 and F.20 into Equation F.2, and rearranging, results in the following relationship for the intrinsic rate constant, k:

$$k = \hat{A}\tilde{k} \cdot exp\frac{-E_a}{R_g T} \qquad \text{F.21}$$

The units of k depend on the reaction order, *i.e.*, the proportionality constant ($\tilde{k}$) adopts its units to yield the intrinsic rate constant in mol/m^2.min. The functional form of this equation reflects Arrhenius-like behaviour with temperature (see, *e.g.*, Atkins & De Paula, 2006). However, the pre-exponential factor ($\hat{A}$) also contains a temperature term and gives the frequency (1/min) of successful exchanges:

$$\hat{A} = \frac{k_b T}{h} \cdot exp\left(1 + \frac{\Delta^{\ddagger}S^{o}}{R_g}\right) \qquad \text{F.22}$$

Even collision theory (see Atkins & De Paula, 2006) leads to a relationship of the form represented by Equation F.21, as well as a temperature term in the pre-exponential factor. In this study it is assumed that the temperature dependencies of both the pre-exponential factor and the activation energy are small compared to the temperature term in the exponent (Eq. F.21). A straight line, with slope $-E_a/R_g$, is then obtained by plotting *ln* k *vs.* 1/T; empirically this is often found to be the case.

F.4 Phenomenological description of the leaching kinetics under surface reaction control (intrinsic kinetics), based on the unreacted shrinking particle (or particle core) model

The above discussions imply that a sulfide mineral particle shrinks as a result of the electrochemical oxidation reaction. The unreacted shrinking core (USC) model envisages a boundary at the surface of the unreacted core that moves towards the centre of a particle and a layer of impervious product (elemental sulphur) that forms on the unreacted core as the reaction proceeds (see, *e.g.*, Crundwell, 1994a). The unreacted shrinking particle (USP) model is identical to the USC model, except that no solid product layer is formed around the unreacted core. These models rely on the assumption that the oxidation reaction occurs at a sharp interface between the surface of the

Stellenbosch University http://scholar.sun.ac.za

unreacted sulfide mineral and the solution. This is known as topochemical kinetics and is in line with the above discussions, which assume that the charge transfer reaction occurs across the Helmholtz double layer.

If no mass transfer effect of the reagent or product is present, the following phenomenological description of the kinetics may be conducted (the derivation is based on the discussions of Levenspiel, 1972 & Peters, 1991). Attention is first focused on the leaching behaviour of an individual sulfide mineral particle, without recognition of the solution phase. For the purpose of this discussion, it may be assumed that the majority of sulfide mineral particles in a cleaner concentrate are well liberated and not masked by gangue phases (see Sect. 6.4.3). The rate of leaching (mol/min) of a sulfide mineral particle (n_s moles) is then:

$$\frac{dn_s}{dt} = \frac{\rho_s}{Mw_s} \times \frac{dv_s(\ell,t)}{dt} = \frac{\rho_s}{Mw_s} \times \frac{\partial v_s}{\partial \ell} \frac{d\ell}{dt} \qquad \text{F.23}$$

where ρ_s and Mw_s are the density and molecular weight of the sulfide mineral phase, respectively, while v_s and ℓ represent the volume and one-dimensional size of an unreacted sulfide mineral particle (or particle core), respectively. If r_s is the intrinsic rate of dissolution on the sulfide mineral per unit surface area (mol/m^2.min), the following relationship is obvious:

$$\frac{-dn_s}{dt} = a_s r_s \qquad \text{F.24}$$

where a_s is the surface area of the unreacted sulfide mineral particle or particle core. Substitution of Equation F.24 into Equation F.23, and rearranging, then yields the following relationship:

$$\frac{d\ell}{dt} = -\frac{Mw_s}{\rho_s} \times \left(a_s(\ell,t) / \frac{\partial v_s}{\partial \ell} \right) \times r_s(t) \qquad \text{F.25}$$

Firstly, expressions for $a_s(\ell,t)$ and $\partial v_s/\partial \ell$ are required. The following two equations give the relationship between the area and size, and the volume and size of the unreacted sulfide mineral particle (or particle core), respectively:

$$a_s = \Phi_a(\ell,t) \cdot \ell^2 \qquad \text{F.26}$$

$$v_s = \Phi_v(\ell,t) \cdot \ell^3 \qquad \text{F.27}$$

where Φ_a is the area shape factor (π for a perfect sphere) and Φ_v is the volume shape factor ($\pi/6$ for a perfect sphere). It is customary to assume that these shape factors are independent of the size, *i.e.*, the unreacted particle or particle core maintains its shape as it shrinks. This is a good assumption if the gangue or more noble sulfide mineral phases do not hinder (obstruct) the sulfide mineral being leached. This is assumed to be the case during initial oxidation because the inert phases are

Stellenbosch University http://scholar.sun.ac.za

minority constituents in the concentrates used in this study (Sect. 6.4.3). However, this is not necessarily the case for some of the particles when leached close to completion. Nevertheless, if the shape is maintained for most of the dissolution process, Equation F.27 may be differentiated with respect to the size. Substitution of this differentiated equation and the area term (Eq. F.26) into Equation F.25 leads the following expression:

$$k_\ell = \frac{d\ell}{dt} = -\frac{1}{3}\frac{Mw_s}{\rho_s}\frac{\Phi_a}{\Phi_v}\times r_s(t) \qquad \text{F.28}$$

This equation clearly illustrates that the rate of shrinkage of an unreacted sulfide mineral particle (or particle core) under surface reaction control, *i.e.*, intrinsic kinetics (no diffusion effects), is not dependent on its size. If the mass of an unreacted sulfide mineral particle (or particle core) at a particular point in time is given by w_s, the surface area per unit mass of the particle is:

$$\frac{a_s}{w_s} = \frac{1}{\rho_s}\frac{\Phi_a}{\Phi_v}\frac{\ell^2}{\ell^3} \qquad \text{F.29}$$

The surface area per initial particle mass ($w_{s,o}$) is then:

$$\frac{a_s}{w_{s,o}} = \frac{1}{\rho_s}\frac{\Phi_a}{\Phi_v}\frac{\ell^2}{L_o^3} \qquad \text{F.30}$$

where L_o is the initial particle size. The following relationship is obtained after dividing Equation F.30 by Equation F.29:

$$\frac{w_s}{w_{s,o}} = 1 - X_s = \frac{\ell^3}{L_o^3} \qquad \text{F.31}$$

The fractional amount of sulfide mineral leached is represented by X_s. If the intrinsic reaction rate, r_s, remains constant with time, Equation F.28 may be integrated to yield an analytical expression. Substitution of this expression into Equation F.31 then yields the USP (or USC) model for intrinsic leaching under constant reaction rate conditions:

$$1-(1-X_s)^{\frac{1}{3}} = k_s t \qquad \text{F.32}$$

where k_s is the overall, observed leaching rate constant (1/min):

$$k_s = -\frac{1}{3}\frac{Mw_s}{\rho_s}\frac{\Phi_a}{\Phi_v}\frac{r_s}{L_o} \qquad \text{F.33}$$

Equations F.32 and F.33 are directly utilised to evaluate the experimental leaching data. If the term, $1-(1-X_s)^{1/3}$ is plotted against time, and the intrinsic leaching reaction controls the rate, a straight line should be obtained with slope k_s. However, it is obvious from Equation F.33 that a straight line would only be obtained if the particles are screened to a narrow size range, L_o, and the reaction

Stellenbosch University http://scholar.sun.ac.za

rate, r_s, is kept constant over the course of the leach, *i.e.*, the solution composition is kept constant. Equation F.32 may also be rearranged to yield the following useful relationship:

$$X_s = 1 - \left(1 - \frac{t}{\tau_s}\right)^3 \qquad \text{F.34}$$

where τ_s is the time constant ($1/k_s$), which gives the time (min) for complete oxidation of a sulfide mineral. Finally, the differential form of Equation F.32 yields the mineral extraction rate:

$$\frac{dX_s}{dt} = 3k_s(1 - k_s t)^2 \qquad \text{F.35}$$

Substitution of Equation F.32 into F.35, and rearranging, then yields the following differential form of the USP (or USC) model when the intrinsic oxidation reaction controls the kinetics:

$$\frac{dX_s}{dt} = 3k_s(1 - X_s)^{\frac{2}{3}} \qquad \text{F.36}$$

Stellenbosch University http://scholar.sun.ac.za

APPENDIX G. DETAILED BATCH LEACH TEST RESULTS (HBMS 777 CHALCOPYRITE CONCENTRATE)

This appendix summarises the detailed batch leaching testwork results in sequential order, as discussed in Chapter 6 (Sect. 6.5). The detailed size distributions of the narrow-sized head samples (HBMS 777 chalcopyrite cleaner concentrate) are tabled first, after which the detailed leaching results are presented. All these tests were conducted in the 2-litre Parr autoclave (Sect. 6.4.1). The first series of tests focused on verifying the experimental procedure. This was then followed by a series of tests conducted to identify the different reaction regimes. The next series of tests quantified the effect of initial particle size and acid concentration. The final series of tests attempted to obtain the reaction stoichiometries and information regarding the sulfide mineral oxidation mechanisms. These include various tests that attempted to quantify the effect of varying solution composition (sulfate salt concentration) and temperature. The (regressed) rate constant values of all the tests used to derive the intrinsic rate equations are summarised in figure format at the end of each section. The detailed experimental procedures are summarised in Section 6.4.1.

G.1 Detailed size distributions of the head samples

The particle size distributions of the four head samples (HBMS 777) were measured with a Malvern MasterSizer 2000 (Sect. 6.4.3); the detailed results are presented below.

		Sample A	**Sample B**	**Sample C**	**Sample D**
		Obscuration (%)	Obscuration (%)	Obscuration (%)	Obscuration (%)
		8.5	5.4	13.1	6.0
Size (µm)	Size (avg.) (µm)	Cum. vol. (%)	Cum. vol. (%)	Cum. vol. (%)	Cum. vol. (%)
0.55	0.5145	0.00	0.00	0.00	0.00
0.631	0.5905	0.17	0.00	0.00	0.00
0.724	0.6775	0.86	0.00	0.00	0.00
0.832	0.778	2.35	0.00	0.05	0.00
0.955	0.8935	4.96	0.00	0.16	0.00
1.096	1.0255	8.99	0.00	0.28	0.00
1.259	1.1775	14.65	0.00	0.39	0.00
1.445	1.352	22.03	0.00	0.47	0.00
1.66	1.5525	31.00	0.00	0.53	0.00
1.905	1.7825	41.23	0.13	0.60	0.00
2.188	2.0465	52.16	0.84	0.71	0.00
2.512	2.350	63.11	2.53	0.88	0.00

Stellenbosch University http://scholar.sun.ac.za

		Sample A	**Sample B**	**Sample C**	**Sample D**
Size (µm)	Size (avg.) (µm)	Cum. vol. (%)	Cum. vol. (%)	Cum. vol. (%)	Cum. vol. (%)
2.884	2.698	73.34	5.62	1.14	0.00
3.311	3.0975	82.20	10.44	1.46	0.00
3.802	3.5565	89.25	17.11	1.83	0.00
4.365	4.0835	94.34	25.58	2.26	0.00
5.012	4.6885	97.56	35.50	3.07	0.00
5.754	5.383	99.33	46.30	4.88	0.00
6.607	6.1805	99.92	57.27	9.21	0.00
7.586	7.0965	100.00	67.72	16.80	0.01
8.71	8.148	100.00	77.02	29.10	0.18
10	9.355	100.00	84.75	44.79	1.33
11.482	10.741	100.00	90.72	61.79	4.34
13.183	12.3325	100.00	94.97	77.06	10.08
15.136	14.1595	100.00	97.68	88.55	19.12
17.378	16.257	100.00	99.19	94.94	31.27
19.953	18.6655	100.00	99.90	98.3	45.55
22.909	21.431	100.00	100.00	99.59	60.36
26.303	24.606	100.00	100.00	100.00	73.93
30.2	28.2515	100.00	100.00	100.00	84.88
34.674	32.437	100.00	100.00	100.00	92.52
39.811	37.2425	100.00	100.00	100.00	97.05
45.709	42.76	100.00	100.00	100.00	99.20
52.481	49.095	100.00	100.00	100.00	99.92
60.256	56.3685	100.00	100.00	100.00	100.00
69.183	64.7195	100.00	100.00	100.00	100.00

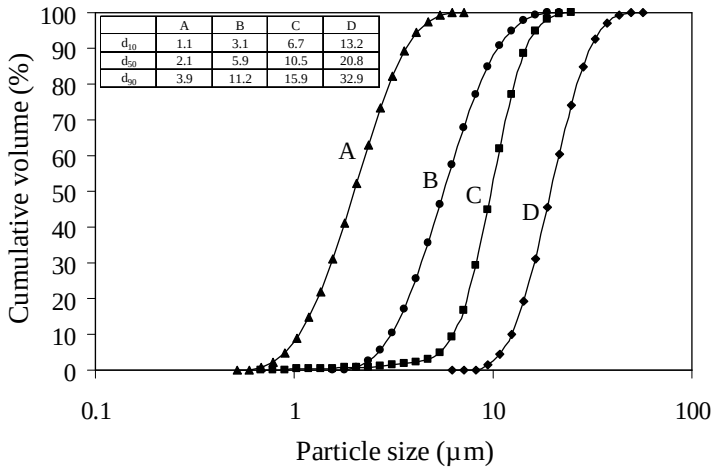

Stellenbosch University http://scholar.sun.ac.za

G.2 Verifying the experimental procedure

These tests focussed on developing and verifying a suitable experimental procedure to obtain accurate rate constant values.

PLA1	Temp.	Imp. speed	P_g	p_{O2}°	Solids	Solids	Solution	Density
Sample C	150°C	1000 rpm	473 kPa	3 kPa	2.0 wt %	20 g	980 g	1079 g/L
LS, QB	Cu	Zn	–	Fe (II)	H_2SO_4	–	SO_4	H_2O
0.00 g/L	35 g/L	0 g/L	–	0 g/L	0 g/L	–	52.9 g/L	898.9 g
min (test)	Sld. (g)	Colour	Sln. (g)	Vol. (mL)	Colour	[a] Dens (g/L)	[a] E_{Ag} (mV)	[a] pH
–	–	–	–	–	–	–	–	–
30 (A12)	19.1	Black	897.0	825	Blue	1087	–	–
–	–	–	–	–	–	–	–	–
–	–	–	–	–	–	–	–	–
–	–	–	–	–	–	–	–	–
Solids	Cu (%)	Zn (%)	Fe (%)	–	S^{2-} (%)	S° (%)	SO_4 (%)	S^T (%)
Head	28.5	4.6	29.5	–	35.5	0.0	0.0	35.5
–	–	–	–	–	–	–	–	–
30 (A12)	29.9	4.2	29.0	–	35.2	0.1	0.5	34.4
–	–	–	–	–	–	–	–	–
–	–	–	–	–	–	–	–	–
–	–	–	–	–	–	–	–	–
Solution	Cu (g/L)	Zn (g/L)	Fe^T (g/L)	FeII (g/L)	H_2SO_4 (g/L)	–	SO_4 (g/L)	–
–	–	–	–	–	–	–	–	–
30 (A12)	37.25	0.15	0.36	0.33	2.3	–	59.4	–
–	–	–	–	–	–	–	–	–
–	–	–	–	–	–	–	–	–
–	–	–	–	–	–	–	–	–
Extraction	[b] Cu (%)	[b] Zn (%)	[b, c] Fe (%)	–	S^{2-} (%)	[d] S° (%)	–	[b] S^T (%)
–	–	–	–	–	–	–	–	–
30 (A12)	< 0 (97)	13 (100)	5 (99)	–	5	3	–	(99)
–	–	–	–	–	–	–	–	–
–	–	–	–	–	–	–	–	–
–	–	–	–	–	–	–	–	–

[a] 20°C; [b] Elemental accountability in brackets; [c] Fe (sln)/Fe (sld+sln)×100%; [d] S° yield, *i.e.*, $S°/S^{2-}{}_{rx}$×100%.

Stellenbosch University http://scholar.sun.ac.za

PLA2	Temp.	Imp. speed	P_g	$p_{O2}°$	Solids	Solids	Solution	Density
Sample C	150°C	1000 rpm	473 kPa	3 kPa	1.0 wt %	10 g	990 g	1035 g/L
LS, QB	Cu	Zn	–	Fe (II)	H_2SO_4	–	SO_4	H_2O
0.00 g/L	15 g/L	0 g/L	–	0 g/L	0 g/L	–	22.8 g/L	954.5 g
min (test)	Sld. (g)	Colour	Sln. (g)	Vol. (mL)	Colour	[a] Dens (g/L)	[a] E_{Ag} (mV)	[a] pH
–	–	–	–	–	–	–	–	–
30 (A22)	9.59	Copper	800.7	763	Blue	1050	–	–
–	–	–	–	–	–	–	–	–
–	–	–	–	–	–	–	–	–
–	–	–	–	–	–	–	–	–
Solids	Cu (%)	Zn (%)	Fe (%)	–	S^{2-} (%)	S° (%)	SO_4 (%)	S^T (%)
Head	28.5	4.6	29.5	–	35.5	0.0	0.0	35.5
–	–	–	–	–	–	–	–	–
30 (A22)	29.9	3.95	28.1	–	33.9	0.1	0.5	33.0
–	–	–	–	–	–	–	–	–
–	–	–	–	–	–	–	–	–
–	–	–	–	–	–	–	–	–
Solution	Cu (g/L)	Zn (g/L)	Fe^T (g/L)	FeII (g/L)	H_2SO_4 (g/L)	–	SO_4 (g/L)	–
–	–	–	–	–	–	–	–	–
30 (A22)	18.58	0.06	0.27	0.26	1.7	–	30.5	–
–	–	–	–	–	–	–	–	–
–	–	–	–	–	–	–	–	–
–	–	–	–	–	–	–	–	–
Extraction	[b] Cu (%)	[b] Zn (%)	[b, c] Fe (%)	–	S^{2-} (%)	[d] S° (%)	–	[b] S^T (%)
–	–	–	–	–	–	–	–	–
30 (A22)	< 0 (99)	18 (92)	7 (98)	–	8	0	–	(99)
–	–	–	–	–	–	–	–	–
–	–	–	–	–	–	–	–	–
–	–	–	–	–	–	–	–	–

[a] 20°C; [b] Elemental accountability in brackets; [c] Fe (sln)/Fe (sld+sln)×100%; [d] S° yield, *i.e.*, $S°/S^{2-}{}_{rx}$×100%.

Stellenbosch University http://scholar.sun.ac.za

PLB1	Temp.	Imp. speed	P_g	p_{O2}°	Solids	Solids	Solution	[b] Density
Sample C	150°C	1000 rpm	1090 kPa	700 kPa	1.5 wt %	15 g	985 g	1094 g/L
[a] LS, QB	Cu	Zn	–	Fe (II)	H_2SO_4	–	SO_4	H_2O
0.35 g/L ea.	35 g/L	0 g/L	–	0 g/L	15 g/L	–	67.8 g/L	890.2 g
min (test)	Sld. (g)	Colour	Sln. (g)	Vol. (mL)	Colour	[b] Dens (g/L)	[b] E_{Ag} (mV)	[b] pH
–	–	–	–	–	–	–	–	–
30 (B12)	12.2	Red brown	896.5	808	Blue	1.109	465	1.05
–	–	–	–	–	–	–	–	–
–	–	–	–	–	–	–	–	–
120 (B15)	11.1	Deep red	911.8	825	Blue	1107	503	1.14
Solids	Cu (%)	Zn (%)	Fe (%)	–	S^{2-} (%)	S° (%)	SO_4 (%)	S^T (%)
Head	28.5	4.6	29.5	–	35.5	0.0	0.0	35.5
–	–	–	–	–	–	–	–	–
30 (B12)	20.8	0.8	33.9	–	24.3	10.2	0.1	34.4
–	–	–	–	–	–	–	–	–
–	–	–	–	–	–	–	–	–
120 (B15)	2.8	0.0	38.3	–	4.9	26.6	3.4	32.4
Solution	Cu (g/L)	Zn (g/L)	Fe^T (g/L)	FeII (g/L)	H_2SO_4 (g/L)	–	SO_4 (g/L)	–
–	–	–	–	–	–	–	–	–
30 (B12)	41.20	0.81	0.39	0.02	12.2	–	76.6	–
–	–	–	–	–	–	–	–	–
–	–	–	–	–	–	–	–	–
120 (B15)	41.91	0.79	0.18	0.01	12.8	–	77.7	–
Extraction	[c] Cu (%)	[c] Zn (%)	[c, d] Fe (%)	–	S^{2-} (%)	[e] S° (%)	–	[c] S^T (%)
–	–	–	–	–	–	–	–	–
30 (B12)	42 (100)	87 (107)	7 (99)	–	45	51	–	(96)
–	–	–	–	–	–	–	–	–
–	–	–	–	–	–	–	–	–
120 (B15)	93 (97)	100 (93)	3 (98)	–	90	62	–	(96)

[a] Norlig A, Orfom 2 (no pre-drying); [b] 20°C; [c] Elemental accountability in brackets; [d] Fe (sln)/Fe (sld+sln)×100%; [e] S° yield, *i.e.*, $S°/S^{2-}{}_{rx}$×100%.

Stellenbosch University http://scholar.sun.ac.za

PLB2	Temp.	Imp. speed	P_g	p_{O2}°	Solids	Solids	Solution	[b] Density
Sample C	150°C	1000 rpm	1090 kPa	700 kPa	0.5 wt %	5 g	995 g	1094 g/L
[a] LS, QB	Cu	Zn	–	Fe (II)	H_2SO_4	–	SO_4	H_2O
0.35 g/L ea.	35 g/L	0 g/L	–	0 g/L	15 g/L	–	67.8 g/L	899.3 g
min (test)	Sld. (g)	Colour	Sln. (g)	Vol. (mL)	Colour	[b] Dens (g/L)	[b] E_{Ag} (mV)	[b] pH
–	–	–	–	–	–	–	–	–
30 (B22)	3.6	Dark grey	939.1	856	Blue	1097	475	1.05
–	–	–	–	–	–	–	–	–
–	–	–	–	–	–	–	–	–
120 (B25)	3.8	Red	956.3	869	Blue	1100	506	1.13
Solids	Cu (%)	Zn (%)	Fe (%)	–	S^{2-} (%)	S° (%)	SO_4 (%)	S^T (%)
Head	28.5	4.6	29.5	–	35.5	0.0	0.0	35.5
–	–	–	–	–	–	–	–	–
30 (B22)	23.3	0.9	31.1	–	25.9	12.6	0.5	38.7
–	–	–	–	–	–	–	–	–
–	–	–	–	–	–	–	–	–
120 (B25)	1.7	0.0	37.8	–	6.7	23.6	1.5	31.0
Solution	Cu (g/L)	Zn (g/L)	Fe^T (g/L)	FeII (g/L)	H_2SO_4 (g/L)	–	SO_4 (g/L)	–
–	–	–	–	–	–	–	–	–
30 (B22)	35.3	0.25	0.25	0.04	14.1	–	68.4	–
–	–	–	–	–	–	–	–	–
–	–	–	–	–	–	–	–	–
120 (B25)	36.42	0.28	0.19	0.01	13.2	–	69.0	–
Extraction	[c] Cu (%)	[c] Zn (%)	[c, d] Fe (%)	–	S^{2-} (%)	[e] S° (%)	–	[c] S^T (%)
–	–	–	–	–	–	–	–	–
30 (B22)	42 (93)	86 (106)	14 (90)	–	48	53	–	(93)
–	–	–	–	–	–	–	–	–
–	–	–	–	–	–	–	–	–
120 (B25)	95 (95)	100 (105)	11 (107)	–	86	58	–	(94)

[a] Norlig A, Orfom 2 (no pre-drying); [b] 20°C; [c] Elemental accountability in brackets; [d] Fe (sln)/Fe (sld+sln)×100%; [e] S° yield, *i.e.*, $S°/S^{2-}{}_{rx}$×100%.

Stellenbosch University http://scholar.sun.ac.za

PLC1	Temp.	Imp. speed	P_g	p_{O2}°	Solids	Solids	Solution	[b] Density
Sample D	150°C	1000 rpm	1090 kPa	700 kPa	1.5 wt %	15 g	985 g	1051 g/L
[a] LS, QB	Cu	Zn	–	Fe (II)	H_2SO_4	–	SO_4	H_2O
0.35 g/L ea.	15 g/L	0 g/L	–	0 g/L	25 g/L	–	47.3 g/L	924.8 g
min (test)	Sld. (g)	Colour	Sln. (g)	Vol. (mL)	Colour	[b] Dens (g/L)	[b] E_{Ag} (mV)	[b] pH
30 (C11)	9.6	Black	970.2	916	Green	1059	481	0.90
45 (C12)	8.6	Dark grey	955.5	901	Blue	1060	491	0.86
60 (C13)	7.6	Dark grey	945.0	893	Green	1058	503	0.80
90 (C14)	8.0	Red	954.9	898	Blue	1063	596	0.82
150 (C15)	9.1	Red	898.8	843	Blue	1066	500	0.80
Solids	Cu (%)	Zn (%)	Fe (%)	–	S^{2-} (%)	S° (%)	SO_4 (%)	S^T (%)
Head	28.5	4.6	29.5	–	35.5	0.0	0.0	35.5
30 (C11)	30.7	0.3	24.9	–	30.5	14.1	0.3	45.2
45 (C12)	27.4	0.1	24.1	–	29.5	19.0	0.5	46.3
60 (C13)	26.9	0.1	22.6	–	29.5	22.8	0.4	51.8
90 (C14)	17.9	0.0	30.2	–	20.2	26.2	1.1	46.3
150 (C15)	5.5	0.0	35.9	–	7.5	28.5	2.3	38.0
Solution	Cu (g/L)	Zn (g/L)	Fe^T (g/L)	FeII (g/L)	H_2SO_4 (g/L)	–	SO_4 (g/L)	–
30 (C11)	17.09	0.69	2.34	0.67	18.8	–	50.9	–
45 (C12)	17.42	0.75	2.82	0.69	17.6	–	51.5	–
60 (C13)	18.04	0.75	3.00	0.50	18.4	–	53.9	–
90 (C14)	19.26	0.78	2.05	0.40	19.2	–	54.2	–
150 (C15)	20.62	0.81	1.18	0.01	21.2	–	56.4	–
Extraction	[c] Cu (%)	[c] Zn (%)	[c, d] Fe (%)	–	S^{2-} (%)	[e] S° (%)	–	[c] S^T (%)
30 (C11)	31 (101)	96 (96)	48 (102)	–	45	56	–	(98)
45 (C12)	45 (99)	99 (99)	57 (104)	–	52	59	–	(96)
60 (C13)	52 (99)	99 (98)	61 (99)	–	58	56	–	(99)
90 (C14)	67 (102)	100 (102)	42 (96)	–	70	56	–	(98)
150 (C15)	88 (98)	100 (99)	23 (96)	–	87	56	–	(95)

[a] Norlig A, Orfom 2 (no pre-drying); [b] 20°C; [c] Elemental accountability in brackets; [d] Fe (sln)/Fe (sld+sln)×100%; [e] S° yield, *i.e.*, $S°/S^{2-}{}_{rx}$×100%.

Stellenbosch University http://scholar.sun.ac.za

PLC2	Temp.	Imp. speed	P_g	p_{O2}°	Solids	Solids	Solution	[b] Density
Sample D	150°C	1000 rpm	1090 kPa	700 kPa	1.0 wt %	10 g	990 g	1052 g/L
[a] LS, QB	Cu	Zn	–	Fe (II)	H_2SO_4	–	SO_4	H_2O
0.35 g/L ea.	15 g/L	0 g/L	–	1 g/L	25 g/L	–	49.0 g/L	926.9 g
min (test)	Sld. (g)	Colour	Sln. (g)	Vol. (mL)	Colour	[b] Dens (g/L)	[b] E_{Ag} (mV)	[b] pH
15 (C21)	8.7	Black	899.6	846	Green	1063	457	0.80
30 (C22)	7.1	Black	875.7	825	Green	1062	489	0.83
45 (C23)	6.3	Grey	873.2	820	Green	1065	494	0.84
60 (C24)	5.5	Grey	764.7	702	Green	1089	487	0.74
–	–	–	–	–	–	–	–	–
Solids	Cu (%)	Zn (%)	Fe (%)	–	S^{2-} (%)	S° (%)	SO_4 (%)	S^T (%)
Head	28.5	4.6	29.5	–	35.5	0.0	0.0	35.5
15 (C21)	27.3	3.95	27.1	–	31.3	5.1	0.0	36.8
30 (C22)	28.4	2.2	26.6	–	33.6	6.7	0.0	42.3
45 (C23)	26.5	1.3	27.2	–	31.9	8.2	0.0	44.8
60 (C24)	26.8	1.2	23.6	–	28.0	15.6	0.0	48.7
–	–	–	–	–	–	–	–	–
Solution	Cu (g/L)	Zn (g/L)	Fe^T (g/L)	FeII (g/L)	H_2SO_4 (g/L)	–	SO_4 (g/L)	–
15 (C21)	17.4	0.14	1.84	1.05	25.3	–	55.3	–
30 (C22)	17.8	0.39	2.11	0.51	23.3	–	55.4	–
45 (C23)	18.18	0.47	2.16	0.61	23.3	–	56.3	–
60 (C24)	22.10	0.65	3.54	0.53	22.7	–	65.5	–
–	–	–	–	–	–	–	–	–
Extraction	[c] Cu (%)	[c] Zn (%)	[c, d] Fe (%)	–	S^{2-} (%)	[e] S° (%)	–	[c] S^T (%)
15 (C21)	17 (101)	25 (100)	40 (101)	–	23	33	–	(99)
30 (C22)	29 (98)	66 (104)	45 (93)	–	33	41	–	(96)
45 (C23)	41 (98)	82 (103)	45 (90)	–	43	34	–	(95)
60 (C24)	48 (100)	86 (113)	64 (97)	–	57	43	–	(94)
–	–	–	–	–	–	–	–	–

[a] Arbo A02, Orfom 2 (no pre-drying); [b] 20°C; [c] Elemental accountability in brackets; [d] Fe (sln)/Fe (sld+sln)×100%; [e] S° yield, *i.e.*, $S°/S^{2-}{}_{rx}$×100%.

Stellenbosch University http://scholar.sun.ac.za

PLD1	Temp.	Imp. speed	P_g	p_{O2}°	Solids	Solids	Solution	[b] Density
Sample C	150°C	1000 rpm	1090 kPa	700 kPa	1.5 wt %	15 g	985 g	1101 g/L
[a] LS, QB	Cu	Zn	–	Fe (II)	H_2SO_4	–	SO_4	H_2O
0.35 g/L ea.	35 g/L	0 g/L	–	0 g/L	35 g/L	–	87.4 g/L	873.0 g
min (test)	Sld. (g)	Colour	Sln. (g)	Vol. (mL)	Colour	[b] Dens (g/L)	[b] E_{Ag} (mV)	[b] pH
15 (D11)	10.0	Grey	943.7	846	Green	1116	481	0.79
30 (D12)	7.9	Grey	917.2	820	Green	1118	493	0.82
60 (D13)	6.0	Grey	906.9	805	Green	1126	506	1.00
90 (D14)	4.8	Drk brown	940.8	835	Green	1127	519	0.94
120 (D15)	5.4	Red brown	914.2	810	Green	1128	533	0.85
Solids	Cu (%)	Zn (%)	Fe (%)	–	S^{2-} (%)	S° (%)	SO_4 (%)	S^T (%)
Head	28.5	4.6	29.5	–	35.5	0.0	0.0	35.5
15 (D11)	27.6	0.9	20.7	–	34.5	13.2	0.0	50.4
30 (D12)	21.9	0.1	17.7	–	32.4	22.0	0.0	54.8
60 (D13)	14.9	0.1	13.9	–	30.0	38.0	0.3	71.6
90 (D14)	10.9	0.1	11.9	–	16.7	55.0	1.7	74.9
120 (D15)	6.0	0.0	13.7	–	6.8	55.8	1.4	63.4
Solution	Cu (g/L)	Zn (g/L)	Fe^T (g/L)	FeII (g/L)	H_2SO_4 (g/L)	–	SO_4 (g/L)	–
15 (D11)	39.5	0.74	2.89	0.65	26.5	–	93.8	–
30 (D12)	40.9	0.82	3.81	0.54	24.2	–	96.3	–
60 (D13)	42.3	0.83	4.58	0.36	22.4	–	98.8	–
90 (D14)	41.8	0.80	4.71	0.05	21.0	–	97.2	–
120 (D15)	44.4	0.87	4.84	0.01	23.0	–	103.6	–
Extraction	[c] Cu (%)	[c] Zn (%)	[c, d] Fe (%)	–	S^{2-} (%)	[e] S° (%)	–	[c] S^T (%)
15 (D11)	36 (102)	88 (102)	55 (101)	–	36	68	–	(100)
30 (D12)	60 (99)	99 (98)	70 (101)	–	52	62	–	(97)
60 (D13)	79 (98)	100 (96)	83 (101)	–	66	64	–	(98)
90 (D14)	88 (99)	100 (96)	88 (101)	–	85	58	–	(97)
120 (D15)	92 (102)	100 (102)	88 (105)	–	93	60	–	(99)

[a] Norlig A, Orfom 2 (no pre-drying); [b] 20°C; [c] Elemental accountability in brackets; [d] Fe (sln)/Fe (sld+sln)×100%; [e] S° yield, *i.e.*, $S°/S^{2-}{}_{rx}$×100%.

Stellenbosch University http://scholar.sun.ac.za

PLD2	Temp.	Imp. speed	P_g	p_{O2}°	Solids	Solids	Solution	[b] Density
Sample C	150°C	1000 rpm	1090 kPa	700 kPa	1.5 wt %	15 g	985 g	1105 g/L
[a] LS, QB	Cu	Zn	–	Fe (II)	H_2SO_4	–	SO_4	H_2O
0.35 g/L ea.	35 g/L	0 g/L	–	0 g/L	35 g/L	–	87.4 g/L	873.4 g
min (test)	Sld. (g)	Colour	Sln. (g)	Vol. (mL)	Colour	[b] Dens (g/L)	[b] E_{Ag} (mV)	[b] pH
30 (D21)	8.6	Grey	921.8	821	Green	1123	462	0.98
45 (D22)	6.7	Brown	902.4	798	Green	1131	476	0.99
60 (D23)	6.2	Brown	892.6	790	Green	1130	481	1.00
90 (D24)	5.9	Brown	938.9	833	Blue	1127	487	0.98
150 (D25)	6.2	Deep red	876.1	773	Blue	1134	514	0.87
Solids	Cu (%)	Zn (%)	Fe (%)	–	S^{2-} (%)	S° (%)	SO_4 (%)	S^T (%)
Head	28.5	4.6	29.5	–	35.5	0.0	0.0	35.5
30 (D21)	21.4	0.1	21.9	–	30.7	18.8	0.2	50.0
45 (D22)	15.4	0.1	17.0	–	26.0	29.9	1.0	56.3
60 (D23)	13.0	0.0	17.1	–	23.1	36.6	1.6	60.5
90 (D24)	10.8	0.1	11.6	–	21.1	39.7	0.4	63.8
150 (D25)	4.4	0.0	19.4	–	5.9	47.9	2.8	54.1
Solution	Cu (g/L)	Zn (g/L)	Fe^T (g/L)	FeII (g/L)	H_2SO_4 (g/L)	–	SO_4 (g/L)	–
30 (D21)	38.73	0.81	2.95	0.55	24.2	–	90.8	–
45 (D22)	41.00	0.83	3.80	0.43	23.6	–	95.9	–
60 (D23)	41.01	0.84	3.81	0.36	23.2	–	95.6	–
90 (D24)	41.72	0.82	4.15	0.33	22.2	–	96.6	–
150 (D25)	43.75	0.90	4.22	0.01	23.4	–	101.4	–
Extraction	[c] Cu (%)	[c] Zn (%)	[c, d] Fe (%)	–	S^{2-} (%)	[e] S° (%)	–	[c] S^T (%)
30 (D21)	58 (95)	99 (96)	54 (96)	–	51	58	–	(92)
45 (D22)	76 (95)	100 (95)	67 (93)	–	68	55	–	(93)
60 (D23)	81 (93)	100 (95)	67 (90)	–	74	57	–	(92)
90 (D24)	85 (100)	100 (97)	77 (92)	–	77	56	–	(97)
150 (D25)	94 (96)	100 (100)	72 (99)	–	93	59	–	(93)

[a] Norlig A, Orfom 2 (no pre-drying); [b] 20°C; [c] Elemental accountability in brackets; [d] Fe (sln)/Fe (sld+sln)×100%; [e] S° yield, *i.e.*, $S°/S^{2-}{}_{rx}$×100%.

Stellenbosch University http://scholar.sun.ac.za

PLD3	Temp.	Imp. speed	P_g	p_{O2}°	Solids	Solids	Solution	[b] Density
Sample C	150°C	1000 rpm	1490 kPa	1100 kPa	1.5 wt %	15 g	985 g	1101 g/L
[a] LS, QB	Cu	Zn	–	Fe (II)	H_2SO_4	–	SO_4	H_2O
0.35 g/L ea.	35 g/L	0 g/L	–	0 g/L	35 g/L	–	87.4 g/L	873.0 g
min (test)	Sld. (g)	Colour	Sln. (g)	Vol. (mL)	Colour	[b] Dens (g/L)	[b] E_{Ag} (mV)	[b] pH
15 (D31)	9.2	Grey	945.8	847	Green	1116	560	1.10
30 (D32)	7.7	Grey	917.2	815	Green	1125	487	0.92
60 (D33)	5.6	Lgt brown	898.0	793	Green	1132	512	0.92
90 (D34)	5.1	Lgt brown	906.7	800	Green	1134	517	0.85
120 (D35)	4.3	Lgt brown	885.8	778	Green	1139	545	0.92
Solids	Cu (%)	Zn (%)	Fe (%)	–	S^{2-} (%)	S° (%)	SO_4 (%)	S^T (%)
Head	28.5	4.6	29.5	–	35.5	0.0	0.0	35.5
15 (D31)	27.0	0.5	19.0	–	32.8	17.2	0.0	50.0
30 (D32)	20.0	0.1	17.8	–	29.7	26.0	0.0	55.7
60 (D33)	12.5	0.1	11.7	–	26.4	44.7	0.9	71.1
90 (D34)	7.8	0.0	10.1	–	21.1	49.8	5.9	71.5
120 (D35)	6.0	0.0	9.2	–	10.7	66.8	4.9	80.8
Solution	Cu (g/L)	Zn (g/L)	Fe^T (g/L)	FeII (g/L)	H_2SO_4 (g/L)	–	SO_4 (g/L)	–
15 (D31)	38.53	0.77	3.19	0.58	23.4	–	90.2	–
30 (D32)	40.54	0.79	3.75	0.48	23.3	–	94.7	–
60 (D33)	43.04	0.81	4.23	0.03	21.6	–	98.5	–
90 (D34)	42.97	0.82	4.83	0.02	21.3	–	99.6	–
120 (D35)	45.10	0.84	4.84	0.01	21.1	–	102.7	–
Extraction	[c] Cu (%)	[c] Zn (%)	[c, d] Fe (%)	–	S^{2-} (%)	[e] S° (%)	–	[c] S^T (%)
15 (D31)	42 (99)	94 (99)	61 (100)	–	44	67	–	(95)
30 (D32)	64 (97)	99 (94)	68 (99)	–	57	65	–	(95)
60 (D33)	84 (98)	100 (92)	75 (90)	–	72	64	–	(95)
90 (D34)	91 (98)	100 (95)	86 (98)	–	80	59	–	(96)
120 (D35)	94 (99)	100 (95)	84 (93)	–	91	59	–	(95)

[a] Norlig A, Orfom 2 (no pre-drying); [b] 20°C; [c] Elemental accountability in brackets; [d] Fe (sln)/Fe (sld+sln)×100%; [e] S° yield, *i.e.*, $S°/S^{2-}{}_{rx}$×100%.

Stellenbosch University http://scholar.sun.ac.za

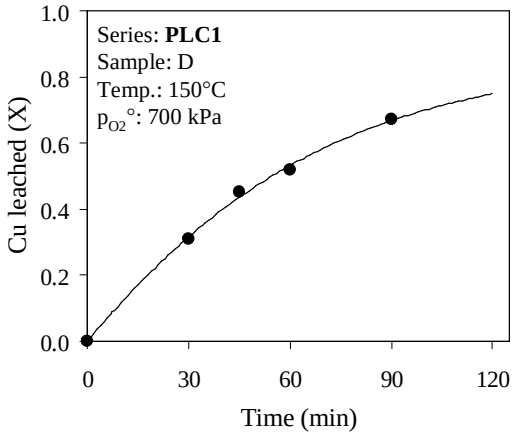

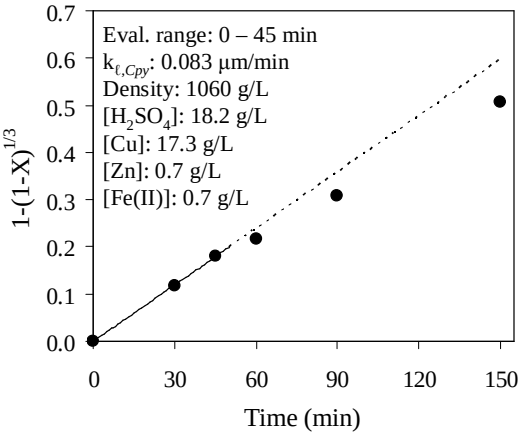

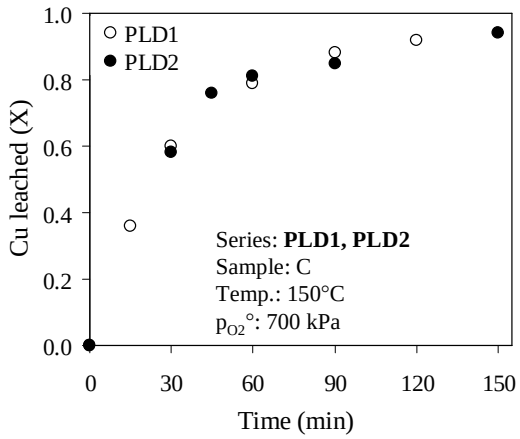

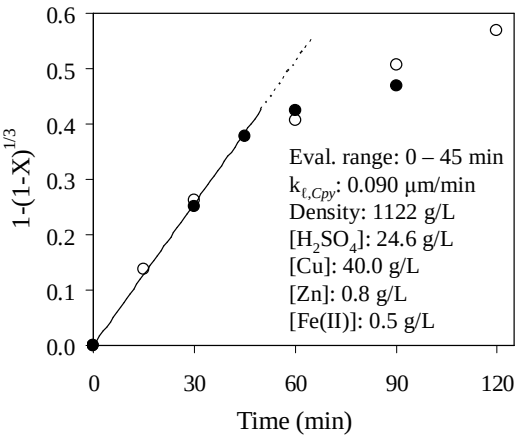

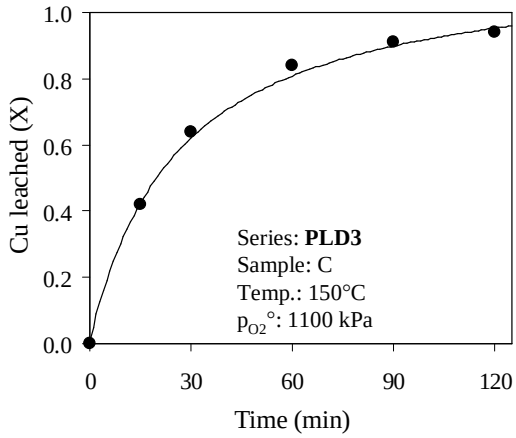

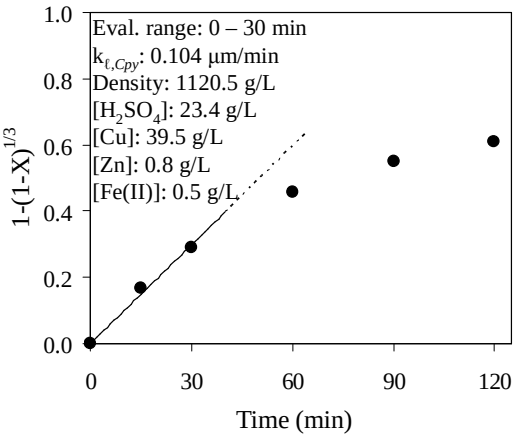

Stellenbosch University http://scholar.sun.ac.za

G.3 Reaction regimes

These tests focused on identifying and elaborating on the different reaction regimes during the oxidation of the HBMS 777 concentrate under MT autoclave conditions.

PLE1	Temp.	Imp. speed	P_g	p_{O2}°	Solids	Solids	Solution	[b] Density
Sample C	150°C	1000 rpm	1090 kPa	700 kPa	1.5 wt %	15 g	985 g	1101 g/L
[a] LS, QB	Cu	Zn	–	Fe (II)	H_2SO_4	–	SO_4	H_2O
0.20 g/L ea.	35 g/L	0 g/L	–	0 g/L	35 g/L	–	87.4 g/L	873.2 g
min (test)	Sld. (g)	Colour	Sln. (g)	Vol. (mL)	Colour	[b] Dens (g/L)	[b] E_{Ag} (mV)	[b] pH
15 (E11)	9.3	Grey	919.4	819	Green	1122	488	0.80
30 (E12)	7.1	Grey	916.4	819	Green	1119	491	0.85
60 (E13)	5.5	Grey	908.9	804	Green	1130	516	0.87
90 (E14)	5.0	Lgt brown	949.6	840	Green	1130	522	0.85
120 (E15)	5.8	Drk brown	915.9	813	Green	1127	545	0.87
Solids	Cu (%)	Zn (%)	Fe (%)	–	S^{2-} (%)	S° (%)	SO_4 (%)	S^T (%)
Head	28.5	4.6	29.5	–	35.5	0.0	0.0	35.5
15 (E11)	31.2	0.7	16.3	–	32.6	17.8	0.0	49.9
30 (E12)	24.0	0.2	15.0	–	31.3	27.5	0.0	56.4
60 (E13)	15.9	0.1	9.8	–	26.5	41.2	0.4	67.8
90 (E14)	8.4	0.1	8.9	–	17.7	55.9	1.0	73.8
120 (E15)	5.2	0.1	16.0	–	9.3	50.0	1.7	60.3
Solution	Cu (g/L)	Zn (g/L)	Fe^T (g/L)	FeII (g/L)	H_2SO_4 (g/L)	–	SO_4 (g/L)	–
15 (E11)	41.1	0.73	3.72	0.62	24.4	–	96.2	–
30 (E12)	42.9	0.80	4.25	0.55	22.3	–	98.5	–
60 (E13)	44.1	0.78	5.17	0.33	21.0	–	101.6	–
90 (E14)	42.4	0.74	5.03	0.24	19.6	–	97.3	–
120 (E15)	44.4	0.81	4.82	0.01	21.4	–	101.9	–
Extraction	[c] Cu (%)	[c] Zn (%)	[c, d] Fe (%)	–	S^{2-} (%)	[e] S° (%)	–	[c] S^T (%)
15 (E11)	33 (102)	91 (95)	68 (102)	–	44	61	–	(98)
30 (E12)	60 (103)	98 (97)	78 (102)	–	59	62	–	(98)
60 (E13)	80 (102)	99 (91)	93 (105)	–	73	58	–	(98)
90 (E14)	90 (101)	99 (90)	95 (105)	–	84	62	–	(98)
120 (E15)	93 (102)	99 (95)	88 (109)	–	90	60	–	(98)

[a] Norlig A, Orfom 2 (no pre-drying); [b] 20°C; [c] Elemental accountability in brackets; [d] Fe (sln)/Fe (sld+sln)×100%; [e] S° yield, *i.e.*, $S°/S^{2-}{}_{rx}$×100%.

Stellenbosch University http://scholar.sun.ac.za

PLE2	Temp.	Imp. speed	P_g	p_{O2}°	Solids	Solids	Solution	[b] Density
Sample C	150°C	1000 rpm	1090 kPa	700 kPa	1.5 wt %	15 g	985 g	1101 g/L
[a] LS, QB	Cu	Zn	–	Fe (II)	H_2SO_4	–	SO_4	H_2O
0.50 g/L ea.	35 g/L	0 g/L	–	0 g/L	35 g/L	–	87.4 g/L	873.0 g
min (test)	Sld. (g)	Colour	Sln. (g)	Vol. (mL)	Colour	[b] Dens (g/L)	[b] E_{Ag} (mV)	[b] pH
15 (E21)	9.4	Grey	950.8	850	Green	1118	477	0.91
30 (E22)	8.0	Grey	927.7	831	Green	1116	482	0.73
60 (E23)	4.6	Grey	919.4	817	Green	1125	514	0.87
90 (E24)	5.3	Lgt brown	947.6	843	Green	1124	523	0.84
120 (E25)	4.9	Brown	973.6	866	Green	1124	523	0.88
Solids	Cu (%)	Zn (%)	Fe (%)	–	S^{2-} (%)	S° (%)	SO_4 (%)	S^T (%)
Head	28.5	4.6	29.5	–	35.5	0.0	0.0	35.5
15 (E21)	28.8	0.5	19.5	–	32.8	16.1	0.0	50.4
30 (E22)	22.9	0.1	20.2	–	34.8	20.1	0.0	55.0
60 (E23)	14.3	0.1	7.8	–	31.3	45.5	0.0	72.8
90 (E24)	9.1	0.0	11.4	–	18.9	52.5	0.3	75.1
120 (E25)	5.5	0.0	13.8	–	13.5	55.6	1.5	69.9
Solution	Cu (g/L)	Zn (g/L)	Fe^T (g/L)	FeII (g/L)	H_2SO_4 (g/L)	–	SO_4 (g/L)	–
15 (E21)	39.7	0.76	2.96	0.64	24.3	–	92.2	–
30 (E22)	39.7	0.80	3.36	0.74	24.9	–	93.8	–
60 (E23)	41.7	0.84	4.83	0.35	21.0	–	97.2	–
90 (E24)	41.2	0.81	4.78	0.27	20.3	–	95.6	–
120 (E25)	42.5	0.80	4.83	0.21	20.9	–	98.4	–
Extraction	[c] Cu (%)	[c] Zn (%)	[c, d] Fe (%)	–	S^{2-} (%)	[e] S° (%)	–	[c] S^T (%)
15 (E21)	37 (102)	93 (100)	56 (97)	–	43	66	–	(98)
30 (E22)	58 (98)	99 (97)	63 (99)	–	48	62	–	(96)
60 (E23)	85 (98)	100 (99)	88 (96)	–	73	53	–	(94)
90 (E24)	89 (99)	100 (98)	90 (104)	–	81	64	–	(98)
120 (E25)	94 (101)	100 (99)	88 (108)	–	88	58	–	(99)

[a] Norlig A, Orfom 2 (no pre-drying); [b] 20°C; [c] Elemental accountability in brackets; [d] Fe (sln)/Fe (sld+sln)×100%; [e] S° yield, *i.e.*, $S°/S^{2-}{}_{rx}$×100%.

Stellenbosch University http://scholar.sun.ac.za

PLE3	Temp.	Imp. speed	P_g	p_{O2}°	Solids	Solids	Solution	[b] Density
Sample C	150°C	750 rpm	1090 kPa	700 kPa	1.5 wt %	15 g	985 g	1105 g/L
[a] LS, QB	Cu	Zn	–	Fe (II)	H_2SO_4	–	SO_4	H_2O
0.35 g/L ea.	35 g/L	0 g/L	–	0 g/L	35 g/L	–	87.4 g/L	873.4 g
min (test)	Sld. (g)	Colour	Sln. (g)	Vol. (mL)	Colour	[b] Dens (g/L)	[b] E_{Ag} (mV)	[b] pH
15 (E31)	9.8	Grey	966.5	865	Green	1117	491	0.83
45 (E32)	7.0	Brown	922.1	814	Green	1133	484	0.93
150 (E35)	6.5	Red	888.3	784	Blue	1133	503	0.91
Solids	Cu (%)	Zn (%)	Fe (%)	–	S^{2-} (%)	S° (%)	SO_4 (%)	S^T (%)
Head	28.5	4.6	29.5	–	35.5	0.0	0.0	35.5
15 (E31)	30.1	0.8	18.2	–	36.1	13.1	0.0	49.1
45 (E32)	16.1	0.0	17.7	–	27.1	32.3	0.2	58.0
150 (E35)	6.5	0.0	22.1	–	7.1	46.6	2.5	53.0
Solution	Cu (g/L)	Zn (g/L)	Fe^T (g/L)	FeII (g/L)	H_2SO_4 (g/L)	–	SO_4 (g/L)	–
15 (E31)	40.10	0.77	2.94	0.89	25.3	–	93.5	–
45 (E32)	40.40	0.91	3.35	0.75	22.8	–	96.4	–
150 (E35)	44.12	0.79	4.50	0.01	24.2	–	103.4	–
Extraction	[c] Cu (%)	[c] Zn (%)	[c, d] Fe (%)	–	S^{2-} (%)	[e] S° (%)	–	[c] S^T (%)
15 (E31)	32 (106)	88 (107)	57 (97)	–	34	70	–	(101)
45 (E32)	74 (98)	100 (106)	74 (102)	–	65	64	–	(96)
150 (E35)	90 (99)	100 (89)	78 (110)	–	91	61	–	(97)

[a] Norlig A, Orfom 2 (no pre-drying); [b] 20°C; [c] Elemental accountability in brackets; [d] Fe (sln)/Fe (sld+sln)×100%; [e] S° yield, *i.e.*, $S°/S^{2-}{}_{rx}$×100%.

Stellenbosch University http://scholar.sun.ac.za

PLE4	Temp.	Imp. speed	P_g	p_{O2}°	Solids	Solids	Solution	[b] Density
Sample C	150°C	1000 rpm	1090 kPa	700 kPa	1.5 wt %	15 g	985 g	1101 g/L
[a] LS, QB	Cu	Zn	–	Fe (II)	H_2SO_4	–	SO_4	H_2O
0.35 g/L ea.	35 g/L	0 g/L	–	0 g/L	35 g/L	–	87.4 g/L	873.0 g
min (test)	Sld. (g)	Colour	Sln. (g)	Vol. (mL)	Colour	[b] Dens (g/L)	[b] E_{Ag} (mV)	[b] pH
60 (E43)	6.4	Grey	965.0	855	Green	1129	500	0.92

Solids	Cu (%)	Zn (%)	Fe (%)	–	S^{2-} (%)	S° (%)	SO_4 (%)	S^T (%)
Head	28.5	4.6	29.5	–	35.5	0.0	0.0	35.5
60 (D43)	15.2	0.1	14.0	–	31.5	37.4	0.1	69.8

Solution	Cu (g/L)	Zn (g/L)	Fe^T (g/L)	FeII (g/L)	H_2SO_4 (g/L)	–	SO_4 (g/L)	–
60 (D43)	41.4	0.77	4.66	0.55	23.3	–	98.3	–

Extraction	[c] Cu (%)	[c] Zn (%)	[c, d] Fe (%)	–	S^{2-} (%)	[e] S° (%)	–	[c] S^T (%)
60 (D43)	77 (102)	99 (95)	89 (109)	–	62	71	–	(103)

[a] Norlig A, Orfom 2 (no pre-drying) injected at 0 min **& after 45 min**; [b] 20°C; [c] Elemental accountability in brackets; [d] Fe (sln)/Fe (sld+sln)×100%; [e] S° yield, *i.e.*, $S°/S^{2-}_{rx}$×100%.

Stellenbosch University http://scholar.sun.ac.za

PLE5	Temp.	Imp. speed	P_g	p_{O2}°	Solids	Solids	Solution	[b] Density
Sample C	150°C	1000 rpm	1090 kPa	700 kPa	1.5 wt %	15 g	985 g	1057 g/L
[a] LS, QB	Cu	Zn	–	Fe (II)	H_2SO_4	–	SO_4	H_2O
0.35 g/L ea.	15 g/L	0 g/L	–	0 g/L	35 g/L	–	57.1 g/L	915.8 g
min (test)	Sld. (g)	Colour	Sln. (g)	Vol. (mL)	Colour	[b] Dens (g/L)	[b] E_{Ag} (mV)	[b] pH
15 (E51)	9.8	Grey	932.5	872	Green	1069	476	0.76
30 (E52)	7.5	Grey	927.6	865	Green	1073	452	0.86
45 (E53)	6.5	Grey	927.6	862	Green	1076	471	0.91
60 (E54)	6.1	Grey	884.6	821	Green	1077	504	0.60
90 (E55)	5.5	Red brown	890.3	823	Green	1082	523	0.57
150 (E56)	5.3	Red	950.7	884	Green	1076	516	1.05
Solids	Cu (%)	Zn (%)	Fe (%)	–	S^{2-} (%)	S° (%)	SO_4 (%)	S^T (%)
Head	28.5	4.6	29.5	–	35.5	0.0	0.0	35.5
15 (E51)	27.5	0.8	19.9	–	36.6	11.3	0.0	47.5
30 (E52)	22.9	0.1	21.0	–	29.5	23.3	0.8	52.1
45 (E53)	18.3	0.1	14.5	–	27.2	33.4	0.7	61.0
60 (E54)	16.4	0.0	14.8	–	23.4	39.9	1.2	61.0
90 (E55)	13.4	0.0	16.9	–	18.6	45.5	1.3	64.0
150 (E56)	5.1	0.0	20.7	–	7.3	52.7	2.4	60.8
Solution	Cu (g/L)	Zn (g/L)	Fe^T (g/L)	FeII (g/L)	H_2SO_4 (g/L)	–	SO_4 (g/L)	–
15 (E51)	17.65	0.73	2.94	0.69	26.6	–	61.0	–
30 (E52)	18.64	0.79	3.12	0.76	24.7	–	61.1	–
45 (E53)	19.84	0.82	4.25	0.59	22.4	–	63.8	–
60 (E54)	20.49	0.84	4.14	0.55	24.0	–	66.1	–
90 (E55)	21.66	0.86	4.57	0.14	22.3	–	67.7	–
150 (E56)	20.33	0.76	4.10	0.01	23.3	–	65.4	–
Extraction	[c] Cu (%)	[c] Zn (%)	[c, d] Fe (%)	–	S^{2-} (%)	[e] S° (%)	–	[c] S^T (%)
15 (E51)	37 (99)	88 (103)	57 (101)	–	33	62	–	(96)
30 (E52)	61 (97)	99 (98)	60 (95)	–	59	55	–	(92)
45 (E53)	73 (100)	99 (102)	81 (102)	–	67	60	–	(96)
60 (E54)	77 (97)	100 (99)	76 (96)	–	74	61	–	(94)
90 (E55)	83 (101)	100 (101)	83 (104)	–	81	57	–	(95)
150 (E56)	94 (99)	100 (96)	80 (105)	–	93	55	–	(96)

[a] Norlig A, Orfom 2 (no pre-drying); [b] 20°C; [c] Elemental accountability in brackets; [d] Fe (sln)/Fe (sld+sln)×100%; [e] S° yield, *i.e.*, $S°/S^{2-}{}_{rx}$×100%.

Stellenbosch University http://scholar.sun.ac.za

PLE6	Temp.	Imp. speed	P_g	p_{O2}°	Solids	Solids	Solution	[b] Density
Sample C	150°C	1000 rpm	1090 kPa	700 kPa	1.5 wt %	15 g	985 g	1021 g/L
[a] LS, QB	Cu	Zn	–	Fe (II)	H_2SO_4	–	SO_4	H_2O
0.35 g/L ea.	0 g/L	0 g/L	–	0 g/L	35 g/L	–	34.4 g/L	896.0 g
min (test)	Sld. (g)	Colour	Sln. (g)	Vol. (mL)	Colour	[b] Dens (g/L)	[b] E_{Ag} (mV)	[b] pH
60 (E63)	5.9	Grey	947.3	915	Green	1035	487	0.64
90 (E64)	4.9	Grey	905.9	872	Green	1039	518	0.62

Solids	Cu (%)	Zn (%)	Fe (%)	–	S^{2-} (%)	S° (%)	SO_4 (%)	S^T (%)
Head	28.5	4.6	29.5	–	35.5	0.0	0.0	35.5
60 (E63)	12.7	0.0	14.5	–	18.7	40.7	0.3	60.0
90 (E64)	11.7	0.0	9.9	–	19.5	54.6	0.6	74.0

Solution	Cu (g/L)	Zn (g/L)	Fe^T (g/L)	FeII (g/L)	H_2SO_4 (g/L)	–	SO_4 (g/L)	–
60 (E63)	3.76	0.72	3.88	0.74	23.6	–	39.4	–
90 (E64)	4.56	0.74	4.43	0.30	21.8	–	40.7	–

Extraction	[c] Cu (%)	[c] Zn (%)	[c, d] Fe (%)	–	S^{2-} (%)	[e] S° (%)	–	[c] S^T (%)
60 (E63)	83 (96)	100 (94)	79 (98)	–	80	56	–	(93)
90 (E64)	87 (105)	100 (92)	86 (97)	–	82	60	–	(93)

[a] Norlig A, Orfom 2 (no pre-drying); [b] 20°C; [c] Elemental accountability in brackets; [d] Fe (sln)/Fe (sld+sln)×100%; [e] S° yield, *i.e.*, $S°/S^{2-}{}_{rx}$×100%.

Stellenbosch University http://scholar.sun.ac.za

PLE7	Temp.	Imp. speed	P_g	p_{O2}°	Solids	Solids	Solution	[b] Density
Sample C	150°C	1000 rpm	1090 kPa	700 kPa	1.5 wt %	15 g	985 g	1057 g/L
[a] LS, QB	Cu	Zn	–	Fe (II)	H_2SO_4	–	SO_4	H_2O
0.35 g/L ea.	15 g/L	0 g/L	–	0 g/L	35 g/L	–	57.1 g/L	915.8 g
min (test)	Sld. (g)	Colour	Sln. (g)	Vol. (mL)	Colour	[b] Dens (g/L)	[b] E_{Ag} (mV)	[b] pH
60 (E73)	6.3	Grey	968.1	903	Green	1072	499	0.59
90 (E74)	5.0	Grey	918.9	857	Green	1072	512	0.59
Solids	Cu (%)	Zn (%)	Fe (%)	–	S^{2-} (%)	S° (%)	SO_4 (%)	S^T (%)
Head	28.5	4.6	29.5	–	35.5	0.0	0.0	35.5
60 (E73)	13.8	0.1	13.8	–	20.8	42.6	0.6	62.5
90 (E74)	10.3	0.0	9.3	–	18.0	55.0	0.6	71.0
Solution	Cu (g/L)	Zn (g/L)	Fe^T (g/L)	FeII (g/L)	H_2SO_4 (g/L)	–	SO_4 (g/L)	–
60 (E73)	18.28	0.76	3.84	0.60	22.2	–	60.1	–
90 (E74)	19.89	0.82	4.30	0.40	22.4	–	64.1	–
Extraction	[c] Cu (%)	[c] Zn (%)	[c, d] Fe (%)	–	S^{2-} (%)	[e] S° (%)	–	[c] S^T (%)
60 (E73)	80 (95)	100 (98)	77 (96)	–	76	65	–	(94)
90 (E74)	88 (96)	100 (100)	82 (92)	–	83	61	–	(94)

[a] Norlig A, Orfom 2 (no pre-drying) injected at 0 min **& after 45 min**; [b] 20°C; [c] Elemental accountability in brackets; [d] Fe (sln)/Fe (sld+sln)×100%; [e] S° yield, *i.e.*, $S°/S^{2-}_{rx}$×100%.

Stellenbosch University http://scholar.sun.ac.za

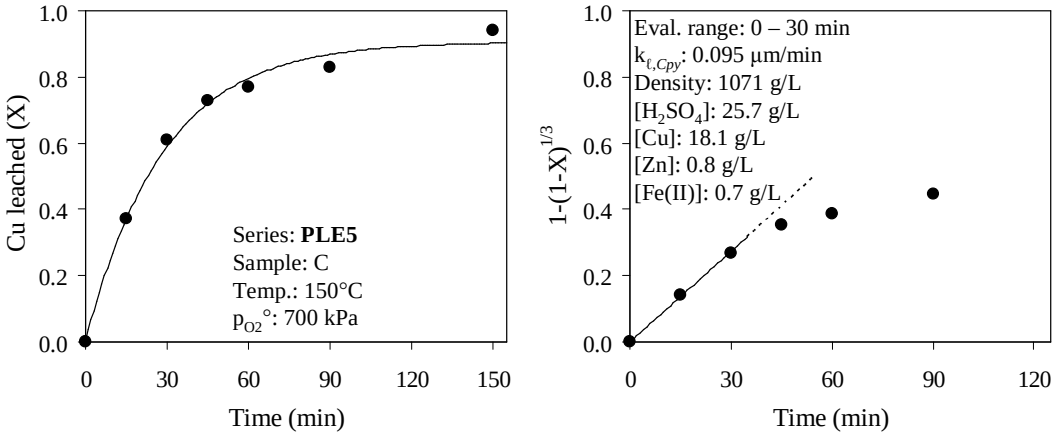

Stellenbosch University http://scholar.sun.ac.za

G.4 Particle size effects at different acid concentrations

These tests investigated the effects of different particle sizes at various acid concentrations during the oxidation of the HBMS 777 concentrate under MT autoclave conditions.

PLF1	Temp.	Imp. speed	P_g	p_{O2}°	Solids	Solids	Solution	[b] Density
Sample A	150°C	1000 rpm	1090 kPa	700 kPa	1.5 wt %	15 g	985 g	1046 g/L
[a] LS, QB	Cu	Zn	–	Fe (II)	H_2SO_4	–	SO_4	H_2O
0.35 g/L ea.	15 g/L	0 g/L	–	0 g/L	15 g/L	–	37.5 g/L	933.9 g
min (test)	Sld. (g)	Colour	Sln. (g)	Vol. (mL)	Colour	[b] Dens (g/L)	[b] E_{Ag} (mV)	[b] pH
7.5 (F11)	9.4	Brown	935.0	885	Green	1057	470	1.08
15 (F12)	10.0	Brown	934.1	884	Green	1057	479	1.08
30 (F13)	9.8	Lgt brown	939.9	889	Green	1057	490	1.08
45 (F14)	8.8	Org brown	940.1	889	Grn blue	1057	485	1.02
60 (F15)	9.6	Org brown	950.0	900	Blue	1056	490	1.06
Solids	Cu (%)	Zn (%)	Fe (%)	–	S^{2-} (%)	S° (%)	SO_4 (%)	S^T (%)
Head	28.5	4.6	29.5	–	35.5	0.0	0.0	35.5
7.5 (F11)	14.9	0.1	28.8	–	15.0	23.7	4.0	39.0
15 (F12)	7.8	0.1	33.4	–	6.5	26.7	6.6	34.9
30 (F13)	1.6	0.1	36.0	–	2.5	26.7	6.5	29.4
45 (F14)	1.5	0.1	42.6	–	2.0	26.4	4.0	29.2
60 (F15)	1.1	0.0	44.9	–	1.2	26.0	4.0	28.6
Solution	Cu (g/L)	Zn (g/L)	Fe^T (g/L)	FeII (g/L)	H_2SO_4 (g/L)	–	SO_4 (g/L)	–
7.5 (F11)	17.97	0.75	1.69	0.05	9.7	–	42.3	–
15 (F12)	18.22	0.72	1.07	0.03	11.5	–	42.8	–
30 (F13)	18.78	0.76	0.61	0.01	12.6	–	43.6	–
45 (F14)	18.97	0.78	0.42	0.01	13.3	–	44.1	–
60 (F15)	19.03	0.75	0.36	0.01	13.2	–	43.9	–
Extraction	[c] Cu (%)	[c] Zn (%)	[c, d] Fe (%)	–	S^{2-} (%)	[e] S° (%)	–	[c] S^T (%)
7.5 (F11)	67 (94)	98 (98)	34 (95)	–	73	57	–	(93)
15 (F12)	82 (92)	98 (94)	21 (97)	–	88	57	–	(93)
30 (F13)	96 (92)	99 (99)	12 (92)	–	95	51	–	(92)
45 (F14)	97 (92)	99 (101)	8 (93)	–	97	45	–	(91)
60 (F15)	98 (94)	100 (98)	7 (105)	–	98	48	–	(92)

[a] Norlig A, Orfom 2 (no pre-drying); [b] 20°C; [c] Elemental accountability in brackets; [d] Fe (sln)/Fe (sld+sln)×100%; [e] S° yield, *i.e.*, $S°/S^{2-}{}_{rx}$×100%.

Stellenbosch University http://scholar.sun.ac.za

PLF2	Temp.	Imp. speed	P_g	p_{O2}°	Solids	Solids	Solution	[b] Density
Sample B	150°C	1000 rpm	1090 kPa	700 kPa	1.5 wt %	15 g	985 g	1046 g/L
[a] LS, QB	Cu	Zn	–	Fe (II)	H_2SO_4	–	SO_4	H_2O
0.35 g/L ea.	15 g/L	0 g/L	–	0 g/L	15 g/L	–	37.5 g/L	933.9 g
min (test)	Sld. (g)	Colour	Sln. (g)	Vol. (mL)	Colour	[b] Dens (g/L)	[b] E_{Ag} (mV)	[b] pH
15 (F21)	12.8	Red brown	930.6	886	Green	1050	484	1.10
30 (F22)	12.4	Red	933.9	890	Blue	1050	488	1.06
45 (F23)	11.6	Red	939.2	890	Blue	1055	459	1.09
60 (F24)	11.4	Red	922.9	874	Blue	1056	466	1.09
90 (F25)	10.7	Red	928.9	878	Blue	1058	468	1.10
Solids	Cu (%)	Zn (%)	Fe (%)	–	S^{2-} (%)	S° (%)	SO_4 (%)	S^T (%)
Head	28.5	4.6	29.5	–	35.5	0.0	0.0	35.5
15 (F21)	16.4	1.8	31.0	–	18.1	12.3	2.0	31.2
30 (F22)	6.6	0.3	35.1	–	5.9	20.8	3.2	27.2
45 (F23)	4.6	0.2	37.3	–	4.6	22.6	3.5	28.3
60 (F24)	2.2	0.1	37.1	–	3.4	23.4	2.8	28.3
90 (F25)	1.4	0.1	40.7	–	1.8	26.2	3.7	30.7
Solution	Cu (g/L)	Zn (g/L)	Fe^T (g/L)	FeII (g/L)	H_2SO_4 (g/L)	–	SO_4 (g/L)	–
15 (F21)	16.98	0.50	0.69	0.31	12.0	–	39.9	–
30 (F22)	18.51	0.68	0.39	0.05	12.3	–	42.2	–
45 (F23)	18.87	0.75	0.31	0.01	14.1	–	44.4	–
60 (F24)	19.12	0.81	0.39	0.01	13.2	–	44.2	–
90 (F25)	20.21	0.82	0.21	0.01	12.9	–	45.1	–
Extraction	[c] Cu (%)	[c] Zn (%)	[c, d] Fe (%)	–	S^{2-} (%)	[e] S° (%)	–	[c] S^T (%)
15 (F21)	51 (93)	66 (98)	14 (103)	–	56	53	–	(91)
30 (F22)	81 (94)	95 (93)	8 (106)	–	86	56	–	(92)
45 (F23)	88 (94)	97 (100)	6 (104)	–	90	55	–	(95)
60 (F24)	94 (92)	98 (104)	8 (103)	–	93	54	–	(93)
90 (F25)	96 (97)	99 (105)	4 (103)	–	96	55	–	(95)

[a] Norlig A, Orfom 2 (no pre-drying); [b] 20°C; [c] Elemental accountability in brackets; [d] Fe (sln)/Fe (sld+sln)×100%; [e] S° yield, *i.e.*, $S°/S^{2-}{}_{rx}$×100%.

Stellenbosch University http://scholar.sun.ac.za

PLF3	Temp.	Imp. speed	P_g	p_{O2}°	Solids	Solids	Solution	[b] Density
Sample C	150°C	1000 rpm	1090 kPa	700 kPa	1.5 wt %	15 g	985 g	1046 g/L
[a] LS, QB	Cu	Zn	–	Fe (II)	H_2SO_4	–	SO_4	H_2O
0.35 g/L ea.	15 g/L	0 g/L	–	0 g/L	15 g/L	–	37.5 g/L	933.9 g
min (test)	Sld. (g)	Colour	Sln. (g)	Vol. (mL)	Colour	[b] Dens (g/L)	[b] E_{Ag} (mV)	[b] pH
30 (F31)	12.0	Brown	985.0	942	Blue	1057	448	1.25
45 (F32)	11.6	Red brown	926.9	876	Blue	1058	439	1.41
60 (F33)	11.5	Red	875.4	824	Blue	1062	444	1.32
90 (F34)	11.2	Red	921.6	870	Blue	1059	452	1.28
150 (F35)	10.8	Red	837.9	788	Blue	1064	465	1.21
Solids	Cu (%)	Zn (%)	Fe (%)	–	S^{2-} (%)	S° (%)	SO_4 (%)	S^T (%)
Head	28.5	4.6	29.5	–	35.5	0.0	0.0	35.5
30 (F31)	18.2	0.1	33.2	–	22.1	11.2	1.2	33.7
45 (F32)	14.1	0.0	35.2	–	16.4	15.9	1.8	32.7
60 (F33)	9.8	0.0	37.6	–	13.6	18.6	2.1	33.6
90 (F34)	6.5	0.0	39.0	–	10.6	21.2	1.0	32.5
150 (F35)	2.2	0.0	42.2	–	2.8	27.0	1.2	29.6
Solution	Cu (g/L)	Zn (g/L)	Fe^T (g/L)	FeII (g/L)	H_2SO_4 (g/L)	–	SO_4 (g/L)	–
30 (F31)	18.31	0.77	0.45	0.01	12.5	–	42.4	–
45 (F32)	18.03	0.76	0.39	0.01	13.0	–	42.3	–
60 (F33)	19.75	0.80	0.36	0.01	13.1	–	45.0	–
90 (F34)	20.29	0.79	0.26	0.01	13.1	–	45.5	–
150 (F35)	22.82	0.89	0.17	0.01	13.9	–	50.0	–
Extraction	[c] Cu (%)	[c] Zn (%)	[c, d] Fe (%)	–	S^{2-} (%)	[e] S° (%)	–	[c] S^T (%)
30 (F31)	50 (96)	98 (96)	8 (97)	–	51	49	–	(93)
45 (F32)	62 (94)	99 (96)	8 (98)	–	65	52	–	(93)
60 (F33)	74 (94)	99 (94)	7 (103)	–	71	56	–	(93)
90 (F34)	83 (100)	99 (99)	5 (102)	–	78	56	–	(97)
150 (F35)	95 (99)	100 (100)	3 (104)	–	94	57	–	(94)

[a] Norlig A, Orfom 2 (no pre-drying); [b] 20°C; [c] Elemental accountability in brackets; [d] Fe (sln)/Fe (sld+sln)×100%; [e] S° yield, *i.e.*, $S°/S^{2-}{}_{rx}$×100%.

Stellenbosch University http://scholar.sun.ac.za

PLF4	Temp.	Imp. speed	P_g	p_{O2}°	Solids	Solids	Solution	[b] Density
Sample D	150°C	1000 rpm	1090 kPa	700 kPa	1.5 wt %	15 g	985 g	1046 g/L
[a] LS, QB	Cu	Zn	–	Fe (II)	H_2SO_4	–	SO_4	H_2O
0.35 g/L ea.	15 g/L	0 g/L	–	0 g/L	15 g/L	–	37.5 g/L	933.9 g
min (test)	Sld. (g)	Colour	Sln. (g)	Vol. (mL)	Colour	[b] Dens (g/L)	[b] E_{Ag} (mV)	[b] pH
30 (F41)	11.1	Brown	945.0	898	Blue	1052	475	1.16
45 (F42)	11.7	Red brown	942.2	896	Blue	1051	466	1.06
60 (F43)	12.0	Deep red	923.8	876	Blue	1054	473	1.03
90 (F44)	11.5	Deep red	919.3	871	Blue	1056	473	1.08
150 (F45)	11.0	Deep red	922.9	874	Blue	1056	474	1.08
Solids	Cu (%)	Zn (%)	Fe (%)	–	S^{2-} (%)	S° (%)	SO_4 (%)	S^T (%)
Head	28.5	4.6	29.5	–	35.5	0.0	0.0	35.5
30 (F41)	26.0	1.0	30.6	–	28.0	10.5	0.4	39.4
45 (F42)	19.6	0.3	34.7	–	23.1	10.9	0.7	35.1
60 (F43)	16.8	0.2	33.5	–	21.2	11.1	0.5	34.0
90 (F44)	12.2	0.1	37.7	–	12.9	19.7	1.3	33.0
150 (F45)	7.5	0.0	40.3	–	7.6	23.1	0.9	31.9
Solution	Cu (g/L)	Zn (g/L)	Fe^T (g/L)	FeII (g/L)	H_2SO_4 (g/L)	–	SO_4 (g/L)	–
30 (F41)	15.82	0.63	1.31	0.05	11.2	–	39.3	–
45 (F42)	16.39	0.68	0.64	0.01	13.2	–	40.5	–
60 (F43)	17.71	0.71	0.57	0.01	14.3	–	43.5	–
90 (F44)	18.11	0.72	0.40	0.01	13.5	–	42.9	–
150 (F45)	19.18	0.71	0.26	0.01	13.4	–	44.0	–
Extraction	[c] Cu (%)	[c] Zn (%)	[c, d] Fe (%)	–	S^{2-} (%)	[e] S° (%)	–	[c] S^T (%)
30 (F41)	32 (93)	85 (97)	27 (103)	–	42	53	–	(94)
45 (F42)	46 (92)	95 (95)	13 (105)	–	49	49	–	(94)
60 (F43)	53 (95)	97 (93)	11 (102)	–	52	48	–	(97)
90 (F44)	67 (93)	99 (91)	8 (106)	–	72	59	–	(94)
150 (F45)	81 (96)	100 (91)	5 (105)	–	84	57	–	(95)

[a] Norlig A, Orfom 2 (no pre-drying); [b] 20°C; [c] Elemental accountability in brackets; [d] Fe (sln)/Fe (sld+sln)×100%; [e] S° yield, *i.e.*, $S°/S^{2-}{}_{rx}$×100%.

Stellenbosch University http://scholar.sun.ac.za

PLG1	Temp.	Imp. speed	P_g	p_{O2}°	Solids	Solids	Solution	[b] Density
Sample A	150°C	1000 rpm	1090 kPa	700 kPa	1.5 wt %	15 g	985 g	1051 g/L
[a] LS, QB	Cu	Zn	–	Fe (II)	H_2SO_4	–	SO_4	H_2O
0.35 g/L ea.	15 g/L	0 g/L	–	0 g/L	25 g/L	–	47.3 g/L	924.8 g
min (test)	Sld. (g)	Colour	Sln. (g)	Vol. (mL)	Colour	[b] Dens (g/L)	[b] E_{Ag} (mV)	[b] pH
7.5 (G11)	6.4	Grey	957.2	900	Green	1064	465	1.06
15 (G12)	7.9	Red brown	935.5	880	Green	1063	506	0.82
30 (G13)	9.0	Red	935.6	883	Blue	1059	497	0.78
45 (G14)	11.3	Red	944.4	888	Blue	1062	512	0.79
60 (G15)	9.8	Red	945.2	891	Blue	1061	521	0.77
Solids	Cu (%)	Zn (%)	Fe (%)	–	S^{2-} (%)	S° (%)	SO_4 (%)	S^T (%)
Head	28.5	4.6	29.5	–	35.5	0.0	0.0	35.5
7.5 (G11)	20.0	0.2	16.5	–	28.0	30.7	0.0	59.0
15 (G12)	7.0	0.1	28.6	–	8.0	37.7	2.1	46.0
30 (G13)	1.4	0.0	34.1	–	1.8	33.8	3.3	36.1
45 (G14)	0.5	0.0	35.0	–	0.7	28.7	3.4	31.7
60 (G15)	0.4	0.0	36.5	–	0.5	31.8	3.6	32.7
Solution	Cu (g/L)	Zn (g/L)	Fe^T (g/L)	FeII (g/L)	H_2SO_4 (g/L)	–	SO_4 (g/L)	–
7.5 (G11)	17.66	0.74	3.40	1.41	15.7	–	50.9	–
15 (G12)	19.28	0.74	2.54	0.43	18.0	–	54.2	–
30 (G13)	19.41	0.75	1.47	0.05	19.5	–	53.5	–
45 (G14)	19.70	0.73	1.00	0.01	19.7	–	52.9	–
60 (G15)	19.74	0.73	0.92	0.01	21.6	–	54.6	–
Extraction	[c] Cu (%)	[c] Zn (%)	[c, d] Fe (%)	–	S^{2-} (%)	[e] S° (%)	–	[c] S^T (%)
7.5 (G11)	70 (94)	98 (98)	69 (93)	–	66	56	–	(94)
15 (G12)	87 (96)	99 (96)	51 (102)	–	88	63	–	(96)
30 (G13)	97 (94)	99 (96)	29 (99)	–	97	59	–	(94)
45 (G14)	99 (96)	100 (94)	20 (109)	–	99	62	–	(95)
60 (G15)	99 (96)	100 (94)	18 (99)	–	99	59	–	(96)

[a] Norlig A, Orfom 2 (no pre-drying); [b] 20°C; [c] Elemental accountability in brackets; [d] Fe (sln)/Fe (sld+sln)×100%; [e] S° yield, *i.e.*, $S°/S^{2-}{}_{rx}$×100%.

Stellenbosch University http://scholar.sun.ac.za

PLG2	Temp.	Imp. speed	P_g	p_{O2}°	Solids	Solids	Solution	[b] Density
Sample B	150°C	1000 rpm	1090 kPa	700 kPa	1.5 wt %	15 g	985 g	1051 g/L
[a] LS, QB	Cu	Zn	–	Fe (II)	H_2SO_4	–	SO_4	H_2O
0.35 g/L ea.	15 g/L	0 g/L	–	0 g/L	25 g/L	–	47.3 g/L	924.8 g
min (test)	Sld. (g)	Colour	Sln. (g)	Vol. (mL)	Colour	[b] Dens (g/L)	[b] E_{Ag} (mV)	[b] pH
15 (G21)	8.4	Lgt brown	947.8	893	Green	1061	469	0.98
30 (G22)	8.5	Red brown	947.3	891	Blue	1063	485	0.91
45 (G23)	10.3	Red	942.9	888	Blue	1062	480	0.90
60 (G24)	10.9	Red	927.4	873	Blue	1062	488	0.89
90 (G25)	9.6	Red	919.9	865	Blue	1063	514	0.89
150 (G26)	10.1	Deep red	937.4	881	Blue	1064	521	0.86
Solids	Cu (%)	Zn (%)	Fe (%)	–	S^{2-} (%)	S° (%)	SO_4 (%)	S^T (%)
Head	28.5	4.6	29.5	–	35.5	0.0	0.0	35.5
15 (G21)	24.0	0.1	24.8	–	25.7	22.3	0.1	48.0
30 (G22)	8.7	0.1	30.9	–	7.7	31.8	3.0	39.5
45 (G23)	3.9	0.0	34.2	–	5.5	28.0	2.3	35.1
60 (G24)	1.7	0.0	34.6	–	5.0	27.1	2.7	34.1
90 (G25)	0.4	0.0	38.6	–	0.4	32.2	3.1	33.1
150 (G26)	0.2	0.0	38.6	–	0.4	31.7	3.2	32.3
Solution	Cu (g/L)	Zn (g/L)	Fe^T (g/L)	FeII (g/L)	H_2SO_4 (g/L)	–	SO_4 (g/L)	–
15 (G21)	17.93	0.77	2.34	0.68	16.2	–	49.7	–
30 (G22)	19.19	0.71	1.79	0.41	17.4	–	51.5	–
45 (G23)	19.73	0.76	1.24	0.02	22.8	–	56.6	–
60 (G24)	19.93	0.79	0.92	0.02	19.7	–	53.1	–
90 (G25)	19.93	0.83	0.87	0.01	20.3	–	53.6	–
150 (G26)	19.74	0.84	0.87	0.01	20.8	–	53.8	–
Extraction	[c] Cu (%)	[c] Zn (%)	[c, d] Fe (%)	–	S^{2-} (%)	[e] S° (%)	–	[c] S^T (%)
15 (G21)	53 (98)	99 (100)	47 (94)	–	59	59	–	(93)
30 (G22)	83 (97)	99 (93)	36 (95)	–	88	58	–	(92)
45 (G23)	91 (98)	100 (98)	25 (104)	–	89	61	–	(101)
60 (G24)	96 (96)	100 (100)	18 (103)	–	90	62	–	(95)
90 (G25)	99 (94)	100 (104)	17 (101)	–	99	58	–	(92)
150 (G26)	100 (95)	100 (107)	17 (105)	–	99	61	–	(94)

[a] Norlig A, Orfom 2 (no pre-drying); [b] 20°C; [c] Elemental accountability in brackets; [d] Fe (sln)/Fe (sld+sln)×100%; [e] S° yield, *i.e.*, $S°/S^{2-}{}_{rx}$×100%.

Stellenbosch University http://scholar.sun.ac.za

PLG3	Temp.	Imp. speed	P_g	p_{O2}°	Solids	Solids	Solution	[b] Density
Sample C	150°C	1000 rpm	1090 kPa	700 kPa	1.5 wt %	15 g	985 g	1051 g/L
[a] LS, QB	Cu	Zn	–	Fe (II)	H_2SO_4	–	SO_4	H_2O
0.35 g/L ea.	15 g/L	0 g/L	–	0 g/L	25 g/L	–	47.3 g/L	924.8 g
min (test)	Sld. (g)	Colour	Sln. (g)	Vol. (mL)	Colour	[b] Dens (g/L)	[b] E_{Ag} (mV)	[b] pH
30 (G31)	8.9	Brown	915.7	858	Green	1067	458	1.23
45 (G32)	7.2	Brown	918.9	859	Green	1070	474	1.22
60 (G33)	7.7	Red brown	935.9	875	Green	1069	477	1.95
90 (G34)	9.9	Red	862.4	807	Blue	1069	488	1.63
150 (G35)	10.1	Red	872.7	818	Blue	1067	495	1.48
Solids	Cu (%)	Zn (%)	Fe (%)	–	S^{2-} (%)	S° (%)	SO_4 (%)	S^T (%)
Head	28.5	4.6	29.5	–	35.5	0.0	0.0	35.5
30 (G31)	22.8	0.1	27.0	–	27.9	19.2	1.6	45.6
45 (G32)	19.4	0.1	24.5	–	22.9	28.1	1.3	50.4
60 (G33)	11.7	0.1	25.4	–	18.6	29.7	2.8	49.8
90 (G34)	4.0	0.1	40.6	–	3.9	28.2	2.6	32.9
150 (G35)	0.6	0.0	40.3	–	0.5	35.2	2.6	36.0
Solution	Cu (g/L)	Zn (g/L)	Fe^T (g/L)	FeII (g/L)	H_2SO_4 (g/L)	–	SO_4 (g/L)	–
30 (G31)	18.85	0.77	2.22	0.57	16.7	–	51.4	–
45 (G32)	19.46	0.80	3.00	0.47	14.9	–	52.7	–
60 (G33)	19.86	0.78	2.57	0.44	15.1	–	52.4	–
90 (G34)	22.30	0.89	0.99	0.01	20.5	–	57.8	–
150 (G35)	22.22	0.82	0.91	0.01	19.6	–	56.5	–
Extraction	[c] Cu (%)	[c] Zn (%)	[c, d] Fe (%)	–	S^{2-} (%)	[e] S° (%)	–	[c] S^T (%)
30 (G31)	53 (99)	99 (95)	42 (96)	–	54	58	–	(92)
45 (G32)	68 (98)	99 (98)	57 (96)	–	70	54	–	(92)
60 (G33)	79 (99)	99 (98)	50 (93)	–	74	57	–	(94)
90 (G34)	91 (100)	99 (103)	18 (107)	–	93	56	–	(92)
150 (G35)	99 (99)	99 (96)	17 (107)	–	99	66	–	(94)

[a] Norlig A, Orfom 2 (no pre-drying); [b] 20°C; [c] Elemental accountability in brackets; [d] Fe (sln)/Fe (sld+sln)×100%; [e] S° yield, *i.e.*, $S°/S^{2-}{}_{rx}$×100%.

Stellenbosch University http://scholar.sun.ac.za

PLG4	Temp.	Imp. speed	P_g	p_{O2}°	Solids	Solids	Solution	[b] Density
Sample C	150°C	1000 rpm	1090 kPa	700 kPa	1.5 wt %	15 g	985 g	1051 g/L
[a] LS, QB	Cu	Zn	–	Fe (II)	H_2SO_4	–	SO_4	H_2O
0.35 g/L ea.	15 g/L	0 g/L	–	0 g/L	25 g/L	–	47.3 g/L	924.8 g
min (test)	Sld. (g)	Colour	Sln. (g)	Vol. (mL)	Colour	[b] Dens (g/L)	[b] E_{Ag} (mV)	[b] pH
15 (G41)	9.7	Black	950.5	898	Green	1059	470	1.20
30 (G42)	8.5	Brown	951.1	896	Green	1062	487	1.04
45 (G43)	7.4	Brown	942.9	887	Blue	1063	519	1.30

Solids	Cu (%)	Zn (%)	Fe (%)	–	S^{2-} (%)	S° (%)	SO_4 (%)	S^T (%)
Head	28.5	4.6	29.5	–	35.5	0.0	0.0	35.5
15 (G41)	28.9	0.4	25.4	–	30.8	13.7	0.3	46.0
30 (G42)	21.9	0.1	25.3	–	26.0	22.7	0.8	49.2
45 (G43)	17.4	0.1	23.0	–	26.0	25.4	0.8	53.4

Solution	Cu (g/L)	Zn (g/L)	Fe^T (g/L)	FeII (g/L)	H_2SO_4 (g/L)	–	SO_4 (g/L)	–
15 (G41)	17.72	0.73	2.06	0.76	17.8	–	50.1	–
30 (G42)	18.26	0.75	2.49	0.71	16.7	–	51.1	–
45 (G43)	19.12	0.75	3.13	0.59	14.3	–	51.8	–

Extraction	[c] Cu (%)	[c] Zn (%)	[c, d] Fe (%)	–	S^{2-} (%)	[e] S° (%)	–	[c] S^T (%)
15 (G41)	34 (102)	95 (100)	42 (97)	–	44	57	–	(96)
30 (G42)	56 (99)	99 (99)	50 (99)	–	59	62	–	(96)
45 (G43)	70 (100)	99 (97)	63 (101)	–	64	55	–	(95)

[a] Norlig A, Orfom 2 (no pre-drying); [b] 20°C; [c] Elemental accountability in brackets; [d] Fe (sln)/Fe (sld+sln)×100%; [e] S° yield, *i.e.*, $S°/S^{2-}{}_{rx}$×100%.

Stellenbosch University http://scholar.sun.ac.za

PLH1	Temp.	Imp. speed	P_g	p_{O2}°	Solids	Solids	Solution	[b] Density
Sample A	150°C	1000 rpm	1090 kPa	700 kPa	1.5 wt %	15 g	985 g	1057 g/L
[a] LS, QB	Cu	Zn	–	Fe (II)	H_2SO_4	–	SO_4	H_2O
0.35 g/L ea.	15 g/L	0 g/L	–	0 g/L	35 g/L	–	57.1 g/L	915.8 g
min (test)	Sld. (g)	Colour	Sln. (g)	Vol. (mL)	Colour	[b] Dens (g/L)	[b] E_{Ag} (mV)	[b] pH
7.5 (H11)	6.0	Grey	933.6	871	Green	1072	470	0.73
15 (H12)	4.9	Grey	944.7	880	Green	1073	496	0.84
30 (H13)	4.1	Lgt brown	940.7	877	Green	1073	513	0.87
45 (H14)	4.0	Lgt brown	936.7	873	Green	1073	528	0.87
60 (H15)	3.9	Lgt brown	915.7	850	Green	1077	530	0.82
Solids	Cu (%)	Zn (%)	Fe (%)	–	S^{2-} (%)	S° (%)	SO_4 (%)	S^T (%)
Head	28.5	4.6	29.5	–	35.5	0.0	0.0	35.5
7.5 (H11)	20.9	0.3	10.8	–	28.7	36.8	0.0	65.5
15 (H12)	6.7	0.0	14.5	–	15.9	62.3	0.2	79.0
30 (H13)	3.1	0.0	6.6	–	5.5	74.5	0.0	80.2
45 (H14)	0.9	0.0	8.9	–	0.5	83.4	0.0	83.9
60 (H15)	0.5	0.0	10.2	–	0.3	82.3	0.2	83.0
Solution	Cu (g/L)	Zn (g/L)	Fe^T (g/L)	FeII (g/L)	H_2SO_4 (g/L)	–	SO_4 (g/L)	–
7.5 (H11)	18.97	0.74	4.20	2.37	24.1	–	62.3	–
15 (H12)	19.71	0.78	3.99	0.72	23.9	–	64.2	–
30 (H13)	19.34	0.78	4.29	0.38	24.2	–	65.0	–
45 (H14)	19.60	0.80	4.15	0.23	23.8	–	64.8	–
60 (H15)	19.79	0.82	4.18	0.05	25.0	–	66.5	–
Extraction	[c] Cu (%)	[c] Zn (%)	[c, d] Fe (%)	–	S^{2-} (%)	[e] S° (%)	–	[c] S^T (%)
7.5 (H11)	71 (97)	98 (96)	83 (97)	–	68	61	–	(95)
15 (H12)	92 (97)	100 (99)	79 (96)	–	85	67	–	(98)
30 (H13)	97 (94)	100 (99)	85 (91)	–	96	60	–	(96)
45 (H14)	99 (94)	100 (101)	82 (90)	–	100	63	–	(96)
60 (H15)	100 (92)	100 (101)	80 (89)	–	100	60	–	(95)

[a] Norlig A, Orfom 2 (no pre-drying); [b] 20°C; [c] Elemental accountability in brackets; [d] Fe (sln)/Fe (sld+sln)×100%; [e] S° yield, *i.e.*, $S°/S^{2-}{}_{rx}$×100%.

Stellenbosch University http://scholar.sun.ac.za

PLH2	Temp.	Imp. speed	P_g	p_{O2}°	Solids	Solids	Solution	[b] Density
Sample B	150°C	1000 rpm	1090 kPa	700 kPa	1.5 wt %	15 g	985 g	1057 g/L
[a] LS, QB	Cu	Zn	–	Fe (II)	H_2SO_4	–	SO_4	H_2O
0.35 g/L ea.	15 g/L	0 g/L	–	0 g/L	35 g/L	–	57.1 g/L	915.8 g
min (test)	Sld. (g)	Colour	Sln. (g)	Vol. (mL)	Colour	[b] Dens (g/L)	[b] E_{Ag} (mV)	[b] pH
15 (H21)	8.0	Grey	926.7	865	Green	1071	498	0.60
30 (H22)	7.1	Grey	927.7	865	Green	1072	495	0.67
45 (H23)	5.0	Lgt brown	949.8	888	Green	1070	505	0.71
60 (H24)	4.5	Lgt brown	945.7	880	Green	1075	509	0.74
90 (H25)	4.9	Lgt brown	950.6	884	Green	1075	528	0.76
Solids	Cu (%)	Zn (%)	Fe (%)	–	S^{2-} (%)	S° (%)	SO_4 (%)	S^T (%)
Head	28.5	4.6	29.5	–	35.5	0.0	0.0	35.5
15 (H21)	23.1	0.4	19.2	–	31.0	22.5	0.0	49.3
30 (H22)	10.4	0.1	13.6	–	23.8	34.6	0.0	58.6
45 (H23)	7.9	0.1	16.2	–	11.7	60.3	0.0	72.0
60 (H24)	5.6	0.0	12.3	–	9.8	65.3	0.0	75.0
90 (H25)	2.7	0.0	14.2	–	7.4	65.5	0.0	74.4
Solution	Cu (g/L)	Zn (g/L)	Fe^T (g/L)	FeII (g/L)	H_2SO_4 (g/L)	–	SO_4 (g/L)	–
15 (H21)	17.76	0.74	3.04	0.68	24.8	–	59.7	–
30 (H22)	18.72	0.74	3.57	2.90	23.7	–	61.4	–
45 (H23)	19.14	0.79	4.19	0.49	20.9	–	61.1	–
60 (H24)	20.15	0.83	4.23	0.31	21.0	–	63.1	–
90 (H25)	20.70	0.81	4.03	0.01	21.4	–	64.0	–
Extraction	[c] Cu (%)	[c] Zn (%)	[c, d] Fe (%)	–	S^{2-} (%)	[e] S° (%)	–	[c] S^T (%)
15 (H21)	57 (94)	96 (97)	59 (103)	–	53	63	–	(91)
30 (H22)	83 (93)	99 (94)	70 (106)	–	68	68	–	(94)
45 (H23)	91 (95)	100 (102)	84 (104)	–	89	64	–	(93)
60 (H24)	94 (99)	100 (105)	84 (103)	–	92	60	–	(94)
90 (H25)	97 (101)	100 (104)	81 (103)	–	93	65	–	(97)

[a] Norlig A, Orfom 2 (no pre-drying); [b] 20°C; [c] Elemental accountability in brackets; [d] Fe (sln)/Fe (sld+sln)×100%; [e] S° yield, *i.e.*, $S°/S^{2-}{}_{rx}$×100%.

Stellenbosch University http://scholar.sun.ac.za

PLH3	Temp.	Imp. speed	P_g	p_{O2}°	Solids	Solids	Solution	[b] Density
Sample D	150°C	1000 rpm	1090 kPa	700 kPa	1.5 wt %	15 g	985 g	1057 g/L
[a] LS, QB	Cu	Zn	–	Fe (II)	H_2SO_4	–	SO_4	H_2O
0.35 g/L ea.	15 g/L	0 g/L	–	0 g/L	35 g/L	–	57.1 g/L	915.8 g
min (test)	Sld. (g)	Colour	Sln. (g)	Vol. (mL)	Colour	[b] Dens (g/L)	[b] E_{Ag} (mV)	[b] pH
15 (H31)	12.5	Black	914.5	859	Green	1065	474	0.49
30 (H32)	11.1	Black	916.7	860	Green	1066	478	0.56
45 (H33)	10.0	Grey	949.7	890	Green	1067	483	0.55
60 (H34)	9.1	Grey	934.7	874	Green	1070	498	0.62
90 (H35)	8.0	Grey	926.7	865	Green	1071	506	0.64
150 (H36)	5.9	Grey	920.7	856	Green	1075	519	0.61
Solids	Cu (%)	Zn (%)	Fe (%)	–	S^{2-} (%)	S° (%)	SO_4 (%)	S^T (%)
Head	28.5	4.6	29.5	–	35.5	0.0	0.0	35.5
15 (H31)	26.5	1.2	25.3	–	32.5	6.5	0.0	40.2
30 (H32)	24.0	1.2	24.3	–	32.7	10.1	0.0	42.3
45 (H33)	22.7	0.6	23.6	–	29.2	14.4	0.0	43.0
60 (H34)	21.8	0.1	22.5	–	27.0	21.2	0.0	45.2
90 (H35)	20.6	0.1	21.9	–	26.0	25.5	0.0	52.9
150 (H36)	18.7	0.0	19.7	–	25.9	35.9	0.0	61.8
Solution	Cu (g/L)	Zn (g/L)	Fe^T (g/L)	FeII (g/L)	H_2SO_4 (g/L)	–	SO_4 (g/L)	–
15 (H31)	15.90	0.65	1.16	0.73	29.4	–	56.3	–
30 (H32)	16.60	0.64	1.74	0.61	28.7	–	58.3	–
45 (H33)	16.57	0.70	1.91	0.61	28.8	–	58.9	–
60 (H34)	17.05	0.77	2.47	0.45	27.9	–	60.4	–
90 (H35)	17.94	0.76	2.70	0.45	28.0	–	62.4	–
150 (H36)	18.85	0.77	3.33	0.05	26.3	–	64.1	–
Extraction	[c] Cu (%)	[c] Zn (%)	[c, d] Fe (%)	–	S^{2-} (%)	[e] S° (%)	–	[c] S^T (%)
15 (H31)	23 (93)	78 (103)	23 (94)	–	24	65	–	(91)
30 (H32)	38 (93)	81 (99)	34 (95)	–	32	66	–	(92)
45 (H33)	47 (93)	92 (99)	38 (92)	–	45	60	–	(94)
60 (H34)	54 (92)	98 (99)	49 (95)	–	54	67	–	(93)
90 (H35)	61 (94)	99 (96)	53 (92)	–	61	63	–	(96)
150 (H36)	74 (94)	100 (96)	64 (91)	–	71	56	–	(95)

[a] Norlig A, Orfom 2 (no pre-drying); [b] 20°C; [c] Elemental accountability in brackets; [d] Fe (sln)/Fe (sld+sln)×100%; [e] S° yield, *i.e.*, $S°/S^{2-}{}_{rx}$×100%.

Stellenbosch University http://scholar.sun.ac.za

PLI1	Temp.	Imp. speed	P_g	p_{O2}°	Solids	Solids	Solution	[b] Density
Sample A	150°C	1000 rpm	1090 kPa	700 kPa	1.5 wt %	15 g	985 g	1061 g/L
[a] LS, QB	Cu	Zn	–	Fe (II)	H_2SO_4	–	SO_4	H_2O
0.35 g/L ea.	15 g/L	0 g/L	–	0 g/L	45 g/L	–	66.9 g/L	906.8 g
min (test)	Sld. (g)	Colour	Sln. (g)	Vol. (mL)	Colour	[b] Dens (g/L)	[b] E_{Ag} (mV)	[b] pH
7.5 (I11)	5.8	Grey	948.2	880	Green	1078	451	0.69
15 (I12)	4.2	Grey	982.2	911	Green	1078	498	0.52
30 (I13)	4.1	Lgt yellow	950.2	882	Green	1077	512	0.49
45 (I14)	4.0	Lgt yellow	940.7	872	Green	1079	528	0.45
60 (I15)	3.8	Lgt yellow	943.1	872	Green	1081	534	0.66
Solids	Cu (%)	Zn (%)	Fe (%)	–	S^{2-} (%)	S° (%)	SO_4 (%)	S^T (%)
Head	28.5	4.6	29.5	–	35.5	0.0	0.0	35.5
7.5 (I11)	20.7	0.3	10.8	–	30.5	38.0	0.1	68.0
15 (I12)	6.4	0.0	13.9	–	14.9	72.3	0.2	87.0
30 (I13)	2.4	0.0	2.6	–	1.1	79.4	0.5	80.7
45 (I14)	1.2	0.0	3.3	–	0.9	86.0	0.5	87.8
60 (I15)	0.8	0.0	3.4	–	0.6	88.8	0.5	89.1
Solution	Cu (g/L)	Zn (g/L)	Fe^T (g/L)	FeII (g/L)	H_2SO_4 (g/L)	–	SO_4 (g/L)	–
7.5 (I11)	18.18	0.74	3.87	1.98	33.1	–	69.5	–
15 (I12)	18.43	0.75	3.74	0.65	31.0	–	68.6	–
30 (I13)	19.35	0.75	4.47	0.38	31.7	–	72.8	–
45 (I14)	20.40	0.78	4.75	0.19	32.6	–	76.2	–
60 (I15)	19.74	0.74	4.72	0.01	33.4	–	76.0	–
Extraction	[c] Cu (%)	[c] Zn (%)	[c, d] Fe (%)	–	S^{2-} (%)	[e] S° (%)	–	[c] S^T (%)
7.5 (I11)	72 (94)	97 (97)	77 (91)	–	67	62	–	(93)
15 (I12)	94 (94)	100 (99)	77 (90)	–	88	65	–	(93)
30 (I13)	98 (94)	100 (96)	89 (91)	–	99	62	–	(94)
45 (I14)	99 (98)	100 (98)	94 (96)	–	99	65	–	(98)
60 (I15)	99 (95)	100 (94)	93 (96)	–	100	64	–	(97)

[a] Norlig A, Orfom 2 (no pre-drying); [b] 20°C; [c] Elemental accountability in brackets; [d] Fe (sln)/Fe (sld+sln)×100%; [e] S° yield, *i.e.*, $S°/S^{2-}{}_{rx}$×100%.

Stellenbosch University http://scholar.sun.ac.za

PLI2	Temp.	Imp. speed	P_g	p_{O2}°	Solids	Solids	Solution	[b] Density
Sample B	150°C	1000 rpm	1090 kPa	700 kPa	1.5 wt %	15 g	985 g	1061 g/L
[a] LS, QB	Cu	Zn	–	Fe (II)	H_2SO_4	–	SO_4	H_2O
0.35 g/L ea.	15 g/L	0 g/L	–	0 g/L	45 g/L	–	66.9 g/L	906.8 g
min (test)	Sld. (g)	Colour	Sln. (g)	Vol. (mL)	Colour	[b] Dens (g/L)	[b] E_{Ag} (mV)	[b] pH
15 (I21)	8.1	Grey	948.8	881	Green	1077	459	0.69
30 (I22)	6.5	Grey	932.2	865	Green	1078	473	0.72
45 (I23)	4.9	Lgt grey	925.1	857	Green	1079	502	0.64
60 (I24)	4.1	Lgt yellow	948.8	879	Green	1080	498	0.60
90 (I25)	4.6	Lgt yellow	944.7	874	Green	1081	496	0.67
Solids	Cu (%)	Zn (%)	Fe (%)	–	S^{2-} (%)	S° (%)	SO_4 (%)	S^T (%)
Head	28.5	4.6	29.5	–	35.5	0.0	0.0	35.5
15 (I21)	22.3	0.2	22.4	–	29.0	21.8	0.5	50.5
30 (I22)	10.5	0.1	12.6	–	19.2	38.8	1.7	58.7
45 (I23)	8.7	0.1	13.4	–	8.7	62.0	0.5	71.0
60 (I24)	5.2	0.0	10.3	–	6.7	72.3	0.2	79.0
90 (I25)	3.1	0.0	9.3	–	4.4	73.3	0.5	76.0
Solution	Cu (g/L)	Zn (g/L)	Fe^T (g/L)	FeII (g/L)	H_2SO_4 (g/L)	–	SO_4 (g/L)	–
15 (I21)	16.96	0.73	2.74	1.01	36.4	–	68.7	–
30 (I22)	18.97	0.74	3.90	0.92	35.0	–	73.5	–
45 (I23)	20.07	0.74	4.03	0.62	32.5	–	73.3	–
60 (I24)	20.52	0.78	4.32	0.34	32.0	–	74.6	–
90 (I25)	20.55	0.80	4.40	0.12	30.0	–	73.1	–
Extraction	[c] Cu (%)	[c] Zn (%)	[c, d] Fe (%)	–	S^{2-} (%)	[e] S° (%)	–	[c] S^T (%)
15 (I21)	58 (92)	98 (95)	55 (96)	–	56	59	–	(93)
30 (I22)	84 (94)	99 (94)	76 (95)	–	77	62	–	(95)
45 (I23)	90 (97)	100 (93)	78 (93)	–	92	62	–	(93)
60 (I24)	95 (100)	100 (100)	86 (95)	–	95	59	–	(96)
90 (I25)	97 (99)	100 (102)	87 (97)	–	96	66	–	(95)

[a] Norlig A, Orfom 2 (no pre-drying); [b] 20°C; [c] Elemental accountability in brackets; [d] Fe (sln)/Fe (sld+sln)×100%; [e] S° yield, *i.e.*, $S°/S^{2-}{}_{rx}$×100%.

Stellenbosch University http://scholar.sun.ac.za

PLI3	Temp.	Imp. speed	P_g	$p_{O2}°$	Solids	Solids	Solution	[b] Density
Sample C	150°C	1000 rpm	1090 kPa	700 kPa	1.5 wt %	15 g	985 g	1061 g/L
[a] LS, QB	Cu	Zn	–	Fe (II)	H_2SO_4	–	SO_4	H_2O
0.35 g/L ea.	15 g/L	0 g/L	–	0 g/L	45 g/L	–	66.9 g/L	906.8 g
min (test)	Sld. (g)	Colour	Sln. (g)	Vol. (mL)	Colour	[b] Dens (g/L)	[b] E_{Ag} (mV)	[b] pH
15 (I31)	10.9	Black	936.5	874	Green	1072	454	0.68
30 (I32)	7.1	Grey	918.9	852	Green	1079	452	0.55
45 (I33)	6.4	Grey	926.7	860	Green	1078	461	0.60
60 (I34)	5.8	Grey	903.5	834	Green	1083	493	0.55
90 (I35)	5.1	Grey	932.2	761	Green	1093	508	0.52
150 (I36)	4.0	Brown	985.0	928	Green	1090	511	0.54
Solids	Cu (%)	Zn (%)	Fe (%)	–	S^{2-} (%)	S° (%)	SO_4 (%)	S^T (%)
Head	28.5	4.6	29.5	–	35.5	0.0	0.0	35.5
15 (I31)	25.2	1.1	24.9	–	31.0	12.2	0.3	46.0
30 (I32)	21.2	0.1	16.2	–	29.9	30.3	0.3	60.0
45 (I33)	15.2	0.1	16.9	–	25.1	38.0	0.5	62.0
60 (I34)	12.6	0.1	10.7	–	22.5	48.3	0.2	70.2
90 (I35)	10.0	0.1	5.6	–	18.6	56.9	0.5	75.0
150 (I36)	7.4	0.0	4.3	–	18.3	65.2	1.0	84.0
Solution	Cu (g/L)	Zn (g/L)	Fe^T (g/L)	FeII (g/L)	H_2SO_4 (g/L)	–	SO_4 (g/L)	–
15 (I31)	17.11	0.67	2.00	0.87	37.2	–	67.9	–
30 (I32)	18.88	0.83	3.60	0.77	32.7	–	70.6	–
45 (I33)	18.54	0.80	3.94	0.68	33.2	–	71.5	–
60 (I34)	19.50	0.90	4.83	0.38	34.2	–	76.6	–
90 (I35)	21.97	1.03	5.21	0.39	34.1	–	81.4	–
150 (I36)	22.52	1.00	5.46	0.30	32.0	–	80.9	–
Extraction	[c] Cu (%)	[c] Zn (%)	[c, d] Fe (%)	–	S^{2-} (%)	[e] S° (%)	–	[c] S^T (%)
15 (I31)	36 (97)	82 (102)	39 (101)	–	37	68	–	(95)
30 (I32)	65 (96)	99 (102)	68 (94)	–	61	65	–	(92)
45 (I33)	78 (93)	100 (99)	75 (99)	–	70	64	–	(93)
60 (I34)	83 (93)	100 (108)	89 (103)	–	76	68	–	(97)
90 (I35)	88 (94)	100 (112)	88 (94)	–	82	65	–	(93)
150 (I36)	93 (98)	100 (111)	95 (99)	–	86	56	–	(93)

[a] Norlig A, Orfom 2 (no pre-drying); [b] 20°C; [c] Elemental accountability in brackets; [d] Fe (sln)/Fe (sld+sln)×100%; [e] S° yield, *i.e.*, $S°/S^{2-}{}_{rx}×100\%$.

Stellenbosch University http://scholar.sun.ac.za

PLI4	Temp.	Imp. speed	P_g	p_{O2}°	Solids	Solids	Solution	[b] Density
Sample D	150°C	1000 rpm	1090 kPa	700 kPa	1.5 wt %	15 g	985 g	1061 g/L
[a] LS, QB	Cu	Zn	–	Fe (II)	H_2SO_4	–	SO_4	H_2O
0.35 g/L ea.	15 g/L	0 g/L	–	0 g/L	45 g/L	–	66.9 g/L	906.8 g
min (test)	Sld. (g)	Colour	Sln. (g)	Vol. (mL)	Colour	[b] Dens (g/L)	[b] E_{Ag} (mV)	[b] pH
15 (I41)	12.1	Black	929.8	868	Green	1071	450	0.68
30 (I42)	10.9	Black	913.4	853	Green	1071	472	0.50
45 (I43)	9.1	Black	943.6	879	Green	1073	482	0.60
60 (I44)	8.0	Grey	941.7	877	Green	1074	490	0.60
90 (I45)	7.6	Grey	972.4	905	Green	1074	500	0.61
150 (I46)	6.2	Grey	943.3	875	Green	1078	506	0.63
Solids	Cu (%)	Zn (%)	Fe (%)	–	S^{2-} (%)	S° (%)	SO_4 (%)	S^T (%)
Head	28.5	4.6	29.5	–	35.5	0.0	0.0	35.5
15 (I41)	27.0	2.5	28.4	–	35.0	6.2	0.2	40.0
30 (I42)	24.4	0.6	25.9	–	34.7	9.8	0.6	44.0
45 (I43)	24.6	0.1	23.7	–	32.9	16.7	0.1	49.4
60 (I44)	24.5	0.1	20.1	–	32.4	23.0	0.1	55.4
90 (I45)	21.5	0.1	18.9	–	32.5	24.3	0.1	56.2
150 (I46)	20.4	0.0	15.8	–	30.0	34.1	0.1	64.4
Solution	Cu (g/L)	Zn (g/L)	Fe^T (g/L)	FeII (g/L)	H_2SO_4 (g/L)	–	SO_4 (g/L)	–
15 (I41)	17.28	0.39	1.51	0.74	38.2	–	67.5	–
30 (I42)	16.76	0.72	1.93	0.67	36.9	–	67.1	–
45 (I43)	16.82	0.76	2.46	0.68	35.1	–	66.9	–
60 (I44)	17.21	0.76	2.88	0.59	34.6	–	68.1	–
90 (I45)	17.49	0.74	2.99	0.45	34.0	–	68.3	–
150 (I46)	18.01	0.76	3.62	0.44	32.2	–	69.0	–
Extraction	[c] Cu (%)	[c] Zn (%)	[c, d] Fe (%)	–	S^{2-} (%)	[e] S° (%)	–	[c] S^T (%)
15 (I41)	24 (100)	56 (93)	30 (107)	–	20	69	–	(93)
30 (I42)	38 (93)	90 (99)	37 (101)	–	29	69	–	(91)
45 (I43)	48 (94)	98 (98)	49 (98)	–	44	65	–	(92)
60 (I44)	54 (94)	99 (97)	57 (93)	–	51	67	–	(93)
90 (I45)	62 (96)	99 (98)	61 (94)	–	54	65	–	(95)
150 (I46)	70 (94)	100 (97)	71 (94)	–	65	61	–	(92)

[a] Norlig A, Orfom 2 (no pre-drying); [b] 20°C; [c] Elemental accountability in brackets; [d] Fe (sln)/Fe (sld+sln)×100%; [e] S° yield, *i.e.*, $S°/S^{2-}{}_{rx}$×100%.

Stellenbosch University http://scholar.sun.ac.za

PLI5	Temp.	Imp. speed	P_g	$p_{O2}°$	Solids	Solids	Solution	[b] Density
Sample D	150°C	1000 rpm	1090 kPa	700 kPa	1.5 wt %	15 g	985 g	1061 g/L
[a] LS, QB	Cu	Zn	–	Fe (II)	H_2SO_4	–	SO_4	H_2O
0.35 g/L ea.	15 g/L	0 g/L	–	0 g/L	45 g/L	–	66.9 g/L	906.8 g
min (test)	Sld. (g)	Colour	Sln. (g)	Vol. (mL)	Colour	[b] Dens (g/L)	[b] E_{Ag} (mV)	[b] pH
60 (I54)	8.4	Grey	918.4	853	Green	1077	480	0.72

Solids	Cu (%)	Zn (%)	Fe (%)	–	S^{2-} (%)	S° (%)	SO_4 (%)	S^T (%)
Head	28.5	4.6	29.5	–	35.5	0.0	0.0	35.5
60 (I54)	22.1	0.2	20.2	–	29.0	23.0	0.1	52.0

Solution	Cu (g/L)	Zn (g/L)	Fe^T (g/L)	FeII (g/L)	H_2SO_4 (g/L)	–	SO_4 (g/L)	–
60 (I54)	18.59	0.76	3.11	0.71	35.4	–	71.5	–

Extraction	[c] Cu (%)	[c] Zn (%)	[c, d] Fe (%)	–	S^{2-} (%)	[e] S° (%)	–	[c] S^T (%)
60 (I54)	57 (97)	96 (98)	60 (98)	–	54	67	–	(94)

[a] Norlig A, Orfom 2 (no pre-drying); [b] 20°C; [c] Elemental accountability in brackets; [d] Fe (sln)/Fe (sld+sln)×100%; [e] S° yield, *i.e.*, $S°/S^{2-}{}_{rx}$×100%.

Stellenbosch University http://scholar.sun.ac.za

PLJ1	Temp.	Imp. speed	P_g	$p_{O2}°$	Solids	Solids	Solution	[b] Density
Sample B	150°C	1000 rpm	1090 kPa	700 kPa	1.5 wt %	15 g	985 g	1051 g/L
[a] LS, QB	Cu	Zn	–	Fe (II)	H_2SO_4	–	SO_4	H_2O
0 g/L	15 g/L	0 g/L	–	0 g/L	25 g/L	–	47.3 g/L	924.8 g
min (test)	Sld. (g)	Colour	Sln. (g)	Vol. (mL)	Colour	[b] Dens (g/L)	[b] E_{Ag} (mV)	[b] pH
30 (J12)	9.7	Red brown	936.2	884	Blue	1059	511	0.76

Solids	Cu (%)	Zn (%)	Fe (%)	–	S^{2-} (%)	S° (%)	SO_4 (%)	S^T (%)
Head	28.5	4.6	29.5	–	35.5	0.0	0.0	35.5
30 (J12)	17.1	0.3	29.8	–	21.2	18.5	3.1	40.5

Solution	Cu (g/L)	Zn (g/L)	Fe^T (g/L)	FeII (g/L)	H_2SO_4 (g/L)	–	SO_4 (g/L)	–
30 (J12)	18.06	0.69	1.76	0.52	19.7	–	51.9	–

Extraction	[c] Cu (%)	[c] Zn (%)	[c, d] Fe (%)	–	S^{2-} (%)	[e] S° (%)	–	[c] S^T (%)
30 (J12)	61 (96)	96 (92)	35 (101)	–	61	55	–	(95)

[a] No surfactant injection; [b] 20°C; [c] Elemental accountability in brackets; [d] Fe (sln)/Fe (sld+sln)×100%; [e] S° yield, *i.e.*, $S°/S^{2-}_{rx}$×100%.

Stellenbosch University http://scholar.sun.ac.za

PLJ2	Temp.	Imp. speed	P_g	$p_{O2}°$	Solids	Solids	Solution	[c] Density
[a] **(PLI44)**	150°C	1000 rpm	1090 kPa	700 kPa	0.6 wt %	6.2 g	933.8 g	1074 g/L
[b] LS, QB	Cu	Zn	Fe (III)	Fe (II)	H_2SO_4	–	SO_4	H_2O
0.35 g/L ea.	17.2 g/L	0.8 g/L	2.3 g/L	0.6 g/L	34.6 g/L	–	68.1 g/L	908.7 g
min (test)	Sld. (g)	Colour	Sln. (g)	Vol. (mL)	Colour	[c] Dens (g/L)	[c] E_{Ag} (mV)	[c] pH
45 (J23)	4.1	Grey	933.0	866	Green	1077	494	0.57

Solids	Cu (%)	Zn (%)	Fe (%)	–	S^{2-} (%)	S° (%)	SO_4 (%)	S^T (%)
Head	28.6	0.2	26.2	–	38.0	0.0	0.0	38.0
45 (J23)	22.1	0.1	22.8	–	32.0	15.8	0.1	48.0

Solution	Cu (g/L)	Zn (g/L)	Fe^T (g/L)	FeII (g/L)	H_2SO_4 (g/L)	–	SO_4 (g/L)	–
45 (J23)	19.02	0.73	3.37	0.51	30.3	–	67.9	–

Extraction	[d] Cu (%)	[d] Zn (%)	[d, e] Fe (%)	–	S^{2-} (%)	[f] S° (%)	–	[d] S^T (%)
45 (J23)	49 (98)	85 (89)	68 (90)	–	44	63	–	(92)

[a] PLI44 residue after elemental sulfur removal; [b] Norlig A, Orfom 2 (no pre-drying); [c] 20°C; [d] Elemental accountability in brackets; [e] Fe (sln)/Fe (sld+sln)×100%; [f] S° yield, *i.e.*, $S°/S^{2-}_{rx}$×100%.

Stellenbosch University http://scholar.sun.ac.za

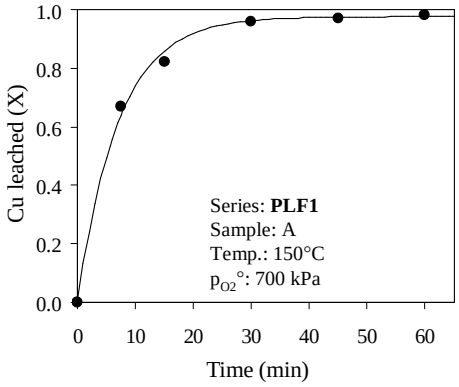

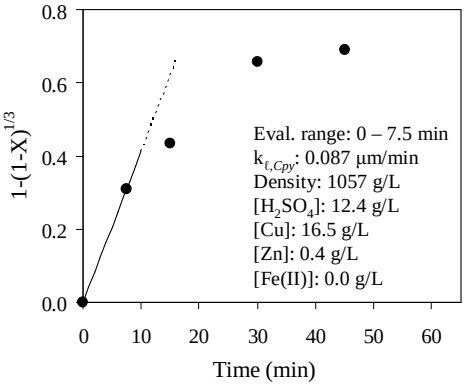

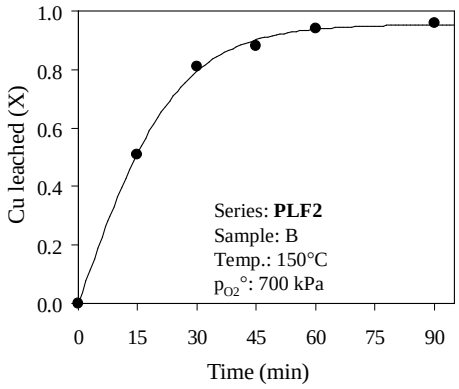

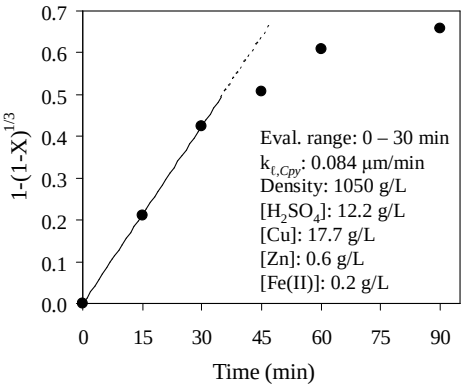

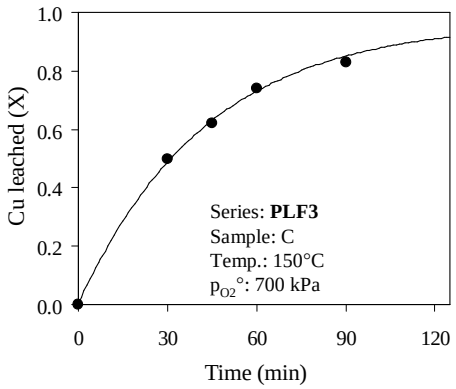

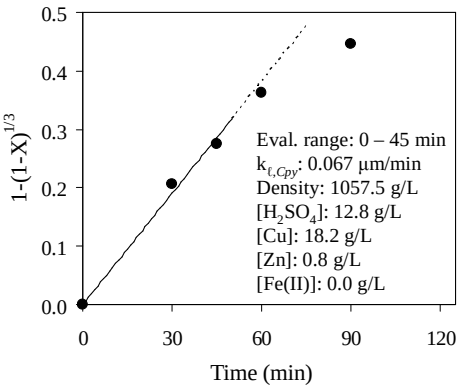

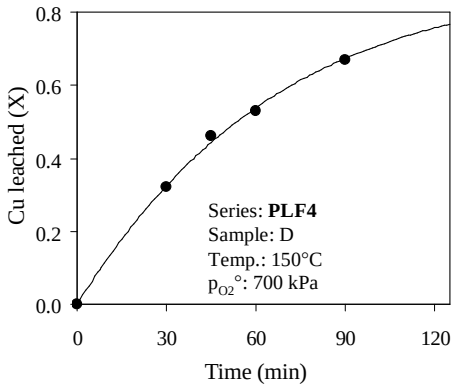

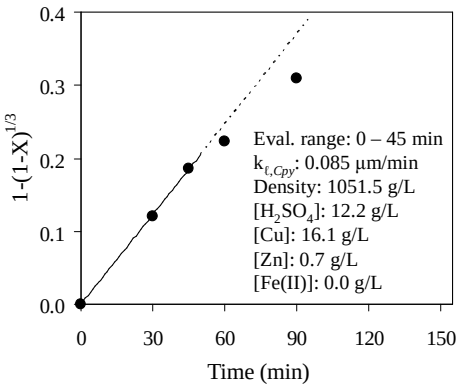

Stellenbosch University http://scholar.sun.ac.za

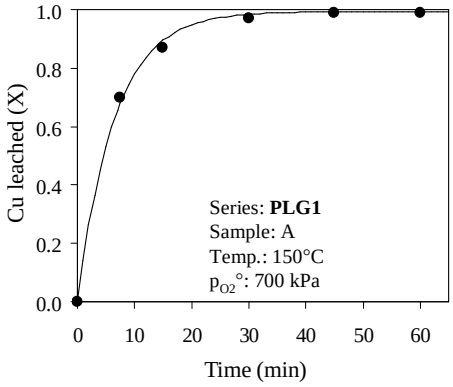

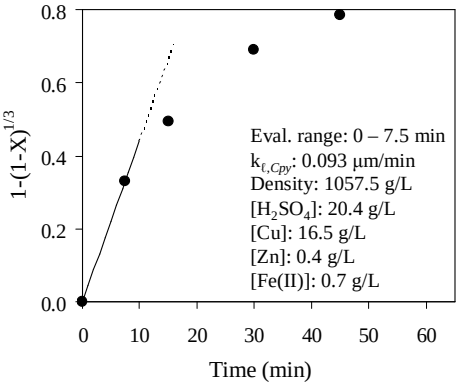

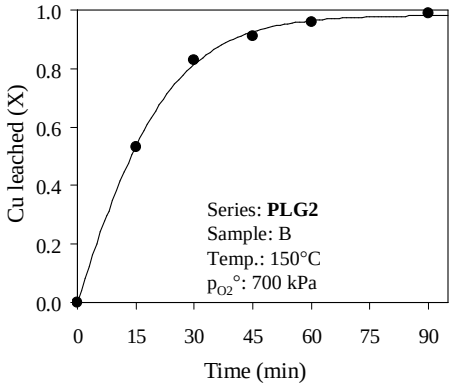

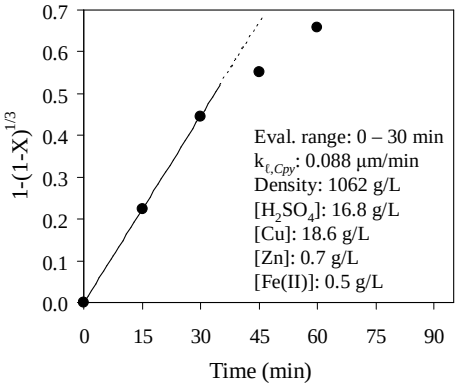

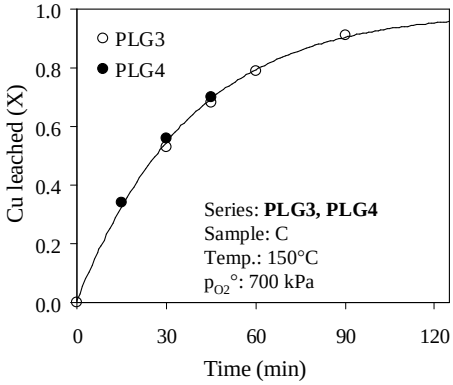

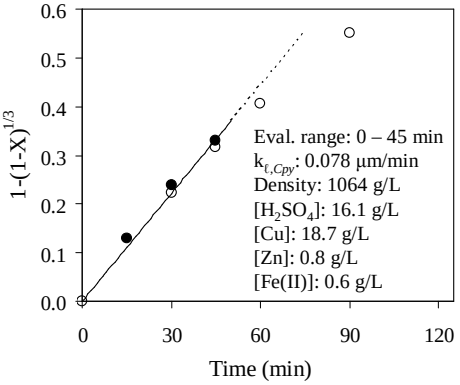

Stellenbosch University http://scholar.sun.ac.za

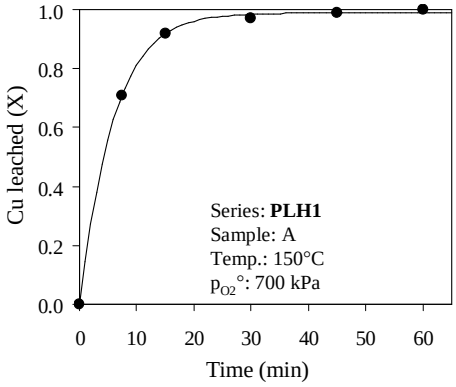

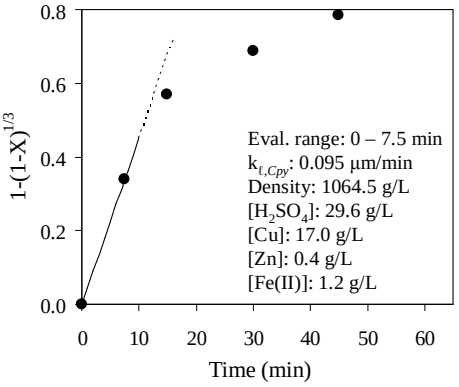

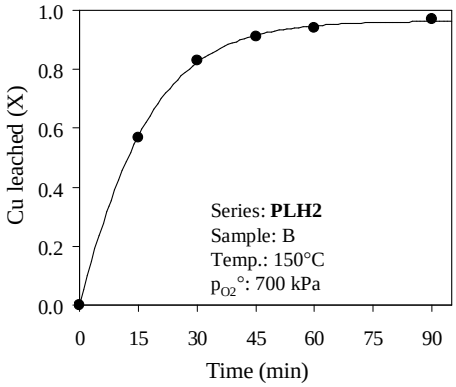

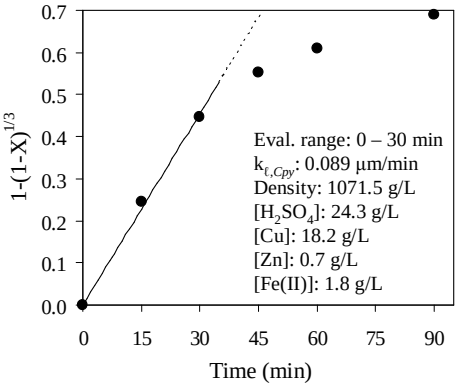

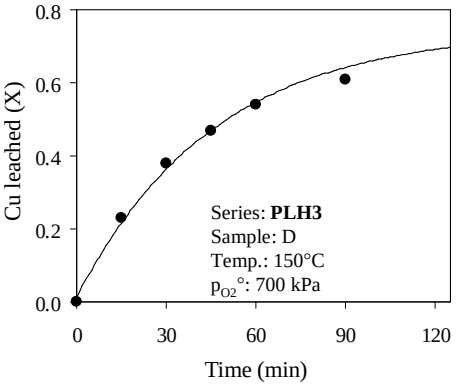

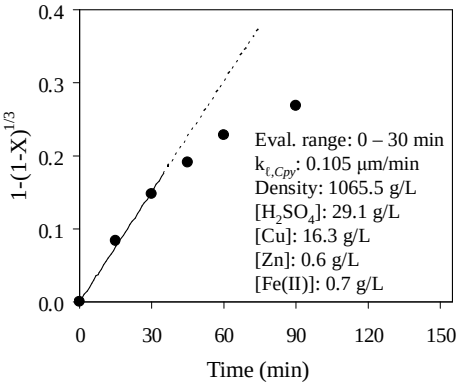

Stellenbosch University http://scholar.sun.ac.za

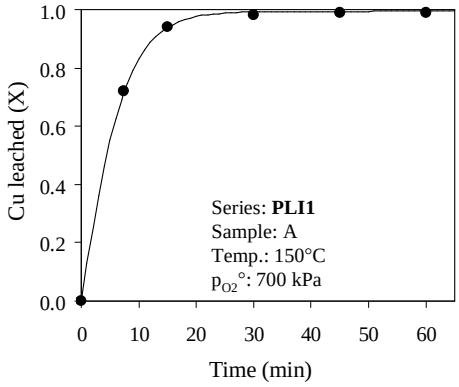

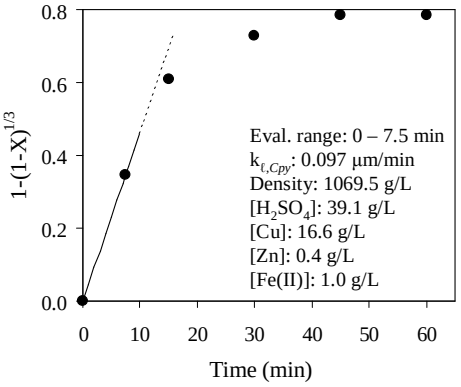

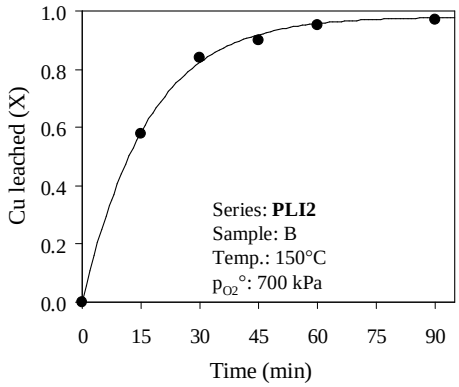

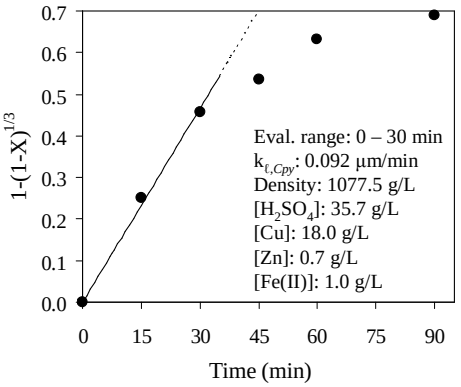

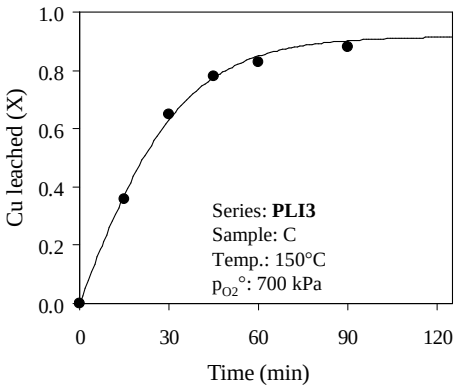

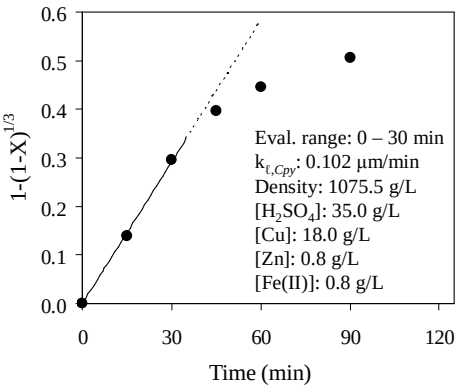

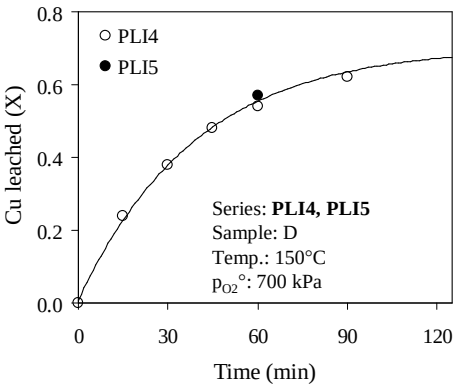

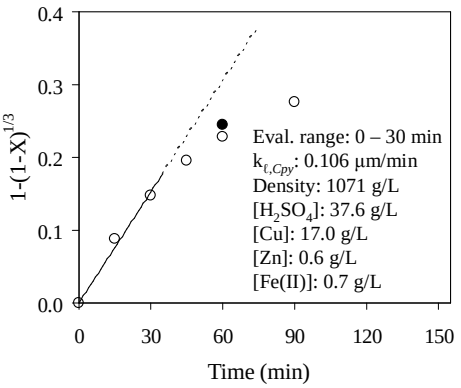

Stellenbosch University http://scholar.sun.ac.za

G.5 Oxidation chemistry and mechanism

These tests aimed to generate information on the chemistry (stoichiometry) and mechanisms of the important oxidation reactions (HBMS 777 concentrate oxidation under MT autoclave conditions).

PLK1	Temp.	Imp. speed	P_g	p_{O2}°	Solids	Solids	Solution	[c] Density
[a] **(PLE52)**	150°C	1000 rpm	1090 kPa	700 kPa	0.6 wt %	5.8 g	994.2 g	1073 g/L
[b] LS, QB	Cu	Zn	–	Fe (II)	H_2SO_4	–	SO_4	H_2O
0.35 g/L ea.	18.6 g/L	0.8 g/L	–	0 g/L	24.7 g/L	–	53.5 g/L	921.5 g
min (test)	Sld. (g)	Colour	Sln. (g)	Vol. (mL)	Colour	[c] Dens (g/L)	[c] E_{Ag} (mV)	[c] pH
30 (K12)	3.6	Grey	950.3	883	Blue	1076	495	0.82

Solids	Cu (%)	Zn (%)	Fe (%)	–	S^{2-} (%)	S° (%)	SO_4 (%)	S^T (%)
Head	30.3	0.1	28.1	–	38.9	0.0	0.4	39.0
30 (K12)	17.1	0.0	23.4	–	26.8	23.3	0.4	50.0

Solution	Cu (g/L)	Zn (g/L)	Fe^T (g/L)	FeII (g/L)	H_2SO_4 (g/L)	–	SO_4 (g/L)	–
30 (K12)	20.36	0.75	1.06	0.36	21.3	–	55.4	–

Extraction	[d] Cu (%)	[d] Zn (%)	[d, e] Fe (%)	–	S^{2-} (%)	[f] S° (%)	–	[d] S^T (%)
30 (K12)	65 (98)	83 (90)	57 (109)	–	57	66	–	(95)

[a] PLE52 residue after elemental sulfur removal; [b] Norlig A, Orfom 2 (no pre-drying); [c] 20°C; [d] Elemental accountability in brackets; [e] Fe (sln)/Fe (sld+sln)×100%; [f] S° yield, *i.e.*, $S°/S^{2-}_{rx}$×100%.

Stellenbosch University http://scholar.sun.ac.za

PLL1	Temp.	Imp. speed	P_g	$p_{O2}°$	Solids	Solids	Solution	[b] Density
Sample C	150°C	1000 rpm	640 kPa	250 kPa	1.5 wt %	15 g	985 g	1051 g/L
[a] LS, QB	Cu	Zn	–	Fe (II)	H_2SO_4	–	SO_4	H_2O
0.35 g/L ea.	15 g/L	0 g/L	–	0 g/L	25 g/L	–	47.3 g/L	924.8 g
min (test)	Sld. (g)	Colour	Sln. (g)	Vol. (mL)	Colour	[b] Dens (g/L)	[b] E_{Ag} (mV)	[b] pH
30 (L12)	10.9	Grey	932.8	878	Green	1061	452	0.78
45 (L13)	8.8	Grey	931.2	875	Green	1064	469	0.93
60 (L14)	8.7	Grey	920.2	866	Green	1063	468	0.86
90 (L15)	7.5	Grey	927.1	871	Green	1065	476	0.89
Solids	Cu (%)	Zn (%)	Fe (%)	–	S^{2-} (%)	S° (%)	SO_4 (%)	S^T (%)
Head	28.5	4.6	29.5	–	35.5	0.0	0.0	35.5
30 (L12)	28.3	0.6	26.9	–	34.0	10.4	0.0	44.3
45 (L13)	26.2	0.1	23.1	–	34.5	16.3	0.0	50.9
60 (L14)	24.7	0.1	24.4	–	34.0	18.8	0.0	51.0
90 (L15)	22.1	0.0	21.5	–	30.3	24.3	0.0	53.6
Solution	Cu (g/L)	Zn (g/L)	Fe^T (g/L)	FeII (g/L)	H_2SO_4 (g/L)	–	SO_4 (g/L)	–
30 (L12)	17.06	0.76	1.69	0.96	17.3	–	47.6	–
45 (L13)	17.66	0.77	2.35	0.82	16.2	–	49.2	–
60 (L14)	17.86	0.82	2.49	0.94	16.3	–	50.0	–
90 (L15)	18.60	0.84	2.76	0.92	16.0	–	51.5	–
Extraction	[c] Cu (%)	[c] Zn (%)	[c, d] Fe (%)	–	S^{2-} (%)	[e] S° (%)	–	[c] S^T (%)
30 (L12)	28 (99)	91 (106)	33 (100)	–	30	71	–	(93)
45 (L13)	46 (97)	99 (99)	46 (92)	–	43	63	–	(93)
60 (L14)	50 (96)	99 (104)	49 (97)	–	44	69	–	(93)
90 (L15)	61 (97)	100 (106)	54 (91)	–	57	60	–	(94)

[a] Norlig A, Orfom 2 (no pre-drying); [b] 20°C; [c] Elemental accountability in brackets; [d] Fe (sln)/Fe (sld+sln)×100%; [e] S° yield, *i.e.*, $S°/S^{2-}{}_{rx}$×100%.

Stellenbosch University http://scholar.sun.ac.za

PLL2	Temp.	Imp. speed	P_g	$p_{O2}°$	Solids	Solids	Solution	[b] Density
Sample C	150°C	1000 rpm	1890 kPa	1500 kPa	1.5 wt %	15 g	985 g	1051 g/L
[a] LS, QB	Cu	Zn	–	Fe (II)	H_2SO_4	–	SO_4	H_2O
0.35 g/L ea.	15 g/L	0 g/L	–	0 g/L	25 g/L	–	47.3 g/L	924.8 g
min (test)	Sld. (g)	Colour	Sln. (g)	Vol. (mL)	Colour	[b] Dens (g/L)	[b] E_{Ag} (mV)	[b] pH
30 (L22)	7.2	Grey	906.7	851	Green	1066	504	0.84
45 (L23)	7.1	Brown	921.6	864	Green blue	1067	507	0.88
60 (L24)	9.0	Red	908.7	852	Green blue	1066	505	0.82
90 (L25)	8.6	Red	940.3	881	Blue	1067	510	0.79
Solids	Cu (%)	Zn (%)	Fe (%)	–	S^{2-} (%)	S° (%)	SO_4 (%)	S^T (%)
Head	28.5	4.6	29.5	–	35.5	0.0	0.0	35.5
30 (L22)	21.4	0.1	24.3	–	30.5	25.5	0.0	55.2
45 (L23)	14.7	0.0	24.5	–	22.7	33.8	0.0	55.5
60 (L24)	9.3	0.0	33.6	–	12.8	28.4	1.4	40.8
90 (L25)	4.0	0.0	36.7	–	6.3	34.3	2.1	41.0
Solution	Cu (g/L)	Zn (g/L)	Fe^T (g/L)	FeII (g/L)	H_2SO_4 (g/L)	–	SO_4 (g/L)	–
30 (L22)	19.49	0.80	2.71	0.39	15.8	–	53.0	–
45 (L23)	20.27	0.78	2.62	0.34	14.8	–	52.9	–
60 (L24)	20.75	0.77	1.45	0.05	16.8	–	52.8	–
90 (L25)	21.26	0.71	1.07	0.05	18.7	–	54.4	–
Extraction	[c] Cu (%)	[c] Zn (%)	[c, d] Fe (%)	–	S^{2-} (%)	[e] S° (%)	–	[c] S^T (%)
30 (L22)	64 (99)	99 (99)	52 (92)	–	59	59	–	(94)
45 (L23)	75 (101)	100 (98)	51 (91)	–	70	65	–	(95)
60 (L24)	80 (101)	100 (96)	28 (96)	–	78	61	–	(92)
90 (L25)	92 (104)	100 (91)	21 (93)	–	90	62	–	(96)

[a] Norlig A, Orfom 2 (no pre-drying); [b] 20°C; [c] Elemental accountability in brackets; [d] Fe (sln)/Fe (sld+sln)×100%; [e] S° yield, *i.e.*, $S°/S^{2-}{}_{rx}$×100%.

Stellenbosch University http://scholar.sun.ac.za

PLM1	Temp.	Imp. speed	P_g	p_{O2}°	Solids	Solids	Solution	[b] Density
Sample C	150°C	1000 rpm	1090 kPa	700 kPa	1.5 wt %	15 g	985 g	1064 g/L
[a] LS, QB	Cu	Zn	–	Fe (II)	H_2SO_4	–	SO_4	H_2O
0.35 g/L ea.	25 g/L	0 g/L	–	0 g/L	15 g/L	–	52.6 g/L	911.2 g
min (test)	Sld. (g)	Colour	Sln. (g)	Vol. (mL)	Colour	[b] Dens (g/L)	[b] E_{Ag} (mV)	[b] pH
30 (M11)	13.0	Brown	911.2	842	Green	1082	454	1.24
45 (M12)	12.4	Red	928.5	859	Blue	1081	456	1.19
60 (M13)	11.9	Deep red	868.0	800	Blue	1085	458	1.19
90 (M14)	11.5	Deep red	906.8	836	Blue	1085	471	1.19
150 (M15)	10.7	Deep red	847.3	777	Blue	1091	487	1.16
Solids	Cu (%)	Zn (%)	Fe (%)	–	S^{2-} (%)	S° (%)	SO_4 (%)	S^T (%)
Head	28.5	4.6	29.5	–	35.5	0.0	0.0	35.5
30 (M11)	19.9	0.3	28.6	–	24.5	9.9	1.3	34.5
45 (M12)	17.4	0.2	32.8	–	19.8	14.2	2.3	34.6
60 (M13)	12.1	0.0	34.7	–	14.8	18.6	1.2	33.2
90 (M14)	5.6	0.1	36.2	–	6.9	25.4	1.7	33.1
150 (M15)	1.9	0.0	38.6	–	2.5	28.8	2.7	33.2
Solution	Cu (g/L)	Zn (g/L)	Fe^T (g/L)	FeII (g/L)	H_2SO_4 (g/L)	–	SO_4 (g/L)	–
30 (M11)	30.76	0.78	0.69	0.05	12.1	–	61.4	–
45 (M12)	30.56	0.85	0.43	0.02	12.1	–	60.6	–
60 (M13)	35.29	0.96	0.40	0.01	12.7	–	68.4	–
90 (M14)	33.30	0.88	0.31	0.01	11.6	–	64.0	–
150 (M15)	35.94	0.99	0.30	0.01	13.2	–	69.7	–
Extraction	[c] Cu (%)	[c] Zn (%)	[c, d] Fe (%)	–	S^{2-} (%)	[e] S° (%)	–	[c] S^T (%)
30 (M11)	41 (104)	94 (99)	13 (95)	–	41	58	–	(100)
45 (M12)	50 (103)	97 (107)	8 (99)	–	55	59	–	(99)
60 (M13)	67 (108)	99 (110)	7 (99)	–	67	61	–	(102)
90 (M14)	85 (104)	99 (105)	6 (98)	–	85	63	–	(99)
150 (M15)	95 (102)	100 (110)	5 (97)	–	95	60	–	(99)

[a] Norlig A, Orfom 2 (no pre-drying); [b] 20°C; [c] Elemental accountability in brackets; [d] Fe (sln)/Fe (sld+sln)×100%; [e] S° yield, *i.e.*, $S°/S^{2-}{}_{rx}$×100%.

Stellenbosch University http://scholar.sun.ac.za

PLM2	Temp.	Imp. speed	P_g	p_{O2}°	Solids	Solids	Solution	[b] Density
Sample C	150°C	1000 rpm	1090 kPa	700 kPa	1.5 wt %	15 g	985 g	1077 g/L
[a] LS, QB	Cu	Zn	–	Fe (II)	H_2SO_4	–	SO_4	H_2O
0.35 g/L ea.	25 g/L	0 g/L	–	0 g/L	25 g/L	–	62.4 g/L	902.9 g
min (test)	Sld. (g)	Colour	Sln. (g)	Vol. (mL)	Colour	[b] Dens (g/L)	[b] E_{Ag} (mV)	[b] pH
30 (M21)	9.0	Grey	936.7	859	Green	1090	462	1.06
45 (M22)	7.8	Brown	926.9	848	Green	1093	464	1.15
60 (M23)	8.5	Red brown	905.4	828	Blue	1094	470	1.03
90 (M24)	12.3	Red	913.8	837	Blue	1092	485	0.89
150 (M25)	11.6	Red	844.3	767	Blue	1101	494	0.96
Solids	Cu (%)	Zn (%)	Fe (%)	–	S^{2-} (%)	S° (%)	SO_4 (%)	S^T (%)
Head	28.5	4.6	29.5	–	35.5	0.0	0.0	35.5
30 (M21)	24.7	0.3	25.6	–	32.9	15.5	0.0	49.9
45 (M22)	21.4	0.1	23.5	–	29.8	20.6	1.3	49.9
60 (M23)	14.4	0.0	27.5	–	19.0	24.4	2.1	44.6
90 (M24)	3.9	0.0	36.0	–	5.5	22.2	3.2	28.7
150 (M25)	0.7	0.0	38.3	–	1.2	28.1	3.3	30.0
Solution	Cu (g/L)	Zn (g/L)	Fe^T (g/L)	FeII (g/L)	H_2SO_4 (g/L)	–	SO_4 (g/L)	–
30 (M21)	28.2	0.76	2.18	0.55	15.7	–	64.5	–
45 (M22)	29.4	0.81	2.24	0.51	15.4	–	66.2	–
60 (M23)	30.5	0.80	1.82	0.47	17.4	–	68.8	–
90 (M24)	31.8	0.84	0.53	0.01	18.6	–	69.1	–
150 (M25)	33.8	0.86	0.55	0.01	19.6	–	73.1	–
Extraction	[c] Cu (%)	[c] Zn (%)	[c, d] Fe (%)	–	S^{2-} (%)	[e] S° (%)	–	[c] S^T (%)
30 (M21)	49 (97)	96 (97)	42 (93)	–	45	57	–	(93)
45 (M22)	62 (98)	99 (98)	42 (83)	–	57	52	–	(92)
60 (M23)	72 (97)	100 (95)	33 (85)	–	70	55	–	(93)
90 (M24)	89 (100)	100 (100)	10 (108)	–	87	58	–	(93)
150 (M25)	98 (96)	100 (94)	9 (108)	–	97	62	–	(90)

[a] Norlig A, Orfom 2 (no pre-drying); [b] 20°C; [c] Elemental accountability in brackets; [d] Fe (sln)/Fe (sld+sln)×100%; [e] S° yield, *i.e.*, $S°/S^{2-}{}_{rx}$×100%.

Stellenbosch University http://scholar.sun.ac.za

PLM3	Temp.	Imp. speed	P_g	p_{O2}°	Solids	Solids	Solution	[b] Density
Sample C	150°C	1000 rpm	1090 kPa	700 kPa	1.5 wt %	15 g	985 g	1083 g/L
[a] LS, QB	Cu	Zn	–	Fe (II)	H_2SO_4	–	SO_4	H_2O
0.35 g/L ea.	25 g/L	0 g/L	–	0 g/L	35 g/L	–	72.2 g/L	894.3 g
min (test)	Sld. (g)	Colour	Sln. (g)	Vol. (mL)	Colour	[b] Dens (g/L)	[b] E_{Ag} (mV)	[b] pH
30 (M31)	8.4	Grey	918.2	836	Green	1098	473	0.88
45 (M32)	7.6	Grey	923.4	839	Green	1101	476	0.93
60 (M33)	6.4	Grey	892.5	809	Green	1103	478	0.93
90 (M34)	6.1	Grey	910.5	824	Green	1105	493	0.98
150 (M35)	6.1	Red	885.3	788	Blue	1124	507	1.04
Solids	Cu (%)	Zn (%)	Fe (%)	–	S^{2-} (%)	S° (%)	SO_4 (%)	S^T (%)
Head	28.5	4.6	29.5	–	35.5	0.0	0.0	35.5
30 (M31)	23.3	0.1	21.5	–	32.0	19.2	0.7	51.5
45 (M32)	19.4	0.1	18.2	–	28.3	29.6	0.6	57.5
60 (M33)	19.3	0.1	19.2	–	25.3	35.0	0.7	58.7
90 (M34)	15.9	0.0	14.0	–	20.3	39.6	0.4	60.9
150 (M35)	2.3	0.0	18.5	–	3.8	49.8	2.0	54.5
Solution	Cu (g/L)	Zn (g/L)	Fe^T (g/L)	FeII (g/L)	H_2SO_4 (g/L)	–	SO_4 (g/L)	–
30 (M31)	27.96	0.77	3.09	0.61	24.2	–	74.7	–
45 (M32)	28.84	0.82	3.83	0.46	24.5	–	78.4	–
60 (M33)	30.71	0.86	4.13	0.51	24.6	–	82.2	–
90 (M34)	30.56	0.83	4.33	0.11	22.5	–	80.7	–
150 (M35)	32.77	0.89	4.61	0.01	23.9	–	86.4	–
Extraction	[c] Cu (%)	[c] Zn (%)	[c, d] Fe (%)	–	S^{2-} (%)	[e] S° (%)	–	[c] S^T (%)
30 (M31)	55 (94)	99 (92)	57 (97)	–	50	59	–	(92)
45 (M32)	66 (95)	99 (98)	71 (102)	–	60	69	–	(96)
60 (M33)	72 (96)	100 (99)	74 (102)	–	70	59	–	(94)
90 (M34)	78 (97)	100 (98)	79 (98)	–	77	58	–	(94)
150 (M35)	97 (96)	100 (100)	81 (106)	–	96	59	–	(95)

[a] Norlig A, Orfom 2 (no pre-drying); [b] 20°C; [c] Elemental accountability in brackets; [d] Fe (sln)/Fe (sld+sln)×100%; [e] S° yield, *i.e.*, $S°/S^{2-}{}_{rx}$×100%.

Stellenbosch University http://scholar.sun.ac.za

PLN1	Temp.	Imp. speed	P_g	p_{O2}°	Solids	Solids	Solution	[b] Density
Sample C	150°C	1000 rpm	1090 kPa	700 kPa	1.5 wt %	15 g	985 g	1094 g/L
[a] LS, QB	Cu	Zn	–	Fe (II)	H_2SO_4	–	SO_4	H_2O
0.35 g/L ea.	35 g/L	0 g/L	–	0 g/L	15 g/L	–	67.8 g/L	890.2 g
min (test)	Sld. (g)	Colour	Sln. (g)	Vol. (mL)	Colour	[b] Dens (g/L)	[b] E_{Ag} (mV)	[b] pH
30 (N11)	12.5	Brown	914.5	827	Blue	1106	455	1.12
45 (N12)	12.6	Deep red	932.6	843	Blue	1106	456	1.19
60 (N13)	11.4	Red	908.3	819	Blue	1109	464	1.09
90 (N14)	11.2	Red	924.1	835	Blue	1107	473	1.03
150 (N15)	10.7	Red	912.5	821	Blue	1111	496	1.16
Solids	Cu (%)	Zn (%)	Fe (%)	–	S^{2-} (%)	S° (%)	SO_4 (%)	S^T (%)
Head	28.5	4.6	29.5	–	35.5	0.0	0.0	35.5
30 (N11)	21.3	0.7	33.5	–	24.8	10.2	0.3	35.4
45 (N12)	17.5	0.3	33.8	–	19.1	12.1	1.8	32.8
60 (N13)	12.8	0.0	37.1	–	13.7	19.0	1.7	33.1
90 (N14)	6.8	0.0	38.3	–	7.3	24.5	1.2	33.1
150 (N15)	1.8	0.0	39.6	–	1.2	28.1	1.8	30.3
Solution	Cu (g/L)	Zn (g/L)	Fe^T (g/L)	FeII (g/L)	H_2SO_4 (g/L)	–	SO_4 (g/L)	–
30 (N11)	40.92	0.77	0.36	0.01	11.9	–	75.8	–
45 (N12)	41.80	0.76	0.26	0.01	12.3	–	77.2	–
60 (N13)	44.30	0.90	0.34	0.01	13.2	–	82.3	–
90 (N14)	45.18	0.91	0.24	0.01	12.5	–	82.7	–
150 (N15)	46.46	0.93	0.13	0.01	12.6	–	84.5	–
Extraction	[c] Cu (%)	[c] Zn (%)	[c, d] Fe (%)	–	S^{2-} (%)	[e] S° (%)	–	[c] S^T (%)
30 (N11)	39 (102)	88 (103)	7 (100)	–	43	55	–	(98)
45 (N12)	49 (104)	94 (97)	5 (99)	–	56	51	–	(100)
60 (N13)	66 (105)	99 (106)	6 (100)	–	71	56	–	(101)
90 (N14)	83 (107)	100 (109)	5 (100)	–	85	59	–	(103)
150 (N15)	96 (107)	100 (109)	2 (97)	–	98	57	–	(102)

[a] Norlig A, Orfom 2 (no pre-drying); [b] 20°C; [c] Elemental accountability in brackets; [d] Fe (sln)/Fe (sld+sln)×100%; [e] S° yield, *i.e.*, $S°/S^{2-}{}_{rx}$×100%.

Stellenbosch University http://scholar.sun.ac.za

PLN2	Temp.	Imp. speed	P_g	p_{O2}°	Solids	Solids	Solution	[b] Density
Sample C	150°C	1000 rpm	1090 kPa	700 kPa	1.5 wt %	15 g	985 g	1099 g/L
[a] LS, QB	Cu	Zn	–	Fe (II)	H_2SO_4	–	SO_4	H_2O
0.35 g/L ea.	35 g/L	0 g/L	–	0 g/L	25 g/L	–	77.6 g/L	881.7 g
min (test)	Sld. (g)	Colour	Sln. (g)	Vol. (mL)	Colour	[b] Dens (g/L)	[b] E_{Ag} (mV)	[b] pH
30 (N21)	9.5	Brown	908.3	814	Green	1116	468	1.07
45 (N22)	7.1	Brown	922.4	825	Green	1118	470	1.37
60 (N23)	10.5	Red	904.6	807	Blue	1121	467	1.28
90 (N24)	10.2	Deep red	907.3	809	Blue	1121	471	1.32
150 (N25)	10.5	Deep red	895.0	799	Blue	1120	492	1.17
Solids	Cu (%)	Zn (%)	Fe (%)	–	S^{2-} (%)	S° (%)	SO_4 (%)	S^T (%)
Head	28.5	4.6	29.5	–	35.5	0.0	0.0	35.5
30 (N21)	22.3	0.1	28.2	–	27.2	16.7	0.7	44.5
45 (N22)	19.0	0.1	27.5	–	24.8	25.3	1.0	50.1
60 (N23)	9.8	0.0	34.9	–	11.9	25.2	1.5	38.6
90 (N24)	3.5	0.0	38.8	–	4.4	28.9	2.6	34.7
150 (N25)	0.9	0.0	40.5	–	0.9	31.1	3.1	35.0
Solution	Cu (g/L)	Zn (g/L)	Fe^T (g/L)	FeII (g/L)	H_2SO_4 (g/L)	–	SO_4 (g/L)	–
30 (N21)	41.82	0.85	1.93	0.43	17.1	–	86.0	–
45 (N22)	44.35	0.90	2.65	0.42	15.7	–	90.4	–
60 (N23)	44.79	0.90	1.22	0.01	19.2	–	91.2	–
90 (N24)	45.23	0.92	0.52	0.01	20.1	–	90.9	–
150 (N25)	45.00	0.96	0.47	0.01	20.8	–	91.2	–
Extraction	[c] Cu (%)	[c] Zn (%)	[c, d] Fe (%)	–	S^{2-} (%)	[e] S° (%)	–	[c] S^T (%)
30 (N21)	51 (101)	99 (99)	35 (94)	–	52	56	–	(96)
45 (N22)	69 (106)	99 (106)	49 (92)	–	68	49	–	(99)
60 (N23)	76 (104)	100 (104)	22 (103)	–	77	63	–	(99)
90 (N24)	92 (103)	100 (107)	9 (97)	–	92	59	–	(98)
150 (N25)	98 (101)	100 (110)	8 (103)	–	98	61	–	(97)

[a] Norlig A, Orfom 2 (no pre-drying); [b] 20°C; [c] Elemental accountability in brackets; [d] Fe (sln)/Fe (sld+sln)×100%; [e] S° yield, *i.e.*, $S°/S^{2-}{}_{rx}$×100%.

Stellenbosch University http://scholar.sun.ac.za

PLO1	Temp.	Imp. speed	P_g	p_{O2}°	Solids	Solids	Solution	[b] Density
Sample C	150°C	1000 rpm	1090 kPa	700 kPa	1.5 wt %	15 g	985 g	1107 g/L
[a] LS, QB	Cu	Zn	–	Fe (II)	H_2SO_4	–	SO_4	H_2O
0.35 g/L ea.	25 g/L	15 g/L	–	0 g/L	25 g/L	–	84.5 g/L	871.5 g
min (test)	Sld. (g)	Colour	Sln. (g)	Vol. (mL)	Colour	[b] Dens (g/L)	[b] E_{Ag} (mV)	[b] pH
30 (O11)	9.9	Drk brown	889.4	790	Green	1126	466	1.10
45 (O12)	10.8	Red brown	887.0	788	Green	1126	456	1.00
60 (O13)	10.3	Red brown	923.1	822	Blue	1123	465	1.04
90 (O14)	10.2	Red	900.9	799	Blue	1127	466	1.09
150 (O15)	10.3	Deep red	864.3	761	Blue	1135	477	1.19
Solids	Cu (%)	Zn (%)	Fe (%)	–	S^{2-} (%)	S° (%)	SO_4 (%)	S^T (%)
Head	28.5	4.6	29.5	–	35.5	0.0	0.0	35.5
30 (O11)	23.3	0.3	27.8	–	28.1	14.6	2.0	44.3
45 (O12)	17.3	0.1	31.6	–	18.9	18.5	3.1	38.5
60 (O13)	13.1	0.1	36.1	–	15.1	22.4	3.0	39.2
90 (O14)	6.8	0.1	36.0	–	8.0	26.8	3.1	37.1
150 (O15)	1.6	0.1	39.5	–	1.6	31.8	3.9	35.6
Solution	Cu (g/L)	Zn (g/L)	Fe^T (g/L)	FeII (g/L)	H_2SO_4 (g/L)	–	SO_4 (g/L)	–
30 (O11)	30.11	17.24	2.02	0.44	18.0	–	93.5	–
45 (O12)	30.44	17.07	1.23	0.04	18.6	–	92.6	–
60 (O13)	30.25	16.72	1.18	0.01	18.9	–	92.0	–
90 (O14)	31.51	17.34	0.89	0.01	20.1	–	95.3	–
150 (O15)	34.44	18.67	0.56	0.01	21.7	–	102.4	–
Extraction	[c] Cu (%)	[c] Zn (%)	[c, d] Fe (%)	–	S^{2-} (%)	[e] S° (%)	–	[c] S^T (%)
30 (O11)	47 (98)	96 (97)	35 (97)	–	49	55	–	(94)
45 (O12)	57 (97)	98 (96)	21 (97)	–	62	59	–	(93)
60 (O13)	69 (99)	99 (98)	22 (104)	–	71	60	–	(95)
90 (O14)	84 (97)	99 (99)	16 (97)	–	85	59	–	(95)
150 (O15)	96 (99)	99 (101)	9 (100)	–	97	62	–	(97)

[a] Norlig A, Orfom 2 (no pre-drying); [b] 20°C; [c] Elemental accountability in brackets; [d] Fe (sln)/Fe (sld+sln)×100%; [e] S° yield, *i.e.*, $S°/S^{2-}{}_{rx}$×100%.

Stellenbosch University http://scholar.sun.ac.za

PLO2	Temp.	Imp. speed	P_g	$p_{O2}°$	Solids	Solids	Solution	[b] Density
Sample C	150°C	1000 rpm	1090 kPa	700 kPa	1.5 wt %	15 g	985 g	1130 g/L
[a] LS, QB	Cu	Zn	–	Fe (II)	H_2SO_4	–	SO_4	H_2O
0.35 g/L ea.	25 g/L	25 g/L	–	0 g/L	25 g/L	–	99.2 g/L	851.9 g
min (test)	Sld. (g)	Colour	Sln. (g)	Vol. (mL)	Colour	[b] Dens (g/L)	[b] E_{Ag} (mV)	[b] pH
30 (O21)	11.2	Brown	909.3	794	Green	1145	452	0.90
45 (O22)	11.0	Red brown	930.2	815	Green	1142	456	0.91
60 (O23)	10.7	Red brown	867.2	754	Blue	1150	463	0.87
90 (O24)	10.5	Red	927.0	807	Blue	1149	471	0.83
150 (O25)	10.7	Deep red	886.1	771	Blue	1150	480	0.88
Solids	Cu (%)	Zn (%)	Fe (%)	–	S^{2-} (%)	S° (%)	SO_4 (%)	S^T (%)
Head	28.5	4.6	29.5	–	35.5	0.0	0.0	35.5
30 (O21)	21.1	0.6	28.7	–	24.2	15.9	2.0	40.4
45 (O22)	15.7	0.2	30.5	–	20.1	18.8	3.0	40.4
60 (O23)	12.5	0.2	33.4	–	16.5	20.9	3.9	38.8
90 (O24)	5.6	0.1	35.0	–	7.7	26.9	2.8	35.9
150 (O25)	0.8	0.1	37.4	–	0.9	31.2	4.2	33.8
Solution	Cu (g/L)	Zn (g/L)	Fe^T (g/L)	FeII (g/L)	H_2SO_4 (g/L)	–	SO_4 (g/L)	–
30 (O21)	28.82	26.95	1.40	0.34	19.2	–	105.5	–
45 (O22)	29.39	27.85	1.30	0.03	19.1	–	107.6	–
60 (O23)	31.65	27.69	0.90	0.01	19.9	–	110.5	–
90 (O24)	31.10	27.29	0.80	0.01	19.6	–	108.5	–
150 (O25)	32.46	28.00	0.52	0.01	20.5	–	111.8	–
Extraction	[c] Cu (%)	[c] Zn (%)	[c, d] Fe (%)	–	S^{2-} (%)	[e] S° (%)	–	[c] S^T (%)
30 (O21)	46 (97)	91 (95)	25 (96)	–	50	66	–	(94)
45 (O22)	60 (98)	97 (101)	24 (98)	–	59	64	–	(98)
60 (O23)	69 (96)	98 (93)	15 (94)	–	67	61	–	(93)
90 (O24)	87 (98)	99 (98)	14 (96)	–	85	61	–	(96)
150 (O25)	98 (96)	98 (96)	9 (98)	–	98	63	–	(94)

[a] Norlig A, Orfom 2 (no pre-drying); [b] 20°C; [c] Elemental accountability in brackets; [d] Fe (sln)/Fe (sld+sln)×100%; [e] S° yield, *i.e.*, $S°/S^{2-}{}_{rx}$×100%.

Stellenbosch University http://scholar.sun.ac.za

PLO3	Temp.	Imp. speed	P_g	p_{O2}°	Solids	Solids	Solution	[b] Density
Sample C	150°C	1000 rpm	1090 kPa	700 kPa	1.5 wt %	15 g	985 g	1155 g/L
[a] LS, QB	Cu	Zn	–	Fe (II)	H_2SO_4	–	SO_4	H_2O
0.35 g/L ea.	25 g/L	35 g/L	–	0 g/L	25 g/L	–	113.9 g/L	833.4 g
min (test)	Sld. (g)	Colour	Sln. (g)	Vol. (mL)	Colour	[b] Dens (g/L)	[b] E_{Ag} (mV)	[b] pH
30 (O31)	10.5	Grey	944.3	814	Green	1160	461	0.94
45 (O32)	10.8	Drk brown	985.5	853	Green	1155	458	1.05
60 (O33)	10.8	Deep red	893.8	761	Blue	1174	461	0.94
90 (O34)	11.0	Deep red	912.3	781	Blue	1168	465	0.91
150 (O35)	10.7	Deep red	834.7	707	Blue	1181	480	0.87
Solids	Cu (%)	Zn (%)	Fe (%)	–	S^{2-} (%)	S° (%)	SO_4 (%)	S^T (%)
Head	28.5	4.6	29.5	–	35.5	0.0	0.0	35.5
30 (O31)	21.5	0.8	25.5	–	30.7	12.8	1.9	44.9
45 (O32)	16.0	0.2	28.5	–	22.2	17.2	3.3	41.6
60 (O33)	11.9	0.1	32.0	–	15.3	21.8	2.3	37.1
90 (O34)	6.6	0.1	34.4	–	9.0	25.3	3.4	35.3
150 (O35)	0.8	0.1	37.6	–	0.9	31.2	4.2	33.3
Solution	Cu (g/L)	Zn (g/L)	Fe^T (g/L)	FeII (g/L)	H_2SO_4 (g/L)	–	SO_4 (g/L)	–
30 (O31)	27.21	35.84	1.96	0.40	17.3	–	115.6	–
45 (O32)	27.76	35.94	1.53	0.03	17.2	–	115.7	–
60 (O33)	30.55	38.12	1.17	0.01	19.1	–	124.1	–
90 (O34)	31.30	36.67	0.88	0.01	19.3	–	122.5	–
150 (O35)	34.94	39.61	0.58	0.01	20.9	–	133.2	–
Extraction	[c] Cu (%)	[c] Zn (%)	[c, d] Fe (%)	–	S^{2-} (%)	[e] S° (%)	–	[c] S^T (%)
30 (O31)	48 (95)	88 (96)	35 (95)	–	40	61	–	(95)
45 (O32)	60 (99)	97 (100)	29 (97)	–	56	61	–	(99)
60 (O33)	70 (96)	98 (95)	20 (97)	–	69	63	–	(94)
90 (O34)	83 (98)	98 (94)	15 (99)	–	82	63	–	(94)
150 (O35)	98 (97)	98 (92)	9 (98)	–	98	63	–	(92)

[a] Norlig A, Orfom 2 (no pre-drying); [b] 20°C; [c] Elemental accountability in brackets; [d] Fe (sln)/Fe (sld+sln)×100%; [e] S° yield, *i.e.*, $S°/S^{2-}{}_{rx}$×100%.

Stellenbosch University http://scholar.sun.ac.za

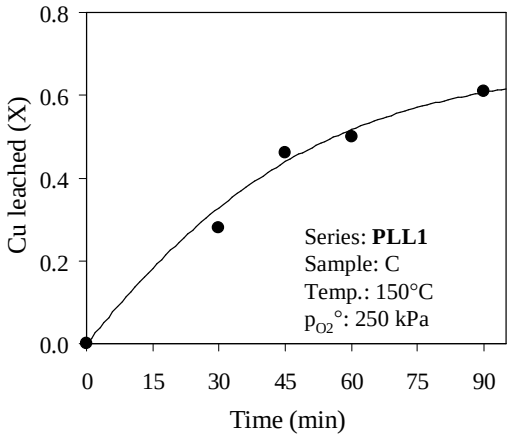

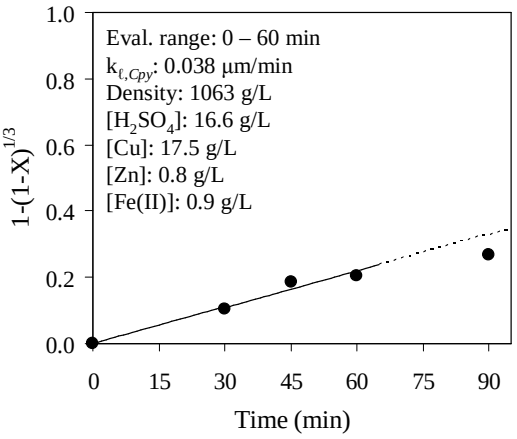

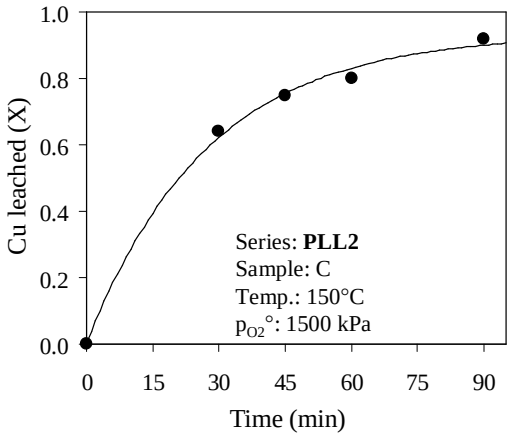

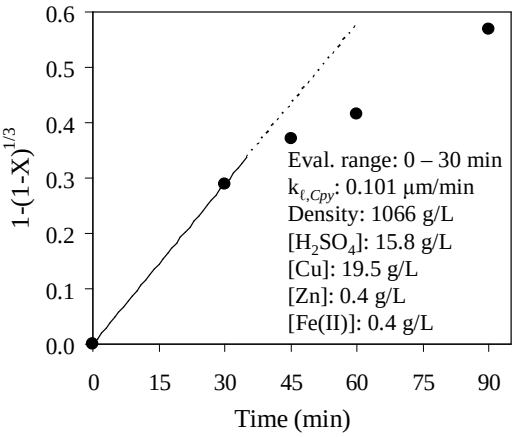

Stellenbosch University http://scholar.sun.ac.za

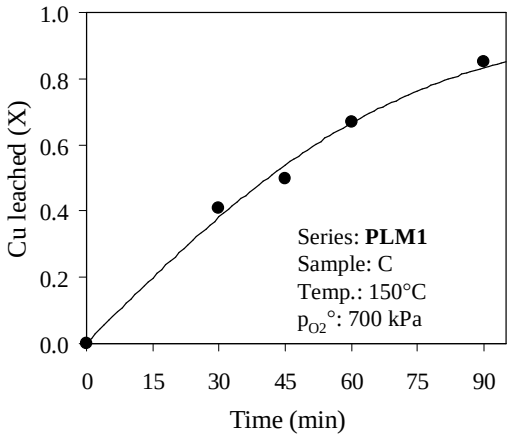

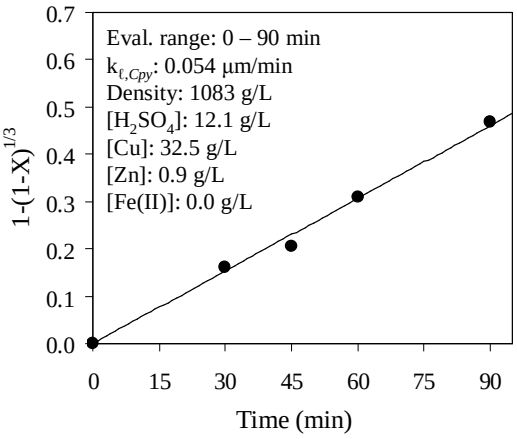

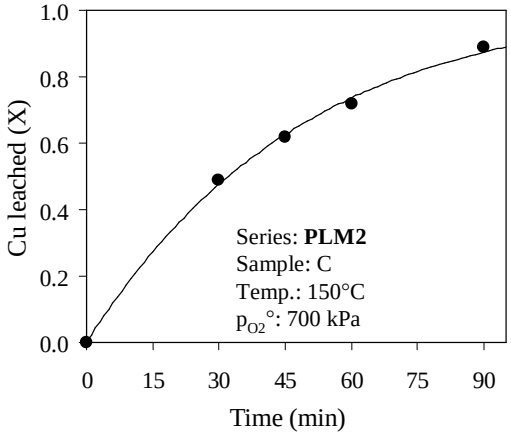

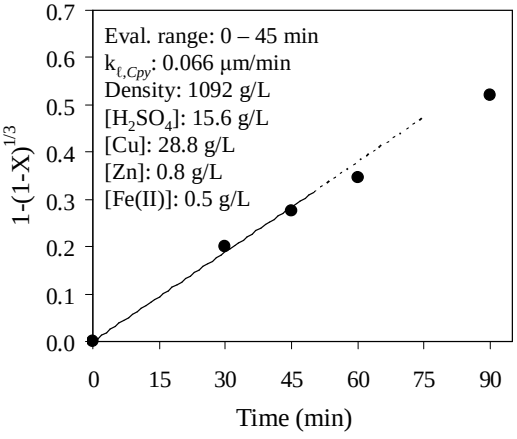

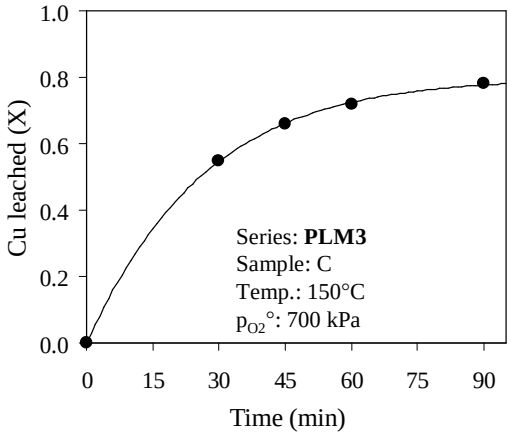

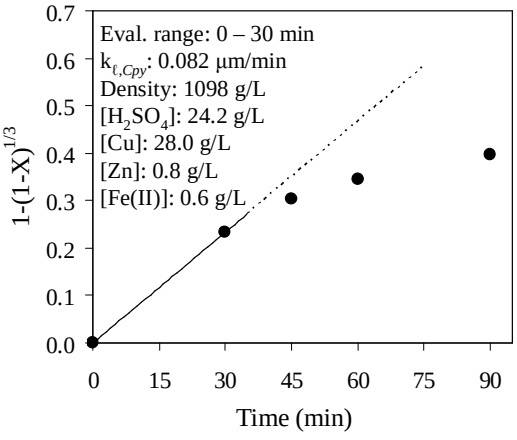

Stellenbosch University http://scholar.sun.ac.za

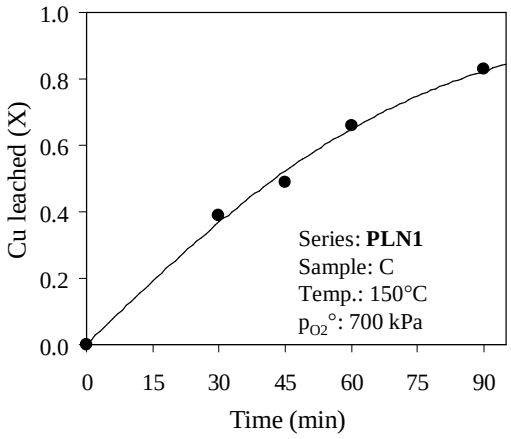

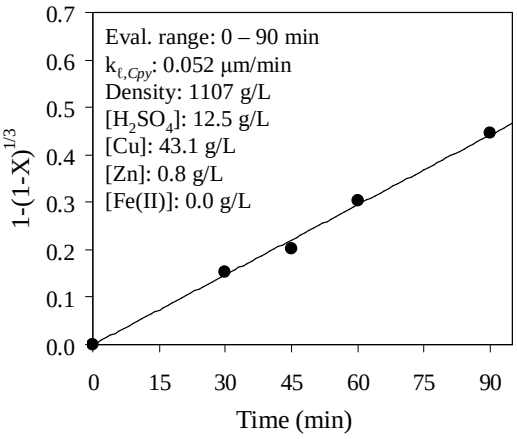

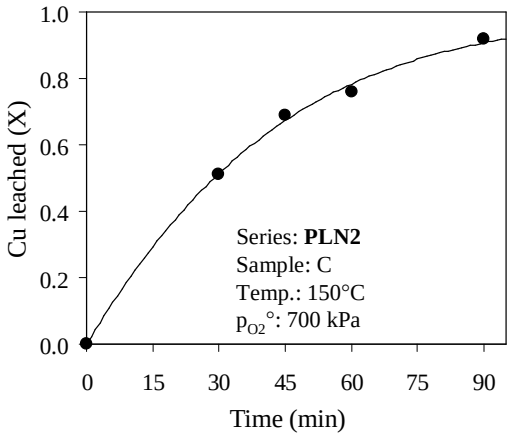

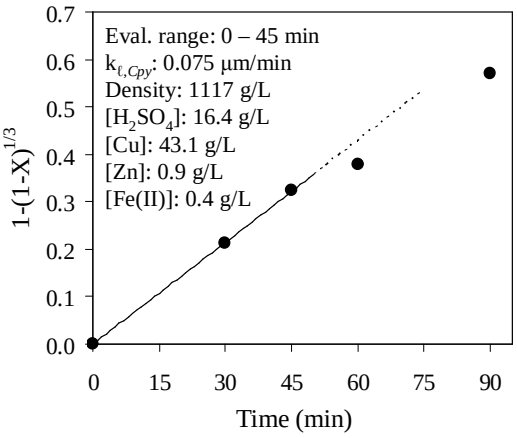

Stellenbosch University http://scholar.sun.ac.za

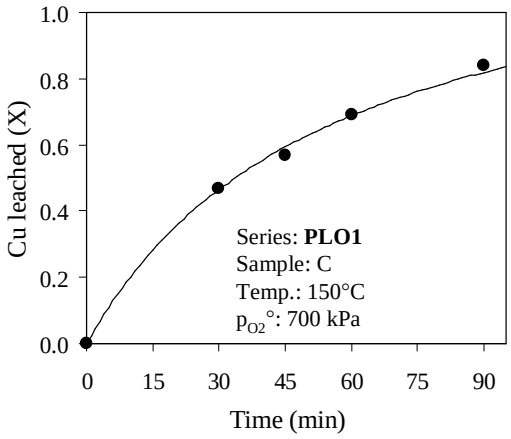

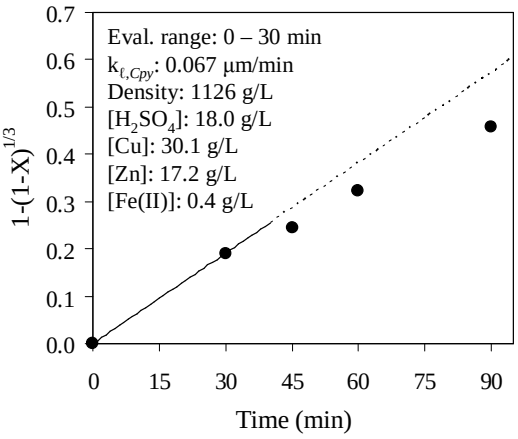

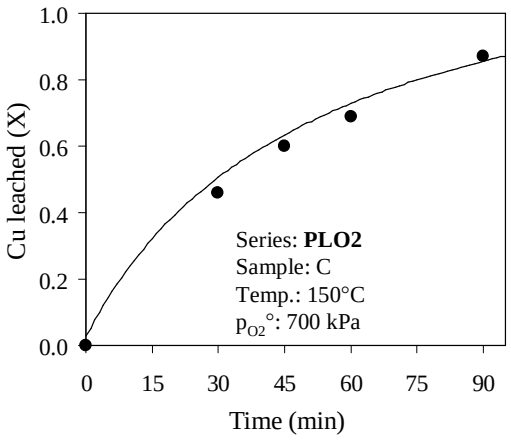

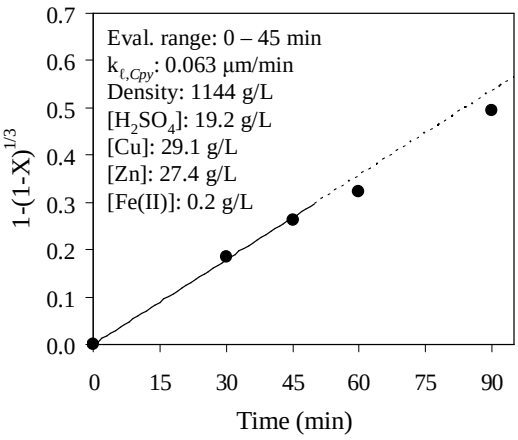

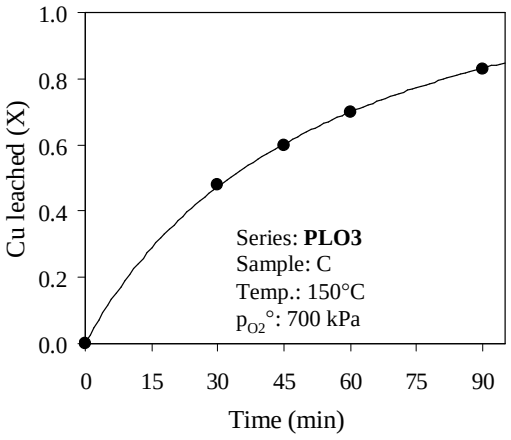

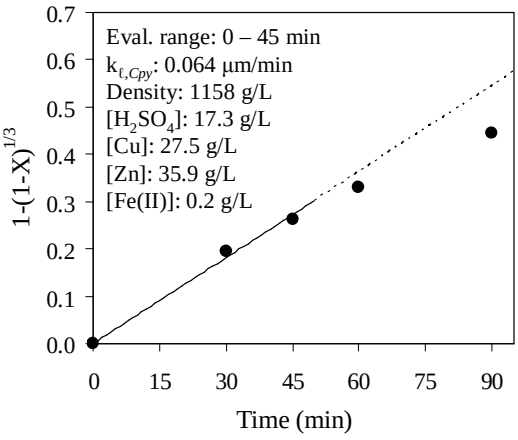

Stellenbosch University http://scholar.sun.ac.za

APPENDIX H. MACROSCOPIC POPULATION BALANCE FOR CONTINUOUS STIRRED TANK AND BATCH REACTORS

This appendix presents the mathematical derivation of the population balance (PB) model for a series of continuous stirred tank reactors (CSTRs). All the theoretical concepts are obtained from Randolph and Larson (1988; Ch.3), unless indicated otherwise. Although these authors presented the general theory of particulate processes from a crystallisation perspective, the principles remain equally applicable to leaching. The general derivation of the PB balance is presented first, followed by mathematical simplification and manipulation in order to obtain the macroscopic form of the PB, which is directly applicable to a series of ideal CSTRs. Finally, the PB is adapted to describe leaching in a batch stirred tank reactor (BSTR).

H.1 Derivation of the PB model for a single reactor under chemically controlled kinetics

The concept of particle phase space may be used to describe a property distribution. This particle space is subdivided into external and internal coordinates. External coordinates refer to the spatial distribution of particles in a certain volume, while internal properties refer to each individual particle. The vector $\boldsymbol{\upsilon}$ denotes the velocity of this particle phase space in a closed volume and has an internal (i) and external (e) term:

$$\boldsymbol{\upsilon} = \boldsymbol{\upsilon}_i + \boldsymbol{\upsilon}_e \qquad \text{H.1}$$

The general mass conservation equation is used as a starting point:

$$\text{Accumulation} = \text{Input} - \text{Output} + \text{Net generation} \qquad \text{H.2}$$

If a Lagrangian viewpoint is taken, *i.e.*, the external particle volume (under consideration) moves convectively with the particles, the following general equation of the number continuity, in particle phase space, is obtained (see details in Randolph & Larson, 1988):

$$\frac{\partial n}{\partial t} + \boldsymbol{\nabla} \cdot (\boldsymbol{\upsilon} n) = B - D \qquad \text{H.3}$$

This general PB equation states that the accumulation of any particle number distribution property in the time dimension, $\partial n(V,t)/\partial t$, where V represents an arbitrary volume, can be expressed by the expansion of the distribution in terms of the above internal and external velocity terms. The mathematical summation ($\boldsymbol{\nabla}$) makes provision for all possible external (x, y, z) and internal coordinates in which the particle distribution needs to be described. The terms B and D refer to the birth and death rates of the distribution property, respectively. Equation H.3 may, by convention, be integrated over the effective reactor volume of gas- and solids-free solution (V_l):

Stellenbosch University http://scholar.sun.ac.za

$$\int_{V_l}\left(\frac{\partial n}{\partial t} + \nabla \cdot \boldsymbol{\upsilon}_i n + \nabla \cdot \boldsymbol{\upsilon}_e n + D - B\right) dV_l = 0 \qquad \text{H.4}$$

This PB equation may be averaged (macroscopic approach) over the external phase space because the CSTR is assumed to operate under conditions of perfect micro-mixing. This assumption of maximum-mixedness allows n, D and B to be excluded from the volume integration, *i.e.*, these properties only become functions of time in the internal particle property coordinates. The remaining term, an integral over the volume of the spatial divergence of the population flux in the reactor, can now be converted into a surface integral of the population flux. This integral operates over the total surface, S_m, moving through the reactor at an average velocity, ν_n, normal to the surface:

$$\int_{V_l} \nabla \cdot \boldsymbol{\upsilon}_e n \, dV_l = \int_{S_m} \nu_n n \, dS_m \qquad \text{H.5}$$

The term, S_m, can be subdivided into three components:

1) The total moving surface, S_k, due to the in- and outflow of *k* slurry streams, where Q_l refers here to the volumetric flowrate (the sign convention states that flow in an outward direction, normal to the surface, is positive):

$$\int_{S_k} \nu_n n \, dS = \sum_k Q_{l,k} n_k \qquad \text{H.6}$$

2) The total moving surface, S_l, due to a change in solids- and gas-free liquid in the reactor. The reactor operates at steady state and this term reduces to zero, *i.e.*:

$$\int_{S_l} \nu_n n \, dS = 0 \qquad \text{H.7}$$

3) The total moving surface, S_e, due to changes in the solids- and gas-free liquid, resulting from changes in the void fraction of solids in the reactor. If it is assumed that the volume occupied by solids is small compared to the solids- and gas-free liquid volume, *i.e.*, 'thin' suspensions, this terms also reduces to zero, *i.e.*:

$$\int_{S_e} \nu_n n \, dS = 0 \qquad \text{H.8}$$

With these assumptions, Equation H.5 may be rewritten as follows:

$$\int_{V_l} \nabla \cdot \boldsymbol{\upsilon}_e n \, dV_l = \sum_k Q_{l,k} n_k \qquad \text{H.9}$$

This term may now be substituted into Equation H.4, to yield:

$$\left(\int_{V_l} \frac{\partial n}{\partial t} dV_l\right) + (\nabla \cdot \boldsymbol{\upsilon}_i n)V_l + \sum_k Q_{l,k} n_k + (D - B)V_l = 0 \qquad \text{H.10}$$

Stellenbosch University http://scholar.sun.ac.za

Since the reactor operates at steady state, the change of the particle distribution in the time dimension, $\partial n/\partial t$, may be omitted. Furthermore, the death and birth rate functions, which account for discrete changes in the population, *e.g.*, due to breakage, coalescence or agglomeration, may be assumed negligible in the case of leaching of sulfide mineral particles. These assumptions yield the spatial-averaged PB equation in a steady-state leaching reactor:

$$\sum_k Q_{l,k} n_k + (\nabla \cdot \boldsymbol{\upsilon}_l n) V_l = 0 \qquad \text{H.11}$$

Furthermore, since the reaction extent of intrinsic leaching is captured be the change in the unreacted core size distribution only, the first term may be translated as follows (for single feed & exit slurry streams):

$$\sum_k Q_{l,k} n_k = Q_{l,out} \psi_{l,out} - Q_{l,in} \psi_{l,in} \qquad \text{H.12}$$

where ψ_l represents the average (unreacted) core size (number) distribution, defined per unit volume solution. If the volumetric flowrate of bubble- and solids-free solution is not significantly affected by the reactions, Q_l may be used as a convenient basis to define the in- and outflows of the particle size distributions. Since the reactor is micro-mixed, with the solid phase ideally suspended, Equation H.11 may be represented as follows:

$$Q_l(\psi_l - \psi_{l,in}) + V_l \frac{\partial(\upsilon_\ell \psi_l)}{\partial \ell} = 0 \qquad \text{H.13}$$

where the velocity vector is replaced by the (one-dimensional) rate of core size (ℓ) change, υ_ℓ, due to leaching. If the volumetric flowrate of bubble-free solution is approximately constant, a common reference may be used to define $\psi_{l,in}$ and ψ_l, *i.e.*, the average residence time, τ (Ch. 7; Eq. 7.1), may be substituted into Equation H.13, resulting in the continuous macroscopic PB equation:

$$\frac{\partial(\upsilon_\ell \psi_l)}{\partial \ell} + \frac{\psi_l}{\tau} = \frac{\psi_{l,in}}{\tau} \qquad \text{H.14}$$

H.2 Solving the macroscopic PB for a series of CSTRs

If the rate of shrinkage is constant, *e.g.*, when no inhibiting (elemental) sulfur product layers are formed (see discussions in Sect. 6.3.5), the following holds:

$$\frac{\partial \upsilon_\ell}{\partial \ell} = 0 \qquad \text{H.15}$$

Equation H.14 may now be expressed for reactor, *j*, where subscript *j*-1 refers to the previous reactor in the series (overflows into reactor *j*):

Stellenbosch University http://scholar.sun.ac.za

$$\upsilon_\ell \frac{\partial \psi_j}{\partial \ell} + \frac{\psi_j}{\tau_j} = \frac{\psi_{j-1}}{\tau_j} \qquad \text{H.16}$$

Equation H.16 is a first-order differential equation and the equation can be solved using the well-known method of integrating factors (Herbst, 1979). The boundary condition, $\psi \rightarrow 0$ as $\ell \rightarrow \ell_{max}$, which practically means that no particle can remain totally unleached, yields the following equation of the marginal distribution of core sizes in the exit stream (Crundwell & Bryson, 1992; Sepulveda & Herbst, 1993):

$$\psi_j(\ell) = \frac{1}{\tau_j \upsilon_\ell} exp\left(\frac{-\ell}{\tau_j \upsilon_\ell}\right) \int_{\ell_{max,\,j-1}}^{\ell} exp\left(\frac{\ell'}{\tau_j \upsilon_\ell}\right) \psi_{j-1}(\ell')\, d\ell' \qquad \text{H.17}$$

The symbol $\ell_{max,j-1}$ refers to the largest unreacted size in the feed distribution to reactor j, while ℓ' refers to the initial unreacted core size (obviously between ℓ & $\ell_{max,j-1}$), that yields the exit density distribution, ψ_j, at size ℓ. In this study, the feed and exit number density distributions (ψ_{j-1} & ψ_j, respectively) were expressed per unit mass water flowing out of the reactor. This is a convenient basis, as it is independent of density variation, is consistent with the molality scale, *i.e.*, the scale chosen to express the abundance of solute species, and results in a more elegant mass balance representation of the CSTR (see Sect. 7.2.3).

H.3 Solving the macroscopic PB for a batch stirred tank reactor (BSTR)

The PB for the batch reactor may be derived starting with Equation H.10. Since there is no flow in and out of the reactor, and no breakage or coalescence of particles occurs, the PB reduces to:

$$\left(\int_{V_l} \frac{\partial n}{\partial t} dV_l\right) = -(\nabla \cdot \boldsymbol{\upsilon}_i n) V_l \qquad \text{H.18}$$

As in the case of the continuous reactor, the spatial-averaged balance needs to be considered for a well-mixed batch stirred tank reactor, *i.e.*, the PB over the macroscopic external coordinate region. Furthermore, since the intrinsic leaching extent is captured by the one-dimensional change in the unreacted core size distribution only, the macroscopic PB may be expressed as follows:

$$\frac{\partial [V_l \cdot n(\ell, t)]}{\partial t} = -V_l \frac{\partial [\upsilon_\ell \cdot n(\ell, t)]}{\partial \ell} \qquad \text{H.19}$$

To be consistent with the methodology used to describe the continuous reactor, the unreacted core size number distribution is defined per unit mass water in the BSTR, *i.e.*, $\psi(\ell)$, which then yields:

$$\frac{\partial [W_{H_2O} \cdot \psi(\ell, t)]}{\partial t} = -W_{H_2O} \frac{\partial [\upsilon_\ell \cdot \psi(\ell, t)]}{\partial \ell} \qquad \text{H.20}$$

Stellenbosch University http://scholar.sun.ac.za

where W_{H2O} is the mass of water in the batch reactor. The formal solution of this first-order differential equation, subject to side conditions, is (see analogous expressions in Herbst, 1979):

$$\psi(\ell, t)\, d\ell = \psi(L_o)\, dL_o \qquad \text{H.21}$$

where

$$\ell = L_o + \int_0^t \upsilon_\ell\, dt \qquad \text{H.22}$$

Since the velocity term, υ_ℓ, is dependent on the solution composition, which would vary with time, these equations need to be solved simultaneously with the various mass balance equations.

An expression of the fractional extent of sulfide oxidation, X_s, may now be obtained, using the following obvious relationship:

$$X_s = 1 - \frac{W_s}{W_{s,o}} = 1 - \frac{\int_0^{\ell_{max}} \rho_s \Phi_v \ell^3 \psi(\ell)\, d\ell}{\int_0^{L_{o,max}} \rho_s \Phi_v L_o^3 \psi(L_o)\, dL_o} \qquad \text{H.23}$$

This equation is rearranged, after substituting Equation H.21, to yield (after Crundwell, 2003):

$$X_s = 1 - \frac{W_s}{W_{s,o}} = 1 - \int_0^{L_{o,max}} \frac{\ell^3}{L_o^3} \cdot \left(\frac{\rho_s \Phi_v L_o^3 \psi(L_o)}{\int_0^{L_{o,max}} \rho_s \Phi_v L_o^3 \psi(L_o)\, dL_o} \right) dL_o \qquad \text{H.24}$$

which may be simplified to:

$$X_s = 1 - \frac{W_s}{W_{s,o}} = 1 - \int_0^{L_{o,max}} [1 - X_{s,n}] W_{f,n}\, dL_o \qquad \text{H.25}$$

where $W_{f,n} = W_f(L_{o,n})$ is the fractional mass of original mineral feed particles in a size-class *n*, with average size, $L_{o,n}$, (histogram) and $X_{s,n}$ is the fractional (leaching) extent, *i.e.*, corresponding to that class. Following from discussions of Appendix F.4, the reaction extent for a narrow-sized fraction (size-class *n*) can also be represented as follows:

$$1 - X_{s,n} = \left(1 + \frac{\upsilon_{\ell,n} t}{L_{o,n}} \right)^3 \qquad \text{H.26}$$

where $\upsilon_{\ell,n}$ refers to the one-dimensional core size velocity rate for particles in original size-class *n*. Substitution of Equation H.26 into Equation H.25, followed by discretization, results in the following general form of the leaching extent of a multi-sized particle feed in a BSTR:

$$1 - X_s(t) = \sum_{-\upsilon_\ell t}^{L_{o,max}} \left(1 + \frac{\upsilon_{\ell,n}(t) \cdot t}{L_{o,n}} \right)^3 W_{f,n} \qquad \text{H.27}$$

Stellenbosch University http://scholar.sun.ac.za

APPENDIX I. DETAILED FOLLOW-UP BATCH LEACHING TEST RESULTS (HBMS 777 CLEANER, LT CLEANER AND MV ROUGHER CONCENTRATES)

This appendix summarises the detailed batch testwork results in sequential order, as discussed in Chapter 7. The detailed particle size distributions (PSDs) of the pilot plant feed and narrow-sized samples are presented first (App. I.1 & I.2, respectively), *i.e.*, the HBMS 777 cleaner material (pilot plant feed & narrow-sized Sample E), the two Las Tortolas (LT) size fractions (Samples F & G), and a rougher size fraction (Sample H) from Manto Verde (MV). The bulk modal analyses of the head and residue samples are presented in Appendix I.3, while the detailed leaching results can be found in Appendix I.3, I.4, I.5 and I.6, all conducted in the 2-litre Parr autoclave (see Sect. 6.4.1). The detailed experimental procedures are summarised in Section 7.3.

I.1 Detailed PSDs of the HBMS pilot plant feed material (*ref.* Periods P1-P4)

The feed PSDs of the four evaluation periods (P1-P4) during continuous pilot testing were measured with a Malvern MasterSizer 2000 (see Sect. 6.4.3). The detailed results are presented in the following table.

	Period P1		**Period P2**	**Periods P3 & P4**
Size (avg.) (μm)	Cum. vol. (%)	Size (avg.) (μm)	Cum. vol. (%)	Cum. vol. (%)
0.497	0	0.55	0	0
0.561	0.07	0.631	0.05	0.09
0.634	0.27	0.724	0.18	0.33
0.717	0.74	0.832	0.51	0.88
0.81	1.50	0.955	1.13	1.84
0.915	2.65	1.096	2.21	3.39
1.034	4.29	1.259	3.89	5.66
1.168	6.49	1.445	6.34	8.78
1.32	9.33	1.66	9.70	12.84
1.491	12.87	1.905	14.06	17.87
1.684	17.13	2.188	19.44	23.82
1.903	22.11	2.512	25.78	30.58
2.15	27.77	2.884	32.93	37.96
2.429	23.02	3.311	40.65	45.71
2.745	40.74	3.802	48.65	53.52
3.101	47.77	4.365	56.58	61.08
3.503	54.94	5.012	64.11	68.10

Stellenbosch University http://scholar.sun.ac.za

	Period P1		**Period P2**	**Periods P3 & P4**
Size (avg.) (µm)	Cum. vol. (%)	Size (avg.) (µm)	Cum. vol. (%)	Cum. vol. (%)
3.958	62.05	5.754	70.97	74.36
4.472	68.92	6.607	76.95	79.71
5.053	75.37	7.586	81.97	84.12
5.709	81.26	8.71	86.03	87.62
6.45	86.48	10	89.24	90.33
7.287	90.94	11.482	91.72	92.38
8.233	94.57	13.183	93.63	93.92
9.302	97.29	15.136	95.10	95.06
10.51	99.06	17.378	96.26	95.92
11.874	99.86	19.953	97.19	96.58
13.426	99.98	22.909	97.97	97.11
15.157	99.99	26.303	98.62	97.57
17.125	100.00	30.2	99.15	97.99
–	–	34.674	99.55	98.39
–	–	39.811	99.82	98.78
–	–	45.709	99.97	99.16
–	–	52.481	100.00	99.51
–	–	60.256	–	99.81
–	–	69.183	–	99.99
–	–	79.432	–	100.00

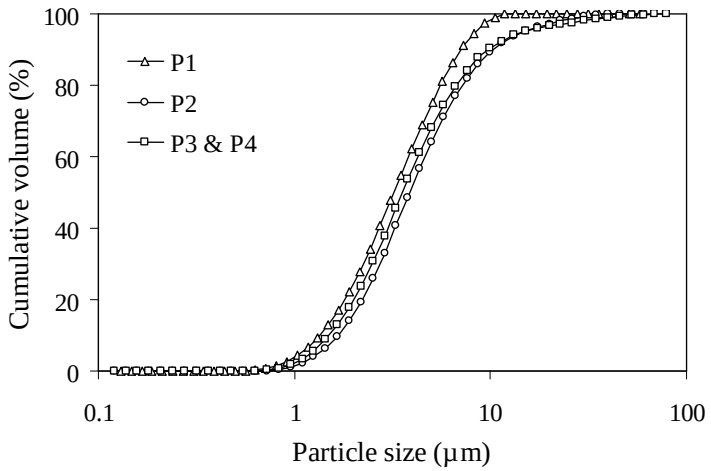

Stellenbosch University http://scholar.sun.ac.za

I.2 Detailed PSDs of the narrow-sized head samples

The PSDs of the four head samples (E, F, G & H) were measured with a Malvern MasterSizer 2000 (see Sect. 6.4.3) and the detailed results are presented in the following table.

	[a] Sample E		[b] Sample F	[b] Sample G		[c] Sample H
	Obscuration (%)		Obscuration (%)	Obscuration (%)		Obscuration (%)
	5.5		8.5	5.4		6.0
Size (avg.) (μm)	Cum. vol. (%)	Size (avg.) (μm)	Cum. vol. (%)	Cum. vol. (%)	Size (avg.) (μm)	Cum. vol. (%)
0.1955	0.04	2.923	0.00	0.07	1.7825	0.01
0.2245	0.15	3.302	0.00	0.19	2.0465	0.18
0.2575	0.29	3.7305	0.00	0.32	2.350	0.60
0.2955	0.45	4.215	0.05	0.45	2.698	1.46
0.3395	0.63	4.7625	0.30	0.55	3.0975	2.92
0.390	0.83	5.381	1.19	0.62	3.5565	5.16
0.448	1.05	6.0795	3.14	0.68	4.0835	8.34
0.5145	1.30	6.8685	6.74	0.73	4.6885	12.62
0.5905	1.60	7.760	12.49	0.82	5.383	18.11
0.6775	1.97	8.7675	20.64	1.06	6.1805	24.86
0.778	2.43	9.906	31.06	1.74	7.0965	32.80
0.8935	3.02	11.192	43.17	3.37	8.148	41.76
1.0255	3.76	12.645	56.00	6.68	9.355	51.38
1.1775	4.67	14.2865	68.38	12.47	10.741	61.21
1.352	5.75	16.141	79.23	21.31	12.3325	70.70
1.5525	7.00	18.2365	87.80	33.18	14.1595	79.31
1.7825	8.39	20.604	93.82	47.31	16.257	86.61
2.0465	9.90	23.279	97.48	62.15	18.6655	92.31
2.350	11.50	26.301	99.35	75.75	21.431	96.36
2.698	13.22	29.7155	99.95	86.45	24.606	98.88
3.0975	15.11	33.5735	99.99	93.62	28.2515	99.93
3.5565	17.29	37.932	100.00	97.50	32.437	100.00
4.0835	19.95	42.8565	–	99.17	–	–
4.6885	23.31	48.420	–	99.76	–	–
5.383	27.59	54.706	–	99.94	–	–
6.1805	32.97	61.808	–	100.00	–	–
7.0965	39.48	–	–	–	–	–
8.148	47.02	–	–	–	–	–
9.355	55.30	–	–	–	–	–

Stellenbosch University http://scholar.sun.ac.za

	[a] Sample E		[b] Sample F	[b] Sample G		[c] Sample H
Size (avg.) (µm)	Cum. vol. (%)	Size (avg.) (µm)	Cum. vol. (%)	Cum. vol. (%)	Size (avg.) (µm)	Cum. vol. (%)
10.741	63.89	–	–	–	–	–
12.3325	72.27	–	–	–	–	–
14.1595	79.93	–	–	–	–	–
16.257	86.46	–	–	–	–	–
18.6655	91.60	–	–	–	–	–
21.431	95.32	–	–	–	–	–
24.606	97.74	–	–	–	–	–
28.2515	99.12	–	–	–	–	–
32.437	99.79	–	–	–	–	–
37.2425	100.00	–	–	–	–	–

[a] HBMS 777 cleaner concentrate; [b] Las Tortolas (LT) cleaner concentrates; [c] Manto Verde (MV) rougher concentrate.

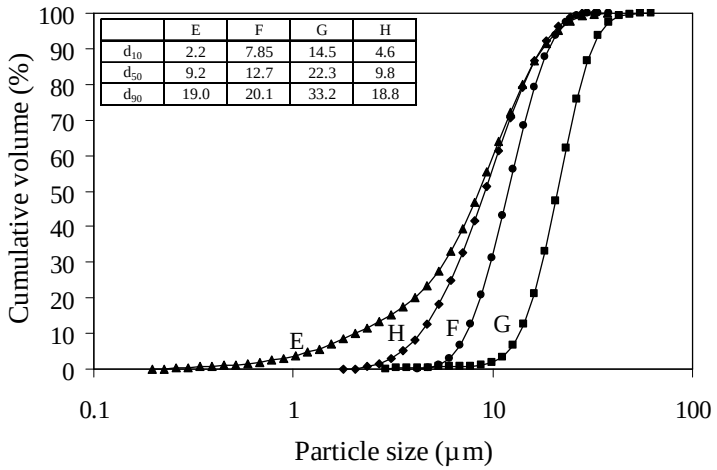

I.3 Bulk modal analyses of the head and residue samples

Series P1, Q1

Mineral	$CuFeS_2$	ZnS (%)	–	–	FeS_2 (%)	Fe_7S_8 (%)	–	SiO_2 (%)
[a] Head	82.3	6.9	–	–	7.5	1.3	–	–
45 (P13)	91.1	0.3	–	–	6.2	0.1	–	–
Head	84.3	7.3	–	–	3.9	1.7	–	–
15 (Q11)	91.9	0.1	–	–	6.2	0.1	–	–
30 (Q12)	93.1	0.2	–	–	2.8	0.1	–	–
45 (Q13)	93.2	0.0	–	–	2.5	0.1	–	–

[a] Mineralogy calc. from avg. elemental composition (*ref.* Ch. 6).

Stellenbosch University http://scholar.sun.ac.za

Series Q2, Q3

Mineral	$CuFeS_2$	ZnS (%)	–	–	FeS_2 (%)	Fe_7S_8 (%)	–	SiO_2 (%)
Head	84.3	7.3	–	–	3.9	1.7	–	–
15 (Q21)	91.7	1.0	–	–	3.8	0.1	–	–
30 (Q22)	94.1	0.2	–	–	2.6	0.0	–	–
45 (Q23)	71.2	0.1	–	–	[b] 18.5	[b] 4.6	–	–
10 (Q31)	90.5	1.8	–	–	4.8	0.1	–	–
20 (Q32)	92.9	0.3	–	–	2.4	0.0	–	–
30 (Q33)	82.3	0.1	–	–	[b] 14.0	0.1	–	–

[b] Interference by iron(III) precipitation products.

Series R1, R2, R3

Mineral	$CuFeS_2$	Cu_2S (%)	CuS (%)	Cu_5FeS_4	FeS_2 (%)	–	–	SiO_2 (%)
Head	63.2	8.9	3.2	4.1	16.3	–	–	–
15 (R11)	67.4	4.4	7.0	0.4	16.6	–	–	–
30 (R12)	70.4	6.2	4.5	0.2	14.8	–	–	–
45 (R13)	74.2	6.7	5.1	0.2	8.6	–	–	–
15 (R21)	67.1	3.4	5.5	0.5	19.1	–	–	–
30 (R22)	69.9	4.2	4.8	0.2	16.6	–	–	–
45 (R23)	74.4	4.5	4.0	0.1	11.5	–	–	–
15 (R31)	67.5	3.6	5.4	0.4	18.5	–	–	–
30 (R32)	70.8	4.3	5.6	0.4	13.7	–	–	–
45 (R33)	79.6	4.0	4.8	0.3	5.2	–	–	–

Series S1, S2, S3

Mineral	$CuFeS_2$	–	–	–	FeS_2 (%)	Fe_7S_8 (%)	Fe_3O_4 (%)	SiO_2 (%)
Head	27.9	–	–	–	28.1	3.1	7.9	13.4
15 (S11)	27.8	–	–	–	29.9	0.6	6.5	17.2
30 (S12)	27.2	–	–	–	29.7	0.5	6.3	18.6
45 (S13)	27.9	–	–	–	13.4	0.8	9.0	25.3
10 (S21)	26.5	–	–	–	29.4	0.5	7.1	17.1
20 (S22)	24.5	–	–	–	28.5	0.5	7.4	19.3
30 (S23)	27.3	–	–	–	20.9	0.3	7.7	23.1
10 (S31)	26.8	–	–	–	31.5	0.4	7.1	18.4
20 (S32)	24.2	–	–	–	24.2	0.5	9.4	21.0
30 (S33)	23.5	–	–	–	12.9	0.7	10.5	27.4

Stellenbosch University http://scholar.sun.ac.za

I.4 Oxidation of Hudson Bay (HBMS 777) cleaner concentrate (Samples D & E)

PLP1	Temp.	Imp. speed	P_g	p_{O2}°	Solids	Solids	Solution	[a] Density
Sample D	150°C	1000 rpm	1090 kPa	700 kPa	0.87 wt%	10 g	1140 g	1051 g/L
[b] LS, QB	Cu	Zn	–	Fe(II)	H_2SO_4	–	SO_4	H_2O
0.1 g/L	15 g/L	0 g/L	–	0 g/L	25 g/L	–	47.3 g/L	1070.8 g
min (test)	Sld. (g)	Colour	Sln. (g)	Vol. (mL)	Colour	[a] Dens g/L	[a] E_{Ag} (mV)	[a] pH
–	–	–	–	–	–	–	–	–
–	–	–	–	–	–	–	–	–
45 (P13)	5.74	Grey	1075.6	1010	Green	1065	485	0.64
Solids	Cu (%)	Zn (%)	Fe(%)	Si(%)	S^{2-} (%)	S° (%)	SO_4 (%)	S^T (%)
[c] Head	28.5	4.6	29.5	–	35.5	0.0	0.0	35.5
–	–	–	–	–	–	–	–	–
–	–	–	–	–	–	–	–	–
45 (P13)	24.8	0.12	23.9	–	[d] 27.49	[d] 22.11	0.0	49.6
Solution	Cu (g/L)	Zn (g/L)	Fe^T (g/L)	Fe(II) g/L	H_2SO_4 g/L	–	SO_4 (g/L)	–
–	–	–	–	–	–	–	–	–
–	–	–	–	–	–	–	–	–
45 (P13)	17.46	0.38	1.77	0.39	20.9	–	51.9	–
[e] Extent	Cu (%)	Zn (%)	Fe (%)	–	S^{2-} (%)	[f] S° (%)	–	S^T (%)
–	–	–	–	–	–	–	–	–
–	–	–	–	–	–	–	–	–
45 (P13)	51 (100)	98 (85)	54 (107)	–	56	64	–	(98)
[g] Modal	$CuFeS_2$	ZnS (%)	–	–	FeS_2 (%)	Fe_7S_8 (%)	–	SiO_2 (%)
[h] Head	82.3	6.9	–	–	7.5	1.3	–	–
–	–	–	–	–	–	–	–	–
–	–	–	–	–	–	–	–	–
45 (P13)	71.0	0.2	–	–	4.8	0.1	–	–
[i] Oxidation	[j] $CuFeS_2$	ZnS (%)	–	–	FeS_2 (%)	Fe_7S_8 (%)	–	[k] $W_{f,t}$ (%)
–	–	–	–	–	–	–	–	–
–	–	–	–	–	–	–	–	–
45 (P13)	51 (50)	98	–	–	63	97	–	57.4

[a] At 20°C; [b] Arbo A02, Orfom 2 (no pre-drying); [c] Avg. elemental composition (*ref.* Ch. 6); [d] Calc. (Sect. 7.3.2); [e] Reaction extents based on mineralogical analyses (elem. accountabilities in brackets); [f] S° yield, *i.e.*, $S°/S^{2-}{}_{rx}\times100\%$; [g] Bulk modal analyses after % Sº correction (Sect. 7.3.2); [h] Mineralogy calc. from avg. elem. composition (*ref.* Ch. 6); [i] Mineral oxidation extents; [j] Oxidation extents from chem. analyses given in brackets; [k] Fractional weight of residue (*cf.* original sample), based on measured residue mass.

Stellenbosch University http://scholar.sun.ac.za

PLQ1	Temp.	Imp. speed	P_g	$p_{O2}°$	Solids	Solids	Solution	[a] Density
Sample E	145°C	1000 rpm	1029 kPa	700 kPa	0.87 wt%	10 g	1140 g	1051 g/L
[b] LS, QB	Cu	Zn	–	Fe(II)	H_2SO_4	–	SO_4	H_2O
0.15 g/L	15 g/L	0 g/L	–	0 g/L	25 g/L	–	47.3 g/L	1070.8 g
min (test)	Sld. (g)	Colour	Sln. (g)	Vol. (mL)	Colour	[a] Dens g/L	[a] E_{Ag} (mV)	[a] pH
15 (Q11)	6.69	Dark-grey	1084.5	1024	Green	1059	489	0.75
30 (Q12)	5.37	Grey	1107.6	1046	Green	1059	492	0.75
45 (Q13)	4.49	Grey	1111.7	1051	Green	1058	502	0.76
Solids	Cu (%)	Zn (%)	Fe(%)	Si(%)	S^{2-} (%)	S° (%)	SO_4 (%)	S^T (%)
[c] Head	29.3	4.5	29.0	–	34.6	0.0	0.0	34.6
15 (Q11)	24.2	0.05	24.4	–	[d] 27.83	[d] 14.97	0.0	42.8
30 (Q12)	23.5	0.03	22.7	–	[d] 24.16	[d] 23.24	0.0	47.4
45 (Q13)	19.8	0.01	19.4	–	[d] 22.46	[d] 28.24	0.0	50.7
Solution	Cu (g/L)	Zn (g/L)	Fe^T (g/L)	Fe(II) g/L	H_2SO_4 g/L	–	SO_4 (g/L)	–
15 (Q11)	17.0	0.39	1.38	0.42	20.9	–	50.1	–
30 (Q12)	16.9	0.38	1.78	0.41	21.0	–	51.1	–
45 (Q13)	16.6	0.38	2.08	0.37	19.9	–	50.4	–
[e] Extent	Cu (%)	Zn (%)	Fe (%)	–	S^{2-} (%)	[f] S° (%)	–	S^T (%)
15 (Q11)	38 (99)	99 (92)	39 (105)	–	42	75	–	(97)
30 (Q12)	55 (99)	99 (93)	58 (106)	–	59	66	–	(99)
45 (Q13)	65 (96)	100 (93)	67 (105)	–	68	58	–	(97)
[g] Modal	$CuFeS_2$	ZnS (%)	–	–	FeS_2 (%)	Fe_7S_8 (%)	–	SiO_2 (%)
Head	84.3	7.3	–	–	3.9	1.7	–	–
15 (Q11)	78.1	0.1	–	–	5.3	0.1	–	–
30 (Q12)	71.5	0.2	–	–	2.1	0.1	–	–
45 (Q13)	66.9	0.0	–	–	1.8	0.1	–	–
[h] Oxidation	[i] $CuFeS_2$	ZnS (%)	–	–	FeS_2 (%)	Fe_7S_8 (%)	–	[j] $W_{f,t}$ (%)
15 (Q11)	38 (44)	99	–	–	10	97	–	66.9
30 (Q12)	54 (56)	99	–	–	70	98	–	53.7
45 (Q13)	64 (69)	100	–	–	79	98	–	44.9

[a] At 20°C; [b] Arbo A02, Orfom 2 (no pre-drying); [c] Calc. from mineralogical composition; [d] Calc. (Sect. 7.3.2); [e] Reaction extents based on mineralogical analyses (elem. accountabilities in brackets); [f] S° yield, *i.e.*, $S°/S^{2-}{}_{rx}\times100\%$; [g] Bulk modal analyses after % S° correction (Sect. 7.3.2); [h] Mineral oxidation extents; [i] Oxidation extents from chem. analyses in brackets (based on head analysis in Table 7.3); [j] Fractional weight of residue (*cf.* original sample), based on measured residue mass.

Stellenbosch University http://scholar.sun.ac.za

PLQ2	Temp.	Imp. speed	P_g	p_{O2}°	Solids	Solids	Solution	[a] Density
Sample E	150°C	1000 rpm	1090 kPa	700 kPa	0.87 wt%	10 g	1140 g	1051 g/L
[b] LS, QB	Cu	Zn	–	Fe(II)	H_2SO_4	–	SO_4	H_2O
0.15 g/L	15 g/L	0 g/L	–	0 g/L	25 g/L	–	47.3 g/L	1070.8 g
min (test)	Sld. (g)	Colour	Sln. (g)	Vol. (mL)	Colour	[a] Dens g/L	[a] E_{Ag} (mV)	[a] pH
15 (Q21)	6.29	Grey	1087.0	1025	Green	1060	488	0.75
30 (Q22)	4.82	Grey	1104.0	1037	Green	1065	489	0.81
45 (Q23)	4.04	Lgt brown	1110.3	1042	Green	1066	513	0.70
Solids	Cu (%)	Zn (%)	Fe(%)	Si(%)	S^{2-} (%)	S° (%)	SO_4 (%)	S^T (%)
[c] Head	29.3	4.5	29.0	–	34.6	0.0	0.0	34.6
15 (Q21)	25.0	0.39	24.8	–	[d] 25.92	[d] 18.38	0.0	44.3
30 (Q22)	20.4	0.10	22.2	–	[d] 23.21	[d] 26.69	0.0	49.9
45 (Q23)	14.8	0.01	18.6	–	[d] 24.02	[d] 28.88	0.0	52.9
Solution	Cu (g/L)	Zn (g/L)	Fe^T (g/L)	Fe(II) g/L	H_2SO_4 g/L	–	SO_4 (g/L)	–
15 (Q21)	17.9	0.39	1.61	0.42	21.4	–	52.6	–
30 (Q22)	17.9	0.42	1.83	0.20	20.3	–	52.3	–
45 (Q23)	17.1	0.41	2.30	0.27	18.4	–	50.3	–
[e] Extent	Cu (%)	Zn (%)	Fe (%)	–	S^{2-} (%)	[f] S° (%)	–	S^T (%)
15 (Q21)	44 (104)	92 (99)	47 (110)	–	49	74	–	(101)
30 (Q22)	61 (102)	99 (102)	64 (102)	–	65	62	–	(100)
45 (Q23)	76 (96)	100 (98)	67 (108)	–	70	53	–	(95)
[g] Modal	$CuFeS_2$	ZnS (%)	–	–	FeS_2 (%)	Fe_7S_8 (%)	–	SiO_2 (%)
Head	84.3	7.3	–	–	3.9	1.7	–	–
15 (Q21)	74.8	0.8	–	–	3.1	0.1	–	–
30 (Q22)	69.0	0.1	–	–	1.9	0.0	–	–
45 (Q23)	50.6	0.1	–	–	[k] 13.2	[k] 3.3	–	–
[h] Oxidation	[i] $CuFeS_2$	ZnS (%)	–	–	FeS_2 (%)	Fe_7S_8 (%)	–	[j] $W_{f,t}$ (%)
15 (Q21)	44 (45)	[i] 93 (94)	–	–	50	97	–	62.9
30 (Q22)	61 (66)	99	–	–	76	100	–	48.2
45 (Q23)	76 (79)	100	–	–	[k] 0	[k] 0	–	40.4

[a] At 20°C; [b] Arbo A02, Orfom 2 (no pre-drying); [c] Calc. from mineralogical composition; [d] Calc. (Sect. 7.3.2); [e] Reaction extents based on mineralogical analyses (elem. accountabilities in brackets); [f] S° yield, *i.e.*, $S°/S^{2-}{}_{rx}\times100\%$; [g] Bulk modal analyses after % S° correction (Sect. 7.3.2); [h] Mineral oxidation extents; [i] Oxidation extents from chem. analyses in brackets (based on head analysis in Table 7.3); [j] Fractional weight of residue (*cf.* original sample), based on measured residue mass; [k] Interference by iron(III) precipitation products.

Stellenbosch University http://scholar.sun.ac.za

PLQ3	Temp.	Imp. speed	P_g	p_{O2}°	Solids	Solids	Solution	[a] Density
Sample E	155°C	1000 rpm	1157 kPa	700 kPa	0.87 wt%	10 g	1140 g	1051 g/L
[b] LS, QB	Cu	Zn	–	Fe(II)	H_2SO_4	–	SO_4	H_2O
0.15 g/L	15 g/L	0 g/L	–	0 g/L	25 g/L	–	47.3 g/L	1070.8 g
min (test)	Sld. (g)	Colour	Sln. (g)	Vol. (mL)	Colour	[a] Dens g/L	[a] E_{Ag} (mV)	[a] pH
10 (Q31)	6.35	Grey	1116.7	1061	Green	1052	479	0.73
20 (Q32)	4.85	Grey	1090.5	1031	Green	1058	492	0.73
30 (Q33)	4.00	Lgt brown	1106.7	1046	Green	1058	501	0.75
Solids	Cu (%)	Zn (%)	Fe(%)	Si(%)	S^{2-} (%)	S° (%)	SO_4 (%)	S^T (%)
[c] Head	29.3	4.5	29.0	–	34.6	0.0	0.0	34.6
10 (Q31)	25.3	0.77	25.4	–	[d] 26.06	[d] 18.84	0.0	44.9
20 (Q32)	23.3	0.10	22.1	–	[d] 22.73	[d] 27.17	0.0	49.9
30 (Q33)	20.6	0.01	20.6	–	[d] 23.56	[d] 29.64	0.0	53.2
Solution	Cu (g/L)	Zn (g/L)	Fe^T (g/L)	Fe(II) g/L	H_2SO_4 g/L	–	SO_4 (g/L)	–
10 (Q31)	16.2	0.34	1.42	0.47	20.0	–	47.3	–
20 (Q32)	17.0	0.42	1.96	0.43	20.8	–	51.5	–
30 (Q33)	16.9	0.38	2.05	0.38	20.5	–	51.3	–
[e] Extent	Cu (%)	Zn (%)	Fe (%)	–	S^{2-} (%)	[f] S° (%)	–	S^T (%)
10 (Q31)	45 (98)	86 (96)	47 (107)	–	48	78	–	(96)
20 (Q32)	61 (97)	98 (101)	64 (106)	–	65	63	–	(98)
30 (Q33)	73 (97)	100 (93)	69 (102)	–	70	53	–	(97)
[g] Modal	$CuFeS_2$	ZnS (%)	–	–	FeS_2 (%)	Fe_7S_8 (%)	–	SiO_2 (%)
Head	84.3	7.3	–	–	3.9	1.7	–	–
10 (Q31)	73.4	1.5	–	–	3.9	0.1	–	–
20 (Q32)	67.7	0.2	–	–	1.7	0.0	–	–
30 (Q33)	57.9	0.1	–	–	[k] 9.9	0.1	–	–
[h] Oxidation	[i] $CuFeS_2$	ZnS (%)	–	–	FeS_2 (%)	Fe_7S_8 (%)	–	[j] $W_{f,t}$ (%)
10 (Q31)	45 (44)	[i] 87 (89)	–	–	37	97	–	63.5
20 (Q32)	61 (61)	99	–	–	78	100	–	48.5
30 (Q33)	73 (71)	100	–	–	[k] 0	98	–	40.0

[a] At 20°C; [b] Arbo A02, Orfom 2 (no pre-drying); [c] Calc. from mineralogical composition; [d] Calc. (Sect. 7.3.2); [e] Reaction extents based on mineralogical analyses (elem. accountabilities in brackets); [f] S° yield, *i.e.*, $S°/S^{2-}{}_{rx}\times100\%$; [g] Bulk modal analyses after % S° correction (Sect. 7.3.2); [h] Mineral oxidation extents; [i] Oxidation extents from chem. analyses in brackets (based on head analysis in Table 7.3); [j] Fractional weight of residue (*cf.* original sample), based on measured residue mass; [k] Interference by iron(III) precipitation products.

Stellenbosch University http://scholar.sun.ac.za

I.5 Oxidation of Las Tortolas (LT) cleaner concentrate (Samples F & G)

PLR1	Temp.	Imp. speed	P_g	p_{O2}°	Solids	Solids	Solution	[a] Density
Sample F	145°C	1000 rpm	1029 kPa	700 kPa	0.87 wt%	10 g	1140 g	1051 g/L
[b] LS, QB	Cu	Zn	–	Fe(II)	H_2SO_4	–	SO_4	H_2O
0.15 g/L	15 g/L	0 g/L	–	0 g/L	25 g/L	–	47.3 g/L	1070.8 g
min (test)	Sld. (g)	Colour	Sln. (g)	Vol. (mL)	Colour	[a] Dens g/L	[a] E_{Ag} (mV)	[a] pH
15 (R11)	7.98	Grey	1104.9	1049	Blue	1053	420	0.73
30 (R12)	6.45	Grey	1107.1	1052	Green	1052	418	0.74
45 (R13)	5.10	Grey	1101.3	1046	Green	1053	432	0.76
Solids	Cu (%)	–	Fe(%)	Si(%)	S^{2-} (%)	S° (%)	SO_4 (%)	S^T (%)
[c] Head	33.6	–	27.3	–	33.8	0.0	0.0	33.8
15 (R11)	28.7	–	27.7	–	[d] 34.19	[d] 4.41	0.0	38.6
30 (R12)	26.4	–	26.3	–	[d] 32.28	[d] 8.62	0.0	40.9
45 (R13)	25.7	–	22.3	–	[d] 29.35	[d] 12.75	0.0	42.1
Solution	Cu (g/L)	–	Fe^T (g/L)	Fe(II) g/L	H_2SO_4 g/L	–	SO_4 (g/L)	–
15 (R11)	17.4	–	0.35	0.10	23.9	–	50.7	–
30 (R12)	16.2	–	0.81	0.34	23.2	–	49.2	–
45 (R13)	16.2	–	1.54	0.39	21.3	–	49.2	–
Extent	[e] Cu (%)	[f] Cu (%)	[e] Fe (%)	[f] Fe (%)	[e] S^{2-} (%)	[f] S^{2-} (%)	[g] S° (%)	[f] S^T (%)
15 (R11)	28	30 (105)	21	22 (91)	19	19	54	(101)
30 (R12)	43	48 (96)	39	40 (90)	38	38	43	(96)
45 (R13)	54	60 (93)	57	60 (97)	56	56	35	(93)
[h] Modal	$CuFeS_2$	Cu_2S (%)	CuS (%)	Cu_5FeS_4	FeS_2 (%)	–	–	SiO_2 (%)
Head	63.2	8.9	3.2	4.1	16.3	–	–	–
15 (R11)	64.4	4.2	6.7	0.4	15.9	–	–	–
30 (R12)	64.3	5.7	4.1	0.2	13.5	–	–	–
45 (R13)	64.7	5.8	4.4	0.2	7.5	–	–	–
[i] Oxidation	$CuFeS_2$	Cu_2S (%)	CuS (%)	Cu_5FeS_4	FeS_2 (%)	[j] FeS_2 (%)	–	[k] $W_{f,t}$ (%)
15 (R11)	19	62	-67	93	22	26.9	–	79.8
30 (R12)	34	59	17	97	46	52.0	–	64.5
45 (R13)	48	67	29	98	77	88.8	–	51.0

[a] At 20°C; [b] Arbo A02, Orfom 2 (no pre-drying); [c] Calc. from mineralogical composition; [d] Calc. (Sect. 7.3.2); [e] Reaction extents based on mineralogical analyses; [f] Reaction extents based on chem. analyses (head analyses are in Table 7.3) (elem. accountabilities in brackets); [g] S° yield, *i.e.*, $S°/S^{2-}{}_{rx}\times100\%$; [h] Bulk modal analyses after % S° correction (Sect. 7.3.2); [i] Mineral oxidation extents; [j] Extents based on Fe balance, $CuFeS_2$ & Cu_5FeS_4 mineral contents (Sect. 7.4.2); [k] Fractional weight of residue (*cf.* original sample), based on measured residue mass.

Stellenbosch University http://scholar.sun.ac.za

PLR2	Temp.	Imp. speed	P_g	$p_{O2}°$	Solids	Solids	Solution	[a] Density
Sample G	150°C	1000 rpm	1090 kPa	700 kPa	0.87 wt%	10 g	1140 g	1051 g/L
[b] LS, QB	Cu	Zn	–	Fe(II)	H_2SO_4	–	SO_4	H_2O
0.15 g/L	15 g/L	0 g/L	–	0 g/L	25 g/L	–	47.3 g/L	1070.8 g
min (test)	Sld. (g)	Colour	Sln. (g)	Vol. (mL)	Colour	[a] Dens g/L	[a] E_{Ag} (mV)	[a] pH
15 (R21)	8.27	Grey	1099.9	1049	Blue	1049	409	0.72
30 (R22)	7.12	Grey	1102.9	1047	Blue	1053	414	0.70
45 (R23)	5.71	Grey	1090.5	1034	Green	1055	419	0.71
Solids	Cu (%)	–	Fe(%)	Si(%)	S^{2-} (%)	S° (%)	SO_4 (%)	S^T (%)
[c] Head	33.6	–	27.3	–	33.8	0.0	0.0	33.8
15 (R21)	28.8	–	28.5	–	[d] 35.41	[d] 2.49	0.0	37.9
30 (R22)	26.4	–	27.8	–	[d] 34.08	[d] 4.82	0.0	38.9
45 (R23)	25.7	–	24.7	–	[d] 31.17	[d] 9.53	0.0	40.7
Solution	Cu (g/L)	–	Fe^T (g/L)	Fe(II) g/L	H_2SO_4 g/L	–	SO_4 (g/L)	–
15 (R21)	15.2	–	0.52	0.22	21.1	–	45.0	–
30 (R22)	15.6	–	0.86	0.29	23.0	–	48.3	–
45 (R23)	16.2	–	1.25	0.36	22.3	–	49.5	–
Extent	[e] Cu (%)	[f] Cu (%)	[e] Fe (%)	[f] Fe (%)	[e] S^{2-} (%)	[f] S^{2-} (%)	[g] S° (%)	[f] S^T (%)
15 (R21)	28	27 (94)	13	17 (102)	13	13	46	(91)
30 (R22)	38	43 (93)	28	30 (102)	28	28	36	(95)
45 (R23)	51	55 (93)	47	50 (95)	47	47	34	(94)
[h] Modal	$CuFeS_2$	Cu_2S (%)	CuS (%)	Cu_5FeS_4	FeS_2 (%)	–	–	SiO_2 (%)
Head	63.2	8.9	3.2	4.1	16.3	–	–	–
15 (R21)	65.4	3.3	5.4	0.5	18.6	–	–	–
30 (R22)	66.5	4.0	4.6	0.2	15.8	–	–	–
45 (R23)	67.4	4.1	3.6	0.1	10.4	–	–	–
[i] Oxidation	$CuFeS_2$	Cu_2S (%)	CuS (%)	Cu_5FeS_4	FeS_2 (%)	[j] FeS_2 (%)	–	[k] $W_{f,t}$ (%)
15 (R21)	14	69	-39	90	6	19.3	–	82.7
30 (R22)	25	68	-2	97	31	39.7	–	71.2
45 (R23)	39	74	35	99	64	76.1	–	57.1

[a] At 20°C; [b] Arbo A02, Orfom 2 (no pre-drying); [c] Calc. from mineralogical composition; [d] Calc. (Sect. 7.3.2); [e] Reaction extents based on mineralogical analyses; [f] Reaction extents based on chem. analyses (head analyses are in Table 7.3) (elem. accountabilities in brackets); [g] S° yield, *i.e.*, $S°/S^{2-}{}_{rx}\times100\%$; [h] Bulk modal analyses after % S° correction (Sect. 7.3.2); [i] Mineral oxidation extents; [j] Extents based on Fe balance, $CuFeS_2$ & Cu_5FeS_4 mineral contents (Sect. 7.4.2); [k] Fractional weight of residue (*cf.* original sample), based on measured residue mass.

Stellenbosch University http://scholar.sun.ac.za

PLR3	Temp.	Imp. speed	P_g	p_{O2}°	Solids	Solids	Solution	[a] Density
Sample G	155°C	1000 rpm	1157 kPa	700 kPa	0.87 wt%	10 g	1140 g	1051 g/L
[b] LS, QB	Cu	Zn	–	Fe(II)	H_2SO_4	–	SO_4	H_2O
0.15 g/L	15 g/L	0 g/L	–	0 g/L	25 g/L	–	47.3 g/L	1070.8 g
min (test)	Sld. (g)	Colour	Sln. (g)	Vol. (mL)	Colour	[a] Dens g/L	[a] E_{Ag} (mV)	[a] pH
15 (R31)	7.77	Grey	1098.2	1043	Blue	1053	410	0.62
30 (R32)	6.12	Grey	1103.2	1047	Blue	1054	419	0.49
45 (R33)	4.57	Grey	1085.7	1028	Green	1056	440	0.63
Solids	Cu (%)	–	Fe(%)	Si(%)	S^{2-} (%)	S° (%)	SO_4 (%)	S^T (%)
[c] Head	33.6	–	27.3	–	33.8	0.0	0.0	33.8
15 (R31)	26.6	–	28.8	–	[d] 34.32	[d] 4.98	0.0	39.3
30 (R32)	25.5	–	26.4	–	[d] 31.97	[d] 8.43	0.0	40.4
45 (R33)	26.2	–	25.5	–	[d] 28.98	[d] 12.42	0.0	41.4
Solution	Cu (g/L)	–	Fe^T (g/L)	Fe(II) g/L	H_2SO_4 g/L	–	SO_4 (g/L)	–
15 (R31)	15.2	–	0.60	0.23	24.0	–	48.1	–
30 (R32)	16.3	–	1.16	0.35	23.1	–	50.1	–
45 (R33)	17.0	–	1.91	0.34	21.5	–	51.6	–
Extent	[e] Cu (%)	[f] Cu (%)	[e] Fe (%)	[f] Fe (%)	[e] S^{2-} (%)	[f] S^{2-} (%)	[g] S° (%)	[f] S^T (%)
15 (R31)	34	37 (92)	21	21 (101)	21	21	54	(96)
30 (R32)	47	52 (95)	43	43 (100)	42	42	36	(97)
45 (R33)	59	63 (96)	61	59 (110)	61	61	28	(95)
[h] Modal	$CuFeS_2$	Cu_2S (%)	CuS (%)	Cu_5FeS_4	FeS_2 (%)	–	–	SiO_2 (%)
Head	63.2	8.9	3.2	4.1	16.3	–	–	–
15 (R31)	64.1	3.4	5.1	0.4	17.6	–	–	–
30 (R32)	64.8	3.9	5.1	0.4	12.5	–	–	–
45 (R33)	69.7	3.5	4.2	0.3	4.6	–	–	–
[i] Oxidation	$CuFeS_2$	Cu_2S (%)	CuS (%)	Cu_5FeS_4	FeS_2 (%)	[j] FeS_2 (%)	–	[k] $W_{f,t}$ (%)
15 (R31)	21	70	-25	93	16	17.1	–	77.7
30 (R32)	37	73	2	95	53	55.1	–	61.2
45 (R33)	50	82	40	97	87	80.6	–	45.7

[a] At 20°C; [b] Arbo A02, Orfom 2 (no pre-drying); [c] Calc. from mineralogical composition; [d] Calc. (Sect. 7.3.2); [e] Reaction extents based on mineralogical analyses; [f] Reaction extents based on chem. analyses (head analyses are in Table 7.3) (elem. accountabilities in brackets); [g] S° yield, *i.e.*, $S°/S^{2-}{}_{rx}\times100\%$; [h] Bulk modal analyses after % S° correction (Sect. 7.3.2); [i] Mineral oxidation extents; [j] Extents based on the Fe balance, $CuFeS_2$ & Cu_5FeS_4 mineral contents (Sect. 7.4.2); [k] Fractional weight of residue (*cf.* original sample), based on measured residue mass.

Stellenbosch University http://scholar.sun.ac.za

I.6 Oxidation of Manto Verde (MV) rougher concentrate (Sample H)

PLS1	Temp.	Imp. speed	P_g	p_{O2}°	Solids	Solids	Solution	[a] Density
Sample H	145°C	1000 rpm	1029 kPa	700 kPa	0.87 wt%	10 g	1140 g	1051 g/L
[b] LS, QB	Cu	Zn	–	Fe(II)	H_2SO_4	–	SO_4	H_2O
0.15 g/L	15 g/L	0 g/L	–	0 g/L	25 g/L	–	47.3 g/L	1070.8 g
min (test)	Sld. (g)	Colour	Sln. (g)	Vol. (mL)	Colour	[a] Dens g/L	[a] E_{Ag} (mV)	[a] pH
15 (S11)	7.57	Grey	1108.9	1052	Blue	1054	412	0.74
30 (S12)	7.10	Grey	1100.9	1043	Blue	1056	409	0.73
45 (S13)	5.68	Grey	1109.8	1048	Green	1059	422	0.72
Solids	Cu (%)	–	Fe(%)	Si(%)	S^{2-} (%)	S° (%)	SO_4 (%)	S^T (%)
[c] Head	10.1	–	29.2	–	26.1	0.0	0.0	26.1
15 (S11)	7.98	–	27.4	–	[d] 23.45	[d] 1.75	0.0	25.2
30 (S12)	7.54	–	22.3	–	[d] 21.48	[d] 1.54	0.0	23.0
45 (S13)	6.88	–	19.0	–	[d] 14.18	[d] 4.32	0.0	18.5
Solution	Cu (g/L)	–	Fe^T (g/L)	Fe(II) g/L	H_2SO_4 g/L	–	SO_4 (g/L)	–
15 (S11)	14.9	–	1.02	0.34	23.5	–	48.1	–
30 (S12)	15.2	–	1.17	0.38	22.6	–	48.0	–
45 (S13)	16.0	–	1.83	0.43	22.8	–	50.9	–
Extent	[e] Cu (%)	[f] Cu (%)	[e] Fe (%)	[f] Fe (%)	[e] S^{2-} (%)	[f] S^{2-} (%)	[g] S° (%)	[f] S^T (%)
15 (S11)	21	31 (95)	25	28 (109)	21	21	28.5	(96)
30 (S12)	33	38 (96)	36	45 (97)	32	32	15	(94)
45 (S13)	46	55 (100)	60	63 (104)	64	64	17	(97)
[h] Modal	$CuFeS_2$	–	–	–	FeS_2 (%)	Fe_7S_8 (%)	Fe_3O_4 (%)	SiO_2 (%)
Head	27.9	–	–	–	28.1	3.1	7.9	13.4
15 (S11)	27.3	–	–	–	29.4	0.6	6.4	16.9
30 (S12)	26.8	–	–	–	29.2	0.5	6.2	18.3
45 (S13)	26.7	–	–	–	12.8	0.8	8.6	24.2
[i] Oxidation	$CuFeS_2$	–	–	–	[j] FeS_2 (%)	Fe_7S_8 (%)	Fe_3O_4 (%)	[k] $W_{f,t}$ (%)
15 (S11)	21	–	–	–	22	85	35	80.7 (75.7)
30 (S12)	33	–	–	–	47	89	45	70.2 (71.0)
45 (S13)	46	–	–	–	81	86	38	56.5 (56.8)

[a] At 20°C; [b] Arbo A02, Orfom 2 (no pre-drying); [c] Calc. from mineralogical composition; [d] Calc.(Sect. 7.3.2); [e] Reaction extents based on bulk modal analyses; [f] Reaction extents based on chem. analyses (head analyses are listed in Table 7.3) & measured mass losses (accountabilities in brackets); [g] S° yield, *i.e.*, $S°/S^{2-}_{rx}\times100\%$; [h] Bulk modal analyses after % S° correction (Sect. 7.3.2); [i] Mineral oxidation extents; [j] Extents based on Fe balance, $CuFeS_2$, Fe_7S_8 & Fe_3O_4 contents (Sect. 7.4.2); [k] Residue fractional weight based on Si tie method (weighed ratio in brackets).

Stellenbosch University http://scholar.sun.ac.za

PLS2	Temp.	Imp. speed	P_g	p_{O2}°	Solids	Solids	Solution	[a] Density
Sample H	150°C	1000 rpm	1090 kPa	700 kPa	0.87 wt%	10 g	1140 g	1051 g/L
[b] LS, QB	Cu	Zn	–	Fe(II)	H_2SO_4	–	SO_4	H_2O
0.15 g/L	15 g/L	0 g/L	–	0 g/L	25 g/L	–	47.3 g/L	1070.8 g
min (test)	Sld. (g)	Colour	Sln. (g)	Vol. (mL)	Colour	[a] Dens g/L	[a] E_{Ag} (mV)	[a] pH
10 (S21)	7.69	Grey	1111.1	1054	Blue	1054	404	0.73
20 (S22)	7.25	Grey	1108.8	1052	Blue	1054	411	0.69
30 (S23)	6.39	Grey	1095.2	1037	Green	1056	415	0.69
Solids	Cu (%)	–	Fe(%)	Si(%)	S^{2-} (%)	S° (%)	SO_4 (%)	S^T (%)
[c] Head	10.1	–	29.2	–	26.1	0.0	0.0	26.1
10 (S21)	7.39	–	26.9	–	[d] 22.47	[d] 1.43	0.0	23.9
20 (S22)	7.09	–	23.8	–	[d] 21.21	[d] 1.49	0.0	22.7
30 (S23)	7.15	–	18.2	–	[d] 16.31	[d] 3.79	0.0	20.1
Solution	Cu (g/L)	–	Fe^T (g/L)	Fe(II) g/L	H_2SO_4 g/L	–	SO_4 (g/L)	–
10 (S21)	14.9	–	0.94	0.36	21.3	–	45.7	–
20 (S22)	14.6	–	1.18	0.36	22.7	–	47.2	–
30 (S23)	14.8	–	1.62	0.46	22.9	–	48.8	–
Extent	[e] Cu (%)	[f] Cu (%)	[e] Fe (%)	[f] Fe (%)	[e] S^{2-} (%)	[f] S^{2-} (%)	[g] S° (%)	[f] S^T (%)
10 (S21)	25	35 (95)	26	28 (106)	23	23	21.5	(92)
20 (S22)	34	41 (93)	43	40 (103)	31	31	15	(93)
30 (S23)	43	47 (92)	53	60 (98)	53	53	20	(93)
[h] Modal	$CuFeS_2$	–	–	–	FeS_2 (%)	Fe_7S_8 (%)	Fe_3O_4 (%)	SiO_2 (%)
Head	27.9	–	–	–	28.1	3.1	7.9	13.4
10 (S21)	26.1	–	–	–	29.0	0.5	7.0	16.9
20 (S22)	24.1	–	–	–	28.1	0.5	7.3	19.0
30 (S23)	26.3	–	–	–	20.1	0.3	7.4	22.2
[i] Oxidation	$CuFeS_2$	–	–	–	[j] FeS_2 (%)	Fe_7S_8 (%)	Fe_3O_4 (%)	[k] $W_{f,t}$ (%)
10 (S21)	24	–	–	–	23	87	28	80.7 (76.9)
20 (S22)	35	–	–	–	41	88	30	75.3 (72.5)
30 (S23)	43	–	–	–	73	94	44	60.1 (63.9)

[a] At 20°C; [b] Arbo A02, Orfom 2 (no pre-drying); [c] Calc. from mineralogical composition; [d] Calc. (Sect. 7.3.2); [e] Reaction extents based on bulk modal analyses; [f] Reaction extents based on chem. analyses (head analyses are listed in Table 7.3) & measured mass losses (accountabilities in brackets); [g] S° yield, *i.e.*, $S°/S^{2-}{}_{rx}\times100\%$; [h] Bulk modal analyses after % S° correction (Sect. 7.3.2); [i] Mineral oxidation extents; [j] Extents based on Fe balance, $CuFeS_2$, Fe_7S_8 & Fe_3O_4 contents (Sect. 7.4.2); [k] Residue fractional weight based on Si tie method (weighed ratio in brackets).

Stellenbosch University http://scholar.sun.ac.za

PLS3	Temp.	Imp. speed	P_g	p_{O2}°	Solids	Solids	Solution	[a] Density
Sample H	155°C	1000 rpm	1157 kPa	700 kPa	0.87 wt%	10 g	1140 g	1051 g/L
[b] LS, QB	Cu	Zn	–	Fe(II)	H_2SO_4	–	SO_4	H_2O
0.15 g/L	15 g/L	0 g/L	–	0 g/L	25 g/L	–	47.3 g/L	1070.8 g
min (test)	Sld. (g)	Colour	Sln. (g)	Vol. (mL)	Colour	[a] Dens g/L	[a] E_{Ag} (mV)	[a] pH
10 (S31)	7.40	Grey	1107.9	1051	Blue	1054	412	0.70
20 (S32)	6.75	Grey	1101.4	1044	Blue	1055	411	0.69
30 (S33)	5.42	Grey	1071.7	1016	Green	1055	430	0.71
Solids	Cu (%)	–	Fe(%)	Si(%)	S^{2-} (%)	S° (%)	SO_4 (%)	S^T (%)
[c] Head	10.1	–	29.2	–	26.1	0.0	0.0	26.1
10 (S31)	7.39	–	25.7	–	[d] 21.9	[d] 2.19	0.0	24.1
20 (S32)	6.75	–	22.9	–	[d] 17.58	[d] 2.52	0.0	20.1
30 (S33)	5.08	–	17.3	–	[d] 12.27	[d] 4.43	0.0	16.7
Solution	Cu (g/L)	–	Fe^T (g/L)	Fe(II) g/L	H_2SO_4 g/L	–	SO_4 (g/L)	–
10 (S31)	14.4	–	1.15	0.35	21.7	–	45.9	–
20 (S32)	14.8	–	1.37	0.43	23.1	–	48.4	–
30 (S33)	16.4	–	1.94	0.38	23.6	–	52.8	–
Extent	[e] Cu (%)	[f] Cu (%)	[e] Fe (%)	[f] Fe (%)	[e] S^{2-} (%)	[f] S^{2-} (%)	[g] S° (%)	[f] S^T (%)
10 (S31)	32	37 (91)	31	34 (108)	28	28	26	(92)
20 (S32)	45	48 (93)	44	47 (103)	47	47	16	(93)
30 (S33)	57	68 (99)	64	68 (101)	70	70	15	(96)
[h] Modal	$CuFeS_2$	–	–	–	FeS_2 (%)	Fe_7S_8 (%)	Fe_3O_4 (%)	SiO_2 (%)
Head	27.9	–	–	–	28.1	3.1	7.9	13.4
10 (S31)	26.2	–	–	–	30.8	0.4	6.9	18.0
20 (S32)	23.6	–	–	–	23.6	0.5	9.2	20.5
30 (S33)	22.5	–	–	–	12.3	0.7	10.0	26.2
[i] Oxidation	$CuFeS_2$	–	–	–	[j] FeS_2 (%)	Fe_7S_8 (%)	Fe_3O_4 (%)	[k] $W_{f,t}$ (%)
10 (S31)	31.5	–	–	–	27	91	36	72.9 (74.0)
20 (S32)	45	–	–	–	51	90	24	65.3 (67.5)
30 (S33)	58	–	–	–	77	89	34	52.1 (54.2)

[a] At 20°C; [b] Arbo A02, Orfom 2 (no pre-drying); [c] Calc. from mineralogical composition; [d] Calc. (Sect. 7.3.2); [e] Reaction extents based on bulk modal analyses; [f] Reaction extents based on chem. analyses (head analyses are listed in Table 7.3) & measured mass losses (accountabilities in brackets); [g] S° yield, *i.e.*, $S°/S^{2-}{}_{rx}\times100\%$; [h] Bulk modal analyses after % S° correction (Sect. 7.3.2); [i] Mineral oxidation extents; [j] Extents based on Fe balance, $CuFeS_2$, Fe_7S_8 & Fe_3O_4 contents (Sect. 7.4.2); [k] Residue fractional weight based on Si tie method (weighed ratio in brackets).

Stellenbosch University http://scholar.sun.ac.za

APPENDIX J. DETAILED HIGH PULP DENSITY BATCH LEACH TEST RESULTS (HBMS 777 AND LT CLEANER CONCENTRATES)

This appendix summarises the detailed results of the batch leaching testwork, conducted at higher pulp densities (~5-9 wt% solids). The detailed particle size distributions (PSDs) of the head samples are presented first, *i.e.*, the three HBMS 777 samples (I, J & K) and the Las Tortolas (LT) cleaner concentrate sample (L) (see App. I.2 for details on LT Sample G). The detailed leaching results are presented in Appendix J.2 to J.6 and were conducted in the 2-litre Parr autoclave (see Sect. 6.4.1). The detailed experimental procedures are the same as those summarised in Sect. 7.3.

J.1 Detailed PSDs of the head samples

The PSDs of the head samples (I, J, K & L) were measured with a Malvern MasterSizer 2000 (see Sect. 6.4.3) and the detailed results are presented below.

[a] HBMS	Sample I	Sample J	Sample K	[b] LT	Sample L
	Obscuration (%)	Obscuration (%)	Obscuration (%)		Obscuration (%)
	10.5	14.4	18.5		12.6
Size (avg.) (µm)	Cum. vol. (%)	Cum. vol. (%)	Cum. vol. (%)	Size (avg.) (µm)	Cum. vol. (%)
0.1480	0.00	0.00	0.02	0.5975	0.14
0.1700	0.00	0.04	0.10	0.6755	0.42
0.1955	0.03	0.15	0.22	0.7635	0.99
0.2245	0.12	0.34	0.40	0.8625	1.89
0.2575	0.25	0.58	0.63	0.9745	3.24
0.2955	0.41	0.89	0.91	1.1010	5.12
0.3395	0.61	1.25	1.24	1.2440	7.61
0.3900	0.85	1.67	1.62	1.4055	10.78
0.4480	1.14	2.15	2.06	1.5875	14.66
0.5145	1.49	2.70	2.58	1.7935	19.26
0.5905	1.92	3.34	3.21	2.0265	24.56
0.6775	2.47	4.10	4.00	2.2895	30.50
0.7780	3.20	5.02	5.01	2.5870	36.97
0.8935	4.16	6.17	6.33	2.9230	43.81
1.0255	5.44	7.62	8.09	3.3020	50.87
1.1775	7.14	9.46	10.43	3.7305	57.96
1.3520	9.38	11.80	13.51	4.2150	64.87
1.5525	12.77	14.76	17.52	4.7625	71.40

Stellenbosch University http://scholar.sun.ac.za

[a] **HBMS**	**Sample I**	**Sample J**	**Sample K**	[b] **LT**	**Sample L**
Size (avg.) (µm)	Cum. vol. (%)	Cum. vol. (%)	Cum. vol. (%)	Size (avg.) (µm)	Cum. vol. (%)
1.2825	15.91	18.44	22.61	5.3810	77.38
2.0465	20.41	22.90	28.86	6.0795	82.68
2.3500	25.80	28.19	36.23	6.8685	87.22
2.6980	32.07	34.27	44.53	7.7600	90.96
3.0975	39.12	41.03	53.41	8.7675	93.93
3.5565	46.77	48.26	62.40	9.9060	96.18
4.0835	54.76	55.70	70.98	11.1920	97.78
4.6885	62.79	63.05	78.68	12.6450	98.82
5.3830	70.52	70.03	85.16	14.2865	99.38
6.1805	77.62	76.37	90.23	16.1410	99.63
7.0965	83.91	81.89	93.92	18.2365	99.75
8.1480	89.15	86.47	96.38	20.6040	99.83
9.3550	93.32	90.11	97.89	23.2790	99.89
10.7410	96.44	92.85	98.73	26.3010	99.95
12.3325	98.56	94.82	99.17	29.7155	99.99
14.1595	99.79	96.18	99.40	33.5735	100.00
16.2570	99.99	97.09	99.55	–	–
18.6655	100.00	97.71	99.68	–	–
21.4310	–	98.16	99.81	–	–
24.6060	–	98.52	99.92	–	–
28.2515	–	98.84	99.99	–	–
32.4370	–	99.13	100.00	–	–
37.2425	–	99.39	–	–	–
42.7600	–	99.61	–	–	–
49.0950	–	99.78	–	–	–
56.3685	–	99.89	–	–	–
64.7195	–	99.96	–	–	–
74.3080	–	100.00	–	–	–

[a] HBMS 777 cleaner concentrate; [b] Las Tortolas (LT) cleaner concentrate.

Stellenbosch University http://scholar.sun.ac.za

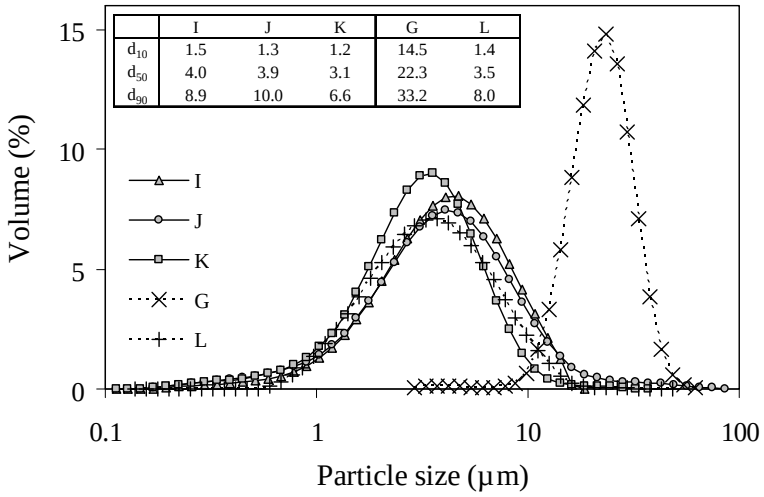

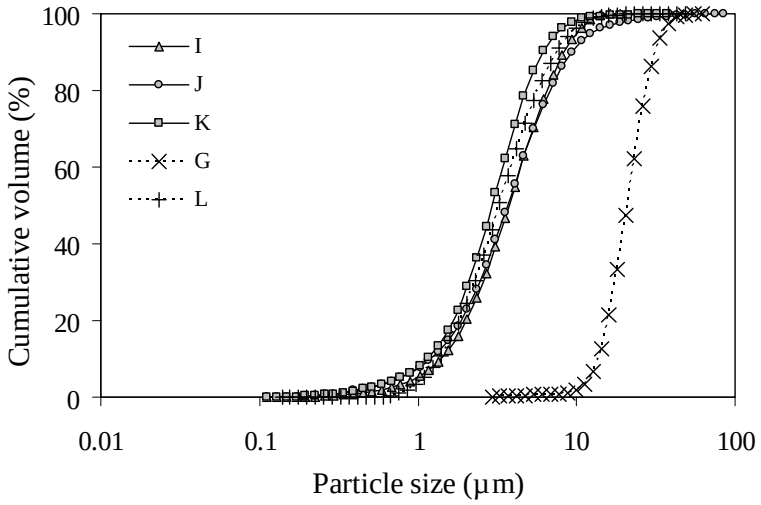

Stellenbosch University http://scholar.sun.ac.za

J.2 Oxidation of HBMS 777 cleaner concentrate (Sample I)

PLT1	Temp.	Imp. speed	P_g	p_{O2}°	Solids	Solids	Solution	[a] Density
Sample I	150°C	1000 rpm	1090 kPa	700 kPa	[b] 8.86 wt%	[c] 110.22 g	1064 g	1064 g/L
[d] LS, QB	Cu	Zn	Fe(III)	Fe(II)	H_2SO_4	Mg	SO_4	H_2O
0.5 g/L	5 g/L	5 g/L	5 g/L	5 g/L	30 g/L	0.1 g/L	66.2 g/L	973.4 g
min (test)	Sld. (g)	Colour	Sln. (g)	Vol. (mL)	Colour	[a] Dens g/L	[a] E_{Ag} (mV)	[a] pH
15 (T11)	86.02	Brown	1008	909	Green-blue	1109	465	0.77
30 (T12)	74.17	Red-brown	984	883	Green-blue	1115	475	0.77
60 (T13)	88.95	Red	986	882	Blue	1118	509	0.72
90 (T14)	79.72	Red	979	881	Blue	1111	490	0.75
Solids	Cu (%)	Zn (%)	Fe (%)	Mg (%)	S^{2-} (%)	[f] S° (%)	SO_4 (%)	S^T (%)
[e] Head	26.0	4.2	28.7	0.22	33.3	0.0	1.4	34.0
15 (T11)	12.1	0.37	33.6	0.16	13.7	13.0	8.9(5)	29.7
30 (T12)	7.62	0.21	35.1	0.16	8.3	20.2	11.4	32.3
60 (T13)	1.66	0.19	38.4	0.16	1.9	19.9	12.7	26.0
90 (T14)	1.48	0.15	37.1	0.16	1.75	21.2	11.2	26.7
Solution	Cu (g/L)	Zn (g/L)	Fe^T (g/L)	Fe(II) g/L	H_2SO_4 g/L	Mg (g/L)	SO_4 (g/L)	[g] Evap. (g)
15 (T11)	18.73	9.3	9.11	2.80	19.1	0.17	82.5	16
30 (T12)	22.69	8.9	7.69	1.45	18.2	0.15	84.4	39
60 (T13)	28.24	8.5	4.18	0.41	23.4	0.18	89.2	19
90 (T14)	27.00	9.3	2.80	0.25	22.3	0.16	84.0	32
[h] Extent	Cu (%)	Zn (%)	Fe (%)	Mg	S^{2-} (%)	[i] S° (%)	–	S^T (%)
15 (T11)	54 (100)	91 (102)	(107)	(101)	59	66	–	(98)
30 (T12)	75 (94)	96 (93)	(94)	(86)	79	66	–	(95)
60 (T13)	93 (96)	95 (89)	(109)	(105)	94	65	–	(96)
90 (T14)	95 (91)	97 (96)	(92)	(94)	95	62	–	(89)
[j] Oxidation	$CuFeS_2$	ZnS (%)	FeS (%)	–	[k] FeS_2 (%)	Fe_7S_8 (%)	[l] $W_{f,Hem}$	[m] $W_{f,t}$ (%)
15 (T11)	53	91	91	–	73	91	53	100
30 (T12)	74.5	96	96	–	91	96	53	86
60 (T13)	93	95	95	–	98	95	61	103
90 (T14)	95	97	97	–	97	97	64.5	92

[a] At 20°C; [b] Per unit mass water; [c] 21.75 wt% moisture; [d] Arbo A02, Orfom 2 (no pre-drying); [e] Avg. elem. composition; [f] Calc. (S balance); [g] H_2O evap., based on total mass accountability; [h] Reaction extents based on chem. analyses (elem. accountabilities in brackets); [i] S° yield, *i.e.*, $S°/S^{2-}{}_{rx}\times100\%$; [j] Mineral oxidation extents (calc. from chem. analyses); [k] Based on residual S^{2-}; [l] Wt. % Hem/(Hem+H-Jar), based on residue SO_4 & Fe balance, assuming 2 wt% S^T in Hem (Ch. 5); [m] Fractional weight of residue (*cf.* original sample), based on residue mass.

Stellenbosch University http://scholar.sun.ac.za

PLT2	Temp.	Imp. speed	P_g	p_{O2}°	Solids	Solids	Solution	[a] Density
Sample I	150°C	1000 rpm	1090 kPa	700 kPa	[b] 8.85 wt%	[c] 110.22 g	1064 g	1064 g/L
[d] LS	Cu	Zn	Fe(III)	Fe(II)	H_2SO_4	Mg	SO_4	H_2O
0.15 g/L	5 g/L	5 g/L	5 g/L	5 g/L	30 g/L	0.1 g/L	66.2 g/L	974.3 g
min (test)	Sld. (g)	Colour	Sln. (g)	Vol. (mL)	Colour	[a] Dens g/L	[a] E_{Ag} (mV)	[a] pH
15 (T21)	91.65	Brown	1000	904	Green-blue	1106	465	0.79
30 (T22)	91.15	Orange	973	877	Blue	1110	475	0.81
60 (T23)	89.09	Red	959	857	Blue	1118	511	0.64
90 (T24)	81.57	Red	991	895	Blue	1107	504	0.65
Solids	Cu (%)	Zn (%)	Fe (%)	Mg (%)	S^{2-} (%)	[f] S° (%)	SO_4 (%)	S^T (%)
[e] Head	26.0	4.2	28.7	0.22	33.3	0.0	1.4	34.0
15 (T21)	11.40	0.13	33.1	0.16	14.0	12.2	9.4	29.3
30 (T22)	8.47	0.18	35.0	0.16	7.3	16.3	9.8	26.9
60 (T23)	3.66	0.18	37.7	0.16	4.5	19.2	10.8	27.3
90 (T24)	3.63	0.18	38.5	0.14	3.95	19.6	10.1	26.9
Solution	Cu (g/L)	Zn (g/L)	Fe^T (g/L)	Fe(II) g/L	H_2SO_4 g/L	Mg (g/L)	SO_4 (g/L)	[g] Evap. (g)
15 (T21)	20.69	9.35	6.08	1.46	16.9	0.17	78.5	4
30 (T22)	24.51	9.25	4.90	1.05	16.5	0.17	79.2	3
60 (T23)	29.10	8.99	2.88	0.29	21.2	0.19	85.9	1
90 (T24)	26.10	8.89	2.46	0.39	21.2	0.20	80.1	16
[h] Extent	Cu (%)	Zn (%)	Fe (%)	Mg	S^{2-} (%)	[I] S° (%)	–	S^T (%)
15 (T21)	53 (106)	97 (99)	(105)	(104)	55	70	–	(98)
30 (T22)	74 (100)	95 (96)	(104)	(102)	77	67	–	(93)
60 (T23)	85 (103)	96 (91)	(104)	(105)	86	69	–	(95)
90 (T24)	87 (96)	96 (94)	(97)	(102)	89	63	–	(89)
[j] Oxidation	$CuFeS_2$	ZnS (%)	FeS (%)	–	[k] FeS_2 (%)	Fe_7S_8 (%)	[l] $W_{f,Hem}$	[m] $W_{f,t}$ (%)
15 (T21)	53	97	97	–	44	97	49	106
30 (T22)	73	95.5	95.5	–	85	95.5	61	106
60 (T23)	85	96	96	–	85	96	64	103
90 (T24)	87	96	96	–	96.5	96	68	95

[a] At 20°C; [b] Per unit mass water; [c] 21.75 wt% moisture; [d] Borrepal U (no pre-drying); [e] Avg. elem. composition; [f] Calc. (S balance); [g] H_2O evap., based on total mass accountability; [h] Reaction extents based on chem. analyses (elem. accountabilities in brackets); [i] S° yield, *i.e.*, $S°/S^{2-}{}_{rx}\times100\%$; [j] Mineral oxidation extents (calc. from chem. analyses); [k] Based on residual S^{2-}; [l] Wt. % Hem/(Hem+H-Jar), based on residue SO_4 & Fe balance, assuming 2 wt% S^T in Hem (Ch. 5); [m] Fractional weight of residue (*cf.* original sample), based on residue mass.

Stellenbosch University http://scholar.sun.ac.za

PLT3	Temp.	Imp. speed	P_g	$p_{O2}°$	Solids	Solids	Solution	[a] Density
Sample I	150°C	1000 rpm	1090 kPa	700 kPa	[b] 8.86 wt%	[c] 110.22 g	1064 g	1064 g/L
[d] LS	Cu	Zn	Fe(III)	Fe(II)	H_2SO_4	Mg	SO_4	H_2O
0.50 g/L	5 g/L	5 g/L	5 g/L	5 g/L	30 g/L	0.1 g/L	66.2 g/L	973.9 g
min (test)	Sld. (g)	Colour	Sln. (g)	Vol. (mL)	Colour	[a] Dens g/L	[a] E_{Ag} (mV)	[a] pH
15 (T31)	83.72	Brown	983	887	Green	1108	466	0.80
30 (T32)	86.08	Red-brown	970	867	Green-blue	1119	470	0.73
60 (T33)	84.98	Red	989	882	Blue	1121	498	0.68
90 (T34)	87.54	Red	992	891	Blue	1113	521	0.68
Solids	Cu (%)	Zn (%)	Fe (%)	Mg (%)	S^{2-} (%)	[f] S° (%)	SO_4 (%)	S^T (%)
[e] Head	26.0	4.2	28.7	0.22	33.3	0.0	1.4	34.0
15 (T31)	11.90	0.42	31.0	0.17	14.0	13.9	10.8	31.5
30 (T32)	5.89	0.27	35.2	0.14	6.7	18.7	12.7	29.7
60 (T33)	2.34	0.26	37.2	0.18	3.0	21.5	11.6	28.45
90 (T34)	1.51	0.26	37.6	0.13	1.9	21.1	13.9	27.6
Solution	Cu (g/L)	Zn (g/L)	Fe^T (g/L)	Fe(II) g/L	H_2SO_4 g/L	Mg (g/L)	SO_4 (g/L)	[g] Evap. (g)
15 (T31)	19.39	8.59	8.30	1.86	15.0	0.17	77.1	17
30 (T32)	25.0	9.13	5.7	1.6	17.8	0.16	82.6	16
60 (T33)	28.0	9.0	3.84	0.34	22.2	0.17	87.6	10
90 (T34)	29.43	8.86	2.15	0.14	22.2	0.17	85.3	1
[h] Extent	Cu (%)	Zn (%)	Fe (%)	Mg	S^{2-} (%)	[I] S° (%)	–	S^T (%)
15 (T31)	56 (99)	90 (93)	(96)	(101)	59	68	–	(96)
30 (T32)	77 (98)	94 (94)	(101)	(88)	80	70	–	(96)
60 (T33)	91 (97)	94 (95)	(101)	(103)	91	70	–	(97)
90 (T34)	94 (100)	94 (94)	(100)	(93)	94	68	–	(96)
[j] Oxidation	$CuFeS_2$	ZnS (%)	FeS (%)	–	[k] FeS_2 (%)	Fe_7S_8 (%)	[l] $W_{f,Hem}$	[m] $W_{f,t}$ (%)
15 (T31)	55	90	90	–	64	90	37	97
30 (T32)	77	64	64	–	87	64	51	100
60 (T33)	91	94	94	–	89	94	62	98.5
90 (T34)	94	94	94	–	96	94	56	101.5

[a] At 20°C; [b] Per unit mass water; [c] 21.75 wt% moisture; [d] Borrepal U (no pre-drying); [e] Avg. elem. composition; [f] Calc. (S balance); [g] H_2O evap., based on total mass accountability; [h] Reaction extents based on chem.. analyses (elem. accountabilities in brackets); [i] S° yield, *i.e.*, $S°/S^{2-}{}_{rx}\times100\%$; [j] Mineral oxidation extents (calc. from chem. analyses); [k] Based on residual S^{2-}; [l] Wt. % Hem/(Hem+H-Jar), based on residue SO_4 & Fe balance, assuming 2 wt% S^T in Hem (Ch. 5); [m] Fractional weight of residue (*cf.* original sample), based on residue mass.

Stellenbosch University http://scholar.sun.ac.za

PLT4	Temp.	Imp. speed	P_g	p_{O2}°	Solids	Solids	Solution	[a] Density
Sample I	150°C	1000 rpm	1090 kPa	700 kPa	[b] 8.86 wt%	[c] 110.22 g	1064 g	1064 g/L
[d] LS, QB	Cu	Zn	Fe(III)	Fe(II)	H_2SO_4	Mg	SO_4	H_2O
0.5 g/L	5 g/L	5 g/L	5 g/L	5 g/L	30 g/L	0.1 g/L	66.2 g/L	973.4 g
min (test)	Sld. (g)	Colour	Sln. (g)	Vol. (mL)	Colour	[a] Dens g/L	[a] E_{Ag} (mV)	[a] pH
–	–	–	–	–	–	–	–	–
–	–	–	–	–	–	–	–	–
60 (T43)	84.93	Red	1008	905	Green-blue	1113	503	0.65
90 (T44)	**S° balls**	–	–	–	–	–	–	–
Solids	Cu (%)	Zn (%)	Fe (%)	Mg (%)	S^{2-} (%)	[f] S° (%)	SO_4 (%)	S^T (%)
[e] Head	26.0	4.2	28.7	0.22	33.3	0.0	1.4	34.0
–	–	–	–	–	–	–	–	–
–	–	–	–	–	–	–	–	–
60 (T43)	3.23	0.38	37.1	0.14	3.3	21.4	10.8	28.3
–	–	–	–	–	–	–	–	–
Solution	Cu (g/L)	Zn (g/L)	Fe^T (g/L)	Fe(II) g/L	H_2SO_4 g/L	Mg (g/L)	SO_4 (g/L)	[g] Evap. (g)
–	–	–	–	–	–	–	–	–
–	–	–	–	–	–	–	–	–
60 (T43)	27.56	8.9	4.45	0.54	22.5	0.19	88.5	5
–	–	–	–	–	–	–	–	–
[h] Extent	Cu (%)	Zn (%)	Fe (%)	Mg	S^{2-} (%)	[i] S° (%)	–	S^T (%)
–	–	–	–	–	–	–	–	–
–	–	–	–	–	–	–	–	–
60 (T43)	88 (101)	91 (97)	(102)	(100)	90	70	–	(99)
–	–	–	–	–	–	–	–	–
[j] Oxidation	$CuFeS_2$	ZnS (%)	FeS (%)	–	[k] FeS_2 (%)	Fe_7S_8 (%)	[l] $W_{f,Hem}$	[m] $W_{f,t}$ (%)
–	–	–	–	–	–	–	–	–
–	–	–	–	–	–	–	–	–
60 (T43)	88	91	91	–	104	91	65	98.5
–	–	–	–	–	–	–	–	–

[a] At 20°C; [b] Per unit mass water; [c] 21.75 wt% moisture; [d] Arbo A02, Orfom 2 (no pre-drying) added over time (50%, 25% & 25% at 0, 30 & 45 min, respectively); [e] Avg. elem. composition; [f] Calc. (S balance); [g] H_2O evap., based on total mass accountability; [h] Reaction extents based on chem. analyses (elem. accountabilities in brackets); [i] S° yield, *i.e.*, $S°/S^{2-}{}_{rx}\times100\%$; [j] Mineral oxidation extents (calc. from chem. analyses); [k] Based on residual S^{2-}; [l] Wt. % Hem/(Hem+H-Jar), based on residue SO_4 & Fe balance, assuming 2 wt% S^T in Hem (Ch. 5); [m] Fractional weight of residue (*cf.* original sample), based on residue mass.

Stellenbosch University http://scholar.sun.ac.za

PLT5	Temp.	Imp. speed	P_g	p_{O2}°	Solids	Solids	Solution	[a] Density
Sample I	155°C	1000 rpm	1157 kPa	700 kPa	[b] 8.86 wt%	[c] 110.22 g	1064 g	1064 g/L
[d] LS, QB	Cu	Zn	Fe(III)	Fe(II)	H_2SO_4	Mg	SO_4	H_2O
0.5 g/L	5 g/L	5 g/L	5 g/L	5 g/L	30 g/L	0.1 g/L	66.2 g/L	973.4 g
min (test)	Sld. (g)	Colour	Sln. (g)	Vol. (mL)	Colour	[a] Dens g/L	[a] E_{Ag} (mV)	[a] pH
–	–	–	–	–	–	–	–	–
30 (T52)	83.7	Red-brown	1064	1000	Green-blue	1117	462	0.65
60 (T53)	88.92	Red	988	888	Blue	1113	512	0.64
–	–	–	–	–	–	–	–	–
Solids	Cu (%)	Zn (%)	Fe (%)	Mg (%)	S^{2-} (%)	[f] S° (%)	SO_4 (%)	S^T (%)
[e] Head	26.0	4.2	28.7	0.22	33.3	0.0	1.4	34.0
–	–	–	–	–	–	–	–	–
30 (T52)	5.41	0.36	33.8	0.14	6.4	19.75	9.8	29.4
60 (T53)	1.07	0.32	38.1	0.16	1.2	20.4	11.3	25.4
–	–	–	–	–	–	–	–	–
Solution	Cu (g/L)	Zn (g/L)	Fe^T (g/L)	Fe(II) g/L	H_2SO_4 g/L	Mg (g/L)	SO_4 (g/L)	[g] Evap. (g)
–	–	–	–	–	–	–	–	–
30 (T52)	25.25	8.9	6.76	1.65	20.0	0.19	87.6	15
60 (T53)	29.0	8.95	2.7	0.25	22.3	0.19	86.3	17
–	–	–	–	–	–	–	–	–
[h] Extent	Cu (%)	Zn (%)	Fe (%)	Mg	S^{2-} (%)	[i] S° (%)	–	S^T (%)
–	–	–	–	–	–	–	–	–
30 (T52)	80 (99)	92 (96)	(99)	(99)	81	71	–	(99)
60 (T53)	96 (97)	92 (97)	(95)	(107)	96	66	–	(94)
–	–	–	–	–	–	–	–	–
[j] Oxidation	$CuFeS_2$	ZnS (%)	FeS (%)	–	[k] FeS_2 (%)	Fe_7S_8 (%)	[l] $W_{f,Hem}$	[m] $W_{f,t}$ (%)
–	–	–	–	–	–	–	–	–
30 (T52)	80	92	92	–	86	92	61	97
60 (T53)	96	92	92	–	102	92	66	103
–	–	–	–	–	–	–	–	–

[a] At 20°C; [b] Per unit mass water; [c] 21.75 wt% moisture; [d] Arbo A02, Orfom 2 (no pre-drying); [e] Avg. elem. composition; [f] Calc. (S balance); [g] H_2O evap., based on total mass accountability; [h] Reaction extents based on chem. analyses (elem. accountabilities in brackets); [i] S° yield, *i.e.*, $S°/S^{2-}{}_{rx}\times100\%$; [j] Mineral oxidation extents (calc. from chem. analyses); [k] Based on residual S^{2-}; [l] Wt. % Hem/(Hem+H-Jar), based on residue SO_4 & Fe balance, assuming 2 wt% S^T in Hem (Ch. 5); [m] Fractional weight of residue (*cf.* original sample), based on residue mass.

Stellenbosch University http://scholar.sun.ac.za

J.3 Oxidation of HBMS 777 cleaner concentrate (Sample J)

PLU1	Temp.	Imp. speed	P_g	p_{O2}°	Solids	Solids	Solution	[a] Density
Sample J	145°C	1000 rpm	1029 kPa	700 kPa	[b] 8.86 wt%	[c] 108.4 g	1064 g	1063 g/L
[d] LS, QB	Cu	Zn	Fe(III)	Fe(II)	H_2SO_4	Mg	SO_4	H_2O
0.5 g/L	5 g/L	5 g/L	2.5 g/L	5 g/L	40 g/L	0.1 g/L	69.5 g/L	973.2 g
min (test)	Sld. (g)	Colour	Sln. (g)	Vol. (mL)	Colour	[a] Dens g/L	[a] E_{Ag} (mV)	[a] pH
15 (U11)	75.78	Brown	1022	925	Green	1104	476	0.97
30 (U12)	71.21	Red-brown	1025	926	Green-blue	1108	491	0.88
45 (U13)	70.91	Red	1020	914	Blue	1116	511	0.76
–	–	–	–	–	–	–	–	–
Solids	Cu (%)	Zn (%)	Fe (%)	Mg (%)	S^{2-} (%)	[f] S° (%)	SO_4 (%)	S^T (%)
[e] Head	26.0	4.2	28.7	0.22	33.3	0.0	1.4	34.0
15 (U11)	16.6	0.23	31.4	0.17	19.6	12.7	10.5	35.8
30 (U12)	9.43	0.19	32.7	0.19	11.4	21.2	9.4	35.7
45 (U13)	4.78	0.11	33.5	0.16	4.2	25.2	10.6	32.9
–	–	–	–	–	–	–	–	–
Solution	Cu (g/L)	Zn (g/L)	Fe^T (g/L)	Fe(II) g/L	H_2SO_4 g/L	Mg (g/L)	SO_4 (g/L)	[g] Evap. (g)
15 (U11)	15.36	8.2	10.05	2.85	12.1	0.18	71.3	8
30 (U12)	21.62	8.12	7.51	1.40	15.9	0.16	79.0	5.5
45 (U13)	25.63	8.23	6.56	0.75	20.4	0.18	87.8	1
–	–	–	–	–	–	–	–	–
[h] Extent	Cu (%)	Zn (%)	Fe (%)	Mg	S^{2-} (%)	[i] S° (%)	–	S^T (%)
15 (U11)	44 (98)	95 (90)	(103)	(100)	48	69	–	(93)
30 (U12)	70 (97)	96 (89)	(94)	(97)	72	73	–	(95)
45 (U13)	85 (98)	98 (88)	(92)	(97)	90	69	–	(95)
–	–	–	–	–	–	–	–	–
[j] Oxidation	$CuFeS_2$	ZnS (%)	FeS (%)	–	[k] FeS_2 (%)	Fe_7S_8 (%)	[l] $W_{f,Hem}$	[m] $W_{f,t}$ (%)
15 (U11)	43	95	95	–	48.5	95	24	88
30 (U12)	70	96	96	–	68.5	96	53	83
45 (U13)	85	98	98	–	112	98	59.5	82
–	–	–	–	–	–	–	–	–

[a] At 20°C; [b] Per unit mass water; [c] 20.43 wt% moisture; [d] Arbo A02, Orfom 2 (no pre-drying); [e] Avg. elem. composition; [f] Calc. (S balance); [g] H_2O evap., based on total mass accountability; [h] Reaction extents based on chem. analyses (elem. accountabilities in brackets); [i] S° yield, *i.e.*, $S°/S^{2-}{}_{rx}\times100\%$; [j] Mineral oxidation extents (calc. from chem. analyses); [k] Based on residual S^{2-}; [l] Wt. % Hem/(Hem+H-Jar), based on residue SO_4 & Fe balance, assuming 2 wt% S^T in Hem (Ch. 5); [m] Fractional weight of residue (*cf.* original sample), based on residue mass.

Stellenbosch University http://scholar.sun.ac.za

PLU2	Temp.	Imp. speed	P_g	p_{O2}°	Solids	Solids	Solution	[a] Density
Sample J	145°C	1000 rpm	1029 kPa	700 kPa	[b] 8.86 wt%	[c] 108.4 g	1064 g	1063 g/L
[d] LS	Cu	Zn	Fe(III)	Fe(II)	H_2SO_4	Mg	SO_4	H_2O
0.5 g/L	5 g/L	5 g/L	2.5 g/L	5 g/L	40 g/L	0.1 g/L	69.5 g/L	973.7 g
min (test)	Sld. (g)	Colour	Sln. (g)	Vol. (mL)	Colour	[a] Dens g/L	[a] E_{Ag} (mV)	[a] pH
15 (U21)	75.04	Yel-brown	999	908	Green-blue	1100	480	0.99
30 (U22)	74.92	Org-brown	1014	914	Blue	1109	501	0.90
–	–	–	–	–	–	–	–	–
–	–	–	–	–	–	–	–	–
Solids	Cu (%)	Zn (%)	Fe (%)	Mg (%)	S^{2-} (%)	[f] S° (%)	SO_4 (%)	S^T (%)
[e] Head	26.0	4.2	28.7	0.22	33.3	0.0	1.4	34.0
15 (U21)	16.9	0.27	30.2	0.14	20.5	13.4	8.7	36.85
30 (U22)	9.53	0.16	34.0	0.12	11.1	16.6	12.5	31.9
–	–	–	–	–	–	–	–	–
–	–	–	–	–	–	–	–	–
Solution	Cu (g/L)	Zn (g/L)	Fe^T (g/L)	Fe(II) g/L	H_2SO_4 g/L	Mg (g/L)	SO_4 (g/L)	[g] Evap. (g)
15 (U21)	15.5	8.86	9.96	2.26	11.8	0.19	72.5	36
30 (U22)	23.94	8.97	7.34	1.20	15.2	0.17	82.8	12
–	–	–	–	–	–	–	–	–
–	–	–	–	–	–	–	–	–
[h] Extent	Cu (%)	Zn (%)	Fe (%)	Mg	S^{2-} (%)	[i] S° (%)	–	S^T (%)
15 (U21)	43 (98)	94 (96)	(98)	(95)	46	76	–	(94)
30 (U22)	68 (106)	97 (96)	(100)	(85)	71	61	–	(93)
–	–	–	–	–	–	–	–	–
–	–	–	–	–	–	–	–	–
[j] Oxidation	$CuFeS_2$	ZnS (%)	FeS (%)	–	[k] FeS_2 (%)	Fe_7S_8 (%)	[l] $W_{f,Hem}$	[m] $W_{f,t}$ (%)
15 (U21)	43	94	94	–	38	94	26.5	87
30 (U22)	68	97	97	–	74	97	42.5	87
–	–	–	–	–	–	–	–	–
–	–	–	–	–	–	–	–	–

[a] At 20°C; [b] Per unit mass water; [c] 20.43 wt% moisture; [d] Borrepal U (no pre-drying); [e] Avg. elem. composition; [f] Calc. (S balance); [g] H_2O evap., based on total mass accountability; [h] Reaction extents based on chem. analyses (elem. accountabilities in brackets); [i] S° yield, *i.e.*, $S°/S^{2-}{}_{rx}\times100\%$; [j] Mineral oxidation extents (calc. from chem. analyses); [k] Based on residual S^{2-}; [l] Wt. % Hem/(Hem+H-Jar), based on residue SO_4 & Fe balance, assuming 2 wt% S^T in Hem (Ch. 5); [m] Fractional weight of residue (*cf.* original sample), based on residue mass.

Stellenbosch University http://scholar.sun.ac.za

PLU3	Temp.	Imp. speed	P_g	p_{O2}°	Solids	Solids	Solution	[a] Density
Sample J	150°C	1000 rpm	1090 kPa	700 kPa	[b] 8.69 wt%	[c] 108.4 g	1064 g	1052 g/L
[d] LS, QB	Cu	Zn	Fe(III)	Fe(II)	H_2SO_4	Mg	SO_4	H_2O
0.5 g/L	5 g/L	5 g/L	2.5 g/L	5 g/L	20 g/L	0.1 g/L	49.9 g/L	992.5 g
min (test)	Sld. (g)	Colour	Sln. (g)	Vol. (mL)	Colour	[a] Dens g/L	[a] E_{Ag} (mV)	[a] pH
10 (U31)	79.92	Lgt brown	977	906	Green-blue	1078	458	1.01
20 (U32)	79.00	Brown	1006	927	Blue	1085	468	0.96
40 (U33)	80.07	Red	998	915	Blue	1091	478	0.88
60 (U34)	81.99	Deep red	1003	917	Blue	1094	479	0.80
Solids	Cu (%)	Zn (%)	Fe (%)	Mg (%)	S^{2-} (%)	[f] S° (%)	SO_4 (%)	S^T (%)
[e] Head	26.0	4.2	28.7	0.22	33.3	0.0	1.4	34.0
10 (U31)	18.3	0.24	31.8	0.17	21.5	9.6	4.6	32.6
20 (U32)	12.4	0.21	32.95	0.17	15.2	13.8	5.6	30.9
40 (U33)	8.44	0.20	37.1	0.16	9.0	17.0	5.8	27.9
60 (U34)	4.71	0.20	39.5	0.16	4.9	19.1	6.2	26.1
Solution	Cu (g/L)	Zn (g/L)	Fe^T (g/L)	Fe(II) g/L	H_2SO_4 g/L	Mg (g/L)	SO_4 (g/L)	[g] Evap. (g)
10 (U31)	13.96	8.69	4.98	2.25	11.8	0.16	57.0	33
20 (U32)	19.18	8.49	3.63	1.35	13.4	0.16	63.4	5
40 (U33)	23.02	8.44	2.03	0.60	15.5	0.17	67.8	8.5
60 (U34)	23.8	8.4	1.93	0.55	18.4	0.18	71.6	(-4)
[h] Extent	Cu (%)	Zn (%)	Fe (%)	Mg	S^{2-} (%)	[i] S° (%)	–	S^T (%)
10 (U31)	35 (99)	95 (93)	(93)	(96)	40	66	–	(94)
20 (U32)	56 (100)	95 (93)	(91)	(98)	58	65	–	(95)
40 (U33)	70 (101)	96 (91)	(98)	(96)	75	63	–	(93)
60 (U34)	83 (93)	95 (91)	(106)	(103)	86	63	–	(94)
[j] Oxidation	$CuFeS_2$	ZnS (%)	FeS (%)	–	[k] FeS_2 (%)	Fe_7S_8 (%)	[l] $W_{f,Hem}$	[m] $W_{f,t}$ (%)
10 (U31)	34	95	95	–	42	95	60	93
20 (U32)	56	95	95	–	49	95	68.5	92
40 (U33)	69.5	96	96	–	93.5	96	81	93
60 (U34)	83	95.5	95.5	–	99	95.5	84	95

[a] At 20°C; [b] Per unit mass water; [c] 20.43 wt% moisture; [d] Arbo A02, Orfom 2 (no pre-drying); [e] Avg. elem. composition; [f] Calc. (S balance); [g] H_2O evap., based on total mass accountability; [h] Reaction extents based on chem. analyses (elem. accountabilities in brackets); [i] S° yield, *i.e.*, $S°/S^{2-}{}_{rx}\times100\%$; [j] Mineral oxidation extents (calc. from chem. analyses); [k] Based on residual S^{2-}; [l] Wt. % Hem/(Hem+H-Jar), based on residue SO_4 & Fe balance, assuming 2 wt% S^T in Hem (Ch. 5); [m] Fractional weight of residue (*cf.* original sample), based on residue mass.

Stellenbosch University http://scholar.sun.ac.za

PLU4	Temp.	Imp. speed	P_g	p_{O2}°	Solids	Solids	Solution	[a] Density
Sample J	150°C	1000 rpm	1090 kPa	700 kPa	[b] 8.55 wt%	[c] 108.4 g	1064 g	1038 g/L
[d] LS, QB	Cu	Zn	Fe(III)	Fe(II)	H_2SO_4	Mg	SO_4	H_2O
0.5 g/L	5 g/L	5 g/L	0.5 g/L	2 g/L	20 g/L	0.1 g/L	39.6 g/L	1008.2 g
min (test)	Sld. (g)	Colour	Sln. (g)	Vol. (mL)	Colour	[a] Dens g/L	[a] E_{Ag} (mV)	[a] pH
10 (U41)	75.53	Drk brown	1009	944	Green-blue	1069	454	1.14
20 (U42)	72.94	Brown	1013	946	Blue	1071	454	1.09
40 (U43)	71.85	Red	1020	943	Blue	1082	464	0.95
60 (U44)	70.67	Deep red	1029	955	Blue	1077	462	0.96
Solids	Cu (%)	Zn (%)	Fe (%)	Mg (%)	S^{2-} (%)	[f] S° (%)	SO_4 (%)	S^T (%)
[e] Head	26.0	4.2	28.7	0.22	33.3	0.0	1.4	34.0
10 (U41)	18.6	0.30	31.8	0.19	22.7	10.5	5.1	34.9
20 (U42)	15.9	0.57	32.5	0.17	19.9	11.8	5.5	33.55
40 (U43)	10.0	0.31	38.5	0.17	12.7	17.1	6.5	32.0
60 (U44)	9.1	0.31	33.6	0.15	11.6	19.6	3.9	32.5
Solution	Cu (g/L)	Zn (g/L)	Fe^T (g/L)	Fe(II) g/L	H_2SO_4 g/L	Mg (g/L)	SO_4 (g/L)	[g] Evap. (g)
10 (U41)	13.57	8.25	3.14	1.75	8.6	0.16	48.3	8
20 (U42)	17.58	8.64	2.23	1.20	9.8	0.15	54.2	16
40 (U43)	20.62	8.38	1.30	0.60	12.9	0.17	59.6	8
60 (U44)	20.57	8.21	1.46	0.60	13.7	0.17	60.5	3
[h] Extent	Cu (%)	Zn (%)	Fe (%)	Mg	S^{2-} (%)	[i] S° (%)	–	S^T (%)
10 (U41)	37 (98)	94 (92)	(99)	(100)	40	69	–	(97)
20 (U42)	48 (102)	89 (98)	(94)	(92)	49	61	–	(97)
40 (U43)	68 (97)	94 (93)	(106)	(95)	68	63	–	(97)
60 (U44)	71 (95)	94 (92)	(92)	(92)	71	68	–	(98)
[j] Oxidation	$CuFeS_2$	ZnS (%)	FeS (%)	–	[k] FeS_2 (%)	Fe_7S_8 (%)	[l] $W_{f,Hem}$	[m] $W_{f,t}$ (%)
10 (U41)	37	94	94	–	29	94	52	88
20 (U42)	48	88.5	88.5	–	36	88.5	59	85
40 (U43)	68	94	94	–	56.5	94	75	83
60 (U44)	71	94	94	–	61	94	86	82

[a] At 20°C; [b] Per unit mass water; [c] 20.43 wt% moisture; [d] Arbo A02, Orfom 2 (no pre-drying); [e] Avg. elem. composition; [f] Calc. (S balance); [g] H_2O evap., based on total mass accountability; [h] Reaction extents based on chem. analyses (elem. accountabilities in brackets); [i] S° yield, *i.e.*, $S°/S^{2-}{}_{rx}\times100\%$; [j] Mineral oxidation extents (calc. from chem. analyses); [k] Based on residual S^{2-}; [l] Wt. % Hem/(Hem+H-Jar), based on residue SO_4 & Fe balance, assuming 2 wt% S^T in Hem (Ch. 5); [m] Fractional weight of residue (*cf.* original sample), based on residue mass.

Stellenbosch University http://scholar.sun.ac.za

PLU5	Temp.	Imp. speed	P_g	p_{O2}°	Solids	Solids	Solution	[a] Density
Sample J	150°C	1000 rpm	1390 kPa	1000 kPa	[b] 8.56 wt%	[c] 108.4 g	1064 g	1038 g/L
[d] LS, QB	Cu	Zn	Fe(III)	Fe(II)	H_2SO_4	Mg	SO_4	H_2O
0.6 g/L	5 g/L	5 g/L	0.5 g/L	2 g/L	20 g/L	0.1 g/L	39.6 g/L	1008.0 g
Min (test)	Sld. (g)	Colour	Sln. (g)	Vol. (mL)	Colour	[a] Dens g/L	[a] E_{Ag} (mV)	[a] pH
10 (U51)	75.77	Drk brown	1017	946	Green-blue	1075	465	1.08
20 (U52)	67.73	Brown	1029	948	Blue	1085	471	0.98
40 (U53)	67.76	Red	1020	936	Blue	1090	480	0.95
60 (U54)	69.84	Deep red	1025	941	Blue	1090	484	0.94
Solids	Cu (%)	Zn (%)	Fe (%)	Mg (%)	S^{2-} (%)	[f] S° (%)	SO_4 (%)	S^T (%)
[e] Head	26.0	4.2	28.7	0.22	33.3	0.0	1.4	34.0
10 (U51)	16.25	0.56	31.8	0.20	19.4	11.0	5.8	32.35
20 (U52)	11.4	0.24	35.4	0.19	13.8	16.3	5.9	32.05
40 (U53)	5.1	0.21	37.9	0.20	6.1	21.0	6.9	29.4
60 (U54)	3.2	0.20	40.9	0.20	3.7	19.6	6.7	25.6
Solution	Cu (g/L)	Zn (g/L)	Fe^T (g/L)	Fe(II) g/L	H_2SO_4 g/L	Mg (g/L)	SO_4 (g/L)	[g] Evap. (g)
10 (U51)	14.62	8.53	3.44	1.29	11.9	0.15	54.6	9
20 (U52)	20.47	8.81	2.42	0.95	12.4	0.15	62.0	1
40 (U53)	23.81	8.86	1.31	0.40	14.0	0.15	66.3	4
60 (U54)	25.0	8.92	0.93	0.25	14.5	0.16	67.9	9
[h] Extent	Cu (%)	Zn (%)	Fe (%)	Mg	S^{2-} (%)	[i] S° (%)	–	S^T (%)
10 (U51)	45 (95)	88 (97)	(100)	(100)	49	60	–	(97)
20 (U52)	66 (98)	96 (97)	(96)	(91)	67	57	–	(96)
40 (U53)	85 (93)	96 (96)	(98)	(94)	86	58	–	(95)
60 (U54)	90 (93)	96 (98)	(108)	(98)	91	52	–	(91)
[j] Oxidation	$CuFeS_2$	ZnS (%)	FeS (%)	–	[k] FeS_2 (%)	Fe_7S_8 (%)	[l] $W_{f,Hem}$	[m] $W_{f,t}$ (%)
10 (U51)	44.5	88	88	–	50	88	56	88
20 (U52)	65	95.5	95.5	–	63.5	95.5	73	78.5
40 (U53)	84.5	96	96	–	85	96	79	79
60 (U54)	90	96	96	–	94	96	84	81

[a] At 20°C; [b] Per unit mass water; [c] 20.43 wt% moisture; [d] Arbo A02, Orfom 2 (no pre-drying); [e] Avg. elem. composition; [f] Calc. (S balance); [g] H_2O evap., based on total mass accountability; [h] Reaction extents based on chem. analyses (elem. accountabilities in brackets); [i] S° yield, *i.e.*, $S°/S^{2-}{}_{rx}\times100\%$; [j] Mineral oxidation extents (calc. from chem. analyses); [k] Based on residual S^{2-}; [l] Wt. % Hem/(Hem+H-Jar), based on residue SO_4 & Fe balance, assuming 2 wt% S^T in Hem (Ch. 5); [m] Fractional weight of residue (*cf.* original sample), based on residue mass.

Stellenbosch University http://scholar.sun.ac.za

J.4 Oxidation of HBMS 777 cleaner concentrate (Sample K)

PLV1	Temp.	Imp. speed	P_g	p_{O2}°	Solids	Solids	Solution	[a] Density
Sample K	155°C	1000 rpm	1157 kPa	700 kPa	[b] 5.55 wt%	[c] 77.66 g	1093 g	1038 g/L
[d] LS, QB	Cu	Zn	Fe(III)	Fe(II)	H_2SO_4	Mg	SO_4	H_2O
0.6 g/L	5 g/L	5 g/L	0.5 g/L	2 g/L	20 g/L	0.1 g/L	39.6 g/L	1035.2 g
Min (test)	Sld. (g)	Colour	Sln. (g)	Vol. (mL)	Colour	[a] Dens g/L	[a] E_{Ag} (mV)	[a] pH
10 (V11)	47.22	Drk brown	1057	991	Green-blue	1067	463	0.97
20 (V12)	45.40	Brown	1062	990	Blue	1073	468	0.86
30 (V13)	43.28	Red	1062.5	985	Blue	1079	477	0.84
40 (V14)	45.17	Deep red	1053	975	Blue	1080	484	0.85
Solids	Cu (%)	Zn (%)	Fe (%)	Mg (%)	S^{2-} (%)	[f] S° (%)	SO_4 (%)	S^T (%)
[e] Head	26.0	4.2	28.7	0.22	33.3	0.0	1.4	34.0
10 (V11)	14.5	0.16	28.95	0.18	17.6	13.9	7.5	34.0
20 (V12)	9.40	0.24	32.5	0.21	11.7	16.7	7.4	30.9
30 (V13)	5.52	0.15	34.6	0.19	6.4	20.9	7.5	29.8
40 (V14)	3.37	0.14	34.4	0.17	3.7	23.4	7.6	29.65
Solution	Cu (g/L)	Zn (g/L)	Fe^T (g/L)	Fe(II) g/L	H_2SO_4 g/L	Mg (g/L)	SO_4 (g/L)	[g] Evap. (g)
10 (V11)	13.11	7.37	3.53	1.50	10.7	0.15	49.5	1
20 (V12)	15.20	7.39	2.54	1.05	14.5	0.15	54.3	2
30 (V13)	18.37	7.31	2.35	0.85	14.5	0.15	58.6	7
40 (V14)	19.47	7.40	1.31	0.40	14.8	0.16	58.5	6
[h] Extent	Cu (%)	Zn (%)	Fe (%)	Mg	S^{2-} (%)	[i] S° (%)	–	S^T (%)
10 (V11)	54 (98)	97 (96)	(90)	(100)	57	61	–	(97)
20 (V12)	71 (96)	95 (97)	(90)	(104)	72	55	–	(95)
30 (V13)	84 (101)	97 (95)	(90)	(100)	86	55 **Sº balls**	–	(96)
40 (V14)	90 (101)	97 (95)	(88)	(98)	91	61 **Sº balls**	–	(97)
[j] Oxidation	$CuFeS_2$	ZnS (%)	FeS (%)	–	[k] FeS_2 (%)	Fe_7S_8 (%)	[l] $W_{f,Hem}$	[m] $W_{f,t}$ (%)
10 (V11)	54	97	97	–	49	97	39	82
20 (V12)	71	95.5	95.5	–	65	95.5	62	79
30 (V13)	84	97	97	–	88	97	72	75
40 (V14)	90	97	97	–	96.5	97	74	79

[a] At 20°C; [b] Per unit mass water; [c] 25.96 wt% moisture; [d] Arbo A02, Orfom 2 (no pre-drying); [e] Avg. elem. composition; [f] Calc. (S balance); [g] H_2O evap., based on total mass accountability; [h] Reaction extents based on chem. analyses (elem. accountabilities in brackets); [i] S° yield, *i.e.*, $S°/S^{2-}{}_{rx}\times100\%$; [j] Mineral oxidation extents (calc. from chem. analyses); [k] Based on residual S^{2-}; [l] Wt. % Hem/(Hem+H-Jar), based on residue SO_4 & Fe balance, assuming 2 wt% S^T in Hem (Ch. 5); [m] Fractional weight of residue (*cf.* original sample), based on residue mass.

Stellenbosch University http://scholar.sun.ac.za

PLV2	Temp.	Imp. speed	P_g	p_{O2}°	Solids	Solids	Solution	[a] Density
Sample K	150°C	1000 rpm	1090 kPa	700 kPa	[b] 8.56 wt%	[c] 116.49 g	1064 g	1038 g/L
[d] LS, QB	Cu	Zn	Fe(III)	Fe(II)	H_2SO_4	Mg	SO_4	H_2O
0.6 g/L	5 g/L	5 g/L	0.5 g/L	2 g/L	20 g/L	0.1 g/L	39.6 g/L	1008.0 g
Min (test)	Sld. (g)	Colour	Sln. (g)	Vol. (mL)	Colour	[a] Dens g/L	[a] E_{Ag} (mV)	[a] pH
10 (V21)	76.23	Drk-brown	1025	958	Green-blue	1067	455	1.02
20 (V22)	72.23	Drk brown	1024	946	Blue	1082	460	0.98
30 (V23)	70.26	Red-brown	1020	942	Blue	1083	461	0.91
45 (V24)	66.39	Deep-red	1027	938	Blue	1095	467	0.92
Solids	Cu (%)	Zn (%)	Fe (%)	Mg (%)	S^{2-} (%)	[f] S° (%)	SO_4 (%)	S^T (%)
[e] Head	26.0	4.2	28.7	0.22	33.3	0.0	1.4	34.0
10 (V21)	18.0	0.90	29.3	0.20	22.7	8.2	5.6	32.8
20 (V22)	13.1	0.44	33.9	0.22	14.8	15.55	7.0	32.7
30 (V23)	9.79	0.38	33.4	0.22	11.2	15.3	6.5	28.7
45 (V24)	6.99	0.35	37.7	0.24	7.5	18.9	7.0	28.7
Solution	Cu (g/L)	Zn (g/L)	Fe^T (g/L)	Fe(II) g/L	H_2SO_4 g/L	Mg (g/L)	SO_4 (g/L)	[g] Evap. (g)
10 (V21)	14.90	7.53	3.17	1.50	10.3	0.16	51.2	8
20 (V22)	19.66	8.33	2.92	1.40	12.2	0.15	60.8	7.5
30 (V23)	21.54	8.34	2.07	1.05	13.6	0.15	63.2	11
45 (V24)	24.62	8.25	1.93	0.75	13.5	0.16	67.5	8
[h] Extent	Cu (%)	Zn (%)	Fe (%)	Mg	S^{2-} (%)	[i] S° (%)	–	S^T (%)
10 (V21)	39 (102)	81 (90)	(93)	(104)	40	55	–	(96)
20 (V22)	58 (102)	91 (94)	(100)	(104)	63	62	–	(100)
30 (V23)	69 (99)	93 (93)	(93)	(102)	73	52	–	(93)
45 (V24)	79 (101)	94 (91)	(98)	(105)	83	53	–	(94)
[j] Oxidation	$CuFeS_2$	ZnS (%)	FeS (%)	–	[k] FeS_2 (%)	Fe_7S_8 (%)	[l] $W_{f,Hem}$	[m] $W_{f,t}$ (%)
10 (V21)	38	81	81	–	24	81	37	88
20 (V22)	57	91	91	–	76.5	91	62	84
30 (V23)	69	93	93	–	81	93	70	81.5
45 (V24)	79	94	94	–	96	94	77	77

[a] At 20°C; [b] Per unit mass water; [c] 25.96 wt% moisture; [d] Arbo A02, Orfom 2 (no pre-drying); [e] Avg. elem. composition; [f] Calc. (S balance); [g] H_2O evap., based on total mass accountability; [h] Reaction extents based on chem. analyses (elem. accountabilities in brackets); [i] S° yield, *i.e.*, $S°/S^{2-}{}_{rx}\times100\%$; [j] Mineral oxidation extents (calc. from chem. analyses); [k] Based on residual S^{2-}; [l] Wt. % Hem/(Hem+H-Jar), based on residue SO_4 & Fe balance, assuming 2 wt% S^T in Hem (Ch. 5); [m] Fractional weight of residue (*cf.* original sample), based on residue mass.

Stellenbosch University http://scholar.sun.ac.za

PLV3	Temp.	Imp. speed	P_g	p_{O2}°	Solids	Solids	Solution	[a] Density
Sample K	140°C	1000 rpm	1275 kPa	1000 kPa	[b] 8.56 wt%	[c] 116.49 g	1064 g	1038 g/L
[d] LS, QB	Cu	Zn	Fe(III)	Fe(II)	H_2SO_4	Mg	SO_4	H_2O
0.6 g/L	5 g/L	5 g/L	0.5 g/L	2 g/L	20 g/L	0.1 g/L	39.6 g/L	1008.0 g
Min (test)	Sld. (g)	Colour	Sln. (g)	Vol. (mL)	Colour	[a] Dens g/L	[a] E_{Ag} (mV)	[a] pH
15 (V31)	77.08	Drk-brown	1009	943	Green-blue	1070	454	1.07
30 (V32)	76.85	Drk brown	998	930	Blue	1073	454	1.04
45 (V33)	75.42	Red-brown	1011	936	Blue	1080	463	1.04
60 (V34)	72.76	Red	1020	942	Blue	1082	461	1.03
Solids	Cu (%)	Zn (%)	Fe (%)	Mg (%)	S^{2-} (%)	[f] S° (%)	SO_4 (%)	S^T (%)
[e] Head	26.0	4.2	28.7	0.22	33.3	0.0	1.4	34.0
15 (V31)	18.9	0.93	30.9	0.24	22.3	7.1	4.9	31.0
30 (V32)	15.5	0.47	31.4	0.22	18.0	10.5	5.5	30.3
45 (V33)	12.9	0.36	33.4	0.21	14.4	13.8	5.4	30.0
60 (V34)	11.0	0.27	35.1	0.22	12.2	16.8	5.4	30.8
Solution	Cu (g/L)	Zn (g/L)	Fe^T (g/L)	Fe(II) g/L	H_2SO_4 g/L	Mg (g/L)	SO_4 (g/L)	[g] Evap. (g)
15 (V31)	14.90	8.02	3.78	1.20	10.8	0.14	54.2	17
30 (V32)	16.13	8.25	2.59	0.80	11.6	0.16	54.5	20.5
45 (V33)	19.65	8.43	1.92	0.60	11.8	0.16	58.7	15
60 (V34)	21.51	8.59	1.01	0.45	11.7	0.17	59.5	11
[h] Extent	Cu (%)	Zn (%)	Fe (%)	Mg	S^{2-} (%)	[i] S° (%)	–	S^T (%)
15 (V31)	35 (104)	80 (95)	(100)	(109)	40	47	–	(95)
30 (V32)	47 (98)	90 (92)	(97)	(109)	52	54	–	(94)
45 (V33)	57 (102)	93 (93)	(99)	(107)	62	58	–	(95)
60 (V34)	64 (103)	95 (95)	(97)	(109)	69	62	–	(96)
[j] Oxidation	$CuFeS_2$	ZnS (%)	FeS (%)	–	[k] FeS_2 (%)	Fe_7S_8 (%)	[l] $W_{f,Hem}$	[m] $W_{f,t}$ (%)
15 (V31)	34	80	80	–	49	80	52	89
30 (V32)	46	90	90	–	60	90	61	89
45 (V33)	56	92.5	92.5	–	78	92.5	72	87
60 (V34)	64	95	95	–	83	95	77	84

[a] At 20°C; [b] Per unit mass water; [c] 25.96 wt% moisture; [d] Arbo A02, Orfom 2 (no pre-drying); [e] Avg. elem. composition; [f] Calc. (S balance); [g] H_2O evap., based on total mass accountability; [h] Reaction extents based on chem. analyses (elem. accountabilities in brackets); [i] S° yield, *i.e.*, $S°/S^{2-}{}_{rx}\times100\%$; [j] Mineral oxidation extents (calc. from chem. analyses); [k] Based on residual S^{2-}; [l] Wt. % Hem/(Hem+H-Jar), based on residue SO_4 & Fe balance, assuming 2 wt% S^T in Hem (Ch. 5); [m] Fractional weight of residue (*cf.* original sample), based on residue mass.

Stellenbosch University http://scholar.sun.ac.za

J.5 Oxidation of Las Tortolas (LT) cleaner concentrate (Sample G)

PLW1	Temp.	Imp. speed	P_g	$p_{O2}°$	Solids	Solids	Solution	[a] Density
Sample G	145°C	1000 rpm	1029 kPa	700 kPa	[b] 5.49 wt%	[c] 57.5 g	1093 g	1027 g/L
[d] LS, QB	Cu	–	Fe(III)	Fe(II)	H_2SO_4	Mg	SO_4	H_2O
0.5 g/L	5 g/L	–	0.5 g/L	2 g/L	20 g/L	0.1 g/L	32.3 g/L	1047.95 g
Min (test)	Sld. (g)	Colour	Sln. (g)	Vol. (mL)	Colour	[a] Dens g/L	[a] E_{Ag} (mV)	[a] pH
15 (W11)	46.96	Grey	1066	1019	Green-blue	1046	484	1.08
30 (W12)	46.83	Drk brown	1081	1026	Green-blue	1054	487	1.03
60 (W13)	45.15	Red-brown	1069	1007	Green-blue	1062	490	0.89
–	–	–	–	–	–	–	–	–
Solids	Cu (%)	–	Fe (%)	Mg (%)	S^{2-} (%)	[f] S° (%)	SO_4 (%)	S^T (%)
[e] Head	33.6	–	27.3	0.22	34.7	0.0	0.0	34.7
15 (W11)	26.7	–	28.5	0.12	32.7	5.5	1.4	38.7
30 (W12)	23.7	–	28.5	0.10	28.3	7.5	5.1	37.5
60 (W13)	17.5	–	29.6	0.10	18.3	13.1	8.3	34.2
–	–	–	–	–	–	–	–	–
Solution	Cu (g/L)	–	Fe^T (g/L)	Fe(II) g/L	H_2SO_4 g/L	Mg (g/L)	SO_4 (g/L)	[g] Evap. (g)
15 (W11)	10.35	–	4.92	1.60	9.1	0.16	36.5	6
30 (W12)	12.94	–	5.00	1.45	10.1	0.16	41.7	6
60 (W13)	16.13	–	4.82	1.05	14.7	0.16	50.9	14
–	–	–	–	–	–	–	–	–
[h] Extent	Cu (%)	–	Fe (%)	Mg	S^{2-} (%)	[i] S° (%)	–	S^T (%)
15 (W11)	27 (94)	–	(100)	(92)	23	57	–	(97)
30 (W12)	43 (99)	–	(101)	(88)	34	52.5	–	(101)
60 (W13)	59 (98)	–	(99)	(86)	59	51	–	(103)
–	–	–	–	–	–	–	–	–
[j] Oxidation	–	–	–	–	–	–	–	[k] $W_{f,t}$ (%)
15 (W11)	–	–	–	–	–	–	–	82
30 (W12)	–	–	–	–	–	–	–	81
60 (W13)	–	–	–	–	–	–	–	78.5
–	–	–	–	–	–	–	–	–

[a] At 20°C; [b] Per unit mass water; [c] Dry solids (no moisture); [d] Arbo A02, Orfom 2 (no pre-drying); [e] Avg. elem. composition; [f] Calc. (S balance); [g] H_2O evap., based on total mass accountability; [h] Reaction extents based on chem. analyses (elem. accountabilities in brackets); [i] S° yield, *i.e.*, $S°/S^{2-}{}_{rx}\times100\%$; [j] Individual mineral oxidation extents not uniquely determinable from chem. analyses; [l] Fractional weight of residue (*cf.* original sample).

Stellenbosch University http://scholar.sun.ac.za

J.6 Oxidation of Las Tortolas (LT) cleaner concentrate (Sample L)

PLX1	Temp.	Imp. speed	P_g	p_{O2}°	Solids	Solids	Solution	[a] Density
Sample L	150°C	1000 rpm	1090 kPa	700 kPa	[b] 8.45 wt%	[c] 112.91 g	1064g	1027 g/L
[d] LS, QB	Cu	–	Fe(III)	Fe(II)	H_2SO_4	Mg	SO_4	H_2O
0.6 g/L	5 g/L	–	0.5 g/L	2 g/L	20 g/L	0.1 g/L	32.3 g/L	1020.2 g
Min (test)	Sld. (g)	Colour	Sln. (g)	Vol. (mL)	Colour	[a] Dens g/L	[a] E_{Ag} (mV)	[a] pH
10 (X11)	73.39	Drk-brown	1039	980	Blue	1060	461	1.12
20 (X12)	66.10	Brown	1053	981	Blue	1073	463	1.06
30 (X13)	63.63	Red-brown	1053	976	Blue	1079	474	0.97
–	–	–	–	–	–	–	–	–
Solids	Cu (%)	–	Fe (%)	Mg (%)	S^{2-} (%)	[f] S° (%)	SO_4 (%)	S^T (%)
[e] Head	30.2	–	24.7	0.22	30.7	0.0	0.3	30.8
10 (X11)	18.1	–	28.6	0.12	22.9	6.7	5.1	31.3
20 (X12)	11.1	–	30.6	0.15	14.2	12.9	5.8	29.0
30 (X13)	8.6	–	31.3	0.15	10.3	14.6	5.6	26.8
–	–	–	–	–	–	–	–	–
Solution	Cu (g/L)	–	Fe^T (g/L)	Fe(II) g/L	H_2SO_4 g/L	Mg (g/L)	SO_4 (g/L)	[g] Evap. (g)
10 (X11)	18.14	–	3.69	1.88	9.4	0.15	45.1	4.5
20 (X12)	23.25	–	3.76	1.55	10.8	0.15	54.7	6
30 (X13)	24.93	–	3.21	1.20	13.4	0.15	58.7	0
–	–	–	–	–	–	–	–	–
[h] Extent	Cu (%)	–	Fe (%)	Mg	S^{2-} (%)	[i] S° (%)	–	S^T (%)
10 (X11)	49 (99)	–	(103)	(79)	37	51	–	(100)
20 (X12)	72 (97)	–	(100)	(84)	65	50	–	(98)
30 (X13)	79 (95)	–	(96)	(83)	75	47	–	(96)
–	–	–	–	–	–	–	–	–
[j] Oxidation	–	–	–	–	–	–	–	[k] $W_{f,t}$ (%)
10 (X11)	–	–	–	–	–	–	–	85
20 (X12)	–	–	–	–	–	–	–	77
30 (X13)	–	–	–	–	–	–	–	74
–	–	–	–	–	–	–	–	–

[a] At 20°C; [b] Per unit mass water; [c] 23.62 wt% moisture; [d] Arbo A02, Orfom 2 (no pre-drying); [e] Avg. elem. composition; [f] Calc. (S balance); [g] H_2O evap., based on total mass accountability; [h] Reaction extents based on chem. analyses (elem. accountabilities in brackets); [i] S° yield, *i.e.*, $S°/S^{2-}{}_{rx}\times100\%$; [j] Individual mineral oxidation extents not uniquely determinable from chem. analyses; [l] Fractional weight of residue (*cf.* original sample).

Stellenbosch University http://scholar.sun.ac.za

PLX2	Temp.	Imp. speed	P_g	p_{O2}°	Solids	Solids	Solution	[a] Density
Sample L	155°C	1000 rpm	1157 kPa	700 kPa	[b] 8.45 wt%	[c] 112.91 g	1064g	1027 g/L
[d] LS, QB	Cu	–	Fe(III)	Fe(II)	H_2SO_4	Mg	SO_4	H_2O
0.6 g/L	5 g/L	–	0.5 g/L	2 g/L	20 g/L	0.1 g/L	32.3 g/L	1020.4 g
Min (test)	Sld. (g)	Colour	Sln. (g)	Vol. (mL)	Colour	[a] Dens g/L	[a] E_{Ag} (mV)	[a] pH
10 (X21)	72.52	Drk-brown	1041	981	Blue	1062	460	0.97
20 (X22)	71.32	Drk-brown	1043	982	Blue	1062	463	0.97
40 (X23)	61.24	Red-brown	1052	968	Blue	1087	476	0.86
60 (X24)	61.11	Red	1044	957	Blue	1091	506	0.75
Solids	Cu (%)	–	Fe (%)	Mg (%)	S^{2-} (%)	[f] S° (%)	SO_4 (%)	S^T (%)
[e] Head	30.2	–	24.7	0.22	30.7	0.0	0.3	30.8
10 (X21)	17.0	–	29.9	0.15	21.1	6.9	5.65	29.9
20 (X22)	13.4	–	31.0	0.16	17.1	10.2	7.8	29.9
40 (X23)	5.06	–	34.5	0.12	6.0	17.2	8.0	25.9
60 (X24)	2.31	–	34.7	0.12	1.8	18.7	7.4	23.0
Solution	Cu (g/L)	–	Fe^T (g/L)	Fe(II) g/L	H_2SO_4 g/L	Mg (g/L)	SO_4 (g/L)	[g] Evap. (g)
10 (X21)	19.66	–	2.51	1.25	11.9	0.15	47.4	2
20 (X22)	20.31	–	2.84	1.00	12.8	0.15	50.3	6
40 (X23)	29.25	–	3.08	0.55	16.9	0.16	68.9	0.5
60 (X24)	29.39	–	1.17	0.30	18.8	0.16	66.2	4
[h] Extent	Cu (%)	–	Fe (%)	Mg	S^{2-} (%)	[i] S° (%)	–	S^T (%)
10 (X21)	53 (101)	–	(101)	(87)	42	45	–	(98)
20 (X22)	63 (94)	–	(104)	(90)	54	51	–	(100)
40 (X23)	88 (101)	–	(101)	(77)	86	46	–	(101)
60 (X24)	95 (95)	–	(93)	(76)	96	45	–	(93)
[j] Oxidation	–	–	–	–	–	–	–	[k] $W_{f,t}$ (%)
10 (X21)	–	–	–	–	–	–	–	84
20 (X22)	–	–	–	–	–	–	–	83
40 (X23)	–	–	–	–	–	–	–	71
60 (X24)	–	–	–	–	–	–	–	71

[a] At 20°C; [b] Per unit mass water; [c] 23.62 wt% moisture; [d] Arbo A02, Orfom 2 (no pre-drying); [e] Avg. elemental composition; [f] Calc. (S balance); [g] H_2O evap., based on total mass accountability; [h] Reaction extents based on chem. analyses (elem. accountabilities in brackets); [i] S° yield, *i.e.*, $S°/S^{2-}{}_{rx}\times100\%$; [j] Individual mineral oxidation extents not uniquely determinable from chem. analyses; [l] Fractional weight of residue (*cf.* original sample).